



Advanced Virgo Technical Design Report



The Virgo Collaboration

VIR-0128A-12

April 13, 2012



The Virgo Collaboration

T. Accadia¹², F. Acernese^{6ac}, M. Agathos^{15a}, A. Allocca^{8ac}, P. Astone^{9a}, G. Balestri^{8a},
G. Ballardin³, F. Barone^{6ac}, M. Barsuglia¹, A. Basti^{8ab}, Th. S. Bauer^{15a},
M. Bebronne¹², M. Bejger^{17c}, M.G. Beker^{15a}, A. Bertolini^{15a}, M. Bitossi^{8a},
M. A. Bizouard^{11a}, M. Blom^{15a}, F. Bondu^{2b}, L. Bonelli^{8ab}, R. Bonnand¹⁴, V. Boschi^{8a},
L. Bosi^{7a}, B. Bouhou¹, S. Braccini^{8a}, C. Bradaschia^{8a}, M. Branchesi^{4ab}, T. Briant¹³,
A. Brillet^{2a}, V. Brisson^{11a}, T. Bulik^{17b}, H. J. Bulten^{15ab}, D. Buskulic¹², C. Buy¹,
G. Cagnoli¹⁴, E. Calloni^{6ab}, B. Canuel³, F. Carbognani³, F. Cavalier^{11a}, R. Cavalieri³,
G. Cella^{8a}, E. Cesarini^{4b}, E. Chassande-Mottin¹, A. Chincarini⁵, A. Chiummo³,
F. Cleva^{2a}, E. Coccia^{10ab}, P.-F. Cohadon¹³, C. N. Colacino^{8ab}, A. Colla^{9ab},
M. Colombini^{9b}, A. Conte^{9ab}, J.-P. Coulon^{2a}, E. Cuoco³, S. D'Antonio^{10a}, V. Dattilo³,
M. Davier^{11a}, R. Day³, K. de Roo^{15a}, R. De Rosa^{6ab}, G. Debreczeni¹⁸, J. Degallaix¹⁴,
W. Del Pozzo^{15a}, L. Di Fiore^{6a}, A. Di Lieto^{8ab}, M. Di Paolo Emilio^{10ac},
A. Di Virgilio^{8a}, A. Dietz¹², M. Doets^{15a}, M. Drago^{16ab}, R. Elsinga^{15b}, G. Endr oczy¹⁸,
V. Fafone^{10ab}, I. Ferrante^{8ab}, F. Ferrini³, F. Fidecaro^{8ab}, I. Fiori³, R. Flaminio¹⁴,
J.-D. Fournier^{2a}, J. Franc¹⁴, S. Franco^{11a}, S. Frasca^{9ab}, F. Frasconi^{8a}, M. Galimberti¹⁴,
L. Gammaitoni^{7ab}, F. Garufi^{6ab}, M. E. G asp ar¹⁸, G. Gemme⁵, E. Genin³, A. Gennai^{8a},
A. Giazotto^{8a}, R. Gouaty¹², M. Granata¹⁴, S. Gras¹³, H. Groenstege^{15a},
G. M. Guidi^{4ab}, J.-F. Hayau^{2b}, A. Heidmann¹³, H. Heitmann², P. Hello^{11a},
G. Hemming³, E. Hennes^{15a}, R. Hermel¹², P. Jaranowski^{17d}, R.J.G. Jonker^{15a},
M. Kasprzack^{3,11a}, I. Kowalska^{17b}, M. Kraan^{15a}, A. Kr olak^{17ae}, B. Lagrange¹⁴,
N. Leroy^{11a}, N. Letendre¹², T. G. F. Li^{15a}, M. Lorenzini^{4a}, V. Lorette^{11b},
G. Losurdo^{4a}, C. Magazz u^{8a}, E. Majorana^{9a}, I. Maksimovic^{11b}, V. Malvezzi^{10a},
N. Man^{2a}, M. Mantovani^{8a}, F. Marchesoni^{7a}, F. Marion¹², J. Marque³, F. Martelli^{4ab},
A. Masserot¹², C. Michel¹⁴, L. Milano^{6ab}, Y. Mimenkov^{10a}, T. Mingam¹², M. Mohan³,
N. Morgado¹⁴, A. Morgia^{10ab}, S. Mosca^{6ab}, B. Mours¹², P. Mugnier¹², F. Mul^{15a},
L. Naticchioni^{9ab}, I. Neri^{7ab}, F. Nocera³, E. Pacaud¹², L. Palladino^{10ac}, C. Palomba^{9a},
F. Paoletti^{8a,3}, R. Paoletti^{8ac}, A. Paoli³, G. Parguez³, M. Parisi^{6ab}, A. Pasqualetti³,
R. Passaquietti^{8ab}, D. Passuello^{8a}, M. Perciballi^{9a}, G. Persichetti^{6ab}, M. Pichot^{2a},
F. Piergiovanni^{4ab}, L. Pinard¹⁴, R. Poggiani^{8ab}, M. Prato⁵, G. A. Prodi^{16ab},
M. Punturo^{7a}, P. Puppato^{9a}, D. S. Rabeling^{15ab}, I. R acz¹⁸, P. Rapagnani^{9ab}, V. Re^{10ab},
T. Regimbau^{2a}, F. Ricci^{9ab}, F. Robinet^{11a}, A. Rocchi^{10a}, L. Rolland¹², R. Romano^{6ac},
D. Rosi nska^{17cf}, J. Rosier^{15b}, P. Ruggi³, E. Saracco¹⁴, B. Sassolas¹⁴, F. Schimmel^{15a},
D. Sentenac³, L. Sperandio^{10ab}, R. Sturani^{4ab}, B. Swinkels³, M. Tacca³,
L. Taffarello^{16c}, A. P. M. ter Braack^{15a}, A. Toncelli^{8ab}, M. Tonelli^{8ab}, O. Torre^{8ac},
E. Tournefier¹², F. Travasso^{7ab}, G. Vajente^{8ab}, M. van Beuzekom^{15a},
J. F. J. van den Brand^{15ab}, C. Van Den Broeck^{15a}, S. van der Putten^{15a}, M. Vasuth¹⁸,
M. Vavoulidis^{11a}, G. Vedovato^{16c}, D. Verkindt¹², F. Vetrano^{4ab}, A. Vicer e^{4ab},
J.-Y. Vinet^{2a}, G. Visser^{15a}, S. Vitale^{15a}, H. Vocca^{7a}, H. Voet^{15b}, R. L. Ward¹,
M. Was^{11a}, K. Yamamoto^{16bd}, M. Yvert¹², A. Zadro ny^{17e}, J.-P. Zendri^{16c}

¹APC, AstroParticule et Cosmologie, Universit  Paris Diderot, CNRS/IN2P3, CEA/Irfu, Observatoire de Paris, Sorbonne Paris Cit , 10, rue Alice Domon et L onie Duquet, 75205 Paris Cedex 13, France

²Universit  Nice-Sophia-Antipolis, CNRS, Observatoire de la C te d'Azur, F-06304 Nice^a;

- Institut de Physique de Rennes, CNRS, Université de Rennes 1, 35042 Rennes^b, France
- ³European Gravitational Observatory (EGO), I-56021 Cascina (PI), Italy
- ⁴INFN, Sezione di Firenze, I-50019 Sesto Fiorentino^a; Università degli Studi di Urbino 'Carlo Bo', I-61029 Urbino^b, Italy
- ⁵INFN, Sezione di Genova; I-16146 Genova, Italy
- ⁶INFN, Sezione di Napoli ^a; Università di Napoli 'Federico II'^b Complesso Universitario di Monte S. Angelo, I-80126 Napoli; Università di Salerno, Fisciano, I-84084 Salerno^c, Italy
- ⁷INFN, Sezione di Perugia^a; Università di Perugia^b, I-06123 Perugia, Italy
- ⁸INFN, Sezione di Pisa^a; Università di Pisa^b; I-56127 Pisa; Università di Siena, I-53100 Siena^c, Italy
- ⁹INFN, Sezione di Roma^a; Università 'La Sapienza'^b, I-00185 Roma, Italy
- ¹⁰INFN, Sezione di Roma Tor Vergata^a; Università di Roma Tor Vergata, I-00133 Roma^b; Università dell'Aquila, I-67100 L'Aquila^c, Italy
- ¹¹LAL, Université Paris-Sud, IN2P3/CNRS, F-91898 Orsay^a; ESPCI, CNRS, F-75005 Paris^b, France
- ¹²Laboratoire d'Annecy-le-Vieux de Physique des Particules (LAPP), Université de Savoie, CNRS/IN2P3, F-74941 Annecy-Le-Vieux, France
- ¹³Laboratoire Kastler Brossel, ENS, CNRS, UPMC, Université Pierre et Marie Curie, 4 Place Jussieu, F-75005 Paris, France
- ¹⁴Laboratoire des Matériaux Avancés (LMA), IN2P3/CNRS, F-69622 Villeurbanne, Lyon, France
- ¹⁵Nikhef, Science Park, Amsterdam, the Netherlands^a; VU University Amsterdam, De Boelelaan 1081, 1081 HV Amsterdam, the Netherlands^b
- ¹⁶INFN, Gruppo Collegato di Trento^a and Università di Trento^b, I-38050 Povo, Trento, Italy; INFN, Sezione di Padova^c and Università di Padova^d, I-35131 Padova, Italy
- ¹⁷IM-PAN 00-956 Warsaw^a; Astronomical Observatory Warsaw University 00-478 Warsaw^b; CAMK-PAN 00-716 Warsaw^c; Białystok University 15-424 Białystok^d; NCBJ 05-400 Świerk-Otwock^e; Institute of Astronomy 65-265 Zielona Góra^f, Poland
- ¹⁸WIGNER RCP, RMKI, H-1121 Budapest, Konkoly Thege Miklós út 29-33, Hungary

Contents

| | |
|--|-----------|
| Introduction | 1 |
| 1 Advanced Virgo overview | 3 |
| 1.1 Reference configuration | 3 |
| 1.2 Sensitivity | 7 |
| 1.3 Other system requirements | 10 |
| 1.4 Sensitivity and detector commissioning | 11 |
| 2 Optical simulation and design (OSD) | 13 |
| 2.1 Introduction | 13 |
| 2.1.1 Scope of the subsystem and deliverables | 13 |
| 2.1.2 Design summary and changes with respect to the baseline design | 14 |
| 2.2 Simulation tools | 18 |
| 2.2.1 FFT codes | 19 |
| 2.2.2 Modal codes | 21 |
| 2.2.3 Other codes | 22 |
| 2.3 Optical layout | 23 |
| 2.3.1 Mirror positions and modulation frequencies | 23 |
| 2.3.2 Optocad layout | 26 |
| 2.3.3 Core optics characteristics | 30 |
| 2.4 Secondary beams extraction | 33 |
| 2.4.1 Extraction with large angles (> 1 deg) | 33 |
| 2.4.2 Extraction with small angles (fraction of degree) | 34 |
| 2.4.3 CP secondary beam extraction | 36 |
| 2.4.3.1 Extraction through small tilt | 36 |
| 2.4.3.2 Extraction through 20 mrad tilt | 39 |
| 2.4.4 BS secondary beam extraction | 40 |
| 2.4.5 Secondary beams from ITMs and choice of the ITM AR face geometry | 43 |
| 2.5 Extraction of the pickoff beam used for ITF control | 45 |
| 2.6 Arm-cavity design | 47 |
| 2.6.1 Bi-concave geometry | 47 |
| 2.6.2 Choice of the RoCs | 47 |
| 2.6.3 Absolute RoC tolerances | 47 |
| 2.6.4 Finesse | 49 |
| 2.7 Recycling cavities design | 50 |
| 2.7.1 Choice of the RoCs | 50 |

| | | |
|----------|--|-----------|
| 2.7.2 | Power recycling cavity finesse | 50 |
| 2.7.3 | Signal recycling cavity finesse | 51 |
| 2.8 | Test masses polishing specifications | 52 |
| 2.8.1 | Specification summary | 52 |
| 2.8.2 | Arm cavity mirror flatness specification | 53 |
| 2.8.3 | Definitions | 53 |
| 2.8.4 | Round trip loss budget | 53 |
| 2.8.5 | Simulations | 54 |
| 2.9 | Central area optical path length distortion requirements | 58 |
| 2.9.1 | Characterization | 58 |
| 2.9.2 | Sources of optical path length distortions | 59 |
| 2.9.2.1 | Surface figure errors | 59 |
| 2.9.2.2 | Substrate index inhomogeneity | 61 |
| 2.9.2.3 | Distortions induced by the suspension system | 61 |
| 2.9.3 | Requirements | 61 |
| 2.9.4 | Differential mode optical path length distortions | 63 |
| 2.9.5 | Tolerances in RoCs | 64 |
| 2.9.6 | Compensation of optical path length defects | 65 |
| 2.9.6.1 | Correction axisymmetric distortions | 65 |
| 2.9.6.2 | Compensating the non-axisymmetric distortions | 66 |
| 2.10 | Future upgrades | 67 |
| 2.10.1 | Reduction of quantum noise | 67 |
| 2.10.1.1 | Injection of squeezed light | 67 |
| 2.10.1.2 | The GEO experience | 68 |
| 2.10.1.3 | Expected sensitivity gain | 69 |
| 2.10.2 | Use of higher order optical modes | 71 |
| 2.11 | Conclusion | 73 |
| 3 | Prestabilized laser (PSL) | 75 |
| 3.1 | Overview and deliverables | 75 |
| 3.1.1 | Overview | 75 |
| 3.1.2 | Deliverables | 77 |
| 3.2 | Location, requirements | 78 |
| 3.2.1 | Location | 78 |
| 3.2.2 | Requirements | 78 |
| 3.3 | Interfaces with other subsystems | 78 |
| 3.3.1 | Interfaces with INJ | 79 |
| 3.3.2 | Interfaces with ISC and INF | 79 |
| 3.4 | The fiber amplifier system | 79 |
| 3.4.1 | The seed laser | 80 |
| 3.4.2 | The HP amplifier stage | 80 |
| 3.4.2.1 | Fiber amplifier principle | 80 |
| 3.4.2.2 | Amplifier stages overall description | 80 |
| 3.4.2.3 | Beam shape | 81 |
| 3.5 | Frequency prestabilization | 82 |
| 3.6 | Power stabilization | 83 |
| 3.6.1 | RIN at the AdV auxiliary modulation frequencies | 84 |

| | | |
|----------|---|-----------|
| 3.6.2 | RIN in AdV bandwidth | 84 |
| 3.6.2.1 | Free-running noise and servo loop | 84 |
| 3.6.2.2 | Photodiode sensitivity homogeneity issue | 86 |
| 3.7 | Coherent addition of two lasers | 87 |
| 3.8 | Beam stabilization: the pre-mode cleaner | 88 |
| 3.8.1 | Beam jitter filtering | 88 |
| 3.8.2 | Optical and mechanical design | 90 |
| 4 | Injection (INJ) | 93 |
| 4.1 | Scope of the subsystem and general requirements | 93 |
| 4.2 | Subsystem overview | 93 |
| 4.3 | Functional requirements | 95 |
| 4.4 | Interfaces with other subsystems | 96 |
| 4.4.1 | Prestabilized Laser (PSL) | 96 |
| 4.4.1.1 | Optical parameters | 96 |
| 4.4.1.2 | Frequency prestabilization | 96 |
| 4.4.1.3 | Laser beam power stabilization | 97 |
| 4.4.2 | Superattenuator (SAT) | 97 |
| 4.4.3 | Thermal compensation (TCS) | 97 |
| 4.4.4 | Detection (DET) | 97 |
| 4.4.5 | Payloads (PAY) | 98 |
| 4.4.6 | Suspended benches (SBE) | 98 |
| 4.4.7 | Vacuum (VAC) | 98 |
| 4.4.8 | Mirrors (MIR) | 99 |
| 4.4.9 | Infrastructures (INF) | 99 |
| 4.4.10 | Data acquisition (DAQ) | 99 |
| 4.5 | INJ optical design | 99 |
| 4.5.1 | Optical specifications | 100 |
| 4.5.2 | External injection bench layout | 100 |
| 4.5.3 | Suspended injection benches layout | 102 |
| 4.6 | EOM and RF Modulation | 104 |
| 4.6.1 | Requirements | 104 |
| 4.6.2 | Electro-optic crystal choice | 104 |
| 4.6.3 | Proposed configuration: electro-optical modulator | 105 |
| 4.6.3.1 | EO modulation principle | 105 |
| 4.6.3.2 | Technical realization of the modulator | 106 |
| 4.6.4 | Proposed configuration: RF modulation | 107 |
| 4.6.4.1 | RF generation | 107 |
| 4.6.4.2 | RF amplification | 107 |
| 4.6.4.3 | RF distribution | 107 |
| 4.6.4.4 | Local RF phase adjustment | 109 |
| 4.6.4.5 | RF amplitude and phase stability | 109 |
| 4.7 | Input beam jitter monitoring and control | 110 |
| 4.7.1 | Requirements on input beam jitter | 111 |
| 4.7.2 | Beam pointing control system | 112 |
| 4.7.3 | Input beam jitter monitoring system | 112 |
| 4.8 | Input power control | 114 |

| | | |
|----------|--|-----|
| 4.8.1 | Requirements | 115 |
| 4.8.2 | Configuration chosen | 115 |
| 4.9 | High power beam dumps and baffles for INJ | 116 |
| 4.9.1 | High power in-air beam dump | 117 |
| 4.9.2 | Medium power high vacuum compatible beam dumps | 118 |
| 4.9.3 | High power high vacuum compatible beam dumps | 120 |
| 4.9.4 | Baffles for INJ | 121 |
| 4.10 | Input mode cleaner | 121 |
| 4.10.1 | Geometry and finesse | 121 |
| 4.10.2 | Cavity input/output mirrors | 122 |
| 4.10.2.1 | Dihedron description | 122 |
| 4.10.2.2 | Substrate specifications | 123 |
| 4.10.2.3 | Mirrors specifications: surface characteristics. | 123 |
| 4.10.2.4 | The support | 125 |
| 4.10.3 | Cavity end mirror | 128 |
| 4.10.3.1 | Radius of curvature | 128 |
| 4.10.3.2 | Mirror Roughness | 129 |
| 4.10.3.3 | IMC end mirror payload | 132 |
| 4.10.3.4 | CHRoCC IMC - Central heating RoC correction | 135 |
| 4.10.4 | IMC cavity longitudinal and angular control | 136 |
| 4.10.4.1 | Local control | 136 |
| 4.10.4.2 | Angular accuracy requirements | 137 |
| 4.10.4.3 | Angular control system | 138 |
| 4.10.4.4 | Control noise projection | 139 |
| 4.10.4.5 | IMC longitudinal control | 140 |
| 4.11 | The reference cavity system | 140 |
| 4.11.1 | System overview | 140 |
| 4.11.2 | Requirements and functionalities | 141 |
| 4.11.3 | RFC system design | 141 |
| 4.11.3.1 | General specifications | 141 |
| 4.11.3.2 | RFC characteristics and optical layout on SIB1 | 142 |
| 4.11.3.3 | RFC input beam path optical design | 143 |
| 4.11.3.4 | RFC input beam path mechanical design | 144 |
| 4.11.3.5 | RFC input beam polarization | 145 |
| 4.11.3.6 | RFC transmitted beam path optical design | 145 |
| 4.11.3.7 | Optical design of the RFC reflected beam path | 146 |
| 4.11.3.8 | Automatic alignment | 146 |
| 4.11.4 | Pickoff beam sent to the power stabilization photodiodes box | 148 |
| 4.12 | Faraday isolator | 148 |
| 4.12.1 | Requirements | 148 |
| 4.12.2 | Proposed solution | 148 |
| 4.12.3 | Prototype performances | 149 |
| 4.12.4 | Technical description | 151 |
| 4.12.5 | Other Faraday isolators | 154 |
| 4.13 | ITF mode matching telescope | 154 |
| 4.13.1 | General requirements | 155 |
| 4.13.2 | Telescope overview | 155 |

| | | |
|----------|--|------------|
| 4.13.2.1 | Tolerancing study | 156 |
| 4.13.2.2 | Alignment procedure | 160 |
| 4.13.3 | Diffused and backreflected light study for INJ | 160 |
| 4.13.3.1 | Projection of scattered/backreflected light noise coming from ITF MMT optics | 160 |
| 4.13.3.2 | Backreflected light from the meniscus lens | 162 |
| 4.13.3.3 | Light backscattered from telescope optics | 162 |
| 4.13.3.4 | Amount of backreflected and backscattered light not recou- pled into the ITF | 165 |
| 4.14 | Input beam monitoring system | 165 |
| 4.14.1 | Optical design: division in subsystems | 165 |
| 4.14.1.1 | Space requirements | 167 |
| 4.14.2 | Input power requirements | 167 |
| 4.14.3 | Optical components | 167 |
| 4.14.4 | Description of the adjustment systems | 167 |
| 4.15 | INJ main milestones | 169 |
| 5 | Mirrors (MIR) | 171 |
| 5.1 | Scope of the subsystem and deliverables | 171 |
| 5.2 | Introduction | 171 |
| 5.3 | Substrates | 172 |
| 5.3.1 | List of the Advanced Virgo substrates | 172 |
| 5.4 | Polishing | 174 |
| 5.4.1 | Strategy for polishing in Advanced Virgo | 176 |
| 5.5 | Coating | 178 |
| 5.5.1 | Mechanical losses | 179 |
| 5.5.2 | Absorption losses | 179 |
| 5.5.3 | Coating uniformity | 180 |
| 5.5.4 | Coating performances for the auxiliary beams: Hartmann beams and auxiliary lasers | 181 |
| 5.6 | Metrology | 182 |
| 5.7 | Cleaning | 184 |
| 5.8 | Main Milestones | 185 |
| 6 | Thermal compensation (TCS) | 187 |
| 6.1 | Scope and requirements of the subsystem | 187 |
| 6.2 | Design overview | 187 |
| 6.3 | Core optics defects | 189 |
| 6.3.1 | Thermal effects | 189 |
| 6.3.2 | Cold defects | 190 |
| 6.4 | Compensation plates | 191 |
| 6.4.1 | CP geometry and position | 192 |
| 6.4.2 | Influence of the CP on alignment and longitudinal controls | 192 |
| 6.5 | TCS actuators: ring heater | 195 |
| 6.5.1 | Ring heater design guidelines | 195 |
| 6.5.2 | Vacuum compatibility | 199 |
| 6.6 | TCS actuators: CO ₂ laser projector | 200 |
| 6.6.1 | Axisymmetric compensation: Double Axicon System | 201 |

| | | |
|----------|--|------------|
| 6.6.2 | Nonsymmetric compensation: scanning system | 207 |
| 6.7 | TCS actuator noise | 209 |
| 6.7.1 | CO ₂ laser noise coupling | 210 |
| 6.7.2 | Ring heater noise coupling | 213 |
| 6.8 | ”Cold RoC” Correction | 215 |
| 6.9 | TCS sensing | 221 |
| 6.9.1 | Hartmann wavefront sensor | 222 |
| 6.9.2 | Hartmann beam sources | 224 |
| 6.10 | Recycling cavities wavefront sensing | 225 |
| 6.10.1 | HWS Optical layout | 225 |
| 6.10.2 | Phase camera | 229 |
| 6.11 | High reflectivity surface sensing | 231 |
| 6.12 | HWS in transmission on the end benches | 233 |
| 7 | Detection (DET) | 235 |
| 7.1 | Scope of the DET subsystem | 235 |
| 7.1.1 | Overview of the beams to be extracted | 235 |
| 7.1.2 | DET main functions | 237 |
| 7.1.3 | Overview of the DET benches | 238 |
| 7.2 | Interfaces with other subsystems | 239 |
| 7.2.1 | Specifications from other subsystems to the DET subsystem | 239 |
| 7.2.2 | Specifications provided by the DET subsystem to other subsystems | 241 |
| 7.3 | Output mode cleaners | 243 |
| 7.3.1 | Requirements on side band and HOM filtering | 243 |
| 7.3.2 | Main guidelines for the baseline design | 244 |
| 7.3.2.1 | Impact of the finesse and length on the OMC filtering | 244 |
| 7.3.2.2 | OMC length noise and locking accuracy | 245 |
| 7.3.2.3 | Choice of the cavity geometry | 246 |
| 7.3.2.4 | Choice of the substrate material | 248 |
| 7.3.2.5 | Choice of the finesse | 248 |
| 7.3.2.6 | Choice of the radius of curvature | 249 |
| 7.3.2.7 | Consequences of the requirements for side-band filtering | 252 |
| 7.3.2.8 | Choice of the angle of incidence on the OMC surfaces | 253 |
| 7.3.3 | Presentation of the baseline design | 254 |
| 7.3.3.1 | Filtering of side bands and high order modes | 255 |
| 7.3.3.2 | Parameter tolerancing | 257 |
| 7.3.3.3 | Length control strategy | 258 |
| 7.3.4 | Constraints on side band RIN for the INJ subsystem | 258 |
| 7.3.5 | Discussion of alternative solutions | 259 |
| 7.3.6 | OMC alignment and beam matching | 260 |
| 7.3.6.1 | OMC alignment | 260 |
| 7.3.6.2 | OMC mode matching | 261 |
| 7.3.7 | OMC loss budget | 261 |
| 7.3.8 | OMC planning | 262 |
| 7.4 | Bench components | 262 |
| 7.4.1 | Optics | 262 |
| 7.4.2 | Mounts and motors | 263 |

| | | |
|---------|--|-----|
| 7.4.3 | Diaphragms | 264 |
| 7.4.4 | High power beam dumper | 264 |
| 7.5 | Longitudinal photodiodes and electronics | 264 |
| 7.5.1 | Photodiodes used for DC detection | 264 |
| 7.5.2 | Control photodiodes | 264 |
| 7.5.2.1 | Photodiodes | 265 |
| 7.5.2.2 | Preamplifier | 265 |
| 7.5.2.3 | Demodulation electronics | 266 |
| 7.5.3 | Photodiode airbox | 268 |
| 7.6 | Quadrants and electronics | 268 |
| 7.6.1 | Power on photodiodes | 270 |
| 7.6.2 | Modulation frequencies | 270 |
| 7.6.3 | Front-end electronics | 270 |
| 7.6.4 | Noise contributions | 271 |
| 7.6.4.1 | Shot noise | 271 |
| 7.6.4.2 | Electronic noise | 271 |
| 7.6.4.3 | Dark current noise | 273 |
| 7.6.4.4 | Thermal noise | 273 |
| 7.6.4.5 | Quantization noise | 274 |
| 7.6.5 | Expected performance | 275 |
| 7.6.6 | Seismic isolation and hardware implementation | 275 |
| 7.6.7 | Demodulation electronics | 276 |
| 7.6.8 | Quadrants used for OMC alignment | 276 |
| 7.7 | Phase cameras | 277 |
| 7.7.1 | Phase camera options and workings | 277 |
| 7.7.1.1 | Scanning phase camera | 278 |
| 7.7.1.2 | InGaAs FPA based phase camera | 279 |
| 7.7.1.3 | Time of Flight measurement systems as phase camera | 280 |
| 7.7.2 | Development timeline | 280 |
| 7.7.3 | Concluding remarks on the phase camera development | 283 |
| 7.8 | Detection benches | 283 |
| 7.8.1 | Functions and requirements | 283 |
| 7.8.2 | Dark fringe to OMC mode matching telescope | 285 |
| 7.8.2.1 | General requirements | 285 |
| 7.8.2.2 | Telescope overview | 285 |
| 7.8.2.3 | Performances of the system | 287 |
| 7.8.2.4 | Tolerancing study: radii of curvature of the optics | 288 |
| 7.8.2.5 | Tolerancing study: input beam errors | 290 |
| 7.8.2.6 | Tolerancing study: tilt and decenter errors of the optics | 290 |
| 7.8.2.7 | Back-scattered and back-reflected light recoupled in the ITF | 292 |
| 7.8.2.8 | Back-scattered and back-reflected light not recoupled | 294 |
| 7.8.3 | Hartmann beam injection | 294 |
| 7.8.4 | Faraday isolator | 296 |
| 7.8.5 | Extraction of secondary beams | 296 |
| 7.8.6 | Optical layout | 296 |
| 7.8.7 | Detection losses budget | 299 |
| 7.8.8 | Bench mechanical design | 300 |

| | | |
|----------|--|------------|
| 7.8.9 | Bench local controls | 301 |
| 7.9 | End benches | 302 |
| 7.9.1 | Functions and requirements | 302 |
| 7.9.2 | End bench telescopes | 303 |
| 7.9.2.1 | General requirements | 303 |
| 7.9.2.2 | Telescope overview | 303 |
| 7.9.2.3 | Performances of the system | 304 |
| 7.9.2.4 | Tolerancing study: errors in the ROCs | 304 |
| 7.9.3 | Optical layout | 307 |
| 7.10 | Pick-off bench | 308 |
| 7.10.1 | Functions and requirements | 308 |
| 7.10.2 | Telescope design | 309 |
| 7.11 | SIB2 bench | 309 |
| 8 | Interferometer sensing and control (ISC) | 311 |
| 8.1 | General description of the subsystem | 311 |
| 8.2 | Input from other subsystems and basic assumptions | 312 |
| 8.3 | Longitudinal control system: steady state control | 314 |
| 8.3.1 | Definition of degrees of freedom | 314 |
| 8.3.2 | Definition of available output ports and signals | 316 |
| 8.3.3 | DC readout offset | 316 |
| 8.3.4 | Accuracy requirements | 317 |
| 8.3.5 | Consequences of the accuracy requirements on OMC filtering | 319 |
| 8.3.6 | Design and performances of the control systems | 320 |
| 8.3.7 | Requirements on modulation and demodulation noises | 321 |
| 8.3.8 | ITF asymmetries and coupling of laser noises | 324 |
| 8.3.8.1 | Power recycled configuration at 25 W | 325 |
| 8.3.8.2 | Dual recycled configuration at 125 W | 325 |
| 8.3.9 | Second stage of frequency stabilization | 325 |
| 8.3.10 | Input mirror etalon tuning | 331 |
| 8.4 | Longitudinal control system: lock acquisition | 331 |
| 8.4.1 | Lock acquisition of the arm cavities | 332 |
| 8.4.2 | Lock acquisition in power recycled configuration | 332 |
| 8.4.3 | Lock acquisition in dual recycled configuration | 336 |
| 8.5 | Auxiliary lasers | 336 |
| 8.5.1 | Goals of the auxiliary lasers | 336 |
| 8.5.2 | Implementation and requirements | 337 |
| 8.6 | Sideband aberration risk reduction strategy | 339 |
| 8.7 | Angular control system | 339 |
| 8.7.1 | Introduction | 339 |
| 8.7.2 | Radiation pressure effect and angular modes | 340 |
| 8.7.3 | Accuracy requirements | 341 |
| 8.7.4 | Quadrants and demodulations | 342 |
| 8.7.5 | Automatic alignment control scheme | 343 |
| 8.7.5.1 | Sensing scheme | 343 |
| 8.7.5.2 | Control of the arm degrees of freedom | 344 |
| 8.7.5.3 | Control of the central cavity degrees of freedom | 345 |

| | | |
|-----------|---|------------|
| 8.7.5.4 | Discussion | 345 |
| 8.7.6 | Performances of the angular control system | 346 |
| 8.7.7 | Quadrant diode suspension requirements | 347 |
| 8.8 | Parametric instabilities | 350 |
| 8.9 | Software requirements | 353 |
| 8.9.1 | Fast realtime control | 353 |
| 8.9.2 | Slow control | 354 |
| 8.10 | Interfaces with other subsystems | 354 |
| 8.10.1 | OSD | 354 |
| 8.10.2 | MIR | 354 |
| 8.10.3 | INJ | 355 |
| 8.10.4 | SBE | 355 |
| 8.10.5 | DET | 356 |
| 8.10.6 | PSL | 357 |
| 8.10.7 | DAQ | 358 |
| 8.10.8 | SAT | 358 |
| 8.10.9 | PAY | 358 |
| 8.10.10 | INF | 359 |
| 8.11 | Summary and conclusions | 359 |
| 9 | Stray light control (SLC) | 361 |
| 9.1 | Scope and deliverables of the subsystem | 361 |
| 9.2 | Where is the light lost? | 361 |
| 9.2.1 | Arm cavities | 363 |
| 9.2.2 | Recycling cavities | 367 |
| 9.3 | Subsystem overview | 369 |
| 9.3.1 | Suspended baffles | 369 |
| 9.3.2 | Ground connected baffles | 369 |
| 9.3.2.1 | Baffles in the $3km$ vacuum tubes | 369 |
| 9.3.2.2 | Baffles in the other vacuum links | 373 |
| 9.4 | Path to baffle requirements definition | 373 |
| 9.5 | Baffle preliminary design study | 374 |
| 9.5.1 | Absorbing glass | 374 |
| 9.5.2 | Silicon Carbide | 375 |
| 9.5.3 | DLC | 375 |
| 9.5.4 | Oxidized stainless steel | 375 |
| 9.6 | Interfaces with other subsystems | 376 |
| 9.7 | Path to design completion and construction | 377 |
| 10 | Payloads (PAY) | 379 |
| 10.1 | Last Stage Suspension: introduction | 379 |
| 10.1.1 | Main features and general requirements | 379 |
| 10.1.1.1 | Cleanliness and vacuum compatibility | 380 |
| 10.1.1.2 | Geometric constraints and requirements | 381 |
| 10.1.1.3 | Pre-alignment requirements | 383 |
| 10.1.1.4 | Optical local control system | 384 |
| 10.2 | The beam splitter payload: features and solutions exportable to other suspen- sions. | 385 |

| | | |
|-----------|---|------------|
| 10.2.1 | Pre-alignment requirements | 387 |
| 10.2.2 | Optical levers layout for BS | 388 |
| 10.2.3 | Mechanical design overview | 388 |
| 10.2.4 | The marionette and the mirror suspension | 389 |
| 10.2.4.1 | BS payload: example of assembly and integration procedure | 392 |
| 10.3 | Test-mass payloads | 394 |
| 10.3.1 | Input and end mirrors payloads: design overview | 394 |
| 10.3.2 | The monolithic suspensions | 395 |
| 10.3.2.1 | The upper and lower clamps for the fibers | 396 |
| 10.3.2.2 | The ears of the mirrors | 399 |
| 10.3.2.3 | The fibers | 400 |
| 10.3.3 | The compensation plate mount | 406 |
| 10.3.4 | The test mass payload integration with the superattenuator and the safety structure | 408 |
| 10.3.5 | Test and validation procedure during assembly. | 408 |
| 10.4 | The payloads for the recycling cavities | 410 |
| 10.4.1 | The power recycling payload | 410 |
| 10.4.2 | The signal recycling payload | 410 |
| 11 | Superattenuator (SAT) | 413 |
| | Outline | 413 |
| 11.1 | Superattenuator mechanics | 416 |
| 11.1.1 | Virgo superattenuator general mechanics description | 416 |
| 11.1.2 | Superattenuator passive attenuation and AdV requirements | 419 |
| 11.1.3 | Long superattenuators upgrades | 421 |
| 11.1.3.1 | Mechanics for the Control System | 421 |
| 11.1.3.2 | The filter 7 upgrade | 425 |
| 11.1.4 | Signal recycling superattenuator construction | 434 |
| 11.1.4.1 | Signal recycling superattenuator description | 434 |
| 11.1.4.2 | Safety Frame | 435 |
| 11.1.4.3 | Inverted pendulum | 435 |
| 11.1.4.4 | Top stage filter 0 | 435 |
| 11.1.4.5 | Standard filters | 435 |
| 11.1.4.6 | Filter 7 | 438 |
| 11.1.4.7 | Magnetic antisprings | 438 |
| 11.1.4.8 | Centering wires | 439 |
| 11.1.4.9 | Spring blades | 440 |
| 11.1.4.10 | Suspension wires | 442 |
| 11.1.4.11 | Crossbar dampers | 442 |
| 11.1.4.12 | Blade dampers | 442 |
| 11.1.4.13 | Fishing rod | 442 |
| 11.1.4.14 | Cabling | 443 |
| 11.1.4.15 | Crossbar LVDT sensors | 445 |
| 11.1.4.16 | Accelerometers | 445 |
| 11.1.4.17 | Tools | 445 |
| 11.1.5 | Short superattenuators upgrade | 448 |
| 11.1.5.1 | Cabling of short superattenuators | 449 |

| | | |
|-----------|---|------------|
| 11.1.6 | SAT mechanics interfaces | 451 |
| 11.1.6.1 | VAC | 451 |
| 11.1.6.2 | PAY | 451 |
| 11.1.6.3 | INJ & DET | 451 |
| 11.1.6.4 | EGO facilities | 451 |
| 11.2 | SAT control system | 452 |
| 11.2.1 | Introduction | 452 |
| 11.2.2 | Superattenuator | 452 |
| 11.2.3 | Superattenuator control system | 453 |
| 11.2.3.1 | Top stage control | 453 |
| 11.2.3.2 | Payload control | 454 |
| 11.2.3.3 | Motors control | 456 |
| 11.2.4 | Superattenuator control hardware | 457 |
| 11.2.4.1 | Overview | 457 |
| 11.2.4.2 | Signal conditioning electronics | 457 |
| 11.2.4.3 | Data conversion | 460 |
| 11.2.4.4 | Data processing | 465 |
| 11.2.4.5 | Control workstation | 467 |
| 11.2.5 | Superattenuator control system general architecture | 467 |
| 11.2.5.1 | Overview | 467 |
| 11.2.5.2 | Goals | 468 |
| 11.2.5.3 | Requirements | 469 |
| 11.2.5.4 | Design | 470 |
| 11.2.5.5 | Superattenuator control software | 474 |
| 12 | Suspended benches (SBE) | 477 |
| 12.1 | Task description | 477 |
| 12.2 | EIB-SAS | 477 |
| 12.2.1 | Introduction | 477 |
| 12.2.2 | Mechanical design overview | 479 |
| 12.2.3 | EIB-SAS mechanics: inverted pendulum | 481 |
| 12.2.4 | EIB-SAS mechanics: vertical stage | 483 |
| 12.2.5 | Seismic attenuation performance: simulations | 484 |
| 12.2.6 | Controls: sensors and actuators | 487 |
| 12.2.7 | Controls: electronics and DAQ | 489 |
| 12.2.8 | Controls: performance | 489 |
| 12.2.9 | Passive resonant dampers | 491 |
| 12.2.10 | Seismic attenuation performance: measurements | 492 |
| 12.3 | MultiSAS | 496 |
| 12.3.1 | Introduction | 496 |
| 12.3.2 | Mechanical system overview | 496 |
| 12.3.3 | Inverted pendulum | 499 |
| 12.3.4 | Filters | 501 |
| 12.3.5 | Seismic attenuation performance: simulations | 507 |
| 12.3.6 | Controls: sensors and actuators | 509 |
| 12.3.7 | Controls: electronics and DAQ | 513 |
| 12.3.8 | Controls: top stage | 515 |

| | | |
|-----------|--|------------|
| 12.3.9 | Controls: optical bench | 516 |
| 12.3.10 | Interface with vacuum chamber | 516 |
| 12.3.11 | Cleanliness and vacuum compatibility | 517 |
| 12.3.12 | In-vacuum cabling | 518 |
| 12.4 | Minitower: vacuum chambers | 518 |
| 12.4.1 | Requirements and basic design choices | 518 |
| 12.4.2 | Mechanical design | 520 |
| 12.4.3 | Venting and cleanliness | 522 |
| 12.4.4 | Tooling | 523 |
| 12.4.5 | Production strategy and schedule | 523 |
| 13 | Vacuum (VAC) | 525 |
| 13.1 | Introduction | 525 |
| 13.1.1 | Vacuum level requirements | 525 |
| 13.1.2 | Cryotraps | 526 |
| 13.1.3 | Further vacuum upgrades | 527 |
| 13.1.4 | Vacuum compatibility issues | 527 |
| 13.2 | Cryotraps | 528 |
| 13.2.1 | Mechanical design | 528 |
| 13.2.2 | Cryogenics | 531 |
| 13.2.3 | Vacuum performances | 534 |
| 13.2.4 | Vacuum system | 535 |
| 13.2.5 | Impact on the interferometer | 538 |
| 13.2.5.1 | Diffused light | 538 |
| 13.2.5.2 | Thermal effects on test masses | 540 |
| 13.2.5.3 | LN ₂ bubbling and suspension system | 541 |
| 13.2.6 | Liquid nitrogen supply plant | 544 |
| 13.2.6.1 | Storage tanks | 544 |
| 13.2.6.2 | Liquid nitrogen transfer lines | 545 |
| 13.2.7 | Regeneration and baking | 546 |
| 13.2.8 | Safety | 546 |
| 13.2.9 | Prototype action items | 548 |
| 13.3 | Tower vacuum system | 549 |
| 13.3.1 | Requirements and overview | 549 |
| 13.3.2 | Enlarged links | 551 |
| 13.3.3 | Detection tower and injection bench links | 553 |
| 13.3.4 | Central towers pumping | 557 |
| 13.3.5 | Minitowers integration | 558 |
| 13.3.6 | Remote scroll pumping | 561 |
| 13.3.7 | Signal recycling tower upgrade | 564 |
| 13.3.8 | New intermediate vacuum chamber for mirror towers | 564 |
| 13.3.9 | Displacement of towers | 564 |
| 13.4 | Pumping system configuration | 567 |
| 13.5 | Control system | 570 |
| 13.5.1 | Architecture overview | 570 |
| 13.5.2 | Update of existing control stations and new control stations | 570 |
| 13.5.3 | SCADA control software and DAQ interface | 572 |

| | | |
|-----------|---|------------|
| 13.5.4 | Environmental noise aspects | 572 |
| 14 | Data acquisition, general purpose electronics and software (DAQ) | 573 |
| 14.1 | Introduction and requirements | 573 |
| 14.1.1 | Subsystem definition | 573 |
| 14.1.2 | Requirements | 573 |
| 14.1.3 | Main interfaces with other subsystems | 575 |
| 14.1.3.1 | Data collection and digital electronics | 575 |
| 14.1.3.2 | Others interfaces with subsystems and groups | 575 |
| 14.2 | Digital electronics and control | 576 |
| 14.2.1 | Timing system | 576 |
| 14.2.1.1 | The timing distribution network | 576 |
| 14.2.1.2 | Timing distribution box (TDBox) | 577 |
| 14.2.1.3 | Monitoring of the timing system | 579 |
| 14.2.1.4 | Developments of the timing system for AdV | 579 |
| 14.2.2 | Online Architecture for ITF fast controls | 579 |
| 14.2.3 | The TOLM network | 581 |
| 14.2.3.1 | TOLM interface (Timing and Optical Link Module) | 581 |
| 14.2.3.2 | Mux/Demux | 582 |
| 14.2.4 | Real-time processing units | 583 |
| 14.2.4.1 | Real-time PC (RTPC) | 583 |
| 14.2.4.2 | Real-time DSPs | 583 |
| 14.2.4.3 | DAQ-boxes | 585 |
| 14.2.5 | ADC7674 boards | 585 |
| 14.2.6 | DAQ-box general design | 585 |
| 14.2.6.1 | Mezzanine for digital demodulation | 587 |
| 14.2.6.2 | Mezzanine for fast DAC channels | 590 |
| 14.2.6.3 | Mezzanine for fast ADC channels | 590 |
| 14.2.6.4 | Mezzanine for slow control and monitoring | 591 |
| 14.2.6.5 | DAQ-box: planning and foreseen needs | 591 |
| 14.2.7 | Delay of the digital control loop system | 592 |
| 14.2.7.1 | Case of Virgo+ | 592 |
| 14.2.7.2 | Possible improvements for AdV | 592 |
| 14.2.8 | Possible topology of the AdV TOLM network | 593 |
| 14.2.9 | Components of the camera acquisition | 595 |
| 14.2.9.1 | Digital camera | 596 |
| 14.2.9.2 | CameraBox | 596 |
| 14.2.9.3 | Software and data flows | 598 |
| 14.2.10 | Electronics specifications | 598 |
| 14.2.10.1 | Cabling recommendations | 598 |
| 14.2.10.2 | Power supply | 599 |
| 14.2.10.3 | Electronics cooling and power consumption | 600 |
| 14.2.10.4 | Racks specifications | 600 |
| 14.2.10.5 | Installation monitoring: hardware and inventory database | 600 |
| 14.2.10.6 | General specifications | 600 |
| 14.3 | Data collection system | 602 |
| 14.3.1 | Data format: frame | 602 |

| | | |
|----------|---|-----|
| 14.3.2 | Architectural description | 603 |
| 14.3.3 | Data assembly and distribution | 603 |
| 14.3.3.1 | Frame data exchange between servers: Fd library | 603 |
| 14.3.3.2 | Data collection general overview | 605 |
| 14.3.3.3 | Data from slow monitoring stations | 606 |
| 14.3.3.4 | Data from the TOLM network | 606 |
| 14.3.3.5 | The frame collectors (main frame builders) | 606 |
| 14.3.4 | Data streams | 607 |
| 14.3.5 | DAQ system monitoring | 608 |
| 14.3.6 | Online detector monitoring and data visualization | 609 |
| 14.3.6.1 | Detector monitoring | 609 |
| 14.3.6.2 | Data visualization | 610 |
| 14.3.6.3 | Monitoring web pages | 611 |
| 14.3.7 | Online processing | 611 |
| 14.3.7.1 | Online data quality flags | 611 |
| 14.3.7.2 | Online analysis | 611 |
| 14.3.8 | Automation with the Alp software | 612 |
| 14.3.9 | Storage and online network needs | 612 |
| 14.3.9.1 | Data storage | 612 |
| 14.3.9.2 | Online data collection networks | 612 |
| 14.4 | DAQ software environment | 614 |
| 14.4.1 | Framework for communication between servers | 614 |
| 14.4.1.1 | Framework currently used in Virgo | 614 |
| 14.4.1.2 | Possible evolutions for AdV | 614 |
| 14.4.2 | DAQ-oriented software tools | 615 |
| 14.4.2.1 | Hardware inventory and integration database | 615 |
| 14.4.2.2 | Channels database | 616 |
| 14.4.3 | AdV online software management | 617 |
| 14.4.3.1 | Configuration management | 617 |
| 14.4.3.2 | Build tools and development environment | 618 |
| 14.4.3.3 | Software problem report system | 619 |
| 14.5 | Environmental monitoring | 621 |
| 14.5.1 | Slow channel monitoring | 621 |
| 14.5.1.1 | Weather station | 622 |
| 14.5.1.2 | Lightning detector | 622 |
| 14.5.1.3 | Temperature probes | 623 |
| 14.5.1.4 | Humidity probes | 623 |
| 14.5.1.5 | Pressure probes | 623 |
| 14.5.1.6 | Read-out electronics and slow data acquisition | 623 |
| 14.5.1.7 | Probe and electronics location | 624 |
| 14.5.2 | Fast channels | 625 |
| 14.5.2.1 | Seismic probes | 625 |
| 14.5.2.2 | Magnetic probes | 626 |
| 14.5.2.3 | Acoustic probes | 626 |
| 14.5.2.4 | Radio frequency probe | 626 |
| 14.5.2.5 | Voltage sniffer | 627 |
| 14.5.2.6 | Read out electronics | 627 |

| | | |
|-----------|--|------------|
| 14.5.2.7 | Probe and electronics location | 628 |
| 14.6 | Calibration and $h(t)$ reconstruction | 630 |
| 14.6.1 | Signal injection system for the calibration | 630 |
| 14.6.2 | Standard calibration | 631 |
| 14.6.2.1 | Overview | 631 |
| 14.6.2.2 | Frequency domain sensitivity | 632 |
| 14.6.2.3 | Foreseen evolution for AdV and constraints on hardware | 632 |
| 14.6.3 | Photon calibration | 632 |
| 14.6.3.1 | Overview | 632 |
| 14.6.3.2 | Foreseen developments for AdV | 634 |
| 14.6.4 | $h(t)$ reconstruction | 635 |
| 14.6.4.1 | Overview | 635 |
| 14.6.4.2 | Time domain sensitivity | 635 |
| 14.6.4.3 | Foreseen developments for AdV | 636 |
| 15 | Infrastructures (INF) | 637 |
| 15.1 | INF Subsystem overview | 637 |
| 15.2 | Requirements of environmental noise reduction | 637 |
| 15.2.1 | Introduction | 637 |
| 15.2.2 | Noise reduction goals | 639 |
| 15.2.2.1 | Seismic noise | 640 |
| 15.2.2.2 | Acoustic noise | 643 |
| 15.2.3 | General criteria for noise mitigation | 651 |
| 15.2.3.1 | INJ lab silencing | 652 |
| 15.2.3.2 | HVAC systems | 653 |
| 15.2.3.3 | Electronics racks | 655 |
| 15.2.3.4 | Vacuum pumps | 656 |
| 15.2.3.5 | Switching devices | 657 |
| 15.3 | HVAC systems modification works | 657 |
| 15.3.1 | Central Building | 657 |
| 15.3.1.1 | Introduction | 657 |
| 15.3.1.2 | Facility description | 657 |
| 15.3.1.3 | HVAC equipments description | 658 |
| 15.3.1.4 | HVAC air distribution | 660 |
| 15.3.2 | Mode Cleaner | 661 |
| 15.3.2.1 | Introduction | 661 |
| 15.3.2.2 | Facility description | 667 |
| 15.3.2.3 | HVAC equipment description | 667 |
| 15.3.2.4 | HVAC air distribution | 670 |
| 15.3.3 | End Buildings | 671 |
| 15.3.3.1 | General requirements | 671 |
| 15.4 | IMMS upgrades and improvements | 671 |
| 15.5 | Infrastructure modifications for vacuum systems | 673 |
| 15.5.1 | Tower displacements geometry | 673 |
| 15.5.2 | Scroll pumps room | 674 |
| 15.5.3 | Cryotrap power systems and data cable trays | 674 |
| 15.5.4 | Liquid nitrogen tanks external areas | 674 |

| | | |
|--------|--|------------|
| 15.6 | Infrastructure modifications for electronics | 674 |
| 15.6.1 | Electronics room realization | 674 |
| 15.6.2 | Data cable trays for new installations | 676 |
| 15.7 | Infrastructure modifications for minitowers installation | 676 |
| 15.7.1 | INJ lab rearrangements | 676 |
| 15.7.2 | DET lab re-arrangements | 678 |
| 15.7.3 | End buildings rearrangements | 679 |
| | Acronyms | 681 |
| | Bibliography | 689 |

Introduction

Advanced Virgo is the project to upgrade the Virgo detector to a second generation instrument. It is designed to explore a volume of universe about 1000 times larger than Virgo.

The effort of the Virgo Collaboration towards the design of a second generation detector started in 2005 with the *Advanced Virgo White Paper* [1]. In fall 2007 an *Advanced Virgo Conceptual Design* was proposed [2] and submitted to the funding agencies together with a *Preliminary project execution plan and cost plan* [3]. In fall 2008 the *Advanced Virgo Preliminary Design* [4] was released and reviewed by an External Review Committee appointed by the EGO Council. In May 2009 the Virgo Collaboration has released the *Advanced Virgo Baseline Design* [5].

This *Technical Design Report* provides a description of the design solutions adopted for Advanced Virgo. It is meant to be the project reference document for all the design aspects. Each configuration change with respect to what is stated here requires a formal Change Request Procedure.

Chapter 1

Advanced Virgo overview

The aim of Advanced Virgo (**AdV**) is to achieve a sensitivity that is an improvement on the original Virgo by one order of magnitude in sensitivity, which corresponds to an increase of the detection rate by three orders of magnitude. Therefore, most of the detector subsystems have to deliver a largely improved performance to be compatible with the design sensitivity. The choices of the **AdV** design were made on the basis of the outcome of the different R&D investigations carried out within the Gravitational Waves (**GW**) community and the experience gained with Virgo, but also taking into account the budget and schedule constraints. The detailed project schedule is object of a project implementation plan that covers all the necessary tasks until the end of the project. Beside the sensitivity goal described in sec. 1.2, one of the main goals of the project is to have the detector robustly locked in 2015. The phase of installation of **AdV** parts and decommissioning of the Virgo equipment has started in November 2011, while the start of the infrastructure works is scheduled in September 2012.

In this chapter we will describe the **AdV** detector by listing the main features of the **AdV** design (see also fig. 1.1). The required upgrades to convert the Virgo instrument to the **AdV** detector are briefly introduced, while comprehensive and more detailed descriptions can be found in the next chapters. The main requirements at system level are also spelled out. At the end of this chapter a summary of the relevant design parameters for **AdV** is given in the tables 1.1, 1.2.

1.1 Reference configuration

In this section we list the main upgrades to the Virgo configuration, which are detailed in the following chapters:

Interferometer optical configuration (chapter 2)

- **AdV** will be a dual recycled interferometer. Beside the standard power recycling, a Signal Recycling (**SR**) cavity will be present. The tuning of the **SR** parameter allows changing the shape of the sensitivity curve and optimizing the detector for different astrophysical sources.

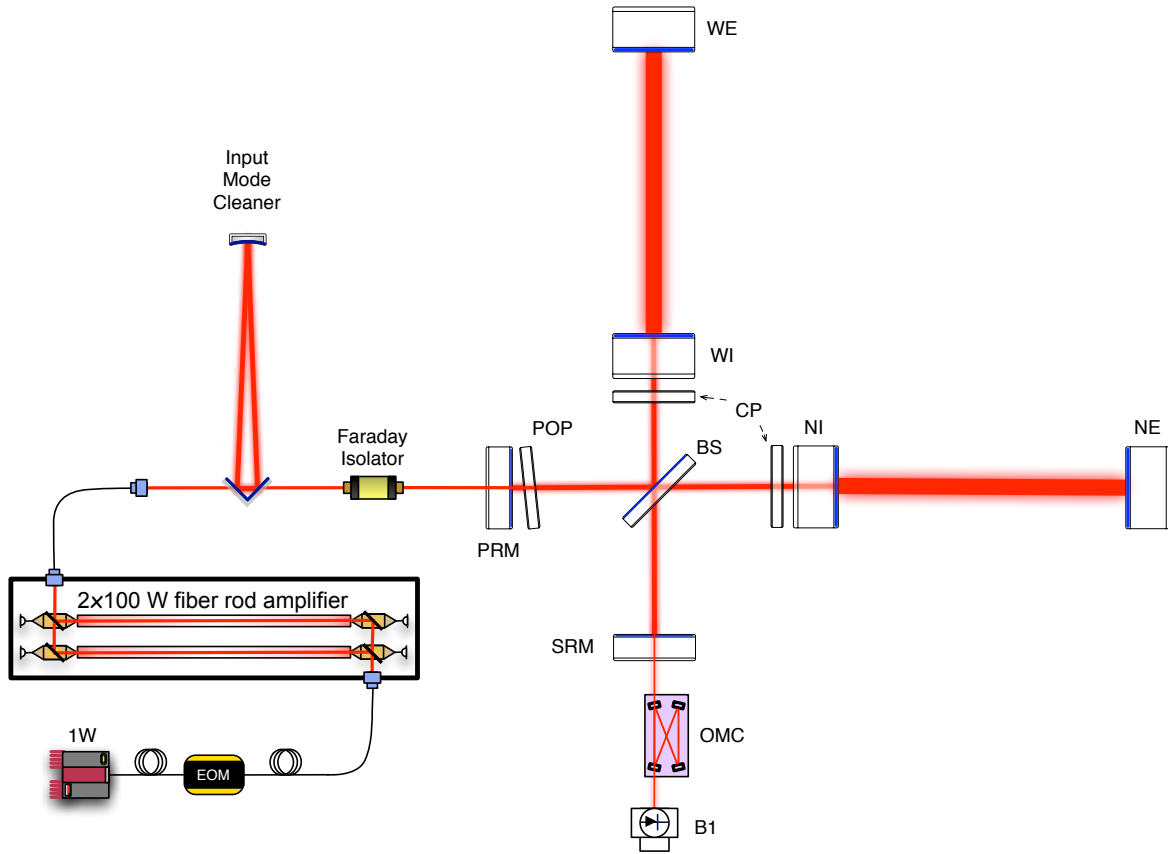


Figure 1.1: AdV optical layout.

- To reduce the impact of the coating thermal noise in the mid-frequency range the spot size on the test masses has been enlarged. Therefore, unlike Virgo, the beam waist will be placed close to the center of the 3 km Fabry-Perot cavities, resulting in beam radii of 48.7 mm and 58 mm for the input and end mirrors, respectively.
- The cavity finesse will be higher with respect to Virgo: a reference value of 443 has been chosen.

Laser (chapter 3) Improving the sensitivity at high frequency requires high power¹. The AdV reference sensitivity is computed assuming 125 W entering the interferometer (after the input mode cleaner). Therefore, considering the losses of the injection system, the laser must provide a power of at least 175 W. AdV will use a rod amplifier. A 100 W prototype is undergoing the final tests. The 200 W ultimate power will be achieved by coherent summation of two 100 W amplifiers.

Injection system (chapter 4)

- The input optics for AdV must be compliant with the 10 times increased optical power. Proper electro-optic modulators and Faraday isolators able to withstand high power have been developed.
- By using better optics the throughput of the IMC will be significantly improved to guarantee the required power (125 W) at the interferometer input.

Mirrors (chapter 5)

- Given the much larger optical power in the cavities, radiation pressure noise becomes a limit in the low frequency range and heavier test masses are needed to reduce it. The AdV test masses have the same diameter as the Virgo ones (35 cm) but are twice as thick (20 cm) and heavy (42 kg).
- Deviations from required flatness is the main source of scattering losses. Stricter flatness requirements (<0.5 nm rms) call for a better polishing. The flatness of the mirrors will be improved by using the corrective coating technique after a standard polishing phase.
- The baseline for the AdV coating is the use optimized multilayer and Ti doped Tantalum for the high-refractive index layers.

Thermal compensation (chapter 6) The AdV Thermal Compensation System (TCS) is designed to manage beam aberrations induced by thermal effects as well as mirror "cold" defects (such as refraction index inhomogeneities). It consists of:

- CO₂ laser projectors shined on dedicated compensation plates through a double-axicon system;
- ring heaters around several suspended optics;

¹Though squeezing is not part of the AdV baseline some works to prepare the infrastructure to host a squeezer in the next years will be performed.

- Hartmann sensors;
- scanning laser systems to cope with non-axisymmetric defects.

The Thermal Compensation System subsystem (**TCS**) will use the initial knowledge of the mirror maps, and more global information like phase camera images.

Detection (chapter 7)

- **AdV** will use a DC detection scheme, which improves the quantum noise and reduces the impact of some technical noises (such as RF phase noise) which would be (close to) limiting the detector sensitivity in case of heterodyne readout.
- The main photodiodes will be placed on the suspended optical bench (in vacuum) to improve the rejection of seismic and acoustic noise.
- A new output mode cleaner compliant with the new requirements on sidebands filtering will be installed.

Interferometer sensing and control (chapter 8) Towers in the central building will be moved in such a way to optimize the locking matrix. The Schnupp asymmetry is reduced to 23 cm.

Stray light control (chapter 9) Out of the 125 W power entering into the interferometer, about 100 W will be lost mainly by scattering around the mirrors and towards the pipes. In order to limit the phase noise due to part of this light being back-scattered into the interferometer, new diaphragm baffles will be installed either suspended around the mirrors, or ground connected inside the vacuum links.

Payloads (chapter 10) The payloads will be modified to be compliant with the thicker and heavier mirrors and to suspend the new components. A new payload layout has been developed, getting rid of the recoil mass and offering the possibility to suspend baffles around the mirrors, compensation plates on the input payloads and ring heaters. The test masses will be suspended by fused silica fibres.

Superattenuators (chapter 11) The Virgo superattenuators provide a seismic isolation compliant with the **AdV** requirements. However, some upgrades are necessary to improve the robustness in bad weather conditions:

- new monolithic inverted pendulum legs will be mounted: the higher resonance frequency will allow to increase the bandwidth of the inertial damping servos;
- piezo actuators will be installed in the inverted pendulum feet, allowing to perform a control of the tilt.

Moreover, the steering filter (or *filter 7*) must be modified to match the new design of the payloads.

Suspended benches (chapter 12) To fulfill the system requirement that all photodiodes to be used in science mode be seismically isolated and in vacuum, a compact vibration isolation system with its vacuum chamber has been realized. Five of such *minitowers* will be installed.

Vacuum (chapter 13)

- The current Virgo vacuum level needs to be improved by a factor of about 100 in order to be compliant with the **AdV** sensitivity. This improvement will be achieved by installing large cryotrap at the ends of the 3 km pipes (their pumping action will reduce the residual pressure by ~ 10 in the pipes even without baking) and then baking out the tubes to reach the final vacuum level.
- Vacuum links in the central area have to be re-designed with lengths compliant with the new positions of the towers and a larger diameter compatible with the larger beam.
- The vacuum separation in the towers must be re-designed to be compliant with the new filter 7 and payload system.

Data acquisition and general purpose electronics (chapter 14) While the general architecture will not change with respect to Virgo, several upgrades of the data acquisition and general purpose electronics are foreseen for **AdV**, to keep up with the increasing number of channels and the more demanding control system for the signal recycling configuration, and to cope with the obsolescence of several boards.

Infrastructure (chapter 15)

- To reduce the influence of environmental noise some noisy machines will be moved out of the experimental halls.
- Important modifications are needed in the central hall to host the minitowers and upgrade the laser lab and the detection lab. The detection lab will be enlarged and become a clean room.

1.2 Sensitivity

The **AdV** reference sensitivity² as well as the main noise contributions are shown in Fig. 1.2. The curve corresponds to a detector configuration with 125 W at the interferometer input and **SR** parameters chosen in order to maximize the sight distance for Binary Neutron Stars (**BNS**). The corresponding inspiral ranges are ~ 135 Mpc for **BNS** and ~ 1 Gpc for $30 M_{\odot}$ Binary Black Holes (**BBH**).

²The sensitivity curves shown in this section have been plotted using *GWINC*, a MATLAB code developed within the LSC [8] and adapted to **AdV** [9]. A document on the **AdV** sensitivity curve and all the contributing noises is available [10].

| AdV Overview, Part I | | |
|--|---|--|
| Subsystem and Parameters | AdV design (TDR) | Initial Virgo |
| Sensitivity | | |
| Binary Neutron Star Inspiral Range | 134 Mpc | 12 Mpc |
| Anticipated Max Strain Sensitivity | $3.5 \cdot 10^{-24} / \sqrt{\text{Hz}}$ | $4 \cdot 10^{-23} / \sqrt{\text{Hz}}$ |
| Instrument Topology | | |
| Interferometer | Michelson | Michelson |
| Power Enhancement | Arm cavities and Power Recycling | Arm cavities and Power Recycling |
| Signal Enhancement | Signal Recycling | n.a. |
| Laser and Optical Powers | | |
| Laser Wavelength | 1064 nm | 1064 nm |
| Optical Power at Laser Output | >175 TEM ₀₀ W | 20 W |
| Optical Power at Interferometer Input | 125 W | 8 W |
| Optical Power at Test Masses | 650 kW | 6 kW |
| Optical Power on Beam Splitter | 4.9 kW | 0.3 kW |
| Test Masses | | |
| Mirror Material | Fused Silica | Fused Silica |
| Main Test Mass Diameter | 35 cm | 35 cm |
| Main Test Mass Weight | 42 kg | 21 kg |
| Beam Splitter Diameter | 55 cm | 23 cm |
| Test Mass Surfaces and Coatings | | |
| Coating Material | Ti doped Ta ₂ O ₅ | Ta ₂ O ₅ |
| Roughness* | < 0.1 nm | < 0.05 nm |
| Flatness | 0.5 nm RMS | < 8 nm RMS |
| Losses per Surface | 37.5 ppm | 250 ppm (measured) |
| Test Mass RoC | Input Mirror: 1420 m End Mirror: 1683 m | Input Mirror: flat End Mirror: 3600 m |
| Beam Radius at Input Mirror | 48.7 mm | 21 mm |
| Beam Radius at End Mirror | 58 mm | 52.5 mm |
| Finesse | 443 | 50 |
| Thermal Compensation | | |
| Thermal Actuators | CO ₂ Lasers and Ring Heater | CO ₂ Lasers |
| Actuation points | Compensation plates and directly on mirrors | Directly on mirrors |
| Sensors | Hartmann sensors and phase cameras | n.a. |

Table 1.1: Main parameters of the AdV Reference Design described in this document (PART 1). The requirement on the mirror micro-roughness has been relaxed with respect to Virgo: while the worsening in terms of scattered light is negligible, it can help achieving a better flatness.

| AdV Overview, Part II | | |
|--|--|----------------------|
| Subsystem and Parameters | AdV design (TDR) | Initial Virgo |
| Suspension | | |
| Seismic Isolation System | Superattenuator | Superattenuator |
| Degrees of Freedom of Inverted Pendulum Inertial Control | 6 | 4 |
| Test mass suspensions | Fused Silica Fibres (optimized geometry) | Steel Wires |
| Vacuum System | | |
| Pressure | 10^{-9} mbar | 10^{-7} mbar |
| Injection System | | |
| Input mode cleaner throughput | >96% | 85% (meas.) |
| Detection System | | |
| GW Signal Readout | DC-Readout | Heterodyne (RF) |
| Output Mode Cleaner Suppression | RF Sidebands and Higher Order Modes | Higher Order Modes |
| Main Photo Diode Environment | in Vacuum | in Air |
| Lengths | | |
| Arm Cavity Length | 3 km | 3 km |
| Input Mode Cleaner | 143.424 m | 143.574 m |
| Power Recycling Cavity | 11.952 m | 12.053 m |
| Signal Recycling Cavity | 11.952 m | n.a. |
| Interferometric Sensing and Control | | |
| Lock Acquisition Strategy | Auxiliary Lasers (different wavelength) | Main Laser |
| Number of RF Modulations | 3 | 1 |
| Schnupp Asymmetry | 23 cm | 85 cm |
| Signal Recycling Parameter | | |
| Signal Recycling Mirror Transmittance | 20 % | n.a. |
| Signal Recycling Tuning | 0.35 rad | n.a. |

Table 1.2: Main parameters of the **AdV** Reference Design described in this document (PART 2).

It must be remarked that different curve shapes are obtained by changing the **SR** tuning and that different choices of such tuning might be driven by scientific or commissioning motivations.

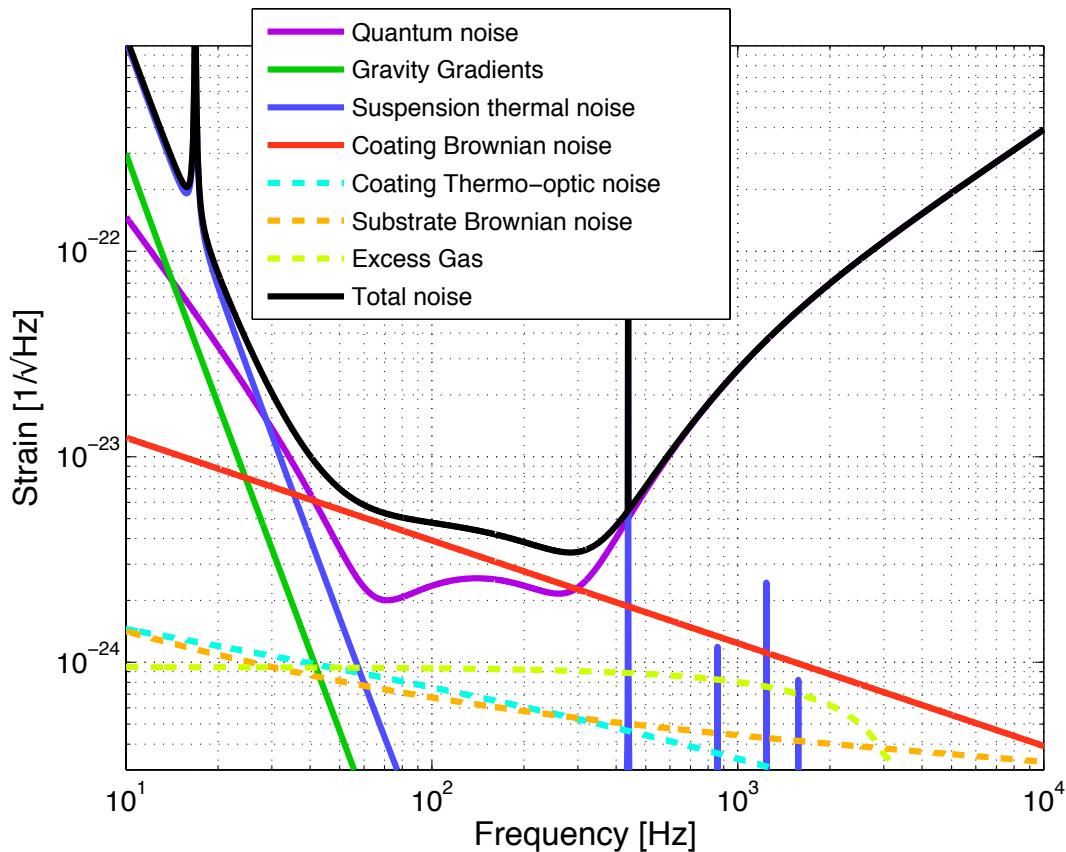


Figure 1.2: Reference **AdV** sensitivity and expected noise contributions. The chosen **SR** tuning optimizes the inspiral range for coalescing binary neutron stars.

1.3 Other system requirements

Some basic assumptions are done in the sensitivity computation that are to be considered as system requirements. Some design choices of different subsystems were made to comply with such requirements:

- **input power:** it is assumed that a laser power of 125 W be available in the TEM_{00} mode after the input mode cleaner;
- **round trip losses:** the power lost in a round trip inside a Fabry-Perot cavity must not exceed 75 ppm;
- **technical noises:** all technical noises must be kept reduced at a level such that the corresponding strain noise is <0.1 of the design sensitivity over the whole frequency range.

1.4 Sensitivity and detector commissioning

The **AdV** detector is tunable in three ways:

- by changing the laser power;
- by changing the transmissivity of the **SR** mirror;
- by tuning the position of the **SR** mirror.

The **SR** mirror transmittance influences the detector bandwidth, while the position of the **SR** mirror at a microscopic scale changes the frequency of the maximal sensitivity. Thus, the presence of the **SR** cavity allows to think of **AdV** as a tunable detector (see chapter 2): the sensitivity curve can be shaped in order to perform runs optimized for targeting different astrophysical sources.

For the sake of simplicity, we refer to four different operation modes:

- **power recycled, 25 W³**;
- **dual recycled, 25 W, tuned signal recycling**;
- **dual recycled, 125 W, tuned signal recycling**;
- **dual recycled, 125 W, detuned signal recycling** (**SR** tuning to optimize BNS inspiral range).

AdV will not be operated in the final configuration since the beginning. The new features will put new problems forward, which must be faced with a step by step approach. The detailed commissioning plan is out of the scope of this document. However, the above-mentioned modes of operation corresponds to commissioning steps of increasing complexity. They should be considered as *reference configurations*, useful as benchmarks. The commissioning will progress through many intermediate steps. Periods of commissioning will be alternated with periods of data taking and such plans will need to be coordinated with Advanced LIGO in order to maximize the network capabilities.

Fig. 1.3 compares the sensitivity curves for the reference scenarios described.

³Reference value for the power after the Input Mode Cleaner (**IMC**)

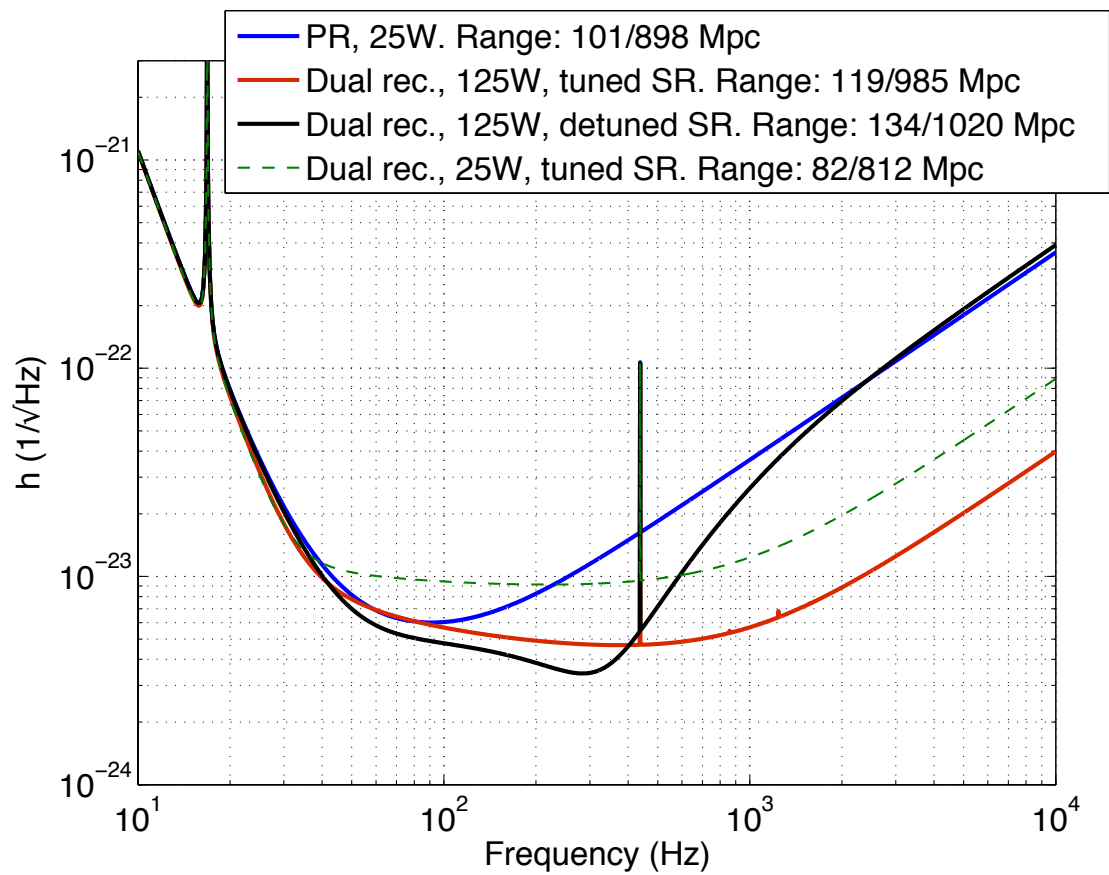


Figure 1.3: Scenario for the evolution of the AdV sensitivity: early operation (blue), 25 W input power, no SR; late operation, wideband tuning (red), 125 W input power, tuned SR; late operation, optimized for BNS (black), 125 W input power, detuned SR (0.35 rad). In the legend, the inspiral ranges for BNS and BBH (each BH of $30 M_{\odot}$) in Mpc are reported. Dual recycling curves are obtained without changing the SR mirror.

Chapter 2

Optical simulation and design (OSD)

2.1 Introduction

2.1.1 Scope of the subsystem and deliverables

The goals and deliverables of the Optical Simulation and Design subsystem (OSD) subsystem are:

- Preparation of the simulation tools for the optical design and commissioning of the interferometer. Deliverables: the optical simulation codes, the detailed configuration scripts and the results from those simulations.
- Definition the optical scheme of the interferometer (geometry of the arm-cavities, geometry of the recycling cavities) and the optical parameters of the interferometer mirrors (positions, optical properties, radii of curvature, etc...). Deliverables: the optical layout of the interferometer and the set of optical parameters.
- Definition of the specifications for the interferometer mirrors, or confirmation that the existing specifications are coherent with the Advanced Virgo performances. Deliverables: specifications for each optic and/or the consequences for the existing specifications.
- Evaluation of the advantages of future upgrades (non gaussian modes, squeezing, etc...) and of their compatibility with the optical design. Deliverables: sensitivity curves demonstrating the interest of future upgrades and evaluation of the impact of future upgrades on the optical design. Plans for future upgrades have not been deeply investigated so far and so are not presented in this chapter.

All the deliverables are given with the links to the relevant documentation (on the Virgo documentation system - TDS [12]).

2.1.2 Design summary and changes with respect to the baseline design

The Advanced Virgo optical layout is shown in Figure 2.1. The basic topology is a dual-recycled Michelson interferometer with Fabry-Perot cavities in the Michelson arms. The interferometer parameters are summarized in table 2.1.

This section provides a brief explanation of the main choices pointing out any changes with respect to the baseline design [13] (2009). A more detailed description is given in the following sections.

Recycling cavities geometry The recycling cavities are marginally stable. This configuration is conceptually similar to the one used in initial Virgo: the power recycling cavity is obtained by the addition of a partially transparent mirror between the input mode-cleaner and the Beam Splitter (BS); Similarly, the signal recycling cavity is obtained by adding another mirror between the BS and the detection system.

Changes from the 2009 baseline: the baseline configuration was Non-Degenerate Recycling Cavity (NDRC). The choice between the Marginally Stable Recycling Cavities (MSRC) configuration and the NDRC has been taken by the Virgo Steering Committee in May 2011. The choice for the MSRC configuration was not driven by optics, but rather by problems related with construction schedule, budget and the increase of suspensions complexity of the NDRC geometry. Details about the trade-off are in [14]. This change has required a complete re-design of the central part of the interferometer, and a complete new study of the impact of optical imperfections on the interferometer fields.

Arm-cavity geometry - choice of the radii of curvature of the test-masses The arm cavities have a bi-concave geometry, with the beam waist roughly in the center of the cavity. The bi-concave geometry is used to increase the beam size (and then reduce coating thermal noise) and to deal with with radiation pressure alignment instabilities.

Changes from the 2009 baseline: the radii of curvature (Radius of Curvatures (RoCs)) of the test masses have been slightly increased, in order to increase the safety factor with respect to possible deviation from specifications.

Arm cavity finesse The use of high finesse in the arm-cavity is necessary to decrease the quantum noise without increasing the power in the transmissive optics (Input Mirrors (IMs) and BS). The combination of high finesse and signal recycling can preserve the optical transfer function of the instrument.

Changes from the 2009 baseline: the arm-cavity finesse has been decreased by a factor 2 (from 900 to 443), mainly in order to deal with possible extra losses inside the arm-cavities and Signal Recycling (SR) cavity, to ease the lock acquisition procedure, and to ease requirements on signal recycling cavity length noise.

Power recycling mirror transmission The Power Recycling Mirror (PR) transmission is a trade-off between the need to maximise the circulating power in the arms compatible with a reasonable value of arm-cavity round-trip losses, and the need to decrease the susceptibility

of the power recycling cavity to optical imperfections. The first objective can be achieved by matching the reflectivity of the power recycling mirror with the apparent reflectivity of the arm cavities (so with a **PR** transmission 2.8%), while the second can be achieved by lowering the recycling cavity finesse.

Changes from the 2009 baseline: the power recycling mirror transmission has been changed from 4.6% (this value was chosen for critically coupling the Advanced Virgo baseline design, which had higher arm-cavity finesse) to 5%. We choose this value to reduce the effect of imperfections in the Virgo Ientral interferometer (**CITF**). The result is a 14% reduction in the stored optical power compared to the case with the optimal reflectivity coupling.

Signal recycling tuning The signal recycling tuning is optimized to have the best Signal to Noise Ratio (**SNR**) for a given type of gravitational wave source. Two configurations are considered here: the Resonant Sideband Extraction (**RSE**) configuration (zero tuning), and a ‘tuned’ configuration, optimized for Binary Neutron Stars (**BNS**) inspiral searches.

Changes from the 2009 baseline: the detuning corresponding to the **BNS**-optimized configuration has been recomputed taking into account the change in the arm-cavity finesse and the change in the Signal Recycling Mirror (**SR**) transmission. The corresponding detuning is now 0.35 radians.

Signal recycling mirror transmission The **SR** transmission is chosen, in combination with the arm cavity finesse and signal recycling detuning, to optimize the detector sensitivity to astrophysical sources.

Changes from the 2009 baseline: to compensate the decrease of arm-cavity finesse, the recycling mirror transmission is roughly increased by a factor of 2 (T=20%)

Pick-off for interferometer control At least one pickoff inside the power recycling cavity is needed for the longitudinal and alignment control. The choice is to add a low reflectivity plate (reflectivity of 300 ppm) near the power recycling mirror. The plate is suspended in the same way as the compensating plates.

Secondary beams extraction Secondary beams (often called *ghost beams*) are generated by the AR surface of the beam splitter and by the surfaces of the plates inside the power recycling cavity (compensating plates and pickoff plate). The proper handling of these beams is essential in order to avoid stray light noise or excessive noise couplings. Such control is made by inserting wedges or tilting the components. The value of the wedge/tilts have been determined through FFT simulations and ray tracing packages.

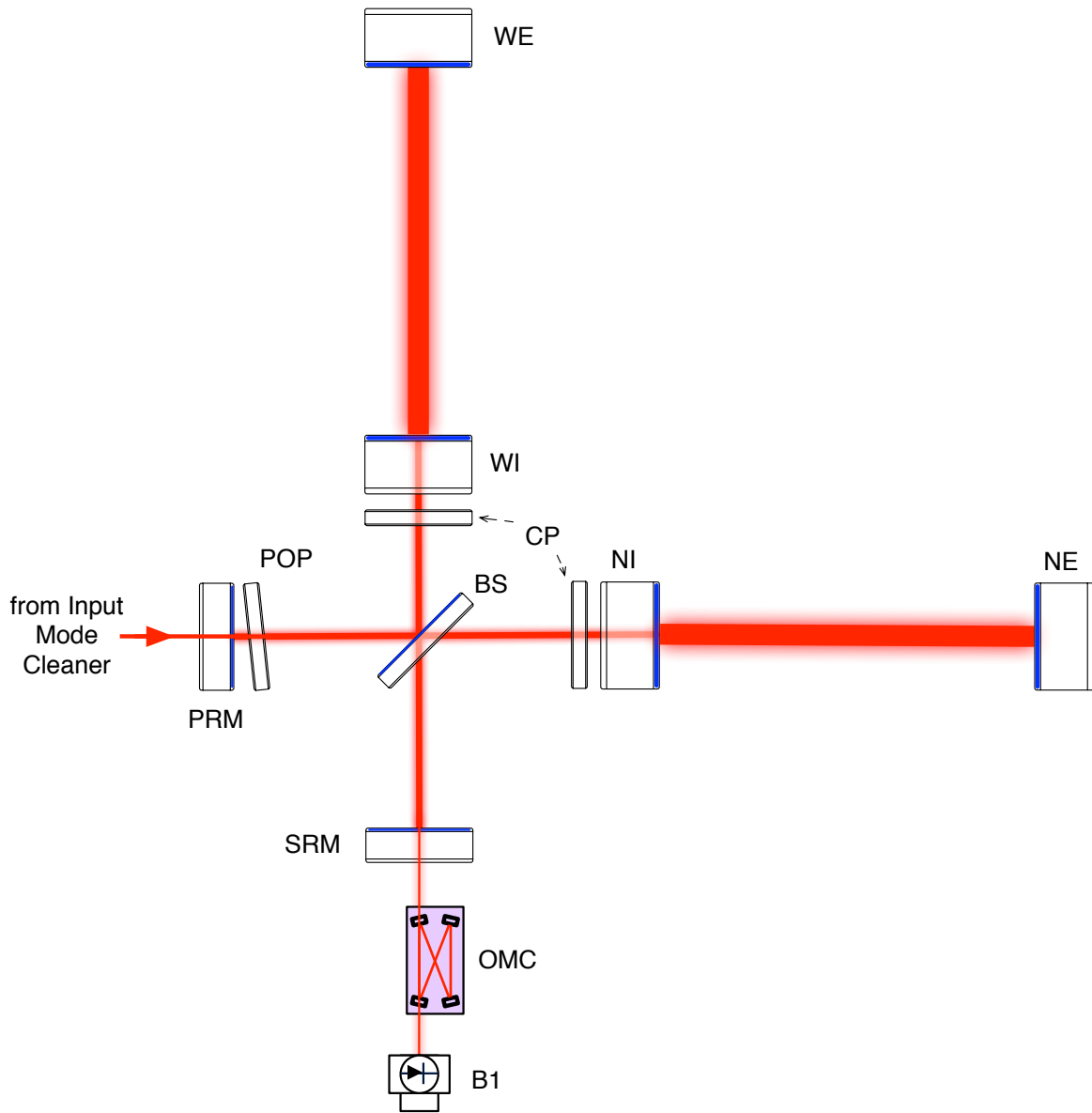


Figure 2.1: Simplified optical layout of the core of the Advanced Virgo interferometer.

| Advanced Virgo main optical parameters | | | |
|---|----------|-------------------------------|----------|
| Light Power | | | |
| Arm cavity power | 650 kW | Power on the BS | 4.9 kW |
| Arm cavity geometry | | | |
| Cavity length | 2999.8 m | | |
| IM RoC | 1420 m | EM RoC | 1683 m |
| Beam size on IM | 48.7 mm | Beam size on EM | 58.0 mm |
| Waist size | 9.69 mm | Waist position from IM | 1363 m |
| Arm cavity finesse | | | |
| Transmission IM | 1.4% | Transmission EM | 1 ppm |
| Finesse | 443 | Round-trip losses | 75 ppm |
| Power recycling cavity | | | |
| Transmission PR | 5% | Recycling gain | 37.5 |
| PRC length | 11.952 m | Beam size on PR | 49.1 mm |
| Signal recycling cavity | | | |
| Transmission SR | 20% | Finesse | 26 |
| SRC length | 11.952 m | SRM tuning | 0.35 rad |

Table 2.1: Main parameters of the final configuration of the Advanced Virgo interferometer. The reflectivity and tuning of **SR** are optimised to maximise the likelihood of detection of **BNS**. Detailed parameters for the core optics are given in tables 2.6,2.8,2.9 and 2.7.

2.2 Simulation tools

The development of the optical simulation tools is one of the primary tasks of the OSD subsystem. The fields inside Advanced Virgo can not be simply derived from analytical models, especially in the presence of asymmetries or mirror defects.

The simulation tools are thus clearly important for the baseline design phase, but an updated and relevant set of simulation tools is also crucial during the construction phase in order to check the design consistency using the real mirrors parameters and results from the pre-commissioned subsystems (laser, Thermal Compensation System subsystem (TCS)). Furthermore, simulation is an essential tool to ease the commissioning process.

For Advanced Virgo, three main types of codes are used: FFT codes (SIS, DarkF, OSCAR, FOG and SIESTA), modal codes (Finesse and MIST) and codes including radiation-pressure (Optickle). DarkF, OSCAR, FOG, SIESTA and MIST are developed within the Virgo Collaboration. SIS and Optickle are developed within the LIGO project and Finesse in GEO.

None of the codes can simulate every aspect of the interferometer, and so this collection of codes with different strengths is necessary to try to answer as many questions as possible. In addition, where there is overlap of capability, the use of these different independent codes enables the crosschecking of results. Furthermore the development of codes in several laboratories of the Virgo Collaboration increases the expertise of the collaboration members in optical simulation.

In the modal codes the electric field is expanded in a base of Hermite-Gaussian or Laguerre-Gaussian modes. For our purposes one convenient base is the eigenmodes of the perfect and ‘cold’ (no thermal effect) 3-km arm-cavity. These codes are in general very useful in the early phases of the design, where no big defects are considered, since a low number of modes is required.

In the FFT codes the electric field is expanded in plane wave components (through the FFT transform). The plane waves are propagated independently through free space and optical components. The resulting electric fields are then computed by inverse Fourier transform; the process is repeated until the resulting electric fields have converged to stable values. The advantage of these codes is their accuracy, even in the case of realistically imperfect optical systems. The drawback is that these codes are computationally more expensive than the modal codes and so their use is less effective in the first phases of the design, when large parameter spaces need to be explored. However, due to the large sensitivity of the marginally stable recycling cavity to optical aberrations and the choice to use small wedges on optics within the recycling cavity, the FFT codes are an essential tool for the OSD work, as the modal codes do not converge to stable results under the current computational limits.

The existing modal and FFT codes do not contain radiation pressure effects. In order to understand the audio frequency dynamics of the interferometer, it is necessary to include the effects of radiation pressure. This is especially necessary for the design of proper control systems.

In addition to these aforementioned classes of simulation, GWINC is a top level interferometer optimization tool used to calculate detector design sensitivity, and Optocad is a ray tracing code used to generate interferometer layouts.

In the following paragraphs we will briefly describe the different simulation tools that have been used during the OSD studies. The table 2.2 summarizes the simulation tools.

2.2.1 FFT codes

DarkF is an FFT simulation code written in Fortran90 which can simulate simple systems such as Fabry Perot cavities (resonant or not), Michelson interferometers or complex systems such as Virgo (for the carrier and for the sidebands) and Advanced Virgo with signal recycling. Mirror surface maps and thermal effects phase maps can be included in the simulation after correction of the residual tilt and the piston. Various results can be obtained from these simulations, such as, power of the different beams, the losses, the coupling defect and the coupling of the main beams with a perfect TEM₀₀ mode. Recently DarkF has been used for OSD, to study the problem of secondary beam extraction, for several configurations of BS wedge and compensating plates. The recent on-going update in the DarkF program, is the simulation of the Audio-Sidebands, created by a passing Gravitational Waves (**GW**) at a specific frequency.

FOG is an FFT based simulation code written in Matlab which has been developed within the optics group of EGO. It can currently simulate the entire interferometer of Advanced Virgo. In the full Interferometer (**ITF**) configuration FOG uses the accelerated convergence scheme [18] to run complete simulations in just a few minutes. This feature has been used for defining the aberration budget in the power recycling cavity. FOG simulates the Michelson interferometer and so an aberration budget may be defined for both common and differential aberrations. In addition, such simulations may be used to determine the quantity of higher order modes generated in the arm cavities that end up on the dark fringe, which helps in setting requirements for the Output Mode Cleaner. FOG has also been used to study the effects of the second reflection of the wedged beamsplitter and the reflections off the antireflection coatings of the compensation plates in the recycling cavity. FOG treats each secondary surface as an additional cavity mirror. It therefore reproduces multiple reflections off the secondary surfaces and so simulates correctly the so-called ‘pickoffs of pickoffs’. It also has a novel feature of using rectangular grids (resulting in different resolutions in the two directions), which permits the study of larger wedge angles than possible with DarkF. FOG has also been used to determine **RoC** tolerances of the arm cavities using realistic mirror maps.

FOG is still in development and has not been rigorously tested or officially released and so therefore no documentation is available to date. However, it has been very useful in providing an independent cross-check for more mature simulation tools such as DarkF and SIS.

OSCAR is a FFT based optical simulation package used to simulate Fabry-Perot cavities or interferometers with realistic optics [17]. The code is written in Matlab, easy to use and is well documented. Typical OSCAR simulations include cavity round trip loss estimations and calculations of steady state fields in interferometers. For the design of Advanced Virgo, OSCAR has been used to find the specifications for the arm cavity mirror flatness and to calculate the loss in sideband power in the recycling cavities. A special version of OSCAR using a beam in 1 dimension has also been developed to quickly simulate secondary beams

| Optical simulation tools | | | | |
|---------------------------------|-----------------------|-----------|-----------|-----------------|
| Name | optical configuration | language | documents | comments |
| FFT codes | | | | |
| SIS | double cavity | C | [15] | |
| DarkF | Advanced Virgo | Fortran90 | [16] | |
| OSCAR | CITF | Matlab | [17] | 1D or 2D option |
| FOG | Advanced Virgo | Matlab | | |
| Siesta-FFT | simple cavity | C | [56] | |
| Modal codes | | | | |
| Finesse | Advanced Virgo | C | [28] | HG based |
| MIST | Advanced Virgo | Matlab | [32] | HG based |
| Radiation pressure code | | | | |
| Optikle | Advanced Virgo | Matlab | [33] | only 3 modes |
| Detector sensitivity | | | | |
| GWINC | Advanced Virgo | Matlab | [34] | |
| Ray tracing | | | | |
| Optocad | Advanced Virgo | Fortran95 | [35] | |

Table 2.2: OSD simulation tools. For each code the most advanced optical configuration that can be simulated is given.

with large angles. For the 2D simulations of the secondary beams, OSCAR used a rectangular grid with typically 32 times more points in the direction of the tilt than in the other transverse direction.

SIESTA the Virgo simulation tool [19], can run either modal or FFT optical simulations. Modal simulations have been widely used in the past, whereas the FFT capabilities have been improved recently. Current capabilities of SIESTA-FFT which are of interest for the simulations of Advanced Virgo includes: computation of the Fabry Perot steady state electric fields (with accelerated convergence scheme [18]), computation of the steady state of a power-recycled interferometer with arm cavities, possibility of loading mirror surface maps or generating random surface maps with a user-defined spectral density of defects and possible use of Hermite-Gauss or Laguerre-Gauss modes.

SIESTA-FFT has been positively cross-checked with SIS and OSCAR. The results obtained for a power-recycled interferometer [24] are compatible with those of DarkF. For AdV, it has been employed for the definition of the polishing specifications of the arm cavity mirrors (see section 2.8; [20, 21, 22, 23]). In this context, a nice feature which has been massively exploited is the use of bash scripts to create SIESTA configuration files and to run a few thousands of simulations automatically.

SIESTA runs under Linux; the latest release is available in the Virgo Common Software Distribution [25]. Source code and documentation can also be obtained via CVS [26].

SIS (Stationary Interferometer Simulation tool) is an FFT based simulation tool developed to determine the specifications of the Advanced LIGO core optics components. SIS is currently capable of simulating a three-mirror coupled cavity. It is written in C, is fast and easy to use with a complete manual, and has numerous features that make quick studies of steady state fields under various conditions in the interferometer relatively easy. These include loading mirror maps, generating mirror maps from PSDs, automatically measuring and subtracting Zernike terms from maps, the ability to specify nearly every parameter of the simplified interferometer (or have the parameter auto-magically determined), detailed stationary state beam analysis using modal expansions, calculation of the RF and audio sidebands, and automatic locking in length degrees of freedom. SIS can also use an adaptive window resolution to, e.g., simulate the Advanced LIGO recycling cavity which has strongly focusing beams. SIS has been used to study thermal effects in the Advanced Virgo recycling cavities and to set specifications on the surface quality of the optics in the recycling cavities. The SIS manual is available on the LIGO DCC [15].

2.2.2 Modal codes

Finesse [28] is a simulation tool able to describe the interferometer behavior in the frequency domain (steady state interferometer). It accepts user configuration files (.kat files) where virtually any optical configuration can be depicted. In the same file, commands about the parameters to be tuned during the simulation are given. Starting from this file, the interferometer description is translated into a set of linear equations that are solved numerically for each set point of the configuration. Finesse employs modal expansion of the fields

in doing that, and can handle Hermite-Gauss High Order Modes (**HOMs**) with no intrinsic limitation, although the computational load increases quickly with the maximum order of the involved modes. Effects related to beam mismatch and/or misalignment can easily be tackled with the use of **HOMs**, and transfer functions can easily be computed by adding lines at a given frequency to almost any parameter of the interferometer. Recently, Finesse was given also the ability to take into account mirror maps describing figure defects for reflective and transmissive interfaces, even though no maps are available nor foreseen for beam splitters. In [29, 30] a study was performed to validate Finesse predictions against well established FFT programs, such as DarkF, showing that Finesse is able to give comparable results when Virgo-like interferometers were studied. An important limitation, however, arose when using Finesse to study marginally stable cavities with figure defect maps. Actually, it was shown in [31] that too many **HOMs** had to be included in order for the simulation to converge towards reliable results, so making impractical the use of Finesse in this configuration. The versatility of Finesse in quickly setting up simulations for arbitrary configurations is an asset, but users should always check the convergence with respect to increasing the mode order.

MIST [32] is a tool developed in Virgo for modal simulation of a dual recycled interferometer. It is based on the MATLAB environment. It implements analytical equations to compute the field behavior inside the optical system. This limits its flexibility (it can be used only for subsets of a dual recycled interferometer) but allows shorter computational times with respect to similar tools such as Finesse. It was extensively used to compute the effect of thermal lensing in the input mirror on the sideband recycling gain as a function of interferometer parameters such as the power recycling cavity finesse. It was also used to study the convergence speed of modal simulations as a function of the number of higher order modes used. The main limitations of the code are the reduced flexibility and the lack of mirror map implementations.

2.2.3 Other codes

Optickle [33] is a tool developed by the LSC community, based on the MATLAB environment, with the goal of simulating the frequency domain behavior of a general optical setup including dynamic effects due to radiation pressure. This tool works mainly in the plane wave approximation, without including any high order Gaussian mode. The only exception is the first transverse mode which is partially considered in a section of the code used to simulate alignment effects. This lack of high order modes is the main limitation of the code. Optickle is mainly used for ISC purposes (simulation of interferometer optical response) but it was also used for **OSD** topics such as the simulation of the interferometer optical response to differential strain to be used as a calibration function.

GWINC [34] (Gravitational Wave Interferometer Noise Calculator) is a simulation tool developed by the LSC community, based on the MATLAB environment. It is used to compute the fundamental noise contribution to the advanced detector sensitivity, such as quantum and thermal noise. The tool implements directly equations describing the known noise sources, as determined from publications and standard models. It does not include any description of technical noise such as longitudinal and angular control noise or laser noise. It has been used in

the design of Advanced Virgo since the beginning to compute the design sensitivity. Recently it has been used to find the dependence of the detector sensitivity on optical parameters such as the arm cavity finesse and the power and signal recycling reflectivity [27]. All other parameters (such as those regarding coating and suspension thermal noise) were computed at the time of the first baseline design and were not updated recently.

Optocad is a Gaussian beam tracing program [35]. It has been used in GEO and Virgo for more than 10 years. Its simplicity (limited to Gaussian beam propagation) is also its force: it allows to propagate the beam through all optics (1000 in Virgo+) and deduce what should be their precise positions. It is the reference tool in Virgo to compute the towers positions in Advanced Virgo. It is also used to propagate secondary beams and verify that beam dumps are well dimensioned. Optocad was extensively used to design the optical layout of Advanced Virgo. The main limitation of Optocad is that beams can be propagated only in the horizontal plane. This is not an issue as long as tilts and wedges are all in the horizontal plane. Very recently, a new version has been released which can deal with aspherical and off-axis surfaces. The realistic input and output parabolic telescopes of Advanced Virgo are now well taken into account (in particular, secondary beams which are not centered on the parabolic telescope mirrors are propagated in the right way with this new version).

2.3 Optical layout

2.3.1 Mirror positions and modulation frequencies

In this section the choice of the positions of the interferometer mirrors is described. This choice is intrinsically coupled with the constraints given by the existing vacuum infrastructure (see VAC chapter and [36]) and with the choice of modulation frequencies (see ISC, INJ, DET chapters).

Four modulation frequencies (Fmod1, Fmod2, Fmod3 and Fmod4) are used to provide an adequate sensing matrix for all the interferometer degrees-of-freedom.

Assuming the arm length is 2999.8m, assuming the Schnupp asymmetry has been set to 23 cm (see ISC chapter), assuming also the detailed geometry of each optic (see Tables 2.6, 2.8, 2.9 and 2.7), the choice of the modulation frequencies has been made in order to minimize the PR, SR and IMC tower displacements, while respecting the required properties of resonance of the various fields in the interferometer,

All the modulation frequencies should generate sidebands transmitted by the Input Mode Cleaner (IMC) cavity. Other specific properties are:

- Fmod1 generates sidebands resonant in the power recycling cavity and not resonant in the arms and in the signal recycling cavity.
- Fmod2 generates sidebands not resonant in the arms, and resonant in the power and signal recycling cavities.
- Fmod3 generates sidebands not resonant in the interferometer.

| Name | Frequency [MHz] |
|-------|-----------------|
| Fmod1 | 6.270777 |
| Fmod2 | 56.436993 |
| Fmod3 | 8.361036 |
| Fmod4 | 131.686317 |

Table 2.3: Summary of the modulation frequencies

- Fmod4 has the same properties as Fmod2 except that the sidebands generated by Fmod4 should have a very low finesse in the recycling cavities.

The sidebands are chosen to be near the anti-resonance of the arm cavities (with an offset of 300 Hz, corresponding to 3 times the FWHM to the arm-cavities, in order to avoid the presence of sidebands of sidebands resonant in the arm cavities).

The detail of the computation of the modulation frequencies is the following:

- The **FSR** of the arm cavities is $FSR_{arm} = c / (2L_{arm}) = 49968.74$ Hz
- $F_{mod1} = 125.5 \times FSR - 300$ Hz = 6270777 Hz
- The power and signal recycling lengths are $PRCL = SRCL = (1-0.5) \times c / (2F_{mod1}) = 11.952$ m
- $F_{mod2} = 9 \times F_{mod1} = 56436993$ Hz
- The **IMC** cavity length is $L_{imc} = 3c / F_{mod1} = 143.424$ m and then the **FSR** of the **IMC** cavity is $FSR_{imc} = c / (2L_{imc}) = 1045130$ Hz
- $F_{mod3} = 8 \times FSR_{imc} = 8361036$ Hz
- $F_{mod4} = 21 \times F_{mod1} = 131686317$ Hz

All modulation frequencies are summarized in Table 2.3.

Inter-component distances are summarized in Table 2.4, and final tower positions as well as displacement with respect to current positions are summarized in Table 2.5. The positions are given in the *optical reference system*, defined as follows: the origin corresponds to the center of the **BS** hole in the pavement of the central building, the x-axis is along the west arm oriented towards east, and the y-axis is along the north arm oriented towards north. The position of the towers correspond to the center of mass position of the main optics components (i.e., for the input test masses, the center of the towers is also the center of the input test masses substrate). The tower positions have been computed properly considering the propagation in the substrates (**IM**, Pickoff Plate (**POP**), Compensation Plate (**CP**) and **BS**).

Note that the detection tower has been displaced so that the distance between the Injection tower and **PR** is the same as the distance between the Detection tower and **SR**. This allows reaching a perfectly symmetric interferometer (apart from the Schnupp asymmetry). In addition, **PR** and **SR** are similar substrates.

| Components | Dist. [m] | Cavity | Optical Path Length (OPL) [m] |
|--------------|-----------|---------|-------------------------------|
| NI NE | 2999.800 | N ARM | 2999.800 |
| WI WE | 2999.800 | Y ARM | 2999.800 |
| NI NCP | 0.200 | | |
| WI WCP | 0.200 | | |
| NCP BS | 5.367 | Schnupp | 0.230 |
| WCP BS | 5.245 | | |
| BS POP | 5.814 | PRC | 11.952 |
| POP PR | 0.06 | | |
| BS SR | 5.943 | SRC | 11.952 |
| BStickness | .065 | | .108 |
| IMthickness | .200 | | .290 |
| CPthickness | .035 | | .051 |
| POPthickness | .035 | | .051 |

Table 2.4: Inter-component physical distances measured from surface to surface(left) and the optical path lengths (right).

| Tower | position in X [m] | position in Y [m] | disp in X [m] | disp in Y [m] |
|-------|-------------------|-------------------|---------------|---------------|
| INJ | -0.027 | -11.000 | +0.000 | +0.001 |
| PRM | -0.017 | -6.085 | +0.006 | -0.082 |
| BS | 0.003 | 0.023 | +0.003 | +0.005 |
| NI | 0.000 | 5.774 | +0.000 | -0.624 |
| NE | 0.000 | 3005.774 | +0.000 | -0.626 |
| WI | -5.600 | 0.000 | -0.001 | -0.002 |
| WE | -3005.600 | 0.000 | +0.000 | -0.001 |
| SRM | 6.044 | 0.018 | +0.043 | -0.002 |
| SDB | 10.958 | 0.017 | -0.043 | +0.019 |

Table 2.5: Tower positions in the optical reference system (left) and displacement with respect to current position (right). The position of the towers correspond to the center of mass position of the main optics components (i.e., for the input test masses, the center of the towers is also the center of the input test masses substrate). The X direction is along the north arm whereas the Y direction is along the west arm

2.3.2 Optocad layout

The gaussian beam tracing of this design has been done in Optocad and is shown in figure 2.2. Zooms (not to scale) provides further information about wedge and tilt orientations of the various optics. See fig. 2.3, 2.5 and 2.4.

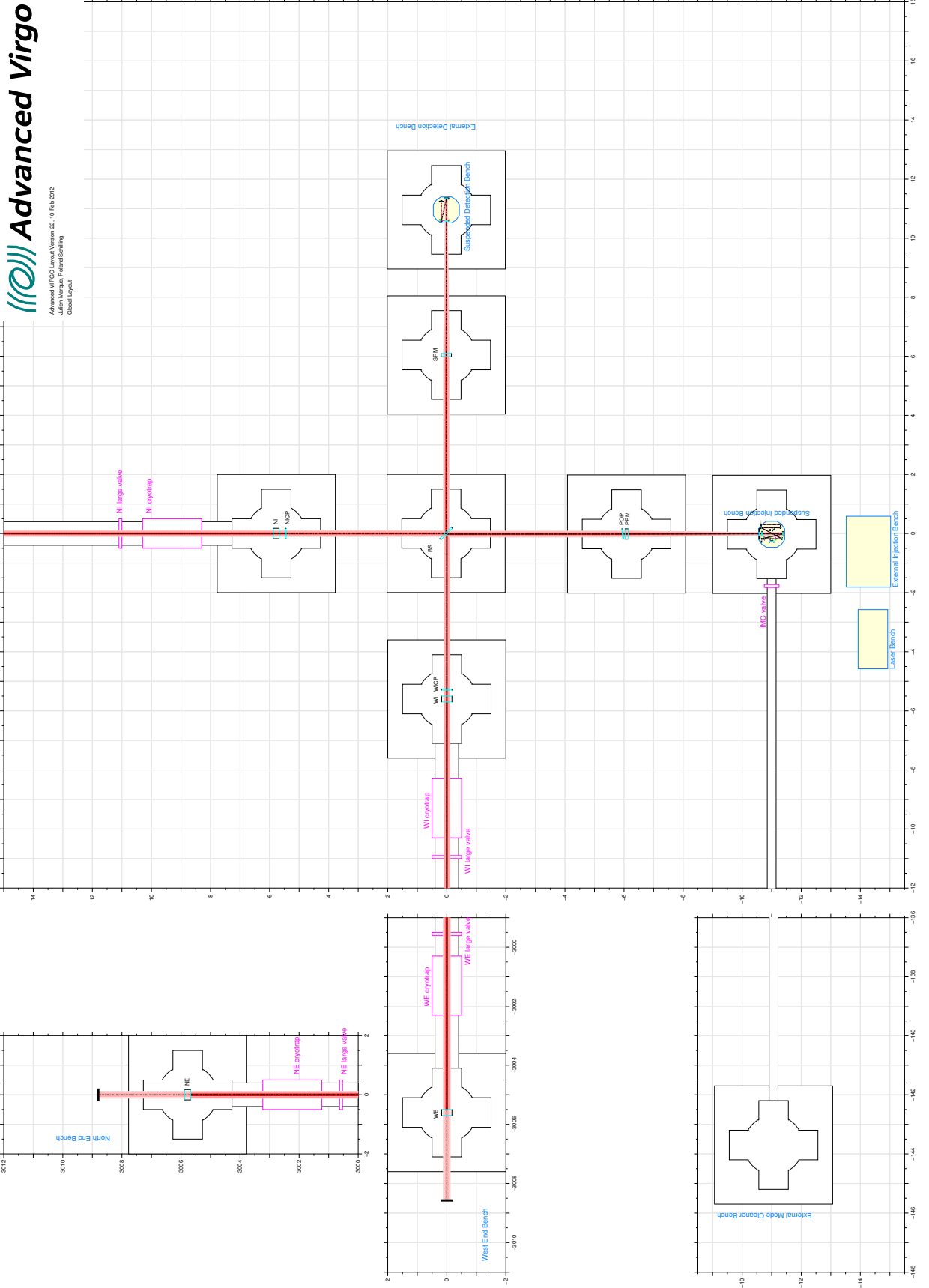


Figure 2.2: General optical layout obtained with Optocad.

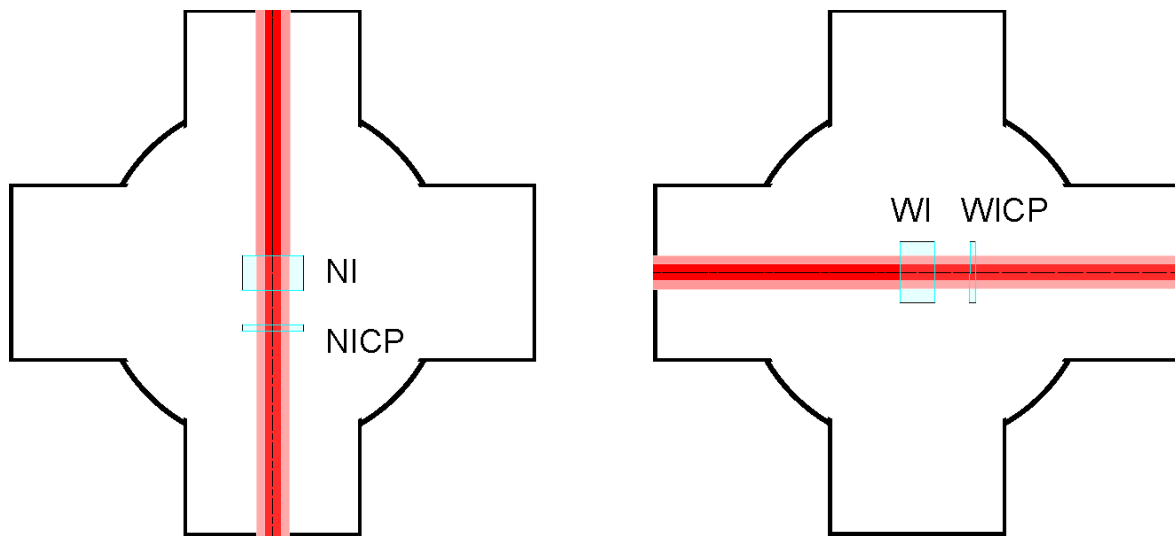


Figure 2.3: Zoom on the North arm IM and CP (left) and East arm IM and CP (right) optical layout obtained with Optocad.

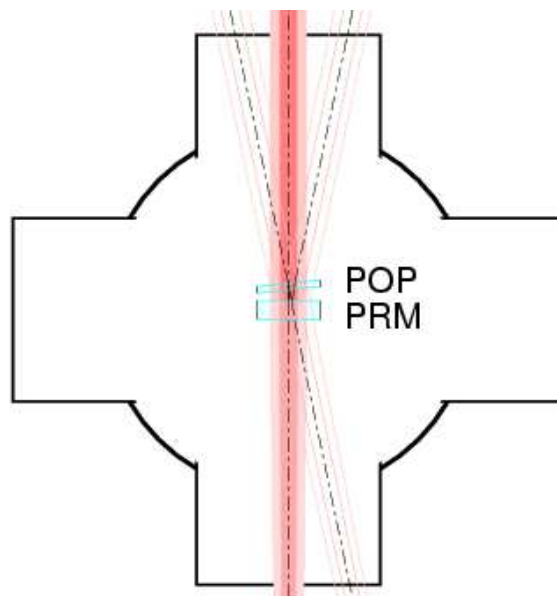


Figure 2.4: Optical layout of the PR and POP obtained with Optocad.

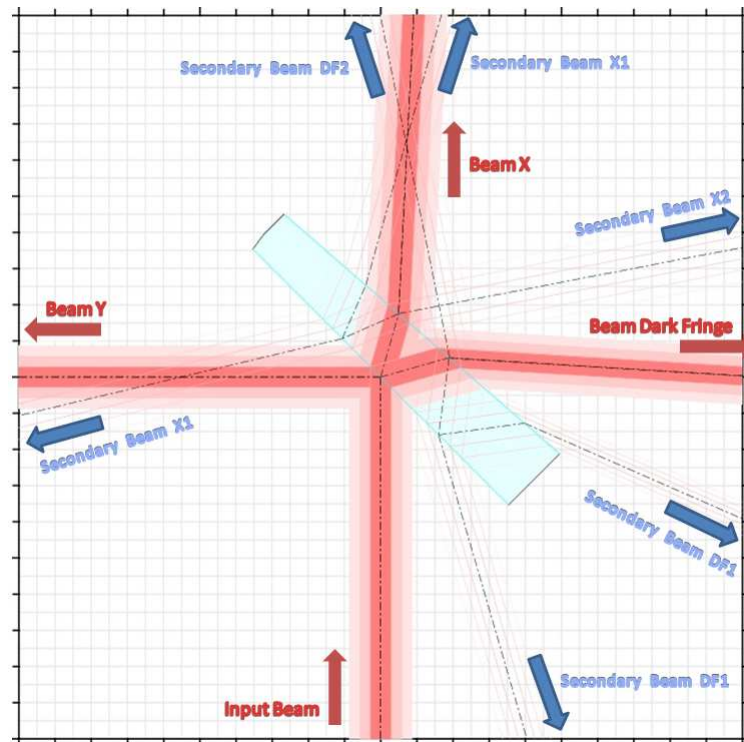


Figure 2.5: BS optical layout obtained with Optocad. The main beams (input beam, beam, beam Y, and beam dark fringe) as well as secondary beams generated by the AR second surface (secondary beam X1, secondary beam X2, secondary beam DF1 and secondary beam DF2) are shown. For this picture, the BS has been well exaggerated, in reality the secondary beams are almost parallel to the main beams.

2.3.3 Core optics characteristics

In the tables (Tables 2.6, 2.8, 2.9 and 2.7), we give for each of the core optics, the main characteristics and requirements. For the simulation works, the clear aperture is given by the diameter of the baffle around the mirror (330 mm), 10 mm smaller than the coating size.

| | | IM | EM |
|------------------------------------|--------------|---------------|--------------|
| Substrate material | | Suprasil 3002 | Suprasil 312 |
| Material absorption | [ppm/cm] | <0.3 | <3 |
| Geometry | | | |
| Thickness | [mm] | 200 | 200 |
| Diameter | [mm] | 350 | 350 |
| Wedge | [μ rad] | <3 | 1000 |
| RoC of High Reflectivity (HR) face | [m] | 1420 | 1683 |
| RoC of AR face | [m] | 1420 | >100000 |
| Coating | | | |
| Coating diameter | [mm] | 340 | 340 |
| Baffle clear aperture | [mm] | 330 | 330 |
| HR coating | | R=0.986 | T<1ppm |
| AR coating | | TBD | R<100ppm |
| Absorption | [ppm] | <1 | <1 |

Table 2.6: Parameters for the Input Mirror (IM) and End Mirror (EM) for the arm cavities. The etalon effect in the input mirror substrates will be able to compensate for asymmetry in the HR reflectivity of the IMs. So the value of the AR coating of the IM which control the amplitude of the etalon effect will only be calculated after the HR reflectivities has been measured.

| BS | | |
|---------------------|--------------|---------------|
| Substrate material | | Suprasil 3001 |
| Material absorption | [ppm/cm] | <0.3 |
| Geometry | | |
| Thickness | [mm] | 65 |
| Diameter | [mm] | 550 |
| Wedge | [μ rad] | 430 |
| RoC of HR face | [km] | >100 |
| RoC of AR face | [km] | >100 |
| Coating | | |
| Coating diameter | [mm] | 530 |
| Baffle aperture | [mm] | 500 |
| HR coating | | R=0.5 |
| AR coating | | R<100ppm |
| Absorption | [ppm] | <1 |

Table 2.7: Beam splitter (BS) parameters.

| | | PR | SR (power recycling) | SR (dual recycling) |
|-----------------------|--------------|--------------|--------------------------------|-------------------------------|
| Substrate material | | Suprasil 312 | Suprasil 312 | Suprasil 312 |
| Material absorption | [ppm/cm] | <3 | <3 | <3 |
| Geometry | | | | |
| Edge thickness | [mm] | 100 | 100 | 100 |
| Diameter | [mm] | 350 | 350 | 350 |
| Wedge | [μ rad] | <300 | <300 | <300 |
| RoC of HR face | [m] | 1430 | 1430 | 1430 |
| RoC of AR face | [m] | 3.59 | 3.59 | 3.59 |
| Coating | | | | |
| Coating diameter | [mm] | 340 | 340 | 340 |
| Baffle clear aperture | [mm] | 330 | 330 | 330 |
| HR coating | | R=0.95 | R<100ppm | R=0.80 |
| AR coating | | R<100ppm | R<100ppm | R<100ppm |
| Absorption | [ppm] | <1 | <1 | <1 |

Table 2.8: Power/signal recycling mirrors parameters. Two different versions of **SR** are given, one for the first phase of Advanced Virgo where the interferometer will run only in power recycling mode (so the transmission of **SR** is 1) and the second version is for the final configuration. SRM must always be present as it is an essential part of the output telescope due to its curved surfaces.

| | | POP | CP |
|---------------------------------|--------------|----------------|----------------|
| Substrate material | | Suprasil 312SV | Suprasil 312SV |
| Material absorption [ppm/cm] | | 0.5 | 0.5 |
| Geometry | | | |
| Thickness | [mm] | 35 | 35 |
| Diameter | [mm] | 350 | 350 |
| Wedge | [μ rad] | 1000 (TBC) | <3 |
| Tilt | [mrad] | 105 | 0.750 |
| RoC of 1st face | [km] | >100 | >100 |
| RoC of 2nd face | [km] | >100 | >100 |
| Coating | | | |
| Coating diameter | [mm] | 340 | 340 |
| Baffle diaphragm clear aperture | [mm] | 330 | 330 |
| Coating 1st face | | R=300ppm | R<100ppm |
| Coating 2nd face | | R<100ppm | R<100ppm |
| Absorption | [ppm] | <1 | <1 |

Table 2.9: POP and CP parameters. The substrates for the CPs and POP are cut out from Virgo+ IMs.

2.4 Secondary beams extraction

The so called *secondary beams* are generated by AR coated surfaces of the optics inside the recycling cavity. They need to be properly separated from the main beam to minimize noise couplings and interference with the control system. Once separated those beams are then properly dumped or extracted, to avoid stray light noise. In Advanced Virgo, secondary beams are generated by the following AR coated surfaces:

- the Input Test Mass (ITM) AR surface,
- both surfaces of the CPs
- the AR surface of the BS

In the following we will describe first the different solutions to extract the secondary beams, underlying the pros and cons. Then we will give the trade-off analysis for the optical surfaces mentioned above.

2.4.1 Extraction with large angles (> 1 deg)

A direct way to extract the secondary beams is to put a wedge large enough to separate the secondary beams from the main beam before they reach other optics. Considering the Virgo vacuum and infrastructure constraints, there are two possibilities:

- A wedge (for BS and ITMs) or an angle (for CPs) of about 6 degrees (0.1 rad). In this case it is possible to send the secondary beams directly out of the vacuum tank in which they are generated, and to extract them with a dedicated hardware.

This solution cannot be adopted for BS and ITM because it will make the main beam highly astigmatic, with a consequent reduction of the Radio Frequency (RF) sidebands recycling gain [37].

The situation for the CP is different: a tilt of the CP will not give any astigmatism, but it has been demonstrated that, if the thermal correction is applied on the CP tilted by 6 degrees, the efficiency of the correction is significantly affected with respect to a correction applied on a plate that is not tilted [40].

- A wedge (for BS and ITMs) or an angle (for CPs) of about 1.2 degrees (20 mrad) can separate the secondary beams over a distance of 6 m.

This solution cannot be adopted for BS and ITMs, for the same reason: the astigmatism introduced on the main beam is too high. For example, simulations done with SIS have shown that a BS with wedge angle of 11 mrad will be enough to reduce the sidebands gain by more than 50%.

The CP tilt by 20 mrad is possible from the TCS point of view. In this case the secondary beams can be dumped at the level of the BS tank, by the diaphragm which is planned to be around the beam splitter in order to dump diffused light (suspended to the BS superattenuator). This solution puts constraints on the aperture of the vacuum infrastructure (vacuum pipe and valves) and on the dimensions of the diaphragm around the BS.

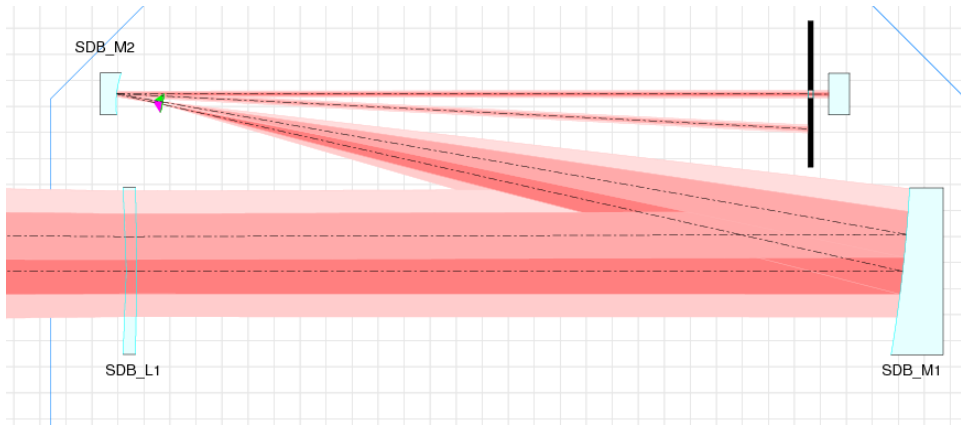


Figure 2.6: Example of a secondary beam generated by a $400\ \mu\text{rad}$ BS wedge (equivalent to a CP tilt of $720\ \mu\text{rad}$) after a realistic detection telescope of magnification 40. L1, M2 and M1 are the three telescope components (L1 is a meniscus lens, M2 and M1 are parabolic mirrors). The drawing has been done with Optocad

2.4.2 Extraction with small angles (fraction of degree)

A wedge (or an angle, for CP) less than 1 mrad can be used to separate the secondary beams from the main beam, since in this case they are almost superposed inside the central area. This means that the separation should be achieved outside the interferometer, through the injection and detection telescopes. The telescopes will reduce the size of the main and secondary beams (by a factor 40 or 20) and so at they will also increase the angular separation by roughly the telescope magnification. The secondary beams can be, in principle, dumped by a diaphragm after the injection/detection telescope. The role of the diaphragm is to block the secondary beam and to let pass the main beam (as example, see fig. 2.6).

The output telescope will reduce the beam size from 5 cm (in the central part of the interferometer) to 1.25 mm at the output. A small beam size is required to facilitate the mode matching with the output mode cleaner. On the other side, the injection telescope will have a magnification of 20. A larger beam is preferable at the input of the telescope in order to reduce the thermal lensing effect in the Faraday isolator located between the input mode cleaner and the interferometer.

In order to choose the best angles for BS, ITMs and CPs we have defined some figures of merit and some requirements:

Clipping on the interferometer mirrors The first figure of merit (FOM1) is a measurement of the light clipped by mirror apertures, since the secondary beams are not centered on the mirrors. FOM1 is defined as the sum of the power lost outside all the mirror apertures for 1 W ITF input power.

This light will be in principle absorbed, with a certain efficiency, by the diaphragm baffles around each mirrors and suspended to the superattenuators (see PAY chapter); but, we want to define a threshold for this light in order to be sure that this will not degrade the interferometer sensitivity.

The requirement is that FOM1 should be lower than the light already lost by the mirror micro-roughness scattering and surface defect, and already going towards the diaphragm baffles around each mirror or towards the vacuum pipes. A realistic value for such loss for AdV mirror surfaces has already been defined by MIR for the arm cavity mirrors and has been calculated to be 10 ppm per surface (similar to what has also been used for Advanced LIGO [39]). Assuming a recycling gain of 40 and 17 surfaces in the recycling cavity for one round-trip, the total power lost because of micro-roughness scattering in the central interferometer for 1 W input power is $10 \times 40 \times 17 = 6800 \mu\text{W}$.

In principle, following a naive approach, the light clipped on the interferometer mirrors will increase with the angle of separation between the main beam and the secondary beams, and then small angles would be preferred. We will see in the following paragraphs that the relation between the clipping loss and the angle of separation between the main beam and the secondary beams seems to be more complex.

Contamination of the dark fringe by the secondary beams The second figure of merit (FOM2) is a measurement of the contamination of the dark fringe main beam by the secondary beams. FOM2 is defined as the power of the secondary beam (for 1 W **ITF** input power) contained in the dark fringe beam after the detection telescope and after a diaphragm with a diameter of 5 times the beam radius.

The corresponding requirement has been set by ISC [41]: the secondary beam power after the output mode-cleaner should be less than $5 \mu\text{W}$ for 1 W input power. The requirement for the secondary beam before the Output Mode Cleaner (**OMC**) is in principle less stringent, since part of the secondary beam mode is not coupled with the output mode-cleaner fundamental mode. However, as safety factor we consider here that the coupling between the secondary beam and the **OMC** is 1, and we keep the requirements above.

Constraints from the injection/detection telescopes In addition to the figures of merit described above, the separation between the secondary beams and the main beams should be possible with the injection/detection telescope. In particular, since the secondary beams are not centered on the telescope optics, the separation angle should be low enough to allow the secondary beam to stay within the telescope optics apertures (see for example fig. 2.6).

Simulation of secondary beams with small angles Since the angle is very small, the secondary beams in this case do not directly leave the recycling cavity, but experience several roundtrips before going outside the mirror apertures and so could interfere with themselves. This means that simple models, or ray tracing simulations cannot be used to understand the secondary beam shapes and power.

Three FFT propagation optical simulations (DarkF, OSCAR and FOG) have been used therefore to compute the figures of merit.

We briefly describe the main features of these simulations at the time of this OSD-FDR chapter release. The work continues to develop more realistic simulations however we do not expect major changes from the results presented in this section.

- DarkF can use a rectangular grid with different resolution in x and y to deal with high wedge values (for BS or CP) and can simulate a dual recycled interferometer.
- FOG uses a power-recycling Michelson interferometer configuration. The signal recycling cavity is not simulated, but the signal recycling mirror aperture is simulated for the computation of the clipping losses. It uses a rectangular grid, which allows an higher resolution in the plane of the secondary beams, and then it can simulated angles up to 1 mrad.
- OSCAR uses a dual-recycling Michelson interferometer configuration. Full 2D simulations with a rectangular grid (different resolution along the x/y directions) has been implemented to simulate CP tilt with large angles. Recently, OSCAR has also been able to simulate the input and output telescopes of Advanced Virgo.

Angle of separation between the main beam and the secondary beams The angle of separation between the secondary beam and the main beam is related to the wedge/angle, by the relations:

- For a BS wedge angle of α , the angle of separation is $2 \times \alpha \times \sqrt{2n^2 - 1}$
- For an IM wedge angle of β , the angle of separation is $2 \times \beta \times n$
- For a CP tilt angle of γ , the angle of separation is $2 \times \gamma$

Where $n=1.44963$ is the refraction index of fused silica [38]

In the following we analyze the extraction of the secondary beams from the three optical components (CPs, BS, and ITMs).

2.4.3 CP secondary beam extraction

As already discussed, the extraction of the CP secondary beams can be made in two ways: with a small (<1 mrad) or with a large (1 deg) tilt. The CPs cannot be parallel to the ITMs, since otherwise they will disturb the alignment control [42].

2.4.3.1 Extraction through small tilt

As explained before, FFT simulations have been performed to compute the figures of merit for the secondary beams generated by a tilt of the CP. One of the two AR surfaces (AR reflectivity of 100 ppm) of one of the two CPs have been simulated. Figure 2.7 shows a scan of the CP tilt between 0.1 and 1 mrad obtained with OSCAR in the power recycling and dual recycling configurations.

In the case of the power recycling configuration, the simulation results show a big decrease in the clipping loss as a function of the tilt angle, with a minimum around around 700-800 μ rad. In this region the losses are below 1 μ W, more than three order of magnitudes lower than the requirements given by the micro-roughness and surface defect of the surfaces.

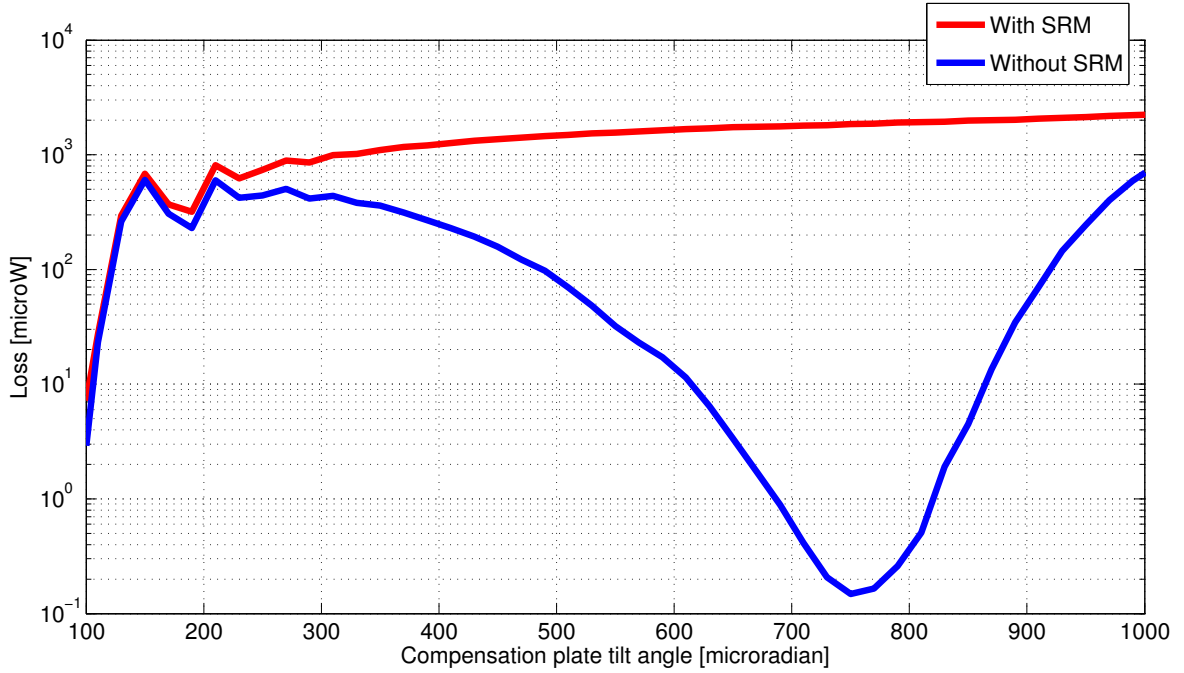


Figure 2.7: OSCAR simulations of FOM1 (power lost by clipping on all the interferometer mirrors for 1 W ITF power) versus the CP tilt. FOG and DarkF simulations give similar results.

The dip in the loss is due to the Schnupp asymmetry which induces different phase shifts for the pick off beams traveling in the north and west Michelson arms. For a CP tilt around 750 μrad , the difference of phase shift between the tilted pick off beams traveling in the two arms is π , resulting in destructive interference toward the power recycling mirror. As the result, the pick off beams power does not build up and the beams exit directly through the dark port. Simple analytical model has been used to confirm the position of the dip.

For the dual recycling configuration, the clipping loss is much higher and the previous dip in the loss is no longer present. That is because the pick off beams can no longer exit directly through the dark port and must circulate in the power and signal recycling cavity. The clipping loss for a CP tilt of 750 μrad is slightly less than 2000 μW . So in the case of dual recycling the total amount of light hitting the baffles in the central area will be of the same order as the scattered light from the surface optics.

The corresponding images of the circulating beams on the PR and SR for 750 μrad wedges are reported in fig.2.8. In those images, both the (on axis) main beam and the (off axis) secondary beams are present.

The reflected and dark port beams are propagated through a telescope of magnification respectively 20 and 40 and imaged 50 cm after the telescope. In order to quantify the separation between the main beams and the secondary beams (FOM2), a second simulation is done only with the main beam (the 100 ppm of reflection of the BS AR coating is replaced with 100 ppm absorption). The complex field of this second simulation is subtracted from the first, so at the end, only the pick off beam can be displayed. The power of the secondary

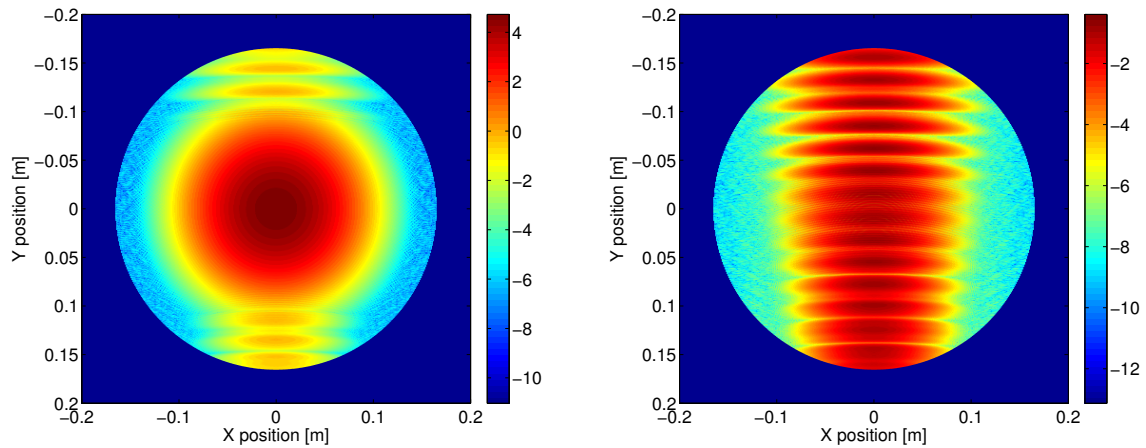


Figure 2.8: Circulating fields in the power recycling cavity (left) and on the dark port (right) for a CP *vertical* tilt of $750 \mu\text{rad}$. This figure is the results of simulations of Advanced Virgo (dual recycling) done with OSCAR and displayed with log color scale. The main beam on axis beam has not been subtracted. The field on PRM is dominated by the on axis field circulating in the PRC whereas the dark port field is mainly constituted by the secondary beam (which is the sum of two beams propagating at opposite angle).

beam within an aperture of diameter 5 times the beam radius centered around the main beam is finally computed to deduce FOM2.

Figure 2.9 shows the result of FOM2 versus the CP tilt computed by OSCAR for a power recycling and dual recycling interferometers. As expected, the global trend is clear: the contamination of the dark fringe with the secondary beams decreases as the CP tilt increases. As the tilt angle of the secondary beams increases, the spatial separation between those beams and the main beam becomes larger and larger at the output of the telescope.

It is also interesting to note that the decrease in FOM2 with the increase of the CP tilt is slower in the case of the ITF reflection than at the dark port. That is a direct consequence of the difference of magnification between the injection and the detection telescope. Since the magnification for the output telescope is twice that of the input, the diaphragm aperture at the detection is two times smaller and at the same time, for a given CP tilt the separation between the pick off and the main beam after the telescope is two times larger at the detection compared to the injection.

In the CP tilt region of interest between 700 and $800 \mu\text{rad}$, FOM2 for one AR side of one CP is $0.04 \mu\text{W}$ for the power recycling Michelson configuration and $0.8 \mu\text{W}$ for the dual recycling. Since in total we have 4 CP surfaces, FOM2 is always below the limit of $5 \mu\text{W}$ [41].

It is possible to find the power from the pick off beams even before the telescope. It is found that at the dark port, the power in the secondary beams is more than two times smaller with signal recycling than without [43]. That is coherent with the fact that with signal recycling more power of the secondary beams is clipped inside the central interferometer (see figure 2.7) so the secondary beams leaving the interferometer at the dark port and in reflection are globally less powerful. However that does not necessary mean that the dark fringe contamination (FOM2) must be smaller with signal recycling since the shape of the

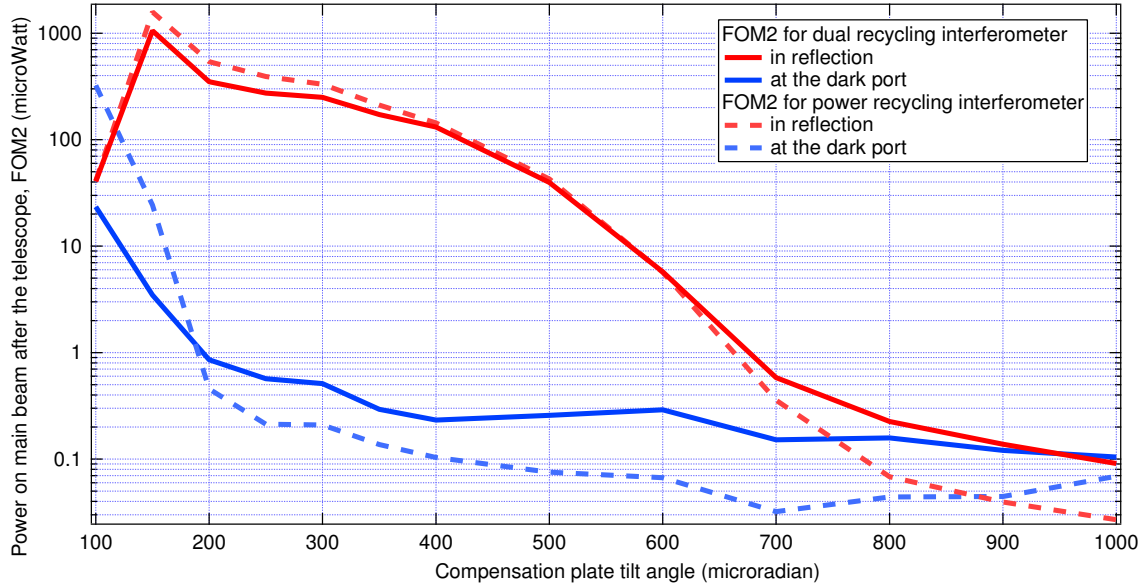


Figure 2.9: OSCAR simulations for power recycled and dual recycling interferometers of FOM2 (dark fringe contamination) versus the CP tilt. For the simulations, only one side of one of the two CPs has been included. The FOM2 limits from all the pick off is $5 \mu\text{W}$.

secondary beams is altered by the presence of the signal recycling mirror [45].

For a CP tilt in the range of 700-800 μrad , most of the pick off leaving the interferometer is at the dark port. For example without signal recycling, the power of the pick off at the dark port is 25 times greater than the pick off power in reflection. That explains why even if the telescope in reflection has a smaller magnification than the detection one, FOM2 is still on the same order in reflection and at the dark port.

The images after the telescope for a CP tilt of 750 μrad are shown in figure 2.10 for both in reflection (top) and at the dark port (bottom). On those pictures, the main beam has been subtracted, so only the pick off beam is present. The difference between the two plots is well explained by the difference of magnification between the injection telescope ($\times 20$) and the detection one ($\times 40$).

An estimation of the power lost by clipping on the optics of the output telescope has also been computed using OSCAR. The losses are negligible for the on axis main beam but they can become substantial for the tilted pick off beams which can hit the telescope optics off center. It was found that on the four optics composing the output telescope (SR, SDB L1, SDB M1 and SDB M2 as shown in figure 2.6), the losses are dominated by the two central optics: the lens SDB L1 and the parabolic mirror SDB M1. For a CP tilt of 750 μrad , 1W of input power, for the clipping loss to be less than 1 μW on SDB L1 and SDB M1, the optics must have a diameter superior to 140 mm [44].

2.4.3.2 Extraction through 20 mrad tilt

The extraction of the CP secondary beams is possible through a tilt of about 20 mrad. In this case the secondary beams make no roundtrip in the recycling cavity and should be directly

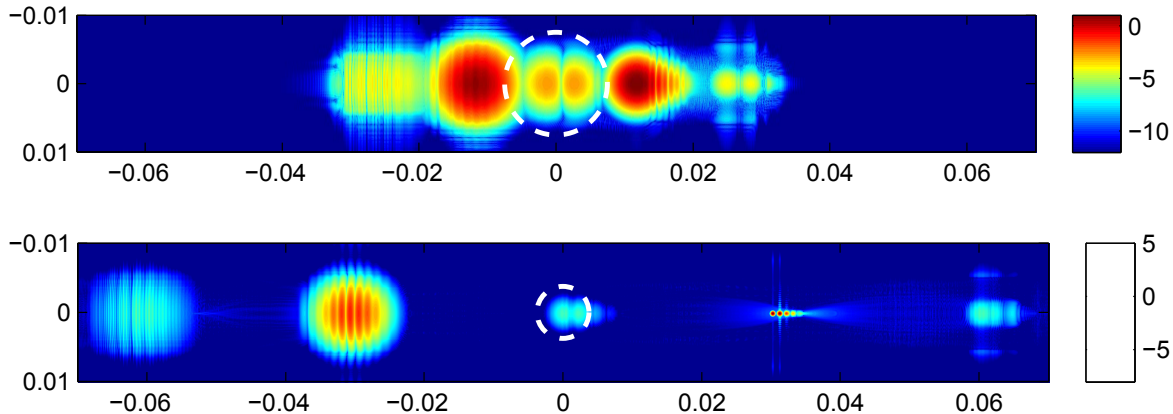


Figure 2.10: Image in amplitude and log scale of the pick off beam in reflection of the interferometer (top) and at the dark fringe (bottom) for a CP tilt of $750 \mu\text{rad}$. Both images are taken 50 cm after the last mirror of the telescope where a diaphragm (represented by the white dashed circle) will be inserted.

dumped by a baffle around the BS and suspended to the BS superattenuator. The potential advantage of this solution is that this will avoid the proliferation of secondary beams on the injection/detection telescopes. The drawback is that it requires a larger vacuum aperture (with respect to the one requested for the only main beam) and a larger BS baffle.

Conclusions: The reference solution to extract the secondary beams from the CP is a tilt of about $750 \mu\text{rad}$. The profile of the loss as a function of the CP tilt is understood and OSCAR and FOG have similar results, giving us confidence in our results. This tilt angle of $750 \mu\text{rad}$ is compatible with the requirements of light lost by clipping and dark fringe contamination with and without signal recycling mirror. Simulations are still on going to confirm these results with all the four CP AR surfaces included.

In the reference configuration, the CP tilt is vertical, so the secondary beams are in the vertical plane (however the simulations were done indifferently in the vertical or horizontal planes since the problem has a cylindrical symmetry). The possibility to tilt the CP in the other directions (for example in diagonal), is also being explored. This would allow to identify the various secondary beams and, if possible, use them for diagnostic purposes.

2.4.4 BS secondary beam extraction

As already discussed, a wedge of the order of 1 degree (or higher) will introduce an important astigmatism on the main beam. **The only possibility to extract the BS secondary beams is then to have a small ($<1 \text{ mrad}$) wedge on the BS.** We have then studied the best value of the wedge in terms of the three requirements defined above.

Thanks to recent progress in simulation development and the use of rectangular grid with different resolutions along the vertical and horizontal axis, it is now possible to achieve simulations with scan of the beamsplitter wedge angle.

The result for FOM1 (sum of power clipped on all the interferometer mirrors for 1 W ITF power) with DarkF is shown in the figure 2.11 for power recycling and dual recycling inter-

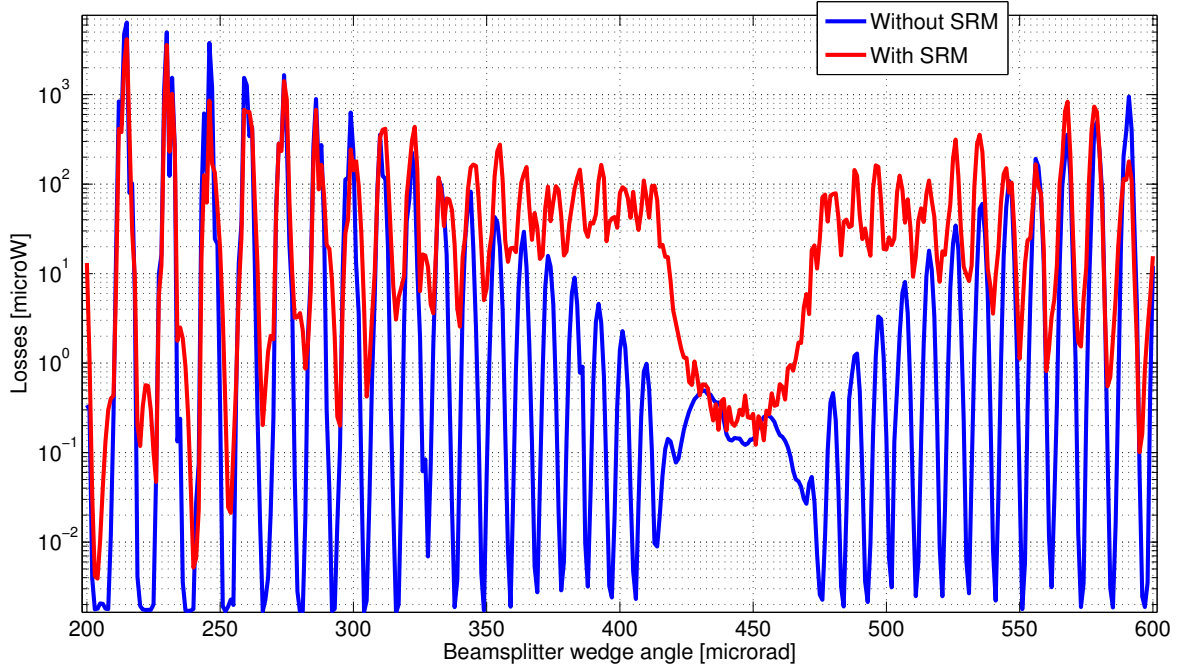


Figure 2.11: DarkF simulation of FOM1 for power recycled and dual recycled interferometer. FOM1 (power lost by clipping on all the interferometer mirror for 1 W ITF power) for a BS wedge from 200 μrad to 600 μrad .

ferometer.

We notice that for certain angles the clipping can be enhanced by orders of magnitude; this is in correspondence with the resonance of the secondary beams inside the recycling cavity. That happens since the secondary beams from the **BS AR** sides are mode matched with the mirrors of the power recycling cavity (it was not the case for the secondary beams from the **CPs**). Similar results were also found by FOG. Since the precision on the wedge value is about 50 μrad , it is not possible to select a wedge angle to avoid such resonances and so region with rapid variation of loss should be avoided.

Figure 2.11 shows that the region around wedge angles of 430 μrad presents a minimum in loss. This behavior is similar to what has been found for the CP as shown in figure 2.7. The value of BS wedge of 430 μrad corresponds to a separation angle between the main beam and the secondary beams of 1540 μrad , equivalent to the one produced by a CP tilted by 770 μrad , tilt value where we have the minima in loss. Since for 430 μrad FOM1 is also much lower than the requirements given by the micro-roughness (7000 μW), we select this value for the BS wedge.

The corresponding images of the secondary beams on the **PR** and **SR** for 400 μrad wedges are reported in figure 2.12.

In order to compute FOM2, the near fields of beams through the PR and SR mirrors are propagated through a telescope of magnification 20 and imaged 50 cm after the telescope. In order to quantify the separation between the main beams and the secondary beams, (FOM2) a second simulation is done with only the main beam (the 100ppm of reflection of the BS AR coating is replaced with 100 ppm absorption). The complex field of this second simulation

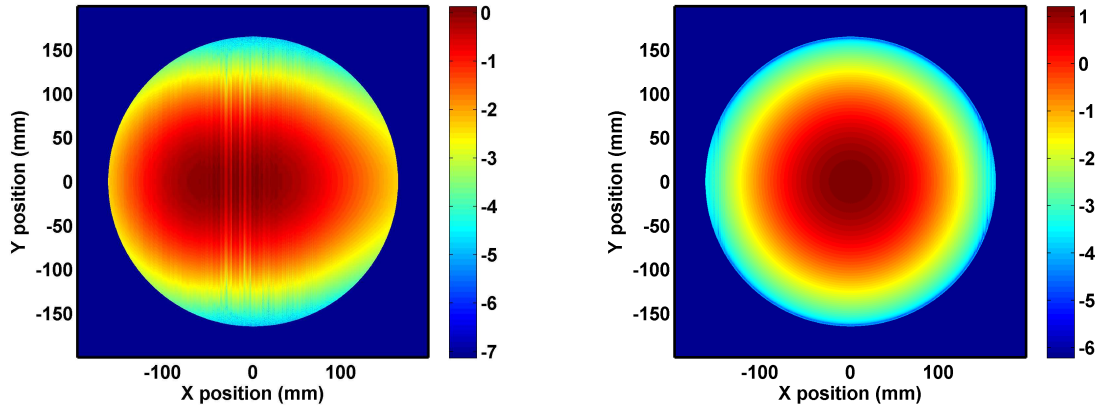


Figure 2.12: FOG simulation (power recycled interferometer, including SR mirror aperture). Image in amplitude and log scale of the SRM (up) and PRM (down) for a for a BS wedge of $400 \mu\text{rad}$. The main beam is not subtracted.

is subtracted from the first. The power inside 5 times the beam radius centered around the main beam is finally computed.

The simulations were done with an output telescope of magnification 20 (former design), whereas in the baseline design the magnification will be 40 (as used for the CP tilt simulations). Due to lack of time, we were not able to update the results. However if the main beam and the secondary beam are already enough separated with a telescope of magnification 20, increasing the magnification can only improve FOM2.

The images are shown in figure 2.13 (for the antisymmetric port) and in figure 2.14 (for the symmetric port). On the left, figure containing the main beam are shown, on the right figures containing only the secondary beams. The diaphragm with a diameter of 5 times the beam radius is indicated with a dotted circle.

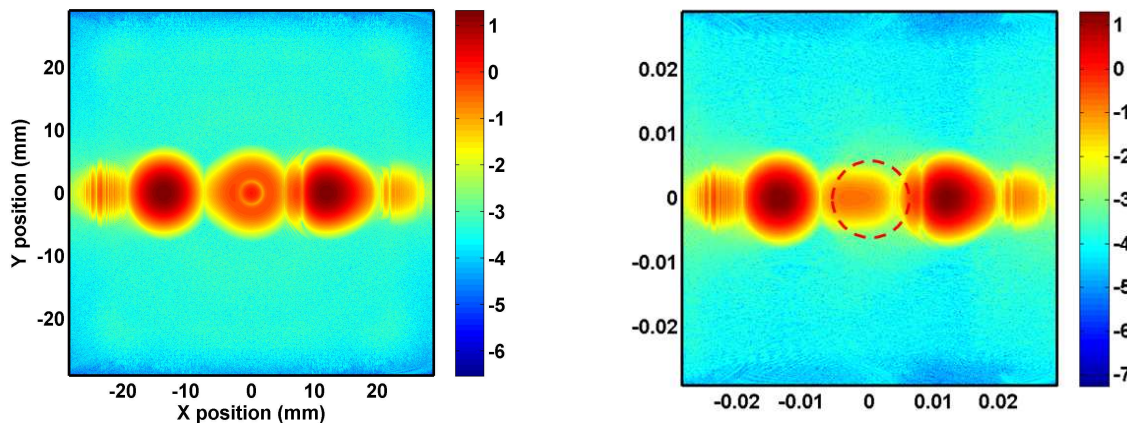


Figure 2.13: FOG simulation. Image in amplitude and log scale of the antisymmetric port (dark fringe) after a telescope of magnification 20 and 50 cm propagation for a BS wedge of $400 \mu\text{rad}$. Left: secondary beam + main beam. Right: only secondary beams

For a BS wedge of $400 \mu\text{rad}$, The value computed by FOG for FOM2 is a fraction of μW ,

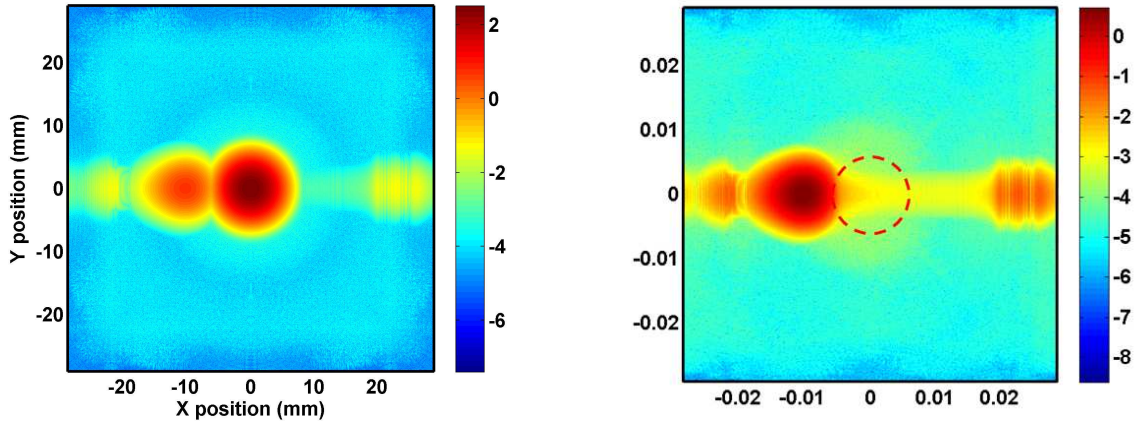


Figure 2.14: FOG simulation. Image in amplitude and log scale of the symmetric port (ITF reflection) after a telescope of magnification 20 and 50 cm propagation for a BS wedge of $400 \mu\text{rad}$. Left: secondary beam + main beam. Right: only secondary beams

less than the requirement for the dark fringe contamination ($5 \mu\text{W}$, [41]).

Conclusions: The reference solution to extract the secondary beams from the BS is a wedge of $430 \mu\text{rad}$. This value seems compatible with the requirements of clipping of the interferometer mirrors and dark fringe contamination. Simulations are still on going to confirm the value of FOM2 in presence of signal recycling.

The BS wedge is horizontal whereas the CPs tilt is vertical. So after the detection telescope, the secondary beams from the BS and CPs can be separated. The secondary beam from the BS, called B5 is used for example for the alignment of the OMC.

2.4.5 Secondary beams from ITMs and choice of the ITM AR face geometry

The interest to have an etalon effect on the ITMs has been pointed out by ISC and it has been considered a guideline for the design. In the current design, the two surfaces of the ITMs are then parallel, with a curvature of 1420 m. This choice has the advantage that there are no secondary beams from the AR face.

This choice is not possible with the current metrology. In order to measure the sub nanometer RMS precision needed for the test masses HR surfaces, the substrate should have wedges of at least 1 mrad, to avoid the contamination of the HR surface maps. A new metrology, based on the *wavelength shifting interferometry* allows to measure sub nanometer surfaces without the necessity to put wedges. The direct drawback of this solution is a cost increase.

Conclusions: in the current solution there are no secondary beams from the ITMs. If a 1 mrad wedge is needed for metrology reasons, the corresponding simulations should be performed (FOM1, FOM2 and clipping on the telescope mirrors). These simulations are not yet performed since computation with these large wedge needs high computational power and time.

Note: If the reference solution is changed after the project tradeoff and the 1 mrad solution

is eventually chosen the following parameters of the optical design described in this report must be changed:

- Position of the towers (< 1 cm)
- RoCs of the PR/SR mirrors. If the input mirror wedge solution is selected, the AR face of the ITMs will be flat. In that case the PR and SR RoCs will be around 1 km instead of 1.4 km.

2.5 Extraction of the pickoff beam used for ITF control

One pickoff beam in the central interferometer is required for the alignment and longitudinal control. This pickoff beam will be used for **BS** alignment and MICH longitudinal controls (see ISC chapter).

Two solutions have been studied to extract the pickoff and then discarded:

- The use of one of the beam generated by the **CP**, tilted of 6 deg. This solution has been discarded for two reasons: (1) it has been demonstrated that, if the thermal correction is applied on the **CP** tilted by 6 degrees, the efficiency of the correction is significantly affected with respect to a correction applied on a plate that is not tilted, (2) space constraints become a serious issue as many systems have to be installed at the same location: pickoff optical setup, Hartman wavefront sensing, thermal correction projection on the **CP**.
- The use of one of the secondary beam generated by **BS** or **CP** with a small (< 1 mrad) angles. This solution has been discarded, since various studies have showed that the error signals generated by these beams have spurious offsets larger than the required locking accuracy. This option has then been discarded.

Therefore it has been decided to add a plate tilted by 6 degrees and located close to the power recycling mirror (see optical layout on fig.2.4 and opto-mechanical drawing on fig.2.15). This plate is called the **POP**. Adding an extra plate requires an extra effort of construction (its opto-mechanical design is essentially a copy of the **CP**) and increases the optical losses budget of the recycling cavity. But, this choice has also some advantages:

- the pickoff beam optical setup will be on the common part of the interferometer where possible noise couplings are much less important than on the differential part. The fact that the **POP** is an opto-mechanical copy of the **CP** should guarantee that the noise introduced by this plate is lower than the noise introduced by the compensating plates
- at this location, the **POP** can be used to inject both the Hartman beams to sense the aberrations of the optical path to North Input (**NI**) and to West Input (**WI**) (see TCS chapter)
- the pickoff plate can potentially be used as an extra **TCS** actuator (for example to correct for common aberrations while the **CPs** can be used to correct for differential aberrations)

The secondary beams generated by the **POP** will be directed to an optical bench which will be suspended and in vacuum. This optical bench will be significantly similar to the ones in transmission of the arm cavities. The wedge of the **POP** is not yet confirmed (so far, the simulations were done for a wedge of 1000 μ rad). The **POP** will have a wedge to guarantee that the beams reflected from its two sides are well separated on the pick off bench. The separation of the two beams on the bench depends on the magnification of the telescope which has not been designed. As soon the telescope for the pick off is known, we can recalculate the suitable **POP** wedge angle and if necessary updates the mirror positions.

The required reflectivity for the **POP** is 300 ppm.

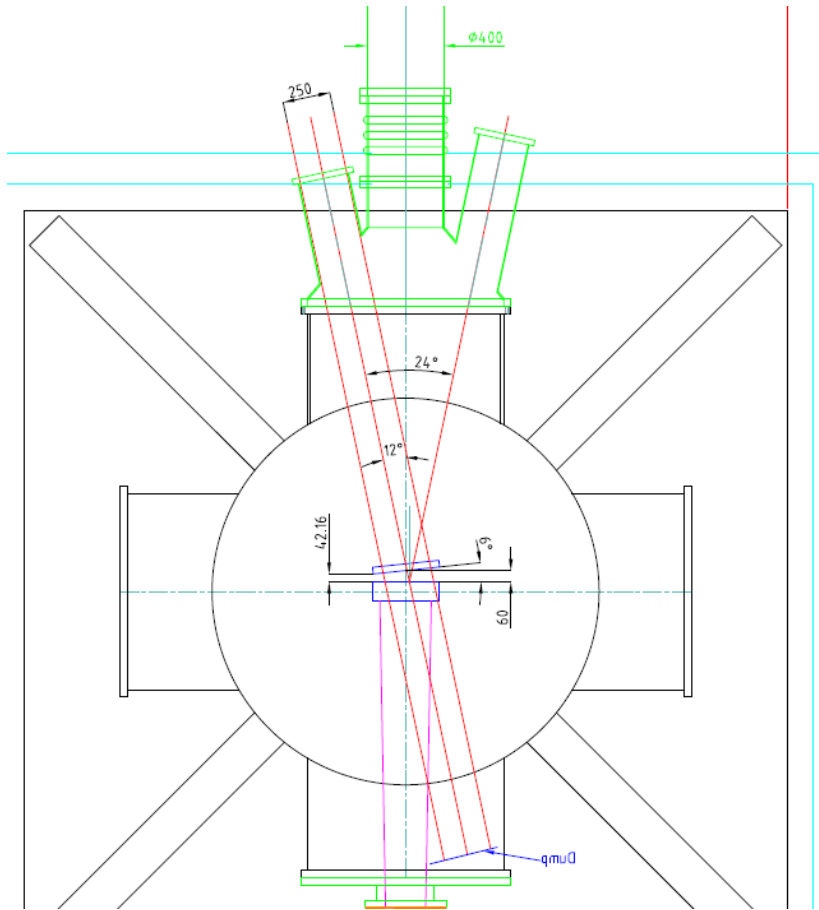


Figure 2.15: Opto-mechanical design of the POP

2.6 Arm-cavity design

2.6.1 Bi-concave geometry

The arm cavities have a bi-concave geometry, with each test mass mirror having a concave radius of curvature of slightly larger than half the arm cavity length. Such a near-concentric resonator configuration is chosen for two principle reasons: (1) to increase the beam size at the mirrors, thus averaging over a larger area of the mirror's surface and reducing the relative contribution of mirror coating thermal noise, and (2) to limit the effect of radiation-pressure induced alignment instabilities [46].

This type of topology means that the cavity waist is near the middle of the arm cavity. Having different radii of curvature for the two cavity mirrors displaces the waist toward the mirror with the smaller radius of curvature, and the beam size on that mirror is also reduced. This can actually cause an increase in detector sensitivity, as the input mirror will have fewer coating layers and so its coating thermal noise contribution is actually slightly smaller for identical beam sizes on the two mirrors. We thus choose to have the End Test Mass (**ETM**) with a larger radius, and thus larger beam size, than the **ITM**.

2.6.2 Choice of the RoCs

Several competing factors must enter the decision. These include mirror thermal noise, cavity stability, clipping losses as beams become larger, and tolerance to manufacturer errors in mirror production, which can limit the cavity stability in the cold (uncorrected) state. Figure 2.16 shows the consequences of changing the mirror radii of curvature, for the easily illustrated case of a symmetric cavity. Increasing the radius of curvature decreases the spot size on the mirror, and thus reduces detector sensitivity. Conversely, decreasing the radius of curvature increases sensitivity, until the spot size becomes too large for the mirror and clipping losses become important.

The **RoCs** should also be chosen in such a way as to minimize the accidental degeneracy of higher-order-modes in the arm cavities. We thus choose an average radius of 1551 m, which means the cavity mode is situated directly between higher-order-mode degeneracies of order 8 and 9. Next, as described above, we reduce the **ITM RoC** and increase the **ETM RoC** to minimize the impact of mirror thermal noise while also keeping the clipping losses low by limiting the final beamsizes on the **ETM**. This procedure yields mirror radii of 1420 m for the **ITM** and 1683 m for the **ETM** [47]. The resulting parameters are included in table 2.1.

2.6.3 Absolute RoC tolerances

For **RoCs** of approximately 1 km, we expect manufacturer errors of around 1%, perhaps slightly less. To guarantee the required optical performance, even more stringent requirements on the **RoCs** may be necessary. In this paragraph we confirm the choice of the **RoC** through FFT simulation and we compute the absolute tolerances.

With realistically imperfect mirrors, the errors in the surface flatness can excite higher-order-modes (**HOMs**) in the arm cavities. The excitation of **HOMs** has a number of undesirable

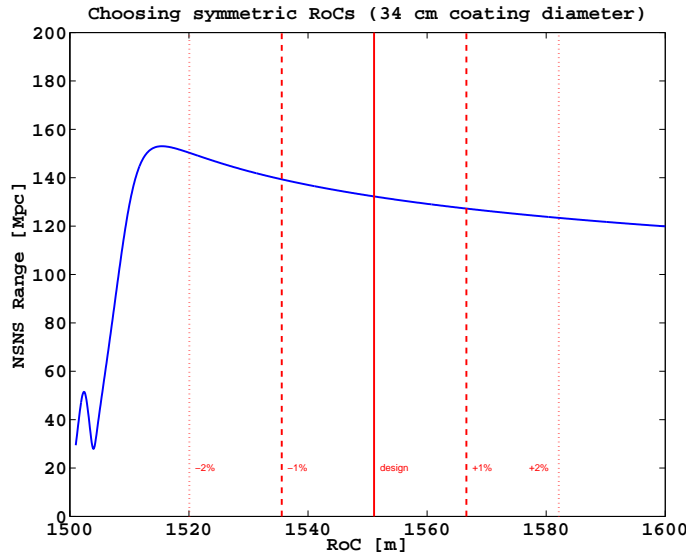


Figure 2.16: Small changes in the main test mass mirror radii of curvature can have a significant effect on the detector sensitivity. This figure depicts the average **RoC** of the IM and EM, because variations in this quantity have the most severe effect on sensitivity. The arm cavity is perfectly unstable at **RoC** = 1500m, but clipping losses in the naive calculation will begin to severely limit detector performance at **RoCs** < 1515m. Losses in realistic cavities can become important for even larger **RoCs**.

effects:

- Increased clipping losses in arm cavity reducing cavity power.
- **HOMs** on dark fringe increasing contrast defect.
- **HOMs** generating noise on alignment signals

The main criteria for the absolute **RoC** tolerances is to ensure that these effects are kept to an acceptable level, or at least to minimize them.

To study the clipping losses as a function of mirror **RoC** in the presence of realistic mirror imperfections we use the FFT codes OSCAR and FOG to simulate an arm cavity with randomly generated mirror maps having the same power spectral density of defects as an Advanced Virgo mirror with corrective coating. Figure 2.17 shows the measured round trip losses when changing the radii of curvature of the cavity mirrors from their nominal values.

We clearly see the increase in round-trip losses below and above the nominal ac**RoC** due to clipping losses of the excited **HOMs**. We set the requirement that the round-trip losses must not increase by more than 10% from their nominal value. Using the results of figure 2.17 we may therefore set a **RoC** tolerance of ± 2 m for each mirror.

This level of precision likely exceeds the current manufacturer capabilities, and so it must be ensured by the **TCS** system (see **TCS** chapter). Since a polishing precision of ± 10 m around the central value is compatible with the foreseen **TCS** dynamics, we set the polishing specification as ± 10 m, and the **TCS** system will make up the difference between this polishing specification and the optical requirement. In our simulations, we did not yet include the change of the **RoC** due to the coating process since research are still ongoing to improve the

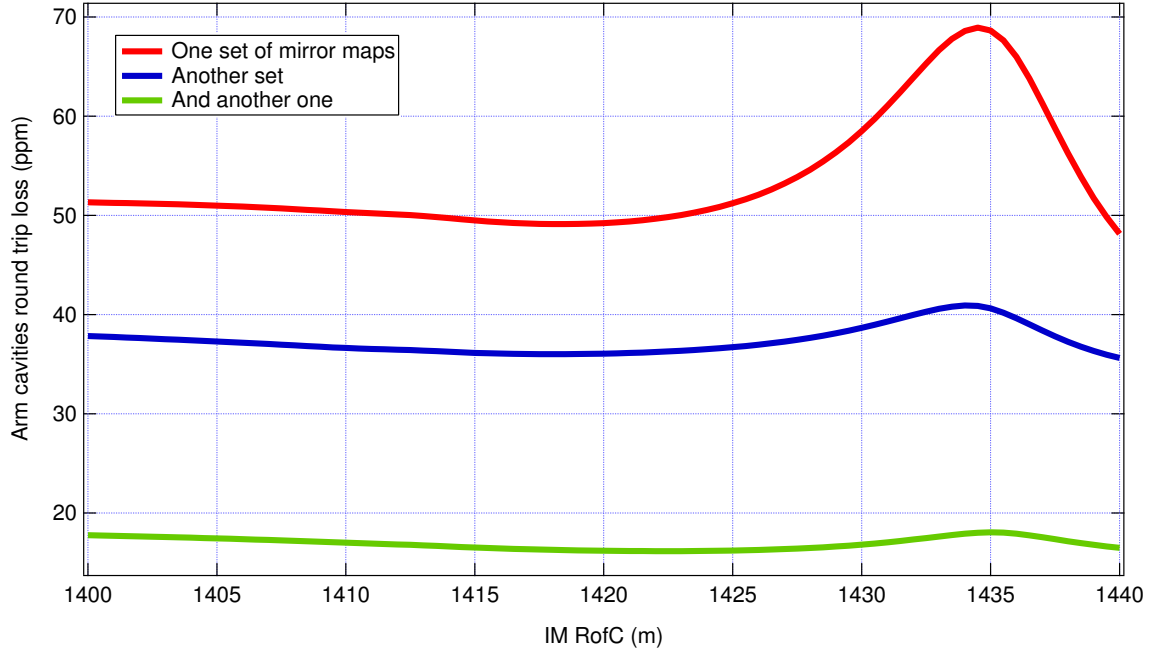


Figure 2.17: Round trip losses as a function of arm cavity radii of curvature using random Advanced Virgo mirror maps as done with OSCAR. Each curve corresponds to a different pair of random maps. Since the cavity is symmetric, a scan of the cavity end mirror give the same result.

coating uniformity. Realistic value for the **RoC** change will be known when the Advanced LIGO mirrors will be coated or when the planetary system will be tested.

The summary of the specifications are in table 2.11.

A **RoC** asymmetry between the two arm cavities will result in excess Laguerre-Gauss modes on the dark fringe. A second specification is also given to ensure that all the mirrors **RoC** are within 5 m of each other.

2.6.4 Finesse

In initial detectors such as Virgo and LIGO the choice of arm cavity finesse, and thus the arm cavity input mirror transmissivity, was a critical factor in determining the sensitivity of the detector: the finesse, in combination with the arm length, uniquely determined the detector bandwidth and frequency response.

For Advanced Virgo, which will use the signal recycling technique, the detector response will vary with the arm cavity input mirror transmissivity, the signal recycling mirror transmissivity, the signal recycling cavity length, and the circulating power. This combination of factors means that the detector bandwidth depends only weakly on the specific choice of arm cavity finesse, since changes in the arm cavity input mirror transmissivity can be compensated by changing one of the other parameters.

Factors other than the ideal sensitivity curves thus drive the choice of arm cavity finesse. These factors include thermal loading in the central interferometer, length noise coupling

from auxiliary degrees of freedom, and the relative impact of losses in the arm and signal recycling cavities. Details of the trade off studies can be found in [47].

We choose a value of finesse around 450. This represents a decrease from the previous design by a factor of 2, and is chosen because sufficient investigation of the resulting increased thermal load in the central interferometer has already been done, lending confidence that this value is still safe. The resulting input test mass mirror transmission is in table 2.1.

2.7 Recycling cavities design

The recycling cavity are marginally stable. This means that the high-order modes can resonate at the same time as the fundamental one, since the Gouy phase accumulated during the free space propagation inside the recycling cavity is not enough to separate the various modes.

This situation is similar to Virgo, but in Advanced Virgo the increase of the beam size from about 2 to 5 cm decrease the Gouy phase and then enhances the degeneracy. This explain why, according to the simulations, the marginally stable power recycling cavity is more sensitive to interferometer imperfections and thermal effects than the Virgo power recycling cavity [48, 49].

2.7.1 Choice of the RoCs

The RoCs of the power and signal recycling mirrors are determined by the arm-cavity RoCs and by the curvature of the AR surfaces of the ITMs. They are chosen to phase match the beam coming from the arm-cavities. The values are reported in table 2.8.

2.7.2 Power recycling cavity finesse

In the presence of realistic limits on the laser power and optical losses in the interferometer, the best use of available laser power would mean choosing the power recycling mirror transmittance such that the interferometer is critically coupled, so that the circulating power is maximised. Such a choice however reduces the strength of several signals in reflection from the interferometer which are needed to control the power-recycling cavity length and alignment. We thus choose a transmittance of the power recycling mirror higher than the one for optimal matching (i.e. maximum circulating power). Furthermore, lowering the finesse of the power recycling cavity lowers the susceptibility of the cavity to optical aberrations (see section 2.9, [63]). We thus choose a power recycling mirror transmission of 5%, which yields a power recycling gain of 37.5 with round-trip losses in the power recycling cavity of 1500 ppm as detailed in the table 2.10.

Not all the losses described in 2.10 create scattered light in the power recycling cavity. In fact the dominant loss is from the POP whose two secondary beams will be properly dumped outside the cavity. Only the light scattered by the surfaces (170 ppm) and a fraction of the secondary beams will be lost inside the recycling cavity. The quantity of the secondary beam hitting the baffles around the mirrors will depend on the presence or not of the signal recycling mirror as explained in 2.4.3.1.

| Loss origin | Loss per round trip [ppm] |
|--------------------|---------------------------|
| POP HR | 2×300 |
| POP AR | 2×100 |
| 2 CPs | 2×200 |
| BS AR | 100 |
| Surface scattering | 17×10 |
| Absorption | 40 |
| Total Loss | 1510 |

Table 2.10: Estimated loss budget in the power recycling cavity. The losses are defined per round trip and are equivalent to loss defined in the common path, so between PR and BS.

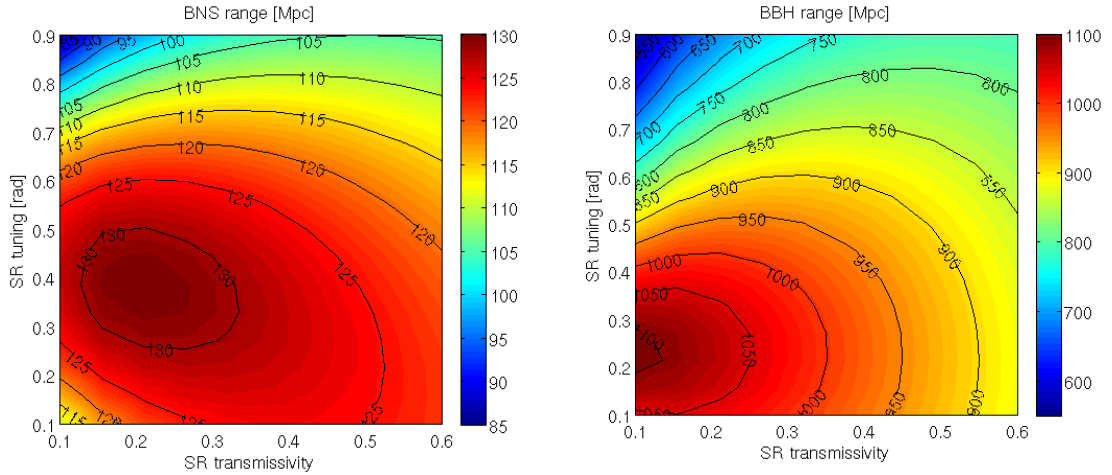


Figure 2.18: BNS inspiral range (left) and BBH inspiral range (right) shown as functions of the signal recycling mirror transmission and the signal recycling cavity detuning phase. We choose a signal recycling mirror transmission of 0.2 and a detuning of 0.35 radians.

2.7.3 Signal recycling cavity finesse

With the arm cavity input mirror transmittance of 1.4%, we can choose the recycling mirror transmittance to optimize the detector sensitivity to astrophysical sources (see [51] for a discussion). Using GWINC to calculate the inspiral ranges, we choose the signal recycling mirror transmittance as a compromise between the following trade-offs: optimized sensitivity to BNS inspirals, optimized sensitivity to Binary Black Holes (BBH) inspirals, and optimized sensitivity in a broadband (zero detuning) configuration. Figure 2.18 (from [50]) shows the ranges for BNS and BBH for different values of the signal recycling mirror transmission. A signal recycling mirror transmission of 20% with a detuning of 0.35 radians is near the maxima of both the BNS and BBH ranges, with an emphasis on the BNS range. Moreover, a 20% SRM also yields a good range for both BNS and BBH even with zero detuning. We thus choose a SR transmission of 20%.

| RoC | Central value [m] | Polishing error [m on \varnothing 150 mm] | Absolute error (after TCS) [beam-weighted m] |
|-----|----------------------|--|---|
| ITM | 1420 | ± 10 | ± 2 |
| ETM | 1683 | ± 10 | ± 2 |

Table 2.11: Test mass mirror HR side RoC specifications

| Property | Spatial frequency [m^{-1}] | Specification [nm] | \varnothing [mm] |
|---------------|---------------------------------------|--------------------|--------------------|
| RMS flatness | $50 < f < 1000$ | < 0.15 | 150 |
| RMS flatness | $f < 1000$ | < 1.5 | 150 |
| RMS flatness | $f < 1000$ | < 3 | 300 |
| RMS roughness | $f > 1000$ | < 0.1 | 150 |

Table 2.12: Mirror flatness specifications for the high reflectivity side of the arm cavity mirrors.

2.8 Test masses polishing specifications

In this section, the polishing specifications for the test masses of the Advanced Virgo interferometer are described.

2.8.1 Specification summary

The mirror of the arm cavity are made of high uniformity and low absorption fused silica glass from Heraeus. The input and end mirrors of the arm cavity have the same dimensions: 350 mm of diameter for a thickness of 200 mm. All the substrates have already been delivered to LMA.

The polishing specifications in term of radius of curvature are presented in table 2.11 and flatness and roughness are presented in table 2.12. The maximum acceptable loss for the light stored in the arm cavities (75 ppm per round trip) constrains directly the surface quality of the mirrors. For the table 2.12, we assume that the technique of corrective coating will be done in LMA to bring down the mirror RMS flatness from 1.5 nm to 0.5 nm. Since corrective coating only improves low spatial frequency features, a specification for the high frequency has also to be given.

As already explained in the paragraph 2.6, the tolerances for the radius of curvature (around +/- 1%) comes from what could be relatively easily achieved by the polisher keeping in mind that in any case thermal tuning of the radius of curvature is planned to control the mirror radius of curvature with about 1 m accuracy. The flatness specifications were derived from simulations detailed in section 2.8.2. The roughness specification comes from the experience gained from the Virgo+ mirrors and the loss measured by diffusion on those mirrors.

2.8.2 Arm cavity mirror flatness specification

The arm cavity mirrors are critical to achieve the expected sensitivity of the interferometer. Indeed the mirrors should have a very low flatness in order to ensure minimal optical power loss inside the arm cavities. In this section we described the simulations done to define the arm cavity mirrors flatness to meet the specifications of the Advanced Virgo Baseline, given in section 2.8.4.

2.8.3 Definitions

The mirror flatness can be defined as the deviation from an ideal surface, plane or spherical depending on the mirror. To quantify this flatness the parameter that is commonly used is the root-mean square (RMS) fluctuation in height of the mirror, computed over a given diameter. In this section the RMS is computed over the central part of diameter 150 mm if not otherwise specified.

Another useful way to describe the surface of the mirror is the Power Spectral Density (PSD). The PSD describes the surface via the distribution in spatial frequencies of the square amplitude of the defects.

The Round Trip Losses (RTL) is used to quantify the losses in the Fabry-Perot arm cavity, in the following we use the definition via the energy conservation law as defined in [53]:

$$\text{RTL} = \frac{P_{in} - (P_{ref} + P_{trans})}{P_{circ}} \quad (2.1)$$

All the calculations to derive the mirror specifications were done on the round trip loss of the fundamental cavity eigenmode (sometimes call in the Virgo jargon ‘loss on all the modes’). Not much difference exists between this loss and the round trip loss defined on the TEM00 [53] for Advanced Virgo like mirror since the cavity eigen mode is very close to the ideal fundamental Gaussian beam. That is a direct consequence of the action of the corrective coating since all the low order aberrations are becoming extremely small, the circulating mode in the cavity is not distorted and is extremely close to be perfectly Gaussian [54].

2.8.4 Round trip loss budget

The Advanced Virgo Baseline Design [13] specifies that the round-trip losses in the arm cavities should be smaller than 75 ppm. These losses are due to absorptions, transmission, surface defects and diffraction at low and high spatial frequencies. The losses due to absorption and transmission are estimated to be of not more than 5 ppm. The losses due to surface point defects and micro-roughness High Spatial Frequency (HSF) (i.e for spatial frequency above 10^3 m^{-1}) are estimated to be 2×10 ppm. Therefore the losses due to Low Spatial Frequency (LSF) should be smaller than 50 ppm. The LSF contains the defects that are in the range $10^0 \text{ m}^{-1} - 10^3 \text{ m}^{-1}$, typically the range that can be measured with a Phase-Shifting Interferometer. In the following we will concentrate on these low spatial frequencies.

2.8.5 Simulations

FFT simulations have been performed on SIESTA [19] and OSCAR[17] to determine the acceptable flatness of the mirror surface.

We simulated an Advanced Virgo Fabry-Perot arm cavity with the parameters given in 2.1 and a random surface on the ITM and ETM . The FFT parameters used in the simulations are carefully chosen and are dependent on the simulation as explained in [52]. Looking at the PSD for different substrates polished by different polishers shown in figure 2.19, we see that the shape of the PSD depends on the polisher. For example, the CSIRO substrate exhibits much higher high frequency than any others substrates.

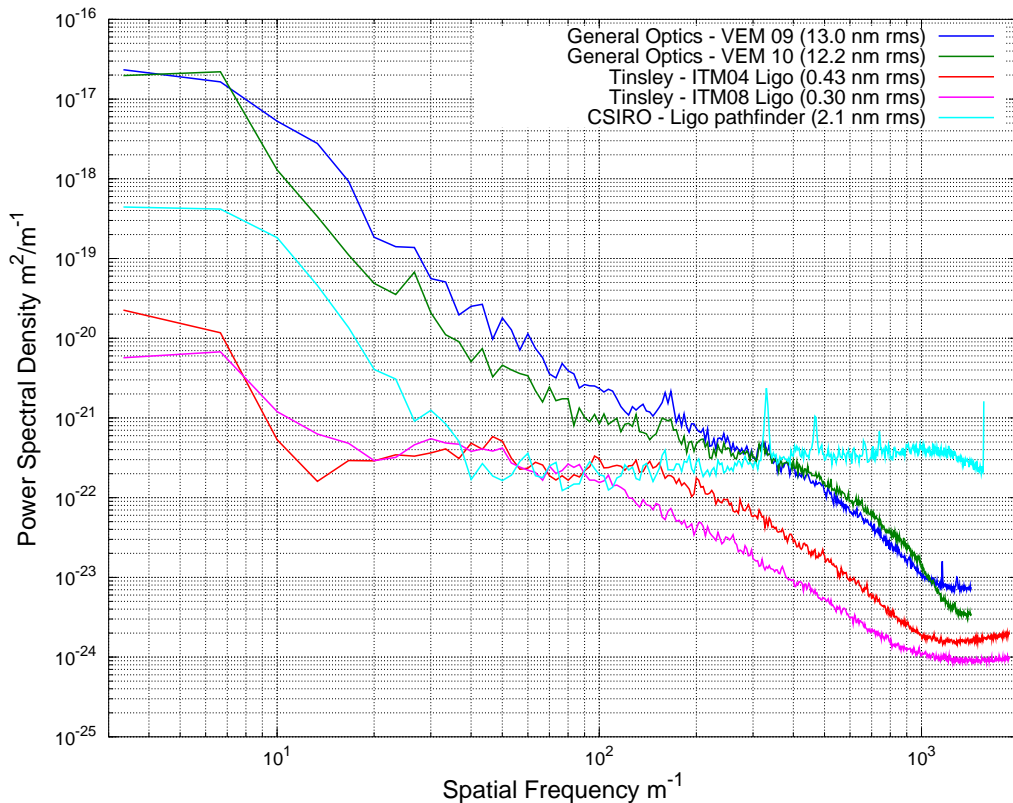


Figure 2.19: PSDs of mirror maps from different polishers computed over a diameter of 300 mm.

We performed thousands of simulations with a given flatness on each cavity mirror with different PSD shape corresponding to General Optics (GO) and CSIRO polishing. 5000 simulations are performed with mirrors having a PSD shape characteristic of GO polishing, with a flatness in the range 0.5 - 2.5 nm rms. The results are shown in figure 2.20 where we can see that the dispersion in terms of RTL for a given flatness is quite important. We can compute the fraction of simulations which give a RTL smaller than 50 ppm. Doing so, we see that according to our simulations mirrors having a flatness of 1 nm rms will give losses smaller than 50 ppm with a 95% confidence.

The same kind of simulations are performed with mirrors having CSIRO-like PSD shapes. 1000 simulations are performed with a flatness spanning the interval 0 - 2.5 nm rms. The

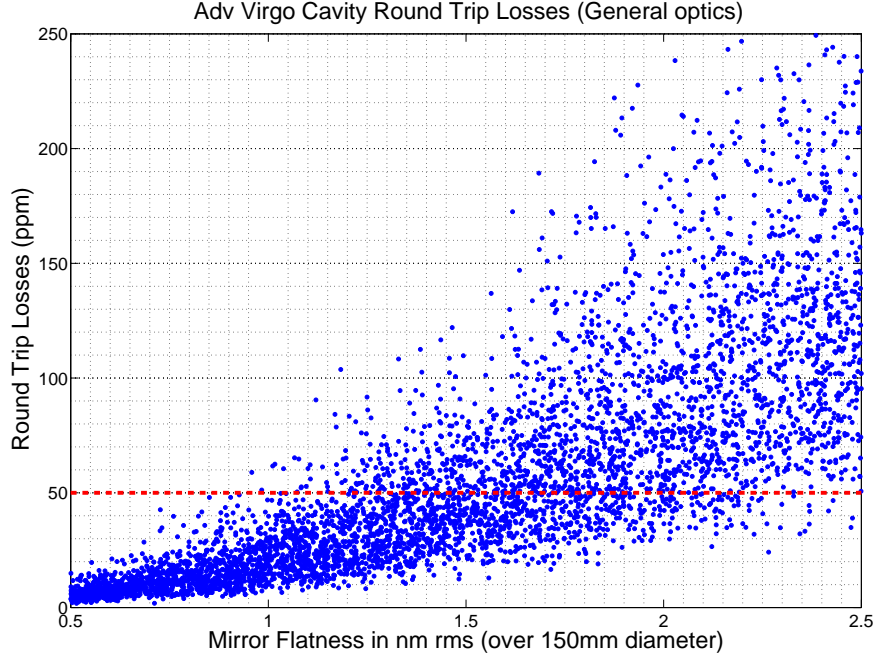


Figure 2.20: Round-Trip Losses for GO-like surfaces.

results in terms of **RTL** in the Advanced Virgo cavity are plotted in figure 2.21, we see that the losses start to cross the 50 ppm limit for mirrors having a flatness of about 0.5 nm rms. Again we can compute that to achieve round trip losses smaller than 50 ppm with a 95% confidence we need to have mirrors having a flatness of 0.5 nm rms or less with CSIRO polishing.

From these simulations, we discovered that mirrors having the same flatness rms can still give different losses in a Fabry-Perot cavity depending on their **PSD** shapes. **We propose to give two specifications for the flatness, one in the spatial frequency range $50 m^{-1} - 1000 m^{-1}$ and the other in the whole range.** The choice of the $50 m^{-1}$ border is driven by two reasons. The first one is the geometrical parameters of the Fabry-Perot arm cavity. The angle θ at which the light is diffracted is related to the spatial frequency of the defects f by the relation $\theta = \lambda \times f$ with λ the light wavelength. Assuming that most of the power is contained at the center of the mirror, we find that the light escapes the cavity when diffracted by defects with spatial frequency higher than $50 m^{-1}$. The other reason for the $50 m^{-1}$ threshold is that the corrective coating technique should be able to correct defects below this threshold. Simulations have been performed with mirrors having defects only above $50 m^{-1}$ with **PSD** shape in $PSD = f^{-n}$, with n equal to 2.3 (GO like), 0 and -1 (growing PSD). We see that the **RTL** are not dependent on the **PSD** shape above the $50 m^{-1}$ frequency and that it follows the law:

$$\text{Losses (per mirror)} = \left(\frac{4 \times \pi \times RMS}{\lambda} \right)^2 \quad (2.2)$$

Then, we propose to set a specification for the higher part of the **LSF**, that is to say above $50 m^{-1}$. Since the losses due to these higher **LSF** will be hard to correct, we request them to

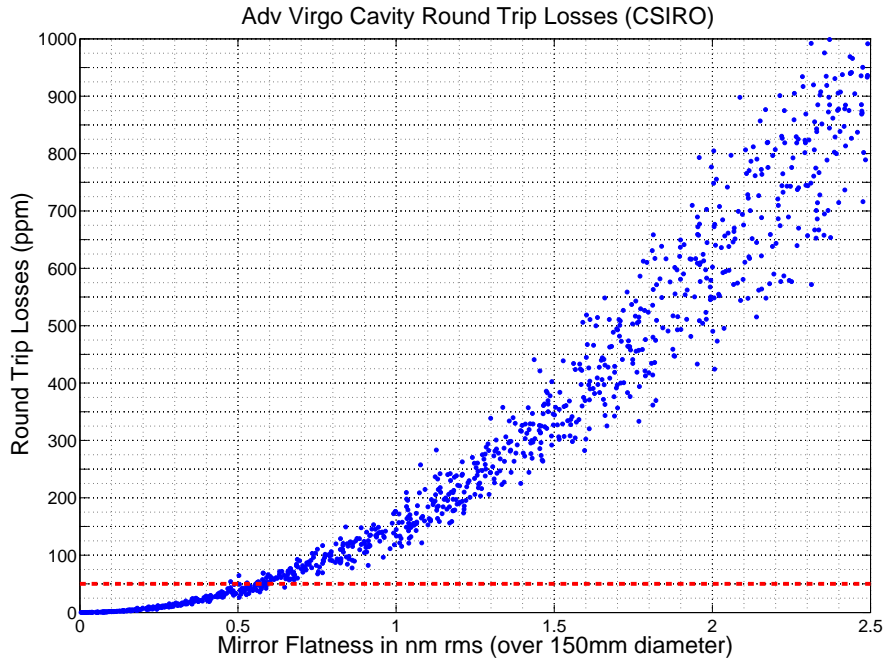


Figure 2.21: Round-Trip Losses for CSIRO-like surfaces.

be smaller than 20% of the losses due to **LSF**, i.e 10 ppm. So we propose to set a specification of 0.15 nm rms in the range 50 m^{-1} – 1000 m^{-1} . Some details can be found in [55].

Considering that classical polishing does not permit to obtain a low enough flatness surface, we studied the effect of the corrective coating technique. Based on tests that took place in 2003 at LMA, the effect of the technique is to flatten the **PSD** below a certain spatial frequency. This frequency is related to the beam of matter size used. It is similar to the effect of the ion beam polishing (see "Tinsley" curve in fig 2.19) which is basically the same technique except that it ion beam polishing removes material instead of adding it. We performed the simulation of the corrective coating in two ways: the first simulation was performed in the spatial frequency domain, considering that the corrective coating flattens the spectra for frequencies below 50 m^{-1} , corresponding to a beam of matter of 2 cm. The second simulation was done in the space domain, directly adding material at the surface where needed and assuming a scanning beam of matter. The two simulations give similar results.

Then we simulate the corrective coating by applying a filter characteristic of the corrective coating action on the **PSD** of random map.

This filter flattens the **PSD** below a cutoff frequency that corresponds to the mask used in corrective coating process. The figure 2.22 shows the **PSD** of a simulated map after and before correction with a cutoff of 50 m^{-1} . The **PSD** is flattened below the cutoff frequency. These corrected maps are put in a the simulation of the Advanced Virgo arm cavity and the **RTL** are computed. We see that starting from maps having a flatness of 4 nm rms (the Virgo+mirrors), the corrective coating does not permit to reach the 50 ppm. 1000 simulations have been performed and only 1 % of them give a **RTL** smaller than 50 ppm (see table 2.13).

The same procedure has been done starting with mirrors having a flatness of 3 nm rms,

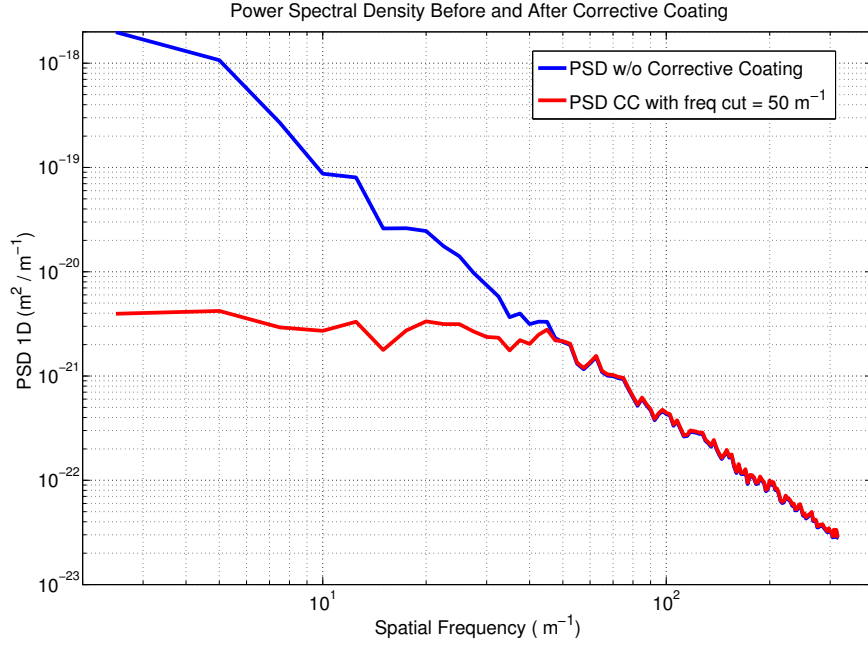


Figure 2.22: Power Spectral Density of simulated map before and after correction with the corrective coating acting below 50 m^{-1} .

2 nm rms and 1.5 nm rms. The table 2.13 shows the percentage of simulations that give a **RTL** smaller than 50 ppm. We can see that starting with mirrors having a flatness of 1.5 nm rms and with the use of the corrective coating technique we should be able to meet the Advanced Virgo specifications on the round-trip losses in the arm cavity of the interferometer.

Thus the specifications on the arm mirror flatness should be of 1.5 nm rms below 1000 m^{-1} with a flatness of 0.15 nm rms in the range $50 \text{ m}^{-1} - 1000 \text{ m}^{-1}$.

| Mirrors flatness | No Corrective Coating | Corrective Coating ($f_c = 50 \text{ m}^{-1}$) |
|------------------|-----------------------|--|
| 4 nm rms | 0 % | 1% |
| 3 nm rms | 0.3 % | 23.8 % |
| 2 nm rms | 13.9 % | 88.4 % |
| 1.5 nm rms | 61.3 % | 95.9 % |

Table 2.13: Percentage of the simulations that gives a RTL smaller than 50 ppm, with and without corrective coating at 50 m^{-1}

At the beginning of 2012, tests will take place at LMA to assess the performances of the real corrective coating. If the corrective coating does not have the expected performance, the mirrors will have to be polished with ion beam polishing and the specifications should then be 0.5 nm rms below 1000 m^{-1} with a flatness of 0.15 nm rms in the range $50 \text{ m}^{-1} - 1000 \text{ m}^{-1}$.

2.9 Central area optical path length distortion requirements

The Advanced Virgo recycling cavities are marginally stable recycling cavities (MSRC), with a cavity Gouy phase of approximately 1.7 milliradians. Simulations have shown that this level of stability leaves the optical performance of the recycling cavities vulnerable to imperfections in the optical components that make up the cavities [58].

The optical performance of a marginally stable cavity is thus critically dependent on high quality optical components. Both the surfaces and substrates need to be uniform to high precision (nm-level) in order to not spoil the optical performance. In order to set requirements on the quality of the optical components, the performance of the recycling cavities in the presence of imperfections has been studied within the OSD framework using multiple FFT simulation tools, including DarkF, SIS, FOG, and OSCAR.

We use the term ‘optical path length distortion’ to encompass any deviation from perfection in optical components, which includes surface flatness errors and inhomogeneities in the index of refraction of the optics.

2.9.1 Characterization

In order to simply characterize a given set of optical path length distortions, we used the figure-of-merit of a beam-intensity weighted rms deviation from ideal. This figure of merit has been studied and found to be a good predictor of optical performance in a cavity [61].

The beam weighted rms (strictly speaking, the square root of the weighted variance about a weighted mean) for a given set of map-like data is described in [61], and repeated here:

$$\sigma_g^2 = \frac{\sum m, n^{M,N} G(xm, yn) [h(xm, yn) - hg]^2}{\sum m, n^{M,N} G(xm, yn)} \quad (2.3)$$

where $h(x, y)$ is the map height at point (x, y) , $G(x, y)$ is the beam intensity at (x, y) , and hg is given by

$$hg = \frac{\sum h(xm, yn) G(xm, yn)}{\sum m, n^{M,N} G(xm, yn)}. \quad (2.4)$$

When using a realistic map in a simulation, it is customary to first subtract from the map the dominant terms which can be relatively easily corrected in a real interferometer. These terms include piston & tilt (which are corrected by the length and alignment automatic control systems), and any residual radius of curvature (which can be corrected by, e.g., a ring-heater or a CHRoCC). The computation of these terms is done by doing a beam intensity weighted least squares fit to a generalized paraboloid (cf. equation 2.5):

$$f(x, y) = C0 + C1x + C2y + C3xy + C4x^2 + C5y^2. \quad (2.5)$$

Once the fit is made, the paraboloid is subtracted from the map with the substitutions $C3^{sub} = 0$ and $C4^{sub} = C5^{sub} = (C4 + C5)/2$.

2.9.2 Sources of optical path length distortions

The optical path length distortions arise from imperfections in the production and polishing of the glass used for the various substrates in the recycling cavity. Figure 2.23 shows the optics in a recycling cavity. The surface figure errors on each reflective surface contribute directly to the total optical path length distortion. In addition to this, surface figure errors on transmissive surfaces also contribute to optical path distortions, with a factor of $n - 1$ where n is the index of refraction of the material. Finally, spatial variations in the index of refraction of the substrates also contribute to optical path length distortions.

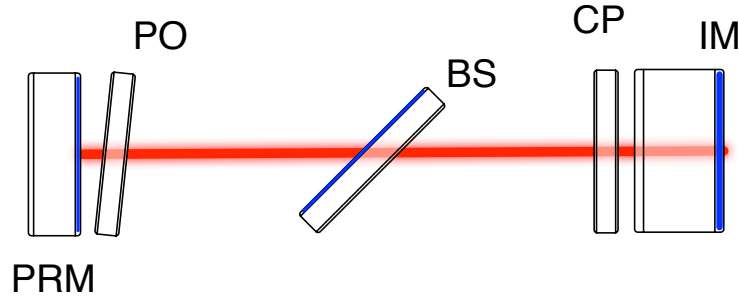


Figure 2.23: The Advanced Virgo recycling cavity.

2.9.2.1 Surface figure errors

As already explained in section 2.8, the process of figuring and polishing the fused silica substrates leaves a surface with residual deviations from perfect sphericity. The level of these surface figure errors is well characterized by the power spectral density, several examples of which from different polishing vendors can be seen in figure 2.19. It is primarily the low-frequency (less than 50 m^{-1}) errors which contribute to optical performance. The choice of polishing vendor (and thus, process) can thus have a strong impact on optical performance.

Pragmatically, there are only two meaningful options for the polishing quality level of core optics components in Advanced Virgo: the so-called ‘standard polishing’ and ‘test-mass quality’ polishing. Standard polishing is considered to produce a map with an overall rms deviation of 2 nm on the central diameter of 150 mm. As there are multiple surfaces in the recycling cavity, including the transmissive AR coated surfaces, even standard polishing for each surface can yield a wide spread of possible total distortions. Figure 2.24 shows the resulting beam weighted rms of the total optical path length distortion when Standard Polishing (SP) and maps after corrective coating are individually simulated¹ for each surface in the recycling cavity. Transmissive surfaces are added with a prefactor of $n - 1$, where n is the refractive index of the substrate material. It is this beam-weighted rms which is considered as a figure-of-merit for optical performance.

Test-mass quality polishing is essentially standard polishing followed by a corrective coating, and has a sub nanometer rms over the central 150 mm, with a typical value quoted for Advanced Virgo as 0.5 nm (see, for example, [57], for a computation of this value). Adding together multiple maps in the same manner as done for figure 2.24 yields a central value

¹These surfaces are simulated using a code based on F. Bondu’s MirrorShape package.

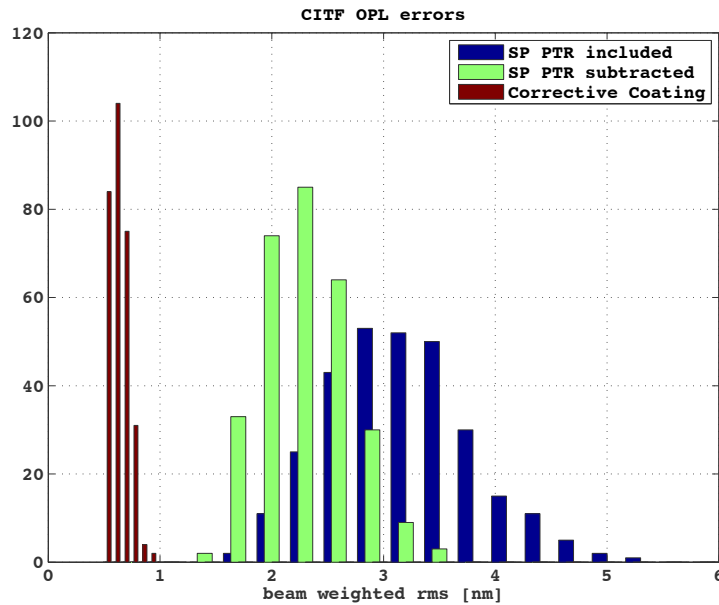


Figure 2.24: Likely statistical spread of beam weighted rms resulting from use of standard polishing (SP) and maps after corrective coating (CC) for the optical surfaces in the central interferometer. The statistics are for a single map, added to seven maps with the same polishing level multiplied by $n - 1$ as they represent transmissive surfaces in the CITF. For the SP, results are shown for the final OPL with and without subtraction of piston, tilt, and RoC (PTR). The mean of the distribution for SP without PTR subtracted is 3.1 nm and standard deviation is 0.65 nm. The mean of the distribution with PTR subtracted is 2.2 nm and standard deviation is 0.39 nm. For the maps after corrective coating the mean is 0.6 nm and standard deviation is 0.1 nm; the subtraction of PTR does not change the distribution. Substrate index inhomogeneity is not included.

around (or slightly less than) 1 nm, with spread smaller than 0.5 nm. Test-mass quality polishing is, however, significantly more expensive and more time-consuming to produce.

2.9.2.2 Substrate index inhomogeneity

The fused silica used for the substrates in the Advanced Virgo interferometer is of very high quality, but nonetheless the specification for spatial variation in the refractive index of the material is limited. For the Advanced Virgo input mirrors (made of Heraeus Suprasil 3002), the specification for this variation (peak-to-valley) is ≤ 2.5 ppm over \varnothing 200 mm and ≤ 0.5 ppm over \varnothing 100 mm. For a substrate of 20 cm thickness, this latter specification can entail a variation of the optical path length of ~ 100 nm. Such a distortion is significant enough to severely limit the optical performance of a **MSRC**. Three of the four delivered input mirror substrates are about five times better than the specification (in peak-to-valley terms), but we do not yet have map data that can be used in simulation.

The left part of figure 2.28 shows an example of a substrate inhomogeneity in a sample of Heraeus Suprasil 3001 (an Advanced LIGO substrate), a similar material that has the same specifications as Suprasil 3002 for this quantity. The level of inhomogeneity in this sample is large enough to severely impact the performance of the recycling cavities [58]. Measurements made on this Advanced LIGO substrate show variation of the optical path length of 16 nm rms (beam weighed) without subtraction of piston-tilt and curvature, and 3.1 nm after subtraction of the piston-tilt-curvature. The measurement of the substrate inhomogeneity done on another Advanced LIGO **ITMs**, gives an RMS of 5.6 after subtraction of piston-tilt-curvature.

2.9.2.3 Distortions induced by the suspension system

Advanced Virgo mirrors are not free floating in space but are suspended through glass fiber attached to the mirror with ears. Like any attachment system, the suspension can induce small deformations of the mirror surface or wavefront distortion in transmission.

Simulations were done in ANSYS and results can be found in [69, 66]. The largest deformations of the mirror surface are around 4 nm in amplitude and were found next to the ears. In the central part of diameter 150 mm, the deformations are much smaller: the RMS is below 0.15 nm. That is negligible compared to other distortions that can be met in the power recycling cavities.

The suspension also creates non-uniform change in the refractive index via the photoelastic effect. The change of the refractive index is directly calculated by multiplying the strain tensor of the suspended mirror (exported from ANSYS) with the photoelastic tensor. In the central part, the wavefront distortion in transmission was found to be less than 0.1 nm which is totally negligible in front of the substrate refractive index inhomogeneity.

2.9.3 Requirements

With a marginally stable recycling cavity, the laser carrier field (which will carry the gravitational-wave signal) is almost completely dominated by the field in the high-finesse arm cavities, which

are stable. The carrier-field in the recycling cavity is thus largely insensitive to optical path length distortions within the recycling cavity itself; using 'standard polishing' maps for the surfaces in the recycling cavity leads to carrier recycling gain variations on the order of 2%.

We thus choose to use the recycling gain of the **RF** sidebands used for control of auxiliary degrees of freedom of the interferometer as our figure-of merit for optical performance. We have set an optical performance goal of 50% of the nominal, ideal recycling gain (for the TEM00 mode) of the **RF** sidebands. This value should leave enough light in the **RF** sidebands for all the auxiliary loops to continue functioning at a low-enough noise level to not spoil interferometer performance. Moreover the value of 50% seems like a reasonable goal. It can be inferred from figure 2.25 that this requires the total distortions to be less than 2 nm rms (beam weighted). Figure 2.25 in particular was computed with FOG, but similar results have been achieved with SIS and OSCAR.

These requirements are valid for Fmod1, the modulation frequency which will be used in *science mode*. Fmod4 has much lower finesse in the recycling cavity, due to the higher leaking onto the dark port, and then it is much less susceptible to interferometer defects. Fmod4 could then be used during the commissioning phase, to tune the **TCS** system, and during the lock acquisition to reduce sensitivity to thermal transients [60].

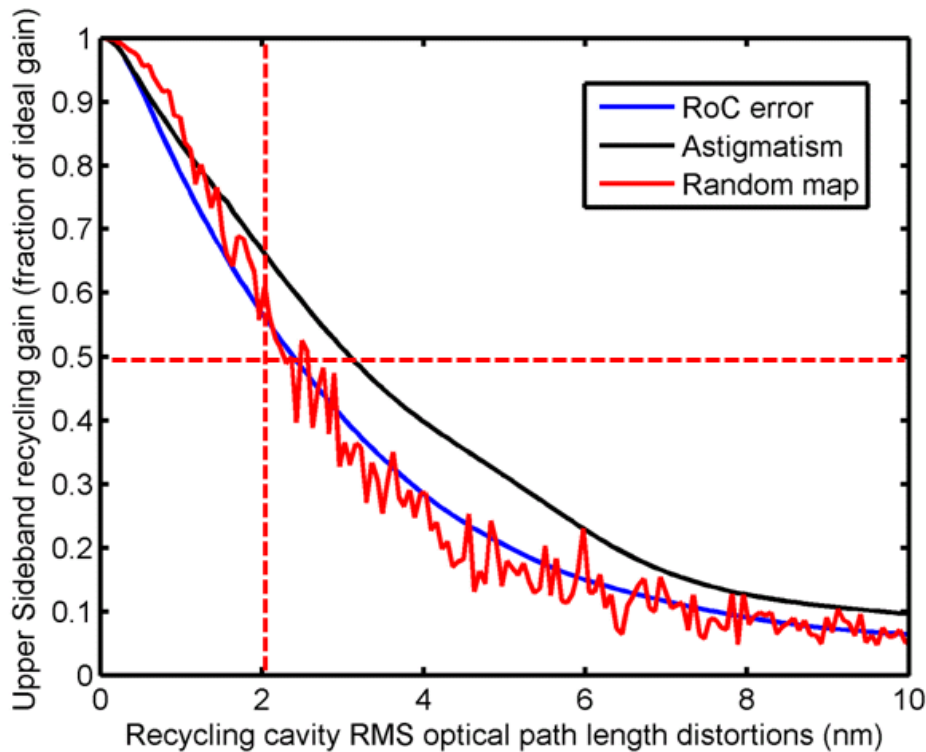


Figure 2.25: The **RF** sideband recycling gain declines sharply as the total optical path distortions in the recycling cavity are increased. The curves show the dependence of recycling gain on three types of distortions: **RoC** errors, astigmatism, and general polishing errors. Each type of error has been plotted according to its equivalent magnitude in beam weighted rms, which is shown along the abscissa. A cross-hair is drawn at the 50% recycling gain level, which occurs at approximately 2 nm rms. We can see that this 2 nm requirement is sufficient for any type of distortion. For simplicity, in this simulation all optical path length distortions are collected on the surface of the power recycling mirror

Audio sideband performance The sensitivity of the audio sidebands (those that carry the gravitational-wave signal) to the mirror surface imperfections has also been studied. These sidebands are expected to be less sensitive than **RF** sidebands to optical path length distortions for two reasons: (1) the signal recycling cavity finesse is lower than the power recycling cavity finesse and (2) the audio sidebands are also resonating in the arm cavities.

Using SIS, a coupled system of one arm cavity with a signal recycling cavity has been simulated. SIS allows the user to define a GW signal originating in the arm cavity with a given frequency and then compute the gain of the GW sidebands in the signal recycling cavity. The relative effect of the **SR** surface quality on the GW sidebands is presented in figure 2.26.

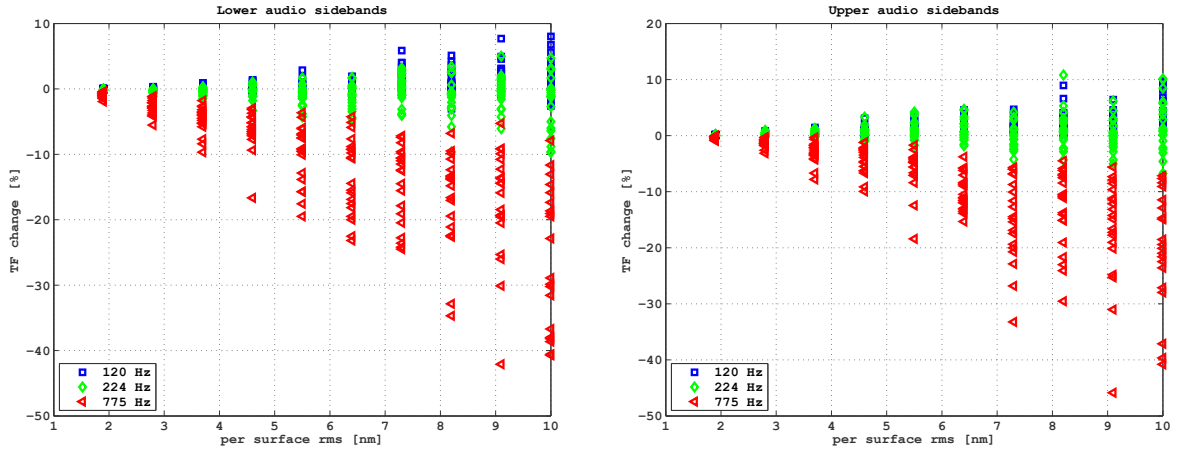


Figure 2.26: Relative GW sidebands gain in the signal recycling cavity as a function of the flatness of the signal recycling mirror. Each RMS has been simulated 20 times with random maps with tilt and piston subtracted. The transfer functions were calculated for three different frequencies of the GW signal: 120 Hz, 224 Hz and 775 Hz.

As expected the surface of the signal recycling mirror is less critical compared to other optics in the power recycling cavity. A surface quality of 2 nm RMS for SRM only marginally decreases (2%) the GW sidebands gain [58]. The increase of the transfer function for large RMS of surface maps may likely be due to a local detuning of the signal recycling mirror. So far only SIS can simulate GW sidebands, but in a near future other FFT simulations code will be adapted to reproduce the results presented here.

2.9.4 Differential mode optical path length distortions

The requirements discussed so far pertain to common mode optical path length distortions. A preliminary study has also been done of the requirements on differential aberrations [60], in order to limit the amount of diffuse light at the dark port. The sidebands dark fringe power as a function of the differential surface defaults is presented in figure 2.27. Quantifying the maximal tolerable amount of sidebands light at the dark port will necessitate further interaction with DET and ISC, but a preliminary appraisal indicates that the same 2 nm rms requirement set for the common mode aberrations should also be sufficient in the differential mode.

The carrier gain in the PRC is almost unaffected by common aberration.

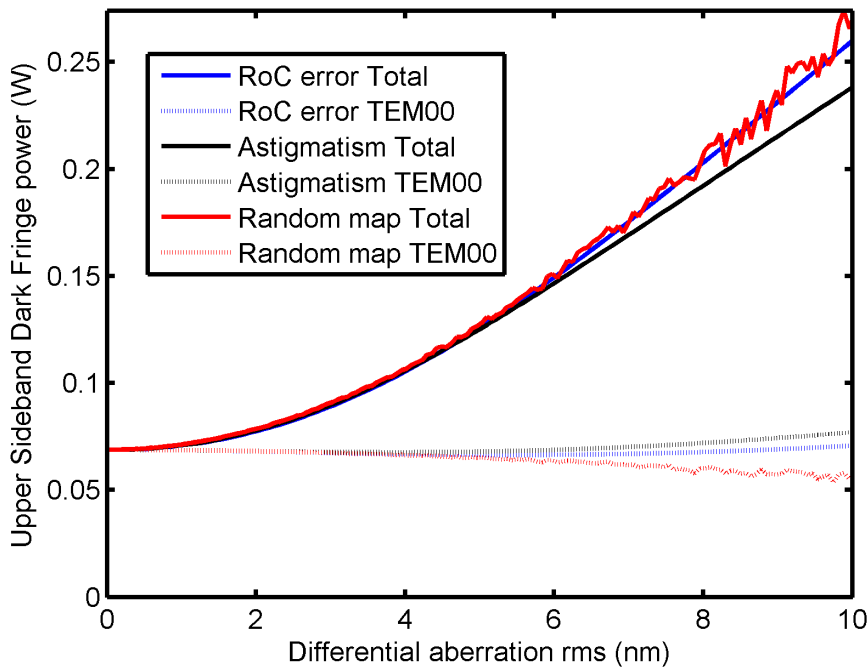


Figure 2.27: Power in the 6 MHz RF sideband present at the dark port, per Watt of sideband input power.

| Surface | RoC [m] | Absolute tolerance [m] |
|----------------|---------|------------------------|
| PRM S1 | 1430 | 8 |
| SRM S1 | 1430 | 8 |
| PRM S2 | 3.590 | .01 |
| SRM S2 | 3.590 | .01 |
| Astigmatism S1 | 0 | 15 |

Table 2.14: Recycling cavity design tolerances. S1 corresponds to the HR side whereas S2 stands for the AR side.

2.9.5 Tolerances in RoCs

The recycling gain of the RF sidebands versus errors in RoCs of the PR/SR mirrors has been studied as well [60]. Using the same performance criterion of 50% of the nominal ideal gain for the sidebands, we define the tolerances given in table 2.14. Those are tolerances to guarantee good performances of the interferometer, specific tolerances will also be set for the polishing and for the coating process (see the MIR chapter).

Since the absolute tolerances for the RoCs are rather tight, TCS will be installed on PR and SR to have the possibility to tune the RoCs. TCS on PR can also be used to corrected common spherical aberration.

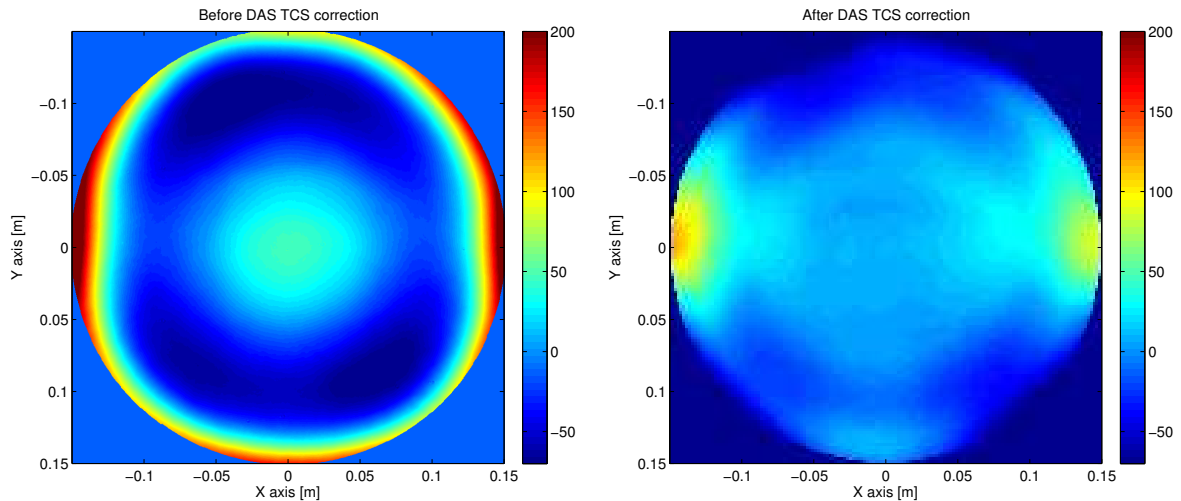


Figure 2.28: Index inhomogeneity in a Heraeus Suprasil 3001 substrate (left) and the residual optical path length defects after compensation with DAS. The color bar indicates the optical path length in nanometers. The Advanced Virgo *ITMs* are made Heraeus Suprasil 3002 but must present similar inhomogeneity.

2.9.6 Compensation of optical path length defects

Cold and hot optical distortions can usually be separated into two kind: the distortions with radial symmetry and the non symmetric other one. To be compensated, both distortions required specific actuators with specific dynamic range and as a first step, the two distortions can be treated separately.

2.9.6.1 Correction axisymmetric distortions

Axisymmetric distortions represent distortions invariant across rotations around the optical axis. In general, such distortions are due to optics with suboptimal radii of curvature or due to the presence of thermal lenses in the case of a hot interferometer. Compensation of such aberrations can be done by thermal tuning the radius of curvature of a mirror inside the PRC or using the Double Axicon System (*DAS*) which can create a divergent lens inside the compensation plates.

Once of the first source of distortion to be compensated from the start of Advanced Virgo is the input mirror substrate inhomogeneity as already mentioned in section 2.9.2.2. Studies have already been undertaken in the *TCS* group to find the necessary heating pattern using a double-axicon system to compensate the substrate inhomogeneity shown in the left part of figure 2.28, resulting in the compensated map shown in the right part of the same figure. The right map includes the effects of the substrate inhomogeneity, thermal lensing at 25 W of input power (negligible), and the compensation achievable with the *DAS*. The beam-weighted rms of this compensated map is 2.8 nm (whereas the beam-weighted rms of the substrate inhomogeneity alone was 16 nm).

The performance of the CITF with this *DAS* compensated map has been studied in optical simulations [62]. The level of compensation does not meet the optical requirements (the RF sideband losses are greater than 50%). So an additional *TCS* system must thus be developed

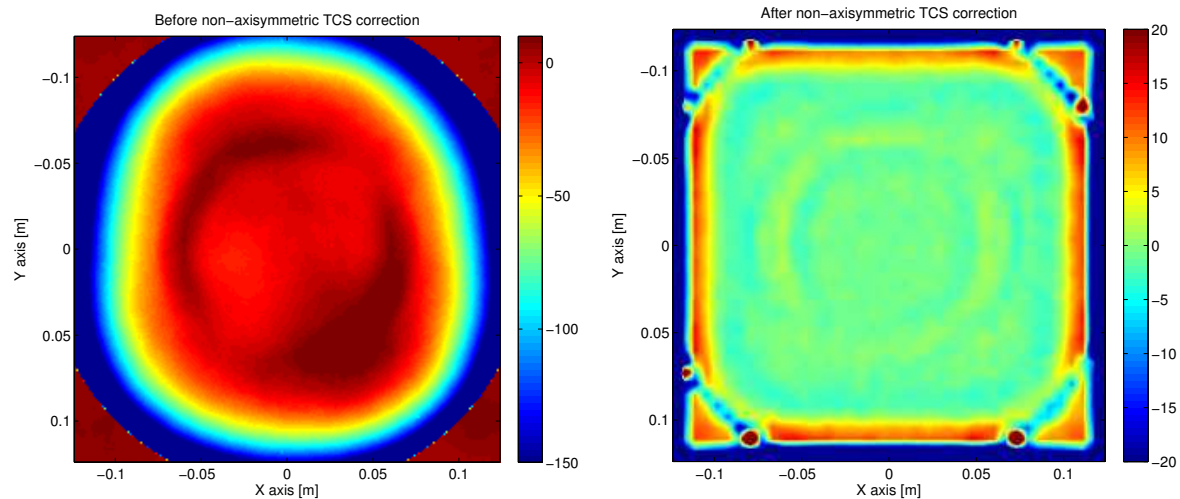


Figure 2.29: Total distortion maps in the PRC before (left) and after compensation (right) using a non on-axisymmetric compensation system. With such a system, the amplitude aberrations can be reduced by a factor 10. The color bar indicates optical path length in nanometers. In the corrected map, a piston offset has been removed.

which can bring down the level of optical path length distortion below 2 nm, correcting for any kind of distortions. The first theoretical performances of such a system are presented in the next section.

2.9.6.2 Compensating the non-axisymmetric distortions

A thermal compensation system can be designed where heat is only applied with a well defined pattern or on only to specific parts of the mirror. For example, that system can be achieved with a scanning CO₂ laser as already demonstrated by LIGO people 10 years ago [65].

To simulate the compensation system, fake distortion maps representing the total accumulated optical distortion in the power recycling cavities have been created. The maps included the effects from all the surfaces encountered by the laser beam as well as the measured substrates inhomogeneity maps for the beamsplitter and the input mirrors. On these maps the residual curvatures have been removed, assuming that a perfect DAS has been first applied.

The uncorrected maps of the total optical path distortion in the PRC is shown in the left part of figure 2.29. The map has a RMS of 5.6 nm. After the correction is applied, the RMS of the optical path went down to 0.5 nm as seen in the right part of figure 2.29. A SIS simulation of the PRC with the corrected maps showed that the sidebands gain only decreased by 5%, confirming the excellent compensation.

The performances of the correction presented here are optimal. The thermal simulations assumed perfect sensing of the distortions as well as perfect actuation which will, of course, not be the case in reality.

2.10 Future upgrades

Similarly to the initial Virgo interferometer which was upgraded to Virgo+ in 2010, it is likely that Advanced Virgo will also receive an upgrade at the end of this decade. This major improvement can serve two goals: first increase the sensitivity of Advanced Virgo to increase the detection rate and second test some key technologies for third generation detectors.

The two upgrades presented here are not part of the initial Advanced Virgo baseline. However dedicated researches are on going on these topics within the Virgo collaboration and special considerations were taken in the design of Advanced Virgo to ensure that the interferometer will be compatible with these upgrades.

2.10.1 Reduction of quantum noise

The sensitivity of advanced interferometers is expected to be limited by the quantum nature of light over a wide frequency range. In the last decades, non classical techniques have been developed ([72] for a summary) to demonstrate that the standard quantum noise may not be the ultimate limitation of a measurement as previously thought.

In this section, we will only focus on the injection of squeezed light to reduce the quantum noise level of Advanced Virgo. This technique is mature, proven and does not require large infrastructure changes (see INF chapter).

It is important to underline that reduction of the quantum noise is only worth when the interferometer is limited by quantum noise, which is easy to achieve at high frequency with the shot noise but could be challenging at low frequency (radiation pressure noise). In the frequency region where the interferometer is limited by thermal noise or technical noise, the use of the squeezed light is of no help.

2.10.1.1 Injection of squeezed light

Ideally, the sensitivity of Advanced GW interferometer will be limited over a wide frequency range, from tens of Hertz to several kiloHertz, by the quantum nature of light.

At low frequency, the contribution from the quantum world comes from radiation-pressure noise whose origin is related to the photon number fluctuation; this noise is important only at low frequency because of the mechanical response of the free mass while the photon-momentum is transferred to the mirrors. The equivalent strain induced by this noise increases as the injected power increases. At high frequency, on the contrary, when all the other technical noises fall down, the quantum limit is due to the uncertainty on the arrival time of the photons to the detection port, this noise is termed shot-noise and is a white noise. The equivalent strain induced by shot noise decreases as the injected power increases.

The photon picture can be a little misleading, however, in that it could suggest a modification of the injected laser light in order to overcome the standard quantum limit. Switching from the particle-like picture to a true field quantization can give a deeper understanding. The two aforementioned quantum noises are the manifestation of the fluctuations respectively in amplitude and phase quadratures of the light field circulating in the interferometer. These two

quadratures are non-commuting observables and must therefore obey Heisenberg uncertainty principle, a principle that holds true even for null-average fields, such as the vacuum field entering the interferometer through all the unused ports, including "virtual" ports originated by loss mechanism. It can be shown that the standard quantum limit is ultimately due to the fluctuations of the vacuum fields entering the interferometer [76], mainly through the detection port. So an engineering of the vacuum field leaking through the detection port (and a struggling effort to keep the effective losses as low as possible) can lead to a lower level of quantum noise that interferes with the field carrying the gravitational-wave signal. For instance, injecting squeezed vacuum with phase quadrature noise below the standard quantum limit can reduce the level of the shot noise on the detection photodiode.

This technique has been demonstrated both in tabletop suspended prototype and full-scale gravitational wave interferometers [74, 75, 73]. Unfortunately, due to Heisenberg principle, reducing the phase quadrature noise implies a corresponding increase of the amplitude quadrature noise in order to keep constant their product. This, in turn, means that radiation pressure noise is increased, and the net effect is the same as the increase of the injected power. This could be anyway useful to mimic power increase without dealing with huge thermal effects, but would not reduce the overall quantum noise of the interferometer.

Since the radiation-pressure and shot noises limit the interferometer sensitivity in different frequency bands, it is possible to inject a "frequency-dependent" squeezed vacuum, featuring amplitude noise reduction where radiation pressure noise dominates and phase noise reduction where the shot noise is limiting [82]. The possibility of such squeezer has already been demonstrated experimentally but not in the audio frequency band relevant to GW detector [81].

The place required for a squeezed light source and the attached electronics has already been saved in the detection lab of the Advanced Virgo main building .

The major advantage of this upgrade remains that the squeezed light source runs independently and does not require any change for the interferometer. A shutter can be simply added to block the injection of the squeezed light beam inside the interferometer, if no sensitivity improvement is noticed. Compared to other major upgrades possible (change of laser, mirrors or suspension), the injection of squeezed vacuum is totally reversible and almost risk free.

2.10.1.2 The GEO experience

The GEO 600 detector is the first interferometer to have demonstrated on a large scale that the injection of squeezed vacuum light at the dark port can effectively reduce the shot noise level at high frequency [73]. A squeezed light source, mounted on a stand alone breadboard was installed at the output of GEO in April 2010, and after few months of commissioning, the sensitivity of GEO at high frequency was improved by 3.5 dB.

The squeezing breadboard has first been assembled and tested in Hannover (so outside the GEO site). To achieve squeezing even at low frequency (up to 10 Hz), ultra-clean environment and super-polished optics are required. At the output of breadboard a squeezed beam with a quantum noise reduction of more than 10 dB is available for injection in GEO. Details of the squeezed light source can be found in [70]. The breadboard is relatively compact with a size of 1.35 m \times 1.13 m, weighting in total 130 kg.

In parallel to the squeezing breadboard assembly during the years 2007-2009, works were also going on in GEO to prepare for the squeezer arrival. At that time to facilitate the injection of squeezed light, GEO switched from heterodyne control with RF sidebands to DC readout and from detuned to tuned signal recycling. Space was allocated for the breadboard in the GEO clean room, near the detection tank. A fraction of the GEO input laser beam was transported by optical fiber to arrive at the future breadboard location to phase lock the squeezed light source to the GEO laser. And finally, a Faraday rotator was installed just before the OMC for the injection of the squeezed vacuum noise.

The squeezing breadboard arrived during spring 2010 the best squeezing level achieved so far was -3.5 dB after six months of sporadic commissioning. The installation as well as the interfacing with GEO existing hardware and software went without major trouble. To be compatible with the long observation time of GW detectors, the squeezer has been automated to run with GEO continuously over several tens of hours and a duty cycle exceeding 99% has been measured [71].

Even if around 10 dB of squeezed vacuum is available at the output of the squeezed light source only a 3 dB improvement is measured effectively on the GEO sensitivity curve. The amount of quantum noise reduction is reduced by all the optical losses accumulated along the path of the squeezed light beam, from the squeezer source to the detection photodiode via the reflection off from the interferometer. This can be better understood by thinking of losses as an open port which the ordinary vacuum field leaks through, in order to preserve commutation relations between quadrature operators. The superposition of the squeezed field with the ordinary vacuum spoils the obtained level of squeezing [76]. For GEO, according to the current squeezing level achieved at the detection, the losses encountered by the squeezed beam should totalize around 55%.

The three quarters of the total losses is well understood. For example, the three major culprits, which generate more than half of the known losses are: the OMC, the detection photodiode with a relative low quantum efficiency of 91% and the mode matching between the squeezed beam and the interferometer. All these three sources of loss will be reduced during the first half of 2012, a new OMC is being built, a photodiode with a quantum efficiency of 99% will be installed and finally the mode matching will be improved. The candidates responsible for the unknown extra losses are: imperfect squeezing beam alignment to GEO and phase noise in the loop that locks the squeezing phase to the dark port light.

2.10.1.3 Expected sensitivity gain

As seen in the previous sections, the technology for vacuum squeezing in the gravitational wave audio band is quite well developed [78, 79, 77], with enough squeezing and stability at low frequencies to make the technique an attractive upgrade. The remaining technological hurdle is thus stable operation of a squeezer integrated with an interferometer, and ensuring the total losses in the interferometer and in the secondary optics which match the squeezed field to the interferometer, are low enough.

Preliminary work in [64] indicates that optical losses resulting from using test-mass quality polishing for the **SR**, while important, are not critical. The key result, obtained using SIS, is that the losses from a test-mass quality polishing level for the **SR**, combined with the index inhomogeneity in the **IMs** substrate after compensation by the double-axicon system, can

be approximated by a one-way beamsplitter loss of 0.75%, or a round-trip Signal Recycling Cavity (SRC) loss of 1.5%. Compensation by the non-axisymmetric TCS will of course reduce this loss further.

Figures 2.30 and 2.31 show the impact on sensitivity of losses in the signal recycling cavity, and compare this impact to that from losses in the photo detection chain, for a frequency-independent input squeezing of 6dB. These figures are for a signal-recycled interferometer with 25W input power and a broadband SR tuning, and the results have been computed using the formalism described in [80]. Figure 2.30 shows that SRC losses primarily reduces the utility of the squeezing at high-frequencies, while photodetector losses reduce the utility at all frequencies. It is important to note that the negative impact of the anti-squeezing at low-frequencies (i.e., the increase in radiation pressure noise) is not appreciably affected by losses.

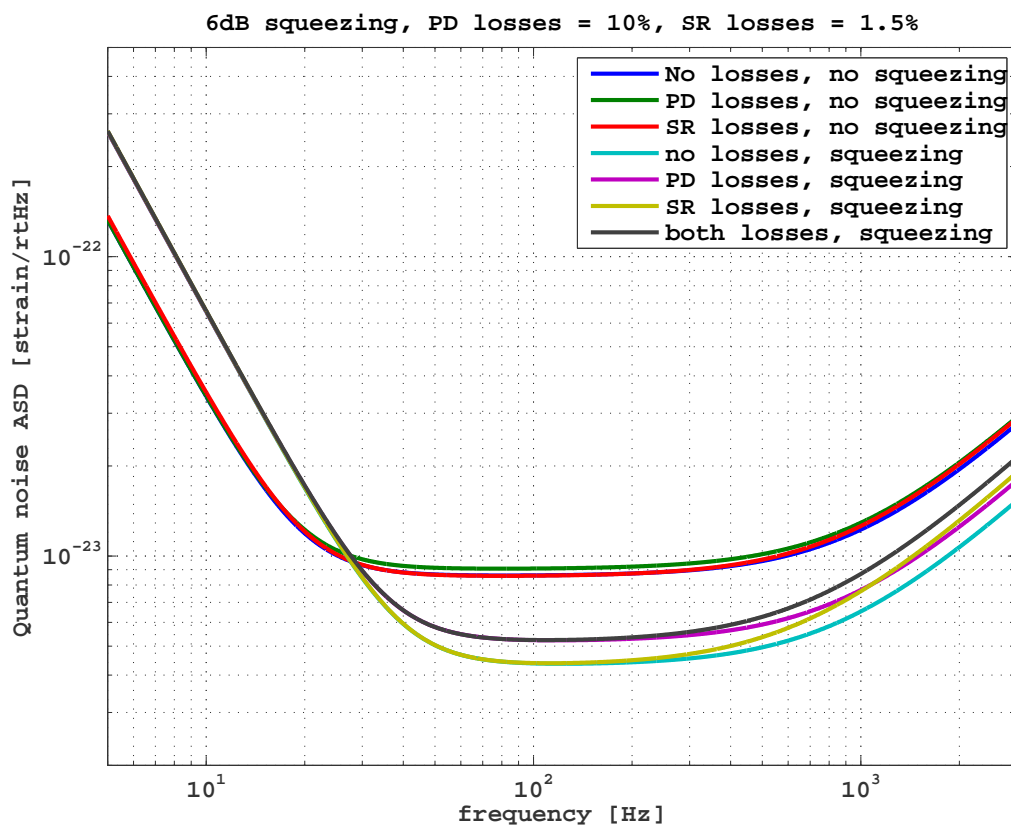


Figure 2.30: Quantum-noise spectral density (in strain unit) for a signal recycled interferometer, with varying amounts of squeezing and losses. The loss in the arm cavity are fixed and set to 75 ppm.

Figure 2.31 shows the impact of photodetector and SRC losses on the binary inspiral range. Here it can be seen that a 1.5% loss in the SRC leads to a loss of 1 Mpc of range, while a 10% loss in the photodetection chain leads to a 9 Mpc range loss. The differing slopes of the two curves indicate that losses in the detection chain are more important than losses in the recycling cavity. It is thus imperative that all optics in the detection chain (steering mirrors, telescopes, the OMC, Faraday Isolator) be of extremely high quality in order to take

appropriate advantage of input squeezing.

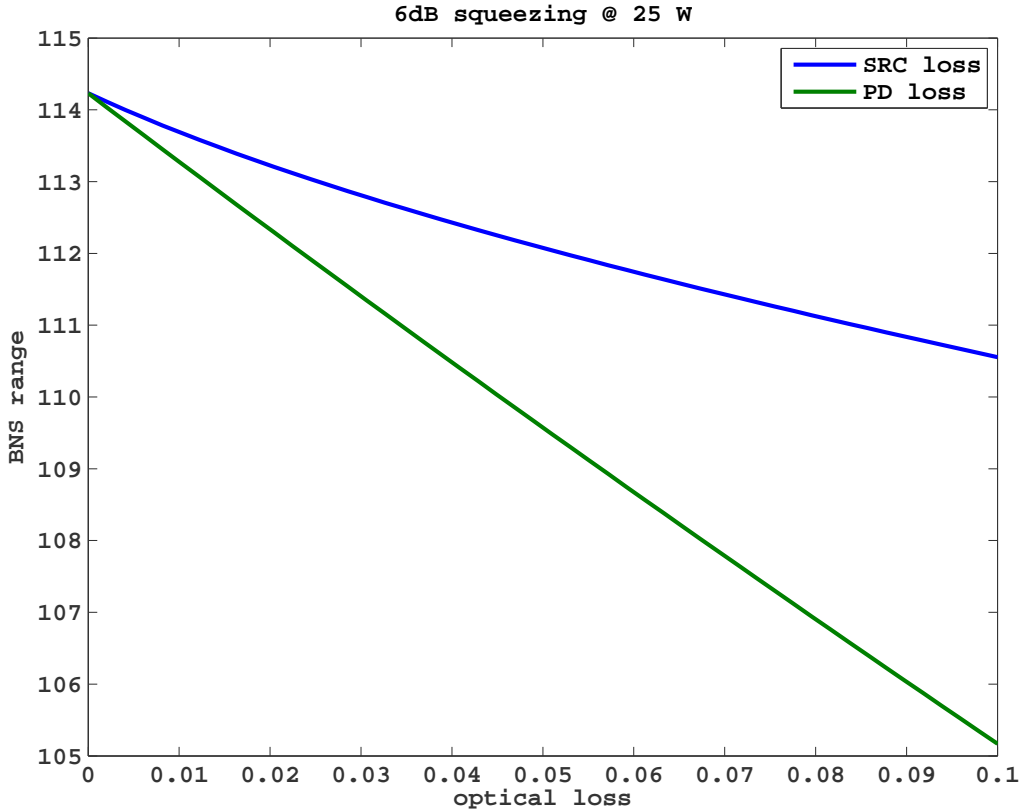


Figure 2.31: Dependence of BNS range on photodetector losses and SRC losses, for a signal recycled interferometer with 6dB of squeezed vacuum injected into the dark port. The photodetector losses are used to represent all the optical losses accumulated by the squeezed beam on the injection and detection paths whereas the SRC losses represent the squeezed beam losses within the interferometer.

Since frequency independent squeezing increases the interferometer sensitivity at high frequencies but decreases it at low frequencies, we do not have a gain in the BNS horizon by injecting squeezed vacuum light (even with 25W of input power [68]). However squeezing is definitively attractive to target high frequencies GW sources.

It is very easy to rotate the squeezing ellipse and reduce the radiation pressure noise instead of the shot noise if one is more interested at gaining sensibility at low frequency. This modification is simply achieved by changing the demodulation phase of an error signal (i.e. turning a knob) on the squeezing breadboard.

2.10.2 Use of higher order optical modes

The higher-order Laguerre-Gauss (LG) modes have been proposed to reduce the influence of the mirror thermal noise on the interferometer sensitivity [83].

Because of their wider intensity distribution, LG modes can average the fluctuations due to the thermal noise over a bigger portion of the mirror surface. Other beam profiles have been

investigated [84][85], but LG modes are attractive because they resonate in a cavity composed of spherical mirrors.

The LG modes are solutions of the paraxial wave equation [86]. The LG mode of radial number p and azimuthal number l is given by the expression²:

$$\begin{aligned}
 u^\ell p(r, \phi, z) &= \sqrt{\frac{2p!}{\pi(p+|\ell|)!}} \frac{1}{w(z)} \exp\left[\frac{-r^2}{w^2(z)}\right] \\
 &\times \left(\frac{\sqrt{2}r}{w(z)}\right)^{|\ell|} L^{|\ell|} p\left[\frac{2r^2}{w^2(z)}\right] \exp[-i\ell\phi] \\
 &\times \exp\left[-i\left(k\frac{r^2}{2R(z)} - (2p + |\ell| + 1)\Phi G\right)\right],
 \end{aligned} \tag{2.6}$$

where $w(z)$ is the beam radius, z and $R(z)$ is the curvature of the phase front, $\Phi G = \arctan(z\lambda/\pi w^2)$, $w_0 = w(z=0)$ is the beam waist, and $L^\ell p$ is the Laguerre generalized polynomial. These modes have a power profile composed of continuous rings separated by p non-axial radial nodes. Modes with $l \neq 0$ have a phase singularity at $r=0$, no power in the center of the beam and $p+1$ concentric rings.

The use of LG can also allow to reduce the thermal deformations of the mirrors [87], decreasing the requirements for the thermal compensation system.

The status of the art of the LG modes research can be summarized on the following facts:

- The total mirror thermal noise reduction using a LG33 (instead of a gaussian mode) for equivalent clipping losses (1 ppm) for the Advanced Virgo mirrors is 1.76 [88].
- The gaussian parameter of the beam inside the arm-cavities in order to have 1 ppm clipping losses are different for the gaussian beam and the LG33. Passing from a gaussian mode to a LG33 mode, the radii of curvature (ROC) of the test masses should be different by about 200 m. The possibility to change the ROC thermally has been suggested [89].
- LG modes (as defined as above) are not resonant in the triangular Fabry-Perot cavities [90, 91]. The main problem for Advanced Virgo is the use of a triangular input mode-cleaner. Possible solutions (to be investigated) are the transformation of the input mode-cleaner in a 4-mirrors cavity or the use of sinusoidal modes (sum of helicoidal modes, described above, with opposite azimuthal index).
- The basic interferometry with Laguerre-Gauss modes have been tested on table-top prototypes [91, 92]. Test of LG33 interferometry with suspended system is on-going at Glasgow [93]; test with a more complex interferometric configuration (Fabry-Perot Michelson interferometer) is on-going at APC-Paris.
- The production of a pure LG33 mode starting by a standard laser and using a silica phase plate and a pre-mode-cleaner has been tested at APC [92]. Tests of production of high-power LG modes with a phase plate are on going in Hannover [93].

²LG defined in this way are sometimes called helicoidal Laguerre-Gauss modes

- According to numerical simulations and analytical computations performed by different groups [94, 95, 96], the main potential problem in the use of LG modes is the degradation of the beam quality in the arm-cavities due to the degeneracy of modes with the same Gouy phase (same order $2p+1$). This put strong constraint on the mirror figure errors, in order to avoid mode mixing, and especially on the amplitude of low spatial frequency modes [96]. According to [95], in order to have a contrast defect of 10^{-3} an RMS of the order to 0.05 nm is needed, roughly an order of magnitude below our current requirements for mirror polishing. Some ideas to reduce these constraints have also been explored [95].

2.11 Conclusion

In the chapter, the optical design for the arm and recycling cavities of Advanced Virgo has been defined. The positions and characteristics of each optics were specified to ensure that the interferometer meets its performance goal. Below, two of the most challenging points highlighted by the simulations are summarized:

1. The Fabry-Perot arm cavities are 3 km long with the laser beam waist almost at the center of the cavities. To guarantee a light round trip loss inferior to 75 ppm, the surface flatness of the mirrors for the central 150 mm diameter must be less than 0.5 nm RMS. To achieve this surface quality, a strategy has been derived which involved a first phase of standard mechanical polishing and then a second phase using the technique of corrective coating developed at LMA.
2. The power and signal recycling cavities are marginally stable cavities similar in design to what has been implemented to the initial Virgo interferometer. Since the recycling cavities are degenerated, the gain of the sidebands only circulating in those cavities is extremely sensitive to the optical aberrations. In order to keep the recycling gain of the RF sidebands above 50%, the requirement for the common total defects (surfaces and substrates) is about 2 nm RMS. That results is independent of the state of the interferometer and so the requirement is still valid for a hot interferometer. First results from the non-axisymmetric TCS seems promising since most of the sidebands gain has been recovered.

In the following months, the OSD group will focus on consolidating the results presented in the chapter and keep doing crosscheck between optical simulations codes.

Chapter 3

Prestabilized laser (PSL)

3.1 Overview and deliverables

The Prestabilized Laser (PSL) system is located at the input of the interferometer: it comprises the High Power (HP) laser followed by the stabilizations of its output beam in order to match the AdV requirements. The HP laser and most of the optical components will sit on the laser bench inside the laser lab. Guiding beams through fibers from the seed laser to the amplifiers will decrease the number of optical components of the bench, resulting in an improved maintenance simplicity, as well as the compactness of the layout. Figure 3.1 gives the schematic of the PSL, and the different parts presented here are described in the chapter (except the Input Mode Cleaner (IMC), part of the INJ subsystem).

3.1.1 Overview

The HP continuous wave laser will deliver around 200 W in a stable monomode beam such that at least 175 W in TEM₀₀ mode are available at the input of the INJ subsystem (see INJ chapter, table 1). The seed¹ (1 W Nd:YAG laser from Innolight) is amplified to 100 W in parallel by two rod amplifiers (Eolite). Both 100 W beams are added coherently to generate a single 200 W beam. The stabilization of the laser consists in:

- the frequency prestabilization which locks the laser frequency to a short term stable cavity (reference cavity or mode cleaner cavity) to bring the laser linewidth to less than one Hz, i.e. at a level where it can be locked to the cavity arms by the Second Stage of Frequency Stabilization (SSFS) (this servo being part of the ISC subsystem). This prestabilization loop will be very similar to the loop which has been developed for Virgo and Virgo+;
- the amplitude control which uses the beam filtered by the IMC and received by uniform and fast photodiodes sitting under vacuum on the Suspended Injection Bench (SIB)1.

¹The word seed is used in case of amplifiers: as there is no more injection locked laser, so no slave laser and no more master laser. Along the chapter we will use the generic name seed laser instead of master laser when it comes to the low power stable laser used in AdV.

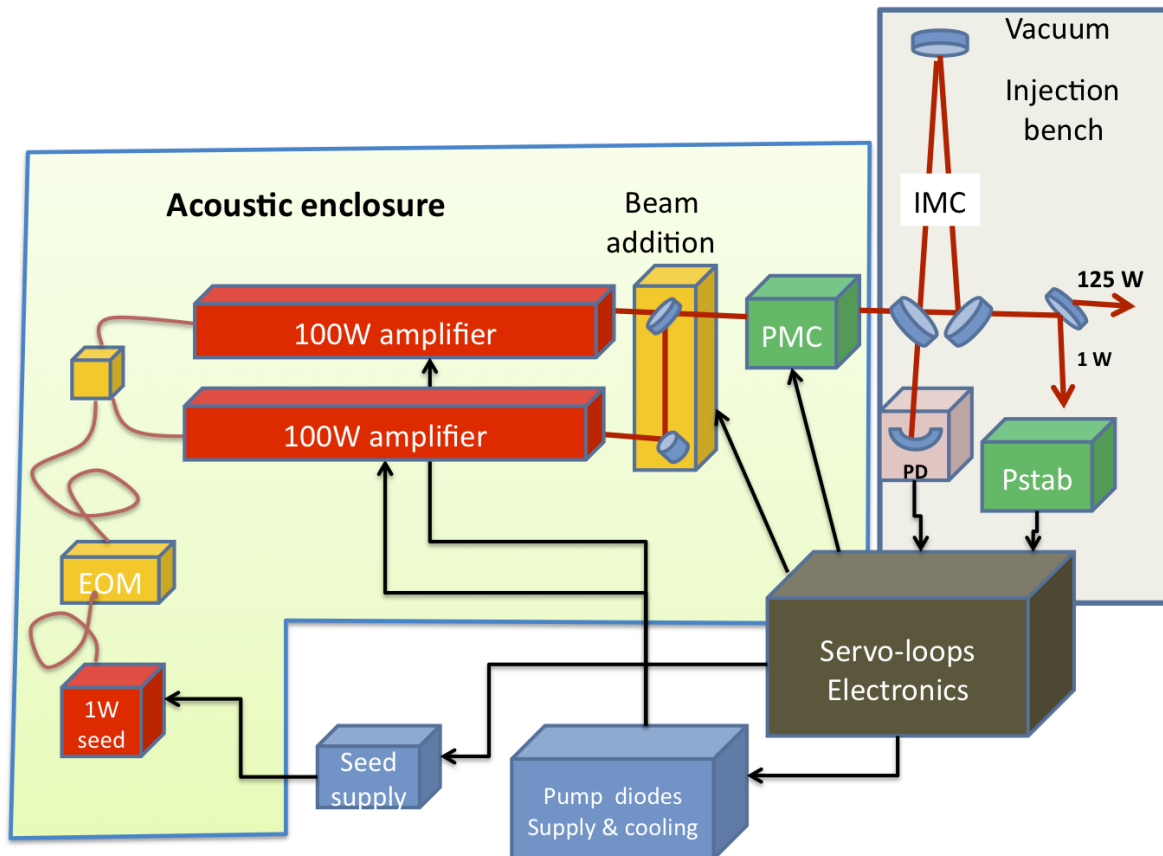


Figure 3.1: Schematic of the PSL: the green shade indicates the parts sitting on the laser bench that will be protected by an acoustic enclosure.

Its principle is the same as in Virgo: the servo loop acts on the current of the pump diodes of the amplifiers;

- the beam jitter and the beam geometry of the laser beam will be cleaned by two short cavities acting as mode cleaners (block Pre-Mode Cleaner (**PMC**) of Fig 3.1) sitting on the laser bench to filter out any unwanted beam geometry and beam pointing fluctuations.

This TDR will describe the **HP** laser, the controls and the pre-mode cleaners. A 100 W prototype made by the French company Eolite for Virgo, has already been tested in our lab and gave some promising results shown below. Besides that, the controls of the laser will be extensively described, as they are well proved and worked for the Virgo and Virgo+ generations. And finally a basic solution for the **PMC** will be given in terms of requirements for filtering the beam jitter and high frequency intensity noises of the laser.

3.1.2 Deliverables

The system consists of the following elements (Fig 3.1):

- the seed laser (“1 W seed”);
- the Electro-Optical Modulator (**EOM**), which provides the fast channel of the frequency control “EO”;
- the 100 W amplifiers;
- the beam addition system, with a Piezo-electric Transducer (**PZT**) phase control;
- the “**PMC**”, or pre-mode cleaner, which consists in a series of two Fabry-Perot cavities;
- a high power photodiode, to extract the Pound-Drever error signal from the reflection of the **IMC** (“PD”), sitting on the External Injection Bench (**EIB**);
- a high power photodiode system for power stabilization, (“Pstab”), sitting on the **SIB 1**
- laser and amplifiers power supplies and cooling systems. Wideband, low noise, feedback electronics for all the servo loops.

The **PSL** system does not include:

- the optics and mechanics of the suspended **IMC**;
- the design of the **EIB** which will be shared with INJ subsystem;
- the optical scheme and optics foreseen to feed the power stabilization sensors on the **SIB** should also be shared between INJ and **PSL**.

| Requirement | Value |
|-----------------|--|
| Power | 175 W on TEM ₀₀ at the input of INJ |
| Laser linewidth | < 1 Hz ² |
| Power Noise | -172 dB/Hz ($2.5 \cdot 10^{-9}/\sqrt{\text{Hz}}$ in the AdV bandwidth, ref. [97]) |
| Beam jitter | see Figs. 4.12, 4.13 |

Table 3.1: PSL requirements

3.2 Location, requirements

3.2.1 Location

As for Virgo, the prestabilized laser will be located in the laser lab that houses the laser bench and the EIB shared with the INJ subsystem. The laser lab needs to be an ISO8 (class 100 000) clean room to ensure dust free and clean conditions with a temperature regulated to better than 0.5 °C for having a stable environment. The EIB will be arranged and specified once the layout of the injection bench (and the input mode cleaner) will be done. The high power laser will be enclosed in a sound proof enclosure as it has been done for the initial Virgo, because the laser frequency and the beam jitter have been found to be very sensitive to local acoustic noise. The seed laser should be also in an acoustic enclosure as it defines the frequency of the HP laser. To avoid the perturbations due to the fans, all the electronics which require fans will be placed outside, except boards with stringent requirements of noise and bandwidth. The pumping laser diodes, their power supplies and the noisy chillers will be located in a separate room outside the laser lab. This room should be relatively clean, so that failed pump diodes could be exchanged on site, using a portable laminar flux.

3.2.2 Requirements

In order to reach the AdV sensitivity, the laser has to fulfill a number of specifications among which there are the beam requirements in terms of output power and stability. Its location at the front end of the interferometer results in little interference with other subsystems. Actually, the important inputs are coming from the ISC subsystem directly for the Relative Intensity Noise (RIN) requirement or through INJ for the frequency and beam jitter requirements. The table 3.1 summarizes quickly these data through noise curves mentioned in the TDR.

3.3 Interfaces with other subsystems

The PSL subsystem will interface with other subsystems:

- ISC to define the frequency range and the dynamics of the prestabilization and to implement the final frequency stabilization loop (SSFS) as well as the RIN specifications at the ITF input;
- INJ to provide the high power (HP) compatible EOM and Faraday Isolator (FI) used on the laser bench and for integrating of the power stabilization photodiode on the

injection bench;

- INF, for the sound proof enclosure, the maintenance of laser lab cleanliness and the installation of the laminar flow around the pumping diodes outside the laser lab;
- DAQ for the control and monitoring requirements.

3.3.1 Interfaces with INJ

The interfaces with INJ concern a few points:

- the beam sent from the laser bench to the **EIB** which is taken care of by INJ: the requirements of beam jitter have been computed by INJ, starting from the allowed beam jitter at the entrance of the interferometer. The beam pointing noise of the beam delivered to the **EIB** will match the specifications of Table 3.1.
- the dimension of the power stabilization photodiode sitting on the **SIB** which will be around 250 mm x 300 mm. INJ will take care of matching the beam to the sensors. **PSL** will send to INJ the beam characteristics as soon as the sensors board is finalized. Any heat removal necessity from the board will be managed by INJ.
- the beam waist or the maximum diameter beam size fitting in the EOM which are provided by INJ to **PSL**, which is not larger than 0.5 mm, in S-polarization and located within 5 cm of the output of **PSL**.
- INJ will integrate on **EIB** the frequency prestabilization photodiodes made by **PSL** as well as delivering the reference signal and phase shifters for demodulation.

3.3.2 Interfaces with ISC and INF

As in Virgo and Virgo+, the laser frequency will be prestabilized to the **IMC** length to take advantage of the good seismic isolation of the **SIB**, and at low frequency, the **IMC** length itself is stabilized to the rigid reference cavity (RFC) to control the drifts of the suspended **IMC** end mirror. This prestabilization allows for the final stabilization to the arm length [98]. The link between the frequency noise at the interferometer input and the control loops on the arms has been computed and ISC has given a requirement of the laser noise at the ITF input (see table 3.1). INF will decide where **PSL** could install the pumping diodes with a non-permanent laminar flow and the control electronics, power supply or cooling systems (chiller), which is too noisy inside the laser lab. This place should be as far as possible around the laser lab. Chiller and power supplies can be remotely controlled through RS232 connections. Monitoring signals can be made available either through RS232 for slow monitoring, or converted through the Adv DAQ channels, depending on the signal frequency range and precision of interest.

3.4 The fiber amplifier system

To reach the 200 W **HP** output, the baseline solution proposed in this TDR is to add coherently two lasers delivering 100 W each. The 100 W source is a two-stage amplifier made out

of Ytterbium doped fibers seeded by a monolithic laser similar to the laser already used in Virgo and Virgo+. The following paragraphs describe successively the parts of the 100 W amplifier and the coherent summation of two 100 W lasers will be described in section 3.7.

3.4.1 The seed laser

The seed laser is a laser similar to the master laser used for Virgo+ (NPRO from Innolight). Noise figures of such a laser (RIN, frequency, long term stability) made it fully compliant with AdV (based on Virgo+ experience, see also PMC chapter). The needed power depends on the high power amplifier scheme, and 0.3 W to 1 W is used, which anyway is fully available in the standard version. The seeder is connected to the amplifier through single mode polarization maintaining fibers. Hence, it makes unambiguous the alignment of the seeder with the amplifier and keeps it stable over time. As a consequence it will ease diagnostics and maintenance.

3.4.2 The HP amplifier stage

3.4.2.1 Fiber amplifier principle

The HP amplifier stage is based on the rod type fiber technology. This new scheme combines several advantages over solid state lasers and conventional fiber lasers. Rod type fibers are rigid silica fibers with an air-silica microstructure feature. The microstructures allow keeping single mode propagation of light in a large core, and getting pump light confined close to the core and far from the outer edge of the fiber. As a result the power intensity in the core is lowered (like for large mode area fiber), and the pump light is effectively absorbed in the core over a very short length (typically 1 meter). Both effects combine to reduce nonlinear issues when high power matters (stimulated Brillouin scattering [99] more specifically) and makes a 100 W laser readily available. Another interesting feature is that the core is Ytterbium doped. Ytterbium has a high absorption cross section around 980nm which makes the quantum gap between 1064 nm emission and absorption much smaller than in the case of the Nd:YAG crystals used for the Virgo+ laser (Neodymium doped YAG crystals are usually pumped at 808 nm). The pump power is therefore more efficiently transferred to useful photons, and the thermal load due to the pump power gets much reduced. Remark: Ytterbium has a much larger gain at 1030 nm than at 1064 nm, therefore a Yb amplifier is more efficient to amplify a 1030 nm wavelength and 200 W would already be available. This option has been discarded since moving the AdV laser wavelength from 1064 to 1030 nm has prohibitive side effects.

3.4.2.2 Amplifier stages overall description

A 100 W HP amplifier has been developed for AdV and tested at Eolite site. The box contains two stages of amplification: a preamplifier that brings the seed laser power of around 300 mW to 12 W, this preamplifier stage being pumped by a 130 W diode working at 60 W. This 12 W output is then brought to 100 W by the second amplifier which is pumped by a 200 W diode working at 160 W. A double stage scheme has been selected to manage the thermal load in the rods and keep the single mode feature of the output as much as possible. The

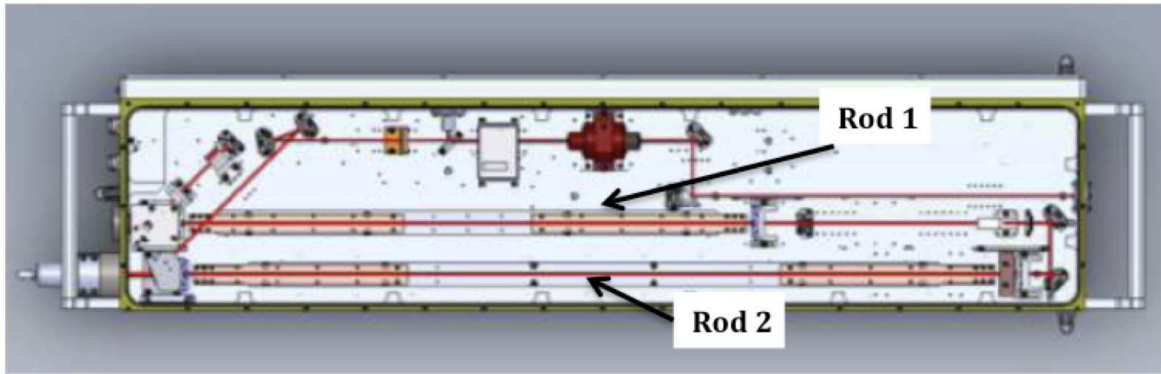


Figure 3.2: Picture of the Eolite two stages rod type amplifier. Due to industrial confidentiality we cannot give all the details of the parts, one needs only to know the location of input and output ports. The seed laser is injected through fiber cable connected on the left part of the box. The output port is situated on the right part of the box.

lengths of the rods are adjusted for optimizing the single mode behavior of the amplifier: for the present prototype, they are successively around 750 mm and 1080 mm (1st/2nd stages). The size of a 100 W Eolite amplifier head is about 1200 mm x 300 mm. According to the requested configuration, the optical path is adjusted to feed in series the preamplifier (short rod) and the amplifier stage (long rod) with the seeder. Besides that, the two laser diodes of 130 W and 200 W and their cooling system sit in a box and linked to the amplifier head by fiber cables. Last but not least are the 2 diodes power supplies connected to the diodes box by electric cables and receiving the feedback signal for the power stabilization (same principle as Virgo/Virgo+). Figure 3.2 gives the picture of this Eolite head.

The other parts of the Eolite head that are added by the company on our request, specifically for the PSL monitorings, are:

- some photodiodes to monitor the power at each stage of the amplifier (input, first stage, second stage);
- some photodiodes to monitor the pump power;
- a “trigger” photodiode to switch off the amplifier in case the input beam is interrupted and to prevent any Q-switch behavior of the amplifier (possible rod failures).

3.4.2.3 Beam shape

At an output of 60 W, more than 94% of the output beam follows a TEM_{00} Gaussian mode as it was measured by coupling within a Fabry-Perot cavity similar to the reference cavity of Virgo. It is linearly polarized in a ratio higher than 98.8%. Around 100 W HP output power, the coupling within the same Fabry-Perot is more than 92.6% in a TEM_{00} Gaussian mode; this shows some constant behavior of the beam shape vs. the output power. Figure 3.3 shows the output beam shape vs. the HP power and no noticeable change appears up to 95 W.

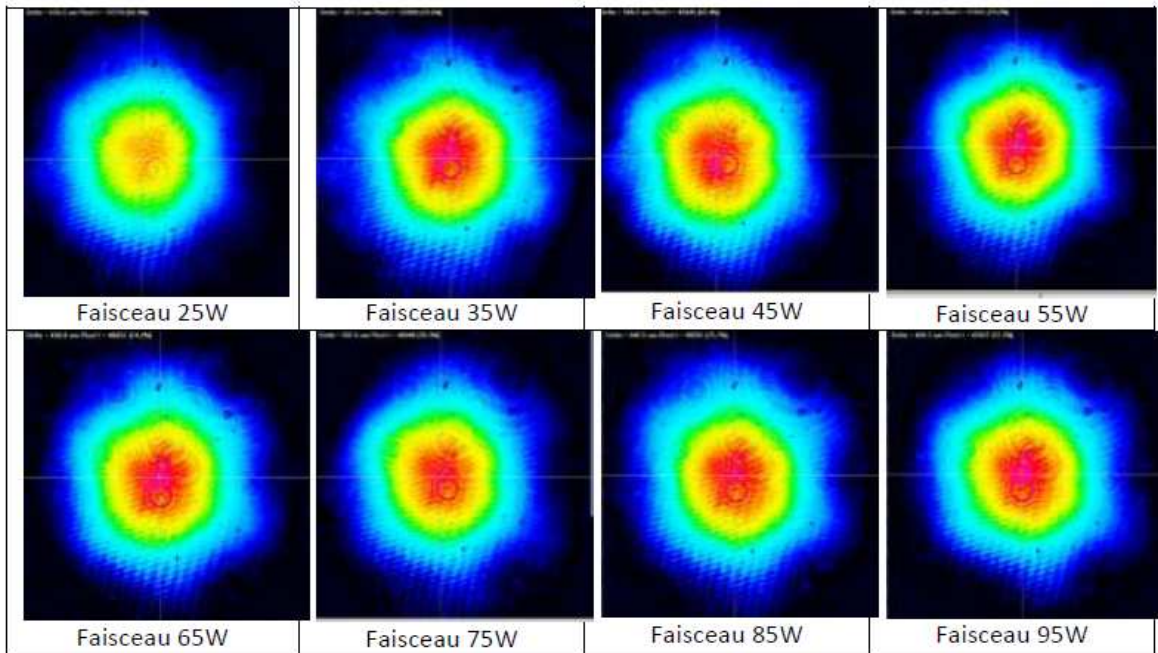


Figure 3.3: Beam shape of the Eolite HP amplifier vs. output power.

3.5 Frequency prestabilization

We show in the following paragraphs some noise figures (frequency and power fluctuations) for the HP rod amplifiers that have been taken when the prototype was operating at 60 W and tested in a quiet lab environment (Nice lab). The data about the RIN and beam jitter were obtained at 100 W output at the Eolite lab before the prototype started the process of long term tests.

In the PSL subsystem, the laser frequency is prestabilized, this prestabilization being the first stage of a series of stabilizations to bring the laser frequency down to the level required for the arms resonances. The series of stabilizations is described by the ISC subsystem and according to the sensitivity expected for AdV, ISC has specified to PSL the level of prestabilization required (which is less than $1 \text{ Hz}/\sqrt{\text{Hz}}$, see Tab. 3.1). As mentioned above, we recall that the beams used to construct the error signals for prestabilization are provided by the INJ subsystem and sent to a fast photodiode and a servo loop, both of them provided by PSL. Figure 3.4 plots the free running frequency noise (amplifier output was 55 W) and the usual $10 \text{ kHz}/f$ behavior of Virgo/Virgo+ master laser: one can see that this amplifier does not bring extra frequency noise, when seeded by the same master Virgo/Virgo+ laser. The requirement for AdV is not more stringent than for Virgo, therefore the same servo loop can be used for AdV. As for Virgo/Virgo+, the prestabilization loop will act on the seed laser through three actuators: the fast actuator is an EOM the intermediate range is covered by a piezo bonded to the laser crystal, the slow actuator is the temperature control of the crystal. This triple loop can have a unity gain frequency of a few hundred kHz, to provide a very high gain at low frequencies. It relocks automatically after a few seconds in case of accidental unlock. The frequency noise is measured after the HP amplifier, so that its additional noise

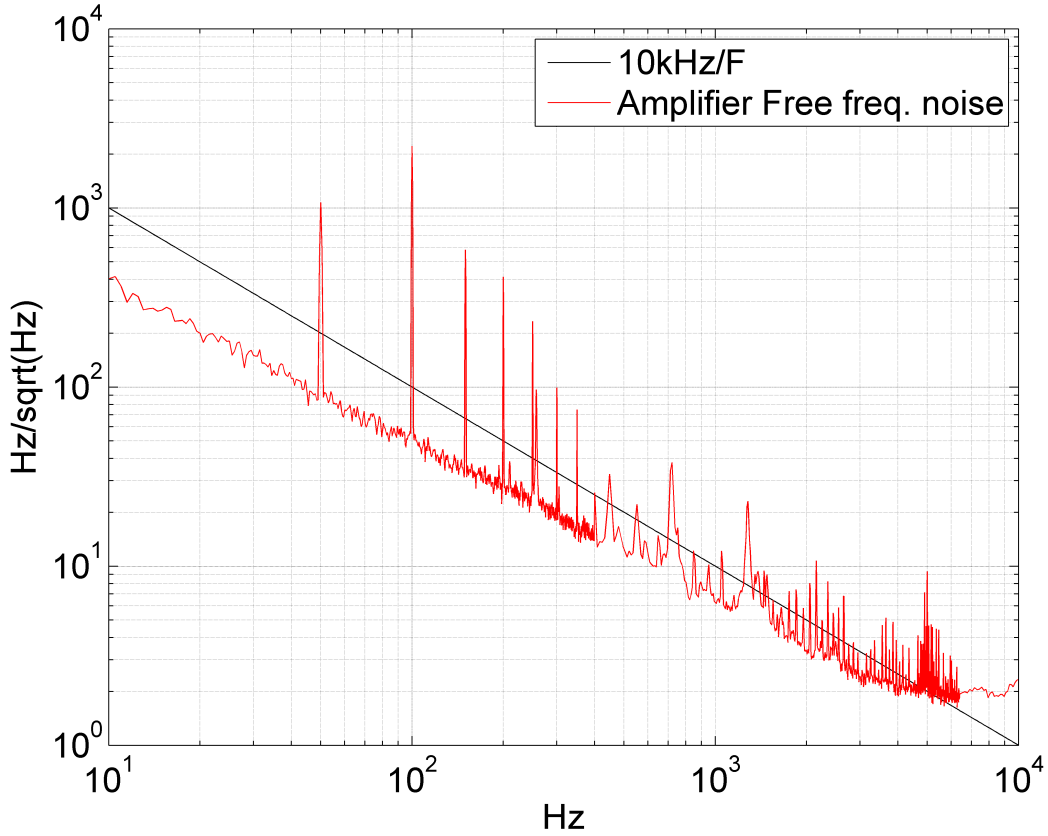


Figure 3.4: Free running frequency noise of the 100 W HP fiber laser operated at 55 W (red curve). Black curve: Typical Virgo+ master laser-like contribution.

is corrected by the feedback loop.

3.6 Power stabilization

The specifications of power stabilization are of two kinds: First make sure that the power detected at the AdV auxiliary modulation frequencies (6.27, 8.36, 56.4 MHz) be shot noise limited for 0.1 W detected, which is -175 dB/Hz ($1.78 \cdot 10^{-9}/\sqrt{\text{Hz}}$) [97]. And keep the RIN low enough in the AdV detection bandwidth, ie -172 dB/Hz ($2.5 \cdot 10^{-9}/\sqrt{\text{Hz}}$) @ 30 Hz [100] To reach this level in the detection bandwidth, the laser needs to be stabilized via a photodiode capable of detecting more than 50 mA (shot noise limit for a noise of $2.6 \cdot 10^{-9}/\sqrt{\text{Hz}}$). Recent R&D conducted in our lab with a 20 W laser has shown the importance of a coupling between the residual Beam Jitter (BJ) and residual spatial non-homogeneity of the photodiode sensitivity, a factor that we name “K” (in m^{-1}). We will raise the issue in section 3.6.2.

3.6.1 RIN at the AdV auxiliary modulation frequencies

We have checked with the **HP** rod fiber amplifier that no extra noise is added to the **RIN** for the frequencies around several MHz and within a detection limit of our setup (80 mA of photocurrent, 0.1 W detected power). It means that above several MHz, the **HP** amplifier copies the **RIN** of the seed laser. If we take a seed laser identical to the Virgo+ master laser, the **RIN** at 6 MHz is lower than -155 dB/Hz ($1.78 \cdot 10^{-8}/\sqrt{\text{Hz}}$) [101]. To reach -175 dB/Hz ($1.78 \cdot 10^{-9}/\sqrt{\text{Hz}}$) no servo loop can be used at those RF frequencies, but the passive filtering through two **PMC**, which is the baseline solution, will bring at least a 30 dB attenuation (see **PMC** paragraph below).

3.6.2 RIN in AdV bandwidth

In the AdV bandwidth two issues are relevant for the **RIN** performances: first ensure that a servo loop has enough gain for the purpose, and ensure that the photodiodes sensitivity spatial uniformity is good enough (K factor, see section 3.6.2.2).

3.6.2.1 Free-running noise and servo loop

Figure 3.5 shows the free-running **RIN** of the amplifier on the upper parts: one can note that the **RIN** we measured at 100 W is higher than at 55 W likely due to the different environment, the 100 W being measured in the Eolite lab. The amplifier **RIN**, although rather noisier than the Virgo laser, remains still manageable using power stabilization techniques developed for Virgo+ laser. We benefit from reasonable bandwidth (100 kHz) and high dynamics (10% of the output power and more) to actuate on the amplifier diode pumps. On the same Fig 3.5 we have added the performance of the power stabilization of the amplifier operated at 55 W, compared to the requirements. Finally the green curve shows the ultimate performance of that specific loop: the low level reached below the AdV specifications is quite important (factor 50 @ 100 Hz, and factor 20 @ 1 kHz): it shows also the spare gain of the open loop transfer function. Therefore even if the **RIN** of the **HP** at 100 W is somewhat more important than at 55 W the available servo loop is able to deal with the extra noise. Moreover it can be shaped and optimized to show larger gain below kHz region.

The second issue to reach such a low **RIN** level is the photodiode sensitivity spatial homogeneity, combined with the effect of dust particles in the optical path. Consequently this photodiode will be inserted under vacuum at a point where beam jitter is minimized and must follow some specifications regarding its spatial homogeneity. The location after the **IMC** has been proven convenient in initial Virgo and this position is taken as the baseline solution. In addition the plan is to add a second, out-of-loop photodiode to measure the real performance of the servo, a quadrant photodiode in order to monitor beam position and beam jitter at the photodetector surface, and some remotely controlled mirrors in order to be able to center the beam on the photodiode.

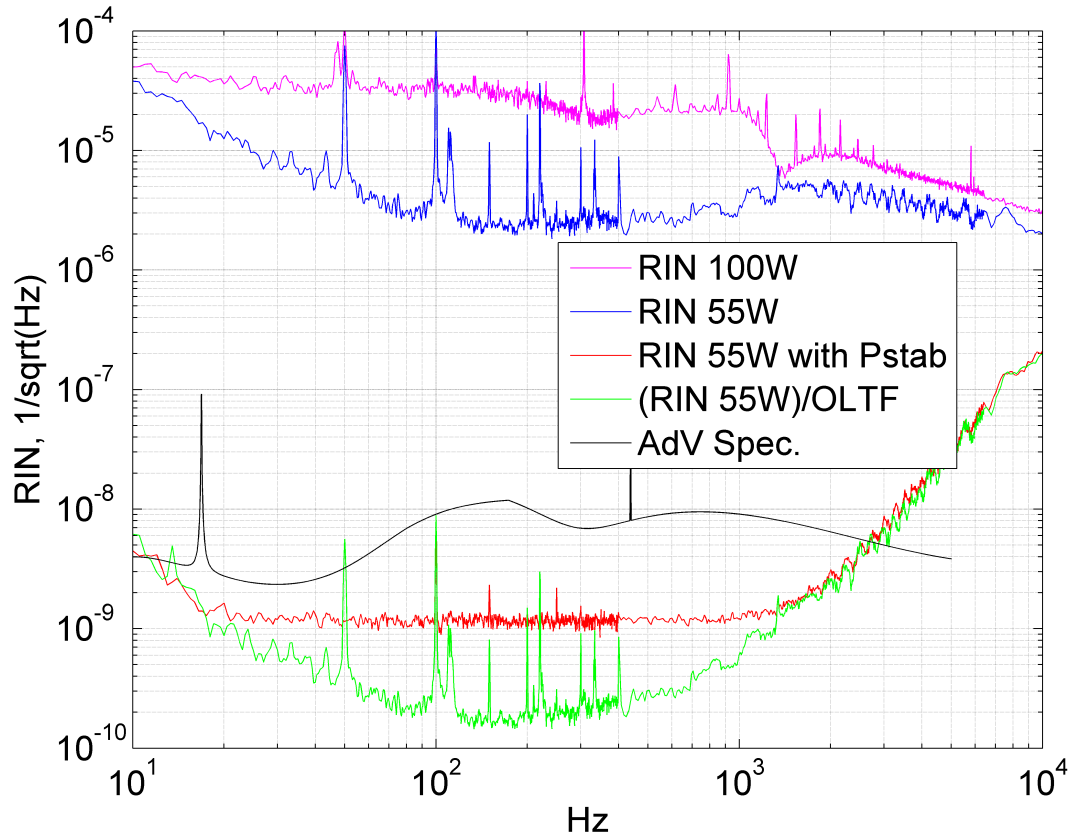


Figure 3.5: The magenta curve is the RIN of 100 W HP amplifier. Blue curve: RIN of the 55 W amplifier. Red curve: RIN of the 55 W amplifier after stabilization. Green curve: 55 W RIN divided by the open loop transfer function of the servo loop. Black curve: AdV specification.

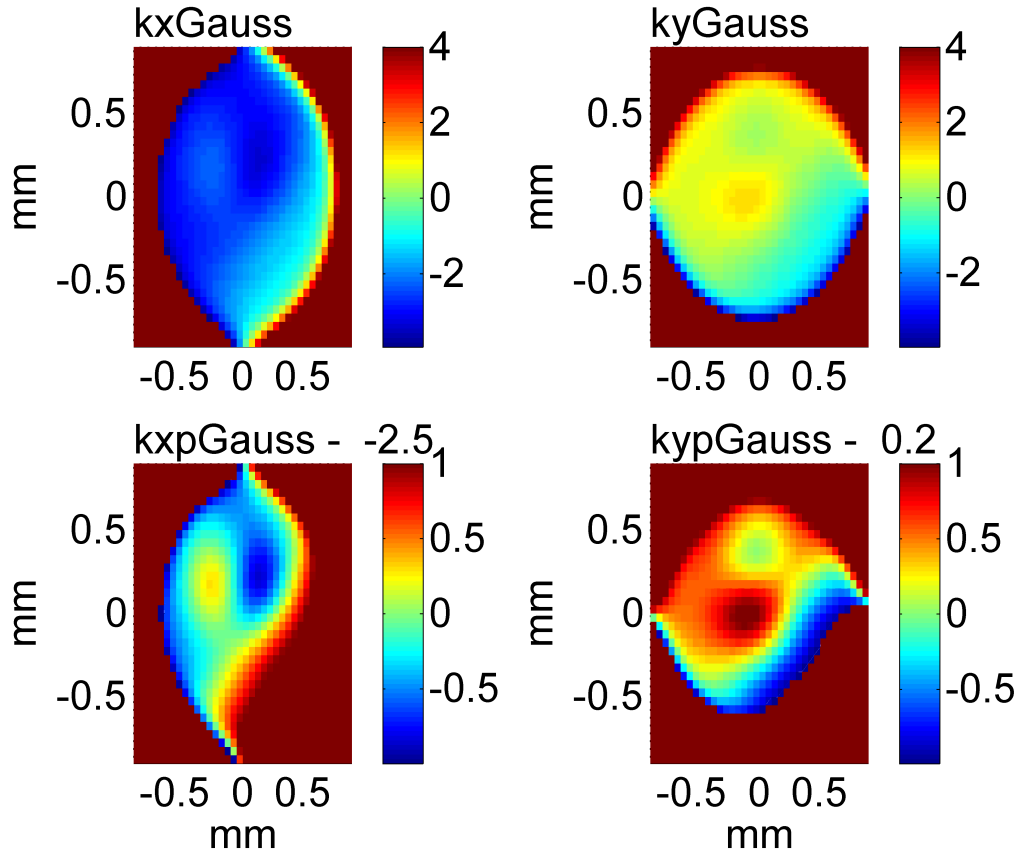


Figure 3.6: Upper plots: K factor for a selected photodiode. “kxGauss” means the derivative along x axis (horizontal) of the relative photodiode sensitivity, and averaged with a 400 microns radius Gaussian beam. Lower plots: same as upper, but with the DC component removed for legibility (-2.5 m^{-1} and $+0.2 \text{ m}^{-1}$).

3.6.2.2 Photodiode sensitivity homogeneity issue

The homogeneity of the sensitivity of a few photodiodes from different manufacturers has been measured and was found compliant with the AdV beam jitter specification after the IMC for most of the photodiodes we could test.

Figure 3.6 plots the gradient along x/y axis of the relative sensitivity S of the photodiode, named the K factor ($K = \partial S / \partial x$, or $\partial S / \partial y$); therefore the RIN induced by the BJ coupling to the photodiode non-homogeneity is expressed as $\text{RIN} = \partial x \times K$ (∂x being the lateral BJ at the photodiode surface, standing for ∂x or ∂y). K is expressed in m^{-1} , and we have assumed a 400 microns beam radius feeding the photodiode. For the three selected photodiodes we have found that one must keep the beam in an area of 1 mm diameter to keep K below a few m^{-1} .

Taking into account the BJ specifications at IMC output we have evaluated the associated lateral BJ at the photodiode location given a realistic telescope between IMC and photodiode in order to match both apertures. Two telescope configurations have been tested (Focal length 3 and 6m) which both reduce the IMC transmitted beam down to a 400 microns beam radius, where the photodiode stands. Figure 3.7 plots the lateral beam jitter at the

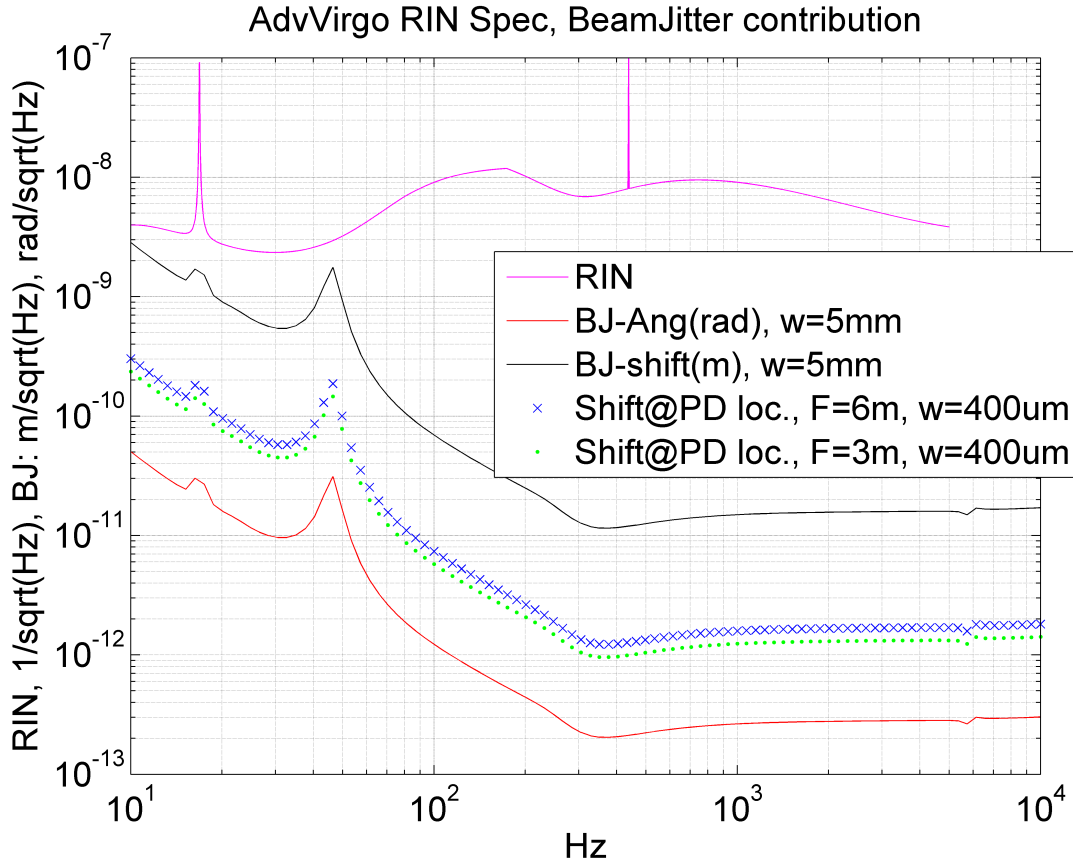


Figure 3.7: The dotted lines are the estimated lateral BJ at the photodiode surface in $\text{m}/\sqrt{\text{Hz}}$. Blue solid line: AdV **RIN** specification in $1/\sqrt{\text{Hz}}$. Red and black solid lines: AdV BJ specifications after the **IMC**, in $\text{m}/\sqrt{\text{Hz}}$ for lateral BJ and $\text{rad}/\sqrt{\text{Hz}}$ for angular BJ.

photodiode location for both telescope configurations (dotted lines) and reminds the AdV **RIN** specifications and the AdV **BJ** specifications right after the **IMC** (beam waist is 5 mm). This makes obvious that a K factor lower than 10 should be enough to keep BJ induced **RIN** below the AdV **RIN** specifications. As mentioned above, for the three tested photodiodes it should be just a matter of keeping the beam within a 1 mm diameter target to get K below a few m^{-1} . Up to now several photodiodes have been purchased and selected and some of them kept as spare.

3.7 Coherent addition of two lasers

To deliver the 175 W required by INJ, the baseline is to add coherently two 100 W prototypes together. The addition of two lasers is not a big technical difficulty and we experienced it a long time ago with quite noisy lasers [102] and with no surprise on the results. What remains to be done is the check out of the different noises on the resulting beam. An extra servo loop to control the length of one laser path relatively to the second laser path has to be implemented. This should not present any difficulty, as this servo loop is a slow one to prevent mechanical drifts and is internal to both the frequency and power stabilization loops.

| Cavity (Virgo+ PMC) | Beam plane | Horizontal attenuation | Vertical attenuation |
|-----------------------------|------------|------------------------|----------------------|
| 1 cavity | Horizontal | 0.0032 | 0.017 |
| 1 cavity | Vertical | 0.017 | 0.0032 |
| 2 dual cavities | H + V | 5.4×10^{-5} | 5.4×10^{-5} |

Table 3.2: Attenuation factors achieved with one cavity and 2 cavities

3.8 Beam stabilization: the pre-mode cleaner

The role of the **PMC** is twofold:

- Filter out the high order modes inherent to the **HP** amplifier stage and lower the beam jitter at the INJ input port
- Lower the laser **RIN** at the Adv auxiliary modulations frequencies

3.8.1 Beam jitter filtering

According to the stringent beam jitter specifications at the INJ input port (see Table 3.1) some extra beam jitter filtering after the **HP** laser becomes mandatory. Moreover, even though the **HP** laser uses rod type fiber technology, the present Adv prototypes we have tested do show an output beam imprinted with non negligible beam jitter. This could be due to a noisy environment, but could also be explained by the high level of pump power required to reach 100 W output power, which, by dumping a significant thermal load in the rod, changes the guidance properties of the rod fiber and leads to a weaker modal selectivity of the rod. The issue can be minimized through the optical configuration of the **HP** laser (length of the rod fiber, combination of rod fibers) and is part of the work of the laser manufacturer. For the following curves, we take the beam jitter measured with the 100 W **HP** laser as reference values. To evaluate the filtering action of a cavity, Fig 3.8 shows the filtering effect of the Virgo+ **PMC** [103] lying in the vertical plane as an example: the lateral/angular **BJ** specifications given by INJ and evaluated at **PSL** output port, are normalized to relevant beam waist/divergence. Only lateral **BJ** has been plotted for sake of legibility (angular **BJ** appears to be about the same as lateral **BJ**). We recall that the specifications are not the same on horizontal and vertical **BJ** as it comes from the **IMC** that has a better filtering in horizontal.

It is obvious that an attenuation factor 20 is missing for horizontal **BJ** and 10 for vertical **BJ**. As a non negligible attenuation factor is missing in vertical direction, we propose as baseline solution the use of a two stage filtering with a scheme with two cavities in series one in a horizontal plane and the second in a vertical plane. The **PMC** block in Fig 3.1 will then be a box of two cavities. If we keep for both of them the same parameters as the Virgo+ **PMC**, the intra-cavity power is only increased by a factor three and remains easily manageable with appropriate coatings (175 W for Adv instead of 60 W for Virgo+). Table 3.2 gives the attenuation factors used for one cavity and two crossed cavities assuming the Virgo+ **PMC** design parameters given in table 3.3. Virgo+ **PMC** pole is 1.07 MHz, therefore 2 cavities will provide an attenuation at 6.27 MHz equal to $1/[1+(6.27/1.07)^2]$ (31 dB).

Figure 3.9 represents the expected performances of **BJ** with two cavities. Compared to the

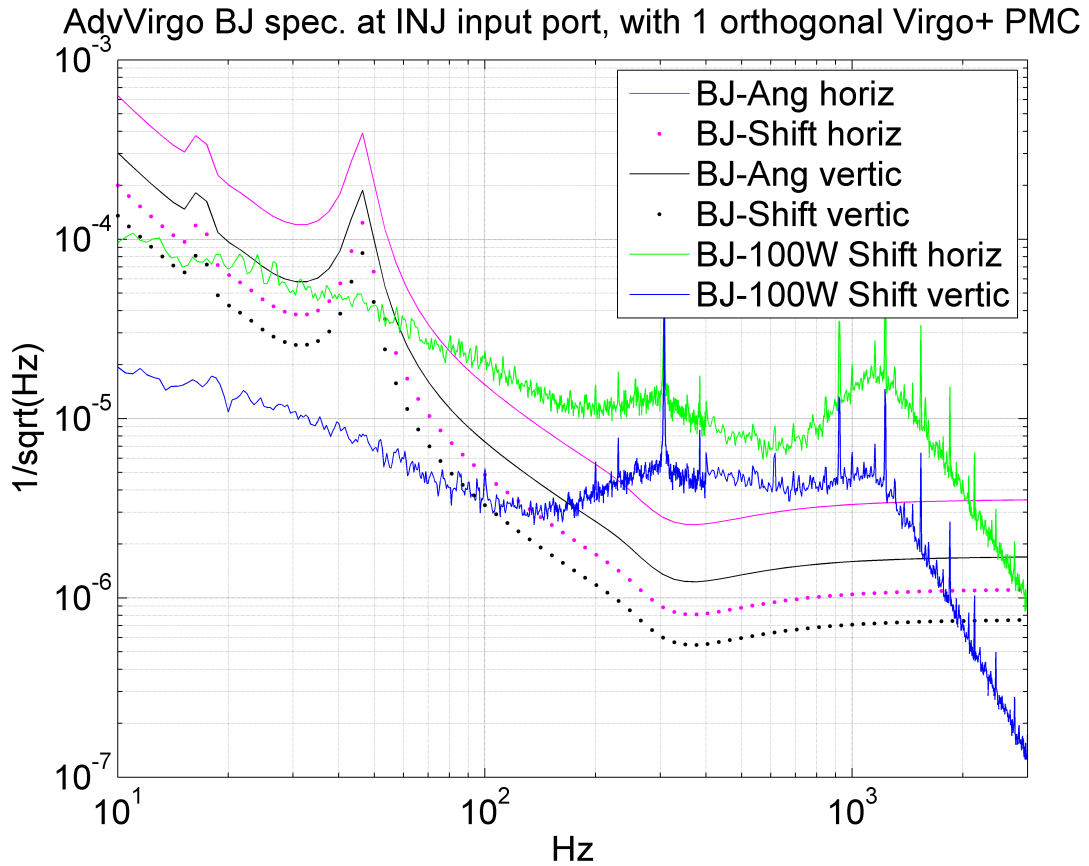


Figure 3.8: Expected Adv lateral BJ spectra of 100 W HP amplifier filtered by one Virgo+ PMC (angular data are similar to lateral and are not plotted for sake of clarity). In that specific case we assume that the PMC is lying in a vertical plane. Regular lines are the specifications of the BJ at PSL output port for vertical (dark curves) and horizontal (magenta curves) direction and expressed according to angular (solid curves) and lateral (dotted curves) (see INJ chapter, sec. 1.7). BJ specifications are normalized to the associated beam parameters.

| Mode waist | Mode divergence | Finesse | Length | End mirror curvature | Triangular cavity | Pole Pole |
|-------------------|---------------------|---------|--------|----------------------|-------------------|-----------|
| 500 μm | 675 μrad | 500 | 0.14 m | 4.2 m | | 1.07 MHz |

Table 3.3: Virgo+ PMC design parameters

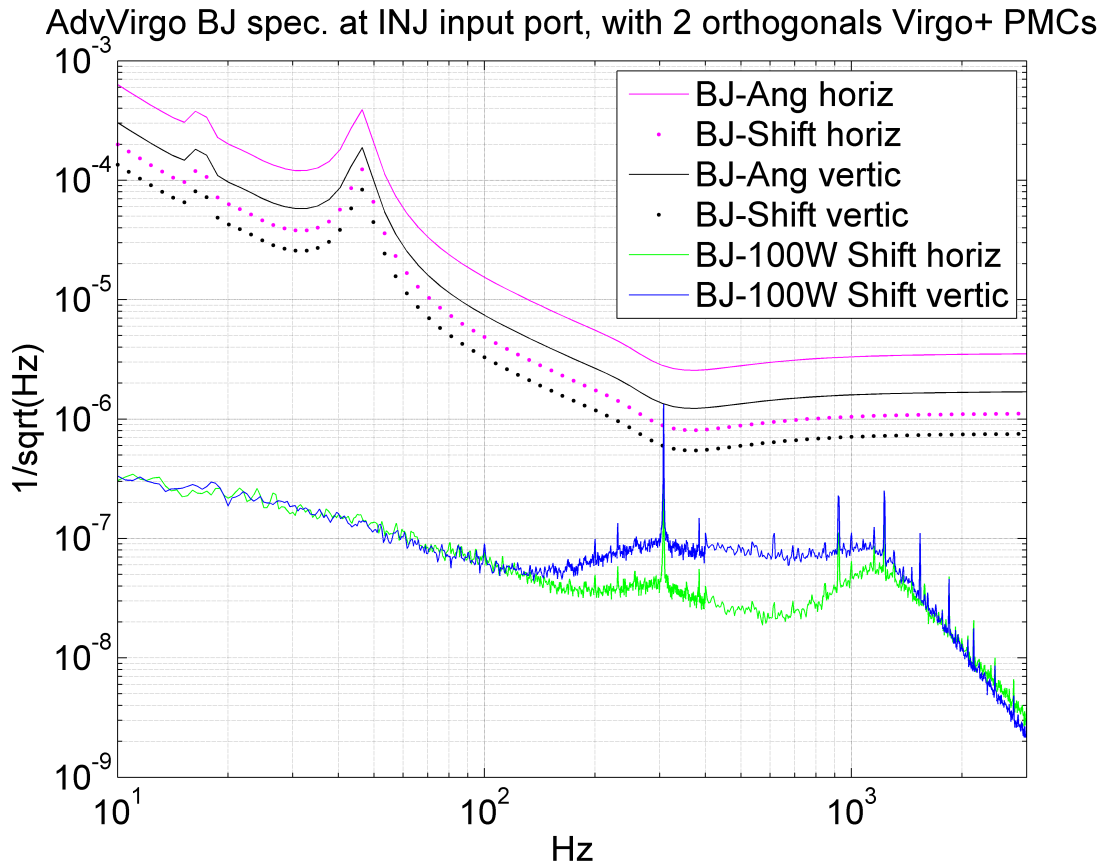


Figure 3.9: Expected lateral BJ spectra of 100 W HP amplifier filtered by 2 cavities (Virgo+ like). Regular lines are the specifications as in Fig 3.8.

requirements put by INJ, the residual BJ are far below.

3.8.2 Optical and mechanical design

Each filtering cavity of the PMC block is a three mirror (two plane and one curved) ring cavity inserted into the main beam path and has a high transmission for the fraction of the light in the TEM₀₀ mode. A length control system based on a PZT mounted curved mirror is needed to keep the cavity resonant with the incoming beam and to compensate for large drifts over long periods of time. A Pound-Drever-Hall loop or a tilt locking loop will be used to pick up the signal reflected by the PMC. Following the amount of power distributed on high order modes, the finesse of the PMC will be designed as a trade-off between spatial filtering, noise filtering and circulating power. Today the PMC of Virgo+ (Fig. 3.10) stands a power of about 60 W without mirror damage thanks to high quality coated mirrors by LMA-Lyon and a vacuum enclosure to keep it air-free and dust-free. Vacuum enclosure (Fig. 3.11) may appear as oversized thanks to our experience with Virgo + and we may consider using a simple sealed box to overcome cleanliness issues. The PZT mounting sits behind the curved high reflectivity mirror and it will be mounted in a negative/positive expansion design in order to minimize any heating effect due to residual transmission of the high reflectivity

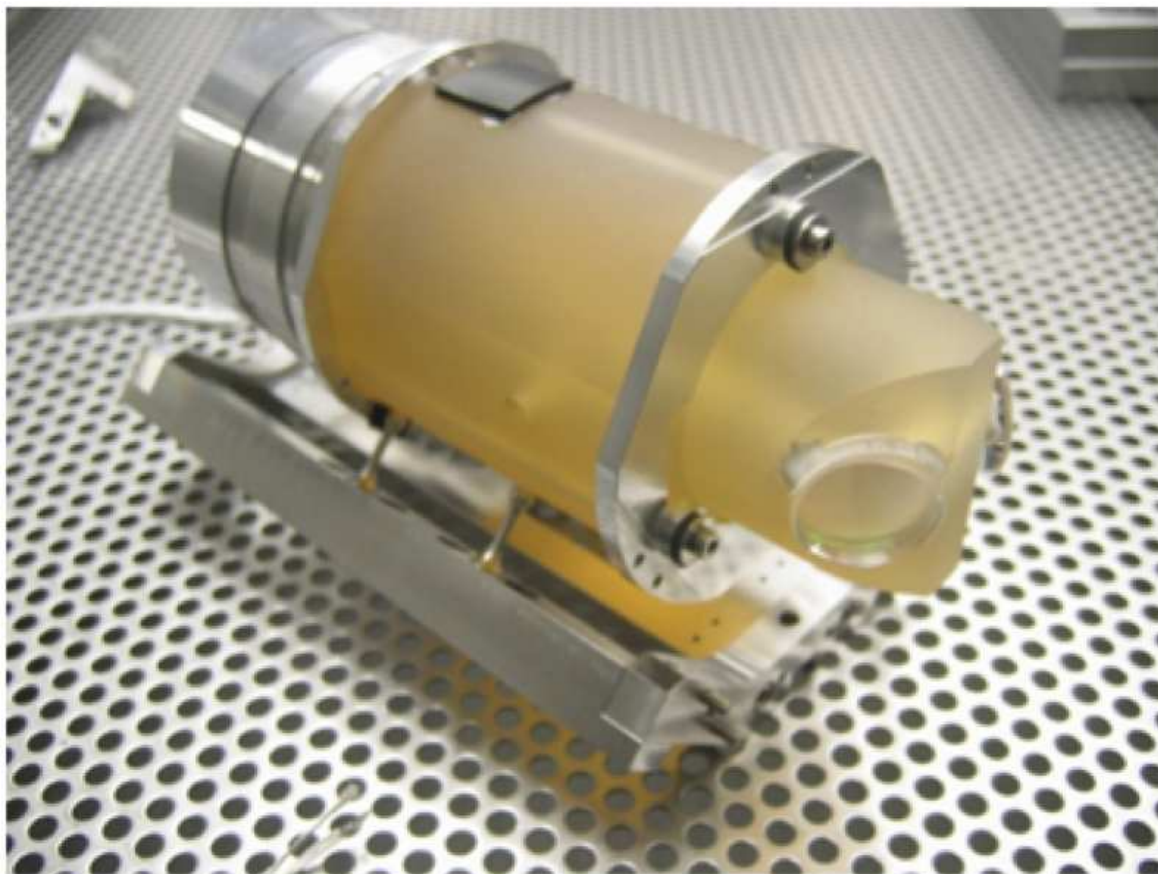


Figure 3.10: Virgo+ PMC: mechanical mounting

mirror. The two-cavity PMC will be enclosed into a simple sealed metallic box to overcome cleanliness issues.



Figure 3.11: Virgo+ PMC vacuum tank

Chapter 4

Injection (INJ)

4.1 Scope of the subsystem and general requirements

The Injection subsystem (INJ) subsystem of Advanced Virgo takes care of the optics downstream of the high power laser, and of the interface between these optics and the laser. The whole system must deliver a beam with the required power, geometrical shape, frequency and angular stability. The general requirements for the AdV INJ subsystem are given in Tab. 4.1, considering the fact that the high power Advanced Virgo (AdV) laser delivers 175 W in the TEM₀₀ mode, and the AdV sensitivity goal [104]. Moreover, all the components used in the injection system at places where the beam is powerful will have to be designed for high power operation (Faraday isolator, electro-optical modulators,...). The injection system ends between the meniscus lens and the power recycling mirror.

| Parameter | Requirement |
|--|--|
| Transmission to the ITF | $> 70\%$ TEM ₀₀ (175 W TEM ₀₀ at INJ input port) |
| Non-TEM ₀₀ power | $< 5\%$ |
| Intensity noise | $2 \times 10^{-9}/\sqrt{\text{Hz}}$ at 10 Hz (from ISC) |
| Beam Jitter | $< 10^{-12}$ rad/ $\sqrt{\text{Hz}}$ ($f > 10$ Hz) |
| Frequency noise (for lock acquisition) | < 1 Hz rms (from ISC) |

Table 4.1: AdV INJ general requirements.

The expected overall power loss budget for the INJ subsystem is given in Tab. 4.2.

4.2 Subsystem overview

An overview of the INJ subsystem can be seen in Fig. 4.1. The general layout proposed here is expected to fulfill the requirements asked to the INJ subsystem in terms of laser beam

| Parameter | Value |
|--|-------|
| Electro-optic modulators | 3% |
| Faraday isolator (between the laser and IMC cavity) | 5% |
| Input power control system (before IMC) | 2% |
| IMC cavity coupling losses | <5 % |
| IMC intra-cavity losses | <4 % |
| In-vacuum Faraday isolator | 5% |
| Input power control system (ITF input port) | 2% |
| Other losses(RFC/power stabilization pickoff and optics) | 2% |
| ITF coupling losses | 1% |
| Total power lost budget | <30% |

Table 4.2: INJ power budget.

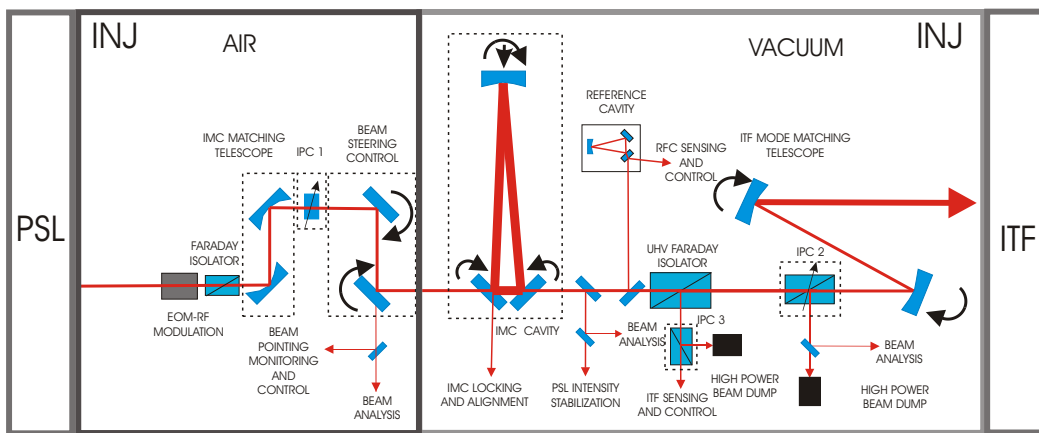


Figure 4.1: General optical scheme of the INJ subsystem.

pointing, frequency and amplitude stability given in Tab. 4.1 and the power loss budget given in Tab. 4.2.

An Electro-Optical Modulator (**EOM**) system will provide the needed radio frequency phase modulations (for control and sensing purposes). A power adjustment system, Input Power Control (**IPC**), consisting of a half wave plate and a few polarizers, will be used in order to tune the Interferometer (**ITF**) input power (important for ITF lock acquisition). A matching and steering system in air will be used to properly couple the beam into the in-vacuum suspended Input Mode Cleaner (**IMC**) cavity. The IMC will geometrically clean the beam and reduce its amplitude and beam pointing fluctuation. The resonant IMC, whose length is locked on the Reference Cavity (**RFC**), will also serve as a first stage of frequency stabilization. After the IMC an intensity stabilization section will provide the signal for stabilizing the laser Relative Intensity Noise (**RIN**). An in-vacuum Faraday isolator will prevent interaction of the light rejected by the interferometer with the IMC and the laser system. An ITF mode matching telescope will give to the beam the correct dimension for matching it to the interferometer. Finally, INJ should provide a way to monitor laser beam properties at different points of the INJ subsystem to keep track of every change and be able to accurately adjust the beam provided to the ITF (input beam monitoring system).

4.3 Functional requirements

Going further into the details, the functional requirements for each subpart of the INJ subsystem are given in this section.

- Electro optical modulation (EOM) system, radio frequency generation and distribution (see section 4.6): An EOM system will provide the radio frequency modulations of the laser beam as required by ISC subsystem (for ITF and IMC control and locking). This system will have to fulfill AdV requirements in terms of phase noise and residual amplitude modulation at the modulation frequencies. The generation and distribution of RF modulations will be provided by INJ and should also respect specifications in terms of phase and amplitude noise.
- Beam Pointing Control (BPC) (see section 4.7): The purpose of this control loop is to reduce angular and lateral beam jitter of the beam at low frequency before entering the vacuum vessel. This system should also help to properly tune the absolute beam position and direction. A particular care is required for the actuator selection and actuator mounts design in order to fulfil AdV requirements in terms of beam jitter.
- Input Beam Jitter Monitoring (IBJM) (see section 4.7): This system will monitor beam shifts and tilts over the whole sensitivity curve bandwidth.
- IPC (see section 4.8 for more details): It is used to remotely tune the laser power from low (a few Watts) up to full power. This system will be based on the Virgo+ IPC system. We propose to adjust the laser power in three places of the INJ subsystem:
 - Before the IMC cavity;
 - On the suspended injection bench (Suspended Injection Bench 1 (SIB1)) after all the optical elements that are sensitive to laser beam heating, in order to adjust the laser power at the interferometer input port (during the commissioning phase);
 - On the ITF reflection beam.
- High Power Beam Dump (HPBD): Low diffusion beam dumps able to withstand up to high continuous laser power (200 W) should be provided by INJ (see 4.9 for more details).
- Input Mode Cleaner cavity: The laser light must be frequency stabilized and spatially filtered before it can be used in the interferometer. The input mode cleaner (IMC) provides active frequency stabilization through feedback to the laser, passive frequency noise suppression above its cavity pole frequency, and passive spatial filtering at all frequencies. In particular, the input mode cleaner cavity filters out laser beam jitter (see 4.10). After the IMC an intensity stabilization section will provide the signal for stabilizing the laser RIN (see PSL).
- Reference cavity (RFC): A reference cavity is used to prestabilize the laser frequency. It should be possible to perform alignment and matching of the RFC system independently from the ITF beam. In science mode, the RFC will be used in the low frequency stabilization loop of the ITF. More details are given in 4.11.
- Faraday Isolators (FI): A high power compatible, 20 mm clear aperture, in-vacuum

Faraday isolator, compensated in terms of thermal lensing and depolarization, with the possibility to remotely tune the isolation, will be provided. Its optical isolation at full power should be higher than 40 dB (see 4.12 for further details). Other Faraday isolators with a smaller clear aperture to be used in air will have to be provided mainly to isolate AdV laser from back-traveling light coming from the IMC or the ITF.

- Mode Matching Telescopes (MMT): Two telescopes of this kind will be part of INJ. One will be used to match the beam onto the IMC cavity, and the other one to match the beam onto the ITF (see section 4.13). These devices should be remotely adjustable and use the input beam monitoring system (see section 4.14) for the fine adjustment of the matching on the IMC cavity and the ITF.
- Input Beam Monitoring System (IBMS): (see section 4.14) It should provide some useful tools to characterize the ITF input beam properties. This system should be used to:
 - Adjust laser beam properties in different places of INJ.
 - Characterize thermal effects in INJ.
 - Potentially provide error signals for a thermal compensation system.

4.4 Interfaces with other subsystems

4.4.1 Prestabilized Laser (PSL)

The interface between PSL and INJ is described with more details in the INJ/PSL interface control document [105]. The main interfaces are described here.

4.4.1.1 Optical parameters

The output beam from PSL will be delivered to the INJ subsystem at the output of the optical table (laser bench), leaving enough space to install 2 or 3 electro-optic modulators (about 30 cm are needed) along the main beam path. The spot size at the beam waist of the PSL output beam shall be 0.5 mm (maximum dimension limited by the EOM's clear aperture). The PSL output beam waist location shall be within 5.0 cm of the PSL output beam location. The beam should be S-polarized.

4.4.1.2 Frequency prestabilization

PSL will provide the photodiodes to be used in the frequency pre-stabilization loop. INJ will take care of integrating these photodiodes on the injection benches. INJ will provide the reference signal as well as electronic phase shifters for the demodulation of the photodiode signal. INJ will provide the frequency of the Radio Frequency (RF) phase modulation used in IMC sensing and control to PSL. Optical phase modulation of the laser beam at 22.38 MHz will be generated using an electro-optical modulator as presented in section 4.6.

4.4.1.3 Laser beam power stabilization

INJ will match part of the beam transmitted after the IMC to the sensors board. The sensor board will be designed and developed by PSL. Information on beam characteristics to be sent to the sensor board will be provided by PSL. The PSL power stabilization box maximum dimension is 250 mm x 250 mm (TBC) according to the suspended injection bench optical layout (see Fig. 4.6). INJ will study how to manage the heat removal of the box, to be installed under vacuum.

4.4.2 Superattenuator (SAT)

SAT will install one extra filter in the injection and mode cleaner towers in order to gain some safety margin, taking into account the expected IMC length noise projection given in 4.10 (see Fig. 4.30). The weight of the SIB1 payload (bench + opto-mechanical parts) has been estimated to be 160 kg. The weight of the new MC payload with marionette has been estimated to be around 147 kg (see Fig. 4.36).

4.4.3 Thermal compensation (TCS)

The generation of Hartmann beams and the sensing of thermal effects happening in the West input mirror is expected to be done through the injection benches. A space of 1.2 m x 0.4 m has been reserved on the External Injection Bench (EIB) (see Fig. 4.3). The Hartmann beam will be injected through the pickoff used to extract the beam for the phase camera as explained in section 4.5.2. A projection of diffused light noise from this setup has been made; it is expected to be negligible if we have enough attenuation of the 1064 nm wavelength laser beam as shown in Fig. 4.2. In order to compute the amount of scattered light that can be recoupled in the ITF we used the same method as the one used to compute the contribution of the mode matching telescope optics to the AdV noise budget [139].

4.4.4 Detection (DET)

INJ will provide one beam to install a phase camera on it.

INJ will design and construct the optical setup for the interferometer reflected beam (telescope for single element and quadrant photodiodes and imaging camera). Vacuum compatible photodiodes to be installed on the new suspended bench (Suspended Injection Bench (SIB) 2) that will host the ITF reflected beam setup will be provided by DET: single element photodiodes (2 for ITF reflection and 2 for RFC reflection), and quadrant photodiodes (2 for ITF reflection). INJ provides to DET RF reference signals for demodulation purposes. The level of each reference signal is expected to be as high as +7dBm.

The INJ subsystem delivers diagnostic beams for interferometer length and alignment control to the ISC/DET subsystems (reflected beam from the ITF). These beams will have spot size and Gouy phase adapted to what is requested by DET/ISC. DET provides to INJ the new Suspended Injection Bench 2 (SIB2) bench plane on top of which will be mounted the optics of the ITF and RFC reflection setups.

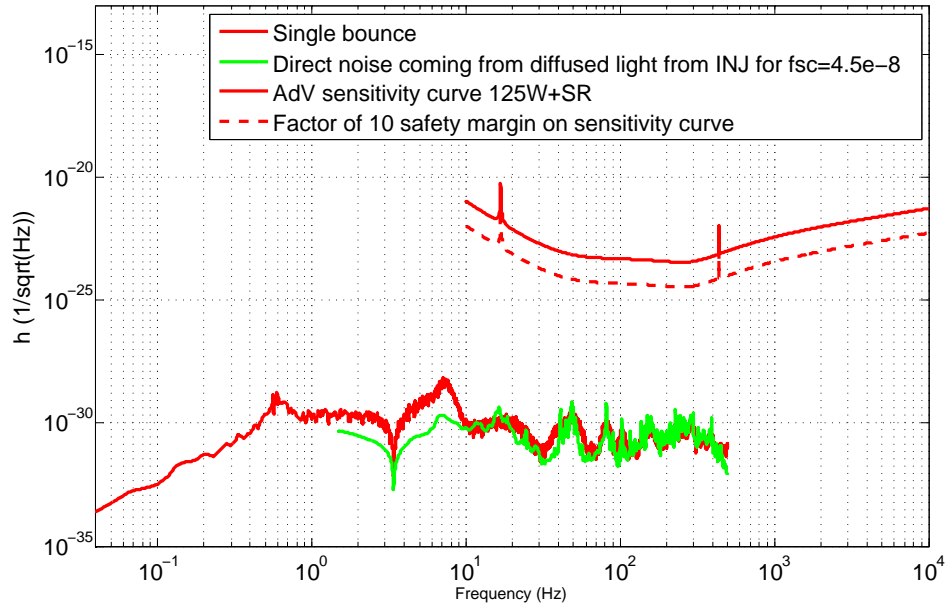


Figure 4.2: Projection of diffused light noise coming from the TCS Hartmann setup installed on the **EIB**. The residual motion resulting from the **EIB-SAS** isolation system has been used in this projection. We have considered that less than 0.5% of the light reflected by the **ITF** is transmitted through the phase camera pickoff mirror.

4.4.5 Payloads (PAY)

PAY will provide the interface between the bench plane and SAT subsystem (marionette) and a way to control the bench from the ground and from the marionette. PAY will provide the new payload to suspend the new IMC end mirror that has a diameter of 145 mm and a thickness of 94 mm (twice the Virgo+ end mirror thickness) (see 4.10 and Fig. 4.36 for more detailed numbers).

4.4.6 Suspended benches (SBE)

SBE provides the suspension and control system of the new **SIB2** bench. SBE provides also a Seismic Attenuation System (**SAS**) system to seismically isolate the external injection bench from ground motion that can create some excess of beam jitter noise on the laser beam coupled into the IMC cavity.

4.4.7 Vacuum (VAC)

A residual vacuum pressure of the order of 10^{-6} mbar will have to be ensured in the injection and mode cleaner towers. Windows to enter the vacuum system with the laser beam as well as viewports will be provided according to the needs of INJ. A cryolink will be foreseen between the injection and PR towers to avoid putting any not suspended transmissive optics on the main laser beam path. The clear aperture of this part is expected to be at least

150 mm diameter. The valves should be equipped with windows to allow the work even when the valves are closed. Glass separations have to be foreseen between the **SIB1** and **SIB2** towers. The one that will be installed on the ITF reflected beam should be made of fused silica, since high continuous power will pass through this window. A very good antireflective coating should be put on this window ($R < 0.1\%$). The window installed on the RFC reflected beam can be made of low cost glass such as BK-7. INJ will provide to VAC the value of the displacement needed for the IMC end tower in order to cope with the new ITF parameters.

4.4.8 Mirrors (MIR)

Since the power recycling mirror is part of the ITF mode matching telescope, INJ provides the radius of curvature of the Anti-Reflective (**AR**) face to the MIR subsystem. It is $3.59 \text{ m} \pm 30 \text{ mm}$ (TBC) (see section 4.13 for more details).

4.4.9 Infrastructures (INF)

The laser laboratory should follow the requirements given in [106] concerning air conditioning and cleanliness.

- Temperature: $T = T_0 \pm 0.2 \text{ }^\circ\text{C}$ with T_0 adjustable between 18 and 25 $^\circ\text{C}$; avoid temperature drops when people are working in the laser lab.
- Humidity: $50\% \pm 5\%$.
- Air flow: adjustable between 10 and 100% from remote (the control room) if possible.
- Clean room class: 100000(ISO 7/8) (also in reduced air flow conditions), access rules should be reviewed (consider the possibility to install an air shower).
- Acoustic noise: reduce acoustic noise above 100 Hz as much as possible.

4.4.10 Data acquisition (DAQ)

INJ will provide the list/number of channels to be acquired by DAQ with their sampling rates. DAQ will provide Analog-to-Digital Converters (**ADCs**) to acquire those signals, Digital-to-Analog Converters (**DACs**), real-time PCs and Digital Signal Processors (**DSPs**) that will be used in the INJ control loops.

4.5 INJ optical design

The overall layout of the INJ benches is given in Fig. 4.3. The INJ subsystem consists mainly of 3 benches: the **EIB**, is located outside of the vacuum system, the main suspended injection bench (**SIB1**) located in the injection tower, and the new suspended injection bench (**SIB2**), located in the new injection minitower located in the laser lab safety access system.

Note that all the mirrors and, when possible, all the optics installed on the high power laser beam path will be super-polished optics to reduce as much as possible the scattered light.

4.5.1 Optical specifications

For all the optics hold the following main specifications:

- All the optical components of INJ system should have free apertures diameters larger than 6 times the beam waist on the component itself;
- All the optics are made of fused silica;
- Surface quality: standard quality for mirrors used with low laser power:
 - Surface roughness: $\text{rms} < 1 \text{ nm}$;
 - Flatness peak-to-valley $< \lambda/20$;
 - Scratch/dig better than 20/10;
- Surface quality: superpolished quality for mirrors used with high laser power:
 - Surface roughness: $\text{rms} < 0.1 \text{ nm}$;
 - Flatness peak-to-valley $< \lambda/20$;
 - Scratch/dig better than 20/10;
- All transmitting optical surfaces are AR coated, with $R < 10^{-3}$ at the specified incidence angle and polarization;
- All totally reflecting surfaces are HR coated, with $R > 0.9999$ at the specified incidence angle and polarization;

4.5.2 External injection bench layout

The layout is shown in Fig. 4.3. This bench is hosting the steering and matching optics needed to properly match the beam on the IMC cavity. Moreover a high power compliant Faraday isolator (EIB Faraday isolator), using the same scheme as the In-vacuum compatible one, is added to avoid to have back-reflected light coming from the IMC cavity or the ITF that goes back to the laser and can damage it. One IPC system is installed on the main beam to adjust the power going to the IMC cavity. Quadrants and single element photodiodes used to lock and control angularly the IMC cavity are hosted by this bench. Moreover, a set of quadrant photodiodes and actuators used in the beam pointing control system (see section 4.7) are installed on the EIB. The Input beam monitoring system used to monitor the laser beam properties in several points of INJ is also hosted by this bench. With this system we will have the possibility to characterize up to 5 beams:

- The beam at the input of the IMC cavity
- The beam reflected by the IMC cavity
- The PR mirror or the ITF reflected beam
- The beam located at the output of the In-vacuum Faraday isolator
- The RFC input beam

Finally, some space has been reserved to install the Thermal Compensation System subsystem (TCS) Hartmann sensing setup to inject the Hartmann beam from the INJ subsystem. This beam should be superimposed to the ITF reflection pick-off for the phase camera (see Fig. 4.3). More details on the Hartmann beam and sensing setup are given in the TCS chapter.

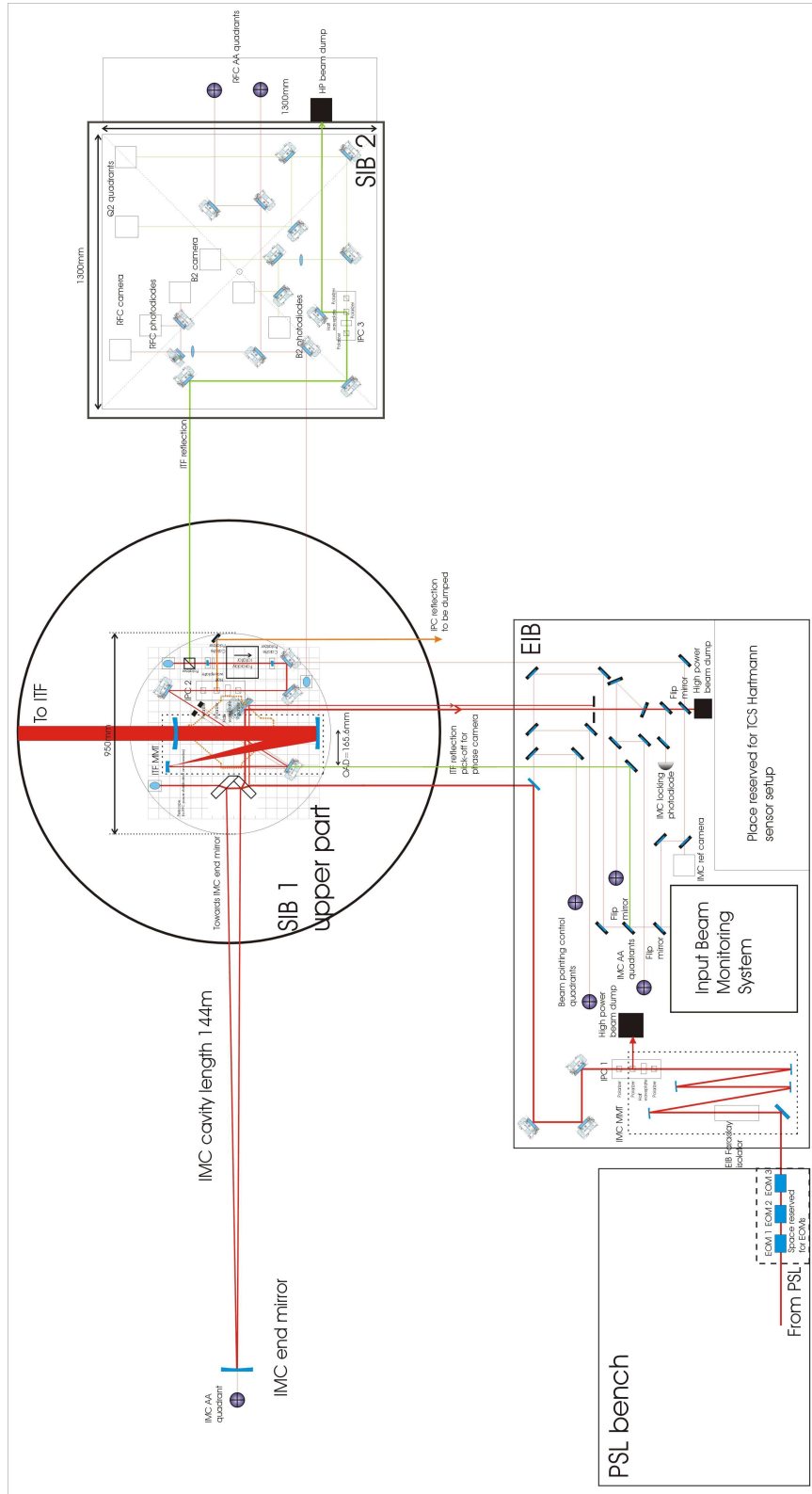


Figure 4.3: General optical layout of INJ benches. See Figs. 4.4, 4.5 and 4.6 for detail views.

4.5.3 Suspended injection benches layout

SIB1 is located in INJ tower and **SIB2** in the new minitower. **SIB1** (see Fig. 4.4) is hosting the IMC flat mirrors (dihedron). The output beam of the IMC cavity is sent to the lower part of **SIB1** as shown in Fig. 4.6. Part of this beam is picked off for the RFC setup and power stabilization photodiodes. The main beam passes through a reducing telescope and is sent with a periscope towards the high power Ultra-High Vacuum (**UHV**) compatible Faraday isolator used to isolate the IMC cavity from the ITF reflection and to send the ITF reflection to **SIB2** in the new tower (see Fig. 4.5). This beam is finally matched to the ITF using the ITF Mode Matching Telescope (**MMT**) (for more details see section 4.13). Moreover, we have reserved some space to install an **IPC** system (**IPC 2**) that could be used during the ITF commissioning phase.

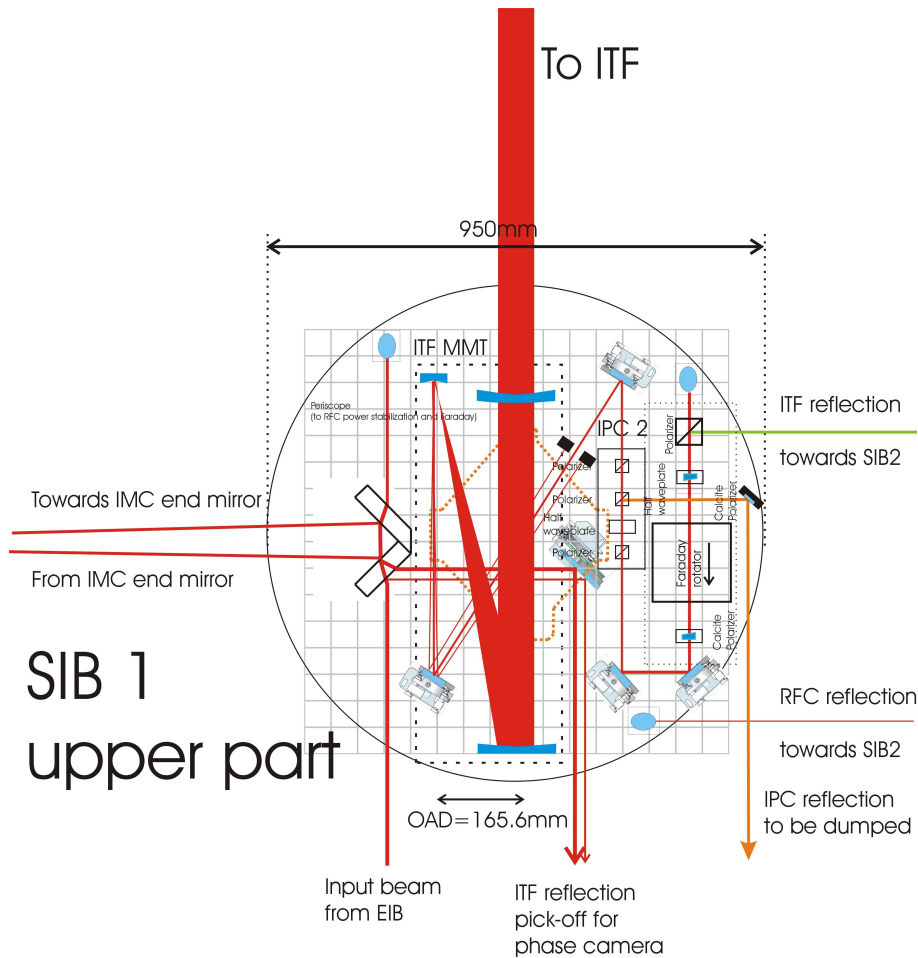


Figure 4.4: Optical layout of the upper part of **SIB1**.

Concerning **SIB2**, we are sending the ITF and RFC reflected beams as shown in Fig. 4.5. An **IPC** system (**IPC 3**) is there to attenuate the high power laser beam reflected by the ITF. The beam to be dumped is sent onto a viewport beam dump (see section 4.9), the light is then sent to longitudinal and quadrant photodiodes provided by DET. The RFC reflection setup is described more in details in section 4.11.

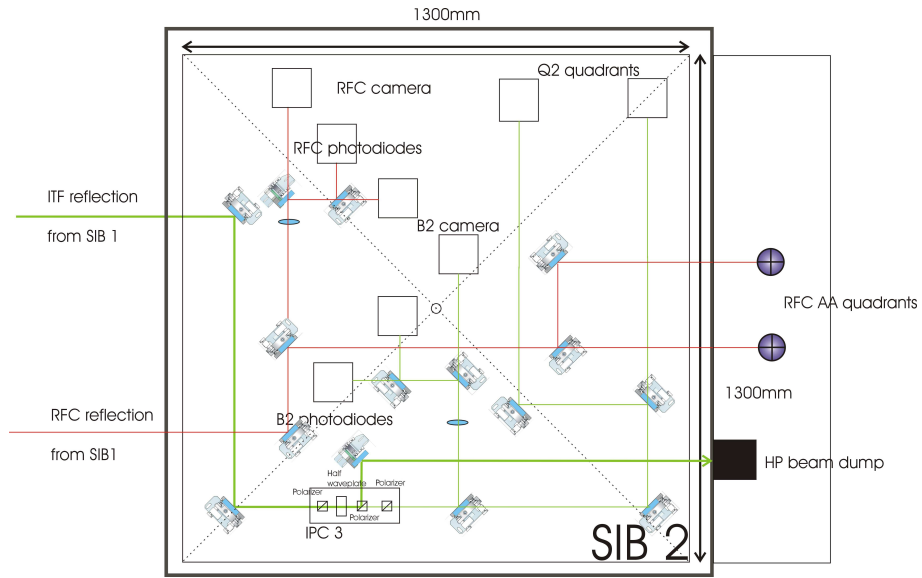
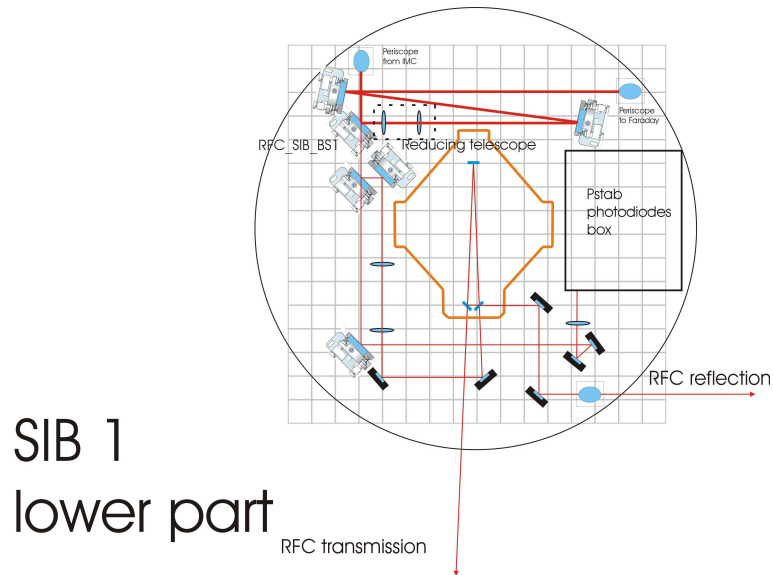


Figure 4.5: Optical layout of the upper part of SIB2.



SIB 1
lower part

Figure 4.6: Optical layout of the lower part of SIB1.

4.6 EOM and RF Modulation

In AdV, **RF** modulation of the laser beam will be used in the control of the interferometer, both for longitudinal and angular controls. The main difference between the electro-optical modulation system to be used in AdV with respect to Virgo is the laser power that it will have to withstand; it will be almost 10 times higher (about 200 W instead of 20 W). Thermal effects become more significant [107], and the choice of the appropriate material (electro-optic (EO) crystal) becomes crucial to limit as much as possible the consequences of these thermal effects on **EOM** properties. Indeed, it is important to select the right material not only to limit wavefront aberrations but also to limit heating that can induce slow variations of the modulation index and a disturbance of the **ITF** control. Requirements in AdV for Electro-Optical (**EO**) modulation will also be different. Many of these parameters affect the driving electronics and signal generator choices with respect to Virgo. Requirements on phase and amplitude noise were provided by the ISC subsystem [108]. In the following paragraphs, we give an overview of the requirements used in the design of the **EOM** system. Then we briefly introduce the absorption measurements made on different electro-optical materials that led to the choice of Rubidium Tytanil Phosphate (**RTP**) crystals. Finally the proposed configuration for AdV will be presented as well as the generation and distribution of radio frequency signals.

4.6.1 Requirements

Five modulation frequencies will be needed in AdV, three for the interferometer control, one for the IMC cavity control and one to facilitate the lock acquisition of the interferometer. The highest modulation frequency used for the ITF control in science mode is not expected to be higher than 56 MHz (see ISC section).

The 3 modulation frequencies used for ITF control are: $f_1=6\,270\,777$ Hz, $f_2=56\,436\,993$ Hz and $f_3=8\,361\,036$ Hz. A fourth radio frequency signal will be used for the ITF lock acquisition $f_4=131\,686\,317$ Hz. The modulation frequency used to control the IMC cavity should stay close to the one we are using in initial Virgo: $f_5=22.38$ MHz. The modulation depth m should be of the order of 0.1 according to preliminary simulations done by ISC [109]. Nevertheless, in order to get a bit of margin, we consider that the modulation depth could be as high as 0.2 even for the highest modulation frequency (f_4) which is technically the most difficult. Sideband amplitude noise and phase noise requirements have been provided by ISC [110] and are given in Tab. 4.3, quoting only the most stringent requirement for each frequency. These numbers have been computed based on simulation of all photodiode signals except B1 and therefore are not depending on Output Mode Cleaner (**OMC**) design. The numbers for B1 have been provided by DET considering the filtering properties of two **OMC** cavities (DET design). For f_1 , the sideband amplitude noise should be as low as $2.5 \times 10^{-7}/\sqrt{\text{Hz}}$ above 100 Hz as shown in the DET chapter.

4.6.2 Electro-optic crystal choice

From the 3 different kinds of high-power resistant crystals [111] considered in the High Power Input Optics (**HPIO**) R&D program: potassium titanyl phosphate (KTP, used already in

| Name | Frequency (Hz) | Phase Noise [Rad/\sqrt{Hz}] | Amplitude Noise [$1/\sqrt{Hz}$] |
|-------|----------------|---------------------------------|-----------------------------------|
| f_1 | 6 270 777 | 1.8×10^{-6} | 1.7×10^{-7} |
| f_2 | 56 436 993 | 1.1×10^{-6} | 1.1×10^{-6} |
| f_3 | 8 361 036 | 0.27 | 1.7×10^{-7} |

Table 4.3: Requirements on modulation phase noise and amplitude noise for $f > 10$ Hz.

Virgo), rubidium titanyl phosphate (RTP) and lithium niobate doped with MgO, we have chosen RTP from the Raicol company, where an absorption lower than 50 ppm/cm has been measured [112]. A summary of the absorption measurements is given in Tab. 4.4.

| Manufacturer | Type | Dimensions (mm) | Absorption (ppm/cm) |
|------------------------|------------------------|-----------------|----------------------|
| Cristal Laser (France) | KTP | 5x5x12 | $135 < \alpha < 175$ |
| Cristal Laser (France) | RTP | 5x5x12 | $475 < \alpha < 605$ |
| Raicol (Israel) | RTP | 4x4x25 | $38 < \alpha < 50$ |
| Oxyde corp. (Japan) | MgO:LiNbO ₃ | 5x5x20 | $230 < \alpha < 300$ |

Table 4.4: Absorption measurements in electro-optic crystals.

The thermal lens power for each crystal is expected to be lower than 3.5×10^{-2} and will be easily compensated by adjusting the telescope located between the EOM and the IMC cavity.

4.6.3 Proposed configuration: electro-optical modulator

4.6.3.1 EO modulation principle

We will phase modulate the laser beam using the Pockels effect which is the linear electro-optic effect: the refraction index of a medium is modified proportionally to the applied electric field strength. The phase shift induced by the electric field applied along the z axis for a linearly polarized beam with a polarization aligned along the z direction can be written as:

$$\Gamma = \frac{2\pi}{\lambda} n_z L = \frac{2\pi}{\lambda} L (n_e - 0.5 n_e^3 r_{33} E_z)$$

where $E_z = V/d$; V is the voltage applied on the crystal, L the length of the electrode, d the thickness of the crystal, n_e the refraction index of the z -axis without electric field, λ the laser wavelength and r_{33} a coefficient of the material's EO tensor. The electric field of the laser beam at the input of the modulator can be written as $E = E_0 \exp(i\omega t)$. When we apply a voltage modulated at frequency f_m , the electric field of the light at the output of the modulator is expressed as:

$$E_{out} = E_0 \exp(i2\pi f t) \exp(i\Gamma(t))$$

where :

$$\Gamma(t) = \Gamma_0 - (\pi L/\lambda) r_{33} n_e^3 (V_0/d) \sin(2\pi f_m t)$$

It becomes:

$$E_{out} = E_0 \exp(i2\pi f t) \exp(i(\Gamma_0 - m \sin(2\pi f_m t)))$$

where m is the modulation depth:

$$m = (\pi L/\lambda)r_{33}n_e^3(V_0/d) \quad (4.1)$$

In this way, one can note that we are phase modulating the laser beam at f_m with respect to the carrier frequency f .

NB: $n_e=1.8536$ and $r_{33}=39.6\text{pm/V}$.

4.6.3.2 Technical realization of the modulator

During the studies carried out in the framework of the HPIO R&D program [112] we could show that for 30 dBm (1 W) of input power on a specifically designed resonant circuit (see section 4.6.4), we could obtain about 160 V_{rms} applied on the crystal's electrodes for frequencies f_1, f_3 and f_5 and about 118 V_{rms} for frequency f_2 . Using equation 4.1 we deduce that we can obtain $m=0.2$ for an electrode length of about 8 mm for frequencies f_1, f_3 and f_5 and about 11 mm for frequency f_2 . Using EO crystals of about 20 mm long, we propose to use a 2-sections modulator design. This principle was already tested (we applied two different phase modulations at 10 and 65 MHz on the same crystal [112]). This configuration allows us to minimize the losses and avoid as much as possible spurious reflections from input and output faces of the modulators.

Therefore, we propose to use multi section phase modulators as shown in Fig. 4.7. The

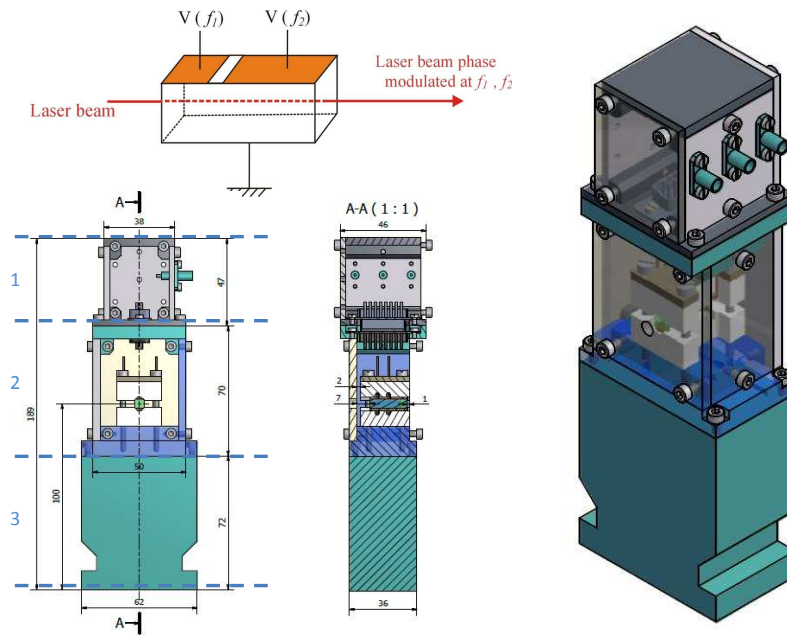


Figure 4.7: Left: Scheme of a 2 sections phase modulator; Right: View of a 2-sections EOM prototype for AdV. 1: electronics; 2: electro-optic crystal and electrodes; 3: support.

20 mm long RTP crystal stands between two sets of copper electrodes; these parts are hold together by a block of Teflon. No glue is used in this design; this facilitates maintenance.

The resonant circuit is placed in a box just above the EO material. For convenience, the box can be plugged/unplugged from the support of the crystal.

We will have three different EOMs on the high power beam in AdV: one for frequencies f_1 and f_3 , another for f_2 and f_5 , both of them having two sets of electrodes. The generation of f_4 will require a dedicated solution. Nevertheless, it seems reasonable to assume that a $m=0.1$ could be achievable with a single, 20 mm long crystal. A prototype is being prepared and will be tested soon to confirm that there is no major problem to use the modulator configuration proposed for f_4 modulation frequency.

4.6.4 Proposed configuration: RF modulation

4.6.4.1 RF generation

INJ takes care of the generation of the 5 modulation frequencies needed for AdV ITF controls and makes them available for both local and global (i.e., interferometer) distribution. f_4 and f_5 RF modulation frequencies do not have as stringent requirements on phase and amplitude stability as the other ones.

The baseline design is to use, as it was done in Virgo, a low-noise synthesizer for the first three RF lines and a quartz for the other two, as shown schematically in Fig. 4.8 and detailed in the following paragraph. To avoid potentially annoying low-frequency beat notes among the specified frequencies or their harmonics, the "interferometer sidebands" will be phase locked.

The reference can be either a 10 MHz source internal to the synthesizer or, as shown, an external one. In addition also the IMC and f_4 sidebands can be phase-locked to the reference, if required. Optionally, the RF source can be locked to Global Positioning System (GPS) as well (not shown).

4.6.4.2 RF amplification

The baseline solution is to use one driving line per each modulation frequency and to couple two frequencies on a single resonant electro-optic modulator. To meet the requirements on the modulation index ($m \geq 0.2$ for f_1 , f_2 , f_3 and f_5 , and $m \geq 0.1$ for f_4), it is necessary to have adequate voltage levels on the crystals, and this in turn requires sufficient quality factors on the resonant circuits built around the modulators themselves and high power for driving them. Building on the results obtained on the high power input optics R&D [112], we can conclude that it is sufficient to drive each resonant circuit with a 1 W amplifier for reaching the desired modulation index with a reasonable electrode length of 8 or 11 mm depending on the considered frequency.

4.6.4.3 RF distribution

All frequencies will be available for distribution right at the output of the generation system (RF source), and the standard amplitude level for all of them is +7dBm.

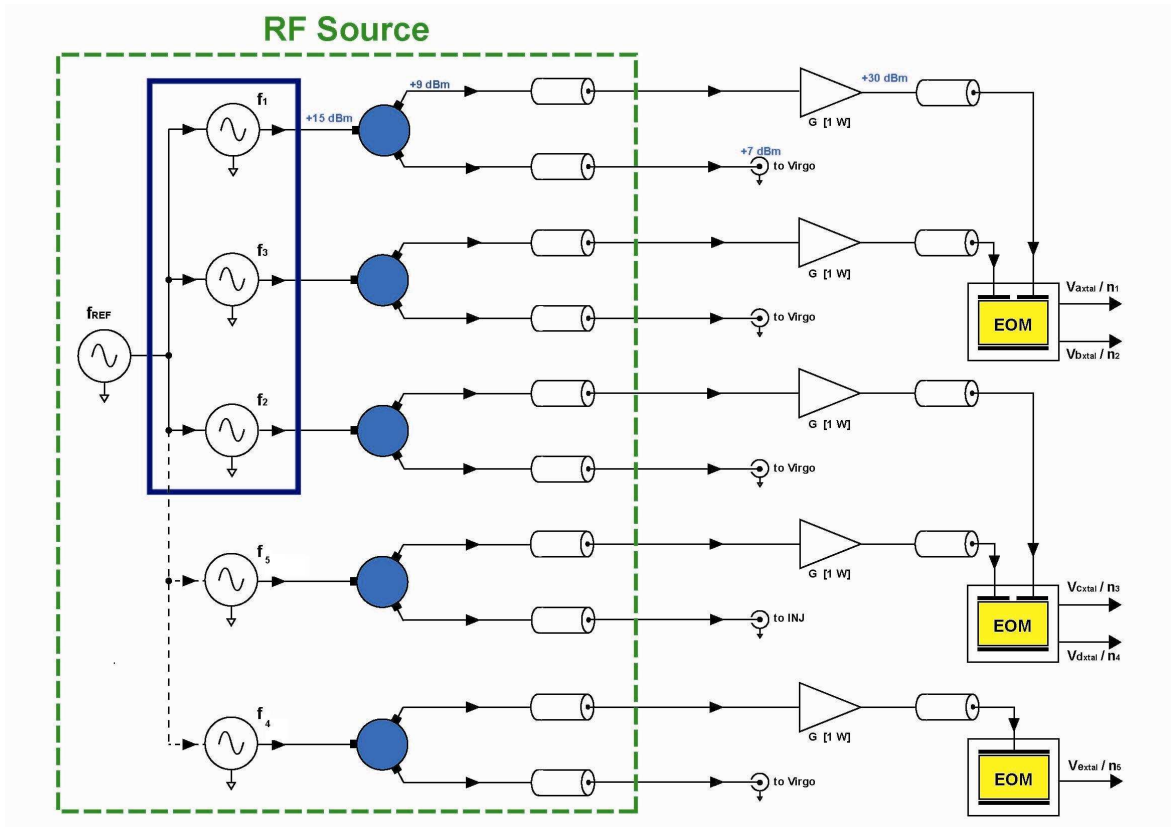


Figure 4.8: AdV RF Beam Modulation System.

4.6.4.4 Local RF phase adjustment

A sixth radio frequency could be present, depending on the solution adopted for the laser. In this case as well it would be used to phase modulate the light beam. Its use would be confined within the laser system; where it would be used, for example, to lock the pre-mode cleaner with the usual Pound-Drever-Hall (PDH) reflection locking technique. Local provision to make this frequency (and the one used in the input mode cleaner lock) available on three additional channels will be present, with the possibility to modify the phase on each of them independently. Phase adjustment can be manual or through a remote computer controlled interface and it will cover 360 degrees per channel, monotonically and in steps of less than one degree (when done via computer). The overall nonlinearity shall not exceed 10%. This system will be based on the Minicircuits' JSPHS component family.

4.6.4.5 RF amplitude and phase stability

The most stringent requirements on sidebands stability set by Interferometer Sensing and Control (ISC) [108] have been provided in table 4.3.

NB: we considered here that we use two output mode cleaner cavities (DET baseline). Measurements done in the EGO electronics lab gave results briefly reported here. The amplitude noise of the synthesizer does not depend on the output frequency as can be seen in Fig. 4.9. We also see on this measurement that far better results can be achieved for example

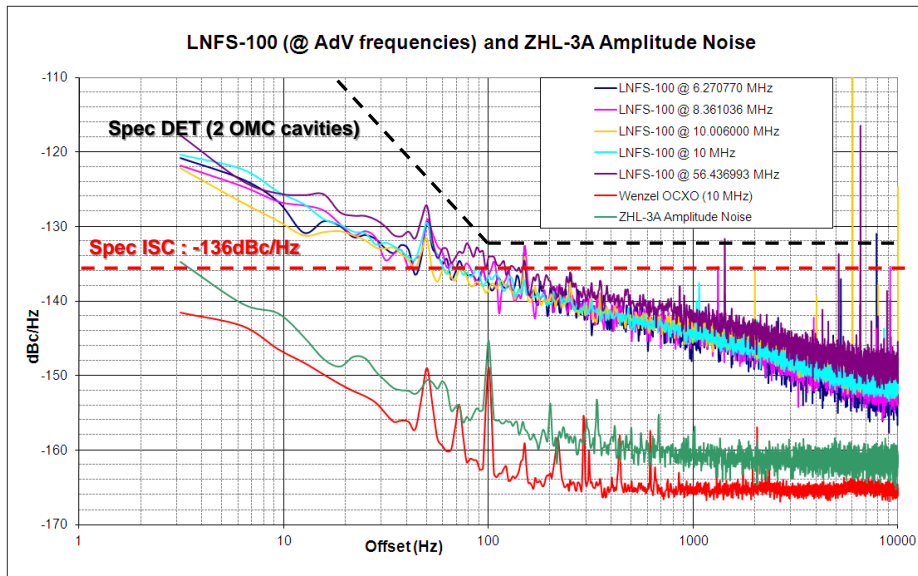


Figure 4.9: Measurement of the residual amplitude modulation noise for f_1, f_2 and f_3 given by the LNFS-100 function generator. Measurement of a Wenzel 10 MHz quartz is given as a reference. The green curve shows the noise contribution from the ZHL-3A RF amplifier. The red dashed line is the requirement from ISC; the black dashed line the requirement from DET.

with a Wenzel oven-controlled quartz oscillator (OCXO) whose frequency cannot be tuned with the dynamic range required using Virgo locking strategy though. The most stringent

requirement in terms of amplitude noise is too close to the performance the RF source can deliver for all frequencies below 10 kHz and therefore meeting the specification requires an additional servo loop to stabilize the residual amplitude modulation.

The working principle of this servo loop is presented in Fig. 4.10: a fraction of the RF signal we want to stabilize is sampled and detected.

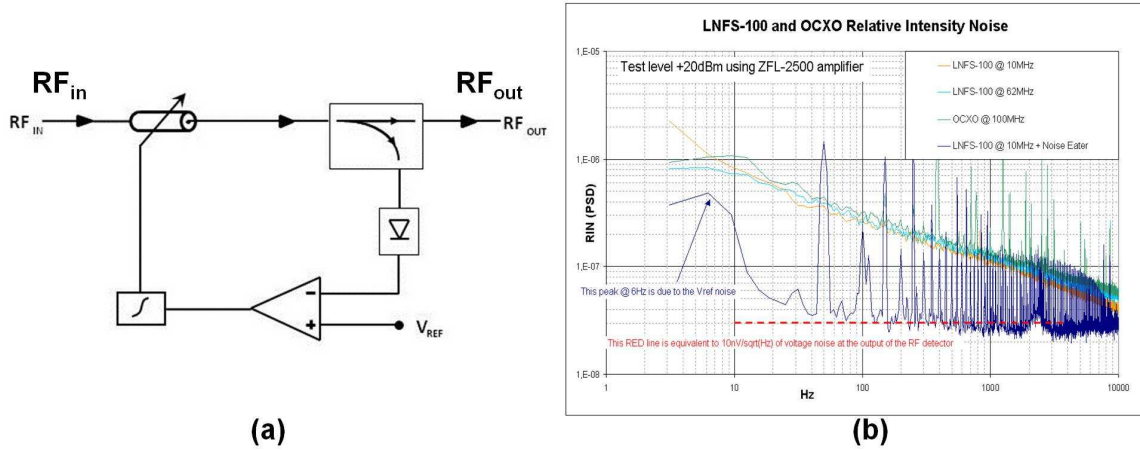


Figure 4.10: a: Scheme of the residual amplitude modulation stabilization loop; b: Experimental result. The noise floor is well below the requirement 1.7×10^{-7} provided by ISC and 2.5×10^{-7} provided by DET above 100 Hz. The 50 Hz harmonics will be cured in the final version of the stabilization loop.

This measurement is compared with a very stable reference and the error signal obtained is filtered and used as input of a voltage controlled attenuator. A prototype servo has been built and tested. Its performance is adequate to the level of suppression desired: unity gain frequency is 300 kHz, gain is larger than 40 dB for frequencies between 10 Hz and 3 kHz. The amplitude noise after stabilization is given in Fig. 4.10.

It is worth mentioning that both the RF amplifier used in the setup (Minicircuits's ZHL-3A; see Fig. 4.9) and the prototype EOM electronics downstream do not contribute to the overall residual amplitude modulation.

The phase noise of the synthesizer is instead markedly dependent on the output frequency: the higher the frequency the higher the phase noise, as can be seen in measurements shown in Fig. 4.11. The ratio between phase noise measured at different output frequencies is frequency independent. The phase noise of the 56 MHz sideband, for which the situation is most critical, is below the requirement level over the entire 10 Hz-10 kHz bandwidth.

Once again, measurements done in the lab show that neither the RF amplifier nor the EOM electronics contribute to the overall phase noise.

4.7 Input beam jitter monitoring and control

Requirements on input beam jitter, the way we monitor this jitter and the way we stabilize the laser beam at low frequency are presented in this section.

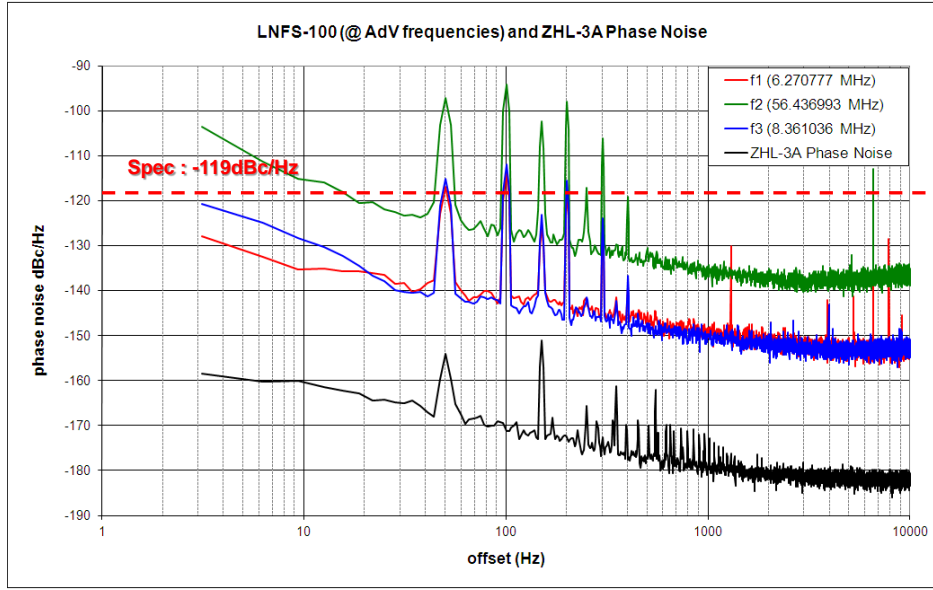


Figure 4.11: Measurement of the phase noise for f_1, f_2 and f_3 delivered by the LNFS-100 function generator. The black curve corresponds to the residual phase noise produced by ZHL-3A RF amplifier.

4.7.1 Requirements on input beam jitter

The requirements on input beam jitter for AdV have been computed using Optikle and Finesse codes. The requirements at the input of the interferometer are given in Fig. 4.12 and 4.13. The red curves show the projected noise from the suspended injection bench residual horizontal motion. Note that Virgo data have been used to make this projection. This noise will be even lower in AdV since we will add an extra filter to the superattenuator of SIB1.

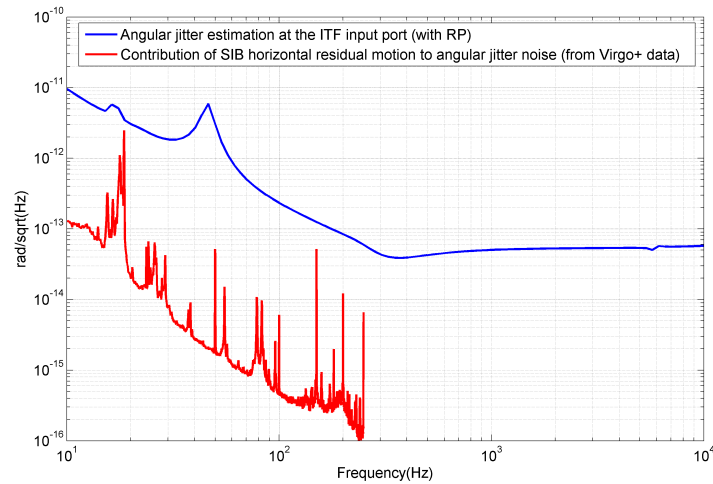


Figure 4.12: Angular beam jitter specifications at the ITF input port (with ITF radiation pressure effect (RP)). The red curve is the expected contribution from SIB motion (Virgo data used).

The requirements at the input of the IMC cavity (output of the EIB) have been computed using the method explained in [113]. Note that radiation pressure has been considered in this

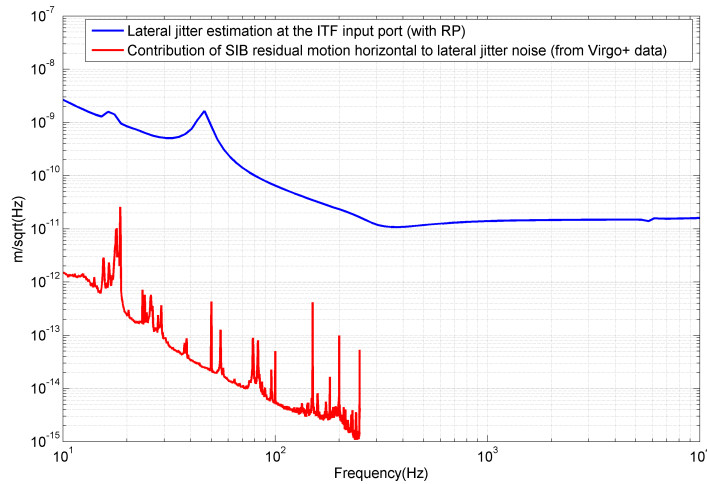


Figure 4.13: Lateral beam jitter specifications at the ITF input port (with ITF radiation pressure effect (RP)). The red curve is the expected contribution from SIB motion (Virgo data used).

study. The requirements are less stringent with respect to the ones that we have at the ITF input due to the filtering properties of the IMC cavity.

4.7.2 Beam pointing control system

The principle scheme is given in Fig. 4.16. The fundamental idea, close to what has been used in the Virgo Beam Monitoring System (BMS)[114], is to use beam pointing sensors as error signals to control beam pointing and reduce this jitter at low frequency. This system should allow to lower the beam jitter at low frequency and keep the beam in a given reference position.

Specifications for the sensors can be deduced from typical jitter noise measured at the output of the laser system (see PSL section) taking into account the optics on the beam path that are located between PSL and the IMC cavity. The bandwidth of this loop is expected to be up to 50 Hz to eventually correct excess of jitter noise in the detection bandwidth between 10 Hz and 50 Hz.

4.7.3 Input beam jitter monitoring system

We propose to have a system that is able to monitor the beam jitter over the whole AdV detection bandwidth (10 Hz-10 kHz). This system is based on an optical system able to monitor beam jitter with a sensitivity better than the required specifications given on figures 4.14 and 4.15. In order to do this job a system similar to what is used in the beam pointing control system (using quadrant photodiodes) will be implemented. Quadrant photodiodes should have better performances above 100 Hz in order to properly monitor beam jitter and for not being limited by acquisition noise. As one can see in Fig. 4.14, the beam jitter level is supposed to reach $5 \times 10^{-5} \mu\text{rad}/\sqrt{\text{Hz}}$ above 300 Hz according to the specification. If we consider a setup similar to the one in Virgo, we get the following numbers. The sensitivity

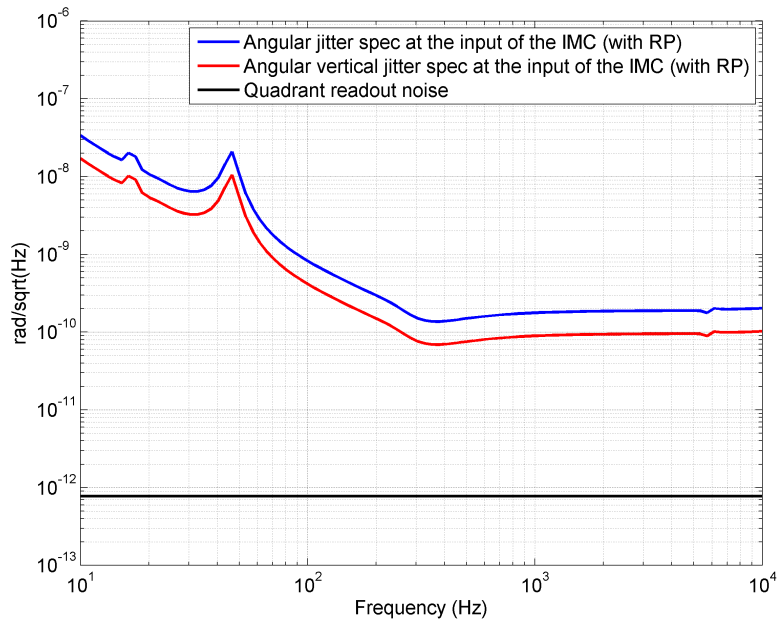


Figure 4.14: Angular beam jitter specifications before the IMC cavity (with ITF radiation pressure effect (RP)). The black line corresponds to the expected quadrant readout noise.

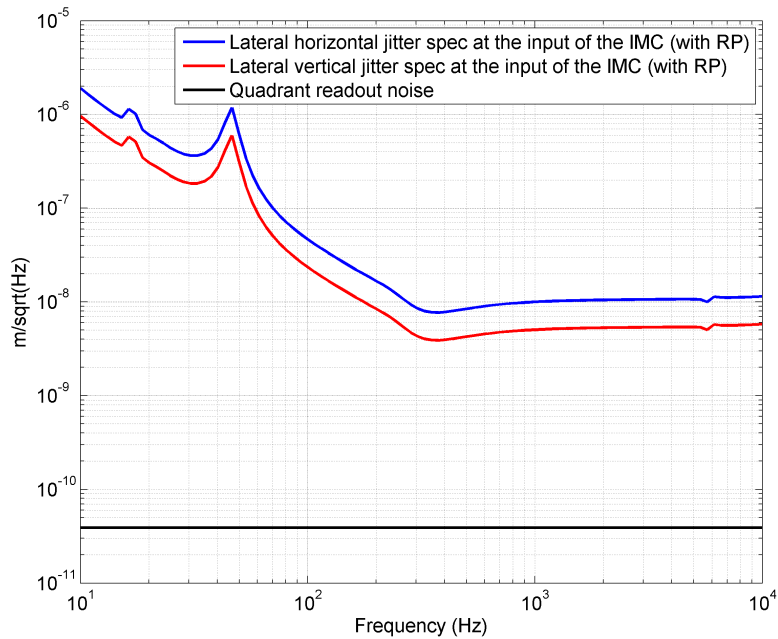


Figure 4.15: Lateral beam jitter specifications before the IMC cavity (with ITF radiation pressure effect (RP)). The black line corresponds to the expected quadrant readout noise.

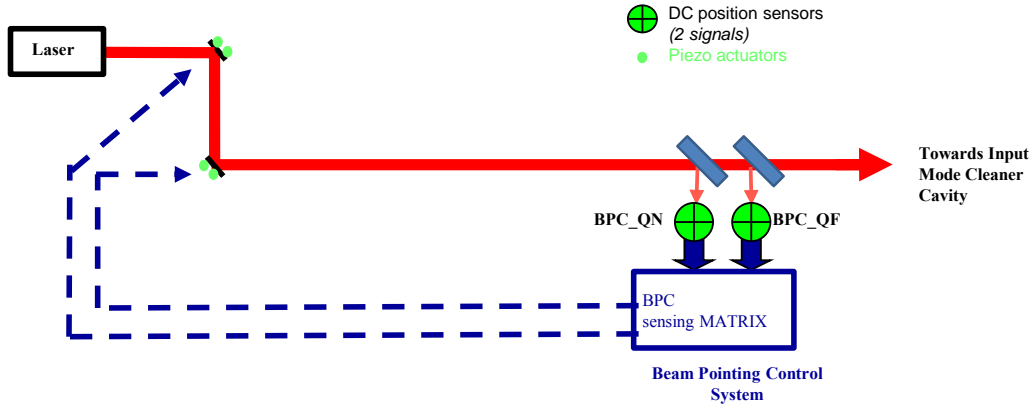


Figure 4.16: Beam Pointing control principle scheme. BPC_QN is the near field quadrant and BPC_QF, the far field quadrant.

of the far field quadrant used for angular jitter monitoring is:

$$S = \frac{2\sqrt{2/\pi}}{w} \times a \times i_{dc}$$

with $a = 8 \times \theta$, where 8 is the equivalent focal length of the telescope in meters, θ is the beam jitter in radians, $w = 500 \mu\text{m}$ is the beam size on the quadrant, and i_{dc} is the overall DC current (0.25 A/W; 2.5 mA for 10 mW).

This means that $S=6.38 \text{ A/rad/mW}$.

If $P=10 \text{ mW}$ (power impinging on the quadrant), then $S=63.8 \text{ A/rad}$, and we need to detect: $3.2 \text{ nA}/\sqrt{\text{Hz}}$.

As one can see in Fig. 4.15, the lateral beam jitter level is supposed to reach $4 \times 10^{-3} \mu\text{m}/\sqrt{\text{Hz}}$ starting from 300 Hz according to the specification.

The sensitivity of the near field quadrant used for lateral jitter monitoring is:

$$S = \frac{2\sqrt{2/\pi}}{w} \times a \times i_{dc}$$

with $a = 0.32 \times d$, where 0.32 is the optical magnification of the near field telescope, d is the beam jitter in meters, $w = 1000 \mu\text{m}$ is the beam size on the quadrant, and i_{dc} is the overall dc current (0.25 A/W; 2.5 mA for 10 mW).

Thus $S=0.127 \text{ A/m/mW}$. If $P=10 \text{ mW}$ (power impinging on the quadrant), then $S=1.27 \text{ A/m}$, and we need to detect: $5.12 \text{ nA}/\sqrt{\text{Hz}}$.

Those numbers are reachable, since we measured a readout electronic noise on the Virgo quadrant photodiodes as low as $50 \text{ pA}/\sqrt{\text{Hz}}$.

4.8 Input power control

The INJ subsystem should provide a way to change the interferometer input power without changing the incident power on elements that can experience possible thermal effects (input

mode cleaner and in vacuum suspended Faraday isolator), and without changing the power on the different detectors used in the control loops of the injection system. For this purpose, INJ will use a system composed of a few polarizers and a wave plate, named **IPC**, placed right before the IMC cavity. To save commissioning time, we will install a second **IPC** system just after the Faraday isolator in order to modify the ITF input power without inducing other changes on the laser and injection systems, and a third one on the ITF reflected beam to easily adjust the laser power on single element and quadrant photodiodes used for the interferometer sensing and control (located on **SIB2**). Simpler and low cost **IPCs** (consisting of a half wave plate mounted in a rotatory mount and a polarizer) will be placed on low power beams (<0.5 W) in front of each photodiode of INJ in order to more easily change the laser power in order to facilitate commissioning of the subsystem and the ITF.

4.8.1 Requirements

The IPC should be able to modify the laser power by two orders of magnitude (from 1% to 99% of the full power) without spoiling the polarization state that should be better than 30 dB for the whole power range. It should also induce no significative thermal distortion at full power. The expected thermal lens power for each fused silica polarizer is expected to be lower than 0.015 diopter, the overall thermal lens power of the system being below 0.045 diopter at full power. As explained in section 4.13, the thermal lensing effect will be easily compensated by adjusting the ITF **MMT**.

4.8.2 Configuration chosen

In order to adjust the power, the most convenient system consists of a half wave plate placed between polarizers as shown in Fig. 4.17. As this system should handle both light going to and reflected back from the interferometer, the two situations are treated here. Light going to the interferometer (S polarization) goes through P1, its polarization is turned by an angle θ by the wave plate and after crossing P2 goes towards the interferometer with S polarisation with a attenuated power of $P_{out} = P_o \cos(\theta)^2$. Light reflected by P2 should go to a high power beam dump. No specific requirements about diffused light are necessary for this beam dump, as its back reflections cannot reenter into the interferometer. Light emerging from P2 goes to an other polarizer P3, aligned along the same direction. This is used to further clean the polarization of the beam when P2 is close to extinction. Use of P3 is mandatory to insure a good polarization quality in low IPC transmission configuration.

Back reflected light coming from the interferometer should go through P3 and P2, its polarization is turned by θ by the wave plate and therefore $P_{back}(1 - \cos(\theta)^2)$ is going back towards the laser system after crossing P1. This element fixes the polarization of light coming back whatever the position of the wave plate. The P polarized light reflected by P1 should go to another high power beam dump. Diffused light from this beam dump can recouple to the interferometer, and therefore a low diffusion system should be used on this beam.

To avoid significant thermal beam distortions, we have identified within the high power input optics R&D program the best suitable polarizers and wave plates to realize this system [112]. It turned out that polarizers should be made of fused silica. Very good results were obtained with thin film brewster plate polarizers (TFPP) from EOTech. For wave plates, standard

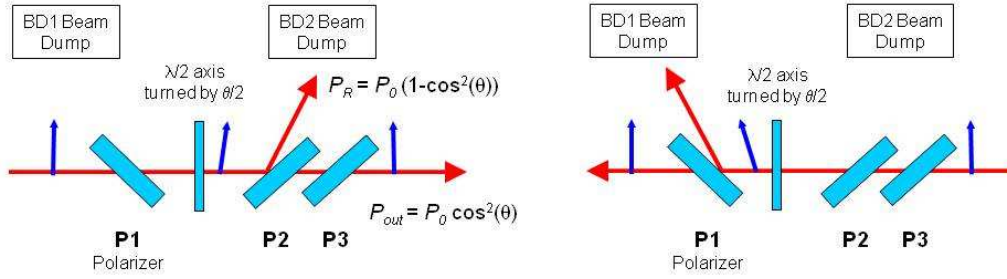


Figure 4.17: IPC principle for light going to the interferometer and back reflected from the interferometer.

zero order optically contacted plates from CVI are performing well [112]. We also tested successfully the use of optically contacted polarizing cubes. With the cubes we can more easily extract the beam that have to be dumped and by slightly tilting these cubes we can easily dump its faces spurious reflections. Using these elements, we realized an IPC prototype that is presented in Fig. 4.18.

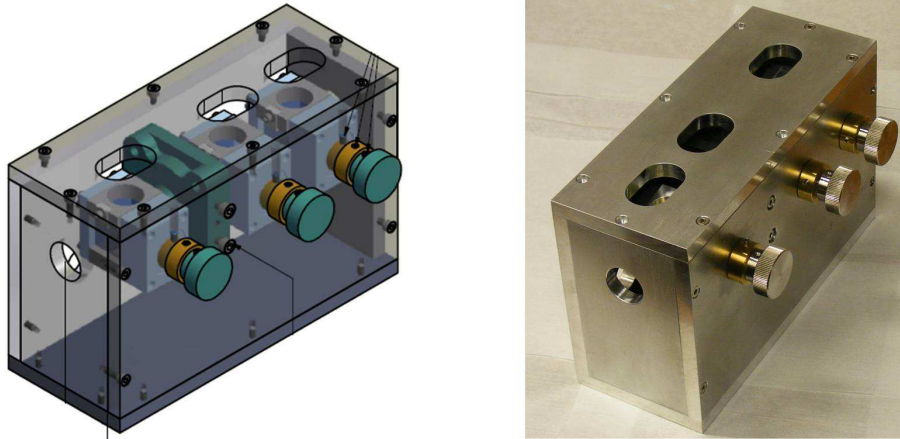


Figure 4.18: Views of the IPC prototype

It is composed of three optically contacted cubes that can be slightly tilted and an adjustable half wave plate. The final version will include a remote adjustment of the wave plate orientation. Figure 4.19 plots the polarization quality of the beam emerging from this prototype for an output power from 1 W up to 125 W (max ITF input power). We observe that the polarization quality remains better than 35 dB.

4.9 High power beam dumps and baffles for INJ

Noise hunting at Virgo showed that light diffused on optics can spoil the ITF sensitivity. This is due to the fact that seismic noise of the optical bench creates some direct and up-converted noise measurable on the dark fringe through the phase-modulation of diffused light re-introduced into the interferometer [115]. Tests were made in the EGO optics lab to determine an optimal beam dump from the diffusion point of view. It turned out that the

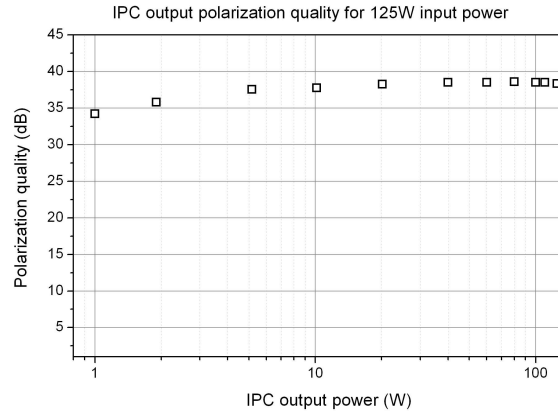


Figure 4.19: Polarization quality of IPC transmission for output power between 1 to 125 W.

best performances could be achieved with absorbing glass. The value of total diffused light from this material (integrated over the whole hemisphere) is in the 10 ppm range, very close to the values obtained with super polished optics. Nevertheless, the problem of absorbing glass is that it is only suitable for low/medium power beams, as it was shown to break at only 2 W for a 1 mm beam waist. This is due to the low conduction coefficient of glass that makes it locally melt.

In the following, we will distinguish three types of beam dumps needed for INJ:

- High power (<200 W) in-air beam dump
- Medium power (<20 W) high vacuum compatible beam dumps
- High power (<125 W) high vacuum compatible beam dumps

All these devices have some common characteristics in terms of diffused light with a Total Integrated Scattering (TIS) lower than 100 ppm. They should also present a limited temperature elevation of less than 150°C to avoid heating nearby opto-mechanical components that can induce drifts on several parts of INJ. In order to realize these low diffusing beam dumps, we propose to use silicon. Silicon is a very interesting material as it has a good conductivity (about $150 \text{ W m}^{-1} \text{ K}^{-1}$ which is close to a good conducting metal such as aluminium), and it can be polished with optical quality. Its absorption at 1064 nm is also quite high: 98% for 5 mm length, and it increases with temperature. Thick plates (5 mm) of this material were tested in the EGO optics lab, and it has been shown that their damage threshold for YAG exposure is as high as 6 kW/cm^2 . Values of total diffused light (70 ppm) are comparable with absorbing glass. In the following section we will give technical details about the realization of the different types of beam dump.

4.9.1 High power in-air beam dump

We developed a prototype that is able to dump a few hundred Watts in air with low diffusing properties. This prototype is presented in Fig. 4.20. It is mainly composed of thick (5 mm) silicon plates with an AR coating. The small transmission of the silicon plate (less than 2% at low power and less than 0.1% when the plate temperature increases when irradiated by

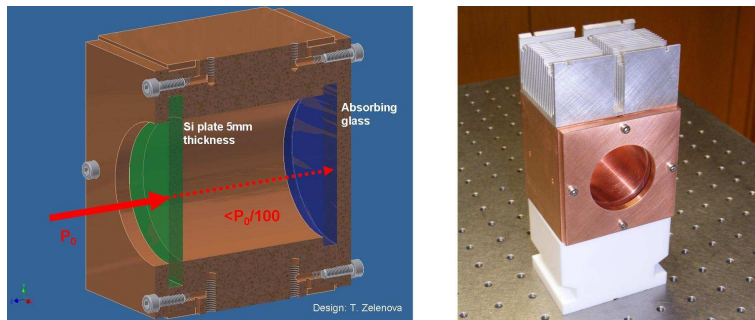


Figure 4.20: IPC beam dump prototype using thick AR coated Si plate. The small transmission of the Si plate is dumped on an absorbing glass. The assembly is made of copper and a radiator insures a good heat evacuation.

a powerful beam as shown in Fig. 4.21) is dumped on an absorbing glass. The assembly is made of copper and a radiator insures a good heat evacuation, which is a key point for dumping high power.

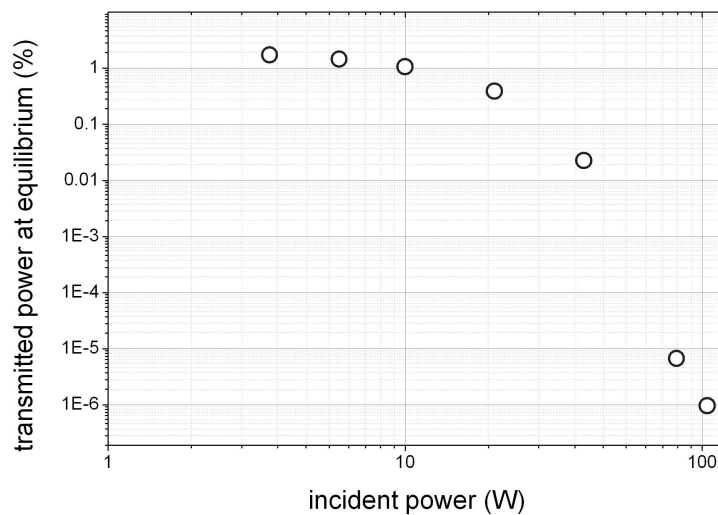


Figure 4.21: Silicon plate transmission change when the laser goes from 3.8 W up to 104 W.

Figure 4.22 shows the measurement of the prototype temperature in function of the heating power.

At maximum tested power (104 W) only 40°C of temperature elevation is reached. This prototype is extremely promising for dumping high power on the external benches such as **IPC** rejected power or **IMC** reflection. Besides, no problem is expected to dump the 200 W from the AdV high power laser if needed.

4.9.2 Medium power high vacuum compatible beam dumps

Based on silicon, we also developed a vacuum compatible version of a low diffusion beam dump. The main challenge there consists in evacuating the heat, and some special design has to be made using high emissivity materials. Figure 4.23 shows a prototype specifically

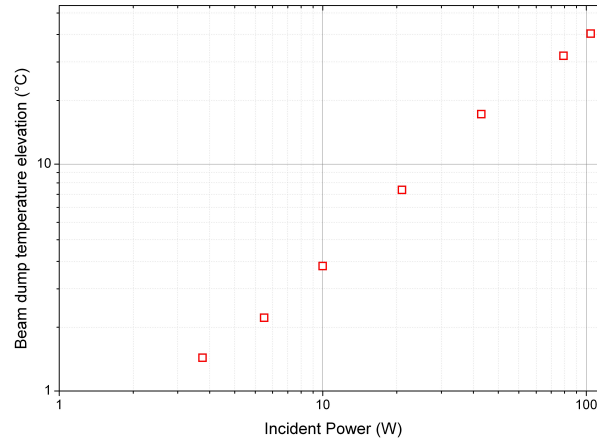


Figure 4.22: Temperature of beam dump prototype presented in Fig. 4.20 as a function of heating power. We observe a linear behavior because of the efficient heat removal by convection.

designed for dumping a few Watts (B1s beam) on the Virgo suspended detection bench (SDB) [116].

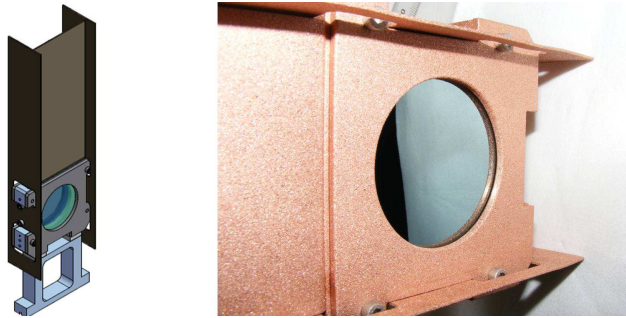


Figure 4.23: High vacuum compatible beam dump prototype. Large vertical plates enable an efficient heat dissipation by radiation. Sanded copper (right picture) is used for its high emissivity and conductivity.

We made the choice to dissipate all heat by radiation in order to avoid conduction through the bench which has a low emissivity. Some vertical radiating plates are therefore added to minimize the working temperature. We chose as material copper with a specific mechanical surface treatment (sanding), which combines very good conductivity to remove heat from the Si plate and good emissivity (around 60-70%) for heat dissipation. This prototype was tested under high vacuum (10^{-6} mbar) with 10 W of impinging power. Experimental results are shown in Fig. 4.24; we measured a temperature elevation of 79°C and a time constant of about 54 min.

By increasing the radiation surface, it seems possible to dump a few tens of Watts under vacuum. Going higher in power seems difficult while keeping a reasonable beam dump temperature (less than 150°C).

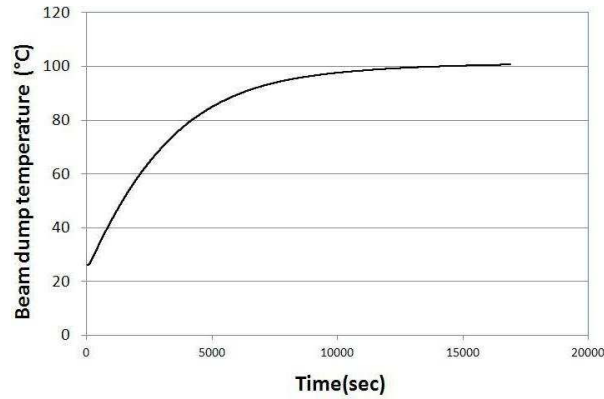


Figure 4.24: Temperature of the beam bump prototype presented in Fig. 4.23 as a function of time.

4.9.3 High power high vacuum compatible beam dumps

In order to dump powerful beams without having to get out of the vacuum system (with the obvious disadvantage to multiply the optical interfaces), we developed a device which dumps the beam under vacuum and dissipates heat, in air, by convection. This system will be useful for dumping the reflection of IPC 2 (placed on the SIB1) and the ITF reflected beam. The design of the prototype can be seen in Fig. 4.25; as for the in-air version, the laser power is dumped by a combination of Si and absorbing glass plates. The whole mount must be attached to a vacuum port. Therefore the external part of the device will be in air, and heat can be dissipated by convection. The device was recently assembled and will be tested soon. We expect to be able to dump around 125 W under vacuum with this design.

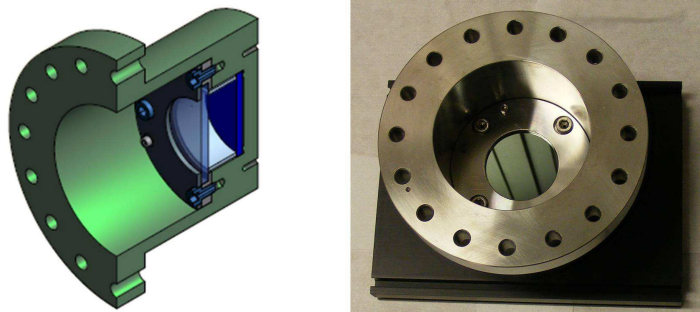


Figure 4.25: Design of the high power, in vacuum beam dump. Heat is dissipated in air by means of a radiator (black piece in left picture).

In Tab. 4.5 we give a summary of the main characteristics of the three beam dump prototypes.

| Type | Maximum incident power | Expected temperature increase |
|-------------------|------------------------|-------------------------------|
| high power in-air | 200 W | 80°C |
| medium power UHV | <20 W | less than 150°C |
| high power UHV | 125 W | probably less than 50°C |

Table 4.5: Main characteristics of the INJ beam dumps

4.9.4 Baffles for INJ

In order to mitigate diffused light and reflection issues of the various INJ optics, some baffling should be foreseen. In some misalignment condition the direct beam may hit these baffles, justifying the need of a high power compatible material. General requirements should be a total diffusion and reflection of the material lower than 1000 ppm and a damage threshold at least at the level of silicon (6 kW/cm^2).

To realize these baffles, we are studying the possibility to use Silicon Carbide (6H-SiC). In comparison with Si, it has the advantage of having an even better conductivity and a higher damage threshold. It can also be manufactured easily in complicated shapes and large plates can be produced. Another advantage is that with a very limited thickness (a few microns) a transmissivity of zero is obtained. Figure 4.26 shows the measurement of thermal maps of Silicon Carbide (SiC) and Si for an absorbed YAG laser power of about 10 W and a beam waist size of 2.5 mm.

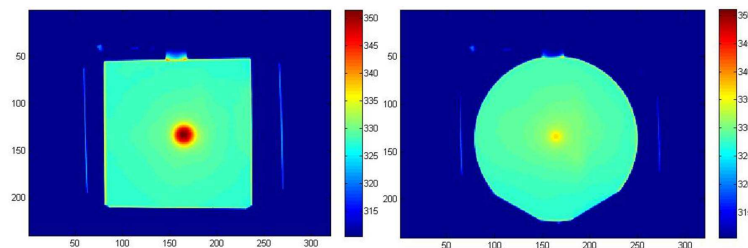


Figure 4.26: Thermal map of Si (left) and SiC (right) for 10 W of absorbed laser power.

We observe that the thermal gradient inside SiC is much smaller than in Si. The peak to peak temperature elevation is 9°C for SiC and 24°C for Si. This seems compatible with conduction values of 490 W/m/K for 6H-SiC found in literature. The damage threshold was measured by slowly ramping up the power incident on the material; a value of 30 kW/cm^2 was found for SiC. We recently developed some diaphragms based on SiC that were designed to dump spurious light on the Virgo Suspended Detection Bench (SDB) [117]. On these rough samples that were coated by CVI we obtained a total reflection and diffusion of 17000 ppm. Far better results are expected with polished samples.

4.10 Input mode cleaner

IMC cavity parameters will be described in this section (geometry, finesse, material choice, polishing requirements and coating properties of the mirrors) as well as the angular control strategy and performances required in order not to spoil the ITF sensitivity.

4.10.1 Geometry and finesse

The IMC cavity is an in-vacuum triangular cavity with suspended optics and a finesse of 1200 (corresponding to an input/output coupler reflectivity of 2500 ppm, and total round trip losses lower than 100 ppm). The finesse and macroscopic length of the cavity are unchanged

with respect to Virgo, as they are still thought to be a good compromise between high spatial filtering effect of the cavity and acceptable issues linked to the high finesse and length, namely radiation pressure, thermal effects and the backscattering at small angle from the end mirror. The design is thus similar to the Virgo case, except that the specifications for the polishing of the mirrors are more stringent (this is detailed in the next paragraphs) in order to cope with the following requirements: less than 4% throughput loss on the TEM₀₀ mode, and less than 4400 ppm of effective "reflectivity" of the IMC due to the mechanism of backscattering at small angle from the end mirror (which associated to the Faraday isolator isolation of 40dB corresponds to less than 0.5 % of fringes amplitude at the output of the IMC cavity [129]) for a finesse of 1200. The waist of the cavity is located on the input/output mirrors which are flat. The half round trip length is 143.424 m (see the OSD chapter). The waist size is 5.17 mm, corresponding to an end mirror radius of curvature of 187 m, in order to minimize losses due to High Order Mode (HOM) resonance. As described in Fig. 4.33, this choice is made to be at about mid-way between the resonance of TEM₁₀ (181 m) and TEM₃ (191 m) which is the best choice in order to minimize the losses due to clipping of HOMs. A corrective system (Central Heating Radius of Curvature Correction (CHRoCC)) will be used to optimize the final operating radius of curvature. In order to have the beam at 45 mm from the external edge of the flat mirrors in the horizontal plane (meaning at 61 mm from the corner angle formed by the 2 flat mirrors as shown in Fig. 4.27), and given the half round trip length of the IMC, the angle between both flat mirrors should be 89° 58' 58" or 89.9828°. An error of 1" corresponds to a miscentering on the flat mirrors of about 1 mm.

4.10.2 Cavity input/output mirrors

The proposed solution not only eliminates the presence of an aperture in front of the mirrors in contrast to what is used in Virgo, but it will also contribute to increase the IMC throughput through an improvement of the mirror surface error. In addition, a monolithic support will be used ensuring a flat transfer function up to more than 800 Hz. The low absorption of the coating (<1 ppm) should ensure that thermal effects in the IMC cavity will be negligible and that the beam shape will not be distorted.

4.10.2.1 Dihedron description

Figure 4.28 gives 3D representations of the dihedron. The concept is the following: two flat rectangular substrate blocks are optically bonded without making use of any material in front of, or behind, the mirrors. No glue will be used. In fact, one of the two faces between which the bonding takes place, is at an angle Θ with respect to the other faces of the block, whereas the second block is completely rectangular. The angle Θ between the two mirrors must be 89° 58' 58" \pm 2". The faces of the mirrors must be polished and coated to meet the required specifications given in the Tab. 4.6. The coating process must take place before the bonding is done taking care of protecting the part of both mirrors that should be optically contacted.

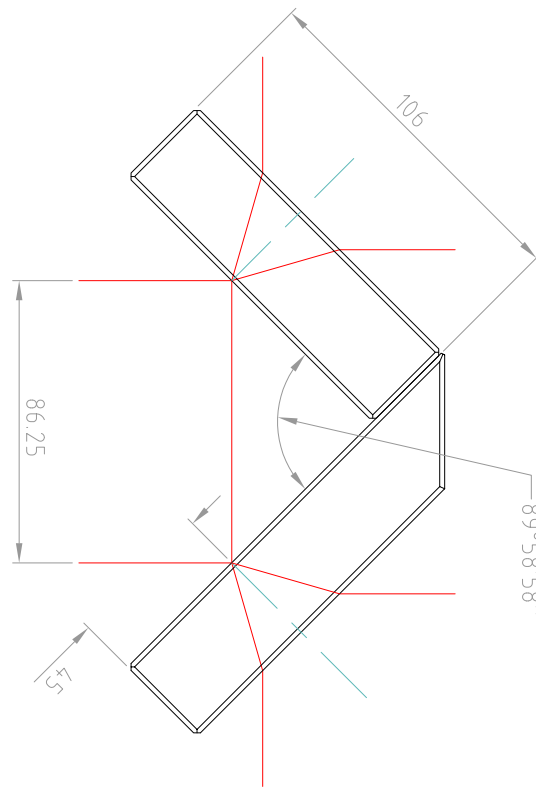


Figure 4.27: IMC flat mirrors assembly; top view with laser beam axis.

4.10.2.2 Substrate specifications

The specifications of the new IMC flat substrates are given in Tab. 4.6. Note that the material chosen is Homosil 101 from Heraeus, a so-called 3D glass, which has a very good homogeneity useful for substrates used in transmission. The substrate absorption should be lower than 20 ppm/cm.

4.10.2.3 Mirrors specifications: surface characteristics.

The principal source of IMC round trip losses is scattering from the rough mirror surfaces. There is a direct relationship between the Power Spectral Density (**PSD**) of a mirror surface and the scattered light. In the case of the IMC, scattered light only contributes to round trip cavity losses when it is generated by high spatial frequency mirror roughness. This is because high spatial frequency mirror roughness scatters light at larger angles which is subsequently lost from the cavity due to the apertures defined by the finite mirror diameters.

| Mirror Substrates | | | |
|---|---|---------------------------|----------|
| Material | Homosil 101 | | |
| Dimensions (mm) | 106 x 30 x 80 \pm 0.5 | | |
| Dimensions (mm) | 136 x 30 x 80 \pm 0.5 | | |
| Bevel | 1.5 mm x 45° | 1.5 mm x 45° | |
| Optical requirements | | | |
| | Side A | Side B | Side C |
| Curvature | ROC>30km (spherical fit) over 22 mm of diameter; | Residual ROC > 1km. | flat |
| | ROC>10km for the rest of the mirror. | | |
| Clear aperture (CA) | \geq 50 mm | \geq 70 mm | |
| Parallelism | < 2" | | |
| Surface error on CA (rms) | < 2 nm on 22 mm diameter and < 5 nm for the rest of the mirror surface (see surface characteristics section). | < 20 nm on CA | polished |
| Wavefront transmitted error | < 20 nm on CA | | |
| Surface defects on CA | \leq 10 scratches \leq 5 digs | | |
| Roughness (rms) | < 0.1 nm on CA | | |
| Coating | | | |
| Wavelength | 1064 nm | | |
| Coating type | HR | AR | NA |
| Incidence angle | 45° | | |
| Polarization | S | S | |
| Transmission (ppm) | The 2 mirrors have to get a similar transmission within few tens of ppm. | | |
| | 2500 ppm \pm 300 ppm (to be reviewed with LMA for absorption optimization) | | |
| Reflection | - | < 300 ppm | |
| Coated area (mm) | 88 mm x 72 mm (See [118]) | 86 mm x 70 mm (See [118]) | |
| Average scattering @ 3deg incidence angle (ppm) | < 5 | < 5 | |
| Absorption | <1 ppm | <1 ppm | |

Table 4.6: General specifications for the flat IMC mirrors.

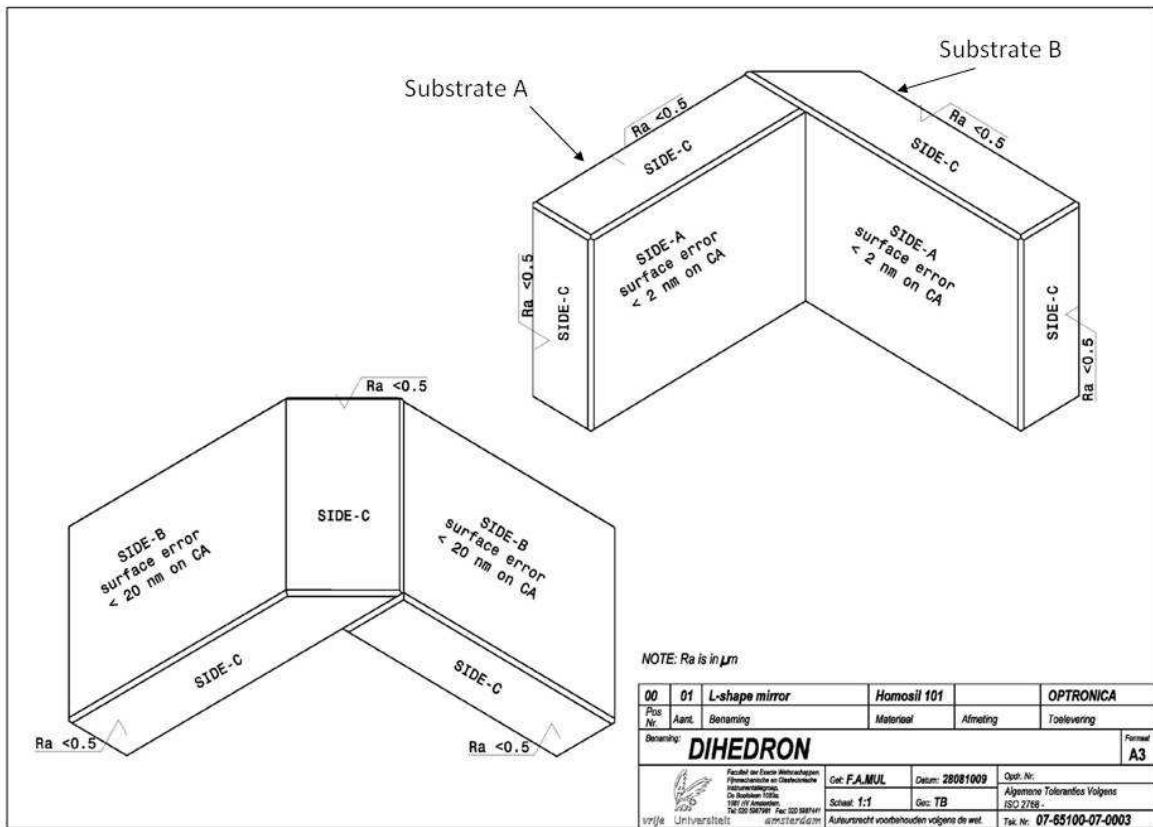


Figure 4.28: IMC flat mirrors assembly 3D view.

The round trip losses may be directly estimated from the mirror surface PSD as explained in a note [119]. We have shown that spatial frequencies below about 100 m^{-1} have very little influence on the round trip losses.

Thus, the requirement for each IMC plane mirror is:

1. an overall mirror roughness rms of less than **2 nm**
2. a round trip loss of less than **15 ppm** (to ensure cavity round trip losses lower than 100 ppm).

In Fig. 4.29, we show a typical PSD which fulfills these requirements.

A set of substrates (see PSD reported in Fig. 4.29) has been polished in The Netherlands and is fulfilling our requirements: the expected round trip loss contribution of each mirror is of the order of 15 ppm [120].

4.10.2.4 The support

Tests have been performed using the Virgo interferometer to obtain an upper limit on the noise coming from the bench creating IMC length noise which is finally projected on the AdV

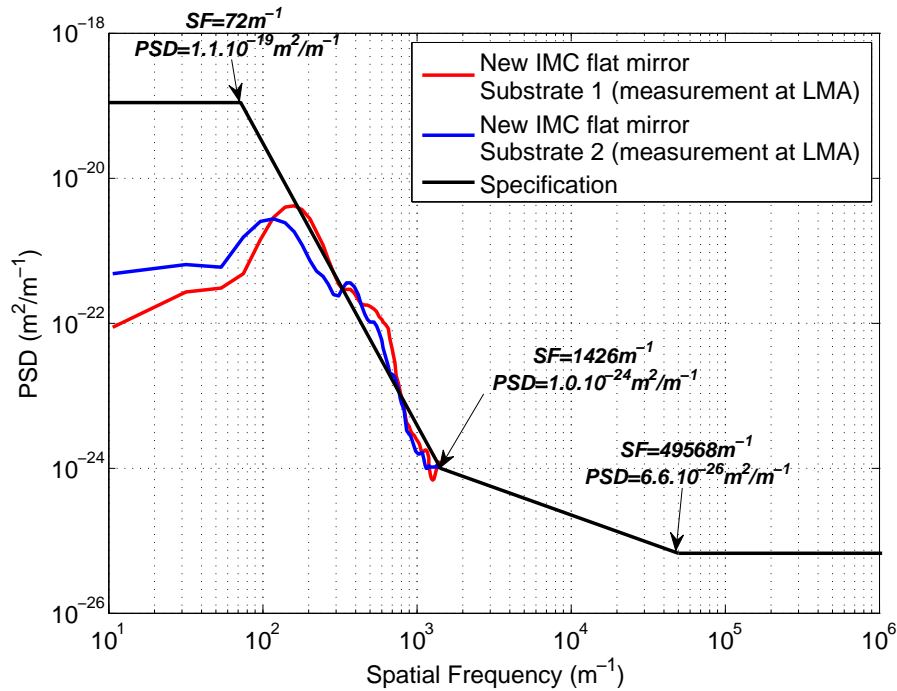


Figure 4.29: IMC plane mirror PSD giving round trip loss of 15 ppm.

sensitivity. The preliminary projection done for Virgo+ [121] has been used to find the one presented in Fig. 4.30. Basically, we have divided the Virgo+ projection by Virgo+ Common Mode Rejection Factor (CMRF) and multiplied the result by the AdV worst case common mode rejection factor given in Fig. 4.57. In Fig. 4.30, it is shown that this noise should not limit the AdV sensitivity since the noise floor remains about a factor of 100 below. Note that this projection has been obtained using Virgo data with the dihedron mounted on a rigid support that shows a first resonant frequency around 240 Hz. Using a rigid support with the dihedron fixed on top of it, we expect an increase of the amplitude of the structures seen above 300 Hz; this is why it was decided to install an extra filter in the SIB1 and MC end mirror superattenuators to have an extra safety factor on this projection.

The proposed support is shown in Fig. 4.31 and Fig. 4.32. It is machined from one piece and consists of a base plate and a support piece ("Pedestal"), which brings the mirrors to the correct height (100 mm). The base plate is directly bolted to the SIB. The surface of the pedestal on which the dihedron rests is completely flat. There is no glue involved, but a clamp is foreseen to prevent the dihedron from oscillating between different possible resting positions. Alternative solutions which make explicit use of three contact points on which the dihedron rests (such as "kinematical positionings" which have been used for the old dihedron) have been eliminated as the contact points between steel and glass act as a spring with intrinsic frequencies in the range of about 240 Hz [121]. At the front side of the pedestal, a border extends 5 mm above the surface. It contains three contact points to allow for a precise positioning of the dihedron in the direction of the IMC. In the horizontal direction, the mirror assembly is kept in place by three little springs which hold it towards the contact points so that it cannot change position.

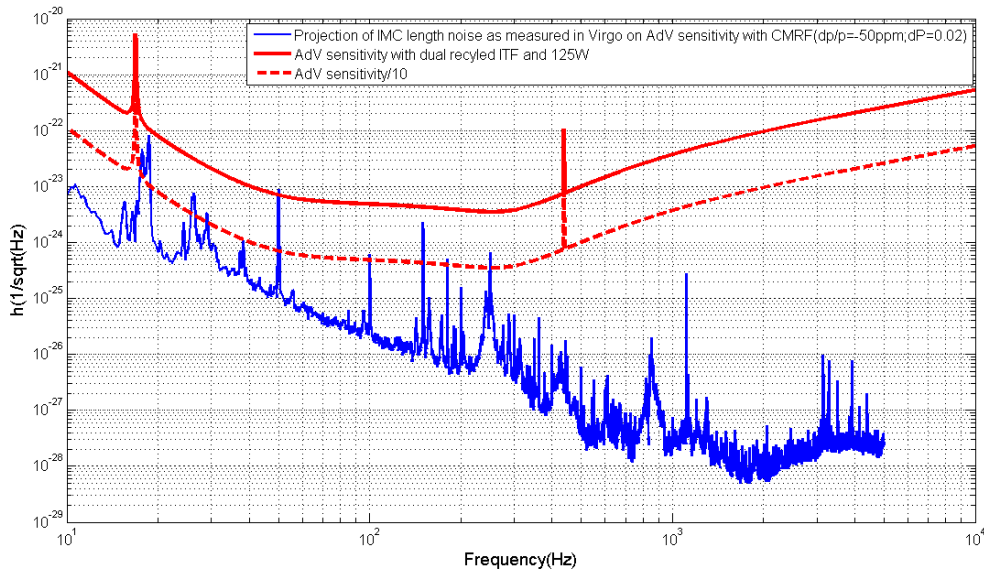


Figure 4.30: AdV reference sensitivity curve in the case of a dual recycled ITF for 125 W input power. The dashed curve is the AdV sensitivity with a factor of 10 safety margin. The blue curve shows the projection of IMC length noise when using a rigid support for the dihedron.

We have measured the transfer function of such a support together with a prototype mirror assembly, and it is flat for frequencies below 800 Hz [121].

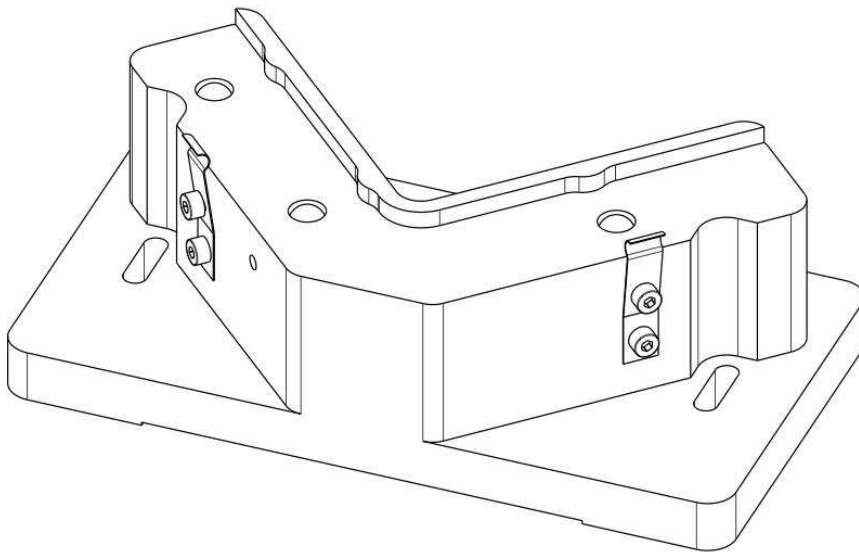


Figure 4.31: A view of the dihedron monolithic support.

Internal frequencies

As there is only one contact face between the two substrates, the (intrinsic) eigenfrequencies of the mirror assembly are expected to be rather low; preliminary FEM analysis yields values starting at about 2100 Hz. This is due in first instance to the ratio between the width of the



Figure 4.32: Dummy dihedron on the monolithic support.

bonding surface and the lengths of the mirror substrates. We have preliminary measurements of the frequency spectrum, and succeeded in FEA simulations to reproduce them at the percent level without adjusting any parameter. This allows us to use the simulations to improve the design. However, one has to consider the whole assembly consisting of mirrors and support mount in order to determine the eigenfrequencies, and the final values will be different from those of the mirror assembly alone. As precise simulations of this are difficult without prior knowledge of the contacts between mounting and mirrors, we will use a prototype mirror assembly and the different mountings to determine the characteristics of the contact points, and to determine the optimal configuration. Of course we will measure the eigenfrequencies of the set up once it is available.

4.10.3 Cavity end mirror

In this section we will discuss the radius of curvature and roughness requirements for the cavity end mirror.

4.10.3.1 Radius of curvature

There are two main requirements that have been used for determining the radius of curvature of the end mirror:

- **RoC weighted by beam intensity:**

Average value of the beam waist in the IMC cavity: We want the average beam radius in the IMC to be $5.1 \text{ mm} \pm 0.1 \text{ mm}$ on the input/output mirrors due to the limited

compensation possibility allowed by the ITF **MMT**. This gives a direct specification on the average Radius of Curvature (**RoC**) of the curved mirror: $187 \text{ m} \pm 3.5\text{m}$.

Astigmatism: The throughput loss due to the ellipticity of the cavity mode induced by the astigmatism of the end mirror should be negligible compared to other throughput loss mechanisms (scattering). This loss should be a factor of 100 smaller than 4.3% (overall throughput losses for the IMC cavity). Thus the astigmatism must be $0 \pm 3.5\text{m}$ to satisfy this requirement.

- **RoC over clear aperture:**

This requirement fixes the radius of curvature as seen by all the **HOMs** that could be circulating in the cavity. Figure 4.33 shows for what radii of curvature the different **HOMs** are in resonance. The radius of curvature must be chosen such that no **HOMs** are in resonance. As the clear apertures of the optics are large, many **HOMs** can resonate. A radius of curvature must be chosen to avoid all HOM resonances. The requirement obtained is a radius of curvature of 187_{-1}^{+0} m over all centered aperture diameters from 33 mm (3 times the beam radius) to 140 mm (end mirror coating aperture). This requirement must hold for the ordinary and extraordinary radii of curvature (RoC_o and RoC_e); therefore it also takes into account astigmatism. Figure 4.34 shows the radii of curvature measured in this way for the Virgo and Virgo+ IMC end mirrors. We see that the variation in radius of curvature with measurement aperture is out of specification for AdV.

Remark: **HOMs** of order higher than $n=20$ start to be clipped, therefore **HOMs** of order higher than 30 will virtually not resonate in the cavity.

The average RoC is equal to $(\text{RoC}_o + \text{RoC}_e)/2$.

Note that a RoC of 187 m has been chosen to be far enough from the degeneracy ($\text{RoC}=191\text{m}$) as shown in Fig. 4.33 in the knowledge that we may increase the RoC by up to 3m using the IMC **CHRoCC**. The second criterion is the most stringent one and will be used as requirement: 187_{-1}^{+0} m .

4.10.3.2 Mirror Roughness

There are two main requirements that have been used for determining the roughness specification:

- **throughput loss:** this requirement is for the maximum amount of power lost from the TEM_{00} mode in transmission of the IMC. The throughput loss due to the end mirror roughness must be less than 0.645 % (this corresponds to 15 ppm round trip losses for this mirror as in the case of the plane mirrors).
- **IMC-ITF parasite cavity:** Light reflected off the interferometer returns into the IMC. Backscattering off the end mirror can cause light to circulate in the IMC in the “reverse” direction. This light may then return to the interferometer thereby generating a non-controlled cavity. The requirement for the effective “reflectivity” of the IMC due to this mechanism of backscattering is less than 4400 ppm (which associated to the Faraday isolator isolation of 40dB corresponds to less than 0.5 % of fringe amplitude at the output of the IMC cavity)

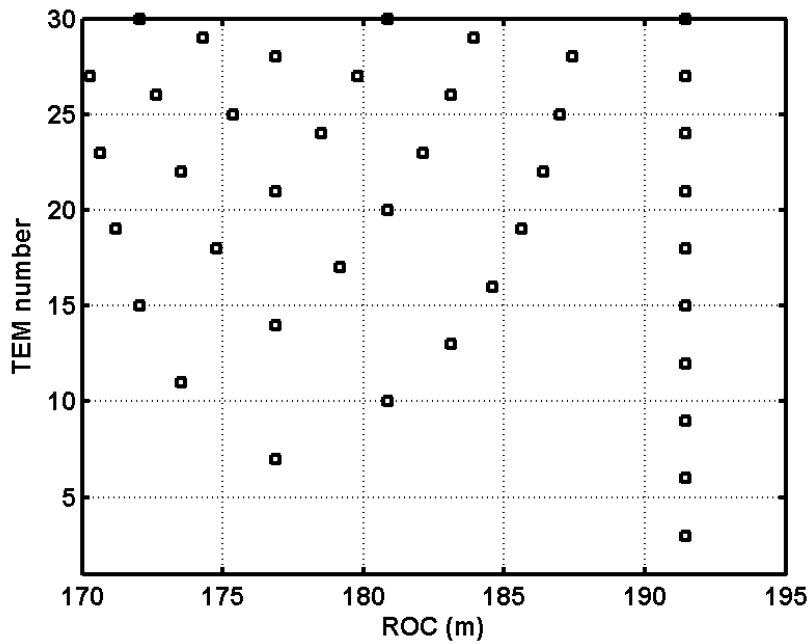


Figure 4.33: End mirror radii of curvature of higher order mode resonances.

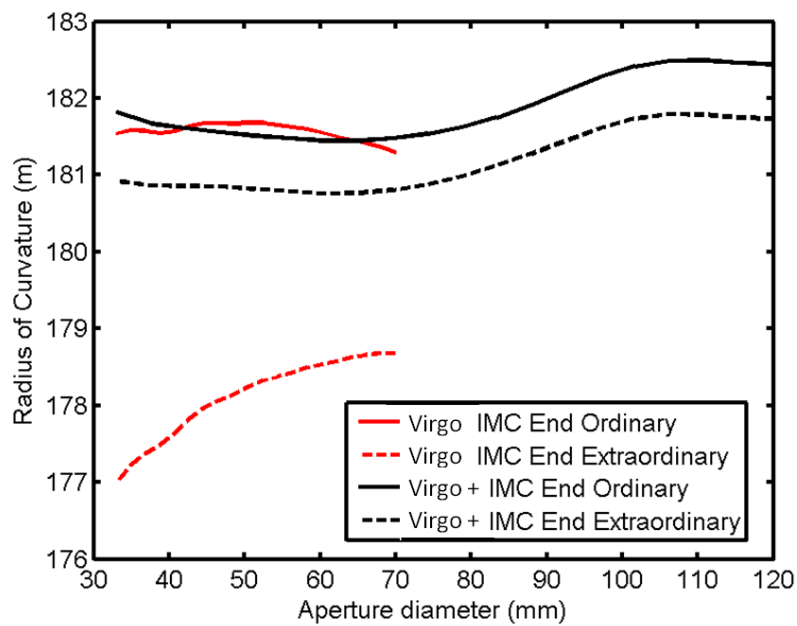


Figure 4.34: End mirror radii of curvature (ordinary and extraordinary axes) as a function of measurement aperture for Virgo end mirror (C03004) and Virgo+ end mirror (C08009).

In order to correctly set the requirements for the end mirror roughness, it is necessary to understand the various mechanisms involved. All of these mechanisms contribute differently depending on the spectral composition of the surface roughness.

For the **throughput loss**, four different mechanisms may be identified.

1. **Scattering:** This loss is due to scattered light that is clipped after one round trip in the cavity. It depends on the rms roughness of the mirror above the spatial frequency cutoff of 150 m^{-1} . The value of this cutoff depends on the mirror apertures in the cavity; the larger the aperture, the higher the cutoff. As the light is scattered from the fundamental cavity mode, the rms roughness measurement is weighted by the fundamental mode intensity.
2. **Backscattering:** A portion of the scattered light from the end mirror that is normally lost by clipping returns to the output mirror. This light is recoupled into the IMC but circulates in the reverse direction. The coupling between the main cavity and this parasite cavity causes power to be lost and “pumped” from the main cavity mode and therefore reduces the throughput. This effect is generated by mirror roughness spatial frequencies between 400 and 700 m^{-1} (These values depends on the angle of incidence on the IMC end mirror). As the light is scattered from the fundamental cavity mode, the rms roughness measurement is weighted by the fundamental mode intensity.
3. **Scattering to HOMs:** Light that is scattered from the end mirror due to mirror roughness with spatial frequencies below the cutoff of 150 m^{-1} is no longer in the fundamental mode but is not lost from the cavity. As this light may be converted back to the fundamental mode by the mechanism of scattering the losses are considerably lower than scattered light that is clipped after one round trip (if the cavity geometry is well chosen so that HOM’s are far from resonance). As the light is scattered from the fundamental cavity mode, the rms roughness measurement is weighted by the fundamental mode intensity.
4. **HOM clipping:** HOMs generated by mirror roughness spatial frequencies near to the cutoff of 150 m^{-1} have a very large TEM number. If the end mirror radius of curvature that they see is such that they are resonant then they will be excited and excessive light will be lost from the cavity by clipping. This loss can be significantly greater than the clipping of scattered light. It is for this reason that the radius of curvature of the end mirror over all apertures must be carefully chosen so that this loss mechanism will be negligible.

For the **IMC-ITF parasite cavity**, one mechanism has been identified:

The **backscattering** off the IMC end mirror.

Having understood the mechanisms involved, the requirement for the end mirror roughness may be described using two conditions:

For the **throughput loss** we may use the condition:

$$aR_{lo}^2 + bR_{med}^2 + cR_{bckscat}^2 + dR_{hi}^2 < 1 \quad (4.2)$$

where R_{lo} is the rms for spatial frequencies below 150 m^{-1} , R_{med} is the rms for spatial frequencies between 150 and 400 m^{-1} , $R_{bckscat}$ is the rms for spatial frequencies between 400 and 700 m^{-1} and R_{hi} is the rms for spatial frequencies above 700 m^{-1} . a , b , c and d are the weighting coefficients.

For the **IMC-ITF parasite cavity** we may use the condition:

$$eR_{bckscat}^2 < 1 \quad (4.3)$$

where e is the weighting coefficient.

The weighting coefficients are determined by FOG simulation (see OSD chapter for more details on FOG) of the IMC using appropriate random maps on the end mirror (with single frequency spatial defects)[122]. The determined coefficients are:

$$a = 0.42nm^{-2} \quad b = 8.43nm^{-2} \quad c = 62.67nm^{-2} \quad d = 8.43nm^{-2} \quad e = 39.90nm^{-2} \quad (4.4)$$

We see from these coefficients that the loss in throughput is considerably higher for spatial frequencies above the cutoff. We may therefore conclude that we should use apertures in the cavity as large as possible as long as we can meet the radius of curvature requirement over the whole aperture.

The conditions 4.2 and 4.3 do not limit the PSD of the end mirror to a specific shape as there is a compromise to be made between high and low spatial frequencies. In Fig. 4.35 we show three example PSDs which all fulfill the requirements.

Taking into account the limitations of polishing technology it would seem that the red curve is the best compromise between low and high spatial frequencies, having a total rms of 0.57 nm. By comparing with the PSD's of the Virgo and Virgo+ IMC end mirror, it should be noted that this requirement is approximately a factor 3 (in amplitude) more stringent than what has been achieved in the past. Specifications for the IMC end mirror are summarized in Tab. 4.7.

4.10.3.3 IMC end mirror payload

The new end mirror has a diameter of 145 mm, and will be 94 mm thick, leading to a mass of 3.399 kg. It has thus a slightly larger diameter (+ 5 mm), and a substantially larger thickness - and mass - than the Virgo IMC end mirror. This leads to the following consequences:

- The spacing between the mirror suspension wires must be increased by 5 mm, or 2.5 mm per wire. The wire yoke in the gear box must be modified correspondingly.
- The reaction mass must be adapted to accommodate the larger mirror thickness.
- The counter mass must be adapted to the increased weight of the mirror and reaction mass.
- The centre of gravity will be below the point in which the marionette is suspended; this must be corrected by adding mass on top of the marionette.
- The total weight of the payload increases, and the suspension must be adapted, cq. retuned.

Most of these changes are small, especially the changes caused by the larger wire spacing. Concerning the reaction mass, the simplest approach is to fabricate a new and slightly adjusted model which accommodates the larger mirror thickness and insures that both, mirror and reaction mass, are suspended in the same z position with respect to the laser beam. Also

| Mirror Substrates | | | |
|-----------------------------------|---|---|----------|
| Material | Herasil 102 | | |
| Outside diameter (mm) | 145 ± 0.1 | | |
| Thickness (mm) | 94 ± 0.1 | | |
| Bevel | 0.5 to 1 mm x 45° | 0.5 to 1 mm x 45° | |
| Wedge | 1mrad ± 0.2mrad | | |
| Optical requirements | | | |
| | Side A | Side B | Side C |
| Curvature | Residual RoC > 1km | RoC* = 187 ⁺⁰ ₋₁ m weighted by the beam profile RoC* = 187 ⁺⁰ ₋₁ m over clear aperture | |
| Surface error (rms) | < 20 nm on 50 mm diameter | see PSDs (Fig. 4.35) | polished |
| Surface defects on Clear Aperture | ≤ 10 scratches on 145 mm diameter ≤ 5 digs on 145 mm diameter | | |
| Roughness (rms) | < 10 Å on CA | see PSDs (Fig. 4.35) | |
| Coating | | | |
| Wavelength | 1064 nm + 633 nm | 1064 nm | |
| Coating type | AR @ 1064 nm on 140 mm diameter R=70% @ 633 nm on 90 mm diameter | HR @ 0° on 140 mm diameter | NA NA |
| Polarization | S | S | |
| Transmission | | T < 1 ppm | |
| Reflection | < 100 ppm @ 1064 nm | | |
| Absorption | < 10 ppm | < 1 ppm | |
| Scattering | < 5 ppm | | |

Table 4.7: General specifications of the IMC end mirror.

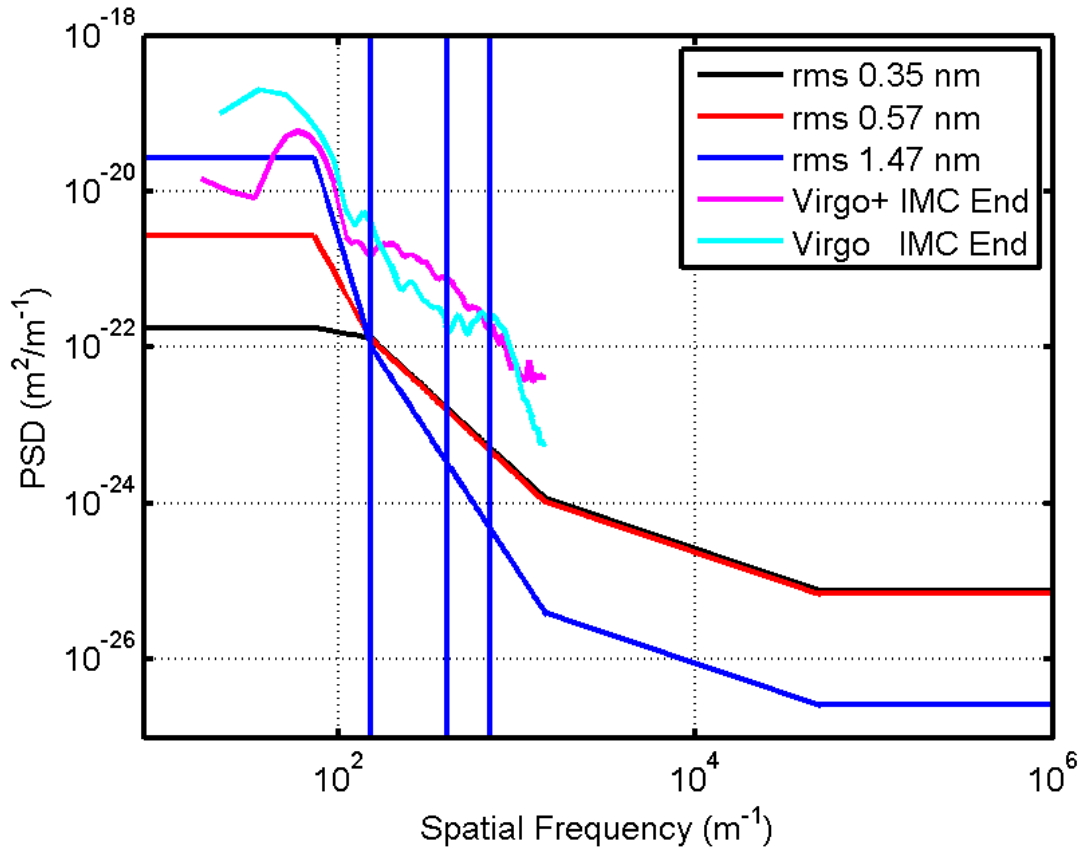


Figure 4.35: Three sample PSDs meeting requirements (black, red and blue curves) with total RMS of 0.35, 0.57 and 1.47 nm. Blue vertical lines indicate 4 different spatial frequency regions (below 150, 150-400, 400-700 and above 700). PSD's for Virgo IMC end mirror (C03004) and Virgo+ IMC end mirror (C08009) included for comparison. All PSD calculations weighted by fundamental cavity mode intensity.

the change of the centre of gravity is easy to correct by adding a new, heavier metal ring on top of the marionette.

However, all these actions increase the weight of the payload, especially the new reaction mass, the correspondingly heavier counter weight, and the correction of the centre of gravity. Since in any case, the suspension chain has to be retuned due to the addition of a filter, a weight adjustment of the payload is possible. It is certainly worthwhile to investigate whether a reaction mass can be designed without increasing its weight - or possibly even in such a way as to compensate also the increased mass of the mirror - in order that the weight of the payload remains (essentially) unchanged, as shown in the preliminary design presented in Fig. 4.36.

In addition, there is one minor item: the larger mirror dimensions require also remanufacturing of part of the installation tool.

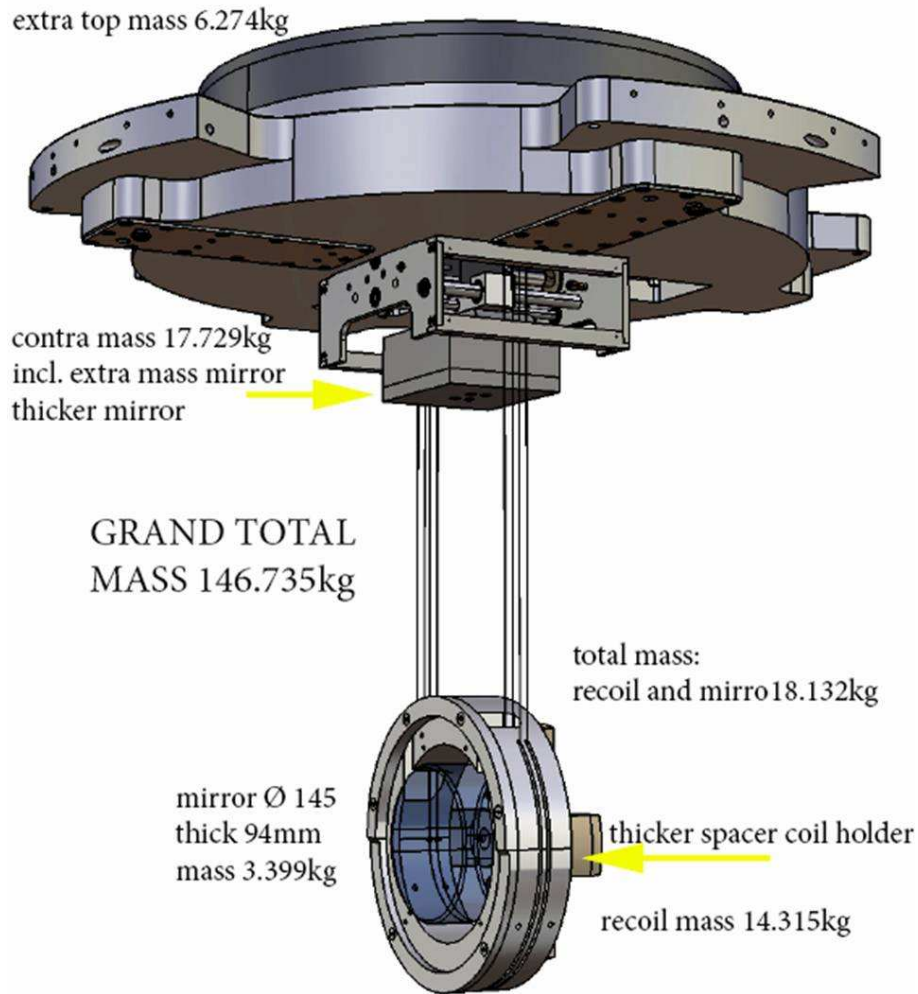


Figure 4.36: Preliminary design of the IMC end mirror payload for AdV.

4.10.3.4 CHRoCC IMC - Central heating RoC correction

HOMs resonance in the cavity can become a dominant source of round trip losses. It depends on cavity geometry and in particular on the end mirror RoC[124]. To reduce the round trip losses due to HOM resonating in the IMC cavity, the radius of curvature of the IMC end mirror in AdV will be changed with respect to Virgo+. The risk due to a possible RoC error of the new mirror will be mitigated by a RoC correcting system. It will help to accurately tune the radius of curvature in case the end mirror's RoC is close to HOM degeneracy.

This corrective system is a central Heating Radius of Curvature Correction (CHRoCC). It allows to increase the RoC of the IMC mirror by projecting a heat pattern onto the center of the mirror HR surface. This heat pattern comes from a vacuum compatible source, an alumina substrate that acts as a black body emitter. The parabolic reflector of the IMC CHRoCC (see Fig. 4.37-right) projects the infrared pattern on the mirror surface. The power absorbed in the mirror depends on the temperature of the heat source. The maximum

temperature of actuation is 1200 °C; this corresponds to a maximum absorbed power of 7.5 W. By working at 500 °C, which corresponds to 3 W of absorbed power, the increase of the RoC is sufficient to go far from the HOM degeneracy. The IMC CHRoCC was installed in the IMC tower during the final phase of Virgo+ commissioning; it was able to induce an RoC increase of 3 m. Some tests have been done with a thermal camera to verify the heat pattern of the CHRoCC on the IMC mirror (see Fig. 4.37-left). They have shown good agreement with simulations.

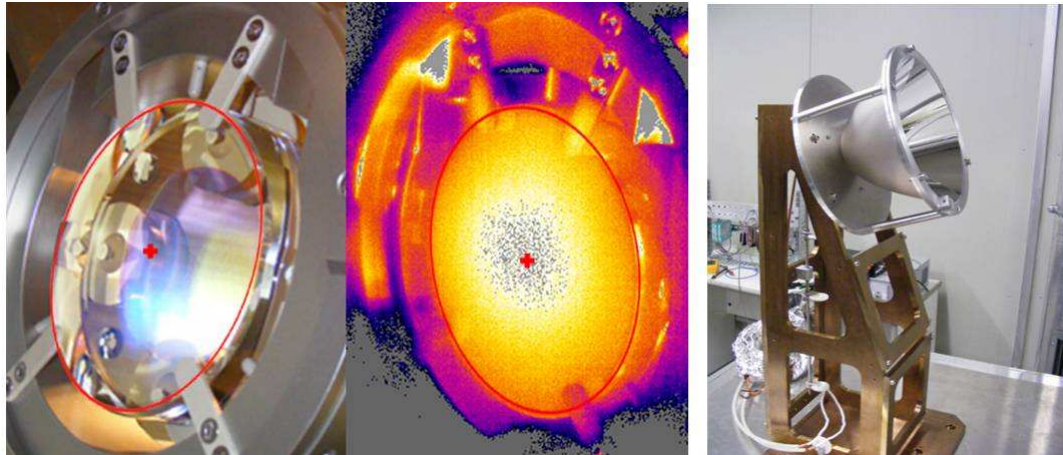


Figure 4.37: Left: Heat pattern of the CHRoCC on the IMC end mirror; Right: IMC CHRoCC during tests under atmospheric pressure.

Note that the CHRoCC will not worsen the RoC uniformity. Figure 4.38 shows a Zemax/ANSYS simulation of the RoC induced by the IMC CHRoCC. This example shows the CHRoCC working at half its full dynamic range (RoC increased by 1.5m). We see that the RoC non-uniformity is well below the requirement of 1m (solid and dashed black curves) defined in the RoC requirements paragraph.

4.10.4 IMC cavity longitudinal and angular control

In order to ensure long locking periods of the IMC, the mirrors have to be continuously kept aligned with respect to the main beam. First, the MC mirror and the dihedron, placed on the Suspended Injection Bench (SIB1), are aligned by means of auxiliary devices called Local Control (LC), whose goal is to keep their position stable for allowing to acquire the lock of the IMC cavity. Then, when the residual mirror angular displacement is reduced below some tenths of microradians, a global alignment control, based on the wavefront sensing technique, is engaged.

4.10.4.1 Local control

The local control is a servo system based on optical levers which maintains the angular position of the mirrors with respect to local references. The main purposes of the LC are to suppress longitudinal and angular pendulum oscillations and to recover the angular and longitudinal reference position without exciting resonances.

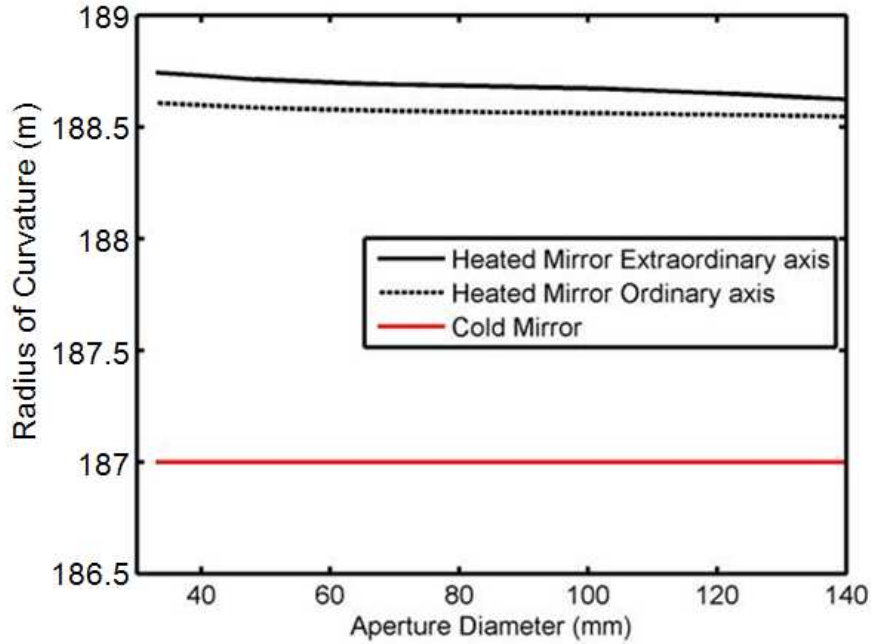


Figure 4.38: Expected IMC CHRoCC uniformity when working at half dynamic range.

The angular accuracy requirements for the local control system are set in order to maintain the mirrors within the linear regime of the Automatic Alignment (AA) error signals. In order to evaluate the LC angular accuracy requirements for the AdV IMC, some measurements have been performed in the Virgo+ IMC. This extrapolation is possible since no modification to the AA control scheme is planned in the AdV IMC design.

In order to be able to switch from local control to global control, the mirror has to be locally controlled within the linear range of the global signals. We have measured the AA error signals as a function of the angular misalignment in the Virgo+ IMC cavity. The measured values of the linear regime are in a range between a few μrad and $15\mu\text{rad}$. These results are in agreement with the present LC performances, which have a typical accuracy of the order of a fraction of a microradian for both pitch and yaw. So the present LC performances are compliant with the AdV requirements.

4.10.4.2 Angular accuracy requirements

The angular accuracy requirements have been estimated by modeling the whole IMC cavity with the frequency domain simulation tool Finesse. This simulation took into account the pitch and yaw degrees of freedom of the SIB¹ and the mode cleaner end mirror (MC). The angular accuracy requirements have been fixed in order to have the maximum cavity power variation of $dP/P \sim 10^{-3}$.

Figure 4.39 shows the effect of a misalignment of the SIB by an angle θ in the yaw direction.

¹Due to the fact that the dihedron origin O and the SIB center of rotation are not coincident (see Fig. 4.39) in the simulation for the SIB yaw requirement evaluation a tilt plus a small translation, proportional to $d \cdot \theta$, has been applied. The translation effect is negligible, but it could become relevant if the distance between the dihedron origin and the SIB center of rotation will significantly increase.

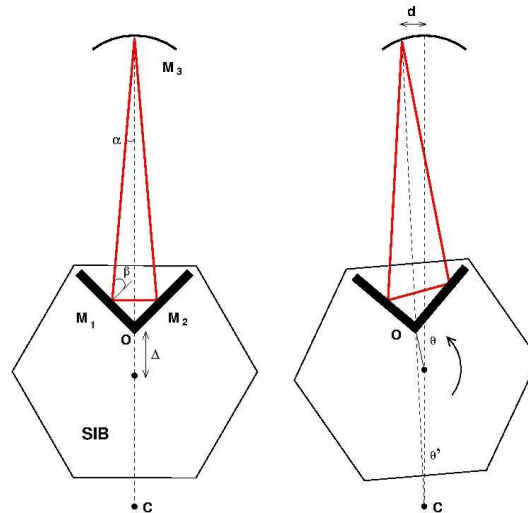


Figure 4.39: Effect of a misalignment of the SIB by an angle θ in the yaw direction.

Moreover, in order to validate the simulation results, a measurement of the cavity power variation as a function of the IMC misalignment has been performed. The simulations are in agreement with the experimental data within a factor two. The discrepancy obtained between the simulation and the measurement could be even smaller since the MC LC error signals, which have been used to perform the measurement, are not perfectly calibrated.

Even with this small mismatch the currently achieved control accuracy remains below the requirements by a factor ~ 10 . So the present control system is already compliant with the Advanced Virgo angular accuracy requirements.

Table 4.8 collects the measured and the simulated values for a cavity power variation of $\sim 10^{-3}$.

| | simulated [μrad] | measured [μrad] | achieved [μrad] |
|-------------------|-------------------------------|------------------------------|------------------------------|
| MC $_{\theta_x}$ | 0.87 | 0.58 | 0.11 |
| MC $_{\theta_y}$ | 0.47 | 0.31 | 0.02 |
| SIB $_{\theta_x}$ | 0.93 | 1.86 | 0.09 |
| SIB $_{\theta_y}$ | 1.1 | 1.1 | 0.10 |

Table 4.8: Comparison between the simulated and measured requirements, expressed in total rms. The simulated requirements are in agreement with the measured ones within a factor 2, due to possible mistuning in the simulation and a not perfect calibration of the LC signals. In the last column the present angular control accuracies are shown. The discrepancy is not worrying since both requirements, measured and simulated, are well above the current IMC performances, by a factor ~ 10 .

4.10.4.3 Angular control system

The angular control system deals with six degrees of freedom, four for the injection bench ($\theta_x, \theta_y, \theta_z, z$) and two for the mode cleaner end mirror (θ_x, θ_y). In this section only θ_x, θ_y of the SIB and Mode cleaner (MC) are considered. The control is based on a wavefront sensing technique, which uses interferometric signals, in transmission of the MC end mirror and in

reflection of the IMC cavity. This system allows the control of all angular degrees of freedom within $0.1 \mu\text{rad}$ (see Tab. 4.8) with a unity gain frequency of about 1 Hz. The automatic alignment of SIB and MC end mirror is made using DSPs.

4.10.4.4 Control noise projection

The complete treatment of the automatic alignment control noise projection is described in [123]. The evaluation of the IMC angular control noise has been done by evaluating the equivalent IMC length noise caused by the cavity misalignment and projected to the dark fringe using the simulated transfer function (TF) between the IMC length noise and the gravitational wave signal. Figures 4.40 and 4.41 show the automatic alignment control noise projection to the AdV sensitivity, both for the low and the full power configurations.

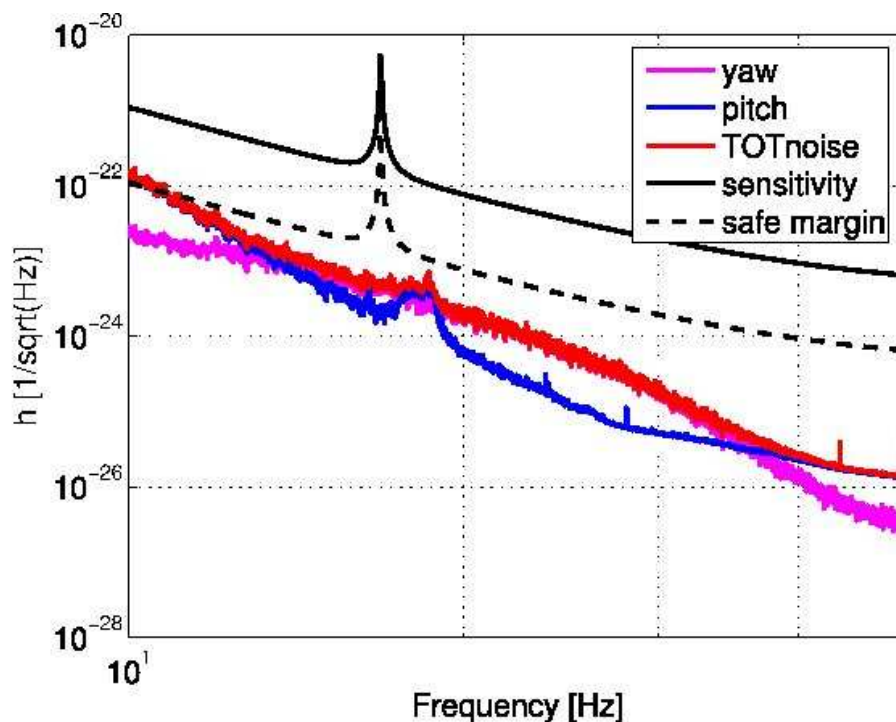


Figure 4.40: Automatic alignment control noise projection to the Advanced Virgo sensitivity for the low power configuration.

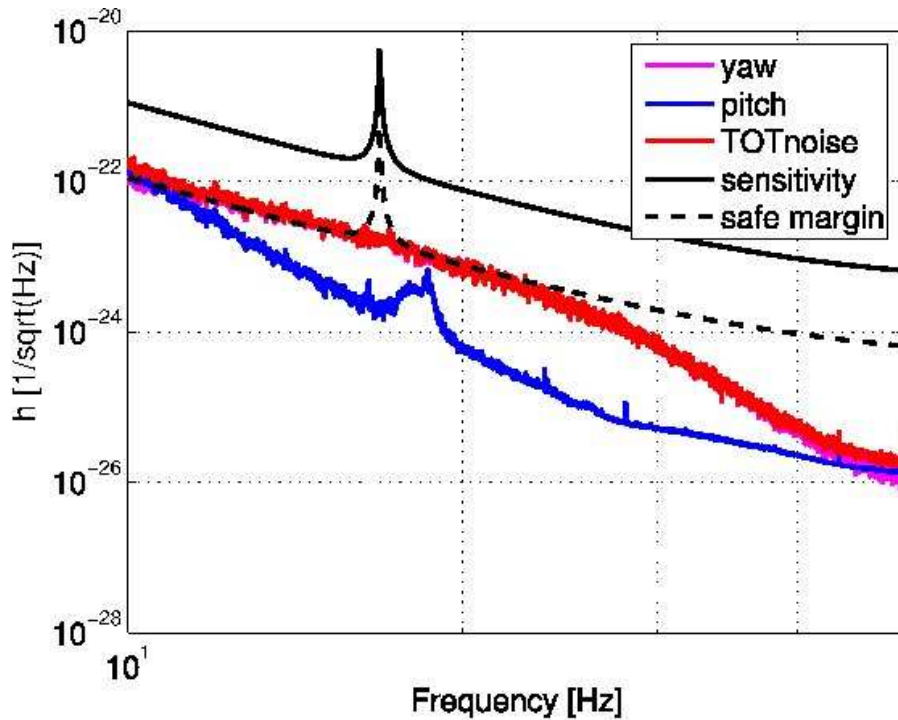


Figure 4.41: Automatic alignment control noise projection to the Advanced Virgo sensitivity for the full power regime.

In the low power configuration, in which the radiation pressure effects can be considered negligible, and in the high power configuration, considering 180 W of input power which will be the standard situation, the automatic alignment control noises are fulfilling the AdV requirements, remaining below the design sensitivity by about a factor of ten.

4.10.4.5 IMC longitudinal control

The locking strategy is quite similar to what has been used in Virgo. The error signal is taken in reflection of the IMC cavity and the correction is sent to the laser, whose wavelength is changed to follow the IMC cavity length change. See the PSL chapter for more details.

4.11 The reference cavity system

4.11.1 System overview

The **RFC** system is used in AdV to provide a low frequency stabilization reference for the laser frequency stabilization. The monolithic **RFC** is the reference for the laser frequency prestabilization: the laser frequency will be locked on the IMC and the IMC length will be locked on the RFC. In a first stage, it is the low frequency reference for the prestabilized beam, and then it is used as main **ITF** low frequency reference for controlling the interferometer common mode (CARM) in science mode. The assumed topology is analogous to the one already successfully used in Virgo and Virgo+.

4.11.2 Requirements and functionalities

The top level requirements for the RFC system are defined hereafter [104].

- Provide a reference for the prestabilized laser loop and for the ITF lock (for reducing frequency noise at low frequency) to get a frequency stability sufficient for locking the long arms.
- Provide a reference to stabilize at low frequency the ITF common mode
- The residual frequency fluctuation requirement provided by the RFC for Advanced Virgo is $\delta\nu < 1$ Hz rms up to 0.1 Hz (see the **ISC** chapter).

In order to fulfill the requirements, the main functions to be included in the RFC system are:

- Alignment and matching of the input beam on the RFC: possibility to check and tune remotely the alignment and matching on the RFC.
- – RFC transmission: the RFC system provides the pickoff, alignment and collimation of the RFC transmitted beam. It is used for locking threshold triggering, monitoring and diagnostic.
- – RFC reflection: the RFC reflected beam is used for providing the beam for the Pound-Drever-Hall signal extraction for the longitudinal locking on the RFC resonance, the beam for the RFC AA signal extraction by the wavefront sensors and the DC signal for monitoring and diagnostic of the RFC status.
- It must be possible to perform alignment and matching of the RFC system independently from the ITF beam.
- An automatic alignment system of the RFC keeps the incident beam aligned on the RFC.
- RFC monitoring and diagnostic: the RFC system includes the diagnostic and monitoring for the RFC DC alignment and matching. Beam characterization will be performed using the input beam monitoring system (see **IBMS** section).

4.11.3 RFC system design

4.11.3.1 General specifications

As shown in [111] and [104], the reference cavity has to be isolated from the ground seismic noise. The RFC cavity and the corresponding optics will be located in the lower part of **SIB1**. Any vibration noise introduced by the components of the RFC system has to be lower than the residual noise of **SIB1**. All the suspended RFC components are able to operate in the environmental conditions of the **SIB1** tower.

The total weight of the suspended part of the RFC system does not exceed 45 kg. All suspended components are vacuum compatible for at least 10^{-6} mbar residual pressure. On the bottom part of the SIB, the distance of the optical path from the bench surface is 17 cm (given by the RFC housing dimension).

4.11.3.2 RFC characteristics and optical layout on SIB1

We will use the original Virgo RFC in Adv. The RFC is mounted inside its separate tank below SIB1, as shown in Fig. 4.42. Maximum 30 mW (TBC) of power of the main beam are picked up to feed the RFC.

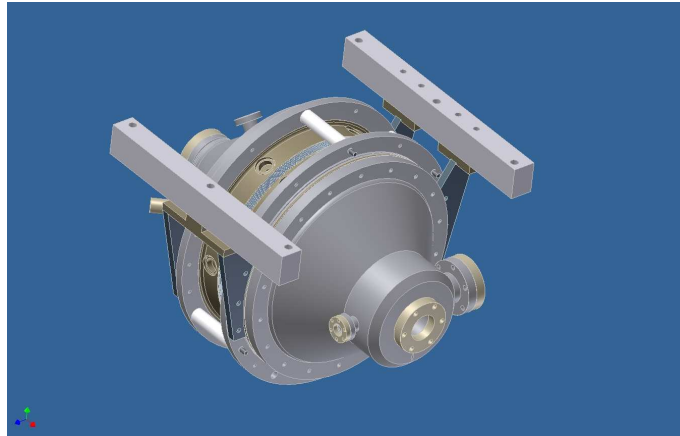


Figure 4.42: 3D view of the RFC in its vacuum tank.

All the requirements of the RFC and its mechanical envelope are those described in [125] and are identical to Virgo and Virgo+. The optical and mechanical specifications of the monolithic (ULE) cavity are also those of the Virgo RFC [125] and are given in Tab. 4.9.

| Parameter | Denomination | Dimension | Unity |
|--------------------------|------------------|----------------------|---------------|
| Block mass | M | 13 | kg |
| Silica block length | L | 300 | mm |
| Block radius | R | 100 | mm |
| Block Young modulus | Y | 6.7×10^{10} | Pa |
| Optical cavity length | z | 307.5 | mm |
| Free Spectral Range | FSR | 490 | MHz |
| Optical curvature radius | R_{curv} | 500 | mm |
| Spatial mode spacing | $\Delta\nu_{01}$ | 137 | MHz |
| Cavity waist | w_0 | 286 | μm |
| Finesse S pol. | F_s | 30,000 | - |
| Finesse P pol. | F_p | 800 | - |

Table 4.9: RFC physical and optical parameters

The overall layout is shown in Fig. 4.43.

The beam sent to the RFC is picked up right after the IMC, before entering into the SIB Faraday isolator. In this way a double advantage is obtained:

- The beam entering into the RFC is geometrically stable in shape and lateral jitter. The geometrical stability is that of the IMC transmitted beam (about a factor of 500 lower than specifications presented in section 4.7). This improves the matching with the RFC and makes requirements on the RFC AA less stringent.

SIB 1 lower part

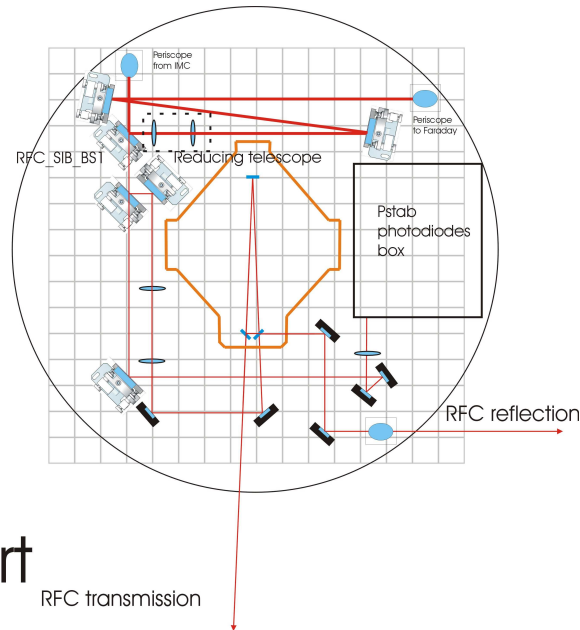


Figure 4.43: Optical layout the lower part of the SIB with the RFC system.

- The RFC alignment is decoupled from the alignment of the main beam and from matching adjustments on the ITF.

The beam is sent to the lower part of **SIB1** with a periscope (see section on optical design and Fig. 4.43). After the periscope the beam splitter RFC-SIB-BS1 (see Fig. 4.43) transmits part of the light to the RFC system, while the largest part is reflected and sent to the Faraday isolator. The amount of the light transmitted to the RFC system does not exceed 330 mW: 30 mW maximum for the RFC, 300 mW for the power stabilization photodiodes box. The reflectivity of the first face of RFC-SIB-BS1 is therefore $R=0.997$ ($T=0.003$). The second face is AR coated: $R<0.1\%$ (S polarization).

4.11.3.3 RFC input beam path optical design

The reflection and transmission values of all the optics of the RFC input beam path are selected in order to limit the amount of light arriving to the RFC, in any interferometer configuration, below the RFC damage threshold: the maximum power arriving at the input of the RFC in any ITF configuration does not exceed 30 mW in order to get less than 1 MW/cm² in the cavity for S polarization.

The picked off beam follows an optical path contained in the lower part of the SIB. The optical path is designed in order not to interfere with any other subsystem and to limit the amount of scattered light.

The matching telescope is designed in order to allow to tune the waist dimension around the design value of 286 μm and to change the position around the RFC input waist position by several millimeters (Fig. 4.44). The waist position is changed by moving the whole telescope along the optical path. The waist dimension is changed by changing the distance between the two lenses: this changes also the waist position, which is then compensated by moving the whole telescope.

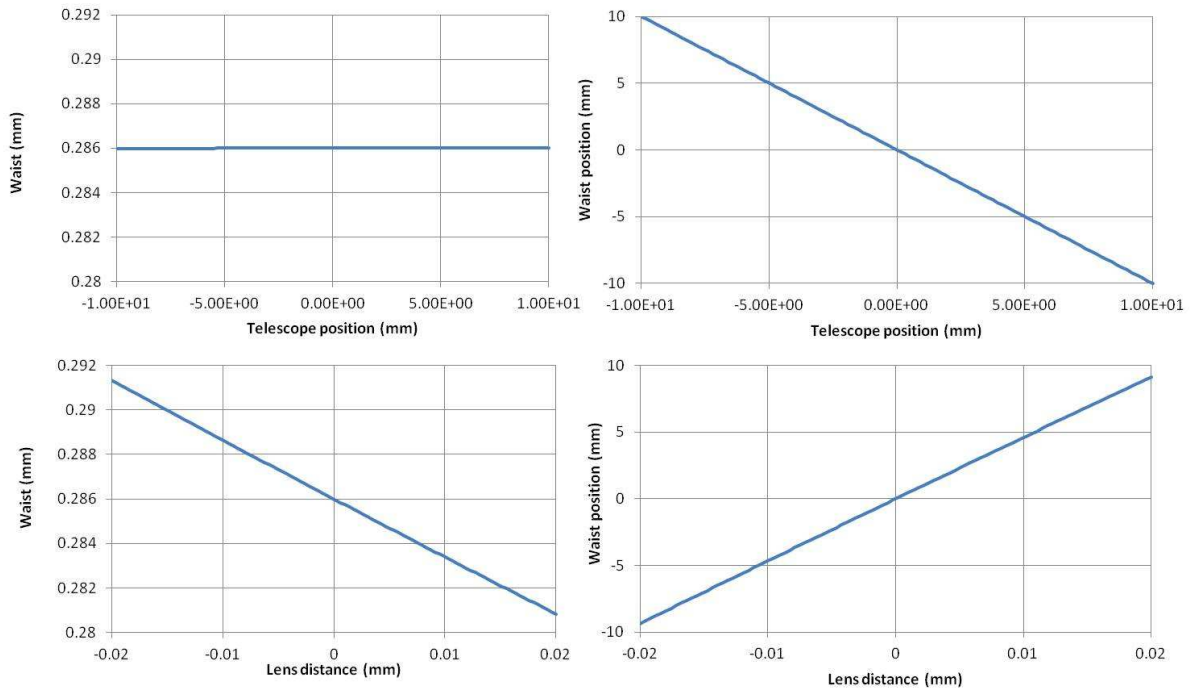


Figure 4.44: Waist dimension and position when changing the position of the telescope as a block and the distance between the two lenses.

4.11.3.4 RFC input beam path mechanical design

Means to fully remotely align the beam on the RFC, including angles and translations, are provided. It is possible to perform remotely the alignment with the RFC locked and in vacuum. The alignment adjustment is monitored via the RFC optical signals and actuators encoders. DC alignment stability is maintained after having performed the alignment procedure (stability in time and repeatability of actuator positioning). The actuation for the automatic alignment loop is provided by the two last RFC steering mirrors. The alignment and matching requirements are satisfied in the layout presented in Fig. 4.43 by allowing the ranges of actuation (given in Tab. 4.10) of the optics used to match and align the beam on the RFC.

| Element | Range | Resolution and Repeatability |
|-----------------------------------|-----------------------|------------------------------|
| 50 mm diameter steering mirror | ± 1 mm (TBC) | 1 μm |
| Matching telescope block actuator | ± 10 mm | 1 μm |
| Matching telescope L_2 | ± 10 mm | ± 1 mm |
| 25 mm diameter steering mirrors | $< \pm 1 \mu\text{m}$ | $< \pm 1$ nm |

Table 4.10: RFC SIB actuators ranges and resolutions.

4.11.3.5 RFC input beam polarization

It is possible to operate the RFC in low and high finesse by turning the polarization of the light impinging onto the RFC with a half wave plate. The half wave plate will be placed between the two last steering mirrors before the RFC cavity, and it will be turned remotely.

4.11.3.6 RFC transmitted beam path optical design

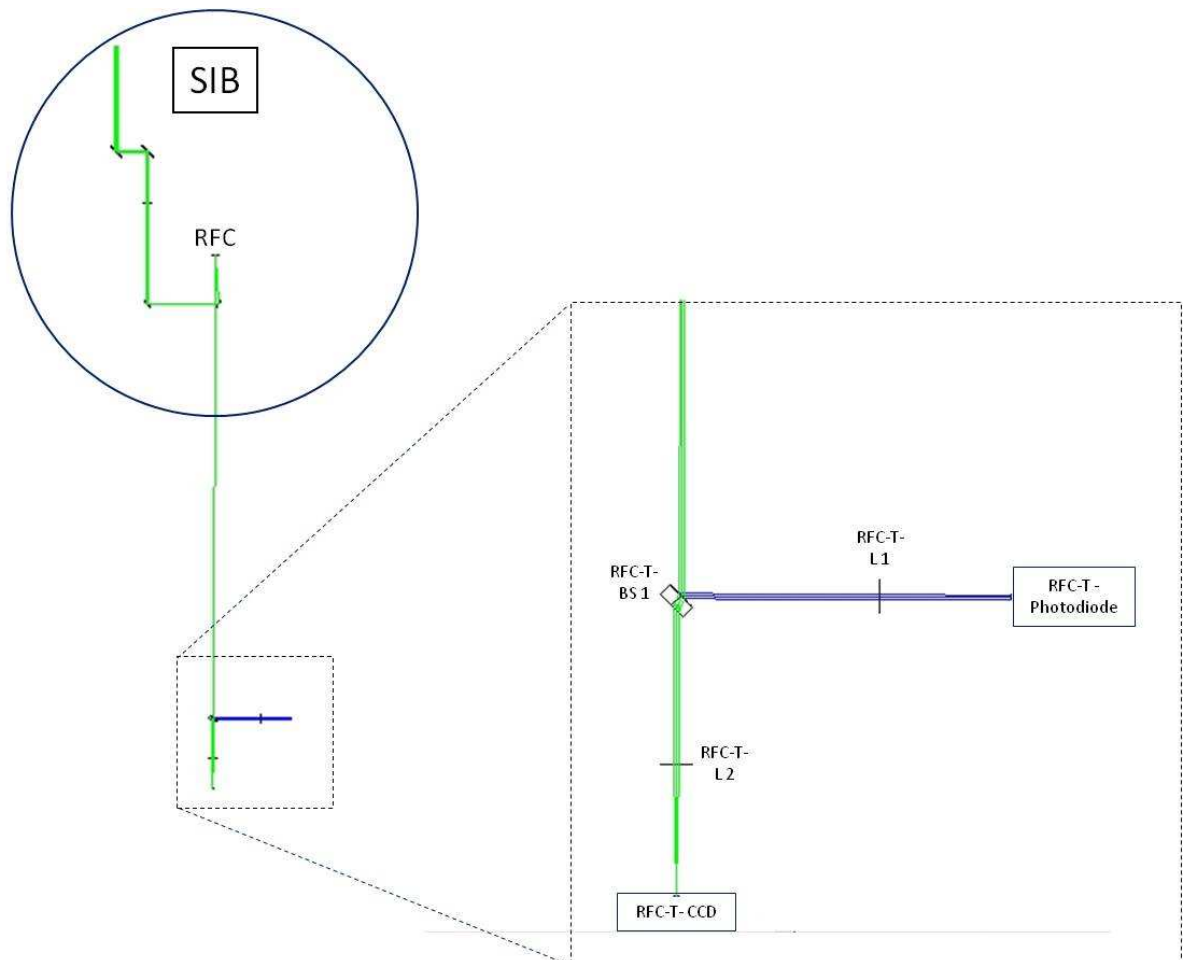


Figure 4.45: RFC transmission optical setup: the zoomed view is showing the splitting to the RFC-T-DC-PD and RFC-T-CCD monitoring camera.

The light transmitted by the RFC when locked will be redirected outside the SIB vacuum chamber to a dedicated external bench located in the laser lab, as shown in Fig. 4.45, then collimated and split according to Tab. 4.11. The distance of this RFC transmission bench from the RFC is about 1500 mm. The bench contains manual alignment and collimation opto-mechanics. Part of the RFC transmitted beam is sent to a CCD camera before reaching the RFC transmission photodiode.

The beam is impinging on a DC photodiode. This signal is used for monitoring and diagnostic and to provide the resonance passing triggering signal for the RFC locking. Lens RFC-T-L₂

| RFC Transmission to | Max power | Beam waist size |
|---------------------|-------------|--|
| DC photodiode | 10 mW (TBC) | 100 μm < w < 500 μm |
| CCD | 1 mW (TBC) | 500 μm < w < 2000 μm |

Table 4.11: RFC transmission parameters

collimates the beam on the photodiode with a waist of 300 μm .

- spot dimension on the RFC-T-CCD (image of the RFC waist): < 2 mm;
- spot dimension on the RFC-T-DC-PD: about 300 μm .

4.11.3.7 Optical design of the RFC reflected beam path

The light reflected by the RFC, in any RFC configuration (locked / not locked) and interferometer status, will be redirected outside the **SIB1** vacuum chamber to **SIB2**, as shown in Fig. 4.46. It is used for diagnostics (RFC-R-DC-PD photodiode and RFC-R-DC-CCD camera), for RFC locking with the standard Pound-Drever-Hall technique (RFC-R-HF-PD), and for extraction of the RFC automatic alignment error signals (quadrant diodes RFC-R-AA-QP1 and RFC-R-AA-QP2). The remote vacuum-compatible alignment and collimation opto-mechanics for the RFC reflected beam alignment and collimation on the detectors is contained in the **SIB2** tower. The total reflection at the resonance of the RFC is 5 mW (with 30 mW input power and in low finesse configuration). The polarization status depends on the position of the half wave plate. The optical coatings are therefore not polarization dependent (UNP). The power is split in the way presented in Tab. 4.12.

| RFC reflection to | Max power | Beam waist size |
|-------------------|--------------|--|
| DC photodiode | 0.3 mW (TBC) | 100 μm < w < 500 μm |
| HF photodiode | 2 mW (TBC) | 100 μm < w < 500 μm |
| CCD | 0.2 mW (TBC) | 500 μm < w < 1000 μm |
| AA WFS | 2.5 mW (TBC) | 100 μm < w < 1000 μm |

Table 4.12: RFC reflection parameters

The optical setup of the RFC reflection on **SIB2** is shown in Fig. 4.46.

4.11.3.8 Automatic alignment

The RFC input beam path includes the RFC AA circuit. The signal, detected by two quadrants in quadrature of the Gouy phase, is used to act on the RFC-SIB-M3 and RFC-SIB-M4 (TBC) (see Fig. 4.43). The actuators of the steering mirrors of the RFC will provide a closed loop bandwidth of 10 Hz (TBC).

- The AA of the RFC is performed with the Ward technique. The RFC optical specifications impose the parameters for the AA.
- The signals for the RFC AA are provided by the AA quadrant photodiodes (RFC-AA-QP-1 and RFC-AA-QP-2, placed on the RFC reflection path (see Fig. 4.46).

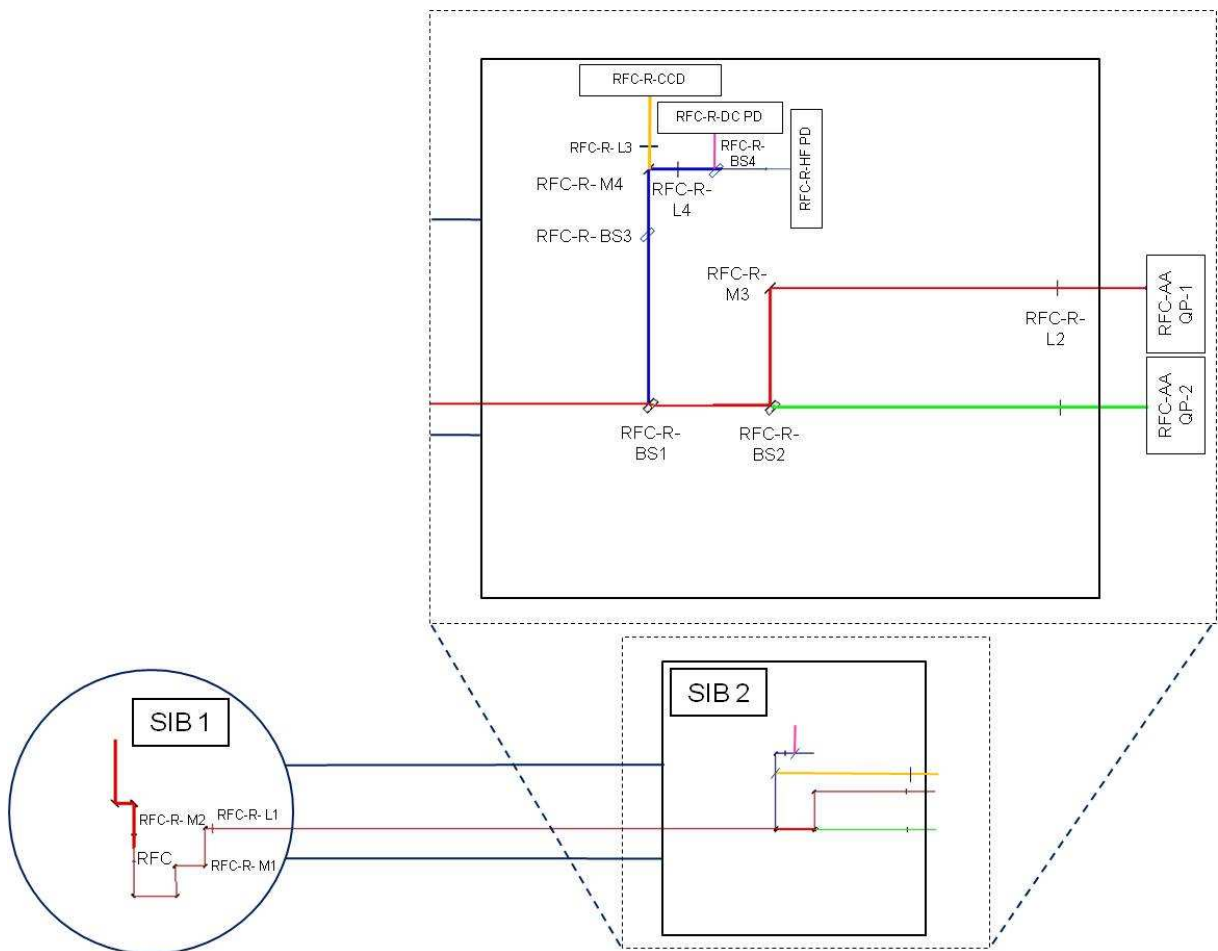


Figure 4.46: RFC reflected beam path optical setup: the setup in the new suspended injection bench (SIB2) is shown enlarged.

- The automatic alignment of the RFC is performed using the two last steering mirrors on the optical path of the beam impinging on the RFC.

4.11.4 Pickoff beam sent to the power stabilization photodiodes box

Requirements for the power stabilization photodiode box are:

- waist dimension: TBD
- power: $P_{in} = 300mW$ at full power (125 W).

4.12 Faraday isolator

4.12.1 Requirements

The expected performances and characteristics of the AdV ultra high vacuum compatible Faraday isolator defined in the INJ design requirements document [126] have been recently reviewed and are given in Tab. 4.13. Moreover, the weight of the device must be reduced as much as possible since this device should be installed on the suspended injection bench. To have enough margin on the weight, the Faraday rotator body should be lighter than 15 kg.

| Parameter | Requirement |
|-------------------------|---|
| Isolation(low to 150 W) | ≥ 40 dB |
| Total throughput | $\geq 95\%$ |
| Residual thermal lens | > 100 m or < 0.01 diopters at 150 W |
| Clear aperture | ≥ 20 mm |
| Vacuum compatibility | $< 10^{-6}$ mBar |

Table 4.13: AdV Faraday requirements.

Note that the isolation requirements have been defined considering that we don't want to have fringes with amplitude bigger than 0.5% in reflection of the IMC cavity. Those fringes are coming from the spurious cavity formed by the IMC and PR mirror (there is room for improving those fringes if needed by controlling the distance between the suspended injection bench and the power recycling/interferometer).

The full power considered now is 150 W (125 W input power + Power reflected by the ITF (20% of 125 W)($R_{ITF}=20\%$)).

A residual thermal focal lens of 80 to 100m can be easily compensated by small adjustment of the ITF mode matching telescope (see section 4.13.2.1).

4.12.2 Proposed solution

Light backreflected by the ITF towards the IMC has already been an issue in Virgo [127] [128]. This problem will become more significant with the higher power of AdV. The solution for this problem has consisted in installing an in-vacuum Faraday isolator between the IMC and the interferometer. With the higher AdV laser power (ITF input power=125 W), a standard

Faraday isolator will exhibit loss of optical isolation due to thermally induced birefringence and modification of mean angle rotation due to heating of the TGG (Terbium Gallium Garnet) crystals. It will also exhibit very high thermal lensing that it is mandatory to correct at the level of the Faraday itself.

In order to reach a good level of optical isolation (more than 40 dB) a custom designed Faraday isolator has to be used, including the compensation of thermal depolarization, the ability to fine tune the mean angle of rotation of the Faraday system and the passive correction of its thermal lensing. A design developed during many years of experimentation has already been adopted by LIGO, and fits also AdV needs.

Such a system has been developed in collaboration with the Institute of Applied Physics (IAP) (Russia) that has extensive experience in this field [130], [131] and developed a prototype for LIGO that demonstrated 49 dB of isolation with more than 100 W of input power [132]. The schematic of the AdV Faraday isolator that will be based on the same design is shown in Fig. 4.47.

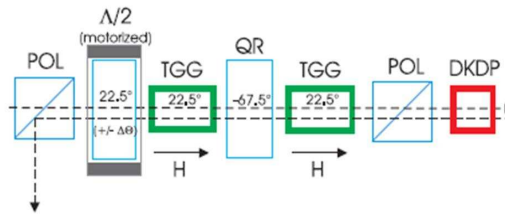


Figure 4.47: High power compatible Faraday isolator scheme compensated in terms of thermal lensing, depolarization and with remotely adjustable isolation.

It consists of an input polarizer, a half wave plate, two TGG crystals rotating the polarization by 22.5° and separated by a -67.5° quartz rotator, an output polarizer and a DKDP (Deuterated Potassium Dihydrogen Phosphate, KD_2PO_4) plate.

By using two TGG crystals separated by a quartz rotator, it is possible to limit the effects of thermal depolarization [133]. The variation of the mean angular rotation of the two TGG crystals can be compensated by slightly turning the half wave plate (this can be done remotely). This also makes it possible to compensate for the modification of isolation observed with the whole setup when it is tuned in air and then placed in vacuum [134] (where thermal dissipation is very different). Finally, a DKDP plate is used to compensate the thermal lensing created inside the TGG crystals, due to its large negative thermo-optic coefficient [135]. After a design stage [136], a prototype of this isolator has been built by IAP group.

4.12.3 Prototype performances

The magnetic system of the isolator was assembled on the Virgo site by IAP experts. Then all the optics composing the Faraday (except DKDP) were coated by Laboratoire des Matériaux Avancés (LMA) to achieve a good overall transmission ($T > 95\%$). Then high power tests were done at EGO on all these single components in terms of depolarization and thermal lensing, which allowed to complete the assembly of the Faraday seen in Fig. 4.49-right. We assessed the low power isolation performance ('cold' state) to be as good as **43 dB** [112] during the assembling phase in the EGO clean rooms. An isolation ratio higher than 48dB

could be achieved during the high power characterization phase (see Fig. 4.50). We could also validate the throughput (95 %) and the vacuum compatibility of the system.

The thermal lensing of the two TGGs was measured at high power and agrees with simulations for an absorption of **2300 ppm/cm** (± 100 ppm/cm) for TGG n°1 and **2600 ppm/cm** (± 100 ppm/cm) for TGG n°2 [137]. To compensate for this thermal lensing, the IAP delivered a DKDP crystal cut to the right length. On Fig. 4.48, a measurement of the residual thermal lens power is given.

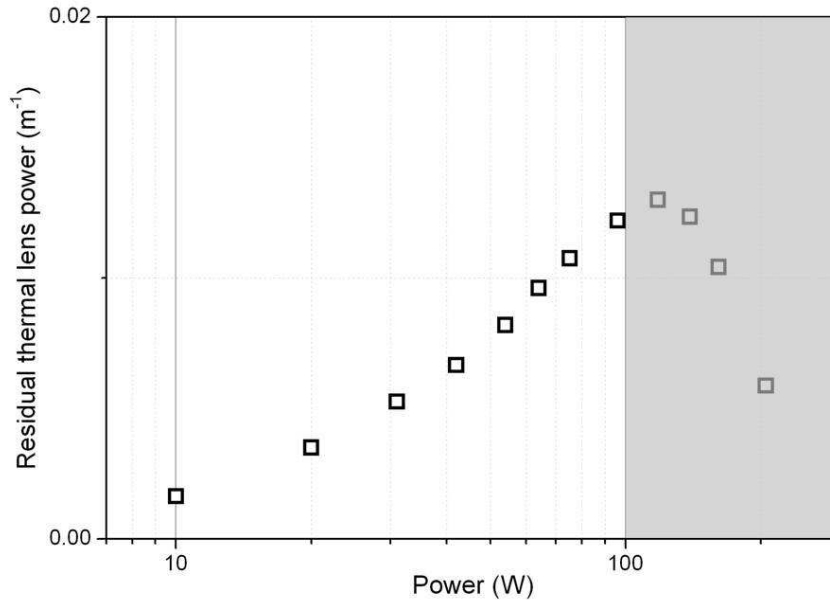


Figure 4.48: Residual thermal lens power in the Faraday isolator after compensation of thermal lensing with DKDP plate.

As one can see the compensation is quite efficient considering that without compensation the residual lens power at 125 W is about 0.1 diopters. At 125 W, we get about 0.0125 diopters of residual thermal lens power which is a bit out of the specifications but we know how to improve this in the construction process of the Faraday isolator for AdV. In order to improve the compensation, once the TGG crystals will be coated by LMA they will be sent back to Russia where the DKDP plate will be produced using an iterative process that consists in finding the right lens of the DKDP in order to reach 0.01 diopters at 150 W. Note that the lensing effect is starting to decrease from laser power of 130 W and above (grey zone in Fig. 4.48) but we are convinced that this is an artefact of the measurement (thermal effects in the pump beam setup are affecting the measurement at high power).

High power tests have been performed under vacuum with a residual pressure close to 10^{-6} mBar (the expected vacuum level in the AdV INJ tower). To this purpose we developed a dedicated chamber of cylindrical shape seen in Fig. 4.49-left which allowed us to quickly carry out the tests.

Figure 4.50 shows the isolation in vacuum of the Faraday isolator as function of power going from 20 to 250 W (residual). For each power, the remotely controllable half wave plate is adjusted to minimize the effect of thermal variation of Verdet constant and therefore gets the optimum isolation. As shown in Fig. 4.50, with 150 W inside the Faraday Isolator (FI) the

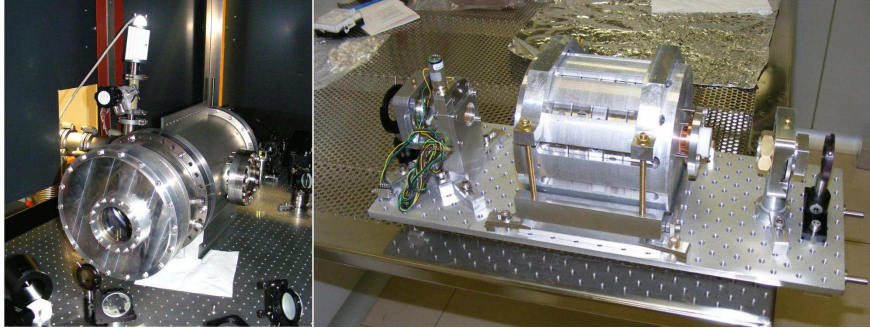


Figure 4.49: Left: Cylindrical vacuum chamber that will be used in order to test the Faraday prototype at high power with a vacuum level of 10^{-6} mBar. Right: The Faraday prototype assembled on its breadboard, ready to be mounted inside the vacuum chamber.

isolation is better than 40 dB. More results about characterization of the Faraday isolator prototype are given in [137].

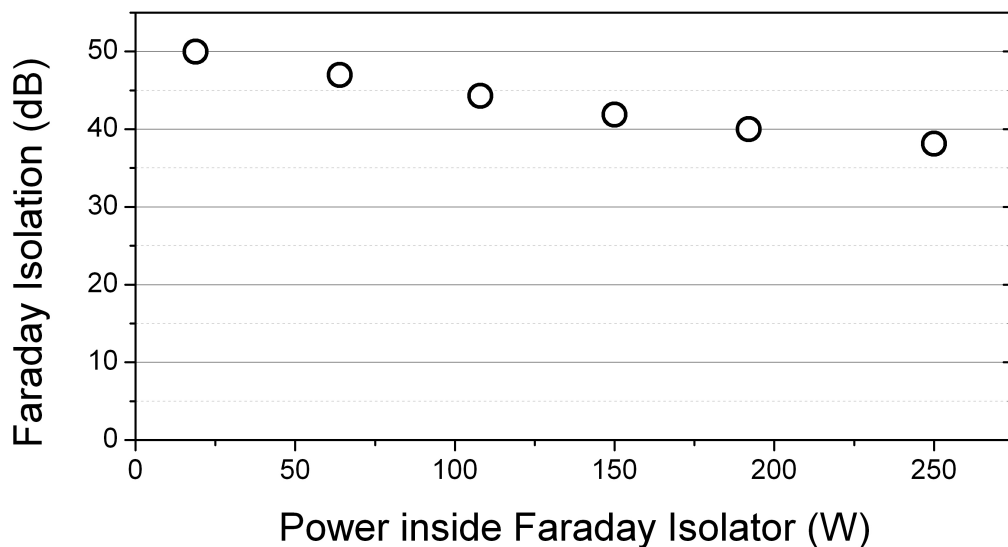


Figure 4.50: Faraday isolator isolation factor versus laser power traveling through the FI. Tests done with a residual pressure close to 10^{-6} mBar.

NB: all the tests have been done using a 2.5 mm waist laser beam.

A summary of the optical characterization of the prototype is given in Tab. 4.14.

4.12.4 Technical description

The schematics of the different parts of the Faraday isolator can be seen in Fig. 4.51 on its dedicated breadboard. In the following, we give more precise specifications concerning the magnetic system, the mechanics and the optics of the FI.

The magnetic system (MS) of this Faraday isolator consists in an assembly of Nd-Fe-B permanent magnets. It contains a total of 7 magnetic rings. Six of these rings are composed by

| Characteristic | Expected Value | Measured Value |
|--|--------------------|---|
| Isolation | ≥ 40 dB | > 40 dB at 150 W |
| Power lost by depol. | $\ll 1\%$ | $< 0.2\%$ at 200 W |
| Power lost due to Verdet constant change | $< 1\%$ | $< 2\%$ |
| Power lost by absorption | $< 1\%$ | 0.45% |
| Power lost by reflectivity of each surface | $< 1\%$ | 0.6% |
| Total throughput | $> 95\%$ | $> 95\%$ |
| Residual thermal lens | > 100 m at 150 W | > 80 m at 125 W |
| Vacuum compatibility | $< 10^{-6}$ mBar | $< 10^{-6}$ mBar (for the magnetic assembly) |
| Faraday rotator weight | < 15 kg | 12.7 kg |

Table 4.14: AdV Faraday prototype expected characteristics and experimental performances.

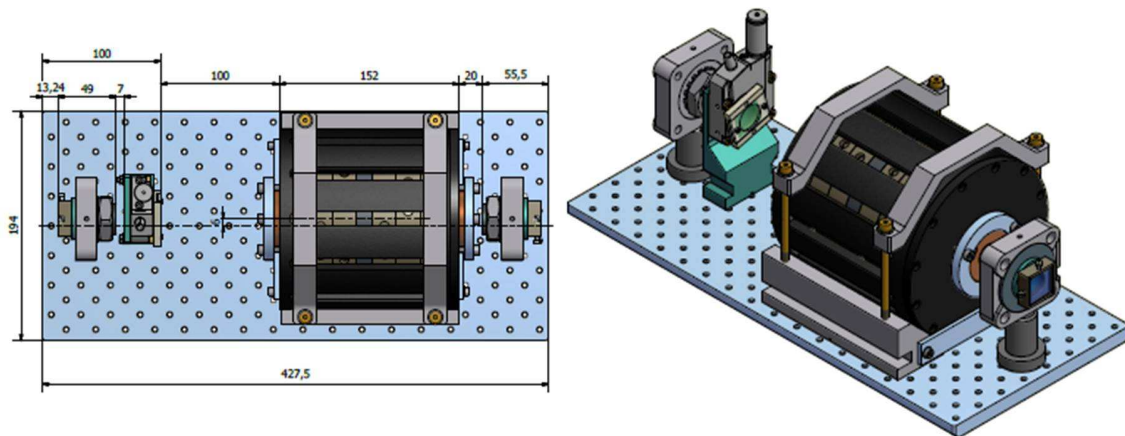


Figure 4.51: Schematics of the Faraday isolator

8 single magnetic elements (shown in Fig. 4.52-left). These 6 rings produce a radial direction



Figure 4.52: Components of the magnetic system of the AdV isolator prototype. Left: composite rings with radial direction of the magnetization vector. Center: monolithic ring with axial direction of the magnetization vector. Right: aluminium case used to mount the assembly of magnetic rings.

of the magnetization vector. For three of them, the magnetization vector is directed towards the center. The other ones are oriented in the opposite sense. The last ring is monolithic and produces an axial direction of the magnetization vector (see Fig. 4.52-center). All the rings are assembled in an aluminium case shown in Fig. 4.52-right. With this setup, the obtained magnetic field along the isolator direction is reported in Fig. 4.53 where we see that the maximum is about 18 kOe at the center of the device. In this figure, we also report the position of the 2 magneto-optic elements and the quartz rotator.

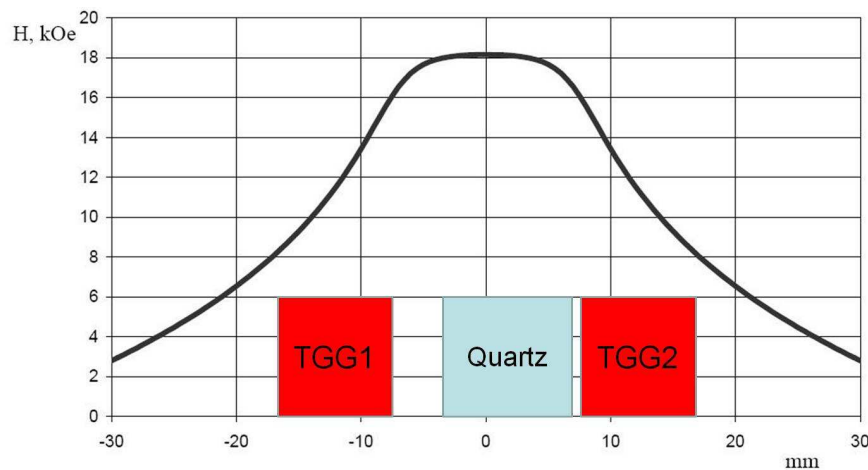


Figure 4.53: Spatial distribution of the magnetic field along the isolator. The origin of the horizontal axis corresponds to the magnetic system center. Physical location of TGG crystals and quartz rotator is also given on this plot.

The list and characteristics of the Faraday isolator optics are the following:

- 2 TGG crystals, cylindrical shape, $L=9$ mm, $D=20.7$ mm, cold depolarization $\sim 1.6 \cdot 10^{-5}$
- 1 quartz rotator, cylindrical shape, $L=10.7$ mm, $D=20.7$ mm, cold depolarization $\sim 3.7 \cdot 10^{-5}$
- 1 half wave plate, square shape, 25×25 mm, $L=0.9$ mm, cold depolarization $\sim 2.5 \cdot 10^{-5}$

- 2 calcite wedge polarizers, square shape, 25×25 mm, $L=3$ to 5 mm (wedge= 7°), cold depolarization $< 1 \cdot 10^{-5}$
- 1 DKDP crystal, cylindrical shape, $L=5$ mm, $D=25$ mm.

The TGG crystals and the quartz rotator are mounted inside the magnetic housing by means of two copper holders shown in Fig. 4.54. A thin layer of indium is put between the TGG crystal and the copper holder. In this way, we obtain a good conductivity of the whole assembly and the heat absorbed in the TGG at high power can be efficiently evacuated. This helps to limit the thermal effects linked to the mean temperature elevation of the crystal. Using two different holders it is possible to tune independently the position of each TGG crystal with respect to the magnetic field in order to tune accurately the mean rotation angle obtained with each crystal. Note that the half wave plate will be mounted in a remote controllable mount to finely tune the isolation once in vacuum.

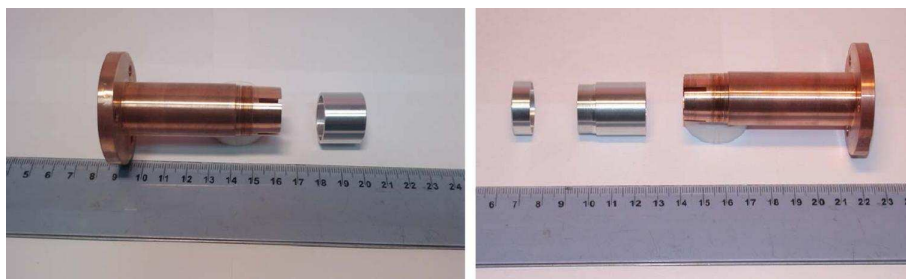


Figure 4.54: The copper holders used to mount the crystals inside the magnetic assembly. One of the holders is longer (right) to mount together one of the two TGG crystals and the quartz rotator.

4.12.5 Other Faraday isolators

High power compliant and low power Faraday isolators will be used in air. Those parts are expected to be produced by the Institute of Applied Physics as it is the case for the vacuum compatible FI. One high power compatible Faraday isolator compensated in terms of depolarization, Verdet constant, change with temperature and thermal lensing will be installed between the EOM system and the IMC cavity (see section 4.5). The clear aperture is expected to be 10 mm. Other smaller aperture and simpler Faraday isolators may be installed on important beams such as the IMC cavity reflection beam.

4.13 ITF mode matching telescope

In this section, we present the general requirements of the Interferometer Mode Matching Telescope (ITF MMT). Then, a description and the main characteristics of the telescope are given, as well as a summary of the tolerancing study we performed to define the actuation range needed on each optic of the telescope. Finally we give the projection of back-reflected and back-scattered light noise coming from the ITF MMT optics on the Advanced Virgo sensitivity curve.

4.13.1 General requirements

The general requirements of the ITF MMT are given in Tab. 4.15.

| Parameter | Requirement |
|---|--|
| Mode matching (on the ITF) | $\geq 99\%$ |
| Noise coming from diffused and back-reflected light | $\leq \text{AdV sensitivity}/10$ |
| Magnification | 19 |
| Telescope dimensions | $< 800 \text{ mm} \times 350 \text{ mm}$ |

Table 4.15: ITF MMT requirements.

Considering manufacturing errors on optical elements parameters (radius of curvature, surface deviation,...) and alignment errors, the telescope should have the capacity to recover a good matching ($> 99\%$ as said above).

Finally, the magnification of the telescope should be sufficient to separate properly the secondary beams coming from the ITF with respect to the main beam (this depends on the angle of incidence of the pickoff beams at the MMT input; see OSD chapter for this particular point).

4.13.2 Telescope overview

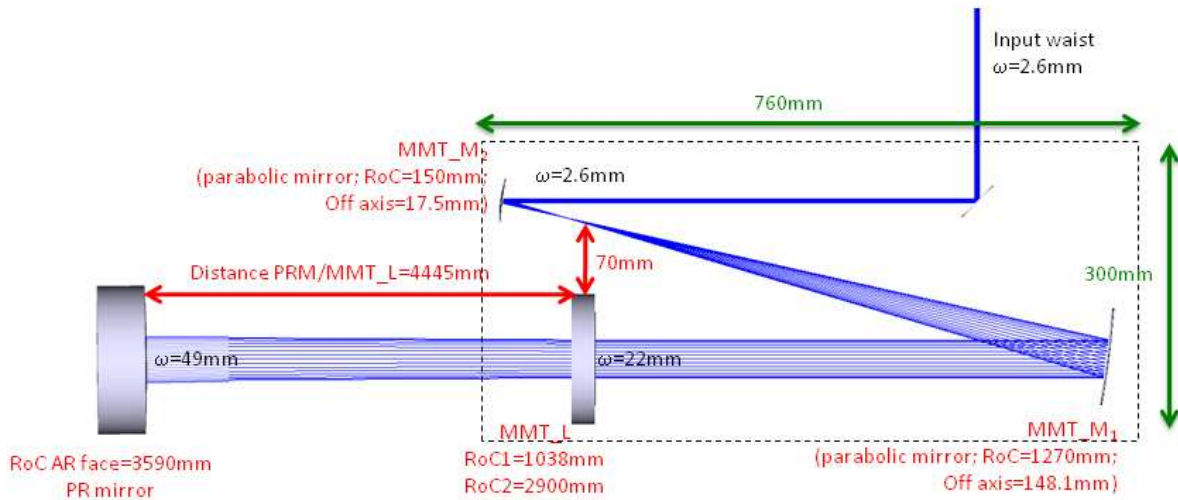


Figure 4.55: Overview of the catadioptric telescope.

This telescope has been proposed at the beginning of the design work on the Marginally Stable Recycling Cavities (MSRC) configuration for AdV that has started in February 2011 [138, 140]. An alternative design has also been studied [142] that uses only reflecting optics on the benches at the cost of having a somewhat less compact telescope. Finally, the design choice has been driven by the space constraints on the suspended injection bench and the fact that we had to reduce as much as possible aberrations of the telescope, since the rear face of the PR mirror has to be curved for reducing the size of the mode matching telescope elements on the bench

[139]. This telescope (see Fig. 4.55) consists of an afocal off axis parabolic telescope made of 2 mirrors (MMT_M1 and MMT_M2), that increases the beam size by a factor of 8.5 (from 2.6 to 22 mm). Then a diverging lens (MMT_L) is used in combination with the PR mirror to match the beam to the interferometer. The big advantage of this configuration is that it is quite compact. This compactness of the telescope is an advantage for the SIB design, considering that we have a lot of bulky elements to install on it, such as Faraday isolator, reference cavity, dihedron, input power control system and flat IMC mirrors. The shape of the diverging lens (meniscus shape) has been optimized in order to compensate spherical aberrations induced by the recycling mirror. This optimization enables us to reach by design a matching of the input beam on the interferometer higher than 99.9% as explained in [139]. The telescope magnification (19) has been optimized in order to easily separate the pickoff beams as explained in [141]. The input beam waist size is about 2.6 mm in the configuration that is presented in this document (see Fig. 4.55). In this configuration the dimension of the telescope can be estimated to be around 76 cm x 30 cm taking into account the opto-mechanical mounts. The radius of curvature as well as the clear aperture of each surface of the telescope optics and the distance between the optics are given in Tab. 4.16. Note that we have checked the maximum diameter of the optics that can be hosted by the SIB; the maximum clear aperture allowed is 145 mm. The meniscus lens will be made of fused silica and its thickness is 25 mm in the center.

| Parameter | Value | Characteristic |
|---|-----------|--------------------------|
| PR mirror AR face RoC (mm) | 3590 | spherical |
| Meniscus lens face 1 RoC (mm) | 1038 | spherical |
| Meniscus lens face 2 RoC (mm) | 2900 | spherical |
| MMT_M1 RoC (mm) | 1270 | parabolic (OAD=148.1 mm) |
| MMT_M2 RoC (mm) | 150 | parabolic (OAD=17.5 mm) |
| PR mirror clear aperture (mm) | 370 | |
| Meniscus lens clear aperture (mm) | 140 (TBC) | |
| MMT_M1 RoC clear aperture (mm) | 140 (TBC) | |
| MMT_M2 RoC clear aperture (mm) | 50 | |
| Distance PR_AR face/ Meniscus lens face 1 (mm) | 4445 | |
| Distance Meniscus lens face 2/ MMT_M1 (mm) | 600 | |
| Distance MMT_M1/MMT_M2 (mm) | 710 | |

Table 4.16: Telescope optics radii of curvature, clear aperture and distance between the optics. OAD: off-axis distance.

4.13.2.1 Tolerancing study

Definition of the tolerancing study

The tolerancing study was performed using the Zemax software (Monte Carlo simulation method). All this work is well explained and the output of this study is given in [139]. We considered errors on the surface of the optics of the telescopes: the radii of curvature (RoCs) and the surface irregularities in particular and also errors in the alignment of the

| Optical element | RoC value (mm) |
|--------------------|----------------|
| MMT_M ₁ | 1270 +/- 13 |
| MMT_M ₂ | 90 +/- 1.5 |
| MMT_L face 1 | 1038 +/- 11 |
| MMT_L face 2 | 2900 +/- 29 |
| PR_AR | 3590 +/- 36 |

Table 4.17: RoC errors for the tolerancing study of the catadioptric telescope.

| Optics | MMT_M ₁ / MMT_M ₂ (mm) | PR_AR / MMT_L (mm) |
|--------------------|--|--------------------|
| MMT_M ₁ | ±6 | ±150 |
| MMT_M ₂ | ±0.8 | ±25 |
| MMT_L face 1 | ±2 | ±50 |
| MMT_L face 2 | ±0.7 | ±21 |
| PR_AR | ±3 | ±81 |

Table 4.18: Ranges of the compensators of the catadioptric telescope necessary to compensate separately RoC errors of the optics of ± 1 %.

optics and on input beam parameters. Table 4.17 shows the errors on the RoCs considered for the catadioptric telescope optics. We defined compensators in order to compensate for these errors and recover an optimal matching on the interferometer (higher than 99%). The 2 compensators are the distance between the two parabolic mirrors and the distance between the meniscus lens and the PR mirror.

Radius of curvature of the optics

We studied separately the RoC errors of each optic of the telescopes to define the maximum ranges of the compensators. More details are given in [139]. For example, using the distance between the meniscus lens and PR mirror as compensator we are able to recover RoC errors on the back face of the power recycling mirror as shown in Fig. 4.56. A coupling higher than 99% is recovered by moving the meniscus lens with respect to the power recycling mirror.

Note that we are also able to recover errors in the RoC of the PR back face by adjusting the distance between the two parabolic mirrors. Table 4.18 summarizes the ranges of the compensators necessary to compensate separately each RoC error of the optics.

Notes:

- By playing with the two compensators, we can relax the ranges. The ranges defined here will help us in making the appropriate choice of actuators and in the design of the mechanical mounts of telescope optics (we can stay within the expected range of a MMT_L displacement ± of 100 mm).
- A first contact with the polishers showed that the error on the RoCs could be smaller than ± 0.5%, if needed.

Tolerancing study for surface irregularities of the optics

As the RoC of the optics cannot be perfect, their surfaces may present irregularities. Typically, the manufacturers give an accuracy on the Peak-to-Valley (PtV) surface irregularities

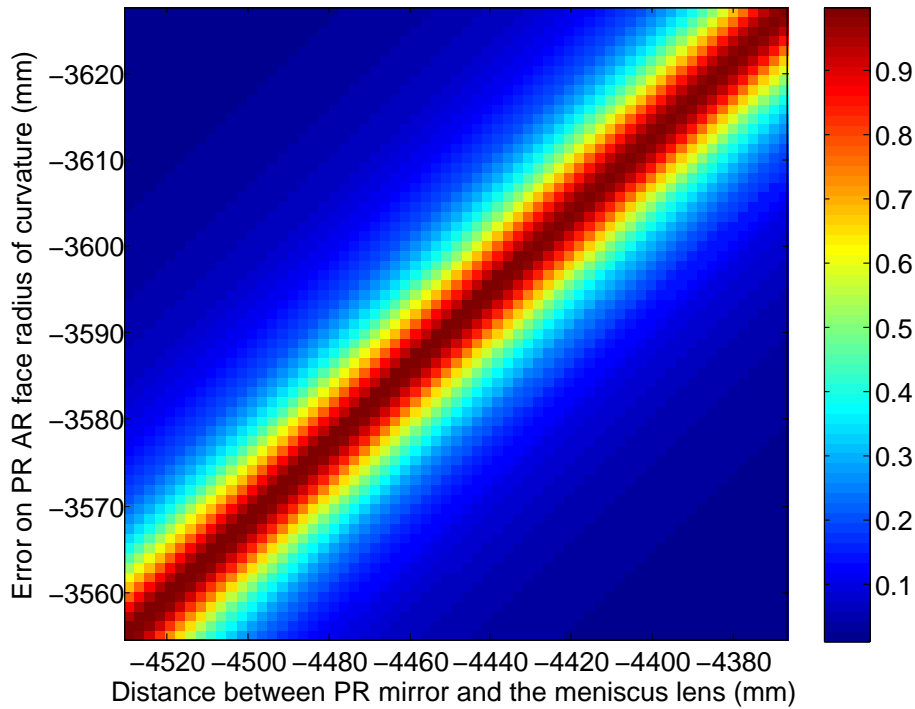


Figure 4.56: Coupling efficiency as a function of the RoC of the back face of the PR mirror and the distance between the meniscus lens and the PR mirror.

of the order of $\lambda/5$ and an rms of $\lambda/50$. As in the case of RoC errors, two compensators can be used to recover a good coupling in the interferometer. This could relax a lot the displacement needed to apply on the meniscus lens and on the parabolic mirrors. In this computation, performed with Zemax, we considered deviations of the surface with respect to a perfectly parabolic surface described with Zernike polynomials. Computations using this method and considering a rms error of the surface of the order of $\lambda/50$ (achieved for Virgo parabolic mirrors) has been performed. To compensate for this error and recover a matching higher than 99.7%, the distance between the 2 parabolic mirrors should be adjusted by ± 0.6 mm and the distance between the meniscus lens and the PR mirror by ± 15 mm, which looks easily manageable.

Tolerancing study for input beam geometry errors

The input beam coming from the Faraday isolator (FI) could present errors on the waist size, the waist position or both, and we studied the possibility to compensate such errors by adjusting a defined compensator. If we consider errors on the input beam waist size (4%) and input beam waist position (500 mm) (that looks reasonable considering that the telescope located between the IMC cavity and the ITF MMT is made from off-the-shelf optics), we could

| | MMT_M ₁ | MMT_M ₂ | MMT_L |
|--------------|--------------------|--------------------|-------------------|
| Tilt | 5 mrad | 0.4 mrad | 17 mrad |
| Miscentering | 300 μm | 300 μm | 100 μm |

Table 4.19: Maximum tilt and miscentering allowed for the optics of the catadioptric telescope, in order to keep a coupling efficiency higher than 99%.

| Parameter | Value |
|------------------------------------|--|
| Shift of the ITF beam vs PR motion | 170 $\mu\text{m}/\mu\text{m}$ |
| Tilt of the ITF beam vs PR motion | $1.2 \cdot 10^{-4}$ rad/ μm |
| Shift of the ITF beam vs PR tilt | 650 $\mu\text{m}/\mu\text{rad}$ |
| Tilt of the ITF beam vs PR tilt | $1 \cdot 10^{-6}$ rad/ μrad |

Table 4.20: Shift and tilt of the beam in the interferometer at the waist position (almost 1363 m from ITM) versus the PR mirror motion and tilt, for the catadioptric telescope. The maximum motion of the ITF beam compatible with keeping a matching higher than 99% is 900 μm .

check that it is possible to recover a matching higher than 99.9% by adjusting the distance between the PR mirror and the meniscus lens by less than 1 mm. Note that matching on the ITF can also be recovered by adjusting the distance between the two off-axis parabolic mirrors (more details are given in [139]).

NB: We also gave a look to the effect of a residual thermal lens of the order of 100 m induced by the Faraday isolator. The effect on the coupling in the ITF is of the order of 0.1% and can be easily recovered by playing with the compensators of the catadioptric telescope.

Tolerancing study for tilt and decentering errors of the optics

A tilt or a decentering of the optics of the telescope will induce coma and spherical aberrations on the beam. To keep a matching of the input beam with the ITF beam higher than 99%, we computed the maximum tilt and decentering allowed on the optics mounts of the catadioptric telescope. The results are presented in Tab. 4.19. The constraints are realistic and seem manageable according to the expected actuators precision. Note that for the particular case of the meniscus lens, in order to center it with the expected precision, we will install 3 translation stages on its mount: 2 for vertical and horizontal adjustment with respect to the beam axis, and another one that moves the lens along the main beam axis to adjust the distance between the meniscus lens and the power recycling mirror.

Moreover, we computed the shift and the tilt of the beam in the ITF as a function of the shift and the tilt of the PR mirror. The results are presented in Tab. 4.20. Assuming that the matching is higher than 99% if the beam shift in the ITF is less than 900 μm [143], it implies that the vertical and horizontal motions of the PR mirror should be smaller than 5.3 μm and the tilt motion should be smaller than 1.4 μrad , for the catadioptric telescope. These requirements for the PR mirror are not stringent, compared with alignment requirements (see alignment section of ISC chapter).

The same study has been made to derive the requirements for the SIB. The vertical and horizontal motions of the bench should be smaller than 5.3 μm and the tilt motion should be smaller than 1.6 μrad , for the catadioptric telescope. These requirements seem to be manageable and similar to displacement and angular motion of the Virgo suspended injection

bench [144] [139].

4.13.2.2 Alignment procedure

For this telescope, there should be 2 phases in the matching adjustment. First of all, a rough adjustment/ fine alignment of the telescope will be done during the assembling phase in the EGO clean rooms. This phase should be divided in 2 steps:

- Afocal parabolic telescope alignment using the procedure explained in [145].
- Alignment and rough adjustment of the meniscus lens (the distance between the second parabolic mirror and the meniscus lens does not matter). For the transversal alignment of the meniscus lens, the idea is to use the reflection of one or both faces of the telescope to properly center it during the prealignment phase in the clean room. We can either use the YAG beam or an auxiliary He-Ne laser beam.

The second phase consists in performing the fine alignment once the **SIB1** will be installed on the interferometer. The fine tuning will be done by using 2 tunable parameters: the distance between the 2 parabolic mirrors and the distance between PR mirror and the meniscus lens. The mode matching on the ITF will be adjusted performing a scan of the arm cavities to analyze the spectral content of the laser beam (the arm cavities are used as spectrum analyzers). This is an iterative process that aims to reduce the mismatching mode amplitude below 1% by adjusting the 2 parameters of the catadioptric telescope.

4.13.3 Diffused and backreflected light study for INJ

One of the limiting noises that can come from the telescope optics is attributed to diffused light created by imperfections of the surface polishing of each optic. This noise can spoil the ITF sensitivity either through an upconversion process or a direct coupling. Moreover, since the mode matching telescope uses a lens, we have also to consider the noise coming from the backreflection of the 2 faces of this lens.

4.13.3.1 Projection of scattered/backreflected light noise coming from ITF MMT optics

The optical phase noise $\delta\varphi(t)$ induced at the ITF input port by a diffusing/backreflecting object moving by $\delta x(t)$ is written as follows:

$$\delta\varphi(t) = \sqrt{f_{sc}} \sqrt{\frac{P_r}{P_{in}}} \sin\left(\frac{4\pi}{\lambda} \delta x(t)\right)$$

where P_r is the power reflected by the ITF, P_{in} the power at the ITF input port and f_{sc} the fraction of scattered/backreflected light recoupled in the ITF.

The frequency noise induced at the ITF input port is equivalent to a differential arm length that can be written:

$$\tilde{h} = \frac{\delta\nu}{\nu_{las}} \text{CMRF}$$

where CMRF is the common mode rejection factor and ν_{las} the laser frequency.

$$\tilde{h} = \frac{f\delta\varphi}{\nu_{las}G_{SSFS}}\text{CMRF}$$

If δx is small ($< \lambda/30$) this formula can be approximated by:

$$h(f) = G \frac{4\pi}{\lambda} \delta x(f)$$

where

$$G = \frac{f}{\nu_{las}G_{SSFS}}\text{CMRF} \sqrt{f_{sc}} \sqrt{\frac{P_r}{P_{in}}}$$

To make the projection, we considered the worst case for CMRF: Losses asymmetry = -50 ppm and finesse asymmetry = -2% (green curve in Fig. 4.57). CMRF for several finesse and losses asymmetry is shown in Fig. 4.57 (data from ISC).

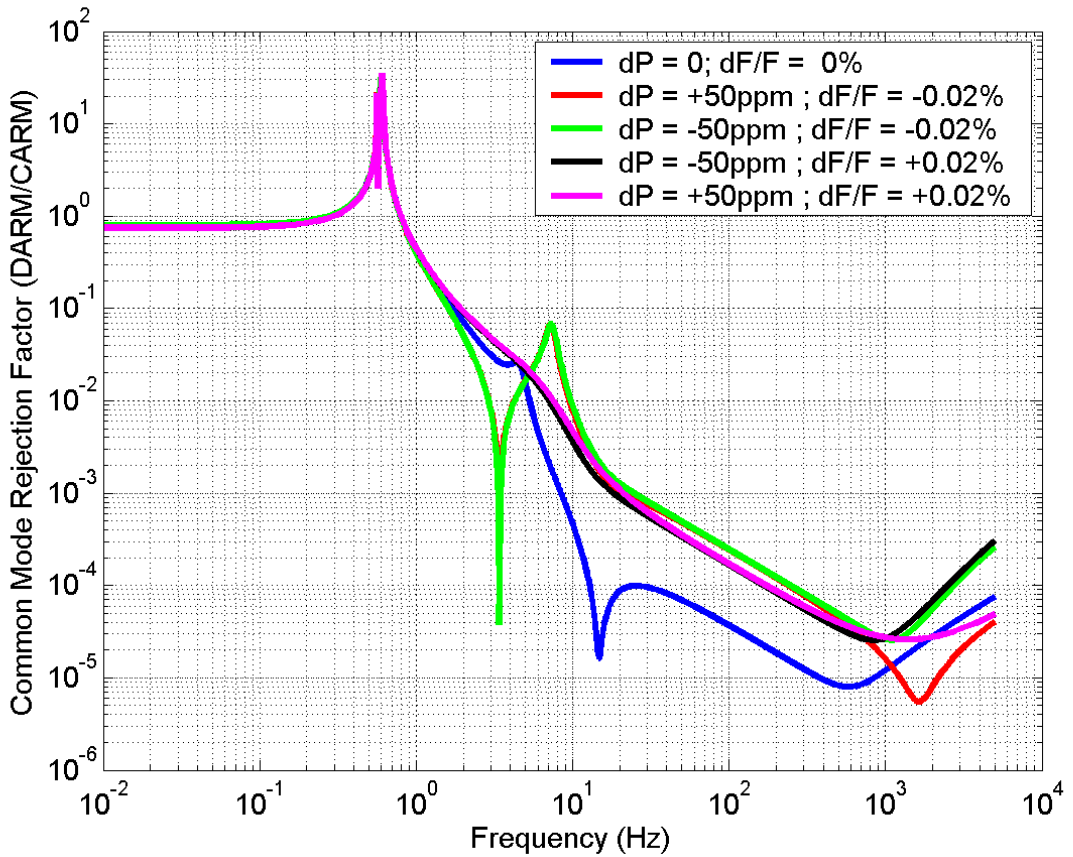


Figure 4.57: Common mode rejection factor (CMRF) for AdV.

Moreover, we have estimated the residual horizontal displacement of the Virgo suspended injection bench in Fall 2011 [139]. This is considered to be an upper limit of the AdV SIB displacement since a new filter will be added to the suspension chain having the effect of reducing the residual motion of this bench (see SAT chapter).

To make the projection we also considered that the power incident on the ITF P_{in} is 125 W and the power reflected by the ITF P_r is $0.2 P_{in}$. The projection of diffused light noise for the INJ telescope on the AdV sensitivity curve is given in Fig. 4.59.

4.13.3.2 Backreflected light from the meniscus lens

Since we are using a lens that is perpendicular (or almost perpendicular) to the optical axis of the main beam, the direct reflection of the faces of the lens can be recoupled in the interferometer and the fact that this optic is moving not in phase with the ITF is producing unwanted perturbations on the dark fringe signal, thus spoiling AdV sensitivity.

The amount of backreflected light coming from both faces of the meniscus lens that is recoupled in the ITF has been computed. In the worst case (meniscus lens face 2 radius of curvature = 2.9 m), we found that the amount of backreflected light recoupled in the ITF is of the order of 7×10^{-11} as explained in [139] and [146].

NB: Each surface (secondary faces of PR and all lens surfaces) has been modeled considering that the AR coating reflectivity was as high as 100 ppm.

Upconverted noise In both cases (power recycled and dual recycled ITF), if the rms motion around 300 mHz is lower than $2 \mu\text{m/s}$, the noise does not enter inside the detection bandwidth. The residual motion in normal conditions is much lower than this requirement, since in [147] it is measured that the rms speed of the payload is lower than $0.1 \mu\text{m/s}$ for a full superattenuator chain. We could confirm that even in case of high microseismic activity this requirement is fulfilled.

Linear coupling The requirements are quite relaxed for the SIB because, assuming a safety factor of 10, the bench must move less than $0.7 \times 10^{-8} \text{ m}/\sqrt{\text{Hz}}$ from 10 Hz up to 10 kHz, and the Virgo SIB has demonstrated to move much less than that [146] [139].

NB: These numbers are computed in the case of 100 ppm of backreflection of the AR coating.

4.13.3.3 Light backscattered from telescope optics

In the case of backscattered light, we computed the f_{sc} factor using 3 methods:

- An analytical model already used to compute the contribution of each optic of Virgo's end benches to the diffused light noise [148];
- The second based on FFT code [149];
- Finally, Zemax software has been used to make simple cross checks of the analytical model.

NB: Details on the methods used are given in a note that justifies the choice of the catadioptric telescope as ITF MMT [139].

Fraction of diffused light recoupled in the interferometer Four surfaces have been considered as diffusing element in the ITF MMT:

- MMT_L face 1, first face of the meniscus lens
- MMT_L face 2, second face of the meniscus lens;
- MMT_M₁, the biggest parabolic mirror;
- MMT_M₂, the smallest parabolic mirror.

In order to estimate the contribution of the 2 faces of the lens, we used a typical diffusion law of superpolished optics (the main contribution is given at low spatial frequencies that means low diffusion angle). The PSD and the corresponding Bidirectional Reflectance Distribution Function (BRDF) used in the computation are shown in Fig. 4.58.

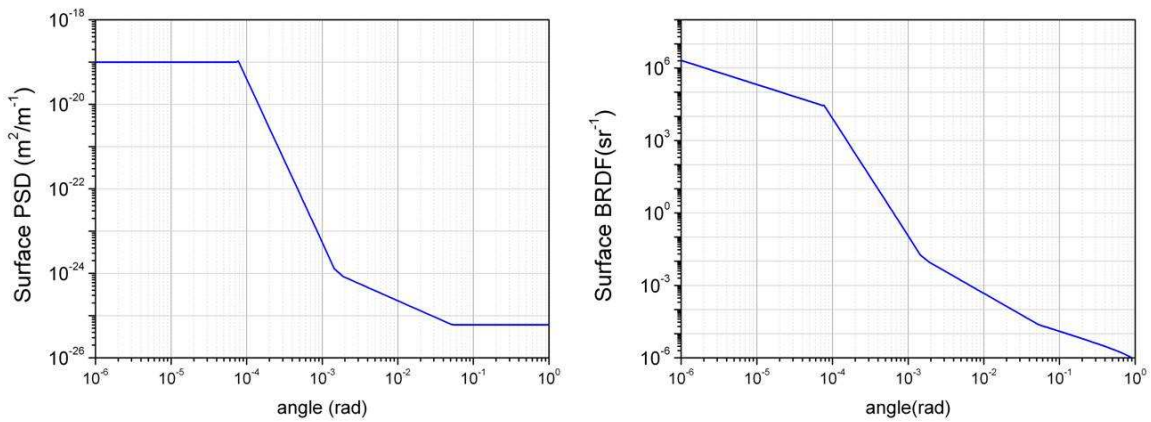


Figure 4.58: Left plot: Typical PSD of a superpolished optic (corresponding to about 2 nm rms). Right plot: corresponding BRDF.

NB: To carry out the calculation, since we have no realistic small angle BRDF of transmissive optics, we used the BRDF expected for the IMC flat mirror. So the numbers found for the meniscus lens should be considered as an upper limit.

For the 2 parabolic mirrors, we estimated the contribution of each optical element of the telescope using Lambertian distribution (its diffusion appears the same from any angle of view) as diffusion law. The Total Integrated Scattering (TIS) has been chosen to be equal to 500 ppm (similar to what has been measured on Virgo parabolic mirrors).

The results obtained with the analytical model are given in Tab. 4.21. As one can see, the second face of the meniscus lens is the main contributor of the backscattered light recoupled in the ITF. To have a further margin on our projection and to be as conservative as possible, we considered a safety margin of 100 on f_{sc} (factor of 10 on the ITF sensitivity), thus projecting the contribution of a diffusing element with a $f_{sc}=3.7 \cdot 10^{-7}$. It is shown in Fig. 4.59 that we are orders of magnitude below Adv sensitivity. This means that back-reflected or back-scattered light coming from INJ telescope optics should not limit Adv sensitivity. Note that in the projection, we also considered double and triple bounce contributions (coefficients used for simulation of double and triple bounce have been taken from Virgo experience with DET suspended detection bench lens [150]).

| Optical element | f_{sc} (with TIS=500 ppm for parabolic mirrors) |
|---------------------------------|---|
| MMT_L (face 1) (RoC=1038 mm) | $4.2 \cdot 10^{-10}$ |
| MMT_L (face 2) (RoC=2900 mm) | $3.7 \cdot 10^{-9}$ |
| MMT_M ₁ | $4.3 \cdot 10^{-13}$ |
| MMT_M ₂ | $9.35 \cdot 10^{-11}$ |

Table 4.21: Fraction of scattered light recoupled in the ITF for the catadioptric telescope computed using the analytical model.

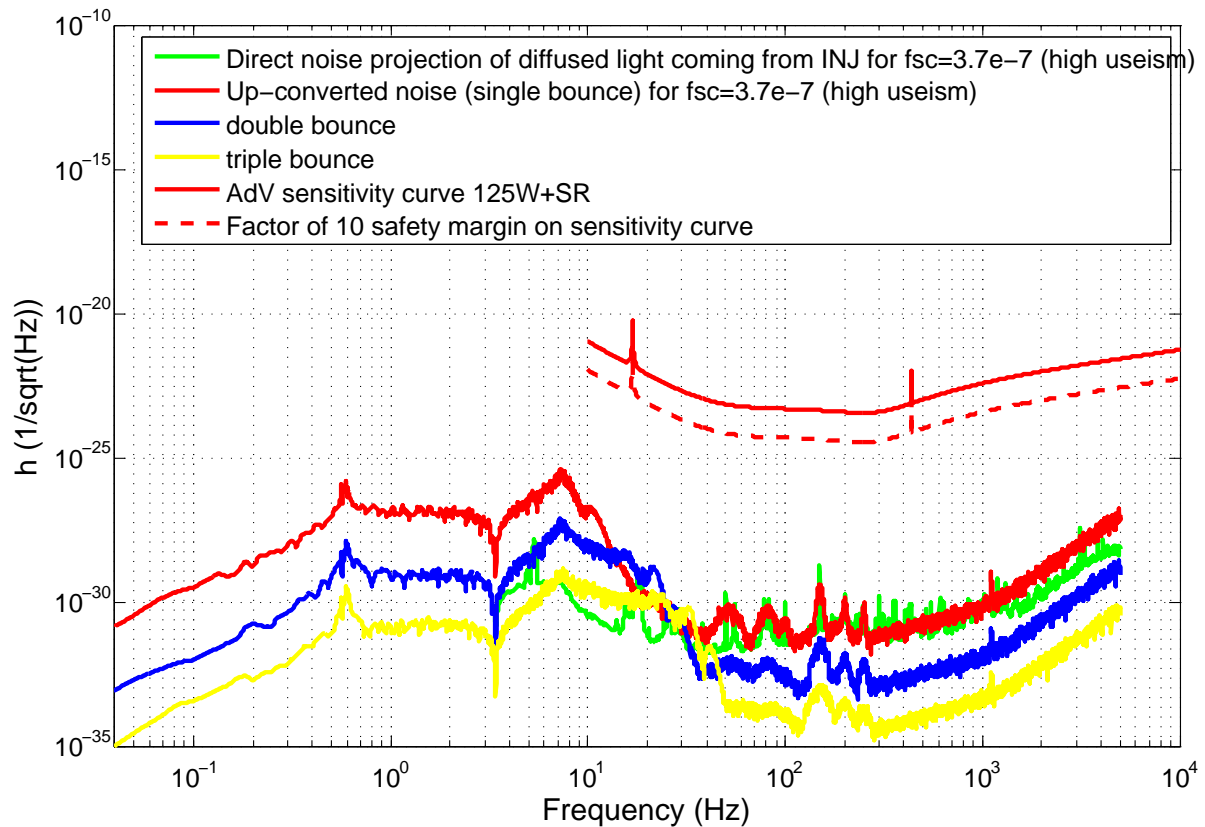


Figure 4.59: Projection of diffused light noise coming from INJ telescope in the case of high micro-seismic activity.

4.13.3.4 Amount of backreflected and backscattered light not recoupled into the ITF

It looks reasonable to ask what is the amount of reflected or scattered light that is not recoupled into the interferometer, because this light could also spoil the interferometer sensitivity. In any case, we can make a simple computation based on the definition of Figure of Merit 1 (FOM1)² presented in the OSD chapter. We should have at maximum 100 ppm (AR coating reflectivity) for each face of the meniscus lens that can fall out of the ITF optics clear aperture. If we consider $P_{in}=1$ W incident power on those faces, we have: $P_{in} \times 100$ ppm = 0.1 mW. This number has to be compared with FOM1 for the central ITF, that is equal to: $P_{out}=1.4$ ppm $\times 17 \times G_{rec} \times P_{in}=1.4$ ppm $\times 17 \times 40 \times P_{in}=0.95$ mW, where 17 is the number of surfaces in the central ITF, 1.4 ppm is the amount of light diffused by the mirrors at large angle (due to micro-roughness), and G_{rec} is the recycling gain. In conclusion the amount of scattered light coming from the meniscus lens that has to be dumped is 9.5 times lower than the amount of scattered light that has to be dumped in the central ITF, so this should not be a problem; it can be dumped by using appropriate baffles. Note that the design and the construction of these baffles will be carried out by the SLC subsystem.

4.14 Input beam monitoring system

The input beam monitoring system is used to monitor the laser beam properties in several points of the INJ system. In this paragraph, we will describe the technical solution adopted and give the optical layout of the system. The beam monitoring system will measure the intensity distribution and wavefront shape for the different fields of the injected beam and at different points of the injection system. This tool will principally be employed during the commissioning phase of Advanced Virgo for characterization, alignment and troubleshooting. It is therefore important to have a tool that can be used quickly and easily for any beam of INJ. In order to measure the parameters presented in Tab. 4.22, the test beam will be shared among five diagnostic tools: two CCD cameras (near field & far field), a wavefront sensor (WFS), a scanning Fabry-Perot interferometer (SFPI) and a phase camera.

4.14.1 Optical design: division in subsystems

To perform all the relevant measurements, a single beam is shared among the diagnostic instruments. Due to its installation on the EIB, the measurement device has to be conceived like a “black box”: the test beam is injected at the input and will be automatically adjusted in terms of power, alignment and size for the receiving measurement devices (see Tab. 4.23). The beam adaptation to the diagnostics tools is separated in several successive steps: one subsystem for each kind of adjustment is controlled by a specific servo loop. At each step of the procedure, the beam is interrupted by mirrors mounted on flip mounts to avoid damages on the measurement devices.

²FOM1 is defined as the sum of the power lost by clipping outside of the mirror apertures in the central interferometer for 1 W ITF input power. It should be lower than the light already lost by the mirror microroughness scattering and surface defect.

| Measured Parameter | Measurement device | Accuracy |
|--|------------------------|---|
| Intensity map | | |
| Global | Wavefront sensor | Rel acc. rms: $\lambda/100$ |
| For each field (USB, LSB, CAR) | Phase camera | Rel acc. rms: $\lambda/500$ |
| Wavefront map | | |
| Global | Wavefront sensor | Rel acc. rms: $\lambda/300$ |
| For each field (USB, LSB, CAR) | Phase camera | Rel acc. rms: $\lambda/500$ |
| Relative power of each field (USB, LSB, CAR) | Scanning Fabry - Perot | Resolution: 1.5 MHz Finesse >200 |
| High resolution intensity images in near and far field | NF & FF camera | Resolution: 1360 x 1024 Pixel size: 4.65 μm |
| Zernike decomposition of wavefront map | Wavefront sensor | Rel acc. rms: $\lambda/300$ |
| Hermite – Gauss decomposition of each field | Phase camera | Rel acc. rms: $\lambda/500$ |

Table 4.22: Parameters to be measured by the IBMS and the accuracy of the measurement devices.

| Control Parameter | Range Control Requirement | Control device and Control accuracy |
|-------------------|---------------------------|--------------------------------------|
| Beam radius size | From 1 mm to 2.87 mm | NF & FF Cameras – 4.65 μm |
| Beam power | From 1 mW to 5.5 W | Photodiode – 0.7 mW |
| Beam position | From 0 to TBD | NF & FF Cameras - 4.65 μm |

Table 4.23: Beam parameters to be controlled by the IBMS and the corresponding control devices.

4.14.1.1 Space requirements

The input beam monitoring system shall be constructed and aligned on its own breadboard and it has to cover a surface of no more than 0.4m^2 . The actual breadboard covers a surface of 0.36 m^2 . It includes the NF & FF cameras, the scanning Fabry-Perot interferometer and the wavefront sensor. Due to its size, the phase camera is placed outside the breadboard. The working height of the optics shall be the standard height of 10 cm which includes the height of the bread board. It would be desirable that the system be covered in order to protect it from light, dust and inadvertent tampering. The “manual alignment” system part shall be left free to allow an easier access of the user to this part.

4.14.2 Input power requirements

Due to its low damage threshold, the wavefront sensor has to work in a power range of $10\ \mu\text{W}$. The working value in the system is chosen such as to have the minimum power injected into the SFPI. According to calculations, it means that the power has to be regulated at around 55 mW after the **IPC** (see the automatic power control paragraph below). This working value allows to reduce the number of optical attenuators in the system. We consider that the IPC can produce a linear attenuation by a factor of 100: The IPC can accept a maximum input value of 5.5 W . So a pre-attenuation is needed before the **IBMS**. Total losses on high reflected (HR) mirrors are not included in the calculation and are evaluated to be around 0.25%.

4.14.3 Optical components

When the system adjusts the beam, it has to correctly maintain the beam properties: each error or aberration introduced at this stage will be measured by the whole set of tools. To preserve the beam properties through the system, high quality optical components specially designed for IR applications are used: Nd:YAG HR mirrors, lens, polarizing prisms, wedged beam splitters and attenuators. Furthermore, IBMS uses Virgo devices such as standard galvanometers pairs, CCD cameras and software tools.

4.14.4 Description of the adjustment systems

An overview of the IBMS setup is shown in Fig. 4.60.

These four systems are described hereafter:

Manual alignment

Even though there is an automatic control of beam parameters it is necessary to carry out rough alignment during the first installation and maintenance works. This subsystem is composed of four mirrors and two alignment targets. 2 of the mirrors are tunable. By adjusting these two mirrors while observing the alignment targets a preliminary alignment of the beam is made. The alignment targets may be a combination of a crosshairs and a threaded alignment disk mounted to 90° flip mounts in order to remove them when the alignment is completed.

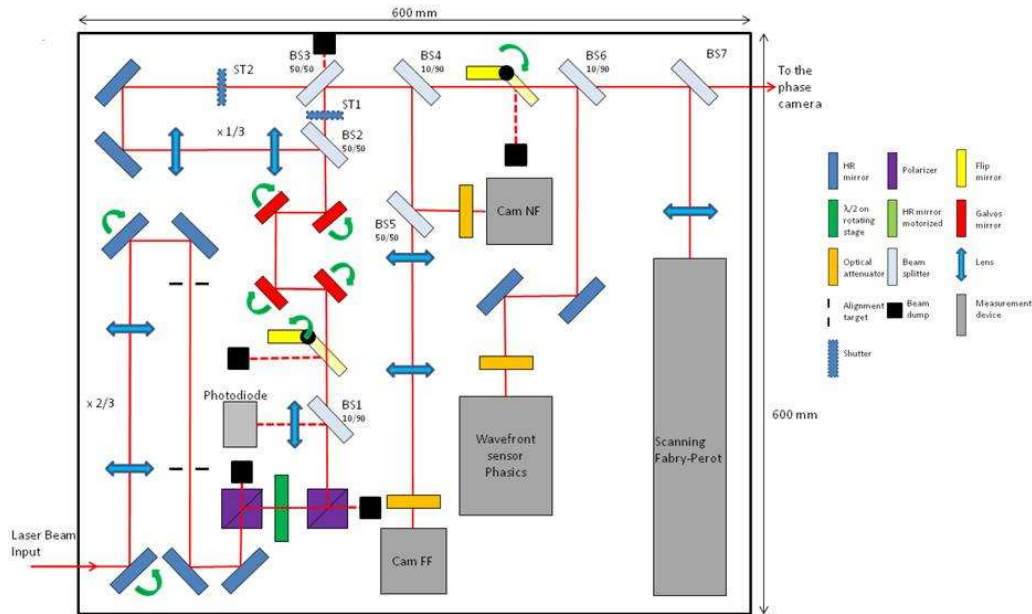


Figure 4.60: Scheme of IBMS setup on its breadboard.

Automatic power control

Based on the IPC principle (see section 4.8), it consists of a rotating half wave plate placed between two polarizers. The error signal comes from a photodiode which is calibrated to monitor the power of the light that continues to the automatic alignment control. The wave plate angle is controlled such as to obtain a predetermined power. The power on the WFS has to be stable at $8.8 \mu\text{W} \pm 0.2 \mu\text{W}$, so the working value has to be 54.9 mW after the wave plate. According to constructor specifications, the minimum incremental motion of the rotation stage is $5 \mu\text{rad}$. This means that the power can be controlled at $35 \mu\text{W}$. Limitations on power precision are therefore coming from the photodiode that has to have a minimum precision of 0.7 mW .

During the power adjustment process the flip mirror remains in the closed position in order to avoid damaging the measurement instruments. Once the predetermined power has been obtained the flip mirror is set to the open position. This control is iterative and, to protect the system, the opening and closing of the flip mirror depend on two different loops: the opening order is given when a stable power is observed, and each acquisition is under surveillance of a control loop in case the determined power value threshold is crossed.

Automatic precision alignment control

Once the system is installed on the **EIB**, we need an active system to maintain the alignment for the measurement devices and telescopes in order to allow a correct measurement of the beam parameters. This is performed using two standard Virgo galvanometer pairs, servo-

controlled in voltage; the output control is made using the NF and FF cameras. These cameras are diagnostics tools that give high resolution intensity distribution of the beam in different Gouy phases. As the FF camera is insensitive to the beam tilt because of a Galilean telescope, each pair of galvanometers is associated to one camera to control independently tilt and translation. With the optical and frequency decoupling, we can align the beam for each camera separately. The tests of the mechanical response confirm that the amplitude of rotation for each galvanometer is sufficient to align the beam in the system. With this system, based on a method used for the Virgo quadrant diodes, we have a stable method to align and maintain the beam in the center of the cameras at less than $5 \mu\text{m}$.

Beam size control

In the INJ subsystem, the beam size can vary from 1 to 5 mm. However, it is limited in the system by the beam clipping: we can assume that beam clipping occurs from 0.1% of the maximum beam intensity and the system is built with 1" optical components, mostly at an angle of 45° with respect to the optical axis. So the beam radius is limited to 2.87 mm at the input and then to 2.12 mm by the galvanometers. For the WFS, the beam size has to be reduced from 2.87 mm to 0.72 mm, a reduction by a factor 4. The beam size control subsystem consists therefore in two telescopes and allows beam size measurement and adaptation for the measurement devices. The first telescope is used consistently to reduce the input beam size by a factor 1.5. The error signal is given by the NF camera. If the result is superior to 0.7 mm, the input beam is redirected to a two lens telescope that reduces beam size and radius of curvature in order to insure diagnostics.

4.15 INJ main milestones

Here is a list of the main INJ milestones:

- September 2011: Faraday isolator (FI) prototype validated: Prototype tested and compliant with AdV requirements.
- September 2011: EOM (phase modulator) prototype validated: Prototype tested and compliant with AdV requirements.
- Fall 2011: IMC cavity finesse and end mirror dimensions choice.
- October 2011: ITF MMT configuration chosen.
- December 2011: IMC end mirror substrate ordering.
- Spring 2012: AdV INJ technical design release.
- Faraday isolators ordering: Spring 2012.
- Electro-optic crystals ordering: Spring 2012.
- ITF MMT mirrors and lens substrates ordering: Spring 2012.
- Spring 2013: Electro optical modulation system ready to be installed.
- Spring 2013: Ultra high vacuum compatible Faraday isolator ready to be installed.
- May 2013: AdV INJ components ready to be installed.

- Mid 2013: AdV INJ optics, mechanics and electronics installation start.
- Beginning of 2014: INJ SS precommissioning start.

Chapter 5

Mirrors (MIR)

5.1 Scope of the subsystem and deliverables

The MIR subsystem concerns the procurement and preparation of the Advanced Virgo test masses and spares: Input Mirror (**IM**), End Mirror (**EM**), Beam Splitter (**BS**), the mirrors for the power recycling and signal recycling cavities, the Compensation Plate (**CP**) and finally the Pickoff Plate (**POP**). The mirrors will have larger dimensions than the Virgo mirrors. This will induce modifications in the coating process (cleaning system, manipulation devices) and also in the metrology benches (stronger and larger sample-holders). One of the main goal is to provide substrates/mirrors having a flatness better of 0.5 nm RMS. For that purpose, the "Corrective coating" solution has been chosen. It allows the correction of the substrate flatness. For that purpose, the construction of a new robot (sample-holder) for the coating machine is necessary to reach the flatness specifications.

5.2 Introduction

As it is shown in Fig. 1.2, mirrors play a crucial role in the sensitivity of Advanced Virgo (**AdV**). On one side the mechanical losses in the coating determine the quality factor of the mirror and as a consequence the displacement of the mirror surface due to its thermal vibration. On the other side the optical losses in the coatings determine the amount of power which is lost in the Fabry-Perot cavity and as a consequence the power that is stored in the recycling cavity. This quantity determines the quantum noise which is expected to limit the sensitivity at the higher frequencies. R&D was done at Laboratoire des Matériaux Avancés (**LMA**) to improve the mechanical performances of coating without degrading the optical performances. Titanium doped Ta_2O_5 coatings recently developed at **LMA** are the best solution known so far [151].

The **AdV** design foresees the use of mirrors, for the Fabry-Perot cavities, 35 cm in diameter and 20 cm thick i.e. mirrors having the same diameter as Virgo but twice as thick.

A larger substrate is required for the beam-splitter as this component lies at 45 degrees with respect to the beam axis. A substrate 55 cm in diameter and 6.5 cm thick will be used. For the power recycling and signal recycling cavities, a solution similar to the Virgo one was

chosen (one large mirror for each cavity: 35 cm in diameter and 10 cm thick). Due to the thermal compensation implemented in **AdV**, two **CP** will be necessary. At last, a new type of component is also foreseen : a pickoff plate used to extract the pickoff beams. The size of this plate will be the same as the Compensation Plate one. After coatings and assembling of the mirror ears in the **LMA** clean room (like in Virgo+), all the mirrors will be delivered to the Virgo site.

5.3 Substrates

The **AdV** mirror substrates (Table 5.1) will be made of fused silica. Tests on sapphire were done at **LMA** in the context of the Advanced LIGO pathfinder. The results obtained favored the choice of fused silica [152]. No alternative material is being considered today by Virgo. It was decided also to buy the fused silica substrate from the Heraeus company in Germany. New types of fused silica with smaller absorption (Suprasil 3001/3002) are available today. The bulk absorption for this material is 3 times smaller than the one used for Virgo (measurements made at **LMA**, 0.2 ppm/cm [156]). Moreover, the other performances (quality factor, index homogeneity, residual strain, birefringence) are still the same. The cost of this new type of silica is comparable to the one used for Virgo. Reducing the absorption in the substrates is certainly of interest as the power absorbed causes thermal lensing in all transmissive optics. The problems increase with the power stored in the interferometer and with the thickness of the substrates. On the other hand one should remind that so far thermal effects are dominated by coating absorption, and this will be enhanced by the very high circulating power in **AdV**. From this point of view it is more important to improve the absorption of the coatings than to improve the absorption of the silica. The power absorbed in the coating on **IM** is ten times higher than in the 20 cm thick substrate. Both for the old type of silica used for Virgo as for the new one recently developed, it is possible to obtain pieces of the size requested for **AdV**.

5.3.1 List of the Advanced Virgo substrates

- **Input test masses:** they will be made of a high quality fused silica (Suprasil 3002) having a very low bulk absorption (0.2 ppm/cm), as these optics transmit a relatively large amount of power (of the order of 2 kW).
- **End test masses:** fused silica of a lower optical has been chosen (Suprasil 312) as in this case the mirrors are reflecting most of the light. However, Suprasil 312 has a mechanical quality factor sufficiently high to avoid increasing the thermal noise above the level determined by the mechanical losses in the coating [157].
- **Beam splitter:** high quality fused silica (Suprasil 3001) was chosen. This particular type of Suprasil is particularly suitable for the **BS** because this is an optically isotropic 3D-material. It is highly homogeneous and has no striations in all three directions.
- **Compensation plates, pickoff plate:** these components will be machined out of the Virgo/Virgo+ **IM** (4 silica blocks available, diameter 35 cm, thickness 10 cm). The material is Suprasil 312 SV and the absorption measured on this silica blanks was lower than 1 ppm/cm. The silica blocks will be cut in two (feasibility checked with polishing companies) to produce two **CP** or two **POP**.

| | Input Mirror IM | End Mirror EM | Beam Splitter BS | Compensation Plates CP | Power Recycling Mirror PR | Signal Recycling Mirror SR | Pick Off Plate POP |
|---------------------|--|--|--|--|--|--|--|
| Number of parts | 4 | 4 | 3 | 4 | 3 | 3 | 3 |
| Fused Silica Nature | Suprasil 3002 | Suprasil 312 | Suprasil 3001 | Suprasil 312 SV | Suprasil 312 SV | Suprasil 312 | Suprasil 312 SV |
| Diameter | 350 mm | 350 mm | 550 mm | 350 mm | 350 mm | 350 mm | 350 mm |
| Thickness | 200 mm | 200 mm | 65 mm | 35 mm | 100 mm | 100 mm | 35 mm |
| Bulk Absorption | <0.3 ppm/cm | typical 3 ppm/cm ≤ 5 ppm/cm | <0.3 ppm/cm | <1 ppm/cm | typical 3 ppm/cm ≤ 5 ppm/cm | typical 3 ppm/cm ≤ 5 ppm/cm | <1 ppm/cm |
| Index homogeneity | ≤5 10 ⁻⁷ PV in central 100 mm | ≤3 10 ⁻⁶ PV in central 200 mm | ≤5 10 ⁻⁷ PV in central 100 mm | ≤3 10 ⁻⁶ PV in central 200 mm | ≤3 10 ⁻⁶ PV in central 200 mm | ≤3 10 ⁻⁶ PV in central 200 mm | ≤3 10 ⁻⁶ PV in central 200 mm |

PV : Peak to Valley

Table 5.1: Specifications of the bulk substrates for the Adv mirrors.

- Power/signal recycling mirrors: after verification and confirmation by the Thermal Compensation System subsystem (TCS) subsystem, the choice of the silica for the Power Recycling (PR)/Signal Recycling (SR) substrate was done (same as CP : Suprasil 312). The thickness of PR/SR mirror was fixed to 10 cm because, for convenience, this is a standard dimension formerly used in Virgo.

In Adv, the scheme followed to determine the number of spare parts for each type of substrates was exactly the same used for Virgo. The aim is to anticipate some accidents in the interferometer itself, during the coating phase or during the transportation.

- For the Input and End test masses (IM, EM), it is necessary to have two spare cavities (this means 2 spare IM and 2 spare EM). This is the minimum solution because of the high cost of these parts.
- The same arguments were used to determine the number of spares (two) for the CP and the POP, mirrors that were not present in Virgo.
- For the Beam Splitter, the arguments are different to determine the number of spare parts, which was fixed to two, although only one BS is used in the interferometer. The coating that should be done on the BS is one of the most difficult to perform. The risk that the coating has not the good optical performance is higher than for all the other parts.
- For the recycling mirrors (PR, SR), it was decided to have 2 spare parts for each of them

(for Virgo, 4 recycling mirrors were ordered at the beginning). In fact we need some flexibility in the future to change the recycling factor of the cavities easily, if necessary. Moreover, the substrates of these cavities are not very expensive.

The **IM**, **EM**, **BS** blank substrates have been ordered and delivered (4 **IM**, 4 **EM**, 3 **BS**, see Fig. 5.1). The **PR** and **SR** blanks substrates were also ordered to Heraeus and are under production.



Figure 5.1: Input Mirror Blank (35 cm diameter, 20 cm thick, left), **BS** blank substrate (55 cm diameter, 6.5 cm thick, right)

5.4 Polishing

Traditionally, the polishing quality is characterized by two different parameters: the flatness and the micro-roughness. The first parameter gives the RMS of the difference between the perfect surface (typically a sphere for spherical mirrors) and the actual surface as measured by phase map interferometer. For Virgo this parameter was measured to be in the range of a few nm [153, 154]. The second parameter gives a measurement of the mirror surface roughness at small scale lengths (from a few microns, up to about 1 mm). For the Virgo mirrors this parameter was found to be of the order of 0.05 nm.

The distinction between these two different length scales originates in the fact that different instruments are used to measure them: both effects contribute to scatter the light from the fundamental mode to higher order modes. They generate losses and extra noise. These polishing losses will play an even more important role in **AdV** due to the higher finesse of the cavities. Depending on the difference in the losses between the two cavities they could be the source of finesse asymmetry and contrast defect thus modifying the constraints on other subsystems.

The losses in Virgo+ deduced from the measurement of the recycling gain are about 500 ppm per round trip. This is compatible with the value predicted by the simulation using the real mirror maps measured at **LMA** (around 300 ppm per round trip) [155] and much more than the value measured for the absorption losses on site (between 1 and 6 ppm [165]). Anyhow the losses foreseen by the simulation alone exceed by a large fraction the losses assumed in **AdV** (~ 75 ppm per round trip: 50 ppm due to the flatness defects, 25 ppm due to transmission/absorption/scattering losses). To meet the round trip losses requirement in

the **AdV** cavities, simulations were carried out to define the flatness specification for the cavity mirrors that will be sent to the polishing companies. We estimate that the contribution of the mirror surface due to the (Low Spatial Frequency (**LSF**)) (i.e. smaller than 1000 m^{-1}) should not exceed 50 ppm.

The difference between the input cavity mode (perfect Gaussian TEM_{00}) and the circulating mode in the cavity can also generate additional losses, called coupling losses. However it was shown that the circulating cavity mode is very close to be fundamental Gaussian [167] thanks to the action of the corrective coating. So, the coupling losses can be considered negligible and are not taken into account in the simulations presented here.

Starting from there, we derived the specifications on the **LSF** for the arm cavity mirrors surface. Using a Monte Carlo approach we performed 1000s of simulations. We were able to find that a final flatness of 0.5 nm RMS on 150 mm diameter is necessary (Fig. 5.2)[162].

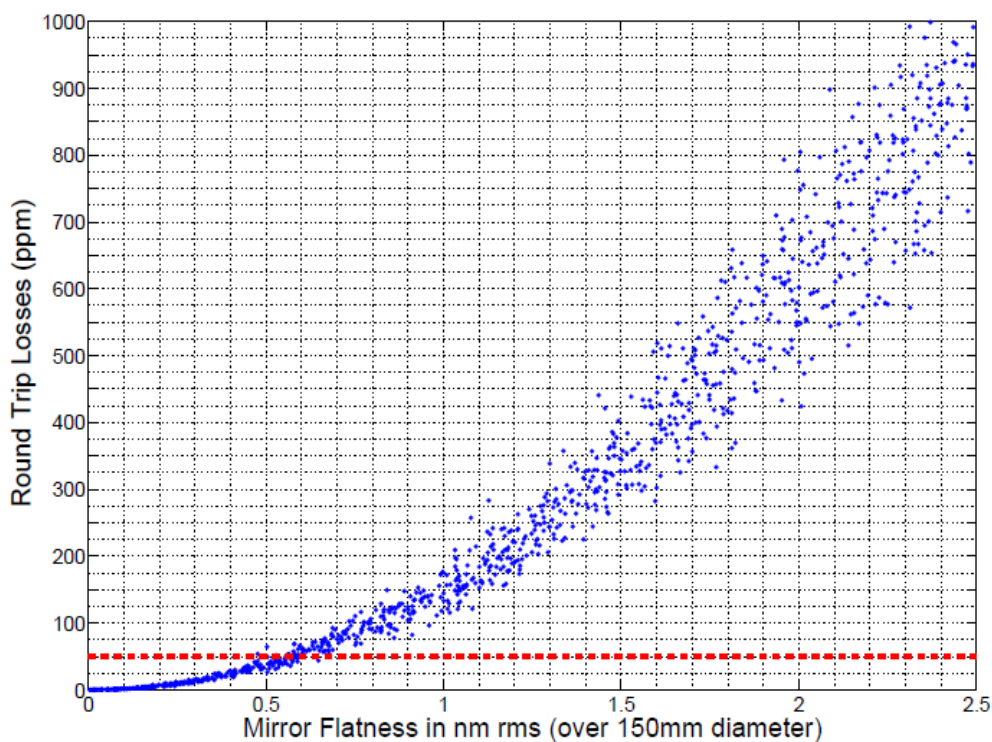


Figure 5.2: Influence of the mirror RMS flatness on the round trip losses in the **AdV** cavities.

These simulations underline also that expressing the flatness only in terms of RMS is not enough. The Power Spectral Density (**PSD**) shape of the surfaces is important as different **PSD** shapes gives different losses in a Fabry-Perot (**FP**) cavity for an equal flatness. We also showed that the light diffracted by defects having a spatial frequency above 50 m^{-1} never reach the other hand of the cavity and so the shape of the **PSD** does not matter any more. Then we decided to give a specification in the frequency range $50\text{ m}^{-1} - 1000\text{ m}^{-1}$, this specification is set to be 0.15 nm RMS [162].

There is also a point that can be a problem: the machining and polishing of the flats on the large beam splitter. It is foreseen to have small flats on the **BS** but, during discussions with some polishers, it appears that it can be impossible to create these flats because of the large

diameter of this part (diameter out of range on the polishing machine). Depending on the polishing companies answers after the call for tender, an interaction with the PAY subsystem should be done to study alternative solutions.

A summary of the main specifications for the AdV substrate polishing can be seen in Table 5.2

| | Input Mirror IM | End Mirror EM | Beam Splitter BS | Compensation Plates CP | Power Recycling Mirror PRM | Signal Recycling Mirror SRM | Pick Off Plate POP |
|--|-----------------------------------|-----------------------------------|---------------------------------|---------------------------------|---------------------------------|---------------------------------|------------------------------------|
| Shape Surface 1 Reflective side | Concave 1420 m | Concave 1683 m | Flat | Flat | Concave 1430 m | Concave 1430 m | Flat |
| Shape Surface 2 | Convex 1420 m | Flat | Flat | Flat | Convex 3.59 m | Convex 3.616 m | Flat |
| Accuracy on ROC Surface 1 | +/- 10 m | +/- 10 m | - | - | +/- 10 m | +/- 10 m | - |
| Accuracy on ROC Surface 2 | +/- 10 m | +/- 10 m | - | - | +/- 1 % TBC | +/- 1 % TBC | - |
| Wedge | 0 μ rad TBC | 1 mrad +/- 0.1 mrad | 400 μ rad +/- 50 μ rad | 0 μ rad | < 300 μ rad | < 300 μ rad | 400 μ rad +/- 50 μ rad TBC |
| Roughness Surface 1 | $\leq 1 \text{ \AA}$ RMS | $\leq 1 \text{ \AA}$ RMS | $\leq 1 \text{ \AA}$ RMS | $\leq 1 \text{ \AA}$ RMS | $\leq 1 \text{ \AA}$ RMS | $\leq 1 \text{ \AA}$ RMS | $\leq 1 \text{ \AA}$ RMS |
| Roughness Surface 2 | $\leq 1 \text{ \AA}$ RMS | $\leq 2 \text{ \AA}$ RMS | $\leq 1 \text{ \AA}$ RMS | $\leq 1 \text{ \AA}$ RMS | $\leq 1 \text{ \AA}$ RMS | $\leq 1 \text{ \AA}$ RMS | $\leq 1 \text{ \AA}$ RMS |
| RMS Flatness Surface 1 Reflective side | < 0.5 nm RMS \varnothing 150 mm | < 0.5 nm RMS \varnothing 150 mm | < 2 nm RMS \varnothing 250 mm | < 2 nm RMS \varnothing 150 mm | < 2 nm RMS \varnothing 150 mm | < 2 nm RMS \varnothing 150 mm | < 2 nm RMS \varnothing 150 mm |
| RMS Flatness Surface 2 | < 2 nm RMS \varnothing 150 mm | < 5 nm RMS \varnothing 150 mm | < 2 nm RMS \varnothing 250 mm | < 2 nm RMS \varnothing 150 mm | < 2 nm RMS \varnothing 150 mm | < 2 nm RMS \varnothing 150 mm | < 2 nm RMS \varnothing 150 mm |

Table 5.2: Polishing specifications of the AdV substrates.

5.4.1 Strategy for polishing in Advanced Virgo

For AdV, the polishing strategy (baseline solution) is defined as follows. The classical steps of "mechanical" polishing will be done by external companies. Then, the second step will consist in improving the mirror surface figure by using the so-called corrective coating technique. This technique, originally developed at LMA, consists in measuring the mirror surface map and correcting it by adding an additional layer of silica wherever is necessary. A R&D project was carried out at LMA within the first EGO R&D program in 2002. The corrective coating (CC) technique was tested on a 150 mm diameter flat mirror with good performances (surface rms: 0.9 nm, surface Peak-to-Valley (PV): 9 nm, see Fig. 5.3). In this test, the substrate central part was not corrected properly due to the robot behavior: a hole can be seen in Fig. 5.3. Without this central hole, the RMS flatness is 0.7 nm RMS (PV value around 3 nm) so

very close to the **AdV** specifications. The maximum thickness that will be deposited during the corrective coating will be around 10 nm if the polishing company is working well. So the impact of this layer on the coating thermal noise will be negligible. Moreover the mechanical losses of the SiO_2 layer is twice lower than the Ta_2O_5 one.

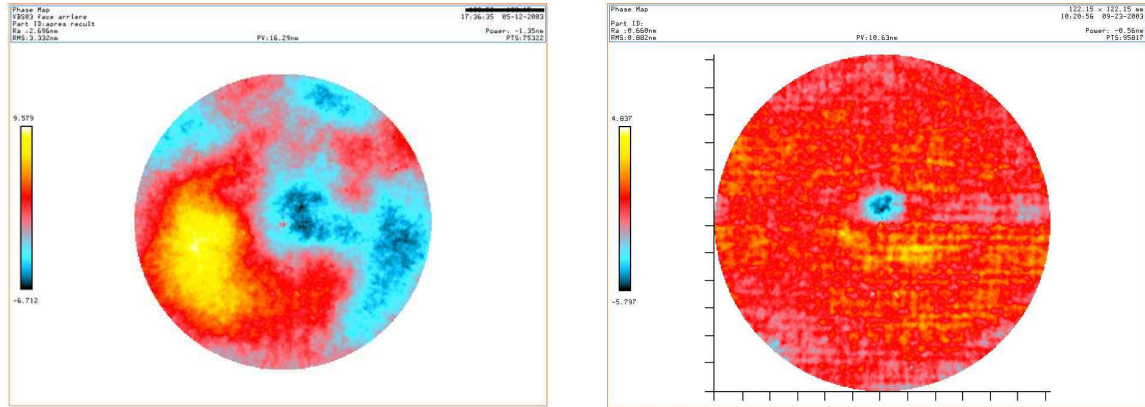


Figure 5.3: Wavefront maps of a 150 mm diameter silica substrate before (left, 3.3 nm RMS) and after (right, 0.9 nm RMS) corrective coating.

To understand how much the corrective coating will be able to correct the flatness of a substrate, we simulate the corrective coating technique in the spatial frequency domain. These simulations will allow us to find out the level of flatness required in the first polishing phase (i.e. the classical polishing) that allows the CC to be efficient enough [160, 162]. Using the results presented in Fig. 5.3, we plot the power spectral density of the substrate surface before and after correction (Fig. 5.4). We were able to notice that the corrective coating acts as a high-pass filter on the PSD (frequency cut 50 m^{-1} , correction of the low spatial frequencies) [162].

The conclusion that appears in these calculations is that, for the Corrective Coating (CC) to be efficient at the level needed for **AdV**, it is necessary to start from a substrate with a flatness of 1.5 nm RMS at least.

In order to reach the **AdV** specifications on the flatness, a new robot for the Virgo large coating machine in Lyon was developed in collaboration with LAPP. It was installed in July 2011 on the vacuum chamber (Fig. 5.5). The calibration and test in real conditions have started. The aim is to provide a witness sample corrected by CC having the flatness needed for Advanced Virgo and it should be done at the end of the first quarter of 2012.

The polishing strategy for the cavity mirrors (**EM**, **IM**) is the following. As soon as the CC final test is performed and if it is positive, the wavefront of all the **IM** and **EM** substrates will be corrected by CC. If not, the backup solution will be the Ion Beam Figuring and a complementary order will be passed. In both cases, a "classical" polishing phase is needed. The aim of this phase is to provide substrates with a flatness of 1.5 nm RMS on the central area. That means that the polishing order can be placed without having the CC test result, in order to save time.

Concerning the polishing order, the draft of the general specifications for the **IM** and **EM** polishing is ready as the optical design of **AdV** is finished. The wedge value of the **IM** was defined in the OSD chapter to be 0 degree. The choice has a direct consequence on the

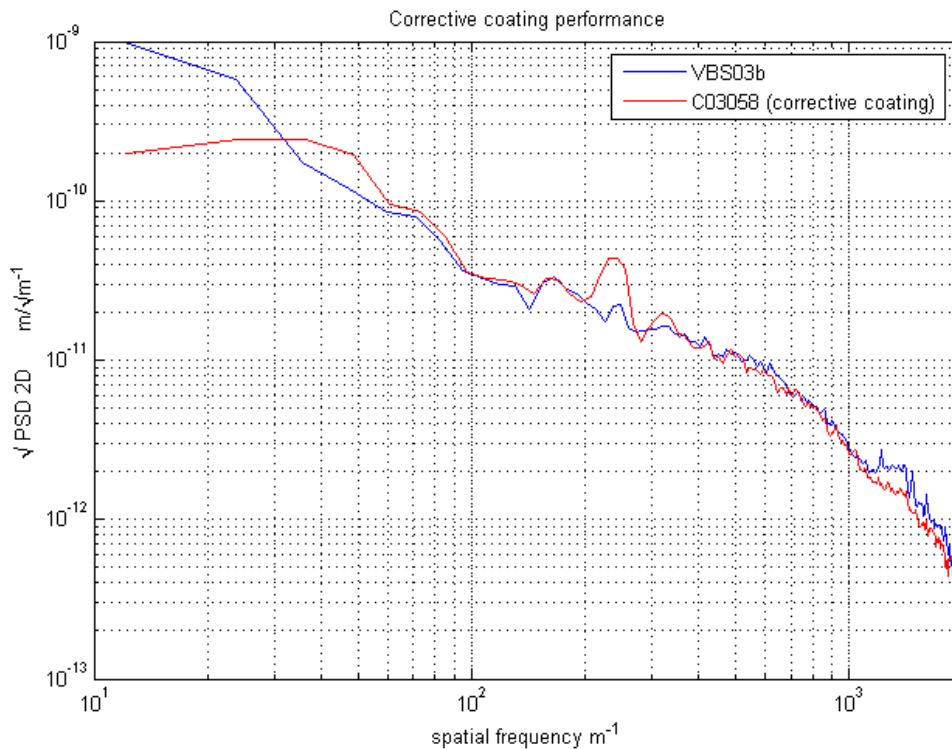


Figure 5.4: PSD of the 120 mm diameter substrate before and after corrective coating from the 2003 test

flatness metrology. Indeed, it is impossible to fully suppress the interference between the 2 parallel surfaces of the **IM** substrates. In that configuration, we are not able to control sample with a very low flatness using standard phase-shifting interferometer.

This implies a new type of flatness metrology (wavelength shifting interferometry) to get rid of the back side contribution during the wavefront measurement. This is something new on which we have no experience. Secondly, the flatness metrology problem underlined will be also present for the polishing company. The consequence of that can be a reduction of the number of polishing company able to answer to the call for tender (because they have not the metrology) or a cost increase of the polishing if the companies decide to purchase the metrology tools (included in the non recurring costs).

5.5 Coating

The coatings of the **AdV** components are certainly the most sensitive component of the mirrors and among the most important in the interferometer as they determine both the total mechanical losses of the mirrors and their optical losses.



Figure 5.5: Pictures of the new robot for the CC installed on the Virgo coating chamber.

5.5.1 Mechanical losses

Since many years, R&D programs on the coating mechanical losses were carried out at LMA, some of them were funded by EGO. At present, the lowest mechanical losses measured for Ta₂O₅ coating are those obtained with Ti doped Ta₂O₅. The losses value is within the AdV requirement of $2.3 \cdot 10^{-4}$ [151]. It is clear that the sensitivity of the detector will directly benefit of a further decrease of the mechanical losses. One of the main difficulties in this context is to find materials with low mechanical losses without degrading the performances in terms of optical losses. The best available recipe will be used for the AdV mirror coating. The coating design foreseen originally for AdV is the quarter wave stack as the AdV sensitivity curve is calculated with this assumption. Moreover, with a quarter wave design it is easier to adjust the reflectivity needed at the wavelength of the auxiliary laser used for lock acquisition. Indeed, this design is less sensitive to layer thickness errors that can occur during the coating process.

Nevertheless, an option to reduce the mechanical losses consists in optimizing the thickness of the different coating layers (Ta₂O₅ and SiO₂). This new design can be called "optimized coatings". Since the losses are mostly concentrated in the Ta₂O₅ layers, it is possible to reduce the mechanical losses of the multi-layer by reducing the amount of Ta₂O₅ and increasing the amount of SiO₂. For a given required reflectivity it is possible to find an optimum combination. Recently at LMA a mirror was coated using this technique and delivered to Caltech. The estimated gain can be around 10% on the coating thermal noise. The layer thickness control is more critical in this case but the very recent tests done on the LIGO coatings have shown that the coating machine is able to produce such optimized multilayers with a quite good accuracy. Thanks to this result, the "optimized coatings" for the IM and EM will be used for AdV.

5.5.2 Absorption losses

The absorption losses of the coatings play also an important role as they determine the power absorbed in the test mass and thus the thermal lensing effect. The lower are the losses in the coating the lower is the required thermal compensation. The high reflectivity coatings of the first generation of Virgo mirrors had an absorption of 1.2 ppm for the input mirrors and 0.7

ppm for the end mirrors. Since then, the absorption in the coating has been reduced [164]. An absorption level lower than 0.5 ppm is currently achieved on high reflectivity mirrors (**EM**) thanks to the use of Ti doped Ta_2O_5 . For the **IM**, an absorption level lower than 1 ppm is reachable. These absorption levels have been obtained on the mirrors installed for Virgo+. This is also true for the "optimized coatings" (measurements done at **LMA**). Nevertheless, due to the increase of the finesse, the absorption in the coating is likely to remain the main origin of the mirror heating.

Moreover, we found that the details of the polishing process of the silica substrate can play a very important role on the the final coating absorption value for "transmissive" optics (like the **IM**). Indeed, when putting several samples in the same run coming from different polishing companies, we found sometimes that the mirror absorption can vary by more than a factor 4. The physicochemical explanation has not yet been found. At the present time, these absorption levels are the best values ever obtained and, unless new R&D is done, they are representatives of the absorption of the Advanced Virgo mirrors.

5.5.3 Coating uniformity

In order to maintain after coating the substrate flatness, a very good coating uniformity is needed. Since the Virgo+ mirrors, a strong improvement of the uniformity was done. We were able to produce mirrors with a flatness RMS close to 0.5 nm RMS on a diameter of 160 mm. The coating configuration used for this part is a single rotation of the sample inside the coating machine; this means that we are able to coat only one substrate per run. The goal we have is, like in Virgo+ for the **IM**, to coat two parts in a coating run to have the same optical performances. In this configuration, the transmission of the two mirrors should be equal. Thus, the **AdV** cavities will be identical. Otherwise, the asymmetry in finesse and power on the dark fringe might be too large. The finesse asymmetry is dominated by the transmission mismatch between the two **IM** rather than the losses induced by the flatness of the cavity mirrors (as in **AdV**, the mirror RMS flatness is very low). We found that, if we coat two fixed substrates with only an axis of rotation between the two, the coating uniformity reached is not satisfactory (1.6 nm RMS on 150 mm in diameter).

The only possible solution is the planetary motion. In this case, we add a rotation of the two substrates to the previous rotation. Optical simulations have been done to see what kind of uniformity we can reach with this configuration for the **IM** and **EM**. The first results (Fig. 5.6) seem very promising and compliant with the **AdV** needs in term of uniformity (no Zernike terms greater than 0.5 nm, sagitta variation¹ around 1 nm).

According to this simulation results, the construction of a planetary motion is being considered at **LMA**. A mechanical drawing of a planetary motion system already exists and can be seen in Fig. 5.7.

The table in Table 5.3 summarizes the main coating characteristics at 1064 nm of the different type of mirrors for **AdV**.

Concerning the **SR** mirror, in the first phases of **AdV**, this particular component will not be used as a mirror but only as a lens. In this case, the coatings put on the two surfaces will be antireflective coatings working at normal incidence. The characteristics of these AR coatings

¹Radius of curvature variation due to coating.

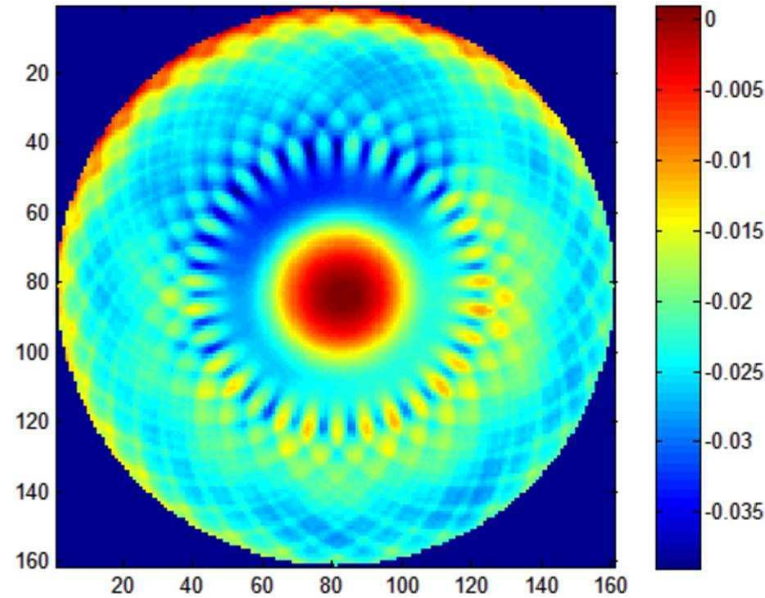


Figure 5.6: Simulation of the **EM** coating uniformity using the planetary motion with masking (1 nm **PV**, 0.2 nm **RMS**.)

are the same as the **CP** ones (see Table 5.3). When **AdV** will be in its final configuration with signal recycling, this lens will be replaced by a **SR** mirror and it will be repolished.

5.5.4 Coating performances for the auxiliary beams: Hartmann beams and auxiliary lasers

The classical coating designs used in Virgo/ Virgo+, working at 1064 nm, must be modified due to the use in **AdV** of auxiliary beams. They are of two kinds:

- the Hartmann beams at 800 nm used by the **TCS** to control the thermal effect in the **IM** (see **TCS** chapter for more details): this requires a proper coating design for the **PR**, **SR** and **BS** (high reflective and antireflective coatings);
- an auxiliary beam used for the lock acquisition at 1319 nm (see Interferometer Sensing and Control (**ISC**) chapter for more details): this requires a proper coating design for the **EM** coatings.

Nevertheless, the priority is to preserve the coating performances (reflectivity, absorption) at 1064 nm for all the mirrors that must be modified. The reflexion/transmission specifications linked to these two beams are summarized in the table 5.4

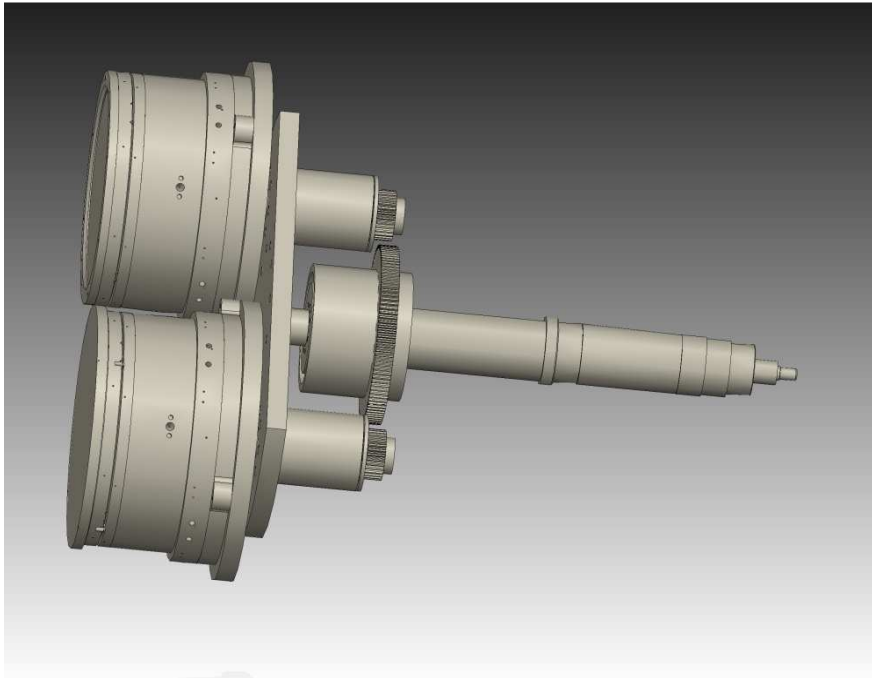


Figure 5.7: Mechanical drawing of the sample holder with planetary motion.

5.6 Metrology

The metrology tools, necessary to completely characterize the Virgo mirrors, have already been developed for the first mirror generation (absorption, scattering, transmission, wavefront, radius of curvature, roughness, point defect detection). The size (diameter greater than 400 mm for the beam splitter) of the **AdV** mirrors will impose modifications of the several sample holders to be able to map the scattering, the transmission, the reflection and the absorption losses, because of the size and the weight increase. Here is the list of modifications on the metrology benches that must be done for **AdV**.

- **Scattering measurement:** a new sample holder must be manufactured to be able to move larger and heavier samples (40 kg, diameter 55 cm for the **BS**).
- **Absorption measurement:** an upgrade of the existing sample holder is needed due to the mirror weight increase (40 kg). The two motors of the Y axis have been replaced by stronger ones.
- **Metrology mounts:** new metrology mounts will be manufactured because of the new mirror size (20 cm thick for the **IM** and **EM**, 55 cm diameter of the **BS**).
- **Flatness measurement:** to be able to measure the flatness of the **AdV** substrates and mirrors at the level required (RMS flatness of 0.5 nm), a new bench will be developed to measure wavefronts at 0° and 45° for the beam splitter with a better accuracy and reproducibility. This bench is also crucial for the "corrective coating" to be efficient. A R&D program supported by EGO started on this subject. For **AdV**, an upgrade

| | Input Mirror IM | End Mirror EM | Beam Splitter BS | Compensation Plates CP | Power Recycling Mirror PRM | Signal Recycling Mirror PRM | Pick Off Plate POP |
|------------------------------------|--------------------------------|----------------------------|------------------------|------------------------------|-------------------------------------|--------------------------------------|---------------------------------|
| Incident angle | 0° | 0° | 45° | 0° | 0° | 0° | 6° |
| Coating diameter Surface 1 | 340 mm | 340 mm | 530 mm | 340 mm | 340 mm | 340 mm | 340 mm |
| Coating diameter Surface 2 | 340 mm | 340 mm | 530 mm | 340 mm | 340 mm | 340 mm | 340 mm |
| Coating Surface 1 | HR T = 1.4% | HR T = 1 ppm | R=T= 50% +/- 0.5% | AR R <100 ppm | HR T = 5 % | HR T = 20 % | R = 300 ppm +/- 100 ppm |
| Coating Surface 2 | AR R ≈ 300 ppm (TBC) (*) | AR R < 100 ppm (TBC) | AR R <100 ppm | AR R <100 ppm | AR R <100 ppm | AR R <100 ppm | AR R <100 ppm |
| Coating absorption Surface 1 | < 1 ppm | < 0.5 ppm | < 2 ppm | - | < 2 ppm | < 2 ppm | - |
| Scattering Surface 1 | <10 ppm | <10 ppm | <10 ppm | <10 ppm | <10 ppm | <10 ppm | <10 ppm |
| RMS Flatness Surface 1 | 0.5 nm RMS Ø 150 mm | 0.5 nm RMS Ø 150 mm | < 2 nm RMS Ø 250 mm | < 2 nm RMS Ø 150 mm | < 2 nm RMS Ø 150 mm | < 2 nm RMS Ø 150 mm | <3 nm RMS (TBC) Ø 150 mm |
| RMS Flatness Surface 2 | < 2 nm RMS Ø 150 mm | < 5 nm RMS Ø 150 mm | < 2 nm RMS Ø 250 mm | < 2 nm RMS Ø 150 mm | < 2 nm RMS Ø 150 mm | < 2 nm RMS Ø 150 mm | <40 nm RMS (TBC) Ø 150 mm |

(*) This specification is for the baseline solution (no wedge on the IM).

Table 5.3: A summary of the coatings main features of the AdV mirrors at 1064 nm.

of the present flatness measurement is necessary and the main things that must be improved are the vibration isolation and the perturbation due to turbulences, which are the two main limitations. It was decided to install the new bench in the clean room plenum (basement of the clean room) which is a more stable area. The study of the turbulence effect was done and we know how to minimize this problem, especially by encapsulating well the measurement area. At the beginning, we intended to use the same configuration as the one used for Virgo: 6" phase-shifting interferometer present at LMA coupled to stitching interferometry. But, we are now convinced that reaching with this configuration the accuracy level needed for AdV (0.1 nm RMS on the central mirror area) is impossible. Indeed, moving the substrate/mirror to do the stitching is a source of vibrations and suppressing the turbulences is more complicated as the substrate is moving in front of the interferometer. The best way to proceed is to use a new phase-shifting interferometer at 1064 nm coupled to a large beam expander (12" or 18"). This type of configuration is used by Caltech to control the Advanced LIGO mirrors and the accuracy achieved is the one we need. Another point found with recent tests is that it is absolutely necessary to use reference sphere for the measurement instead of reference flat, to measure very low flatness values of curved surfaces, because the number of fringes due to the mirrors curvature is too high in AdV. This has a strong impact on the measurement. The optical design detailed in the Optical Simulation and

| | End Mirror EM HR coating | Beam Splitter BS HR coating | Beam Splitter BS AR coating | Power/Signal Recycling Mirror PR/SR HR coating | Power/Signal Recycling Mirror PR/SR AR coating |
|----------------------------|--------------------------------|-----------------------------------|-----------------------------------|---|---|
| Reflectivity at 1319 nm | 70% +/- 10% | - | - | - | - |
| Reflectivity at 800 nm | - | R > 98 % at 45° inc. | R < 0.1% at 45° inc. | R < 0.5% | R < 0.5 % |

Table 5.4: Coating performances needed for the auxiliary beams at 800 nm and 1319 nm.

Design subsystem (**OSD**) chapter specifies that the **IM** will have no wedge. This implies that the baseline configuration for this new bench is a wavelength shifting interferometer (instead of a phase-shifting interferometer) coupled to a beam expander to be able to measure very low flatness value, with a high accuracy, on parallel plates. The wavelength shifting technique is the only one able to get rid of the interferences due to the substrate backside. This method is expected to have at least the same performances (or even better) than the phase shifting.

Finally, in [166], the simulations showed that the deformation induced by the way the mirror is put in front of the interferometer for the measurement (V shape mount) is negligible on the 150 mm center part (few tenths of nm Peak to Valley).

5.7 Cleaning

During the coating process the mirrors are cleaned several times. Due to safety reasons, the cleaning procedures used for Virgo cannot be simply transposed to the larger mirrors that will be used in **AdV**. A different cleaning procedure (wet cleaning) was tested in the past at **LMA** on small silica sample (120 mm diameter). This process is as efficient as the classical cleaning procedure used for Virgo. A new procedure has been identified and its development had been already proposed and supported by EGO in the context of the 2nd R&D program. Thus, we were able to test the efficiency on small substrates (120 mm diameter) of a large cleaning machine manufactured by Minaservices on the basis of our requirements and compatible with the large **AdV** substrates. The results were totally satisfactory [163]. Indeed, less than 10 particles (diameter max 4 microns) were present on the surface on the 120 mm center

part. There are four steps to clean the component. After a preliminary hand wash with special tissues and soap, the mirror will go in the first tray equipped with ultrasonics devices. Then, there is the rinsing step in deionized water. After, the component goes in a third tray equipped with megasonics devices which helps to remove very small particles (< 100 nm). And the final steps is the drying. The new cleaning machine is now installed in the **LMA** clean room (Fig.5.8). After installation, cleaning tests were made on real Virgo substrates and the results obtained were totally satisfactory. The cleaning process is validated. This machine will also be able to clean a mirror having ears glued on the two flats.



Figure 5.8: New wet cleaning machine needed for **AdV** installed in the clean room.

Before being sent on the Virgo site, the mirrors will have to be protected against contamination and properly packed. Special boxes adapted to the larger size of the **AdV** mirrors will be manufactured. Like in Virgo, all the mirrors will be delivered in Cascina to be mounted on the payloads.

5.8 Main Milestones

- September 2009 - Robot construction start: the new robot installed in the coating chamber is needed for the corrective coating to improve the polishing of the large test masses.
- December 2009 - Large substrates procurement: the input and end substrates were ordered to the manufacturer Heraeus.
- April 2010 - New wet cleaning station ready: this system is needed to clean the large test masses
- September 2010 - New wet cleaning station installed in the clean room

- December 2010 - Large substrates procurement: order of the Beam Splitters blank substrates.
- November 2011 - Large substrates procurement: order of the **PR** and **SR** blank substrates.
- March 2012 - Corrective coating test on a scale 1 substrate: after construction and installation in the Virgo coating chamber, the corrective coating technique will be tested on a real 35 cm in diameters substrates to check if the polishing requirement for **AdV** are achieved, and so confirm the polishing strategy. If not, the other polishing solution will be chosen through a change request.
- June 2012 - Large test masses (**IM**, **EM**) polishing: the polishing of the **IM** and **EM** substrates will be ordered.
- December 2012 - New flatness metrology bench available (new wavelength shifting interferometer with a beam expander)
- February 2013 - 2 **IM** polished: the two first **IM** will be delivered by the polishing company.
- September 2013 - 2 **IM** ready (coated + characterized): the two first **IM** are ready to be installed on the payload.
- July 2014 - All mirrors ready (coated + characterized): all the mirrors needed for **AdV** (2 **IM**, 2 **EM**, 1 **BS**, 2 **CP**, 1 **PR**, 1 **SR**, 1 **POP**) will be coated and characterized.

Chapter 6

Thermal compensation (TCS)

6.1 Scope and requirements of the subsystem

The Thermal Compensation System (TCS) will sense and correct aberrations in the core optics to a level that allows AdV to acquire the lock and run at full power, without spoiling the sensitivity of the detector. The correction provided by the TCS concerns:

- optical path length distortions (thermal lensing, mirror figure errors, inhomogeneity of the substrate refraction index), which give raise to wave front distortions in the signal recycling (SRC) and power recycling (PRC) cavities (sections 6.3.1 and 6.3.2);
- change of the profile of the high reflective surface, due to thermal expansion (thermoelastic deformation), in both ITMs and ETMs, affecting the FP cavity (section 6.3.1);
- correction of manufacturing error of the Input Test Mass (ITM), End Test Mass (ETM) and Recycling Cavity (RC) mirrors Radius of Curvature (RoC) (section 6.8).

TCS must provide as much flexibility as possible for corrections. The noise introduced into the detector by the TCS must not exceed the requirement imposed to technical noises. Based on the experience of Virgo/Virgo+, TCS is designed so that most of the apparatus lives outside vacuum and can be easily upgraded as new understanding of the Interferometer (ITF) is realized. Table 6.1 reports the general requirements for the AdV TCS.

| Parameter | Requirement |
|--|---------------------------------------|
| RC residual optical path length RMS | < 2 nm (from OSD) |
| TM RoC precision | ± 2 m (from OSD) |
| RM RoC precision (without other distortions) | ± 8 m (from OSD) |
| Noise | factor of 10 below design sensitivity |

Table 6.1: AdV TCS general requirements.

6.2 Design overview

The actuation and sensing schemes are shown in Fig. 6.1 and comprise:

- CO₂ lasers that will shine the appropriate heating pattern (see sections 6.6.1 and 6.6.2) on additional transmissive optics in the recycling cavities named compensation plates (CP) to correct for aberrations in the cavities themselves. The presence of the CP allows to control independently the thermal lensing in the RC and the RoC of the ITM and makes the level of the noise coupling of the CO₂ laser compliant with the AdV sensitivity requirements (see section 6.7.1);
- ring heaters (RH), placed around each Test Mass (TM), Power Recycling Mirror (PR) and Signal Recycling Mirror (SR), that will restore the proper radius of curvature; the possibility to realize some of the actuations with central heating (CO₂ laser or radiative source) is also discussed (section 6.8 for details);
- Hartmann sensors that will measure the wave front distortions and the thermoelastic deformation of the High Reflectivity (HR) face directly from the optics themselves (details in section 6.9 and 6.11).

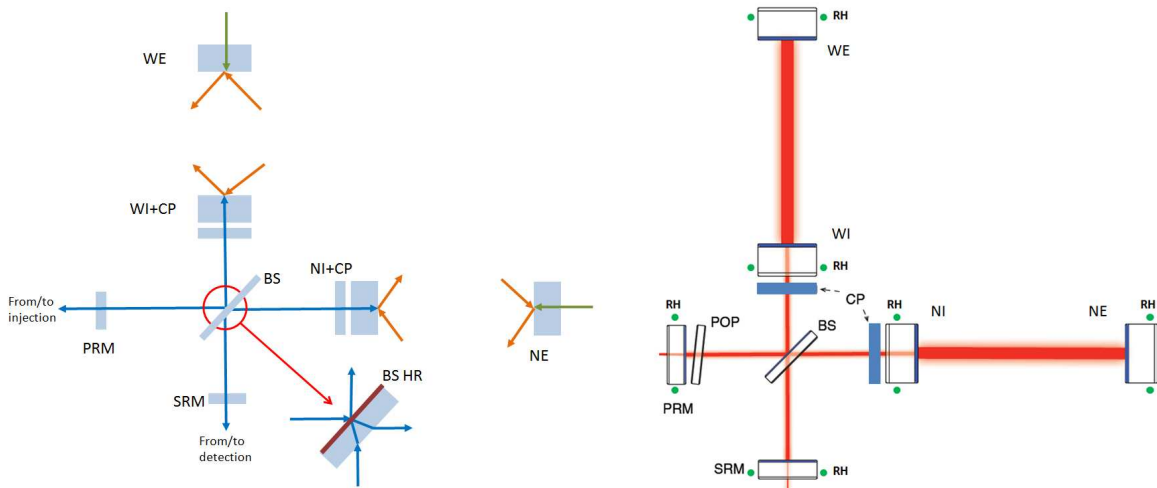


Figure 6.1: AdV TCS layout. Left: sensing scheme. Phase distortions are probed in transmission (blue and green beams), surface deformations are measured in reflection (orange beams). Right: actuation scheme, the green dots represent the ring heaters, the blue rectangles represent compensation plates.

Changes with respect to the 2009 baseline design

- CP diameter: from 28 cm to 35 cm (see section 6.4.1);
- CO₂ heating pattern generator: from single axicon Virgo-like to double axicon (see section 6.6.1);
- nonsymmetric compensation added due to the choice of marginally stable recycling cavities (section 6.6.2);
- added PRM and SRM RoC tuning.

6.3 Core optics defects

The figures of merit chosen to describe the amount of aberrations are the coupling losses and the Gaussian weighted RMS of the optical path length (OPL) increase. We remind in the following the definition of these two FOMs. The coupling losses L represent the fractional power scattered out from the TEM₀₀ mode [168, 169]:

$$L = 1 - A^*A, \quad (6.1)$$

where

$$A = \frac{\langle E_0|E \rangle}{\langle E_0|E_0 \rangle} = \frac{\langle E_0|e^{i\frac{2\pi}{\lambda}h(x,y)}|E_0 \rangle}{\langle E_0|E_0 \rangle} = \int dx \int dy e^{i\frac{2\pi}{\lambda}h(x,y)} |E_0(x,y)|^2. \quad (6.2)$$

E_0 is the undisturbed cavity field before being subjected to the optical distortion, $h(x,y)$ is the value of the OPL at point (x,y) , λ the field wavelength and E the distorted field.

The Gaussian weighted RMS of the OPL is defined as [170]:

$$\sigma_g^2 = \frac{\sum_{m,n} G(x_m, y_n) [h(x_m, y_n) - h_g]^2}{\sum_{m,n} G(x_m, y_n)}, \quad (6.3)$$

where $G(x,y)$ is the interferometer beam intensity at (x,y) , and h_g is given by

$$h_g = \frac{\sum_{m,n} G(x_m, y_n) h(x_m, y_n)}{\sum_{m,n} G(x_m, y_n)}. \quad (6.4)$$

The procedures for the optimization of the CP parameters (section 6.4.1) and of the heating pattern (sections 6.6.1 and 6.6.2) use the OPL increase as error signal: flattening the OPL corresponds to minimizing both the coupling losses and the RMS.

6.3.1 Thermal effects

Thermal lensing. The absorption losses foreseen for the optics are summarized in Tab. 6.2. The power absorbed is computed for 125 W input power, an arm cavity finesse of 443 and a recycling cavity gain of 37.5.

With the parameters mentioned above, the coupling losses due to thermal lensing turn out to be of the order of $5 \cdot 10^5$ ppm and the corresponding RMS is about 125 nm. The right graph of Fig. 6.2 shows the simulated optical path length increase, corresponding to a lens with focal length of about 5 km. The left plot shows the thermoelastic deformation which would be experienced by the HR surface of an AdV test mass ¹.

The value of 1 ppm takes into account only the average coating absorptions. However, there is a degree of nonuniformity that gives rise to nonsymmetric phase distortion [172], as shown in Fig. 6.3. From optical simulations (reported in the OSD chapter), also these phase

¹The results shown in this figure have been obtained with an ANSYS finite element model and crosschecked with the Hello-Vinet analytical solution [168], showing an excellent agreement [171]

| | Substrate absorption (ppm/cm) | Coating absorption (ppm) | Absorbed power (mW) |
|-----|----------------------------------|-----------------------------|------------------------|
| ITM | 0.3 | 1 | 694 |
| ETM | 3 | 0.5 | 330 |
| BS | 0.3 | 2 | 34 |
| PRM | 3 | 2 | 13 |
| CP | 1 | 1* | 26 |
| POP | 1 | 1* | 52 |

Table 6.2: Expected absorptions in the optics as given in the MIR chapter. The absorbed power is computed for the ITF at 125 W. *This value is taken from Table 8 in the OSD chapter and is considered as the reference value for the AR coating absorption.

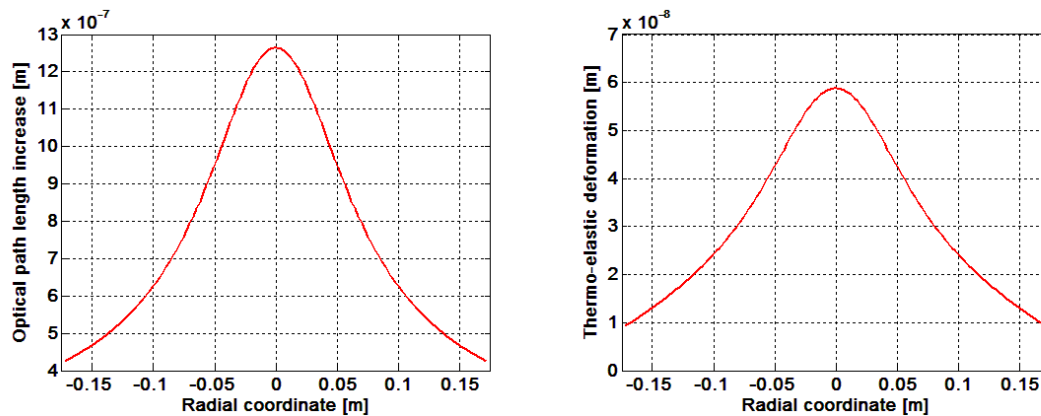


Figure 6.2: Left: optical path length increase in AdV TM due to substrate and coating absorption, corresponding to a focal length of about 5 km. Right: thermoelastic deformation of the HR surface in AdV TM, corresponding to a Gaussian weighted RoC increase of the test masses of about 44 m (about 10 m for unweighted fit).

distortions give a non negligible contribution to the decrease of the recycling cavity gain and must therefore be compensated.

HR face deformation. Due to thermal expansion, the temperature gradient will also change the profile of the high reflectivity surface: the thermoelastic deformation of the test mass faces will be of the order of 50 nm (see Fig. 6.2). The Gaussian weighted RoC of the test masses will increase by about 44 m (about 10 m for unweighted fit) for the input and 22 m for the end, out of the OSD requirements.

6.3.2 Cold defects

It has been demonstrated (see chapter Optical Simulation and Design subsystem (OSD) 2) that the surface defects and the inhomogeneity of the refraction index of the substrates in the AdV optics will have an impact on the behavior of the marginally stable recycling cavities. An example of these aberrations, usually referred to as "cold defects", is shown in Fig. 6.4. As for thermal effects, also the cold defects contain a major contribution with axial symmetry plus a smaller fraction of nonsymmetric terms, revealed by a decomposition of a test mass

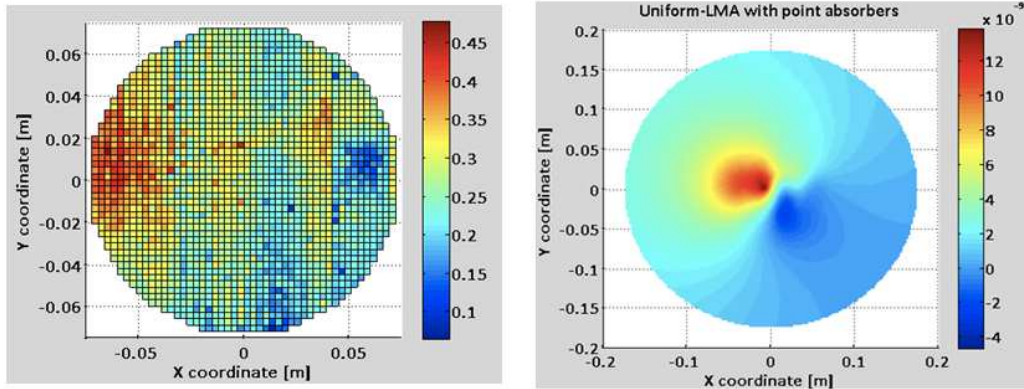


Figure 6.3: Left: coating absorption map measured at LMA on an Advanced LIGO test mass. Right: resulting non uniformity of the OPL for 125 W of ITF input power. Color scale in meters.

transmission map into Zernike polynomials [173].

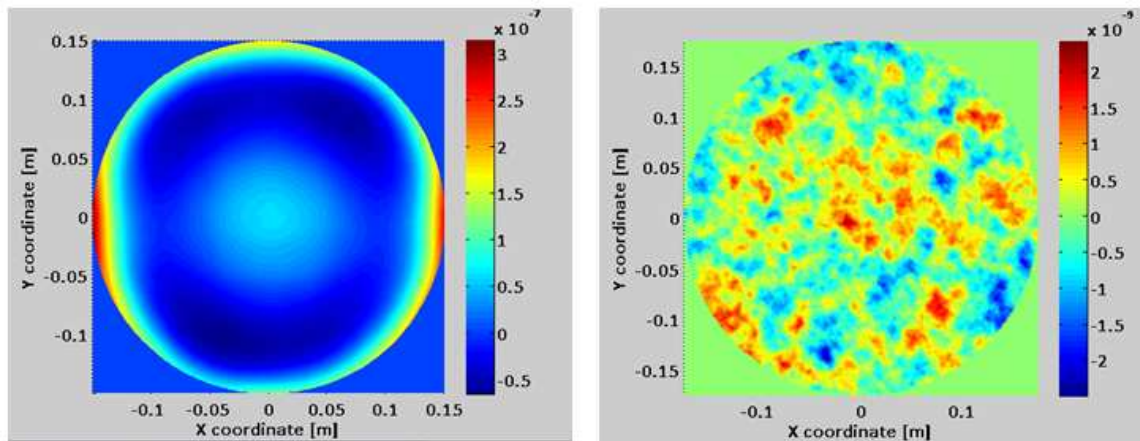


Figure 6.4: Left: substrate transmission map measured at LMA on an Advanced LIGO test mass. Right: simulated surface map. Color scale in meters.

The expected manufacturing error on the RoCs of the test masses is about 1%, but more stringent requirements have been put by OSD to guarantee the needed optical performance. Also for the recycling mirrors, the accuracy achievable in the fabrication process is not compliant with the optical constraints. The TCS must fill the gap between the fabrication accuracy and the optical requirement.

6.4 Compensation plates

The Compensation Plate (**CP**) interacts directly with the interferometer beam. As such, it must satisfy requirements like those of a core optic with respect to displacement noise, absorption and scattering, index homogeneity, antireflection coatings.

6.4.1 CP geometry and position

The geometry and position of the CP have been defined by optimizing the TCS performances, also taking into account the constraints coming from the payload design. We report in the following the results of this investigation using the coupling losses as a FOM.

CP diameter. The diameter of the CP has been fixed at the same value as the TM, in order not to add clipping of the ITF beam.

CP thickness investigation. In order to investigate the effect of the CP thickness on the TCS performance, a setup where CPs are far from the TMs [174] has been considered for the simulations. In this way, the radiative coupling between TM and CP is cancelled and the effect of the thickness only is put in evidence. The thickness range 3.5-10 cm has been investigated. The choice of these values depends on considerations about the minimum resonance frequency of the CP (see below). Simulations have been run for three different values of the thickness (10 cm, 6.5 cm, 3.5 cm). As a case study, a setup with the RH always on at the power and position needed to recover the cold RoC (see section 6.5) and a simple annular heating pattern on the CP is considered. Results show a quadratic dependence of the minimum coupling losses as a function of the thickness: the minimum increases by a factor of ten when the thickness goes from 3.5 cm to 10 cm.

These results clearly show that a thin CP is better than a thick one. This is due to the fact that a thick CP will radiate more heat from its lateral surface than a thin CP. The choice of a thin CP allows also to avoid a big increase in the mass of the payload and the need for a gold coating on the barrel of the CP.

The analysis of the resonance mode for an unconstrained 3.5 cm thick CP, shows that the lowest mode (butterfly mode) is at 1.7 kHz, higher than the lowest resonant mode of the beam splitter (1.3 kHz). Thus, the thickness of the AdV CP has been set to 3.5 cm.

CP position investigation. The effect of thermal interaction between the CP and the test mass has been evaluated by changing the distance between the test mass and CP, in the range 20 cm (maximum allowed by the design of the payload) and 1 cm. As a consequence of the CP-TM radiative interaction [174], the heat radiated toward the TM concentrates mainly in the center of the TM itself, thus increasing the amount of thermal lensing and the minimum coupling losses achievable (by about a factor of 6 going from 20 cm to 1 cm). Another unwanted consequence of the radiative coupling between CP and TM is that the RoC depends also from the CO₂ power so that RH and CO₂ powers are coupled. From these considerations, the distance between CP and TM is fixed to its maximum value of 20 cm. At this distance, the residual effect of the CP heat on the ITM RoC is about -0.26 m/W [174].

6.4.2 Influence of the CP on alignment and longitudinal controls

The presence and exact value of a wedge on the CP, either to allow a reduction of the etalon effect or to extract pick off beams, has been defined in the frame of the general optical design of the interferometer (see OSD chapter). Since the request from OSD is for a wedge $< 3 \mu\text{rad}$, in the following considerations a wedge in the range from 0 to $3 \mu\text{rad}$ has been considered, taking in each calculation the most conservative value.

Longitudinal controls

A FFT simulation made with FOG has been used to estimate the fraction of the power reflected by one AR side of one of the tilted compensation plates that couples back into the main dark fringe beam. More precisely, the total power falling inside a diaphragm centered on the main beam is computed. This might give an overestimate of the real number, since it does not take into account the real coupling of the reflected beam with the Gaussian mode at the interferometer output.

The relative distance between the compensation plate and the input mirror was swept over a full wavelength. As expected interference fringes are visible in the dark fringe carrier power, see Fig. 6.5, which refers to the power recycled case for 1 W input power. Compensation

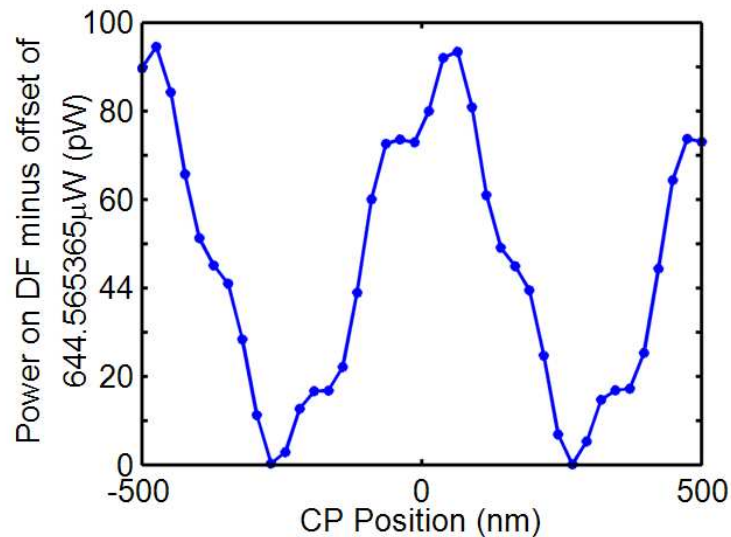


Figure 6.5: Power variations at dark port (for 1 W input power) created by a motion of the compensation plates over one entire wavelength.

plate motion can couple to the detector sensitivity through two main phenomena. Large low frequency displacements can couple to the sensitivity through upconversion. The maximum speed that the compensation plates can reach before the upconverted noise enters the detector bandwidth is of the order of $2 \mu\text{m/s}$. This has been computed with the same procedure used for similar cases in other subsystems (see for example INJ chapter for backscattering from the meniscus lens), taking into account the actual position of the involved optical components. Besides upconversion effects, there is a direct coupling of CP motion to power noise at the dark fringe, as shown by the fringes in Fig. 6.5. The worst case coupling is given by the maximum slope of Fig. 6.5, which corresponds to 10^{-3} W/m (for 1 W input power).

The expected signal on the dark fringe photodiode corresponding to the design sensitivity can be computed using the transfer function computed with Optickle [256] simulations [175]. A requirement for the maximum CP motion can be obtained requiring the CP induced power fluctuations to be ten times below the signal corresponding to the design sensitivity. The result, in power recycling configuration, is shown in Fig. 6.6. The effect of the output mode cleaner, that reduces the coupling of the light reflected from the CP, is not taken into account in the simulation.

The simulation in dual recycled configuration is under study.

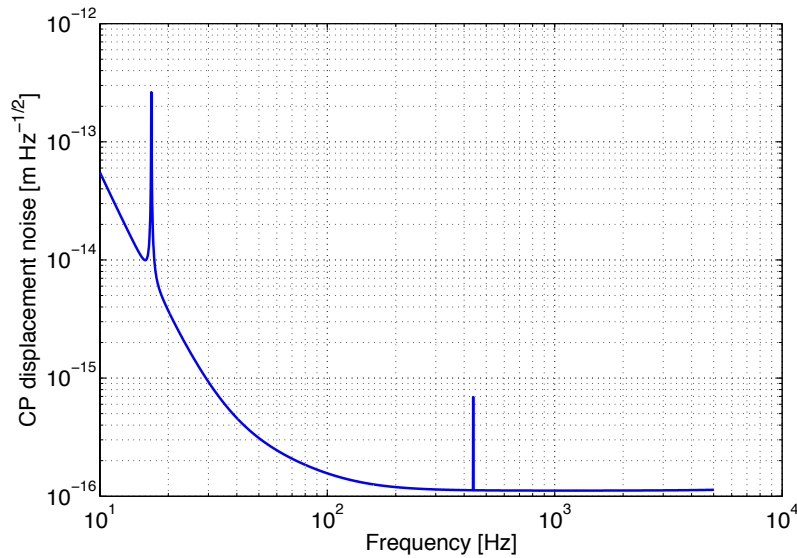


Figure 6.6: Requirement on compensation plate motion, relative to input mirror, corresponding to a safety factor 10 below the design sensitivity. In power recycled configuration.

Alignment

The effects of the presence of a CP on the automatic alignment control system have been simulated by modeling a single cavity with the code Finesse and introducing a 100 ppm mirror behind the NI mirror.

The first effect studied is the CP etalon effect, considering the case with no wedge. The etalon tuning produces a very small optical gain variation on the automatic alignment error signals, of the order of 1 per thousand.

To study the effects of the CP misalignment with respect the North Input (NI) mirror, a wedge of $3 \mu\text{rad}$ has been used. The major consequence of using a wedged compensation plate arises when the face of the CP looking at the FP cavity is slightly misaligned with respect the NI HR face. The misalignment produces an amount of higher order modes which corresponds to a nonnegligible cavity mirror misalignment. If we lock the cavity, longitudinally and angularly, a CP front face misalignment induces the Automatic Alignment control loop to misalign the cavity mirror, as it is shown in Fig. 6.7, of about 6 nrad for a $50 \mu\text{rad}$ of CP misalignment. It has to be noticed that this effect disappears for CP misalignment larger than 0.1 mrad, thus in order to avoid it the CP front face should be misaligned, with respect the NI front face, more than that. The thermal effects on the CP mirror, which essentially modify the RoC of the CP to $\sim 2700 \text{ m}$, when the ITF is operated at full power, do not introduce significant variations on the previous results.

From the above considerations, a tilted CP must be used. The tilt of $750 \mu\text{rad}$ reported in the OSD chapter satisfies this requirement.

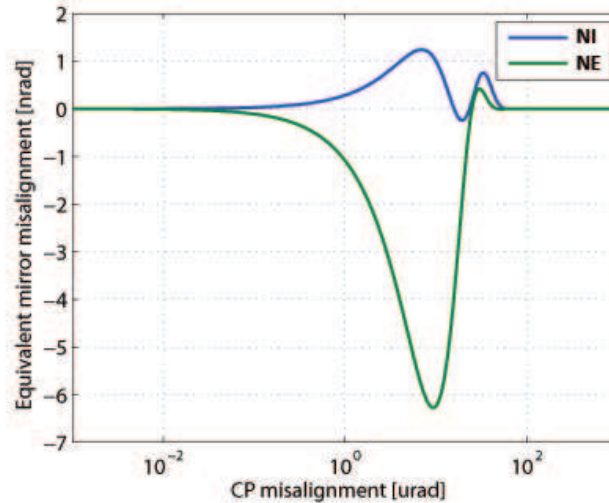


Figure 6.7: Effect of the CP front face misalignment on the automatic alignment error signal, which produce an equivalent cavity angular displacement up to nrad. The solution is to angularly displace the CP front face more than 0.1 mrad with respect to the ITM front face.

6.5 TCS actuators: ring heater

The general requirements for the RH are the following:

- it must provide a correction for the HR surface of the TMs with the required dynamics and precision (see Tab. 6.1). This correction will be used to compensate the thermoelastic deformation due to the YAG absorption and to provide a static curvature correction of the core optics RoCs due to possible fabrication errors (see section 6.8). The input mirror ring heaters also provide limited compensation of thermo-optic effects in the recycling cavities. The possibility to use the Ring Heater (RH) to tune transverse mode frequencies away from parametric instabilities [176] has been highlighted in the past, but no detailed study has been yet finalized.
- it must provide a correction for the RoCs of the RC mirrors (see Tab. 6.1);
- it must be compatible with high temperature operation under vacuum;
- the noise introduced must be compliant with the AdV sensitivity curve;
- it must radiate mainly toward the optic and minimize the interactions with the surrounding hardware.

6.5.1 Ring heater design guidelines

A simple ring heater is a very inefficient solution, since only a small fraction of the emitted power reaches the optic. By adding a reflecting shield around the ring heater, the amount of emitted power reaching the mirror will increase, thus decreasing the required total emitted power. This behavior has been checked with a simple Zemax [303] simulation. The dimensions of the RH have been chosen in order to guarantee a good radiative coupling with the optic.

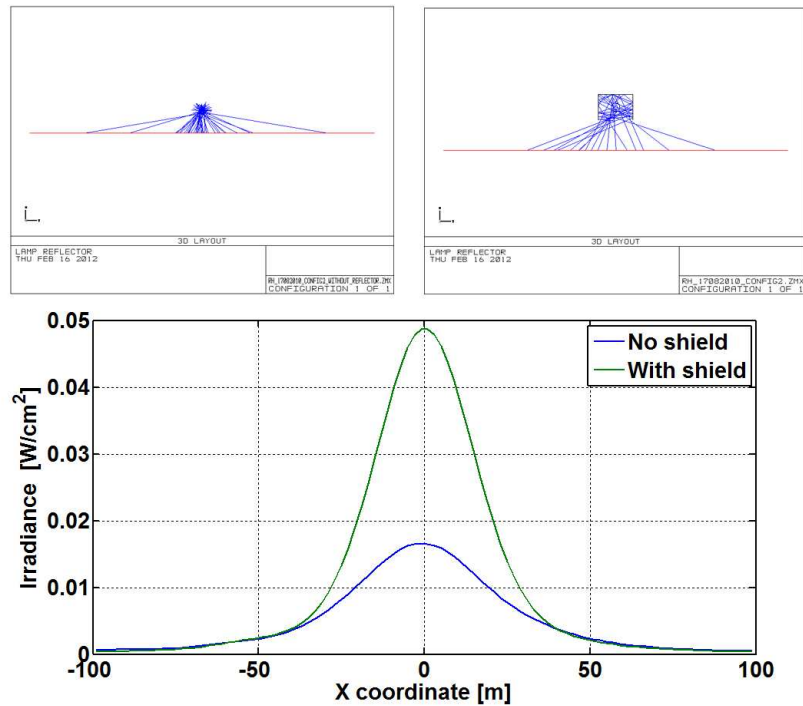


Figure 6.8: Zemax simulation of a radiating element. Up: ray tracing for a simple RH (left) and for a shielded radiating element (right). Bottom: comparison of the two power distributions on the barrel. With a reflecting shield, the power reaching the optic increases by a factor of 2.

As a case study, a ring with an internal diameter of 370 mm and a thickness of 5 mm has been considered. The results are shown in Fig. 6.8. It can be seen that for the same emitted power, the shield makes the RH more effective, with a consequent increase of its dynamics. The presence of the reflecting shield also reduces the heating of the surrounding structures.

From the Zemax simulation it is found that the intensity profile of the radiation reaching the optic has a Gaussian shape (see Fig. 6.9).

In order to study the RH dynamics, an ANSYS coupled thermostructural finite element analysis has been developed. The model considers a Gaussian intensity profile, heating for example the barrel of the TM. The result is reported in Fig. 6.10 and shows the RoC change as a function of the position of the RH along the barrel of the TM and of the deposited power. As it can be seen from Fig. 6.10, a ring heater placed along the barrel of the TM can only decrease the RoC. Instead, the thermal lensing introduced by the RH on the TM substrate is independent from the RH position.

From the figure it is clear that, to have the highest dynamics (-1.6 m/W), the position of the RH around the TM must be set to about 18 cm from the HR face. In this case, the RH power needed to compensate the thermoelastic deformation at full ITF power is about 28 W for the ITM and 14 W for the ETM. The residual deformation of the ITM HR face is shown in Fig. 6.11, that can be compared with the right plot in Fig. 6.2.

The dependence of the heating pattern from the geometry of the RH and of the reflecting shield has been investigated with Zemax. Both parabolic and rectangular profiled shields have been considered and no relevant difference has been put in evidence on the efficiency

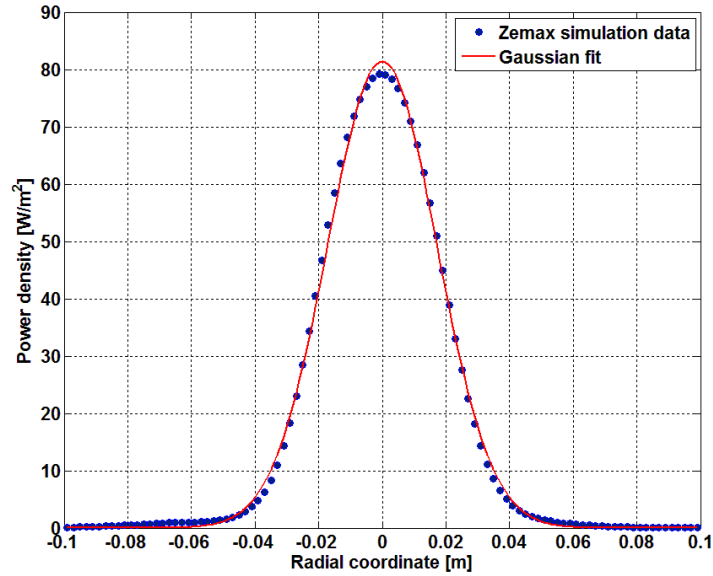


Figure 6.9: Intensity profile (blue dots) on the barrel of the optic together with a Gaussian fit (red line).

of the shield itself. Thus in the simulations a rectangular profile has been used, changing the main parameters of the system: dimensions of the shield (D and d), distance of the RH from the TM (H) and its thickness r and distance between the RH and the shield (h) (see Fig. 6.12).

Table 6.3 reports the parameter space investigated. Also a configuration with a rectangular RH transversal section has been studied.

The Zemax result shows in Fig. 6.13 the dependence of amplitude and size of the heating pattern on the geometrical parameters. However, what is most important is that the RH dynamics is negligibly affected by its geometrical parameters in the interval investigated (see Fig. 6.14).

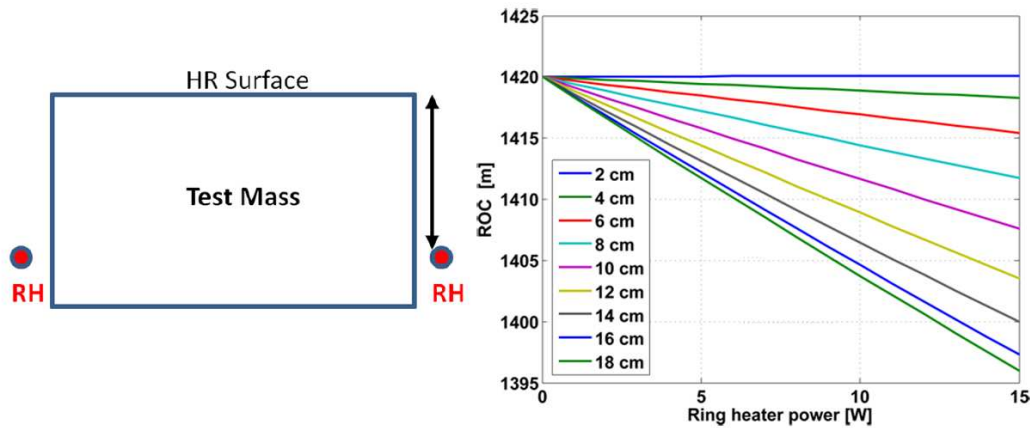


Figure 6.10: Left: scheme of the positioning of the RH along the barrel of the TM. Right: plot of the RoC of the TM as a function of the power deposited by the RH at different positions along the TM side.

This leaves some flexibility in the design of the RH and allows to choose the geometry in order to take into account practical aspects that can ease the construction and installation, such as the thickness that plays a role in the working temperature (see Fig. 6.15) and robustness.

Two designs are at present being used for the production of a full scale prototype: a RH with a glass former and a RH with an aluminum support coated with electrically insulating material. A non conductive support is necessary because no insulated wire has been found with the required mechanical properties and high vacuum compatibility [177].

Two designs have been studied to allow different winding geometries: a toroidal winding around the glass former with a circular cross section and an annular winding around the aluminum core with a rectangular cross section (see Fig. 6.16 for an example of the two winding geometries). The two winding geometries can provide different features in terms of temperature profile, deliverable power, operating temperature. Both must be assembled in counter flux configurations in order to minimize the stray magnetic field (see section 6.7.2).

The wire must satisfy the following requirements:

- a resistivity compliant with the delivery of the needed power (the maximum current is limited to 1 A due to the size of the cables through the conductance pipe of the intermediate vacuum chamber);
- weak dependence of the resistivity on the temperature;
- mechanical properties that make it suitable for winding around the support.

Three possible materials meet the requirements: manganine, nichrome and phosphorus bronze. They will be tested on the two different supports for the final selection. Optimization of the reflecting shield around the RH and of the thermal contacts between the RH and the shield is in progress using the down scaled prototypes already built: measurements are performed on the temperature profile of the RH and on the thermal coupling with the shield and will be compared with the thermal model to take into account the geometry of the mirrors (presence of the flats and suspension wires).

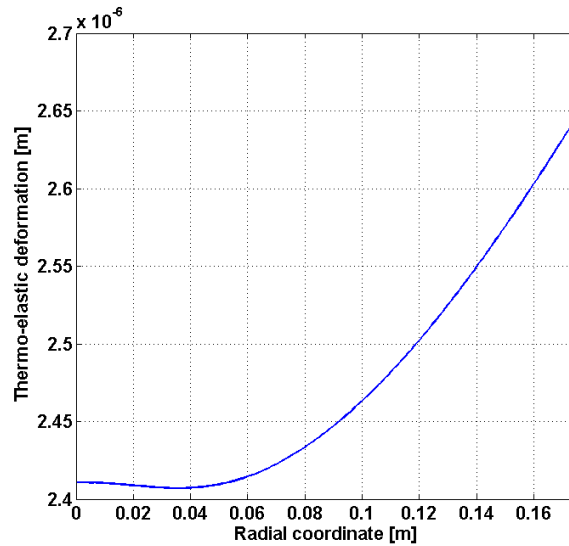


Figure 6.11: Residual thermoelastic deformation of the ITM HR face for the interferometer at full power and the RH on (28 W deposited on the TM). This profile corresponds to a Gaussian weighted RoC of about 1420 m.

Since both designs are compatible with the noise requirements (see section 6.7.2), the down-selection of the RH model will be done on the basis of the results of the measurements on the two prototypes in terms of temperature profile, reliability, and integration in the payload structure. Definition of the mounting of the RH around the mirrors and electrical cabling is in progress in collaboration with PAY.

6.5.2 Vacuum compatibility

The glass former does not present any issue regarding the vacuum compatibility.

In order to validate the design with the aluminum support, samples have been coated with alumina through a plasma spray deposition process. Three samples (see Fig. 6.17) of Al

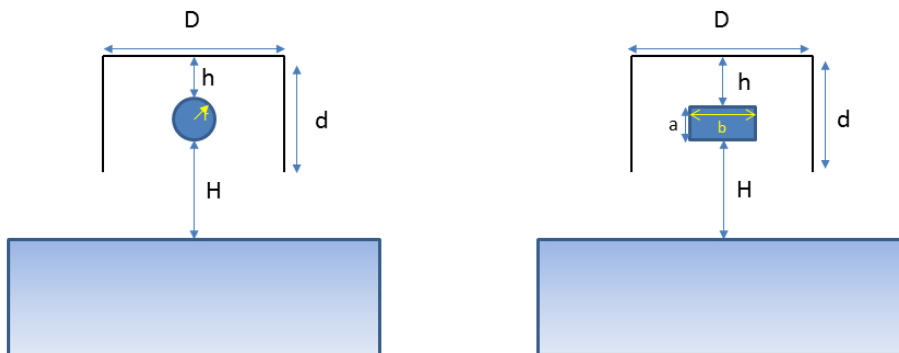


Figure 6.12: Schematic of the RH geometrical parameters.

| Configuration number | r (cm) | D (cm) | d (cm) | h (cm) | H (cm) |
|----------------------|-----------|--------|--------|--------|--------|
| 1 | 0.5 | 2 | 2 | 0.5 | 0.5 |
| 2 | 0.5 | 4 | 4 | 1.5 | 0.5 |
| 3 | 0.5 | 2 | 4 | 1.5 | 0.5 |
| 4 | 0.5 | 2 | 3 | 1.5 | 0.5 |
| 5 | 0.5 | 2 | 3 | 1.5 | 1.5 |
| 6 | 0.5 | 2 | 4 | 1.5 | 1.5 |
| 7 | 0.5 | 4 | 4 | 1.5 | 1.5 |
| 8 | 0.5 | 2 | 2 | 1.5 | 1.5 |
| 9 | 0.3 | 2 | 1 | 0.5 | 0.5 |
| 10 | 0.3 | 2 | 3 | 1.5 | 1.5 |
| 11 | 0.3 | 2 | 2 | 1.5 | 1.5 |
| 12 | 0.3 | 2 | 1.3 | 0.5 | 0.5 |
| 13 | 0.3 | 2 | 1.3 | 0.5 | 1 |
| 14 | 0.3 | 2 | 1.6 | 0.5 | 1 |
| 15 | 0.3 | 3.2 | 1.8 | 0.5 | 1 |
| 16 | 0.3 | 4 | 2.5 | 1.5 | 1 |
| Configuration number | b; a (cm) | D (cm) | d (cm) | h (cm) | H (cm) |
| 17 | 1; 0.6 | 2 | 2 | 0.5 | 1.2 |

Table 6.3: Geometrical parameters of the investigated configurations

coated with alumina (coated surface: around 62 cm²) have been tested up to 180°C in order to check their outgassing rate and possible released pollutants in vacuum. The outgassing rates proved to be sufficiently low for the foreseen purpose and Residual Gas Analyzer (RGA) spectra showed no major pollution due to the samples, even at high temperatures [178].

6.6 TCS actuators: CO₂ laser projector

The TCS CO₂ projectors will provide correction for optical aberrations in the recycling cavities by shining the appropriate heating pattern on the compensation plates. The requirement set by OSD on the residual optical path length RMS is 2 nm, as shown in Tab. 6.1. Since optical aberrations have both an axisymmetric and a nonsymmetric contribution, the TCS strategy to compensate for these aberrations is to use a double axicon² system for the symmetric part and a scanning system for the residual distortions (see sections 6.6.1 and 6.6.2).

²An axicon is a type of lens with a conical surface

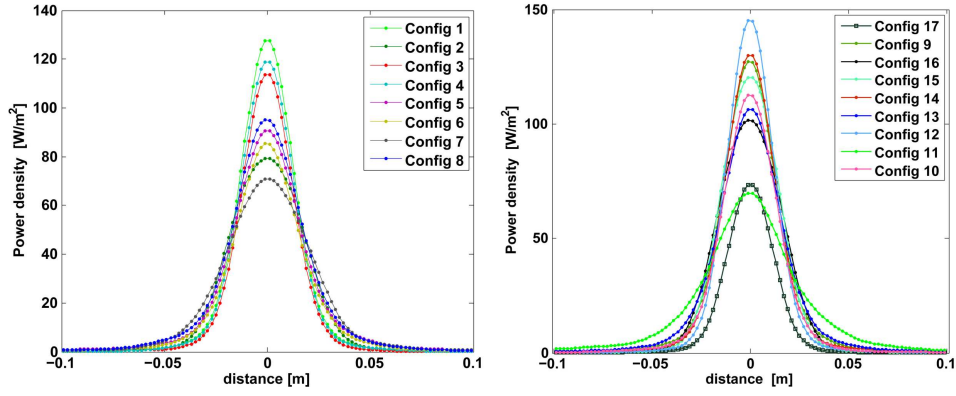


Figure 6.13: Intensity patterns for the configurations investigated. Config 17 refers to a rectangular RH.

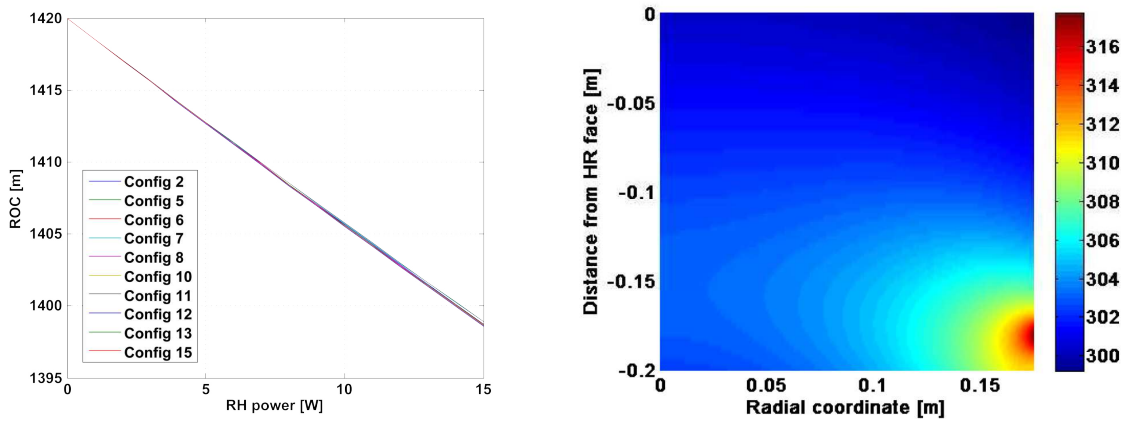


Figure 6.14: Left: RoC as a function of the RH power for some of the different configurations. It is important to note that the dynamics is not affected by the geometrical parameters in the range investigated. Right: example of temperature distribution inside the TM for 20 W heating power.

6.6.1 Axisymmetric compensation: Double Axicon System

Heating pattern

Optical simulations have shown that the heating profile generated by a single axicon (as in Virgo and LIGO) is not the optimal one for the correction of axisymmetric defects (see for example [168, 179] for the investigation in case of thermal lensing). This is due to the heat loss via radiation from the barrel of the optic. The optimum correction pattern for axisymmetric aberrations has been determined using an ANSYS based linear iterative optimization process. The code makes use of the Optical Path Length (OPL) increase (ΔOPL) as error signal, and calculates at each iteration the next step heating pattern from the previous one and from the corresponding OPL increase:

$$H_{path}(n+1) = H_{path}(n) + K_L \cdot \Delta OPL(n), \quad (6.5)$$

where H_{path} is the CP heating pattern and K_L is the loop gain. The procedure is applied to the complete system made of ITM, CP and RH. The improvement with respect to previous

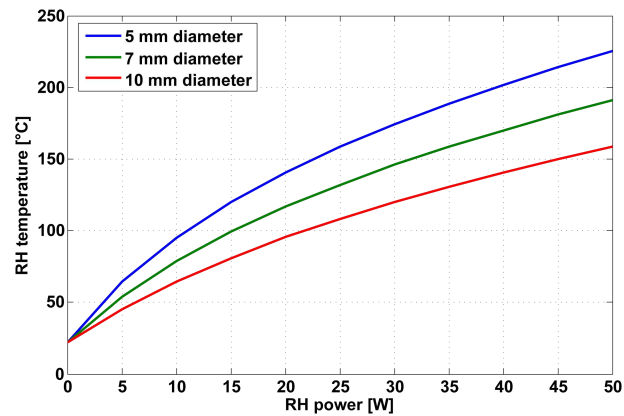


Figure 6.15: RH temperature as a function of the emitted power for three different thicknesses.

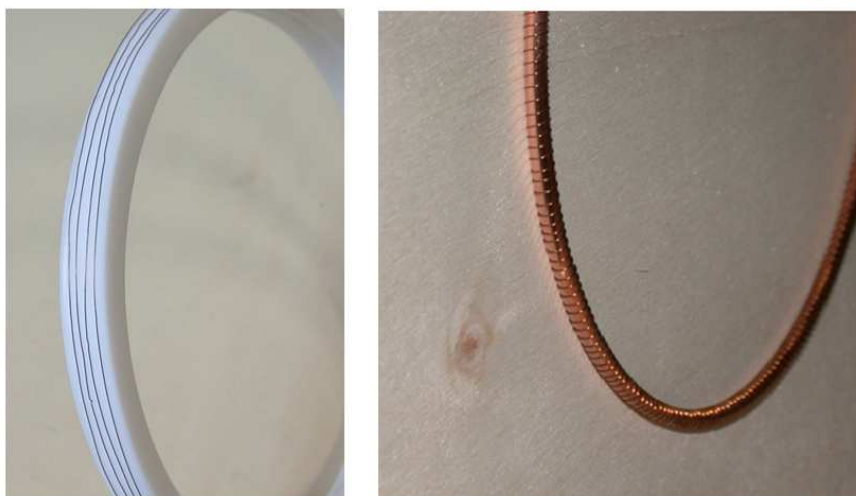


Figure 6.16: Pictures of the RH prototypes with the different winding geometries.

heating pattern optimizations [168, 180] is that this computation takes into account the presence of the ring heater and the radiative coupling between CP and TM.

An example of the optimized heating pattern and optical path length increase is shown in Fig. 6.18 for thermal effects at 125 W input power. The corresponding residual coupling losses amount to 6 ppm for an RMS of 0.4 nm. The total CO₂ power needed is about 18 W.

The solution chosen for the AdV TCS CO₂ projector is based on known technology and allows to approximate the optimized heating pattern by combining the action of two axicon generated heating patterns [181].

Figure 6.19 shows a conceptual design of the Double Axicon compensation System (DAS). A linearly polarized CO₂ beam passes through a $\lambda/2$ plate that rotates the incident polarization. A fixed polarizer splits the incident polarization into two orthogonal components. Thus each of the two beams goes through a non-polarization-rotating power control, a focusing lens and an axicon. The beams are then recombined using a polarizer. This setup assures that there would be no interference between the beams at recombination. Each axicon pattern can be freely modified by changing the distance of the focusing lens from the axicon itself. With



Figure 6.17: Picture of the Al samples tested for the high vacuum compatibility. Sample 1: rectangle of 10 cm × 1 cm × 0.5 cm, with etched grooves for the wire winding. Sample 2 and 3: ring section - curved length about 21 cm, width = 1 cm, height = 1.5 mm. Coating thickness is 0.10 mm for samples 1 and 2 and 0.15 mm for sample 3. The maximum voltage applicable to this coating is about 140 V/ 0.1 mm.

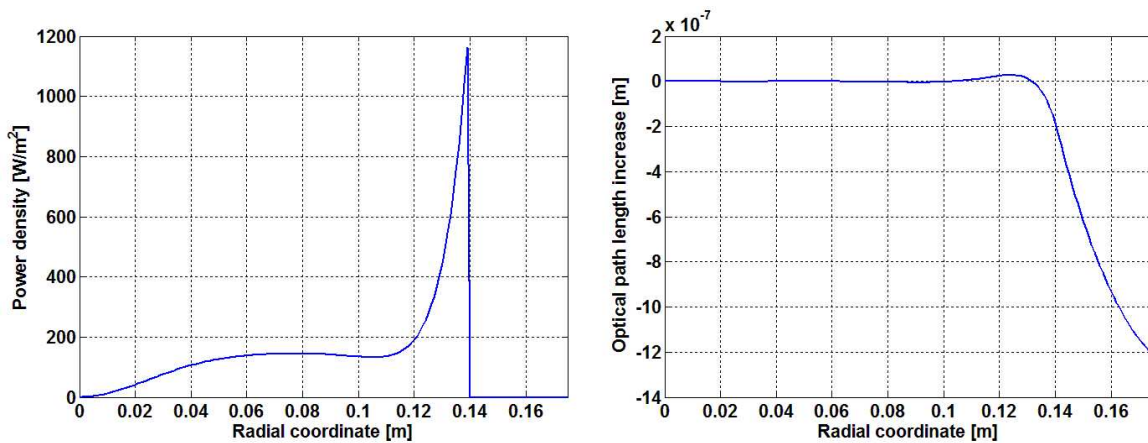


Figure 6.18: Left picture shows the optimized heating pattern. Right: the corresponding optical path length increase.

such a setup it is possible to generate a heating pattern that approximates the optimal one, as shown in the left plot of Fig. 6.20.

The right plot in Fig. 6.20 shows a comparison of the OPL increase for the optimized heating pattern, single and double axicons systems; the improvement of the DAS with respect to the single axicon can be expressed in terms of a factor of 10 lower coupling losses (about 300 ppm instead of 3000). The RMS computed with the DAS compensation amounts to 3 nm. The DAS can correct all kinds of axisymmetric aberrations: not only thermal lensing, but also the symmetric contribution of cold defects, such as the inhomogeneity of the substrate refraction index [173]. The extra CO₂ power needed to compensate the axisymmetric contribution of the cold map defects shown in Fig. 6.4 is about 2 W.

Optical layout

The preliminary optical layout of the AdV TCS DAS projector is shown in Fig. 6.21.

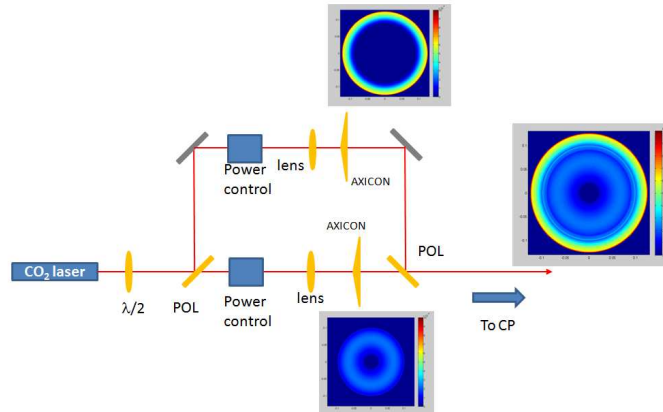


Figure 6.19: Conceptual design of a double axicon compensation system.

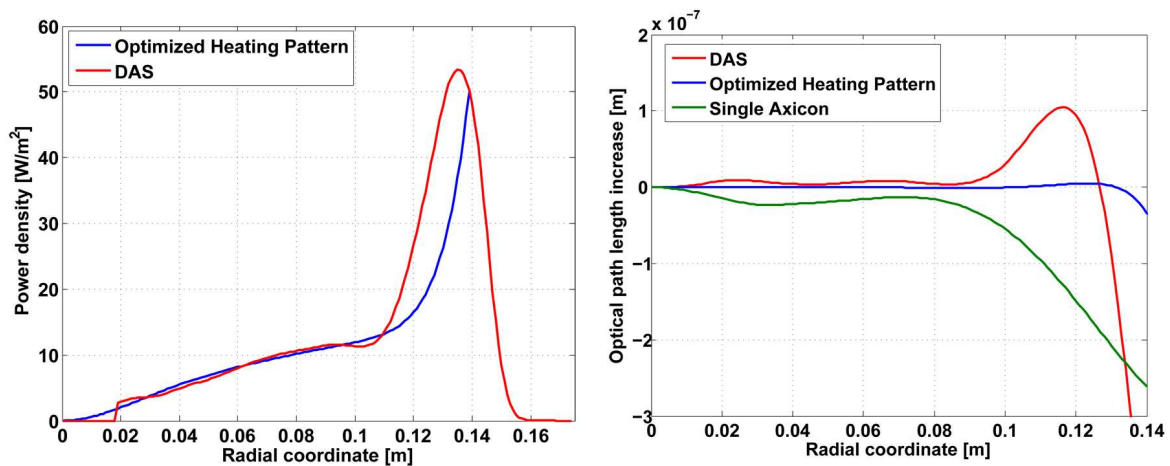


Figure 6.20: Left: the double axicon heating pattern (red) compared to the optimized heating pattern (blue). Right: corresponding optical path length increase (optimized heating pattern is in blue and the DAS is in red). Also the OPL given from a single axicon system (green) is reported for comparison.

The layout includes a laser intensity stabilization system, made of an Acousto-Optic Modulator (AOM) and two photodiodes, to make the noise compliant with the AdV sensitivity (see section 6.7.1). An automatic alignment system (galvo or piezo mirror and a quadrant photodiode) will minimize pointing instabilities and jitter noise. A telescope will collimate the beam, mostly to ease the delivery of a part of the beam to the scanning system. For this reason a partial reflector is placed before the arms of the Double Axicon System (DAS). The beam is then split by polarization into two arms. The power in each arm is controlled independently with a $\lambda/2$ wave plate and polarizer pair. Measurement of the power in each arm is performed by placing a power meter on the reflected/transmitted beam of the polarizer. This scheme is intended to maximize the power efficiency of the bench. A focusing lens and one axicon lens (each placed on a three axis motorized linear translation stage) will provide control over the geometrical parameters of each ring (inner and outer radii, intensity distribution). A polarizer will be used to recombine the rings from the two arms. An optical system will then image the pattern after the polarizer on the compensation plate. The quality of the heating pattern is monitored by a high sensitivity infrared camera. A cross hair red laser will be

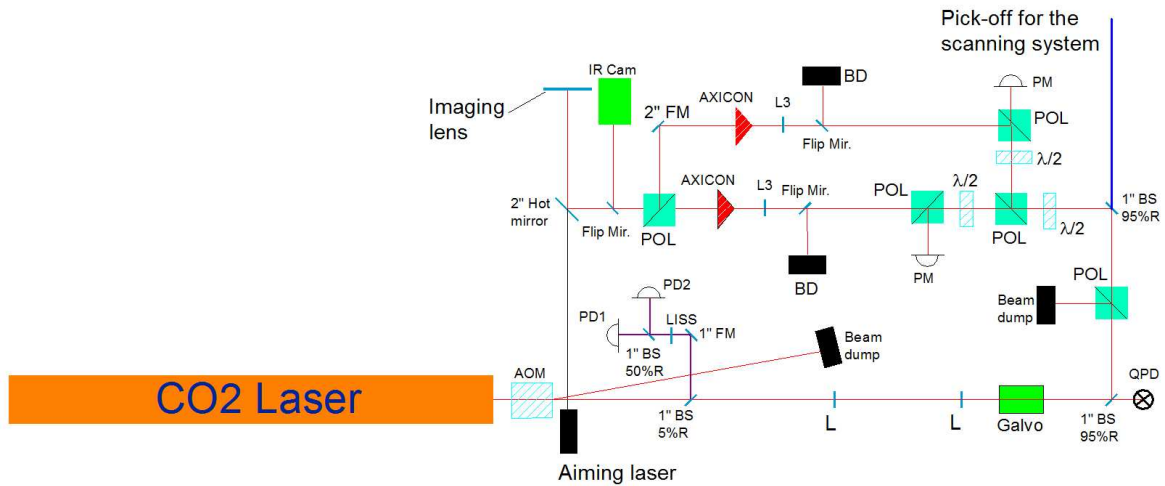


Figure 6.21: Optical layout of the AdV TCS benches using a double axicon system to generate the CP heating pattern.

superposed to the CO_2 beam through a dichroic mirror for the coarse alignment of the DAS onto the compensation plate. All the optics crossed by the CO_2 beam are in ZnSe. All the mirrors are gold coated with silicon substrates to handle the high impinging power.

The access of each CO_2 beam is through a viewport located on the vacuum links between Beam Splitter (BS) and input towers (Fig. 6.22). The bench close to the links will also house a remotely controllable steering mirror and the scanning system hardware. The steering mirror will be used for the alignment of the CO_2 beam onto the compensation plate. The benches and the pipe between them will be acoustically isolated. From the preliminary design of the links, the angle of incidence of the beam on the CP has been estimated to be about 11° . This angle of incidence generates an ellipticity of the intensity distribution on the CP of the order of 2%. The possibility to use a pair of anamorphic prisms to correct only for the angle of incidence is considered.

As far as the design of the links is progressing, the exact positioning of the benches is defined with some uncertainty. A preliminary design of the imaging system has been developed with Zemax (Fig. 6.23) using axicons with a base angle of 4.3° , but axicons with different base angles are also being considered to tune the divergence of the beam. In the preliminary design the dimensions of some relevant optics are the following: the imaging lens has a diameter of 4 inches and a focal length of about 150 mm, for a telescope magnification of about 28. The steering optic on the second bench has a diameter of 3 inches. Since this optic will also be used to recombine the DAS to the scanning system, it will be made of a partial reflector 85% R. The viewport on the link must have a minimum clear aperture of 90 mm. As already anticipated above, the beam quality will be monitored with a high sensitivity infrared camera. A flip mirror will deviate the beam towards the camera and an optical system will image it onto the CCD. The device selected is the LaserDec 500 from Cinogy Technologies. With respect to the Spiricon camera used in Virgo, the LaserDec has the following advantages:

- higher spatial resolution;
- high power operation;

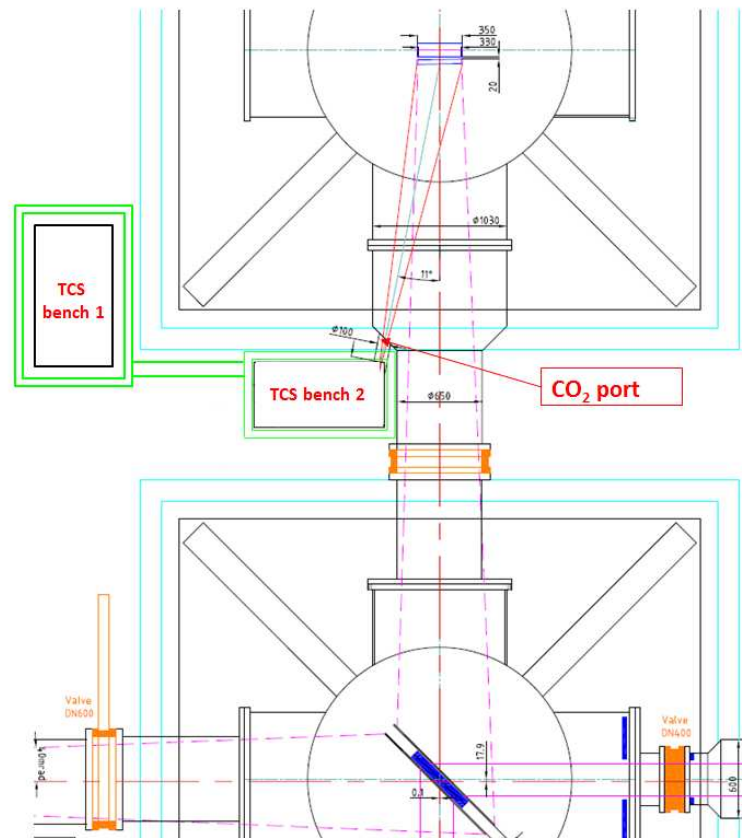


Figure 6.22: Sketch of the position of the CO₂ benches (not in scale) in the central building.

- no moving parts: the Spiricon has a chopper running at 24 Hz, evidence for a noise line at this frequency in the DF spectrum has been reported several times in the Virgo Logbook and the camera has always been kept off during science mode.

As a consequence of the capability of the LaserDec to handle high power, the layout of the monitoring system has been modified with respect to the Virgo TCS (see Fig. 6.21). This allows to correct the main issue of the Virgo setup: the annular beam was passing through a high reflectivity partial reflector and, as a consequence, the intensity distribution on the CCD was not representative of what was being imaged on the ITM.

An analysis of the power lost by the DAS is used to evaluate the total power required by the CO₂ laser projector. About 10% is absorbed and 5% is diffracted by the acousto-optic modulator; 15% is picked off and sent to the scanning system; 15% is lost at the partial reflector that recombines the DAS with the scanning system and about 12% is reflected by the CP. Also, about 2.5 W are required for the intensity stabilization servo photodiodes and about 0.2 W are needed for the quadrant photodiode of the automatic alignment system. The losses in the other optical elements are negligible. If we assume that the CO₂ laser delivers 50 W, this means that about 28 W are available for the DAS. From simulations, the power required to compensate 1 ppm coating absorption at 125 W ITF input power is about 18 W. Thus, with a 50 W laser, the DAS has a safety margin of about 50% with respect to increase in coating absorptions.

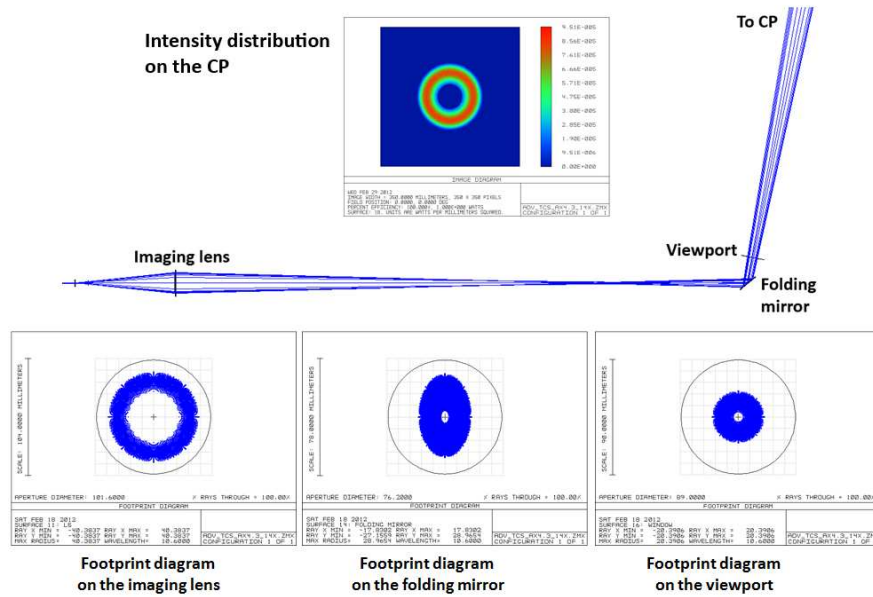


Figure 6.23: Zemax layout of one of the arms of the DAS together with the footprint diagrams of some relevant optics.

The laser selected for the AdV TCS CO₂ projector is the LASY-50 from Access Laser Company³, capable of delivering up to 50 W CW. The LASY-50 has an internal system for power stabilization: the length of the Radio Frequency (RF) cavity is actively controlled with a piezo actuator. Moreover, the RF drivers of all the CO₂ lasers will be fed by an external generator with the same RF frequency, thus avoiding those beatings that, in Virgo, have introduced lines in the noise spectra of the lasers and on the Virgo dark fringe spectrum.

The Virgo+ TCS has shown that the CO₂ laser is very sensitive to temperature fluctuations, both in the laser itself and in the laser housing. Figure 6.24 shows the typical temperature driven instabilities observed on one of the Virgo TCS benches.

Drifts of the laser beam have been observed for temperature variations of about 1°C. These cause a misalignment of the beam on the axicons, resulting in a change of the heating pattern on the test mass.

For these reasons, each of the AdV CO₂ laser will be equipped with a dedicated high precision (0.01°C) chiller. A separate chilling machine will be used to cool beam dumps and AOMs. Inclusion of the laser into a thermalized box is being considered.

6.6.2 Nonsymmetric compensation: scanning system

Heating pattern

To compute the corrective pattern to compensate for the residual non symmetric defects, the same algorithm developed for DAS has been used by extending it to 3D [182]. The

³This is the same vendor that provided the CO₂ lasers for Virgo+, that have proven to have a good reliability over the three years of almost continuous operation.

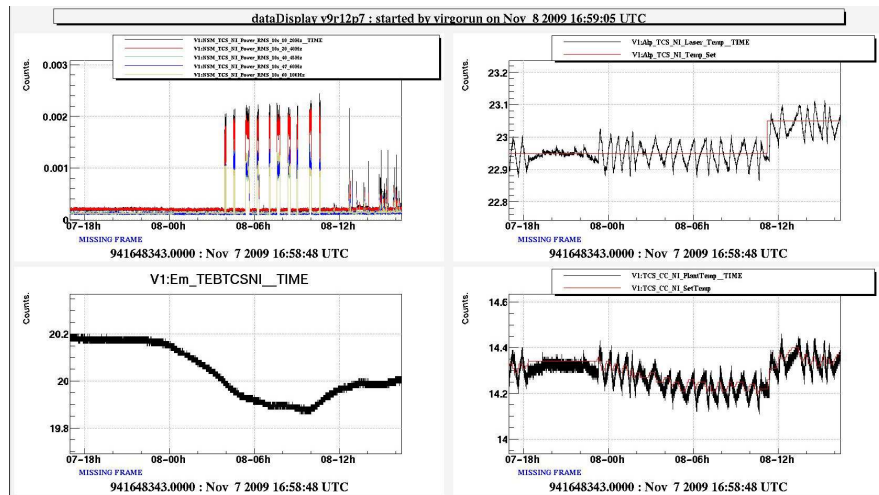


Figure 6.24: Up left: plot of the RMS of the laser noise. Up right: laser body temperature. Bottom left: acoustic enclosure temperature. Bottom right: chiller temperature.

study has been carried on with two sets of maps with cold non symmetric defects, provided by LMA. Since from optical simulations [181] it turns out that the OPL must be flattened within a radius of 8 cm (for a 5 cm waist probe beam), the analysis has been carried out on a 16 cm by 16 cm area with a scanning spot 1 cm in diameter. The results of the optimization procedure show that the residual optical path length RMS is reduced by a factor of 20 for spatial frequencies below 40 m^{-1} [182] and amounts to 0.35 nm, within the requirements set by OSD. The corresponding coupling losses are about 7 ppm. An example of the results of the optimization procedure are shown in Fig. 6.25, where also the effect of non uniform absorptions at 25 W has been included. As the main contribution to non symmetric aberrations comes from the substrate inhomogeneity, this result is well representative also for higher input powers.

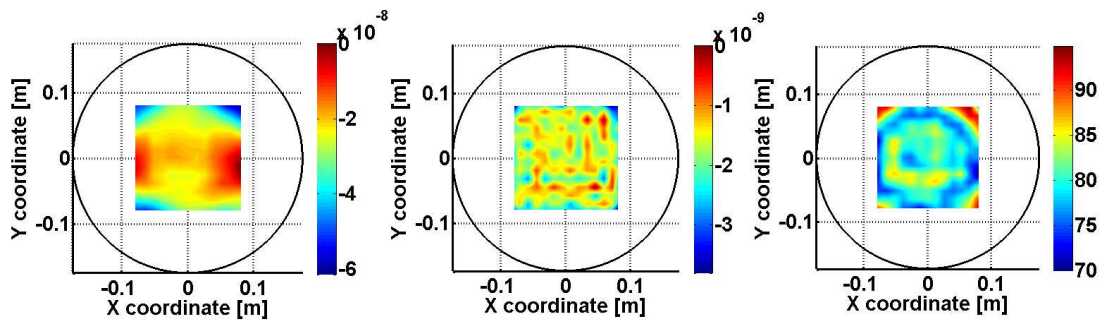


Figure 6.25: Left image: optical path length increase due to coating non uniform absorptions for 25 W ITF input power, substrate residual inhomogeneity and mirror figure error. Peak-to-valley is about 60 nm. This represents the residual optical path length after the correction provided by the DAS. Centre image: residual optical path length after the correction with the heating pattern shown in the right picture; the peak-to-valley is about 3.5 nm. Right image: heating pattern to be applied on the CP to correct for the optical path length shown in left image. The color scale is in W/m^2 . The total integrated power is about 2 W.

Since the scanning system is used only to correct the residual nonsymmetric defects, the total

power needed for the compensation is small (a few Watts). Moreover, the scanning system has a high degree of flexibility and can be easily adapted to the needs of the ITF.

Optical layout

As mentioned above, the scanning system hardware will be hosted on the TCS bench located near the vacuum links. Figure 6.26 shows a very simple schematic of the hardware.

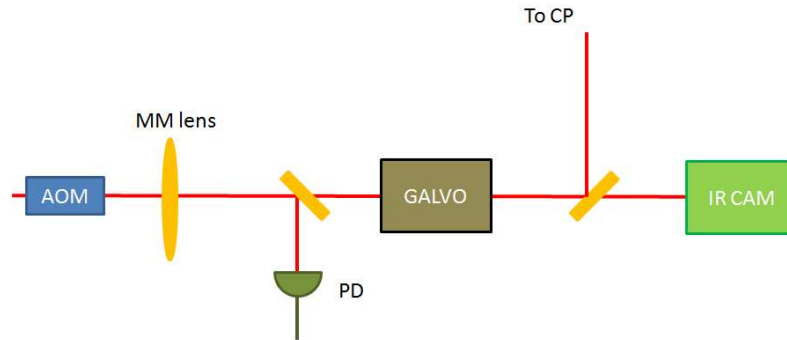


Figure 6.26: Schematic of the scanning system hardware.

The modulation of the power in each scanning spot will be provided by an acousto-optic modulator⁴ and measured by a photodiode. In fact, since the scanning frequency is of the order of a few Hertz, a standard power meter is not fast enough to follow the power variations. At the same time, the AOM has a response time of about 1 ms, thus providing a large enough actuation bandwidth. A mode matching lens will adjust the size of the beam on the CP to about 0.5 cm, same size of the aberrations to be corrected. A pair of galvo mirrors⁵ will be used to "draw" the scanning pattern on the CP. Figure 6.27 shows some examples of possible scanning patterns. As for the DAS, the heating pattern will be monitored by a high sensitivity camera. Investigation to define the optimal scanning pattern is in progress. Finally, the DAS and the scanning system beams will be recombined using the 3 inch partial reflector described above.

6.7 TCS actuator noise

The physical mechanisms responsible for the noise injected by the TCS actuation into the gravitational channel are the following [183]:

- thermorefractive effect: fluctuations in locally deposited heat cause fluctuations in local refractive index;
- thermoelastic effect: fluctuations in locally deposited heat cause fluctuations in local thermal expansion;

⁴The AOM is the same model and brand as those for the CO₂ laser intensity stabilization: AGM-406B1 from IntraAction Corporation.

⁵Instead of galvo mirrors, radiofrequency optical deflectors are being considered to move the scanning frequency to the MHz region.

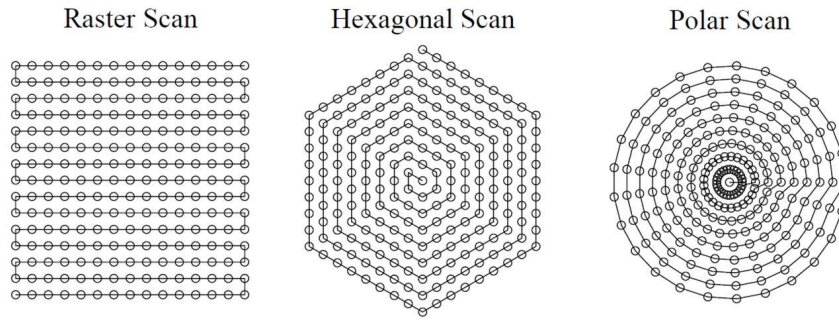


Figure 6.27: Scanning pattern examples.

- flexure: fluctuations in locally deposited heat cause fluctuations in global shape of the optic;
- elasto-optic effect: strain fields associated with flexure change the index of refraction of the optic;
- radiation pressure: variations in the light power change the force on the optic. This has two consequences. The force will compress the optic, and the optic will recoil from the force.

All the above mechanisms are related to fluctuations in the heat deposited on the optic by the actuator. Therefore, they can act both on the CP and the TMs. The relevance of the couplings is different for the two optics due to the different actuators. There are other noise contributions, specific to each actuator, and their relevance will be evaluated in the following sections, deriving the corresponding noise requirements.

6.7.1 CO₂ laser noise coupling

It has been demonstrated [183] that, among the above listed noise sources, the dominant contributions are the thermoelastic and thermorefractive terms that can be evaluated analytically. They act on the CP through the two actuators: the DAS and the scanning system.

Thermoelastic and thermorefractive noise

In the case of the DAS, the noise requirement has been calculated considering a 35 cm diameter CP heated with the optimized heating pattern for 18 W of TCS (ITF at full power). It is compared in Fig. 6.28 with the Relative Intensity Noise (RIN) measured on the Virgo+TCS.

For the scanning system, the RIN requirement has been computed with the following assumptions, consistent with the simulation shown in section 6.6.2:

- the area scanned by the system has a diameter of 16 cm;
- the size of the scanning spot has a radius of $w=0.5$ cm, for a total number of spots equal to 200;
- the map of the injected power is the same as in Fig. 6.25;

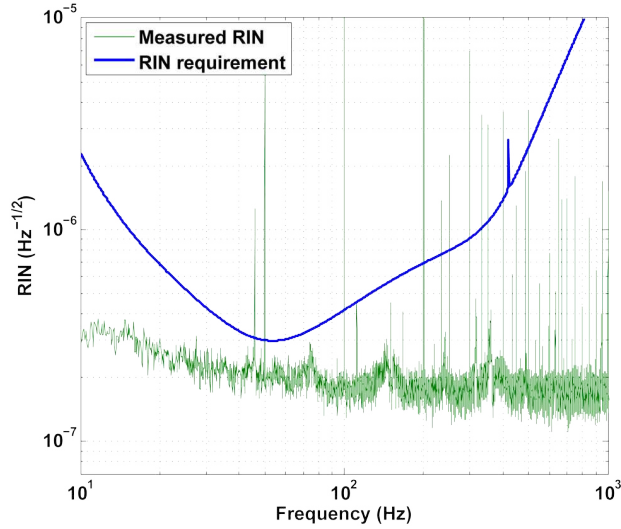


Figure 6.28: DAS noise projection. The blue curve represents the maximum allowed RIN of the CO₂ laser to be a factor of ten below the AdV sensitivity curve. This is compared with the measured RIN in the Virgo+ TCS (green curve).

- pattern repetition frequency equal to 0.05 Hz and laser amplitude modulation frequency of 10 Hz. The repetition frequency is much larger than the typical thermal time constants of fused silica:

$$\tau \sim \pi w^2 \frac{\rho C}{k} \simeq 95 \text{ s} \left(\frac{w}{0.5 \text{ cm}} \right)^2 \quad (6.6)$$

where ρ is the density, C the heat capacity and k the thermal conductivity.

For all the spots in the scanning pattern, the superposition integral with the ITF beam has been evaluated. The RIN requirement, shown in Fig. 6.29, is given for the spot that has the largest superposition integral. In the frequency band 30 Hz-80 Hz, the RIN measured on the Virgo+ TCS is a factor of 8 below the AdV sensitivity, instead of a factor of 10 as required for technical noises. Since the RIN in Virgo+ is limited by the photodiodes dark noise, a reduction factor of $\sqrt{2}$ can be easily gained, if needed, by increasing the number of in loop photodiodes from one to two⁶. In the meanwhile, the photodiode preamplifier is being redesigned to decrease the electronic noise.

The radiative coupling between **ITM** and **CP** would suggest that the CO₂ laser intensity fluctuations act indirectly upon the ITM. However, the time scale for the CP to heat the ITM through radiative coupling is hours and this mechanism must not be considered as a possible noise source.

In the case of the DAS, the dependence of optic infrared absorption with incident angle must be also taken into account, as it converts incident beam jitter into absorbed power fluctuations. From the computation of this noise contribution, the requirement on the CO₂ beam jitter will be derived.

Beam jitter noise

⁶Use of alternative photodiodes (SiAs) to increase the output current is also being considered.

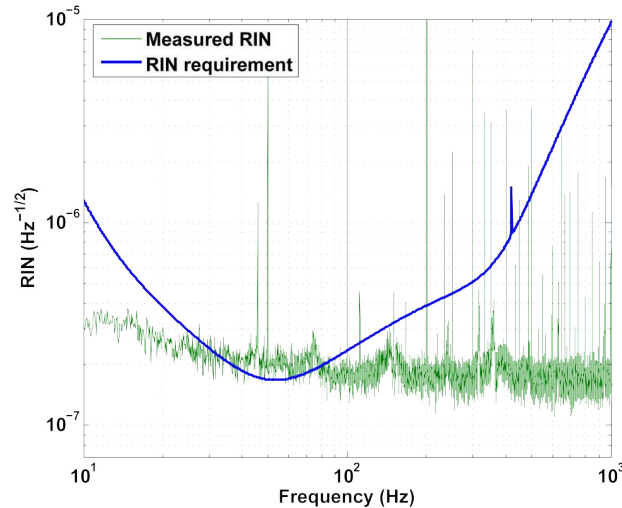


Figure 6.29: Scanning system noise projection. The blue curve represents the maximum allowed RIN of the CO₂ laser to be a factor of ten below the AdV sensitivity curve. This is compared with the measured RIN in the Virgo+ TCS (green curve). A further $\sqrt{2}$ reduction of the measured RIN is easily gained by using two in loop photodiodes instead of one.

A detailed analysis of this noise source can be found in [183]. We will report here the main results. The jitter noise acts through two mechanisms:

- it changes the beam's incidence angle and, since the power absorption depends on the angle of incidence, this translates into fluctuations in the absorbed power;
- it produces displacement of the incident beam that changes linearly with the projected beam distance and this translates into variations of the superposition between the CO₂ and the ITF beams.

We will report in the following the requirements on the CO₂ beam jitter noise for both contributions, in order to be compliant with the AdV sensitivity.

Angular absorption dependence

Figure 6.30 shows the angular dependence of the absorption of the CO₂ beam by the CP. Since the AR coating does not show any absorption peak at 10.6 μm , it is assumed that the absorption of the AR coating is the same as for fused silica.

Since the angle of incidence of the CO₂ beam on the CP is 11°(section 6.6.1), the rate of change of the absorption is about $4 \times 10^{-5}/\text{mrad}$. We take the maximum allowable RIN spectrum from Fig. 6.28 and convert it into maximum allowable angular jitter noise spectrum, using the angular absorption dependence scaled by the overall absorption (about 0.85 for either polarization) as a conversion factor. The resulting spectrum in $\text{mrad}/\sqrt{\text{Hz}}$ is shown in Fig. 6.31. The reflectance of the CO₂ bench gold coated mirrors does not depend on the angle of incidence.

Jitter fluctuations in CO₂-YAG beam overlap

The direct thermoelastic and thermorefractive noise couplings arise because the TCS projector beam overlaps with the interferometer beam. If the TCS beam moves on the CP, the

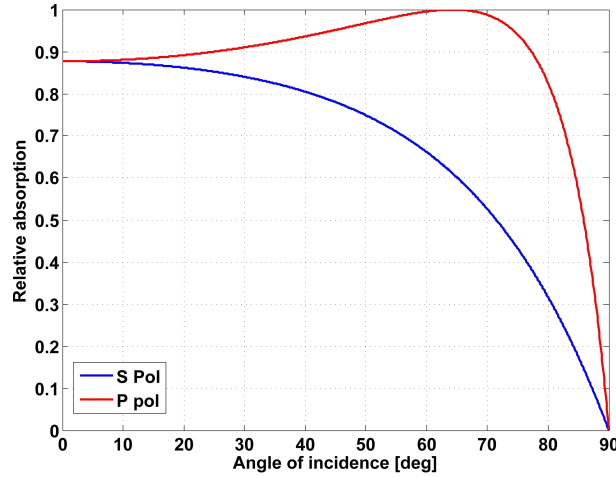


Figure 6.30: Absorption vs. incident angle for $10.6 \mu\text{m}$ radiation on fused silica.

amount of overlap will change. The amount of coupling will depend on the alignment of the TCS beam relative to the interferometer beam. We denote by δ the misalignment of the CO_2 on the CP. Considering as worst case the optimized heating pattern and that the jitter is in the same direction as the misalignment, the variation in the overlap is:

$$90 \text{ W/m}^2 + 3.5 \cdot 10^4 \delta^2 \text{ W/m}^4. \quad (6.7)$$

We can now convert the direct thermoelastic and thermorefractive intensity noise spectrum into a displacement jitter noise spectrum taking the derivative of the overlap function as a conversion factor. That is:

$$\Delta z_{TE+TR} = \left[(n-1)(1+\sigma)\alpha + \frac{dn}{dT} \right] \frac{7.0 \cdot 10^4 \text{ W/m}^4 \cdot \delta}{2\pi i f \rho C} \Delta x, \quad (6.8)$$

where Δx is the displacement jitter amplitude (assumed small compared to the offset δ). Assuming $\delta = 1 \text{ mm}$ and a CO_2 beam path 10 m long, the required beam jitter noise spectrum is shown in Fig. 6.32.

6.7.2 Ring heater noise coupling

The noise considerations made in the following sections are specialized to the TMs case. For the RHs installed on the RC optics the noise coupling is reduced by a factor $\pi/2F$.

The noise introduced on the test mass is due to the fluctuations of the power emitted by the ring heater. Regarding those that imply heat deposition in the TM, the design with the RH around the barrel is less sensitive to power fluctuations than designs that heat the HR surface, because the heating is entirely on the substrate far from the ITF beam. This implies that direct thermoelastic and thermorefractive couplings to the optical path in the substrate of the ITM may be ignored. In fact, the thermal fluctuations penetrate only about $35 \mu\text{m}$ inside the TM [184].

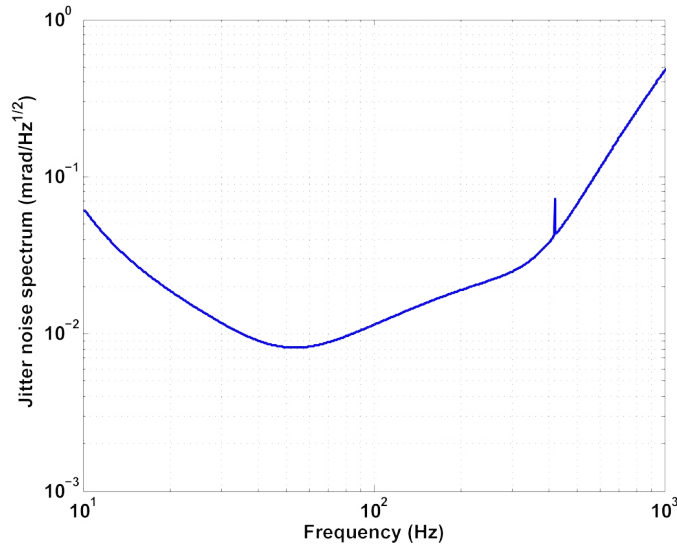


Figure 6.31: Requirement on jitter noise spectrum due to angular dependence of CP absorption of TCS projector light.

The elasto-optic contribution, also in this case, is negligible compared to the others. In fact, its magnitude is of the same order as the flexure noise, but it is injected in the recycling cavity only, thus profiting from the reduction factor $2F/\pi$, due to the arm cavity finesse.

With a RH around the TM, the radiation pressure averages to zero over the test mass, making its contribution negligible.

Regarding the flexure noise, there is a coupling of overall power fluctuations to HR surface displacement. In fact, the ring heater changes the radius of curvature of the test mass's HR surface by flexing the mirror and, since the position of the centre of the HR surface relative to the test mass centre of gravity varies with the flexure, any power fluctuation in the ring heater will create displacement noise. The ring heater thermal inertia will passively smooth power fluctuations on its input supply, thus making it easier to meet the noise requirements. This noise contribution has been evaluated for different RH assemblies [185] and the requirements have been found to be quite feasible even in the most stringent case (maximum power fluctuation about a few $\text{mW}/\sqrt{\text{Hz}}$).

In the case of the ring heater, two more noise sources must be considered: the magnetic and the electrostatic noise.

Magnetic stray field coupling

To characterize the magnetic stray field, down scaled RH samples with different winding density have been produced in the two geometries: annular and toroidal windings, both in counterflux configurations. Measurements of magnetic field maps *vs.* position and magnetic field *vs.* frequency have been performed. The annular winding geometry has also been simulated (with Opera-3D ⁷) and the results have been compared with the experimental data showing excellent agreement (see Fig. 6.33). This check has allowed the use of a simulated

⁷This is a finite element environment for the complete analysis of electromagnetic applications in 3 dimensions by Cobham CTS Limited (USA).

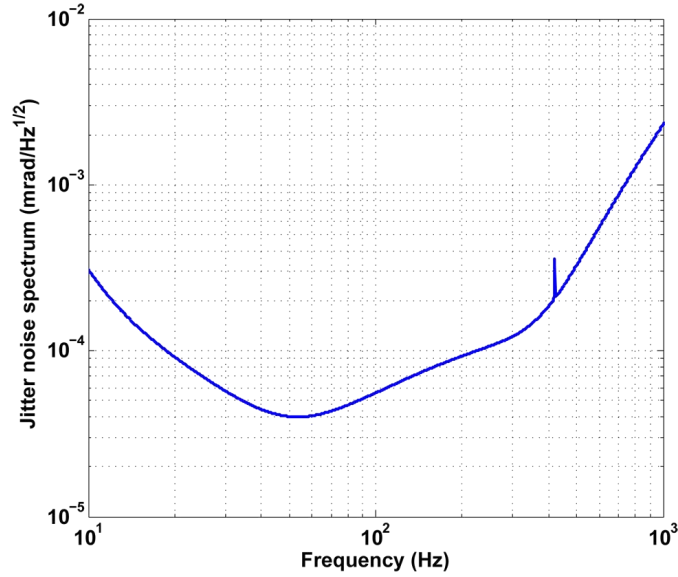


Figure 6.32: Requirement on jitter noise spectrum due to transversal displacement of the TCS projector light if 1 mm misalignment is assumed. The requirement scales linearly with δ .

full scale RH to make an evaluation of the noise projection due to the magnetic stray field. This translates in a requirement on the noise level of the RH power supply. The results show that a current noise of $1 \text{ nA}/\sqrt{\text{Hz}}$, that can be easily achieved, keeps the magnetic noise well below the AdV sensitivity [186]. Since the measurements on toroidal winding geometry in counterflux configuration give the same order of magnitude values, both configurations are suitable for AdV in terms of magnetic noise.

Electrostatic coupling

The ring heater is essentially a wire with a voltage gradient held in proximity to the test mass. Therefore, it will exert an electrostatic force on the test mass. If the voltage is fluctuating, then the electrostatic force too will fluctuate and inject displacement noise into the interferometer. The electrostatic force can be exerted along the longitudinal or transversal directions or as a torque. Computation of the voltage noise requirements has been done in [183] and shows that the most stringent requirements come from the longitudinal component, but also in this case they can be easily met, as the maximum allowed voltage fluctuation is about $10^{-3} \text{ V}/\sqrt{\text{Hz}}$.

6.8 "Cold RoC" Correction

In the following we describe the solutions needed to correct the possible fabrication errors in the RoCs exceeding the OSD requirements. In fact, the accuracy of the RoC after polishing will not be better than $\pm 10 \text{ m}$ while that required by OSD is $\pm 2 \text{ m}$ for the TMs and $\pm 8 \text{ m}$ for RC mirrors (see Tab. 6.1). We will set in the following the specifications for the RoC of the ITF mirrors, compatible with the TCS actuation, that must be met after all the fabrication

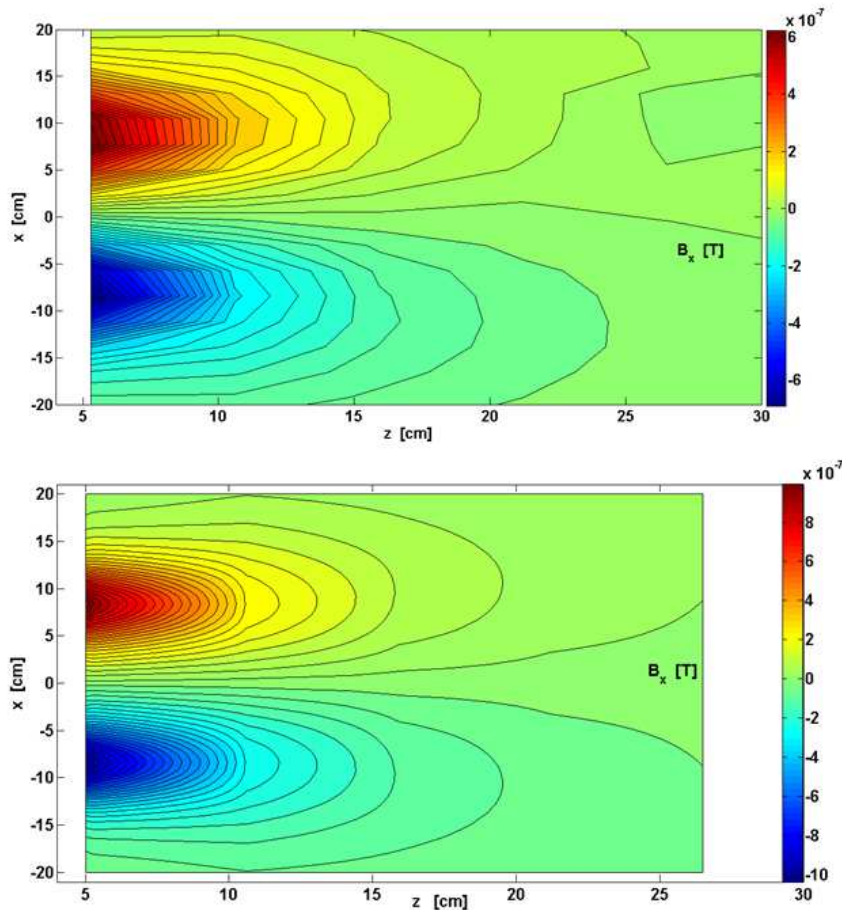


Figure 6.33: Comparison of the measured (upper) and simulated (lower) z component of the magnetic field due to 1 A circulating in an annular geometry with 3+3 counter flux windings. On the horizontal axis the distance from the RH plane is reported and on the vertical axis the radial distance from the centre. The amplitude of the magnetic field is given by the color scale, the range is 10^{-7} T.

process (coating included ⁸).

There are several ways to heat an optic in order to change its RoC. They have been all modeled and their dynamics evaluated [187, 188]. The result shows that the most efficient and viable are: central heating on the HR face and RH around the barrel of the optic. The main differences between the two are that the central heating increases the RoC, while the RH decreases it. The central heating requires less power than the RH to change the RoC by the same amount, but it produces a larger deviation from sphericity in the deformed surface. We will discuss in the following the most suitable choice for the different optics.

ITMs

In the case of the *ITMs*, the choice of the most appropriate strategy to correct the RoC must take into account that the actuator will also introduce thermal lensing. The central heating would add a thermal lens of the same sign as that due to the YAG thus increasing the thermal

⁸The coating process may change the RoC by ± 5 m, depending on the technique used (planetary motion or double mirror process)

effects in the ITF. For central heating, the amount of power required to cover the dynamics depends on the size of the heating beam (defined as the waist of a Gaussian beam): the smaller the beam, the smaller the required heating power. However, smaller beams introduce larger deviations from sphericity in the deformed HR surface. The results of the study are given in [187, 188]. Table 6.4 reports the required central heating power for each beam size to increase the RoC by 10 m and the corresponding increase of absorbed power with respect to the amount of YAG power absorbed by the ITM (about 690 mW).

| Beam Size (cm) | Required Power (mW) | Relative absorbed power increase |
|----------------|---------------------|----------------------------------|
| 2 | 67 | 10% |
| 5 | 156 | 23% |
| 10 | 476 | 70% |
| 12 | 667 | 100% |

Table 6.4: Required central heating powers as a function of the beam size.

While TCS has been designed with a safety margin of about a factor of 1.5 to cope with possible higher coating absorptions, it is evident that using central heating to correct the RoC of the ITMs will greatly reduce such a margin. Thus, central heating is not an adequate method in increasing the ITM RoC.

Reference solution: ITM RoC correction with ring heater.

When considering the actuation for the TMs, it is necessary to take into account the RoC increase due to thermal effects. Figure 6.34 shows the RoC behavior as a function of the ITF input power for 1 ppm coating absorption. As it can be seen, the RoC depends linearly on

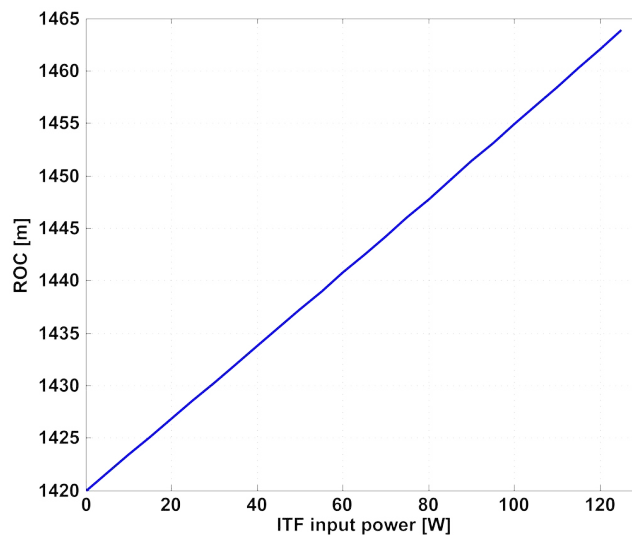


Figure 6.34: Change in the ITM RoC as a function of the ITF input power for 1 ppm coating absorption. The slope is about 0.35 m/W.

the power and already at 25 W the RoC increase is about 9 m. Thus an error of -10 m would be "naturally" corrected by thermal effects at 25 W. At lower input powers, or if coating absorptions are less than 1 ppm, the "YAG thermal" correction would not be sufficiently

strong to meet the optical requirements. As a consequence, the specifications for the RoC should be fixed accordingly: (1420_{-5}^{+15}) m is a viable choice. This is compatible with an actuation made using a ring heater. In fact by heating the TM around its barrel, the RoC changes linearly with the power deposited with a slope of -1.6 m/W (without introducing additional non sphericity on the HR face); this means that to change the RoC by -15 m, about 9 W of absorbed power are required. In this configuration, a predicted maximum power of 37 W is needed at 125 W input power.

ETMs

Reference solution: ETM RoC correction with ring heater.

The same evaluation done for the ITMs regarding the actuation with a ring heater can be applied to the **ETMs**. The expected absorptions of the ETM coating are lower, so the specifications on the RoC can be given accordingly as (1683_{-3}^{+17}) m. In this case, a predicted maximum power of 25 W is needed at 125 W input power.

Considerations about ETM RoC correction with two actuators.

In the ETM there is no thermal lensing to take into account. Thus, also a combination of ring heater and central heating is in principle viable, if deviation from sphericity in the RoC of the ETM is not an issue (to be confirmed by optical simulations). With this setup the specifications could be set at (1683 ± 10) m.

Concerning the technique to apply the central heating, it is possible to produce the spot pattern with a CO_2 projector: the noise introduced for the required dynamics ($+10$ m) is shown in Fig. 6.35. This system also allows to avoid astigmatism of the beam on the TM (see [189] as an example for a study made for Virgo). Nevertheless the CO_2 source requires a relatively complex setup. From this point of view, it would be easier to use an infrared source, as done in Virgo with the CHRoCC (Central Heating Radius of Curvature Correction) to tune the ETMs RoC [190]. The CHRoCC implemented in Virgo generates a quite astigmatic heating pattern on the TMs, but there could be margin for improvement. The optical simulations must still fix the requirements on the maximum astigmatism allowed in the FP cavities. If the upgrade of the CHRoCC and/or the results of the simulations on the astigmatism give a positive answer, the solution with a CHRoCC seems to be preferable with respect to the CO_2 .

PRM

The RoC of the **PR** does not change significantly because of thermal effects: the absorbed power is a factor of F/π times lower than that absorbed by the TMs, for a maximum change in the RoC of about 0.6 m at full input power. In this case, the methods to modify the RoC of PRM must take into account the presence of the Pickoff Plate (**POP**) (so the HR face of PRM is not accessible for central heating) and the fact that the plate is tilted by 6° to allow the extraction of the pick off beam.

Moreover, the thermal lensing in the POP will decrease the apparent RoC of the PRM as [187]:

$$\frac{1}{RoC_{PRM}^{hot}} = \frac{1}{RoC_{PRM}} + \frac{1}{f_{POP}^{hot}}. \quad (6.9)$$

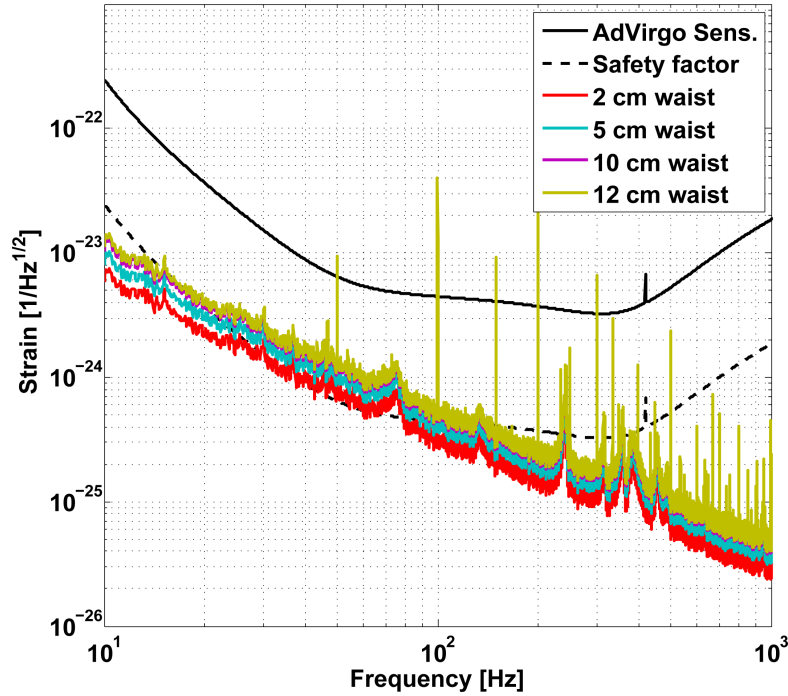


Figure 6.35: Noise projection for a CO₂ central heating.

Figure 6.36 shows the change in the apparent RoC of PRM as a function of the ITF input power: the slope is about -0.31 m/W.

Different RoC correction methods to be implemented on the PRM or on the POP have been studied [187] and their applicability has been evaluated in terms of dynamic range, type and amplitude of the aberrations introduced in the recycling cavity. All the methods have the required dynamic range. The actuation on the POP always introduces aberrations (due to the 6° tilt angle). Among the different possibilities to act on the POP, the one that generates the least aberrations is the ring heater (aberrations dominated by tilt - this would be corrected by the AA system) that increases the apparent RoC of the PRM. A ring heater on PRM introduces no aberration at all and decreases the RoC. This implies that, from the point of view of induced aberrations, the solutions with a RH around PRM or around POP are to be preferred; the specifications for the RoC must be set considering that the actuators have effects with opposite signs.

Reference solution: RH around the PRM.

The dynamics of a RH around the barrel of the PRM, approximately 8-9 cm from the HR surface, is -2 m/W [187]. Taking into account the effect of the RH and the thermal lensing in the POP, the specifications on the RoC could be set as (1475 ± 10) m. In this case, at low ITF input powers, the RH should deposit about 18 W or 28 W on PRM to reach 1430 m for an initial RoC value of 1465 m or 1485 m respectively. These power values are compatible with the RH design. As the ITF input power increases, the RH power is decreased accordingly. When the IFT works at full power, the "hot" RoC becomes 1426 m for an initial value of 1465 m, within the specs set by OSD, while for a starting RoC of 1485 m the thermal effects decreases it down to 1446, thus requiring 8 W deposited from the ring heater. The precurving

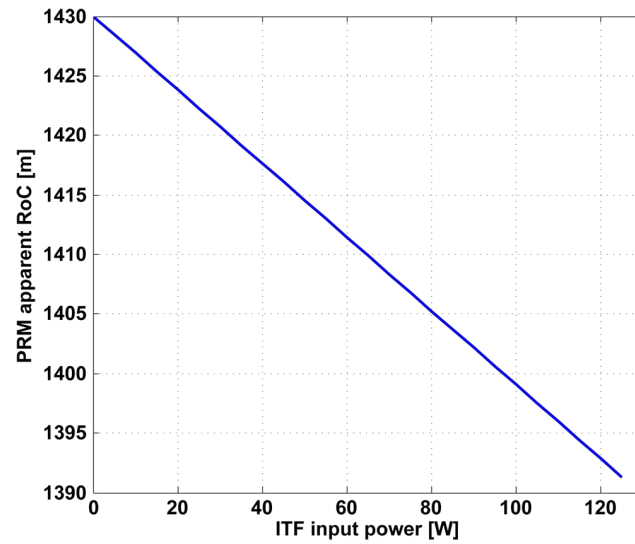


Figure 6.36: Change in the PRM apparent RoC as a function of the ITF input power for 1 ppm coating absorption. The slope is about -0.31 m/W.

of PRM allows to compensate the thermal lensing in the POP thus making the task of the CO_2 laser actuator lighter.

RH around the POP.

A RH around the POP is very efficient as it can exploit the dependence of the refraction index on the temperature. It has the opposite effect as the thermal lensing in the POP itself, thus increasing the RoC of PRM with a slope of 30 m/W [187]. A viable choice of the RoC specifications could be (1430^{+0}_{-20}) m. In fact, if the initial RoC is 1410 m, the RH must deliver to the POP an amount of power that ranges from 0.6 W to 2 W as the ITF input power is increased. Otherwise, if the cold RoC is 1430 m, the RH must be off at low input powers and deliver a maximum power of 1.3 W when the ITF is operated at 125 W.

The feasibility if this solution depends upon the possibility to suspend a RH around the POP. No interaction with PAY has yet started to define this issue.

SRM

The **SR** will experience no dynamical change of the RoC (neither real nor apparent) since no power is impinging on SRM itself. Moreover, there is no thermal lensing to take into account, making both central heating and ring heater viable solutions. However, since it is known that central heating introduces some degree of non sphericity on the HR surface, *the solution with a ring heater is proposed as the reference solution*. Thus, the RoC specification can be set as (1430^{+20}_{-0}) m. In this way, if the RoC is wrong by +20 m, the RH will have to deliver a maximum power of 10 W to meet the specifications, as the RH dynamics is the same as for PRM (-2 m/W).

We report in Tab. 6.5 the summary of the specifications for the RoC of the ITF mirrors, compatible with the TCS actuation, that must be met after all the fabrication process (coating included), compared with the specifications by OSD.

| | OSD request | Specs set by TCS |
|-----|-------------------|-----------------------|
| ITM | (1420 ± 10) m | (1420^{+15}_{-5}) m |
| ETM | (1683 ± 10) m | (1683^{+17}_{-3}) m |
| PRM | (1430 ± 8) m | (1475 ± 10) m |
| SRM | (1430 ± 8) m | (1430^{+20}_{-0}) m |

Table 6.5: Summary of the RoC specifications coming from OSD and the corresponding specifications set by TCS to meet the OSD requirements.

6.9 TCS sensing

During Virgo+ operation, the TCS was mainly operated on a "set-and-leave" basis, only looking at phase camera images and other ITF channels during commissioning. In AdV, due to the increased complexity of the TCS (increased number of actuators) and of the ITF (increased sensitivity to optical defects), this kind of operation will not be possible anymore. Thus, AdV TCS actuators require error signals for their optimized operation. The outcome

of the optical simulations on the need to correct also for the "cold" aberrations, confirms the scheme already proposed for the TCS sensing in the AdV baseline design document [191], thought as a blend of different sensors: Hartmann wavefront sensors and phase cameras, plus some ITF channels, as shown in Fig. 6.37.

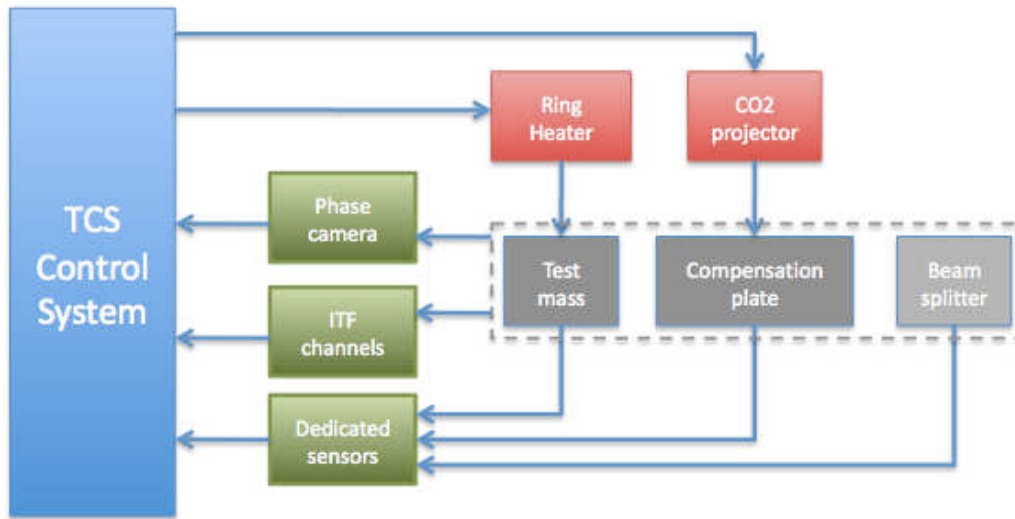


Figure 6.37: Conceptual scheme of the TCS sensing and actuation.

A technical description of the phase camera can be found in Detection Subsystem (DET) chapter 7. The Hartmann sensor is described in the following section.

6.9.1 Hartmann wavefront sensor

The Hartmann wavefront sensor (HWS) is a differential sensor, which needs a reference wavefront. Thus it is not suitable for the measurement of "cold" defects, while it can detect thermal aberrations with an extremely high sensitivity. This makes the HWS suitable for measuring both the wavefront distortions in the RC and the thermoelastic deformation of the HR surface of the TMs. Since the area over which the RC distortions must be corrected has a radius of about 8 cm, the sensing must be performed on an area slightly larger. For this reason, the required size of the HWS on the ITM is set to 10 cm Gaussian waist. This same beam size on the HR face of the TMs allows a RoC reconstruction compliant with the OSD requirements.

The sensor chosen for the AdV TCS has been developed by the University of Adelaide (Australia) and will also be used for the Advanced LIGO TCS. The characterization performed on a table top experiment has shown a shot-to-shot reproducibility of $\lambda/1450$ at 820 nm, which can be improved to $\lambda/15500$ with averaging (see Fig. 6.38) and an accuracy of $\lambda/6800$ [192].

The HWS assembly is shown in Fig. 6.39. The plate has holes 150 μm in diameter, for a pitch of 420 μm and is screwed onto the CCD body through a 6 mm thick spacer.

The CCD is a modified ⁹ Dalsa Pantera 1M60, 1024 by 1024 pixels for an active area of 1.2 cm

⁹The CCD protection window has been removed.

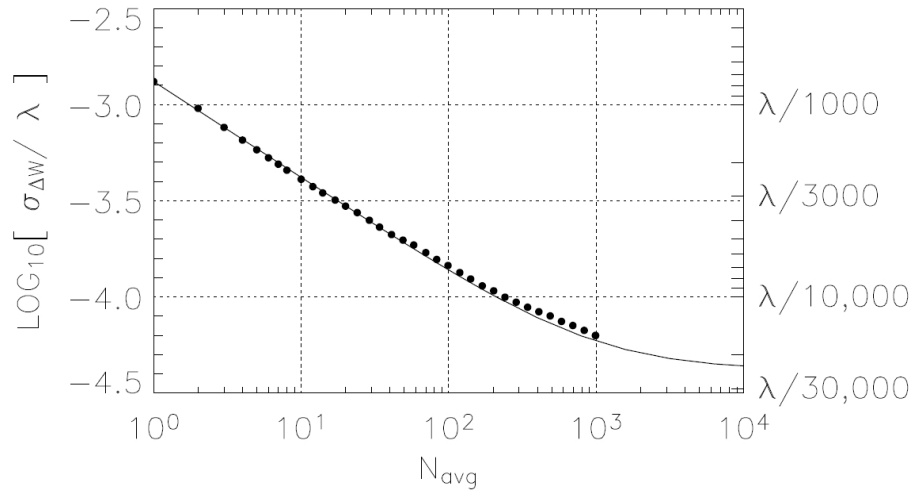


Figure 6.38: HWS measured noise level as a function of the number of averages.

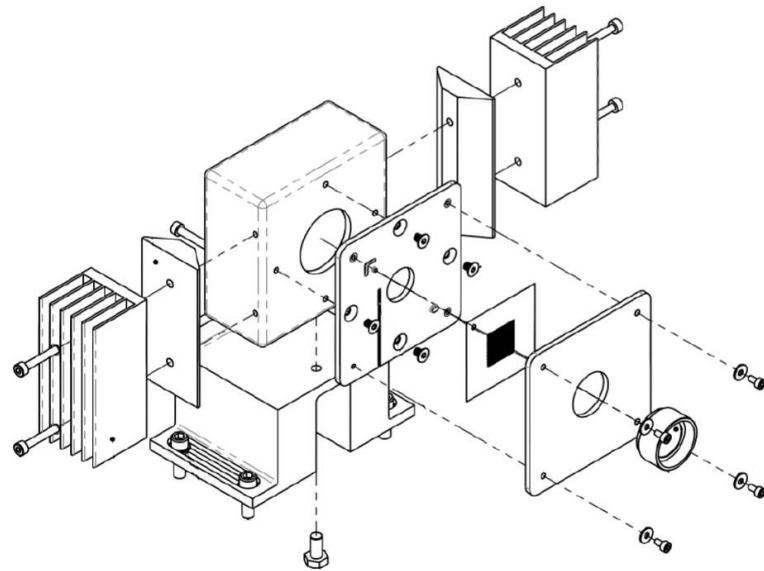


Figure 6.39: A view of the HWS assembly.

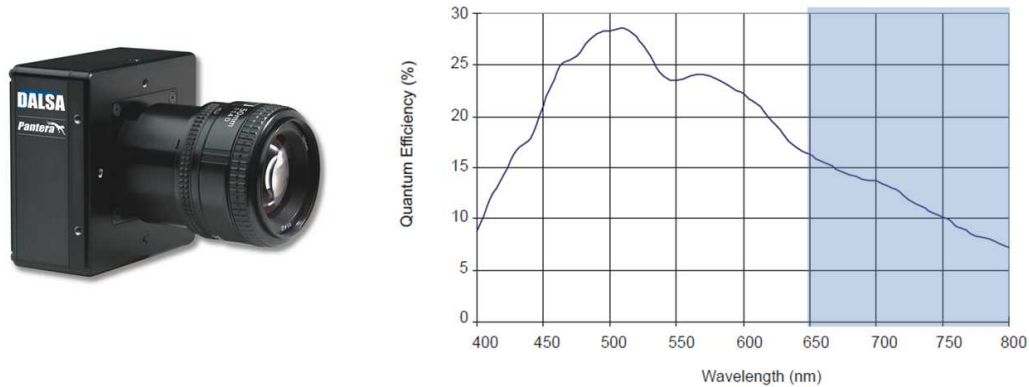


Figure 6.40: The Dalsa Pantera 1M60 and its quantum efficiency as a function of the wavelength.

by 1.2 cm, with a maximum frame rate of 60 fps. Figure 6.40 shows the quantum efficiency of the camera as a function of the wavelength and the shaded area represents the frequency range in which SLED sources (see below) are available. The sensor is controlled and its data acquired and analyzed by a dedicated PC. Connection with the PC is through the C-link digital data protocol. The control and analysis software (developed in collaboration with the University of Adelaide) is written in MATLAB and runs under CentOS or Ubuntu. In order to avoid the use of a dedicated PC, the possibility to have the same CCD equipped with a Giga Ethernet connection is being investigated with Dalsa.

The minimum optical power impinging on the detector required to run it at full speed has been estimated to be about 10 to 14 μW in the wavelength range 700-900 nm. This translates into a requirement on the total transmittance/reflectivity of the optical path of the probe beam, limited by the reflectivity and transmittance of the involved optics. The Gaussian beam radius at the HWS, optimized to have a reasonably uniform intensity over the CCD, is the CCD diameter (12.29 mm) divided by $\sqrt{2} = 8.69$ mm.

6.9.2 Hartmann beam sources

Probe beams for the Hartmann sensors will be generated using Superluminescent Diode (SLED) sources, characterized by a very low spatial coherence. This property has been demonstrated [193] to improve the noise performances of the Hartmann sensor. Table 6.6 reports some of the sources commercially available.

The wavelength ranges between 650 nm and 900 nm because:

- no source is commercially available below 650 nm;
- for wavelengths higher than 900 nm, the quantum efficiency of the Dalsa camera becomes smaller than 5%;
- the wavelength of the Hartmann probe beams must be kept far from that of the ITF.

Suitable sources to generate the Hartmann probe beams are the Superlum SLD-33-HP and SLD-38-HP, with a centre wavelength tunable between 790 and 830 nm and a peak output

| EXALOS | | Superlum | |
|------------------------|-----------------|------------------------|-----------------|
| Centre wavelength (nm) | Peak power (mW) | Centre wavelength (nm) | Peak power (mW) |
| 650 | 1 | 680 | 5 |
| 750 | 2.5-5 | 780 | 7.5-25 |
| | | 790 | 10-30 |
| 800 | 1.5-5 | 825 | 7.5-25 |
| 830 | 1.2-8 | 830 | 10-30 |
| 840 | 5 | 840 | 7.5-25 |
| | | 845 | 7.5-25 |
| 850 | 5 | 855 | 7.5-25 |
| 870 | 5 | 860 | 10-30 |
| 880 | 5-7 | 935 | 3.5-10 |

Table 6.6: List of the commercially available SLED sources in the wavelength range of interest.

power of 25-30 mW.

6.10 Recycling cavities wavefront sensing

Due to the requirement on the residual optical path length RMS of 2 nm, roughly speaking corresponding to a peak-to-valley maximum amplitude of 8 nm, the precision of the RC wavefront sensing must be of the order of 0.8 nm, corresponding to $\lambda/1000$ @ 800 nm (to be compared with the measured noise level of $\lambda/15500$).

6.10.1 HWS Optical layout

The conceptual layout of the Hartmann Wavefront Sensor (**HWS**) beams in the RC is shown in Fig. 6.41. In the picture, the beams have different colors for the sake of clarity; but the wavelength is in fact the same for both beams. The beams will be injected/extracted from the suspended injection/detection benches, and superposed to the main ITF beam with a dichroic mirror at the level of the mode matching telescopes. This scheme allows for on axis double pass wavefront measurement and for probing of all the optics in the recycling cavity. Another advantage of this layout is that the HWS beams are magnified under vacuum. In fact, during tests performed at the Gingin High Optical Power Test Facility, degradation of the HWS noise floor due to air currents has been reported [194].

Additional optics are necessary to fulfill the main optical requirements for HWS beams: image a plane around the ITM-CP pair on the Hartmann plate, illuminate the ITM with a Gaussian beam 10 cm in size and match the optimal beam size on the CCD.

In order to maximize the power coming back to the sensor and to keep the measurement of the thermal lensing in the two input test masses well decoupled, special coatings on the RC optics must be applied. The requirements at the HWS beam wavelength are: the HR coating of the **BS** must have a reflectivity higher than 95%; the transmittance of all other coatings must be higher than 95%. A theoretical feasibility study has been carried out by

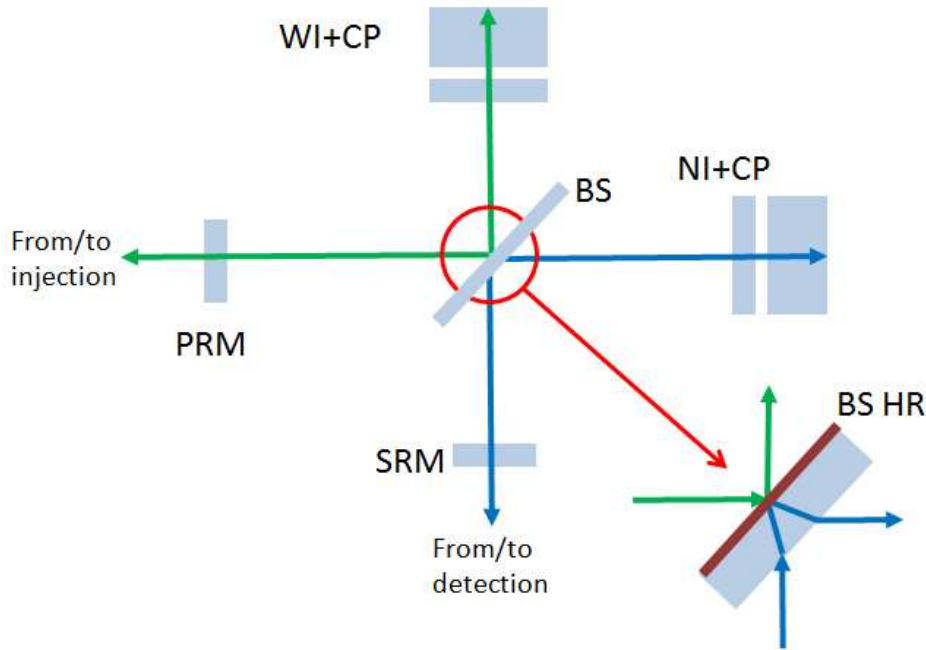


Figure 6.41: Conceptual layout of the HWS probe beams in the recycling cavity. For the sake of clarity the beams have different colors, but the wavelength is the same.

MIR subsystem for $\lambda = 800$ nm with positive results; experimental validation is in progress¹⁰. The optimized coating spectra, released by MIR, have been used to compute the total two way transmittance spectra (shown in Fig. 6.42) for the two arms.

Even if there are wavelengths at which the transmittance is higher than that at 800 nm, the source must be chosen with a centre wavelength close to 800 nm, since the reflectivity of the HR face of the BS has been optimized to decouple the beams of the two arms at 800 nm.

HWS imaging telescope

A Zemax simulation of the whole telescope for both INJ and DET¹¹ sides has been set up to study the propagation of the HWS beam generated by a fiber coupled SLED. The size of the optics of the telescopes have been optimized to the dimensions of the YAG beam. Since the HWS beams are approximately twice the size of the YAG, a clipping of about 0.6% occurs on the meniscus lens, that is the optic with the smallest clear aperture. Diffraction not only

¹⁰A possible fallback solution in case the tests will not be satisfactory, is to inject one of the HWS beams from DET superposed to B5 instead of B1. This beam would partially reflect off the AR surface of the BS. Since the BS is wedged, the beam injected from DET would only sense the North ITM+CP pair. On the other hand, the beam coming from the INJ bench, which should sense West ITM+CP pair only, would also contain a 50% pollution from the North ITM+CP pair, as it is partially transmitted by the BS (depending on the transmittance of the BS HR and AR coatings at the HWS beam wavelength). This contribution should be removed using the information from the beam injected from DET. This scheme has not been studied in detail. For sure a severe drawback of this scheme is that the beam splitter is not sensed by any beam, thus requiring a dedicated setup (additional bench, dedicated viewports of suitable clear aperture, perhaps in vacuum optics, this latter issue being critical due to the size and complexity of the BS payload).

¹¹The considerations in this section apply to the design of the DET telescope as known at the time of writing. If a new design from DET will be released this section must be modified accordingly.

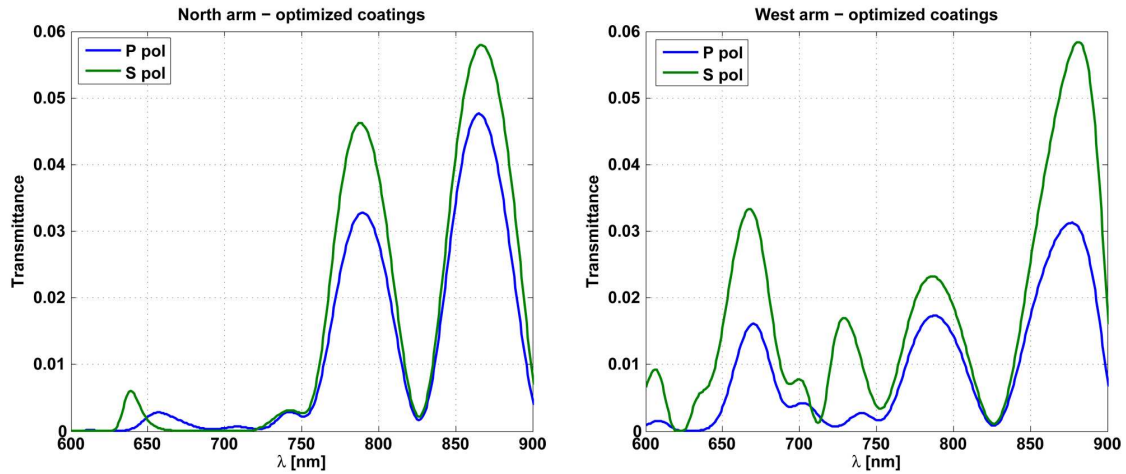


Figure 6.42: Transmittance spectra for the North and West arm HWS probe beams for P (blue) and S (green) polarizations.

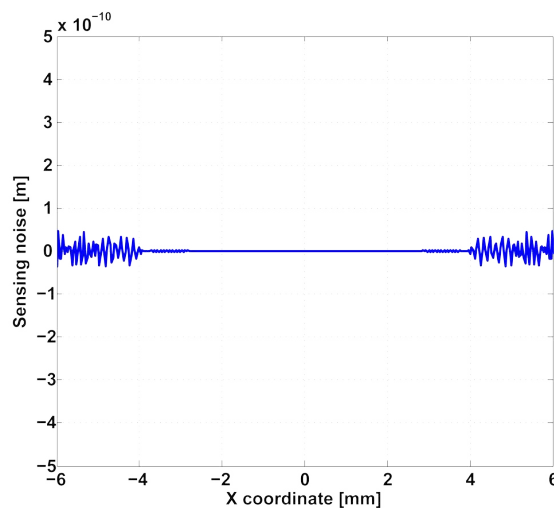


Figure 6.43: Static optical path distortion due to diffraction on the HWS.

reduces the amount of power in the HWS beam, but also introduces distortions of the wave front. This has been evaluated with the Zemax simulation. The result, shown in Fig. 6.43, is below the HWS sensitivity requirement. This calculation concerns only the static optical path distortion without the effect of thermal lensing. The inclusion of thermal effects and the evaluation of how the wavefront distortions affect the noise of the HWS are in progress.

One additional optic after the INJ/DET telescope is required to fulfill the imaging and the CCD size matching conditions. The propagation of the HWS beam through the telescope is shown in Fig. 6.44.

The hardware for the HWS beams will be hosted on the external injection and detection benches as displayed in Figs. 4.3 and 7.33 of the INJ and DET chapters, respectively.

A scheme of the HWS setup is given in Fig. 6.45.

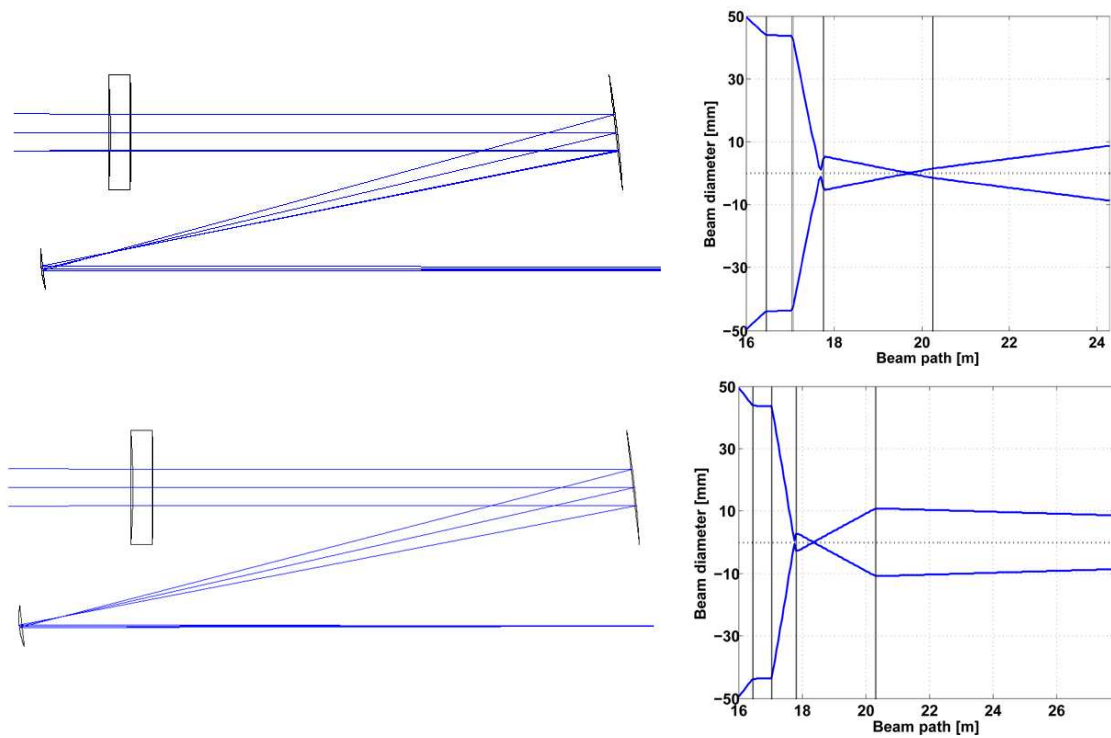


Figure 6.44: Top left: Zemax propagation through the INJ telescope. Top right: calculated size of the HWS beam through the INJ telescope to the Hartmann plate (from the meniscus lens). Bottom left: Zemax propagation through the DET telescope. Bottom right: calculated size of the HWS beam through the DET telescope to the Hartmann plate (from the meniscus lens). The black vertical lines represent the different optics. Distances are measured from the ITM HR face.

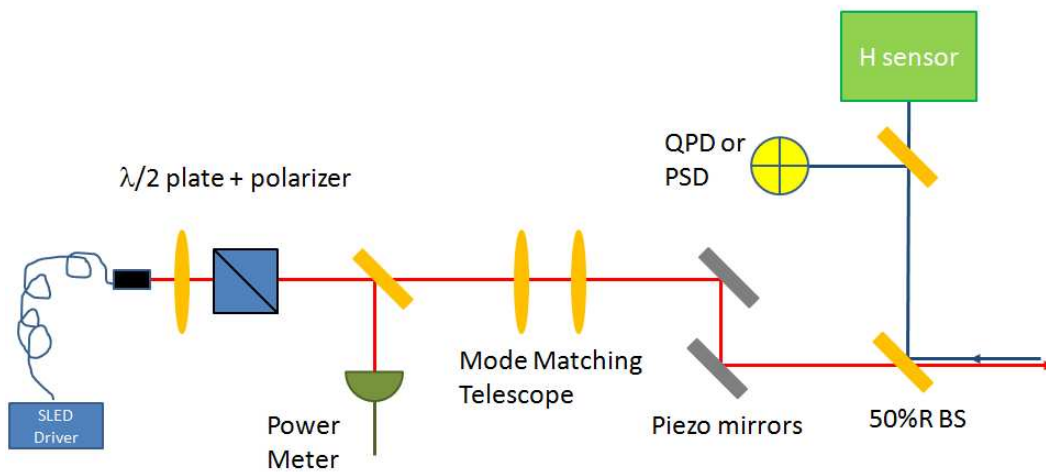


Figure 6.45: A schematic of the HWS optical layout. The imaging optic to the far right is not shown in the picture. The red beam is entering the ITF, the blue beam is the returning one.

- A telescope will match the size of the SLED beam (approximately 1.6 mm radius) to twice the size of the YAG on the dichroic mirror and with the right divergence in order to collimate the beam at the output of the telescopes.
- A $\lambda/2$ plate and a polarizer will be used to select the correct polarization state (S according to the transmittance spectra shown in Fig. 6.42); they will also be used for power control (even is this is also possible by changing the SLED current).
- A power meter will measure the SLED output power and provide the error signal to keep the power constant by changing the SLED current.
- Two steering mirrors will be piezo actuated in order to keep the alignment of the beam on the sensor.
- The beam coming back from the ITF will be sent towards the HWS by means of a beam splitter. A small fraction of the returning beam will be sent to a quadrant photodiode¹² to provide the error signal for the alignment system.

Since some of the imaging optics of the HWS are hosted on the suspended benches and others on the external benches, there might be a source of systematic error in the wavefront measurement, usually referred to as "thermal defocus". Changes in the distance between the imaging optics due to temperature fluctuations in the central building may introduce a fake RoC in the wavefront of the probe beam. This error can be accurately monitored with a "two color system": besides the wavelength that measures the aberrations in the recycling cavity optics, there will be another that makes the same path till the suspended bench and is then retro reflected, to monitor the distance between the suspended and external benches. The implementation of the two color system requires a second source and a mirror on the suspended benches and is being considered as a risk reduction (also for the other Hartmann sensor setups described in the following sections).

6.10.2 Phase camera

The Hartmann sensor is the primary sensor for measuring all thermal effects in the input test masses. It can measure very precisely relative distortions independently on both test masses. The complementary sensor, required to measure the "cold" defects in the recycling cavity, is the phase camera described in the DET chapter.

The phase camera allows us to measure independently the amplitude and phase of the carrier and RF sidebands on different beams in the interferometer [195], notably inside the recycling cavity and on the dark fringe. As the RF sidebands are strongly degraded by the aberrations in the recycling cavity we may use them to determine these same aberrations. Unlike the Hartmann sensor, the phase camera does not permit to make independent measurements in the North and West arm of the central interferometer (CITF). However, in the OSD chapter it is explained that the recycling gain is affected only by the common aberrations and higher order modes of the RF sidebands leaking onto the dark fringe is affected by the differential aberrations. Simulations using FOG have shown that information from the phase camera may be used to determine these common and differential aberrations which may then be compensated using the actuators on the compensation plates. The information given by the

¹²Also a position sensing detector or the use of the camera itself are being considered.

phase camera may be used in many different ways. The current strategy for determining aberrations is shown in the following.

Measurement of common aberrations. The current strategy for measuring common aberrations is to use the phase of the RF sideband relative to the carrier phase for the beam inside the recycling cavity. The recycling cavity acts as a low pass filter as can be seen in Fig. 6.46, so the phase image is dominated by low spatial frequency aberrations.

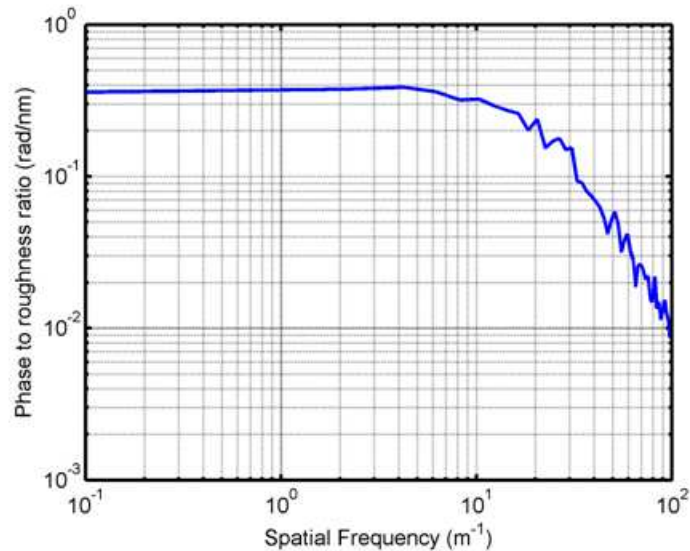


Figure 6.46: FOG simulation. Response of sideband phase for different spatial frequency roughness.

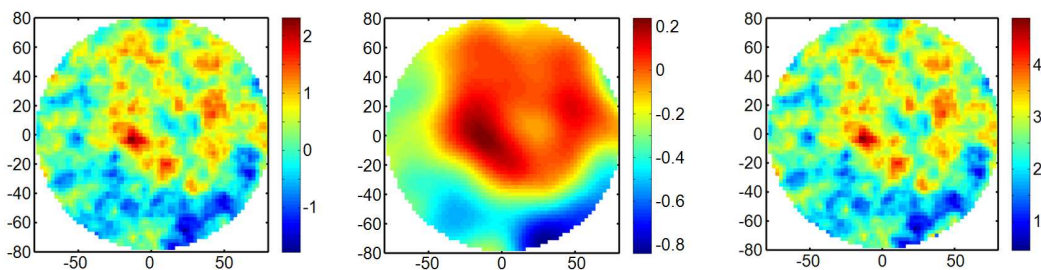


Figure 6.47: FOG simulation. Left: common aberration in recycling cavity (color scale in nm). Middle: phase difference between upper sideband and carrier (color scale in rad). Right: Resulting aberration map after filtering phase difference map (color scale in nm). Horizontal and vertical scales in mm.

In Fig. 6.47 we see a typical phase camera image resulting from a common aberration.

We see that, even though the image is dominated by low spatial frequencies, after filtering using the transfer function shown in Fig. 6.46 we are able to reconstruct the optical aberrations.

Measurement of differential aberrations. This information is not found in the phase information of the phase camera. However we can use the sideband amplitude on the dark fringe to have a qualitative measurement of differential aberrations which should be sufficient when used in loop. Figure 6.48 shows the result of a FOG simulation. Differential aberrations

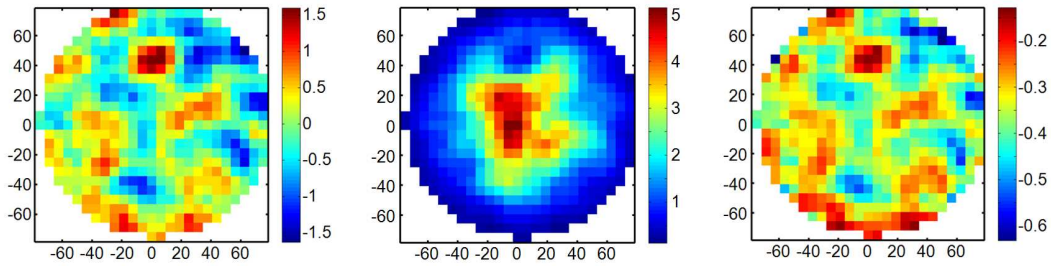


Figure 6.48: FOG simulation. Left: differential aberration in recycling cavity (color scale in m). Middle: lower sideband amplitude on dark fringe. Right: Difference between lower sideband and carrier amplitude normalized by carrier amplitude. Horizontal and vertical scales in mm.

in the recycling cavity result in a distorted sideband beam on the dark fringe. The amplitude image of this beam can then be compared with the "ideal" carrier beam to reconstruct a map of the differential aberrations. This resulting map does not give a quantitative measure of aberrations but may be used as an error signal for the compensation.

Modulation frequencies to use. The measurements using the phase camera are very sensitive to aberrations; as a result they have a low dynamic range (about 3 nm RMS for the 6 MHz modulation frequency) and therefore are easily saturated, due to wrapping issues of the phase images. For this reason it is planned to carry out the sensing and compensation in two steps. We begin by using the 131 MHz modulation frequency sidebands, because they are 10 times less sensitive to aberrations allowing us to carry out a "coarse" compensation. Once this is done, we will switch to the 6 MHz modulation frequency sidebands which will allow us to complete the process with the "fine" compensation.

6.11 High reflectivity surface sensing

Deformation of the TM HR surfaces will be monitored in reflection (see Fig. 6.1), performing a double pass measurement of the change of the phase in a probe beam with the HWS. Since the HR surfaces are essentially planes, there is no parallax, and off axis sensors give unambiguous results. The requirements given by OSD on the precision of the TM RoCs (from Tab. 6.1) are ± 2 m.

Figure 6.49 shows the amplitude of the signal on the HWS for 1 m RoC change in the ITMs and ETMs.

Since the measurement is performed in reflection, the choice of the probe beam source wavelength can be based only on the reflectivity spectrum of the HR coating. The wavelength range that maximizes the power returning to the HWS is in the interval 780-800 nm. Dedicated benches are placed close to the TMs towers to host the HWS hardware and telescope.

The conceptual scheme is shown in Fig. 6.50. The HWS probe beam is injected through a lateral viewport, steered by two in vacuum mirrors on the HR face of the TM and retro reflected by a third mirror, thus performing a double pass measurement in reflection. The layout of the first part of this setup is the same as for the HWSs measuring the wavefronts in the RCs described in Fig. 6.45. The second part, comprising the magnifying telescope, is peculiar to this setup and is described below:

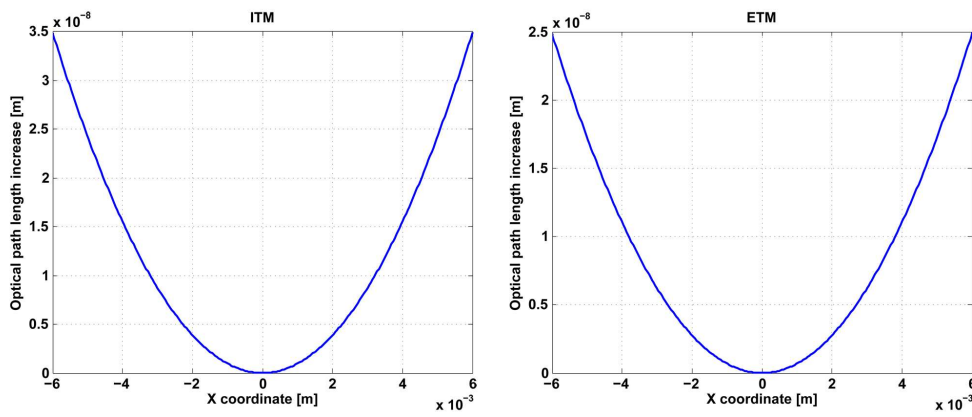


Figure 6.49: Optical path length increase on the HWS induced by a 1 m change in the RoC of the ITM (left) and ETM (right).

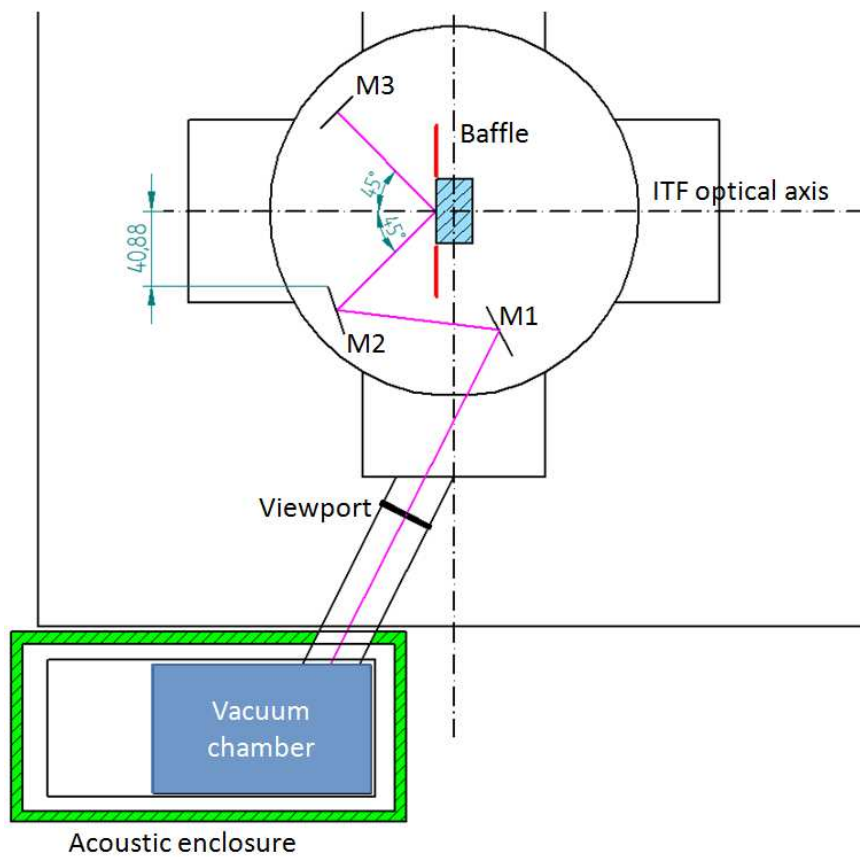


Figure 6.50: Preliminary layout of the baseline solution.

- the beam enters the tower from a viewport placed on the lateral flange of the tower;
- to minimize the noise introduced by air currents, the telescope will be housed in a small vacuum chamber, connected to the viewport on the tower with a pipe (vacuums in the chamber and in the tower are kept separated by the viewport);
- three in vacuum mirrors are needed to steer the beam onto the TM (M1 and M2) and to retro reflect it towards the HWS (M3);
- a cylindrical optic is used on the bench to correct the astigmatism of the beam on the TM due to the 45° angle of incidence;
- mirrors M2 and M3 will be remotely actuated to align the probing beam;
- the distance between the ITF optical axis and the edge of M2 is about 41 cm.

The setup has been simulated with Zemax to determine the size of the optics and of the apertures that keep clipping losses of the order of 1% in order to have the same noise level as in the HWS setup for the measurement of the wavefront in the RCs (see Fig. 6.43). The diameter of M1 is 300 mm; M2 and M3 both have a diameter of 280 mm. If the thickness of the mirrors is set to 3 cm, the lowest vibrational mode is at 1.9 kHz. The viewport must have a clear aperture of 280 mm.

6.12 HWS in transmission on the end benches

The TCS sensing scheme comprises one HWS on each ETM to measure the wavefront distortions in transmission with the main purpose to monitor the absorptions of the ETMs ¹³.

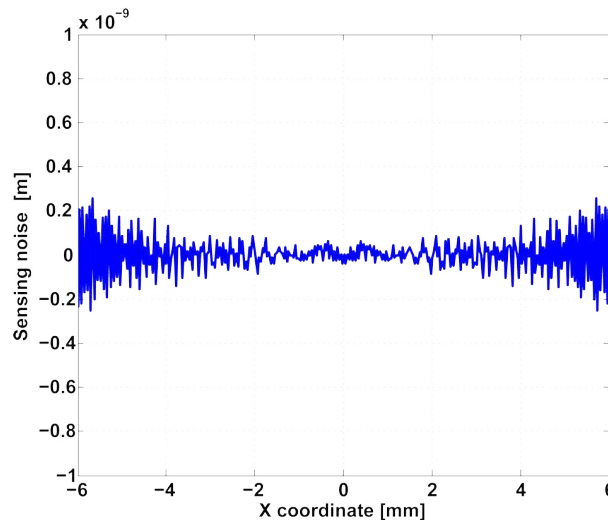


Figure 6.51: Static optical path distortion due to diffraction from the "Lentone" on the HWS.

¹³Combining this measurement with that of the deformation of the HR surface, it is also possible to evaluate with great accuracy the dn/dT

The HWS beam setup [196] is hosted on the external end bench together with auxiliary lasers hardware. Figure 7.33 in the DET chapter shows a schematic layout of the SEB with the HWS beam path included.

The HWS and the auxiliary beams would be superposed onto the YAG using the same dichroic mirror. MIR is currently evaluating the feasibility of a coating with high reflectivity at 1064 nm and high transmittance at 800 and 1319 nm. The HWS probe beam would profit from the telescope already foreseen and designed for the YAG. Since the clear aperture of the "Lentone" is 220 mm, the clipping losses amount to about 9% (established by a Zemax simulation) and the corresponding optical path length distortion is shown in Fig. 6.51.

This effect is larger than that for the other HWS setups. In case it turned out to represent a limitation for the precision of the measurement, a reduction of the size of the HWS beam can be considered.

Chapter 7

Detection (DET)

7.1 Scope of the DET subsystem

This section gives an overview of the main functions fulfilled by Detection Subsystem (DET). The primary goal of the DET subsystem is to extract the Interferometer (ITF) signals from the dark fringe beam and the auxiliary beams. The dark fringe beam carries information about a change in the Differential Arm Length (DARM) and is thus sensitive to a Gravitational Waves (GW). Auxiliary beams are sensitive to other degrees of freedom of the ITF, providing signals needed for the ITF control systems (see ISC chapter).

7.1.1 Overview of the beams to be extracted

The beams that need to be extracted for Advanced Virgo are shown in Fig. 7.1 and listed below (we use the naming conventions introduced for Virgo in [197]):

- B1 is the dark fringe beam obtained in transmission of two Output Mode Cleaner (OMC) cavities. The Direct Current (DC) channels of the photodiodes receiving the B1 beam will provide the GW channel;
- B1p is a pickoff of the dark fringe before the beam enters the first OMC;
- B1s1 is the beam reflected by the first OMC;
- B1t is a pickoff of the beam resonating inside the first OMC;
- B1s2 is the beam reflected by the second OMC;
- B2 is the beam of the symmetric port (reflection from the interferometer towards the laser lab);
- B4 is a pickoff beam in the Power Recycling (PR) cavity. It will be extracted by using the pickoff plate placed in front of the PR mirror;
- B5 is a pickoff beam originating from the reflection of the beam coming from the north arm on the Anti-Reflective (AR) face of the Beam Splitter (BS) mirror;

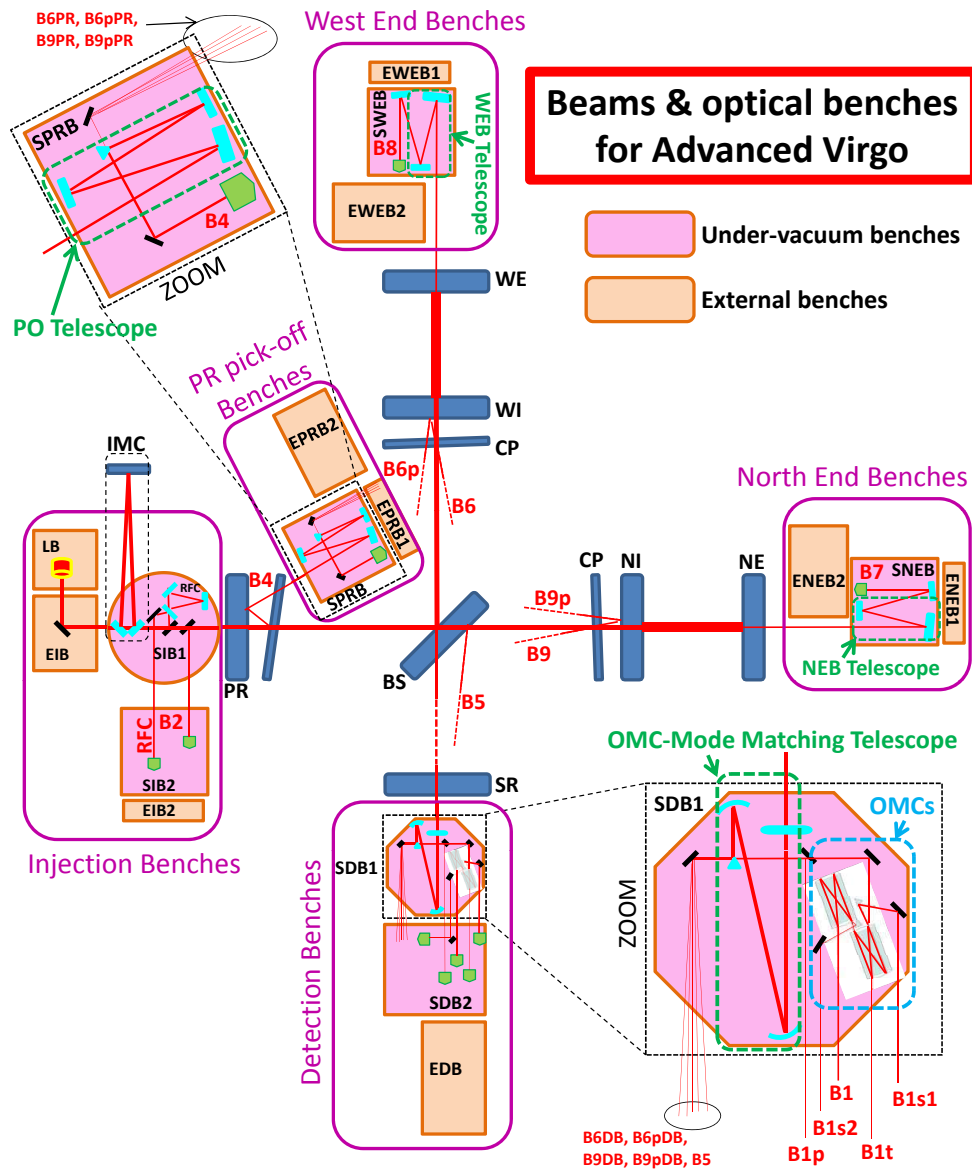


Figure 7.1: Functional scheme of the ITF beams and the optical benches foreseen for Advanced Virgo.

- B6 and B6p (respectively B9 and B9p) are the pickoff beams originating from the reflections on the tilted faces of the west (respectively north) arm Compensation Plate (**CP**). Two different extraction scheme can be envisioned for these beams. They propagate towards the **ITF** anti-symmetric port and need to be separated from the dark fringe beam at the level of the detection benches, where they are named as B6DB, B6pDB, B9DB and B9pDB. The **CP** pickoff beams also propagates towards the **ITF** symmetric port and could be extracted at the level of the **PR** pickoff benches, where they are named as B6PR, B6pPR, B9PR and B9pPR;
- B7 (respectively B8) is the beam transmitted by the north (respectively west) end mirror.

7.1.2 DET main functions

In order to achieve the goal of extracting the **ITF** signals, the **DET** subsystem must provide the functions described below.

- The size of the **ITF** beams must be adapted to the aperture of the sensors, which is achieved with telescopes. Spatially overlapping beams such as B1, B5, B6DB, B6pDB, B9DB and B9pDB need to be separated at the output of the telescopes. Telescope designs will be presented in sections 7.8.2, 7.9.2 and 7.10.2.
- High Order Mode (**HOM**) in the dark fringe beam must be filtered out in order to minimize the contrast defect and to maximize the detector sensitivity. This is achieved with two **OMC** cavities. In order to be compliant with **DC** detection, the **OMC** cavities of Advanced Virgo must also filter out the side band components of the optical field. The proposed **OMC** design will be described in section 7.3.
- Appropriate sensors (longitudinal photodiodes and quadrants) must be provided for each beam containing signals to be extracted. The main photodiodes will be placed on suspended benches under vacuum to improve the rejection of acoustic noise and seismic noise. The output currents of each photodiode or quadrant must be converted into digitalized signals with a readout electronics designed to match stringent noise requirements. Sensor specifications as well as the proposed strategy for the choice of photodiodes/quadrants and their electronics will be discussed in sections 7.5 and 7.6.
- The **DET** subsystem must plan the injection of auxiliary beams into the **ITF**, such as the Hartmann beams used by the Thermal Compensation System subsystem (**TCS**) and the auxiliary lasers at 1319 nm foreseen by Interferometer Sensing and Control (**ISC**) for the lock acquisition. The design of the telescopes and optical benches must be compliant with those beams.
- The **DET** subsystem will provide the phase cameras used by the **TCS**. A description of the possible designs of the phase cameras will be given in section 7.7.
- The components of the **DET** subsystem must be designed in such a way to minimize the risk of introducing environmental noise into the **ITF**. In particular special care must be taken to minimize the coupling of seismic and acoustic noise through the light back-scattered by optics and sensors. To this purpose, most of the components will be placed under vacuum on seismically isolated benches. The most critical optics will be

super-polished. A Faraday isolator will be placed in front of the **OMC** to isolate the **ITF** from the spurious light induced by back-reflection or back-scattering on the OMC cavities or the other optics located after this Faraday isolator. The use of beam dumps and diaphragms to dump spurious light rays will be systematic and coordinated with Stray Light Control subsystem (**SLC**).

- Benches need to have mechanical properties compliant with the sensitivity requirements (in particular mechanical resonances should be avoided inside the core of the detector band-width), and be locally controlled with sufficient accuracy. The proposed mechanical design of the benches and their local control will be discussed in sections 7.8.8 and 7.8.9.

7.1.3 Overview of the DET benches

Figure 7.1 gives an overview of the optical benches needed for Advanced Virgo. The DET subsystem is responsible for the design and the production of the following benches:

The Detection Benches:

Located at the **ITF** anti-symmetric port, these benches will be used to extract the dark fringe beam (B1, B1p, B1s1, B1s2, B1t), and the secondary beams due to reflections on the **BS AR** face (B5) or on the **CP** faces (B6DB, B6pDB, B9DB, B9pDB). The Suspended Detection Bench 1 (**SDB1**) is located in the former Virgo detection tower, suspended to a short Superattenuator (**SA**) suspension, and will host the Output Mode Cleaner Mode Matching Telescope (**OMC-MMT**), a Faraday isolator, and the two **OMC** cavities. The Suspended Detection Bench 2 (**SDB2**) will be located inside a new vacuum chamber (the mini-tower presented in the SBE chapter) and suspended to a new multi-stage seismic attenuation system (*MultiSAS*). The SDB2 bench will host the main photodiodes and quadrants of the anti-symmetric port, in particular the ones dedicated to DC detection. Finally the External Detection Bench (**EDB**) will host phase camera and scanning Fabry-Perot systems, and will be shared with the **TCS** group to host also the Hartmann beam setup. A full description of the detection benches will be presented in section 7.8.

The North/West End Benches:

The DET subsystem is responsible for the Suspended North End Bench (**SNEB**) and the External North End Bench 1 (**ENE1**) as well as their equivalents for the west arm. The suspended benches will be placed under vacuum in a new mini-tower and suspended to a MultiSAS suspension. These benches will host the end bench telescopes and the main photodiodes used to extract the end mirror transmissions (B7 and B8). The first external benches will be mostly used to install the Charge-Coupled Device (**CCD**) cameras involved in the suspended bench local controls. The End Benches will be described in section 7.9. The additional External North End Bench 2 (**ENE2**) and its equivalent for the west arm will host the auxiliary laser and Hartmann beam setups and are therefore under the shared responsibility of **ISC** and **TCS**.

The PR pickoff Benches:

These benches will be used to extract the **PR** pickoff beams (B4, and possibly B6PR, B6pPR, B9PR, B9pPR). The Suspended Power Recycling pickoff Bench (**SPRB**) will be placed under vacuum inside a mini-tower and suspended to the MultiSAS suspension. It will host the pick-

off telescope and the main photodiodes and quadrants for this port. Two external benches (the External Power Recycling Pickoff Bench 1 (**EPRB1**) and the External Power Recycling Pickoff Bench 2 (**EPRB2**)) are foreseen for a phase camera and secondary photodiodes. The PR pickoff Benches will be described in section 7.10.

The Suspended Injection Bench 2 (SIB2) and Second External Injection Bench (EIB2):

These benches will be shared between INJ and DET subsystems. The mechanical design and production of the benches will be performed by the **DET** subsystem as the **SIB2** will be suspended inside a similar mini-tower as the ones foreseen at the other **ITF** ports. The **DET** subsystem will also provide the photodiodes, quadrants and associated electronics used to extract the **ITF** symmetric port (B2), as well as the photodiodes used to extract the beam reflected by the Reference Cavity (**RFC**). The Injection subsystem (**INJ**) will provide the general optical layout of the benches, the main optics, and the in-air quadrants needed for the **RFC** beam. The design of these benches will be further discussed in section 7.11.

7.2 Interfaces with other subsystems

This section enumerates the main dependencies existing between the **DET** subsystem and the other subsystems.

7.2.1 Specifications from other subsystems to the DET subsystem

OSD

Optical Simulation and Design subsystem (**OSD**) provides the characteristics of the beams (position, size and curvature) reaching the detection benches. This information is used to design the telescopes as it will be discussed in sections 7.8.2, 7.9.2 and 7.10.2.

ISC

Several requirements for the **DET** subsystem have been defined in the **ISC** chapter as mentioned below.

The signals and demodulation frequencies needed for the longitudinal and angular controls have been defined at each interferometer port. **ISC** requests that two quadrants are placed at each port involved in the automatic alignment with a Gouy phase difference $\delta\phi_g = 90 \pm 20$ degrees. This sets constraints on the design of the telescopes and the bench layouts as it will be discussed in sections 7.8, 7.9, and 7.10.

The **ISC** subsystem requests paths on the end benches layout for the introduction of auxiliary lasers. This is taken into account in the design of the benches.

The **ISC** subsystem gives specifications on the maximum acceptable readout noise for the photodiodes and quadrants used in science mode. The total readout noise of the Radio Frequency (**RF**) signals provided by the longitudinal photodiodes should not exceed $2.06 \times 10^{-10} \text{ W}/\sqrt{\text{Hz}}$ per photodiode, which corresponds to the shot noise of a photodiode receiving a power (P_{dc})

equal to 50 mW. The shot noise has been computed with the following formula:

$$\delta n_{sn} = \sqrt{2} \sqrt{\frac{2h\nu P_{dc}}{\eta}} \quad (7.1)$$

where the quantum efficiency (η) is assumed to be 88%, and the factor $\sqrt{2}$ is due to the demodulation.

The total readout noise of the **RF** signals provided by the quadrants should not exceed $1.46 \times 10^{-10} \text{ W}/\sqrt{\text{Hz}}$ per photodiode, which corresponds to the shot noise of a quadrant receiving 25 mW. The corresponding noise specification for the DC signals is $1.03 \times 10^{-10} \text{ W}/\sqrt{\text{Hz}}$. There is an exception concerning the quadrants that will be placed on the **SDB2** and will received only 2.5 mW. Their noise specification is thus divided by $\sqrt{10}$.

The specifications on the total readout noise are summarized in Tab. 7.1.

| | RF | DC |
|----------------------------------|---|---|
| Longitudinal Photodiodes (50 mW) | $2.06 \times 10^{-10} \text{ W}/\sqrt{\text{Hz}}$ | NA |
| Quadrants (25 mW) | $1.46 \times 10^{-10} \text{ W}/\sqrt{\text{Hz}}$ | $1.03 \times 10^{-10} \text{ W}/\sqrt{\text{Hz}}$ |
| Dark Fringe Quadrants (2.5 mW) | $4.62 \times 10^{-11} \text{ W}/\sqrt{\text{Hz}}$ | $3.26 \times 10^{-11} \text{ W}/\sqrt{\text{Hz}}$ |

Table 7.1: Requirements on sensing noise provided by **ISC** for the photodiodes and quadrants used in control loops. The powers are given per photodiode.

The **ISC** subsystem defines the requirements for the band-width of the photodiode and quadrant electronics. The maximum frequency that will need to be extracted with stringent requirements on readout noise is at 56.4 MHz. A modulation frequency at 131 MHz will also need to be extracted for the lock acquisition but can afford relaxed noise specifications.

Specifications on phase noise at the level of the mixer have also been given in the **ISC** chapter. The most stringent requirement corresponds to a phase noise of $1.1 \times 10^{-6} \text{ rad}/\sqrt{\text{Hz}}$ at 10 Hz for the 56.4 MHz side band.

Overall specifications on the electronics used for longitudinal photodiodes and quadrants will be discussed in the sections 7.5 and 7.6 respectively.

The **ISC** subsystem gives requirements on the **OMC** cavity filtering in order to guarantee that the side bands Relative Intensity Noise (**RIN**) does not spoil the accuracy of the **DARM** loop. The consequences for the **OMC** design are presented in section 7.3.1.

TCS

The **TCS** subsystem sets constraints on the benches layout by requesting a path for the injection of the Hartmann beams. These beams should be twice as large as the YAG beam, and diffraction effects should be limited in order to not spoil the sensitivity of the Hartmann setup. This puts constraints on the minimum aperture of the telescopes (see **TCS** chapter).

Another type of constraint coming from the **TCS** subsystem is the need for phase cameras that will provide additional error signals. The **TCS** subsystem is requesting a phase camera on the B1p beam and another one on the B4 beam. Both phase cameras must be capable of monitoring the 6.27 MHz and 131 MHz side bands. The monitoring of the 56 MHz side band will also be foreseen for the **ITF** optical characterization.

7.2.2 Specifications provided by the DET subsystem to other subsystems

OSD

An interaction between the **DET** and **OSD** subsystems has taken place in order to define the specifications on **BS** wedge, **CP** tilt, and **PR** plate wedge angles. The wedge and tilt angles need to be sufficiently large in order to allow a correct separation and extraction of the secondary beams reaching the SDB1 and the SPRB benches. To this purpose a separation of about 10 beam radii after the telescopes has been asked. The wedge and tilt angles should also not be too large in order to avoid clipping of the secondary beams by the telescope optics. The reference solutions presented in the **OSD** chapter (**BS** wedge of $430 \mu\text{rad}$, **CP** tilt of $750 \mu\text{rad}$ and **PR** plate wedge of $400 \mu\text{rad}$) represent a good trade-off satisfying these requirements.

In order to be able to extract the secondary beams from the **BS** and the **CP**, the beams should be localized in different planes. As presented in the OSD chapter, the baseline design foresees that the **BS** wedge is set in the horizontal plane while the **CP** are tilted in the vertical plane. This leads to the configuration shown in Fig. 7.2.a (left side) where the beams are imaged in the transversal plane a few tens of centimeters after the OMC mode matching telescope. This configuration allows to extract the B5 beam that will be used as reference for the alignment of the detection suspended benches, at least in the power recycled configuration. The possibility to extract the **CP** secondary beams will also be investigated as these beams might provide some information about the CP reflectivities. This could be achieved, for instance, by tilting the CP in both the vertical and horizontal planes to obtain the configuration shown in Fig. 7.2.b (right side).

MIR/OSD

The curvature of the **AR** side of the Signal Recycling (**SR**) mirror must be defined according to the design of the OMC mode matching telescope (described in section 7.8.2). The baseline design foresees a curvature of 3590 mm.

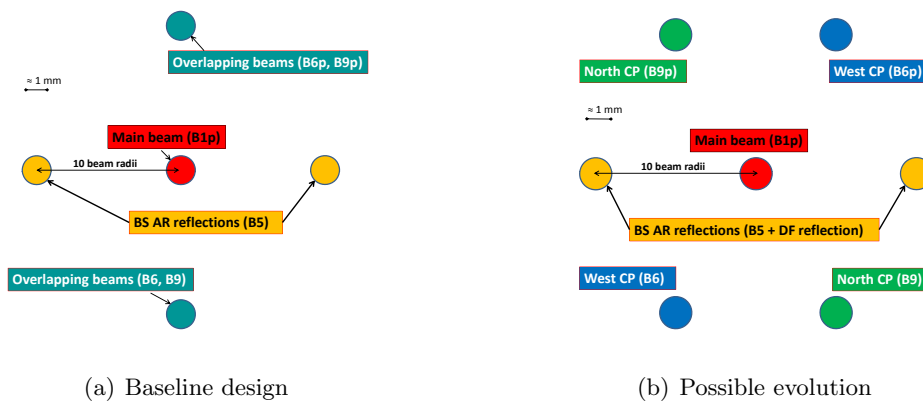


Figure 7.2: Schematic drawing of the dark fringe and secondary beams observed in the transversal plane after the OMC mode-matching telescope. The second beam reflected on the **AR** side of the **BS** mirror (pickoff of the dark fringe) will simply be dumped at the level of the **SDB1** bench.

SLC

The **DET** subsystem interacts with the **SLC** subsystem in order to determine the position of the baffles that are needed to dump the back-scattered/reflected light from the bench optics.

SBE

DET sets constraints on the mini-tower design, in particular for what concerns the position and aperture of the flanges (which result from the bench optical layouts presented in sections 7.8.6 and 7.9.3), the inner size of the vacuum chamber (resulting from the benches mechanical design discussed in section 7.8.8), and the required seismic isolation.

The most stringent constraints on the residual bench motion have been given by the **ISC** subsystem for the end benches [228], where the quadrants **DC** signals involved in the automatic alignment should not be spoiled by the effect of the bench motion. These constraints, which include the effect of the end bench telescopes, are summarized in Tab. 7.2.

| | Requirements |
|---|---|
| Translation noise at 10 Hz (δl) | 2×10^{-12} m/ $\sqrt{\text{Hz}}$ |
| Angular noise at 10 Hz ($\delta\theta$) | 3×10^{-15} rad/ $\sqrt{\text{Hz}}$ |
| Translation RMS motion (l_{RMS}) | 20 μm |
| Angular RMS motion (θ_{RMS}) | 0.03 μrad |

Table 7.2: Requirements on the residual displacement of the end suspended benches.

SAT

The **DET** subsystem set constraints on the needed seismic isolation for the suspended detection bench **SDB1**. Some requirements are driven by considerations on the **OMC** alignment ([198, 199]) and set constraints on the residual angular seismic motion of the bench in absolute Root Mean Square (**RMS**), and at frequencies above 10 Hz. These requirements are given in section 7.3.6.1. The mitigation of scattered light noise induced by the **OMC** Mode Matching Telescope (see section 7.8.2, Fig. 7.29) also adds constraints on the **SDB1** seismic isolation. In order to minimize the risk of scattered light it is asked to add an extra filter to the **SDB1** suspension.

INF

The **DET** subsystem asks for a rearrangement of the detection laboratory and sets constraints on cleanliness (see Infrastructure subsystem (**INF**) chapter).

VAC

A cryolink has to be foreseen between the **SR** tower and the tower hosting the **SDB1** bench in order to avoid any not suspended transmissive optics on the beam path. The required aperture in this area is expected to be at least 250 mm diameter.

DAQ

The **DET** subsystem provides requirements on the number and location of channels to be acquired, as well as the needs in term of Digital-to-Analog Converter (**DAC**) (see sections 7.5 and 7.6).

ISC

A nominal **DC** power of 80 mW is assumed for the B1 beam (TEM_{00} of the dark fringe). This power corresponds to a differential offset of 10^{-11} m in the dual recycled configuration at full power (see **ISC** chapter). As explained in [201] this offset value allows to keep the contribution of the contrast defect to the shot noise lower than 1%, assuming differential losses in the arms of the order of 30 ppm.

The value of the differential offset has also a direct impact on the constraints on the side band filtering by the **OMC** cavity (see section 7.3.1). A larger value of the differential offset would increase the power of the carrier reaching the dark port and relax these constraints. However, as reported in the **ISC** chapter, a larger differential offset would also increase the coupling between **ITF** degrees of freedom and make the mirrors control more difficult. On the other hand, reducing the differential offset would make the constraints on the **OMC** cavity harder. The baseline design of the **OMC** cavity (discussed in section 7.3) allows to reach the constraints on the side band filtering set by **ISC** (see [200] and the **ISC** chapter) by assuming a carrier power of 80 mW. It must be underlined that a reduction of the differential offset could jeopardize the **DARM** locking accuracy, specially for what concerns the power recycled intermediate configuration.

INJ

As already discussed in section 7.1.3, the **SIB2** and **EIB2** benches will be shared between the **INJ** and **DET** subsystems. The bench production is under the **DET** responsibility while **INJ** takes care of the optical layout. **DET** will provide the B2 photodiodes and quadrants, as well as the RFC photodiodes.

The **DET** subsystem sets constraints on the side bands **RIN** above 10 Hz. Side bands **RIN** translate into power fluctuations in transmission of the **OMC** cavities, whose amplitude depends on the **OMC** filtering performances. In order for these power fluctuations to not affect the Advanced Virgo sensitivity, the side bands **RIN** must be compliant with the specifications given in Fig. 7.10 for the baseline design with two **OMC** cavities.

7.3 Output mode cleaners

Preliminary designs of the Advanced Virgo **OMC** have been presented in [201, 202]. The design has evolved in order to meet the requirements set by **ISC** on the side band filtering. The main guidelines for the choice of the design are summarized under this section, and the baseline design is presented.

7.3.1 Requirements on side band and HOM filtering

The goal of an **OMC** is to filter the dark fringe beam from components not carrying information on **DARM**. This allows to minimize the contrast defect and to reduce the shot noise. The **OMC** filtering also reduces the impact of technical noises such as side band **RIN** noise. To these purposes, the **OMC** must filter out the beam **HOM** as well as the side bands transmitted at the dark port (ie the side bands at 6.27 MHz and 56.44 MHz in science mode, and, with relaxed requirements, the side band at 131.7 MHz foreseen for lock acquisition).

The most stringent constraints on the filtering of side bands come from the requirements on the **DARM** longitudinal control loop accuracy as it is explained in the **ISC** chapter and in [200]:

- the requirement on the **DARM** loop accuracy itself has been set in order to guarantee that the up-conversion of low frequency residual **DARM** motion around high frequency lines (a consequence of the non linear **ITF** response in DC readout) remain a factor 10 below the nominal Advanced Virgo sensitivity. This leads to the requirements given in [200], ie a **DARM** accuracy of 6×10^{-16} m in the power recycled 25 W configuration and 10^{-15} m in the dual recycled 125 W configuration;
- the **DARM** degree of freedom is controlled by using the **DC** channel of the B1 beam as error signal. Side band **RIN** at low frequency will produce spurious power fluctuations in the **DARM** error signal if the side bands are not sufficiently filtered out by the **OMC** cavity. In order to guarantee that the readout noise induced by the side band **RIN** does not affect the **DARM** loop accuracy, it has been requested in the **ISC** chapter that this noise remains a factor 10 below the amplitude of the **DARM** error signal to be measured. This leads to a specification on the side band transmission by the **OMC** cavity of 0.075 mW for the power recycled 25 W configuration and 0.080 mW for the dual recycled configuration (see [200]). These constraints should apply both to the TEM_{00} and the **HOM** of the side bands.

For what concerns the carrier **HOM**, one may expect the **HOM** fluctuations to be correlated with the TEM_{00} power fluctuations, which would relax the requirements on the residual **HOM** transmitted power. Due to the large uncertainty on the **HOM** fluctuations, a more conservative approach has been followed, which assumes that the carrier **HOM** fluctuations can be as large as the side bands fluctuations. Thus, we also require the residual power of the carrier **HOM** to be lower than 0.08 mW after the **OMC** cavities.

7.3.2 Main guidelines for the baseline design

7.3.2.1 Impact of the finesse and length on the **OMC** filtering

When the carrier field is kept resonant in the **OMC** cavity, the **OMC** transmission at a modulation frequency f_{mod} is given by:

$$T_{OMC}(f_{mod}) = \frac{1}{1 + \left(\frac{2F_{OMC}}{\pi}\right)^2 \sin^2\left(\frac{2\pi f_{mod} l_{opt}}{c}\right)} \quad (7.2)$$

where F_{OMC} is the finesse of the **OMC** cavity and l_{opt} is its optical length.

The previous equation shows that the filtering performances of the **OMC** cavity can be improved by increasing the parameters F_{OMC} and l_{opt} .

7.3.2.2 OMC length noise and locking accuracy

As computed in [202], if the OMC is away from the resonance by a constant offset Δl_0 , then OMC length fluctuations δl give a variation of the power transmitted by the cavity:

$$\frac{\delta P}{P} = 32F_{OMC}^2 \frac{\Delta l_0}{\lambda} \frac{\delta l}{\lambda} \quad (7.3)$$

By requesting that the power fluctuations due to OMC length noise stay a factor 10 below the shot noise of the dark fringe signal, one obtains the following requirement on the OMC length noise and locking accuracy:

$$\Delta l_0 \delta l \leq \frac{1}{10} \frac{1}{64} \frac{\lambda^3}{FL_{off}} \sqrt{\frac{2h\nu}{P_0 G_{PRC} T_{SR} F_{OMC}^2}} \quad (7.4)$$

where F is the arm cavity finesse ($F = 443$), L_{off} the differential offset ($L_{off} = 10^{-11}$ m), P_0 the power injected in the interferometer ($P_0 = 125$ W), G_{PRC} the power recycling gain ($G_{PRC} = 37.5$), T_{SR} the SR mirror transmission ($T_{SR} = 0.20$).

Equation 7.4 shows that for a given locking accuracy, the constraint on the OMC length noise becomes more stringent as the inverse of the square of the finesse. Assuming for instance a finesse $F_{OMC} = 210$, equation 7.4 becomes:

$$\Delta l_0 \delta l \leq 1.9 \times 10^{-28} \text{ m}^2 \text{Hz}^{-1/2} \quad (7.5)$$

An upper limit on the locking accuracy of the Virgo OMC cavity has been measured [203, 204], giving: $\Delta l_0 \leq 6 \times 10^{-12}$ m.

Assuming that the same locking accuracy can be reached with the Advanced Virgo OMC the maximum acceptable length noise will be:

$$\delta l \leq 3.2 \times 10^{-17} \text{ mHz}^{-1/2} \quad (7.6)$$

An upper limit on the Virgo OMC length noise has been measured [204], giving: $\delta l \leq 6 \times 10^{-16} \text{ m}/\sqrt{\text{Hz}}$ at 100 Hz, and $\delta l \leq 10^{-16} \text{ m}/\sqrt{\text{Hz}}$ at 1 kHz. As explained below, this upper limit is several orders of magnitude above the fundamental limit on the OMC length noise, given by the thermal noise.

Calculations of thermal noise in rigid reference cavities have been presented in [205]. One can try to extrapolate these results for the Advanced Virgo OMC by approximating it with a cylindrical cavity of similar geometry as the cavities described in [205]. This extrapolation leads to a cavity thermal noise given by:

$$\delta l_{th}(f) \approx \frac{4k_B T}{2\pi f} \frac{L}{3\pi R^2 E} \phi \quad (7.7)$$

where R is the radius of the cylinder, L is the length, E is the Young's modulus, ϕ is the mechanical loss, and T is the temperature. Using the following values $T = 300$ K, $R = 1$ cm, $L = 6$ cm, $E = 7.3 \times 10^{10}$ Pa (Fused Silica value), and $\phi = 10^{-6}$ (same value as the one quoted in [205] for the Fused Silica), one obtains at 100 Hz:

$$\delta l_{th}(f) \approx 1.5 \times 10^{-19} \text{ m.Hz}^{-1/2} \quad (7.8)$$

This naive calculation gives a result that is a factor 200 lower than the requirement on the OMC length noise shown in Eq.7.6. The mechanical loss used in the previous calculation is

probably underestimated as the Advanced Virgo OMC will be stressed inside a box containing a PZT actuator (used for length modulation). Nevertheless the large margin factor found above indicates that the target set for the Advanced Virgo OMC length noise is reachable. A special care must be paid to the design of the OMC mechanics (this cavity needs to be controlled to keep the carrier TEM_{00} resonant), in order to not spoil the length noise performances. In particular, the actuation system used to control the OMC length should not introduce too much noise, and the resonances of the OMC and its mechanical support should be kept outside of the detection bandwidth.

7.3.2.3 Choice of the cavity geometry

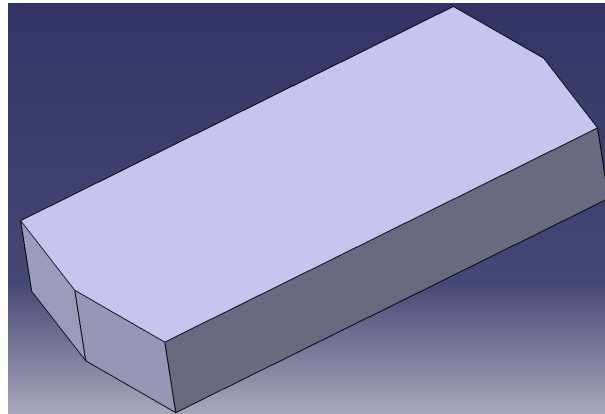


Figure 7.3: 3D view of the OMC cavity designed for Advanced Virgo.

In order to minimize the length noise, a compact, monolithic cavity has been chosen for the OMC design. As discussed above, the expected thermal noise is compliant with the specifications. The proposed geometry corresponds to a bow-tie cavity, which is a geometry compatible with the possible use of High Order Laguerre Gauss Modes in the future. A 3D view of the proposed cavity is shown in Fig. 7.3 and a preliminary technical drawing is shown in Fig. 7.4. The geometrical length of this cavity is 6.150 cm. This choice results from the following trade-off:

- The optical length has been increased by a factor 5 (from 3.6 cm to 17.8 cm) with respect to the Virgo OMC design [207] in order to be able to filter the side bands for DC detection.
- The length could not be chosen too large in order to avoid mechanical resonances inside the detection bandwidth.

A modal analysis performed with CATIA indicates that the first mechanical resonance of the OMC cavity is located at 79kHz. Resonances of the mechanical system made of the OMC cavity, its support and enclosing box are expected to be lower. A measurement of the mechanical resonances of the Virgo OMC mounted on its support was performed before its installation [208, 209]. The result of this measurement is shown in Fig. 7.5 and indicates that the first resonance is near 14kHz. The geometry of the Advanced Virgo OMC slightly differs from the Virgo OMC. Its geometrical length is 2.4 times longer (which tends to lower the

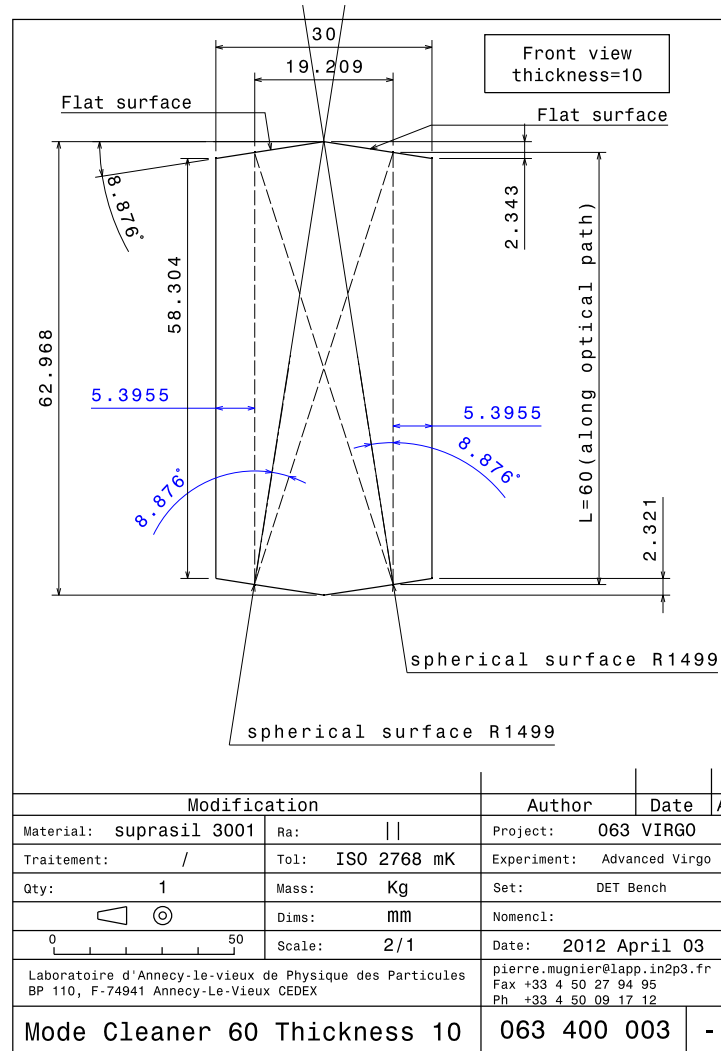


Figure 7.4: Technical drawing of the Advanced Virgo OMC cavity. The dashed lines indicate the beam path inside the cavity.

resonance frequency which varies as the inverse of the length) and it is also broader (which should compensate partially the effect of the length increase). Therefore the resonance frequency of the Advanced Virgo OMC cavity with its support is expected to be of the order of 10 kHz for the proposed geometry. Measurements with a first OMC prototype are scheduled in the next months to verify the frequency position of the first mechanical resonances.

The other advantage of this monolithic design is that it allows to use a simple, low noise, thermal control for the lock, as it was already implemented for the Virgo OMC cavity [208, 209].

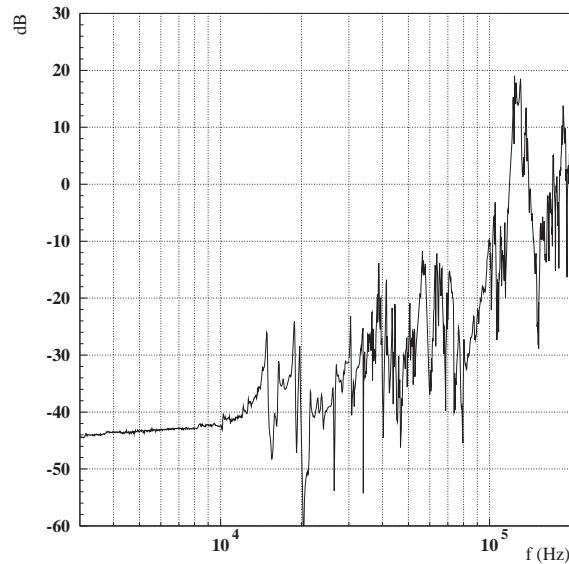


Figure 7.5: Measured mechanical transfer function of the Virgo OMC. The system is excited using a PZT actuator placed on top of the cavity, and the response is measured with the OMC error signal (photodiode AC output).

7.3.2.4 Choice of the substrate material

In order to limit the absorption losses and the thermal effects in the OMC cavity [201], the substrate will be made of fused silica, Suprasil 3001, which is a very low absorption material. The absorption losses at 1064 nm (≤ 0.3 ppm/cm) are at least 10 times lower than the absorption in the Virgo OMC made of Homosil 101. This should allow us to increase the OMC finesse without introducing too much absorption.

7.3.2.5 Choice of the finesse

The choice of the finesse is driven by several needs:

- the filtering needed for the sidebands and the high order modes (see section 7.3.1) requires an increase of the finesse with respect to the value chosen for the Virgo OMC;

- the finesse should remain low enough to ensure that the lock of the cavity is feasible (as the cavity resonance becomes narrower when the finesse increases), and that a sufficiently low locking accuracy can be reached (see Eq.7.4). As discussed above, a worsening of the locking accuracy would make the requirements on the OMC length noise more stringent, and consequently would put more stress on the OMC control and its mechanical design. Although this criterion has not been quantified at the time of the TDR writing (as an absolute measurement of the length noise of the OMC with its mechanics is not yet available), this argument pleads for a design with a moderate increase of finesse;
- the losses inside the cavity (dominated by surface losses) should be kept sufficiently low.

A finesse of 210 has been chosen by requesting that the cavity intrinsic losses remain below 1%. As computed in [201], this criterion is satisfied if the diffraction losses are lower than 30 ppm per face (which is a realistic assumption).

As it will be discussed in section 7.3.5, the finesse could be increased further if larger losses are accepted and if we remove the requirement of controlling the OMC length.

7.3.2.6 Choice of the radius of curvature

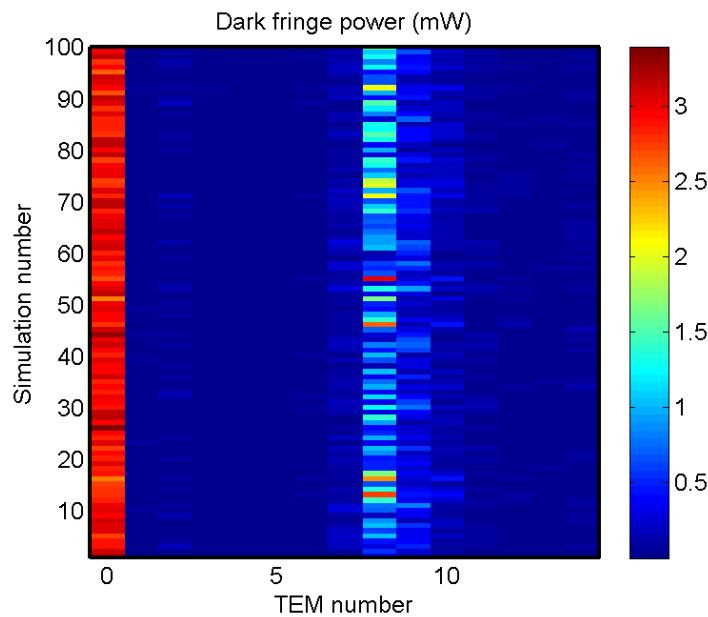


Figure 7.6: Power in the carrier HOM at the dark fringe as predicted by an Advanced Virgo simulation including mirror roughness maps [212, 213]. The HOM powers at the dark fringe are given for an injected power of 1 W. The x axis indicates the order of the mode. One hundred simulation results (obtained with different random maps) are reported along the y axis.

As shown in Fig. 7.4 two surfaces of the OMC cavity are spherical. The presence of a curvature is mandatory in order to avoid degeneracy between the TEM_{00} and HOM modes. The choice of the RoC of the two spherical surfaces is made according to two criteria:

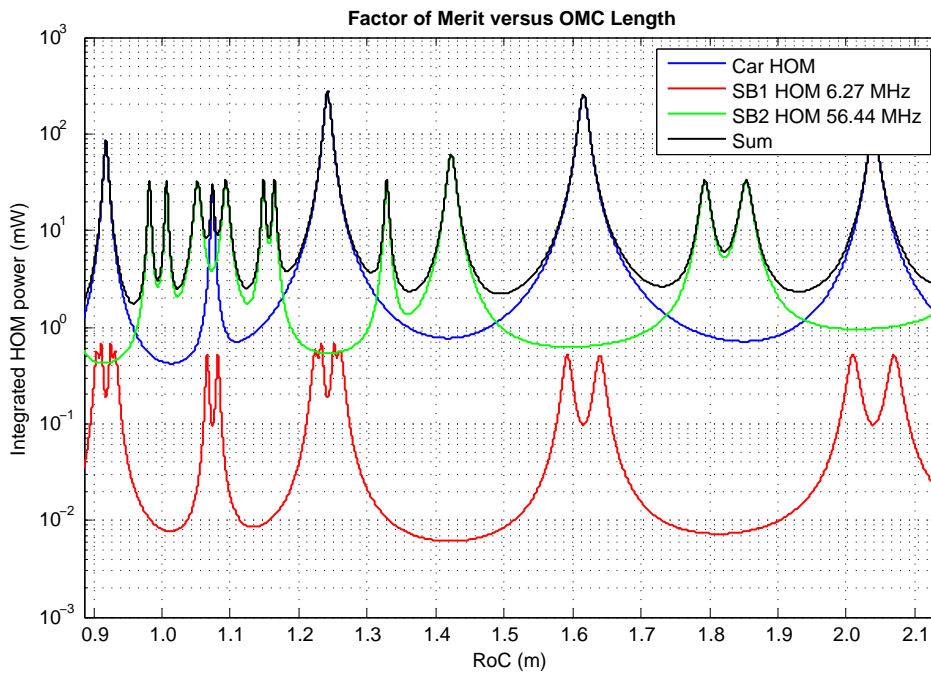


Figure 7.7: Figure of merit for the choice of the OMC RoC. Only one OMC cavity with a finesse of 210 is considered.

| Order $m + n$ | 0 | 1 | 2 | 3 | 4 | 5 | 6 | 7 | 8 | 9 | 10 | 11 | ... | 14 |
|---------------|-----|-----|-----|-----|-----|-----|-----|-----|-----|-----|-----|-----|-----|-----|
| Carrier (mW) | 80 | 200 | 25 | 10 | 10 | 10 | 50 | 150 | 150 | 75 | 25 | 10 | ... | 10 |
| SB1 (mW) | 8.4 | 20 | 3.2 | 3.2 | 3.2 | 3.2 | 3.2 | 3.2 | 3.2 | 3.2 | 3.2 | 3.2 | ... | 3.2 |
| SB2 (mW) | 116 | 260 | 45 | 45 | 45 | 45 | 45 | 45 | 45 | 45 | 45 | 45 | ... | 45 |

Table 7.3: Assumptions on TEM_{00} and HOM power used to calculate the RoC figure of merit, in the power recycled configuration (25 W of injected power).

| Order $m + n$ | 0 | 1 | 2 | 3 | 4 | 5 | 6 | 7 | 8 | 9 | 10 | 11 | ... | 14 |
|---------------|-----|-----|----|----|----|----|----|-----|-----|----|----|----|-----|----|
| Carrier (mW) | 80 | 200 | 60 | 25 | 25 | 25 | 60 | 250 | 250 | 95 | 60 | 25 | ... | 25 |
| SB1 (mW) | 2.5 | 6.3 | 1 | 1 | 1 | 1 | 1 | 1 | 1 | 1 | 1 | 1 | ... | 1 |
| SB2 (mW) | 160 | 400 | 62 | 62 | 62 | 62 | 62 | 62 | 62 | 62 | 62 | 62 | ... | 62 |

Table 7.4: Assumptions on TEM_{00} and HOM power used to calculate the RoC figure of merit, in the dual recycled configuration (125 W of injected power).

- the waist of the **OMC** cavity should not be too small in order to not worsen the amount of back-scattered light that is known to vary as the inverse of the squared waist [210, 211]. The waist of the Virgo **OMC** cavity was of the order of 150 μm . A larger waist is favored for Advanced Virgo;
- the **RoC** must be chosen in order to minimize the transmission of the **HOM** modes for the carrier and for the side bands at 6.27 MHz and 56.44 MHz. More details are given below.

The **RoC** has been chosen by using the figure of merit described in [202]. This figure of merit is obtained by summing the expected power in transmission of the **OMC** cavity for each **HOM** order, for the carrier as well as the two side bands.

In order to compute this figure of merit, some assumptions were made on the power expected at the input of the **OMC** cavity for each frequency component and each mode order. These assumptions are given in Tab. 7.3 for the power recycled configuration (with 25 W injected in the **ITF**) and in Tab. 7.4 for the dual recycled configuration (with 125 W injected in the **ITF**). The power in the TEM_{00} mode has been derived from the analytical calculation. The power in the modes of order 1 (which will depend on the performances of the automatic alignment) has been chosen 3 to 4 times larger than what it was for Virgo. Although realistic this choice is arbitrary as no simulation results concerning the HOM induced by misalignment were available at the time of the TDR writing. The assumptions for the other **HOM** ($m + n \geq 2$) are based on the results of a simulation of the Advanced Virgo **ITF** including mirror roughness maps [212, 213]. An example of simulation results obtained for the carrier HOM at the dark port is shown in Fig. 7.6.

In order to use conservative assumptions for the HOM power extra safety factors have been added to the simulation results: The power in the carrier **HOM** with $m + n \geq 2$ is assumed to be more than 3 times higher than the power predicted in simulation. Moreover the assumptions made for the carrier **HOM** are compatible with two possible **ITF** working points (the nominal arm cavity **RoC** - see **OSD** chapter, and a **RoC** detuned by +30 m). For what concerns the side bands the simulation predicts a total **HOM** power 2.6 times higher than the power in the TEM_{00} for a mirror RMS flatness of 10 nm (which is a conservative value with

respect to the polishing specifications given in the **OSD** chapter). In Tab. 7.3 and Tab. 7.4 the power in the side band **HOM** is assumed to be twice as larger as it is predicted by the simulation.

An example of figure of merit as a function of the **OMC RoC** for the dual recycled configuration is shown in Fig. 7.7. The **RoC** must be chosen at a local minimum of the curve titled "sum", representing the figure of merit combining all carrier and side bands **HOM**. In the Advanced Virgo **OMC** baseline the nominal **RoC** is chosen at 1499 mm, which corresponds to a waist of 263.6 μm .

7.3.2.7 Consequences of the requirements for side-band filtering

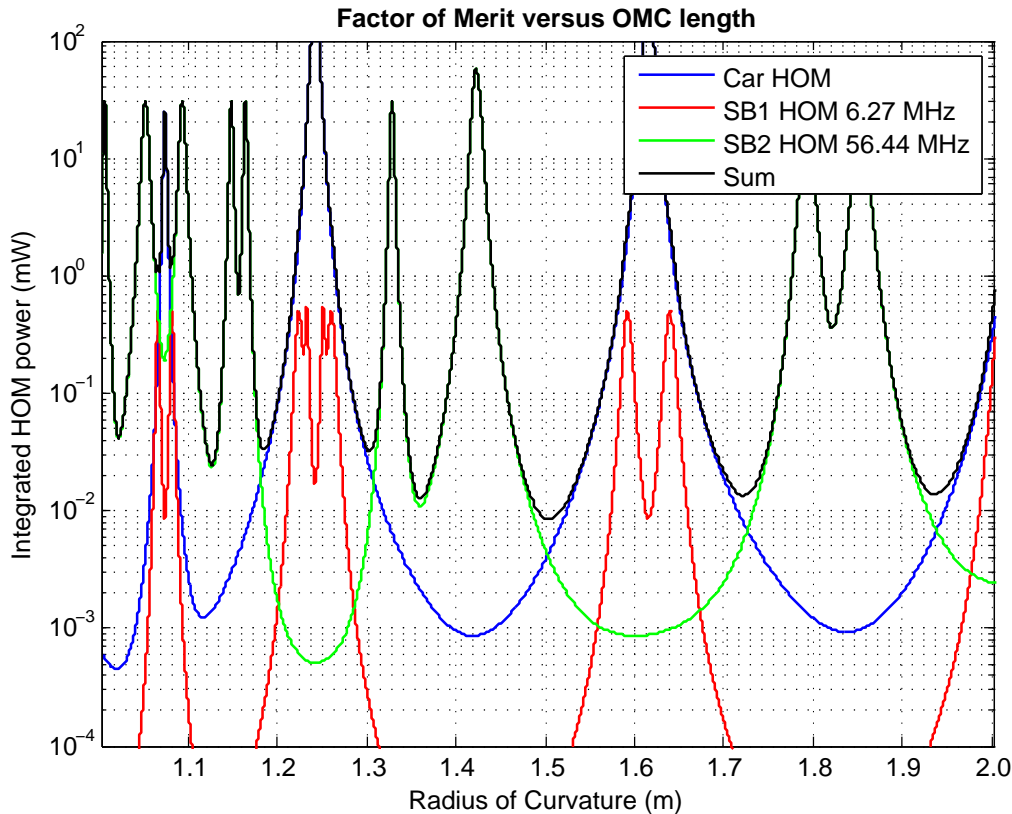


Figure 7.8: Figure of merit for the choice of the **OMC RoC**, with two **OMC** cavities, finesse 210.

The residual powers in the TEM_{00} and **HOM** modes for the carrier and side bands obtained in transmission of a single **OMC** cavity (as designed in [201, 202]) are shown in Tab. 7.5 for the power recycled 25 W configuration and in Tab. 7.6 for the dual recycled 125 W configuration. The total power obtained for each side band must be compared to the specifications given in section 7.3.1. It can be seen that the requirements are not satisfied. For instance, in the power

| | Carrier (mW) | SB1 (mW) | SB2 (mW) |
|------------|--------------|----------|----------|
| TEM_{00} | 80 | 0.78 | 0.15 |
| HOM | 0.78 | 0.027 | 0.67 |
| Total | NA | 0.80 | 0.82 |

Table 7.5: Power transmitted by a single OMC cavity ($F=210$) in the power recycled 25 W configuration.

| | Carrier (mW) | SB1 (mW) | SB2 (mW) |
|------------|--------------|----------|----------|
| TEM_{00} | 80 | 0.24 | 0.20 |
| HOM | 1.24 | 0.008 | 0.96 |
| Total | NA | 0.24 | 1.16 |

Table 7.6: Power transmitted by a single OMC cavity ($F=210$) in the dual recycled 125 W configuration.

recycled 25 W configuration the residual power in the 6 MHz side band (TEM_{00}) exceeds the requirements by a factor 10. In order to tackle this issue the filtering capabilities must be improved, by at least a factor 10 for the 6 MHz side band. This is achieved by placing two OMC cavities in serie. Another alternative could have been to increase the finesse. The two OMC design was preferred over a single OMC cavity with larger finesse for the following reasons:

- as already mentioned previously, a design with a lower finesse is strongly favoured for the controllability of the OMC cavity, and it minimizes the coupling of OMC length noise;
- a single cavity with a finesse of 650 would have equal filtering performances as the two OMC cavities for the 6MHz side band TEM_{00} . However the design with 2 OMC cavities offers better filtering performances of the HOM;
- the price to pay for these improved filtering performances with two OMC cavities is an increase of the intrinsic losses by a factor 2. However this remains lower than the losses that would be induced by a single OMC cavity with large finesse (for instance the losses would be increased by a factor 3 with a finesse of 650).

The figure of merit for the choice of the radius of curvature with two OMC cavities is plotted in Fig. 7.8. It shows that the same radius of curvature ($\rho = 1.499\text{m}$) can be chosen for the design with two cavities. The baseline design consisting of two OMC cavities in serie will be further described in the next section.

7.3.2.8 Choice of the angle of incidence on the OMC surfaces

The choice of the angle of incidence (θ_i) on the OMC surfaces (for the beam resonating inside the cavity) results from the following tradeoff:

- Large angle of incidence are preferred to lower the back-scattering. The diffusion is known to vary with $1/\theta^2$ for angles below typically 5 degrees and constant above.
- On the other hand, the angle of incidence should not be too large in order to not introduce too much astigmatism and losses. One can estimate that for $\theta_i \leq 14$ degrees,

the losses due to the astigmatism should be of the order of 0.1% or less.

In summary, the angle of incidence should be chosen between 5 degrees and 14 degrees.

7.3.3 Presentation of the baseline design

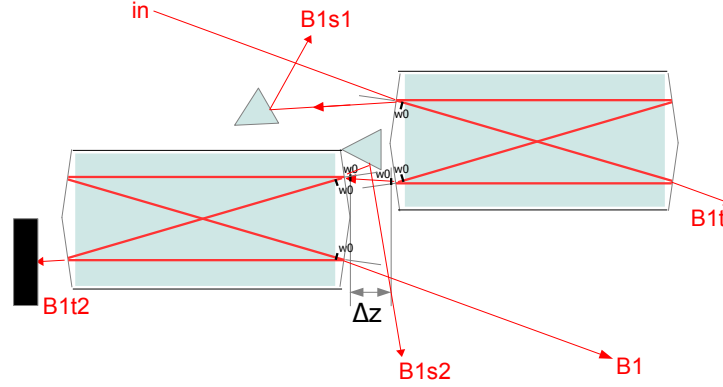


Figure 7.9: Layout of the two **OMC** cavities. The black markers indicate the positions of the beam waist (w_0).

| Finesse | L_{opt} (cm) | L_{geo} (cm) | RoC (cm) | Waist (μm) | Inc. angle ($^\circ$) |
|--------------|--------------------|-------------------|---------------|-------------------------|-------------------------|
| 210 ± 20 | 17.830 ± 0.060 | 6.150 ± 0.020 | 149.9 ± 3 | 263.6 ± 1.5 | 8.876 ± 0.03 |

Table 7.7: Design of the Advanced Virgo **OMC** cavity with allowed manufacturing error bars. L_{geo} refers to the cavity geometrical length and L_{opt} to the optical length ($L_{opt} = 2nL_{geo}$).

This section presents the baseline design of the **OMC** cavities. In order to reach sufficient performances in term of side band filtering, two **OMC** cavities are placed in serie, as shown by the optical layout in Fig. 7.9. The two cavities are designed to be identical. A technical drawing is shown in Fig. 7.4. The optical parameters of both cavities are summarized in Tab. 7.7. They have been derived from the guidelines presented in the previous section.

As shown in Fig. 7.9 the two cavities will be placed as close as possible from each other. This is made possible by choosing an identical waist for both cavities. By minimizing the distance between the two cavities and avoiding intermediate optics, such design allows to reduce the risk of possible alignment drifts between the two cavities due for instance to thermal effects.

The distance Δz indicated in Fig. 7.9 corresponds to the distance under vacuum separating the theoretical waist positions of the two cavities. In the layout drawn in Fig. 7.9 this distance is of the order of 0.9 cm, which translates into an equivalent error (Δz_{err}) on the waist position of 1.3 cm (as expressed in a fused silica medium). This small waist mismatch between the two cavities will induce losses given by:

$$Losses = \left(\frac{\lambda \Delta z_{err}}{2\pi w_0^2} \right)^2 \approx 10^{-3} \quad (7.9)$$

The optical losses due to the relative waist mismatch between the two **OMC** cavities are therefore negligible.

7.3.3.1 Filtering of side bands and high order modes

| power recycling 25 W | | | |
|----------------------|--|--|--|
| Carrier | $l_{geo} = 6.130$ cm $\rho = 1529$ mm | Nominal WP $l_{geo} = 6.150$ cm $\rho = 1499$ mm | $l_{geo} = 6.170$ cm $\rho = 1469$ mm |
| HOM Total | $9.5\mu\text{W}$ | $2.2\mu\text{W}$ | $0.9\mu\text{W}$ |
| Specifications | $\leq 75\mu\text{W}$ | | |
| SB at 6.27 MHz | $l_{geo} = 6.130$ cm $\rho = 1529$ mm | Nominal WP $l_{geo} = 6.150$ cm $\rho = 1499$ mm | $l_{geo} = 6.170$ cm $\rho = 1469$ mm |
| TEM_{00} | $72.7\mu\text{W}$ | $71.8\mu\text{W}$ | $71.0\mu\text{W}$ |
| HOM | $0.4\mu\text{W}$ | $0.07\mu\text{W}$ | $0.02\mu\text{W}$ |
| Total | $73.1\mu\text{W}$ | $71.9\mu\text{W}$ | $71.0\mu\text{W}$ |
| Specifications | $\leq 75\mu\text{W}$ | | |
| SB at 56.44 MHz | $l_{geo} = 6.130$ cm $\rho = 1529$ mm | Nominal WP $l_{geo} = 6.150$ cm $\rho = 1499$ mm | $l_{geo} = 6.170$ cm $\rho = 1469$ mm |
| TEM_{00} | $0.19\mu\text{W}$ | | |
| HOM | $1.1\mu\text{W}$ | $3.6\mu\text{W}$ | $35.4\mu\text{W}$ |
| Total | $1.3\mu\text{W}$ | $3.8\mu\text{W}$ | $35.6\mu\text{W}$ |
| Specifications | $\leq 75\mu\text{W}$ | | |

Table 7.8: Transmission of the carrier **HOM** and side bands after the two **OMC** cavities in the power recycled 25 W configuration. The transmitted power is computed for three different working points (WP): the nominal WP ($\rho = 1499$ mm, $l_{geo} = 6.150$ cm), and two other WPs corresponding to the extrema of the error bars given in Tab. 7.7.

The transmission factors and the residual powers after the two **OMC** cavities have been estimated for each mode up to $m + n = 14$ (where m and n refer to the indexes of the TEM modes). The **OMC** transmission factors have been calculated for three different sets of parameters:

- The nominal set of parameters (or nominal working point) corresponds to the local minimum in the figure of merit obtained with two **OMC** cavities. It is obtained for a geometrical length $l_{geo} = 6.150$ cm and a **RoC** $\rho = 1499$ mm.
- Another set of parameters ($l_{geo} = 6.130$ cm and a **RoC** $\rho = 1529$ mm) has been tested. It corresponds to the worst possible working point in term of transmission of the carrier **HOM**, when the length and the **RoC** stay within the error bars given in Tab. 7.7.
- Another set of parameters ($l_{geo} = 6.170$ cm and a **RoC** $\rho = 1469$ mm) corresponds to the worst possible working point in term of transmission of the **HOM** of the side band at 56.44 MHz, still according to the error bars given in Tab. 7.7.

| Dual recycling 125 W | | | |
|----------------------|--|--|--|
| Carrier | $l_{geo} = 6.130$ cm $\rho = 1529$ mm | Nominal WP $l_{geo} = 6.150$ cm $\rho = 1499$ mm | $l_{geo} = 6.170$ cm $\rho = 1469$ mm |
| HOM Total | $15.8\mu\text{W}$ | $3.7\mu\text{W}$ | $1.4\mu\text{W}$ |
| Specifications | $\leq 80\mu\text{W}$ | | |
| SB at 6.27 MHz | $l_{geo} = 6.130$ cm $\rho = 1529$ mm | Nominal WP $l_{geo} = 6.150$ cm $\rho = 1499$ mm | $l_{geo} = 6.170$ cm $\rho = 1469$ mm |
| TEM_{00} | $21.6\mu\text{W}$ | $21.4\mu\text{W}$ | $21.1\mu\text{W}$ |
| HOM | $0.13\mu\text{W}$ | $0.02\mu\text{W}$ | $8 \times 10^{-3}\mu\text{W}$ |
| Total | $21.7\mu\text{W}$ | $21.4\mu\text{W}$ | $21.1\mu\text{W}$ |
| Specifications | $\leq 80 \mu\text{W}$ | | |
| SB at 56.44 MHz | $l_{geo} = 6.130$ cm $\rho = 1529$ mm | Nominal WP $l_{geo} = 6.150$ cm $\rho = 1499$ mm | $l_{geo} = 6.170$ cm $\rho = 1469$ mm |
| TEM_{00} | $0.26 \mu\text{W}$ | | |
| HOM | $1.6\mu\text{W}$ | $5.0\mu\text{W}$ | $48.8\mu\text{W}$ |
| Total | $1.8\mu\text{W}$ | $5.2\mu\text{W}$ | $49.1\mu\text{W}$ |
| Specifications | $\leq 80 \mu\text{W}$ | | |

Table 7.9: Transmission of the carrier **HOM** and side bands after the two **OMC** cavities in the dual recycled 125 W configuration. Transmission of the carrier **HOM** and side bands after the two **OMC** cavities in the power recycled 25 W configuration. The transmitted power is computed for three different working points (WP): the nominal WP ($\rho = 1499$ mm, $l_{geo} = 6.150$ cm), and two other WPs corresponding to the extrema of the error bars given in Tab. 7.7.

All results concerning the carrier **HOM** and the side bands (6.27 MHz and 56.44 MHz) TEM_{00} and **HOM** are summarized in Tab. 7.8 for the power recycled 25 W configuration and in Tab. 7.9 for the dual recycled 125 W configuration. These tables contains three columns corresponding to the three working points mentioned above. The power expected in the TEM_{00} as well as the sum over all **HOM** are given. For the side bands the sum between the TEM_{00} and the **HOM** modes is also provided. These numbers must be compared to the specifications that have been discussed in section 7.3.1. These specifications are satisfied for the carrier and the two side bands (6.27 MHz and 56.44 MHz).

The transmitted powers for the fundamental and **HOM** modes of the side band at 131 MHz are shown in Tab. 7.10 for the power recycled 25 W and dual recycled 125 W configurations respectively. For this side band, the modulation index is assumed to be 10 times lower than it is for the other side bands, ie $m = 0.01$ (some uncertainty remains on this value as the baseline modulation depth has not been defined yet for the 131MHz side band). This side band will only be used during lock acquisition and its filtering is therefore less critical. The results reported in Tab. 7.10 show that the requirements that apply to side bands used in science mode (maximum transmitted power of 0.08 mW) for the SR 125 W configuration are not satisfied with the 131 MHz side band, when the **OMC RoC** and length are at the margin of the error bars given in Tab. 7.7. It has been checked that the dominating modes are the **HOM** of orders 9 and 14. Since no simulation results for the 131 MHz side band **HOM** are

| power recycling 25 W | | | |
|----------------------|--|--|--|
| SB at 131.7 MHz | $l_{geo} = 6.130$ cm $\rho = 1529$ mm | Nominal WP $l_{geo} = 6.150$ cm $\rho = 1499$ mm | $l_{geo} = 6.170$ cm $\rho = 1469$ mm |
| TEM_{00} | $0\mu\text{W}$ | $0\mu\text{W}$ | $0\mu\text{W}$ |
| HOM | $61.1\mu\text{W}$ | $0.17\mu\text{W}$ | $11.2\mu\text{W}$ |
| Total | $61.1\mu\text{W}$ | $0.17\mu\text{W}$ | $11.2\mu\text{W}$ |
| Dual recycling 125 W | | | |
| SB at 131.7 MHz | $l_{geo} = 6.130$ cm $\rho = 1529$ mm | Nominal WP $l_{geo} = 6.150$ cm $\rho = 1499$ mm | $l_{geo} = 6.170$ cm $\rho = 1469$ mm |
| TEM_{00} | $0\mu\text{W}$ | $0\mu\text{W}$ | $0\mu\text{W}$ |
| HOM | $679\mu\text{W}$ | $1.9\mu\text{W}$ | $125\mu\text{W}$ |
| Total | μW | μW | μW |

Table 7.10: Transmission of the side band at 131.7 MHz after the two **OMC** cavities in the power recycled 25 W configuration and in the dual recycled 125 W configuration. A modulation depth of 0.01 is assumed.

available at the time of the TDR writing, a large uncertainty remains on the estimation of the power in these modes. If the present assumptions are confirmed and if the error on the **OMC RoC** exceeds 1.1% the 131 MHz side band will have to be switched off during science mode in order to not spoil the DARM locking accuracy.

7.3.3.2 Parameter tolerancing

Acceptable error bars for the manufacturing of the **OMC** cavities are shown in Tab. 7.7. Errors of ± 30 mm on the **RoC** and ± 200 μm on the geometrical length are accepted. They are compatible with the specifications on **OMC** filtering previously discussed.

An error of ± 0.03 degrees on the surfaces tilt (that determines also the beam incidence angle) is accepted. Preliminary calculations indicate that this error is small enough to keep the resonating beam inside an optical aperture of 5 mm diameter around the optical centers of the surfaces. According to the polishing company that has been contacted and has accepted our specifications (THALES SESO) a smaller error bar on this angle would increase significantly the production cost.

Specifications for the surface quality are shown in Tab. 7.11. They are driven by the need to minimize scattering losses, and have been accepted by the polishing company previously mentioned.

| Surface clear aperture | Flatness defects | Micro-roughness |
|------------------------|-----------------------|-----------------|
| $\phi \geq 5$ mm | $\leq \lambda/10$ PtV | ≤ 0.3 nm |

Table 7.11: Surface quality specifications for the Advanced Virgo **OMC** cavity.

7.3.3.3 Length control strategy

The baseline solution is to maintain the **OMC** cavities locked on the carrier TEM_{00} by using a thermal control based on Peltier actuators, similarly to what was designed for the Virgo **OMC** cavity (see [208, 209]). Each **OMC** cavity will be surrounded by a box made of copper and the Peltier cells will be put on the sides of the box.

The error signal will be obtained by modulating the optical length of each **OMC** cavity. The two modulation frequencies will be chosen in the range between 15kHz and 30kHz, above the first mechanical resonance. The modulation will be obtained by applying a force (of the order of a few tenths of Newton) on top of the cavity, using a small PZT actuator. The PZT will be pre-constrained by a screw. The strength of this pre-constraint should be tuned so that the induced birefringence losses remain sufficiently small. In Virgo, the **OMC** internal losses were measured to be lower than 1%. In order to avoid thermal dependance of the demodulate output a bridge of Invar (low thermal expansion coefficient) will be used to hold the screw. The error signal for the first **OMC** cavity will be extracted by demodulating the signal provided by the photodiode looking at B1t beam (a pickoff of the power resonating inside the first **OMC**, see Fig. 7.9). The error signal for the second **OMC** will be extracted by demodulating the signal provided by one of the photodiodes looking at the B1 beam (transmission of the second **OMC**).

All the electronic components involved in the **OMC** control will be tested for their vacuum compatibility.

The **OMC** length control loop must be designed so that its bandwidth will extend up to a few tens of mHz, and a locking accuracy of a few 10^{-12} m should be reached (as accomplished with the Virgo **OMC**). The motivation for the required control bandwidth is discussed in [202]. The length of the **OMC** must be controlled to keep the cavity resonant at the laser frequency. Within the bandwidth of the **OMC** servo, any drift in laser frequency is compensated by an appropriate variation of the **OMC** length. For frequencies above the loop unity gain, the fluctuations of the laser frequency with respect to the **OMC** resonance give a residual frequency offset. This frequency offset can couple the **OMC** length noise. Following the calculation presented in [202] and assuming a length noise of $3.2 \times 10^{-17} \text{m}/\sqrt{\text{Hz}}$ (which corresponds to the requirement given by Eq.7.6), one finds that the frequency offset should remain lower than 10kHz to keep the noise a factor 10 below the sensitivity. Frequency fluctuations of a laser stabilized on a rigid reference cavity are expected to be of the order of $1\text{Hz}/\sqrt{\text{Hz}}$ at 10 mHz [205]. Therefore the foreseen **OMC** control bandwidth is sufficiently large.

The mechanical design of the **OMC** box and its thermal control is not yet frozen at the time of the TDR writing. First mechanical tests are foreseen in the coming months.

7.3.4 Constraints on side band RIN for the INJ subsystem

Side band **RIN** above 10 Hz can directly impact the Advanced Virgo sensitivity as it translates into power fluctuations in transmission of the **OMC** cavities. To avoid this problem specifications must be set on the side band **RIN** at the level of the **RF** generator and the

Electro-Optical Modulator (EOM) placed in INJ subsystem.

The required side band RIN above 10 Hz when the side bands are filtered out by two OMC cavities (baseline design) is shown in Fig. 7.10.

7.3.5 Discussion of alternative solutions

The current baseline solution with two OMC cavities has been designed in order to obtain a filtering of the side bands which is compliant with the requirements set by ISC, and under the assumption that the OMC cavities need to be controlled.

As it was discussed in [206] it might be possible to keep the OMC free by locking the laser frequency on the OMC length (this is valid for only one OMC cavity). If it is no longer needed to control the cavity length and if diffraction losses can be kept lower than what was assumed for the OMC design (ie. losses lower than 30 ppm per face) it might be possible to increase by a factor 3 or more the OMC finesse. We could then envision an alternative solution consisting of a single OMC cavity of larger finesse. This alternative solution can be interesting in case of difficulties arising with the present baseline. The draw-backs of using a single OMC with larger finesse are the loss of OMC controllability and an increase of the cavity intrinsic losses. This solution could be more easily implemented if the constraints on side band transmission were relaxed (for instance if the side band low frequency fluctuations are lower than what was assumed for the baseline design).

One should note that using a single OMC cavity might lead to more stringent requirements on the side band RIN above 10 Hz. As example the requirements on the side bands RIN for a single OMC cavity with a finesse of 650 are showed in Fig. 7.11. Measurements made with the Virgo RF generator indicate that these requirements are reachable with the current technology.

One should note that the current baseline design offers the flexibility to go back to a single cavity solution later.

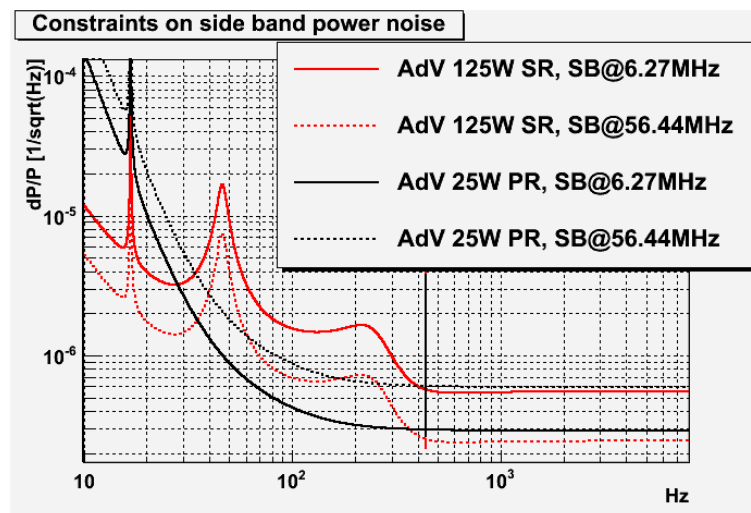


Figure 7.10: Constraints on side bands RIN, assuming filtering by 2 OMC cavities (baseline scenario).

7.3.6 OMC alignment and beam matching

7.3.6.1 OMC alignment

| | Constraints on shift | Constraints on tilt |
|---------------------|---|--|
| Disp. RMS | $x_{omc}^{rms} \leq 7.5 \times 10^{-6}$ m | $\theta_{omc}^{rms} \leq 36 \times 10^{-6}$ rad |
| Disp. noise at 10Hz | $x_{omc}(f) \leq 1.1 \times 10^{-12}$ m/ $\sqrt{\text{Hz}}$ | $\theta_{omc}(f) \leq 5.1 \times 10^{-12}$ rad/ $\sqrt{\text{Hz}}$ |

Table 7.12: Requirements on beam jitter in front of the OMC cavities.

| | Constraints on shift | Constraints on tilt |
|---------------------|---|--|
| Disp. RMS | $x_{bench}^{rms} \leq 590 \times 10^{-6}$ m | $\theta_{bench}^{rms} \leq 0.5 \times 10^{-6}$ rad |
| Disp. noise at 10Hz | $x_{bench}(f) \leq 8.3 \times 10^{-11}$ m/ $\sqrt{\text{Hz}}$ | $\theta_{bench}(f) \leq 6.5 \times 10^{-14}$ rad/ $\sqrt{\text{Hz}}$ |

Table 7.13: Requirements on the residual motion of the SDB1 bench due to the constraints on OMC alignment.

Requirements on beam jitter (beam shift and beam tilt) at the entrance of the OMC cavity have been established in [198, 199]. These requirements are presented in Tab. 7.12. The requirements on the RMS jitter have been obtained by requesting that the TEM_{01} mode leakage to represent less than 1% of the power in the TEM_{00} . The requirements on the jitter noise at 10Hz have been obtained by requesting that the noise due to the power fluctuations in transmission of the OMC cavities remain a factor 10 below the nominal sensitivity.

As explained in [198, 199], the requirements on the OMC alignment translate into constraints for the SDB1 bench residual motion, which are obtained by taking into account the magnification of the OMC-MMT. These constraints are reported in Tab. 7.13.

The requirements on the relative alignment between the two OMC cavities can be obtained by requesting that the TEM_{00} losses in the second OMC cavity due to misalignment remain below 0.5% (which gives a contribution to the loss budget comparable to or lower than the

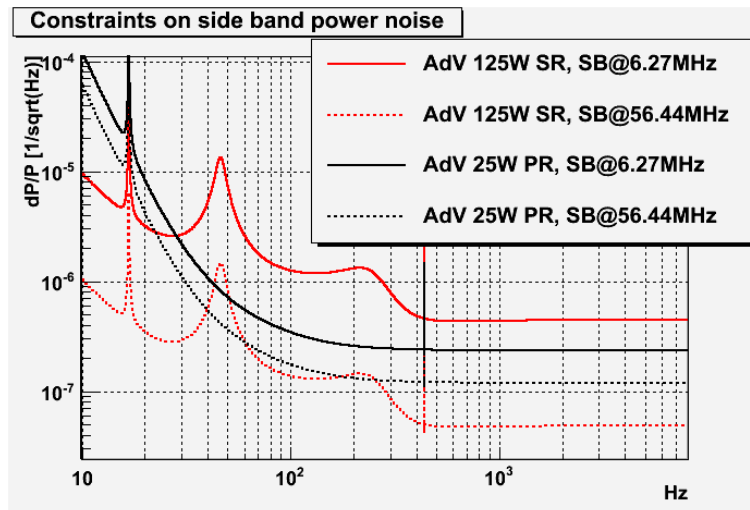


Figure 7.11: Constraints on side bands RIN, assuming filtering by 1 OMC cavity with F=210.

diffraction losses). Using a similar calculation as the one presented in [198, 199], this leads to the following constraints:

- the relative shift between the two OMC cavities must be kept lower than $13\ \mu\text{m}$;
- the relative tilt must be kept lower than $64\ \mu\text{rad}$.

The relative alignment of the two OMC cavities will be performed during a prealignment step on a test bench. Each OMC is surrounded by a copper box. The two boxes will be installed on a common bread-board. During the mechanical conception the first OMC box will be rigidly mounted on the bread-board, while the second OMC will be equipped with temporary motorization allowing a fine adjustment of its relative position with respect to the first OMC cavity. Once this prealignment is completed the second OMC will be rigidly connected to the board.

In order to be able to align the beam with respect to the OMC cavities, two mirrors placed on the SDB1 bench before the first OMC will be equipped with actuators (picomotors or customized PZT). Two complementary methods are proposed for the alignment sensing:

- one solution is similar to a method that has been used already to align the Virgo OMC cavity. This solution consists in using the error signal provided by two quadrants installed on the SDB1 bench on the B5 beam path;
- another complementary solution will be based on the "dithering/beacon" technique already implemented with DC detection at LIGO Hanford [214] and at GEO. This solution does not require any additional hardware.

7.3.6.2 OMC mode matching

The waist of the beam reaching the OMC cavities should be adapted to the cavity waist in order to not induce mismatching losses. This is the goal of the OMC-MMT described in section 7.8.2. When setting constraints for the telescope one needs to account for the systematic mismatch $\Delta z_{err} = 1.3\ \text{cm}$ due to the two OMC optical layout.

By requesting that the mismatching losses remain below 0.5% per OMC one obtains the following constraints for the telescope mode matching (they are computed in a fused silica medium):

- the allowed waist mismatch is: $\delta w \leq \pm 19\ \mu\text{m}$;
- the allowed error on the waist position is: $\delta z \leq \pm 2.9\ \text{cm}$.

7.3.7 OMC loss budget

The following optical losses are anticipated:

- the internal cavity losses (dominated by diffraction losses) should be lower than 2% for the two cavities, assuming losses of 30ppm per surface (which is 3 times worse than the best super-polished optics);
- beam mismatching should induce losses lower than 1% for the two cavities;

- losses due to misalignment should be of the order of 1.5% (with up to 0.5% losses due to the relative misalignment between the two cavities, and 1% losses due to the beam misalignment).

This budget gives total losses of 4.5%.

7.3.8 OMC planning

The preliminary optical design has been completed, and work on the mechanical design is on going. A first OMC prototype (with a finesse of 50) has been ordered in the summer 2011 and is now available at LAPP. This prototype is going to be used for mechanical tests in the next months. Measurements of the mechanical resonances will be performed as well as a preliminary measurement of the OMC length noise. Electronic components will be tested for vacuum compatibility. Results of this prototyping tests should be available in the summer 2012.

The OMC substrates are expected to be ordered when the TDR review is completed.

Once the OMC design is frozen (in particular for the choice of the radius of curvature) and the campaign of prototyping tests is completed, the polishing of 6 cavities (including spares) will be ordered. The polishing should last for up to 6 months.

The OMC cavities will then be sent to LMA for the coating. We plan to ask for one or two cavities with a high finesse ($F \geq 650$), while the other cavities will be coated for a finesse of 210 (baseline design). These OMC cavities should be ready by mid 2013.

The mechanical assembly and the final tests will then be performed on a test bench at LAPP. The high finesse cavity will also be tested (in particular to evaluate its controllability and the internal losses), keeping the flexibility for a possible change of design if any show-stopper arises with the baseline design.

7.4 Bench components

This section describes the various small pieces of hardware (optics mounts, mirrors, motors, diaphragms) that will be installed on the benches.

7.4.1 Optics

Several types of optics are needed:

- lenses: in addition to the meniscus lens or doublets that will be described in the sections related to the telescopes design, we will need smaller lenses to adapt the beam size to the OMC waist or to the photodiodes aperture;
- folding mirrors and splitters;
- dichroic mirrors: they will be needed at each port to separate the YAG beam from the Hartmann beam or from the auxiliary laser;
- polarisator cubes: They will be used to separate the main polarisation (S) from the other spurious polarisations. In particular the amount of not S-polarized light that is sent

to the OMC (B1p) and that is reflected by the OMC (B1s1, B1s2) will be monitored, which will allow us to estimate the amount of P polarization generated inside the OMC due to the birefringence;

- beam dumps: Small glass dumpers will be used to dump low power beams, such as the photodiode reflection.

The typical size of the optics placed on the benches will be 2 inches in diameter. In particular this is necessary for the optical elements that need to be crossed by several separated beams (such as the main beam and secondary beams at the detection port), or by a Hartmann beam which will be roughly twice as large as the YAG beam. There can be some exceptions concerning for instance the splitters placed in front of the photodiodes where the beam is very small (typically smaller than $400\mu\text{m}$). In this case 1 inch optics may be used.

All optics installed on the detection benches (dark port) should be super-polished in order to minimize the amount of back-scattered light. Concerning the end benches and pickoff bench the decision to use super polished optics might be taken as well in order to minimize the risk of back-scattering. This will be confirmed by calculations of scattered light that are currently being checked.

7.4.2 Mounts and motors

This section presents the optics mounts, shutters and required motors. The category of optics will determine the needed type and size of mounts. For each type of mount we need to define which degrees of freedom need to be tunable:

- all mirrors or splitters used to center the beam on sensors (photodiodes, quadrants, cameras) or on the output mode cleaner should stand on mounts equipped with 3 motorized screws allowing rotations in all degrees of freedom;
- lens involved in the tuning of telescope mode matching should stand on mounts equipped with a motorized translation stage. Other lenses will lie on a manual translation stage;
- photodiodes placed inside air boxes (for under-vacuum benches) will lie on a specific support. No screws or motors will be needed, as splitters will already be in place in front of the air boxes to allow to center the beam on all sensors;
- photodiodes located on external benches will be installed on mounts equipped with two screws.

In vacuum motorized mounts will use vacuum compatible motors. Two types of motors are currently envisioned:

- Picomotors, which were already used for the alignment of the Virgo OMC. They induce vibrations when used, but they can be switched off in science mode to not introduce noise.
- Customized PZT actuators, which were already used on the Virgo Injection bench. Their advantage would be to reduce the amount of vibrations during the alignment step. We still need to check their impact in science mode.

Mounts holding the splitters placed in front of photodiodes might also host the glass dump that will absorb the photodiode reflection. Another option is to dump the photodiode reflec-

tion inside the air box.

Motorized shutters will be needed in front of photodiodes or inside air boxes.

Fast shutters must be designed to protect photodiodes from unlocks during which a large part of the optical power stored in the interferometer will exit the asymmetrical port for a short period of time. Preliminary specifications written in the **ISC** chapter suggests that the shutters should be completely closed within 1-2 ms after receiving a trigger. Simulation studies of the **ITF** unlocks are needed in order to provide more reliable specifications.

7.4.3 Diaphragms

Mounts of the optics where the risk of clipping is elevated (such as the main telescope optics) will be equipped with diaphragms made of 6H-SiC. Such diaphragms have been installed and tested on the Virgo suspended detection bench [215, 216].

7.4.4 High power beam dumper

High power, vacuum compatible, beam dumpers will need to be installed on the **SDB1** or **SDB2** benches in order to dump the B1s1 beam (reflection from the first **OMC** cavity). Such beam dumper has already been developed for Virgo [217] and is presented in the **INJ** chapter. It could be used on the Advanced Virgo suspended detection benches or serve as reference to develop other beam dumpers.

7.5 Longitudinal photodiodes and electronics

7.5.1 Photodiodes used for DC detection

The DC photodiodes will sense the dark fringe signal (B1 beam). For this beam, the goal is to have each of the technical noises coming from the sensing chain (photodiode quantum efficiency, front end electronic, ADC noise) a factor 10 below shot noise. This is challenging since this means for instance, that the quantum efficiency must be as good as 99%, a number difficult to reach although such efficiency might have been achieved on photodiodes used by GEO. The design of the preamplifier will also be different from the one of the control photodiodes because of this tighter noise requirement. Notice however, that the bandwidth of the DC photodiode is limited to a few tens of kHz. The design work as well as the photodiode selection is still in progress at the time of writing the TDR.

7.5.2 Control photodiodes

The purpose of the control photodiode is to sense the interferometer control signals coming from the various sidebands. The main challenge for the sensing chain is a large number of demodulation frequencies (see Tab.7.14), up to five for a single beam, with frequencies values like 56 MHz for f_2 or 131 MHz for f_4 being at the limit of the bandwidth of a typical

| Port | Needed signals | Motivations |
|----------------------------------|---|--|
| Symmetric port (B2) | DC, f_1 , $3f_1$, f_2 , f_3 , f_4 | ITF control |
| Dark port after OMC (B1) | DC $2f_1$, $2f_2$ | DC readout and ITF control Monitoring |
| Dark port before OMC (B1p) | DC, f_1 , f_2 , $2f_1$, $2f_2$, f_4 | Lock acquisition, monitoring |
| First OMC reflection (B1s1) | DC, f_1 , f_2 , $2f_1$, $2f_2$, f_4 | Monitoring |
| Second OMC reflection (B1s2) | DC | Monitoring |
| First OMC pickoff (B1t) | DC, $2f_1$, $2f_2$ | OMC control and monitoring |
| Power recycling pickoff (B4) | DC, f_1 , f_2 , $2f_1$, $2f_2$, f_4 | ITF control |
| Beam splitter pickoff (B5) | DC, f_1 , f_2 , $2f_1$, $2f_2$ | ITF control fall-back |
| Arm cavity transmission (B7, B8) | DC, f_1 | Lock acquisition |

Table 7.14: List of needed signals and demodulation frequencies at each interferometer output port for the longitudinal photodiodes, with $f_1 = 6.27$ MHz, $f_2 = 56.44$ MHz, $f_3 = 8.36$ MHz, $f_4 = 131.7$ MHz. The signals demodulated at f_4 will not be used in science mode and can have a worsened SNR.

photodiode.

7.5.2.1 Photodiodes

On the photodiode front, no significant progresses have been made over the last 20 years. The photodiode used for Virgo are not anymore produced and new type have still a large capacitance (typically 200 pF) and resistance (typically 10 ohms), introducing a cutoff at a few tens of MHz. The diameter of the photodiode will be 3 mm, large enough for convenient alignment. A smaller diameter makes the alignment more difficult and the benefit of the reduce capacitor is canceled by the increase of the internal resistance, therefore without noticeable change of the photodiode bandwidth.

A first investigation of the available photodiodes has been made (see [226]), but tests of the photodiodes are still in progress and the final selection has not been made. It is anticipated that the maximum power handled by a photodiode will be around 100 mW, like for initial Virgo, with an operation point at about half power (50 mW) or slightly above. A couple of photodiodes are expected to be used to handle the needed power and to provide the demodulated signals with a signal to noise ratio equivalent to a 100 mW shot noise limited signal (this is the value used by ISC for the design of the control loops). The exact number of photodiodes and value for the operating power will be decided once the full photodiode plus electronic chain will be characterized, since for control photodiodes there is some freedom in the selection of the power used, as well as on the selection of the signal amplitude via the modulation index for instance.

7.5.2.2 Preamplicifier

To be able to meet the goal of a signal to noise ratio equivalent to a 100 mW shot noise limited signal with a reasonable used power, the target for the electronic design is to have a

noise floor below the shot noise level, hopefully a factor 2 below (in this case, 121 mW would be used to meet the goal).

Since multiple demodulation frequencies will be used, a wideband design of the preamplifier is selected. Two options are possible for the preamplifier: a simple load resistor by a voltage amplifier or a transimpedance preamplifier. First, we tested various low noise transimpedance amplifiers. The high impedance input is source of instability at low gains. In fact, proper operation was not possible below a gain of 100 or even more, depending on the amplifier. It has the effect of reducing the bandwidth (see Fig. 7.12 for the typical bandwidth for two amplifiers used with their lowest gain). The minimal required gain could also be a problem in the case of the THS3201 since it exceeds the maximum value needed to fit the signal in the dynamical range of the amplifier output. Furthermore, the impedance of the photodiode creates a zero in the noise gain response. Therefore, this front-end type shows a noise peak which exceeds the shot-noise at 56 MHz (see Fig. 7.12 top right and bottom left). We also tested the simple load resistor option (bottom right on Fig. 7.12). We were able to have the electronic noise floor below shot noise at 56 MHz in this last configuration, which therefore has been selected. Development is ongoing to provide the final electronic with this technique.

The typical resistance load will be 30 Ohms. A larger value would limit the bandwidth, given the typical internal capacity of the photodiode. In this condition, the thermal noise of the resistance is around $0.6 \text{ nV}/\sqrt{\text{Hz}}$ and the shot noise of 50 mW is around $3.3 \text{ nV}/\sqrt{\text{Hz}}$, with about a factor 2 attenuation at 56 MHz.

7.5.2.3 Demodulation electronics

As already explained, the number of demodulation signals will increase with Advanced Virgo. Furthermore, the selection of the frequencies used might change according to the configuration of the interferometer and effective behavior of the sidebands in the interferometer, as it already happened in the past. Therefore, we are looking for a more flexible design, with the possibility to select online the demodulation frequency. The solution under development is to digitize the signal at high frequency (400 or 500 MHz) and then perform a digital demodulation. With such a scheme, although the noise of the digitization chain is larger than a pure analog demodulation scheme, it offers the possibility to multiple demodulations at no extra cost for the noise point of view, contrary to the case were the RF photodiode signal is split to multiple analog demodulation circuits. Another benefit of such a solution is a more compact front end electronic with integrated digital processing which could be put on the suspended bench hosting the photodiode(s). This will reduce the number of cables going out which usually spoiled the performances of the seismic isolation.

The candidate ADC is the ISLA214P50 from Intersil. It offers a 72 dB dynamic and samples the data at 500 MHz. Since the total peak to peak amplitude of the AC signal is expected to be limited to 5.7 mW, or 0.13 V after the resistor, the gain of the front end voltage amplifier before the ADC has to be around 15 to match the input dynamic of the ADC (2 V). The level of the shot noise will therefore be $50 \text{ nV}/\sqrt{\text{Hz}}$ at the input of the ADC, which is above

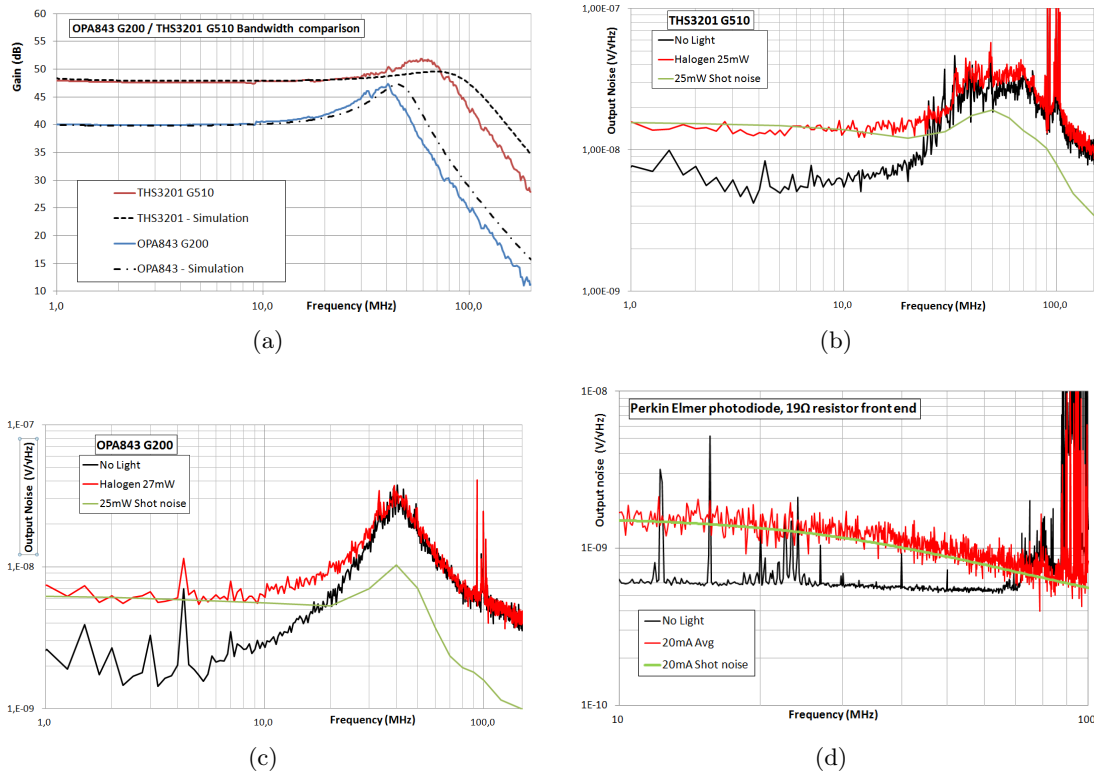


Figure 7.12: Results from the prototyping of the AC photodiode readout. Top left: simulated and measured transfer functions for two types of amplifier. Top right: electronic noise floor and shot noise (measured with a halogen lamp and predicted) with the THS3201 amplifier. Bottom left: same curves for the OPA843 amplifier. Bottom right: same curves for a single load resistor.

the expected input noise floor of the ADC: $22 \text{ nV}/\sqrt{\text{Hz}}$.

The demodulation will be performed in two steps. The main step will be made by a Stratix IV GX FPGA (model EP4SGX70HF35C3N), which will output demodulated signals at about 1 MHz. Then further low pass digital filtering will be performed on the onboard DSPs, like for the existing Virgo 7476 ADCs.

There is not much margin in this design, with challenging issues on the jitter noise of the ADC clock for instance, beside the ADC noise floor. The construction of an evaluation board is in progress to assess the feasibility of this solution. This evaluation board includes another possible ADC: the ADS5475 from Texas Instrument. First results are expected in April 2012 and will tell us if the digital solution could be confirmed as baseline. In case of limited result, the backup solution will be to use analog mixers, like for initial Virgo, with digital demodulation for the less critical signals.

7.5.3 Photodiode airbox

Several photodiodes have to be placed on under vacuum benches. The front-end electronics of the photodiodes is not vacuum compliant therefore a special airbox hosting the photodiode and its preamplifier needs to be designed. Each airbox contains only one photodiode. A preliminary space constraint of $10 \times 10 \text{ cm}$ is considered for this box.

Air boxes also need to be developed for the quadrants photodiodes described in section 7.6.

7.6 Quadrants and electronics

Quadrant photodiodes (QPD) are used for the linear alignment [229] of the various optical components in Advanced Virgo. The location of the QDPs is shown in Fig. 7.13. As described in the ISC chapter two QDPs each are used at the symmetric port (B2), the anti-symmetric port (B1p), the PR pickoff port (B4), and at the North arm (B7) and West arm (B8) end mirror transmissions for the ITF alignment. Two QPDs will also be foreseen on the SDB2 bench for the BS pickoff (B5) as possible fall-back solution for the ITF alignment. Two additional QPDs will be placed on the SDB1 bench for the OMC alignment (they might be equipped with a simplified front-end as it was done in Virgo). This implies that in total up to $7 \times 2 = 14$ QPDs front-ends need to be installed for Advanced Virgo.

For a Gaussian beam with radius w incident on the center of a QPD with diameter $D = 6w$, a fraction $\text{erfc}(3\sqrt{2}) = 1.97 \times 10^{-9}$ of the intensity is not contained in the QPD. With the baseline telescope configurations (see section 7.8.2 and section 7.9.2) the beam sizes of the laser light impinging on the sensors will range within $300 - 400 \mu\text{m}$. In case of future evolution in the baseline design, the beam sizes on the bench could be increased to $1100 - 1500 \mu\text{m}$ if needed. In the latter case it may be possible to employ the 11 mm diameter QPDs used for Virgo+, while in the former case new 5 mm diameter QPDs (QP45 from First Sensor is under consideration) may be used. The 5 mm QPDs have a lower capacitance and allow operation at higher frequencies.

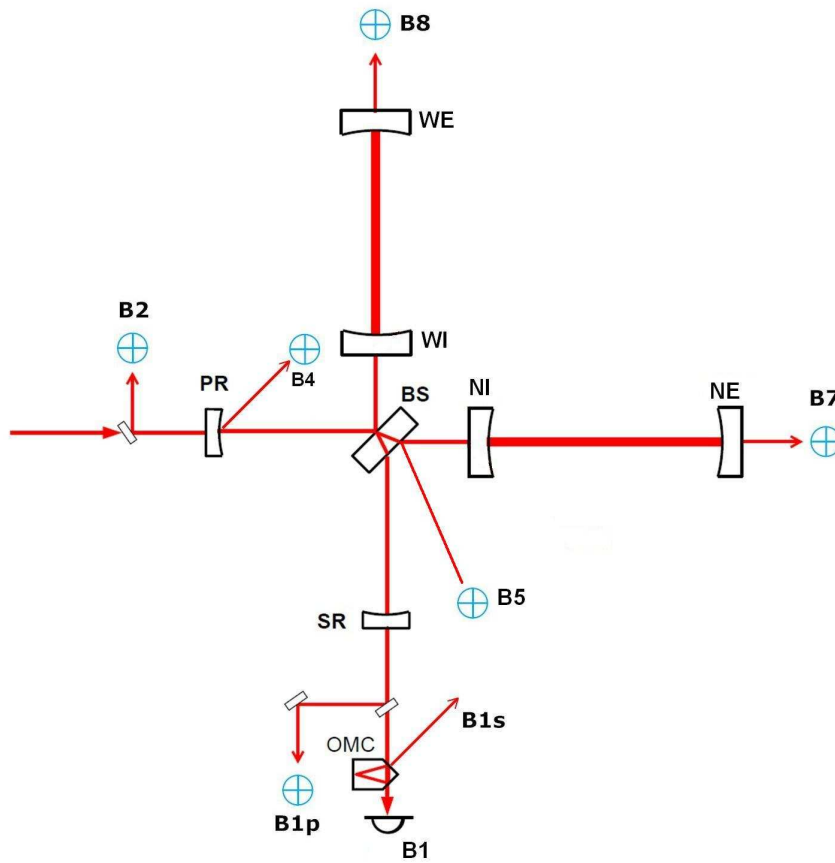


Figure 7.13: Position of the various beams and quadrant photodiodes in Advanced Virgo.

7.6.1 Power on photodiodes

We discriminate between the following definitions for DC power. We have P_{nom} and P_{max} which are the nominal DC and maximum DC power, respectively. Powers can be different during lock acquisition mode and science mode of operation of the interferometer.

The expected nominal DC powers (in science mode) for Advanced Virgo are as follows:

- B1p: 2.5 mW per quadrant photodiode;
- B2, B4, B7, B8: 25 mW per quadrant photodiode.

The QPDs are designed for 50 mW maximum light (12.5 mW per quadrant) except for the anti-symmetric Port (5 mW maximum). The AC powers in science mode have been estimated in [229].

7.6.2 Modulation frequencies

The demodulation frequencies for each output port have been determined (see OSD chapter) as

- $f_1 = 6\,270\,777$ Hz
- $f_2 = 56\,436\,993$ Hz
- $f_3 = 8\,361\,036$ Hz

In science mode, the quadrant photodiodes need to measure at various frequencies listed below.

- B2: f_1, f_2, f_3, DC
- B4, B5: f_1, f_2, DC
- B1p: $f_1, f_2, 2f_2, \text{DC}$
- B7, B8: DC

Note that the QPDs for B7 and B8 will be optimized for DC operation (as well as one of the B1p quadrant), while the remainder will be optimized for RF mode of operation. In this manner the noise performance will be optimized for the specific sensors. Moreover, demodulations at $2 \times f_i$ will be used for monitoring purposes only. In addition to these, ISC proposes [230] the use of one additional high frequency modulation (131 MHz) during aberration compensation commissioning. Although requirements on modulation and demodulation efficiency are not yet computed, they will be much relaxed with respect to the other frequencies, since this one will not be used in science mode.

7.6.3 Front-end electronics

The front-end will be equipped with individual outputs for each HF channels (note that this differs from the situation for Virgo+, where LR and UD signals are provided). Individual HF outputs have the advantage that information is available on:

- Is the beam spot at the center of the QPD?
- Is there a signal?
- Do the amplifiers clip?

Obviously, this choice has consequences for the number of cables, feedthroughs, layout of the demodulation board and ADC channels, but we believe that this is warranted through the motivation given above.

For the DC channels, the present choice is to work with differential signals directly from the detector PCB and connect these to the ADCs.

7.6.4 Noise contributions

There will be several noise contributions in the linear alignment signals. The system will be designed such that the noise is dominated by shot noise. Additional noise sources, *e.g.* from electronic and digitization noise, should contribute less than shot noise. Here, we will investigate the various contributions.

7.6.4.1 Shot noise

Signals from 2 quadrants are summed and then the ratio of the difference and sum of 2 of these sums is taken (*e.g.* left and right). For the QPDs for Advanced Virgo we consider the QP45-Q by First Sensor (see Fig. 7.15). These sensors have a responsivity of 0.58 A/W at 1.064 μm . For the QPDs with 25 mW of nominal power, the maximum acceptable current per quadrant segment is estimated at $i_{\text{max}} = 0.0125 \times 0.58 \rightarrow 7.2$ mA, while the nominal current will be 3.6 mA. The corresponding shot noise per quadrant segment is then $\sigma_{i_s} = \sqrt{2ei_s\Delta\nu} \rightarrow 34$ pA for a 1 Hz bandwidth. The relative accuracy of the current measurement on a single quadrant segment is then limited to 9.4×10^{-9} .

For control of various degrees of freedom (*e.g.* D(-), C(-), SRM) the DC information of two QPDs must be combined and the relative uncertainty increases to 1.3×10^{-8} at the shot noise limit¹.

7.6.4.2 Electronic noise

During the design of the front-end electronics for the QPDs for Virgo+, the various contributions from electronic noise: voltage noise, current noise, and $1/f$ noise, were studied in detail [240, 241, 242, 243, 244, 245, 246]. Low-frequency noise measurements were carried out on various prototype QDPs to determine their electronic noise. The QDP prototype for

¹The Virgo+ QPDs can handle 30 mW of light incident on 2 quadrants (in case of equally shared power) before saturating the amplifier. The responsivity at 1.064 μm is 0.45 A/W. This means that a single quadrant has a maximum current of $i_{\text{max}} = 0.015 \times 0.45 \rightarrow 6.75$ mA, while the nominal current will be 3.4 mA. The corresponding shot noise per quadrant segment is then $\sigma_{i_s} = \sqrt{2ei_s\Delta\nu} \rightarrow 33$ pA for a 1 Hz bandwidth. The relative accuracy of the current measurement per segment is then limited to 9.7×10^{-9} , and this equals the uncertainty obtained for a QPD measurement

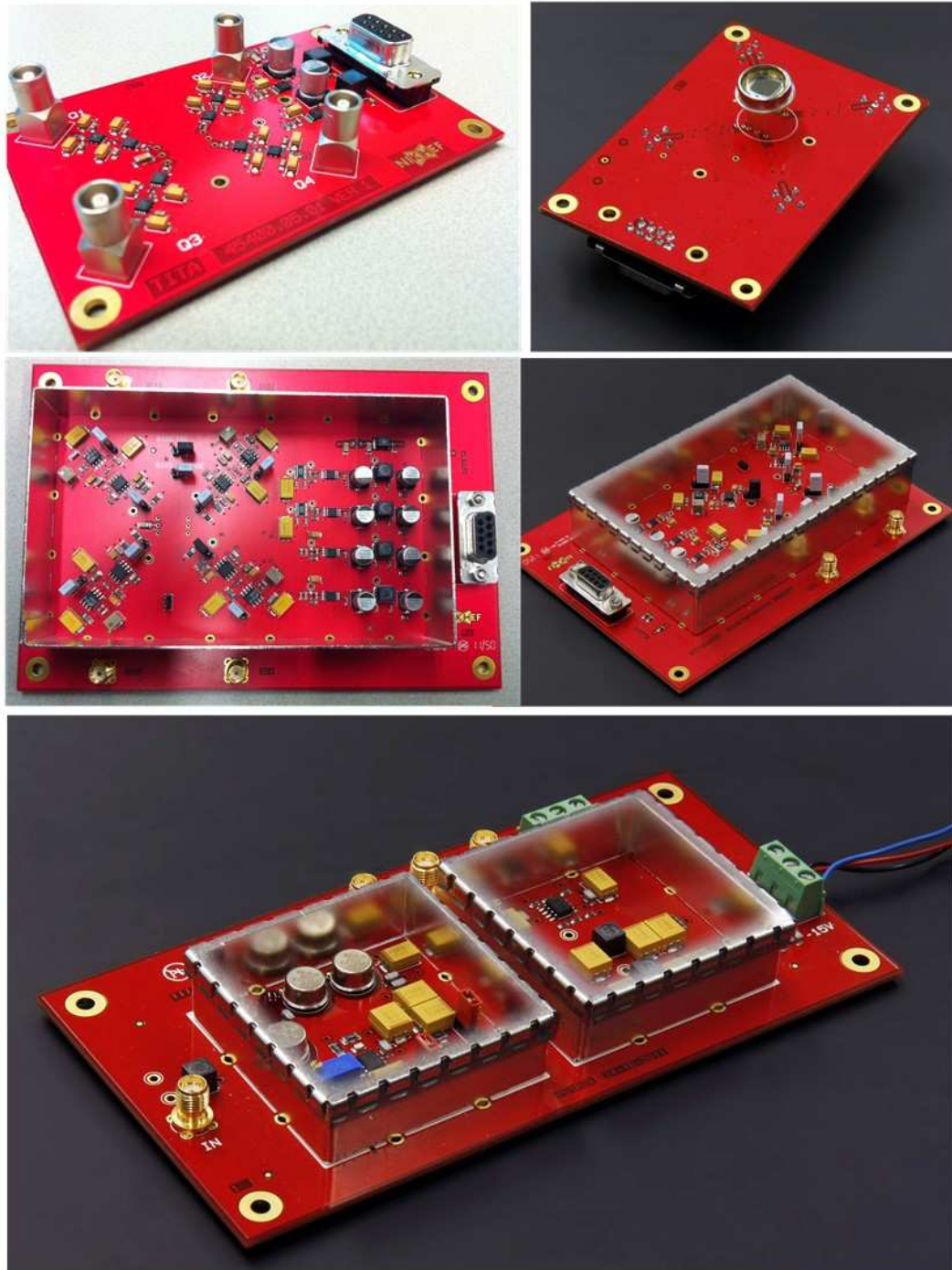


Figure 7.14: Prototype front-ends for Advanced Virgo. Top left: front-end based on ADA4899; top right: QPD; middle left: CS3002 based transimpedance amplifier, middle right: support electronics; bottom: amplifier based on discrete components.



Figure 7.15: QP45-Q by First Sensor features 4 quadrants with 11 mm² surface area. The gap that separates the sensitive regions amounts to 70 μm .

30 mW with the OPA846 front-end amplifier has a voltage noise of about 70 nV/ $\sqrt{\text{Hz}}$ at 10 Hz which decreases to about 50 nV/ $\sqrt{\text{Hz}}$ at 1 kHz. Given the transimpedance of 470 Ω , this corresponds to an equivalent current noise at the input of about 150 pA/ $\sqrt{\text{Hz}}$ at 10 Hz to 105 pA/ $\sqrt{\text{Hz}}$ at 1 kHz. These values exceed the estimated shot noise contribution by a factor 2 to 7, while for Advanced Virgo the electronic noise must be below the shot noise, hopefully a factor 2 below, *i.e.* about 15 pA/ $\sqrt{\text{Hz}}$ for the QP45.

The Virgo+ QPDs were optimized at RF. For the Advanced Virgo end bench QPDs, a front-end design that is optimized for DC readout is needed. In particular the $1/f$ noise should be much lower. In that case the specifications are thought to be within target, although this is not yet demonstrated. Measurements on various prototypes are being performed to test QPD front-end at DC.

7.6.4.3 Dark current noise

Similarly to the photon noise, the random generation of electrons and holes within the depletion region of the diode can be modeled by a Poisson distribution. The dark current depends from many parameters, but generally speaking we have for Si photodiodes currents ranging from 1 to 10 nA (depending on reverse bias voltage), for Ge photodiodes from 50 to 500 nA, and for InGaAs from 1 to 20 nA. The 10 nA or so leakage current from the Virgo+ QPD contributes about 5.6×10^{-14} A/ $\sqrt{\text{Hz}}$. Consequently, dark current noise can be neglected.

7.6.4.4 Thermal noise

Johnson noise is generated by the thermal agitation of the electrons inside an electrical conductor at equilibrium, which happens regardless of any applied voltage. For a photodiode thermal noise can be modeled as a voltage source, Gaussian distribution with a mean value of zero, in series with an ideal resistor R (the photodiode impedance). The transconductance resistance for the 30 mW QPDs used for Virgo+, amounts to 470 Ω . The corresponding

thermal noise amounts to $5.9 \text{ pA}/\sqrt{\text{Hz}}$, which is a factor 5.7 below the Advanced Virgo shot noise.

7.6.4.5 Quantization noise

Virgo employs 18-bit ADCs that allow sampling at 800 kHz of signals in the range $\pm 10 \text{ V}$ ($V_{pp} = 20 \text{ V}$). The effective number of bits (ENOB) is about 16.1 at 2 kHz .

We have measured the power spectral density (PSD) of the quantization noise. The ADC input channels were shorted with 50Ω resistors. The results (the square root of the PSD) are shown in Fig. 7.16.

The theoretical noise power spectral density amounts to:

$$\text{PSD}_{\text{ADC}} = \left(\frac{V_{pp}}{2^{\text{ENOB}}} \right)^2 \frac{2}{12 f_s} = 1.69 \times 10^{-14} \text{ V}^2/\text{Hz} \rightarrow \sigma_{V, \text{ADC}} = 130 \text{ nV}/\sqrt{\text{Hz}}, \quad (7.10)$$

where the sampling frequency is $f_s = 800 \text{ kHz}$. The corresponding current noise per quadrant amounts to $275 \text{ pA}/\sqrt{\text{Hz}}$; whereas it should be lower than $15 \text{ pA}/\sqrt{\text{Hz}}$.

Moreover the measurement results shown in Fig. 7.16 reveal a significant $1/f$ contribution at low frequency below 10 Hz. This noise was found to originate from the input stage of the ADC front-end mezzanine.

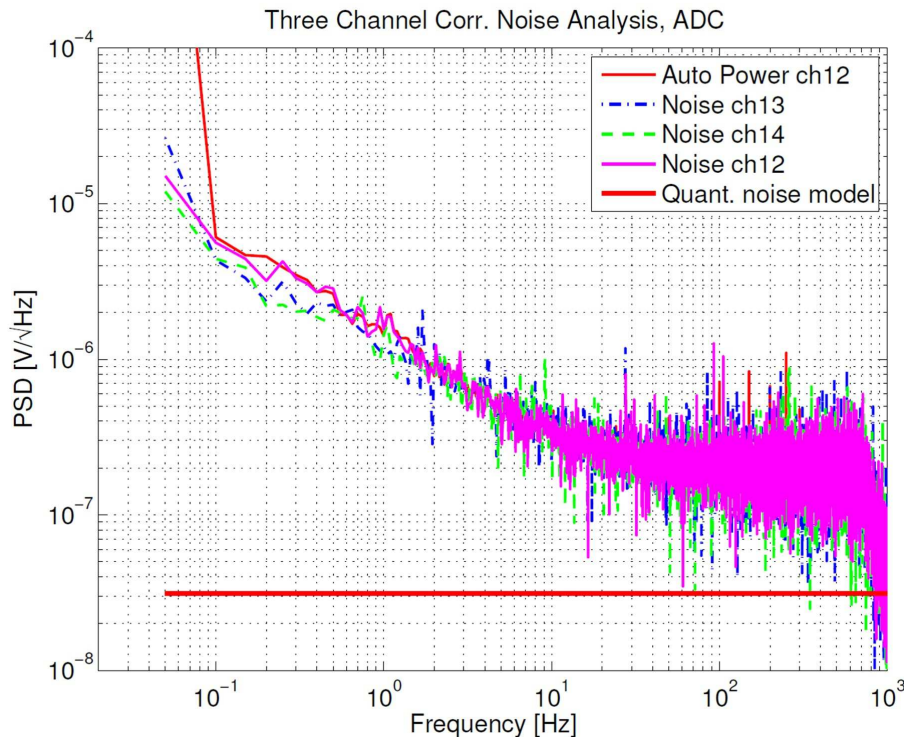


Figure 7.16: Measurement of power spectral density of the ADC noise. The $1/f$ noise contribution originates from the front-end analog mezzanine of the ADC. The red horizontal line at $30 \text{ nV}/\sqrt{\text{Hz}}$ shows the expected quantization noise for a perfect 18 bits ADC (while in practise the effective number of bits is lower) with a differential dynamics of $\pm 10 \text{ V}$.

It will be investigated to what extent the improvement of the front-end analog mezzanine of the ADCs and signal shaping can lead to lower noise values.

7.6.5 Expected performance

A light spot with radius r that is incident on a QPD with radius a yields a displacement signal δ that depends on the shape of the spot and the irradiance distribution. For the left-right difference δ_x we find

$$\delta_x = \frac{u - v}{u + v}, \quad (7.11)$$

where u and v are the summed signals from the left and right quadrants, respectively. We assume that each quadrant segment of the photodiode generates Gaussian distributed noise with zero mean and variance σ_n^2 . In that case the power density function of δ is approximately Gaussian. The worst case for the position error is when the noise between pairs of quadrants is uncorrelated.

The normalized position error in the x direction is given by

$$\frac{\Delta x}{r} = \frac{\pi}{4} \frac{\Delta \delta}{\sqrt{1 - (x/r)^2}}. \quad (7.12)$$

For a well-centered spot ($x \approx 0$), the position error amounts to $\Delta x = \frac{\pi}{4} r \Delta \delta$, and for a shot noise limited QP45 and a 25 mW beam with radius 330 μm , we find $\Delta x = 2.4 \times 10^{-12} \text{ m}/\sqrt{\text{Hz}}$. For a 1650 μm beam, we find $\Delta x = 1,2 \times 10^{-11} \text{ m}/\sqrt{\text{Hz}}$.

Including electronic noise of 220 pA/ $\sqrt{\text{Hz}}$, thermal noise of the transconductance resistor and digitization noise of 123 nV/ $\sqrt{\text{Hz}}$, we obtain for the QP45 $\sigma_i = 241 \text{ pA}$ for each quadrant and thus $\Delta \delta = 6.6 \times 10^{-8}$. The position error then amounts to $\Delta x = 1.7 \times 10^{-11} \text{ m}/\sqrt{\text{Hz}}$ for a 25 mW beam with radius 330 μm . For a 1650 μm beam, we find $\Delta x = 8.5 \times 10^{-11} \text{ m}/\sqrt{\text{Hz}}$.

For the Virgo+ QPDs with 30 mW nominal power, the shot noise limited position uncertainty amounts to $\Delta x = 2.5 \times 10^{-12} \text{ m}/\sqrt{\text{Hz}}$ for a 330 μm beam, and $1.3 \times 10^{-11} \text{ m}/\sqrt{\text{Hz}}$ for a 1650 μm beam. Including electronic noise of 220 pA/ $\sqrt{\text{Hz}}$, thermal noise and digitization noise, we obtain $\sigma_i = 239 \text{ pA}$ for each quadrant and thus $\Delta \delta = 7.0 \times 10^{-8}$. We find $\Delta x = 1.8 \times 10^{-11} \text{ m}/\sqrt{\text{Hz}}$. For a 1650 μm beam, we find $\Delta x = 9.1 \times 10^{-11} \text{ m}/\sqrt{\text{Hz}}$.

7.6.6 Seismic isolation and hardware implementation

Seismic displacement noise at the level of the QPDs cannot be distinguished from the actual signal from mirror movements. Consequently, it is important to mount the optical benches on adequate seismic attenuation systems. The seismic displacement noise must be lower than the shot noise limit [231] and stringent constraints are needed, especially on the tilt degrees of freedom (see section 7.2.2, Tab. 7.2). It requires the realization of multi-stage compact seismic attenuation systems (MultiSAS, see SBE chapter).

The QPDs will be placed on optical benches that are 1.3×1.3 m squares and will be suspended in vacuum. Each bench contains a telescope for beam reduction. Two photodiodes are employed for locking of the cavity (longitudinal alignment). There is a beam path for an auxiliary laser. For linear alignment 2 quadrant photodiodes are installed. The front-end mechanical enclosure of the QPD should be restricted to about $100 \times 200 \times 150$ mm in respectively width, length and height. Note that the current QPD front-ends for Virgo+ have dimensions $48 \times 100 \times 200$ mm.

Tests must be performed to study the operation of QPDs in vacuum, and to determine type and outgassing of cabling, feedthroughs, *etc.* Also the grounding scheme should be evaluated. The power that needs to be dissipated in vacuum will be restricted to about 1 W. This power will be transferred through radiation. Special attention will be paid to minimize the negative effects of cabling on the attenuation performance of the MultiSAS systems.

7.6.7 Demodulation electronics

For Virgo+ demodulation boards have been developed that can demodulate linear alignment signals at frequencies of 6.26 and 8.35 MHz. For Advanced Virgo the signals are modulated at frequencies up to 131 MHz. A prototype demodulation board has been developed and is shown in Fig. 7.17. The system is capable of demodulating QPD signals at frequencies up to



Figure 7.17: Prototype board that is used to demodulate signals from quadrant photodiodes in Advanced Virgo for frequencies up to 200 MHz. The insert shows a demodulated board developed for Virgo+.

200 MHz. In the fall of 2011 further R&D on this task has been put on hold in anticipation of an alternative approach where signals are digitized at high frequency (500 MHz) to allow for digital demodulation (see section 7.5.2).

7.6.8 Quadrants used for OMC alignment

We are planning to use two DC quadrants similar to the one installed on the Virgo suspended detection bench. They will be used for the alignment of the SDB1 bench (and the OMC cavities) with respect to the ITF.

7.7 Phase cameras

The Phase Camera (PC) provides high resolution frequency selective wave-front sensing capabilities that measure the complete spatial profile of any frequency component of a laser field containing multiple frequencies [75, 248]. This type of probe technique was developed to address the necessity of measuring the spatial overlap between the laser carrier field with each sideband component of the fields exiting the many output ports of a gravitational-wave interferometer.

A July 2011 Virgo note [253] investigated the sensing capabilities of the phase camera and the possibility of using its information in a closed loop feedback system to correct for common high spatial frequency mirror aberrations. The simulations presented showed that this technique quantifies common mirror aberrations in the recycling cavity and that aberrations with spatial frequencies below 50m^{-1} have significant effects on the recycling capabilities of the phase modulation sidebands. Using finite element modeling it was shown that a heating pattern, forming a spatial low-pass filter, could be applied as a correction map, restoring significant portions of sideband power.

7.7.1 Phase camera options and workings

There are several working baseline examples from which a phase camera could be constructed. In 2004 Goda *et al.* published a paper in which he described the original idea behind the phase camera, combining an optical heterodyne measurement with a galvanometer scanning system and pinhole detection element. The measurement principle was based on a simple heterodyne interferometer. The phase and amplitude of the wavefront was reconstructed by scanning the galvanometers and recording the quadrature demodulated signals at specific points over a pattern. A similar system, based on the same working principle, is currently operational at Nikhef and Virgo and allows spatial profiling of individual frequency components up to 125 MHz with 10 Hz image update rates [249, 250, 251, 252].

A second method to recover spatio-temporal phase and amplitude information at arbitrary sideband frequencies is based on the wavefront measurement system used for LISA [254]. This method involves two frequency shifters, which themselves contain a (low frequency) heterodyne signal. Using a focal plane array, like a CCD or InGaAs camera, the heterodyne signal can be recorded and processed, giving the phase and amplitude of the wavefront.

Finally, the third measurement method employs a state of the art time of flight CCD/CMOS measurement sensor. These sensors use a technique called "demodulation by sampling" to recover information about some 40 MHz modulation sidebands. By sampling the incoming intensity at exactly four times the modulation frequency we obtain four discrete samples over the period of one modulation cycle. Subsequently recovering the phase from these samples can be done by standard signal processing methods.

7.7.1.1 Scanning phase camera

Fig. 7.18 shows the opto-electronic setup of the system at Nikhef. After some injection optics, the laser light is split into two paths providing a test beam and a reference beam. The reference beam is frequency shifted by an acousto-optic modulator, providing a 80 MHz heterodyne frequency. The test beam passes through a three-mirror traveling wave cavity, which is kept on resonance with the laser frequency using Pound-Drever-Hall locking. A second, broadband, phase modulator is used to excite a sideband frequency corresponding to one of the higher order modes of the optical cavity. Hereafter, the reference and test beams are combined onto a beam-splitter and co-propagate towards the wave-front sensor.

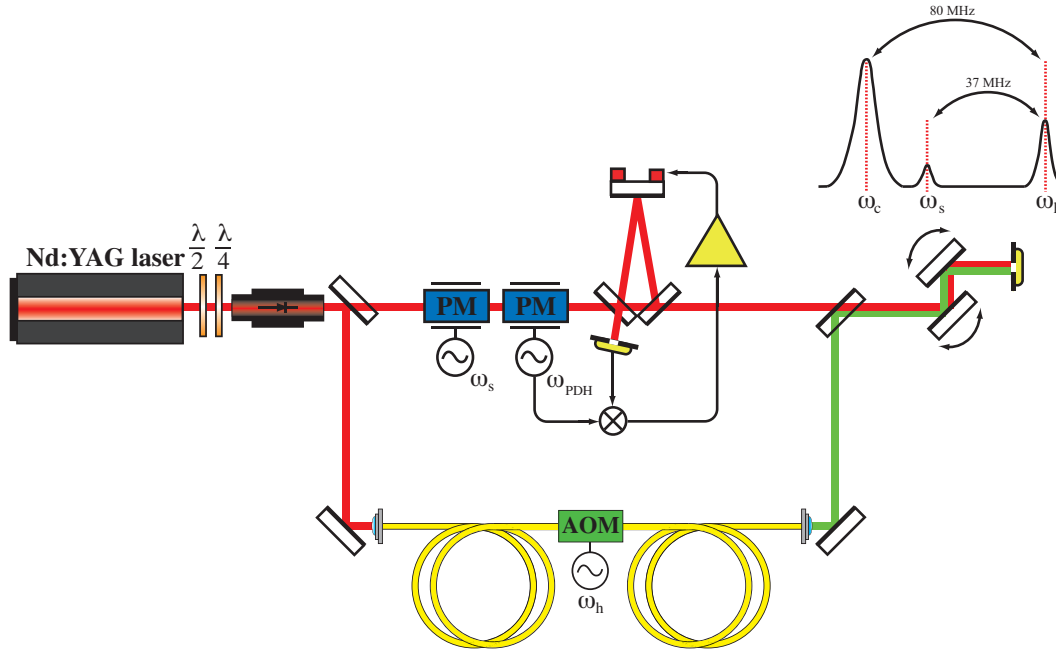


Figure 7.18: Opto-electronic setup for scanning phase camera. The AOM shifts the reference laser beam to the heterodyne frequency ω_h . The mode cleaner is kept resonant with the laser frequency and uses the phase modulation sideband ω_{PDH} for Pound Drever Hall locking. The signal frequency ω_s is set at a frequency that coincides with the frequency offset for the TEM_{mn} , where $m = 3$, and $n = 4$.

The wave-front sensor itself contains two scanning galvanometers (X-Y directions) from Thorlabs (GVS012). The wave-front sensor readout occurs at PD2, which is an InGaAs pinhole photodiode (300 μm diameter active element) from Newfocus (1811-FS-M). Using the scanning galvanometers, the wave-front is scanned over the pinhole diode, allowing the data acquisition system to sample the heterodyne beat frequency at different points over the wave-front. The image acquisition time can be varied from 0.04 to 1 s, with 500 kS in a single-shot scan at 1 s. Fig. 7.19 shows a screen shot of the LabView front panel. The spiral frequency is set to once per second with a sampling rate of 50 kS/s.

The data acquisition system samples seven different channels, including the galvanometer positions, the DC photo-detector output, and the in-phase and quadrature demodulated photo-detector signals (carrier and a single PM sideband). Using LabView, the acquired signals are processed to reconstruct the phase and amplitude of the demodulated signals.

The acquisition system has not been optimized for acquisition speeds faster than 1s per second. This can be amended in follow-up versions of the acquisition system but is not seen as a major undertaking.

Fig. 7.19 shows the typical results of the scanning phase camera at Nikhef. The 80MHz heterodyne signal, originating from the beat between the frequency shifted reference beam and the interferometer test beam, is demodulated using a sine and cosine version of the local oscillator. The baseband signals are fed into the data acquisition system and are sampled simultaneously while scanning the galvanometers across the photodiode. Using the stored coordinates of the scanning pattern, the phase and amplitude distribution are reconstructed at each point.

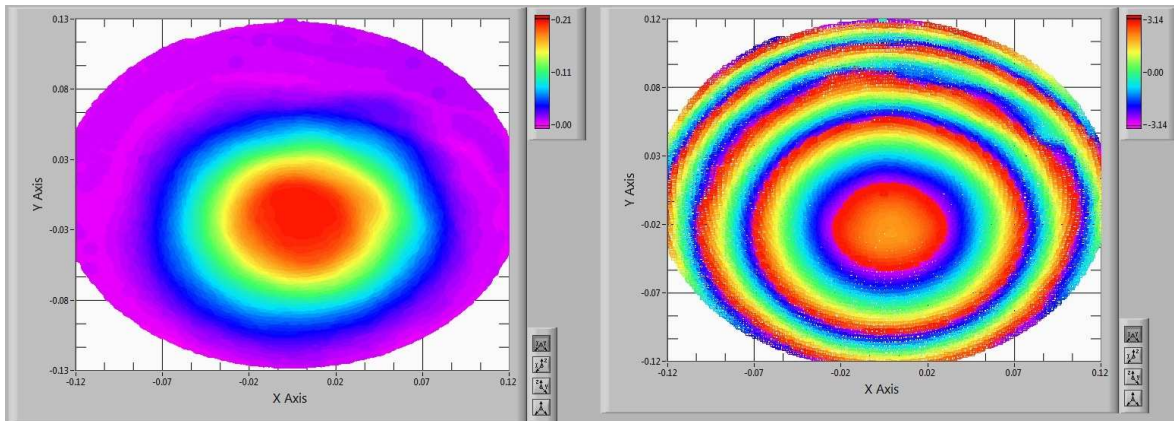


Figure 7.19: Phase camera result for the Nikhef prototype.

7.7.1.2 InGaAs FPA based phase camera

In 2004 Guzman reported on a design and software for a heterodyne Mach-Zehnder interferometer that allowed real-time measurements and display of a laser phase front [254]. The information was displayed in real-time on the graphical user interface (GUI), developed for the application, providing a convenient support for an optimal alignment of interferometer beams. It was proposed that closed loop adjustments of the optical components in the interferometer could optimize the parameters of the interfering beams in order to achieve a homogenization of the spatial distribution of the phase.

Fig. 7.20 shows the opto-electronics setup used by Guzman. After the laser beam was split by the beam splitter, both laser beams were shifted in frequency by an acousto-optic modulator. The frequency shifts contained a frequency difference of 1623 Hz. Subsequently, the two beams were recombined on a beam splitter and both ports of the interferometer were used for detection purposes. One detection port contained a single element photodetector, detecting the heterodyne frequency difference. The detected heterodyne signal drives the input of a comparator every time the heterodyne signal has a zero crossing. The digital output is then used to trigger the FPGA to retrieve data from the CCD/InGaAs focal plane array, which was monitored at the output of the second Mach-Zehnder detection port.

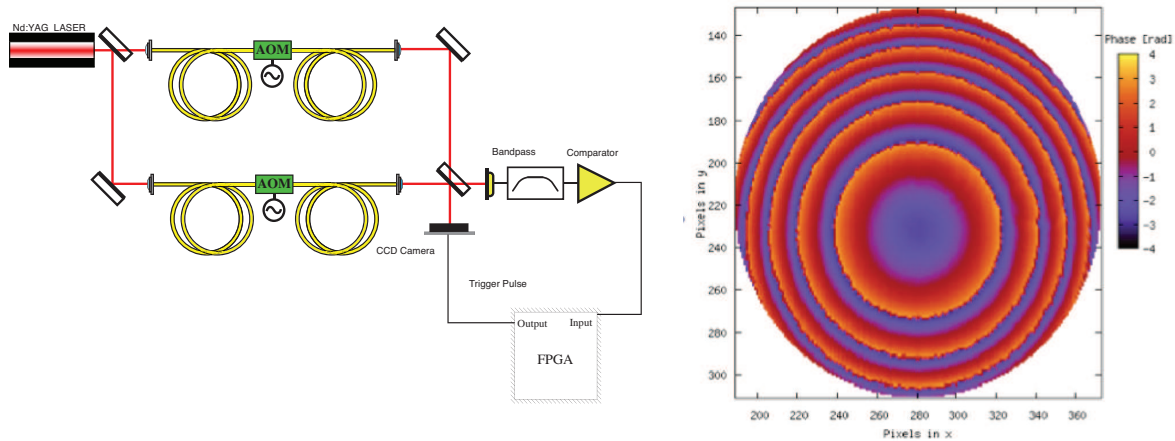


Figure 7.20: Opto-electronic setup for the Mach-Zehnder heterodyne interferometer [254].

Fig. 7.20 shows the phase imaging results using the FPA system. The result was obtained by inserting a lens in one of the recombination arms, creating a strong disparity between the two interfering wavefronts. He also showed that, when interfering mode-matched wavefronts, shows a measurement error of ± 0.15 rad.

7.7.1.3 Time of Flight measurement systems as phase camera

We are currently in the possession of a PMD CamCube 3.0, which is a high resolution all-solid-state ToF (Time of Flight) 3D camera. The optical sensor, with 200x200 pixels, enables the real-time capture of distance and grayscale information. The ToF capabilities originate due to the fact that the camera uses near infrared LEDs which flash at 40 MHz. The camera itself is programmed to collect photons that arrive at each pixel using four separate storage buckets. While averaging over a certain integration period, the camera switches between buckets every quarter of the modulation period. At the end of the camera integration time, the collected photons in each bucket provide quadrature information about the modulated signals, allowing the phase (distance) and amplitude of the modulation frequency to be unambiguously reconstructed. We propose to remove the ToF LED system. The 40 MHz beat frequency will be provided by a heterodyne measurement, which will allow us to retrieve spatial phase and amplitude distribution of the impinging laser beam.

An alternative to the camcube would be the scientific locking pixel module (SLIM), which was developed by MESA imaging. This system allows pixel demodulation at frequencies from 500Hz up to 30 MHz. Fig. 7.21 shows the CAD models of the SLIM camera. The current market price for the SLIM camera is about 24 kEuro.

7.7.2 Development timeline

It is currently anticipated (section 7.2.1) that two phase cameras will be incorporated within the Advanced Virgo control system architecture and their signals will be used within adaptive optics feedback control systems [253]. In order to compare results and performance, and to

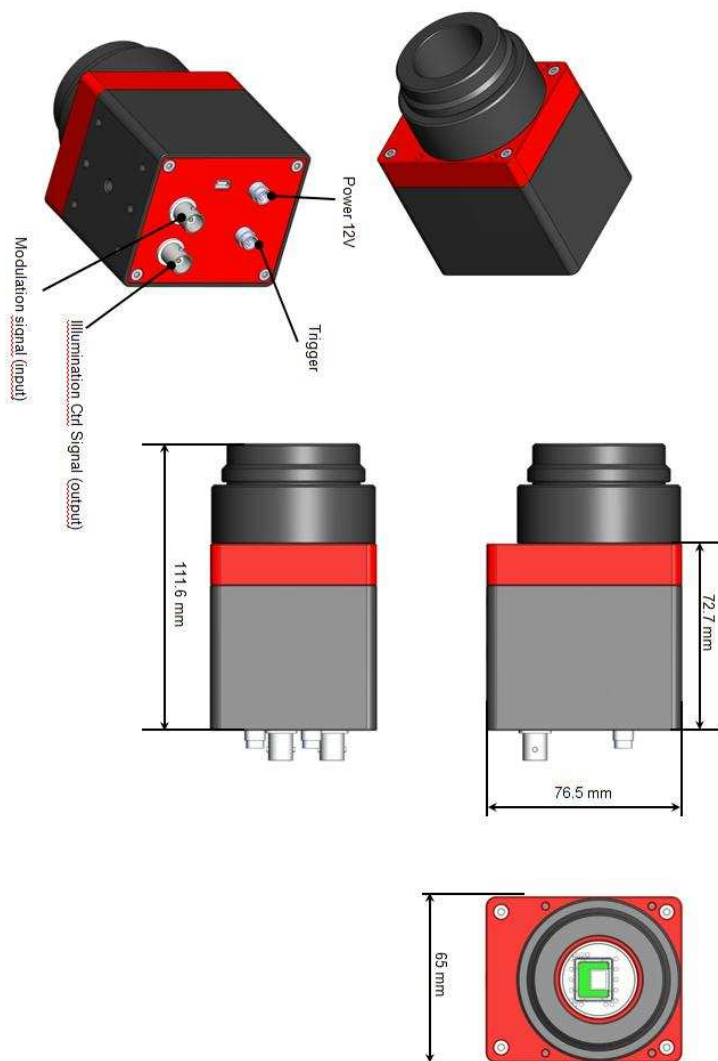


Figure 7.21: Scientific locking pixel module (SLIM) developed by MESA imaging.

keep efforts for system integration to a minimum, it is therefore desirable that data from all prototypes is processed in a similar manner and data flow has a similar structure. Both the scanning and FPA based wave-front sensors have been used to extract the spatial phase and amplitude characteristics of the laser wave-front [254, 253, 249, 252]. The ToF camera is the only sensor that has not been used in a proof of principle experiment to demonstrate its phase imaging capabilities. It is because of this that our R&D efforts will focus on an experimental demonstration of the ToF system as a wave-front sensor and in parallel develop a faster scanning phase camera in case in-vacuum phase cameras are required.

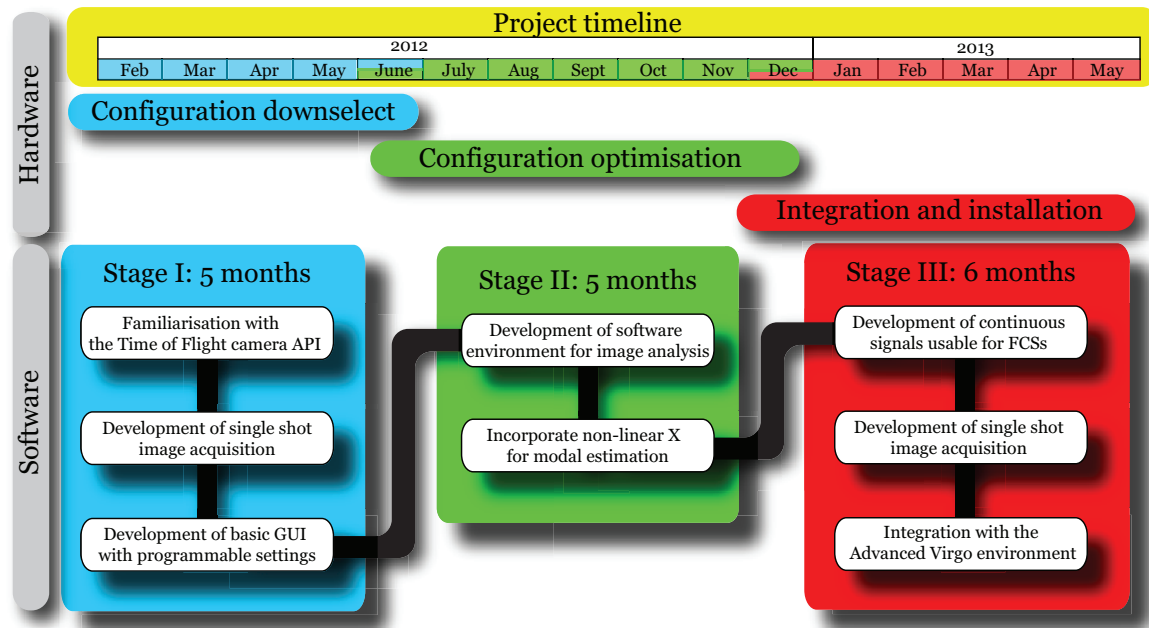


Figure 7.22: 16 month software development program for the Time of Flight phase camera

The current scanning phase camera has a National Instruments LabView environment, which allows the system to take snapshots of the transverse amplitude and phase distribution with a 0.1 s frame acquisition time. Ideally, this rate should be about 5 times faster without significant loss of precision due to the introduction of image blurring by the scanning system. We currently believe that the scan rate can be doubled but much faster will deteriorate the image quality.

It is anticipated that software development will occur in C , which is the native programming language for the Virgo gravitational wave detector control system. The PMD time of flight camera is already supplied with a C based software development kit. The PMD SDK2, as it is called, supplies functionality to access PMD cameras and other data sources. It is possible to set camera parameters, as well as retrieve 2D and 3D images from the data source. This allows simple and fast application development supporting PMD data structures. Since the PMD time of flight camera and its applications as a phase camera have not yet been tested, we will only develop a small subset of the required software to properly test the camera. The software should allow for single shot and continuous recording, preferably with a simple graphical user interface (GUI). The GUI should provide options to set parameters like modulation frequency and integration time on the fly and allow images to be saved for further processing.

Fig. 7.22 shows a rough timeline for the software development, with the software for time of flight sensor as the main deliverable. It is hoped that the developed software, even in its early stage, can be adapted to drive and acquire data from the current scanning phase camera system as well. Documentation on the currently used ADC/DAC would be required for this.

After the initial testing and characterization, which is anticipated to take around three months, a decision will be made on the preferred detection topology using either the scanning phase camera, or the time of flight based camera. After this time, the software will have to incorporate a modal estimation routine and develop more firm analyses. Also, the software should allow to stream data to a monitors with a minimum of 1 s update rates.

7.7.3 Concluding remarks on the phase camera development

Since the three methods have been tested at different facilities without a detailed noise analysis on each of the measurement principles, a quantitative comparison between each measurement system is currently not available. Qualitatively, the requirements of the AdV phase camera dictate that the upper and lower sidebands of all modulation frequencies, including some harmonics, can be accessed, preferably with one device. Only the scanning wave-front detection system will allow such measurements to be performed. Both the ToF and FPA will require a split-path-sensor system with several frequency shifted reference beams to access all required sideband frequencies. Using time division multiplexing, the ToF sensor could image several sideband frequencies (upper and lower) that lie within the bandwidth of the device but, as pointed out, it will not be able to image all frequencies without added reference beams. The FPA sensor will require more reference beams again.

7.8 Detection benches

The detection benches refer to the benches needed to extract the dark fringe signal and other secondary beams directed towards the interferometer output port.

7.8.1 Functions and requirements

The following functions should be fulfilled by the detection benches:

SDB1

The first suspended detection bench will host the OMC cavities needed to filter out the side bands and the carrier HOM. A telescope is also needed to adapt the beam size to the OMC waist.

The optical layout of the bench should also allow the separation and the extraction of the secondary beams due to spurious reflections on the BS AR face and the CP faces. The separation distance allowing to extract all these beams should correspond to about 10 beam radii, which is achieved after the OMC-MMT telescope as shown by simulation results presented in the OSD chapter.

A Hartmann beam needs to be injected along the reversed path of the dark fringe beam. This requires a dichroic mirror.

A Faraday isolator will be implemented on the bench before the OMC cavities in order to isolate the ITF from back-reflected light that could come from the optics or sensors located downstream.

Two DC quadrants need to be installed on the bench. The position of the B5 beam on these quadrants will be used as error signal to align the OMC cavities (or to align the SDB1 bench with respect to the ITF).

SDB2

The second suspended detection bench will host the main photodiodes (such as DC readout photodiodes, quadrants for the automatic alignment), as well as most of the sensors located at the dark port in order to minimize the coupling of scattered light noise:

- up to 4 photodiodes might be needed to extract the B1 beam (transmitted by the second OMC). These photodiodes will be dedicated to DC detection. In the current baseline design, only two of these photodiodes will be actually used, with a nominal power per photodiode of 40 mW;
- an extra photodiode might be used to extract some RF signals of the B1 beam for the monitoring of the $2f_1$ and $2f_2$ signals in transmission of the OMC cavities;
- two photodiodes will be used to extract the B1p beam. These photodiodes will provide DC and RF signals (f_1 , f_2 , f_4 , $2f_1$ and $2f_2$). They will be used during the lock acquisition. A third photodiode with DC readout will be placed on the B1p path to monitor its P polarization;
- two quadrants will be used for the ITF alignment. One of these quadrants will provide DC error signals, while the other quadrant will provide Alternating Current (AC) error signals. The demodulation frequencies of these quadrants should be at f_1 , f_2 and $2f_2$. The $2f_2$ signal will be used as error signal for the beam centering. A galvo fast centering systems is needed to keep the beam centered on the quadrants. The nominal power of these quadrants in science mode should be about 2.5 mW;
- photodiodes will also be needed to monitor the reflections of the OMC cavities. The reflection on the first OMC (B1s1) will be monitored by a photodiode equipped with DC readout and demodulation frequencies at f_1 , f_2 , $2f_1$ and $2f_2$. In order to characterize the first OMC birefringence the fraction of the B1s1 beam that is not S-polarized will be monitored with a second photodiode. Two photodiodes (1 for polarization S, 1 for spurious polarizations) are also foreseen for the reflection of the second OMC (B1s2). As the amount of side bands transmitted by the first OMC is expected to be very small, only the DC signals will be extracted with these photodiodes;
- in order to have an error signal for the thermal control of the first OMC cavity a pickoff of the resonating beam (B1t) will also be extracted. This photodiode will be equipped with DC readout and demodulated signals at $2f_1$ and $2f_2$;
- two photodiodes and two quadrants will be used for the readout of the B5 beam, which could provide fall-back error signals for the ITF control. More importantly the B5 quadrants will be used for the alignment of the SDB2 bench.

The beam size on all photodiodes and quadrants will lie within the range from 300 to 400 μm .

Cameras under vacuum will be installed for the B1, B1p and B1t beams.

EDB

The external detection bench will host the Hartmann setup, as well as a phase camera placed on the B1p path and able to extract the side bands at f_1 , f_2 and f_4 . In addition we need a scanning Fabry-Perot system in transmission of the OMC cavities in order to be able to monitor the beam components at the side band frequencies (while scanning the OMC temperature).

Moreover we are keeping open the possibility to add up to 4 DC photodiodes on the EDB to monitor the secondary beams due to CP reflections.

The EDB will host the cameras needed on the B1s1, B5 and the CP beams.

7.8.2 Dark fringe to OMC mode matching telescope

The aim of this section is to present the design of the OMC-MMT. The requirements are first given. Then the general layout and the performances of the telescope are presented. The tolerancing study to define the actuation range needed for each optics is described.

7.8.2.1 General requirements

The main requirements of the OMC-MMT are given in Tab. 7.15. The OMC-MMT should provide an overall magnification of 186, allowing to reduce the beam size from 49 mm (at the output of the SR mirror) to 263 μm at the waist position of the OMC cavities. Considering manufacturing errors on optics parameters (radii of curvature or surface irregularities) and alignment errors, the OMC-MMT should be able to recover a matching higher than 99%, corresponding to errors on waist size and position respectively $\delta\omega \leq \pm 19 \mu\text{m}$ and $\delta z \leq \pm 2.9 \text{ cm}$.

The telescope has to fit the space constraints on the SDB1 bench which has an octagonal shape with a width of 88cm. It also host a Faraday isolator, two OMC cavities, two quadrants and the optics needed to separate properly the secondary beams from the main beam. The maximum dimensions allowed for the telescope are 800 mm \times 250 mm. Finally, the amount of back-reflected or back-scattered light from the telescope optics should be compliant with the sensitivity requirements (noise \leq AdV sensitivity/10).

| Parameters | Requirements |
|-----------------------------------|---|
| Mode matching on the OMC cavities | $\geq 99\%$ |
| Magnification | 186 |
| Dimensions | $\leq 800\text{mm} \times 250\text{mm}$ |
| Noise coming from spurious light | $\leq \text{AdV sensitivity}/10$ |

Table 7.15: OMC MMT main requirements.

7.8.2.2 Telescope overview

The OMC-MMT telescope is presented in Fig. 7.23. The first part of the telescope (meniscus lens and parabolic mirrors) is similar to the Injection Mode Matching Telescope (see INJ

chapter). Two alternative designs have been studied: a Reflective Telescope (RT) and a telescope with a doublet (a configuration similar to the one selected for the end benches) suspended to the SR superattenuator. The RT used the AR side of the SR mirror as first focusing element to reduce the beam size from 49mm to 21mm at the entrance of SDB1. The part of the RT telescope lying on the bench was made of two parabolic mirrors and several folding mirrors. This configuration is described in more details in [218]. Although interesting from the point of view of scattered light mitigation because it avoids large lens on the bench, this configuration is not compliant with the space constraints on SDB1 and was therefore excluded. The telescope using a lens suspended at the SR superattenuator is interesting from the back-scattered light point of view because the first optical element is well seismically isolated. However, this scheme produces a very small waist on the elements placed on SDB1, and amplifies the fraction of recombined scattered light by the bench components. The possibility to insert a Faraday isolator on SDB1 before the optical components has been explored, but the light scattered by the Faraday optics and the isolation in presence of a strong focused beam are not known at this stage. In conclusion, despite the interest in having the first lens almost at rest with respect to the ITF and a very small telescope on SDB1, this telescope seems too risky due to the extreme sensitivity of the detection port. A careful evaluation of the scattered light is on-going.

The OMC-MMT baseline design consists of a curved AR side of SR mirror in order to reduce the size of the beam at the entrance of the SDB1 bench. A meniscus lens (diverging) is placed on the bench, with a specific shape designed to compensate spherical aberrations induced by the SR mirror. Two off-axis parabolic mirrors (MMT_M₁ and MMT_M₂) are used in an afocal configuration to reduce the beam size by a factor 17 (from 21.9 mm to 1.3 mm). Then two lenses (MMT_L₁ and MMT_L₂) are used to match the beam to the OMC cavities. The dimensions of the telescope is estimated to be around 760 mm×250 mm including the opto-mechanical mounts. The parameters of the telescope are given in Tab. 7.16.

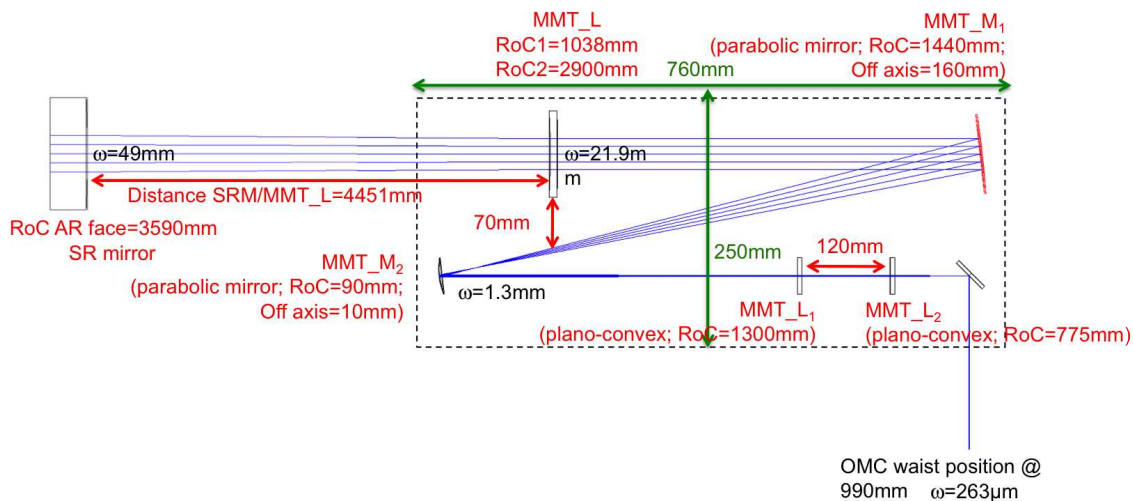


Figure 7.23: Overview of the OMC MMT layout.

| Parameters | Value | Characteristic |
|--|---------|------------------------|
| RoC SR mirror AR side | 3590 mm | spherical |
| RoC meniscus lens side 1 | 1038 mm | spherical |
| RoC meniscus lens side 2 | 2900 mm | spherical |
| RoC MMT_M ₁ | 1440 mm | parabolic (OAD=160 mm) |
| RoC MMT_M ₂ | 90 mm | parabolic (OAD=10 mm) |
| Distance SR AR side/meniscus lens side 1 | 4451 mm | |
| Distance meniscus lens side 2/MMT_M ₁ | 600 mm | |
| Distance MMT_M ₁ /MMT_M ₂ | 765 mm | |
| Distance MMT_M ₂ /MMT_L ₁ | 500 mm | |
| Distance MMT_L ₁ /MMT_L ₂ | 120 mm | |
| Distance MMT_L ₂ /OMC waist position | 990 mm | |
| SR mirror clear aperture | 370 mm | |
| Meniscus lens clear aperture | 140 mm | |
| MMT_M ₁ clear aperture | 140 mm | |
| MMT_M ₂ clear aperture | 50 mm | |

Table 7.16: Optical parameters of the OMC-MMT: radii of curvature, distance between the optics and clear aperture.

7.8.2.3 Performances of the system

As shown in Fig. 7.24, in simulation a matching of the beam on the OMC cavities higher than 99.99% is achieved. This is mainly due to the fact that this configuration has very low aberrations since the parabolic off-axis telescope is used in afocal configuration and the meniscus lens compensates the spherical aberrations introduced by the curved face of SR mirror.

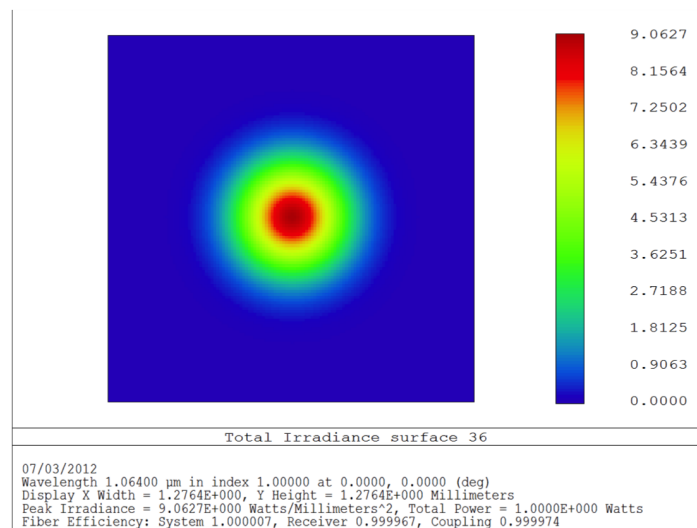


Figure 7.24: Coupling of the beam in the OMC cavities (FFT propagation with Zemax). A matching higher than 99.99% is achieved.

7.8.2.4 Tolerancing study: radii of curvature of the optics

The tolerancing study was performed using the Zemax software through a Monte Carlo simulation. The aim is to find the most critical parameters of the optical system that contribute to the system performances worsening, and define the good compensators to recover optimal performances. This analysis is powerful and useful because all the tolerances can be considered at once. Every parameter is randomly perturbed using appropriate statistical models, all compensators are adjusted and the entire system is evaluated with all defects considered. Tab. 7.17 shows the errors on the RoCs considered for the OMC MMT. We considered errors of the order of $\pm 1\%$ given by the manufacturers. We defined compensators in order to compensate these errors and recover an optimal waist size and position in the OMC cavities, corresponding to an optimal matching higher than 99%. The compensators are the distance between the SR mirror and the meniscus lens, the distance between the two parabolic mirrors, and the distance between the two lenses.

| Optics | RoC value (mm) |
|----------------------|----------------|
| PR_AR | 3590 \pm 36 |
| MMT_M ₁ | 1440 \pm 15 |
| MMT_M ₂ | 90 \pm 1.5 |
| Meniscus lens side 1 | 1038 \pm 11 |
| Meniscus lens side 2 | 2900 \pm 29 |
| MMT_L ₁ | 1300 \pm 13 |
| MMT_L ₂ | 775 \pm 8 |

Table 7.17: RoC errors for the tolerancing study of the OMC MMT.

First, we define a merit function that describe the coupling efficiency. This function is built considering errors on beam waist with respect to the ideal size, error on beam position with respect to ideal position and the remaining aberrations such as spherical aberrations, coma and astigmatism. The ideal configuration gives a coupling efficiency of 99.99%. Without defining any compensators, the most critical parameter is the RoC of the AR side of the SR mirror and the first side of the meniscus lens. Then, playing with the compensators we are able to recover a coupling efficiency higher than 99.99%.

In order to define the maximum ranges of the compensators, we studied separately the RoC errors of each optics. Tab. 7.18 summarizes the ranges of the compensators necessary to compensate separately each RoC errors.

For example, we are able to recover a waist size of 263 μm (and a matching higher than 99.99%) induced by a RoC error on the SR_AR, by using the distance between the two parabolic mirrors as shown in Fig. 7.25. Note that by playing with the three compensators at the same time, we can relax the ranges defined in Tab. 7.18. The values defined below will allow us for the choice of the actuators of the mechanical optic mounts.

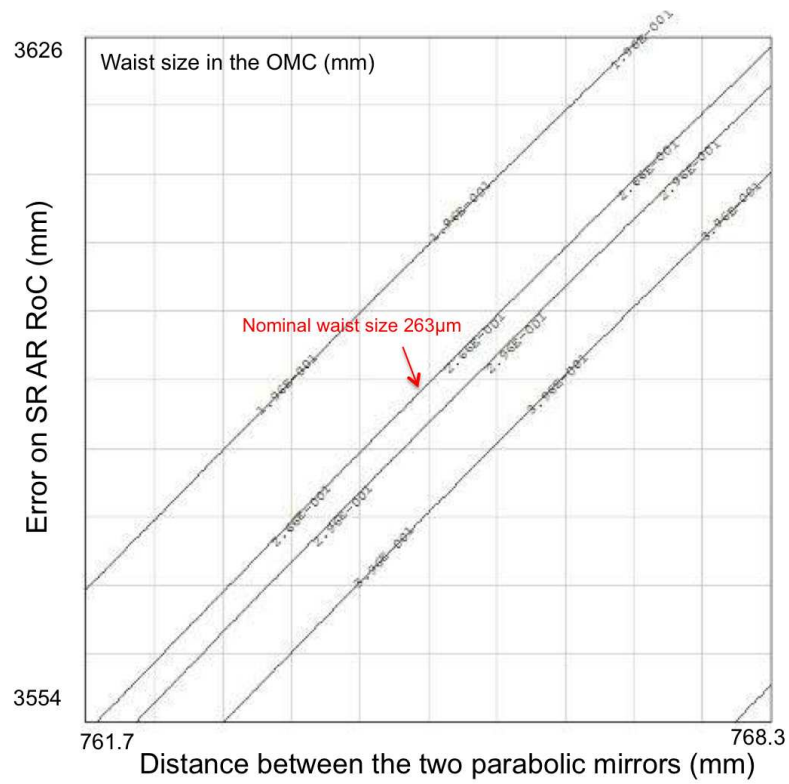


Figure 7.25: Waist size in the OMC as a function of the SRM AR RoC and the distance between the two parabolic mirrors.

| Optics | SR_AR/MMT_L | MMT_M ₁ / MMT_M ₂ | MMT_L ₁ / MMT_L ₂ |
|----------------------|-------------|---|---|
| SR_AR | ±80 | ±3.3 | |
| MMT_M ₁ | ±195 | ±7.5 | |
| MMT_M ₂ | ±18.5 | ±0.7 | |
| Meniscus lens side 1 | ±64 | ±2.5 | |
| Meniscus lens side 2 | ±21 | ±0.8 | |
| MMT_L ₁ | | | ±10 |
| MMT_L ₂ | | | ±30 |

Table 7.18: Ranges of the compensators in mm (distance between SR_AR and the meniscus lens, distance between the two parabolic mirrors, distance between the two lenses) allowing to compensate separately RoC errors of each optics.

7.8.2.5 Tolerancing study: input beam errors

The input beam coming from the ITF could present errors on the waist size and on the waist position. Moreover, the beam at the output of the parabolic mirrors (input of the lenses) could present such errors due to the alignment of the parabolic telescope or to the beam parameters at the entrance of SDB1. We studied the possibility to compensate these errors by using a defined compensator.

In Fig. 7.26, the plots are representing the coupling of the beam in the OMC according to the distance between the SR mirror and the meniscus lens. The nominal and optimal configuration is when the input beam waist is 9.69 mm located at 1363 m from the input mirror. In Virgo, a typical measured coupling between the incident beam and the FP cavities was 98% implying 2% losses [219]. We considered that such losses errors are possible for Advanced Virgo, that is to say an error on the waist size of 14% and an error on the waist position of 78 m. We can see that it is possible to recover a matching higher than 99% (defining a waist size and position in the OMC in the requirements) by adjusting the distance between the SR mirror and the meniscus lens. An optimal matching on the OMC can also be recovered by adjusting the distance between the two parabolic mirrors. In Fig. 7.27, the plots represent the coupling of the beam on the OMC according to the distance between the two lenses. The optimal configuration is when the beam waist size at the output of the parabolic telescope is 1.3 mm located at 1.7 m from the secondary off-axis parabolic mirror. If we consider errors on the waist size of 5% and waist position of 100 mm, we are able to recover a matching higher than 99% by adjusting the distance between the two lenses.

7.8.2.6 Tolerancing study: tilt and decenter errors of the optics

A tilt or a decenter of the optics of the telescope will induce coma, spherical aberrations and astigmatism on the beam. To respect a matching of the input beam with the OMC beam higher than 99%, we computed the maximum tilt and decenter allowed on the optics mounts of the OMC MMT. The results are presented in Tab. 7.19. The constraints are realistic and seem manageable to what we can expect. For the case of meniscus lens, in order to center it with the expected precision, we will install this optical element on a mount with three translation stages: two for the transversal adjustment respect to the beam axis and another

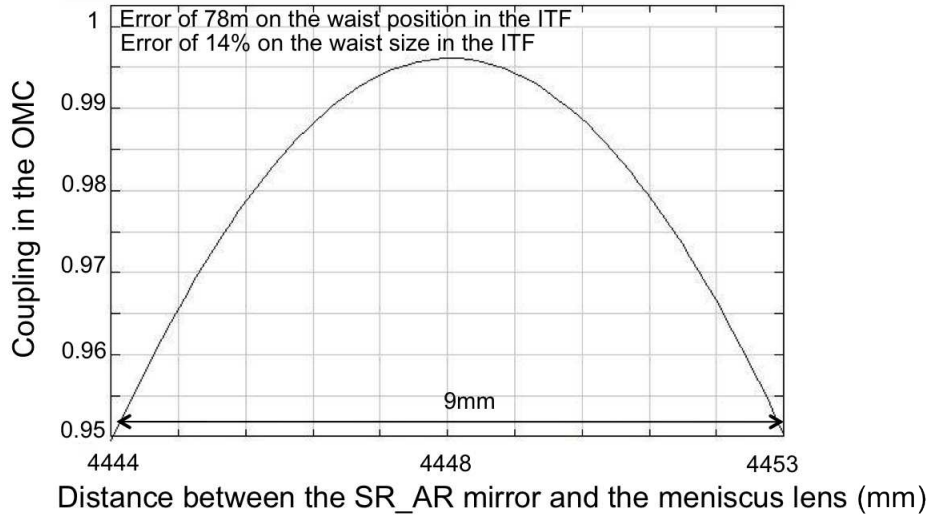


Figure 7.26: Coupling of the beam in the OMC. A matching higher than 99% is recovered when there is an error on input beam parameters, by using the distance between the SR mirror and the meniscus lens.

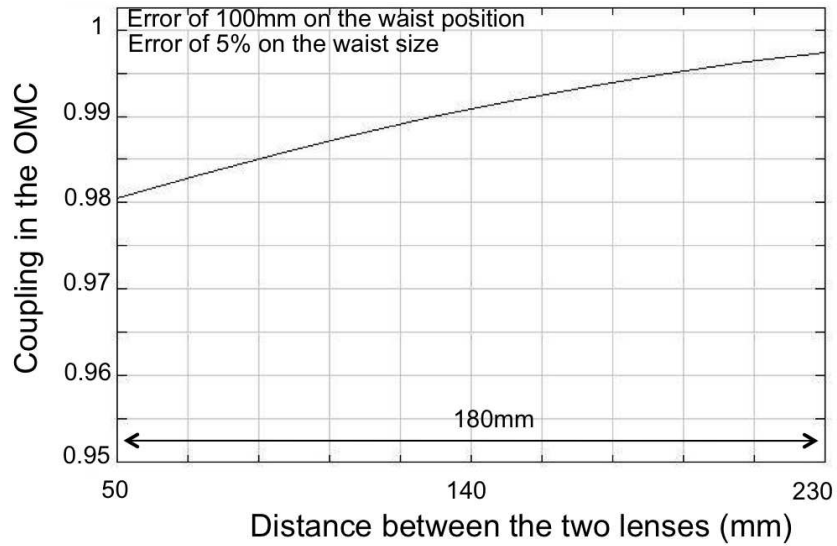


Figure 7.27: Coupling of the beam in the OMC. A matching higher than 99% is recovered when there is an error on parabolic telescope output beam parameters, by using the distance between the two lenses. Both errors on waist size and waist position are plotted.

one for the longitudinal adjustment respect to the beam axis to adjust the distance between the meniscus lens and the signal recycling mirror.

| | MMT_M ₁ | MMT_M ₂ | MMT_L ₁ | MMT_L ₂ | Meniscus lens | SRM |
|----------|--------------------|--------------------|--------------------|--------------------|-------------------|-------------------|
| Tilt | 0.5 mrad | 0.8 mrad | 17 mrad | 17 mrad | 9 mrad | 0.17 mrad |
| Decenter | 100 μm | 100 μm | 1 mm | 1 mm | 400 μm | 400 μm |

Table 7.19: Maximum tilt and decenter allowed for the optics of the OMC MMT, in order to keep a coupling efficiency higher than 99% (fitting the requirements concerning the waist size and position in the OMC).

We also studied the transversal and angular requirements for SDB1. The vertical and horizontal motions of the bench should be smaller than 11 μm and the tilt motion should be smaller than 2.9 μrad , for the catadioptric telescope. These requirements seem to be manageable and similar to what we have currently for the Virgo suspended detection bench.

7.8.2.7 Back-scattered and back-reflected light recoupled in the ITF

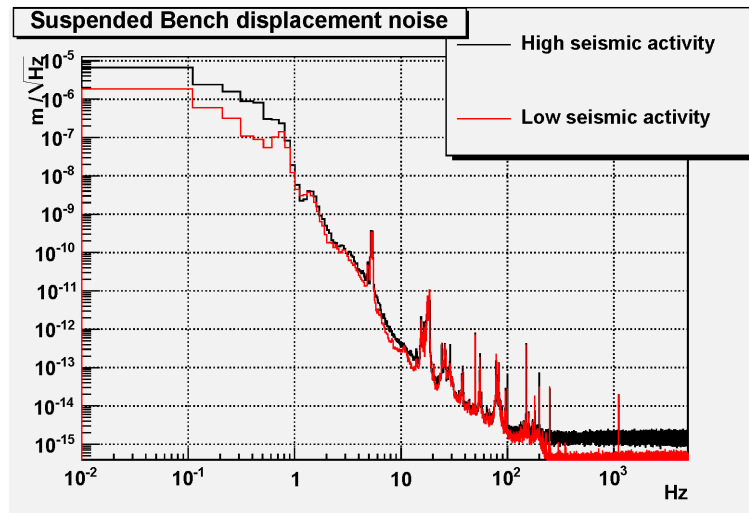


Figure 7.28: Measured horizontal displacement noise for the Virgo Suspended Injection Bench [218] for a period of standard seismic activity (red curve) and for a period of elevated seismic activity (black curve).

Projections of scattered light noise presented in the INJ chapter and in [218] show that the sensitivity requirements are satisfied with a large margin factor for the injection telescope whose design is quite similar to the OMC-MMT. However the ITF dark port is more critical from the point of view of back scattered light as the noise coupling factor is larger ($K_{DET} = 10^{-14}$). This is illustrated by Fig. 7.29 where the projection of back-scattered light noise due to the meniscus lens (which is the element of the telescope for which the larger scattering coefficient f_{sc} is expected) is plotted. This projection was made assuming a scattering coefficient $f_{sc} = 3.7 \times 10^{-9}$ for the meniscus lens, which is the result obtained by an analytical calculation presented in [220] assuming the same Bidirectional Reflectance Distribution Function (BRDF) as it was done in the INJ chapter. No safety factors have been included in this calculation. The scattered light noise has been evaluated by assuming the same bench motion as the one measured for the Virgo suspended injection bench (see [218])

for two periods of different seismic conditions (see Fig. 7.28). Both the suspended injection and detection benches have similar suspensions, and it is expected that equal or better performances can be reached for the SDB1 bench by optimizing or improving the bench control, as it will be discussed below. The evaluation of scattered light noise includes a second and third bounces, whose amplitudes have been extrapolated from the measured bounces with the Virgo suspended detection bench [221].

In standard seismic noise conditions, the back-scattered light noise is dominated by the direct coupling of bench motions. Fig. 7.29 shows that the scattered light noise is in this case compliant with the sensitivity requirements except for a few frequencies where resonances slightly exceed the $h/10$ limit. It is foreseen that Superattenuator subsystem (SAT) will add an extra suspension filter to the superattenuator chain which will provide more safety margin.

In case of marginally elevated seismic activity as shown in Fig. 7.28 (corresponding to bench displacements of about $6\mu\text{m}/\sqrt{\text{Hz}}$ at 0.1 Hz) the back-scattered light noise is dominated by the up-conversion of the low frequency motion (below 1 Hz). Fig. 7.29 shows that in this case the scattered light noise due to the meniscus lens would limit the Advanced Virgo sensitivity up to 30 Hz. For Advanced Virgo the control of the bench (which will be performed by combining local controls as described in section 7.8.9 and an alignment of the bench with respect to the ITF by using the B5 beam) will be optimized so that the bench residual motion should be kept lower than a few microns at 0.1 Hz, in normal science conditions. Moreover, what really matters for the coupling of scattered light noise is not the bench absolute motion but rather the relative displacement of the bench with respect to the ITF. By combining the information about the SR mirror motion at low frequency (that can be obtained from the mirror local controls) with the bench motion one might be able to correct the relative displacement of the bench with respect to the mirror. If this technique, based on the information provided by the local controls, is not sufficient, another way to stabilize better the bench with respect to the ITF would be to use a small interferometric system sensing the relative distance between SR and SDB1. At least one of these techniques will be implemented as risk

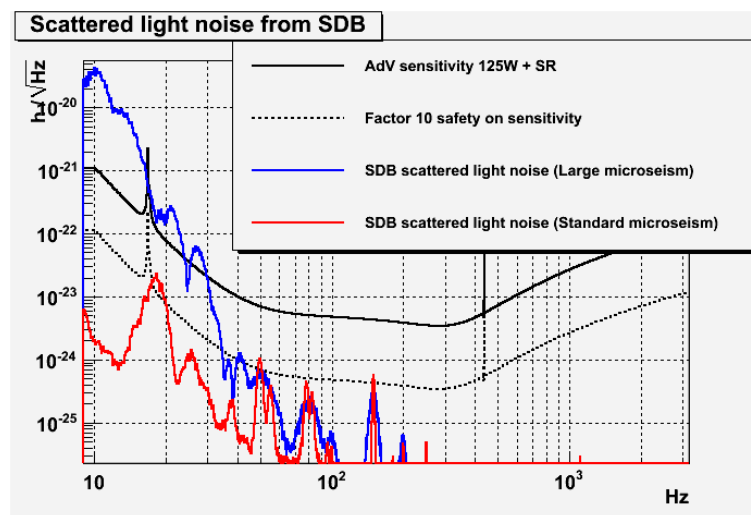


Figure 7.29: Impact on sensitivity of the back-scattered light from the SDB1 bench, assuming that the main contribution to scattered light is due to the meniscus lens of the OMC-MMT.

reduction for the scattered light noise. The choice between the two methods will be done by early 2013.

The contribution to scattered light from the smaller lenses L1 and L2 has not been evaluated at the time of the TDR writing. However the ITF should be partially isolated from this scattered light by adding a Faraday isolator before the small lenses (see section 7.8.4).

7.8.2.8 Back-scattered and back-reflected light not recoupled

If the light is back-scattered or back-reflected at large angles it will not recouple to the main interferometer beam. Instead this light will hit the tubes or the dumpers suspended near the mirrors. The amount of light that can be back-reflected at large angles by the lenses should be of the order of 0.1 mW (assuming 100 ppm for the AR coating and a total dark fringe power of 1 W). This light will need to be dumped by placing baffles at appropriate locations along the vacuum link (see SLC chapter).

7.8.3 Hartmann beam injection

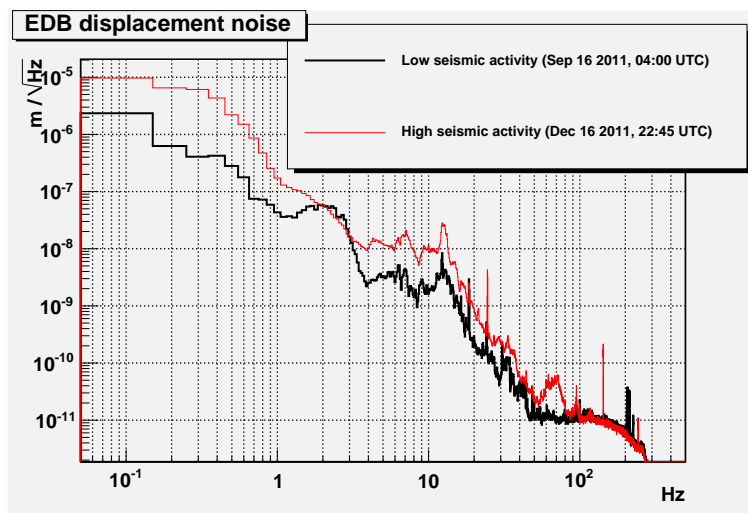


Figure 7.30: Expected displacement spectrum of the external detection bench in period of low or high seismic activity..

The baseline solution for the injection of the Hartmann beam is to follow the reversed path of the dark fringe beam (see TCS chapter). The Hartmann setup will be installed on the EDB bench. The injection of the Hartmann beam will be done at the level of the SDB1 bench by means of a dichroic mirror. The Hartmann beam will be transmitted through the dichroic mirror while the dark fringe beam will be reflected. The coating of the dichroic mirror should allow a high reflectivity for the YAG beam (close to 99.9% if possible) in order to not introduce losses and in order to attenuate the amount of spurious YAG power that could be back-scattered from the Hartmann setup.

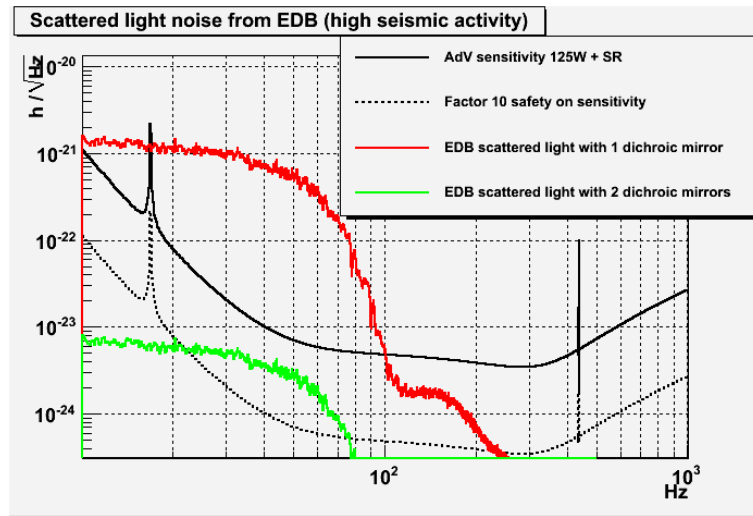


Figure 7.31: Impact on sensitivity of the back-scattered light from the Hartmann setup (located on EDB) during a period of marginally high seismic activity. Two assumptions have been considered on the number of dichroic mirrors used to filter the spurious YAG beam transmitted towards the Hartmann setup.

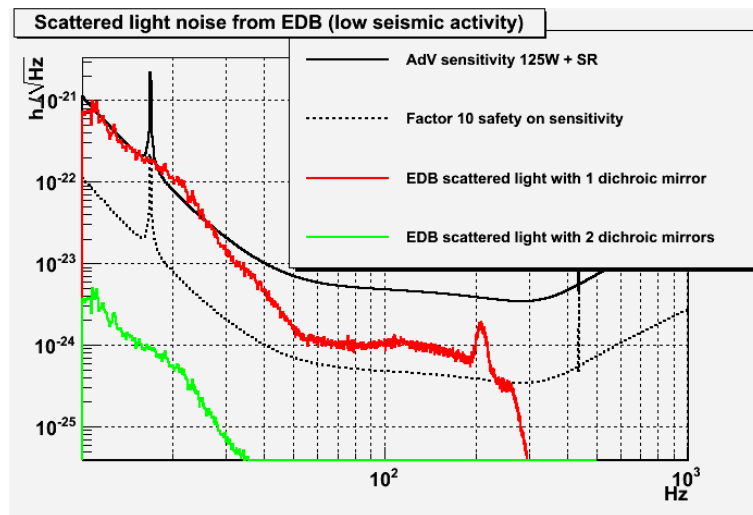


Figure 7.32: Impact on sensitivity of the back-scattered light from the Hartmann setup (located on EDB) during a period of low seismic activity. Two assumptions have been considered on the number of dichroic mirrors used to filter the spurious YAG beam transmitted towards the Hartmann setup.

An estimation of the noise due to the back-scattered light from the **EDB** (where the Hartmann setup will be located) is shown in Fig. 7.31 and Fig. 7.32 for a period of marginally elevated seismic activity and a period of low seismic activity respectively. The **EDB** displacement noise has been estimated by using the data provided by an accelerometer located on the Virgo external bench. The corresponding displacement spectra are shown in Fig. 7.30. The f_{sc} has been computed analytically assuming a transmission of the YAG beam through the dichroic mirror of 0.5% (which should be a conservative assumption).

Fig. 7.31 and Fig. 7.32 show that a single dichroic mirror will not be sufficient to filter out the back-scattered light from the YAG beam. This issue can be solved easily by adding a second (and possibly third) dichroic mirror along the Hartmann beam path.

Losses of the Hartmann beam inside a Faraday isolator have been estimated to be at least of the order of 30% one way. This means that the dichroic mirror separating the YAG beam from the Hartmann must be placed before the Faraday isolator.

7.8.4 Faraday isolator

A Faraday isolator will be placed along the YAG beam path on the **SDB1** bench, after the extraction of the Hartmann beam and the secondary beams (see section 7.8.5). It will be used to isolate the IFT from the light back-reflected (or back-scattered) by optical components placed after this Faraday, for instance the lenses MMT-L1 and MMT-L2 or the **OMC** cavities. The Faraday isolator must have an aperture that corresponds at least to 5 beam radii in order to avoid clipping. The beam size after the second parabolic mirror (M2) is about 1.3 mm. Therefore a Faraday isolator with an aperture above 10 mm, placed after the M2 mirror will be sufficient. Concerning the secondary beams (B5, B6DB, B6pDB, B9, B9pDB), as they are well separated from the main beam after the telescope, they must be extracted before the main beam crosses the Faraday isolator.

The retained solution is to use the same Faraday isolator as the one that was installed on the Virgo Suspended Injection Bench. Its aperture is 20 mm and it should provide an attenuation of 40dB.

7.8.5 Extraction of secondary beams

Secondary beams (such as B5, B6DB, B6pDB, B9DB and B9pDB) need to be separated from the dark fringe beam and extracted at the output of the mode matching telescope. A separation distance of about 10 beam radii should be obtained several tens of cm after the telescope. The beam extraction will be accomplished by using multi-faceted mirrors.

7.8.6 Optical layout

A preliminary optical layout of the two suspended detection benches (**SDB1** and **SDB2**) is shown in Fig. 7.33. It has been established following the specifications given in section 7.8.1 and the telescope design described in section 7.8.2.

The dark fringe beam (spatially overlapped with secondary beams and the Hartmann beam)

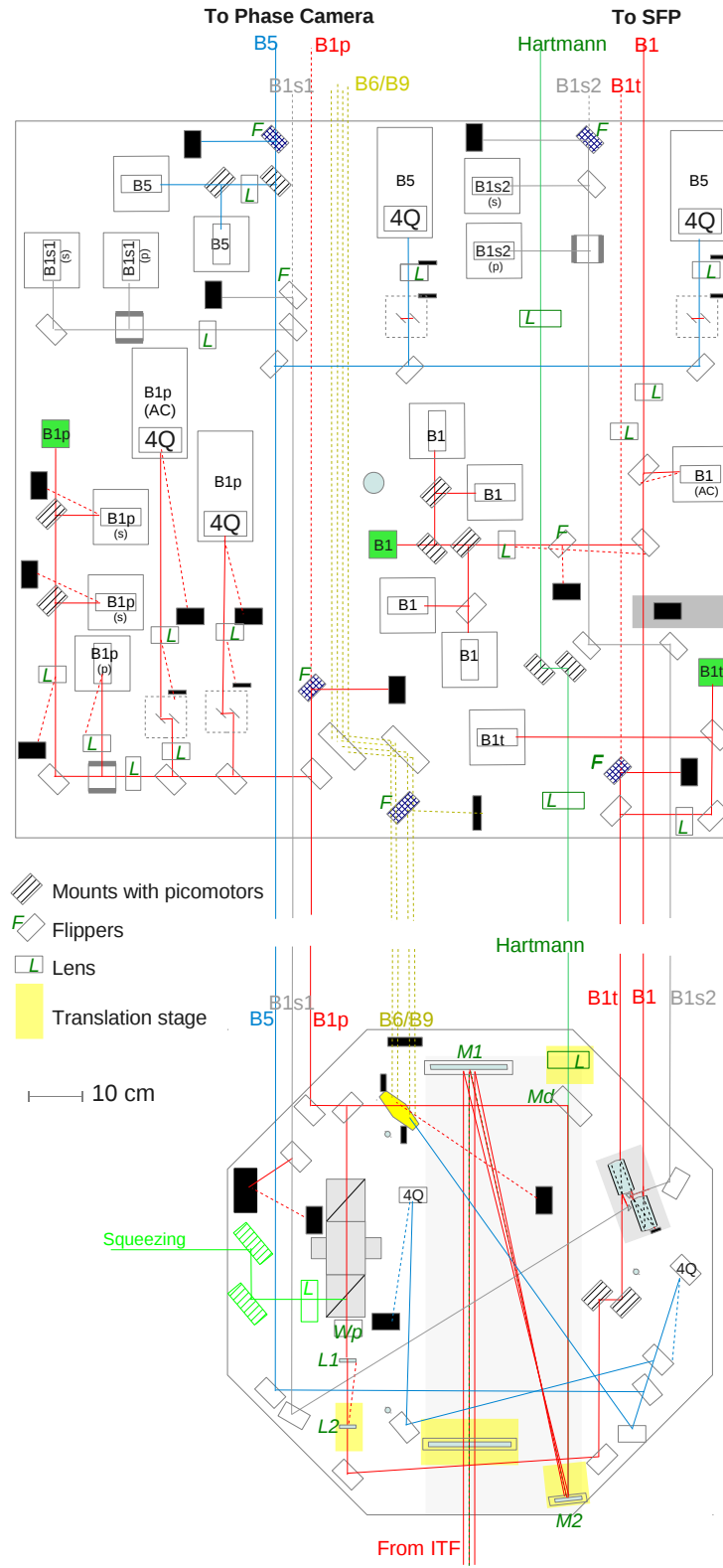


Figure 7.33: Preliminary optical layout of the suspended detection benches (SDB1 and SDB2).

enters the **SDB1** bench through a central aperture in the detection tower (bottom of Fig. 7.33). At the entrance of the bench the beam size is about 21.9 mm. The beams first cross the meniscus lens and are reflected on the two parabolic mirrors of the OMC-MMT. After the M2 mirror, the main beam is almost collimated and its size is about 1.3 mm. The beams are then sent on a dichroic mirror which transmits the Hartmann beam towards the SDB2 and EDB benches, while the YAG beams are reflected.

Three lenses have been placed as illustration purposes along the optical path of the Hartmann beam (one on **SDB1** and two on **SDB2**) in order to adapt its size and curvature with respect to the Hartmann setup located on the **EDB** bench (placed at 3 to 5 m from the first dichroic mirror). The lens focal distances will be accommodated according to the Hartmann setup needs. Two feed-back mirrors tunable in rotation can be used for the Hartmann beam alignment and at least one lens can be placed on a translation stage. Although not represented in Fig. 7.33 there is sufficient space on the SDB2 bench to add a second or third dichroic mirror(s) in order to dump the residual YAG beams that would be transmitted by the first dichroic mirror.

The secondary beams (B5, B6DB, B6pDB, B9DB and B9pDB) are separated from the dark fringe beam by using a multi-faceted mirror. The secondary beams are then sent towards to the SDB2 and EDB benches, while a fraction of the B5 beam is sent on two quadrants placed at different Gouy phases on the **SDB1** bench. The DC signals of these quadrants will be used for the alignment of the SDB1 bench with respect to the ITF.

The YAG beams crosses the Faraday isolator before being sent through the lenses L1 and L2 used to adapt the dark fringe beam to the **OMC** waist. One of these lens will be mounted on a translation stage used to tune the telescope distances.

The dark fringe beam is sent towards the **OMC** cavities where its waist is $263.3 \mu\text{m}$. Two mirrors tunable in rotation and equipped with picomotors will be used for the alignment of the beam with respect to the **OMC** cavities. A small fraction (less than 1%) of this beam (B1p) is extracted before the first OMC and sent towards the **SDB2** bench where it is acquired by two quadrants and three longitudinal photodiodes (1 of them being used for the monitoring of the light that is not S-polarized).

The reflection of the first OMC (B1s1) is sent on a high power beam dumper. A fraction of each reflected beams (B1s1 and B1s2) is also extracted and sent towards the **SDB2** bench for monitoring.

A pickoff of the beam resonating inside the first OMC cavity (B1t) is also sent towards the **SDB2** bench where it will be acquired by a photodiode providing an error signal for the OMC lock.

The transmission of the second OMC cavity (B1) is sent towards the **SDB2** bench where it is extracted for DC detection. Two photodiodes receiving a total power of 80 mW) are foreseen in the baseline, but, as shown in Fig. 7.33, more photodiodes can be used if needed. The B1 beam will also provide an error signal for the lock of the second OMC cavity.

A path for the injection of a squeezing beam on the **SDB1** bench is also shown in Fig. 7.33. Although the implementation of squeezing is not foreseen in the baseline design of Advanced Virgo, it could be added as a future upgrade.

The **SDB2** bench should host all the longitudinal photodiodes foreseen for the B1, B1p, B1s1, B1s2 and B1t beams. It will also host the two quadrants needed for B1p, as well as two quadrants placed on the B5 beam path (which could be used to align **SDB2** with respect

to **SDB1**). A galvanometer will be used to center the beam on the B1p quadrant used in **AC**. Beam splitters placed in front of the longitudinal photodiodes are equipped with picomotors and tunable in rotation, which will allow to center the beams on the photodiodes. Small dumpers might be attached to these beam splitters in order to dump the photodiode reflection (if not done inside the air box).

The vacuum chamber hosting SDB1 is connected to the minitower hosting SDB2 by the mean of a pipe. At the beginning of Advanced Virgo the beams will go from SDB1 to SDB2 by crossing a glass window separating the two vacuums. It is foreseen to later remove this window if scattered light becomes an issue.

A fraction of the B1p and B1 beams must be sent to the **EDB** bench where they will be monitored by a phase camera and a scanning Fabry-Perot system, respectively. The **EDB** bench also hosts the Hartmann setup.

7.8.7 Detection losses budget

| | |
|-------------------------------|-----------------|
| Optical losses | |
| OMC intrinsic losses | $\leq 2\%$ |
| OMC misalignment, mismatching | $\leq 2.5\%$ |
| Telescope coupling losses | $\leq 1\%$ |
| Faraday isolator | $\approx 4\%$ |
| Subtotal | $\leq 9.5\%$ |
| Sensing losses | |
| B1p photodiodes | $\approx 0.3\%$ |
| B1p quadrants | $\approx 2\%$ |
| B1 AC photodiode (or SFP) | $\leq 1\%$ |
| B1p phase camera | $\leq 1\%$ |
| Subtotal | $\leq 4.3\%$ |
| Quantum losses | |
| B1 DC photodiodes | $\leq 2\%$ |
| Total | $\leq 15.8\%$ |

Table 7.20: Detection losses budget.

A preliminary budget for the losses of the dark fringe beam is shown in Tab. 7.20.

The loss budget for the OMC cavities was already presented in section 7.3.7. They should be lower than 4.5 % (with no more than 2 % of intrinsic losses, while the remaining losses are due to misalignment or mode mismatch).

Other optical losses will be induced by the telescope miscoupling ($\leq 1\%$) or the Faraday isolator (which are assumed to be of the order of 4% based on measurement performed with the Virgo injection bench Faraday).

The remaining losses are shared between sensing losses (amount of power that need to be extracted for ITF control or monitoring purposes). Among the sensors the cameras are as-

sumed to be negligible as they can provide an accurate image of the beam with only a few μW . The sensing losses have been estimated by using the following assumptions:

- The B1p photodiodes receive about 5 mW, among which only 0.24 mW correspond to the carrier TEM_{00} . This ratio takes into account the expected side band powers and the amount of HOM predicted by optical simulations ([212, 213]).
- The B1p quadrants receive about 5 mW as TEM_{00} , with only 1.6 mW on the carrier TEM_{00} (the remaining power is on the side bands).
- The power on the B1p phase camera is estimated to 15 mW in total, with only 0.8 mW in the TEM_{00} , based on the Virgo experience.

Finally the quantum efficiency of the DC readout photodiode should be better than 98%.

7.8.8 Bench mechanical design

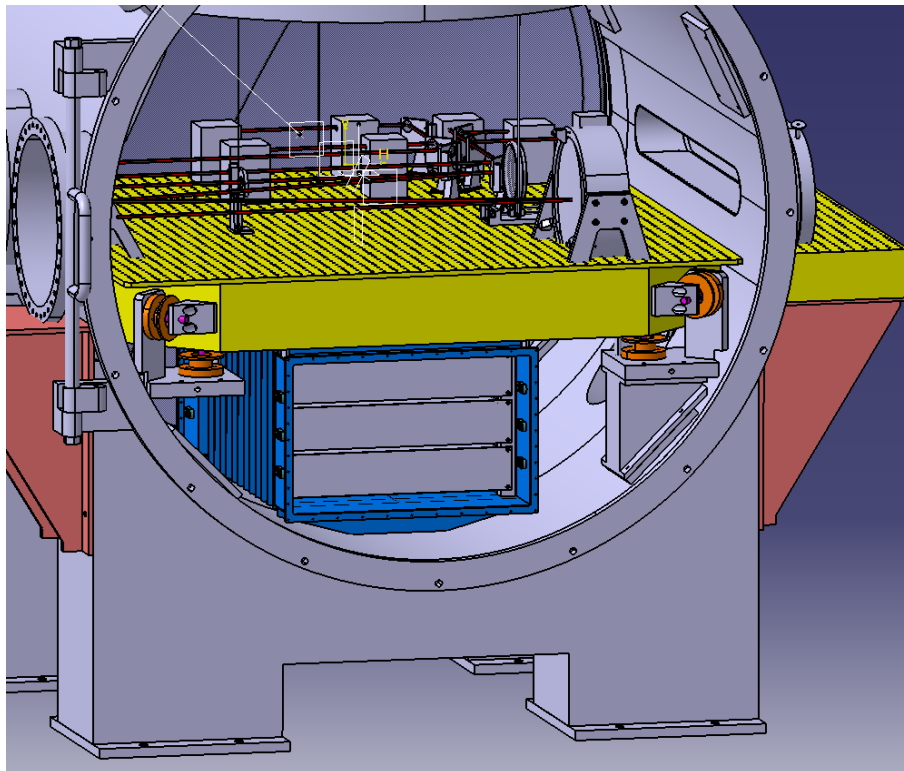


Figure 7.34: Side view of a suspended bench inside its mini-tower..

SDB1

For **SDB1** we plan to reuse the same bench as the Virgo suspended detection bench. This is an octogonal bench whose maximum width is 88 cm. It is suspended to the marionetta using three wires.

SDB2

The **SDB2** bench corresponds to a new bench design that fits inside the new mini-tower (see

Suspended Benches subsystem (**SBE**) chapter). This will be a squared bench with dimensions $130\text{ cm} \times 130\text{ cm}$. Similar benches will be produced for **SNEB**, Suspended West End Bench (**SWEB**), **SPRB** and **SIB2**. A side view of the bench inside its mini-tower is shown in Fig. 7.34.

The actuation of the bench will be fulfilled by using magnets attached at the four corners of the bench and coils attached to the mini-tower.

As it can be seen in Fig. 7.34 a container (shown in blue) is attached under the bench. This air container will host the data acquisition electronics, the camera electronics, the picomotor drivers and the ethernet switch.

The bench will be attached to the short suspension at its center, by a single wire.

EDB

For the **EDB** bench we plan to reuse the same bench as the Virgo external detection bench. This is a rectangular bench whose dimensions are $200\text{ cm} \times 90\text{ cm}$.

7.8.9 Bench local controls

The bench local controls are used to control the bench position with respect to the ground. The same local controls as used in Virgo can be used for **SDB1** [227]: Four mirrors mounted on the suspended bench reflect towards the digital camera the light emitted by four LED-arrays attached to the vacuum chamber (near four viewports). As the bench moves, the image of the LEDs seen by the camera also moves. Image processing permits to extract the displacement of the bench in all of its six degrees of freedom. These signals are then used as error signals for the bench actuation.

In Virgo, this system allowed to maintain the bench at a given position with a precision better than $1\text{ }\mu\text{m}$ and keeping the bench aligned with a precision better than $0.5\text{ }\mu\text{rad}$ in the frequency bandwidth between 1 mHz and 1 Hz .

For **SDB2** (and other suspended benches in mini-towers), three possible control strategies are being considered:

- The error signal could be extracted using a similar system as for **SDB1**, with similar performances. Since less viewports are available, a target would be directly attached to the bench and imaged by a digital camera. If this solution is confirmed it is foreseen to install two targets and two cameras (a priori on the back side of the mini-tower) to extract all the six degrees of freedom of the bench. The digital cameras will be included in the video-system described in the DAQ chapter.
- Another option is to use optical levers, combining **SLED** and **PSD** devices, as foreseen for the **ITF** mirrors.
- The possibility to use **LVDTs** and accelerometers combined with the actuator coils to measure the position of the bench is also investigated.

7.9 End benches

7.9.1 Functions and requirements

The main function of the suspended end benches (**SNEB** and **SWEB**) is to collect the beams transmitted by the end test masses and provide error signals for the **ITF** alignment (with **DC** quadrants) and for the lock acquisition (with longitudinal photodiodes). Their function is also to allow the injection of Hartmann and auxiliary beams. The main requirements for the end benches are the following:

- the end benches must host a telescope to reduce the beam size from 58 mm (in transmission of the end mirrors) to a size that fits the aperture of the sensors;
- the design of the end benches must foresee the injection of a Hartmann beam (at 800 nm) used by the **TCS** and an auxiliary laser at 1319 nm. These beams will be generated and monitored on an external bench under the shared responsibility of **ISC** and **TCS**. Specific viewports must be foreseen to let these beams enter the mini-tower. Dichroic mirrors will be used on the suspended end benches to inject these beams in the reversed path of the B7 and B8 beams;
- the list of sensors needed on the end bench are the following: Two quadrants (used in DC only) will be used for the **ITF** alignment. Each of them will receive about 25 mW of power in science mode. Two longitudinal photodiodes (with **DC** readout and demodulated signals at 6.27 MHz) will be used for monitoring purposes and the for the lock acquisition. One camera is also needed to image the B7 and B8 beams. In addition to these sensors which are part of the baseline design of the bench, we will foresee the possibility to add two extra quadrants that could be potentially useful for the alignment of the auxiliary laser beam injected in the **ITF**. Each of these sensors will be placed inside a specific air box;
- as described in the **ISC** chapter, the quadrants installed on the suspended end benches will provide the error signal to control the angular minus mode of the arm cavity. This mode is equivalent to a pure translation of the beam resonating inside the Fabry Perot cavity. Bench motion induced by seismic noise induces beam jitter in front of the quadrants (such as a cavity angular minus mode would do), and therefore can spoil the alignment error signal. It is therefore crucial that the bench be stabilized with a sufficiently good accuracy at low frequency in order to not spoil the performances of the alignment control loop and be well isolated in the detector frequency bandwidth in order to prevent the introduction of control noise in the interferometer. Requirements on the bench motion are given in the **ISC** chapter. This leads to stringent constraints on the bench isolation and low frequency stabilization, in particular for what concerns the residual angular RMS of the bench ($\theta_{RMS} \leq 0.03\mu\text{rad}$), which is 3 times lower than what was achieved for the Virgo mirrors suspended to the **SA** suspension. As discussed in section 7.9.2 several telescope configurations have been studied with the goal of minimizing the quadrant sensitivity to the bench angular motions.

7.9.2 End bench telescopes

7.9.2.1 General requirements

The main requirements of the End Benches (EB) MMT are given below and summarized in the table 7.21.

- The EB MMT should reduce the ITF beam size from 58 mm (in transmission of the end mirrors) to a size that fits the aperture of the sensors. In the current baseline we will use 5 mm diameter quadrants and 3 mm diameter longitudinal photodiodes, therefore the radius of the beam on the sensors should be in the 300 μm -400 μm range.
- The Gouy phases of the beam on the two quadrants used for the ITF alignment should be separated by a 90 degrees ± 20 degrees .
- The EB MMT should reduce as much as possible the sensitivity of the quadrants sensors (used for the AdV automatic alignment) to the bench motions.
- The telescope should fit the space constraints on the EB. This bench has a square shape with a width of 130 cm.
- The aperture of the telescope should be compliant with the TCS requirements on clipping losses. With the present design the losses are of the order of 9%. If this turns out to limit the precision of the measurement, TCS will consider a reduction of the size of this Hartmann beam. The telescope should also guarantee a sufficiently low distortion of the Hartman beam and of the TEM_{00} .
- The amount of back-reflected or back-scattered light from the telescope optics should be compliant with the sensitivity requirements (noise \leq AdV sensitivity/10).

| Parameters | Requirements |
|----------------------------------|---------------------------|
| Magnification | 165 |
| Noise coming from spurious light | \leq AdV sensitivity/10 |
| Gouy phase difference | 90 deg \pm 20 deg |

Table 7.21: EB MMT general requirements.

7.9.2.2 Telescope overview

Several telescope configurations with all the focusing optics setting on the bench have been studied and they give very similar transfer functions between the bench motions and the signals on the quadrants [224]. Another configuration, with the main focusing element of the telescope suspended to the end mirror superattenuator, allows to reduce the sensitivity to the bench angular motion but it was discarded since it highly increases the constraints on the shifts of the bench [224].

The choice to use lenses, instead of parabolic mirrors, has been driven by considerations on the mechanical designs of the bench itself, tolerancing and alignment procedures, easier for the lenses configuration.

An optical layout of the baseline configuration for the end arm telescope is shown in Fig. 7.35. The main focusing element of the telescope is a doublet (L1) placed at the entrance of the end bench. A similar doublet was designed for Virgo+ [225]. The choice of a doublet instead of a single lens is driven by the need to reduce the spherical aberrations. One extra lens (L2) of two inches diameter will be installed on the bench to reduce the convergence of the beam and to adapt its size to the aperture of the photodiodes and quadrants. The size of the beam on each quadrant is $368 \mu\text{m}$ and the quadrants are placed symmetrically around the waist ($260 \mu\text{m}$) at $\pm z_R$ (the Rayleigh range).

The parameters of the telescope are given in the table 7.22.

7.9.2.3 Performances of the system

The Fig. 7.36 shows the image of the beam (at the waist position) after the telescope. The power on the TEM_{00} is higher than 99%, mainly due to the compensation of the spherical aberrations by the doublet.

In order to reduce the scattered light it may be interesting to tilt the L2 lens by a few degrees. In this case the coupling of the TEM_{00} mode decreases a bit: the coupling efficiency is 99.5% for a tilt of 3 degrees and 96.9 % for a tilt of 5 degrees.

7.9.2.4 Tolerancing study: errors in the ROCs

The tolerancing study was performed using the Zemax software similarly to the one done for the OMC-MMT (see section 7.8.2). Table 7.23 shows the errors on the RoCs ($\pm 1\%$ given by the manufacturers). In order to compensate the errors on the ROCs it is possible to change the distance between the L1 (the doublet) and L2.

The table 7.23 summarizes the range necessary to compensate for each RoC error separately and then recover the ideal waist size and a coupling efficiency higher than 99.9%.

For example, it is possible to recover a waist size of $260 \mu\text{m}$ (and a matching higher than

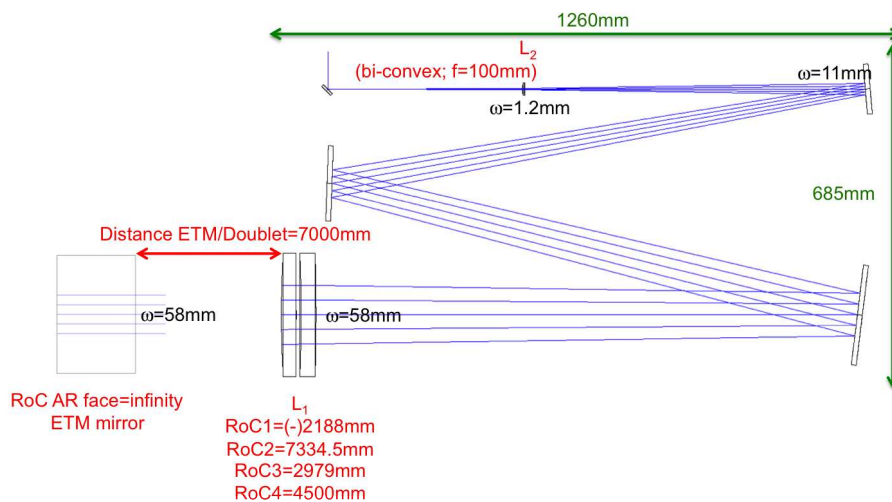


Figure 7.35: Overview of the EB MMT layout.

| Parameters | Value | Characteristic |
|--------------------------------|-------------|-----------------------|
| RoC L1 side 1 | (-)2188 mm | spherical convex |
| RoC L1 side 2 | 7334.5 mm | spherical convex |
| RoC L1 side 3 | 2979 mm | spherical concave |
| RoC L1 side 4 | 4500 mm | spherical convex |
| RoC L2 | 100 mm | spherical - bi convex |
| Distance ETM AR side/L1 side 1 | 7000 mm | |
| Distance L1 side 4/L2 | 3996 mm | |
| ETM mirror clear aperture | 370 mm | |
| L1 clear aperture | 220 mm | |
| L2 clear aperture | 25 mm | |
| ETM beam size | 58 mm | |
| L1 beam size | 58 mm | |
| L2 beam size | 1.2 mm | |
| Waist size on ETM AR | 6.73 mm | |
| Waist position on ETM AR | 1145 m | |
| Waist size after L1 side 4 | 24 μ m | |
| Waist position after L1 side 4 | (-)4084 mm | |
| Waist size after L2 | 260 μ m | |
| Waist position after L2 | (-)965 mm | |

Table 7.22: Optical parameters of the EB MMT: radii of curvature, distance between the optics, clear aperture and beam parameters.

99.9%) induced by a RoC error on the first side of the doublet, by changing the distance between L1 and L2 as shown in Fig. 7.37.

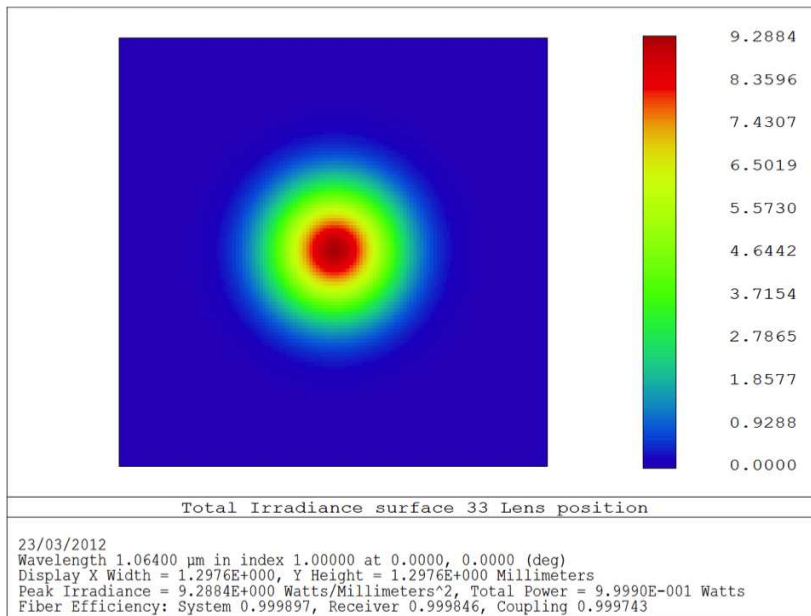


Figure 7.36: Coupling of the beam on the quadrants sensors (FFT propagation with Zemax). A coupling efficiency with a perfect gaussian beam of 99.97% is achieved.

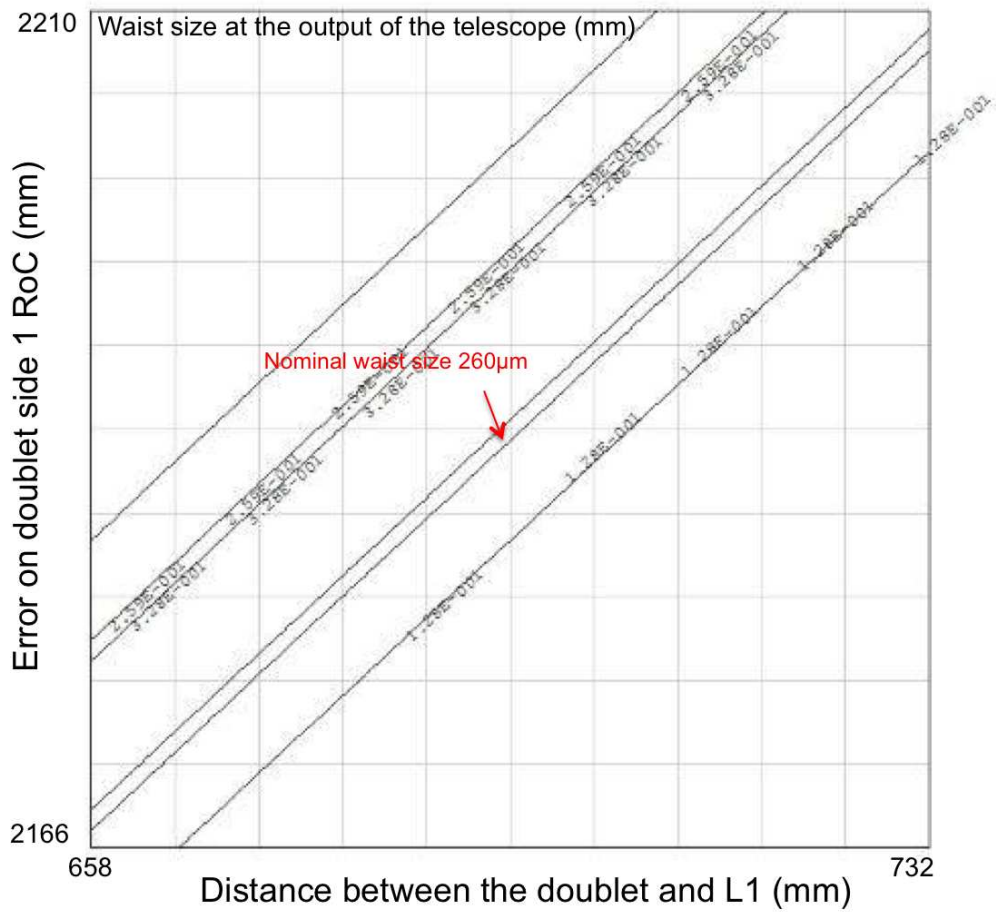


Figure 7.37: Waist size at the output of the telescope as a function of the ROC of the first side of the doublet and of the distance between L1 (doublet) and L2. The different lines correspond to different waist size. The red arrow indicates the line corresponding to the optimal waist size at the output of the telescope

| Optics | RoC errors value (mm) | Distance L1-L2 (mm) |
|-----------|-------------------------|---------------------|
| L1 side 1 | $(-)\text{2188} \pm 22$ | ± 38 |
| L1 side 2 | 7334.5 ± 74 | ± 12 |
| L1 side 3 | 2979 ± 30 | ± 29 |
| L1 side 4 | 4500 ± 45 | ± 19 |
| L2 | $(-)\text{100} \pm 1$ | ± 1 |

Table 7.23: RoC errors for the tolerancing study of the EB MMT, and ranges of the compensator in mm (distance between L1 and L2) needed to compensate separately RoC errors of each optics.

7.9.3 Optical layout

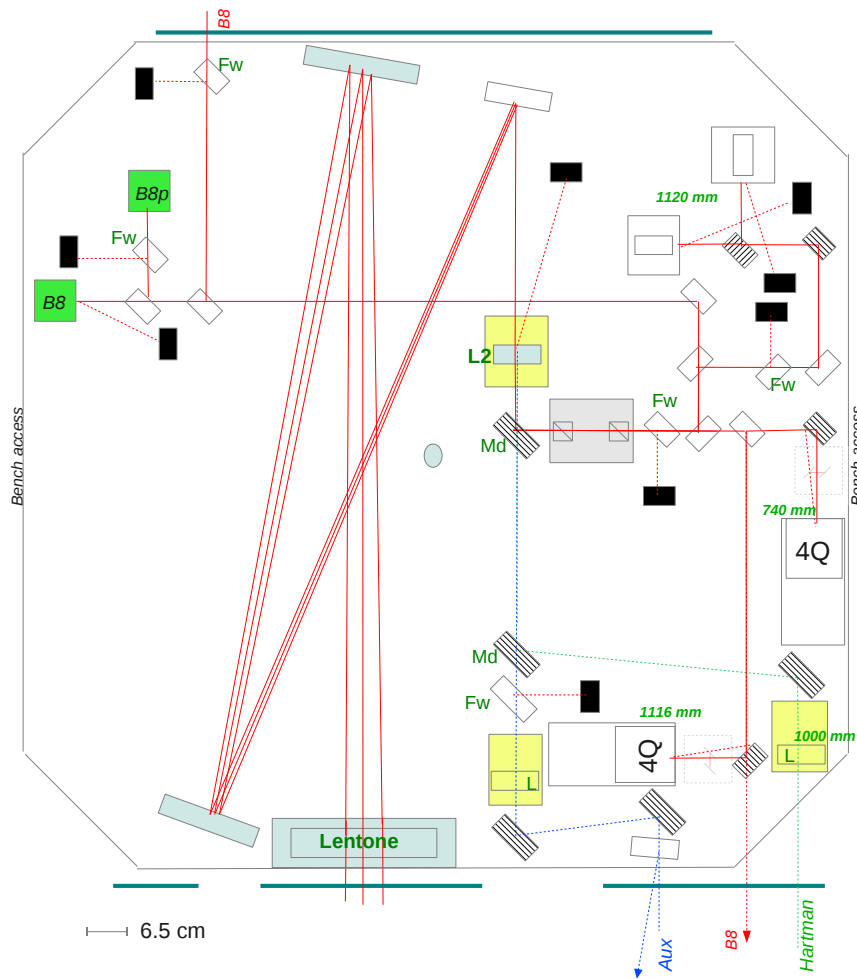


Figure 7.38: Suspended End Bench optical layout.

An optical layout of the end benches is presented in Fig. 7.38.

The main beam (overlapped with the auxiliary laser and the Hartmann beam) enters through a central aperture in the mini-tower. At the entrance of the bench the beam radius is about

58 mm. The beams first propagate through the EB telescope (made of the lentone and the L2 lens). The L2 lens will be mounted on a translation stage allowing a tuning of the telescope distances.

At the output of the telescope, a dichroic mirror is used to extract the Hartmann beam and the auxiliary laser (which are transmitted), while the YAG beam is reflected and sent towards the bench sensors. As shown in Fig. 7.38 the possibility to insert a Faraday isolator along the YAG path to isolate the IFT from the back-reflected light on the sensors is foreseen in the bench layout, although it is not part of the baseline design.

As shown in Fig. 7.38 the Hartmann beam (at 800 nm) and the auxiliary laser (at 1319 nm) are then sent towards the right front of the bench where they exit the minitower through two different viewports (the coating of each viewport is optimized for its specific wavelength). One should highlight that the front right flange of the mini-tower (see SBE chapter) has a diameter of 350 mm and can therefore host several small viewports of a few cm diameter. After exiting the mini-tower, the Hartmann beam and the auxiliary laser beam are collected on an external bench under the shared responsibility of ISC and TCS. In the current optical layout of the suspended bench a lens (mounted on a translation stage) is placed on the path of the Hartmann beam and on the path of the auxiliary laser in order to adapt the beam size with respect to the optics placed on the external bench.

The YAG beam is finally sent on the sensors following the requirements on the Gouy phases given in the section 7.9.1. All these sensors (photodiodes, quadrants and camera) are placed inside dedicated air boxes. The mounts of the splitters or feedback mirrors placed in front of the photodiodes and quadrants must be tunable in rotation and are equipped with picomotors allowing the online centering of the beam with respect to the sensors. The quadrants should also be equipped with translation stages allowing to tune their Gouy phases.

A fraction of the YAG beam is also sent towards the rear side of the mini-tower where a small external bench will host the cameras used for the bench local controls, as well as possible tools for pre-alignment of the telescope.

In the current layout another pickoff of the YAG beam is sent towards the ISC/TCS external bench. This beam is meant to be used as a reference for the alignment of the auxiliary beams. If needed one could add two extra quadrants on the suspended bench for the alignment of the auxiliary laser.

7.10 Pick-off bench

7.10.1 Functions and requirements

The main function of the **SPRB** bench is to extract the pickoff beam B4 that is needed for the longitudinal and angular control of the **ITF**. To this purpose the **SPRB** bench must host two longitudinal photodiodes and two quadrants as described below:

- The B4 longitudinal photodiodes will provide **DC** signals and **RF** signals demodulated at f_1 , f_2 , $2f_1$, $2f_2$ and f_4 . These photodiodes will receive a nominal power of 50 mW in science mode.
- The B4 quadrants will provide **DC** signals and **RF** signals demodulated at f_1 , and f_2 .

These quadrants will receive a nominal power of 25 mW in science mode. It must be highlighted that the **ITF** alignment error signals will be extracted from the **RF** channels of the quadrants, which significantly relax the constraint on the residual bench motion.

The suspended bench must host a telescope that will be used to adapt the size of the beam to the aperture of the photodiodes (of 3 mm diameter) and the quadrants (of 5 mm diameter). At the input of the telescope the beam is about 49 mm and the beam size on the longitudinal photodiodes and the quadrants should lie within the range between 300 and 400 μm .

A fraction of the B4 beam will be sent to an external bench (**EPRB1** or **EPRB2**) where a phase camera capable of monitoring the 6.27 MHz side band and the 131.7 MHz side band will be installed.

The layout of the **SPRB** bench should also allow the separation of all secondary beams (B6PR, B6pPR, B9PR, B9pPR) and their reflection on the second face of the **PR** plate from the B4 beam. To this purpose a multi-faceted mirror (or a diaphragm) will be used.

Due to space constraints around the mini-tower hosting the **SPRB** bench, it is mandatory that the beam enters the mini-tower by the right front flange. The first element of the telescope needs therefore to be installed on the right side of the bench.

7.10.2 Telescope design

The design of the PR pickoff telescope will be very similar to the EB telescope described in section 7.9.2, with doublet (so-called lentone) as main focusing element and a smaller lens L2 about 4 m further to adapt the beam size to the quadrants.

7.11 SIB2 bench

On the **SIB2** bench (shared with the **INJ** subsystem), the **DET** subsystem has the responsibility to provide two longitudinal photodiodes and two quadrants needed for the extraction of the B2 signals:

- The B2 longitudinal photodiodes will provide **DC** signals and **RF** signals demodulated at f_1 , $3f_1$, f_2 , f_3 and f_4 . These photodiodes will receive a nominal power of 50 mW in science mode.
- The B2 quadrants will provide **DC** signals and **RF** signals demodulated at f_1 , f_2 , and f_3 . These quadrants will receive a nominal power of 25 mW in science mode.

The **DET** subsystem will also provide the two RFC photodiodes and the RFC camera that need to be placed under vacuum. An optical layout of the **SIB2** bench is provided in the **INJ** chapter.

The mechanics of the bench and its local controls will follow the design presented in sections 7.8.8 and 7.8.9.

Chapter 8

Interferometer sensing and control (ISC)

8.1 General description of the subsystem

The Interferometer Sensing and Control (ISC) subsystem of the Advanced Virgo project deals with the design of the control systems that will be used both during the lock acquisition of the interferometer and the steady state (*science mode*) operations.

The design requirements to the ISC subsystem are:

- Develop a control strategy capable of maintaining the interferometer controlled at the design sensitivity with good stability and duty cycle. This means that all control loops must have large enough stability margins and that all control noises reintroduced by the loops must contribute at maximum a factor 10 below the design sensitivity.
- Develop a repeatable and robust lock acquisition strategy, capable of bringing the interferometer from a fully uncontrolled state to the final, good sensitivity one in a reasonably short time (of the order of tens of minutes).
- All of the above must be obtained for at least three different optical configurations: power recycled only interferometer at low input power (chosen to be 25 W as reference); dual recycled interferometer at low input power; dual recycled interferometer at full input power (125 W).

The degrees of freedom to be controlled are divided in longitudinal and angular ones (refer to sec. 8.3.1 and 8.7.2 for definitions). Since the cross coupling between the two sets is typically not dominant, the control system design can be carried out separately. In the longitudinal case it is necessary to distinguish between the lock acquisition state and the steady state. In the angular control system case there is no need for such a distinction, since global control loops will be activated only when the interferometer is already close enough to the final working point.

All the designs described in the following sections have been obtained using simulations of the full interferometer based on modal models. The two main frequency domain tools used so far are Finesse [255] and Optickle [256]. Both tools are to some extent incomplete: Finesse can

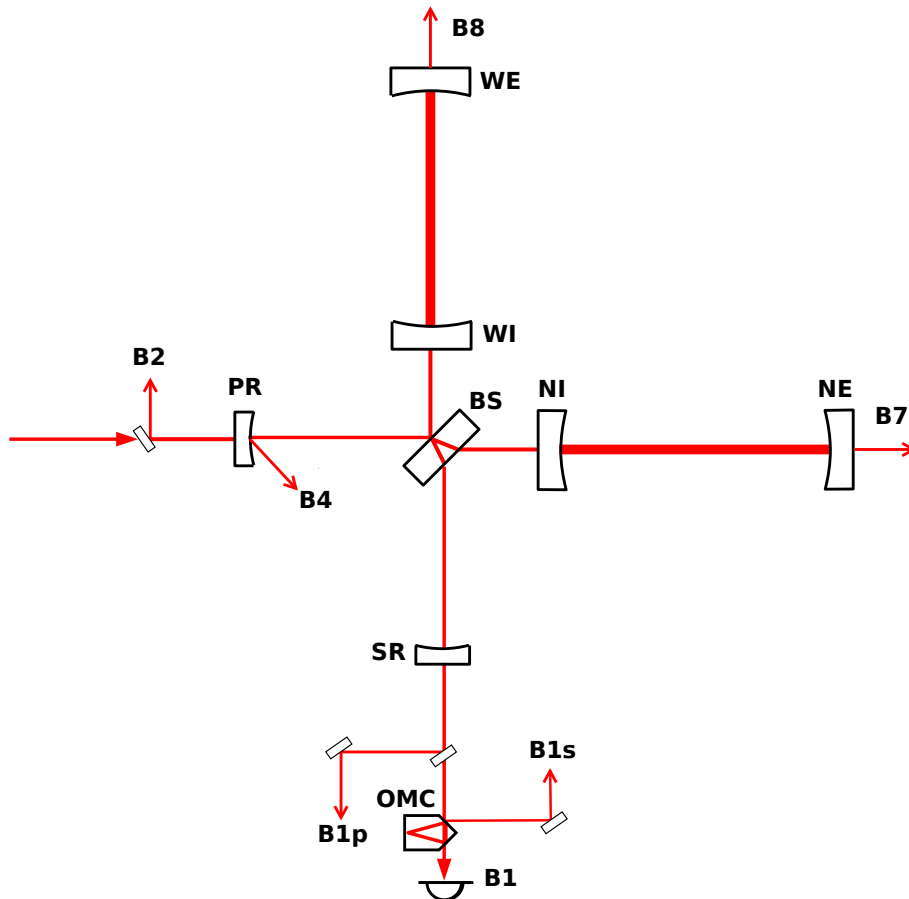


Figure 8.1: Optical layout of the Advanced Virgo interferometer, with mirrors and output ports naming convention.

introduce higher order modes but cannot deal with radiation pressure effects; on the other hand Optickle can deal with radiation pressure but is limited to only the first higher order mode. These limitations are particularly relevant in the design of the angular control system.

Time domain simulations were also used for the study of the lock acquisition procedures. The choice was to use the e2e [257] software, developed by the LIGO Scientific Collaboration, since it is well maintained and widely used for the design of Advanced LIGO lock acquisition.

Optical simulations of thermal effects and mirror defects inside the Power Recycling Cavity (PRC) showed a large impact on radiofrequency sideband aberrations. A risk reduction strategy to have error signals less sensitive to PRC defects and aberrations is proposed. It will help in the first commissioning and locking steps (sec. 8.6).

8.2 Input from other subsystems and basic assumptions

All the main beams exiting from the interferometer (reflection, power recycling pickoff, dark port, transmission of the two arms) need to be probed with suitable photodiodes and quadrant photodiodes for control and monitoring purposes. A scheme of the interferometer layout with

the naming convention is shown in Fig. 8.1.

The DET subsystem fixed the amount of power to be sensed on each beam by longitudinal photodiodes to about 100 mW with a signal-to-noise ratio equivalent of a 100 mW shot noise limited beam down to 10 Hz. The longitudinal control design has been carried out with this assumption. See sec. 8.3.6 for more details.

Similarly DET fixed the amount of power that can be sensed on each quadrant photodiode to 25 mW for each port [259], except for the dark port before the Output Mode Cleaner (OMC), where the power per quadrant is reduced to 2.5 mW to avoid losing too much of the main beam. In the control design the corresponding sensing noise is again required to be dominated by the corresponding shot noise (sec. 8.7.6), thus considering other sources of noise (electronic and bench motion) to be negligible with respect to it.

The gravitational channel extraction foresees the use of a DC readout technique. It implies the addition of an offset on one of the differential degrees of freedom to add a local oscillator carrier field at the dark port. The amount of carrier power at the dark port was fixed by DET to be 80 mW [294], based on considerations explained for example in [293].

A frontal modulation technique will be used to control all longitudinal degrees of freedom, except DARM (see 8.3.1), and most of the angular degrees of freedom. Three modulation frequencies are foreseen in steady state conditions. Their values must be chosen, together with the optical path lengths inside the interferometer, in order to meet the following requirements:

- all modulation frequencies must be transmitted by the Input Mode Cleaner (IMC);
- the first two modulation frequencies must be resonant inside the PRC;
- the third modulation frequency must be antiresonant inside the PRC;
- the second modulation frequency must be resonant also inside the Signal Recycling Cavity (SRC);
- the transmission of the first modulation frequency to the dark port must be as small as possible.

All these requirements constrain the possible frequencies and distances between mirrors. Considering also the requirements coming from infrastructure and vacuum, the set of lengths and modulations listed in the OSD chapter are obtained (Tab. 8.1).

The present design of the INJ subsystem foresees the ability of delivering a modulation index of 0.1 for all main modulation frequencies.

The longitudinal and angular control system have been designed starting from the assumption that the mirror residual motions at low frequency will be of the same order of magnitude of those obtained in Virgo: about 0.5 μm and 0.1 μrad RMS concentrated below a few Hz.

The Advanced Virgo detector in dual recycled configuration is expected to work with different tunings of the SRC. In the design of both angular and longitudinal control systems only the one which optimizes the sensitivity for NS-NS inspirals has been considered. The SRC tuning will be controlled changing the offset added to the Signal Recycling Cavity Length (SRCL) error signal. The available linear range is about double of the tuning corresponding to the NS-NS-optimized configurations. The effect of using different tunings on the control loops and on noise couplings has not been studied yet.

| Parameter | Value |
|--|---|
| Power recycling mirror transmission | 0.05 |
| Input mirror transmission | 0.014 |
| End mirror transmission | 1 ppm |
| Signal recycling mirror transmission | 0.2 |
| Losses per mirror | 32.5 ppm |
| Arm cavity mirror mass | 42 kg |
| Power recycling cavity length | 11.952 m |
| Signal recycling cavity length | 11.952 m |
| Schnupp asymmetry | 0.23 m |
| Arm cavity length | 2999.8 m |
| Modulation frequencies | $f_1 = 6270777$ Hz $f_2 = 56436993$ Hz $f_3 = 8361036$ Hz |
| Suspension last stage resonant frequency | 600 mHz |
| DC readout offset | see Tab. 8.3 |
| Signal recycling cavity detuning | 3.022×10^{-7} m |

Table 8.1: List of relevant parameters used in the Optickle simulation. Reference from [262].

8.3 Longitudinal control system: steady state control

The optical response of the interferometer to longitudinal motions of the mirrors has been simulated using Optickle [256], which is as of today the only tool capable of including radiation pressure effects. Three different configurations have been considered for all the design steps: power recycled only interferometer at low input power, namely 25 W; dual recycled interferometer at low input power (25 W); dual recycled interferometer at full input power, namely 125 W.

The main parameters used in the simulation are summarized in Tab. 8.1. More details on the longitudinal control can be found in the note [260].

8.3.1 Definition of degrees of freedom

In a dual recycled interferometer the length sensing and control system deals with five degrees of freedom. Referring to Fig. 8.2, the microscopic positions (*tunings*) of all mirrors are combined to obtain the following physical degrees of freedom:

$$\begin{aligned}
 \text{DARM} &= \frac{L_N - L_W}{2} \\
 \text{CARM} &= \frac{L_N + L_W}{2} \\
 \text{MICH} &= l_N - l_W \\
 \text{PRCL} &= l_P + \frac{l_N + l_W}{2} \\
 \text{SRCL} &= l_S + \frac{l_N + l_W}{2}
 \end{aligned}$$

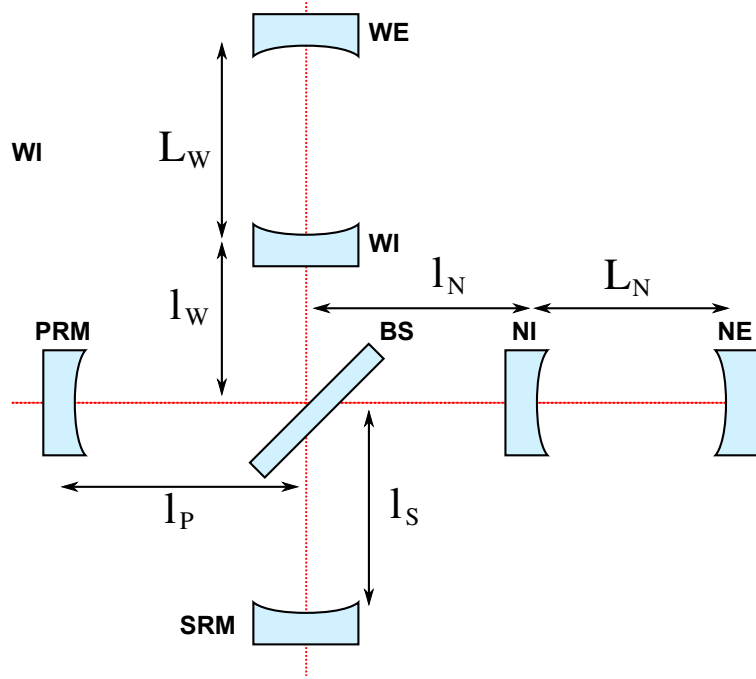


Figure 8.2: Scheme of relevant physical distances between mirrors in a dual recycled interferometer.

| Mirror/DOF | DARM | CARM | MICH | PRCL | SRCL |
|------------|--------|------|--------------|------|------|
| NE | $-1/2$ | -1 | | | |
| WE | $1/2$ | -1 | | | |
| BS | | | $1/\sqrt{2}$ | | |
| PR | | | $-1/2$ | -1 | |
| SR | | | $1/2$ | | -1 |

Table 8.2: Driving coefficients for dual recycled interferometer. In the case of power recycled only interferometer the SR driving is simply removed.

The simplest extension of Virgo driving to Advanced Virgo consists in controlling MICH / PRCL / SRCL using PR / SR / BS. Table 8.2 summarizes the driving matrix for a dual recycled interferometer as it is used in all the following simulations.

In addition to these “mechanical” degrees of freedom one should consider the laser frequency stabilization loop, which locks the laser to the mean length of the two arm cavities with typical bandwidths of a few tens of kHz (sec. 8.3.9). The laser frequency will follow the motion of the mean arm cavity length, called CARM in the previous equations. The typical motion of the CARM degree of freedom, if left free, would correspond to thousands of Hz. To avoid such large fluctuations, the CARM mechanical mode will be controlled by acting on the end mirrors, using an error signal coming from the reference cavity [272]. This is the same strategy adopted in Virgo+ and allowed also to extract the complete position information to be used for the Global Inverted Pendulum Control (GIPC) system.

8.3.2 Definition of available output ports and signals

There are many output ports foreseen in Advanced Virgo:

- The dark fringe or asymmetric port: before the **OMC** a small fraction is extracted and sent to B1p. The transmission of the **OMC** is B1 and the reflection is B1s. Since the **OMC** should filter all sidebands, B1 contains only the fundamental mode carrier field, while all higher order modes and sidebands should therefore go in B1s. For steady state longitudinal control only B1 is used.
- The interferometer reflection or symmetric port, named B2. The amount of power available in this port depends largely on the impedance matching between the PR mirror and the arm cavity reflectivities, which is in turn determined by their round trip losses.
- The transmission of the two arm cavities, named B7 and B8 for North and West, respectively. They will not be used for the longitudinal steady state control.
- The power recycling cavity pickoff port (B4), which will be extracted using a plate in front of the power recycling mirror.

The beam is frontal modulated at three radio frequencies listed in Tab. 8.1, using electro-optical modulators placed before the input mode cleaner, with modulation indexes set to 0.1. The frequencies must therefore be multiples of the **IMC** free spectral range. Not all the possible demodulated signals will be needed at all ports: the B1 beam will not see any sideband, so demodulation is useless on that port; f_3 is antiresonant in the recycling cavity, so signals demodulated at this frequency will be useful only in the B2 beam; the B4 beam finally will contain both f_1 and f_2 sidebands and will provide useful signals at both demodulations. The name convention for signals is: PORT_SBx_yy where x refer to the modulation frequency and can range from 1 to 3, while yy can be DC, P or Q referring respectively to power signal, demodulated in-phase and demodulated quadrature channels. Demodulation phase is chosen in each configuration in order to maximize one chosen degree of freedom in P over Q. Details are given for each configuration separately.

The total power which is sensed at each longitudinal photodiode is 100 mW, according to specifications given by the DET subsystem [259]. All signals are considered limited by the corresponding shot noise, meaning that all sources of electronic noise are required to be negligible.

The reflectivity of the Pickoff Plate (**POP**) was chosen to be 300 ppm. This will provide 100 mW for the longitudinal photodiodes and 50 mW for the quadrant diodes for input power larger than 14 W. In this way it will be possible to fully exploit the shot noise limited sensitivity since the first commissioning steps.

8.3.3 DC readout offset

The DC readout scheme foresees the addition of an offset to a differential degree of freedom, in order to have a static carrier field reaching the dark port, to be used as phase reference for homodyne detection. In principle it is possible to generate such a static field both with an offset in DARM or MICH. The use of a DARM offset introduces a detuning of the arm cavities

| Configuration | Degree(s) of Freedom (DOF) | Offset [m] |
|--------------------|----------------------------|----------------------|
| Power recycled 25W | MICH | $1.6 \cdot 10^{-9}$ |
| Dual recycled 25W | DARM | $2.3 \cdot 10^{-11}$ |
| Dual recycled 125W | DARM | $1.0 \cdot 10^{-11}$ |

Table 8.3: Offsets needed for reaching 80 mW of power at dark port.

from resonance, thus in principle increasing the influence of radiation pressure. Instead using a MICH offset does not move the arm cavities out of resonance. In the presence of a SRC the distinction is however not straightforward. One important point is how optical transfer functions change with the offset, in particular the DARM one and the power and frequency noise couplings.

Results detailed in [260] show that the behavior is different in power recycled and dual recycled configuration. In power recycled only case, if the offset is added to MICH instead of DARM, there is no more any effect of radiation pressure in the DARM optical transfer function. Moreover, in the case of MICH offset, the coupling of frequency and power noises to the output signal is lower, at least in the more critical low frequency region. Therefore the use of a MICH offset is preferable in the case of power recycled only interferometer.

The situation is different in the dual recycled case. Since the DARM optical transfer function is dominated by radiation pressure effects due to the SRC, there is no difference wherever the offset is added. Frequency and power noises instead couple more if a MICH offset is used. It is then preferable to use a DARM offset in the dual recycled case.

In conclusion, in the following simulations, a MICH offset is used in the power recycled interferometer and a DARM one in the dual recycled case. In all three configuration the offset is tuned in order to have 80 mW of carrier fundamental mode power at the dark port. The resulting offsets are summarized in Tab. 8.3.

Moreover, the value of the differential offset (on MICH or DARM) has a strong influence on the angular sensing matrix: the larger the offset, the less diagonal the sensing matrix. Therefore the value of the offset should be maintained as small as possible to improve the angular control system robustness [263].

8.3.4 Accuracy requirements

The accuracy requirements for longitudinal loops are summarized in Tab. 8.4. The reasoning used to derive these numbers is explained in the note [260]. Here only the considerations for DARM and CARM are repeated, since these accuracy requirements are those having stronger impacts on interfaces with other subsystems.

In the DARM case the most stringent requirement comes from the use of DC readout. Indeed the response of the dark fringe power to differential motion is intrinsically non linear: the DC power at B1 varies with very good approximation as a parabola centered at zero offset. The optical gain is given by the derivative of this parabola and therefore it varies linearly even around the nominal operating point.

| DOF | Power rec. 25W | Dual rec. 25W | Dual rec. 125W |
|------------------|-----------------------|-----------------------|-----------------------|
| DARM | $6 \cdot 10^{-16}$ m | $2 \cdot 10^{-15}$ m | $1 \cdot 10^{-15}$ m |
| Frequency | | 7 mHz | |
| CARM | | $4 \cdot 10^{-13}$ m | |
| MICH | $2 \cdot 10^{-13}$ m | $6 \cdot 10^{-13}$ m | $3 \cdot 10^{-13}$ m |
| PRCL | | 2×10^{-11} m | |
| SRCL | | | $3 \cdot 10^{-13}$ m |

Table 8.4: Summary of accuracy requirements for longitudinal control loops.

In general the power at dark port can be described by the following equation:

$$B1 = b_0 + \alpha \delta z + \beta \delta z^2 \quad (8.1)$$

where δz is the residual motion of DARM. The coefficients α and β can be obtained from simulations. However their dependence on the DC readout offset is easily computed, considering the quadratic nature of the B1 power response to DARM motion: β is constant and $\alpha = 2z_0\beta$ where z_0 is the static offset.

One of the effects of the non linear term in the above equation is to create upconversion of low frequency residual DARM motion around high frequency lines. Indeed, the previous equation is correct in the time domain:

$$b(t) = b_0 + \alpha \delta z(t) + \beta \delta z(t)^2 \quad (8.2)$$

which in frequency domain becomes:

$$\tilde{b}(f) = \alpha \tilde{\delta z}(f) + \beta (\tilde{\delta z} \star \tilde{\delta z})(f) \quad (8.3)$$

If we assume the DARM motion to be composed of a low frequency part (residual motion) and of a large spectral line (like for example violin modes) the convolution can be easily computed and the signal on the diode at the line frequency will be

$$\tilde{b}(f) = \alpha z_L \left(1 + \frac{2\beta}{\alpha} z_{\text{RMS}} \right) \delta(f - f_L) \quad (8.4)$$

where z_L and f_L are the amplitude and frequency of the line and z_{RMS} is the residual DARM motion. The second term inside the brackets gives the level of low frequency upconverted noise which falls around the main line. This noise couples directly to the detector sensitivity, thus it must be required to be a factor 10 below the design sensitivity. Assuming to have lines with a Signal to Noise Ratio (SNR) of 1000, which is typical of violin and mirror modes, the term must satisfy:

$$\frac{2\beta}{\alpha} z_{\text{RMS}} < \frac{1}{10} \cdot \frac{1}{1000} = 10^{-4} \quad (8.5)$$

From the relation between α and β one finally finds the following relation which gives the requirement for DARM:

$$\frac{z_{\text{RMS}}}{z_0} < 10^{-4} \quad (8.6)$$

which means that the DARM accuracy must be a factor 10^4 smaller than the actual static offset. This means that for power recycled only configuration at 25 W DARM accuracy must be at the level of $6 \cdot 10^{-16}$ m; for dual recycled at 25 W at $2 \cdot 10^{-15}$ m; for dual recycled at 125 W at $1 \cdot 10^{-15}$ m.

In the CARM case, the very low frequency absolute fluctuation of the laser frequency is dominated by the residual motion of the arm cavity mean length. This is at first order not relevant for the interferometer except for the presence of the output mode cleaner. Indeed any fluctuation of the laser frequency will be equivalent to a change in the length of the **OMC** and will at some level spoil its lock accuracy. If an accuracy δz_{OMC} is needed for avoid the reintroduction of **OMC** length noise in the sensitivity [264], the corresponding tolerable residual motion of the mean arm length is given by

$$\delta z_{CARM} \sim \frac{L_{ARM}}{L_{OMC}} \cdot \delta z_{OMC} \quad (8.7)$$

Assuming for example a length of the **OMC** of about 30 cm [265] and a level of length noise of the **OMC** of the order of $4 \cdot 10^{-17}$ m/ $\sqrt{\text{Hz}}$ at 10 Hz, the required accuracy for **OMC** lock is of the order of $4 \cdot 10^{-13}$ m. This corresponds to a CARM lock accuracy of $4 \cdot 10^{-9}$ m or 400 Hz in terms of laser frequency. In the baseline design, the CARM slow loop will use, as in Virgo+, an error signal in reflection of the reference cavity, with typical bandwidths of few Hz. Alternative schemes are being considered [265], such as controlling the CARM loop directly using the OMC error signal.

8.3.5 Consequences of the accuracy requirements on OMC filtering

In an ideal world only the carrier fundamental mode is transmitted by the **OMC**. However in reality, parts of the sidebands and of higher order modes also leaks through the **OMC**. If these leakage fields fluctuate in amplitude, they will give rise to spurious power fluctuations of the dark fringe photodiode which will be interpreted by the DARM loop as a motion of the physical degree of freedom.

The maximum leakage power which is tolerable depends on the required DARM accuracy and on the expected power fluctuation of the leaking field. The latter is quite difficult to predict. However a reasonable estimate can be obtained looking at the residual intensity fluctuation of sideband fields at the dark port during the last Virgo+ science run. It turned out that sideband power fluctuates typically of about 2%, coherently with interferometer motions especially in the microseismic region [265].

Since at low frequency (below about 1 Hz) the DARM loop has very high gain, any spurious power fluctuation at the dark port is directly converted into a real motion of the DARM degree of freedom, with a conversion factor given by the *purely optical* transfer function of the interferometer. This spurious motion of DARM induced by the loop is not measurable in any way, since the error signal will be squeezed to zero by the high loop gain.

The word purely optical in the last paragraph is relevant in a radiation pressure dominated regime. Radiation pressure creates an optomechanical modification of the transfer function. Any force applied to the DARM degree of freedom creates a potential displacement of the same degree of freedom. This in turn modulates the field inside the arms and induces an additional force on DARM via radiation pressure. The net effect is a reduced real motion

| Configuration | Optical gain (G) | Requirements |
|--------------------|-------------------------|--------------|
| Power recycled 25W | $2.8 \cdot 10^{10} W/m$ | 0.08 mW |
| Dual recycled 25W | $7 \cdot 10^9 W/m$ | 0.07 mW |
| Dual recycled 125W | $1.5 \cdot 10^9 W/m$ | 0.08 mW |

Table 8.5: Requirement on spurious field transmission through the **OMC**, assuming a residual intensity noise of 2%.

of the degree of freedom. However, once the real displacement is properly computed, taking into account the depressing factor due to radiation pressure, the dark fringe power signal responds with a transfer function which depends only on the optics and corresponds to what one would get from computations which do not include radiation pressure.

The spurious DARM motion induced by a leakage field residual intensity noise is given by

$$\delta_{DARM} = \frac{P_s \text{RIN}_s}{G} \quad (8.8)$$

where G is the optical gain of dark fringe with respect to DARM; P_S is the total power of the leaking field and RIN_S is the corresponding residual intensity noise.

To properly control the DARM loop at the level of accuracy δz_{RMS} considered in the previous section, the contribution of spurious motion due to leaking field must be well below this level. If we ask this contribution to sum up to less than 10% of the needed accuracy, the limit on leaking field is given by:

$$P_S < \frac{1}{10} \cdot \frac{\delta z_{\text{RMS}} G}{\text{RIN}_S} \quad (8.9)$$

The resulting requirements on leaking power in transmission of the dark fringe are summarized in Tab. 8.5 as a function of the interferometer configuration.

8.3.6 Design and performances of the control systems

The detailed iterative procedure to design a control scheme compatible with both the accuracy requirements and the noise reintroduction requirements is described in [260]. In each different configuration and for each degree of freedom, the error signal with highest signal-to-(shot)noise ratio has been selected and the corresponding demodulation phase tuned, see Tab. 8.6.

To reduce the coupling of sensing noise to detector sensitivity below the safety factor, it was necessary to assume the implementation of noise subtraction paths [266] with performances of the order of a factor 500 of coupling reduction. This level is the one obtained in Virgo+ and it is considered feasible.

Moreover, during the control loop design it turned out that to achieve the desired accuracy it is necessary to properly diagonalize the sensing matrix. The precision needed for such diagonalization ranges from 10% in the power recycled case to fractions of 1% in the dual recycled case, which is a quite difficult performance to achieve. More investigations in this direction will be needed, in particular to assess the need of adaptive diagonalization of the

sensing matrix. Very simple matrix diagonalization servos were already implemented in Virgo at the time of the first commissioning runs.

The performances in terms of accuracy are listed in Tab. 8.6.

The level of control noise which is coupled to the detector sensitivity in the three configurations is shown in Fig. 8.3. The level of sensing noise is the one corresponding to shot noise limited sensitivity for 100 mW of total sensed power per auxiliary port. In all the configurations the MICH degree of freedom is the most critical and its control noise is at the limit of the factor 10 below design sensitivity.

The filter optimization is a balance between having high gain below 2-3 Hz to be able to reach the accuracy requirements and strong enough roll-off at higher frequencies (above 10 Hz) to avoid reintroducing control noise in the detector sensitivity. The stability of the control loop imposes some limits on the possible optimization. The present design is barely fulfilling the requirements with the minimum acceptable stability margins (30 degree of phase margin and less than a factor 2 of gain margin). Further optimizations of the present scheme are very difficult. Any increase of the sensing noise or of the payload motion would result in the longitudinal control being no more compliant with the design.

Another critical point is the implementation of the DARM loop in the dual recycled case. Indeed in this case the DARM opto-mechanical transfer function contains an unstable pole at some tens of Hz (the frequency is proportional to the input power). To stabilize the system it is therefore necessary to have a much larger bandwidth than in the Virgo+ case. The present design foresees a unity gain frequency of about 400 Hz, which is necessary to stabilize the system with suitable gain and phase margins and reach the required accuracy. The need of significantly increasing the bandwidth of the DARM loop has strong consequences on the design of the real time control system and of the payload. Indeed, the present design of the DARM loop is compatible with a total delay in the control chain of 50 μ s (assuming the phase margin must be larger than 30 degrees). This seems very difficult to achieve. On the payload design side, the structure that will hold the coils used to apply the control forces should not have structural resonances inside the active bandwidth of the loop, otherwise they could get too excited by the control itself. Having all structural resonances above 400 Hz seems very difficult. Both DAQ and PAY considerations triggered the need of a more deep study of the DARM control. It seems feasible to reduce the bandwidth to 200 Hz, even if a detailed design is not available yet. In this way the total delay requirement would be relaxed to 100 μ s and the resonance requirement to 200 Hz.

More details on the final control system design are available in the note [260].

8.3.7 Requirements on modulation and demodulation noises

The main gravitational channel is extracted using DC readout, therefore it is not affected by radiofrequency sideband noises, provided the OMC filtering is adequate. However all the signals used for the auxiliary degrees of freedom control are obtained with a standard demodulation technique. Therefore any phase or amplitude noise of the radiofrequency sidebands will pollute these signals.

The coupling of phase and amplitude noise can be modeled with good accuracy as a cross quadrature coupling [267]. If the Q quadrature of a signal is not perfectly zero, due to an

| Power recycled only at 25 W | | | |
|------------------------------------|---------------------|------------------------|-----------------------|
| D.O.F. | Error signal | Accuracy | Requirement |
| DARM | B1_DC | $5 \cdot 10^{-16}$ m | $6 \cdot 10^{-16}$ m |
| Frequency | B2_SB1_P | 0.6 mHz | 7 mHz |
| MICH | B4_SB1_Q | $1.3 \cdot 10^{-13}$ m | $2 \cdot 10^{-13}$ m |
| PRCL | B2_SB3_P | 2×10^{-12} m | 2×10^{-11} m |

| Dual recycled at 25 W | | | |
|------------------------------|---------------------|------------------------|-----------------------|
| DOF | Error signal | Accuracy | Requirement |
| DARM | B1_DC | $1.1 \cdot 10^{-15}$ m | $1 \cdot 10^{-15}$ m |
| Frequency | B2_SB3_P | 0.05 mHz | 7 mHz |
| MICH | B4_SB2_Q | $1.8 \cdot 10^{-12}$ m | $2 \cdot 10^{-12}$ m |
| PRCL | B2_SB1_P | 1×10^{-13} m | 2×10^{-11} m |
| SRCL | B4_SB2_P | 3×10^{-14} m | 2×10^{-12} m |

| Dual recycled at 125 W | | | |
|-------------------------------|---------------------|------------------------|-----------------------|
| DOF | Error signal | Accuracy | Requirement |
| DARM | B1_DC | $6 \cdot 10^{-16}$ m | $1 \cdot 10^{-15}$ m |
| Frequency | B2_SB3_P | 0.09 mHz | 7 mHz |
| MICH | B4_SB2_Q | $2.4 \cdot 10^{-14}$ m | $2 \cdot 10^{-12}$ m |
| PRCL | B2_SB1_P | 1×10^{-14} m | 2×10^{-11} m |
| SRCL | B4_SB2_P | 3×10^{-15} m | 2×10^{-12} m |

Table 8.6: Summary of error signals and obtained accuracies in: power recycled configuration at 25 W input power (top), dual recycled at 25 W (middle), dual recycled at 125 W (bottom).

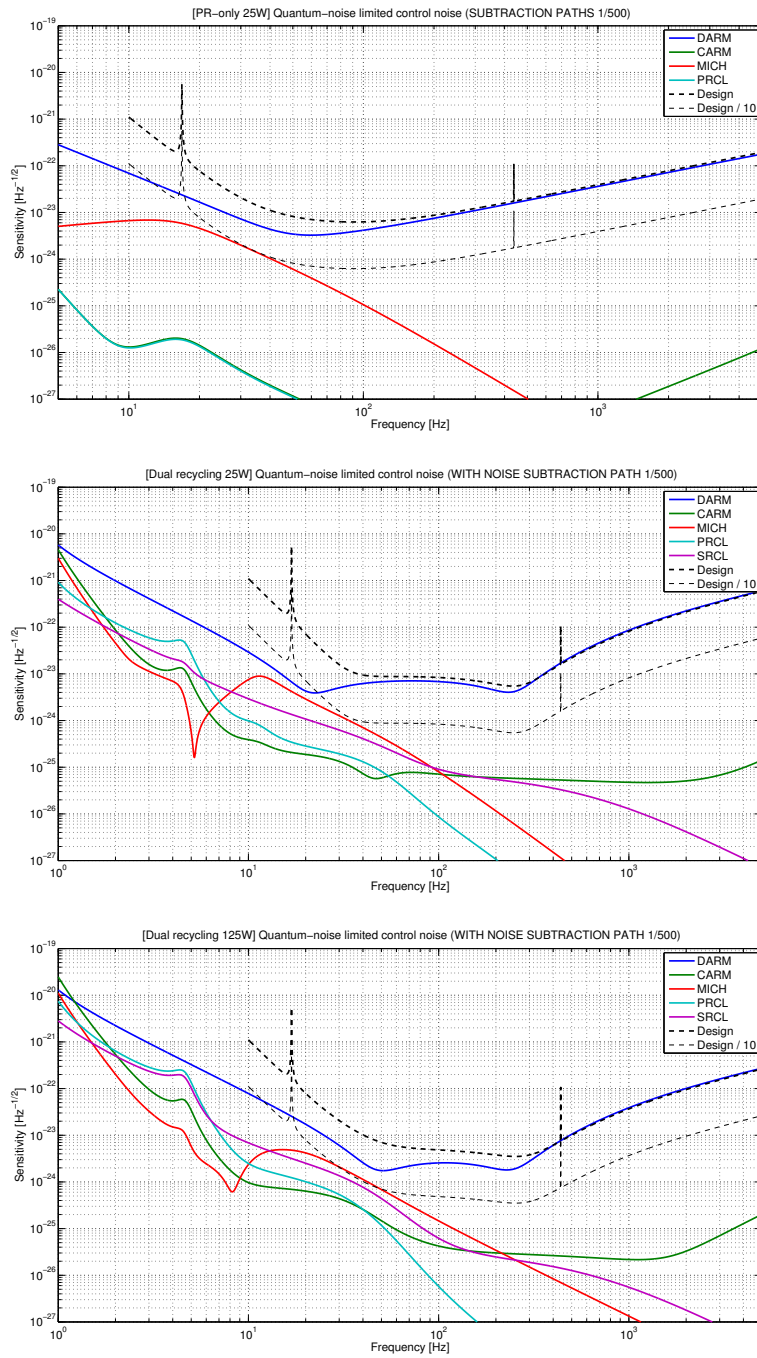


Figure 8.3: Sensing noise reintroduced in the detector sensitivity by longitudinal control loops in the three configurations: power recycled only with 25 W input power (top), dual recycled with 25 W input power (middle), dual recycled with 125 W input power (bottom).

| Frequency | Phase noise [rad/ $\sqrt{\text{Hz}}$] | Rel. ampl. noise [1/ $\sqrt{\text{Hz}}$] |
|-----------|--|---|
| 6.3 MHz | $1.8 \cdot 10^{-6}$ | $1.7 \cdot 10^{-7}$ |
| 56.4 MHz | $1.1 \cdot 10^{-6}$ | $1.1 \cdot 10^{-6}$ |
| 8.4 MHz | 0.27 | $1.7 \cdot 10^{-7}$ |

Table 8.7: Summary of requirements for sideband amplitude and phase noise. Modulation noises enters in the photodiode output signal following two paths. The first one is through the noise at the level of the modulation, which is transmitted to the laser beam and enters on one of the inputs of the mixer. The second path is through noise introduced by the local oscillator distribution system, which enters on the other input of the mixer. The requirements given here apply to the total of the two contributions.

offset or to residual RMS motion, it induces a coupling of phase noise to the P quadrature. A similar coupling exists for the sideband amplitude noise, this time coupling each quadrature with its own RMS motion. The two couplings can be described using the following equations:

$$\tilde{n}_P(f) = \delta Q_{\text{RMS}} \tilde{\phi}(f) \quad (8.10)$$

$$\tilde{n}_P(f) = \delta P_{\text{RMS}} \frac{\tilde{\delta A}(f)}{A} \quad (8.11)$$

where $\tilde{\phi}(f)$ is the spectrum of the phase noise measured in rad/ $\sqrt{\text{Hz}}$, $\frac{\tilde{\delta A}(f)}{A}$ is the residual amplitude noise of the sideband at the given frequency measured in 1/ $\sqrt{\text{Hz}}$, δP_{RMS} , and δQ_{RMS} are the residual motion or offset in the P or Q quadrature. Finally $\tilde{n}_P(f)$ is the resulting noise into the P quadrature. Similar equations hold for the other quadrature.

From the simulations described in the previous sections, the obtained loop accuracy can be translated in residual RMS signals in each port quadrature. Asking the sideband phase and amplitude noise to be a factor 10 below the shot noise, one can obtain requirements on the total modulation and demodulation noises at the mixer input. Results are summarized in Tab. 8.7, quoting only the most stringent requirement for each frequency, regardless of the interferometer configuration. Refer to the INJ chapter (sec. 4.6.4) for a comparison with the expected performances.

8.3.8 ITF asymmetries and coupling of laser noises

In order to assess requirements for power and frequency noises, Optickle was used to simulate the Advanced Virgo interferometer in two configurations: power recycled at 25 W and dual recycled at 125 W.

As well known, Optickle has some limitations, in particular it cannot deal with modes higher than the first order, so it cannot be used to evaluate the effect of geometrical asymmetries such as arm length and/or radius of curvature mismatch, and it cannot even handle figure error maps for the core optics. On the other hand, it is possible to include radiation pressure effects and mechanical transfer functions, that are important at low frequency. Simulations were then carried out in order to evaluate the effects of loss and finesse asymmetries on the coupling of laser power and frequency noises to the dark fringe and the impact on Advanced Virgo sensitivity. Although possible, no control loops were included in the simulation in order to speed up calculations.

8.3.8.1 Power recycled configuration at 25 W

Starting from a situation without any defect, finesse and loss asymmetries were introduced one at a time and together [268, 269]. Frequency noise requirements are reported in Fig. 8.4, both for the no defect case and for some values of finesse and loss asymmetries. Without SRC and without any defect, the requirements for frequency noise are much more relaxed with respect to the dual recycled configuration, but they worsen very quickly as soon as defects are introduced in the simulation. For this configuration loss asymmetry is the worst offender at high frequency, and finesse asymmetry at intermediate frequency.

The situation is more complicated for the power noise requirements (see Fig. 8.4), as for the coupling to the detector sensitivity also the sign of the asymmetries plays a role, but in general we have almost a factor 10 less coupling for power recycled only with respect to dual recycled.

8.3.8.2 Dual recycled configuration at 125 W

Starting from a situation without any defect, finesse and loss asymmetries were introduced one at a time and together [268, 269]. It turned out that loss asymmetry is the worst offender at high frequency (see top plots of Fig. 8.5 and 8.6), while finesse asymmetry plays more a role at intermediate frequency (see bottom plots of 8.5 and 8.6), for the coupling of laser power and frequency noises to DARM. One important thing to notice in those plots is that asymmetries are not symmetrical: the sign does play a role in shaping the coupling of laser noises to DARM, depending on the sign set to the DARM offset, and this could make choosing the sign of this offset a bit tricky, as a situation could occur where the signs of asymmetries require contradictory optimizations with respect to DARM offset sign. Based on those simulations, requirements on input technical noises are drawn considering several combinations of signs for the aforementioned asymmetries (see Fig.8.7, and files attached to [269]).

Triggered by a proposal put forward by the DET subsystem [270], frequency and power noise couplings are also recomputed with an increased offset on the DARM degree of freedom. The aim was to check whether doubling the offset would have had a negative impact on those noise couplings, but as far as only finesse and loss asymmetries are concerned (no other defects introduced in the simulation), there are no dramatic changes in frequency and power noise couplings to sensitivity.

8.3.9 Second stage of frequency stabilization

The Second Stage of Frequency Stabilization (**SSFS**) is used to lock the laser frequency to the arm cavity mean length. It is necessary to meet the requirement on residual frequency noise detailed in sec. 8.3.8. The control architecture is the same as in the Virgo+ case: the correction computed by the **SSFS** controller is added to the error signal of the laser frequency pre stabilization and simultaneously used for the lock of the input mode cleaner [271]. The error signal which will be used is always extracted from the interferometer reflection, demodulated at f_1 or f_3 depending on the optical configuration.

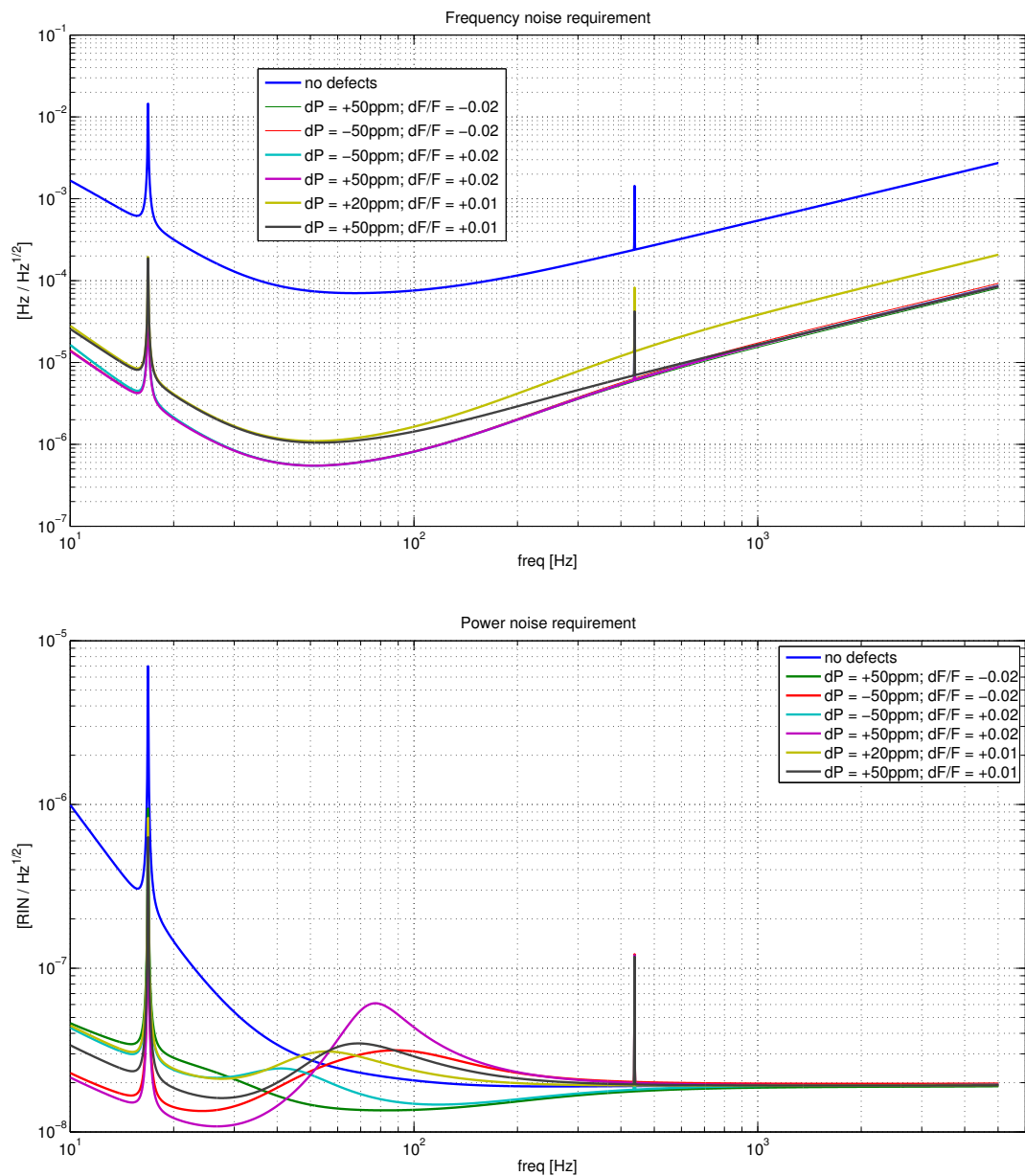


Figure 8.4: Laser and frequency noise requirements for power recycled 25 W configuration; a safety factor of ten has been used to draw the requirements from nominal sensitivity. Different values of finesse and loss asymmetries have been used. Top: laser frequency noise at interferometer input. Bottom: laser intensity noise at interferometer input.

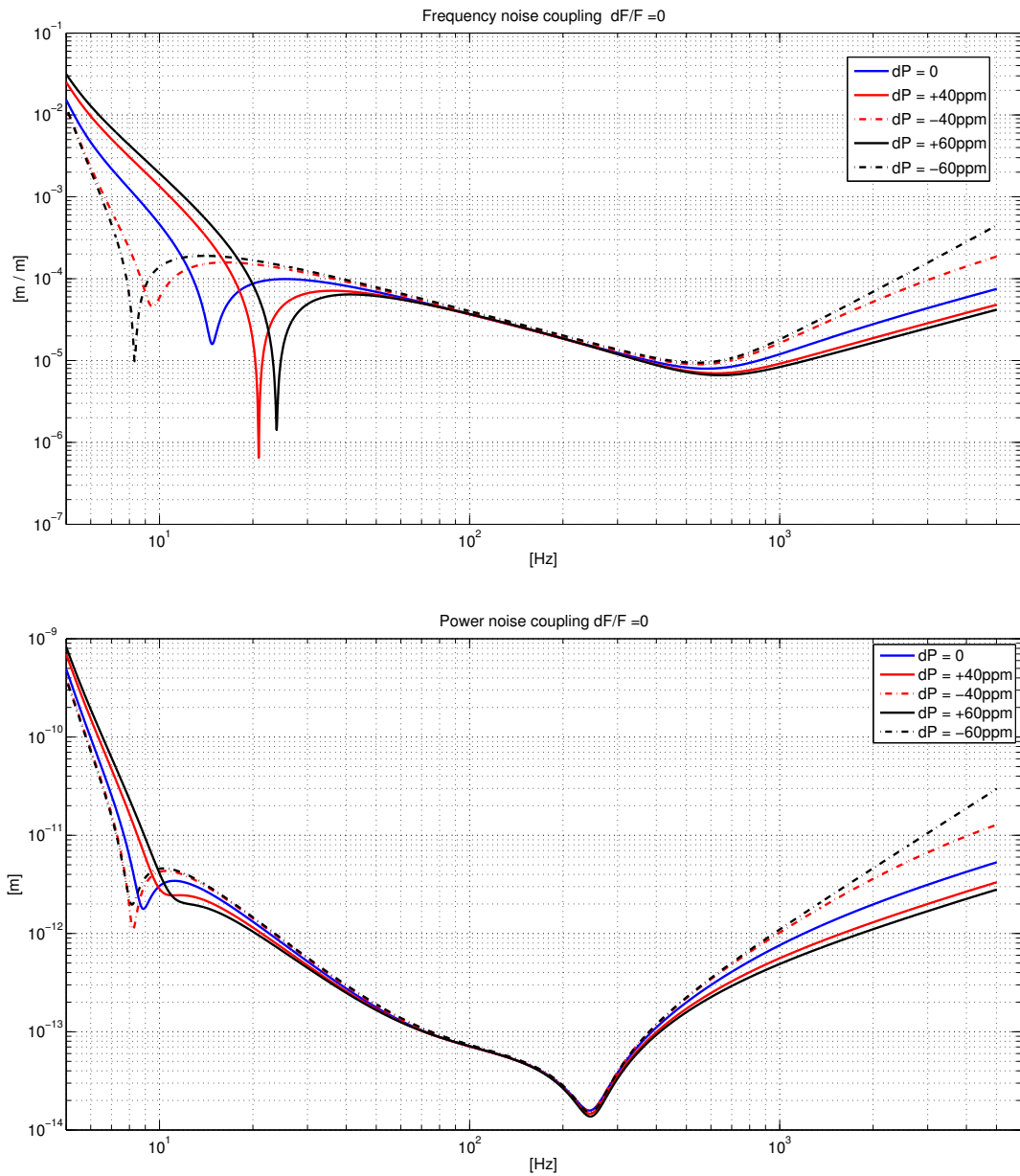


Figure 8.5: Dual recycled full power configuration. Transfer functions in case of equal finesse ($F = 443$) as a function of round trip loss asymmetry. Average round trip losses are 75 ppm. Top: frequency noise transfer function. Bottom: power noise transfer function.

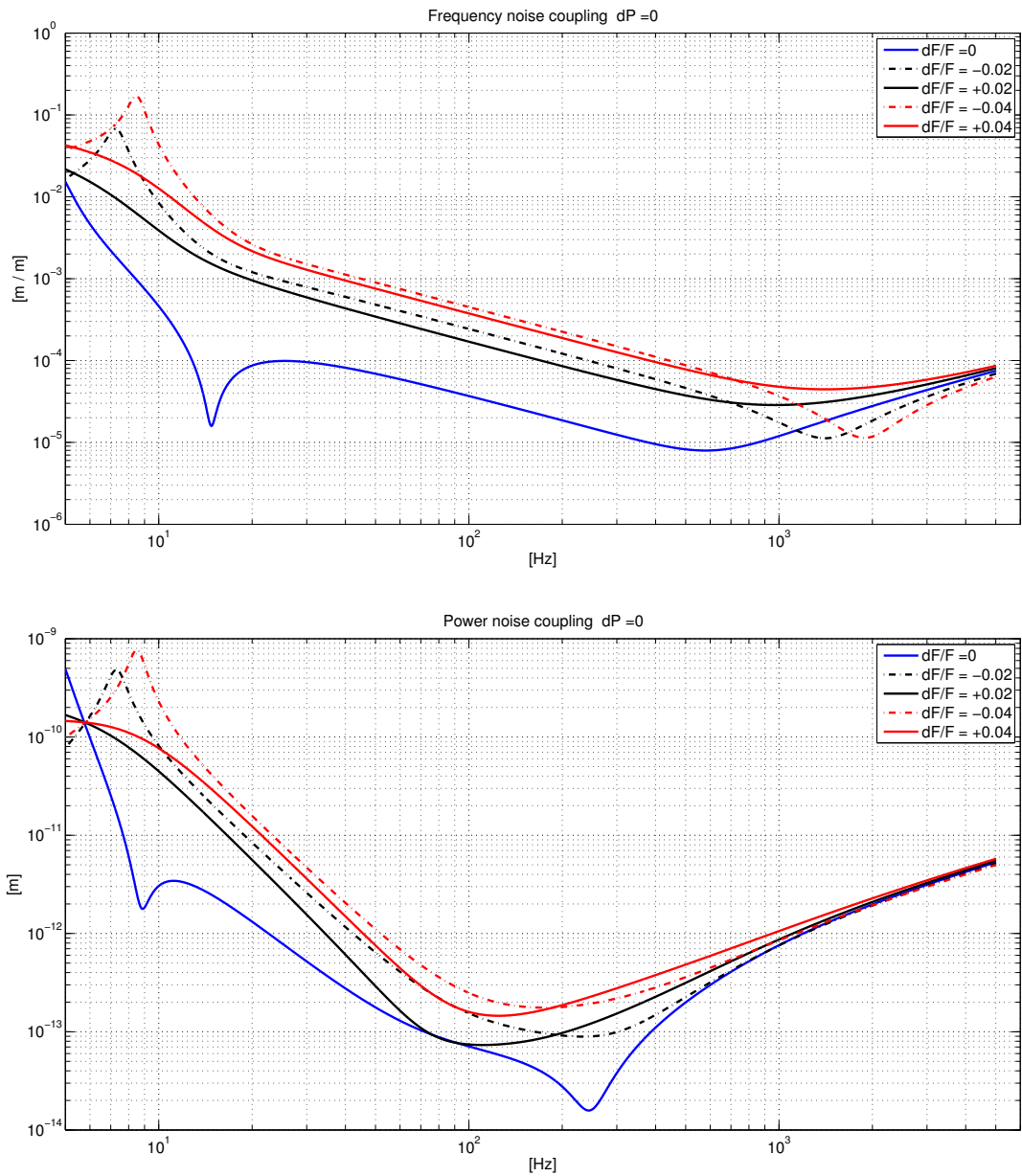


Figure 8.6: Dual recycled full power configuration. Transfer functions in case of equal round trip losses (RTL = 75 ppm) as a function of finesse asymmetry. Average finesse is 443. Top: frequency noise transfer function. Bottom: power noise transfer function.

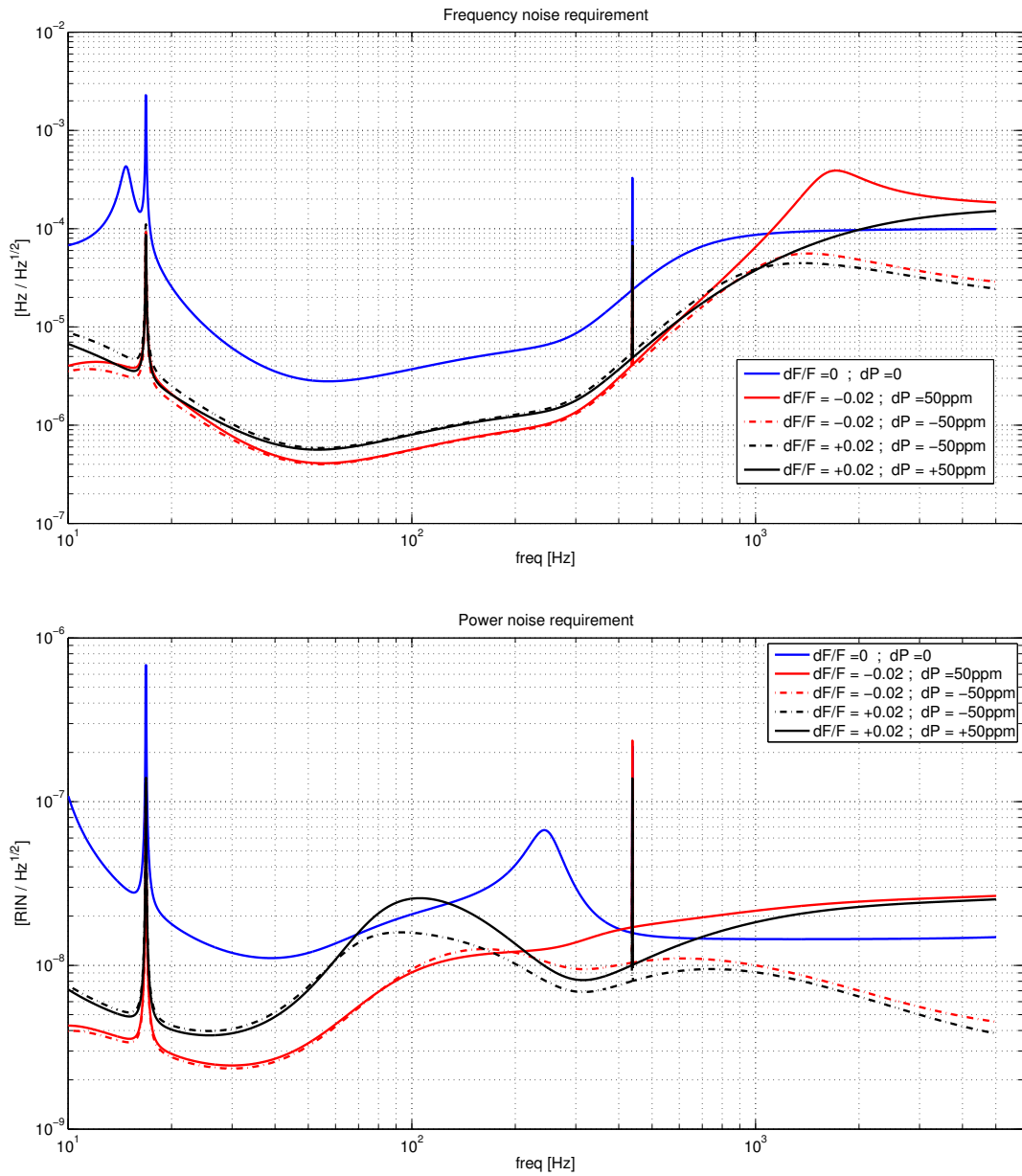


Figure 8.7: Dual recycled full power configuration, frequency and power noise requirements with a safety factor of ten used to draw the requirements from nominal sensitivity. Different values of finesse and loss asymmetries are used. Top: laser frequency noise at interferometer input. Bottom: laser intensity noise at the interferometer input. Blue curve: no defects. Red curves: $dF/F = -2\%$; black curves: $dF/F = +2\%$. Solid curves: $dP = +50$ ppm, dashed curves: $dP = -50$ ppm.

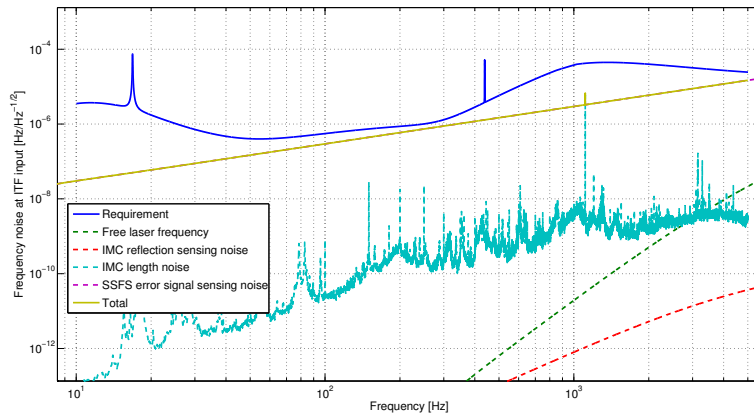


Figure 8.8: Contribution of different noise sources to stabilized laser frequency at the interferometer input, in the dual recycled configuration at full input power (125 W).

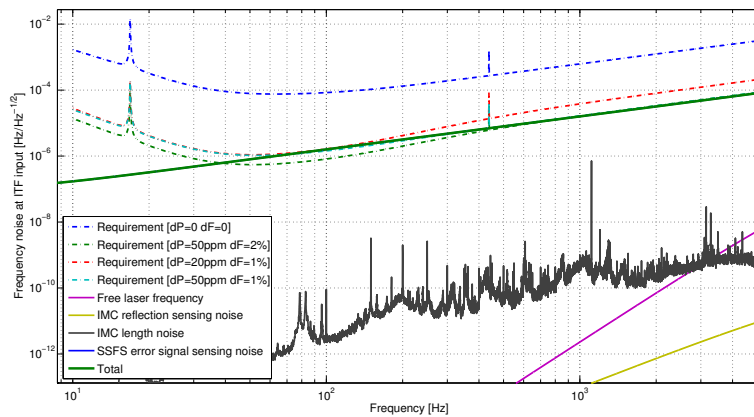


Figure 8.9: Contribution of different noise sources to stabilized laser frequency at the interferometer input, in the power recycled configuration at 25 W input power.

The unity gain frequency of the **SSFS** loop is expected to be at about 20-30 kHz, the upper limit set by the arm cavity free spectral range notch. Controllers with such a high bandwidth are easily built using analog electronics, as done in Virgo+. However it is known that the shape of the interferometer optical transfer function between 3 and 50 kHz depends strongly on sidebands aberrations. The possibility of using an ad hoc digital control system with high sampling rate is being investigated. This would provide the needed flexibility to cope with changes in the optical transfer functions, without the need of rebuilding the analog electronics every time the interferometer behavior changes.

A detailed design of all the paths involved in the full frequency stabilization system has been done [272] and the performances compared with the requirements of sec. 8.3.8. When the laser frequency is stabilized on the interferometer reflection, the limiting factor in the performance is, as expected, the shot noise of the **SSFS** error signal. In the dual recycled case the level of frequency stability meets the requirements even in presence of relatively large interferometer asymmetries (50 ppm of losses asymmetry and 2% of finesse asymmetry), see Fig. 8.8. The power recycled case is instead more critical, see Fig. 8.9: loss asymmetries must remain below 20 ppm and finesse asymmetry below 1% to be able to meet the requirements.

8.3.10 Input mirror etalon tuning

As explained in the previous section, in the power recycled case it is necessary to maintain the finesse asymmetry below 1% in order to meet the requirement on frequency noise coupling to the detector sensitivity. During Virgo commissioning the ability to minimize the coupling of common noises at low frequency has been extensively used and proved crucial to reach good detector sensitivity. The noise sources that coupled proportionally to the finesse asymmetry were only partially identified (frequency noise, limited by the sensor shot noise, and input beam jitter). There remained several noises whose source was not identified, since it was possible to largely reduce their coupling to the detector sensitivity by fine tuning the finesse of the two arms.

For these reasons it is proposed to implement input mirrors with parallel faces, in order to be able to fine tune the finesse asymmetry in a continuous way during the interferometer operations. The plan for Advanced Virgo would be to stabilize the input mirror temperature with slow servo systems. They will use heaters attached to the vacuum towers which will then act as a thermal bath for the input mirrors. This technique has already been tested successfully in Virgo. The needed range of finesse change is under study and will be decided as soon as more detailed simulations will be available.

8.4 Longitudinal control system: lock acquisition

The Advanced Virgo lock acquisition can be divided in mainly three almost decoupled parts. The first is the lock acquisition of the arm cavities, as standalone configuration or as the first step of the full interferometer lock. The second part is the lock acquisition of the interferometer in power recycled configuration. Finally the last part is the lock acquisition of the full dual recycled interferometer.

8.4.1 Lock acquisition of the arm cavities

One of the main differences of Advanced Virgo with respect to Virgo+ is the increase of the finesse of the arm cavities from around 150 to 443. As a result of this, the maximum velocity of the mirrors below which the lock can be acquired will be much lower. This will increase the time needed to lock the cavities or might even make it impossible to lock. One strategy which was tested many years ago at LIGO and TAMA is to first measure the velocity once the cavity sweeps through a resonance and then apply a long rectangular pulse to bring it back to resonance with reduced velocity. Once the velocity is reduced enough, the cavity can be locked with a standard linear feedback loop.

Such strategies have been tested experimentally just before the shutdown of Virgo+ with good results. It was even possible to lock the cavities with a force that was 160 times lower than the maximum available force, see Fig. 8.10. One important observation was that to keep the cavity locked with low force for more than a few seconds, it is necessary to immediately reallocate the low frequency part of the correction to the marionette actuators.

Similar tests were done in simulation using the optical parameters of Advanced Virgo, see Fig. 8.11. They show that the scheme should still work for the optical properties of the future cavities. Still missing from the simulation are an accurate representation of the mechanics and the noise in the detection process. The exact noise level that can be tolerated has still to be determined.

These results indicate that, even with the increase in finesse, the strength of the magnets glued to the mirrors might be reduced somewhat. This is very desirable for reducing the coupling of environmental magnetic noise and for simplifying the design of the payload. How much the magnets can be reduced can only be decided once the design of the new payload is known. More details are given in a separate Virgo note [273].

8.4.2 Lock acquisition in power recycled configuration

In this section the lock acquisition technique proposed for Advanced Virgo in the power recycled configuration is shortly described. It is very similar to the one used in Virgo+ during the last Virgo Science Run (VSR4), which is called the *variable finesse* technique [274].

Arm cavity lock. In order to decrease thermal effects, the idea is to start the lock procedure with low input power and to increase it once the interferometer is steadily locked. The initial state of the uncontrolled interferometer is with all the mirrors roughly aligned except the Power Recycling Mirror (PR), which is misaligned so that its reflection does not return towards the beamsplitter to form a cavity. At the beginning of the lock procedure the two arm cavities are independently locked using the in-phase demodulated signals in transmission with a standard Pound-Drever-Hall (PDH) technique, which are normalized by the powers transmitted by the cavities in order to increase the linear range of the error signals.

The lock of the cavities is obtained by applying small forces to the mirror, with the coils assembled on the cage connected to the filter 7 of the superattenuator. When the lock is reached, the longitudinal correction applied to end and input mirrors is reallocated to the marionette actuators, as described in sec. 8.4.1. Due to the very different amount of

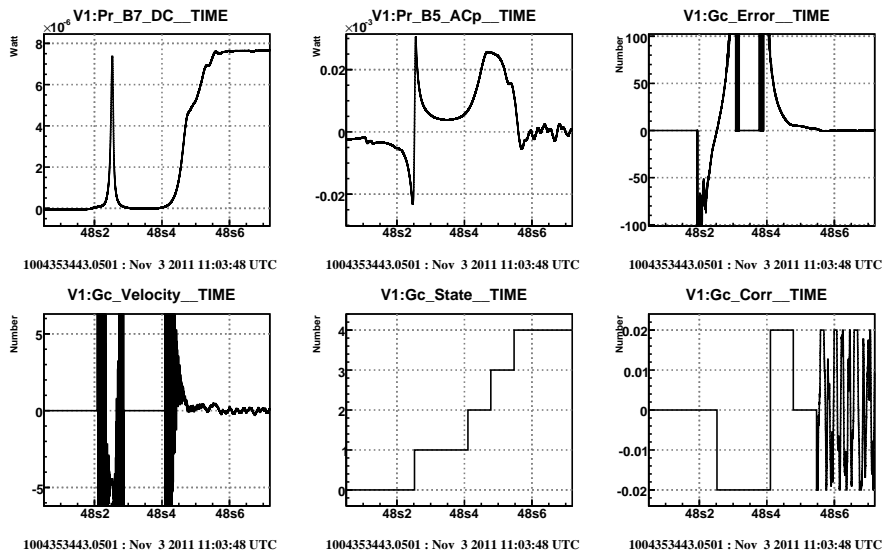


Figure 8.10: Experimental demonstration using Virgo+ of a lock with reduced force implemented in **Gc**. The reflection error signal is normalized with the power transmitted by the cavity. The velocity is estimated as the derivative of the error signal. Two pulses with opposite sign are applied. The lengths of the two pulses are calculated to bring the mirror back at resonance with velocity zero and are proportional to the velocity measured while crossing the resonance. The logic is implemented as a state machine (0 = wait for resonance, 1 = first pulse, 2 = second pulse, 3 = wait for return to resonance, 4 = linear lock). The lock was acquired with a maximum correction of 0.02 Volt on 1 coil pair, while a maximum of 0.8 Volt on 4 coil pairs is available.

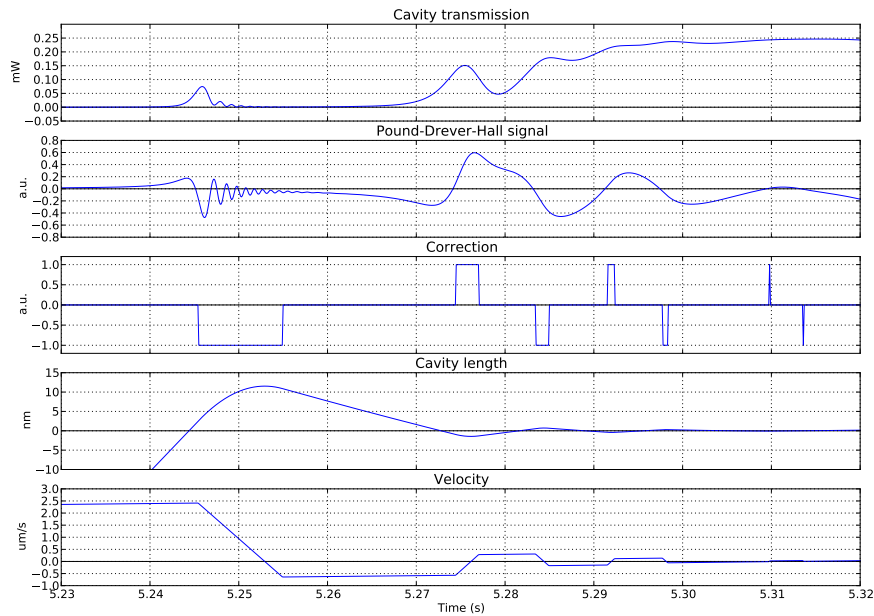


Figure 8.11: Lock acquisition of an Advanced Virgo arm cavity, as simulated with e2e. Note that the cavity length and velocity are properties that are only available in simulation and cannot be observed directly in reality. They are normally estimated, as described in the caption of Fig. 8.10, as the derivative of the error signal on resonance crossing.

power during the lock procedure, two different photodiodes could be needed to detect the transmitted light by the end mirrors: one for low power at the beginning of the procedure and the other for high power in steady state.

Half fringe lock. At the dark port, the resonance condition is initially chosen to be at half fringe (half of the maximum possible power is transmitted), which is outside the linear range of the demodulated signal. A method using the DC powers is therefore used to lock the MICH degree of freedom: the ratio of the power transmitted to the dark port over the power impinging on the arm cavities (read with the PR pickoff beam) gives an estimation of the Michelson fringe value. The fringe offset is set to 0.5 at the beginning, which is a standard side of fringe locking of a Michelson interferometer and does not depend on any optical parameter of the cavities. The lock acquisition of the MICH loop is thus virtually identical to the one used for initial Virgo.

Frequency stabilization. After these first steps, in Virgo and Virgo+ the control strategy of the two arms is modified. The **SSFS**, which keeps the laser frequency locked to the mean length of the arms below some tens of kHz (see 8.3.9 and [272]) is engaged. The control of DARM is made by exploiting an error signal given by the transmission of one of the two cavities. The CARM control is instead implemented using an error signal from the Reference Cavity (**RFC**) reflection with about 1 Hz of bandwidth: in this way the low frequency residual motion of the end mirror and of the laser frequency are reduced to a suitable value (see also sec. 8.3.4 for CARM accuracy requirements).

In the Advanced Virgo case the error signal foreseen for the **SSFS** comes from the interfer-

| | Misaligned PR | Aligned PR | Science Mode |
|-----------------|----------------------|----------------------|----------------------|
| MICH Offset [m] | $1.33 \cdot 10^{-7}$ | $1.33 \cdot 10^{-7}$ | $1.60 \cdot 10^{-9}$ |
| B1p [W] | $2.45 \cdot 10^{-2}$ | $2.41 \cdot 10^{-1}$ | $8.34 \cdot 10^{-3}$ |
| B2 [W] | $1.22 \cdot 10^{-3}$ | $7.48 \cdot 10^{-1}$ | $1.61 \cdot 10^{-1}$ |
| B4 [W] | $1.50 \cdot 10^{-5}$ | $1.48 \cdot 10^{-4}$ | $1.14 \cdot 10^{-2}$ |
| B7 [W] | $6.91 \cdot 10^{-6}$ | $6.82 \cdot 10^{-5}$ | $5.28 \cdot 10^{-3}$ |
| Arm power [W] | 6.91 | $6.82 \cdot 10^1$ | $5.28 \cdot 10^3$ |

Table 8.8: DC powers at various output ports during the lock acquisition, for 1 Watt of input power. Arm cavities are always locked. Note that in the real interferometer the B1p power will depend strongly on contrast defect and higher order mode contents.

ometer reflection (see sec. 8.3.6) and it is not available before the PR is aligned. It might be necessary therefore to modify the described strategy: the SSFS could be engaged after the realignment of the PR (this was done in Virgo at the time of the first commissioning runs) or it could use a different error signal for the lock acquisition (like B4 as done in Virgo and Virgo+) and switch to the final signal later.

PR realignment. At this point of the lock acquisition, the PR is realigned. During this transition the circulating power inside the interferometer increases by a large amount. Therefore all the signals are subjected to a large change in their optical gain, which is compensated by the use of suitable normalization. At the same time the longitudinal control of the PR is engaged using an error signal normalized by the value of the power inside the recycling cavity. Note that the finesse of the recycling cavity is in this configuration dominated by the loss of the short Michelson interferometer at half fringe. The lock acquisition of the PRCL loop should thus be virtually identical to the one used in Virgo and Virgo+. This is the first condition of the interferometer with all mirrors aligned and all longitudinal degrees of freedom controlled.

MICH offset reduction. The locking point of the MICH loop is finally moved in several steps towards its final value, which is close to the dark fringe, see sec. 8.3.3. During this transition the power in the cavities increases by about a factor 100 and gains of the lock loops have to be changed accordingly. An analysis of the different conditions during the lock acquisition procedure has been carried out using the simulation tool e2e [257]. Tab. 8.8 shows the calculated values for the DC power at various output ports during the lock acquisition for 1 W of input power. The large excursion of the power impinging on the diodes might require the use of switchable sets of electronic gain.

Reaching dark fringe. The DARM loop control is then switched to a demodulated signal coming from the beam extracted before the OMC (B1p). The automatic alignment for the all degrees of freedom is engaged.

OMC and low noise configuration. The procedure that brings the OMC to resonance is then started and the DARM loop control is finally switched to the DC readout signal in transmission of the OMC (B1). At this point the interferometer is locked in a robust configuration and the operating point is very close to the final one. When the interferometer is in a steady condition, the input power is increased to the final value. When all the thermal effects connected to the increase of the input power are stabilized, the control filters of all the longitudinal and angular degrees of freedom are optimized in order to reduce control

noise below the requirements. All the actions performed at the end of the lock acquisition procedure are focused to improve as much as possible the sensitivity of the detector (for example engaging of noise subtraction paths, etc.).

As explained in sec. 8.3.3, we do not expect large effects due to radiation pressure in the power recycled configuration, provided that the idea of putting the DC readout offset on MICH is feasible as shown in simulations.

8.4.3 Lock acquisition in dual recycled configuration

So far the lock acquisition of Advanced Virgo in the dual recycled configuration has not been studied yet. One possible solution would be to follow the strategy employed by LIGO, which is briefly explained here. The idea is to first lock the arm cavities using an auxiliary laser, with a technique similar to the one described in the next section 8.5. After this, the lock is transferred to the main laser, using an error signal calculated from the DC signals in transmission of the cavities. A very large offset is applied to the CARM degree of freedom, so that the cavities are almost out of fringe. In this condition, the PRCL and SRCL degrees of freedom are locked. Finally, the offset is adiabatically removed. During this transition, the opto-mechanical resonance of the interferometer shifts in frequency, causing large changes in the optical transfer functions. It appeared that the signals of the central interferometer demodulated at 3 times the modulation frequencies are more robust during this transition, since they depend more on the resonance condition of the sidebands, than on the carrier that resonates in the arm cavities [261].

An alternative method might be to extend the current *variable finesse* technique to the lock of the SRCL degree of freedom. The idea would be to first lock the two arm cavities with both the PR and SR misaligned, lock MICH at half fringe and then align both mirrors one at a time. Finally, the offset of MICH would be adiabatically moved towards the dark fringe.

The lock acquisition strategy for the dual recycled interferometer is at this stage not a high priority task, since it is expected that during the first commissioning phases the Advanced Virgo detector will run in power recycled configuration. Nevertheless the study of the lock acquisition in dual recycled configuration will start in the next months and first results are expected at the beginning of the next year.

8.5 Auxiliary lasers

8.5.1 Goals of the auxiliary lasers

The use of auxiliary lasers was first proposed to lock the initially foreseen very high finesse (first 1200, then 900) arm cavities in the Advanced Virgo design. The idea is to use an auxiliary laser at a wavelength far from 1064 nm so that the finesse seen by it can be chosen independently of the one seen by the main laser. A low finesse (typically lower than 10) makes the lock of the cavity easy and allows to control its length down to a nm precision. It is then sufficient to change the working point of the lock (or the frequency of the laser) to be able to cross a resonance of the main laser and then switch to the latter one for the full control.

With the current finesse for Advanced Virgo (443), it has been shown that even if we reduce the actuator maximum forces by a factor 5 (with respect to Virgo+ during the lock acquisition) we can still lock the long arm cavities with the main laser [275] using a Virgo-like technique. Therefore, as explained in sec. 8.4.2, the lock acquisition strategy in the power recycled configuration will be very similar to the Virgo one and there will be no need of auxiliary lasers.

However we will still face the problem to lock the interferometer with the presence of the signal recycling mirror, which will increase the complexity to acquire the lock. As explained in the previous section, the lock acquisition will be facilitated if we can have the long cavities frozen but off resonance from the main laser. This could be done with an auxiliary laser as long as we can control the long cavities without getting the main laser resonating in the arms during the five minutes planned for the lock acquisition of the central interferometer.

Therefore the design and integration of the auxiliary laser system in Advanced Virgo can be broken down in two steps. The interferometer must be designed in order to be compatible with the system as explained in the next sections, but choosing the correct mirror coating and foreseeing the room of optical benches. If needed and useful, the actual installation could take place only in a second time, when Advanced Virgo will move from power recycled to dual recycled operations.

8.5.2 Implementation and requirements

The present plan is to inject two independent auxiliary lasers from the end station benches. The optical tables will be placed close to the minitowers and on the same concrete slabs. Depending on the telescope design, the optical table may be shared with the Hartmann beam. The different optics on this table will be used to control the beam position and to adapt it to the end arm telescope.

The choice of wavelength is driven mainly by the mirror reflectivity we can have without changing the one planned for the 1064 nm, to obtain a low finesse cavity, see Fig. 8.12. The Nd-YaG solid state laser at 1319 nm seems to satisfy the different requirements and gives a low free running frequency noise.

If we want to lock the cavity on the auxiliary laser, a frequency stabilization loop will however be needed. This could be achieved by using a reference cavity on the optical table like the one used on the injection bench. The requirements also need to take into account that we do not want to cross a 1064 nm resonance during 5 minutes while we are locked on the auxiliary laser. Some simulations were performed to assess the frequency stability for the auxiliary laser using a simple Fabry-Perot cavity in Siesta. The frequency noise spectrum is the one from Virgo given in Fig. 23 of [276] for 1064 nm. The same spectrum has been used for the auxiliary laser. To this noise we also added a long thermal drift (30 Hz/s) as reported in [271]. This preliminary work showed that even by multiplying the frequency noise of the auxiliary laser by more than a factor 10 the goal can still be achieved.

We think we can use two lasers with the same wavelength for the two arms and select a different polarization for each of them. Then a polarizer will be needed for all photodiodes used in the system. The design of the optical table is currently under study. The system will be a standard one with laser and optics to select the polarization, a pickoff towards

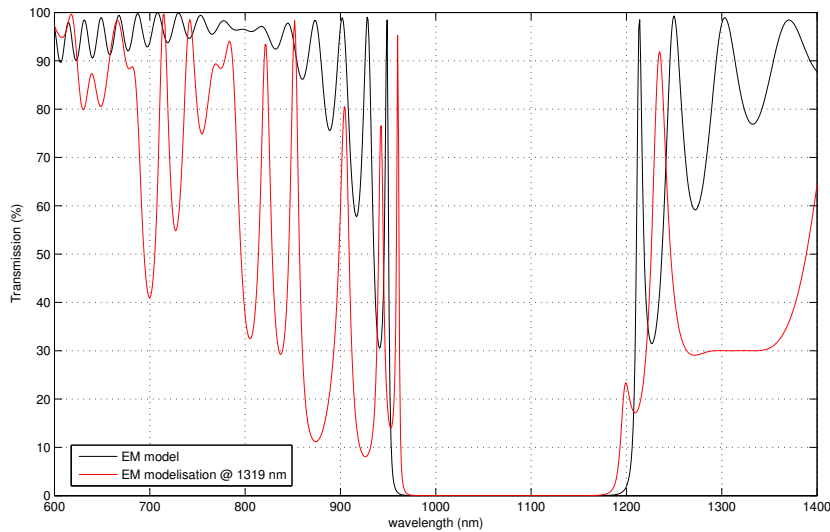


Figure 8.12: Advanced Virgo end mirror transmission model depending on the wavelength. Two models are presented: the current one (black curve) and a possible modification to provide low finesse at 1319 nm. The optimization has been done by LMA to keep the same transmission at 1064 nm and to avoid too many layers on the coating. The new coating has been studied to reduce at maximum the number of layers: between the two designs the width of the coating will be changed by 300 nm (on a total of 7 μm). The impact on thermal noise is expected to be negligible.

the reference cavity, an Electro-Optical Modulator (**EOM**), a telescope to match the beam to the end arm detection table, and some motorized optics for alignment. We will use a set of photodiodes to control the lasers (power and frequency) and the long cavity by using the reflected beam. We will also control the position and alignment of the beam with some quadrant photodiodes. The loops to control the laser will be done locally. The control of the cavity will be performed directly in the locking algorithm of the global control system.

When the lock acquisition procedure will be completed, we will switch off the auxiliary lasers to avoid any perturbation to the detector in science mode.

The auxiliary lasers will not be needed before the installation of the **SR** and so their installation can be delayed up to that time. The different interactions with the MIR, DAQ and DET subsystems have been defined and taken into account in their design. The installation could be done in two steps. We could start to construct the in-air optical table independently and characterize the beam and the different optical elements. This phase may be done in LAL before bringing the elements to the site. Otherwise we could start the installation in the end arm station. Finally we will need to have access to the long cavities to align the beam correctly for at least one month per arm.

Most of the requirements and techniques will be tested on the CALVA platform under commissioning in the LAL laboratory.

8.6 Sideband aberration risk reduction strategy

Simulations of thermal effects and mirror surface and substrate defects in the power recycling cavity showed a large sensitivity of radiofrequency sidebands. Very large aberrations can degrade significantly the quality of the longitudinal error signals. The thermal compensation system is designed to be able to measure and compensate these effects. However it is important, at least in the first stages of commissioning, to have a strategy to robustly control the interferometer even in presence of strong sideband aberrations.

Modal and FFT simulations show that the sideband sensitivity to **PRC** defects depends on their recycling gain. The larger it is the more sensitive the sidebands are to defects [262]. For this reason an additional modulation frequency of 21 times the first one $f_4 = 131.686317$ MHz will be used. The corresponding sideband will have a recycling gain of a few units, and it will be weakly sensitive to **PRC** defects.

Signals from this additional modulation frequency will be needed at all central part ports and they will be used to control the interferometer in the first steps of commissioning of the thermal compensation system. The modulation depth could be smaller than the one of the main modulation and the photodiode requirements in terms of demodulation noise and efficiency could be relaxed, since these signals will be used during the lock acquisition stage when noise performances are not critical.

8.7 Angular control system

8.7.1 Introduction

In order to ensure long data taking periods the interferometer has to be kept on the chosen working point; this means, among other things, that the core mirrors have to be aligned with respect to the beam. So a global angular control system or Automatic Alignment (**AA**) system has to be implemented.

The main differences between the Advanced Virgo and the Virgo interferometer configurations are the higher circulating power and the presence of the signal recycling cavity. These modifications produce an improvement in the interferometer sensitivity, but an increase of complexity for the development of the **AA** control system:

High circulating power: the high amount of laser power produces strong radiation pressure effects, as it will be detailed in sec. 8.7.2, which modify the mechanical transfer functions of the angular degrees of freedom.

Presence of the signal recycling cavity: it adds to the number of degrees of freedom to control and further increases the off-diagonal couplings in the **AA** error signals.

The **AA** control system has been fully designed in the three configurations already described in the introduction: power recycled only at 25 W, dual recycled at 25 W and 125 W.

The design consisted in the definition of accuracy requirements (the maximum allowable misalignments which do not affect the interferometer performances) and the development of the sensing and control scheme, including the evaluation of control noises.

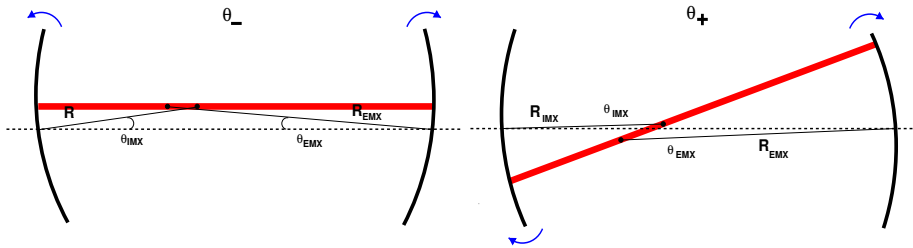


Figure 8.13: Effect of radiation pressure in a Fabry-Perot cavity. The two mirror modes become connected by an optical spring. The Fabry-Perot cavity misalignments can be described using the (+) *plus* and (-) *minus* modes. The combinations of single mirror misalignments giving the two modes depend on the cavity geometry.

This analysis has been carried out using the simulation tools *Finesse* [255] and *Optickle* [256].

Finally requirements for other subsystems are given: quadrant photodiodes specifications (quantity, demodulation frequencies etc.) and suspension requirements for the terminal detection benches.

8.7.2 Radiation pressure effect and angular modes

In a high power interferometer radiation pressure plays an important role. The laser beam acts on the mirror with a force proportional to the power. The effect is largest in the arm cavities, since there the highest amount of laser power is stored, but it must also be evaluated for the central interferometer mirrors.

It is possible to analytically compute the radiation pressure modes using the system energy equations, based on the Sides-Sigg small angle propagation [277]. On the other hand the effects can be simulated numerically using *Optickle*. The eigenvectors of the system are the (+)-mode (the eigenfrequency increases depending on the cavity g parameters and on the radiation pressure, making the mode stiffer), and the (-)-mode (the eigenfrequency decreases making the system softer). The resonant frequency for the (+)-mode increases as the square root of the input power reaching approximately 3.5 Hz at full input power (125 W). The lower eigenfrequency, the (-)-mode, decreases smoothly to 1.1 Hz, remaining stable.

The central interferometer angular degrees of freedom are not significantly affected by radiation pressure due to the low amount of power impinging on the mirrors, see [278].

The single arm cavity angular motions will be described using the physical (+) and (-) modes base. When the entire interferometer is considered, the physical angular degrees of freedom are combinations of the central interferometer and arm cavity mirror misalignments:

- **Central interferometer degrees of freedom**
 - **PR** power recycling mirror
 - **SR** signal recycling mirror
 - Beam Splitter (**BS**), beam splitter mirror

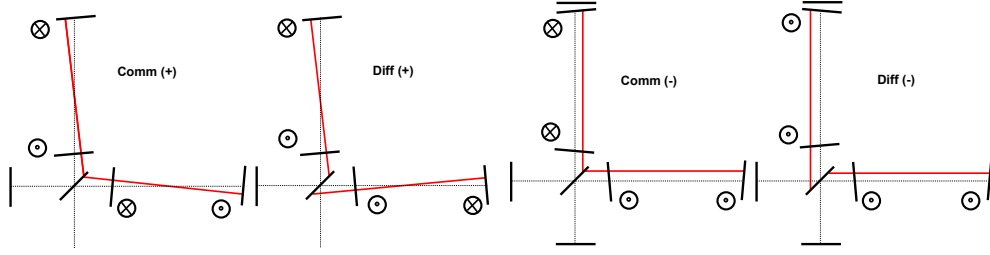


Figure 8.14: Graphical description of the physical modes for the Advanced Virgo interferometer in the yaw direction. Considering the direction of rotation referred to the front side of the optical component defined by the high-reflective coating.

- **Long arm degrees of freedom**

- $\text{Comm}(+) = \frac{(-\alpha \text{ NI} + \beta \text{ NE}) \pm (\alpha \text{ WI} - \beta \text{ WE})}{2}$
- $\text{Comm}(-) = \frac{(\beta \text{ NI} + \alpha \text{ NE}) \pm (-\beta \text{ WI} - \alpha \text{ WE})}{2}$
- $\text{Diff}(+) = \frac{(\alpha \text{ NI} - \beta \text{ NE}) \pm (\alpha \text{ WI} - \beta \text{ WE})}{2}$
- $\text{Diff}(-) = \frac{(\beta \text{ NI} + \alpha \text{ NE}) \pm (\beta \text{ WI} + \alpha \text{ WE})}{2}$

where $\alpha=0.6470$ and $\beta=0.7625$ depend on the cavity geometry, and the \pm are for the yaw (θ_y) and pitch (θ_x) directions respectively, the change of sign is due to the reversing reflection of the beam splitter mirror. Figure 8.14 shows a scheme of these degrees of freedom for the yaw direction.

8.7.3 Accuracy requirements

The angular accuracy requirements for the Advanced Virgo mirrors have been evaluated for the arm cavity mirrors, the **SR** and the **PR** [279]. Since the mirror radii of curvature are of the order of one km the vertical and horizontal mirror displacement requirements are very easily fulfilled.

The RMS accuracy requirements of the cavity mirrors alignment are set in order to have acceptable fluctuations of the carrier and the sidebands power in the cavities, smaller than 10^{-3} relative [280, 281]. For the **SR** the requirements have to be set such as to avoid sensitivity variations by more than a factor 10^{-2} in the whole detection frequency band. Results are given in Tab. 8.9. These requirements are achievable with present Virgo alignment techniques. For example, since the first science run (VSR1) the differential-end pitch and yaw degrees of freedom were controlled with a few nrad of accuracy [282, 283]. Moreover the relatively loose requirement on the **SR** alignment accuracy allows a low bandwidth control (i.e. the Virgo *Drift Control* [283] with tens of mHz of bandwidth and typical accuracy of 100 nrad), which is simpler to implement even with a significantly non-diagonal sensing matrix.

The choice of a factor 10^{-3} for the maximum tolerable power fluctuations is an estimate based on the consideration that in Virgo+ we could reach 1% of stability of the carrier field. Since Advanced Virgo is aiming at a ten times better sensitivity, the goal for angular stability was also tightened by the same factor. More solid estimates might be computed once a

| d.o.f. | req. [nrad] | d.o.f. | req. [nrad] |
|-----------|-------------|-----------|-------------|
| (+)-mode | 2 | (-)-mode | 110 |
| PR | 25 | SR | 280 |

Table 8.9: Angular requirements for the Advanced Virgo optical configuration in the physical mirror modes base.

proper simulation tool will be available for computing the effect of a mirror misalignment on sensitivity.

The requirements are driven by the carrier field fluctuations. Choosing the same requirements for the sidebands might at first seem in contrast with the assumption of 2% fluctuations made in sec. 8.3.5. However it is known from Virgo and Virgo+ commissioning experience that sideband fluctuations are very sensitive to any interferometer defects, mainly aberrations in the **PRC**. Since it is not possible as of today to properly estimate these effects, it was considered safe to compute the angular requirement on a tight basis, and assume a Virgo-like fluctuation to compute OMC requirements.

8.7.4 Quadrants and demodulations

The automatic alignment sensing scheme is based on a set of quadrant diodes placed at the detection ports shown in Fig. 8.1. Each port is instrumented with two quadrant photodiodes, one in near field (XX_A) and one in far field (XX_B). The use of two quadrants is important for being able to digitally combine the outputs in order to fine tune the Gouy phase of the error signal used for the angular control. For being able to obtain arbitrary phases in this way it is necessary that the two quadrants are placed in positions with 90 degrees of Gouy phase difference, which is a slightly less stringent requirement with respect to the near and far field placement. Even the Gouy phase difference between the two sensors does not need to be very accurate. A tolerance of ± 20 degrees is assumed to be enough.

The power impinging on each quadrant diode is 25 mW, considering to have a maximum acceptable impinging power of 50 mW, except for the B1p quadrant diodes which receive 2.5 mW of impinging power. These values are not finalized yet, but since for Virgo+ the high power quadrant diodes can accept 30 mW of impinging power, a maximum tolerance of 50 mW could be feasible. On the other hand the maximum allowed beam power for the B1p quadrants is 2.5 mW to be more conservative, since it is not clear up to now which amount of power at the dark port can be extracted from the main beam for angular control. Clearly if the amount of power will be higher the signal-to-noise ratio will improve with a square root law.

All quadrants will be equipped with fast galvo centering systems. The quadrants on the end benches will also need translation stages that might be used during the prealignment steps.

The quadrants have to be suspended in vacuum to reduce the spoiling of the signals, both demodulated and DC, due to seismic and acoustic noise. In Virgo and Virgo+, error signals, especially in DC, were dominated below the Hz region by air currents. Starting from 10 Hz, where there should be only shot noise, seismic motion was instead the limiting factor (see also sec. 8.7.7). It is important to mention that in Virgo and Virgo+ the error signal used to control the Differential-End **DOF**, which is the most critical one in terms of control noise, was

| Port | Angular control | Beam centering |
|------|---------------------------|----------------|
| B1p | f1, f2 , DC | 2×f2 |
| B2 | f1, f2, f3 | DC |
| B4 | f1 , f2 | DC |
| B7 | DC | |
| B8 | DC | |

Table 8.10: Quadrant diode demodulation frequency specifications. In bold signals used for the control

dominated by the electronic noise given by Analog-to-Digital Converter (ADC) nonlinearities [283, 284, 285, 286]. The very large dynamic range needed for automatic alignment signals (typically of the order of 10^6 - 10^7) must be properly taken into account in the design of the electronic readout system.

For angular control, demodulated signals at all three main frequencies will be used. Needs for each port are summarized in Tab. 8.10. Some signals will be used for angular control of the interferometer mirrors, some others to extract the spot positions used for maintaining the sensor well centered. Not all the signals coming from the detection ports are used in the present control scheme. These are highlighted in bold in Tab. 8.10. Nevertheless in the commissioning phase the possibility to have a larger choice of signals, thus a flexible system, is mandatory. In Virgo the final control system has been developed over the years, obtaining at the end a scheme which was completely different from the one initially foreseen in simulations. This happened due to ITF imperfections and improvements, and also due to the lack of complete and perfectly reliable alignment simulations.

Even for Advanced Virgo there is not a proper simulation tool available which allows to study the behavior of the alignment system as a function of possible unwanted effects (such as thermal effects, robustness versus interferometer working points etc...). As mentioned before the tools presently used are Finesse and Optickle. Optickle can take into account the radiation pressure effect, fundamental in high power interferometers, but considers only the first higher order mode (not allowing the study of thermal effects, beam mismatches etc.), and no mirror static misalignments. On the other hand Finesse can take into account higher order modes but not radiation pressure effects. For all of these reasons, even if the control scheme which has been simulated and designed works properly in simulation, it is important to have enough flexibility and safety margins to be able to use a different control scheme with respect to the designed one, in order to deal with commissioning uncertainties and effects that could not be simulated nor foreseen.

8.7.5 Automatic alignment control scheme

8.7.5.1 Sensing scheme

The automatic alignment control scheme has been modeled with Optickle; its control noise and the control accuracy for each angular degree of freedom have been evaluated with *Pickle* [287], the Optickle tool developed by the Advanced LIGO ISC group for propagating the angular control noise to the sensitivity, together with the residual mirror displacements.

The only noise taken into account in the simulations is the shot noise, thus if the sensing

will be dominated by other sources of noise the angular control scheme has to be completely redesigned and the control noise reevaluated. In other words all quadrant photodiode signals are assumed to be shot noise limited everywhere above 10 Hz.

In order to design the control scheme the sensing has been simulated by optimizing the amplitude of the transfer functions between the angular degree of freedom and the quadrant diodes tuning the Gouy and demodulation phases of the quadrants. The goal was to obtain the best decoupling of the angular degrees of freedom, taking care not to spoil the signal-to-noise ratio. In other words, whenever possible, the signal with larger SNR has been chosen.

It has been decided to use a similar control scheme for all the three optical configurations (low, high power with and without SRC) in the sense that for each configuration a given angular DOF is detected by the same detection port. Nevertheless, in each optical configuration parameters are retuned, such as demodulation and Gouy phases and control gains. Control filters are clearly different in the high and low power regime to take into account radiation pressure effects on the mechanical transfer function.

The optimal sensing scheme is the following:

- B1p demodulated at f_2 used for Differential(+)
- difference of the DC signals coming from the terminal benches for Differential(-)
- B2 demodulated at f_3 used for Common(+)
- sum of the DC signals coming from the terminal benches for Common(-)
- B4 demodulated at f_1 for PR
- B1p DC signal for SR (controlled in *drift control mode*)
- B4 demodulated at f_2 for BS

8.7.5.2 Control of the arm degrees of freedom

The plane of the interferometer is kept fixed by the input beam control system (not taken into account in these simulations) and the (-)-modes, controlled with DC signals using the B7 and B8 quadrants. At low frequency (about 3 mHz) the (-)-modes error signal will be substituted with centering signals (mirror relative to beam) to minimize the angular to longitudinal coupling. Such signals can be obtained using a dithering technique as done for the Virgo input mirrors centering [283]. Otherwise, as recently proposed, processed camera images [288] might provide the needed signals.

A clear difference between the Virgo and the Advanced Virgo angular control is the suppression of the (+)-modes sensing due to the radiation pressure effects. Increasing the circulating power the (+)-modes become more and more stiff, reaching a mechanical resonance frequency of about 3.5 Hz at full power. The decoupling of the sensing matrix is also reduced, making the interferometer more sensitive to possible optical imperfections. As an example, the high power interferometer configuration becomes the most critical configuration for mistuning of the longitudinal working point, as it has been evaluated for the differential offset tuning [263].

8.7.5.3 Control of the central cavity degrees of freedom

The **PR** is controlled by using the first demodulation frequency while the **BS** uses the second one. The **BS** and **PR** error signals can be exchanged if needed by retuning the Gouy and demodulation phases. It was chosen to use the best signal, in terms of SNR, for the **PR** since it is strongly coupled with the Differential(+), especially in the final configuration [263]. This sensing scheme should then assure the lowest **PR** control noise reintroduction in the Differential(+) mode.

The relaxed accuracy requirement for the **SR** (280 nrad) allows to adopt a hierarchical control strategy, using a low frequency control for the **SR** mirror with a bandwidth of some tens of mHz. This strongly simplifies the angular control decoupling. In Virgo the drift control developed for the input mirrors, which used a dithering technique to generate the error signals, achieved a control accuracy of about 100 nrad, which would be already compliant with the Advanced Virgo requirements for **SR**.

8.7.5.4 Discussion

After the control scheme was designed the sensor noise has been projected to the dark fringe. The requirement is, as in the longitudinal case, that all noise contributions must remain a factor 10 below the design sensitivity. In the angular control case this safety factor is even more important since it must also take into account the uncertainty in the simulation results.

In all the three studied configurations the control scheme is compliant with the specifications of control accuracy and control noise and it does not show any evident difficulties for the baseline design (as the decoupling of the sensing, the design of the control filtering etc...) [263]. The most critical degrees of freedom in terms of control noise, for all the three configurations, are the (-)-modes which are controlled with DC signals coming from the terminal benches. For this reason it is mandatory to have these sensors shot noise limited. The performance of the end benches suspension becomes very important, see sec. 8.7.7.

In the power recycled only configuration at 25 W input power, the sensing is very well decoupled and the angular control noise is compliant with the factor 10 of safety below the sensitivity curve. Radiation pressure effects do not affect strongly the cavity modes. This configuration is the closest one to Virgo+. The experience gained in the past years will help the first commissioning phases.

In the dual recycled configuration at 25 W, the angular control scheme is very similar to the first one except for the introduction of the **SRC**. The drift control applied to the **SRC** allows an easy decoupling of the signals which will help the implementation of an angular control system compliant with the sensitivity requirements.

The final configuration, dual recycled at full power, which allows to reach the highest possible sensitivity, is compliant with the control noise sensitivity requirements. This configuration is the most critical one in terms of angular degrees of freedom decoupling, due to the (+)-mode sensing suppression and the presence of the **SRC**. The system is controllable, but its decoupling may become worrying as soon as optical defects occur in the real interferometer [263]. Indeed, in Virgo and Virgo+ we have experienced a strong coupling between the angular DOF of **BS** and **PR** (a sensing ratio of 1:1), which made the commissioning and the

| | PR | SR | BS |
|----------|-------|----|-------|
| B4 f_1 | 103.4 | 0 | -74.4 |
| B1p A DC | 0 | 1 | 0 |
| B4 f_2 | -2.1 | 0 | -4.3 |

Table 8.11: Sensing for the central interferometer degrees of freedom in case of high power configuration with SR cavity, the most coupled configuration.

implementation of the complete automatic alignment system longer and more difficult than initially foreseen. For instance up to VSR4, spring 2011, we could not control both degrees of freedom acting from the marionette. The **PR** had to be controlled by using the reference mass (which is noisier with respect the control from the marionette) due to the fact that in the **PR** error signal the **BS** resonances were visible and not mechanically damped. Table 8.11 shows the sensing matrix for the central interferometer degrees of freedom in the dual recycled configuration.

Moreover, when some optical defects were present in the interferometer (such as thermal transients, higher order modes circulating in the cavities, not optimally tuned working point etc.), it was not possible to find two independent and noiseless signals to control both the BS and the PR mirrors. In VSR3 only the **BS** was globally aligned since the mistuning of the end mirror radii of curvature created lots of higher order modes which affected the angular error signal. The lack of a complete control system yielded a non reliable working point affecting the detector duty cycle and sensitivity. These kinds of issues will make the Advanced Virgo angular control system commissioning more complex and longer.

8.7.6 Performances of the angular control system

The performances of the designed control system can be quantified with the mirror residual motion in the **AA** closed loop configuration, and with the projection of angular control noise to the Advanced Virgo sensitivity. The control filters have been designed in order to meet the sensitivity requirements starting from 10 Hz, while the low frequency part of the controls has been tuned to meet, within a factor 2, the accuracy requirements. Further tunings are not useful at this step of the design, since the mechanical transfer function of the new payloads is not fixed yet. See Fig. 8.15, 8.16 and 8.17: bottom plots for control noise and top plots for accuracy performances.

The residual angular displacements and the **AA** control noise, evaluated with the Optickle simulation, are in agreement with the accuracy and the sensitivity requirements, for all the three configurations. The most critical degrees of freedom in terms of control noise are the (-)-modes, for all the three commissioning configurations.

In the final configuration, the high power dual recycled interferometer, the radiation pressure suppresses the (+)-mode sensing. The consequence is a worse mode reconstruction, especially for the Differential(+), which causes an excess of control noise. This fact is visible in Fig. 8.17, where the control noise due to the Differential(+) mode (dashed blue line) is larger with respect to the B1p diode shot noise contribution (blue line).

This behavior is not critical in simulation since the Differential(+) noise is far from limiting the sensitivity, but the coupling can be stronger in a real interferometer, leading to further

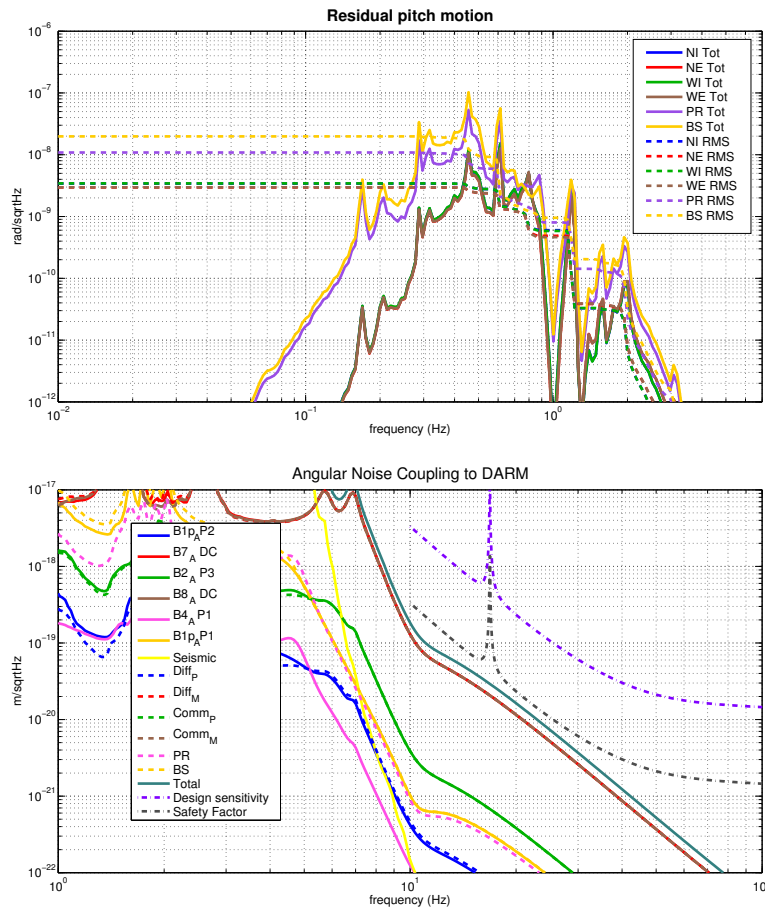


Figure 8.15: Mirror residual displacement and automatic alignment control noise projection for the first commissioning phase (low power interferometer without SRC) in the top and bottom plot, respectively. The mirror residual motions are close to the accuracy requirements and improvement margins have been left in the filter design.

increase of control noise.

8.7.7 Quadrant diode suspension requirements

The requirements for the quadrant diode suspension, in tilt and translation, have been evaluated analytically for the DC signals in transmission of the long arm cavities, used for the control of the (-)-modes [289]. As highlighted before, these are the most critical degrees of freedom in terms of control noise.

A DC signal measures the relative beam-to-quadrant displacement, thus any bench motion fakes the alignment signal generated by the beam displacement due to cavity mirrors misalignment. The bench motion has therefore to be low enough to not spoil the mode angular sensing at low frequency, inside the automatic alignment control bandwidth, i.e. up to a few Hz. It must also not spoil the quadrant sensing noise at high frequency, in the detection bandwidth, i.e. above 10 Hz.

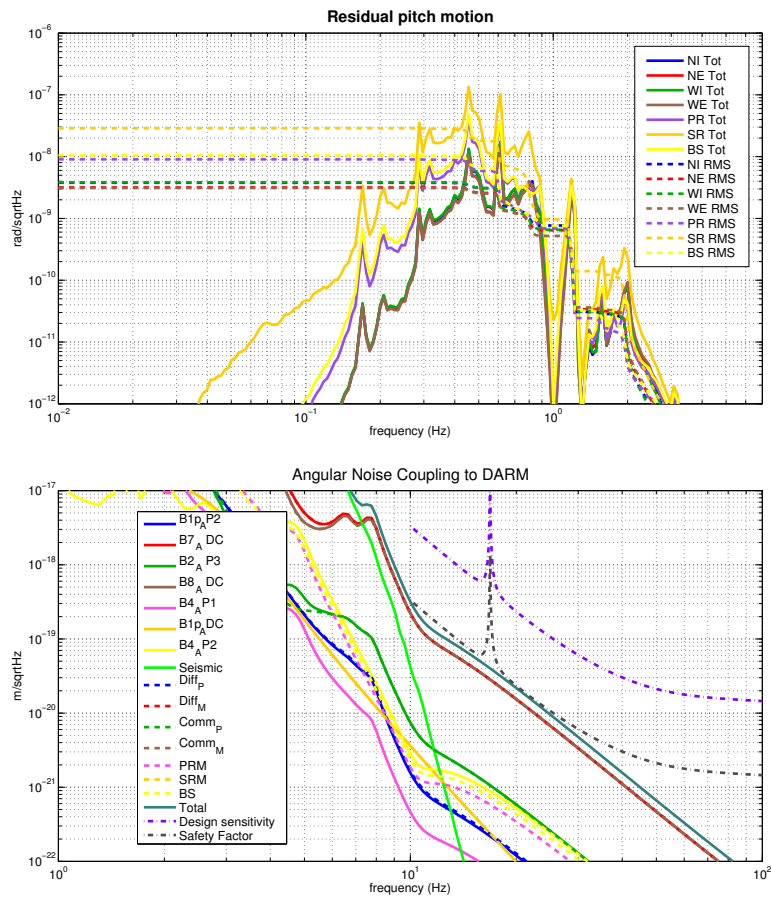


Figure 8.16: Mirror residual displacement and automatic alignment control noise projection for the low power interferometer with SRC in the top and bottom plot, respectively.

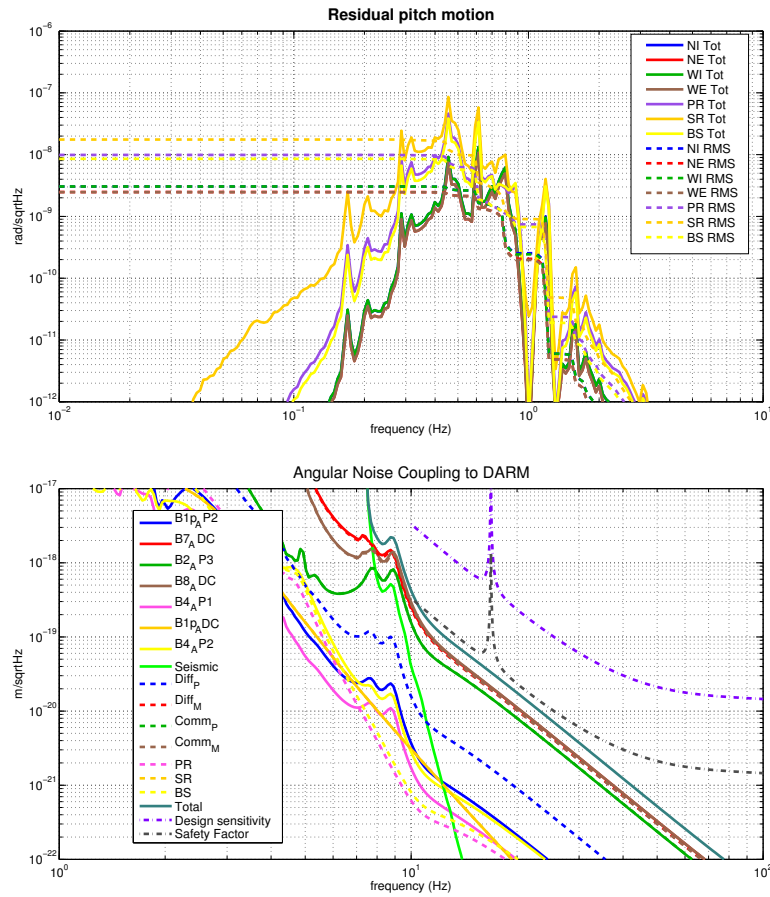


Figure 8.17: Mirror residual displacement and automatic alignment control noise projection for the final commissioning phase (high power interferometer with SRC) in the top and bottom plot, respectively.

| Requirement | | |
|-----------------------|-----------------------|------------------------|
| δh | $2.1 \cdot 10^{-6}$ | $m/\sqrt{\text{Hz}}$ |
| $\delta\theta$ | $3.3 \cdot 10^{-15}$ | $rad/\sqrt{\text{Hz}}$ |
| h_{RMS} | 24 μm | |
| θ_{RMS} | 0.031 μrad | |

Table 8.12: Suspended terminal detection bench displacement requirements. Spectral requirements are valid above 10 Hz.

The requirements have been obtained at low frequency by analytically computing the amplitude of the angular error signal for the (-)-mode misalignment equivalent to the accuracy requirements (110 nrad see Tab. 8.9) taking into account the quadrant diode dimension, the beam size at the quadrant and the telescope transfer function (bench translation and bench tilt to beam displacement on the quadrant) as given by the DET subsystem (baseline telescope design).

At low frequency the spurious signal coming from bench motion is required to be a factor 5 below the real angular error signal. For the high frequency requirements the maximum allowable bench displacement is set to have the equivalent signal below the shot noise by a factor 10. The results are listed in Tab. 8.12.

The most critical requirement is for the residual tilt displacement (θ_{RMS}). The required accuracy is about a factor 3 below the Virgo+ test mass local control performances.

A low frequency control to point the beam on the terminal mirrors, by using the camera images to measure the relative position beam-mirror [288], has been recently proposed. It could relax the requirements only if it can be used with a control bandwidth larger than 500 mHz (for going above the microseismic region where the largest part of the bench motion is located). The limiting factor is the camera sensing noise which must be low enough to not reintroduce control noise in the automatic alignment error signal. Studies and noise evaluations are in progress, but for the moment this solution is not considered in the baseline design.

8.8 Parametric instabilities

The parametric instability (PI) consists in the coherent ringing of a mechanical mode of a cavity mirror by the circulating optical power, which may significantly affect the performance of high-power advanced gravitational wave interferometers [295]. Figure 8.18 presents the mechanical amplification process at play. The incident laser is scattered by the mechanical resonator motion (at frequency Ω_m , yielding both a Stokes and an anti-Stokes band. If a mode detuned to $-\Omega_m$ with respect to the pump laser frequency ω_0 is simultaneously resonant, the Stokes process is favoured over the anti-Stokes one: the net flow of photons from the pump mode to the lower frequency sideband corresponds to a mechanical amplification of the motion (by creation of mechanical phonons).

For a single cavity, the corresponding parametric gain for the mirror motion \mathcal{R} is (for the

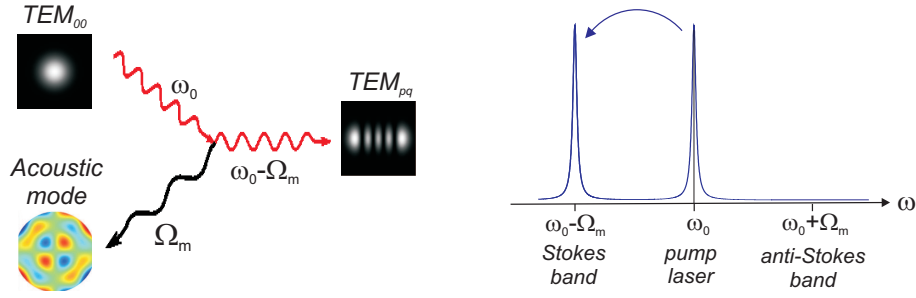


Figure 8.18: Interpretation of the three mode amplification process in terms of photon scattering by mechanical phonons to a different optical mode. Both the pump photon and the scattered one can be simultaneously resonant in the cavity.

Stokes process):

$$\mathcal{R} = \frac{8\mathcal{F}}{\lambda c M \Gamma \Omega_m} P_{\text{in}} \Lambda \left(\frac{\Omega_c^2}{\Omega_c^2 + (\omega_0 - \Omega_m - \omega_{\text{ho}})^2} \right), \quad (8.12)$$

where M is the effective mass of the vibration mode, Γ its damping, ω_{ho} the resonance frequency of the higher order optical mode, \mathcal{F} and Ω_c the associated finesse and optical bandwidth, and Λ the spatial overlap between optical modes and the mechanical one. Mirror motion (such as thermal noise) is amplified by this process up to an instability threshold ($\mathcal{R} = 1$) where the mirror is coherently set into motion by laser light.

Such a 3-mode parametric coupling has already been observed on large test masses in the Australian high-power laser facility [296] and in the LKB group [297], using an almost degenerate optical cavity and a silicon micromirror, even though no experiment to date has been able to reach the parametric instability threshold. The advanced large scale interferometers, with their very high mechanical mode density at frequencies such as tens of kHz, unfortunately are very good candidates to display such an instability.

After the seminal work of Braginsky on a single cavity [295], a number of groups have started modelling a complex interferometer, with dual recycling. The group led by D. Blair has shown that for a given mechanical mode, the overall amplification effect may involve tens of higher order optical modes [298]. The parametric gain should then take into account all optical modes, whether they have an amplification or a damping effect, and can be written for instance, for a single cavity:

$$\mathcal{R} = \frac{8P_{\text{in}}}{\lambda c M \Gamma \Omega_m} \sum_{p,q} \left(\frac{\mathcal{F}_{pq} \Lambda_{pq} \Omega_{cpq}^2}{\Omega_{cpq}^2 + (\omega_0 - \omega_{pq} + \Omega_m)^2} - \frac{\mathcal{F}_{pq} \Lambda_{pq} \Omega_{cpq}^2}{\Omega_{cpq}^2 + (\omega_0 - \omega_{pq} - \Omega_m)^2} \right), \quad (8.13)$$

where the summation is on transverse optical modes $\{p, q\}$. To avoid instability, the gain \mathcal{R} must remain below unity.

Detailed simulations of the impact of the PI by the Perth and MIT groups have shown that in the current Advanced LIGO optical configuration, the number of unstable mechanical modes is unlikely to be below 5 for any set of optical parameters [298, 299]. Such modes are likely to reach a very important vibration amplitude and therefore prevent any stable operation of the interferometer, even though most mechanical modes are outside the detection window. It is therefore of utmost importance to understand, fully compute and mitigate this instability.

The MatLab code first developed by UWA [298] has been adapted to Advanced Virgo and carefully checked. The results so far only include a truncated (but yet significant) set of optical modes. The work already performed includes:

- Ansys computations of the mechanical modes of the test masses (taking into account their exact geometry)
- computation of the mechanical quality factors, taking into account the losses due to the optical coating
- computation of the higher order modes of the cavities of the interferometer, including their optical losses
- computation of the spatial overlap between all possible triplets of modes (TEM₀₀ pump mode, mechanical mode, higher order optical mode)
- parametric gain \mathcal{R} for each mechanical mode by summation of the extension of eq. (8.13) to a dual recycled interferometer.

The computation can be performed for a number of optical configurations: single cavity, interferometer, interferometer with power or dual recycling, etc. Figure 8.19 presents one plot produced by the code: parametric gain \mathcal{R} for each mechanical mode up to 46 kHz, for a dual recycled interferometer with Advanced Virgo specifications and an input power of 125 W. In such a configuration, 13 modes (per test mass) are likely to be unstable, but this is an upper limit, computed under the assumption that the mechanical Qs are effectively limited by coating losses and not clamping losses. The gain is proportional to the input power, so that for a lower one, the number of unstable modes is drastically decreased. In the case of 25 W, about 4 modes per mirror remain unstable. As the results are strongly dependent on the (optical and mechanical) characteristics of the mirrors and the cavities, a statistical analysis has to be performed in order to take into account the expected deviations of the actual mirrors from their specifications.

Possible mitigation strategies include:

- passive damping (with resonant dampers) in order to decrease the Q and increase the PI threshold
- thermal tuning of the RoCs to a 'sweet spot' with a lower number of unstable mechanical modes [300]
- feedback damping [301] by a combination of high speed PI monitoring (at frequencies up to 50 kHz) and efficient actuation on the mirror mode profiles (eg not a global actuation of the mirror center of mass)

The tasks to be completed include:

- Computation of the PI gain with a larger set of optical modes, for a more accurate estimation of \mathcal{R}
- 'Worst case' statistical analysis, to take into account the highly sensitive character of the results to small discrepancies
- evaluation of the impact of the PI over the lock acquisition process
- definition of a mitigation strategy

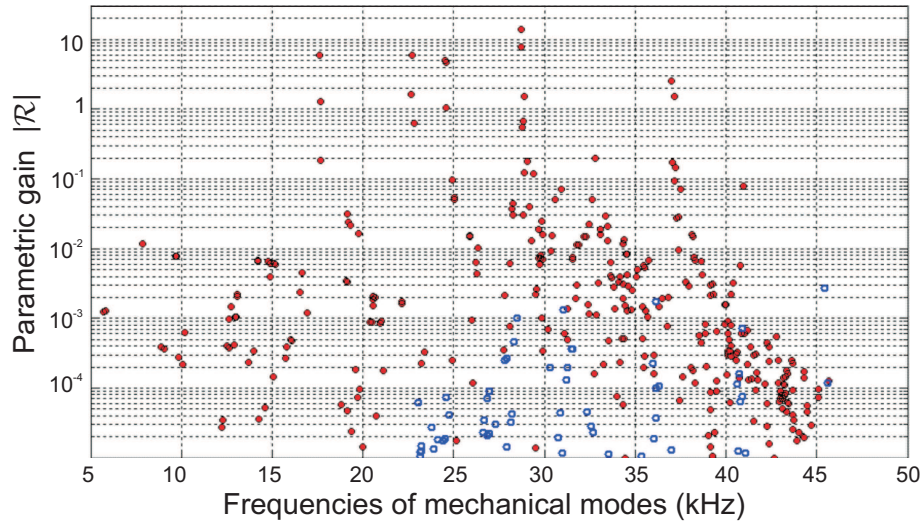


Figure 8.19: Example of a plot obtained with the PI simulation code: parametric gain $|\mathcal{R}|$ computed for all mechanical modes of the suspended mirrors, up to 46 kHz, for a dual recycled interferometer. Red dots indicate amplified modes ($\mathcal{R} > 0$), blue dots damped ones. 13 modes (per test mass) are likely to be unstable.

8.9 Software requirements

8.9.1 Fast realtime control

The realtime system that is currently used for both the lock acquisition and the steady state control consists of a chain of several components (ADC, Photo-diode read-out (Pr), Gc, Digital Signal Processor (DSP) and finally the Digital-to-Analog Converter (DAC)) that run at a sample frequency of 10 kHz. It is expected that the realtime software that will be used for the longitudinal control of Advanced Virgo will not be fundamentally different from the current one. Some minor work might be required to remove some legacy parts or update to the future software environment. The *locking algorithm* (which is part of Gc) will probably be rewritten from scratch, which will be done in parallel with the commissioning activity.

The overall delay of all the components in the chain poses a limit on the unity gain frequency of the locking loops. As discussed in 8.3.6, there might be a need to increase the unity gain frequency to 400 Hz in case of a double recycled interferometer, which is hard to achieve with the current system. A reduction of the delays will be necessary, for example by increasing the sample frequency or optimizing the antialiasing filters. This is discussed in more detail in [xx ref DAQ chapter].

The software chain used for controlling the angular degrees of freedom is pretty similar to the one used for the longitudinal part. The main difference is that it uses quadrant detectors instead of photodiodes and that the control process runs at a much lower frequency (2 kHz typically). Since this is about an order of magnitude slower than the control system used for the longitudinal controls, it poses no extra requirements on the digital or analog delays of the control system.

8.9.2 Slow control

Most of the slow control of Virgo is performed using Automation of the Locking Procedure (**ALP**) servers. The whole lock acquisition currently takes between 10 and 20 minutes. This process is driven by the AlpMain server, which basically executes a long list of Cm commands that are sent to other processes, with the occasional waits and checks to see if a certain state is achieved. The whole sequence of the lock acquisition itself will have to be written from scratch, based on the experience of the commissioning.

In addition to this simple sequencing, a number of servos is active that implement slow feedback loops for stabilizing e.g. a unity gain frequency of a certain loop. Also these are implemented in **ALP** (e.g. AlpLock, AlpTCS, etc.).

Since all the time critical actions are performed using realtime systems, and since **ALP** is mainly used to slowly change the configuration of the interferometer, the requirements on it are not very high. It should therefore be no problem to use **ALP** as it is now to implement the slow control of Advanced Virgo. **ALP** has, however, some limitations when it is used to implement complex logic (e.g. subfunctions, exceptions, inter-process communication) and advanced calculations (e.g. vector math as in Matlab). These kind of operations were already important in Virgo+ and are more critical in Advanced Virgo, given the increased complexity of the system. We therefore propose to investigate the possibility of using an existing scripting language in addition to or in place of **ALP**, instead of upgrading **ALP** to obtain such new features. The migration to the new architecture will be needed only at the time of restart of the commissioning activities, therefore this is not a priority task.

8.10 Interfaces with other subsystems

The design of both longitudinal and angular control systems creates several interfaces with other subsystems. All the requirements are discussed in more details in the corresponding sections.

8.10.1 OSD

In order to control the longitudinal degrees of freedom of the power and signal recycling cavity a pickoff of the beam inside the recycling cavity is needed. This requires the addition of a plate in front of the power recycling mirror to extract the beam.

8.10.2 MIR

The use of the etalon effect in the input mirrors to tune the interferometer finesse asymmetry is an important risk reduction strategy (sec. 8.3.10 and 8.3.9). This implies the need of having input mirrors with parallel faces. To meet the sensitivity requirements, in the power recycled case loss asymmetries must remain below 20 ppm and finesse asymmetry below 1% to be able to meet the requirements.

| Frequency | Phase noise [rad/ $\sqrt{\text{Hz}}$] | Rel. ampl. noise [$1/\sqrt{\text{Hz}}$] |
|-----------|--|---|
| 6.3 MHz | $1.8 \cdot 10^{-6}$ | $1.7 \cdot 10^{-7}$ |
| 56.4 MHz | $1.1 \cdot 10^{-6}$ | $1.1 \cdot 10^{-6}$ |
| 8.4 MHz | 0.27 | $1.7 \cdot 10^{-7}$ |

Table 8.13: Summary of requirements for sideband amplitude and phase noise. Modulation noise enters in the photodiode output signal following two paths. The first one is through the noise at the level of the modulation, which is transmitted to the laser beam and enters on one of the inputs of the mixer. The second path is through noise introduced by the local oscillator distribution system, which enters on the other input of the mixer. The requirements given here apply to the total of the two contributions.

The reflectivity of the power recycling pickoff plate is required to be about 300 ppm, in order to have enough power in the pickoff beam even with low input power (sec. 8.3.2).

Auxiliary lasers at a wavelength different from the main one (sec. 8.5) require a careful evaluation of the mirror coating performances at the new wavelength. We ask to have an arm cavity finesse between 5 and 10 at 1319 nm for the coating of the mirror without changing the value of the 1064 nm parameters. These requirements have already been met for the mirrors installed in the CALVA platform [258].

The angular control system foresees the use, even in science mode configuration, of signals coming from quadrants in transmission of the end mirrors. In order to have a suitable amount of power in the beam a lower limit for the end mirror transmission must be set. In the case of low input power (25 W), a transmission of 1 ppm gives about 150 mW of power on the end benches, which seems a reasonable amount to be shared between diodes, quadrants and cameras. Therefore the end mirror transmission should be $T \geq 1$ ppm.

8.10.3 INJ

The lock acquisition procedure might be strongly affected by the radiation pressure issue. Moreover initial commissioning activities will be for sure carried out in a reduced input power regime. Both these considerations indicate the need of a system to continuously and smoothly tune the input power from its minimum values up to the maximum.

Requirements on modulation phase and amplitude noise have been computed, based on the steady state longitudinal control design. They are summarized in Tab. 8.13 (see sec. 8.3.7 for more details).

8.10.4 SBE

The end mirror transmitted beams will be sensed by two quadrant photodiodes for each port. Spot position (DC) signals will be used to control two angular degrees of freedom. Their required accuracy gives limits on the spurious signal created by bench motion, which should give a contribution not larger than what would be equivalent to a beam translation inside the arm cavity of the order of 20 μm . Provided the magnification properties of the telescope (designed to reduce the beam size to a reasonable value which will fit the sensor) the spot motion on the quadrant can be converted to angular and translational residual motion of

| Requirement | | |
|-----------------------|-----------------------|-------------------------|
| δh | $2.1 \cdot 10^{-6}$ | m/ $\sqrt{\text{Hz}}$ |
| $\delta\theta$ | $3.3 \cdot 10^{-15}$ | rad/ $\sqrt{\text{Hz}}$ |
| h_{RMS} | 24 μm | |
| θ_{RMS} | 0.031 μrad | |

Table 8.14: Suspended terminal detection bench displacement requirements. Spectral requirements are valid above 10 Hz.

| Port | photodiodes | Quadrant photodiodes |
|----------------------------------|----------------------------|----------------------|
| Symmetric port (B2) | DC, $f_1, 3f_1, f_2, f_3$ | DC, f_1, f_2, f_3 |
| Dark port after OMC (B1) | DC | |
| Dark port before OMC (B1p) | DC, $f_1, f_2, 2f_1, 2f_2$ | DC, $f_1, f_2, 2f_2$ |
| OMC reflection (B1s) | DC, $f_1, f_2, 2f_1, 2f_2$ | |
| Power Recycling pick off (B4) | DC, $f_1, f_2, 2f_1, 2f_2$ | DC, f_1, f_2 |
| Arm cavity transmission (B7, B8) | DC, f_1 | DC |

Table 8.15: Needed signals and demodulation frequencies at each interferometer output port.

the end benches. The requirements obtained in this way are quite stringent and reported in Tab. 8.14 (see sec. 8.7.7 for more details).

There are additional requirements on the bench motions inside the detector bandwidth, above 10 Hz. In order to have error signals dominated by shot noise, the maximum bench motion can be computed. With the present telescope design the required maximum bench motions are summarized in Tab. 8.14 (see sec. 8.7.7 for more details).

8.10.5 DET

The different demodulation frequencies needed at each port are summarized in Tab. 8.15. In all ports the two quadrants should be placed in such a way as to have the Gouy phase difference between them as close as possible to 90 degrees. In this way the signals from both quadrants could be mixed digitally to reconstruct with high accuracy the needed Gouy phase. This is necessary to properly decouple the angular degrees of freedom (sec. 8.7.4). All quadrants will use fast galvo centering systems.

The requirements on the DARM longitudinal control loop (sec. 8.3.4), which come from ISC considerations, have an impact on design requirements of the OMC. Any fluctuation of spurious fields (sidebands or higher order modes) transmitted by the OMC is directly translated to a motion of the DARM degree of freedom, thus spoiling the loop accuracy (sec. 8.3.5). From these considerations a requirement on the maximum sideband power which can be tolerated in transmission of the OMC is obtained to be of the order of 0.07 mW. This poses stringent limits on the OMC filtering capabilities. Tab. 8.16 summarizes the filtering requirement in different configurations, using the estimate of sideband powers at the input of the OMC given in [290].

As anticipated in the INJ interface description, requirements on modulation phase and amplitude noise have been computed, based on the steady state longitudinal control design.

| Frequency [MHz] | PR 25 W | SR 25 W | SR 125 W |
|-----------------|---------|---------|----------|
| 6 | 1/120 | 1/7 | 1/36 |
| 56 | 1/1700 | 1/460 | 1/2300 |

Table 8.16: Filtering requirements (in power) for the OMC in different interferometer configurations.

These requirements are given in terms of the total phase and amplitude noises at all mixer inputs, and therefore apply also to the local oscillator distribution network. A summary can be found in sec. 8.3.7 and Tab. 8.13.

Most of the photodiode and quadrant signals will have very large dynamical range (typically 10^6 - 10^7 in Virgo+ angular signals). The full readout chain must be able to handle such large dynamics, without introducing upconversion noise.

Auxiliary lasers (sec. 8.5) will go through the detection benches. Proper space to allow the needed optical path must be prepared. Since a different wavelength will be used we will need a special dichroic element to separate the beams and also avoid any perturbation on the signals observed with the 1064 nm laser. For the latter point some beam dumps may also be needed.

Time domain simulations done at LIGO suggest that in case of an unlock of a double recycled interferometer, a large part of the optical power stored in the interferometer (around 50 Joule) will exit the asymmetrical port in a very short time (less than 20 ms). Since the damage threshold of a typical photodiode is of the order of 100 mJ, a very fast shutter is needed. For avoiding any damage, the shutter must be almost completely closed within 1-2 ms after receiving a trigger, which might be based on the DC power crossing a certain threshold [261]. This seems pretty demanding for a standard mechanical shutter.

The DET subsystem fixed the DC readout offset value in order to have a carrier power at the dark port of 80 mW. From the point of view of ISC, it would be better to reduce as much as possible the offset. As explained in [263] the larger the offset the more coupled the angular sensing matrix becomes.

8.10.6 PSL

The lock acquisition of the long arms requires the residual frequency noise with prestabilized laser to be significantly smaller than the cavity linewidth, namely smaller than about 1 Hz RMS.

Considering the coupling of frequency and power noise at the interferometer input to the detector sensitivity in presence of some reasonable asymmetries, it is possible to draw requirements for the stabilization loops. This is in particular important for the power stabilization at the IMC transmission. The required Relative Intensity Noise (RIN) depends on the interferometer configuration (sec. 8.3.8). A summary of the requirements is given in Tab. 8.17. More details are given in Fig. 8.4 and 8.7.

| Configuration | 10 Hz | 100 Hz | 1000 Hz |
|---------------|-------------------------------------|---------------------------------------|-------------------------------------|
| PR 25 W | $2 \cdot 10^{-8} \text{ Hz}^{-1/2}$ | $1.5 \cdot 10^{-8} \text{ Hz}^{-1/2}$ | $2 \cdot 10^{-8} \text{ Hz}^{-1/2}$ |
| SR 125 W | $4 \cdot 10^{-9} \text{ Hz}^{-1/2}$ | $9 \cdot 10^{-9} \text{ Hz}^{-1/2}$ | $9 \cdot 10^{-9} \text{ Hz}^{-1/2}$ |

Table 8.17: Summary of RIN requirements at the interferometer input. For the full dependence on the frequency refer to Fig. 8.4 and 8.7.

8.10.7 DAQ

All the control loop designs have been carried out without considering the effect of delays introduced by the real time control system. Such delays might play an important role only in the case of the DARM loop for dual recycled configuration, which has a unity gain frequency of about 400 Hz [260]. This would impose a requirement on the total delay of about 50 μs which according to the DAQ subsystem would be difficult to reach. Therefore it is necessary to reconsider the design of the control. It seems feasible, although not yet designed, to reduce the bandwidth to 200 Hz. This would relax the delay requirement to about 100 μs .

The automation of the entire lock procedure and the steady state operations requires an infrastructure to implement scripting and slow servo loop, as was done in Virgo using ALP. A greater flexibility with respect to the scripting and computational capabilities of ALP would be very useful (sec. 8.9) to improve the lock acquisition robustness and speed up the commissioning.

8.10.8 SAT

The issue of total delay in the DARM loop involves also the SAT subsystem, since part of the delay must be accounted to the DSP, coil drivers and DAC controlling the mirror actuators.

The performances of the inertial damping system are important for the total residual RMS motion of the mirrors. Indeed the RMS is almost completely accumulated at frequencies below 1-2 Hz. The requirements for the longitudinal control accuracy are met by the control loops, assuming that the payload motion is the same as measured in Virgo (about 0.5 μm and 0.1 μrad RMS). This implies that the mirror motion in Advanced Virgo must not be larger than in Virgo. Moreover, any reduction of the low frequency mirror motion at the level of the suspension system will help implementing more stable and less noisy longitudinal control loops.

8.10.9 PAY

The force needed to acquire and maintain the interferometer lock can be estimated starting from simple modeling and experimental verifications. The use of nonlinear lock acquisition, which was experimentally proved in Virgo+, reduces the maximum force needed in high power by about a factor 160 with respect to the Virgo+ actuators (sec. 8.4.1). A rough estimation indicates that the maximum force used in Virgo+ was of the order of 3 mN per coil-pair. Keeping some safety margin, we can expect to reduce this by a factor 5-10. The exact value is still to be decided and depends on the mechanics of the new payload and on the amount of sensor noise during the lock acquisition.

Early reallocation to the marionette also virtually eliminates any requirement on the maximum actuation force on the mirror, from the need to maintain the lock.

The need of increasing the DARM loop bandwidth poses stringent requirements on the minimum possible frequency of internal resonances of the structure holding the actuation coils. The present design of the DARM control foresees a bandwidth of 400 Hz. Having all resonances above this frequency seems very difficult, therefore it is necessary to reconsider the design of the control. It seems feasible, although not yet designed, to reduce the bandwidth to 200 Hz.

The issue of parametric instabilities and the possible strategies to damp them, passively or actively, must be deeply investigated with the collaboration of the PAY subsystem.

8.10.10 INF

In the terminal stations, the space for auxiliary laser benches must be allocated near the minitower and on the same concrete slab. Safety issues must be verified with the infrastructure group, as we will be placed on the roof of the clean room. We may also need an acoustic enclosure and we may be able to reuse the one installed around the end arm optical tables.

8.11 Summary and conclusions

The conceptual design of the steady state control of Advanced Virgo, both for angular and longitudinal degrees of freedom, is concluded. Three different configurations have been studied: power recycled only at low input power, dual recycled at both low and full input power.

To be compliant with the detector scientific goal all control noises must remain a factor 10 below the design sensitivity in all studied configurations. To reach these performances the sensing noise of all the error signals cannot exceed the shot noise level, given the maximum power that can be sensed, as set by the DET subsystem.

The accuracy requirements for the control system have been computed based on considerations on the maximum tolerable power fluctuations and on noise upconversion. The control systems are compliant with these accuracy constraints, provided that some requirements to other subsystems are fulfilled. In particular the longitudinal control poses constraints on the **OMC** performances, and the angular control poses constraints on the end benches seismic attenuation system. Requirements on the laser technical noises at the interferometer input and on the interferometer asymmetries are also derived. The need of a precise matching of the two input mirror reflectivities dictates the use of the etalon effect and its control.

The performances of the **ISC** control system have been evaluated using modal simulation tools, namely Finesse and Optickle. The uncertainty in the modeling and in the simulation results is still large. Indeed the large circulating power leads to strong radiation pressure effects. Such effects can be modeled only using Optickle, which on the other hand cannot use higher order modes and therefore does not give completely accurate results in particular for the angular controls. A tool capable of simultaneously handling higher order modes and radiation pressure would be very important. Plans for the development of such a tool are being considered, compatibly with the available manpower.

The study of the lock acquisition procedure has started only since a few months. The lock acquisition of a single arm, even with the increased finesse of Advanced Virgo, will not pose fundamental difficulties. It was shown in simulation and experimentally in Virgo+ that low force lock acquisition techniques are available, allowing a reduction of the needed maximum actuation force at the level of the mirrors.

In the case of the power recycled only interferometer, which will be the first one to be commissioned, the same locking algorithm implemented in Virgo and Virgo+ will be used. The optical configuration is very similar and there are no differences that will make the Variable Finesse technique inadequate. We expect to acquire the lock at reduced power and then increase it to the running one when the interferometer is in a well controlled state. If we use a MICH offset, the switch to DC readout will pose no fundamental difficulty since the controlled system will remain open-loop stable.

The lock acquisition procedure in the dual recycled case has not been studied in depth so far. We expect to be able to profit from the use of auxiliary lasers to maintain the arm cavities locked while acquiring the control of the central part of the interferometer. This would imply a completely different locking scheme with respect to the power recycled case. Another possible strategy that will be considered in the next months is an extension of the Variable Finesse technique.

A risk reduction strategy to cope with sideband aberrations due to thermal effects and mirror defects is proposed. It foresees the use, during the thermal compensation system commissioning, of an additional high frequency modulation. The corresponding sidebands will have very low recycling gain and therefore will be poorly sensitive to recycling cavity defects, providing reliable control signals.

Chapter 9

Stray light control (SLC)

9.1 Scope and deliverables of the subsystem

The Stray Light Control subsystem (**SLC**) subsystem was created in mid-December 2011. The technical design is therefore far from complete. We describe here the scope of the subsystem, the deliverables foreseen so far, and the status of the design study. At this stage, the final requirements are being calculated.

The subsystem is meant to deal with all the light which goes out of the clear aperture of the core optics (the clear aperture is defined as the coating diameter). This light is called stray light. Its origin can be scattering off a surface, as well as spurious reflections off a Anti-Reflective (**AR**) coated surface, or simply clipping of the main fundamental mode.

The **SLC** subsystem extends from the last optics of the Injection subsystem (**INJ**) telescope (meniscus lens) to the first optics of the output telescopes (dark fringe, Fabry-Perot (**FP**) arm cavity transmission and Pickoff Plate (**POP**)). The subsystem is not intended to deal with the backscattered light from the optics of **INJ** and Detection Subsystem (**DET**).

The stray light must be "controlled". It means that the noise due to the recoupling of some of this light into the interferometer must be 10 times lower than the target sensitivity of Advanced Virgo (**AdV**). This can be achieved by integrating baffles into the vacuum chambers of the interferometer. These baffles are required to absorb, as much as it is necessary, the stray light. They should feature low reflectivity and low scattering as well. When this is difficult to achieve, because of requirements on the roughness being too stringent, the baffles are also required to be suspended in order to limit the amplitude of power fluctuations that they can induce on the dark fringe.

The deliverables are therefore a series of baffles which can be made of different materials and have different shapes, which have to be High Vacuum Compatible and must be well interfaced with the other subsystems such as Payload subsystem (**PAY**), Vacuum subsystem (**VAC**), **INJ** and **DET**.

9.2 Where is the light lost?

During the commissioning phase of first generation Gravitational Waves (**GW**) detectors, commissioners faced several issues linked with stray light in the vacuum chambers of the core

optics. We have evidenced such problems by making pictures through the viewports of the Beam Splitter (BS) and West End (WE) vacuum chambers (see pictures 9.1 and 9.2).

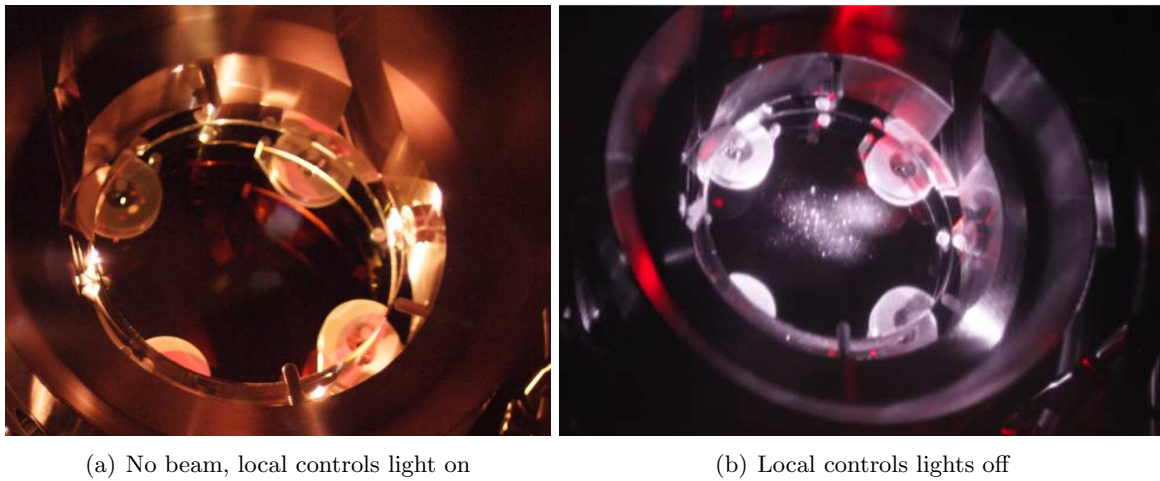


Figure 9.1: Virgo BS payload pictures. The purple light is scattered light from the main beam.

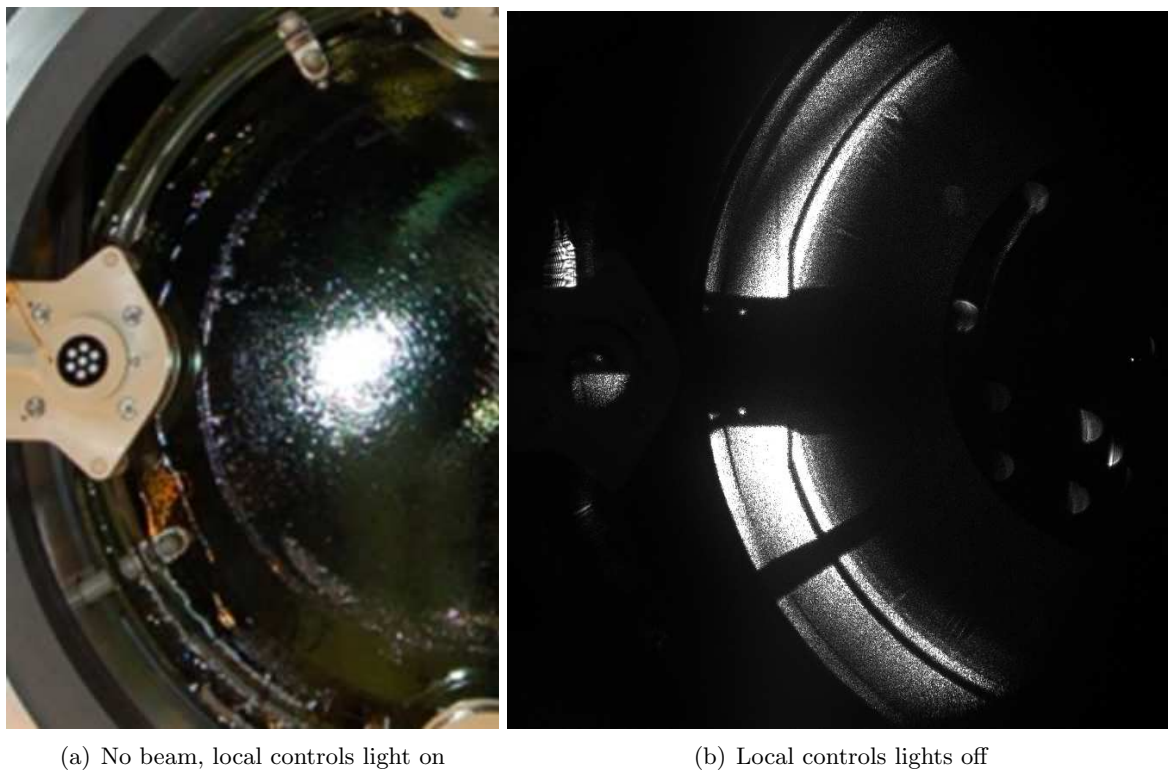


Figure 9.2: Picture of the Virgo+ WE payload taken with lights on during the integration of the payload (left; note that the protecting polymer was not yet removed from the surface of the mirror), and picture of the wall behind the WE payload with lights off while the interferometer is locked (right) which puts in evidence the shadow of the mirror.

9.2.1 Arm cavities

Given the optical design of the **GW** interferometric detectors, the light is mainly lost in the arm cavities. For **AdV**, the power stored in the arms will be 650 kW, and the intra-cavity Round Trip Losses (**RTL**) budget is 70 ppm, leading to 45 W lost in each arm. In this 70 ppm, 50 ppm is budgeted for low spatial frequency figure error of the mirrors (below 10^3 m^{-1}). So, a large amount of the light will be lost at very small angles, meaning just around the coating diameter of the arm cavity mirrors. The rest will be lost in the 3 km vacuum tube.

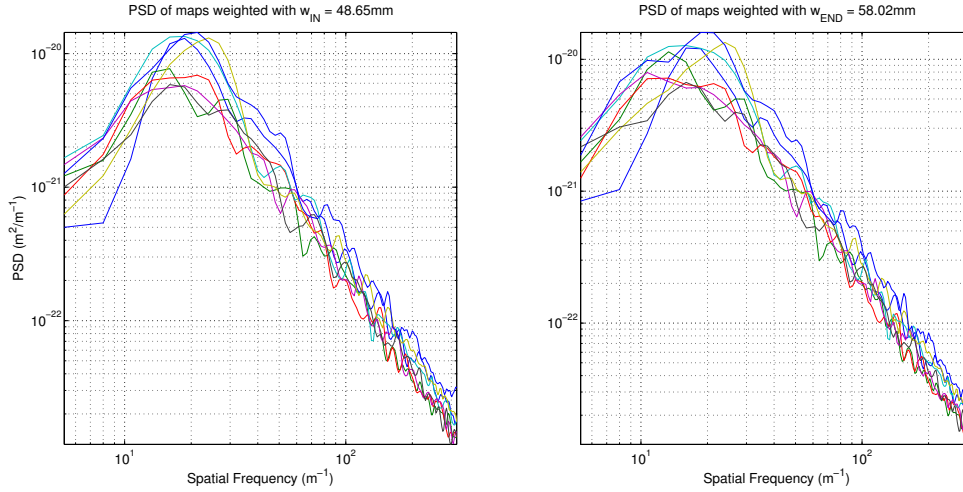
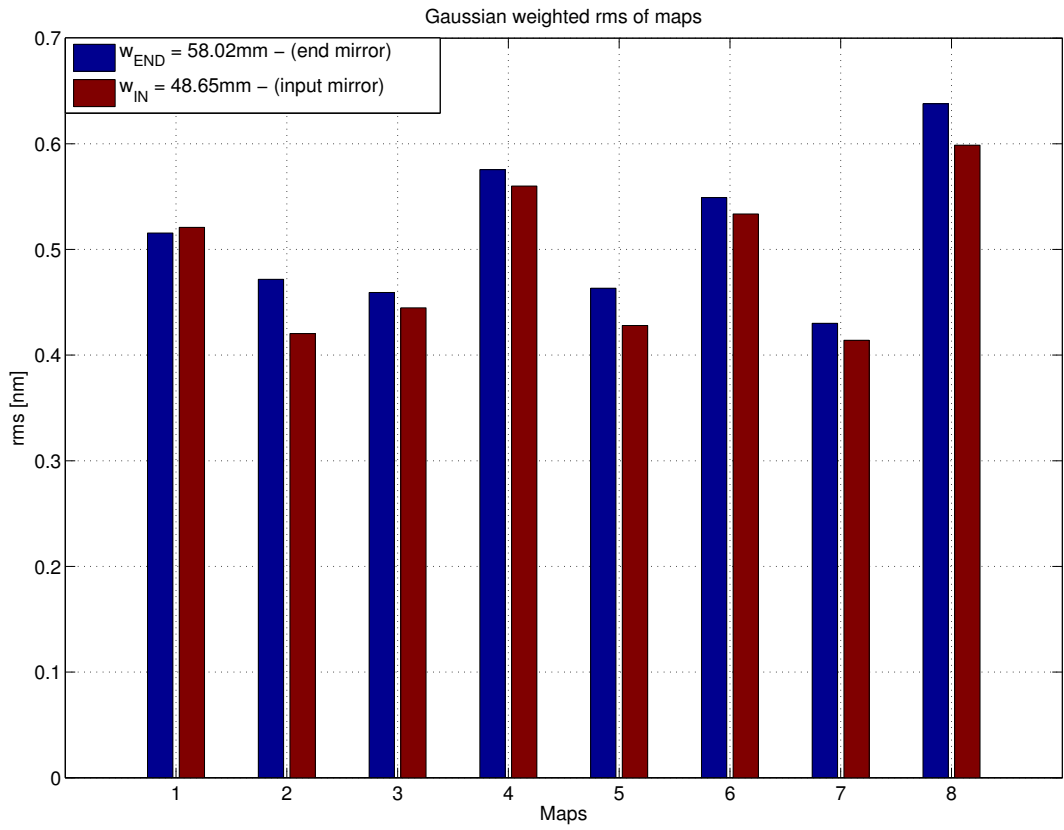


Figure 9.3: PSD of mirror maps used in the simulation campaign, weighted by beam intensity profile on the input mirror (left), and on the end mirror (right).

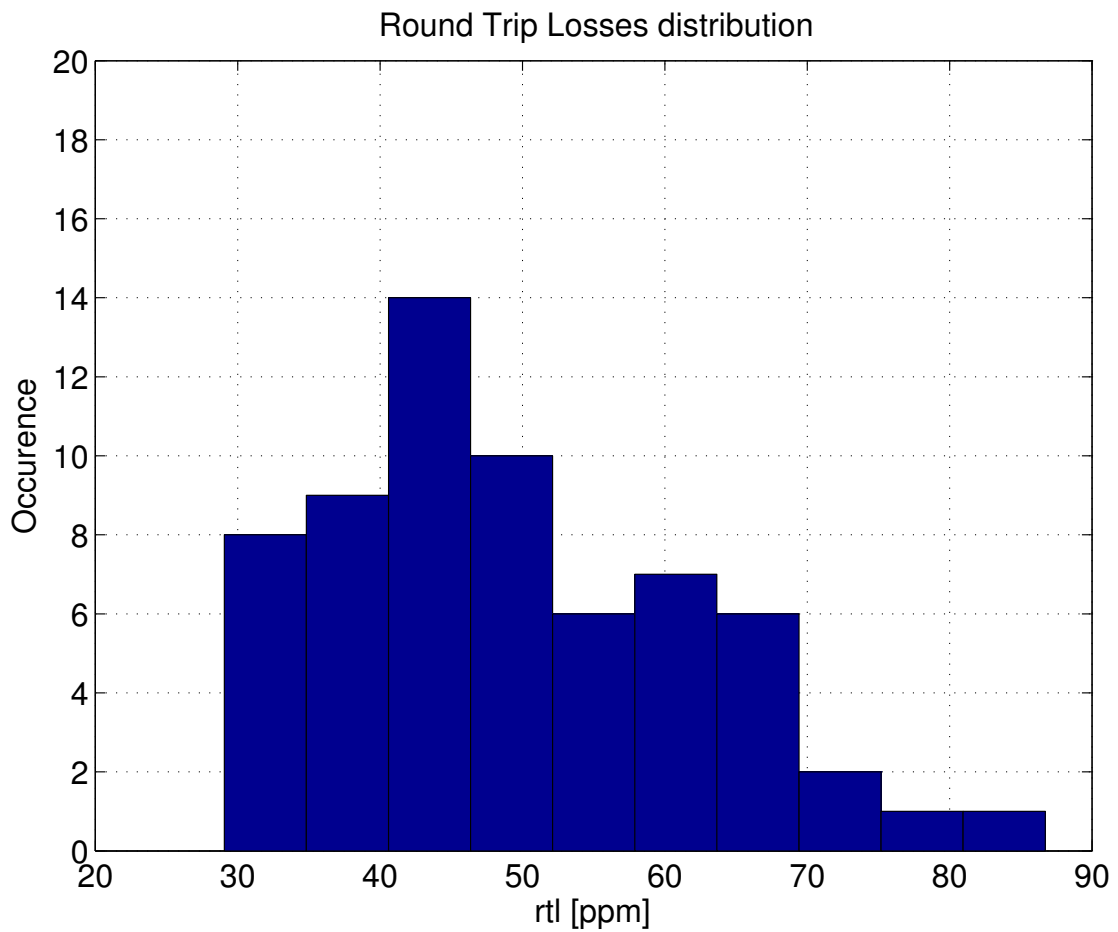
We have used FOG (see Optical Simulation and Design subsystem (**OSD**) chapter) and figure error maps for the mirrors provided by Laboratoire des Matériaux Avancés (**LMA**) to compute the intensity distribution on a virtual baffle with 33 cm internal diameter, located around the mirror. The figure error maps of the mirrors have been pre-processed to remove tilt, piston, and radius of curvature. Those maps feature a **PSD** (see figure 9.3) that is representative of Advanced LIGO core optics, and **LMA** believes that they can achieve such a **PSD** shape by means of the corrective coating. We had eight available maps, and combined them in all the 64 possible associations to simulate the arm **FP** cavity. The maps have a total RMS of about 0.5 nm and give raise to a **RTL** ranging from 30 to 80 ppm (see figure 9.4).

Typical results for the light intensity around the mirrors are given in log-scale (figures 9.5(a) for the input mirror, and 9.5(b) for the end mirror) and linear scale (figure 9.6). Results depend on the map which is used and even on the combination of maps. Figure 9.7 gives some statistics about the total amount of power lost around the input mirror and the output mirror of the arm cavity.

Moreover, it is possible to compute the power density over an annulus (denoted by S_1 in fig.9.8) with $\Delta R = R_{out} - R_{int} = 5 \text{ mm}$, as well as the cumulated power over an annulus (S_2 in fig.9.8) having as inner radius of 165 mm (5 mm less than the coating radius). Both quantities are plotted as a function of the external radius of the annuli. The results are reported in fig.9.9 for the end mirror, and fig.9.10 for the input.



(a)



(b)

Figure 9.4: Characterization of the mirror maps used in the simulation.

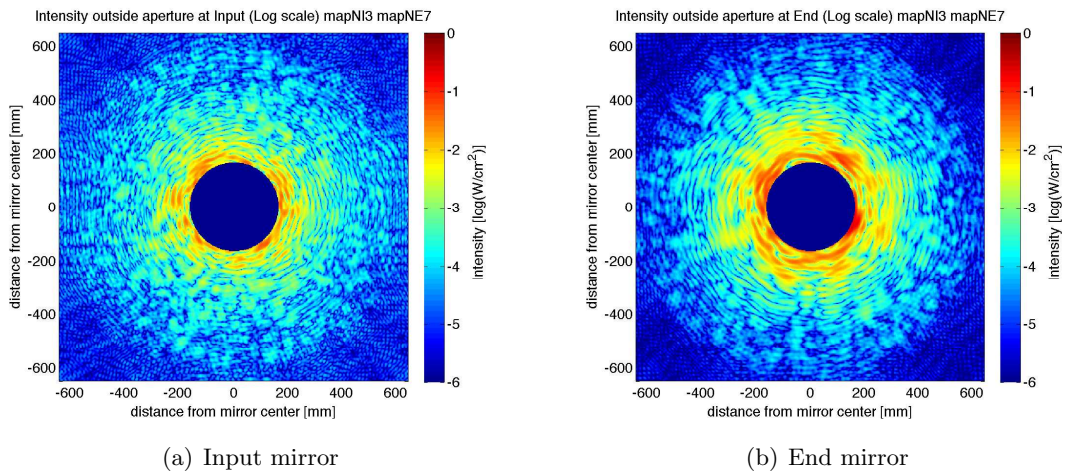


Figure 9.5: Intensity distributions outside the coating area in log scale.

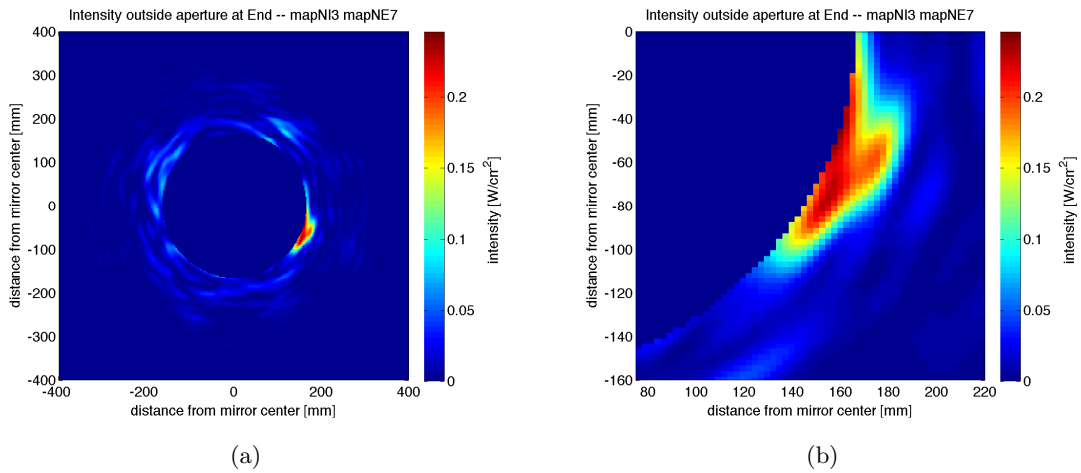


Figure 9.6: Intensity distribution outside the end mirror in linear scale. (a): Intensity distribution on a diameter of 80cm around the end mirror, (b): Detail of hot spot for the intensity distribution.

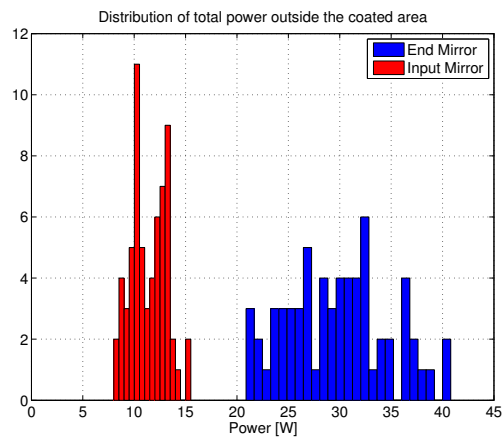


Figure 9.7: Distribution of the power escaping the cavity around the input mirror (red bars) and the end mirror (blue bars) for the various pairs of maps. The power of stray light at the end mirror is about 3 times more than at the input.

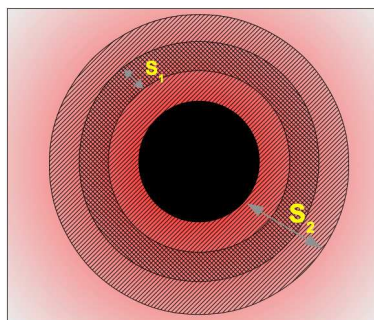


Figure 9.8: Surfaces used to compute average and cumulated intensity distribution in fig.9.9 and 9.10. S_1 : annulus with $\Delta R = R_{out} - R_{int} = 5$ mm, concentric with the mirror. S_2 : annulus with the inner radius equal to 165 mm.

The main results can be summarized as follows:

- **The power lost around the input mirror will be about 12W, and 30W around the end mirror.** The difference is linked to the different beam size on both mirrors.
- **The maximum power intensity around the mirror is 0.25W cm^{-2} .**
- **80 cm external diameter baffles (with 33 cm internal diameter) around input and end mirrors would catch 95 % of the light lost due to low spatial frequency figure errors of the mirrors with 95 % confidence.** An external diameter of 110 cm would be required to catch 99 % of this light with 95 % confidence.

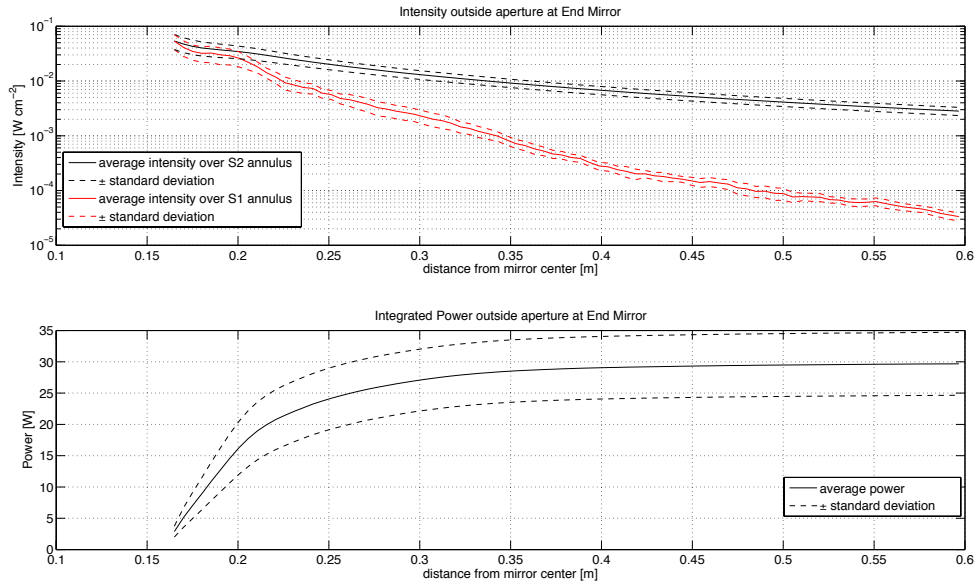


Figure 9.9: Power density distribution and cumulated power over the baffle around the end mirror. Average values and standard deviations computed from the whole simulation data set.

9.2.2 Recycling cavities

A significant amount of power will be lost also in the recycling cavities. The amount of recycled power is 5 kW and the intra-cavity RTL budget is 700 ppm (see OSD chapter) for power lost by scattering and by clipping of secondary beams, leading to 3.5 W of power lost. We will use the results obtained by FOG and Oscar (see OSD chapter) to accurately evaluate the light distribution around each of the core optics in the recycling cavities. We will also use 3D optomechanical simulations to carefully position the necessary baffles in the vacuum links of the recycling cavities dealing with the limited clear aperture of the various elements of the vacuum system such as the cryogenic traps and the valves. Figure 9.11 is an example of the study carried out for the North End (NE) cryogenic trap using Autodesk Inventor [302] (in order to integrate into the simulation the detailed mechanical design), and Zemax [303] (in order to perform Monte-Carlo stray light analysis).

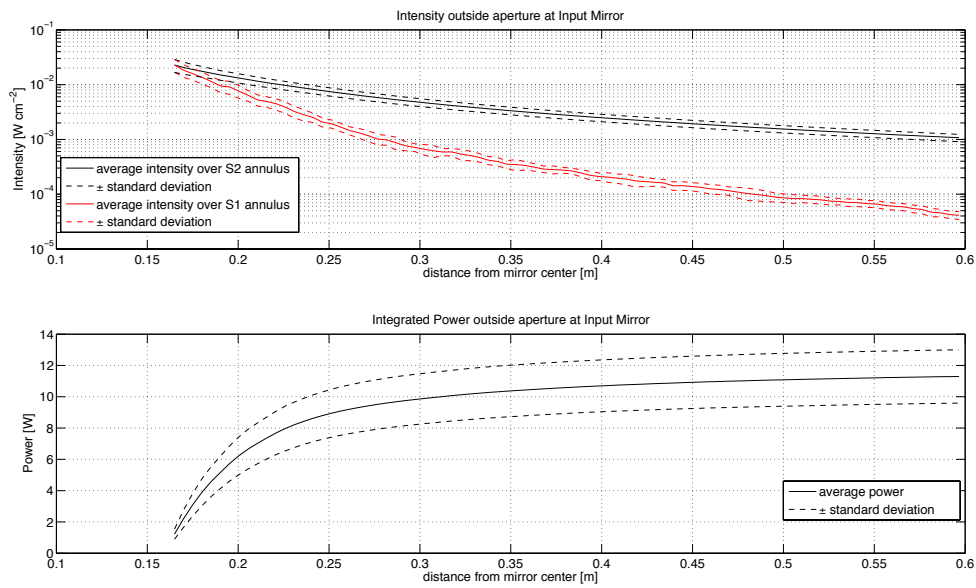


Figure 9.10: Power density distribution and cumulated power over the baffle around the end mirror. Average values and standard deviations computed from the whole simulation data set.

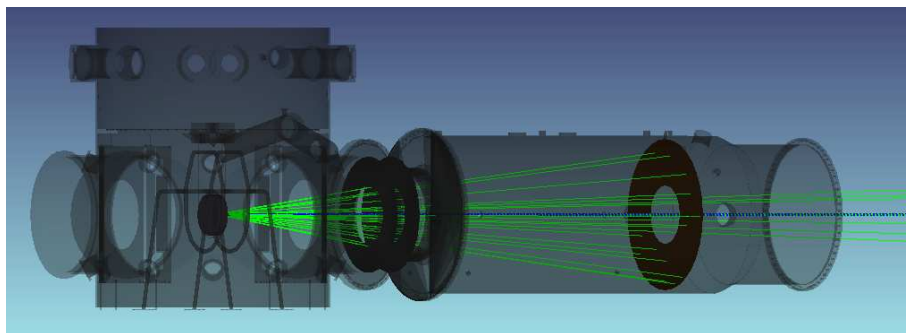


Figure 9.11: Optomechanical study of the baffles for the NE cryogenic trap.

9.3 Subsystem overview

The final system will very likely consist of:

- 16 suspended diaphragm baffles, located around each core optics.
- the 320 baffles that are already installed in the 3 km vacuum tubes.
- about 30 new diaphragm baffles ground-connected in the vacuum links of the recycling cavities and around the cryogenic traps.

The final baffles have obviously to be compliant with noise requirements when the interferometer is in normal working conditions. But two other important features have to be taken into account:

- Some of the baffles will also play the role of "beam parking", for example when Power Recycling (PR) and/or Signal Recycling (SR) mirrors are misaligned for interferometer characterization or lock acquisition purpose,
- The damage threshold of the baffles must be compliant with possible loss of alignment control of any suspended optics.

9.3.1 Suspended baffles

The 16 suspended baffles will be located around all the core optics and attached to the "cage" of the payloads (see PAY chapter). In table 9.1, these baffles with their nomenclature are listed. Figure 9.12 is the optical scheme of AdV including these baffles.

The efficiency of the suspension of the baffles will depend not only on the relative motion between the baffles and the mirrors in the detection bandwidth, but, also, on the amplitude motion at low frequency, due to possible up conversion effects.

9.3.2 Ground connected baffles

9.3.2.1 Baffles in the 3km vacuum tubes

The calculations for scattered light noise in the arm vacuum links were carried out before 1998. There are 2 relevant papers [304, 305], and a Virgo note summarizing calculations and design of these baffles [306]. The arm baffles were designed and constructed in 1998-1999 (see figure 9.13). 160 baffles were installed in each arm during the Virgo construction.

A campaign of measurements was done in 2007 in order to check the performance of these baffles. This was done by shaking the middle of the arm vacuum link and the extremity of the arm vacuum link while the interferometer was fully locked [307]. No extra noise could be seen in the Virgo sensitivity. An upper limit of the noise projection onto the sensitivity has been deduced from these measurements (see figure 9.14). This upper limit is at the level of the AdV sensitivity. The theoretical value for the noise projection, calculated from [306], is compliant with the AdV sensitivity (at least 100 times below the AdV sensitivity).

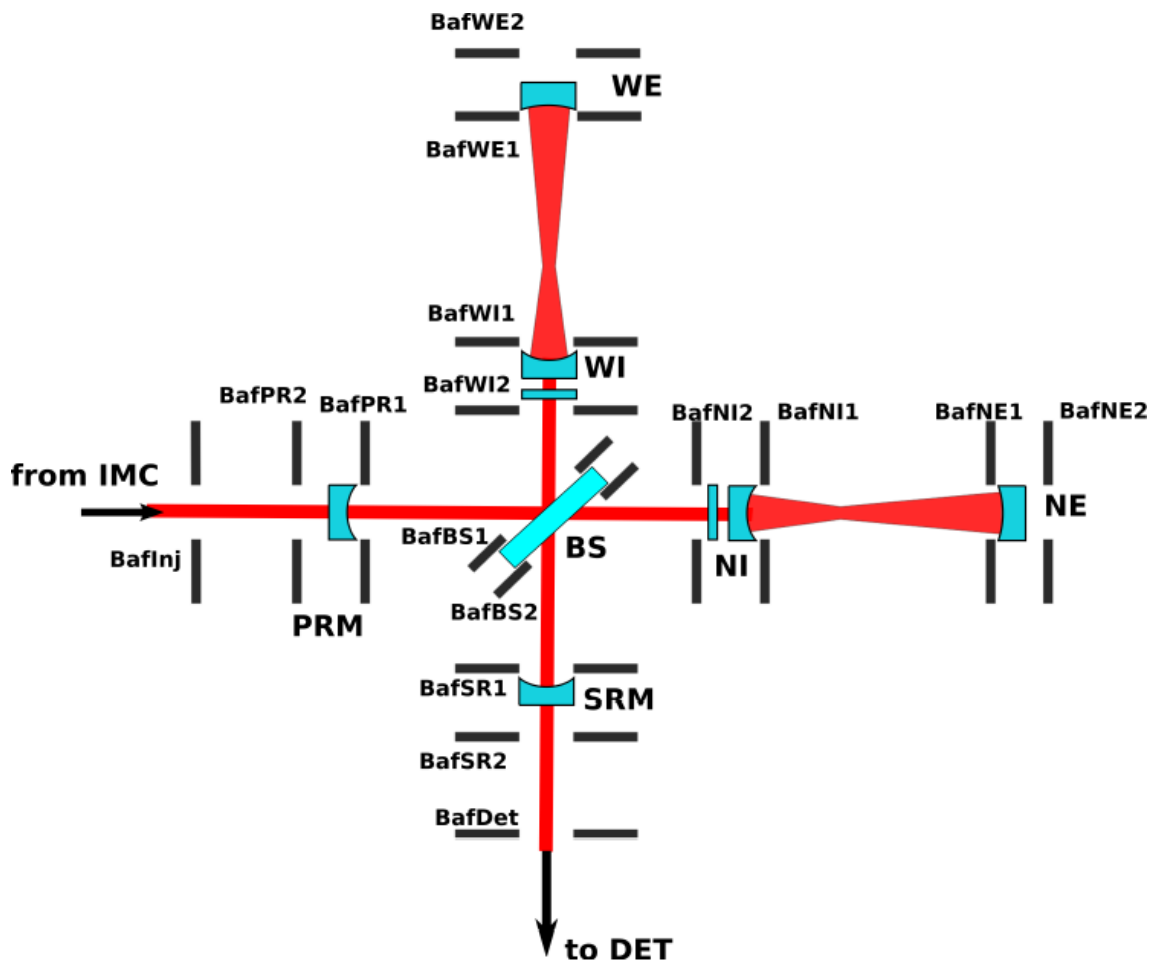
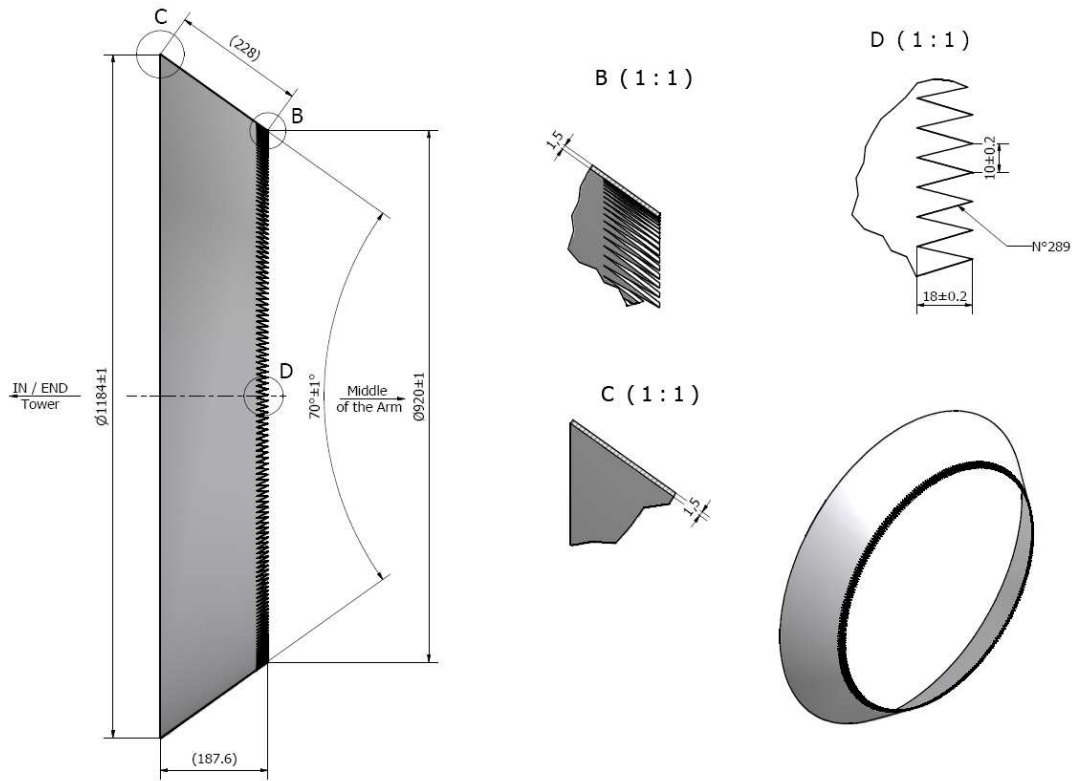
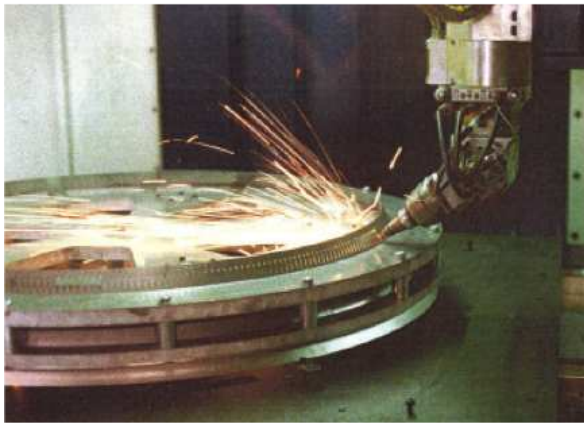


Figure 9.12: Layout of the baffles suspended to the Super Attenuators.



(a) Design



(b) Construction



(c) Inspection

Figure 9.13: Arm baffles are truncated cones made of stainless steel with sharp teeth (left). They have been constructed by laser machining (center). They have been carefully inspected before installation into the arm tubes (right).

| Baffle name | Position |
|-------------|-------------------------------------|
| BafInj | Meniscus of the input telescope |
| BafDet | Meniscus of the detection telescope |
| BafPR1 | PR mirror, HR coated face |
| BafPR2 | PR mirror, AR coated face |
| BafSR1 | SR mirror, HR coated face |
| BafSR2 | SR mirror, AR coated face |
| BafBS1 | BS, semi-reflective coated face |
| BafBS2 | BS, AR coated face |
| BafNI1 | NI mirror, HR coated face |
| BafNI2 | NI mirror, AR coated face |
| BafWI1 | WI mirror, HR coated face |
| BafWI2 | WI mirror, AR coated face |
| BafNE1 | NE mirror, HR coated face |
| BafNE2 | NE mirror, AR coated face |
| BafWE1 | WE mirror, HR coated face |
| BafWE2 | WE mirror, AR coated face |

Table 9.1: List of suspended baffles and nomenclature.

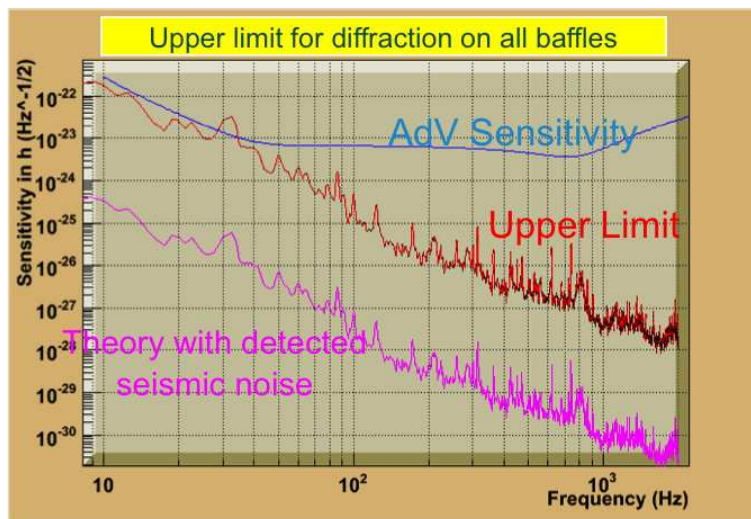


Figure 9.14: Theoretical arm baffle scattered light noise projection and upper limit deduced from measurements done in 2007.

9.3.2.2 Baffles in the other vacuum links

Some of the Virgo baffles will be re-used when possible. At this stage of the design study, there are no detailed plans for the location of these baffles. They will be installed in all links between the towers. The number of new baffles to be installed has been estimated at 30. However, some preliminary studies have already been carried out using Zemax to deal with the light which is backreflected and backscattered from the optics of the input telescope [308]. Indeed, it is important to properly define the position and size of the baffles to mask the links. An example of baffling between PR mirror and INJ tower is given on figure 9.15.

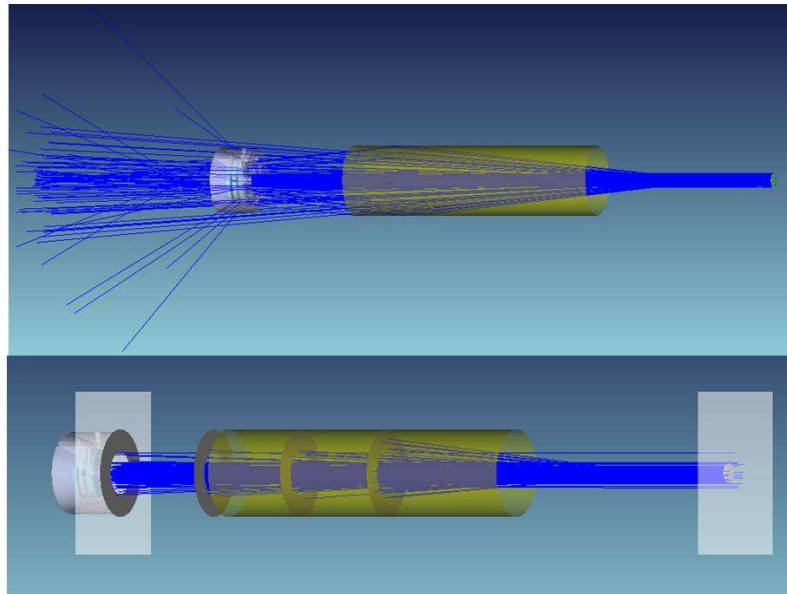


Figure 9.15: Study of baffling of scattered and backreflected light going out of the clear aperture of the optics.

9.4 Path to baffle requirements definition

The baffles are obviously the deliverables of the subsystem. At this stage, we will just provide the list of specifications to be delivered for the construction of the baffles.

The main specifications to be given are:

- Damage threshold,
- External and internal diameter of the baffles,
- Position of the baffles,
- Roughness and reflectivity of the baffles,
- Edge geometry of the baffles (sharp angles!).

The specifications will be derived from the calculation of the requirements. The current method, partially completed, used to compute the requirements consists in 4 steps:

- Use FOG to compute the distribution of the light outside of the coating diameter,
- Use FOG and/or an analytical model to compute how much light from the baffles is then recoupled to the fundamental mode of the interferometer (assuming a Lambertian distribution of the light scattered by the baffles for relevant angles),
- Use Optickle [309] to compute the Transfer Function between baffle motion and power fluctuation on the dark fringe,
- Projection of the noise assuming the specified motion of the various baffles (suspended or ground-connected) by using the model, which has been verified during the Virgo commissioning.

The minimum outer diameter of the suspended baffles, as well as the minimum inner diameter of the ground connected baffles will be defined after making a trade-off study between the various constraints for meeting the required specifications. If the backscattered/reflected light, combined with the residual motion of the baffle, induces too much noise, then either the scattering or the residual motion of the baffle have to be reduced. In order to decrease the amount of scattered light, the quality of the polishing can be improved, whereas suspending the baffle reduces the residual relative motion between the baffle and the core optics.

9.5 Baffle preliminary design study

We describe here the most probable materials that will be used for the construction of the baffles, and the tests that have been done to validate these materials.

The important properties of these materials are: the absorption, the high vacuum compatibility, the roughness, and the possibility to deposit an AR coating. It is also important to state if they are good or bad electrical insulators for avoiding charging issues as well as Eddy current which could affect the mirror position if the baffles are located close to them.

The roughness of the materials is characterized to a first approximation by measuring the Total Integrated Scattering (TIS). This is a good figure of merit in particular for large angle scattering which will be the case for the baffles in the arm cavities since they will be tilted by 3 degrees, and for the baffles in the recycling cavities which will be at normal incidence with respect to the optical axis.

In the following we discuss the different materials available.

9.5.1 Absorbing glass

As in Virgo, we will use absorbing glass there where the required damage threshold is low (well below 1 W cm^{-2}). This glass is highly absorbing ($T = 10^{-7}$ with 3.2 mm thickness) and AR coated ($4 \cdot 10^{-3} < R < 10^{-2}$ depending on angle of incidence). We still have many spare baffles, and about 10 plates of more than 1 m^2 ready to be cut.

9.5.2 Silicon Carbide

Silicon Carbide (**SiC**) is an interesting material for which the absorption is very high (so high that we could not measure the transmission of a 10 mm thick sample) and the damage threshold is high. A damage threshold of 30 kW cm^{-2} has been measured in air (5 times more than Silicon), thanks to its high thermal conductivity. Specific shapes are easy to process and there is no problem to add an **AR** coating. We have already used **SiC** in Virgo+ as detection diaphragm baffles (see picture 9.16).

Due the specific process for fabricating **SiC** objects, and because of its hardness, it is however not straightforward to get a low roughness. This requires the deposition of a layer of CVD **SiC** before polishing. We have tested the entire process of fabrication with small samples and measured a low **TIS** of about 50 ppm. The outgassing of the material is still to be measured but is not really a concern.

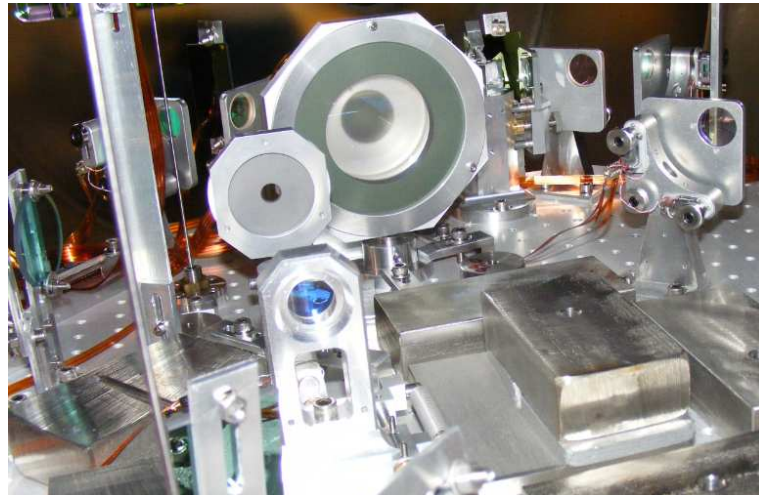


Figure 9.16: **SiC** baffles installed on the suspended detection bench in Virgo+.

9.5.3 DLC

Diamond-Like Carbon (**DLC**) is suitable as large area coating for dumping light in vacuum chambers thanks to its low outgassing and high absorption properties [311]. The **LMA** has a long experience in depositing **DLC** coatings. They recently deposited a $1 \mu\text{m}$ thin film on a glass substrate and the absorption was measured to be 40 % at 1064 nm. A coating $13 \mu\text{m}$ thick would therefore be enough to absorb 99.9% of the light (see figure 9.17). The **TIS** has still to be measured.

9.5.4 Oxidized stainless steel

Many baffles in Advanced LIGO, in particular the ones around the **FP** arm cavity mirrors, are made of oxidized stainless steel with a V shape [312]. This appeared to be more appropriate than porcelainized enameling steel because the first fabricated baffle exhibited a significant amount of shedding of the porcelain surface at critical locations [313]. However, this solution

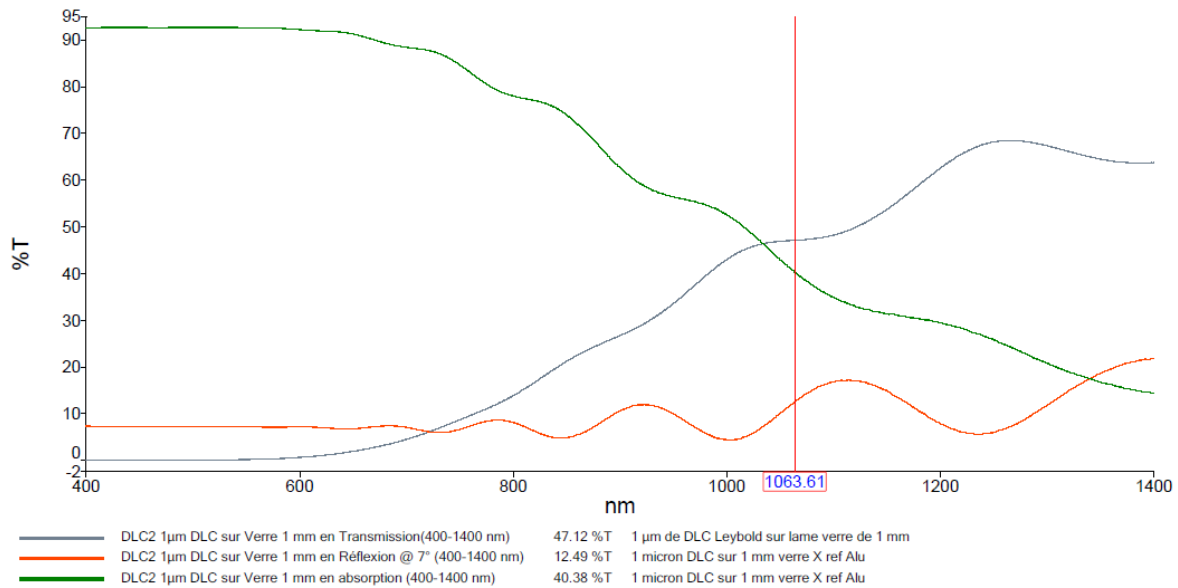


Figure 9.17: Measurement of the absorption of a $1 \mu\text{m}$ thick DLC layer done by LMA.

requires more room inside the vacuum chamber because of its specific geometry as several reflections are necessary in order to absorb the light. It would therefore further constrain many other subsystems in AdV. As a consequence, this is not the preferred solution at this stage.

9.6 Interfaces with other subsystems

There is a large number of interfaces with other subsystems to deal with. Here is a non-exhaustive list of issues that have been identified until now and are under discussion with the other relevant subsystems:

- the weight of the suspended baffles has to be lower than 10 kg (interaction with PAY),
- the frequency of the internal mechanical modes of the suspended baffles has to be higher than 100 Hz (interaction with PAY and OSD),
- the suspended baffles have to be attached to the "cage" of the payloads in an appropriate manner, and will be integrated into the payload only once the payload will be in the vacuum chamber (interaction with PAY),
- the mirror Local Control (LC), Thermal Compensation System subsystem (TCS), and photon calibration systems require a certain clearance for their numerous lasers (interaction with PAY, TCS and Data Acquisition (DAQ)),
- the baffle design has to be compliant with the possibility to misalign the Compensation Plate (CP) (interaction with PAY and OSD),
- the required dynamical range for the misalignment of the mirrors, for lock acquisition or interferometer characterization purpose, taking into account "beam parking" issues, has to be communicated to PAY,

- the position and geometry of the ground-connected baffles are clearly constrained by the clear aperture of the vacuum links (400 mm between towers, 240 mm between interferometer and input/output optics) in the central area, and, cryogenic trap bellows (700 mm) and valves (650 mm) in the tubes (interaction with **VAC**).

9.7 Path to design completion and construction

Here is the list of the main milestones:

- May 2012: delivery of the "SLC final requirements" document; the document will contain all details about the calculations and optical simulations carried out to set the baffle requirements in term of damage threshold, roughness, reflectivity and geometry.
- July 2012: verification of the design of the cryogenic trap and link clear apertures; the compatibility of these elements with SLC requirements will be verified; possible change requests will be delivered.
- September 2012: delivery of the "SLC design study" document; the document will contain all details about the optical and mechanical modeling analysis and measurements carried out, as well as the final trade-off leading to the material and design choices: vacuum compatibility tests, TIS and Bidirectional Reflectance Distribution Function (BRDF) measurements, finite element analysis of the baffles, realistic assessment of the baffle motion with respect to the mirrors, damage threshold measurements, constraints and limitations due to industrial process.
- November 2012: delivery of a document defining all critical interfaces with PAY: weight of the suspended baffles, mechanical interface, detailed geometry, and all other relevant parameters.
- December 2012: delivery of the "SLC Technical Design Report (TDR)" document; the document will contain the final design of the various baffles as well as a clear construction plan and integration procedures.

Chapter 10

Payloads (PAY)

10.1 Last Stage Suspension: introduction

The payload is the last stage of the mirror suspension, located in the lower part of the tower in a dedicated Ultra-High Vacuum (**UHV**) chamber. The role of the last stage suspension is to compensate the residual seismic noise and to steer the optical components maintaining the relative position of the interferometer mirrors. Up to now, the typical configuration of these suspensions both in Virgo and in Virgo+ was essentially a double stage branched system with the so called marionette as first pendulum, and as branches, the recoil mass and the mirror both suspended from it with wires of steel (in Virgo) or of fused silica (in Virgo+). The position of the mirror was controlled by two sets of coil-magnet actuators, one set between the Filter 7 (**F7**) and the marionette and the other between the reaction mass and the mirror. The experience we had with these configurations suggested us to revise the basic configuration of the payload, passing from the branched system to a new configuration where the filter 7 supports not only the coils to act on the marionette, but also those that act on the mirror: the Actuator Cage (**ACA**). In this way, we simplify the payload taking out the recoil mass. In the following we shall detail the reasons of this choice and apply the new configuration to the design of the AdV mirror payloads.

10.1.1 Main features and general requirements

In **Table 10.1** we report the main features of the mirrors to be suspended in AdV. The weight of the test mass mirrors is doubled with respect to Virgo, while the diameter of the beam splitter has increased from 280 mm to 550 mm. Moreover, many new items must be suspended and aligned around the mirrors: the thermal compensation system requires (see Section 6) that a Compensation Plate (**CP**), 350 mm in diameter, and 30 mm thickness, be located at 20 cm from the rear surface of input mirrors. Near the power recycling a Pickoff Plate (**POP**), with size similar to the CP, must be suspended. Moreover, the necessity to mitigate diffused light requires the presence of baffles as large as about 1 m close to the front and the rear faces of each mirror. Other elements to be inserted are several Ring Heaters (**RHs**) (see chapter 6), to be positioned close to mirrors, that will be used as a further tool to adjust the optical parameters of the interferometer. They will be supported by the **ACA**, that will conceptually

| Payload | Mirror Size $\text{\O} \times \text{Thickness (mm)}$ | Susp. Type | Add. Elements |
|---------|---|-------------|---------------------------|
| NI | 350×200 | Monolithic | Large Baffle (LB), CP, RH |
| WI | 350×200 | Monolithic | LB, CP, RH |
| NE | 350×200 | Monolithic | LB, RH |
| WE | 350×200 | Monolithic | LB, RH |
| BS | 550×65 | Steel wires | LB |
| PR | 350×100 | Steel wires | RH, POP, LB |
| SR | 350×100 | Steel wires | RH, LB |

Table 10.1: Main features of the payloads in Adv: NI, WI, NE, NE, BS PR and SR.

ensure a reduced thermal budget with respect to the mirror reaction mass case adopted so far. Indeed, being suspended by steel wires, the recoil mass is almost thermally insulated from the external world, and unwanted heating effects are more difficult to avoid. In any case, the RHs will be thermally insulated from the ACA, but any residual heat flow will be efficiently sunk by the ACA mass, thermally anchored to the filter 7. Finally, monolithic suspensions must be implemented on all test mass mirrors.

10.1.1.1 Cleanliness and vacuum compatibility

Our past experience in the design and assembly of UHV compatible and cleanliness compatible payloads will be our guide also in the design of the new payloads. No major issues are foreseen in the design, concerning vacuum compatibility: we shall use only materials suitable for UHV operation, and test them, in any case, in the vacuum test facility for materials.

To be sure that we insert a clean payload in a clean tower, all operations must be at the same level of cleanliness, starting from the assembly of the payload, until its integration with the superattenuator. This *cleanliness chain* has been refined and verified since the beginning of Virgo, and is now working in a satisfactory way: during the assembly of the monolithic payloads in Virgo+ we recorded a class 100 pollution while assembling the payload, going down to class 1 as human operations stopped [314]. Inside the towers, a class 1 - 10 is usually measured if no operation is underway. However, as a further check, we propose to leave inside each tower some small mirrors, with the same high reflectivity coating of Adv mirrors, on a vertical mount and as close to the real mirror as possible. These small mirrors will be a reference that will be studied, even with destructive techniques, if a degradation of the performance of the mirrors is observed.

We plan to use the central building clean room to assemble the payloads that have steel wires suspensions, i.e. the beam splitter, the power recycling and the signal recycling. The test mass payloads, with monolithic suspensions will be assembled in the 1500 west hall clean room.

10.1.1.2 Geometric constraints and requirements

The new concept is that of a single actuation frame. A rigid cage is clamped on two **F7** legs, and it is used to actuate on both marionette and mirror. The design relies on the possibility of modifying accordingly both the vacuum environment and the **F7** (see chapters 13,11). We started to apply the new configuration in the design of the beam splitter, that embeds the main concept of the **F7** actuation case. The design is complete and soon a prototype for tests will be produced. The development of the **BS** provides the general guidelines for designing the other payloads. Moreover, the design of the new elements for the **BS**, marionette and cage, is used in the design of the all other new payloads. The advantages that will follow through this line are:

- possibility to hold **LB**ss and other components around the mirrors;
- removal of the reaction mass and consequently the absence of differential modes involving the mirror;
- larger room to assemble large optics (such as the beam splitter).

In order to reach the aims above without an unreasonable complication of the system and in order to exploit at the best the available room in Virgo vacuum chambers we adopted two main concepts:

- I a rigid mechanical mount for the optics elements around the mirror;
- II a self-supporting **ACA** which is a single structure and has to serve as a part of the payload assembly frame as well as a safety structure during the operation.

It is important to figure out which are the main implications that must be kept in mind while designing the payload and what are the aspects of the strategy that can be expectedly dealt with later.

The role of the marionette system will still be the same as in the original payload actuated from **F7** coils, hence the angular control of the mirror benefits of the simple double-pendulum transfer function. However, what matters is the effect of the actuation-cage RMS displacement caused by the recoil of the locking force. Such a recoil is modest, since its magnitude is that of the seismic fluctuation reaching the payload, attenuated by the Superattenuator (**SA**), and consequently corrected by the lock, but that implies a position fluctuation of the optical objects surrounding the mirror. For both the baffle and the plate the impact of the **ACA** motion on the residual diffused light produces a demand on the optical requirements of those components. In Sec. 10.3.3 the order of magnitude of RMS displacement of the **CP** mounted on input mirror actuator-cages, is evaluated, but a much more detailed (spectral) evaluation is being performed in order to accurately define the absorption requirement of baffles and other elements mounted on the **ACA** as the prototype design for the test-mass payload will be frozen. Mechanical dynamics issues related to the new design have been considered in order to figure out some aspects of the control that are related to the mechanical design.

In Fig. 10.1 a simulation of the recoil on the actuation cage is shown. In principle, due to the single-wire suspension of the marionette, no effect due to the swinging of the structure reaches the mirror. This behavior has been verified also in Virgo, where the swing of **F7** is not seen by the ITF. However, before the system is locked and its signal re-allocated to the marionette wire suspension point, **F7** pitch control from ground will be necessary to reduce the swing

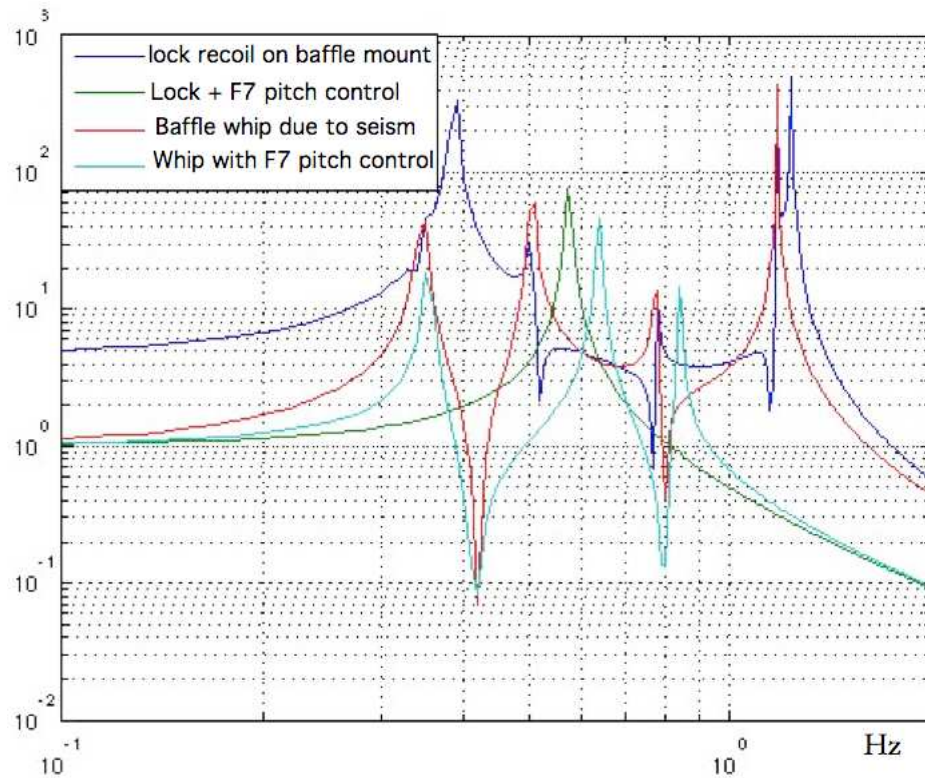


Figure 10.1: The plots show displacement TF from ground and the lowest part of the cage. The net effect (red) is increased by lock recoil (blue), but the whip is strongly reduced by F7 pitch control in absence (cyan) as well as in presence (green) of lock.

| | Marionette Force [mN/A] (Opt. gap [m]) | Marionette Force [mN/A] (Opt. gap [m]) |
|--------------------|--|--|
| Old payload | 2.8 (0.045) | 2.8 (0.015) |
| New payload | 2.5 (0.030) | 0.6 (0.010) |

Table 10.2: Actuator table along longitudinal **DOF** (z): here, smaller magnets 1.5 mm \times 1.5 mm-diameter magnets are considered for the mirror. The gap is meant as the optimal working distance between coil and magnet centres. For the marionette the optimal distance can be reduced safely thanks to the absence mechanical layer (**IVC** separation) in the gap. Coil size reduction is needed for AdV mirror actuators due to the larger size of the beams, hence the actuator cage will be equipped with suitable stops to prevent mirror damage during torsional large oscillations.

of the **ACA** at the same level of the swing of the mirror, enhanced by the mechanical gain of a 2-meter-long structure. Expectedly, it turns out that the removal of the reaction mass implies the need of a careful locking force reallocation to **F7** actuators. Suitable strategies will then be defined within the suspension control context. Coil-magnet actuators have been chosen in order to allow forces similar to those of Virgo+. Provided that the coils are 8, it is also possible to reduce the number of turns and the magnets volume: in order to have the 20 mN/A we shall use 1T magnets, 8 mm in diameter and 4 mm thick. The new marionette system equipped with a full set of actuators, together with the absence of the reaction-mass, allows to avoid the problem arisen in Virgo as the roll bouncing of the mirrors on fused silica fibres, with high quality factor, used to delay the recovery of locking. Roll sensing by optical levers and marionette actuation serve to damp that mode. Common (vertical) bouncing on fibres will be avoided by optimizing sensing and control optimization similarly to what done in Virgo.

In Virgo+ the coils acting on the mirror provide 2.5 mN/A using 1 T magnets with diameter 2.5 mm by 2.5 mm thickness. As in Virgo+, all the magnets of AdV will be Sm₂Co₁₇. Remarkably, the volume of the magnets acting on the mirror can be even significantly smaller [315]: according to the firm which usually provides the magnets for Virgo, magnets as small as 1.5 mm thick 1.5 mm diameter can be produced. In this way, the magnetic moment is reduced by a factor 5, allowing a significant reduction of environmental electromagnetic impact on the sensitivity (10.2),10.2. In order to apply on the mirror such small magnets, they will be included in silica caps bonded by silicate bonding to the mirror substrates.

10.1.1.3 Pre-alignment requirements

The main pre-alignment requirements for AdV will be similar to those of Virgo+. A ground-based local control read-out will be used to drive the motion of the suspended elements of AdV within the linear range of the global control signals. Once this result is achieved, the low-noise control strategy, meant to reach AdV sensitivity, will be applied using a set of actuators acting mainly within the suspension system [316].

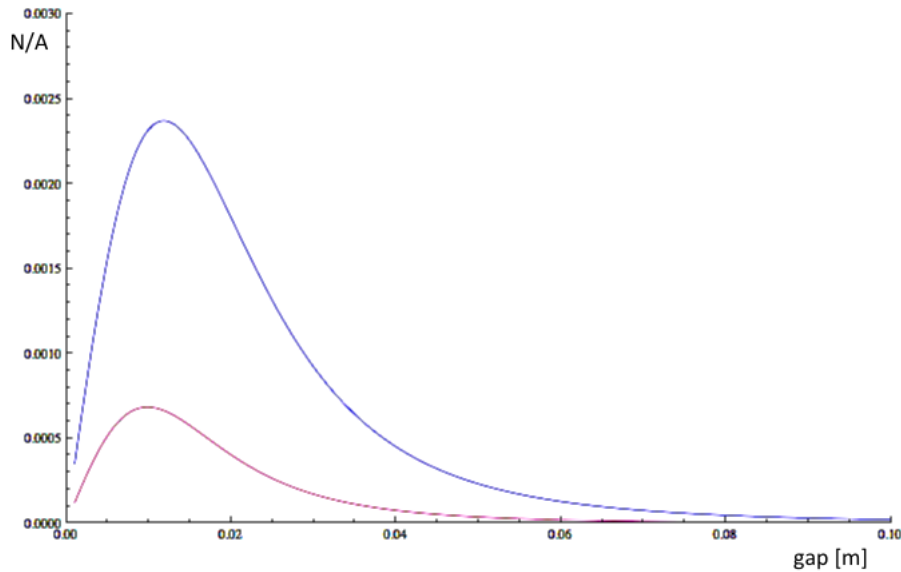


Figure 10.2: Force provided by a single mirror actuator attached to the cage: blue (Virgo+), red (AdV). The shape of mirror coils is such as to provide a smoother range of linearity.

10.1.1.4 Optical local control system

AdV local controls will still make use of optical levers but no coarse mode will be available. Misaligning the recycling mirror by several milliradians (e.g. 8 mrad) is common practice during commissioning. Even though this action can be performed under control using coarse error signals, it has turned out that there is no need to damp the payload and that it is much more convenient to leave the payload in open-loop and apply slowly (e.g. 60 s) a calibrated DC torque (θ_y) ramp. In the last five years we operated Virgo in this way. In case of shocks occurring through the SA, due to mistakes or malfunctioning of the suspension, large oscillations ($\theta > \pm 6$ mrad) will be slowed down by viscous damping, obtained with a suitable elaboration of the signal of an optical lever as it passes on the Position Sensing Device (POSD). That means that the system must be properly pre-aligned within a few milliradians. In the new system, Superluminescent Diode (SLED) technology will be adopted in order to provide better robustness and power adjustment. 2 mW IR SLED Optical Lever (OL) system (Qphotonics) with a single source and optical splitter connected to Single-Mode (SM) fibers has been tested in the Virgo NE payload control [317], Fig. 10.3. A selection among possible diodes in the visible range will be done in 2012. As it will be shown in Sec. 10.2.4, since no branched pendulum suspensions will be present, no differential modes will appear in the mirror. Considering the pendulum modes along z and x , the mode associated to the coupling of the last stage pendulum with the suspension chain will be seen as a mode of the suspension and consequently damped by the inertial damping. The motion angular DOF appearing in the payload will be fully read-out by the optical levers of the marionette Local Control (LC). Thus, in principle no local control sensing would be necessary at the mirror level, but we

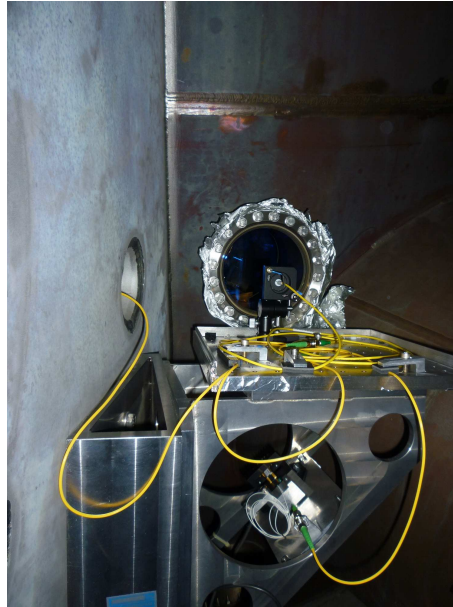


Figure 10.3: Test of LC using SLED source at Virgo NE suspension. Single-mode fibers serve both marionette and mirror optical levers, through a fiber splitter.

prefer to keep using it in order to ensure redundancy in alignment monitoring and the direct read-out of test mass positions. The complete set of the optical levers is summarized in Table 10.3. In order to avoid conversion of chain mode excitation during the microseism into angular modes of the payload, the Center of Mass (COM) of all AdV marionettes, as for Virgo+ test mass payloads, will be adjusted within 1-2 mm to the wire bending point $\lambda = \frac{d^2}{8} \sqrt{\frac{\pi Y}{T}}$ (d and Y are the thickness and the Young modulus).

Hence common modes of pitch and yaw will appear around 200 mHz, below the microseismic bump. That kind of setup makes the payload quite soft and both motorized balance and active control along θ_z (roll) are required. Differently with respect to Virgo+ test mass payloads, whose transversal motion was read-out through the reaction-mass, in AdV the marionette position will be monitored by means of a dedicated mirror below the marionette. Moreover, a further OL will be used to directly monitor the optical plates close the mirror, attached to the cage, i.e. the CP (for NI and WI) and the POP (for PR).

10.2 The beam splitter payload: features and solutions exportable to other suspensions.

The AdV beam splitter payload is peculiar because the shape of the IVC of Virgo, surrounding the coil holders attached to F7 by means of large cylindrical enclosures, would prevent the installation of a mirror suspension with vertical wires. In fact the distance between the walls of the such enclosures is 428 mm, preventing the installation of a marionette meant to suspend a 550 mm diameter substrate. This fact suggested to move the separation between UHV and the High Vacuum (HV) regions of the suspension tower upwards, above the F7. According to this design the last filter of the chain will be in the UHV region. This change in the inner

| Tower | Marionette DOF/Beams | Mirror DOF/Beams | SLEDS/Beams | Viewport | Signals |
|--------------|------------------------------------|---|--------------|---|---------|
| PR | $\theta_x, \theta_y, \theta_z / 2$ | $z, \theta_x, \theta_y,$ θ_x, θ_y (F7:POP) /2 | 2/4 | NUE,NDW SUE,SUW SDW** (WUN,WDS)* | 8 |
| BS | $\theta_x, \theta_y, \theta_z / 2$ | $z, \theta_x, \theta_y, / 1$ | 2/3 | SUW,WDS EUN,NUE | 6 |
| NI | $\theta_x, \theta_y, \theta_z / 2$ | $z, \theta_x, \theta_y,$ θ_x, θ_y (F7:CP) /2 | 2/4 | SUE,SUW NUE,NDW SDW** (WUN,WDS)* | 8 |
| NE | $\theta_x, \theta_y, \theta_z / 2$ | $z, \theta_x, \theta_y, / 1$ θ_x, θ_y (F7:DL) /2 | 2/3 | SUW,SDE NUW,NUE (EUS,EDN)* | 6 |
| WI | $\theta_x, \theta_y, \theta_z / 2$ | $z, \theta_x, \theta_y,$ θ_x, θ_y (F7:CP) /2 | 2/4 | WUN,WDS EUS,EUN EDS** (NDE,NUW)* | 8 |
| WE | $\theta_x, \theta_y, \theta_z / 2$ | $z, \theta_x, \theta_y, / 1$ | 2/3 | EUS,EDN WUN,WUS (SDW,SUE)* | 6 |
| SR | $\theta_x, \theta_y, \theta_z / 2$ | $z, \theta_x, \theta_y,$ θ_x, θ_y (F7:POP) /2 | 2/4 | WUN,WDS EUN,EUN EDS** (SUW,SDE)* | 8 |
| Total | | | 14/25 | 44 (32) | 50 |

Table 10.3: Optical windows identified for LC. In the second and third columns are reported the degrees of freedom controlled and the number of beams, respectively, for the marionette and for the mirror. In the fourth column, the number of SLED sources and the numbers of fiber optic splitters is given. The viewports are coded using location initials (e.g. NUE= North tower base side; U= Up location; E= East corner). Viewports labeled as ** are presently not used by the LC system but their use is needed for direct monitoring the CP and POP, while those labeled as * will not be used if transversal OL will monitor the marionette; however, they cannot be deallocated until the payload prototypes are ready.

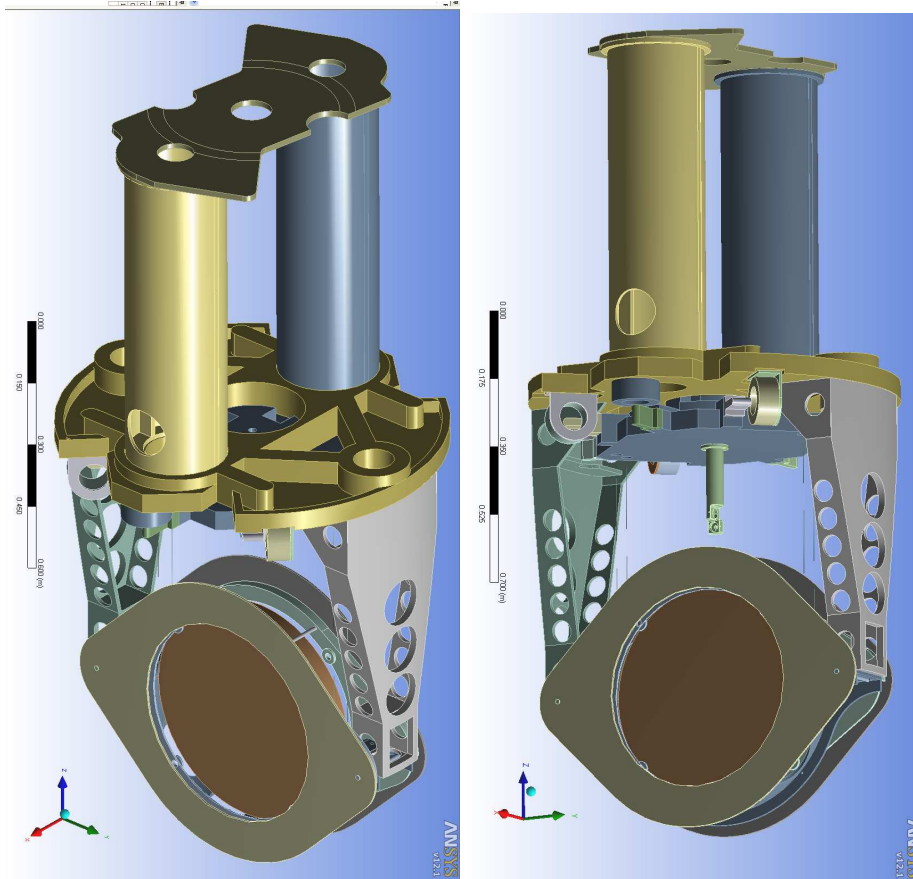


Figure 10.4: Scheme of BS payload.

design of the tower is addressed elsewhere (see chapter 11). In order to limit the impact of the change, the IVC will remain in place (unused), two legs meant for yaw and longitudinal control of the marionette will be removed as well as all the IVC separation enclosures. In the new marionette a set of coils will be installed on a round shaped holder. The two shafts that in Virgo are used to hold pitch coils will be modified and used to keep rigidly the coil holder. In principle, 6 coils are enough to perform a 6 DOF control of new payloads. In the specific case of the BS, due to the large diameter of the substrate and due to the symmetry constrained by the two shafts that remain from the old set up, we keep some redundancy by adopting a symmetric shape with 8 coils. In Fig. 10.4 two views of the payload are shown.

The actuators are meant to provide a force that will globally be the same as for Virgo. Due to the absence of the separation layer in between the F7 coils and marionette magnets, it is possible to design slightly smaller coils with the optimal working point between center of magnet and center of coil set to 30 mm.

10.2.1 Pre-alignment requirements

As it has been said, the new payload system will be balanced in a clean room before the installation into the tower. That means that we expect to suspend the payload within 1 – 2 mrad along θ_x and θ_z . Hence the position of the payload will be governed by θ_y position

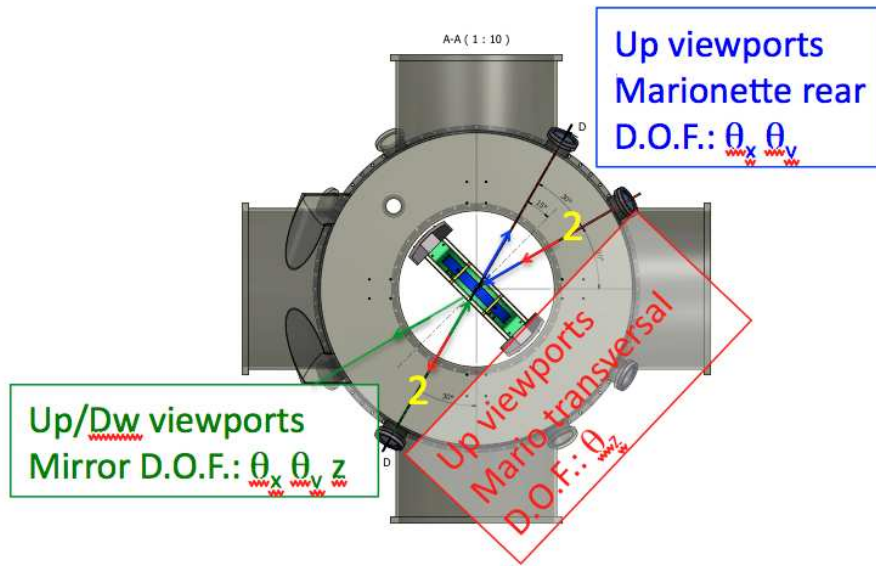


Figure 10.5: Layout of BS optical levers.

of its suspension wire, adjustable through manual (junction-boxes) and motorized rotational stages placed along it (see chapter 11).

The local control system will not operate in coarse mode because no markers will be attached anywhere. Thus ± 6 mrad maximum misalignments will be allowed by the POSD sensing system monitoring the angles of the payload. This means that the assembly of the payload will require an iterated pre-alignment procedure making use of North and West arm and detection ports allowed by a suitably large range of F7 Linear Variable Differential Transformer (LVDT) (see chapter 11). Such a work might be strongly facilitated by marking as a reference the small mirror that is currently used for the BS marionette local control. The center of such a mirror provides pitch and yaw position of the payload. Unfortunately the plane of the optical lever is inclined by 9 deg with respect to the horizontal plane, but its position can be referred to the topographic network of anchor points inside the central building. The feasibility of marking present BS position by means of topographic measurement or other means (further optical levers) should be investigated soon (i.e. before BS payload removal).

10.2.2 Optical levers layout for BS

Optical local control of BS payload will make use of three beams and no additional viewports. Due to the presence of the lateral shafts of the actuation-cage the marionette transversal optical lever has to impinge at a quite large angle (75°) and two viewports will gather the passage of two beams. The layout is shown in Fig. 10.5.

10.2.3 Mechanical design overview

The mechanical design of the BS payload has followed an iterative path using Inventor and ANSYS Workbench platforms. The main issue were related to (I) the attempt to limit the

overall weight of the actuator cage in order not to imply too large changes in the SA filter blade sets, preserving their stiffness; and (II) avoiding to have transversal modes below 50 Hz. This choice was to some extent arbitrary but reasonable if we think that in Virgo we never suffered F7 modes, which fall actually well within the control bandwidth of the locking. The third constraint is specifically related to the further structures attached to the cage, i.e. the baffles which are requested to have frequencies higher than those of the cage structure.

In order not to change other blades than those of F7, which in any case has to be dismantled and modified (see chapter 11) , we should have a weight balance as:

$$\begin{aligned} & (\text{structure} + \text{baffles} + \text{actuators} + \text{mounts} + \text{marionette} + \text{BS} + \text{F7body})_{\text{new}} \\ & = (\text{actuators} + \text{F7})_{\text{old}} - 20\text{kg} \end{aligned}$$

The structure for the BS was conceived to be lighter towards the bottom, in order to maximize the structural frequency. While the prototype will be constructed in aluminum, the real structure of the cage will be partially made using other materials such as titanium and, probably carbon composite materials or PEEK, not only because of mechanical requirements but also to prevent Eddy current flows close to the actuators.

The residual motion of the baffles will be caused by the locking force. Currently the projection of the residual diffused light caused by this motion is under estimation, hence so far it is wise to design the baffles made of the best material available on the market, that is, silicon carbide.

To limit costs, we adopted Al as a test material for the design, keeping in mind that some parts can be optimized by adopting titanium. In Fig. 10.6 we show the simulation of the cage, with the highest frequencies we reached and the modes around the realistic position of the center of mass (the dynamics of the cylinder above the cage mimics the dynamics of the F7 body).

The baffle mount must be quite rigid and light in order to ensure a high enough frequency of its lowest resonances. In Fig. 10.7 the prototype mount of the baffle is shown. Titanium is a natural choice for both the baffle mount and the U-shaped cradle under the BS.

10.2.4 The marionette and the mirror suspension

The BS substrate, weighting 34 kg, will be suspended by two steel C70 wires with 300 μm diameter set at 0.15 mm from the COM section. Silica spacers similar to the present ones will be used. Flats that cut a circular sector at 5 mm height have been set in the drawings.

The marionette will house two motors for θ_x and θ_z DC adjustment. The mechanism is an optimized version of the present motors installed in Virgo+ marionettes. Since the system will be softer, the motor will displace a lighter mass (300 g) along a 60% shorter run. Given the mechanical parameters of the new marionette, the reduction gears (1/10) will allow to fine adjust (2 $\mu\text{rad}/\text{step}$) and DC range about ± 20 mrad. The overall weight of the two motors boxes will be 2 kg, i.e. just 50% larger than an old single motor box.

The modes of the marionette (motors are not inserted) are shown in Fig. 10.8. The design of the support of LC mirrors is similar to that of Virgo+ LC marionette mirrors. This mount will be tested on the prototype, but expectedly it cannot be kept the same as in Virgo+ since

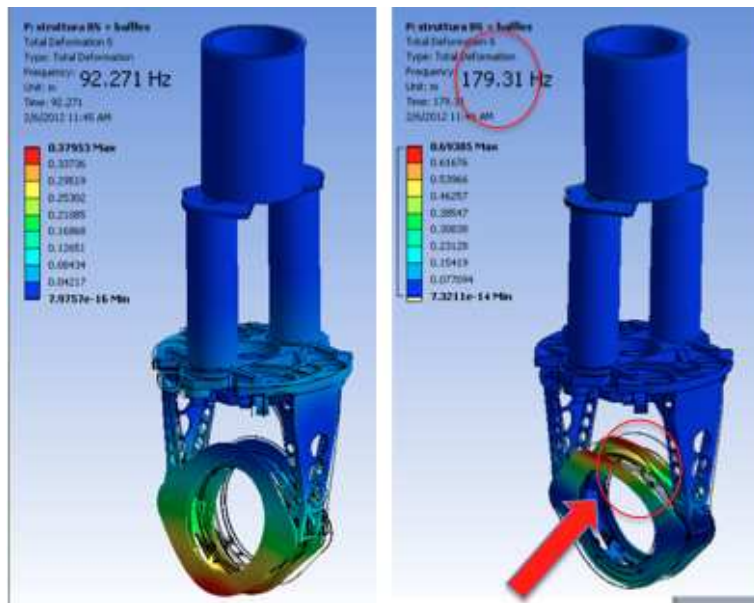


Figure 10.6: The cage structure surrounds the mirror and works as actuator reference as well as safety structure. The lowest structural mode frequency due to the mount of the baffle is maximized by means of the rigid material (Cesic [319]) used in the simulation.

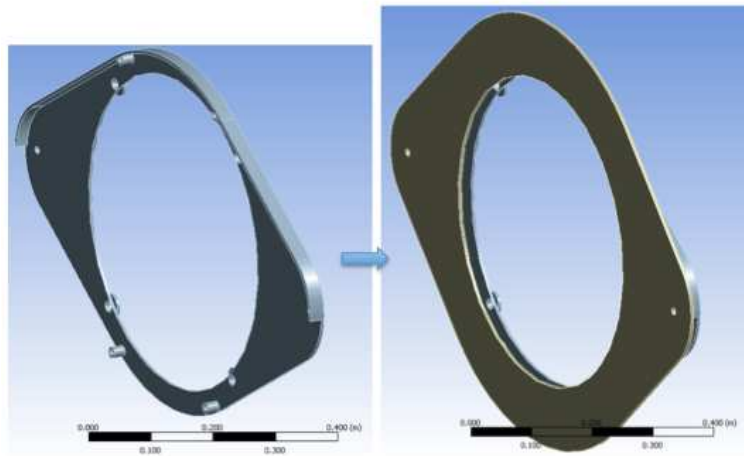


Figure 10.7: The baffle mount inner side will serve as coil holder. Left: the support; right: the baffle mounted on its support.

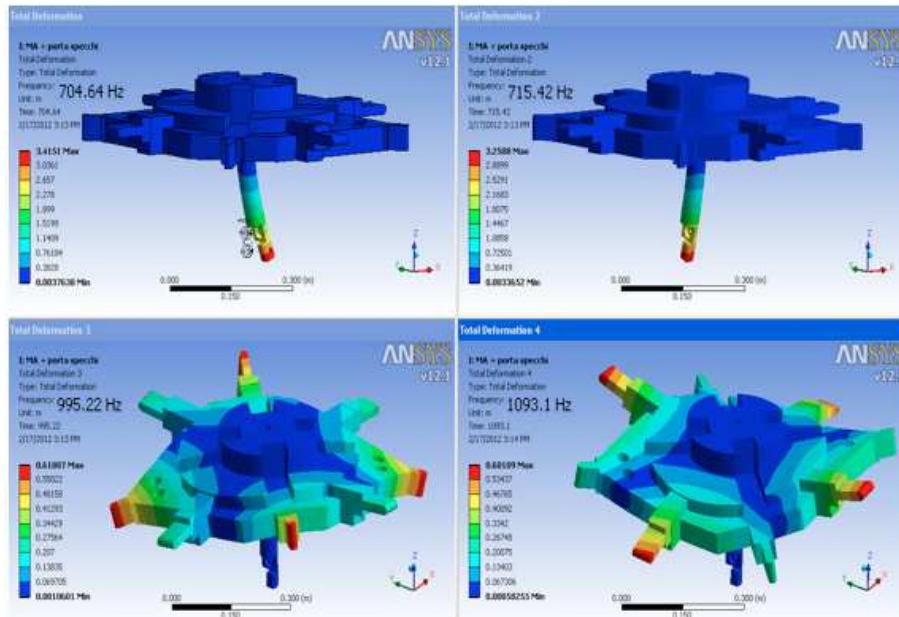


Figure 10.8: The modes of marionette. Motors are not included.

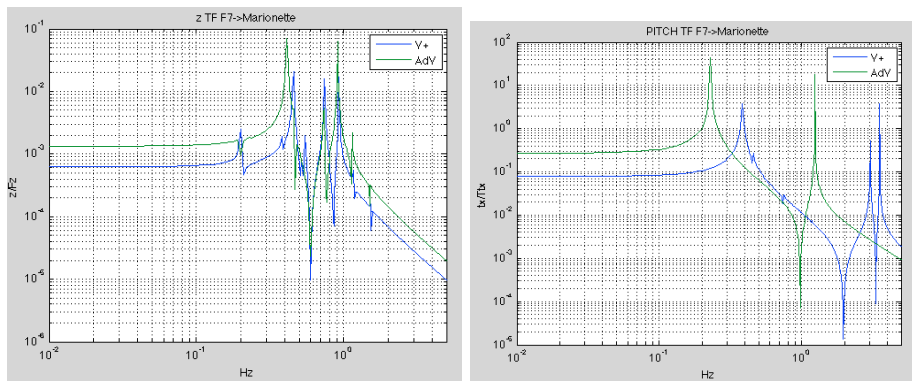


Figure 10.9: Longitudinal and pitch DOF transfer functions from F7 to marionette compared to the Virgo+.

it is planned to install a mirror to provide full angular control of the marionette (10.5, 10.3) and, given the large view angle imposed by the viewports, a wider rectangular mirror (4 cm × 2 cm) will be dedicated to the transversal OL.

The double pendulum system transfer functions from the actuator-cage to the marionette, compared to the present ones, are shown in Figs. 10.9 and 10.10.

The system has been modeled with seed parameters derived from a preliminary design and will be tuned through the prototype. Clearly, angular Transfer Functions (TFs) are significantly simpler than in Virgo+ case, since due to the absence of the reaction mass a zero/pole pair is absent. For the longitudinal DOF along the beam (z) the marionette is still affected by the presence of the SA modes; however, just due to the absence of reaction-mass, the marionette will be well coupled to the mirror motion. The latter feature will simplify the system at least to the extent of damping transversal motion of the mirror (x) that can be easily sensed

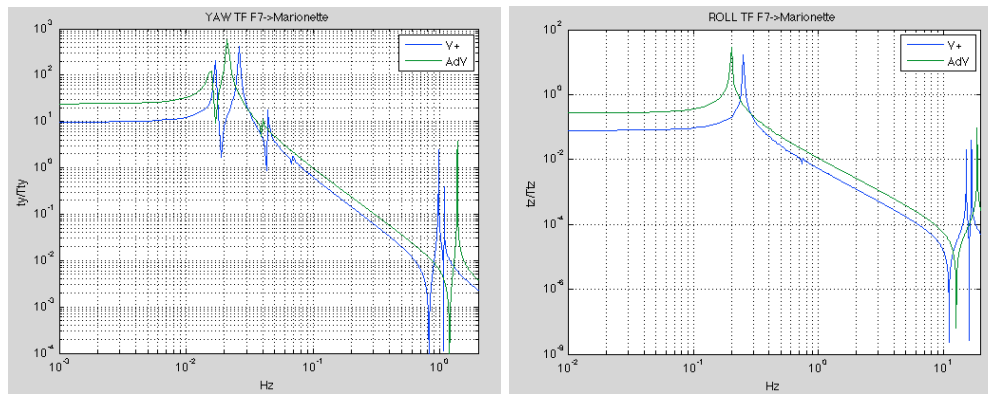


Figure 10.10: Yaw and roll DOF transfer functions from **F7** to marionette compared to the Virgo+.

(and damped) at marionette level. In general, the modes of the last suspension stage (mirror pendulum) can be all sensed through the upper stage.

10.2.4.1 BS payload: example of assembly and integration procedure

As it has been said in Sec. 10.1.1.2 the **ACA** is self-supporting and works also as a safety structure since it is nested into the **IVC**. The mirror and the marionette can be blocked on it. A relevant design activity is related to the assembly procedure. Indeed, before the assembly of the various parts of the payload, the actuator cage does not exist, and a support structure is needed to assemble it and the payload inside it. We conceived such an assembling tool as a structure to be also used during the transportation of the payload and its suspension. Nine main phases have been identified (Figs. 10.11 and 10.12).

- I The coil holder is fixed on the assembly structure.
- II The marionette (naked) is inserted and blocked by means of vertical rods on the holder.
- III 6 coils and the related magnet supports are mounted (except those close to the clamps)
- IV The mirror is inserted from a side onto its U shaped cradle, which sits on an adjustable slide.
- V The mirror is mounted using the slide and the wire tension is adjusted through the apertures.
- VI The last 2 coil/magnet pairs are mounted.
- VII The side walls of the cage are mounted.
- VIII The mirror coil/baffle supports are mounted.
- IX After transportation, inside the tower, the baffles are fixed.

To apply internal forces on the payload in the specific case of **BS**, the **ACA** is the natural choice since it appeared suitable for both purely geometric constraints and requirement of holding large baffles. Remarkably, what developed for the **BS** served to figure out how to approach the general conceptual concerns and will be exported the design of the other payloads. The

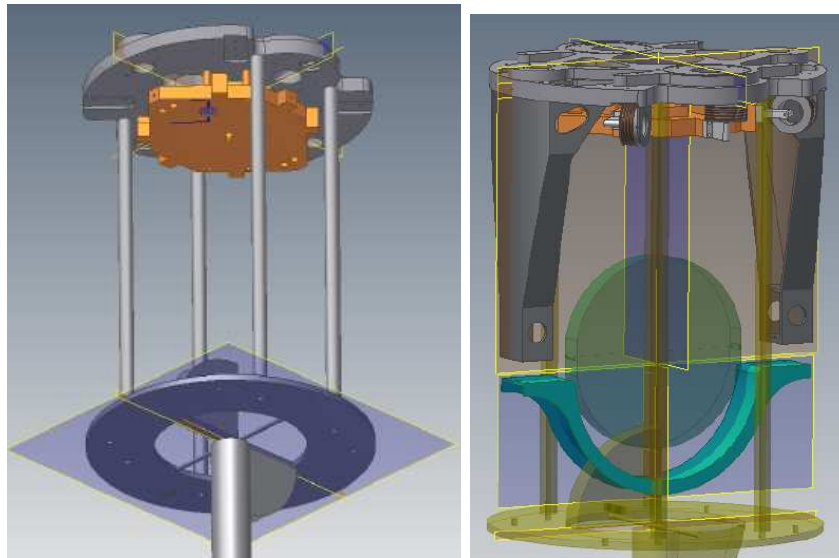


Figure 10.11: Phase II and phases IV,V,VI,VII.

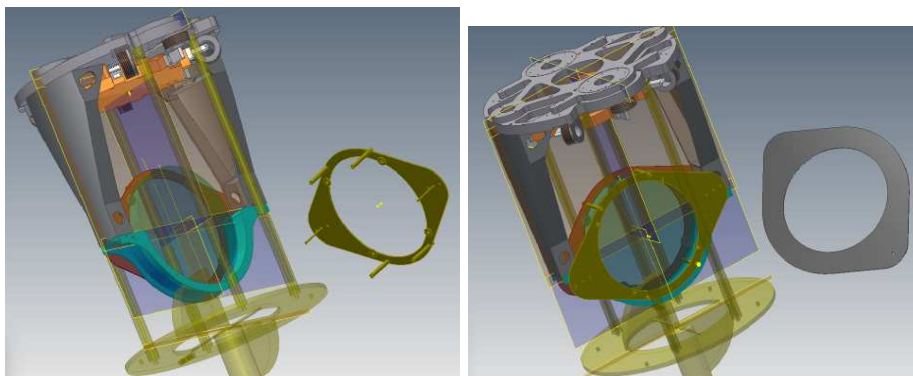


Figure 10.12: Phase VIII and, at last, phase IX: the baffles are attached.

details of this chapter of the Technical Design Report (TDR) will be defined following the path delineated by the following.

- The assembly of the payload in clean rooms and related tools. As seen above the ACA partially replaces the “frame” used in Virgo to assemble the payloads. The further structure sketched in Figs. 10.11 and 10.12 holding from ground the ACA is conceived as a support that is removed after the assembly in clean room and integration in the vacuum chamber.
- Integration with the SA in the bottom vacuum chamber of the towers, whose phases will be necessarily different, whose essentials are that suspending the system composed by ACA+payload implies two vertical displacements of the SA chain, in order to suspend the ACA and marionette to the outer and inner part of the F7.
- Once inside, the ACA will work as primary safety/stop system of the payload, that means, in turn, that the largest mechanical displacements will be blocked through F7 mechanical dynamics. However, just to ensure redundancy, a set of adjustable stops of the ACA, fixed on the bottom vacuum chamber, and accessible, will ensure redundancy to the safety system during operation.
- Some care will concern the electrical cabling of one further marionette motor (roll DOF), while the overall number of coils will remain the same as in Virgo (two more coils for the marionette but absence of x coils on mirrors). Indeed some care will concern the electrical driving of CP orientation but those connection will access the CP through the ACA structure and not along marionette suspension wire.

10.3 Test-mass payloads

10.3.1 Input and end mirrors payloads: design overview

The main feature of test mass payloads is that the mirrors are suspended using silica fibers, to reduce the thermal noise due to their pendulum and bulk motion.

Moreover, in Advanced Virgo, the test mass mirrors are surrounded by large baffles and ring heaters, and the input mirrors have a large optical element (the CP positioned close to their surface). The relevant complexity of the design of a reaction mass including all these parts is one of the main reasons that pushed us in adopting the new scheme for the payloads. Indeed, both end and input mirror payloads will have the same structure as the beam splitter, with a similar marionette and with a cage, rigidly connected to F7, supporting baffles, RHs and, for the input payloads, CPs. A further constraint comes from the locking force that, according to ISC (see chapter 8), will act on the end mirrors payloads when the interferometer will operate in dual recycling mode. In that case, the Differential Arm Length (DARM) loop requires quite a large band width, up to 400 Hz (see chapter 8), and a further stiffening of the cage will be required in order to avoid the excitation of its resonance modes by the locking force. However, further ISC modeling will be performed, aimed to lower the unity gain frequency of DARM control in the dual recycling case down to 200 Hz. We shall make a detailed analysis of the effect of the locking force spectrum on cage, when signal recycling is active, to optimize the response of the payloads, using Octopus [318]. However, with the

increasing of the stiffness of the cage, we shall increase also its mass, and overcome the tight weight limit of the present suspension chains. This means that at least the end mirrors suspension chains need to be retuned to the larger weight, differently to what is possible to achieve concerning the BS design (10.2.3). However, in order to preserve the possibility to act with the wide band locking force also on Input payloads, we shall have all four suspension chains of the test mass payloads retuned. In this way, we have also the additional advantage to have the same model for all test mass payloads.

10.3.2 The monolithic suspensions

Monolithic suspensions were initially developed by GEO and will be used in the advanced detectors both in LIGO and in Virgo. During the years 2008-2011, Virgo (in Virgo+ configuration) performed the science runs VSR3 and VSR4 having the mirrors suspended with fused silica fibers. In VSR3, Virgo was also in coincidence with LIGO S6 run. This experience has allowed us to develop and test our technology: we have defined procedures for fiber production, and for their test and integration with the payloads, for gluing the fibers to the mirrors using silica bonding and for connecting the fibers to the marionette.

Throughout these developments, an important concern has been to achieve a good reliability of the suspended fibers: fibers under stress which come in contact, even lightly, with an object, explode in a fine powder of fused silica, with a consequent pollution of the mirror and potential harm to operators. The result of this effort is in the fact that the fibers of the payloads in Virgo+ have been in operation for two years (until the detector has been shut down for the upgrade to AdV).

Though the performance of the interferometer during VSR3 and VSR4 was not optimal, thanks to monolithic suspensions, we were able to beat for the first time the design sensitivity of initial Virgo in the Vela Pulsar region ($\simeq 22$ Hz) [320].

The AdV monolithic suspensions will be an evolution of the design used in Virgo+. In that old scheme (see Figure 10.13), two *ears* are glued with silica bonding to the mirror. The fiber is extruded from a silica block (*the cone*), inserted in a steel box (*the upper clamp*), and welded to the *anchor*, a silica piece that is silica bonded to the ears when the payload is assembled. The main problem that has been found with this configuration has been an excess of mechanical losses enlightened by means of dedicated measurements at Perugia INFN laboratory. It is crucial to improve the upper clamp of the fibre in AdV.

A deep investigation of losses related to the suspensions and the measured quality factors has been done within the collaboration, with tests performed both on the Virgo interferometer and in Perugia laboratory, and by simulations carried out by various groups (Roma, Perugia, EGO). The main results have been presented both with internal notes [321, 318] and at LSC meetings [322, 323, 324]. One of the main outcome of this effort is that AdV requirements can be achieved by means of a suitable upgrade of Virgo+ monolithic suspensions.

The main features of the new monolithic suspensions are reported hereafter.

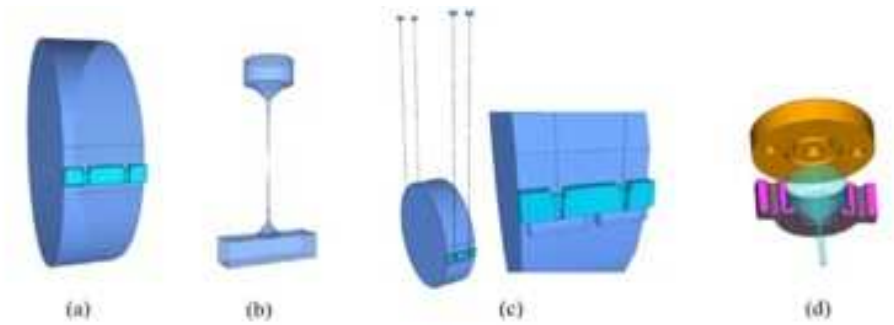


Figure 10.13: Parts of a monolithic payload. (a) Mirror with ears, (b) fiber with upper clamp and anchor, (c) lower clamp, (d) Upper clamp.

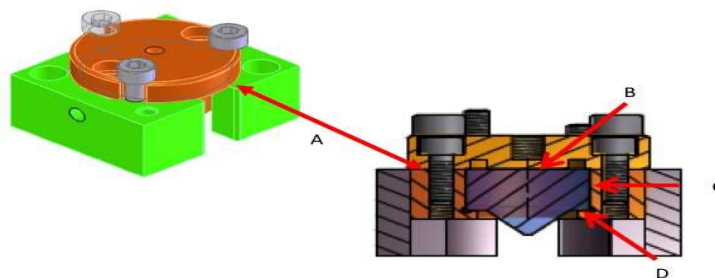


Figure 10.14: A, B, and C: possible frictions between contact surfaces of the box containing the fused silica clamp and the external case; C and D: possible frictions between contact surfaces between the fused silica clamp and its box.

10.3.2.1 The upper and lower clamps for the fibers

In the new scheme, we shall not use any more the silica cone inserted in a metallic block to clamp the fibers to the marionette: both theoretical studies [322] and tests (in progress) show that such a configuration is influenced by the interface between the cone and the box, and also between the box itself and the body of the marionette and can probably account for the low Q s observed in the violin modes in Virgo+.

Indeed, we are currently performing measurements on a fiber suspended with the standard upper clamp metallic box at the test facility in Perugia, (see Fig. 10.17, details can be found in [325]), a very rigid suspension structure dedicated to fiber dissipation measurements under vacuum. Preliminary results show that a change of Q of the violin modes by about an order of magnitude is produced by a small change of the tightening force of the screws connecting the clamp to the marionette.

This effect could be explained by an additional dissipation mechanism due to the friction of the fused silica cone on the stainless steel box and/or of the metallic box itself with the marionette, as it is shown in Fig. 10.14.

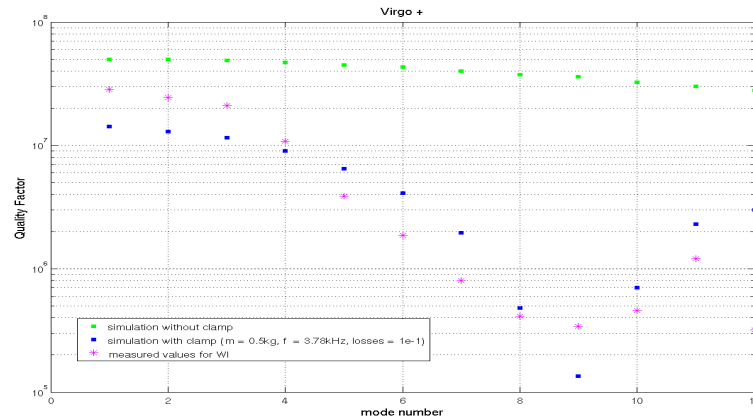


Figure 10.15: In absence of clamping element the model predicts higher Q values (green), while the observed behavior (purple, WI, averaged over four fibres) can be qualitatively fitted by the presence of a further dissipative element with physical mass close to that of the clamp upper box (blue).

For instance, in Fig. 10.15 is shown how the insertion of a further stiffness element (with dissipation lag) in between the upper head of the fiber and the marionette, in the standard Virgo+ scheme, qualitatively explains the observed degradation of the violin modes quality factor around the characteristic frequency of the stiffness element.

Even if the modeled system is not mathematically closed (namely the full identification of the actual system, i.e. the features and number of parasitic elements are unknown a priori) this result supports the hint given by our preliminary measurements in localizing the dissipation source at the upper clamp contact zones between different metallic and fused silica surfaces. Our rough model gives a value $\simeq 0.1$ for the loss angle of these dissipations, which can be easily reduced by decreasing the surface to volume ratio (i.e. increasing the size of the fused silica part of the clamp) and by limiting as much as possible the contact surfaces between metallic and silica parts.

Fig. 10.16 shows that, according to our qualitative model, reducing the dissipation of the upper clamp by factor ten, and increasing its mass by a factor four, this source of dissipation is made negligible.

Hence, we are designing a new marionette, where the upper clamp is a block of fused silica, with a mass at least twenty times greater than the old one (17 g), and with a carefully controlled interface with the metallic surface of the marionette.

Of course, the new scheme will be validated with an extensive set of dedicated tests of the Qs of violin modes in the Perugia test facility.

For risk reduction, we are studying in parallel a more complex solution in which we decouple the silica piece supporting the upper ears from the marionette by using a standard steel wire to suspend it. This scheme, which becomes a three stage lumped system that is fitted in the available vertical room available, is currently being defined from the point of view of thermal noise and control.

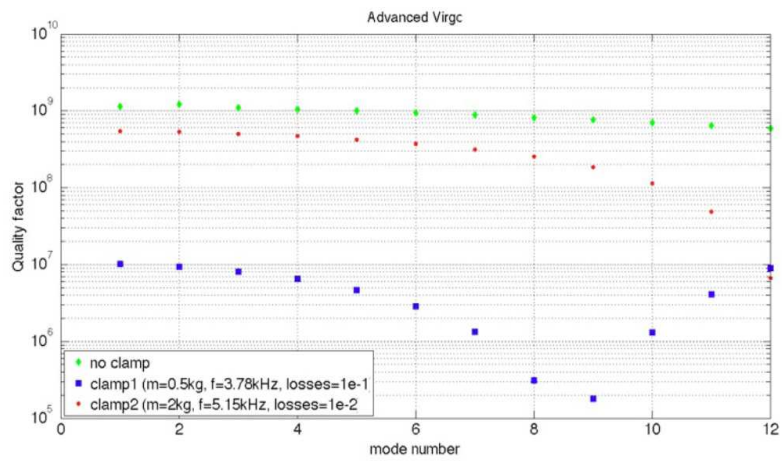


Figure 10.16: Violin mode coupling to the upper clamp in AdV case. The blue dots are related to a Virgo+–like clamp while the red dots are obtained through a different clamp box suitable for AdV.



Figure 10.17: The Perugia test facility for violin modes Q measurements.

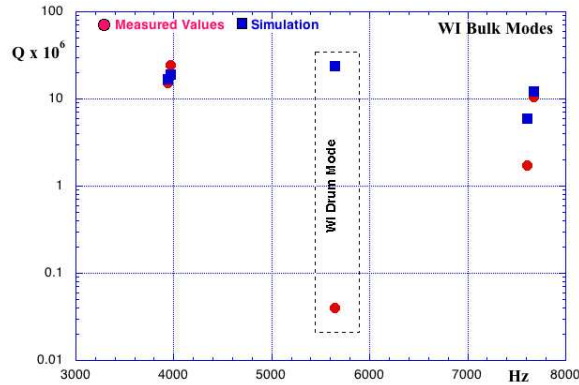


Figure 10.18: Comparison of the measured Q values for the bulk modes with the values given by the simulation. The agreement is good, with the exception of the drum mode. The Q of the drum mode in the WI is so low that it could be due to some wrong procedure during assembly or operation.

10.3.2.2 The ears of the mirrors

The *ears* are the silica pieces that are glued to the lateral surface of the mirrors, acting as support for the anchors. The silica bonding that we have used to attach the ears to the mirrors has proven to be quite reliable, and we shall use the same technique also in AdV.

According to the most recent simulation results, the losses due to the silica bonding of the wire standoffs (ears+anchors) account for the highest Q values observed in bulk modes. For instance, in Fig. 10.18 we show the comparison of the measured Qs for the bulk modes of the WI mirror with the expected values according to simulations. The agreement is good, with the exception of the drum mode. Indeed, the Q value of the drum mode in the WI is so low ($Q \simeq 4 \cdot 10^4$) that it is probably due to some uncontrolled event occurred during assembly or operation: dedicated measurements are being performed in a new vacuum test facility in Rome to identify the cause of this problem.

Thus, according to the simulation, the Q values at the bulk modes are dominated by the losses of the silica bonding of ears and anchors. Hence, a way to reduce this source of losses and increase the overall Q is to reduce the bonded surface of ears and anchors. This is possible because the original design in Virgo+ had a very large safety factor, due to unknown reliability of our silica bonding technology. As a consequence, we are redesigning the wire standoffs reducing the bonded surface by a factor 5 - 10. According to the experience in Virgo+, we do not foresee problems with this reduction.

In parallel with this activity, we shall measure in the vacuum test facility in Rome also the Qs of the bulk modes of the other payloads, in order to understand and quantify the coupling of the modes of the mirrors with the violin modes. This coupling has been identified for the NI drum mode ([321]), but could be relevant also for the others payloads, and must be taken into account for a correct evaluation of the thermal noise.

The measurements will be performed using a properly designed interferometer. The beam of a 25 mW Nd:YAG laser will be injected in the vacuum chamber by using an optical fiber ending with a collimator in the vacuum side. The set-up will be movable, with respect to the AdV mirror, in order to characterize different points of the mirror surface. In order to minimize the electronic noise contribution, the read-out will be performed by using two photodiodes,



Figure 10.19: The Rome vacuum chamber for payload testing.

one on each interferometer port, and analogically subtracting their contribution.

10.3.2.3 The fibers

Our fiber production and testing technology, developed during the installation of Virgo+ on the base of GEO and LIGO experience, has been quite effective. All sixteen fibers suspending the test mass mirrors in Virgo are still working after two years of continuous operation, with mechanical parameters very close to specifications [326]. Thus, in AdV only some minor changes and upgrades of the present set up and procedures will be necessary, as it is briefly described in the following.

Fiber Geometry

The choice of the fibers diameter for the AdV suspensions is driven by the level of safety required in load stress, by the values of the bouncing and violin frequencies and by the performances in terms of thermal noise. Suspending AdV mirrors to a $400\ \mu\text{m}$ diameter fibre, corresponds to a load stress of 780 MPa, about the same of the fibers used for Virgo+ and well below 4-5 GPa, that is the breaking stress estimated by the tests we have carried out before Virgo+ fibers production. Bouncing frequency is about 6 Hz, below the lower limit of the AdV sensitivity and the first violin mode frequency is greater than 400 Hz, hence avoiding problems in control strategy. Fluctuation-dissipation theorem shows that the thermal noise is related to the dissipation of the mechanical energy of the system. For silica fibers there are three dissipation contributions evaluated by three loss angles: $\Phi_{tot} = \Phi_{bulk} + \Phi_{surf} + \Phi_{ThermEl}$, where Φ_{bulk} and Φ_{surf} are the contributions coming from the bulk and the surface of the fibre and $\Phi_{ThermEl}$ is the one due to thermoelastic processes. For a $400\ \mu\text{m}$ diameter fiber in this

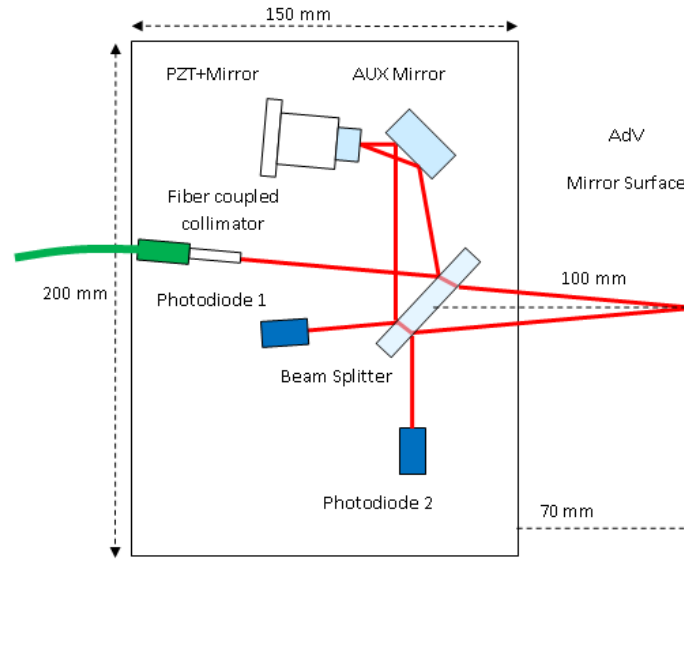


Figure 10.20: Scheme of the measurement device for Mirror Normal Modes.

range of frequencies, this last contribution is the most relevant one. On the other hand, the temperature dependence of the fiber Young modulus contrasts the effect due to thermal expansion, so that there is a certain diameter value of a loaded silica fiber where the thermo elastic dissipations can be totally cancelled [327].

In Figure 10.21 the thermal noise at 10 Hz of the mirror suspensions (last suspension stage) is shown as a function of the fiber diameter. All contributions are taken into account. The bulk contribution is diameter independent, while the surface one decreases as diameter increases, because of the smaller surface to volume ratio. The thermoelastic cancellation mechanism explains the presence of the minimum as was previously pointed out. Finally, also the dilution factor, i.e. the ratio of the total energy (elastic + gravitational) to the elastic one, must be taken into account, since the gravitational force does not include a dissipative component. Increasing the diameter leads to a more rigid fiber, hence a decrease of the dilution factor. Even though a choice of fiber diameters of about $800 \mu\text{m}$ could minimize the thermal noise contribution, these fibers would show a bad set of modes frequencies; mainly, the bouncing mode at about 11 Hz would spoil the sensitivity at low frequency. A solution to this problem [328] is the so called “dumbbell-shaped” fiber shown in Fig. 10.22. In this scheme, most of the fiber length has a diameter of $400 \mu\text{m}$, thus setting the bouncing and violin frequencies at values suitable for the AdV purposes, while at both fiber ends are two short *heads*, with a diameter of $800 \mu\text{m}$. In this way, since most of the bending energy is stored close to the bending points that are inside the $800 \mu\text{m}$ regions (heads), the cancellation mechanism can minimize the thermal noise.

Moreover, the two 3 mm thick ends (bars), can be used to weld the fibre to the rest of the suspension and, also, to set the λ point (bending length) on the right position with respect to the mirror and the marionette. In any case these regions must not be longer than a few millimeters, to limit the bending energy stored there and to make the bending point position

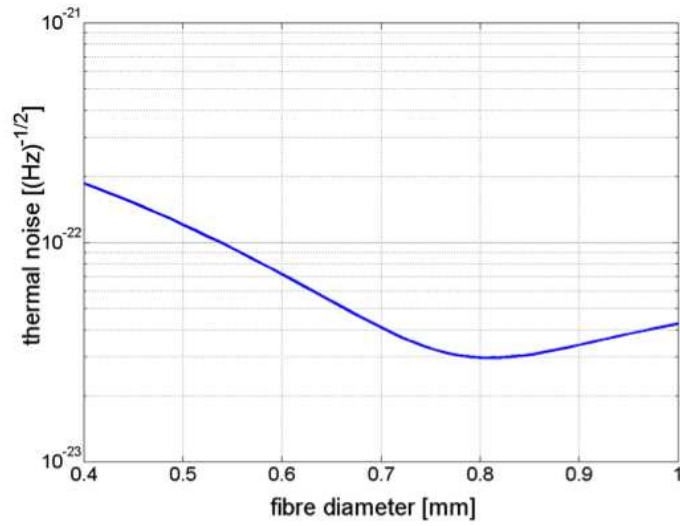


Figure 10.21: Thermal noise at 10Hz of the last stage of the mirror suspension, as a function of the fiber diameter.

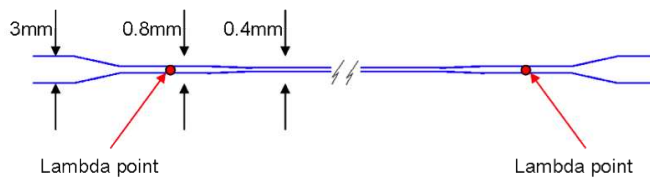


Figure 10.22: Dumb-bell shaped fibre.

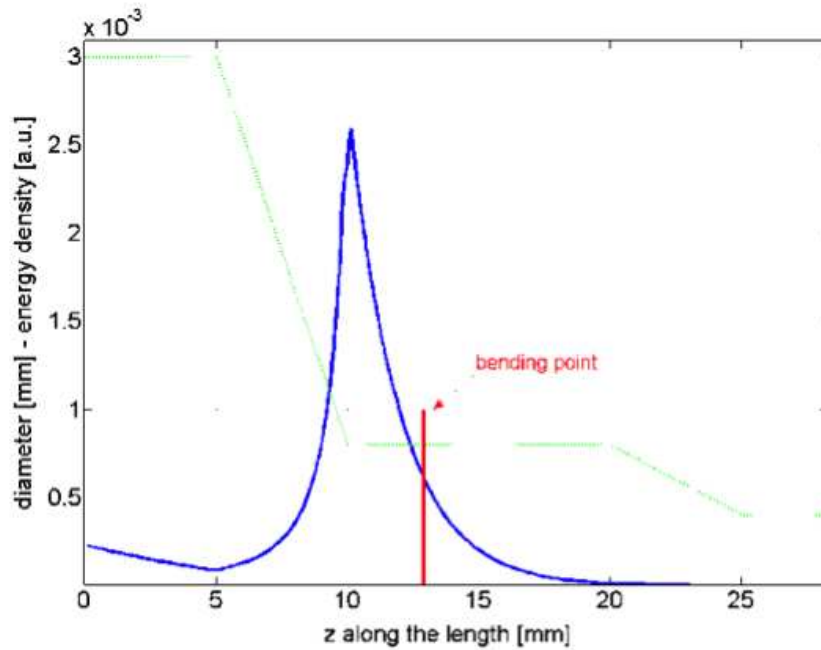


Figure 10.23: Elastic energy distribution along a fiber. The green line is the profile of the fiber.

independent of the welding shape. A finite element model was used to simulate the elastic behavior and to estimate the thermal noise, for fibers with a diameter variable along their length. The model was implemented by a code specifically developed for this purpose (see details in [329]). In Figure 10.23 the elastic energy distribution along the fibre at 10 Hz is shown. In green the first millimeters of the fiber profile.

In Figure 10.24 we plot the shift of the bending point with respect to the length of the bar. For example, if the length of the bar changes from 2 to 4 mm, the bending point shifts by about 0.1 mm towards the fiber end. Hence the change of bending length is only 1.9 mm. It can be noticed that the derivative is growing (in absolute value), so that the position of the bending point becomes more dependent on the bar length and, consequently, also on the welding shape. Below a comparison between different fiber shapes is done. Realistic fiber parameters are considered:

- length of the 3 mm diameter bars = 5 mm;
- length of the 0.8 mm heads = 10 mm;
- length of the transition region 3 mm-0.8mm (welding region) = 5 mm;
- length of the transition region 0.8 mm-0.4 mm (neck region) = 5 mm;
- bending points distance under nominal load (98 N) = 700 mm.

In Figure 10.26 we show the resulting total thermal noise of the last stage of the suspension, assuming a mixing angle of 10^{-3} between horizontal and vertical motions.

These considerations indicate that, for what concerns the total thermal noise balance, the dumbbell-shaped fibers are by far the best solution, and will be implemented in AdV.

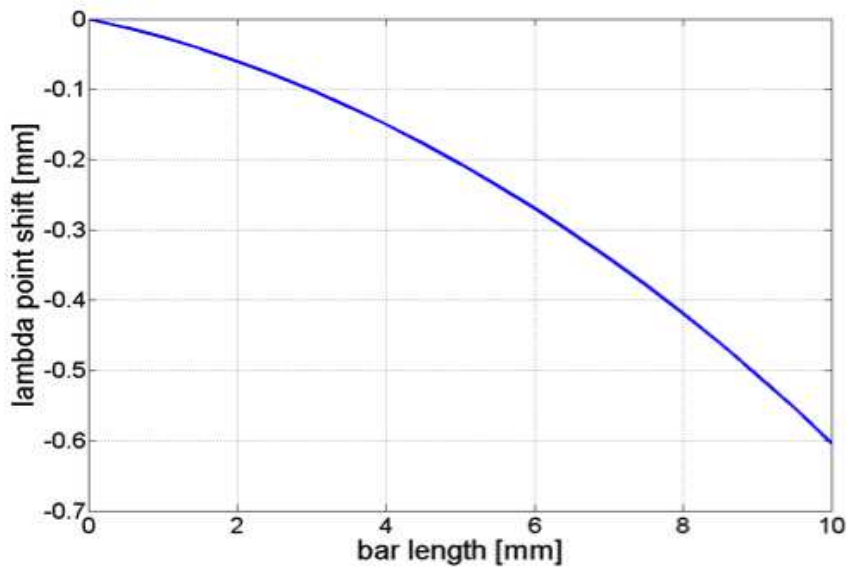


Figure 10.24: Shift of the bending point as function of the bar length.

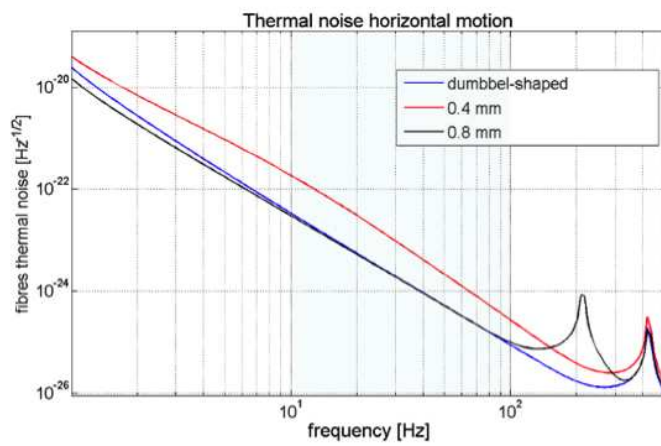


Figure 10.25: Thermal noise induced horizontal motion, for different fiber shapes.

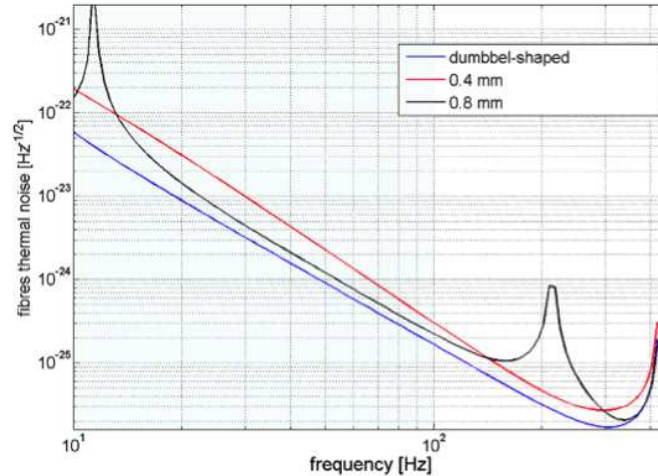


Figure 10.26: Total motion of the last suspension stage due to thermal noise.

Improvements of the production and testing setup for AdV

Presently, fused silica fibers are produced starting from a silica bar that is first welded to the silica parts used for suspending the assembly to the marionette (cones), and for hanging the mirrors, by means of a silicate bonding process (anchors). The silica bar is then melted and pulled to produce the fiber. The melting of silica is obtained with a 120 W CO₂ laser beam, providing also the necessary power to weld the bar to the silica cones and anchors.

In the current setup, displayed in Figure 10.27, the laser beam is first directed on a rotating mirror which allows, together with two other conic mirrors, to heat the silica bar on all sides (see figure below). The upper conic mirror can be moved along the vertical axis, using a PC controlled precision motor. In this way it is possible to move the laser spot along the silica bar. Another identical motor is used to control the upper clamp position. The alignment of the machine pulling axis and of the bar axis can be performed by means of precision slides and tilters, orienting the clamps. After welding the bar to the cone and the anchor, before producing the fibre, the silica bar is heated by moving the laser spot along the bar axis without pulling, to melt all the imperfections and micro-cracks (annealing), whose presence lowers unacceptably the breaking load of the fibre.

Then the fibre is produced by melting the silica bar while pulling upwards the upper clamp and moving downwards the conic mirror. The numerical control of the motors speeds assures to obtain a constant selected diameter fibre (within 10 μm) and to shape the region where the diameter varies from the bar to the fiber value (neck).

Also the laser power is controlled. Indeed, it was noticed that using the full laser power for a rather long time could introduce significant power fluctuations. Thus, full power is used only during the welding process for short time intervals, when heating cones and anchors, where the thickness of silica is relevant. The bar annealing is performed using 55% of the power, while the fibre pulling requires only 45%. It was verified that part of the laser power is lost, due essentially to beam optics. Beam divergence is in fact enhanced after reflection on the conic mirrors: each mirror reflection changes the circular spot into an elliptical one, since

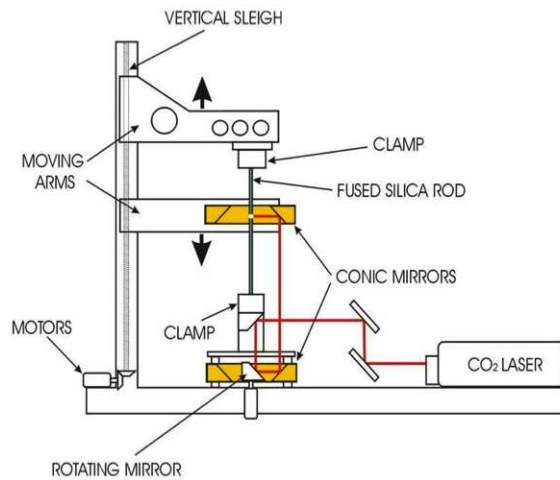


Figure 10.27: Fiber pulling machine, Virgo+ setup.

the curved surface focalizes the light in one direction and leaves it unaffected along the axis perpendicular to the curvature. It has been estimated that almost 40% of the laser power does not reach the silica and is lost.

The geometry of the fibers for AdV is more power demanding because the welding of a 3 mm diameter bar requires more power than in Virgo+. As a consequence, a new more powerful laser (200 W) has been purchased and is being implemented in the fiber production machine.

In parallel also the beam optics is being improved. The lower conic mirror will be changed with a flat one, mechanically fixed to the rotating central mirror, thus avoiding the first focalization of laser beam.

At the same time, the precision on the values of the fibers parameters, such as length and bending points position, is being improved with respect to the current resolution of 10 μm , changing the sensors used to read the positions of the upper clamp and of the mirror.

Finally, also the bending point instrument (λ -machine), is being upgraded, since the measurement must be performed loading the fibre with the operating load, that is greater for AdV mirrors. This requires to change the motor that drives the vertical precision movement with a new one that is able to operate with the increased load.

As it has been already pointed out, fiber reliability has proven to be quite good in the two year long experience of Virgo+ . In any case, a series of careful tests will be performed to verify that this reliability is maintained with the new a fiber geometry.

10.3.3 The compensation plate mount

The compensation plate

The CP has a diameter of 350 mm and a thickness of 35 mm. It must be positioned at 20 cm from the rear surface of the input mirrors. The current solution is to have the CP suspended to the ACA, with a level of stress comparable to that of a standard mirror, so to

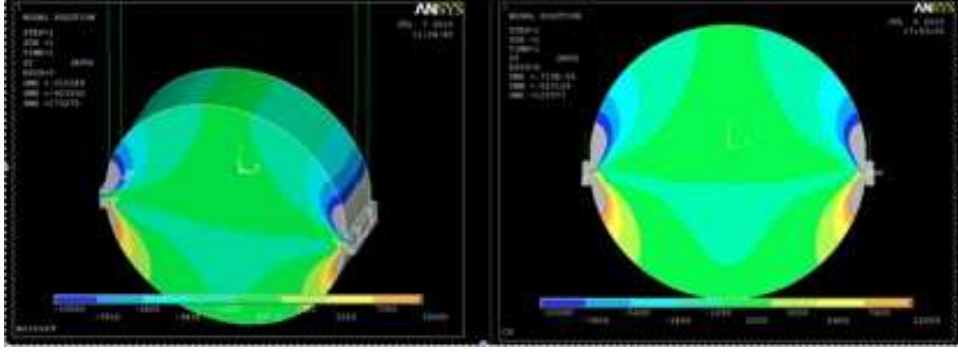


Figure 10.28: Stress on a standard Mirror (left) and on a Compensation Plate (right). The values of stress are of the same order.

limit birefringence effects. The frequencies of the suspension of the CP has been designed so to be inside the detection bandwidth, in order to avoid any coupling with the pendulum modes of the mirror. With this set up, the CP behaves like any other part of the **ACA**. The experience gained with Virgo payloads confirms that the resonant modes of the recoil mass, including the violin modes of the suspending wires, do not affect Virgo sensitivity (because they are related to an element which is in parallel to the mirror suspension). Moreover, in Virgo, some modes of the **F7** body are laying within the locking bandwidth without any significant effect on the payload, due to the single point suspension of marionette wire from **F7**. Hence no resonance of the **ACA** should be visible in the sensitivity curve of Virgo through the direct mechanical path. This means that vibrations of **ACA** parts are not transferred to the output of the interferometer, because of a mechanical or electromagnetic coupling. The only other possible contribution to the output signal due to the CP is optical, by means of the residual coupling of the beam passing through the plate.

According to the requirements defined in chapter 2, the RMS motion of the **CP** vibration should be $\delta z_{RMS} \leq 1$ nm around 100 Hz. Such a constraint will be easily respected by the thermal noise excitation of structural modes of the cage surrounding the mirror, but also by a budget estimate of recoil excitation sustained by lock force.

Indeed, if we overestimate the recoil of the CP by assigning to it the same displacement of the mirror at 100 Hz (that is, according to Virgo sensitivity curve $h(100 \text{ Hz}) \simeq 10^{-22} \text{ Hz}^{-1/2}$), we have: $\delta z_{RMS} \simeq 3 \cdot 10^{-22} \times L_{arm} \times Q_{struct} \times \sqrt{\Delta\nu_{struct}} \sim 10^{-16} \text{ m} \ll 1 \text{ nm}$, where we assume a quality factor $Q_{struct} = 1000$ for a given peak of the cage structure. Indeed, the stiffness of the cage is higher than that of the pendulum suspension, which means that, its displacement due to the recoil is expected to be smaller with respect to the mirror one, which makes this rough estimate conservative

However, a more quantitative evaluation is in progress, and should be ready soon.

The CP mount, meant to hold the CP to the actuator cage structure, sets, according to the current design, the lowest mechanical mode at $\simeq 300$ Hz, with a level of stress on the CP that ensures the same level of birefringence that it is found on the mirror or even lower, if a careful optimization of the suspension attaching points is applied.

The alignment of the CP will be provided by three positioning mechanisms with piezoelectric or motor actuators to ensure the requested sensitivity of $10 \mu\text{rad}$.

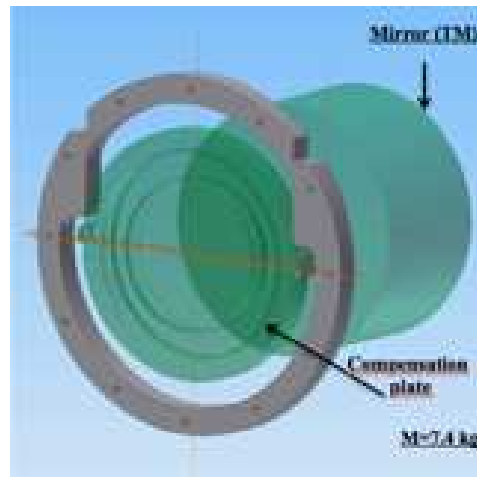


Figure 10.29: Scheme of the compensation plate positioned near the mirror.

The CP assembly has been designed as a part which is separate from the rest of the **ACA** (see Fig.10.29: a full scale prototype is being built and will be tested under vacuum in Rome. After debugging, the prototype could become part of one of the input payloads,

The design of the support of the CP will be replicated, with the necessary changes, for the support of the POP that will be used for the **PR** mirror.

10.3.4 The test mass payload integration with the superattenuator and the safety structure

As for the beam splitter, the **ACA** structure will also act as a support during the integration of the payload into the superattenuator and as a safety structure. The steps of integration will be the same already described for the case of the beam splitter.

10.3.5 Test and validation procedure during assembly.

The experience of Virgo+ has shown that it is important to validate the performance of each payload before its integration in the interferometer. In particular it is essential to be sure that each mirror suspension has the expected dissipation and nothing has gone wrong during the long and complex procedure to assemble the payload. In order to implement such validation procedure, we are designing a vacuum chamber (see Fig. 10.30) to be integrated in the clean room payload assembly facility at the 1500 W Hall at EGO (Fig. 10.31). The tests which are currently underway on the old payloads will allow us to identify the correct set up and procedure that will be used to measure the Q of the violin modes and of the bulk modes of each payload before it is suspended to the superattenuator.

We are designing the vacuum chamber in such a way that it should allow also pendulum measurements on real size payloads up to the level needed for Advanced Virgo. Though such measurements will not be part of the standard diagnostic on payloads, it will be a valuable tool for any further development that payload technology may have in the future.

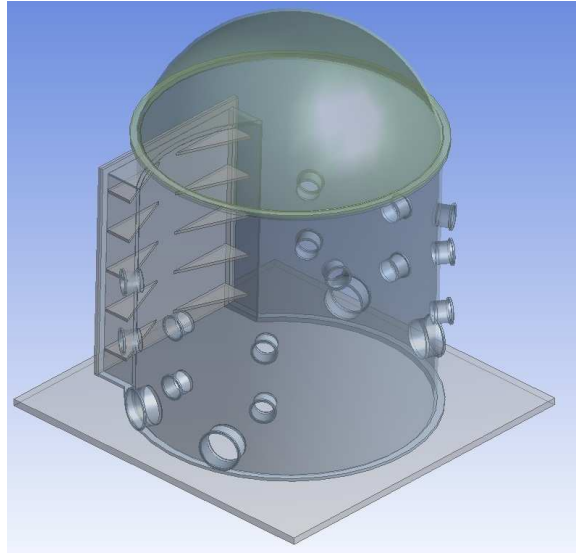


Figure 10.30: The EGO vacuum chamber for payload testing.

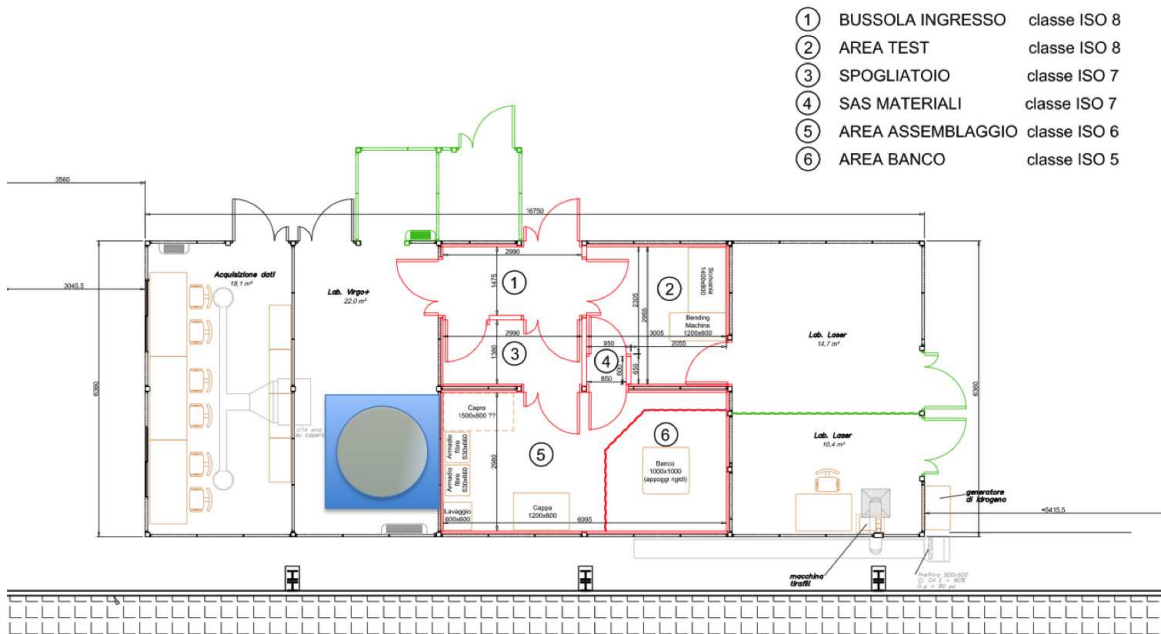


Figure 10.31: Position of EGO vacuum chamber at 1500 W Hall.

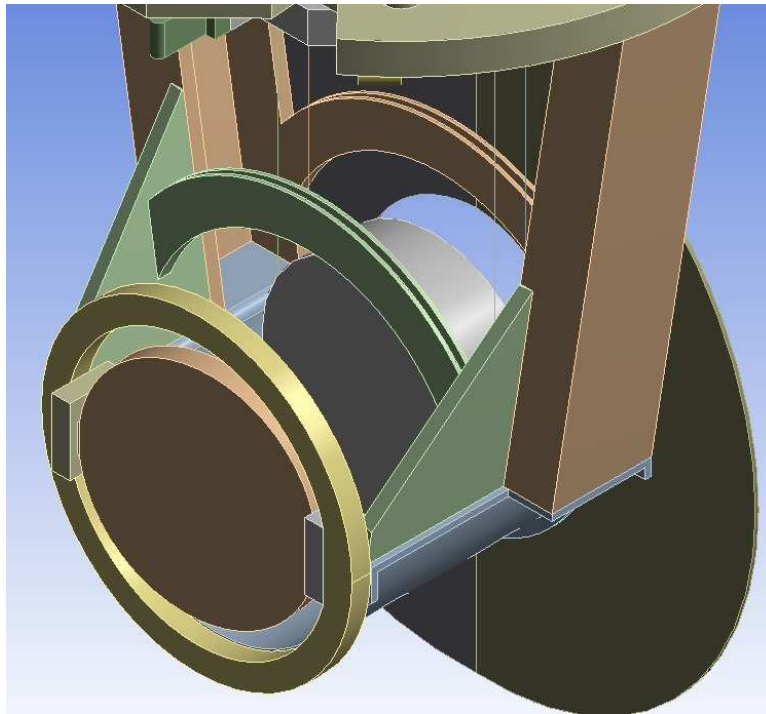


Figure 10.32: Scheme of the PR payload.

10.4 The payloads for the recycling cavities

10.4.1 The power recycling payload

The power recycling mirror (350 mm in diameter, 100 mm thickness) will be suspended using C70 steel wires, the same well known technology used in initial Virgo (see Fig. 10.32). However, in front of the PR we must suspend also a POP for the control of the central cavity. The plate must be positioned 4 cm in front of the mirror, tilted by 6° with respect to the beam axis. We shall suspend the POP with the same technique used for the CP. Moreover, also around PR we must position RHs. So, the structure of the power recycling payload will be similar to the input mirror payloads, of course without the further complication of monolithic suspensions.

Using the OCTOPUS tool we studied the possible effect of a vibration of the POP, as the locking force is applied, on the position of the PR mirror. The result is that, as expected, the frequencies of the POP are not seen by the mirror and will enter only in the sampled signal, at a frequency that is in the range of some hundreds Hz, and that can be easily notched.

10.4.2 The signal recycling payload

The signal recycling mirror will have a diameter of 350 mm and 100 mm thickness. A suspension using standard C70 steel wire will be sufficient. At the moment, it is not foreseen the suspension of any further element close to the SR Mirror, but for the RH: the payload

will be similar to the BS payload, without the further complication of the large size of the mirror.

Chapter 11

Superattenuator (SAT)

Outline

Advanced Virgo (**AdV**) comprises 10 Superattenuators (**SAs**) all operating in Ultra-High Vacuum (**UHV**) chambers. Seven **SAs** are installed in the central building while the additional three are located in north end, west end buildings (3 km far from central area) and mode cleaner building. Each **SA** is identified by a two- or three-character code representing the role of the optical element suspended to it. Two classes of **SAs** are at present foreseen, short and long, depending on actual chain length and number of seismic filters used in the chain.

Long Suspensions:

- NE - north end mirror suspension
- WE - west end mirror suspension
- NI - north input mirror suspension
- WI - west input mirror suspension
- BS - beam splitter mirror suspension
- PR - power recycling mirror suspension
- SR - signal recycling mirror suspension

Short Suspensions:

- INJ - injection bench suspension
- MC - mode cleaner mirror suspension
- DET - detection bench suspension

Superattenuator subsystem (**SAT**) concerns the following main items:

- maintenance and upgrade of the Virgo long **SAs**;
 - mechanics for control system upgrade:
 - * monolithic Inverted Pendulum (**IP**) legs;

- * piezoelectric actuators;
- * tiltmeters and position sensors;
- Filter 7 (**F7**) upgrade to be compliant with the new payload geometry;
- construction and installation of the Signal Recycling (**SR**) suspension;
- maintenance and upgrade of the Virgo short **SAs**;
 - upgrade the short INJ suspension for the Suspended Injection Bench 1 (**SIB1**);
 - upgrade the short MC suspension for the Input Mode Cleaner (**IMC**) end mirror;
 - upgrade the short DET suspension for the Suspended Detection Bench 1 (**SDB1**);
 - * Install **F7** monitoring and Control system
- upgrade of the Superattenuator Control System (**SATCS**);

Long superattenuators upgrade: mechanics for the control system (section 11.1.3.1)

The passive attenuation performance of the long **SAs** was considered to be compliant with the **AdV** requirements since the time of project design. Moreover the latest general specifications for the longitudinal control accuracy are met by the foreseen control loops, assuming the payload motion is the same as measured in Virgo (ISC chapter).

Despite that, the development of a high sensitive sensor for ground tilt is a fundamental tool to tackle a problem of the **SATCS** that becomes relevant during bad weather conditions: the accelerometers on the top stage (see 11.2.4.2) do not distinguish real tilt motion from horizontal acceleration. In addition, the tiltmeter will increase the controllability of the top stage in six degrees of freedom.

Since its design phase the **IP** was conceived with the possibility to install piezoelectric actuators within the three legs structure on which the bottom ring is supported. Maintaining this feature, the new **IP** design has been developed to have its flexural mode ('banana' mode) at higher frequency. In this way it will be possible to improve the feedback control loop gain, presently limited by the presence of a peak structure around 10 Hz in the frequency response curve of the system. The choice of monolithic legs has been also considered the natural solution to have a more rigid structure.

Since a few years **SAT** has started an R&D program to investigate and test the tilt control upgrades. A new **IP** with monolithic legs and commercial piezos have been installed and tested in the environment of the Superattenuator Facility at EGO (**SAFE**). The development of the new advanced tiltmeter has been, as expected, a very challenging task: at present, tests are currently progressing on a prototype of a new kind of accelerometer, designed to be insensitive to tilt, and on a promising commercial hemispherical resonator gyro (HRG), a type of *Coriolis* vibratory gyro, based upon the tilt-driven modulation of the sensor resonance mode (see section 11.2.4.2).

Long superattenuator upgrade: new filter 7 design (section 11.1.3.2)

The **AdV** baseline will have additional suspended optics as the Compensation Plates (**CPs**) in the North Input (**NI**) and West Input (**WI**) test masses and the Pickoff Plate (**POP**) in front of the PR mirror (see OSD chapter). It is also foreseen the implementation of large baffles on all suspended mirrors to reduce the noise caused by the diffused light (see SLC chapter). As a consequence all the payloads will be upgraded to be able to support these new devices and **SAT** is required to upgrade the steering **F7** interfacing the new payloads.

Short superattenuators upgrade (section 11.1.5)

In order to fulfill the **IMC** length noise specifications provided by ISC (see ISC chapter) the installation of an additional standard mechanical filter in each short Injection subsystem (**INJ**) and Mode cleaner (**MC**) chain is required (see INJ chapter) to improve both longitudinal and vertical seismic attenuation performance of these **SAs**. The same kind of upgrade is proposed for the Detection Subsystem (**DET**) chain suspending the **SDB1**, in order to reduce the coupling between the vertical and horizontal Degree(s) of Freedoms (**DOFs**) of the bench and contribute to the scattered light mitigation. As a consequence of this action, the upgrade of the first **SA** stage, the Filter 0 (**F0**), the **IP** flexible joints and partially the cabling, will be necessary.

In all these **SAs** it is also scheduled the installation of the monitoring and control systems of the steering **F7**, as it is presently operating on the long **SAs**. Moreover, as in the long **SA** chains, an upgrade of the mechanics for control system purpose will be done: the **IPs** are already monolithic and the three elastic supports of the **IP** legs are ready to host the piezo actuators.

Upgrade of the superattenuator control system (section 11.2)

The Virgo/Virgo+ **SA** has performed reliably, fulfilling the requirements. However, in order to ensure a long term operation and maintenance for **AdV** and to overcome the hardware physical and technical obsolescence, the **SATCS** electronics has to be upgraded.

11.1 Superattenuator mechanics

11.1.1 Virgo superattenuator general mechanics description

The **SA** suspension mechanics (see Fig. 11.1), was first designed to match the requirements of the Virgo detector [330], and has been operated also in Virgo+ without any upgrade, demonstrating an excellent long term mechanical reliability. Virgo **SAs** are hybrid passive/active systems conceived to achieve two main objectives:

- **passive attenuation** - the ground seismic vibrations have to be attenuated in order to reduce the residual mirror motion along the beam well below the interferometer sensitivity in the detection band.
- **mode damping** - the large mirror motion in the low frequency range below a few Hz, where the seismic noise is amplified by the filter chain resonances, has to be damped to allow low noise hierarchical control of the payload (see section 11.2.4).

A complete Virgo **SA** chain [331] is a five-stage pendulum (Fig. 11.1), where each stage is replaced by a mechanical filter designed to attenuate the seismic vibration in all **DOFs**.

In an n -stage pendulum the horizontal motion of the suspension point, at a frequency f much higher than the frequencies of the normal modes, is transmitted to the suspended mass with a reduction factor proportional to f^{2n} .

In order to decrease the frequency detection threshold it is necessary to reduce the resonant frequencies of the chain and thus to increase the length of the pendula. The Virgo **SA** chain of pendula has an overall height of about 8 m and all its horizontal normal modes are below ~ 2 Hz, providing the required attenuation starting from about 4 Hz. In this way a good safety margin in the detection band (i.e. above 10 Hz) is guaranteed (see section 11.1.2).

Vertical vibrations would be also partially transferred to the laser beam (horizontal) direction because of the unavoidable mechanical couplings between different degrees of freedom (estimated to be below one per cent) and because of the Earth curvature that makes widely separated pendula non parallel to each other (misalignment of 3×10^{-4} rad for 3 km-long arms).

The top stage of the chain is formed by another mechanical filter named **F0** lying over a top table suspended by thin wires from a three-legs elastic structure (the inverted pendulum): the elasticity of the **IP** is given by flexible joints at the base of each leg. By keeping the horizontal resonance frequency of the inverted pendulum at 30-40 mHz, a significant seismic attenuation in the horizontal direction is achieved also in the pendulum chain resonance range (100 mHz - 2 Hz).

The last filter of the chain, for historical reasons named filter 7, was designed to suspend and steer the payload, a system that in Virgo is composed by the *marionette*, the Reference Mass (**RM**) and the mirror. The marionette allows the steering of the mirror with electromagnetic actuators in three **DOFs**. ¹: the displacement along the beam axis (z direction) and the

¹In this chapter the standard Virgo convention for **DOF** naming is adopted: z is the optical axis, x and y are the horizontal and vertical axes respectively, while θ_x , θ_y , θ_z are the rotations about the corresponding axes.

rotations about other the two axes (θ_x, θ_y). The **RM** recoils against the mirror, keeping at rest the system center of mass.

Since the mirror oscillation, in the region where the resonance modes are confined, are fed by the unavoidable injection of seismic noise at the suspension point, an active mode damping is applied. The feedback control is called Inertial Damping (**ID**) because it is based on virtual inertial sensors [332, 333, 334]. Sensing and coil-magnet actuation are at the level of the **IP** top table.

The damping of the vertical resonances of the filter chain is performed at the level of the **F0**. A vertical Accelerometer (**ACC**) placed on the filter movable part (*crossbar*) is used to measure vertical motion of the suspension point. The compensation of the measured vertical displacement is made by a couple of coil-magnet actuators acting on the filter crossbar.

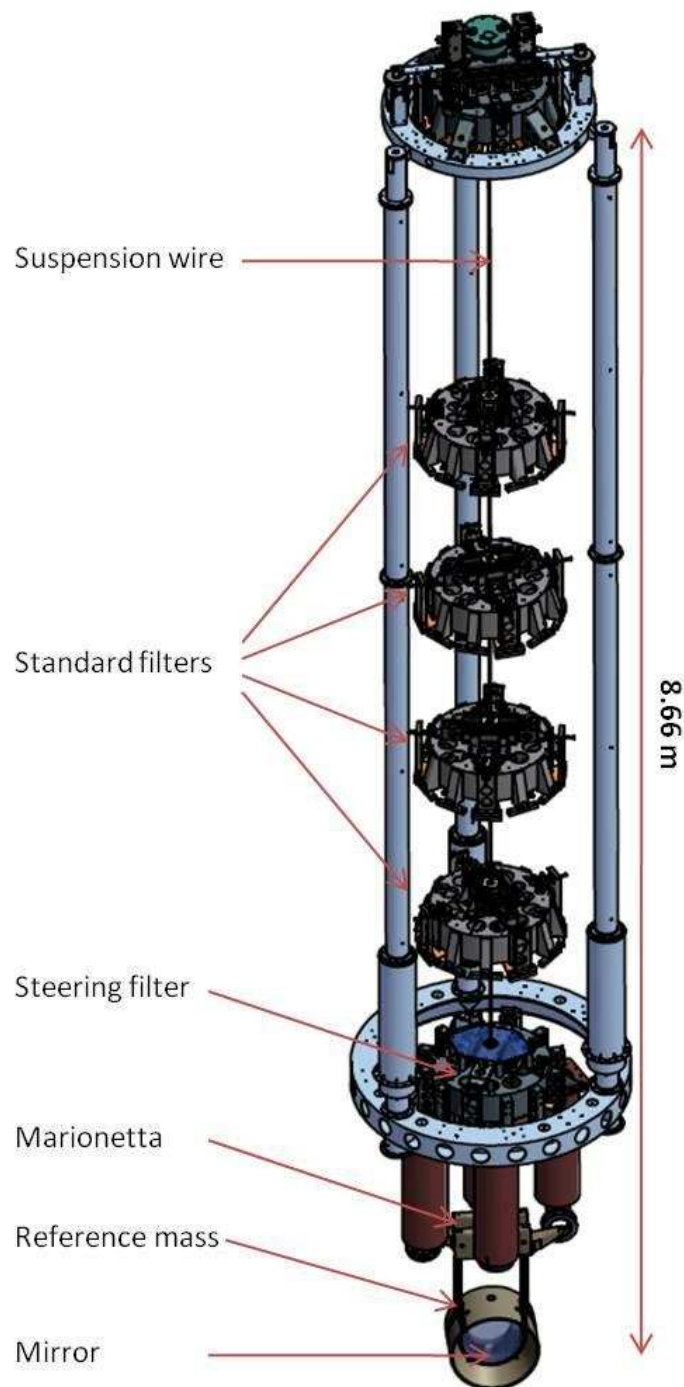


Figure 11.1: The Virgo superattenuator: the mechanical filter chain adopted to attenuate seismic vibration in the detection band, the three-leg inverted pendulum preisolator, the top filter of the chain (**F0**) and the payload are well visible. The inertial damping acts on the top stage to compensate tidal motion and any slow drift motion so that to reduce the mirror swinging within the detection bandwidth (above 10 Hz).

11.1.2 Superattenuator passive attenuation and AdV requirements

The residual displacement at the mirror level is extremely small even when strong excitations are applied to the SA top stage. Consequently, a direct measurement of the total transfer function with commercial instrumentation is not possible. The total transfer function has been extrapolated from the measurement of the 'stage by stage' transfer function [331]. In particular, the 6×6 matrices, connecting the displacements in all the degrees of freedom of each pair of consecutive filters, have been measured using commercial ACCs, and then combined to estimate the total attenuation.

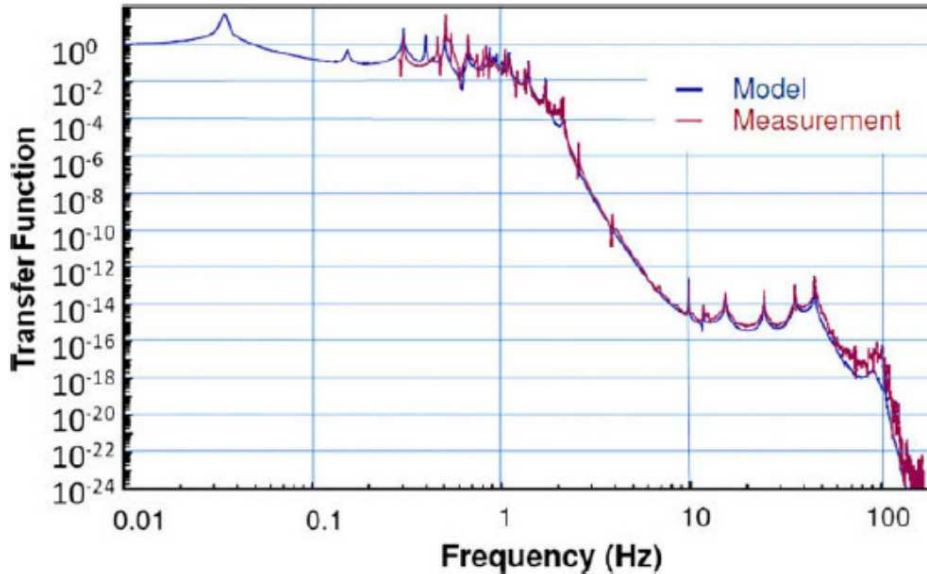


Figure 11.2: The total SA transfer function (red curve), extrapolated by the measurements using the 'stage by stage' technique, is compared with an analytical model (blue curve). The experimental transfer function has to be multiplied by the input seismic noise detected at the ground level, assumed to be isotropic, to obtain the residual mirror displacement along the beam.

The measured isolation for vertical and horizontal seismic noise is in excellent agreement with the analytical simulations and is able to reduce seismic noise below the Virgo sensitivity curve, starting from about 3 Hz. We report in Fig. 11.2 the total transfer function extrapolated by the stage by stage measurement technique discussed in [331]. The curve represents the total transfer function, that is the fraction of ground seismic noise (assumed to be isotropic) that is transmitted to the mirror, towards the beam direction. As shown in [331], above a few Hz, the total transfer function is dominated by the vertical channel, namely by the vertical ground seismic noise that is transmitted through the mechanical filter chain and is coupled to the horizontal direction at the mirror level. Residual couplings, evaluated to be below 1 %, are due to the bending stiffness of the stage-to-stage steel wires connection and to the electric cables that descend the suspension as relatively soft catenaries clamped at each stage of the SA.

The lower attenuation along the vertical axis is due to the first internal mode of the blade springs of the mechanical filters (around 100 Hz). The other resonances appearing at higher frequencies are due to the internal modes of the SA structures (blades, suspension wires, etc.)

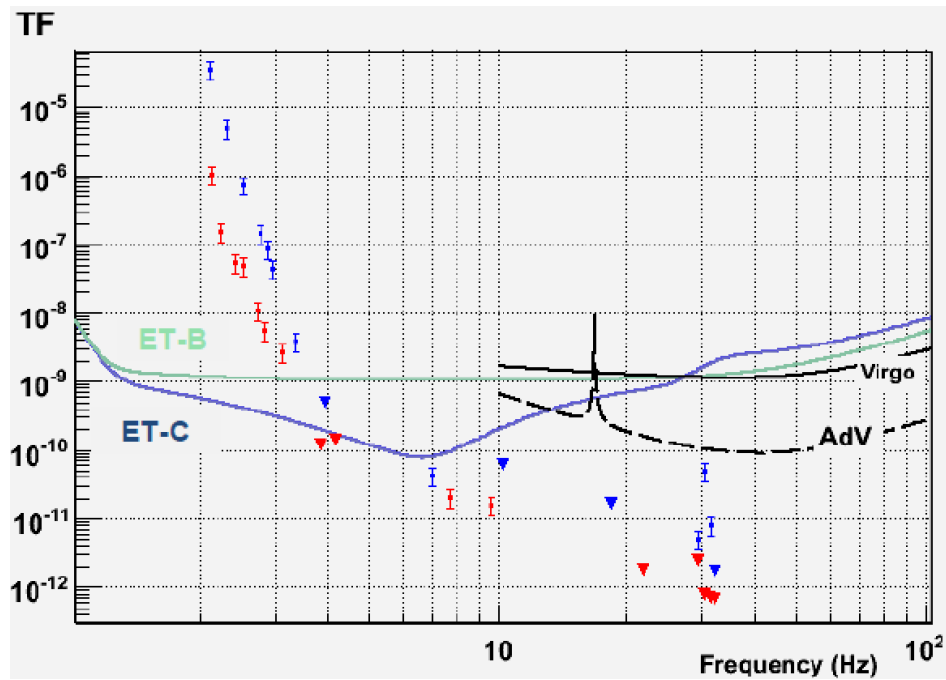


Figure 11.3: The measurement of the SA transfer functions at different frequencies. In red are reported the measurements obtained when a vertical excitation of the top stage is applied. In blue the measurements obtained exciting in horizontal direction are shown. The upper limits are indicated by triangles, while the direct measurements (when a signal is detected at the level of the mirror) are indicated by bars.

[335].

An attempt to measure directly the total attenuation of the SA filter chain has been done a few years ago [336], using as a sensor for the mirror residual motion the Virgo test interferometer (*Central Interferometer* - CITF [337]), and more recently repeated in Virgo+ with higher sensitivity [338, 339].

The experimental results from this measurements campaign compared with the requirements of the future generation detectors are plotted in Fig. 11.3. For the discussion of the error bars see reference [338].

Above 4 Hz, the measured transfer function is compliant with the Adv requirements. Moreover it is important to stress that the further isolation provided by the IP is not included in the transfer functions measurements (which are performed between the IP and the mirror).

11.1.3 Long superattenuators upgrades

The mechanical upgrades of the long Virgo SAs for AdV are meant to enhance the performances of the ID control system and to cope with the requirements and the interface of the new AdV payloads. The foreseen interventions can be summarized by the following scheme:

- mechanics for the control system upgrade:
 - implement a new IP with monolithic legs;
 - install piezo actuators and Linear Variable Differential Transformer (LVDT) displacement sensors below the IP bottom ring;
 - implement a new tiltmeter (see section 11.2.4.2);
- upgrade of the interface for the new AdV payloads:
 - modify the payload steering F7.

11.1.3.1 Mechanics for the Control System

While the Virgo SA passive attenuation of the seismic vibrations in the detection band has been proved to be compliant with the AdV requirements, there is still room for improvements of the ID control to achieve better performances during periods with adverse meteorological conditions (during a few days a year, the amplitude of the microseismic peak could be orders of magnitude larger than the usual one) [340, 341, 342].

As discussed in [343] the seismic noise at low frequency is dominated by tilt. Any attempt to minimize the fraction of seismic noise reintroduced by the LVDTs, moving to lower frequencies the LVDT-ACC blending crossover, would increase the reinjected noise because of the tilt driven contamination of the ACC signals.

It is important to get an independent sensing for the tilt to subtract the tilt signal from the IP ACCs and to provide the error for its control. A tilt control system implemented on the SA would be the straightforward solution to reduce by at least one order of magnitude the mirror swing in 0-200 mHz range and fulfill AdV specifications with a wide safety margin in all weather conditions [344, 345]. This means to introduce new sensors measuring ground tilt motion with a high sensitivity at the level of 10^{-8} rad/ $\sqrt{\text{Hz}}$ in the tens of mHz band (see section 11.2.4.2) [343], and to insert piezoelectric actuators (piezos) below the bottom flange supporting the three IP feet. The tilt control bandwidth will be ~ 1 Hz. It is also possible to conceive the use of these actuators to compensate the excess of vertical seismic noise on the suspension top stage, presently exciting the angular payload motion.

The possibility to perform a tilt control was already foreseen in Virgo suspension and thus a location for tiltmeters and piezos is available. This makes the impact in the AdV construction plan negligible.

The upgrade of the IP legs from a composite to a single aluminum tube is considered useful to make it more robust against the piezos action avoiding dangerous yielding in the junctions and to eliminate undesired structural modes due to the presence of intermediate links. In addition the new legs will have a higher frequency flexural ('banana mode') resonance (from 9 to about 20 Hz), increasing the ID control bandwidth. Other complementary suspension

electronics upgrades are possible to reduce the noise induced by the mirror swinging during windy day (see section 11.2.4). Since a few years SAT has initiated an R&D activity to design and test the tilt control upgrades [346, 347]. Most of the experimental work, in particular those concerning the operation of the monolithic IP prototype with piezos actuators, have been carried on at SAFE.

The Monolithic IP Starting from the present design and keeping the impact of the changes on the mechanical structure of the SA at a minimum level, a new IP has been conceived. The new monolithic legs (see Fig. 11.4) will be about 6 m tall (identical to the present ones). The sectional area will be increased, passing from a cylinder with an outer diameter of 130 mm to a new one of 160 mm, while the thickness will go from 2.5 mm to 5 mm. A prototype designed to have its structural modes at frequencies higher than the actual IP was built and tested in SAFE (see Fig. 11.5).

The Power Spectral Density (PSD) measurements of Fig. 11.6 show that the first IP inner resonances (“banana mode”) appear to be in a region around 25 Hz, more than a factor 2 above the ones of the present Virgo IP.

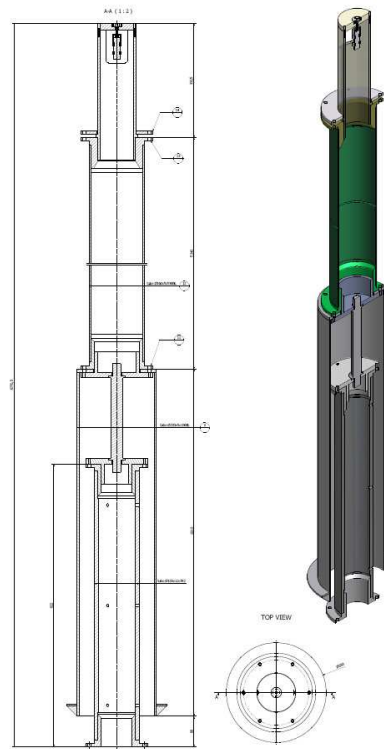


Figure 11.4: Technical drawing of the new IP, based on monolithic legs with increased sectional area.

Piezo Actuators and LVDT Displacement Sensors As mentioned the mechanical structure of the IP was designed since Virgo taking into account the possibility to implement



Figure 11.5: The monolithic IP prototype installed in SAFE.

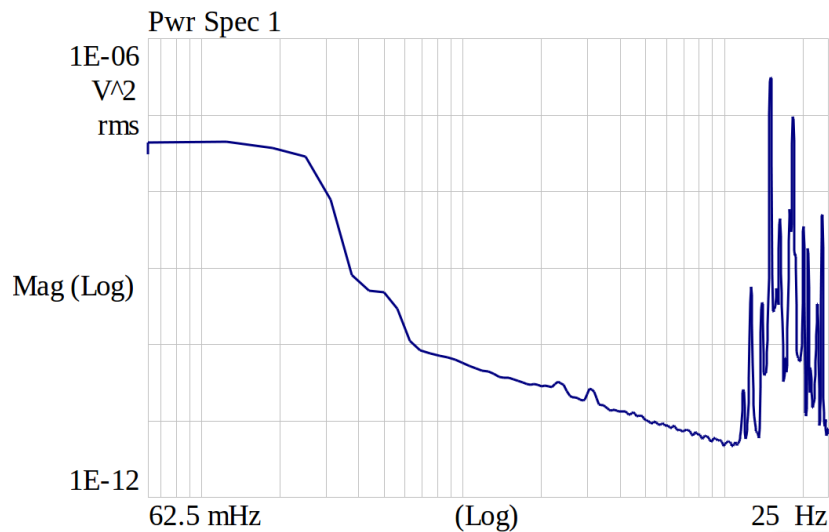


Figure 11.6: Experimental PSD of the monolithic IP prototype.

a tilt control: an elastic element was embedded within its feet (see Fig. 11.7). The piezoelectric actuators Physik Instrumente P-239.30 will be used. They provide a force of 4500 N and a dynamic range of 40 μm . An experimental setup constituted by an IP base ring and three piezos actuators has been tested in SAFE (see Fig. 11.8).

To monitor the IP bottom flange displacement with respect to ground, 3 LVDT sensors will be installed in parallel with the piezo actuators (see Fig. 11.8). The LVDT design is based on the standard model mounted on the SA filters and used to monitor the chain elongation. A 10 kHz AC signal flows in the internal coil, while the external coil, which is the passive element, is composed by two parts wrapped in opposite direction (clockwise and anti-clockwise). When the external coil moves with respect to the symmetric position, the output signal at the passive coil extremities is proportional to the difference between the signals induced on both parts. A 10 kHz signal, whose amplitude is proportional to the relative displacement between the two coils, is induced on the passive elements [348].

This system provides a displacement sensitivity of $10^{-8} \text{ m}/\sqrt{\text{Hz}}$ in the entire band. The electronic performances and the vacuum compatibility of the materials have been already validated in Virgo.

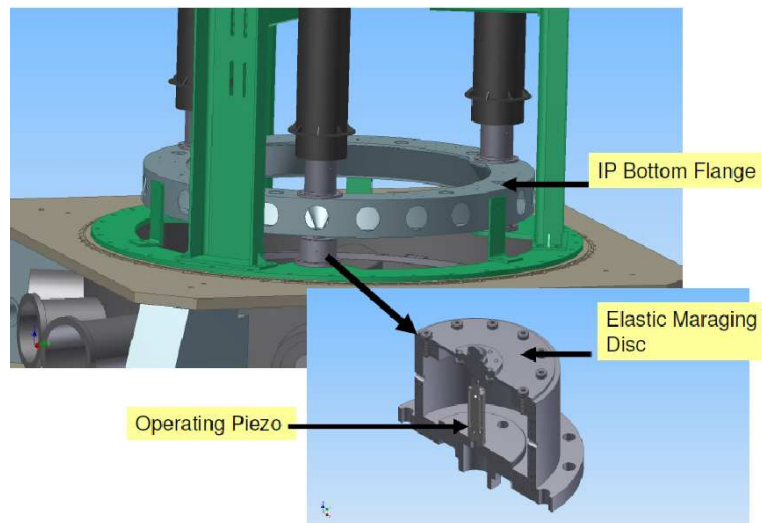


Figure 11.7: Rendering of the piezo installed inside the elastic support of the IP bottom flange.

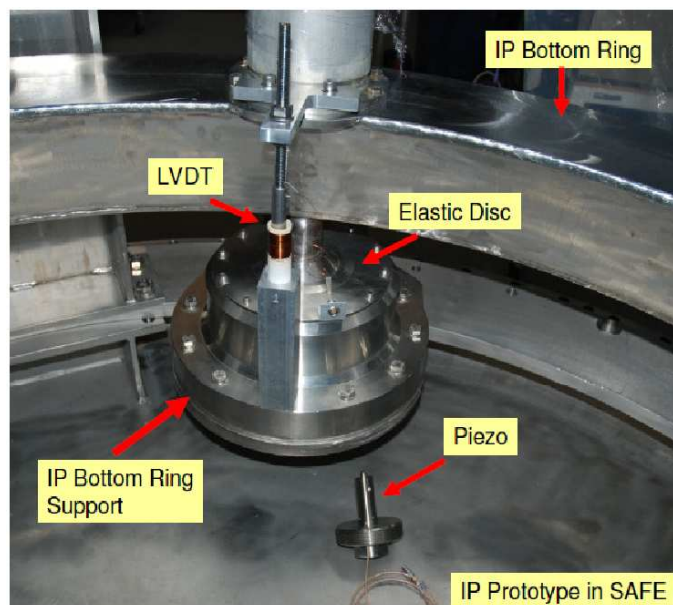


Figure 11.8: Images of the piezo setup in SAFE.

11.1.3.2 The filter 7 upgrade

Beside the mirrors, new large components must be suspended: **CPs** from the **NI** and **WI SAs**, the **POP** from the Power Recycling (**PR SA**). Moreover, large baffles will be suspended around each mirror. Therefore it will be necessary to upgrade all the mirror payloads and consequently the interfacing **F7**.

General description of the filter 7 The last stage **F7** of the present **SA** was designed to suspend and steer the payload [349, 350]. For this reason the bottom of the **F7** body is clamped to a large "sea gull" shaped aluminum flange connected to four aluminum legs with terminal coils each one facing one of the four magnets of the marionette: this coil-magnets system is able to displace the payload along z , θ_x , and θ_y **DOFs** (see Fig. 11.9).



Figure 11.9: Photo of the Virgo **F7** inside the laboratory during the assembly

In Virgo the whole **SA** chain and thus the **F7** body with its legs and coils are separated from the **UHV** environment of the payload by an Intermediate Vacuum Chamber (**IVC**) to preserve the cleanliness of the mirror coating.

The photo in Fig. 11.10 shows the **IVC** installed inside the **SA** tower, the four big holes are the places where **F7** aluminum coil legs go inside, they are contained inside steel pots bolted to the bottom flange of the **IVC** and shaped to face the magnets on each marionette steering arm.

The maraging suspension wire connecting the **F7** with the marionette supports the electric

cabling needed to power the payload control coils and the balancing stepping motors. Cables are arranged inside a pipe fixed coaxially with the suspension wire and crossing the **IVC** through the *conductance pipe* (see Fig. 11.11) [351].

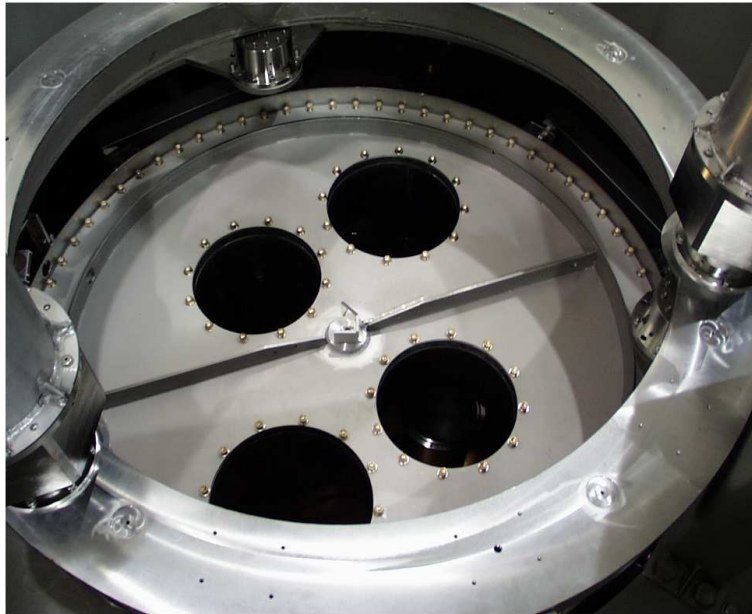


Figure 11.10: Photo of **IVC** inside the **SA** tower, taken during the installation.

The position of **F7** with respect to the **IVC** roof pots and the conductance pipe is controlled in all **DOFs** by the position monitoring and control system. A system of three horizontal **LVDT** sensors/coil actuators is placed in a 120° triangular configuration around the **F7** above the **IP** bottom flange (see Fig. 11.12). Each of these **LVDTs** has also a co-located Maxwell coil-magnet actuator, with the magnet embedded inside the **LVDT** primary and the coils shared with the **LVDT** secondary windings (see the working principle in Fig. 11.13). These actuators are intended to recover the **F7** position in case of strong excitations of the low frequency rotational modes of the **SA** below 1 Hz which, due to their high quality factors, are characterized by long decay times.

The angular tilt around the horizontal axes is monitored by dual-axes precision tiltmeter placed on the top of the filter body. The high sensitivity dynamical range is of 16 mrad and the resolution is of about $0.1 \mu\text{rad}$. The tilt adjustment is performed operating with precision **AML** stepping motors two sliders carrying the counterweight masses (see Fig. 11.12).

In order to achieve the correct angular positioning with respect to the vertical axis, the **F7** has a modified standard filter body to allow rotations with respect to the suspension wire and to the wire suspending the marionette. Two vacuum compatible ceramics ball bearings allow rotations steered by two stepping motors placed respectively above and below the filter body Fig. 11.14.

Design of the upgraded filter 7 The Payload subsystem (**PAY**) reference solution (see **PAY** chapter) foresees the adoption of a new frame that will support the new **CPs**, the **POP** and the baffles. The same structure will carry on the coil actuators both for the marionette

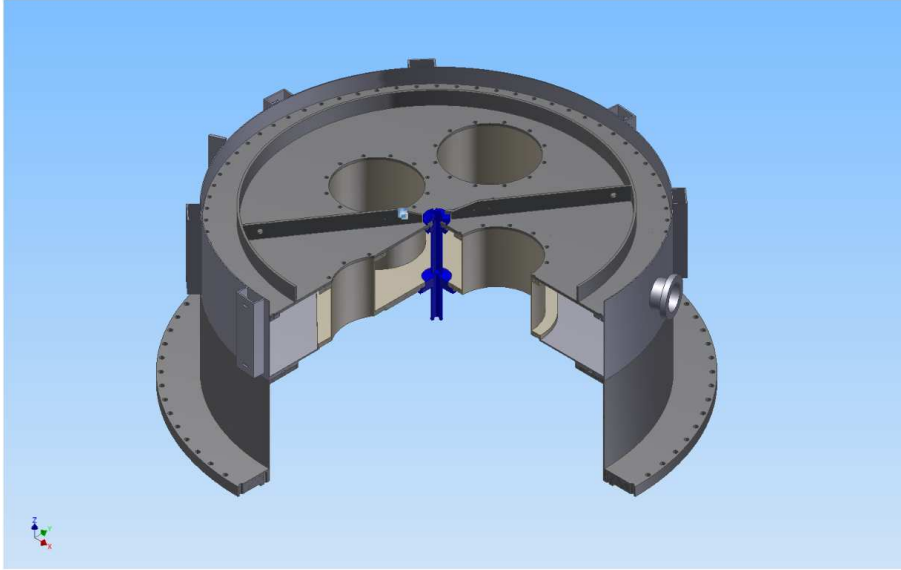


Figure 11.11: IVC section view. The conductance pipe is crossed by the F7 to marionette maraging suspension wire that hosts the coaxial tube containing the electric cables needed by the payload control coils and stepping motors.

and the mirror. This new frame will have a top flange rigidly connected to the F7 by two aluminum legs bypassing the present IVC. The marionette-mirror system suspended by a single maraging wire from the F7 will be conserved, but the RM will be abandoned. The implementation of the interface with this new payload for the case of the Beam Splitter (BS) tower is shown in Fig. 11.15.

The bypass of the IVC will imply the construction of a new vessel lying over the IVC top flange and embodying the F7 body (see VAC chapter), thus separating the rest of the SA from the UHV environment of the payload (see Fig. 11.16). The *cupola* of the vessel has a three petals structure that can be open to access the F7 from top and allow for its eventual maintenance. The IVC conductance pipe (see Fig. 11.11) will be moved above the F7 on top of the new vessel and aligned mechanically to the previous one. Also the cabling pipe will be moved to the maraging suspension wire connecting the F7 to the upper fourth standard filter. In this way one more filter stage is added to attenuate any spurious action from this device. The cabling pipe at present is foreseen to be crossed by about 60 wires of 0.4 mm diameter for coils and sensors (spares included), 38 wires 0.6 mm diameter for stepping motors and ring heaters (spares included) and 6 wires for the piezos (see Tab. 11.1 and schematic in Fig. 11.17).

The Virgo F7 body will have to be modified to avoid the mechanical interferences with the lateral surface of new vacuum separating vessel.

The “sea gull” flange will be removed together with the cylinder bars welded to filter body to connect it, the aluminum legs joining the payload structure will be rigidly connected to the filter body with the help of steel flanges welded to the body (see Fig. 11.18).

The AdV payload marionette is designed to be controllable also along the θ_z DOF (see PAY chapter). Therefore two more coils will be added to the payload control actuators. Since also

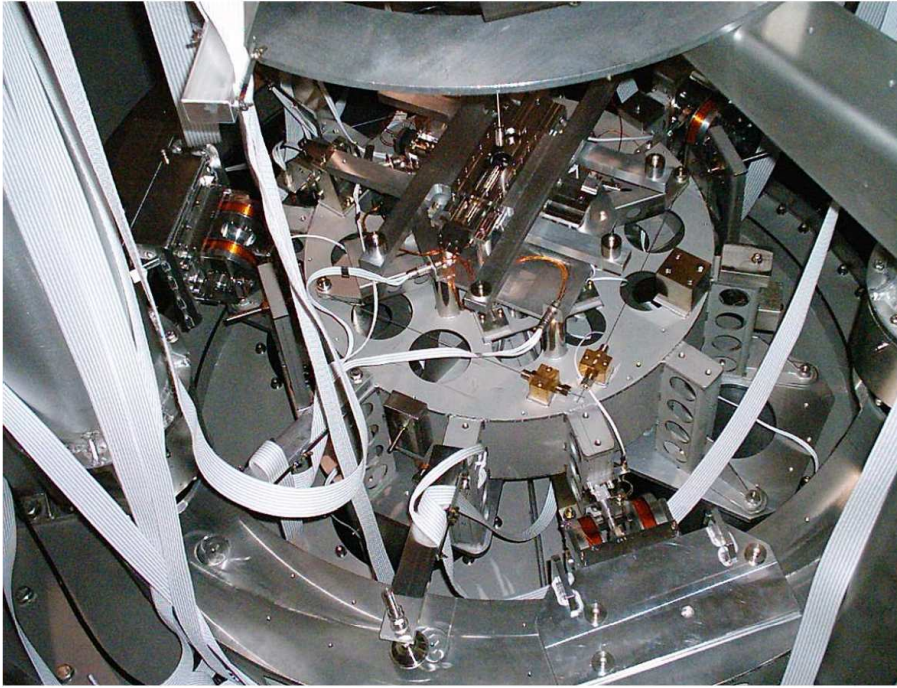


Figure 11.12: Picture of the full **F7** monitoring and control system installed. The motorized balancing system on the top and the 3 **LVDT** sensors/actuators around the filter body are visible.

| Devices | N. of Conductors | Diameter (mm) |
|-----------------------|------------------|---------------|
| 12 Coils | 24 | 0.4 |
| 7 Motors | 28 | 0.6 |
| | 21 | 0.4 |
| 2 Ring Heaters | 4 | 0.6 |
| 2 Temperature Sensors | 4 | 0.4 |
| 3 Piezos | 6 | TBD |

Table 11.1: Summary of the conductors inside the cabling pipe

the **F7** is required to be controlled in θ_z **DOF**, 3 more coil actuators will be needed. Part of **F7** monitor and control system will have to be moved from above the **IP** bottom flange inside the new vacuum separating vessel (see Fig. 11.15).

The arrangement of these wires and the suspension wire has to be done taking into account some constraints:

- to minimize the effective section of the conductance pipe;
- to leave the possibility of a relative motion of ± 5 mm in the horizontal plane between separating vessel and wires;
- to avoid any movement or friction among components of the assembly in order not to deteriorate the quality factor;
- to avoid an excessive lowering of the violin mode of the suspension wire;

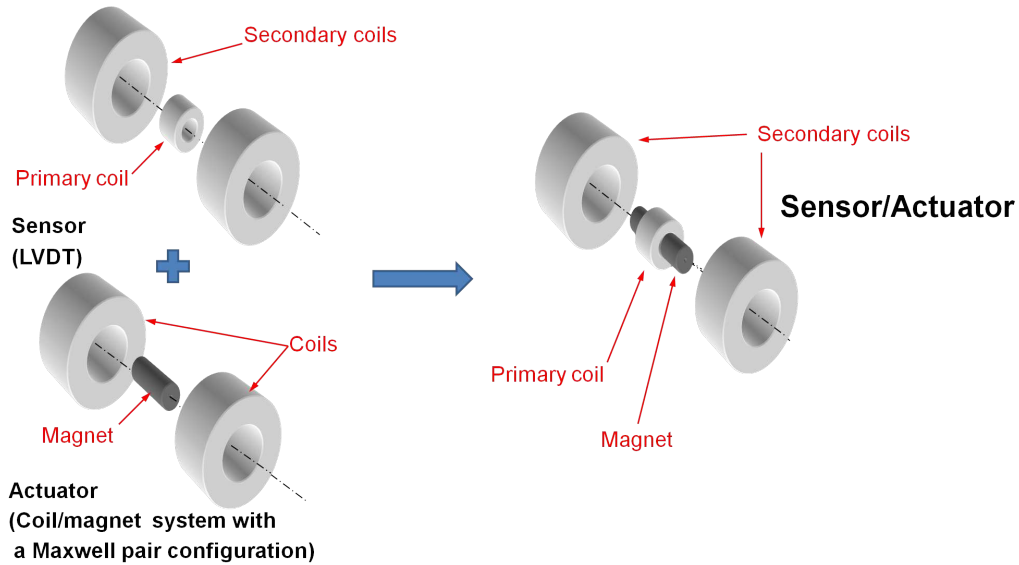


Figure 11.13: Conceptual schemes of the working principle of the **F7** sensor/actuator system. In order to merge the **LVDT** and the coil actuator in a single device, the secondary coils (and therefore their cables) are shared.

- **UHV** compatible with a bake-out up to 150 °C;
- to be easily connected and disconnected in the **SA**.

The basic idea is to put all the wires in a small metal tube and then completely fill it with an **UHV** compatible material.

Particular care is needed during the filling in order to avoid air entrapment in the metal tube that would produce virtual leaks. It is foreseen the use of a special **UHV** glue as filling material: a kind of Araldite with a working time of about one hour and with very low viscosity when heated. The filling is performed by plunging one end of the metal tube in the glue and by means of a vacuum pump connected to the other end which aspires the glue; during the filling the tube and the glue are heated to about 100 °C. Most of these procedures have been

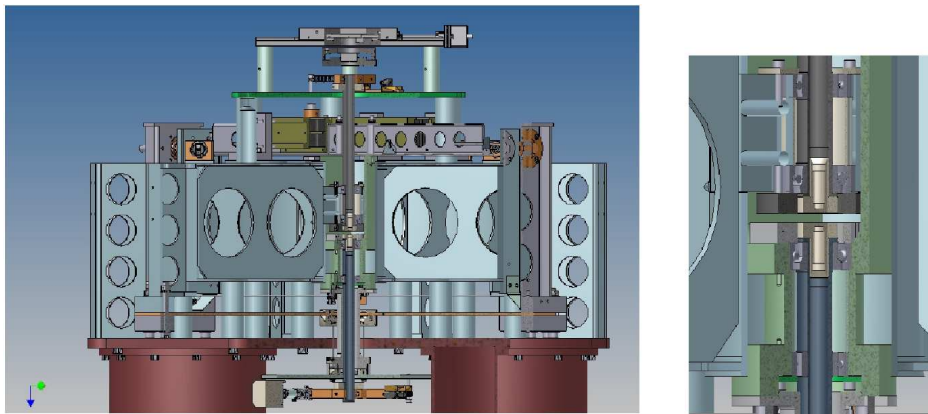


Figure 11.14: Rendering of the **F7** system to allow relative rotations around its axis with respect to the top **SA** chain and to the bottom payload.

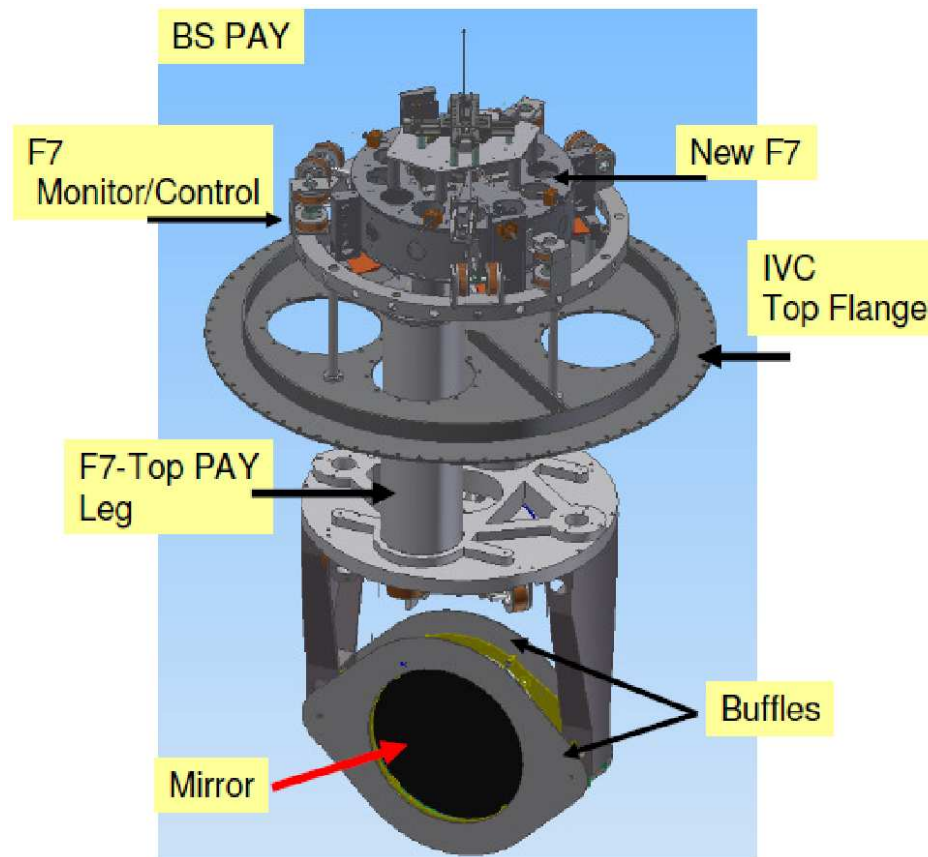


Figure 11.15: Rendering of the AdV F7 as interfaced with the BS payload. The top flange of the IVC is bypassed by the F7 legs and will serve as the support for the F7 Monitor and Control System.

validated for Virgo.

On the overall the new F7 will have to be compliant with the UHV requirements: the new filter body has been designed to be better cleaned and special care will be taken concerning the cleanliness of the magnetic antispring; the whole assembly will be performed in the INFN Pisa clean rooms.

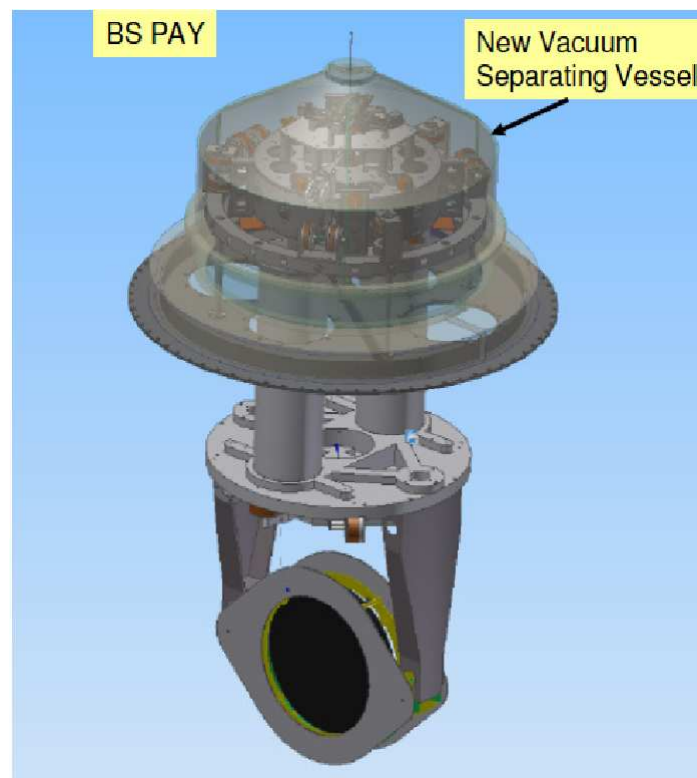


Figure 11.16: Rendering of the new vacuum separating vessel embodying the new F7-PAY-BS system

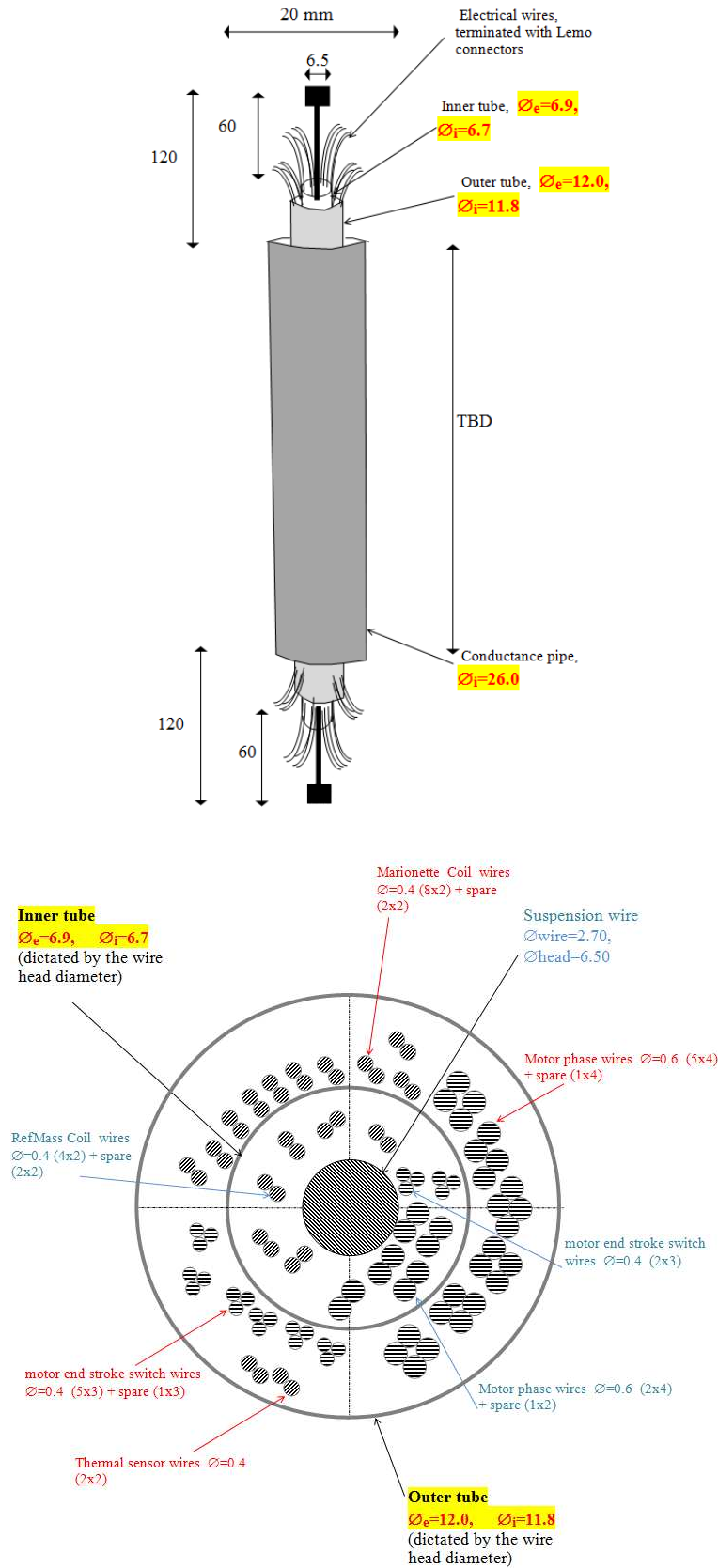


Figure 11.17: Schematics of the cables arrangement inside the new cabling pipe coaxial to the F7-SF4 suspension wire.

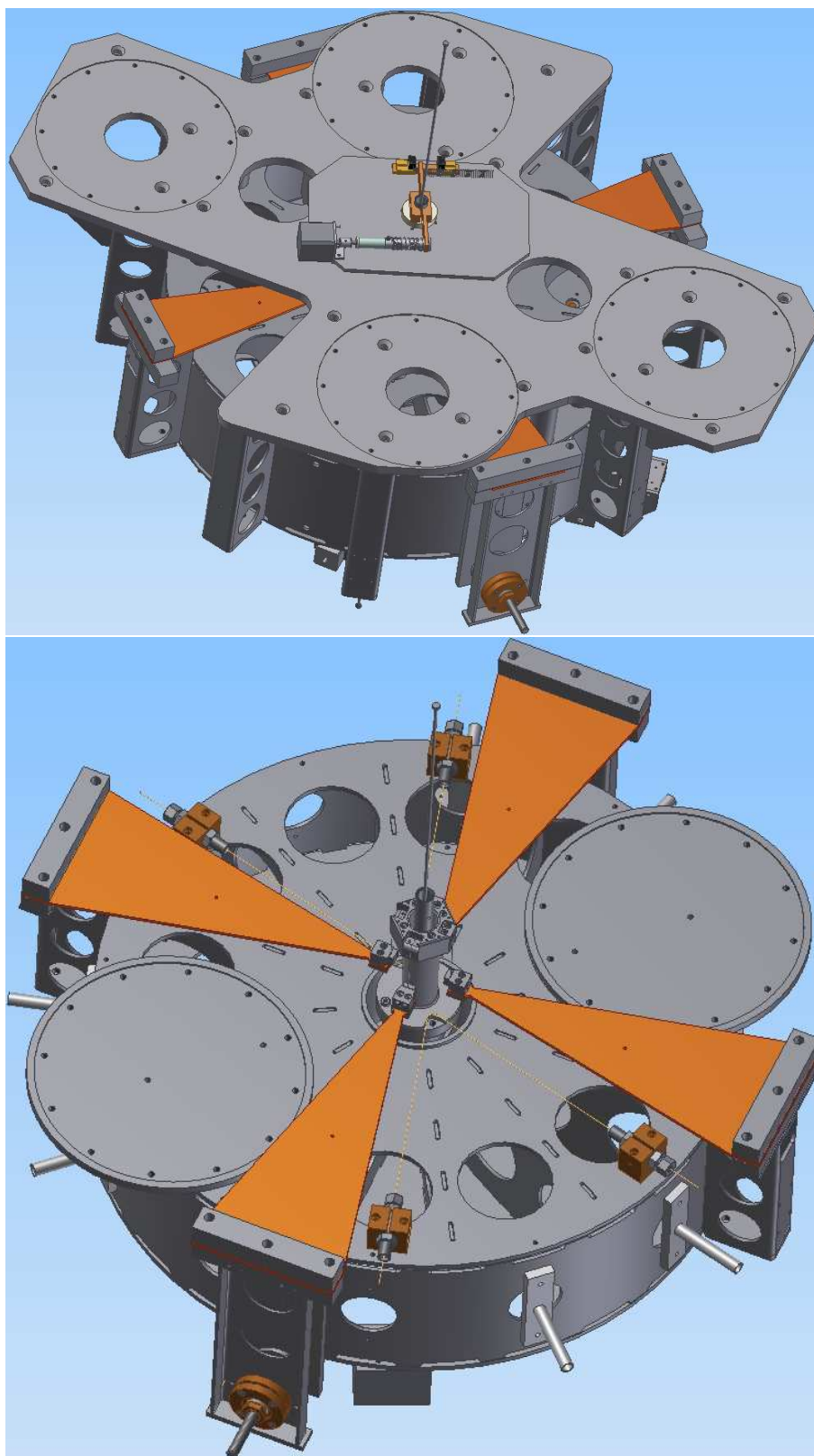


Figure 11.18: The new AdV F7 body (bottom) is compared with the Virgo one (top)

11.1.4 Signal recycling superattenuator construction

11.1.4.1 Signal recycling superattenuator description

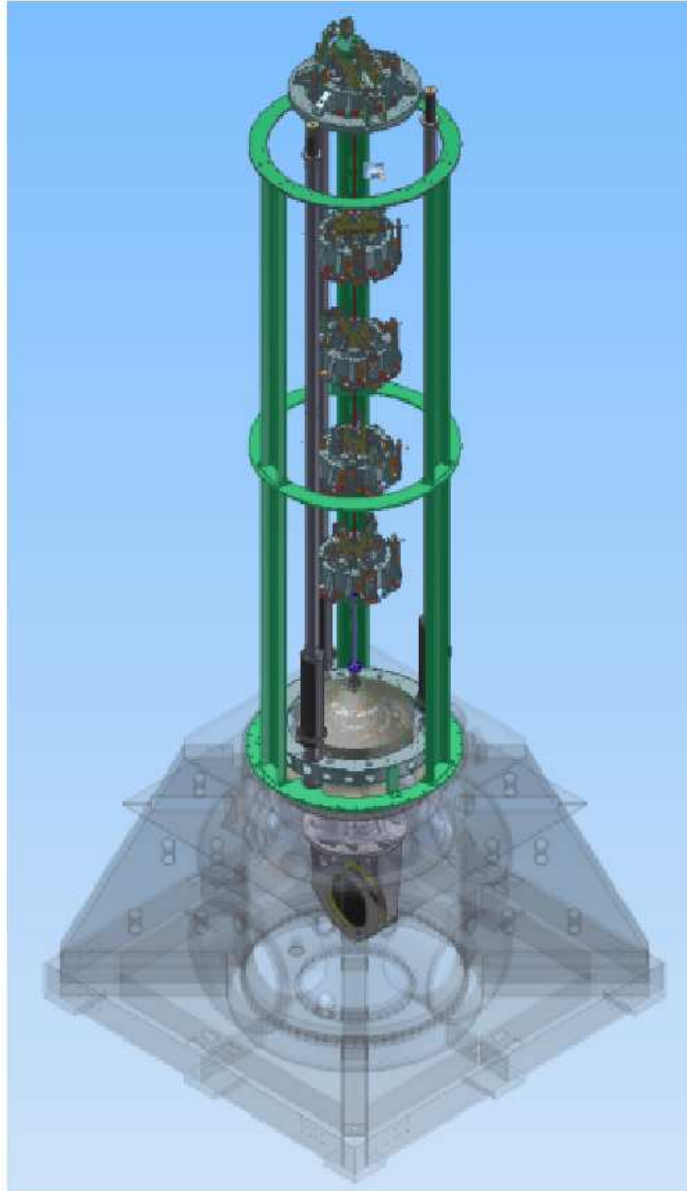


Figure 11.19: Rendering of the Adv long SA assembly (top) together with a detailed view of the new vacuum separation vessel above the F7 stage (bottom).

The SR mirror displacement requirements are of the same order of magnitude as the test masses ($6 \times 10^{-18} \text{ m}/\sqrt{\text{Hz}}$ at 10 Hz [352]). So, a long SA is needed to suspend it. Thus the new SR suspension will essentially reproduce the geometry of an IP+5-stage pendulum Virgo SA [346, 330] with all the foreseen upgrades (see section 11.1.3) implemented. The basic layout of an upgraded long SA is shown in Fig. 11.19.

11.1.4.2 Safety Frame

The entire system is surrounded by an AISI 304-L steel structure, named safety frame, with C-profile connected by rings (see Fig. 11.20). This structure was designed to allow the SA installation and to setup the safety stops of each moving element. Suitable bolts connect the structure to 3 vertical vessels called *viroles*. According with the vertical position of each filter there are shelves which support an internal ring. This ring has a safety function for the accidental breaking of one of the suspension wires. Removable connections between the shelves and the concerning filter are foreseen to keep the filter hooked on the internal structure during the assembly and tuning procedures.

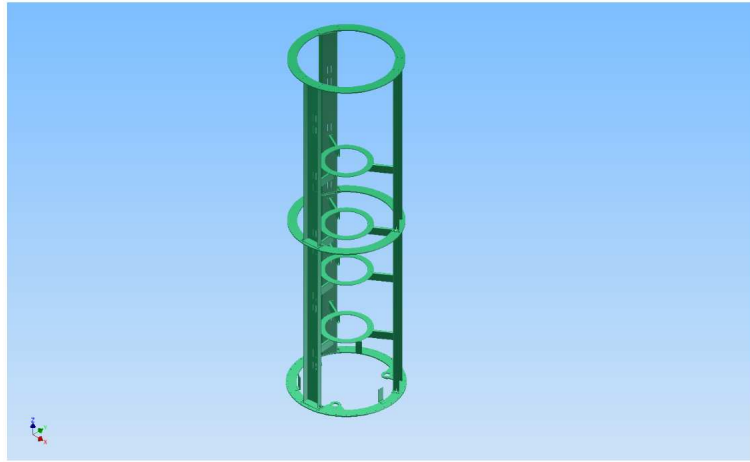


Figure 11.20: Rendering of *Safety Frame*.

11.1.4.3 Inverted pendulum

See section 11.1.3.1.

11.1.4.4 Top stage filter 0

The top stage of the chain is formed by a special filter, the **F0**, rigidly connected to AISI 304-L top ring suspended by three thin wires from the top of the **IP** (see Fig. 11.21). The **F0** is equipped with vertical spring blades and a magnetic antispring system (see next section). The **SA** suspension point is sustained by the **F0** blades and can be adjusted remotely driving a motorized endless with a dynamics of ± 35 mm.

The **SA** top stage hosts all the **ID** sensors and actuators (see section 11.2.4).

11.1.4.5 Standard filters

The first four pendulum stages of the **SA** are denominated *standard filters* (**SF1-SF4**) and are assembled as shown in the renderings Fig. 11.22 and Fig. 11.23.



Figure 11.21: Image of a Virgo SA top stage

The SF is essentially a rigid AISI 304-L steel cylinder (70 cm in diameter and 18.5 cm in height) supporting a set of maraging steel cantilevered triangular blades clamped along the outer surface of the filter body [353].

All the steel blades have a thickness of 3.5 mm, a length of 385.5 mm, while the width of the triangular base changes according with the load to be supported. The number of blades ranges from 12 (in the first filter of the chain) to 4 (in the last filter) according to the suspended load. Blades are pre-curved by cold bending to operate in flat configuration once loaded with almost uniform bending stress along its length.

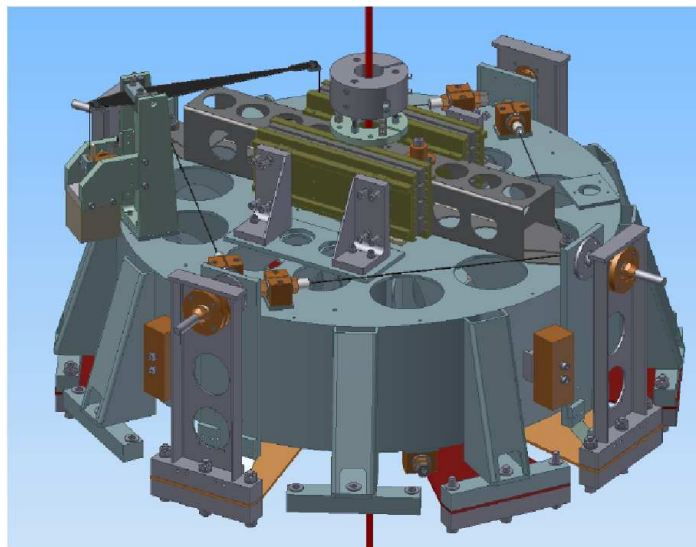


Figure 11.22: Rendering of a SA SF

The tip of each blade is attached to a steel *central column* through a 1 mm diameter piano wire acting as a hinge (see Fig. 11.23). This column is fixed on top of a steel frame named

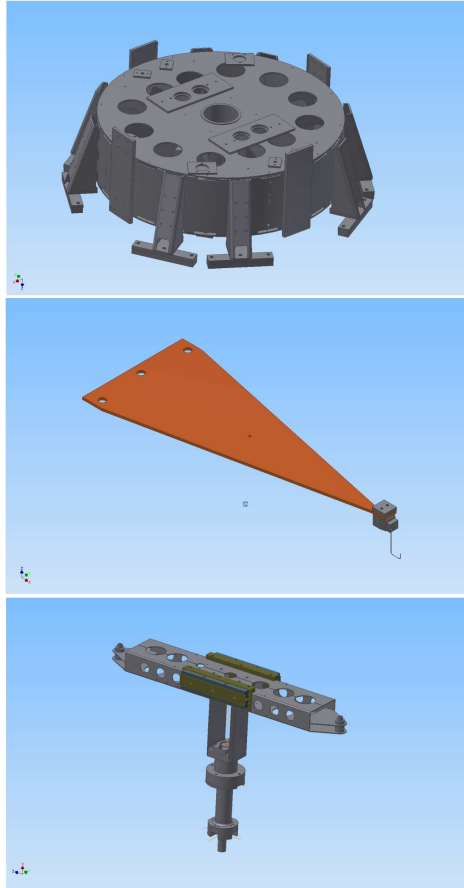


Figure 11.23: From top to bottom: filter body, filter blade, filter central column with crossbar

crossbar. The central column moves freely in the vertical direction and it is constrained to just vertical motion by two systems of four centering wires, respectively clamped on the top and on the bottom of the filter (*centering wires*). In this way a chain of springs is obtained also in the vertical direction.

The central column supports the load of the lower filters through a wire clamped as close as possible to the center of mass of the body.

The vertical working position of the central column (measured by an **LVDT** displacement sensor) can be varied by changing, through a lever arm acting on metal blades, the inclination of some of them. A special system call *fishing rod* (see Fig. 11.24), based on a motor controlled blade acting on the crossbar, is also used for the fine vertical adjustment of the moving part of the filter.

Once properly loaded, the main vertical resonance of the blade system is around 1.5 Hz. A damper is located in the middle of each blade (*blade damper*) in order to damp its first internal mode, while another special crossbar damper filter will be accommodated on the crossbar and tuned to suppress the lowest inner mode (see Fig. 11.25).

A further reduction of the main vertical resonant frequency of the filter, to increase the vertical attenuation, is obtained by softening the spring strength around the filter working

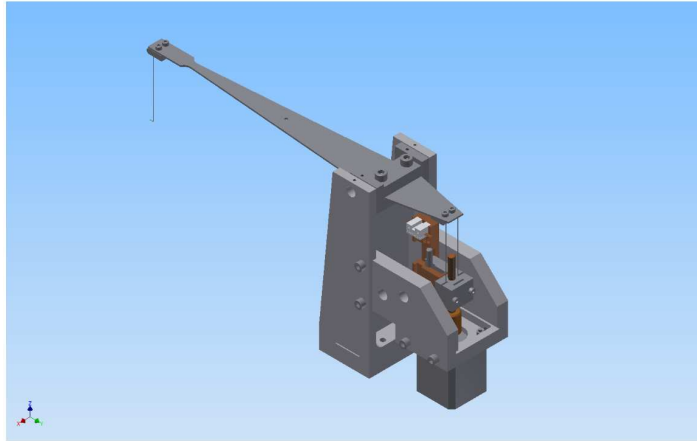


Figure 11.24: *Fishing Rod*

point through a *magnetic antisprings* system. The required antispring stiffness, and hence the number of magnets used for reducing the vertical resonant frequency, depends on the filter load.

11.1.4.6 Filter 7

See section [11.1.3.2](#).

11.1.4.7 Magnetic antisprings

The antispring is placed in parallel to the vertical blade spring mounting two matrices of magnets on the moving part of the filter, along the crossbar (thus connected to the next stage), and two facing matrices on the top of the rigid steel body of the filter (see Fig. [11.26](#)).

Each of the four magnetic matrix mounted on the filter is made of two or four lines of Philips ferroxdure (FXD 330) magnets (6 x 2 x 1.5 cm) producing a nominal magnetic field of 0.36 Tesla in the direction parallel to the 1.5 cm dimension [\[354\]](#). Each line of magnets in the matrix has the sense of the magnetic field opposite both to that of the neighboring line, in the same matrix, and to that of the line facing on the opposite matrix. This configuration allows minimizing the total magnetic dipole of the system, thus reducing the coupling with the external magnetic field.

As mentioned before, the number of magnets in each line is decreased from the top to the bottom filter to match roughly the need of antispring elastic constant. Fine tuning of the antispring force is obtained by setting the horizontal separation of the magnetic matrices. A vertical frequency of 0.4 Hz on the filter can be attained with a separation between the magnetic matrices of about 1 cm.

A full characterization of the antispring system (dependence on the positioning, on the temperature and on the number of magnets) has been given in [\[355, 356, 357, 358\]](#). This work has shown that large tolerances are allowed in the assembly of the antispring matrices.

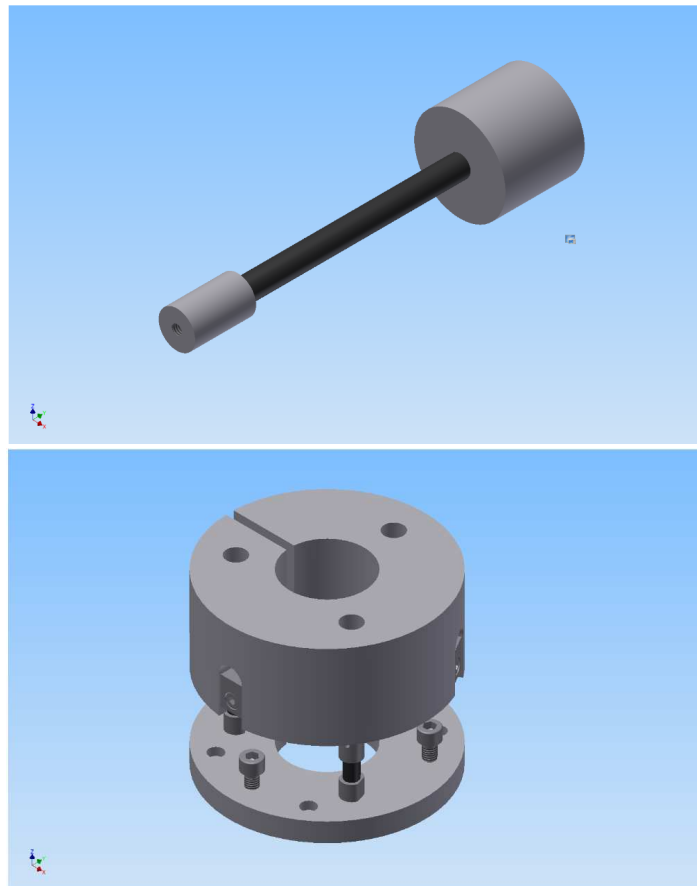


Figure 11.25: Top: *Blade Damper*. Bottom: the crossbar damper filter

The antispring ferrite magnets have been tested under vacuum after the baking outgassing treatment [359]. They exhibit a negligible outgassing rate at room temperature.

The supports are made of titanium, a not ferromagnetic material showing the same thermal dilation coefficient of the magnets.

The glue proposed for attaching the magnets on the supports is VAC-SEAL. This glue has shown a very low outgassing rate [360].

The ferrite magnets and the entire antisprings system can undergo heating until 200 °C without effects on the magnetic and mechanical performances [361].

11.1.4.8 Centering wires

The centering wires are made of piano wires steel (see Fig. 11.27). They will be protected from rust formation by chemical electroless nickel plating. All the centering wires will be set on the bench at a frequency 150 ± 20 Hz, just sufficient to keep the moving part of the filter aligned.

The relevant point is that a large tension of the centering wires induces an extra vertical stiffness on the moving part of the filters, causing a reduction of the vertical attenuation

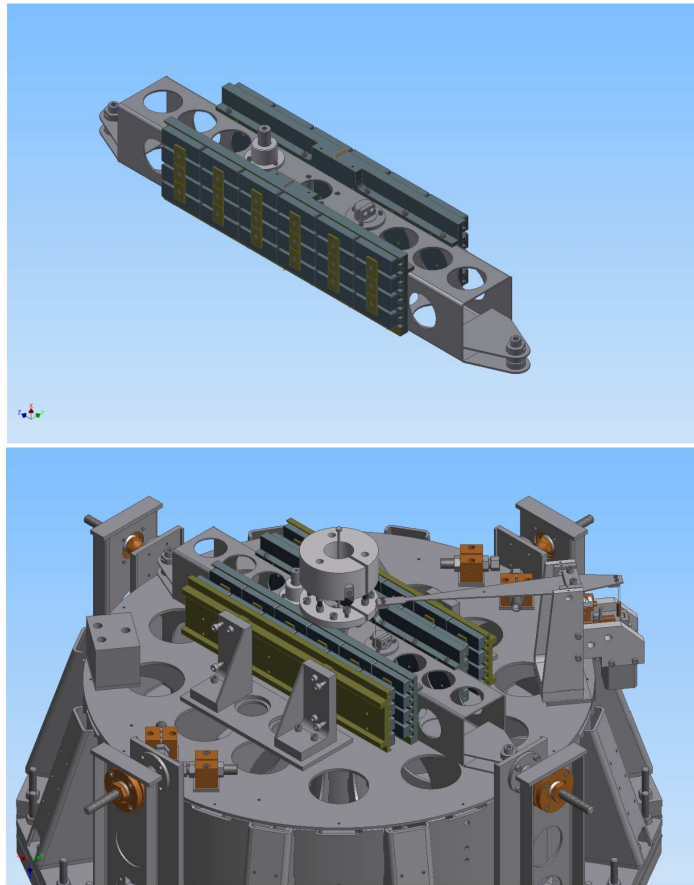


Figure 11.26: Top: crossbar plus magnets. Bottom: SF detail view

performances [362]. In this condition, the tension of the wires is sufficient to keep the central column aligned and it is small enough to avoid overstress (and thus creep) inside the material. The end of each of the 8 centering wires is strongly clamped in a steel mandrel. This system has shown in Virgo to be satisfactorily stable on the long term.

11.1.4.9 Spring blades

The steel blades (see Fig. 11.28) of the mechanical filters [363] have a thickness of 3.5 mm, a length of 385.5 mm, while the width of their base changes according to the load to be supported. The triangular shape gives the blades a rest and stressed shape with a single curvature radius and allows distributing uniformly the stress in the material under load. Bending curvature and dimensions are such that in a loaded cantilever the internal stress is always kept well below $2/3$ of the elastic limit.

The studies that have been performed for the Virgo design [364, 365] have shown that the maraging steel 18% Ni C-250 (Marval 18) steel has to be used to avoid creep in the blades. The following thermal treatment of the Marval 18 has provided the best results in terms of creep, and ultimate tensile strength (UTS):

1. **solubilization:** 840 °C for 1 hour in neutral environment (Ar flux);



Figure 11.27: The centering wires

2. aging: 435 °C for 100 hour in neutral environment (Ar flux).

The yielding and UTS measured are about 1950 MPa [365]. All the blades will be protected from rust formation by a thin layer of chemical electroless nickel plating. After the chemical plating process the blades will undergo a thermal dehydrogenation treatment of 24 hours at 200 °C, to avoid hydrogen embrittlement.

The blades under load exhibit a 1.5 Hz pendulum mode and the first flexural mode at ~ 100 Hz. These blades have been heated under load at 80 °C without significant effects in their mechanical performances. The mechanical performance in Virgo has been satisfactory.



Figure 11.28: A pre-bent blade

11.1.4.10 Suspension wires

The Virgo suspension wires [366, 367], as like as the filter spring blades, are of maraging steel 18% Ni C-250 (Marval 18). The nail head is mounted inside a screw head by means of a split cup washer. The resulting wire headings are then simply screwed in two tapped bridges attached to the upper and lower suspension points of the lower and higher filters. The distance between the attach points of the two wires is only 5 mm in order to keep the rocking frequency of the filter below 1 Hz. The chosen diameters of the suspension wires allow having all the rotational frequencies of the chain below 1 Hz. In order to make possible the removing of a given filter from the chain, and to avoid too long suspension wires (with difficult machining), the wire connecting two contiguous filters are split in three parts operating small and light junctions. Each junction box is essentially a small Ti brick (few cm³) where two holes with the same shape of the connection wire-filter is placed. This means that the attach mechanism of the wire with the junction is identical to the wire-filter one. In order to maximize the resonant frequency of the violin mode of the suspension wire it is mandatory to place the junctions as close as possible to the filter body and to make them as light as possible (few tens of grams).

11.1.4.11 Crossbar dampers

In the Virgo filters there is a resonant mode involving the crossbar. This internal mode is due to the fact that the suspension wire connecting the crossbar to the next filter acts as a spring. The resonance, around 60-80 Hz, is suppressed by using an iron cylindrical mass of 2.5 kg resting on three viton columns at the center of the crossbar (see Fig. 11.25) [368, 369, 370]. The mass oscillates in the vertical direction while the viton columns act as damping springs. The length of the columns is chosen to tune the damping system on the frequency of the crossbar mode. This system is able to reduce by more than one order of magnitude the peak of the vertical transfer function within a tolerance of ± 1 mm in the tuning of the viton columns.

11.1.4.12 Blade dampers

The first flexural mode of each blade (around 100 Hz) can be suppressed by attaching at the point of its maximum oscillation, close to the center of the triangular surface, a short viton rod with a light mass accommodated near its extremity (see picture in Fig. 11.25) [370]. The mass oscillates in the vertical direction inducing a flexure of the viton rod with opposite phase to that of the blade's displacement. The frequency of the viton oscillator can be tuned on the blade first flexural mode by varying the position of the mass along the rod. In this way, the energy of the blade flexural mode is transferred to the dissipative viton oscillator and a strong attenuation is obtained.

11.1.4.13 Fishing rod

The fishing rod is able to tune the position of the crossbar with a precision of few microns and with a dynamic range of few mm. The MARVAL 18 triangular blade has a width of 40 mm,

a flexural length of 254 mm, a maximum load of 20 N, a curvature radius of 823 mm and a stiffness of 255 N/m. The blade is connected through a maraging steel wire (0.6 mm diameter and 200 mm length) to the crossbar. The adopted motor is a commercial ultra high vacuum compatible AML stepping motor chosen on the basis of the mechanical and outgassing tests [371].

11.1.4.14 Cabling

The cabling is used for the electrical connection between the equipment inside the towers and the one outside. Most of the equipment in the tower vacuum environment is mounted on the SA elements or on the optical benches. Cables start their path from the front-end electronics in racks placed sideways each tower, enter in the vacuum environment through a set of electrical feedthroughs mounted on few tower flanges, and reach the top stage, all mechanical filters and the payload.

The vacuum cabling of Virgo is subjected to several constraints which must be taken into account on the selection of the components, on the assembling tools and on clamping. The main design requirements can be summarized as follows:

Vacuum compatibility All the materials used for cabling have to be clean and with a low outgassing rate, to match the Virgo vacuum specifications [372]. Some conductors will be heated by the flowing current: hence some cabling components have to be vacuum compatible also at higher temperature.

Seismic isolation compatibility The cabling must not spoil the attenuation performances of the SA. High mechanical flexibility and clamping at suitable points are required for the cables attached to the SA, in order to prevent vibration transmission or generation of new resonances.

Electrical compatibility Depending on the type of application, some ratings have to be made. These are current, crosstalk, electrical disturbances and impedance. Current ratings are based on the conductor sizes, on the amount of current that will produce certain temperature increases of conductors and contacts, on the thermal capacity and heat transfer capability (in vacuum) of the electrical insulation. Impedance ratings come from the considerable length of the cables (up to 25 m): in fact, in this case, the cable impedance may become comparable with the load impedance, thus reducing the driving capability. Crosstalk is the electrical pickup caused in a conductor by near conductors, while electrical disturbances come from external electromagnetic field or from ground loops. Cables connected to the mirror coils and to the ACCs are particularly sensitive to these effects (in particular to inductive coupling): hence they should be suitably shielded and driven. Finally, cabling should not introduce additional noise, such as microphonics and triboelectric effects in cables or contact noise in connectors.

All the descending cables before the cabling pipe have a diameter of 0.6 mm. As is shown in Tab. 11.1, inside and after the cabling pipe the diameter of some of them is reduced.

Cables can be classified on the basis of their function.

- **Readout cables.** These cables bring back the signals from:
 - LVDT secondary coils;
 - thermal probes
 - LVDT secondary coils of ACCs;
 - end stroke of motors.
- **Control cables.** These cables have to power:
 - coils;
 - stepping motors;
 - accelerometer coils.
- **Driving cables.** These cables provide the driving signal for:
 - LVDT primary coils;
 - LVDT primary coils of ACCs.

Due to the large number of conductors needed for each tower (about 350 conductors), it is necessary to use multi-pole cables. For our applications flat cables are preferred to round cables. The latter exhibit a lower mechanical flexibility and a higher air entrapment inside the insulation. The immunity to electrical disturbances is critical for cables connected to the ACCs, to some LVDTs, to the mirror actuators (i.e. coil-magnet systems), to the optical bench devices. In order to minimize cable mechanical effects on filter performances, the links of cables between two adjacent filters have to be very slack, large bend shaped and with at minimum a 90° cable rotation in each link. A clamp at suitable points is also fundamental to avoid any possible friction. Another improvement in cable flexibility is achieved by using stranded conductors and braided shields, except in the last SA stages, where solid conductors are preferred in order to avoid mechanical friction among the wires of the stranded conductors.

Cables are terminated by mainly using three types of connectors:

- 25 pin type-D subminiature connectors to mate with the electrical feedthroughs;
- 32 pin circular connectors (MIL-C-26482) to mate with the electrical feedthroughs ;
- multipin LEMO connectors to mate with the devices.

The type-D connectors and circular connectors have PEEK insulation and gold plated copper alloy contacts, UHV temperature rated to 200 °C. The same connector may be shared between two cables. The LEMO connectors belong to a multi-pin series having push-pull and bias features; have PEEK insulation and a nickel plated brass shell, with gold plated brass contacts. At the device side, each cable is ended with several LEMO connectors, whose quantity and number of pins depends on the type of connected devices. All the connectors include crimp contacts. For the Virgo vacuum side cabling, the crimping has to be preferred to the soldering because it is cleaner, reproducible and practical. For the connection between SF4 and the upgraded F7 through the new vacuum separating vessel see section 11.1.3.2.

The list of the components, the cable arrangement inside the towers and the technical choices for the purchasing of each component are described in a technical report concerning the cabling procedures in Virgo [373].

11.1.4.15 Crossbar LVDT sensors

Standard Virgo LVDTs [348], with displacement sensitivity of 10^{-10} m/ $\sqrt{\text{Hz}}$ and dynamic range of ± 1 cm, will be adopted.

11.1.4.16 Accelerometers

The horizontal ACCs [374] are based on a mass suspended by means of a low resonant frequency spring system (see Fig. 11.29). A feedback loop keeps the mass on a reference position. Acceleration is derived from the correction signal applied to the ACC. The vertical ACC is based on the same principle as the horizontal one. The mechanics is different to achieve a low resonant frequency while compensating for the acceleration of gravity (see Fig. 11.30). These ACCs show a high sensitivity level in the low frequency region down to about 10 mHz. A measured value of the acceleration spectral sensitivity of about 7×10^{-10} m/s²/ $\sqrt{\text{Hz}}$ below 10 Hz was reported [374].

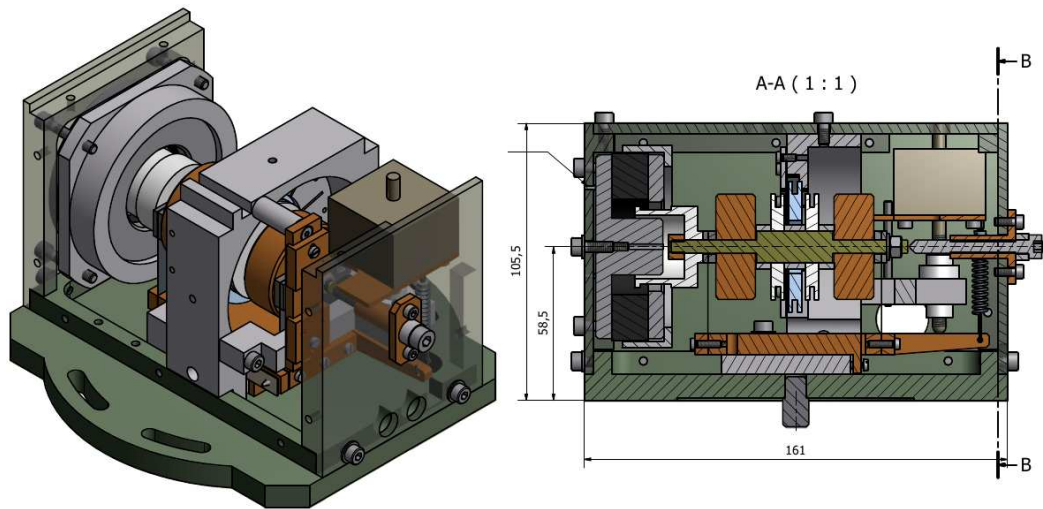


Figure 11.29: CAD renderings of the horizontal ACC.

11.1.4.17 Tools

Special tools are necessary for the production and the quality control of the SA chains. Here we list all the necessary tool sub-items followed by a brief description. The tools are divided in two groups: tools that have been used for Virgo/Virgo+ and are therefore already available and tools that have to be provided for AdV.

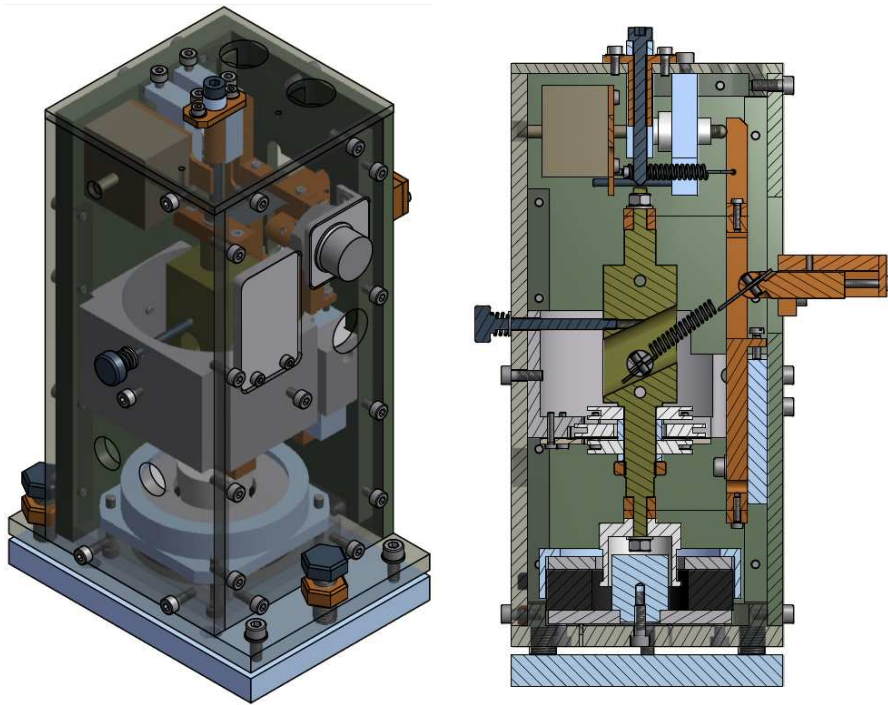


Figure 11.30: CAD renderings of the vertical ACC.

Tools Already Available:

Blade stress machine Each metal spring undergoes mechanical and thermal treatment. The resulting elastic constant has to be measured and the uniformity of strain has to be verified by a hydraulic machine capable of applying a known stress. Metal springs can be also cycled to check as better as possible their mechanical properties.

Oven for blades and suspension wires An oven (able to operate in a protected atmosphere under Ar flux) is also necessary for the thermal treatment of the maraging AdV blades and suspension wires. The system is already available at EGO 1.5 km W-labs.

Oven for cables and coils An oven, already available in the cleaning lab inside the Central Building (CB) is also necessary for the vacuum bake-out of cables and coil wires.

Magnetic force measurement machine Force and the torque between two facing magnetic plates of the antispring system will be measured with a special bench equipped with load cells.

Gaussmeter A commercial Gauss-meter will be used to measure the magnetic field of the magnets. This tool could be used to check the field of all the magnets mounted on the SA.

Tools needed for AdV:

Cleaning tools For the cleaning of all the items and components of the SA few ultrasonic cleaning machines are necessary with suitable dimensions.

Oven for the mechanical filters A large oven is necessary for the mechanical procedures during the production of the filters.

Plating tools A tank with the opportune chemical products is necessary to operate the nickel plating of the maraging steel components.

Hardness measurement tool To perform a quality test on maraging blades a standard hardness measurement tool is necessary. Experience in Virgo has shown that the measurement of the hardness is an exhaustive quality test of the thermal treatment.

Filter quality test setup An experimental test setup with a single filter and a tunable mass will be operated for tuning the main vertical mode, the blade and crossbar dampers and to measure the filter vertical transfer function.

11.1.5 Short superattenuators upgrade

The **IMC** length noise specifications provided by ISC (see ISC chapter) require the installation of another standard mechanical filter along each of the short **INJ** and **MC** chains (see INJ chapter). A similar upgrade will be performed on the **DET SA**. This changes are aimed to improve both the longitudinal and vertical seismic attenuation performances of these **SAs**.

The short Virgo **SAs** are composed by a single stage pendulum chain with the **F7** directly suspended to a **F0** placed over an about 2.5 m-high **IP** (Fig. 11.31).

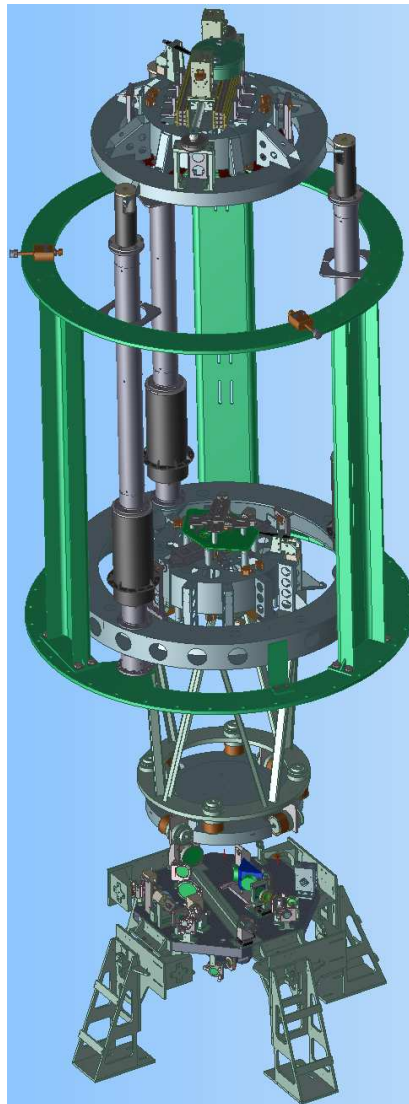


Figure 11.31: Rendering of the short INJ suspension of Virgo+. Apart from the detail of the payload, the **SA** of **SIB1**, **MC** and **SDB1** are the same: composed of one steering **F7** pendulum stage.

The new **SF** (see section 11.1.4.5) will be added between **F0** and **F7** (see Fig. 11.32). The distance between these filters allows the insertion of this additional stage that would increase, with relatively little effort, both the horizontal and vertical attenuation by about 40 dB above the low frequency suspension resonances.

It will be necessary to upgrade the **F0**, adding a few more maraging cantilever blades to sustain the new **SF** load. Also the **IP** flexible joints and partially the **SA** cabling will be upgraded.

In all these **SAs** it is also scheduled the installation of the **F7** monitoring and control system, as the one presently operating on the long **SAs**. Moreover, as in the long suspension chains, the upgrade of the mechanics for control system purpose will be done: the **IPs** are already monolithic and also in this case the three elastic supports of the **IP** legs are ready to host the piezo actuators.

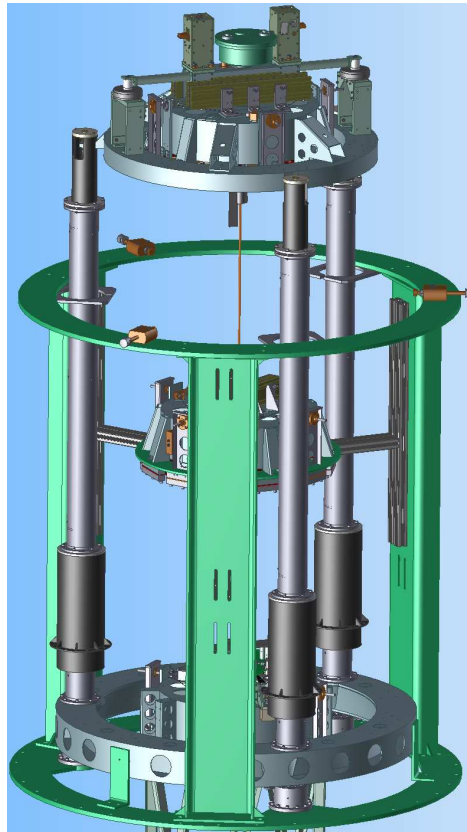


Figure 11.32: Rendering of the Adv short **SAs** assembly with the extra **SF** installed

11.1.5.1 Cabling of short superattenuators

The cabling of short **SAs** will be reshuffled and partially upgraded to connect the new **SF** sensors (Crossbar **LVDT** and **PT100** thermometer) and the fishing rod stepping motor, and to adjust the descending catenaries to the new **SF** clamps. Consequently the existing cables have to be replaced with longer ones. Moreover additional cables are required to connect the increased number of devices on **SIB1** and **SDB1**.

On the short **SAs** the air to vacuum cabling feedthroughs are not of the same standard adopted for the long Virgo **SAs**: a first version of **CF 250** flanges with **SUB-D 25-pins** connectors were installed, while a second version of these flanges for the long **SAs** were equipped with **32-pins**

MIL-C-26482 connectors (see section [11.1.4.14](#)). The experience made during the operation of Virgo suggests upgrading the short SA cabling feedthroughs with this second version of connectors.

11.1.6 SAT mechanics interfaces

11.1.6.1 VAC

The **F7** upgrade (see section 11.1.3.2) requires the installation of a new vacuum separating vessel that will include the **F7** itself in the payload environment. Since the new **F7** will have to be compliant with the **UHV** requirements, all its components will be treated and cleaned according to the standard Virgo procedures [330]. Moreover the new vacuum vessel is designed by VAC keeping into account the mechanical interferences with the **F7**, the **SA** dynamics, and the **SAT** installation and maintenance procedures. The new conductance pipe above the **F7** will be crossed by the **F7** and the payload cabling. The geometry (length and inner clearance radius) will be determined by VAC by differential vacuum needs and could imply a new arrangement of the **SA** filters along the **SA** chain.

11.1.6.2 PAY

The mechanical interface of the **F7** with the new payload (see also the **PAY** chapter) will have to be compliant with the **PAY** requirements. The stiffness of the **F7** legs joining the payload, the accuracy and the noise level of the **F7** control and monitoring system are determined by the specifications for the **PAY** control (see **PAY** chapter). The payload cabling for actuation coils and balancing stepping motors will be part of electric cables descending from the **SA**: the arrangement of the cabling clamps and connections will be settled by joint investigations of their dynamics and electromagnetic compatibility.

The **F7**+payload total weight is foreseen to be approximately maintained in all suspensions except for those supporting the Fabry-Perot test masses (see **PAY** chapter): West End (**WE**), **WI**, North End (**NE**) and **NI**. As a consequence all the filters of these **SAs** will have to be upgraded with new spring blades.

11.1.6.3 INJ & DET

SAT shares with **INJ** and **DET** the cables, dedicated to the suspended benches, descending from the top stage the short **SAs**.

11.1.6.4 EGO facilities

SAT activities foresee a large use of the EGO facilities: the mechanical workshop, the cabling lab, the clean operation devices (the ultrasonic baths, the washing tunnel, the ultra-pure water system [375]), the outgassing baking oven.

11.2 SAT control system

11.2.1 Introduction

Superattenuator control in Virgo and Virgo+ was performed, with hundreds of electronic devices, thousands of line of code and billion of operations per second all cooperating to achieve state of the art performances with a duty cycle close to 100%. During several science runs, suspension control system did not limit neither sensitivity nor duty cycle. Two major upgrades, coil drivers and Digital Signal Processors (DSPs) were changed with minimal down time and impact on Interferometer (ITF) operation.

Most of electronic devices together with the overall architecture was designed in mid 90's and is now in operation since 11 to 13 years almost without any interruption. Devices have become obsolete and components are often no longer available. Analog to digital and digital to analog converter, once state of the art, are today out of production since years. Therefore it is necessary to upgrade the whole control system for being ready to operate AdV SAs in the next ten years, as it has been done for Virgo and Virgo+.

First DSP board, based on Motorola DSP96002, was put in operation in 1998. During the next few years, few minor upgrades produced 3 successive releases of the board. In 2005 the design for a completely new device, based on Analog Devices ADSP21160, started [376]. First prototypes were ready by the end of 2006 and a couple of years were spent in software development. The installation was completed in 2010. Therefore a new design for a processing unit on which rely for the incoming ten years is mandatory, since the 2005 one will be too old even for initial AdV (2015).

11.2.2 Superattenuator

Virgo SAs are complex mechanical structures (Fig. 11.1) controlled by 23 magnet-coil actuators commanded by two distinct DSPs. SA status is observed using more than 20 local sensors. AdV ITF provides additional information on relative displacement of suspended optical elements along three main directions: the beam direction z plus two angles around second horizontal axis x and vertical axis y .

Several actuators are available to set SA operating point and to control payload position within required accuracy: coil-magnet pair actuators are distributed in 3 actuation points (actuation stages):

- F0 and top stage
- F7 and marionette (hosting magnets)
- F7 and mirror (hosting magnets)

In addition to magnet-coil pairs, 18 stepping motors are distributed along the SA chain to set the correct operating point for seismic filters and marionette, DC position and orientation in the z - x plane and vertical DC position of suspended payload.

Along the SA chain several sensors are available.

- Accelerometers

- top stage only
- Displacement sensor:
 - vertical displacement between two seismic filters
 - 4 DOFs monitoring of top stage (vertical + 3 DOFs in the horizontal plane)
 - 6 DOFs monitoring of F7 displacement in respect with local ground
- Optical readout of payload displacement (marionette and mirror or Benches)
- F7 dual-axes electrolytic tiltmeter
 - see section 11.1.3.2.

Several changes to the mechanical structure of Virgo SA were introduced to fulfill AdV requirements. Detailed description of all mechanical changes are described in previous sections (see section 11.1.3 and 11.1.5). Among all changes, the most relevant for the SATCS are the following:

- One additional suspension to be controlled: SR
- Removal of RM used in Virgo and Virgo+ to support the coils acting directly on mirrors and subsequent relocation of these coils on a new mechanical structure rigidly connected to F7
- 6 DOFs control (6 sensors and 6 actuators) of F7
- Tiltmeters and Tilt control
 - Piezoelectric actuators to be located under SA bottom ring together with displacement sensors for piezo closed loop operation.

11.2.3 Superattenuator control system

The SATCS (see diagram of Fig. 11.33) takes care of setting and maintaining the correct operation point for SA and suspended optical elements. It constitutes the core of the Virgo ITF.

SA with its payload is always operated in closed loop mode. Reaction forces are applied on SA and suspended equipment in order to set to zero the difference with a given reference signal (usually a vector defining the operating point for the SAT+payload system). Feedback forces are always derived using a hard real time digital controller implemented using custom DSP boards.

11.2.3.1 Top stage control

The top stage control, also known as Inertial Damping due to the use of inertial sensors, is the digital control loop in charge of the reduction of suspended payload free motion. SA top stage control loops are always active regardless of the status of the ITF.

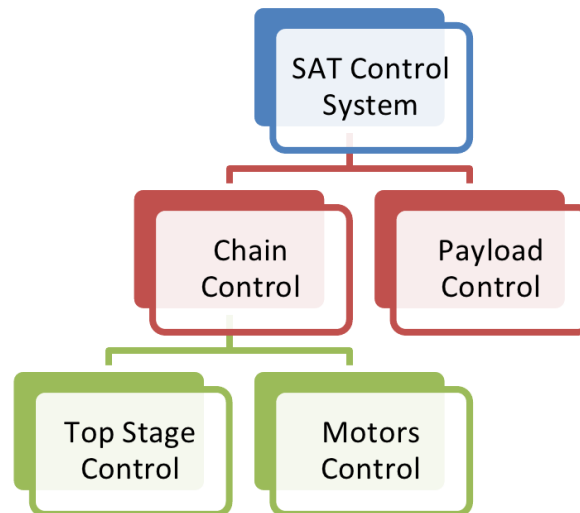


Figure 11.33: Hierarchical diagram of SAT control

The top stage displacement is continuously monitored using inertial sensors (**ACCs**) working in the DC-100 Hz frequency range with an equivalent displacement sensitivity of 10^{-11} m/ $\sqrt{\text{Hz}}$. Together with **ACCs**, the actual position respect to the surrounding supporting structure is monitored using **LVD**T-like displacement sensors, having a sensitivity of 10^{-8} m/ $\sqrt{\text{Hz}}$ and a linear range of ± 2 cm.

The digital control loop operates with a 10 kHz sampling frequency. That is the minimum rate required in order to avoid the introduction of actuation noise in the **ITF** detection bandwidth. The loop unity gain frequency is about 5 Hz.

Three degrees of freedom are currently controlled (two translations in the horizontal plane and the rotation along the vertical axis, as shown in Fig. 11.34) and a fourth one (vertical translation) is active in some **SA**.

The diagonal dominance in the Multiple Input Multiple Output (**MIMO**) system is achieved using static (constant) sensing and driving matrices. Today performances (see the plots of Fig. 11.34) allow a residual displacement less than $1 \mu\text{m}$ at the level of suspended payload and a relative speed between long arm cavities input and end mirrors of about $0.25 \mu\text{m/s}$. Even though this level of performance fulfills **AdV** requirement, the use of optimal and adaptive multivariable feedback design will eliminate the need of control diagonalization and consequently it would be possible to optimize the loop parameters for both the mixed and diagonal term elements of the sensor/actuator transfer function matrix [377].

11.2.3.2 Payload control

The payload control is the digital control loop in charge of the suspended payload positioning. Additional functionality is the damping of unwanted mirror motion.

Two different operational modes can be distinguished. When the interferometer is unlocked, the payload control makes use of measurements made in respect with a local reference frame. When the Virgo interferometer is in locked state, the payload control uses the set points

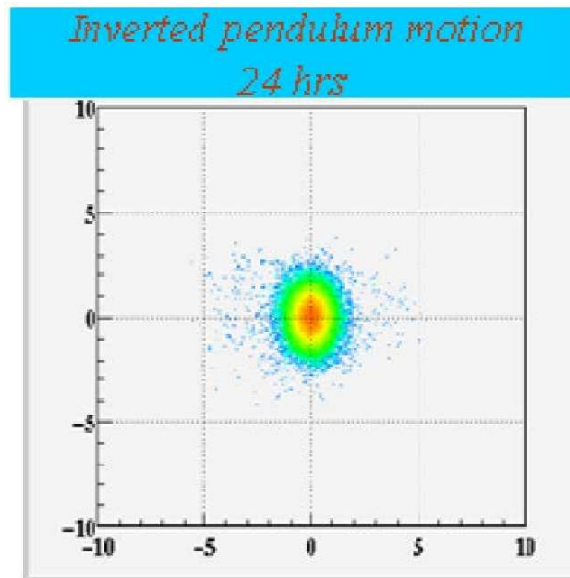
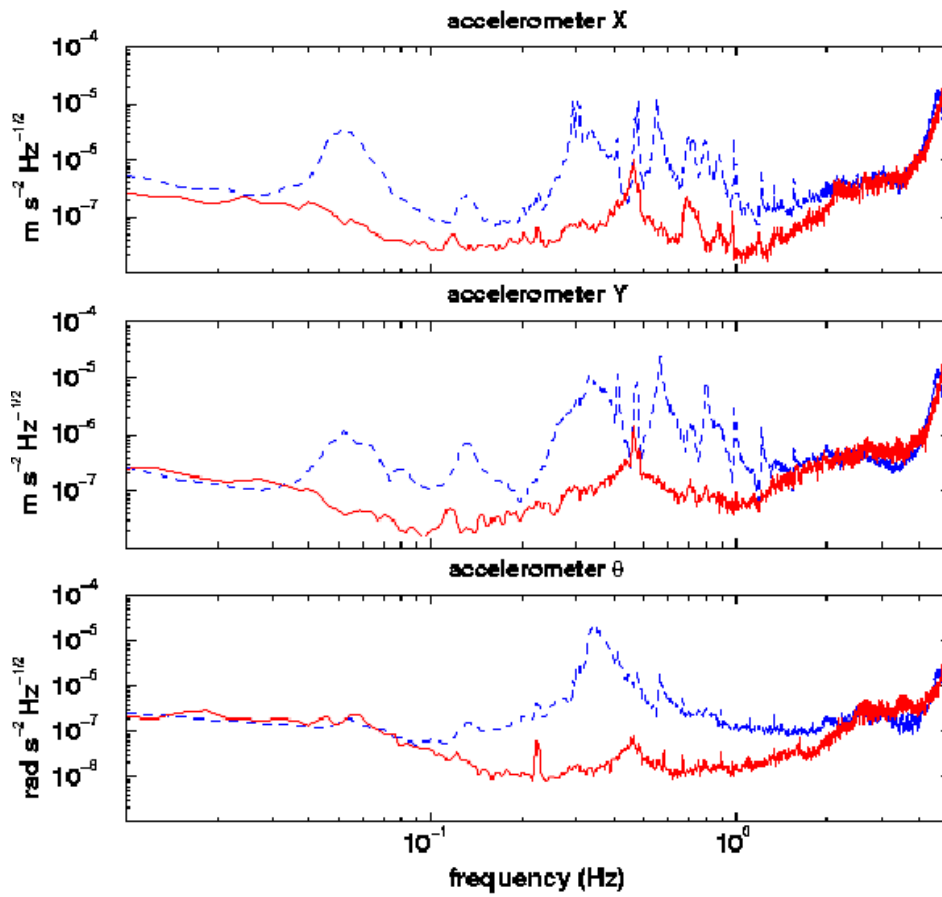


Figure 11.34: Left: Open Loop vs Closed Loop Accelerometers Output top stage. Right: 24 hr motion of the *Inverted Pendulum* (both axes are μm)

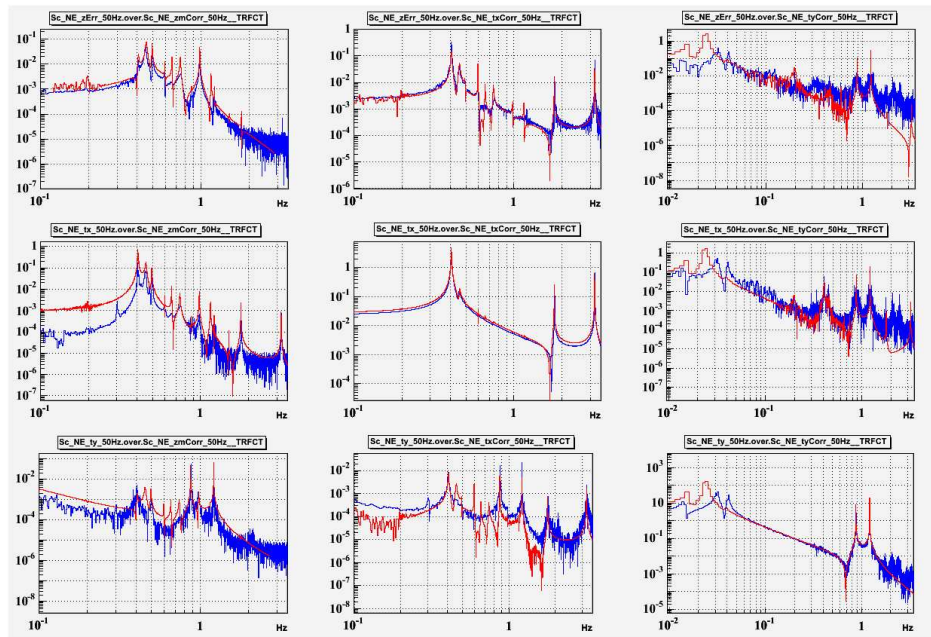


Figure 11.35: Virgo payload measured transfer functions (blue) compared with a model (red). **AdV** payload being different will have a different behavior. These plots are reported here only to give a rough idea of what suspension control system has to deal with.

distributed by global control and alignment computers. The mirror position is corrected along three degrees of freedom: longitudinal displacement (along the Virgo laser beam direction, z), rotation around the vertical axis (θ_y) and rotation along the horizontal axis orthogonal to laser beam direction (θ_x).

The low frequency part (10s of mHz) of the z error signal is forwarded to **SA** top stage control in order to correct the tidal strain acting on top stage, where bigger displacements can be achieved. The local payload position is monitored using two Position Sensing Device (**POSD**) reading marionette and mirror positions respectively plus a Charge-Coupled Device (**CCD**) camera reading the mirror coarse position. The payload measured transfer functions are shown in Fig. 11.35.

The performances of the payload control system meet **AdV** requirements allowing a residual angular displacement of less than $1 \mu\text{rad}$ using local sensors and less than 1 nrad using angular displacement measurements outputs from Virgo **ITF**.

11.2.3.3 Motors control

Along the **SA** chain there are several stepping motors used to set the correct operating state. This paragraph lists the main motors only to give a rough idea of their use:

- one motor for each **ACC** cancels the DC output by moving the **ACC** suspended mass;
- three motors acting on top stage are used for setting the **SA** DC;
- one motor acts on the **SA** suspension point for setting the vertical position of the whole chain;

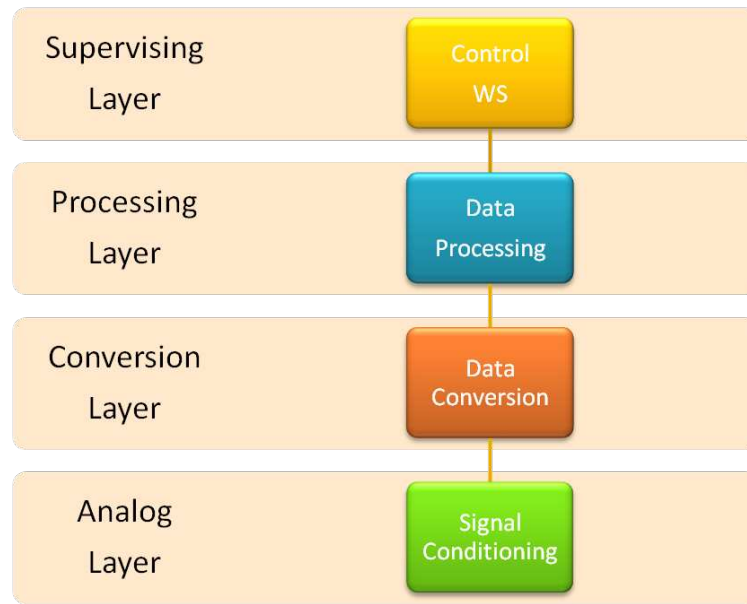


Figure 11.36: Diagram of SA control hardware

- one motor is installed in each SF to steer the *Fishing Rod* blade for setting the anti-spring magnets bar position;
- two motors allow relative rotations of the F7 with respect to the last SF and to the marionette.

Motors are never used during standard operation due to the huge electromagnetic noise produced. Control is always open loop and no more than one motor per tower is operated at the same time.

11.2.4 Superattenuator control hardware

11.2.4.1 Overview

SA control hardware can be split in four main categories (see the diagram of Fig. 11.36): signal conditioning, data conversion, data processing and control workstations.

11.2.4.2 Signal conditioning electronics

The main activity concerning conditioning electronics is managing sensors and actuators placed along the SA chain: ACCs, LVDTs, stepping motors, optical sensors readout, coil drivers and tilt meters.

LVDT The LVDT sensors (inductive position sensor) used in Virgo and Virgo+ to measure the position of the top stage of the suspended chain in the very low frequency band, do not require any particular improvement in their performances in order to be used in AdV. Their

sensitivity is in fact dominated by seismic noise and their dynamical range is compliant with **AdV** requirements.

On the other hand the conditioning electronics of these sensors need to be upgraded for two main reasons. The first one is the age of the electronic components used in the driver that are now obsolete and difficult to maintain; of course and even if not strictly required, using more recent and specific components will produce benefits also in terms of performances. The second reason concerns the possibility to implement a digital output on the driver by using an on-board Analog-to-Digital Converter (**ADC**) to immediately digitize the position signal, and sending it to the processing and control electronics through a digital link. This solution has the clear advantage to greatly reduce interferences and electrical pick-ups from the electromagnetic noise present in the environment. Moreover today converters have such a high resolution that any long cabling between analog source and converter would produce excess noise.

Accelerometers The main upgrade foreseen for the driving electronics is the use of a digital feedback instead of the analog one currently used in addition to the introduction of a digital output for the acceleration signal.

The upgrade of the **ACCs** used to perform the inertial damping of the top stage involves both the sensor and the internal driver (sensors are force-balance **ACCs**). At sensor level minor adjustments are foreseen to enhance the performances. In particular the thermal treatment of the maraging spring element will be improved for enhancing noise performances, especially in the low frequency range, that is the most interesting for the inertial damping application.

The implementation of such digital system would allow the design of more effective feedback for the internal loop, resulting in a wider frequency band, in an improved robustness and in improved noise performances.

Coil Driver Coil drivers are power amplifiers used to drive coil-magnet pair actuators steering Virgo optical elements. Those amplifiers need a wide dynamical range due to the big force impulse required to acquire the lock of Virgo optical cavities and stringent noise behavior during linear regime. The coil driver has two distinct sections: one high power section for lock acquisition and one low noise section for linear regime. The two sections are driven by two independent digital to analog converter channels. The coil driver can supply up to 1 A during the lock acquisition phase with a few pA/ $\sqrt{\text{Hz}}$ of noise during linear regime.

The coil driver were upgraded for Virgo+ and their current performances, in terms of noise, linearity and frequency band are already compliant with the **AdV** requirements [378]. The major upgrade is related to the introduction of a digital input, connected to an on-board Digital-to-Analog Converter (**DAC**) and to a selection of a new **DAC** converter (the one in use is obsolete). The digital link is particularly important since the actuation signals of the coil are the most critical for the **ITF** sensitivity, and a connection between the control and processing electronics that is virtually unaffected by environmental interferences is strongly desirable.

Motors driving No changes are foreseen for the power driving system of the stepper motors working on the suspension. A minor change is related to the control logic that is currently

obsolete.

Piezoelectric actuators drivers As already introduced at the beginning of this document, the presence of piezoelectric actuators placed under the SA base ring are one of the changes in respect with Virgo+ configuration. Today solution for the piezoelectric actuators driving is making use of commercial amplifiers.

Thermal stabilization Since several years a thermal stabilization system, required to control the temperature of the suspension and therefore its length and filters operating points, is ready to be installed. For proper operation of the suspension enclosure, temperature variations shall not exceed ± 0.2 °C. This requirement was up to now fulfilled stabilizing the temperature of the whole central hall and terminal building. Since such requirement could be easily met using heating belts wounded around towers, specifications on air conditioning system can be relaxed, as far as SAT is concerned. It is also worth mentioning that very low frequency variation of the air temperature does not affect at all suspension performances. Therefore a continuous change of mean temperature following seasonal change can be allowed.

Tiltmeter The IP, is actually a low pass filter for seismic noise only along three degrees of freedom: two translations in the horizontal plane and rotation around vertical axis. Ground tilt is transmitted to SA top stage without any attenuation. Moreover acceleration sensors on top stage are sensitive to tilt and produce a signal that is misinterpreted as a horizontal acceleration by the control loop, loop that forces the top stage to move even in absence of horizontal displacement of the ground.

Implementing a tilt control system promise to make the SA control more robust and efficient and thus to improve the detector duty cycle. Virgo detector operates 24 hours a day for several months (maybe up to a couple of years in the next future). Bad weather conditions limit Virgo sensitivity introducing noise at low frequency. Main source of noise was investigated during the last few years inferring that the main cause was ground tilt due to seismic noise. Even if ground seismic tilt was never directly measured by our site, a PSD of the order of $10^{-15}/f^2$ rad²/Hz is expected in good weather conditions. Experimentally (see Fig. 11.37) it was evident that in case of strong wind speed (about 20-30 km/hr) seismic noise grows up to two or three orders of magnitude between 100 mHz and 1 Hz with its maximum between 400 and 500 mHz (micro-seismic peak). A similar increase at lower frequency (between 10 mHz and 100 mHz) was also noticed in case of huge remote earthquakes.

It is worth reminding that the word ‘tiltmeter’ widely used is actually not proper. A tiltmeter by definition measures an angle in respect with the local direction of gravity. A force balanced ACC is well suited for this purpose but unfortunately it is also sensitive to horizontal and vertical acceleration and, simply looking at its output, it is impossible distinguish between acceleration and tilt. What will be most suited would be an angular ACC, sensitive to angular acceleration and insensitive as much as possible to longitudinal accelerations. The problem is not new and is common, for example, to any inertial navigation system where motion must be determined only on the basis of local sensor.

During the last 15 years our group tried to tackle this problem with different approaches [346, 347]. Today there are two parallel studies going on.

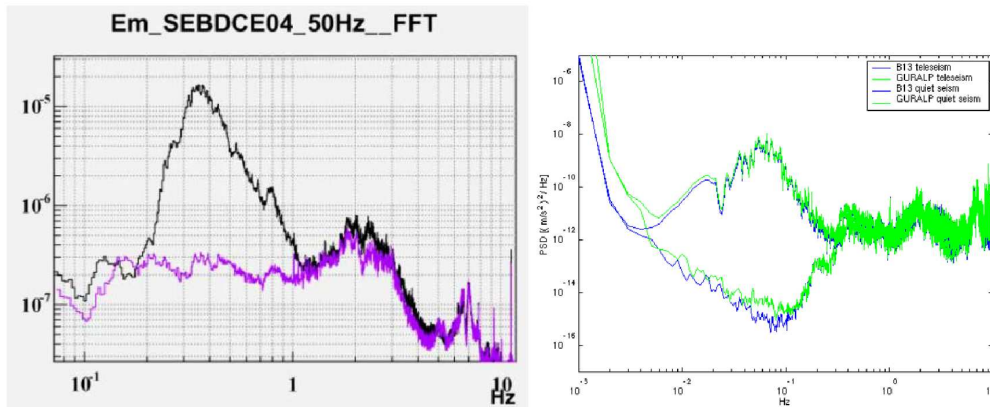


Figure 11.37: Left: Micro-seismic peak due to wind and sea waves (ground displacement [$\text{m}/\sqrt{\text{Hz}}$]). Right: Micro-seismic peak due to remote earthquake (ground acceleration).

The first solution is focused on the construction of a 3-DOFs acceleration sensor not sensitive to tilt by mechanical construction. A preliminary prototype has been built and is currently under test: it is basically composed by a metal disk suspended by a thin wire (see Fig. 11.38). The working principle is based upon the measurement of the relative displacement between the disk and the suspension point at the level of the suspension point itself [379]. This approach, if successful, will allow replacing the current ACC with this new device. The top stage will keep on tilting but tilt will not be converted any longer into a horizontal displacement by control loop. In addition, the same device could anyway output a tilt signal that could be used to drive piezo actuators located under the base ring and virtually zeroing IP tilt.

The second approach is very different and it is based on a principle of operation that only during last decade reached a good sensitivity [380]: the Hemisphere Resonator Gyroscope (HRG). Gyroscopes based on this technology have been recently used in satellite and missile inertial navigation systems with outstanding performances. For this second approach a Russian firm (MEDICON) was contacted to develop a single axis prototype (see Fig. 11.39) to be used for a correct evaluation of performances, possible upgrades and use in AdV.

Unfortunately today is not possible to select one of the two solutions. Therefore they will necessarily go on together until enough measurements are performed to make a decision.

11.2.4.3 Data conversion

With modern analog to digital and digital to analog converters unprecedented performances can be achieved. 24 bit nominal accuracy is nowadays a standard widely used in high level sound devices.

Analog to Digital Converter After an extensive evaluation, our choice for the analog to digital converter is Analog Devices AD7760. AD7760 is a high performance, 24-bit Σ - Δ ADC. It combines wide input bandwidth and high speed with the benefits of Σ - Δ conversion to achieve a performance of 100 dB SNR at 2.5 Mega-Samples Per Second (MSPS), making it ideal for high speed data acquisition. Wide dynamic range, combined with significantly reduced anti-aliasing requirements, simplify the design process. An integrated buffer to drive



Figure 11.38: Left: Image of the new tiltmeter prototype assembly. Right: Scheme of its basic working principle: sensing is realized by means of a spherical sensor S measuring the relative displacement $x_1 - x_4$. The horizontal acceleration of the box induces a sensor S output that is, to the first order in the box tilt angle, insensitive to box tilts.

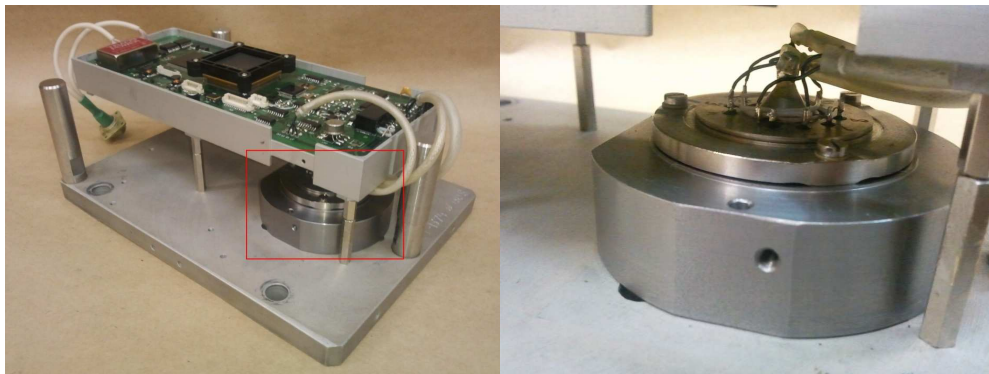


Figure 11.39: Left: a MEDICON HRG sensor prototype and its electronics. Right: The same prototype in a test cradle

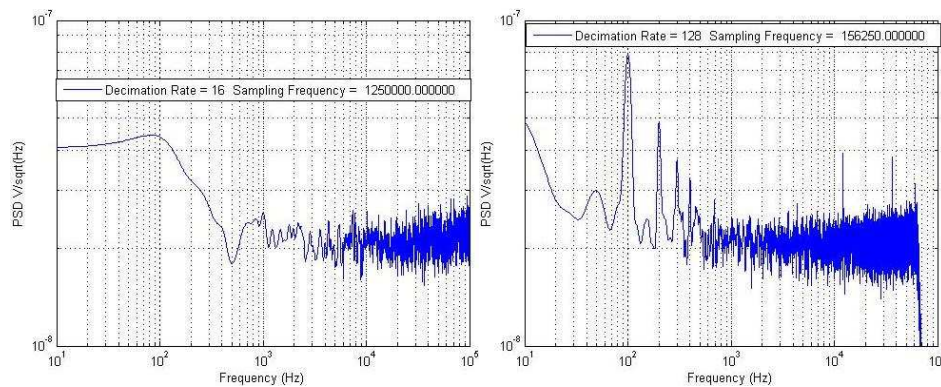


Figure 11.40: Left: **ADC** noise spectra. No signal applied and input closed with a $50\ \Omega$ resistor. Input range is 6.4 V peak to peak. Sampling rate is 1.25 **MSPS**. Right: **ADC** Noise spectra. Sampling rate 156.26 kSPS with a tiny signal applied at **ADC** input.

the reference, a differential amplifier for signal buffering and level shifting, internal gain and offset registers, and a low-pass digital Finite Impulse Response (**FIR**) filter make the AD7760 a compact, highly integrated data acquisition device requiring minimal peripheral component selection. In addition, the device offers programmable decimation rates, and the digital **FIR** filter can be adjusted if the default characteristics are not appropriate for the application. The AD7760 is ideal for applications demanding high SNR without a complex front-end signal processing design.

The differential input is sampled at up to 40 **MSPS** by an analog modulator. The modulator output is processed by a series of low-pass filters, with the final filter having default or user-programmable coefficients. The sample rate, filter corner frequencies, and output word rate are set by a combination of the external clock frequency and the configuration registers of the AD7760.

The reference voltage supplied to the AD7760 determines the analog input range. With our choice of a 4 V reference, the analog input range is ± 3.2 V differential biased around a common mode of 2 V. This common-mode biasing can be achieved using the on-chip differential amplifier, further reducing the external signal conditioning requirements.

To be noticed that all signals generated by **SA** sensors are amplitude modulated with a modulation frequency ranging from 10 kHz up to 50 kHz. The **ADC** will sample at high rate for then producing a decimated output. The minimum time delay that will be introduced by the **ADC** is $1.5\ \mu\text{s}$ with an output data rate of 5 MHz. Decimation down to 10 kHz will cost additional $100\ \mu\text{s}$.

In the left plot of Fig. 11.40 the measured **ADC** noise is reported when input terminals were connected together via a $50\ \Omega$ resistor. Input range was about 6.4 Volts peak-to-peak. Noise in the 1 kHz to 100 kHz range is about $20\ \text{nV}/\sqrt{\text{Hz}}$ that is about 2 orders of magnitude better than what it was in Virgo+ for **SA** accelerometers and **LVDTs**. The right plot of Fig. 11.40 shows the same plot at a different sampling rate and with a tiny signal applied at **ADC** input. Finally Fig. 11.41 shows the **ADC** behavior when a full scale signal is applied at **ADC** input. As visible from the measurement, harmonic distortion is below -100dB, in agreement with what specified by the supplier and the distortion of signal generator used for the measure. In Virgo/Virgo+ noise from **ADC** reading **SA** signals did not limit Virgo

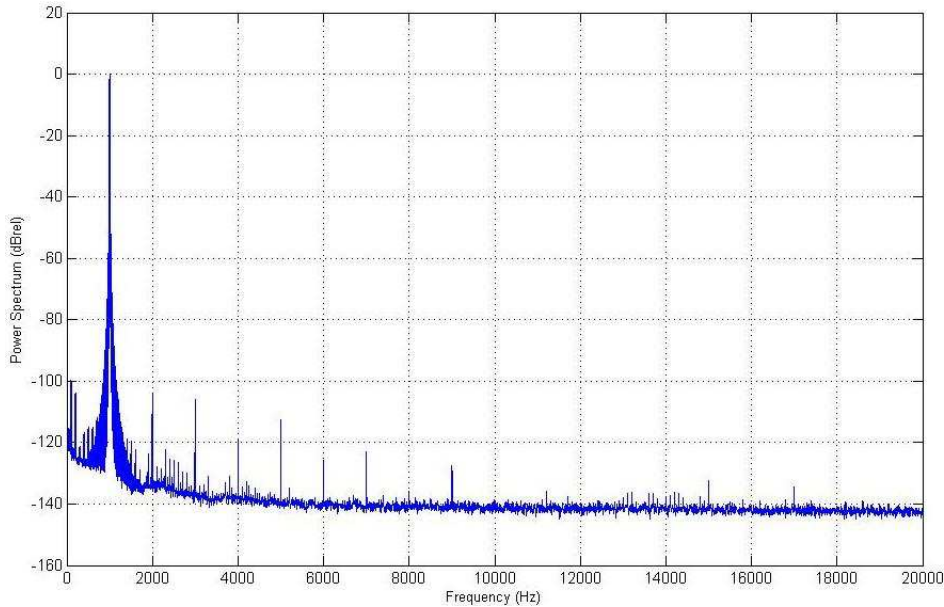


Figure 11.41: Qualitative estimation of an upper limit to ADC distortion. With a full scale sine wave signal applied at ADC input distortion is better than -100 dB that is the distortion of the signal generator.

performances. Nevertheless the suspicion of a possible ADC noise contamination, at ACCs level, has induced the change of some ACCs gain in early Virgo phases. At the same time, it is known that in Virgo/Virgo+ top stage LVDT readout was limited by ADC noise starting from few Hz. With the new ADC the overall system performances will be definitely improved. Moreover, the choice to direct sample modulated signal will allow for a large gain in terms of $1/f$ noise that will become negligible.

Digital to Analog Converters A strong effort to select a DAC for AdV has been made during the last two years. The only point where SATCS can somehow affect overall ITF performances is via the actuators and their driving electronics. Detailed specifications will be presented later in this document but it is worth spending a few lines here to explain selection process. Virgo/Virgo+ experience shows that DAC linearity plays a fundamental role. Feedback forces have usually a huge low frequency contribution that in presence of DAC non linearity produce unwanted up conversion. Glitches cannot be tolerated and therefore a compromise between noise (i.e. effective number of bits), linearity, glitch energy and small conversion time has to be found. The choice was finally set to Analog Device AD1955. AD1955 is a high performance stereo digital audio playback system. It includes a multibit Σ - Δ modulator, high performance digital interpolation filters, and continuous-time differential current output DACs. The choice of an ‘audio’ converter was taken only after accurate testing in the sub-audio frequency range where chip behavior is not fully specified by supplier.

As shown in the left plot of Fig. 11.42, behavior below 20 Hz is excellent regarding both noise and distortion (limited by measurement system).

The expected harmonic distortion has been numerically evaluated: Tab. 11.2 shows our result for an output signal of about 92 Hz with different amplitudes. Measured values are in agreement with what specified by the supplier.

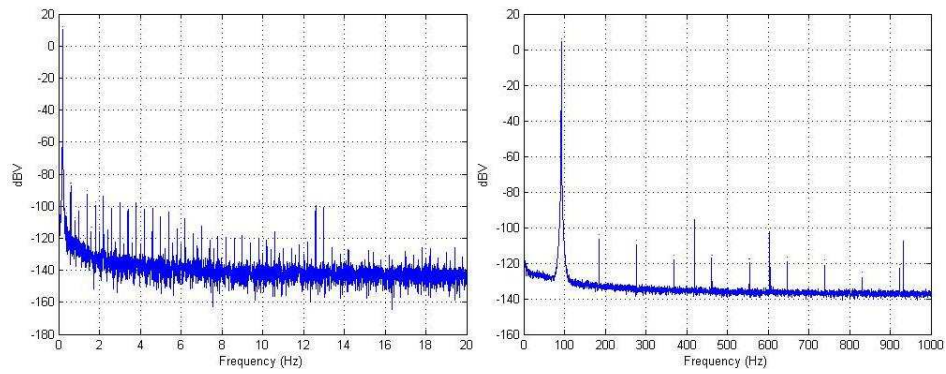


Figure 11.42: Left: AD1955 200 mHz- full scale output spectrum. Right: AD1955 half scale 92 Hz output spectrum

| V (rms) | Frequency (Hz) | 2nd HD (dB) | 3rd HD (dB) | THD (dB) |
|---------|----------------|-------------|-------------|----------|
| 3.890 | 92.4 | -107.6 | -113.4 | -106.5 |
| 1.945 | 92.4 | -110.1 | -113.2 | -107.6 |
| 0.973 | 92.4 | -103.9 | -107.9 | -101.6 |
| 0.486 | 92.4 | -95.6 | -98.1 | -90.4 |
| 0.243 | 92.4 | -102.1 | -79.3 | -78.2 |
| 0.122 | 92.4 | -105.4 | -114.7 | -104.3 |
| 0.004 | 92.4 | -79.5 | -83.6 | -76.3 |

Table 11.2: AD1955 Harmonic Distortion

| V (rms) | Frequency (Hz) | 2nd HD (dB) | 3rd HD (dB) | THD (dB) |
|---------|----------------|-------------|-------------|----------|
| 7.842 | 92.0 | -95.6 | -78.9 | -78.6 |
| 5.845 | 92.0 | -111.6 | -79.0 | -78.4 |
| 4.887 | 92.0 | -112.1 | -81.1 | -80.1 |
| 3.177 | 92.0 | -107.5 | -86.2 | -85.3 |
| 1.602 | 92.0 | -94.2 | -97.7 | -89.7 |
| 0.632 | 92.0 | -99.5 | -91.1 | -88.0 |

Table 11.3: Virgo/Virgo+ DAC Harmonic Distortion

It is interesting to compare the values of Tab. 11.2 with those obtained with the DAC used in Virgo/Virgo+ where harmonic distortion was about 30 dB larger (see Tab. 11.3). It is worth to add that AD1955 shows a much higher spurious free dynamical range.

The new DAC noise safety margin respect to the AdV design sensitivity can be increased up to a factor 10 or more, by reducing the actuation gain and consequently the displacement range. As soon as a new transfer function for the AdV payload is available, the noise budget will be re-evaluated.

It should be also kept into account that the new payload will have in general lower frequency normal modes and a higher number of coils acting on marionette (8 instead of 4) and on F7 (6 instead of 3). Increasing the number of actuation points and actuators of course will allow a further reduction of the DAC noise contribution.

11.2.4.4 Data processing

As digital signal processing was a key role in Virgo/Virgo+, in AdV, dependency on high reliability hard real-time processing will be even higher. In Virgo the total processing load on the SAT control system was in the order of 500 MFLOPS sustained, distributed on 18 processors (2 per suspension). The total IO rate was in the order of 400 Mbit/sec with extremely low latency and time jitter well below 1 μ s. In Virgo DSP took care of three distinct digital loops: local controls (operating at 10 kHz sampling period), automatic alignment (operating at 1 kHz) and longitudinal control (operating at 10 kHz). In AdV all these frequencies will grow due to both increased unity gain frequencies in longitudinal control loops and increased complexity of F7 - payloads combination.

Our choice for the DSP to be used in AdV is Texas Instruments TMS320C6678 a multicore fixed and floating point digital signal processor based on KeyStone Architecture. Texas Instruments's KeyStone Multicore Architecture (see Fig. 11.43) provides a high performance structure for integrating RISC and DSP cores with application specific coprocessors and I/O. KeyStone is the first of its kind that provides adequate internal bandwidth for non-blocking access to all processing cores, peripherals, coprocessors, and I/O. This is achieved with four main hardware elements: Multicore Navigator, TeraNet, Multicore Shared Memory Controller, and HyperLink.

Multicore Navigator is an innovative packet-based manager that controls 8192 queues. When tasks are allocated to the queues, Multicore Navigator provides hardware-accelerated dispatch that directs tasks to the appropriate available hardware. The packet-based system on a chip

(SoC) uses the two Tbps capacity of the TeraNet switched central resource to move packets. The Multicore Shared Memory Controller enables processing cores to access shared memory directly without drawing from TeraNet's capacity, so packet movement cannot be blocked by memory access.

HyperLink provides a 50-Gbaud chip-level interconnect that allows SoCs to work in tandem. Its low-protocol overhead and high throughput make HyperLink an ideal interface for chip-to-chip interconnections. Working with Multicore Navigator, HyperLink dispatches tasks to tandem devices transparently and executes tasks as if they are running on local resources.

The TMS320C6678 **DSP** is the highest-performance fixed/floating-point **DSP** that is based on TI's KeyStone multicore architecture. Incorporating the new and innovative C66x **DSP** core, this device can run at a core speed of up to 1.25 GHz. For developers TMS320C6678 **DSP** offers 10 GHz cumulative **DSP** and enables a platform that is power-efficient and easy to use. In addition, it is fully backward compatible with all existing C6000 family of fixed and floating point **DSPs**.

KeyStone architecture provides a programmable platform integrating various subsystems (C66x cores, memory subsystem, peripherals, and accelerators) and uses several innovative components and techniques to maximize intra-device and inter-device communication that allows the various **DSP** resources to operate efficiently and seamlessly. Central to this architecture are key components such as Multicore Navigator that allows for efficient data management between the various device components. The TeraNet is a non-blocking switch fabric enabling fast and contention-free internal data movement. The multicore shared memory controller allows access to shared and external memory directly without drawing from switch fabric capacity.

For fixed-point use, the C66x core has 4× the multiply accumulate (MAC) capability of C64x+ cores. In addition, the C66x core integrates floating point capability and the per core raw computational performance is an industry-leading 32 MACS/cycle and 16 flops/cycle. It can execute 8 single precision floating point MAC operations per cycle, can perform double- and mixed-precision operations and is IEEE754 compliant. The C66x core incorporates 90 new instructions (compared to the C64x+ core) targeted for floating point and vector math oriented processing. These enhancements yield sizable performance improvements in popular **DSP** kernels used in signal processing, mathematical, and image acquisition functions.

The C6678 **DSP** integrates a large amount of on-chip memory. In addition to 32KB of L1 program and data cache, there is 512KB of dedicated memory per core that can be configured as mapped RAM or cache. The device also integrates 4096KB of Multicore Shared Memory that can be used as a shared L2 SRAM and/or shared L3 SRAM. All L2 memories incorporate error detection and error correction. For fast access to external memory, this device includes a 64-bit DDR-3 external memory interface (EMIF) running at 1600 MHz and has ECC DRAM support.

This family supports a large number of high speed standard interfaces including RapidIO ver 2, PCI Express Gen2, and Gigabit Ethernet, as well as an integrated Ethernet switch. It also includes I2C, UART, Telecom Serial Interface Port (TSIP), and a 16-bit EMIF, along with general purpose CMOS IO. For high throughput, low latency communication between devices or with an FPGA, this device also sports a 50-Gbaud full-duplex interface called HyperLink. Adding to the network awareness of this device is a network co-processor that

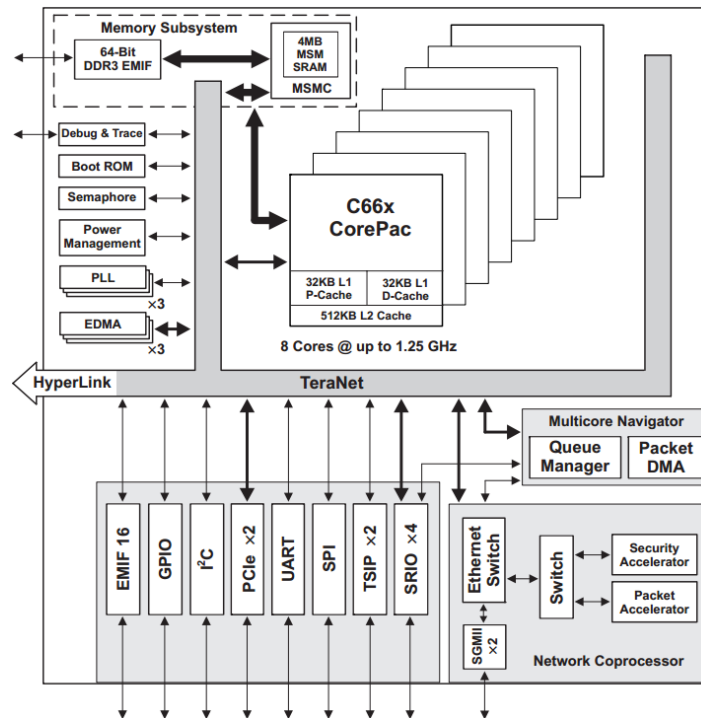


Figure 11.43: DSP TMS320C6678 Functional Diagram

includes both packet and optional security acceleration. The packet accelerator can process up to 1.5 Mpackets/s and enables a single IP address to be used for the entire multicore C6678 device. It also provides L2 to L4 classification, along with checksum and QoS capabilities.

The C6678 device has a complete set of development tools, which includes: an enhanced C compiler, an assembly optimizer to simplify programming and scheduling, and a Windows debugger interface for visibility into source code execution.

11.2.4.5 Control workstation

Moving the computational load entirely to DSP (as it was in Virgo), few space is left for workstation operation. No special requirement is in fact needed at workstation level where only user interface and supervision software is supposed to run. Moreover, having a DSP board provided with Gigabit Ethernet there is no longer the need of a CPU acting as bridge and server for DSPs.

11.2.5 Superattenuator control system general architecture

11.2.5.1 Overview

The starting point of the control system architecture description is a sketch of Virgo/Virgo+ architecture (Fig. 11.44) showing by itself most of the limits that new architecture will overcome.

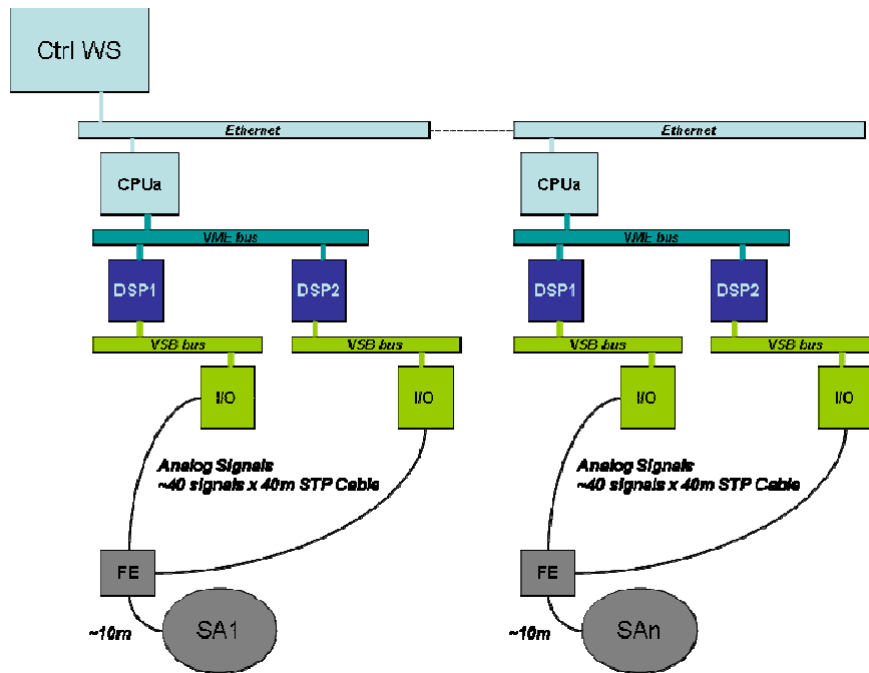


Figure 11.44: Virgo/Virgo+ suspension control system architecture

The architecture shown suffers from several defects:

- Long analog signals' cabling is not compatible with requirement concerning electromagnetic noise immunity and crosstalk between signals. In addition, long cabling requires patch panels to somehow organize the huge mass of conductors and therefore requires several connectors worsening the overall system reliability.
- Communication bandwidth between different DSPs is poor and difficult to be improved, even between the two DSP controlling the same suspension.
- At least one CPUs (two in Virgo/Virgo+) is needed to act as local supervisor and implement communication bridge between the soft real time world at workstation level and the hard real time world at DSP level.
- Communication bandwidth between DSP and IO boards is limited. On a VME system a peak transfer rate of about 10 MB/sec was achieved. Dividing this number by about 20 signals, a peak transfer rate of about 500 kByte/sec per channel have been obtained. Having to deal with high resolution signals, this rate is no longer acceptable and it would be too dangerous for AdV starting operation with such a limit.

The overall architecture for AdV was changed in order to solve all mentioned 'defects'.

11.2.5.2 Goals

The development of the new SATCS is based upon three main guidelines: replace, reduce and improve:

Replacement

- It is required to replace the obsolete components since no longer maintainable.
- It is also required to replace the old components: boards have been running for years and therefore Mean Time Before Failure (**MTBF**) is now too short to start a new decade of operation.

Reduction

- Reducing the number of different devices used in **SATCS** has the benefit to simplify its design and development.
- A strong reduction is also foreseen for the total analog signal path length that will be limited to the minimum. All **SAT** active electronics will continue to be outside the vacuum chambers to be safer against possible duty-cycle consuming maintenance (replacement/adjustments). The only analog cabling allowed will be between in vacuum passive devices (essentially only coils) and electronics that will be located as close as possible to feedthroughs as it was done in Virgo for the front end electronics.
- The number of connectors will be drastically reduced on signals path dismissing most of patch panels used in Virgo.
- The total power will be reduced lowering the operating voltages while taking advantage from the improved resolution of converters.

Improvement As already stated, excluding some new specifications concerning longitudinal control timing that will presumably require a much larger sampling frequency than what has been used in Virgo+ (50-100 kHz instead of 10 kHz as discussed in ISC chapter), requirements for **AdV** do not differ so much from what was already fulfilled in Virgo+. This will let us concentrate on improvement of operability, maintainability and reliability together with a wide margin of improvement also for performances to be able to face rapidly any unforeseen desiderata.

11.2.5.3 Requirements

Not so many changes are foreseen in top level requirements for **SATCS**:

- tiltmeters and tilt control loop with piezos;
- 6 degrees of freedom control of **F7** (only 3 **DOF**s partially controlled in Virgo+);
- 4 **DOF**s marionette control (they were 3 in Virgo+);
- higher closed loop bandwidth for signal recycling requiring much shorter delays and therefore much higher sampling rate (5-10 larger than Virgo+).

Something is then still pending since a few years about software: few bugs still to be corrected, separate **DSP** code from parameters, better GUI, software supervisor, some basic data processing, etc.

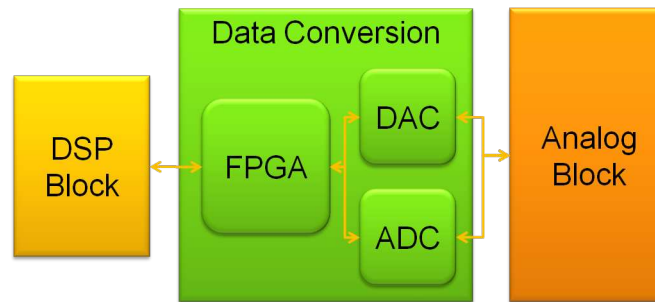


Figure 11.45: Coil driver block diagram

11.2.5.4 Design

The basic conceptual design for **SATCS** foresees a merging between front-end electronics and data converters. This merging solves all problems related to signal analog distribution over long distances. In addition the number of boards to be developed will be reduced down to four: **DSP**, accelerometer, **LVDT** and coil driver. In addition some custom backplane for simplifying signals distribution to boards will have to be developed and also custom power supply boards are planned to be developed.

All electronics will be hosted in Eurocard 6U crates located next to the tower. There will not be any CPU since clients will communicate directly to **DSPs** via Gigabit Ethernet. VME bus will be dropped out, replacing board to board communication with Serial RapidIO.

A certain amount of spare channels for input/output of analog signals will be available in the **SA** cabling distribution box but not on board front panels.

Each board is composed by a small subset of basic blocks:

- **DSP** block:
 - supervising, processing and communication;
- data conversion block:
 - **ADC**, **DAC** and controlling **FPGA**;
- analog block:
 - specific for each board.

For example, new coil driver will be constituted by the blocks sketched in Fig. 11.45.

In general the transition between analog and digital domain will take place according to the top scheme of Fig. 11.46:

Using the following boards configuration, all boards will have the same number of **ADC** and **DAC** channels with a major simplification from firmware and software point of view (see the bottom scheme Fig. 11.46):

- accelerometer:
 - 3 channels per board - 9 analog I/O - 21 to 27 pins (min one GND pin per channel max one GND pin per signal):

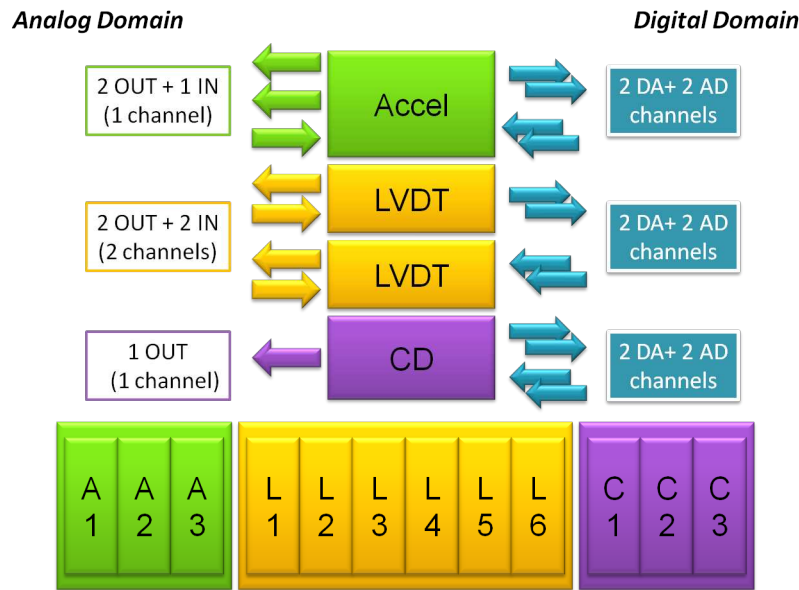


Figure 11.46: Top: Analog to digital domain transition scheme. Bottom: Channel configuration scheme of the accelerometer (green), LVDT (yellow) and coil driver (magenta) boards.

- **LVDT**
 - 6 channels per board - 12 analog I/O (STP) - 30 to 36 pins:
- coil driver (2 **DAC** channels per coil for high power/low noise):
 - 3 channels per board - 3 analog I/O (STP) - 6 to 9 pins (CD out is single ended).

Keeping into account that **F7** control, hosted on top stage control **DSP** in Virgo+, will be better moved onto payload control **DSP**, since new payload - **F7** interactions will be now much stronger, the basic reference configuration for one suspension control is composed by two 12-slots crates (see Fig. 11.47).

Communication The diagram of Fig. 11.48 shows main communication links between **DSP** board (on the left), a generic analog IO board (**LVDT**, accelerometer or coil driver board) and the rest of the world.

TOLM - Virgo Optical Link Real time communication with other Virgo systems like data acquisition, locking and linear alignment is via optical link implemented by Timing and Optical Link Module (**TOLM**) mezzanine board (by LAPP Annecy). **TOLM** mezzanine is configured via a PCI interface and data are provided via 4 link ports (Analog Device standard) exactly as it was in Virgo+

Serial RapidIO (SRIO) **SATCS** boards hosted in the same crate communicate via Serial RapidIO (SRIO). SRIO is implemented by **DSP** and is via a micro TCA backplane, Port 8-11

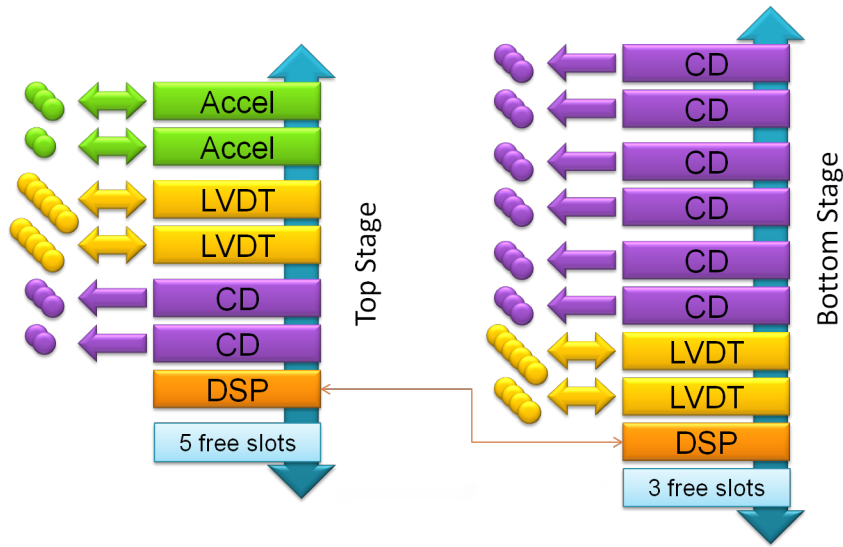


Figure 11.47: Reference configuration for one suspension control

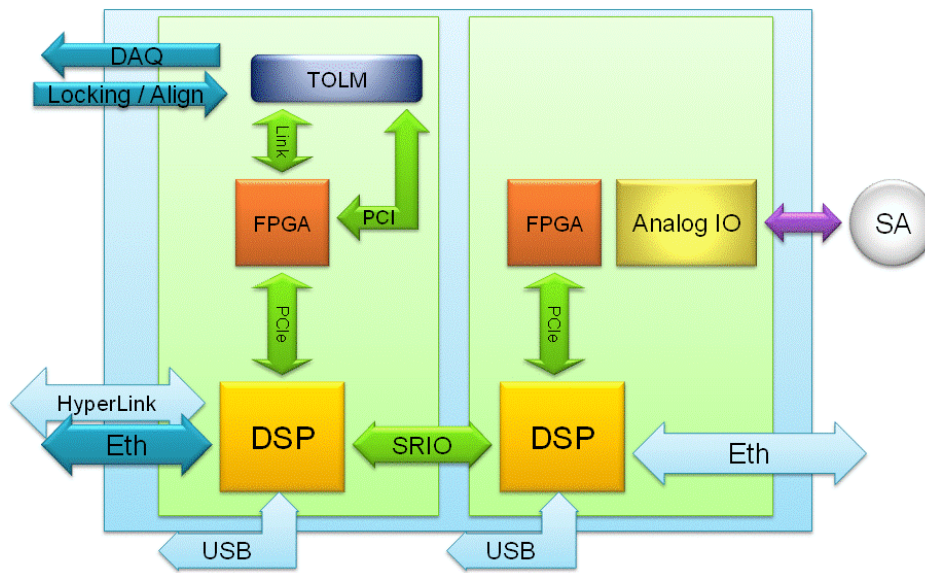


Figure 11.48: Main communication paths

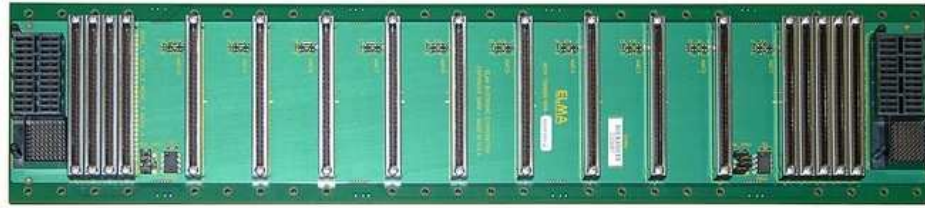


Figure 11.49: microTCA Backplane

mTCA Backplane Standard microTCA backplane (Fig. 11.49) is a 12 slots unit plus 2 power supply slots and 2 MCH for the implementation of the specific ‘Fabric’ (SRIO on port 8-11 in our case).

Gigabit Ethernet Each DSP has two Gigabit Ethernet ports. One of the two ports is available on backplane and allows soft real time communication between DSPs while the second port is available for connection through Virgo Local Area Network (VLAN) to supervising software. This second port is also optionally available on any of the analog IO boards that could become standalone sub systems.

USB Each board is provided with a USB to UART converter for board debugging and configuration.

HyperLink Connection of two crates devoted to the control of the same suspension can be hard real time linked either via TOLM optical link and via Texas Interments HyperLink.

PCIe DSP communicated with on board FPGA via PCIe.

PCI PCI communication is used only for TOLM configuration. In a next future one could think of having PCIe on TOLM dropping the need of PCI.

LinkPort TOLM are programmed to communicate with SATCS via Link port (Analog Devices standard). This standard will be kept only if for some reason PCI performances will not suffice.

Conduction Cooling To reduce vibration in the central hall and terminal buildings, the possibility to remove fan from front end racks is under investigation. Adoption of standard IEEE 1101.2 “Standard for Mechanical Core Specifications for Conduction-Cooled Eurocards” appears to be mandatory in order to remove large fans.

DC supplies distribution Removal of power supplies from the experimental area would produce several benefits:

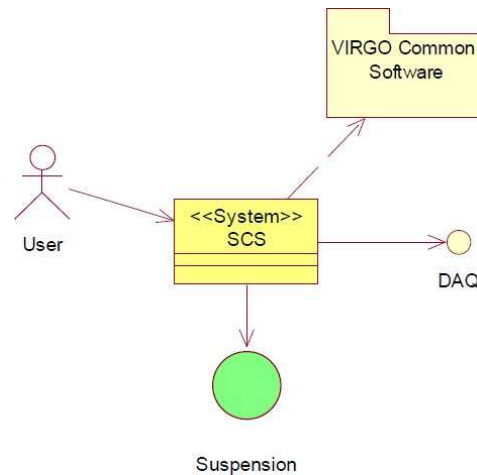


Figure 11.50: Top level context diagram

- Electromagnetic Compatibility (**EMC**) improvements (mainly on mains 50Hz and harmonics)
- Heat reduction
- Power Supply fans vibrations

New system will allow operation with both AC (230V - 50Hz) and DC (48V) supply distribution.

11.2.5.5 Superattenuator control software

The Fig. 11.50 and 11.51 show architecture and layout of suspension control software for **AdV**. The **SATCS** software architecture is constituted by four layers:

- Tools - This layer contains complementary tools like e.g. tools for developing and compiling **DSP** programs.
- Coordination and service - This layer performs the coordination of the distributed control units: commands are received, processed, and forwarded; data is read back and treated accordingly.
- Hardware device management - This layer deals with the associated hardware devices and communicates with the real-time control layer.
- Real-time control - Here real-time control programs run on dedicated **DSPs**. Programs and parameter values come from the Hardware device management layer and a specific subset of parameter values is passed back.

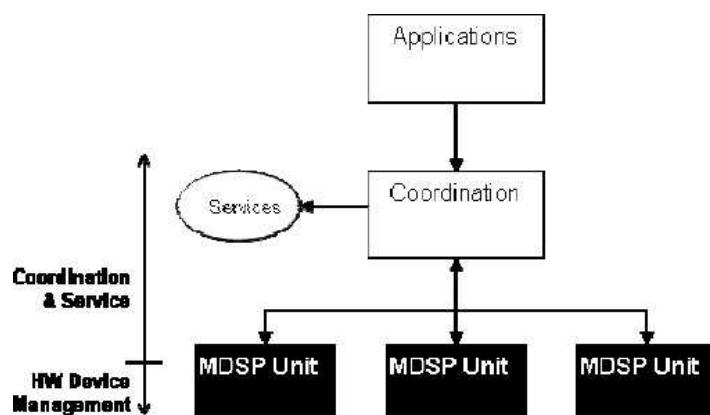


Figure 11.51: Software layout diagram.

Chapter 12

Suspended benches (SBE)

12.1 Task description

The SBE subsystem takes care of the seismic isolation of the suspended optical benches. A single stage, 6 Degree(s) of Freedom (**DOF**) seismic attenuator, called EIB-SAS, will support the External Injection Bench (**EIB**). The **EIB** is located in the Laser Laboratory (**LLab**) and hosts (see INJ chapter of this document) the IBMS and the launching optics to the IMC. A total of five optical benches, SNEB, SWEB, SIB2, SPRB, SDB2, will be suspended in vacuum to host all the photodiodes for longitudinal and angular control to be used in science mode and isolate them from environmental disturbances (see INJ and DET chapters of this document for the details). An integrated system called minitower (see Fig. 12.1), consisting of a multistage vibration isolator named MultiSAS and vacuum chamber, is provided for them. EIB-SAS has been built in 2010 and, after a characterization campaign at Nikhef [381], it has been installed in the Virgo **LLab** in November 2011 (see Fig. 12.2), as the first major hardware upgrade of Advanced Virgo. EIB-SAS provides also a valuable benchmark for MultiSAS, since it makes use of the same subsystems and components.

12.2 EIB-SAS

12.2.1 Introduction

The **EIB** is a known major source of angular and lateral beam jitter in the injection system of Virgo+. Projections of the input beam jitter to the dark fringe signal have shown that input beam jitter could affect the interferometer design sensitivity whether the **EIB** residual motion is not improved [382, 383]. The EIB-SAS design is derived from a prototype device termed HAM-SAS, built by Caltech in 2006 in the framework of the R&D for Advanced LIGO [384]. The system has recently been upgraded and adapted at the Albert Einstein Institut in Hannover, in order to be incorporated in their 10 m prototype interferometer [385].

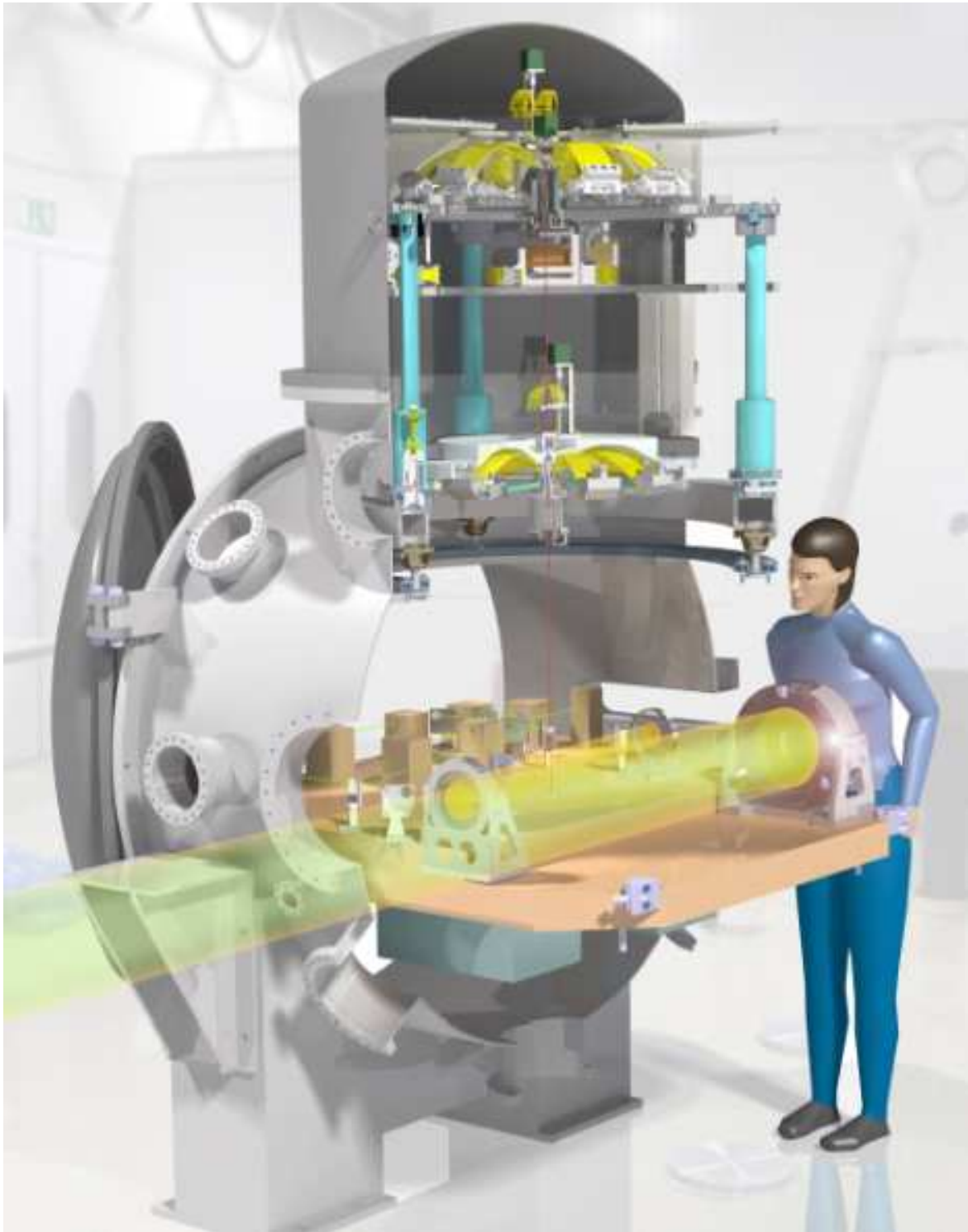


Figure 12.1: Impression of the minitower for the end benches.



Figure 12.2: EIB-SAS as installed in the Virgo LLab.

12.2.2 Mechanical design overview

The EIB-SAS is a single stage vibration isolation system. Passive seismic attenuation is achieved by means of a combination of a short Inverted Pendulum (**IP**) and three Geometric Anti-Springs (**GAS**). The inverted pendulum legs allow the intermediate platform (*spring-box*) to move along x , z , θ_y (see Fig. 12.3)¹. The spring-box hosts the three **GAS** springs that allow the optical bench² to move along y , θ_x and θ_z (see Fig. 12.4)

The EIB-SAS has been engineered in order to prevent its transfer function being higher than one in a broad range of frequencies (see Fig. 12.10). The system is instrumented with position (LVDT) and inertial (geophones) sensors and voice coil actuators to actively damp the low frequency eigenmodes and to stabilize position and orientation of the supported bench. Higher frequency modes, originating from the **GAS** spring lateral compliance and from the vertical compliance of the **IP** structure, are treated with tuned dampers placed on the spring-box. The internal modes of the **IP** legs are cured with eddy current dampers. Positioning of the bench within the resolution of the LVDTs is achievable with the voice coil actuators; stepper motor driven correction springs are used for initial (and periodical on the long term) coarse alignment.

Materials EIB-SAS is almost entirely realized using 6082-T6 aluminum alloy. The exceptions are the spring box and the interface plate between the **GAS** springs and the **EIB**, manufactured using aluminum 5083-H111, and clamps and supports of the elastic elements as well as the **IP** leg tubes machined out AISI 304L. Maraging steel (Maraging C-250) is used

¹In this chapter the standard Virgo convention for **DOF** naming is adopted: z is the optical axis, x is the horizontal orthogonal axis, y is the vertical, θ_z , θ_x , θ_y are the rotations about the corresponding axes. In EIB-SAS x is the direction parallel to the **EIB** long side.

²The **EIB** is a standard 2500×1300 mm optical bench with 840 kg mass.

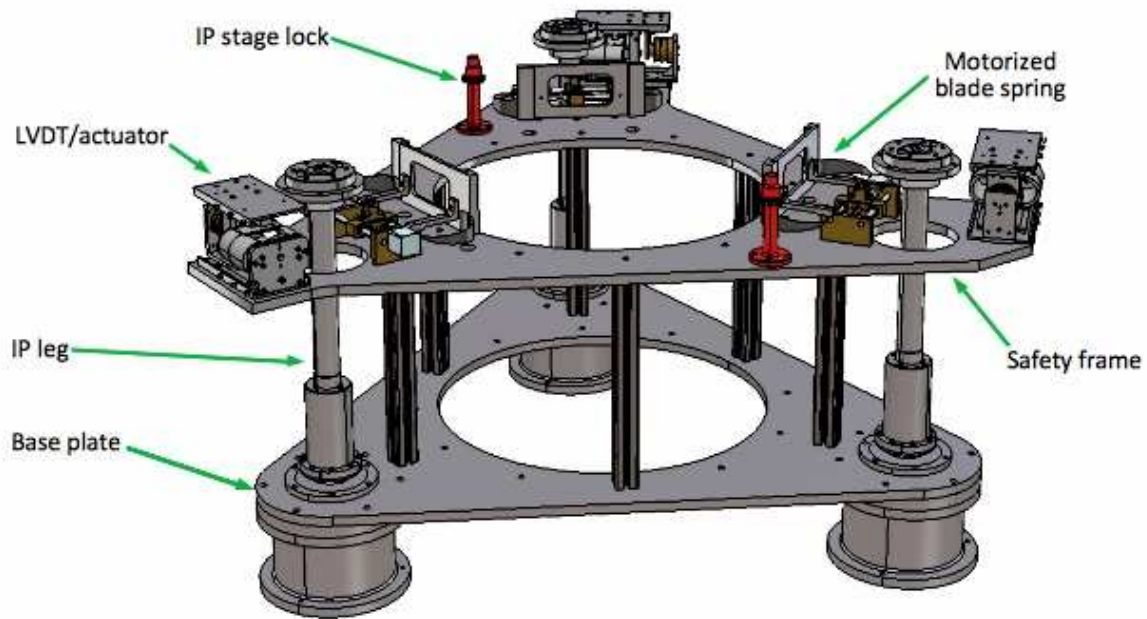


Figure 12.3: EIB-SAS inverted pendulum mechanics and sensing/actuation system.

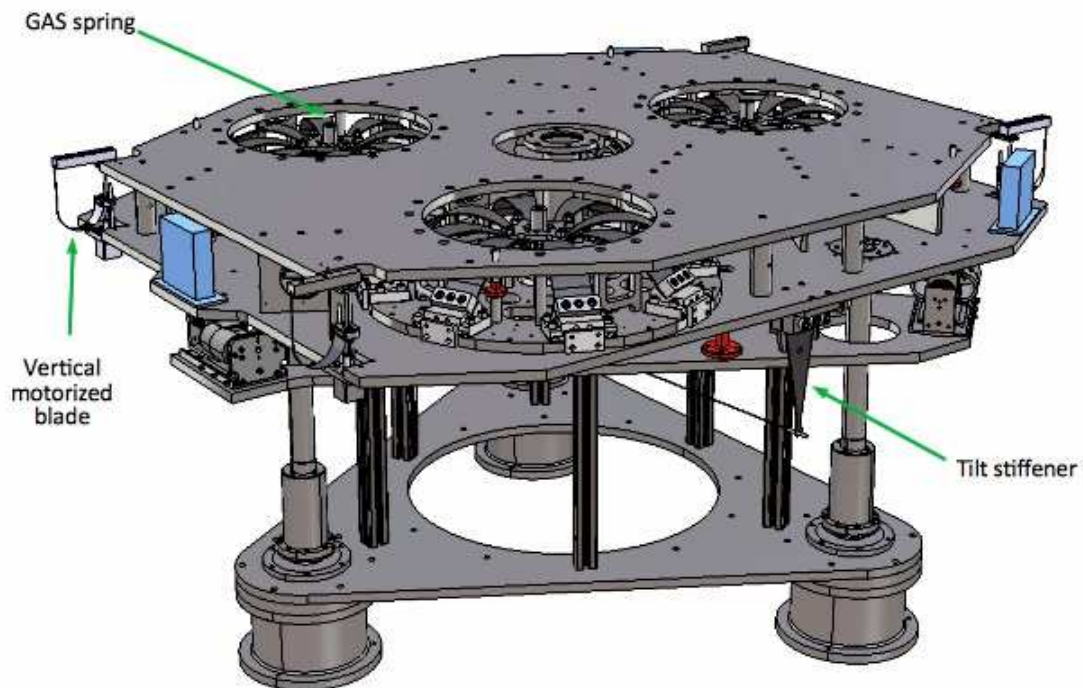


Figure 12.4: EIB-SAS vertical/tilt mechanics. The tilt stiffener allows to adjust pitch and roll natural frequencies independently on the GAS spring vertical tuning.

| | Maraging C-250 | C-17200 |
|------------------------------|----------------|---------|
| Density (g/cm ³) | 8 | 8.25 |
| Young modulus (GPa) | 186 | 130 |
| Shear modulus (GPa) | 73 | 50 |
| Poisson ratio | 0.3 | 0.3 |
| Yield strength (GPa) | 1.94 | 1.4 |

Table 12.1: Mechanical properties of maraging steel and beryllium copper. Yield strength is specified after tempering.

to manufacture all the elastic elements (flexures and blades) of the system. Precipitation hardening is done following the standard Virgo recipe [386] to maximize creep resistance. All maraging steel parts are protected from corrosion by means of nickel flash plating. Auxiliary springs used for DC controls are made out of precipitation hardened (TH04 temper) beryllium copper (C-17200 grade). See Table 12.1 for the material properties.

12.2.3 EIB-SAS mechanics: inverted pendulum

The spring box is supported by three legs each consisting of a 2 mm wall stainless steel tube, 48 mm outer diameter, 438 mm long hinged to the base ring by means of a corner filleted circular cross-section flexure providing the elastic restoring force (see Fig. 12.5 left panel). Shorter, smaller diameter flexures, acting as universal joints, provide the connection between the leg top and the spring box constraining its motion to the horizontal plane. The natural frequency f_0 of the IP is tuned by adjusting the mass of the spring box, exploiting the negative stiffness effect provided by gravity according to (12.1):

$$f_0 = \frac{1}{2\pi} \sqrt{k - \frac{mg}{L}} \quad (12.1)$$

where k is the lower flexure stiffness, L is the leg length and m is the total IP load (EIB+spring box).

The main flexures have been dimensioned, by using Finite Element Analysis (FEA), to obtain an IP translational natural frequency of 200 mHz at a nominal load of 1260 kg. The value of the natural frequency has been chosen to make the system less sensitive to low frequency environmental disturbances, considering the in-air operation. The aspect ratio of the IP lower flexures has been calculated to limit the stress level to 15% of the material yield at the maximum allowed displacement of the spring box from its equilibrium position (± 8 mm). The most relevant design parameters of the EIB-SAS are summarized in Table 12.2.

Damping of the leg internal modes In EIB-SAS the internal modes of the leg are handled with passive eddy current dampers located at the leg top (see Fig. 12.5 right panel). Eddy currents are generated on the leg by its relative movement with respect to a matrix of NdFeB magnets surrounding the leg top with 2-mm gap. Since the steel used for the leg tubes is not a good electrical conductor, copper jackets have been glued around the leg top

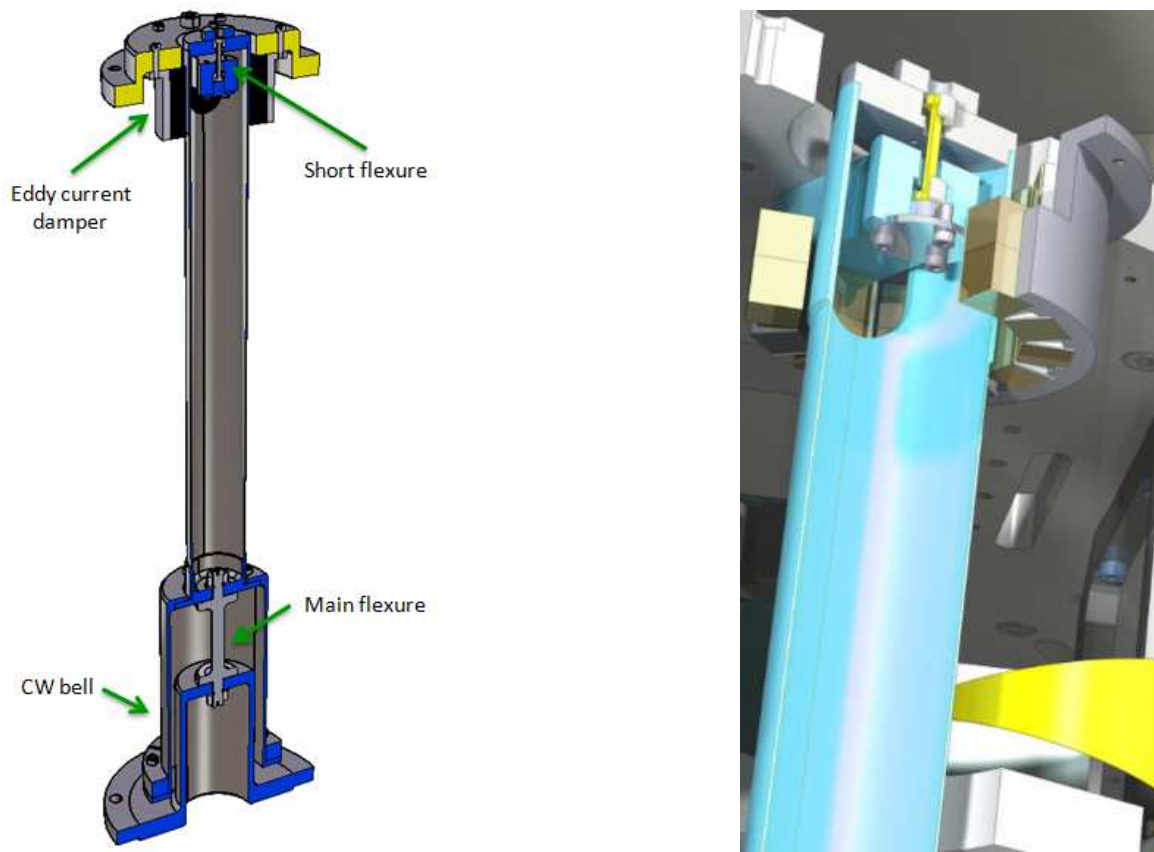


Figure 12.5: (left) IP leg cross section. The optional bell to support the counterweights for the compensation of the leg inertia, not implemented in the final configuration, is also shown. (right) Details of the IP leg top. A matrix of permanent magnets, fixed to the spring box bottom plate, faces the IP leg for eddy current damping of the leg internal modes. Because of the vertical position of the magnets, within a few mm from the upper pivot point of the IP, the low frequency eigenmodes are not influenced significantly by the dampers and the horizontal vibration isolation is not spoiled.

| Parameter | Value |
|------------------------|---------|
| Lower flexure diameter | 11.2 mm |
| Lower flexure length | 50 mm |
| Short flexure diameter | 3 mm |
| Short flexure length | 25 mm |
| Leg length | 438 mm |
| Leg mass | 2.5 kg |
| Total suspended mass | 1260 kg |
| Spring box mass | 320 kg |
| Maximum stress | 320 MPa |

Table 12.2: EIB-SAS inverted pendulum design parameters. The maximum stress corresponds to the maximum allowed displacement of the spring-box from its equilibrium position (± 8 mm).

| Mode shape | Frequency (Hz) | Q without damper | Q with damper |
|--------------|----------------|------------------|---------------|
| rigid leg I | 159 | 400 | 25 |
| rigid leg I | 162 | 400 | 25 |
| torsion mode | 233 | 470 | 40 |
| rigid leg II | 472 | 180 | 95 |
| rigid leg II | 476 | 180 | 95 |

Table 12.3: Eddy current damping of the leg modes. In rigid leg type I modes the leg top is moving hence and forth while the lower flexure is slightly rotating. In type II both top and bottom of the leg move. Because of the already relatively large leg mass, the counterweight bells were not installed to raise the resonant frequencies of the modes.

to increase the damping effect. The dipole term is nulled in the magnet matrix in order to prevent couplings with external magnetic fields. The effect of the eddy current dampers on the leg modes is summarized in Table 12.3. The measured quality factor for the lowest order modes is reduced by almost a factor of 10.

12.2.4 EIB-SAS mechanics: vertical stage

Vertical and tilt compliance of the bench is provided by the three GAS springs placed inside the spring box. GAS springs were developed in the framework of the R&D for Advanced LIGO [387, 388] and have been used in the TAMA 300 seismic isolation system upgrade [389]. A GAS spring (see Fig. 12.6) is a set of radially arranged cantilever *blades* mounted from a common retainer structure (*body*) and opposing each other via a central disk (*keystone*), to which the payload to be isolated is connected.

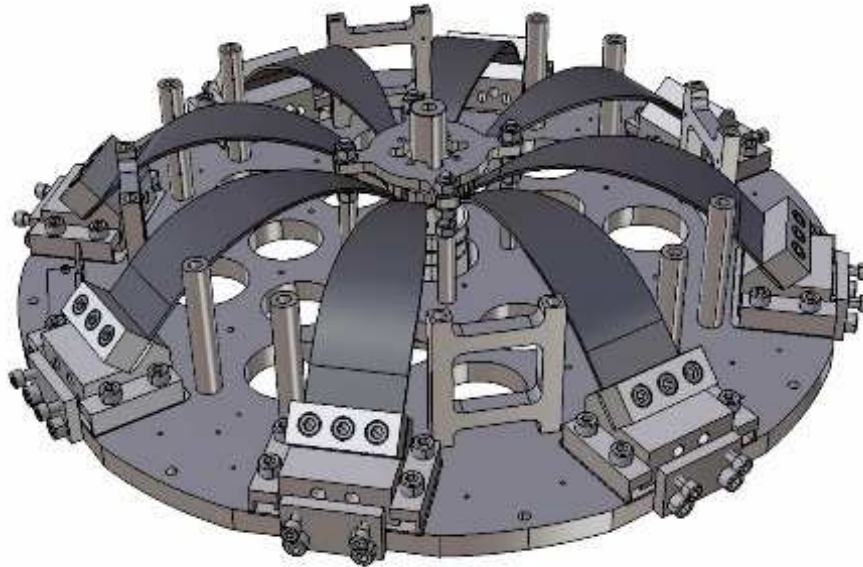


Figure 12.6: EIB-SAS GAS spring. Eight blades are used to support a 314 kg nominal load.

The blades are completely flat when manufactured and flex like a fishing rod under load (see Fig. 12.7). Suitable clamps provide the blade base an initial angle of 45° to accommodate

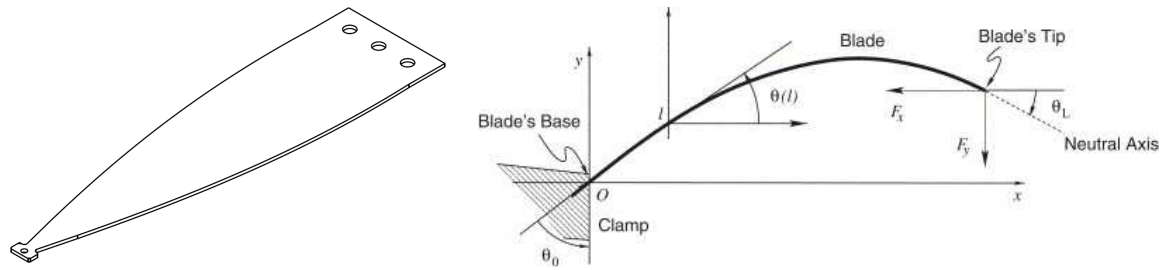


Figure 12.7: (left) GAS blade as manufactured. (right) GAS blade two-dimensional model from Cella *et al.* [390].

the bending. On the other side the blade tip forms a -33° final angle constrained by the geometry of the keystone. The radial position of the clamps is adjusted to realize the required amount of radial/horizontal compression necessary to build up the desired anti-spring effect and lower the vertical natural frequency of the system. A detailed finite element analysis (FEA) model of the GAS blade around its working point was produced to make accurate predictions of stress levels and make modal analysis of complex mechanical systems using GAS springs as building blocks. The FEA model has been extensively benchmarked with Cella *et al.* [390] analytical models and with experimental test on the EIB-SAS blades. In Fig. 12.8 are shown, as an example, the calculated load curves for the eight-blades filters used in EIB-SAS. The optimum working point is predicted at 317 kg load, within a few percent from the actual measured values on the three springs. The blade profile was designed by rescaling for the different load the blades of HAM-SAS. The maximum von Mises stress predicted by FEA is about 1.8 GPa; measurement of the blade radius of curvature at its working point, by means of a coordinate measuring machine, have shown an actual peak stress along the blade length of about 1.65 GPa, corresponding to 85% of the material yield point. Same or comparable design stress levels have been proven to be safe on the long term by TAMA300, HAM-SAS, AEI 10-m prototype experiences, as well as in extended time creep behavior investigations[391]. In EIB-SAS a further creep relief treatment, consisting in a baking under stress at 70°C , has been applied to the GAS springs.

Temperature effects

The vertical position of the keystone is affected by temperature variations that change the GAS blades lifting force by the characteristic coefficient -225 ppm/K [392]. At a 450 mHz tune of the GAS springs, the corresponding vertical stability is about $-290 \mu\text{m/K}$. In Fig. 12.9 the uncontrolled bench position sensor trend data compared with the temperature changes in the Nikhef experimental hall.

12.2.5 Seismic attenuation performance: simulations

Modal analysis of EIB-SAS has been carried out by means of mechanical modeling and experimental validation. A detailed FEA model (see details in [381]), also including the compliance of the GAS springs along the six DOF, has been used for both modal and harmonic analysis (transfer functions). The investigation allowed to identify all the modes of the structure that require damping either with passive dampers or with active control. Twelve

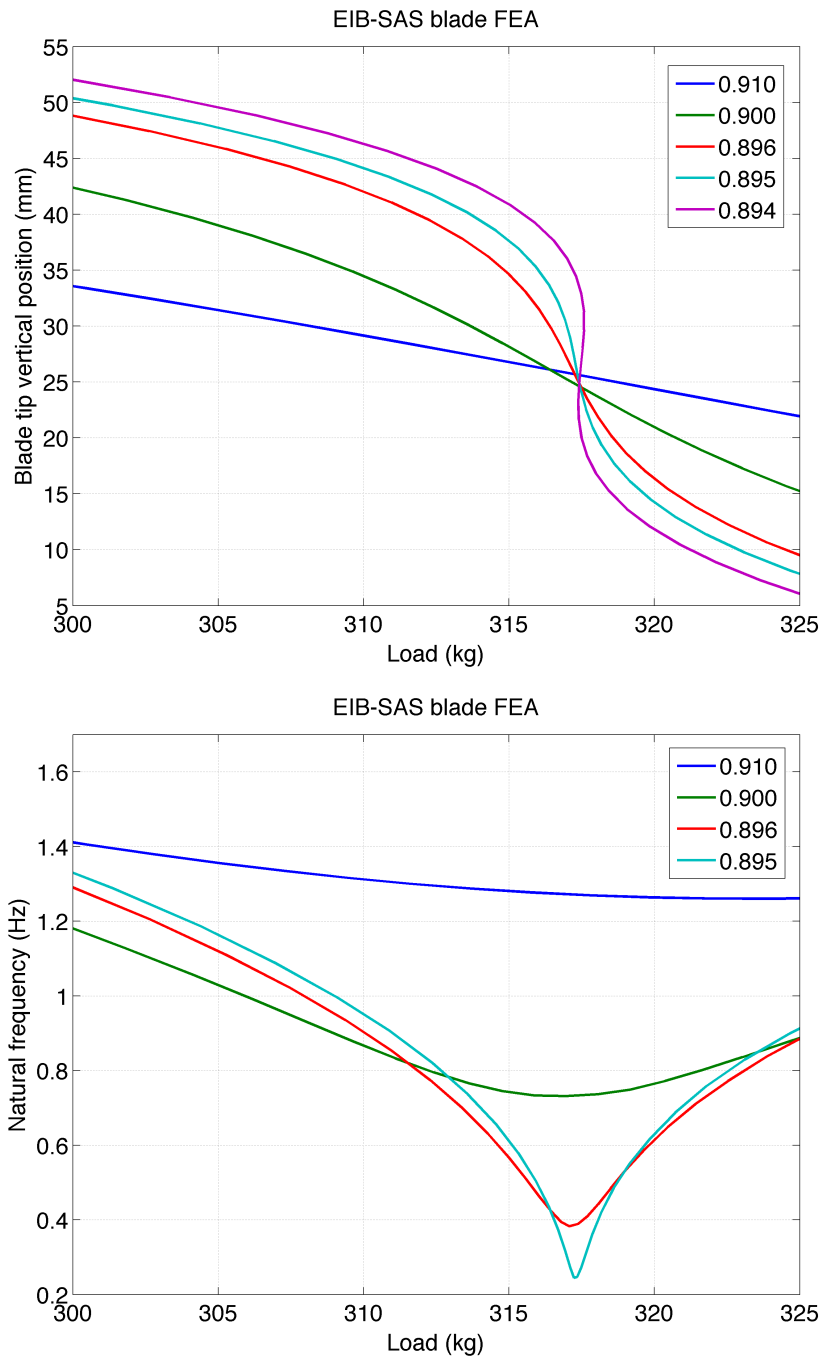


Figure 12.8: FEA modeling of the GAS effect on the eight-blades GAS spring designed for EIB-SAS: (top) predicted keystone vertical position vs. load for different radial compression rates. A bistable behavior (purple line), with two different equilibrium position is achieved for compression exceeding a critical value. (bottom) Corresponding vertical natural frequency vs. load.

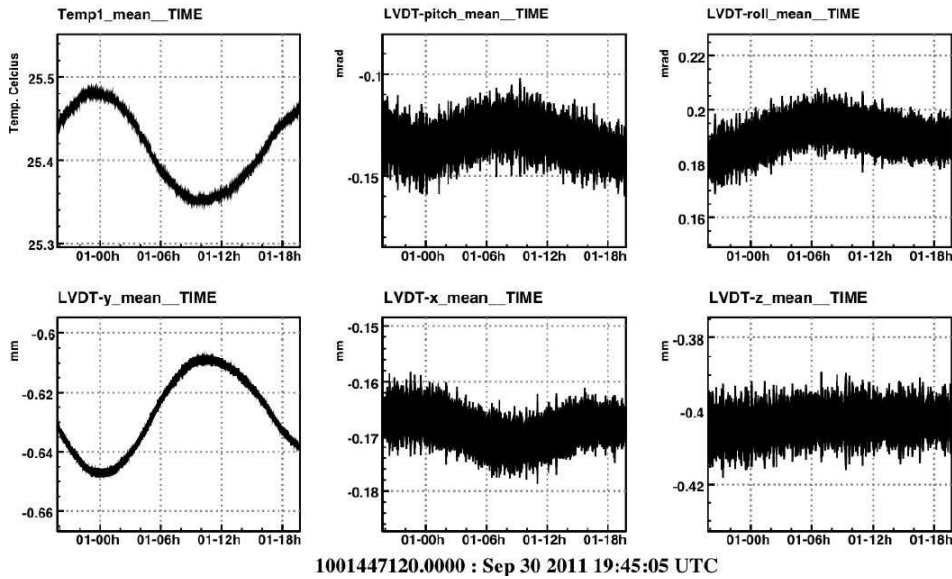


Figure 12.9: Clean-room temperature and open-loop EIB-SAS position measured for 24 hours (a 1-Hz low pass filter have been applied to the signals). The expected strong correlation between the temperature changes and the vertical position (y - channel) is evident.

rigid body modes can be identified related to the integral motion of spring box and bench. The identified modes can be grouped as follows:

- six **IP** and/or **GAS** modes; all at low frequency from 100 to 500 mHz. In these modes the horizontal motion (x , z and θ_y) of bench and spring box are common, *i.e.* in phase. Horizontal and tilt (θ_x and θ_z) **DOF** are strongly coupled as result of the large offset position (more than 20 cm) between the bench center of gravity and the equivalent pivot point of the **GAS** springs (predicted by **FEA** to be a few mm above the keystone). All these modes are electronically damped using the EIB-SAS built-in sensors and actuators;
- three horizontal spring box modes: θ_y (≈ 13 Hz), x and z (both ≈ 18 Hz), in which bench and spring box move (or rotate) in opposite direction, out of phase. The restoring force is delivered by the horizontally displaced **GAS** springs. The measured values are somewhat lower: 11 and 16 Hz. These modes are also handled by the active control;
- three vertical spring box modes: 45 Hz (roll), 57 Hz (pitch) and 60 Hz (vertical). In these modes the top of the **IP** legs are moving vertically up and down. Both short flexure and leg (“in series”) account for the flexibility. The bench recoil is relatively small. For these modes the results are considered as upper limits, due to the assumed rigidity of the spring box. Measured modes are actually rather lower in frequency, starting from about 34 Hz. Damping of these modes is accomplished by means of tuned dampers installed on the spring box itself;

Simulated horizontal and vertical displacement transfer functions (see Fig. 12.10) show that peak attenuation from 50 to 60 dB could be achievable in both **DOF**. Spring box modes would clearly spoil the isolation performance if no countermeasure is taken.

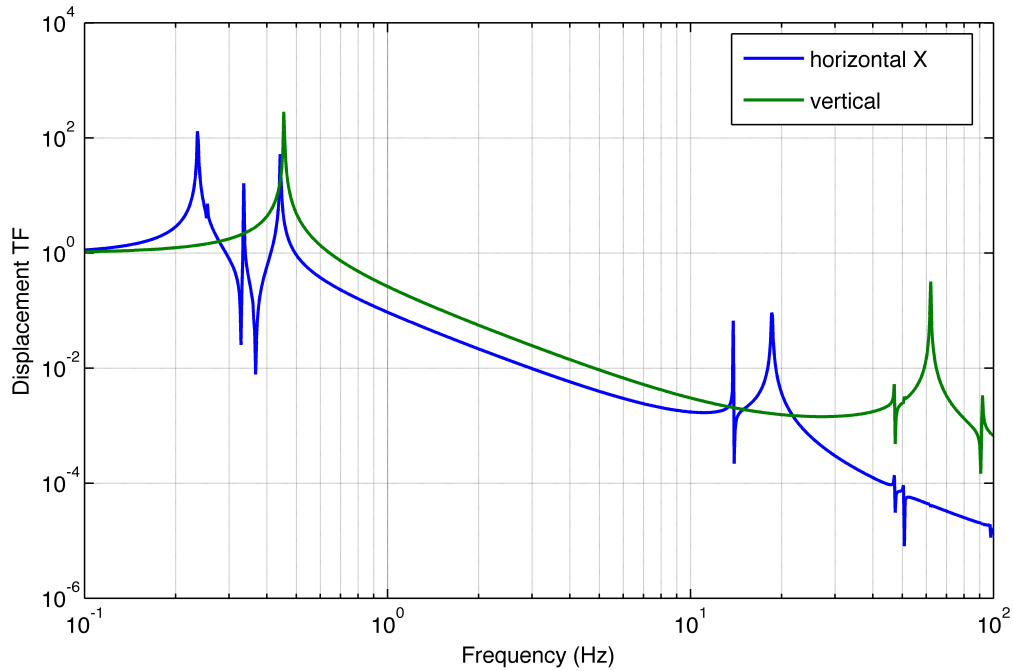


Figure 12.10: EIB-SAS horizontal and vertical simulated transfer functions from ground to bench. Couplings to the other **DOF** are also calculated.

12.2.6 Controls: sensors and actuators

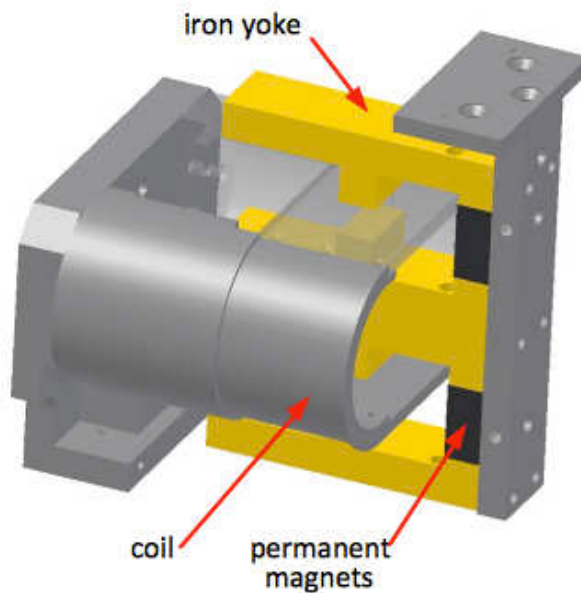


Figure 12.11: Horizontal voice-coil actuator. The racetrack shaped coil and the yoke design provide linear and uniform actuation strength over a large range of relative positions, therefore minimizing seismic noise re-injection.

Static positioning: seven step-motor driven actuators are used to provide the DC positioning of the bench along the six **DOF**; they are mainly used to re-position the bench back to the nominal working point after the bench has been temporarily locked. All the motors are switched off during the normal operation of EIB-SAS.

- **Vertical:** four vertical motorized blade springs located at the four corners of the **EIB** allow to change vertical position and leveling of the bench with respect to the spring box. They are also used to cope with large temperature changes and to correct any very long term drift due to the residual creep of **GAS** blades. The overall actuation range is ± 2 N corresponding to a few mm adjustment of the bench vertical position. The positioning accuracy is better than $1 \mu\text{m}$. The reference signal for the adjustment blades are the three vertical LVDT measuring the position of the keystone with respect to the spring box in each **GAS** spring.
- **Horizontal:** three motorized correction blade springs act on the spring box to translate and rotate horizontally the bench within the range set by the mechanical end stops ± 8 mm. Positioning accuracy achieved is better than $1 \mu\text{m}/1 \mu\text{rad}$.

Dynamic corrections: these include all sensors and actuators used for the active control of the optical bench:

- **horizontal:** very low frequency bench position control and active damping of the EIB-SAS eigenmodes along x , z , θ_y is performed acting on the spring box. The spring box is instrumented with:
 - three horizontal LVDT position sensors [393], in triangular configuration, measuring the spring box motion with respect to the safety frame;
 - three horizontal 1 Hz natural frequency geophones (Sercel L-4C with 5500 Ω series resistance coil and 280 V/m/s throughput), in triangular configuration, measuring the spring box inertial motion³. Being the spring box, at low frequency, tilt rigid, tilt-horizontal coupling effect on the sensors is minimized;
 - three 5 N/A horizontal voice-coil actuators [394](see design features in Fig. 12.11), collocated to the horizontal LVDTs, acting on the top stage from the external frame;
- **vertical:** position control and active damping along y , θ_x and θ_z **DOF** is performed acting on the bench itself. The following sensors and actuators are used:
 - three vertical LVDT position sensors measuring the motion of the three **GAS** spring keystones with respect to the spring box;
 - three vertical 2-Hz natural frequency geophones (Sercel L-22E with 2200 ohm series resistance coil and 98 V/m/s throughput), in triangular configuration, measuring the bench inertial motion;
 - three 10 N/A vertical voice-coil actuator, collocated to the vertical LVDT, acting from the spring box to the three keystones.

³The $1/f^2$ roll-off of the geophone response below its natural frequency is equalized after preamplification by means of a digital filter in the real-time control system, both for horizontal and vertical sensors.

12.2.7 Controls: electronics and DAQ

Please refer to 12.3.7.

12.2.8 Controls: performance

EIB-SAS is controlled using the same approach and techniques described in 12.3.8 for the MultiSAS top stage, but with some peculiarities:

- the control bandwidth that is extended from a few Hz up to 30 Hz in EIB-SAS to cope with the horizontal spring box modes.
- inertial control is used also for the vertical (y, θ_x, θ_x) DOF.

The EIB-SAS is operated with a slow proportional-integral feedback, using the LVDT/geophone blended signal, maintaining the bench set point; in parallel, a broadband weak viscous damping, using the output signals from the geophones, is applied to damp the low frequency eigenmodes as well as the horizontal spring box modes. See the example in Fig. 12.12 and Fig. 12.13.

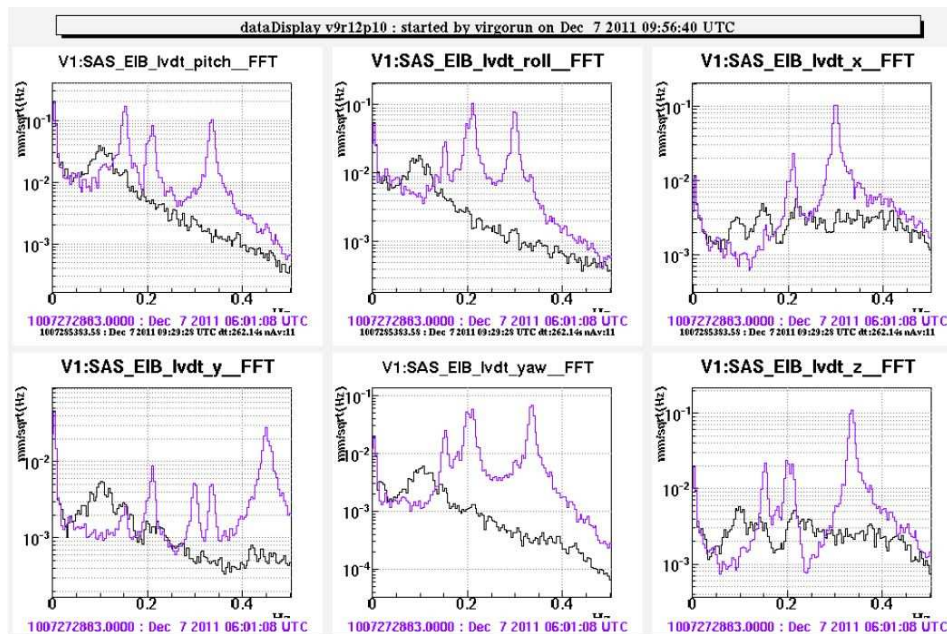


Figure 12.12: Inertial control of EIB-SAS eigenmodes. Pitch and roll correspond to θ_x and θ_y respectively. The black line is with controls on.

EIB-SAS controls are able to maintain the set point over the long term in all the six DOF, as shown in Fig. 12.14. The measured integrated rms displacement over several hours of data taking was well within the design limits (see Table 8).

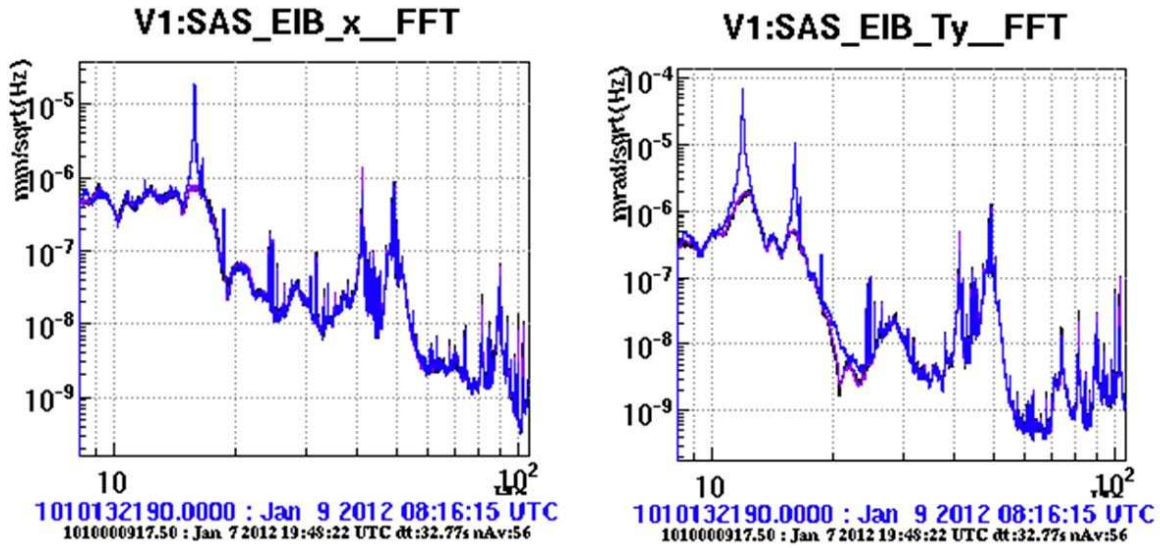


Figure 12.13: (left) Inertial damping of the two horizontal spring box modes at 15.8 and 16 Hz. (right) The spring box yaw mode is also damped by the active control. The purple line is with controls on.

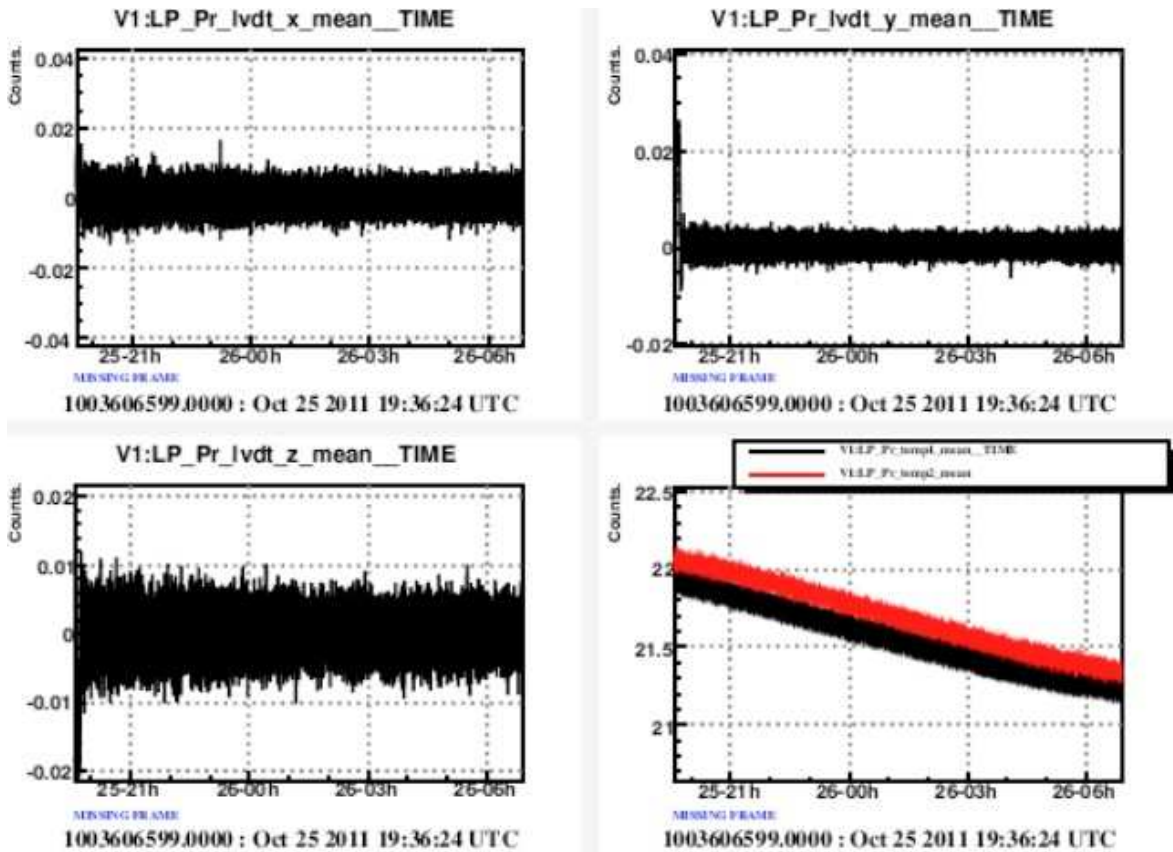


Figure 12.14: EIB-SAS position in closed loop over nine hours. The trend of the three translational DOF is shown. In all the plots of the LVDT signals one count correspond to 1 mm. The control is able to cope with the almost 1 K change in the temperature (bottom right plot); no evidence of the temperature drift appears in the vertical position of the bench.

| d.o.f. | closed loop rms | required rms |
|------------|-------------------|-------------------|
| x | 5 μm | 20 μm |
| z | 2 μm | 20 μm |
| y | 4 μm | 20 μm |
| θ_x | 2 μrad | 5 μrad |
| θ_y | 1 μrad | 5 μrad |
| θ_z | 1 μrad | 5 μrad |

Table 12.4: Integrated rms displacement from the data of Fig. 12.14 compared with the design limits.

12.2.9 Passive resonant dampers

A key factor in reducing the bench residual motion is the control of the spring box modes. While the horizontal modes are efficiently handled by the active control, the three vertical ones are damped passively by using vertical mechanical oscillators (*damper*), with about 3 kg suspended mass, tuned to the frequency of the mode to be suppressed (see Fig. 12.15(left)). The damper spring system is damped by means of eddy currents; the damping factor can be adjusted as well to optimize the energy drain from the spring box resonant modes. Location of the dampers on the spring box has been optimized taking into account the information available from the FEA model. In Fig. 12.15(right) the effect of the tuned damper on one of the two spring box tilt modes is shown; about 20 dB suppression has been achieved.

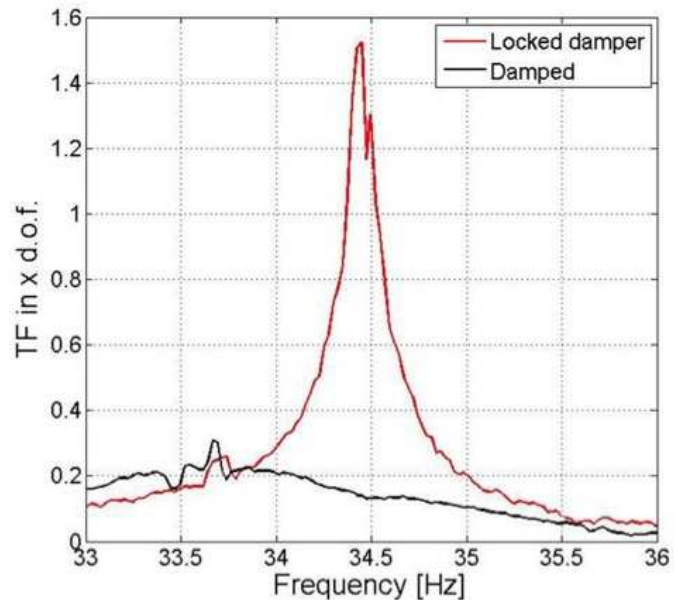


Figure 12.15: (left) Picture of one of the three vertical eddy current damper used to reduce the quality factor of the vertical spring box modes. (right) Damping of the 34.5 Hz tilt mode of the spring box. About 20 dB suppression has been achieved.

12.2.10 Seismic attenuation performance: measurements

The residual motion requirements specified for the new **EIB** support structure are shown in Fig. 12.16, in which the seismic noise (blue curve) measured on top of the Virgo+MS **EIB** is compared with the maximum acceptable noise level represented by the black dashed curve (see [395]). Compliance of EIB-SAS to the requirements was verified by means of transfer function measurements.

Low frequency The transfer function, measured at Nikhef in the low frequency region (see Fig. 12.17 and Fig. 12.18), shows peak seismic attenuation of about 40 dB above a few Hz. The measurement was done using two Trillium 240 seismometers and the environmental microseismic noise as the excitation source. By combining the measured transfer functions with a model of the local ground motion, projections of the residual motion of the bench at the Virgo site have been done (see Fig. 12.19). The analysis shows that EIB-SAS is meeting the requirements in the investigated frequency band.

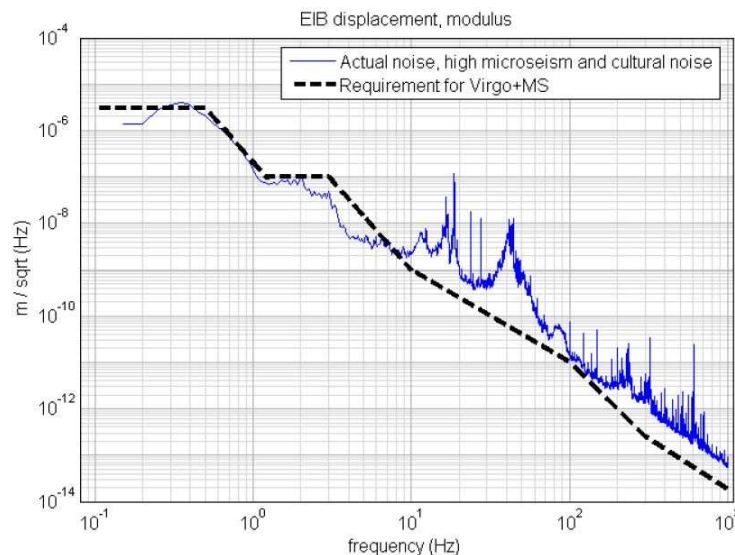


Figure 12.16: Residual displacement requirements for the EIB-SAS. The total displacement is calculated as the quadrature sum of the displacement noise measured along x , y and z .

High frequency A big effort has been made to produce reliable measurements of the transfer function at high frequencies (100 Hz–1 kHz) to confirm in the same band the compliance of EIB-SAS to the requirements. Shaking the ground with an electromagnetic shaker was found to be the correct method after having quantified, with a dedicated test, the signal contribution from the excited ground motion and from the direct acoustic excitation of the suspended bench. Please refer to [381] for the details. The acoustic coupling was found to be not relevant to the quality of the data above 100 Hz and a projection of the EIB-SAS residual motion at the Virgo site, at high frequency, could be made (see Fig. 12.20 and Fig. 12.21). The projected noise must be considered as a lower bound to the actual motion of the **EIB** at these frequencies. The reason is that, with the natural seism excitation, very low coherence

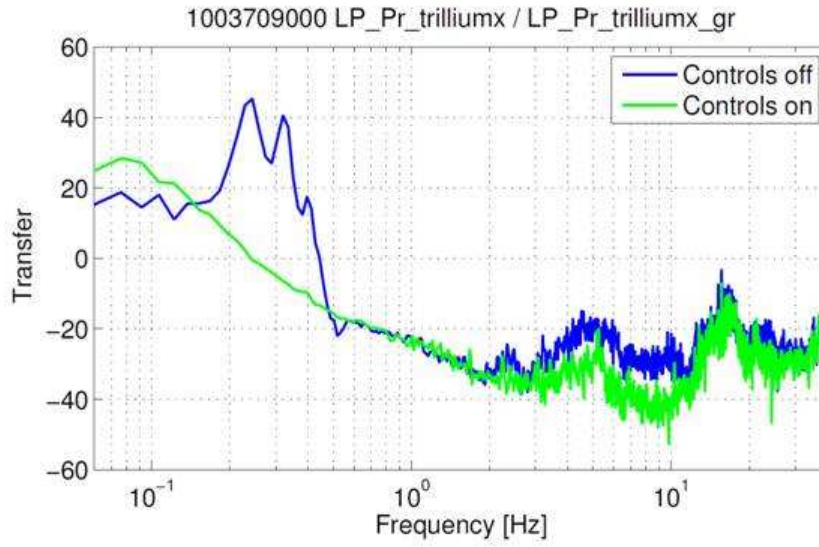


Figure 12.17: Horizontal transfer function in open and closed loop.

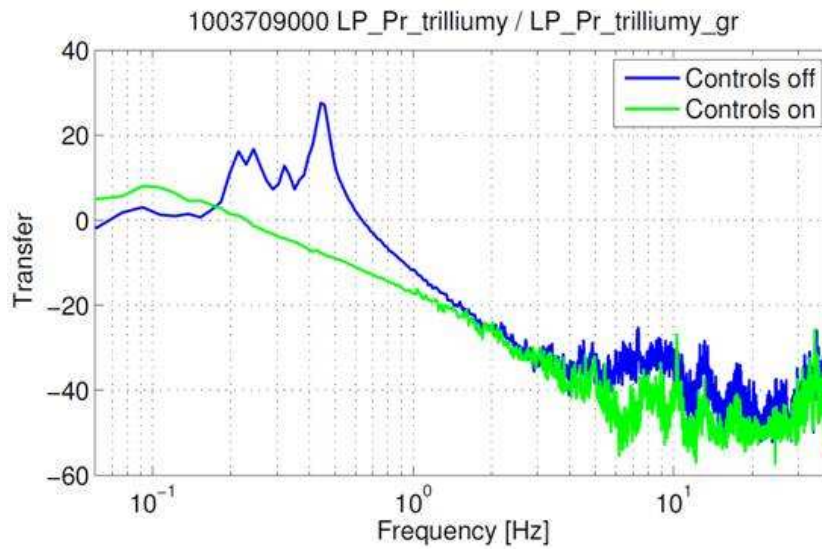


Figure 12.18: Vertical transfer function in open and closed loop.

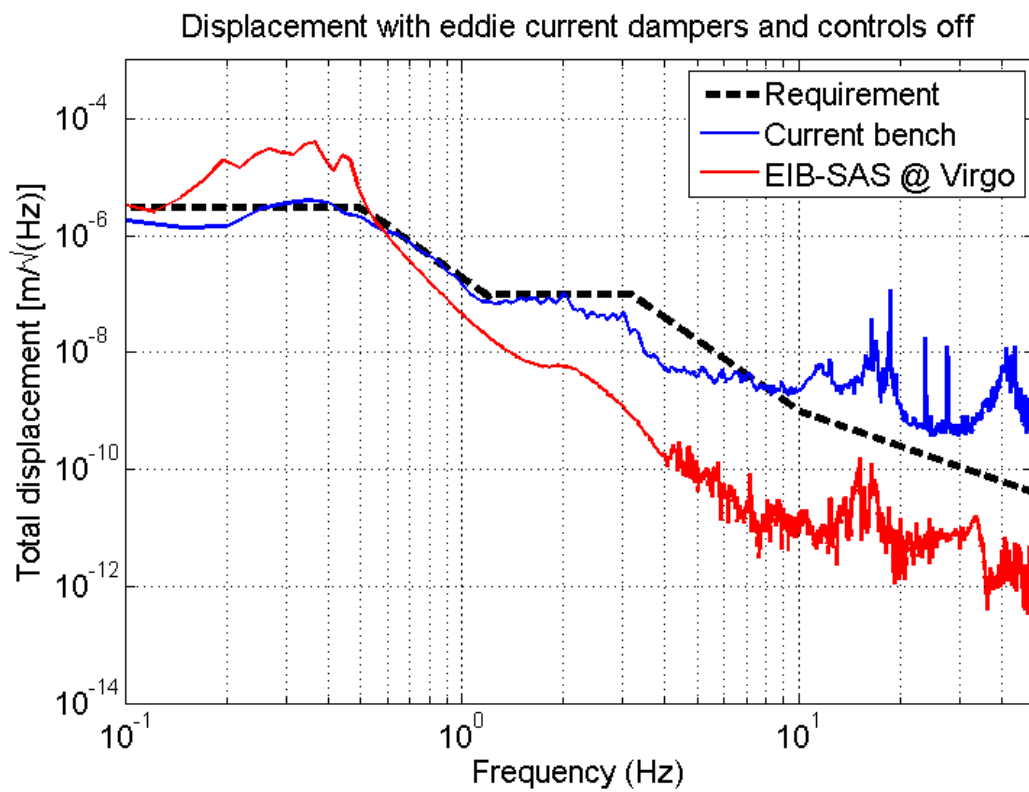


Figure 12.19: Projection of the EIB total displacement at the Virgo site in open loop. Tuned dampers are implemented.

between the motion sensors on the bench and on the ground is observed. On the other side, at the same frequencies, the bench motion is usually well correlated with the local pressure field measured with a microphone. The effect is enhanced by the large cross section of the **EIB**.



Figure 12.20: Ground-to-**EIB** vertical transfer function.

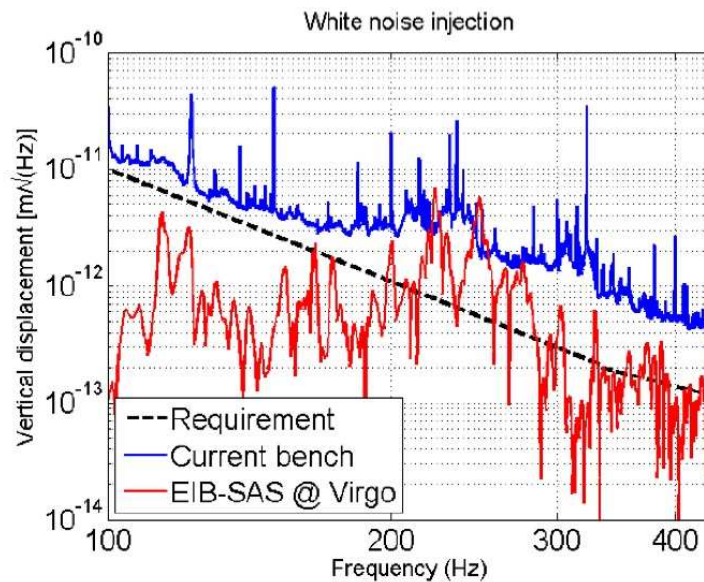


Figure 12.21: EIB-SAS vertical residual displacement expected at the Virgo site, compared with the total displacement of the current bench and the requirement.

12.3 MultiSAS

12.3.1 Introduction

A compact (1200 mm high, 1070 mm in diameter) multi-stage seismic attenuation system, called MultiSAS, has been designed to provide the best possible seismic attenuation for the suspended benches matching the limited space available in the facility. The MultiSAS design has been driven by the requirements of the end benches, the most demanding in terms of seismic isolation. The end benches carry telescopes and DC Quadrant Photodiodes (QPD) for the interferometer automatic alignment, for which shot noise limited controls require QPD residual linear (*horizontal* and *vertical*) and angular (*pitch*, *roll* and *yaw*) motion at 10 Hz of about 10^{-11} m/ $\sqrt{\text{Hz}}$ and $2 \cdot 10^{-14}$ rad/ $\sqrt{\text{Hz}}$ respectively. For details about residual motion requirements for all the suspended benches please refer to the ISC chapter of this document.

MultiSAS, following the philosophy of the superattenuator, is a hybrid seismic isolator in which bulk attenuation is provided passively by means of a chain of low natural frequency (< 500 mHz) mechanical oscillators (*filters*). Filters are realized with pendulums in horizontal and elastic elements in vertical. Feedback is used only to damp the rigid body eigenmodes of the system and to maintain, on the long term, position and orientation of the optical bench. High frequency internal modes are handled, whether necessary, by means of passive resonant dampers. Additional filtering stages, with respect to the minimum number defined by the residual translational motion required at 10 Hz, have been foreseen to make MultiSAS more tolerant to limitations deriving from:

- cross-couplings between different **DOF** due to asymmetries in the mechanics. In particular the horizontal-to-tilt coupling is expected to dominate the residual *pitch* and *roll* motion of the suspended benches;
- larger background transmission of the seismic noise around the high frequency internal modes of the system;
- saturation of the seismic attenuation capability, above a critical frequency, due to the finite mass and moment of inertia of the moving parts of the filters, i.e. deviation from the $1/f^2$ roll-off expected for an ideal spring-mass system;
- parasitic stiffness from cabling.

An overview of the system main components is presented in the next section.

12.3.2 Mechanical system overview

The horizontal ground motion measured at the Virgo site at 10 Hz is around 10^{-9} m/ $\sqrt{\text{Hz}}$. Therefore, the minimum required seismic isolation at the same frequency would be 40 dB, comfortably achievable with a single pendulum stage by assuming a natural period around 1 sec. Nevertheless, considering the challenging requirement on the angular **DOF**, two filter stages have been implemented. The components of the MultiSAS chain are (see Fig. 12.22 and Fig. 12.23):

- A horizontal (x , z and θ_y) pre-isolation stage realized with a short (about 0.5-m) inverted pendulum tuned to a natural frequency below 100 mHz, which attenuates the

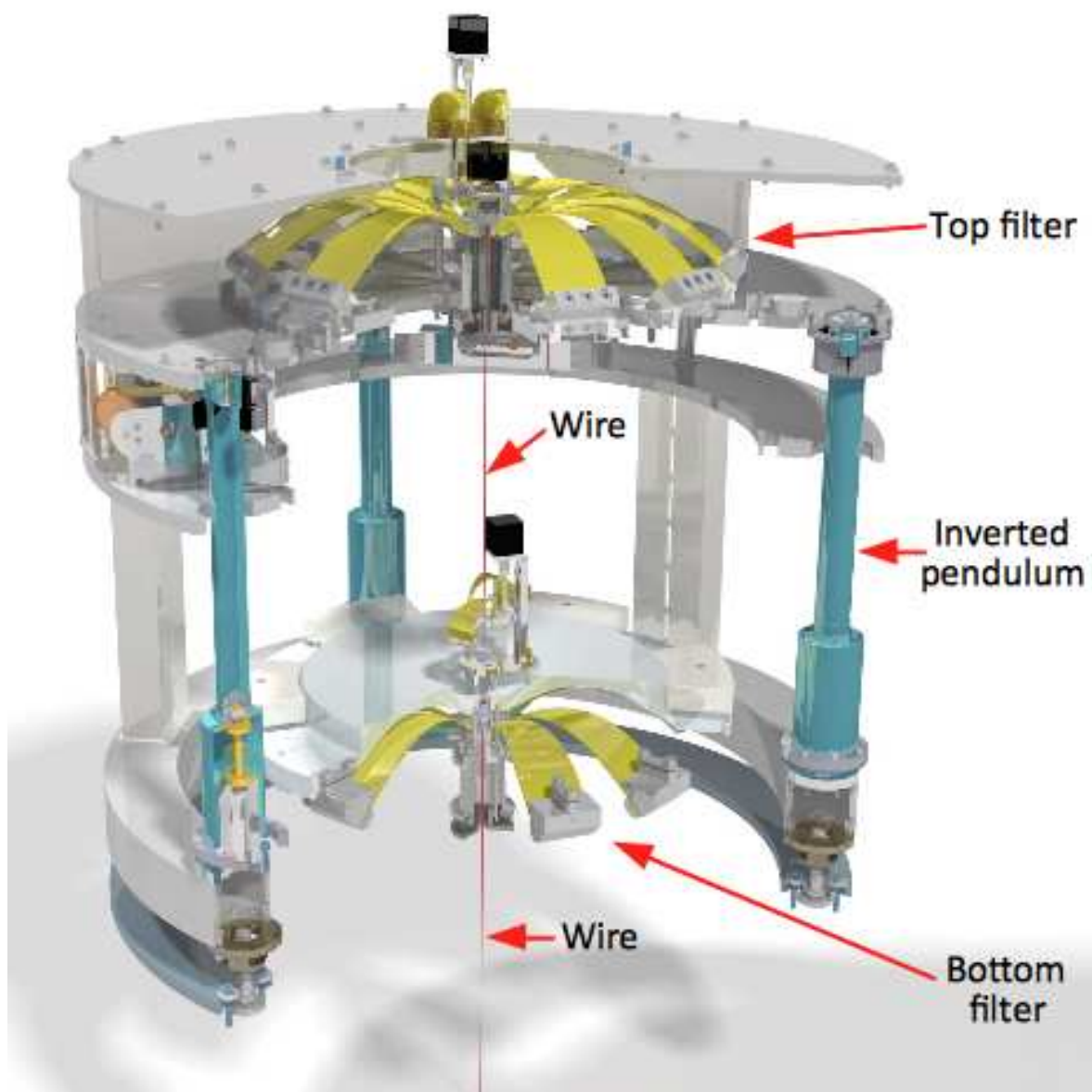


Figure 12.22: MultiSAS prototype assembly.

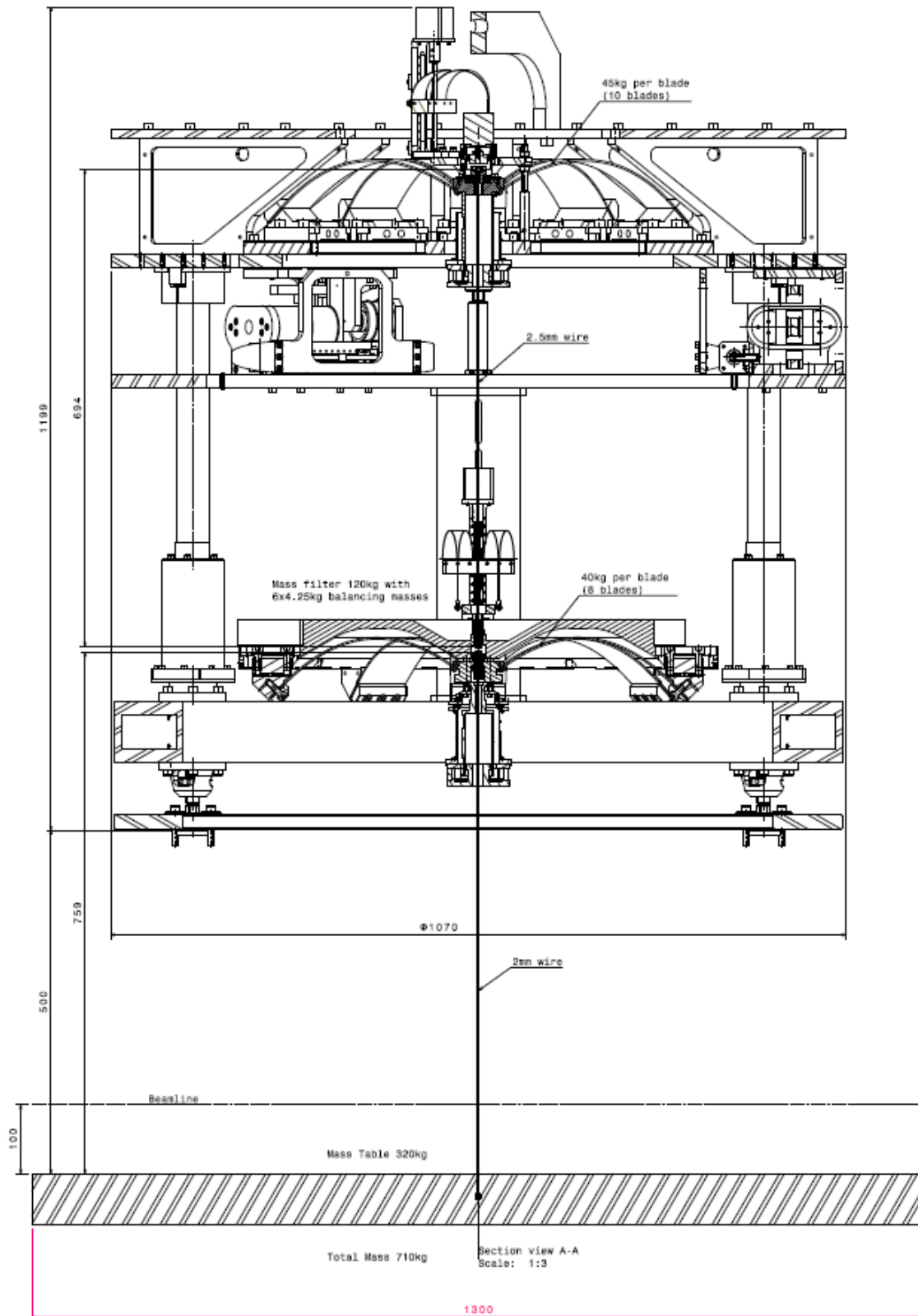


Figure 12.23: MultiSAS prototype dimensions and mass details.

| Parameter | Value |
|-------------------------|---------|
| Lower flexure diameter | 9.4 mm |
| Lower flexure length | 60 mm |
| Short flexure diameter | 2 mm |
| Short flexure length | 25 mm |
| Leg length | 438 mm |
| Leg mass | 0.75 kg |
| Total suspended mass | 650 kg |
| IP platform mass | 200 kg |
| Maximum stress | 290 MPa |

Table 12.5: MultiSAS inverted pendulum design parameters. The maximum stress corresponds to the maximum allowed displacement of the **IP** platform.

bench motion in the microseismic peak band and it allows its precise positioning at very low frequencies. The **IP** also provides an inertial platform on which to detect the recoil and actively damp the rigid body modes of the suspended chain. Passive attenuation between the **IP** itself and the optical bench is exploited to apply controls without re-injecting noise.

- A vertical (y) pre-isolation stage, hereafter called *top filter*, consisting of a **GAS** spring supported by the **IP** platform and tuned to 200 mHz.
- An intermediate stage, hereafter called *bottom filter*, consisting of a **GAS** filter tuned to 400 mHz suspended from the pre-isolation stage via a 694 mm long wire.
- The optical bench suspended from the bottom filter, via a 760 mm long wire. The tilt modes of the bench have been set around 100 mHz for better decoupling from the horizontal pendulum modes of the chain.

Materials The **IP** structure is completely realized in 6082-T6 aluminum alloy except for the flexure mounts. Unlike EIB-SAS both the top filter plate and the bottom filter body are made out of AISI 304L stainless steel. For the mechanical properties of maraging steel and copper beryllium please refer to 12.2.2.

12.3.3 Inverted pendulum

The inverted pendulum design (see Fig. 12.24) is the same as in EIB-SAS. In MultiSAS lighter legs, each consisting of a thin walled (1 mm) aluminum tube, 48 mm outer diameter, 438 mm long, are used. The main flexures have been dimensioned, by using a **FEA** model, to obtain an **IP** translational natural frequency of 70 mHz at a nominal load of 650 kg (including 20 kg of removable ballast mass). The aspect ratio of the flexures has been calculated to limit the stress level to 15% of the material yield at the maximum allowed displacement of the platform from its equilibrium position (± 8 mm).

The most relevant design parameters of the horizontal pre-isolation stage are listed in some detail in Table 12.5.

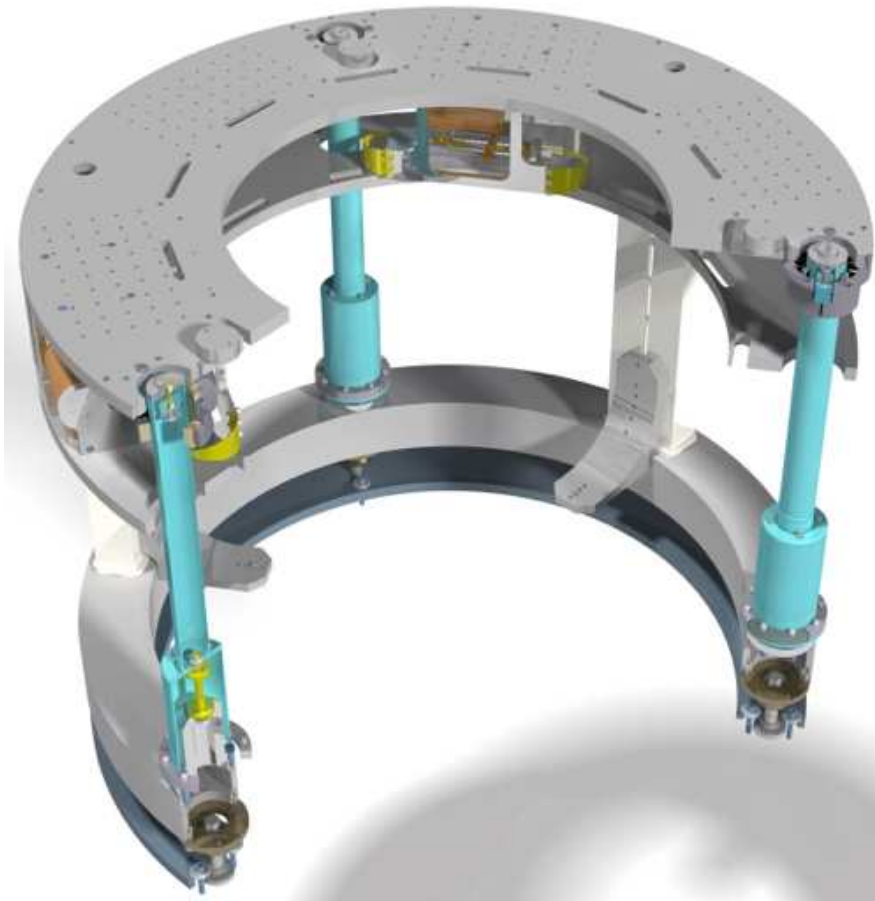


Figure 12.24: Inverted pendulum stage assembly view. A ring-shaped platform is supported by three inverted pendulum legs; an external frame rigidly connected to the base ring hosts the co-located LVDT/actuator pairs, the motorized correction springs and acts as safety structure.

The light weight design of the legs is meant to minimize their inertia in order to reduce the saturation level of the displacement transfer function, the so-called *center of percussion* (c.o.p.) effect [396]. Peak seismic attenuation exceeding 60 dB is expected both from analytical and FEA models⁴ and from extrapolations from experimental results achieved on similar devices [384]. Further improvement of the vibration isolation capability of the IP stage is achievable by tuning the mass of the counterweight bell so that the center of percussion of the leg is moved as close as possible to the center of rotation of the lower flexure. A suitable test jig has been designed for the counterweight tuning procedure.

Horizontal internal modes Besides the c.o.p. effect, the performance of the inverted pendulum at high frequency is limited by the internal modes of the legs, typically showing large quality factors. The corresponding natural frequencies and modal shapes are defined by the stiffness of the flexures, by the leg inertia and they are also influenced by the bell and counterweight masses and by the flexibility of the leg itself. FEA modeling has been made and the following modes were predicted for legs including the bell but without additional counterweights (see Fig. 12.25):

- six so-called first rigid leg modes, at 150 Hz (two per leg, one for each horizontal direction). In this mode, the leg top is swinging hence and forth, while the lower flexure is slightly bending;
- three torsional modes, at 160 Hz (one per leg). This mode is essentially a yaw motion of the leg about its own axis;
- six so-called second rigid leg modes, at 265 Hz (two per leg, one for each horizontal direction). In this mode both leg top and bottom co-move hence and forth;
- six leg modes, at 390 Hz: the so-called *banana* modes.

In the MultiSAS inverted pendulum the effect of the leg internal modes is mitigated by means of passive dampers located at the leg top (please refer to 12.2.3).

Vertical internal modes The top stage is characterized by three vertical/tilt modes related to the axial compliance of the short flexures and of the leg tubes. In the design of the prototype, the ring platform, the filter 0 plate and the stiffening hat add up a rather large mass (200 kg) resulting, according to FEA calculations, to a vertical mode around 66 Hz and to two degenerate tilt modes around 84 Hz.

12.3.4 Filters

The two filter stages (see Fig. 12.26 and 12.27) are realized by combining GAS springs for isolation along the vertical (y) direction and single wire pendular suspensions for isolation in horizontal (x , z and θ_y). The single wires, at the design stress level of 1 GPa, allow to prevent,

⁴Basic Lagrangian models predict a saturation level around $m_l/6M$, where m_l is the mass of the leg and M is the load per leg. For simple leg shapes as in MultiSAS there is a good agreement between Lagrangian and FEA models.

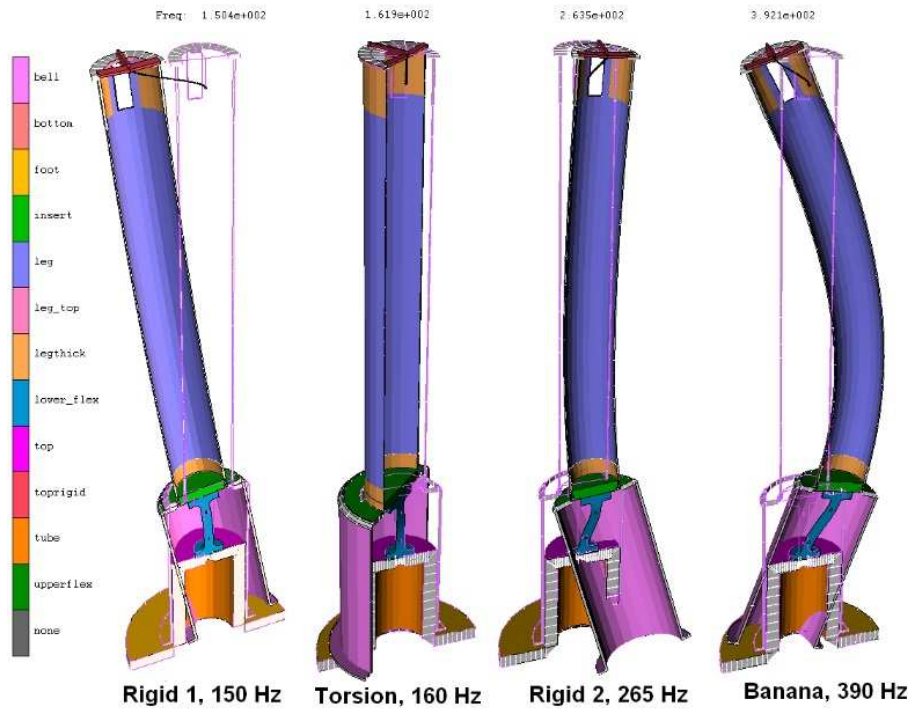


Figure 12.25: FEA model of the IP leg internal modes.

at first order, transmission of the tilt motion through the filter chain⁵. Residual excitation of the angular (θ_x, θ_z) DOF due to the coupling with the horizontal ones is suppressed by locating the effective bending point of the suspension wires as close as possible to the center of mass of the payload at each stage (body of the bottom filter for the top filter, optical bench for the bottom filter).

The blade profile in the bottom filter is calculated according to Cella's model [390]. In the case of the top filter, length and thickness were rescaled by 10% to cope with the larger load. In both cases, the maximum von Mises stress predicted by the FEA at the working point is about 1.7 GPa (Fig. 12.28), corresponding to 87% of maraging yield point. A more realistic value of 80% of the yield stress can be assumed, after taking into account the overestimation factor from the FEA experienced with EIB-SAS blade modeling. The most relevant design parameters for the two filter stages are shown in Table 12.6.

GAS springs: isolation performances Both mass and moment of inertia of the blades are not negligible with respect to that of the payload and it plays a role in the displacement transfer function, similar to the legs in the IP, causing its saturation to a level, typically, around -60 dB (see Fig. 12.29).

A compensating device, called *magic wand*, is foreseen in the bottom filter, to lower the saturation level to -80 dB or better (see Fig. 12.30) [398]. In the magic wand, see Fig. 12.31, a counterweight is fixed to one end of a rigid tube while the other end of the tube is connected

⁵The tilt transmission through a wire of length L scales as e^{-L/L_b} , where L_b is its bending length [397]. In MultiSAS $L_b \simeq 1$ cm

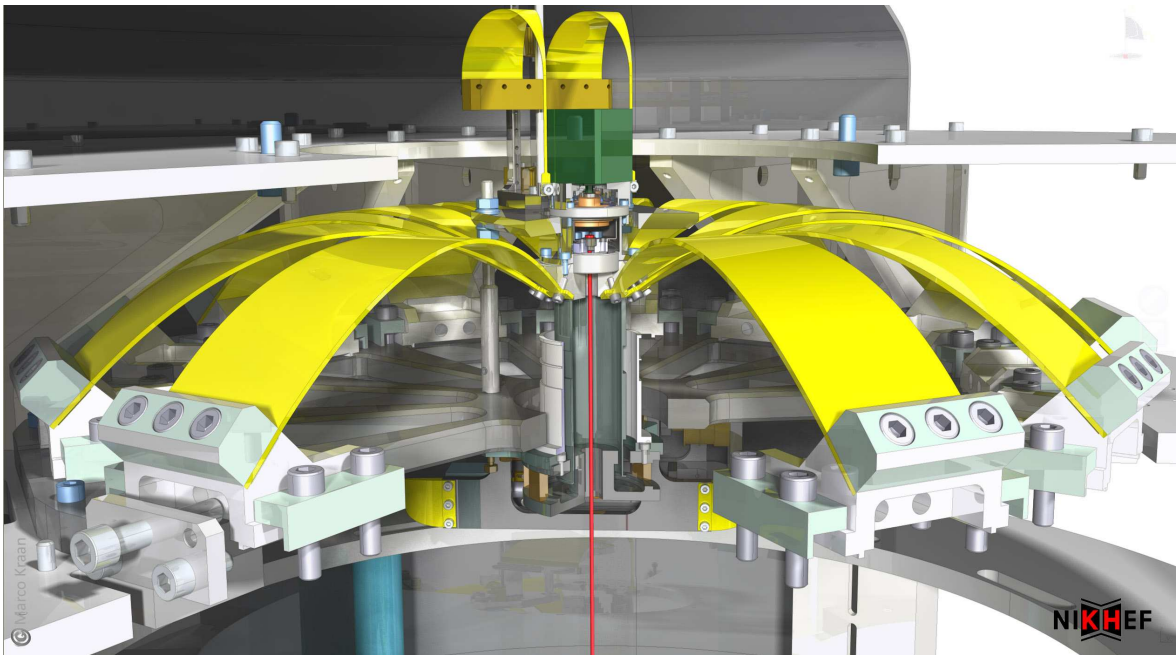


Figure 12.26: Top filter assembly view. It can hosts up to 12 blades for a maximum load of about 600 kg. The vertical DC position of the keystone can be adjusted by means of the dual-blade fishing rod visible on the top of the filter structure.

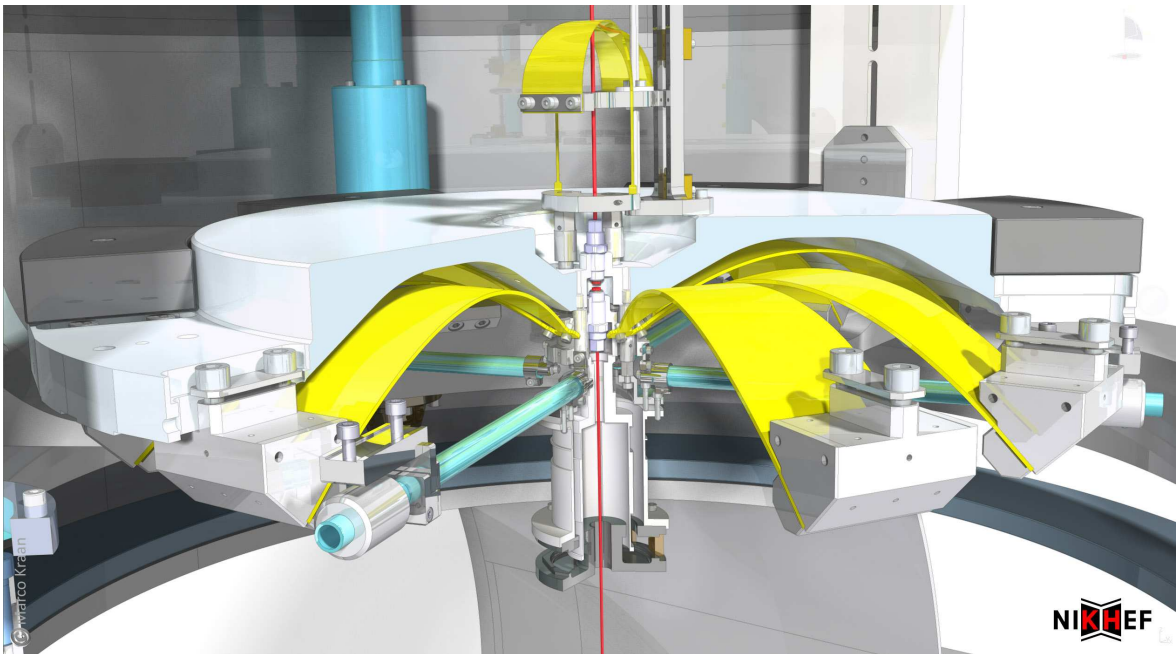


Figure 12.27: Assembly view of the bottom filter.

| Parameter | top filter | bottom filter |
|-----------------------------|------------|---------------|
| Uncoupled natural frequency | 200 mHz | 400 mHz |
| Blade von Mises stress | 1.7 GPa | 1.7 GPa |
| Number of blades | 10 | 8 |
| Load | 450 kg | 320 kg |
| Wire length | 694 mm | 760 mm |
| Wire diameter | 2.5 mm | 2 mm |
| Keystone mass | 1.5 kg | 1 kg |

Table 12.6: MultiSAS filter design parameters.

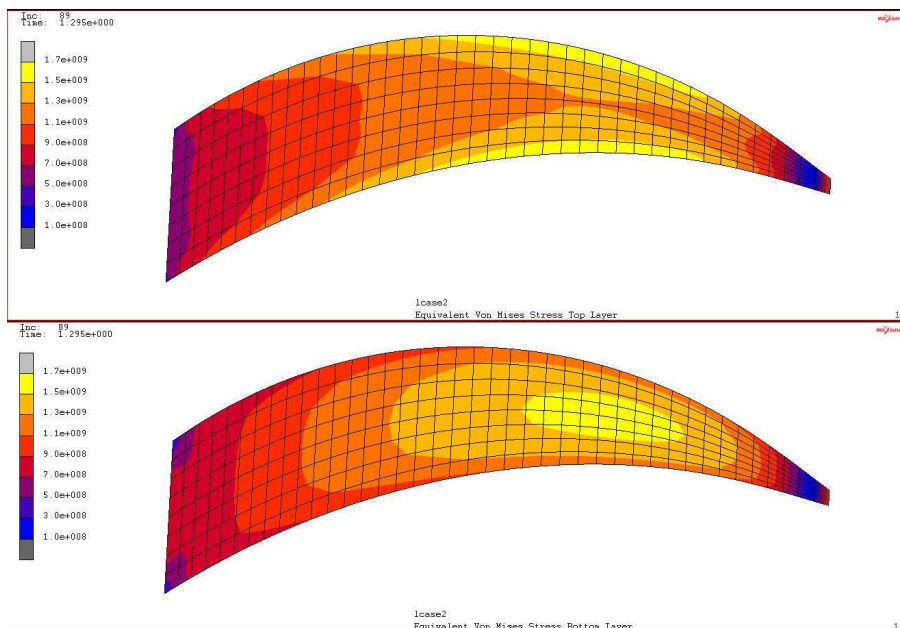


Figure 12.28: Bottom filter blade stress profile at the working point. A peak von Mises stress of 1.7 GPa is predicted. Almost identical results yield for the blades of the top filter.

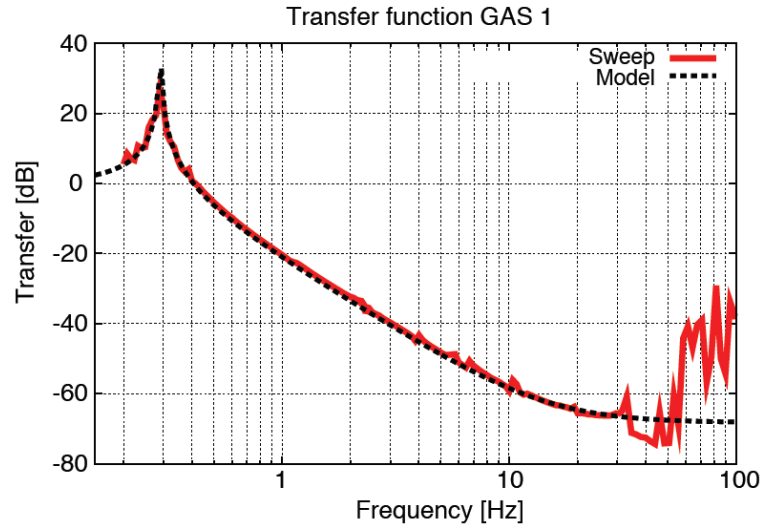


Figure 12.29: EIB-SAS **GAS** spring transfer function. The filter was tuned to 280 mHz natural frequency. Seismic attenuation saturates around -60 dB. The structures above 50 Hz are an artifact of the measurement due to the acoustic coupling of the dummy load with the resonances of the shaking frame.

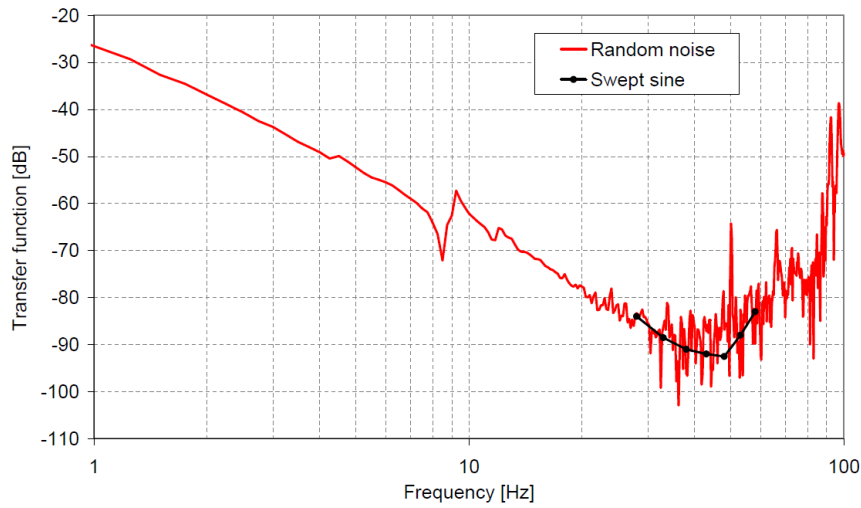


Figure 12.30: AEI-SAS **GAS** spring transfer function. Same device as EIB-SAS but two magic wands are used (courtesy of AEI Hannover). Even in this setup the measurement was limited at high frequencies by the parasitic resonances of the test frame.

to the keystone via a thin flexure. The tube is connected to the filter baseplate via a flexure pivot that allows the counterweight to follow the keystone vertical movement but opposite in phase with respect to the blades (see Fig. 12.27). By tuning mass and/or position of the counterweight the effect of the inertia of the blades can be suppressed; -90 dB residual transmissibility was demonstrated at AEI with the same device. The magic wand introduces a spurious resonance (corresponding to its banana mode) that can spoil the filter vertical transfer function; silicon carbide tubes are used to push the banana-mode above 250 Hz.

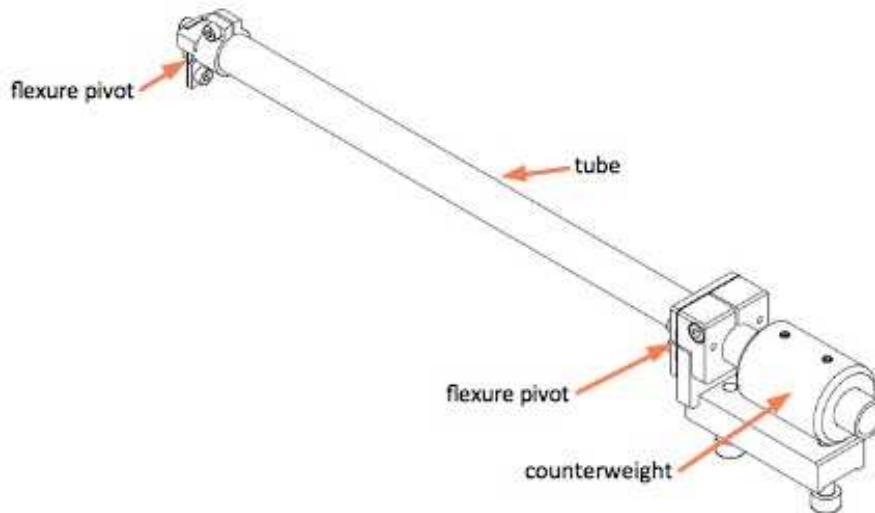


Figure 12.31: Bottom filter magic wand.

Internal modes Besides the usual violin modes of the suspension wires, a number of internal modes related to the compliance of the GAS blades in all the six degrees of freedom characterize the response of the filters. These so-called **keystone modes** involve translation and rotation of the two keystones with respect to the corresponding filter frame. The lowest frequency keystone mode is expected to appear at 67 Hz. For the details we refer to 12.3.5.

GAS springs: temperature effects The vertical position of the keystone is affected by temperature variations that change the GAS blades lifting force by the characteristic coefficient⁶ -225 ppm/K. The corresponding change in the vertical position, dependent on the frequency tuning, is -1.4 mm/K for the top filter and -0.35 mm/K for the bottom filter. Correction for large temperature changes (up to ± 3 K) can be applied using the built-in motorized fishing-rod. The GAS design is very robust with respect to thermal changes of dimensional and elastic parameters. Even at low natural frequency tunes (below 300 mHz) large temperature variations cannot drive the filters towards instability. A dedicated measurement was performed at Nikhef in which the environmental temperature was scanned over 8°C around its nominal value; the results are presented in Fig. 12.32.

⁶Note that the same coefficient in the Virgo standard filters is about -4000 ppm/K due to the large temperature sensitivity of the magnetic anti-spring strength.

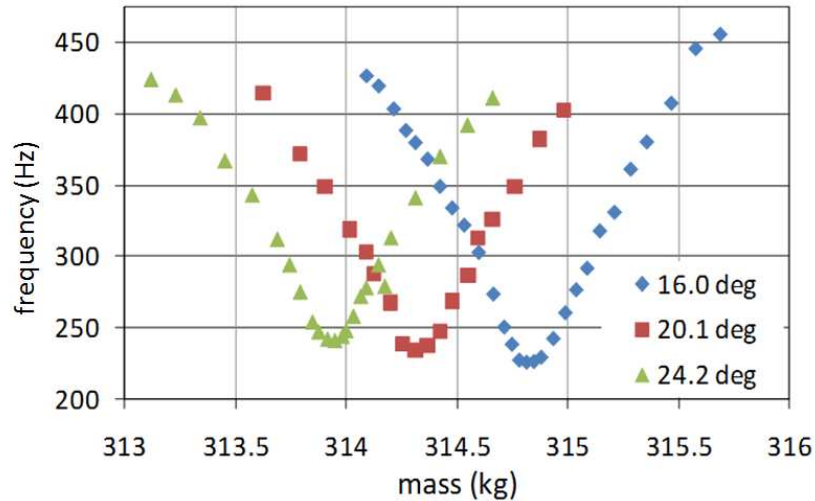


Figure 12.32: GAS filter stability test. An EIB-SAS GAS spring was tuned to 220 mHz and its temperature was changed by $\pm 4^\circ\text{C}$. The natural frequency vs load was measured.

12.3.5 Seismic attenuation performance: simulations

Seismic attenuation performance of MultiSAS have been estimated by means of a comprehensive FEA model of the complete system. In the model, five rigid objects (top stage, bottom filter body, bench, top filter keystone, bottom filter keystone), each provided with its own mass and moment of inertia, are connected with FEA meshed elastic elements (IP flexures, GAS blades, wires). The baseline tuning of IP and GAS filters, specified in Table 12.5 and 12.6, have been used.

In the case of the inverted pendulum, legs also have been considered as deformable objects. Frequencies and modal shapes of the predicted modes (up to about 500 Hz) are listed in Table 12.7. The displacement transfer functions are generated by introducing a large mass rigid body connected to the IP bottom flexures and shaking it at different frequencies. The results of the simulation (see Fig. 12.33, Fig. 12.34 and Fig. 12.35) can be summarized as follows:

- residual displacement spectral density in the horizontal direction will largely overkill the specifications with about 160 dB seismic attenuation at 10 Hz. Actually, above this frequency the coupled vertical motion is expected to be dominating at the bench level. From Virgo superattenuator experience, a 0.1% residual vertical-to-horizontal coupling has been assumed;
- residual tilt displacement spectral density is estimated to be 10% of the horizontal one, therefore well within the requirements.

Performance sensitivity to tuning parameters The same set of transfer functions has been simulated considering a less aggressive tuning of inverted pendulum and top filter. The IP translational mode was set to 220 mHz and the top filter was tuned to 400 mHz. The results are shown in Fig. 12.36, 12.37 and 12.38. No substantial change in the MultiSAS seismic attenuation capability is estimated in the high frequency range (above 10 Hz). This

| Frequency (Hz) | DOF | involved body | Notes |
|----------------|---------------------|-------------------------------|----------|
| 0.010 | θ_y | common | |
| 0.029 | θ_y | + Top stage-Bench, - Filter-1 | |
| 0.084 | x/z | common | 2 modes |
| 0.134 | θ_x/θ_z | Bench | 2 modes |
| 0.152 | y | common | |
| 0.239 | θ_y | Top stage | |
| 0.406 | θ_x/θ_z | Filter-1 | 2 modes |
| 0.518 | y | + Bench, - Filter-1 | |
| 0.743 | z/x | + Top stage, - Bench | 2 modes |
| 1.665 | z/x | + Top stage-Bench, - Filter-1 | 2 modes |
| 66 | y | Top stage | |
| 67 | z/θ_x | Filter-0 keystone | |
| 69 | x/θ_z | Filter-0 keystone | |
| 72 | θ_x/θ_z | Filter-1 keystone | 2 modes |
| 84 | θ_x/θ_z | Top stage | 2 modes |
| 123 | y | Filter-1 keystone | |
| 126 | y | Filter-0 keystone | |
| 150 | x/z | Rigid leg mode <i>I</i> | 6 modes |
| 160 | θ_y | Torsional leg mode | 3 modes |
| 245 | θ_z | Filter-0 keystone | |
| 252 | θ_z/θ_x | Filter-1 keystone | 2 modes |
| 255 | x/z | Upper wire first violin mode | 2 modes |
| 265 | x/z | Rigid leg mode <i>II</i> | 6 modes |
| 267 | x/z | Lower wire first violin mode | 2 modes |
| 269 | θ_x | Filter-0 keystone | |
| 340 | y | Filter-0 blade internal | 10 modes |
| 373 | y | Filter-1 blade internal | 8 modes |
| 378 | θ_x | Filter-0 keystone <i>II</i> | |
| 390 | θ_z | Filter-0 keystone <i>II</i> | |
| 390 | x/z | Banana modes | 6 modes |
| 397 | θ_z | Filter-1 keystone <i>II</i> | |
| 405 | θ_x | Filter-1 keystone <i>II</i> | |
| 428 | θ_y | Filter-0 keystone | |
| 440 | θ_y | Filter-1 keystone | |
| 507 | x/z | Upper wire second violin mode | 2 modes |
| 530 | x/z | Lower wire second violin mode | 2 modes |

Table 12.7: List of the system modes identified by FEA analysis. In the table filter-0 is the top filter, filter-1 is the bottom filter. In the model the same uncoupled 200 mHz uncoupled natural frequency was assumed for the two GAS springs.

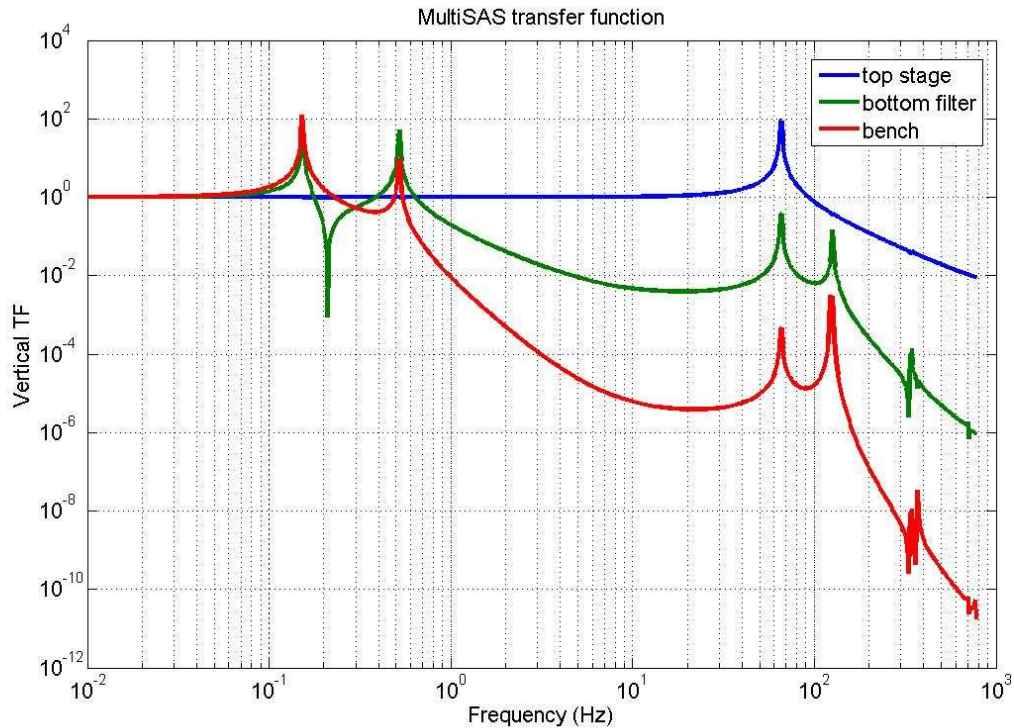


Figure 12.33: Simulated vertical transfer function from ground to the different stages of MultiSAS.

configuration could be chosen to make easier to operate on the suspended benches, at the price of a larger integrated rms motion.

12.3.6 Controls: sensors and actuators

A variety of sensors and actuators distributed in the system are used to control MultiSAS in different frequency bands.

Static positioning: eight step-motor driven actuators are used to provide the DC positioning of the suspended bench along the six **DOF**; all the motors are switched off during normal operation of the interferometer.

- **Vertical:** fishing rod acting on each filter. They are used to cope with large temperature changes and to correct any very long term drift of the chain vertical position due to the residual creep of **GAS** blades. The fishing rod actuation range is ± 2 N corresponding to a few mm adjustment of the filter working point. The positioning accuracy is better than $1 \mu\text{m}$. The reference signal for the fishing rod is the displacement of the keystone with respect to the filter body read by the built-in LVDT.
- **Horizontal:** three motorized correction blade springs act on the inverted pendulum platform to translate and rotate horizontally the entire MultiSAS chain within the range set by the platform end stops ± 8 mm. Positioning accuracy achieved is better than $1 \mu\text{m}/1 \mu\text{rad}$.

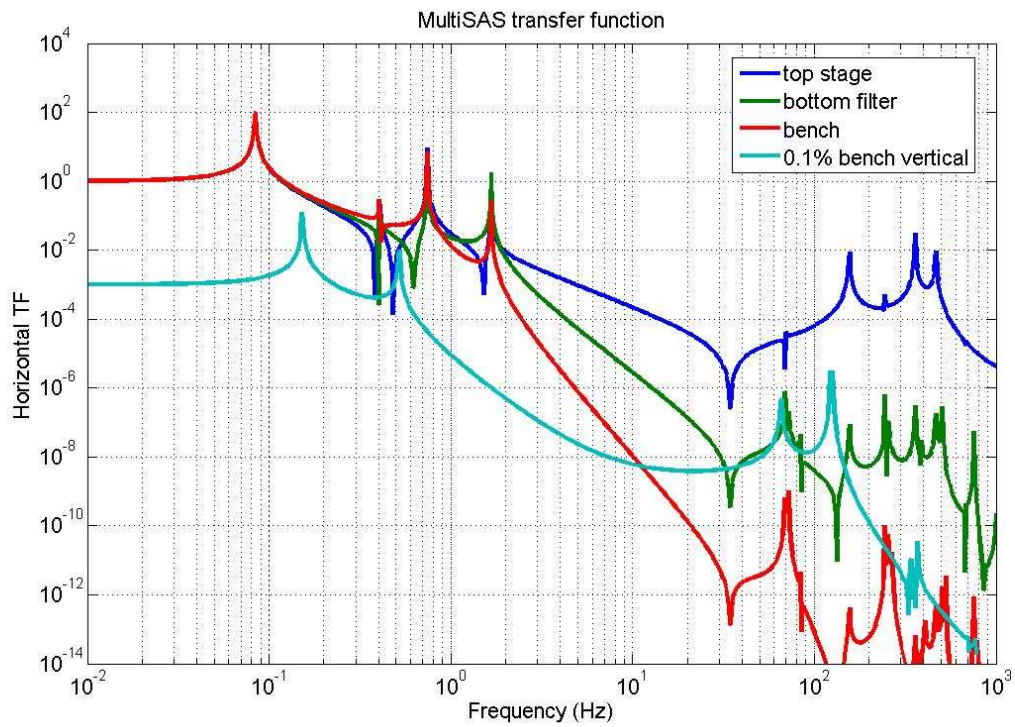


Figure 12.34: Simulated horizontal transfer function from ground to the different stages of MultiSAS. The light blue line shows the expected coupling of the vertical ground motion to the bench horizontal motion. According to the simulation vertical coupling is going to dominate the residual motion above 10 Hz.

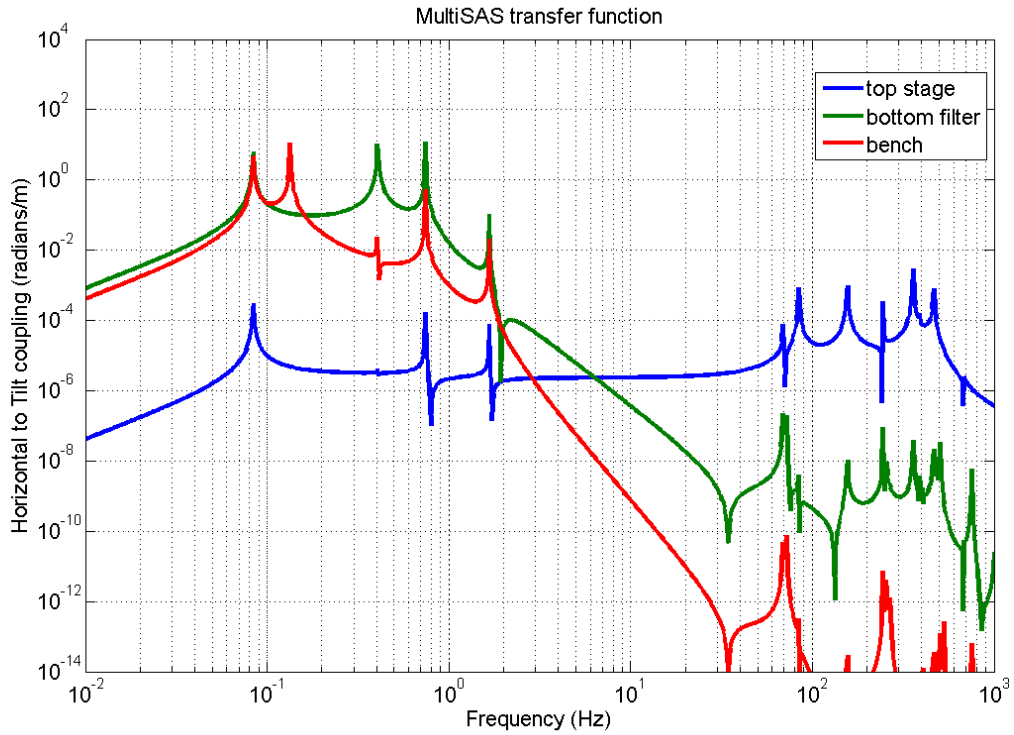


Figure 12.35: Simulated horizontal to tilt transfer function to the different stages of MultiSAS.

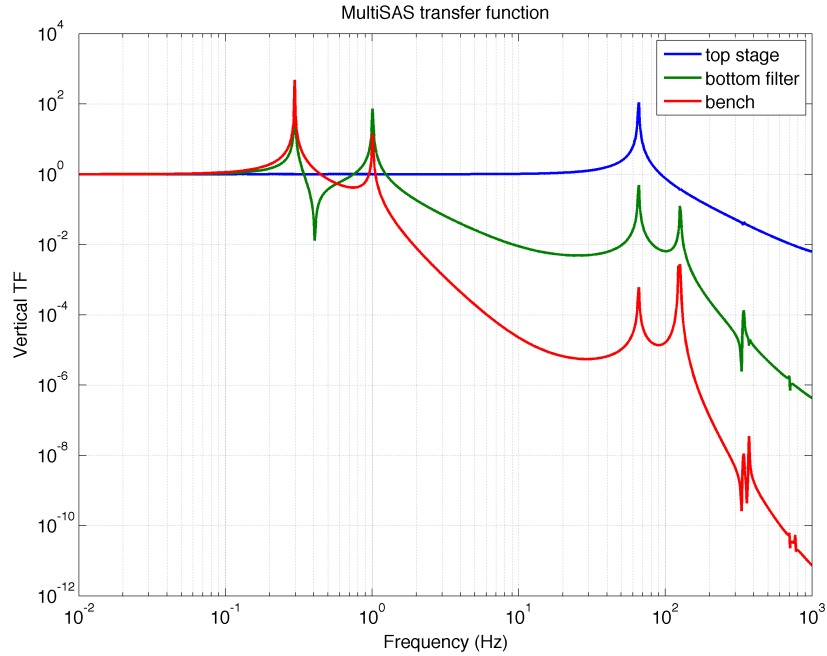


Figure 12.36: Simulated vertical transfer function. In this simulation both top and bottom filter are tuned to 400 mHz.

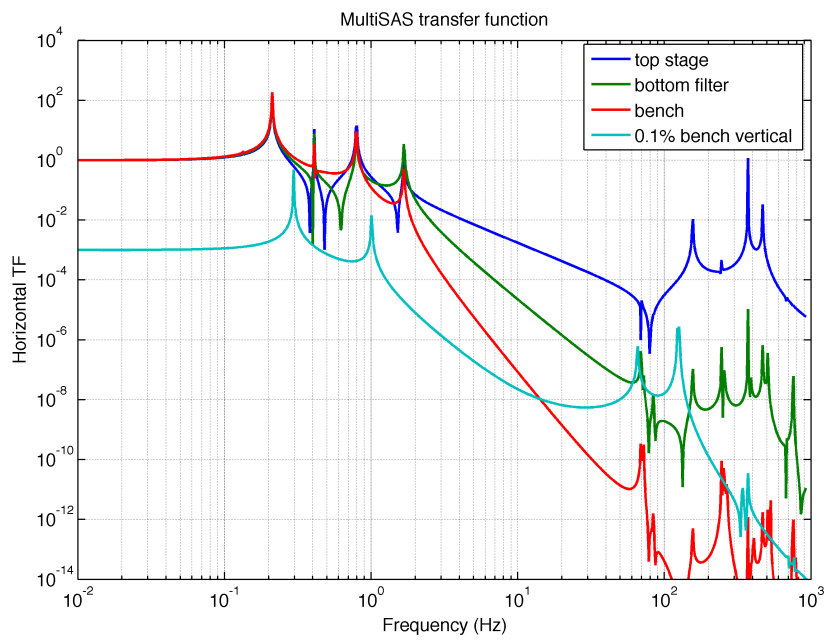


Figure 12.37: Simulated horizontal transfer function. In this simulation the translational IP modes are tuned to 220 mHz.

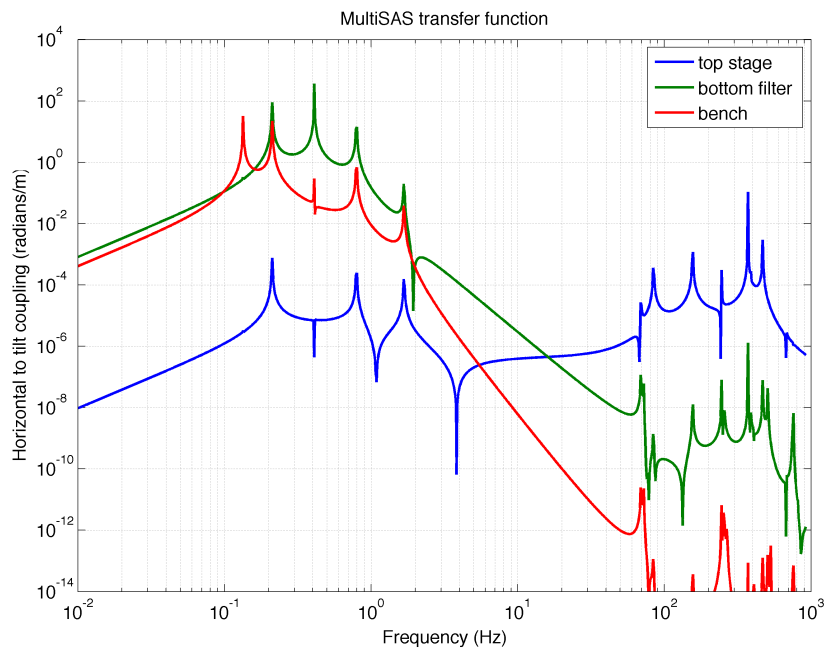


Figure 12.38: Simulated horizontal to tilt transfer function for the up-tuned MultiSAS.

- **Yaw:** differential rotational adjustment between the top stage and the MultiSAS chain can be performed using the gearbox (based on a step-motor driven Harmonic Drive™) located at the top filter keystone. Positioning resolution is around $300 \mu\text{rad}$.
- **Bench tilt:** two motorized mechanisms, located underneath the bench, allow to move counterweights and perform fine leveling. The reference signal is provided by a built-in dual-axis tilt sensor with a resolution better than $1 \mu\text{rad}$.

Dynamic corrections: these include all sensors and actuators used for the active control of the top stage (inverted pendulum platform+top filter baseplate) and for the local control of the optical bench:

- **sensors and actuators on the top stage:** very low frequency bench position control and active damping of the MultiSAS chain eigenmodes along x , y , z , θ_y , is performed acting on the top stage. The top stage is instrumented with
 - three horizontal LVDT position sensors, in triangular configuration, measuring the top stage motion with respect to the MultiSAS external frame;
 - three horizontal 1-Hz natural frequency geophones (Sercel L4-C with 5500 ohm series resistance coil and 280 V/m/s throughput), in triangular configuration, measuring the top stage inertial motion⁷;
 - one vertical LVDT position sensor measuring the motion of the top filter keystone with respect to the top stage;
 - three 5 N/A horizontal voice-coil actuators, collocated to the horizontal LVDTs, acting on the top stage from the external frame (see Fig. 12.39);
 - one 10 N/A vertical voice-coil actuator, collocated to the vertical LVDT, acting from the top filter baseplate to its keystone;
- **sensors and actuators for the bench local control:** bench θ_y , θ_x and θ_z modes are controlled down to very low frequencies by means of optical position sensors and coil-magnet actuators referred to the ground:
 - CCD camera for position readout. Optical levers will be considered to reduce control noise if necessary;
 - eight coil-magnet actuators acting from the vacuum chamber to the bench.

12.3.7 Controls: electronics and DAQ

Electronics Each MultiSAS unit is provided with two crates, one hosting signal conditioning boards for LVDT and tilt sensor, coil driver boards and DC power supply for the geophone preamplifiers, the other hosting the step motor controllers and their dedicated DC power supply. Patch cables (multiple shielded twisted pairs) up to 20 m long connect the crates to a patch panel located next to the minitower; inside the patch panel signals are routed to a

⁷The $1/f^2$ roll-off of the geophone response below its natural frequency is equalized by means of a digital filter in the real-time control system.

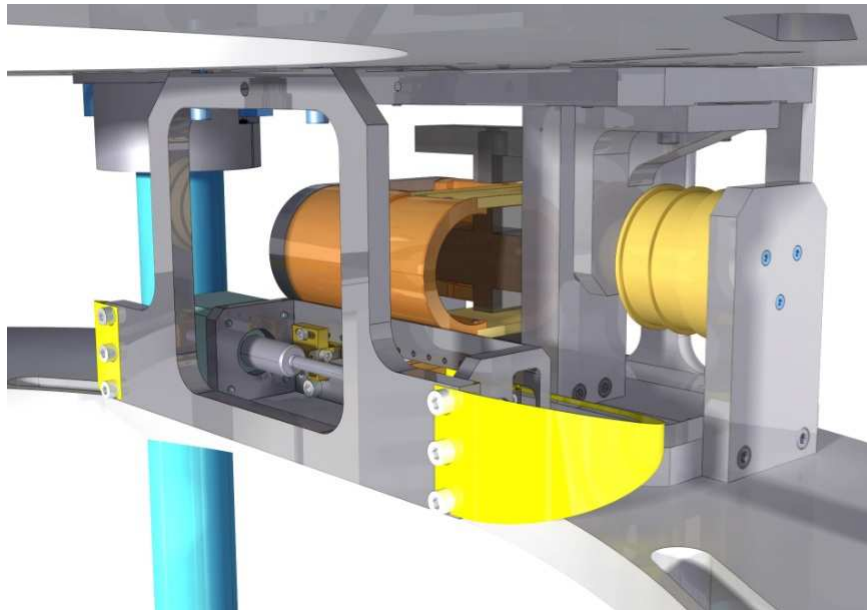


Figure 12.39: View of one of the three horizontal position sensor/actuator sets. The step motor driven blade pair is used for DC positioning.

set of short patch cables connected to the vacuum feedthroughs. The following electronics subsystems are provided to operate MultiSAS:

- the LVDT sensors are conditioned by means of multichannel custom designed boards providing up to 140 dB linear dynamic range at the demodulator differential output. Nanometer level resolution (exceeding the stability of the ground) is achieved over a ± 5 mm displacement;
- the actuator coils are driven by means of multichannel differential input transconductance amplifiers; depending on the voice coil parameters output currents up to 100 mA can be delivered. A differential ended current monitor signal is provided;
- the dual-axis electrolytic tilt sensor used for the remote leveling of the suspended bench is conditioned by a commercial driver from Applied Geomechanics;
- each geophone is provided with a local preamplifier with differential output; the preamplifier PCB is mounted directly on the geophone holder inside the vacuum sealed pod. The necessary DC power supply voltage is generated on board of the LVDT/actuator crate and stabilized to (+12 V) inside the patch panel. The preamplifier, designed at Nikhef, is based on the CS3001 op-amp and it allows to achieve coil Johnson noise limited performance starting from very low frequencies (above 50 mHz);
- two six-channels step motor controller/driver based on commercial Six-pack drivers from Trinamic GmbH. Stepping commands are sent to the driver via Ethernet interface.

DAQ MultiSAS is digitally controlled by means of a real-time control system. DAQ-Box boards are used to digitize the signals and to drive the actuators. Please refer to the DAQ chapter of this document for the details.

12.3.8 Controls: top stage

Lowest frequency rigid body modes of the MultiSAS chain, excited by the natural seism, would increase the rms motion of the bench well above the requirements when active controls are not applied. Most of those modes can be damped applying feedback forces at the top stage level, both in horizontal and vertical direction, taking advantage of the large recoil on it. Only the angular modes of the bench, the yaw at 10 mHz and the two tilt modes at 134 mHz, which are largely decoupled from the top stage, must be handled with local controls by using position sensors and applying feedback force directly on the bench itself. The steps to implement the top stage controls are described hereafter.

- **Pre-filtering and coordinate system change:** a 3X3 base change matrix, including all the measured calibration factors, is applied to the raw signals from LVDT and geophones to geometrically reconstruct the top stage motion along the coordinate system (x, z, θ_y) referred to the optics. The horizontal geophone signals are also digitally prefiltered to provide calibrated displacement output starting from nearly DC. The vertical channel y is independently treated and, in the baseline design, it makes use only of the signal from the vertical LVDT. According to the prototype test results, the implementation of a vertical geophone could be considered in order to reduce seismic noise re-injection.
- **Sensor blending:** LVDT and geophone readouts reconstructed along the same degree of freedom are combined in the frequency domain to provide the error signals for the active control. Practically, blending is realized applying a 5th order low-pass filter, with frequency response $L(s)$ to the LVDT signal, and a complementary high-pass filter, with frequency response $H(s) = 1 - L(s)$, to the geophone signal (see [399] for more details). The blending frequency will be determined experimentally. Relevant parameters of LVDT and geophones are listed in Table 12.8.
- **Actuator diagonalization:** virtual actuators each acting only along one degree of freedom in the xyz coordinate system are determined experimentally. The transformation matrix \mathbf{D} from real to virtual actuators is called *driving* matrix and it is measured according to the following iterative procedure:
 1. the first guess for \mathbf{D} is simply a 3X3 identity matrix. Each real actuator is driven with a very low frequency (as a rule of thumb at a frequency three times below the lowest mode of the top stage) sinewave and the amplitude of the response of each blended sensor is measured; in this way a force-to-displacement transfer function matrix \mathbf{A} in [m/V] units is generated. In the frequency range of the measurement the measured transfer functions between actuation voltage and coordinate amplitude should be real, with phase equals 0 or π , and frequency independent;
 2. the new estimated driving matrix $\mathbf{D} = \mathbf{A}^{-1}$ is applied to the real actuators and a new matrix \mathbf{A} is measured;
 3. step 2 is re-iterated until off-diagonal terms in \mathbf{A} are sufficiently reduced. Typically after two-three iterations residual couplings are reduced well below 10% level.

Standard PID compensation filters are applied to the blended sensors to damp the top stage motion. Unity gain frequencies of a few Hz are foreseen for the control. It is important to

| Sensor | Range | Band (Hz) | Noise @ 0.1 Hz | Noise @ 1 Hz |
|-----------|-----------------|-----------------|---------------------------|-----------------------------|
| LVDT | ± 5 mm | DC \div 300 | 10 nm/ $\sqrt{\text{Hz}}$ | 1 nm/ $\sqrt{\text{Hz}}$ |
| Geophones | ± 0.05 mm/s | 0.01 \div 400 | 10 nm/ $\sqrt{\text{Hz}}$ | 0.01 nm/ $\sqrt{\text{Hz}}$ |

Table 12.8: MultiSAS sensors properties. The listed parameters are the measured ones after digitization with Virgo ADC 7674 board.

notice that the simple diagonalization of the actuators does not resolve the couplings between the different degrees of freedom at the resonances (see Fig. 12.40).

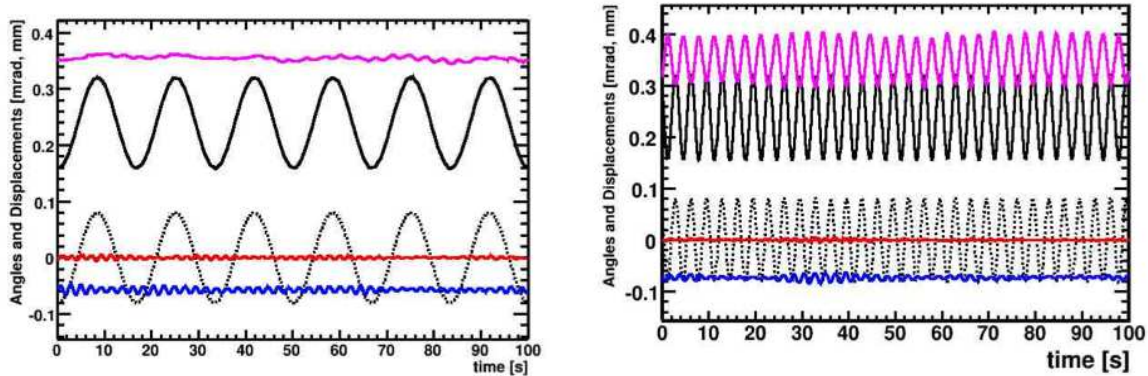


Figure 12.40: Actuation signal (dotted black curve) in the pitch degree of freedom at 60 mHz (left) and 300 mHz (right) as a function of time. The responses in the pitch (black curve), roll (red curve), y (blue curve), and z (pink curve) are simultaneously shown. While at 60 mHz the activation matrix is almost unitary, at 300 mHz actuation of the pitch degree of freedom also induces strong motions along the z-direction.

Care is taken in designing the PID filter to have dominant velocity feedback in the frequency band of the system normal modes so that they get damped independently on the couplings.

12.3.9 Controls: optical bench

MultiSAS benches will use the same camera based position control developed for Virgo SDB [401].

12.3.10 Interface with vacuum chamber

The mechanical interface between SAS and vacuum chamber is provided by a stiff ring-shaped aluminum welded structure called *base* (see Fig. 12.41).

The base is provided with leveling bolts; a clamping device is used to secure the MultiSAS to the vacuum chamber after initial alignment. Vacuum forces could deform the chamber after pumping and change the leveling of the inverted pendulum. A maximum residual tilt of ± 0.1 mrad is required to the vacuum chamber in order to be able to remotely recenter the top stage using the horizontal correction springs. The force needed to correct a leveling error

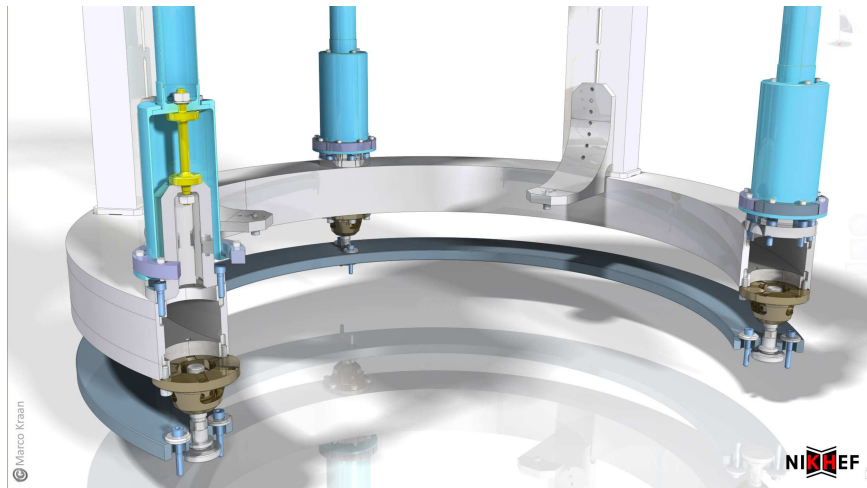


Figure 12.41: View of the inverted pendulum base.

is 6.5N/mrad ⁸ while the maximum overall available pulling force from the DC actuators is 5 N. FEA on the minitower vacuum chamber has shown that the expected tilt error is well within the requirements (see 12.4.2).

12.3.11 Cleanliness and vacuum compatibility

The minitowers vacuum chambers are sealed with Viton O-rings and they are meant to operate in high vacuum. Nevertheless the capability of making a bakeout at 150°C must be preserved. Specific criteria have been followed in designing the MultiSAS and in the planning of the production and assembly procedures.

- **Material selection:** all the materials and components used in the MultiSAS design are UHV compatible: coils of sensors and actuators use Peek™ spools and their windings are made with Pure ML™ kapton coated copper wire; UHV compatible step motors from Arun Microelectronics Ltd are used to power the DC actuators.
- **Geophone pods:** the baseline design of the MultiSAS foresees three horizontal geophones on the IP platform for the top stage control. The geophones are not vacuum compatible and suitable vacuum tight enclosures (*pods*) will be used. The pods will be sealed using conflat flanges and helicoflex gaskets; different tracer noble gases will be blown into each pod before its sealing for leak detection.
- **Cleaning:** all the parts are cleaned according to UHV standard procedures except for the baking that is not required. The cleaned parts will be wrapped in UHV aluminum foil for storage before the assembly, to prevent contamination.
- **Assembly and transportation:** the MultiSAS units will be assembled at Nikhef inside a Class 10000 clean room. After testing each MultiSAS unit, secured in its own transportation jig, will be wrapped first with UHV aluminum foil, then with PET foil and finally sealed inside a moisture barrier bag for shipment.

⁸The force per unit tilt error is calculated just as $mg\theta$, where $m=650$ kg is the IP static load and θ is the misleveling angle.

12.3.12 In-vacuum cabling

The cabling scheme of MultiSAS follows the same criteria as the superattenuator:

- the basic cabling unit is the shielded twisted pair which best matches the balanced nature of sensing and actuating coils used to control the MultiSAS. Low crosstalk between excitation and receiving coils of the LVDT sensors is ensured over long (more than 10 m) distances;
- risk of short circuiting the MultiSAS seismic isolation is minimized by clamping the cables to each stage, starting from the top one, all the way down to the device location. This criterion holds both for MultiSAS controls and for photodiodes and other optical components installed on the optical bench;
- soldering is avoided at most. Connections are realized using crimp contact pins;
- every device is provided with a built-in connector; patch cables are used to reach the feedthroughs;
- feedthroughs use circular 32-pin connectors (MIL-C-26482) with plugs both on air and vacuum side.

High-vacuum compatible cable Standard Virgo cable, used for the controls of the Superattenuators, was produced by Axon S.A. using porous teflon (Celloflon[®]) to provide electrical insulation and jacketing. Porous teflon insulation provides extremely low outgassing rate. Nevertheless the standard cable appears to be still too stiff for MultiSAS since the small volume of the minitower prevents shuffling the cable over large lengths between two adjacent stages. For this reason a much more flexible and lighter cable has been adopted. The new cable is a jacketed single shielded twisted pair (RET 3019 Sh E2) produced by Axon S.A.. The cable is insulated with wrapped and sintered teflon, it has low outgassing rate, it is produced without using lubricants and is bakeable up to 200°C. The nominal outer diameter is 1.7 mm and its weight is 5 gm/meter. Each stranded wire conductor has a nominal diameter of 0.315 mm and it is suitable to carry the maximum average current ($I_{\max} < 100$ mA) deliverable by the MultiSAS controls.

12.4 Minitower: vacuum chambers

12.4.1 Requirements and basic design choices

These chambers are the housing for the benches, and the support for their seismic isolation system. To reduce the development time, a common design has been made for the minitowers of these five benches. The requirements which have driven their design of the minitowers are described hereafter.

- **Suspended bench** - The minitower is designed to host a 1.3×1.3 m bench. Therefore its inner diameter is 1.4 m. The total mass of the equipped suspended bench (with optics, electronic containers) is assumed to be 320 kg. The suspended bench access should be easy: two lateral doors are designed for this purpose.

- **External benches** - Small external optical benches will be attached to the minitower structure. A support structure, attached to the minitower legs is part of the minitower design.
- **Clean air** - The optics on the bench should be kept clean, even when working on the suspended bench. A clean air strategy has been designed.
- **Seismic isolation** - The minitower is the support for the seismic isolation system. Therefore its internal frequencies have to be in the band where the seismic isolation is effective, at least above 20 Hz and the support ring for the seismic isolation should not tilt by more than 100 μ rad when going under vacuum to preserve the performances of the seismic isolation system. A 250 mm diameter flange is needed to accommodate the electrical feedthrough needed to operate the seismic isolation under vacuum.
- **Bench cables** - A 250 mm diameter flange is needed to accommodate the electrical feedthrough needed for the cables coming from the suspended bench. Furthermore a 160 mm diameter flange is needed for the electrical feedthrough of the coils used to control the bench.
- **Optical viewport** - Since the optical layout of the benches is not yet frozen and anyway is likely to evolve as we gain experience, the location of the viewport should be flexible. To fulfill this need, we select large flange on which smaller optical viewports will be installed. A 2° tilt is put on all flanges which may accommodate viewports to easily separate the parasitic reflection on the viewport faces.
- **Beam position** - The design is made assuming that the beam is 1100 mm above ground floor and 100 mm above the top of the bench. When designing the minitower legs, a 20 mm margin is used (i.e. shorter legs) to account floor variation compared to the nominal position. The nominal vertical position will be set by adding spacers underneath the minitower legs.
- **Input beam diameter (end benches towers)** - The maximum aperture of the telescope located on the bench is 230 mm. For initial Virgo, the diameter of the window is slightly less than 200 mm. Therefore the input flange diameter is chosen to be 350 mm, large enough to accommodate a few cm offset of the beam relative to the flange side without introducing clipping.
- **Vacuum** - The minitowers are expected to operate with a glass window separation from the main vacuum chamber at the beginning of AdV. Only rough pumping will be used at that time. However, the design of the minitower should be such that the evolution to ultra high vacuum is possible. Therefore CF flanges and double Viton gaskets will be used. At least two DN40 flanges for rough pumping and gauges are needed, and two 250 mm diameter flanges for possible secondary and ion pumps.
- **Surface** - Some electronic will be put on the bench. Therefore the surface of the minitower should absorb well the infrared light emitted by a heated electronic. A treatment at 400°C of the stainless steel is foreseen for this purpose, which also would be useful for the option of the operation with a good quality vacuum.
- **Space constraints** - In the case of the injection tower, and also for the detection minitower, the available height under the ceiling is limited to 3.6 m. The design of the

chamber and the associated tools should be such that the chamber could be opened and closed with all the elements installed within this limit.

12.4.2 Mechanical design

The minitower will be made of 304L stainless steel. The assembly drawing is proposed in Fig. 12.42. The following list described the available flanges, their purpose, in the case of the NE minitower. Other minitower will have similar assignment, with at least some changes for the input beam of the injection and detection minitowers. The numbering corresponds to the one in Fig. 12.43.

1. DN250 for seismic isolation cables feedthroughs.
2. DN250 for suspended bench cables feedthroughs.
3. Four DN160 for suspended bench view (camera). Some of them might be use as backup solution for clean air injection or local controls.
4. DN350 for input beam.
5. DN350 as backup solution for input beam if later on the input beam need to be more centered. Will be used first to output beams or to inject auxiliary beams.
6. DN160 for output beams.
7. Four DN40 for primary pump and gauges. It is likely that only one side of the minitower will be equipped.
8. DN250 for the possible secondary pump.
9. DN250 for a possible future ion pump.
10. DN250 for the electrical feedthrough of the coils used to control the bench.
11. Custom flange for viewport. This metallic flange will host a few DN100 viewports to let the beam going out, according to the final optical benches layout. This flange will use a double gasket.

All flanges are of type CF (conflat), except for the long window (number 11).

A simplified model of the minitower has been built to study its dynamical performances. The details are given in [400]. The main results are:

- The first normal mode frequency is 53 Hz. This is a lateral oscillation of the top part of the minitower. This is at a frequency where the seismic isolation system is providing a good attenuation.
- When going under vacuum, the deformation of the support ring for the seismic isolation should induce a tilt less than $20 \mu\text{rad}$, if the legs are optimally oriented.
- The vibration induced by devices attached to the minitower have not been computed, but their coupling to the minitower are expected to be small given the mass ratio between the minitower and the objects involved, like the connecting pipe to the main vacuum system.

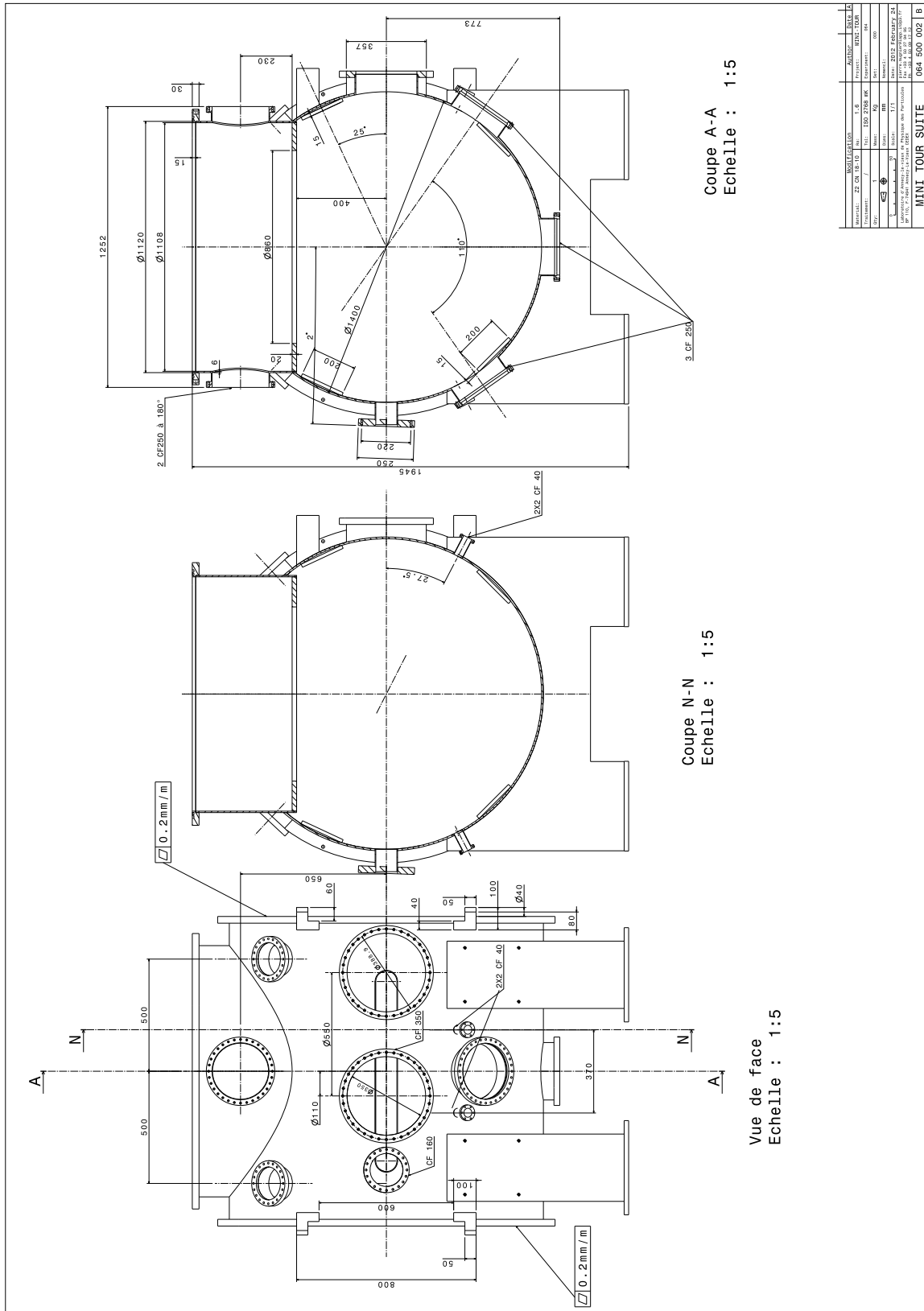


Figure 12.42: Main parameters of the chamber.

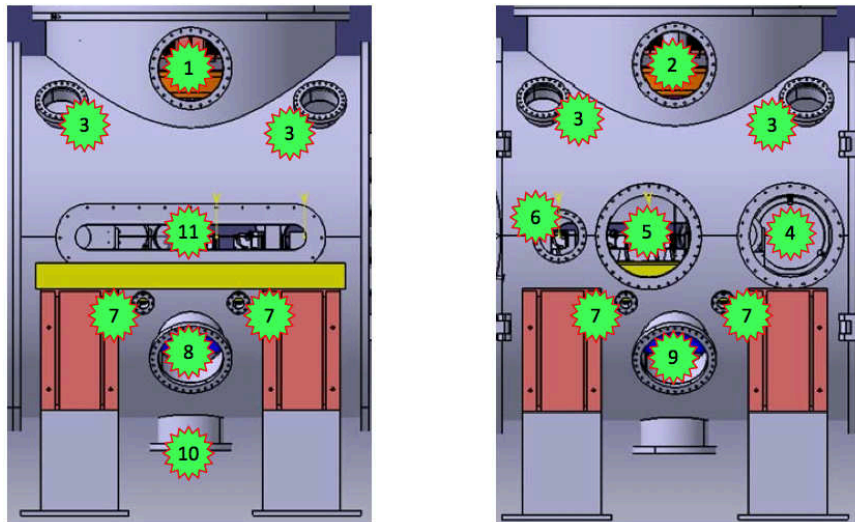


Figure 12.43: View port assignment. See text for the definition of all ports numbers.

12.4.3 Venting and cleanliness

The principle of operation of the minitower from the clean air point of view is described in Fig. 12.44. First, the minitower is expected to be installed in a room with some minimal level of clean air obtain by some overpressure of a clean air flux.

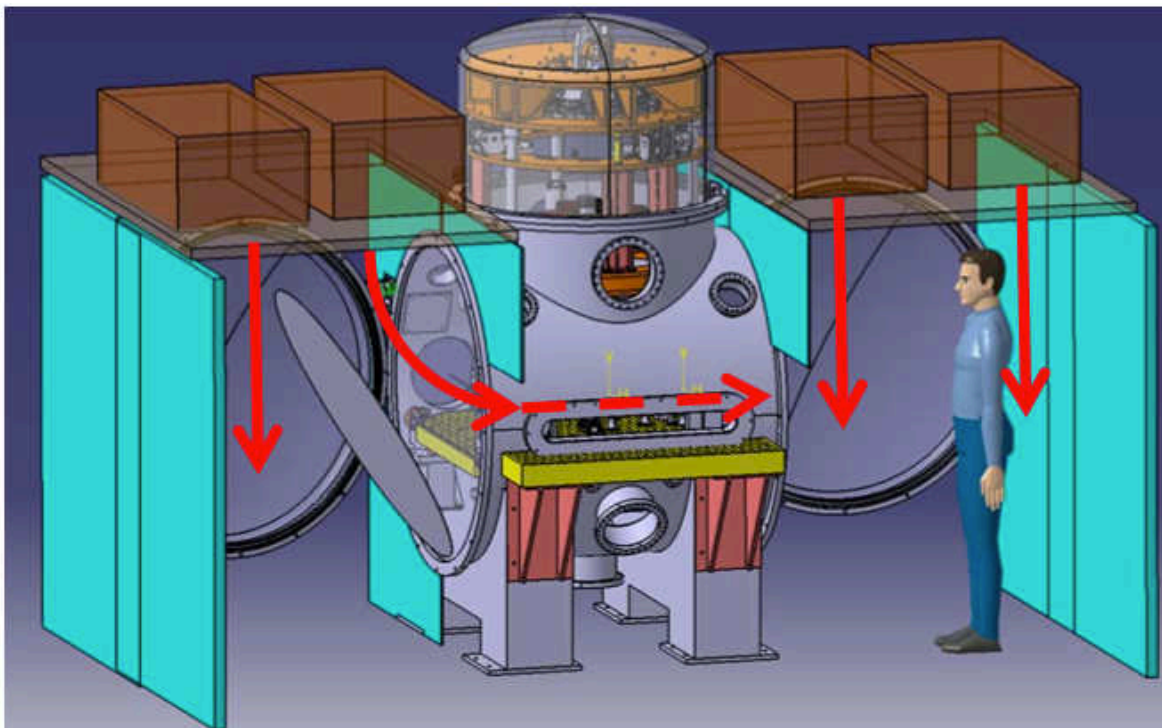


Figure 12.44: Providing clean air flux during operations on the suspended bench.

Then, both doors of the minitower will be under a laminar flux provided by a local light

structure (thin walls and plastic curtains). When opening a door on one side to let the operator working on the bench, the other side will also be opened, and a reflector will be installed to direct part of the air flux coming from the ceiling toward the bench and therefore flushing the bench with clean air. This strategy will be also used when opening the cupola of the minitower (to work on the seismic isolation system) to provide some overpressure inside the minitower.

12.4.4 Tooling

Some specific tools will be developed for the minitower operations.

- **The bench introduction tools:** it should be possible to insert and remove the suspended bench. This will be done through one of the lateral door, after having removed the coils located on the bench corners. A dedicated tool will be designed to remove the bench up to the point where it could be rolled on a cart.
- **Electronic container installation:** it is foreseen to install electronic containers underneath the bench. A tool will be developed to easily install and remove them.
- **Cupola opening:** figure 12.45 is showing the principle of operation with a ceiling located 3.6 m above the floor level, like in the laser lab. Two little cranes attached to rails will lift the cupola which then can be moved away from the minitower. The same cranes could be used to install the seismic isolation system.

12.4.5 Production strategy and schedule

The production strategy is to build the NE and WE minitowers first. One minitower will be initially installed at Nikhef for the prototyping of the seismic isolation system. The second minitower will be installed at LAPP for the integration tests of the detection bench. Both minitowers will then be moved to the site for the final installation. These integration tests will be useful to validate the minitower design before placing the order of the last three articles. This strategy has the benefit of a shorter planning for the construction of the first minitowers since a European call for tender is not needed for the first one. It offers also more time for the possible customization of the minitowers, especially in the case of the power recycling pickoff and for the input and output beams definitions.

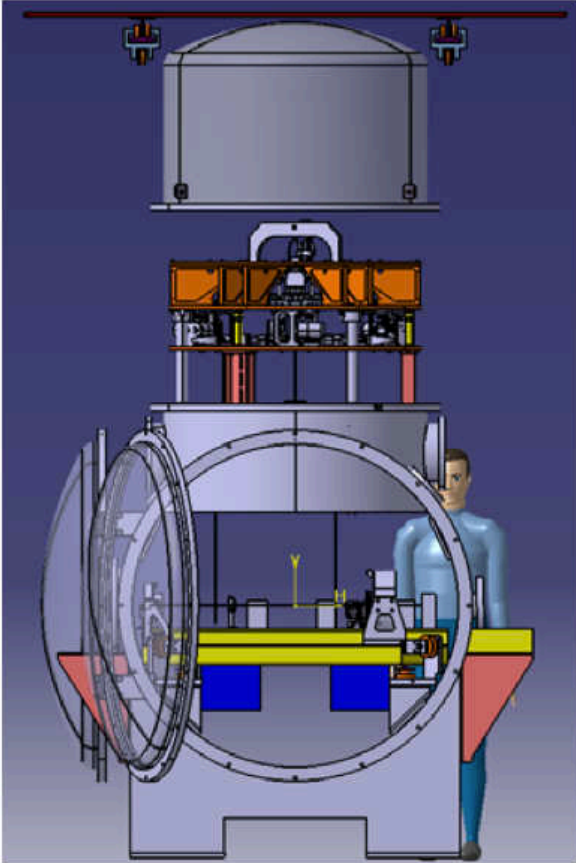


Figure 12.45: Cupola opening tools.

Chapter 13

Vacuum (VAC)

13.1 Introduction

The Vacuum subsystem (VAC) section deals with the upgrades to be performed on the present vacuum system to make it compliant with the Advanced Virgo (AdV) requirements which are:

- cryotrap and the related liquid nitrogen supply plant;
- displacement of towers;
- enlarged links in central area, with related vacuum equipment;
- new Intermediate Vacuum Chamber (IVC) for the mirror towers;
- Signal Recycling (SR) tower upgrade;
- update of the control system of the vacuum equipment.

All tasks involve the phases of design, procurement and installation.

13.1.1 Vacuum level requirements

The enhancement of the Virgo sensitivity by a factor of 10 requires an improvement of the present vacuum level to lower the phase noise given by the residual gas fluctuations inside the 3 km long arm tubes. At present the system operates at about 10^{-7} mbar (dominated by water) although it has been designed and tested to reach a pressure below 10^{-9} mbar (dominated by hydrogen) after an overall bake out. The lowest point of the AdV sensitivity curve, $3 \cdot 10^{-24}$ Hz^{-1/2} between 200 and 400 Hz, is not compatible with the present residual gas noise, at the level of 10^{-23} Hz^{-1/2} [402, 403]. In order not to be dominant in AdV, this noise has to be reduced by at least a factor of 10 (about a factor of three below the AdV design sensitivity). The residual pressure in the tubes has to be reduced by a factor of 100, the noise being proportional to the square root of the partial pressure of the various gas species.

The AdV design sensitivity, expected after arm tubes bake out, is shown in Fig. 1.2 and reported in Tab. 13.1 showing the contributions of the different gases, reported separately.

| Gas species | Pressure (mbar) | Phase noise ($\text{Hz}^{-0.5}$) |
|---------------------------------|---------------------|------------------------------------|
| H_2 | 10^{-9} | $2.1 \cdot 10^{-25}$ |
| H_2O | 10^{-9} | $7.0 \cdot 10^{-25}$ |
| Air + others | $5 \cdot 10^{-10}$ | $6.1 \cdot 10^{-25}$ |
| <i>Hydrocarbons(atomic mass</i> | | |
| <i>units):</i> | | |
| 100 | 10^{-14} | $9 \cdot 10^{-27}$ |
| 300 | | $3 \cdot 10^{-26}$ |
| 500 | | $6 \cdot 10^{-26}$ |
| Total | $2.5 \cdot 10^{-9}$ | $9.5 \cdot 10^{-25}$ |

Table 13.1: Goal pressures and phase noise (baked tubes) in the intermediate frequency band [404].

13.1.2 Cryotrap

The originally planned method of vacuum improvement was based on baking the whole system (the 3 km tubes plus the 7 mirror towers) at 150°C . Baking of towers would have to be repeated after each opening of a tower. With the experience gained running Virgo, we have realized that the tower baking choice as foreseen is not opportune because:

- the long time needed after each tower opening affects excessively the interferometer duty cycle (about 1 month to complete the tower bake out procedure, to be compared to the present two–three days without baking);
- unpredictable detuning effects may be produced by the warmup of the lower stages of the anti-seismic suspension at 50°C or more, involving movements/stresses. Furthermore the recondensation of contaminants on mirrors and detaching of glued or silicate bonded parts are also risks to be considered.

The proposed goal can be met by:

- performing the bake out of the tubes only;
- installing cryogenic traps at tube extremities.

Cryogenic traps are the classical solution to stop the migration of water from unbaked towers to the tubes. Cryotrap are already operating in Virgo and in other large vacuum systems (LIGO has cryotrap at the extremities of the tubes since the beginning), and can be implemented without a long phase of tests and prototypes.

Four cryogenic traps will be installed for **AdV**, one at each tube extremity, inside the link tubes between the relevant tower and the respective large valve [405, 406]. They will consist of hollow cylinder cryostats, 2 m long and with an aperture 0.95 m, cooled to 77 K with a bath of liquid Nitrogen (LN_2). The setup will be completed by an additional large size valve (650 mm aperture) and baffles for diffused light and thermal mitigation. LN_2 will be supplied with a ‘standard’ distribution plant based on large storage tanks and vacuum insulated transfer lines. The estimated overall heat leak for each cryotrap is about 300 W, while the losses of a good quality storage vessel are typically in the range of 1% per day of its content. The LN_2 consumption has been evaluated to 850 l/day for the whole system; the refilling of exhausted tanks will occur by truck coming on site once per week, during the weekly maintenance break.

The tube baking system is already implemented and working in Virgo [407] and will not be described here. Baking will be postponed with respect to traps installation and performed only when convenient for commissioning activity and necessary for sensitivity. A pressure in the tube around 10^{-8} mbar will be obtained without baking, allowing a first period of interferometer commissioning together with a favorable distribution of the manpower and of the economical effort. When required, tubes will be baked during maintenance stops lasting about 1 month per tube.

13.1.3 Further vacuum upgrades

The new optical scheme and the larger beam waist of AdV require new link tubes with larger diameter between the central towers and a full height SR tower

A different position of the ‘mirror towers’ of the central area is also required, including the Mode cleaner (MC) tower. The central area platform structure will be modified.

The vacuum pumps installed at present on the links will be rearranged and in part substituted with ion pumps. The Titanium Sublimation Pumps (TSPs) will be moved on the tubes, after the large valves since they are better suited to work on baked chambers.

The scroll pumps will be displaced away from the towers and installed in an insulated room, to hinder their acoustic and seismic emissions.

The vacuum control system also needs to be renewed, both on the hardware and software sides, including new control stations for the new vacuum devices (cryotrap ...).

The IVC of the mirror towers will be redesigned to fit with the new payloads and with the updated Filter 7 (F7) of the suspension, to be moved in the tower lower compartment.

The two pumping stations at 300 m on the North and West tubes will be activated with TSP pumps, as already foreseen in Virgo.

Finally, 5 new chambers (minitowers) will be integrated into the vacuum system, to provide acoustic insulation for the suspended benches. They will have a basic pumping system and will be separated by glass-windows.

13.1.4 Vacuum compatibility issues

The new components required for AdV which are not yet vacuum qualified (for instance Thermal Compensation System subsystem (TCS) in-vacuum components, Payload and new F7 parts) will be tested for vacuum compatibility according to the procedures already adopted in Virgo. As it is impossible to quantify a contamination limit for which the optics is at risk, Virgo has always taken the policy of a very conservative approach in order to avoid the pollution of the large vacuum chambers, which represents a major - and possibly unrecoverable - risk for the experiment.

Grease lubricants are not admitted.

The contaminants pressure (Residual Gas Analyzer (RGA) fragments over Atomic Mass Unit (AMU) 40, except for 44) has to be lower than 10^{-13} mbar, as extrapolated from components

tested after bake out and correcting for real quantity and tower pumping speed. This limit is based on the conventional monolayer deposition time (set to 10 years for hydrocarbons of high molecular weight with a sticking factor of 0.1) [407].

Components in direct view of mirror surface that incorporate plastic or organic parts should be avoided or limited according to the relative view factor.

The usual Virgo cleaning procedure will be adopted. In particular, all non-metallic components will be baked between 150 and 200°C in vacuum as final cleaning step. Components made of metal (stainless steel, aluminium) will be cleaned by washing in alkaline detergent or solvents depending also on their size. The large ultrasound bath and the ultra-pure water facilities installed in the central building will be used for this purpose.

13.2 Cryotraps

13.2.1 Mechanical design

There is sufficient space to install cryotraps between the towers and the existing DN1000 valves. Fig. 13.1 shows the West End (WE) case, the vacuum vessels of the cryotraps will have different lengths to fit with the different AdV tower axis-large valve distances as listed below (in parenthesis the present distances and the foreseen changes):

| | | |
|------------------------|---|----------------------------|
| WE tower | = | 6000 mm; |
| North End (NE) tower | = | 5374 mm (6000 mm -626 mm); |
| West Input (WI) tower | = | 5400 mm; |
| North Input (NI) tower | = | 5224 mm (4600 mm +624 mm). |

We plan to produce four identical cold vessels for the four cryotraps with a length of 2023 mm and an inner diameter of 950 mm. Special adapter pieces may be needed to adjust the length of the cryotrap outer vessel to the different positions. Optical baffles will be installed inside the stainless steel vacuum vessels; spring lips will be used to hold them inside the inner cylinder. The prototype cryotrap has already been ordered and, after thoroughly laboratory tests, will be installed at WE tower.

The outer vacuum vessel has an outer diameter of 1350 mm (not including the reinforcement ribs welded to the outside of the vessel to avoid buckling of the structure) and it will be constructed of stainless steel 304L. Helicoflex seals will be used on the main flanges.

The vessel is equipped with various pump-out and service ports. A new large size valve (aperture 650 mm) is installed in between the cryotrap and the tower, to allow venting independently the two chambers.

A stainless steel hydro-formed bellows is foreseen as a connecting piece between the trap and the 650 mm valve. The bellows is needed during installation of the cryotrap and to accommodate thermal expansion during bake out. The particular construction has been chosen in order to minimize the atmospheric load on the structures when the tower is vented.

The cold part of the cryotrap will be constructed from aluminum and filled with about 300 l of LN₂. It will be thermally shielded from the outer vacuum vessel by a double aluminum radiation shield to minimize boiling and LN₂ consumption.

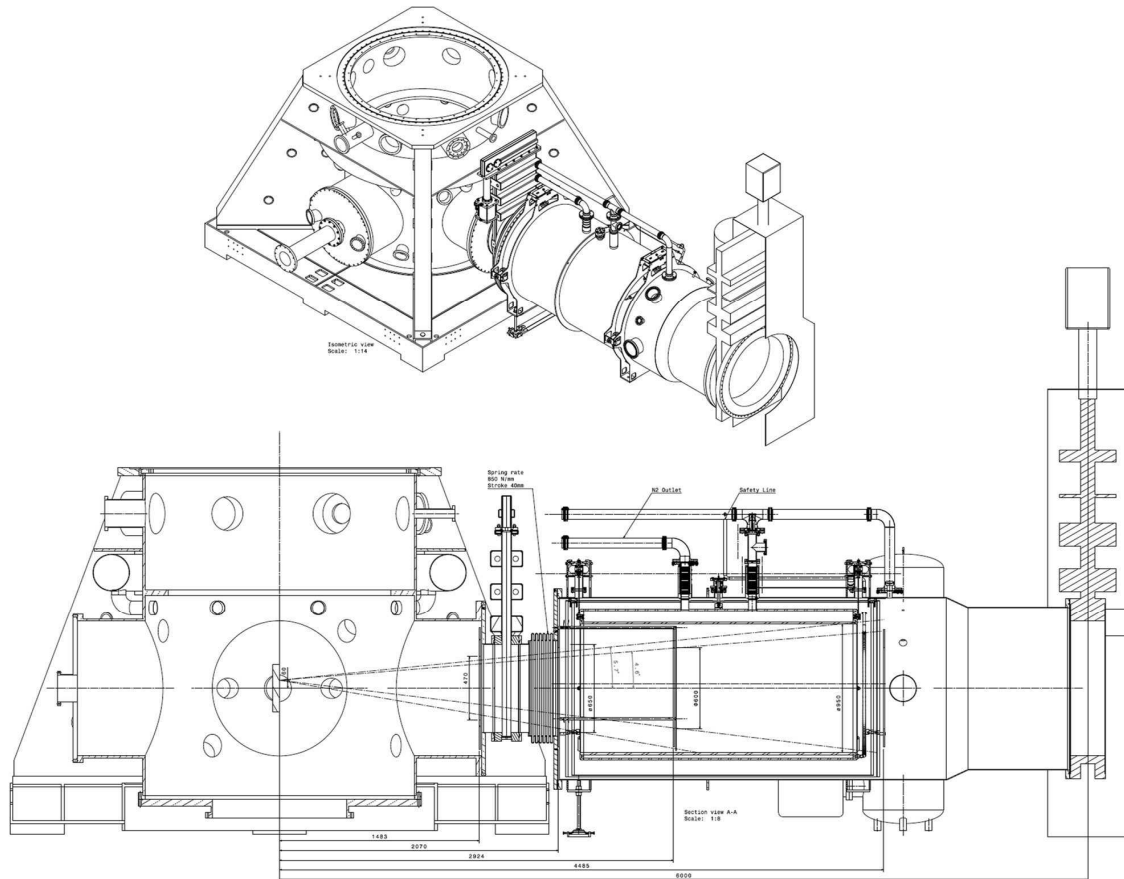


Figure 13.1: Installation of a cryotrap at the WE tower.

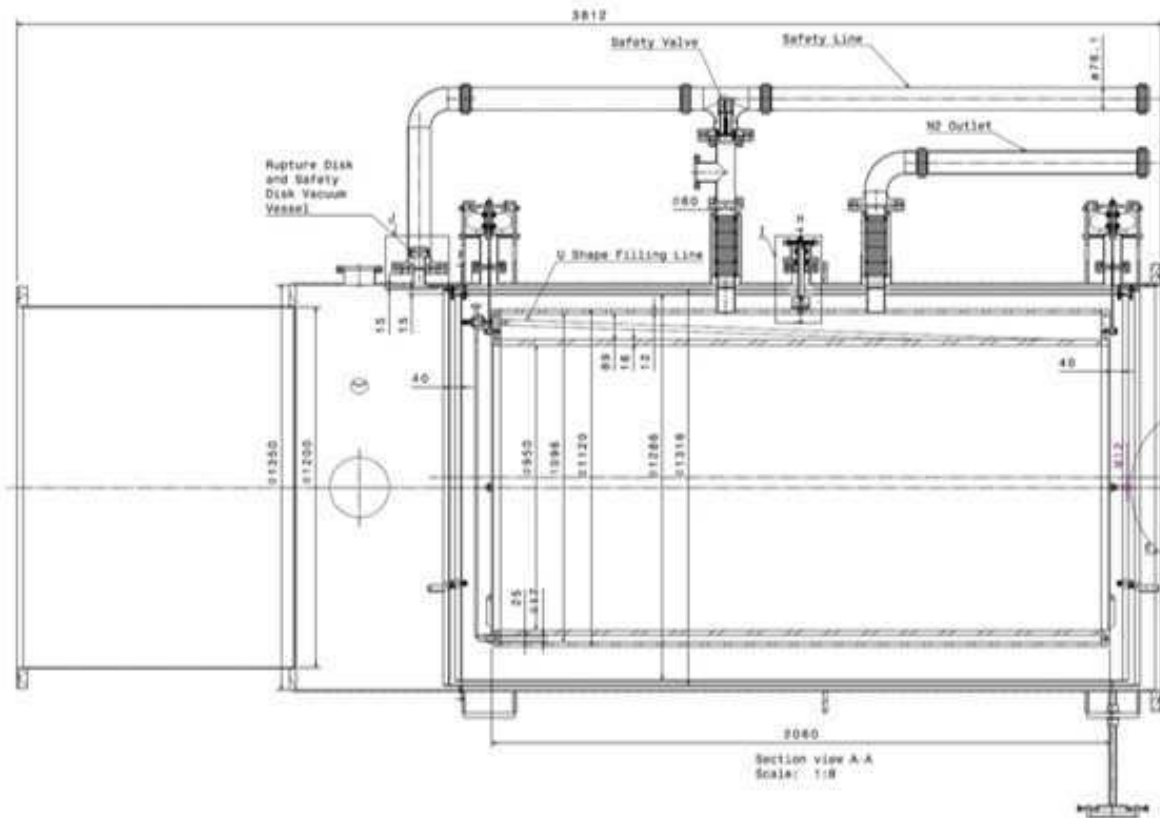


Figure 13.2: Section view of a cryotrap for AdV. Aluminum-stainless steel transition pieces are used to connect the inner vessel to the outside world.

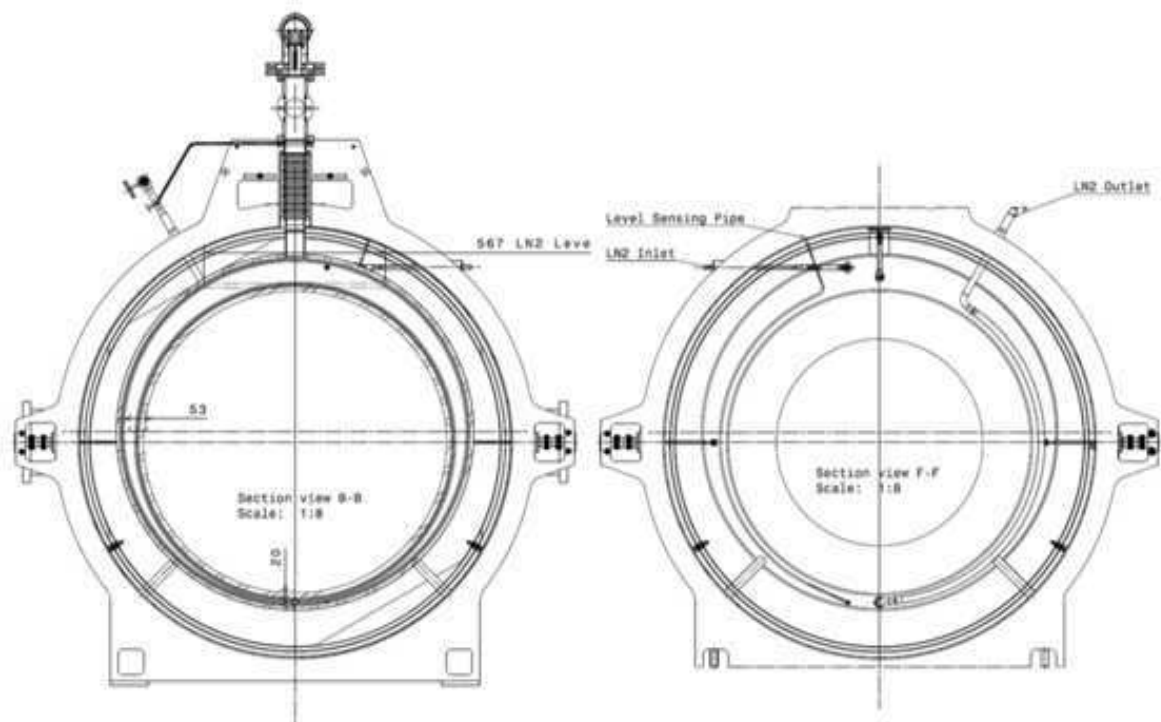


Figure 13.3: Cross-section of the cryotrap. The outer wall of the cryostat vessel is placed off-axis with respect to the vacuum vessel. The inner wall of the cryostat is placed on-axis.

Following specific in-field experience, the design pressure of the inner cryostat will be over-rated with respect to the working pressure (around 1.2 bar) to get an improved safety against mechanical failure of the aluminum welds.

Fig. 13.2 and 13.3 show cross-sections of the cryotrap. The outer cold vessel is placed vertically off-axis by 32 mm: in this way the boiling LN₂ surface width is maximized to 550 mm over the full length of 2000 mm of the cryostat. A large gas/liquid separation surface is in favor of a smooth evaporation and a low bubbling noise.

The inner aluminum cold vessel is suspended from the outer frame of the vacuum vessel by using two double air springs, in combination with longitudinal and transverse suspension systems (see section 13.2.5.3). It will accommodate the thermal expansion (about 4 mm/m) of the inner aluminum vessel (cold) with respect to the outer vacuum vessel (room temperature), also acting as a heat bridge minimizing the thermal losses due to heat conduction.

13.2.2 Cryogenics

A schematic of the cryogenic plant is reported in Fig. 13.4.

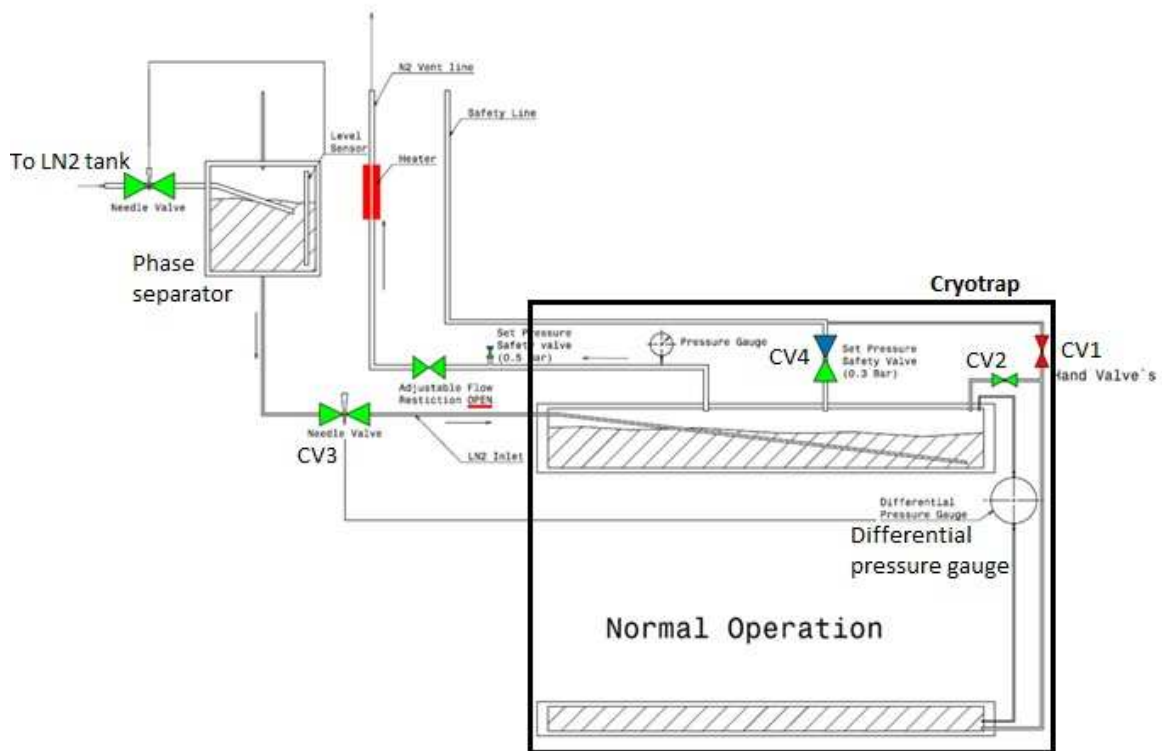


Figure 13.4: Schematic of the cryogenic controls during normal operation of the cryotrap (see also section 13.2.6 for a complete description of cryogenic piping equipment).

The level of liquid nitrogen will be read by a differential pressure gauge and controlled within 10 mm by the automatic refill system. The LN₂ inlet pipe is designed with an inclined U shaped pipe (Fig. 13.2) such that the LN₂ will flow smoothly into the bath while the gas will disengage along the path before entering in the bath. This will minimize the possible noise due to bubbling related to the refill.

In normal operation, the LN₂ level is maintained at 950 mm, covering completely the inner bore of the cryostat. The LN₂ is continuously filled and the Gaseous Nitrogen (GN₂) is exhausted. The inlet flow is regulated by two automatic valves (see section 13.2.6) with proportional aperture. One of them is optional (the phase separator one) and could be just of on/off type.

The cryotrap can be operated for more than one year between regenerations: during this time the water layer deposited on inner surfaces will reach a thickness of the order of one micron. This increases the infrared emissivity [408, 409] from about 0.1 to about 0.2. The resulting heat load turns out to be 250 W, and corresponds to a LN₂ consumption of about 5.6 liters per hour (emissivity 0.2). The estimated gas production is 11 l/s, assuming a temperature of 80 K for the vapor in the vessel. A value of 300 W has been conservatively assumed as heat load for dimensioning the LN₂ supply plant.

The same system allows operating in ‘regeneration mode’ by emptying the cryotrap at first (through valve CV1) with a fair overpressure. The second step is to admit hot GN₂ in order to heat up the cryotrap. The entire cryotrap can be warmed up to 150°C.

Different cryogenic sensors will be used to monitor the temperature distribution and the LN₂ level in the cryostat. The data will be sent to the general Data Acquisition (DAQ) system as for the other parts of the vacuum system, for diagnostics during the Interferometer (ITF) operation. Safety interlocks (closing valves in case of high-temperature alarms) will be implemented at Programmable Logic Controller (PLC) level, fully integrated with the vacuum equipment ones (the cryogenic signals will be acquired by the corresponding ‘vacuum station’). Here is a preliminary list of cryogenic signals, for a single trap:

1. LN₂ level in cryostat from the differential pressure gauge;
2. LN₂ level in the external storage tank from the differential pressure gauge;
3. LN₂ level in phase separator from the differential pressure gauge;
4. pressure in the external storage tank;
5. pressure in the cryostat vessel;
6. 8 temperature probes, PT100 type, installed in cryotrap;
7. opening status of the needle valve to the cryostat;
8. opening status of the needle valve to the phase separator;
9. status of the other cryogenic valves (several relays);
10. status of safety alarms (safety valves status, O₂ sensors) (several relays);
11. electronics regulating the refill (RS232 or better standard for the full set of parameters).

A widely used process control standard for sensors is the "4-20 mA current loop" which uses currents between 4 and 20 mA instead of voltage. All sensors mentioned above will be based on this standard.

13.2.3 Vacuum performances

Cryogenic traps are a proven solution to stop migration of water and of other vapors between different vacuum chambers: the water molecules condense on the surfaces cooled down to 77 K and are thus removed from the gas phase, hence not transmitted through the two openings of the trap [410, 411].

Both in **AdV** and in present Virgo, the water vapor is coming out from the tower chambers because of their frequent venting and consequent water recharging (exposition to humid air). This effect is enhanced by non-metal components that absorb water in their bulk and release it slowly once in vacuum. An example of the present vacuum behavior (without cryotrap) is shown in [412]: the pressure inside the tube rises orders of magnitude above the **AdV** requirements when large valves are opened.

For **AdV** the cryotrap will avoid this behavior maintaining the tube water pressure below 10^{-9} mbar.

The calculation of the trap output has been carried out using a Monte Carlo method for the chosen geometry: 0.95 m cryostat inner diameter, 2 m cryostat length, sticking factor = 0.9, glass baffles with 600 mm aperture installed at both trap extremities and at the tower port, uniform pressure in the tower. The trap has been designed in order to comply with the case of high gas loads present when restarting the **ITF** after tower venting ($4 \cdot 10^{-4}$ mbar l/s, for water, after 2 days of pumping after a mirror tower venting). The pressure at the trap outlet results in this case $6 \cdot 10^{-10}$ mbar, within **AdV** specifications.

The estimated profile of the water pressure along the 3 km tube is shown in Fig. 13.5. The plot is done for baked conditions, including the walls outgassing rate as experimentally obtained during the qualification of the installed tube sections and the distributed pumps in operation (stations at 300 m, 600 m, 1200 m, 1800 m, 2400 m).

The considered load of water coming from the towers corresponds to measurements in the present Virgo. According to Payload subsystem (**PAY**) the **AdV** payloads will have vacuum characteristics similar to the original Virgo ones. The plastic-like parts inserted in the new Virgo+ (**V+**) monolithic payloads will be replaced for **AdV** with suitable parts realized with ceramic and titanium, more favorable for vacuum.

The water load estimation remains anyway not perfectly determined, as it also depends on assembly details, fabrication and cleaning treatments, history of the exposition to atmosphere. In the worst cases extra pumping time will be adopted before restarting the **ITF**: 1 week of pumping would be enough to get an acceptable load ($5 \cdot 10^{-4}$ mbar l/s) according to the experience (for instance, with the recent monolithic payloads, 2nd evacuation of input towers, May 2010).

The trapping effect is shown in Fig. 13.6, which reports the density of the molecular tracks inside the trap [414, 415].

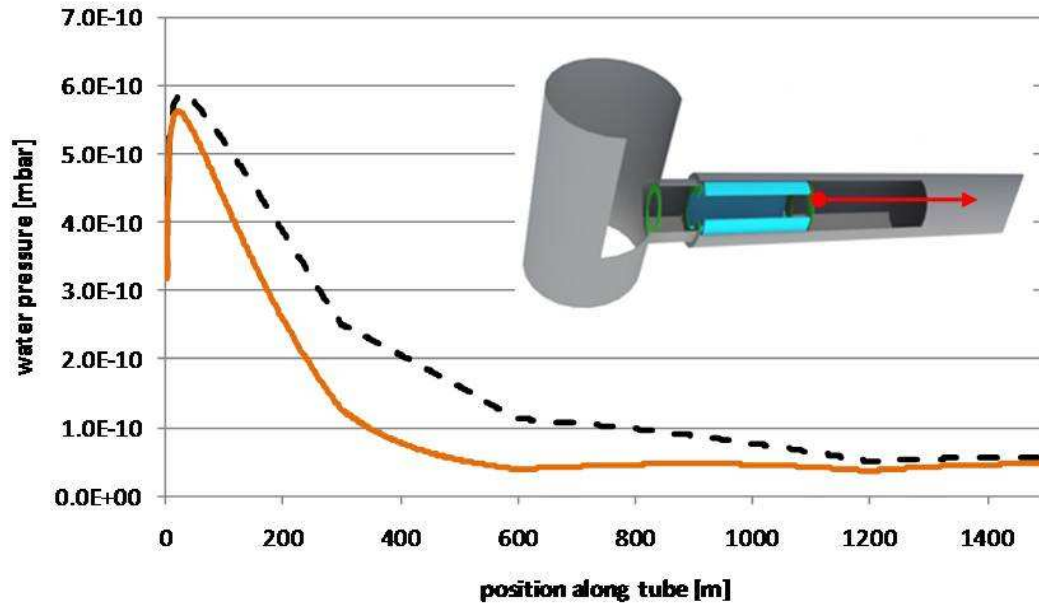


Figure 13.5: Water pressure profile along the 3 km tube calculated for the selected trap geometry. Case of baked tube after a tower venting. Load from tower = $4 \cdot 10^{-4} \text{ mbar l s}^{-1}$; Continuous curve = calculation including re-adsorption of water molecules on the stainless steel walls of the tube [413] after two days from ‘large valves’ opening; dashed curve = calculation without walls re-adsorption, conservative.

Both radius and longitudinal profiles are shown: the molecules closer to the trap axis travel closely packed at the inlet and get sparse at the outlet (tracks density decreases to about 3%). The molecules closer to the trap walls hit the baffles installed at the trap extremities (aperture radius 300 mm): the inlet baffle limits the inlet flow within its aperture and the outlet baffle stops and bounces backward the impacting molecules.

Experience with cryogenic traps exists in LIGO (the traps at LIGO are very similar to the proposed ones) and also in Virgo, thanks to the small trap installed between the Detection Tower (DT) and SR towers, which is behaving as expected; see for example [416].

An estimation of the deposit build up is reported in Fig. 13.7, calculated for 1 year of operation in two load conditions: commissioning and running. In both cases the ice thickness is sufficiently low, of the order of one micron, so that regenerations are not envisaged more often than once per year.

Finally, a benefit of using cryotrap is a large enhancement of the pumping speed for hydrocarbons, more than 10 000 liter/s per trap, increasing by over 10 times the present speed. This will lower the partial pressure of contaminants around mirrors by more than one order of magnitude.

13.2.4 Vacuum system

An auxiliary vacuum pumping system needed to evacuate, regenerate and monitor the trap, is shown below in Fig. 13.8 and the equipment is detailed in Tab. 13.2.

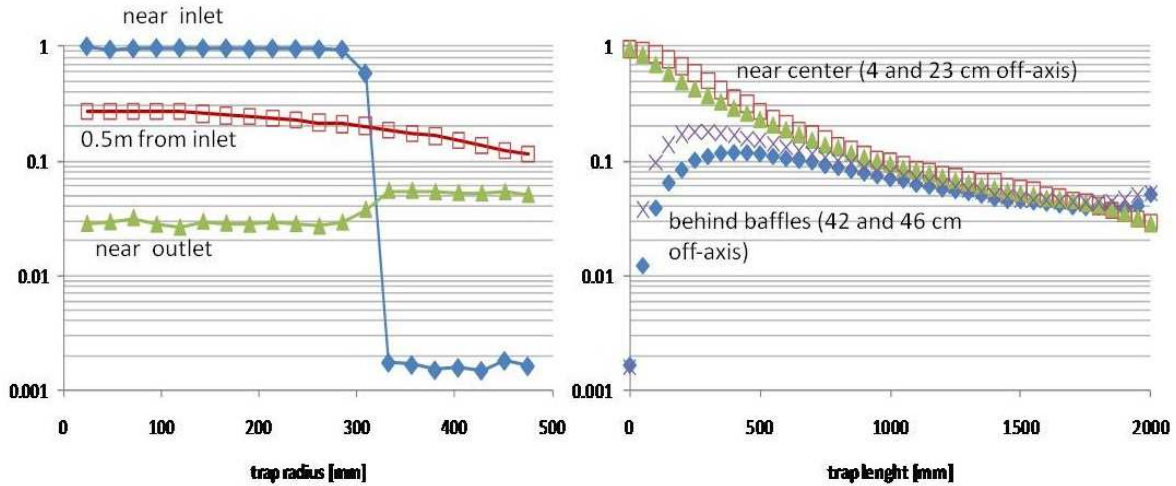


Figure 13.6: Normalized density of molecule tracks inside the trap along the trap radius (left plot, at different longitudinal positions) and along the trap length (right plot, at different distances from the trap axis). Baffles (aperture radius = 300 mm) installed at trap extremities affect the molecule distribution (molecules bounced on baffles and back-traveling are also accounted here). The outlet tracks density represents the escaped molecules fraction, about 0.03. (Molecules re-entered from the tube are not shown, to put in evidence the trapping effect).

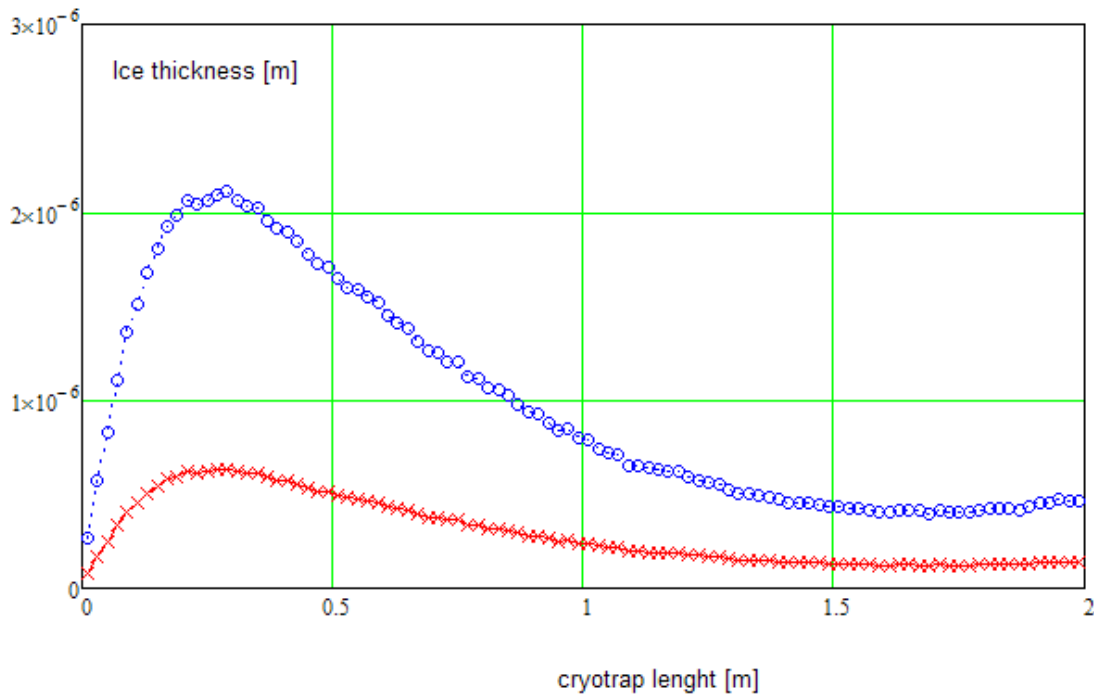


Figure 13.7: Evaluation of the water deposit inside a trap after 1 year of service. Red curve = running conditions (1 g of condensed water); blue curve = commissioning with frequent tower openings (4 g, assumed venting every 2 months.)

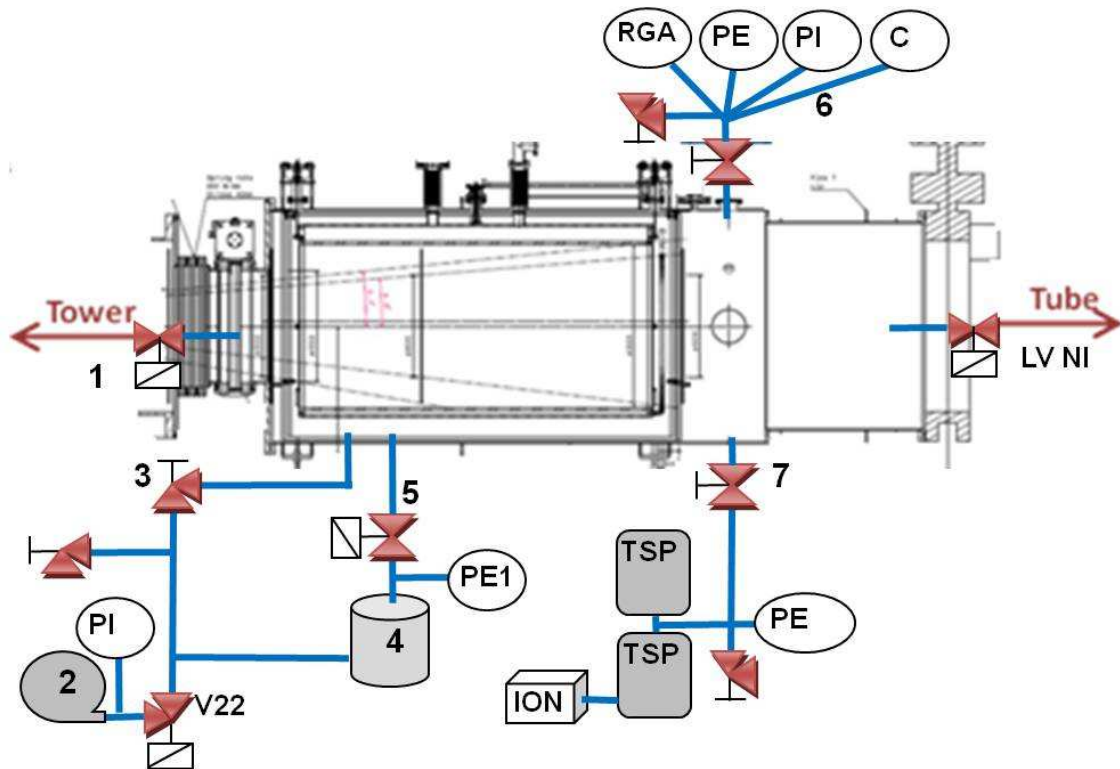


Figure 13.8: Sketch of the cryotrap auxiliary vacuum system.

A large size valve (1) is installed between the trap and the tower, to separate them during tower venting and during trap regenerations. The valve will have a 650 mm aperture, metal seal on bonnet, bellows feed-through and metal gasket flanges. The gate will be Viton sealed, properly degassed as normally established for Virgo. The valve actuator will be driven by compressed air or by an electrical motor, to be evaluated during the call for tender in consultation with the selected manufacturer.

The system will be evacuated with a dry pump (2) through a dedicated port (3) 40 mm diameter, for about 3–4 hours to reach 0.1 mbar. The port will be equipped with an all metal angle valve DN40. Then a turbo-molecular pump (4) will be used through a 150 mm port (5), via an Ultra-High Vacuum (UHV) gate valve, lowering the pressure below the 10^{-6} mbar range. A moderate baking will further improve the vacuum, which will be monitored using the RGA (6), Pirani and Penning gauges.

The bake out of the trap will be done at least once, for cleaning and testing purposes at installation time. Probably it will be necessary to warm up also the large valve by using the existing relevant apparatus to avoid excessive water re-condensation on its large surfaces.

Finally, two TSPs (7) will be used in the UHV regime. These pumps are currently installed on the central area towers but not suited to work for unbaked systems. They will be moved to the ‘tube side’ of the traps, contributing to pump hydrogen, air and other gases not pumped by the cryotrap.

Turbo-molecular and scroll pumps will be used during regeneration and stopped during data taking, see paragraph 13.2.7.

| Item | Quantity |
|--|---------------|
| Turbo-molecular pump | 1 |
| Dry pump | 1 |
| TSP pumps (filament units) | 4 (2 systems) |
| ion pumps | 2 |
| Pirani (PI) gauges | 2 |
| cold cathode (PE) gauges (10^{-10} mbar range) | 4 |
| Capacitance gauge | 1 |
| RGA | 1 |
| DN40CF manual all metal angle valve | 4 |
| DN25KF High Vacuum (HV) electro-pneumatic angle valve | 1 |
| DN150CF UHV electro-pneumatic gate valves | 1 |
| DN200CF manual UHV gate valves | 2 |
| DN63CF manual UHV gate valve | 1 |
| DN25KF HV manual angle valve | 1 |

Table 13.2: Vacuum equipment for each cryotrap

13.2.5 Impact on the interferometer

13.2.5.1 Diffused light

Around the cryotraps, the diffused light problem will be cured with the same approach as in the present Virgo configuration.

At the ends of the Virgo arm tubes, where the cryotraps will be installed (between any input/end tower and the respective large valve), absorbing glass baffles (transmission $< 10^{-7}$, reflection $< 10^{-2}$) will be installed as shown in Fig. 13.9, in a configuration satisfying the following criteria:

- no point of the smooth surface of the vacuum enclosure can be seen simultaneously by the beam spots on two facing mirrors;
- any discontinuity (potential reflecting spot) of the vacuum enclosure is hidden with respect to the beam spot on any mirror;
- the minimum free aperture radius is about five times larger than the local average beam radius (beam radius is 49 mm on the input mirrors and 58 mm on the end mirrors) [417].

The entire inner tube surface of the 3 km arm tubes between the two large valves is hidden from the beam spots on the mirrors by conical stainless steel baffles.

The aperture diameter of the additional valves (DN630) to be installed between each cryotrap and the adjacent tower is 650 mm, more than five times larger than the beam average diameter.

The noise contributions of all processes potentially shining diffused light onto a mirror have been evaluated:

1. splinters on baffle edges;

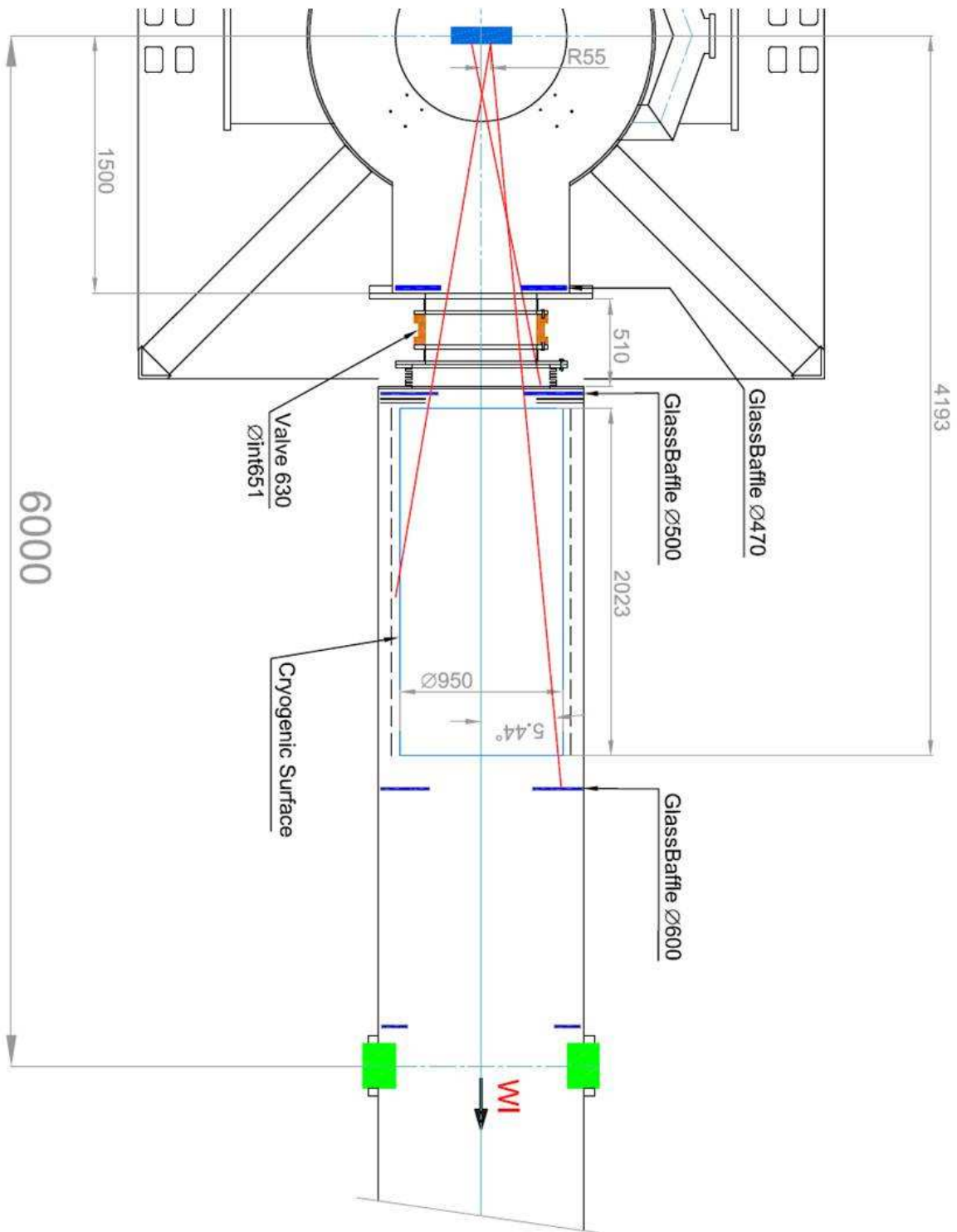


Figure 13.9: Schematic of optical baffles setup around the cryotrap.

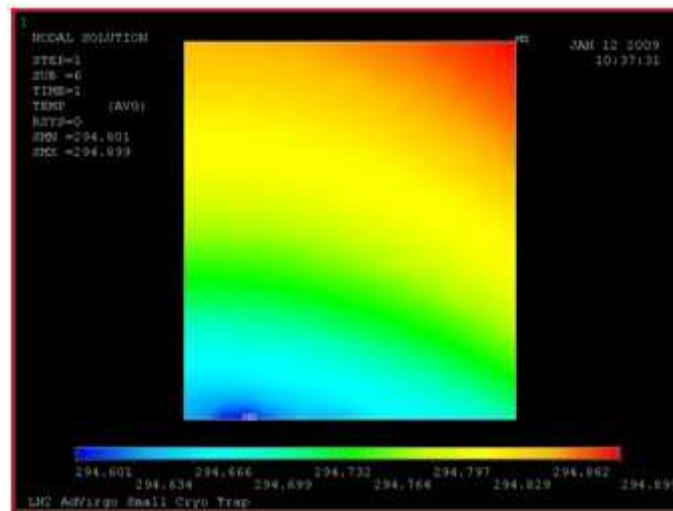


Figure 13.10: TM temperature map. An axial section of the mirror is represented here, the axis of the mirror being the left border of the picture. The mirror side facing the cryotrap is represented on the lower side of the picture. Induced ΔT is approximately 0.4 K.

2. grazing reflection on baffle edges;
3. diffraction on baffle edges;
4. backscattering off inner trap surface.

Calculations [418, 419] show that all diffused light noise sources are well below the AdV sensitivity.

13.2.5.2 Thermal effects on test masses

The relative proximity of cryotrap surfaces cooled to liquid nitrogen temperature with respect to the Test Mass (TMs) will induce thermal effects on the TMs themselves through radiation (see Fig. 13.10). The relevance of these effects, in terms of structural and optical curvature of the TMs, has been analyzed independently by the Nikhef and Roma Tor Vergata groups with finite element thermo-mechanical simulations [420].

The two main effects are:

- a change of the radius of curvature of the TM surface of about 2 m, negligible with respect to its original value of about 1500 m;
- a change in optical path length inside the TM (see Fig. 13.11).

Both are negligible, being smaller and of opposite sign with respect to the changes due to the YAG beam absorption.

Thermal effects on equipment close to the cryostat will be negligible. Some reduced parts of the outer vacuum vessel will be a few degrees below room temperature, but anyway above the room air dew point. Also the glass baffles closer to the cryotrap ports will cool down to a few degrees below room temperature, and similarly the large gate valve when closed. This does not seem to be problematic, an estimation will be provided for completeness.

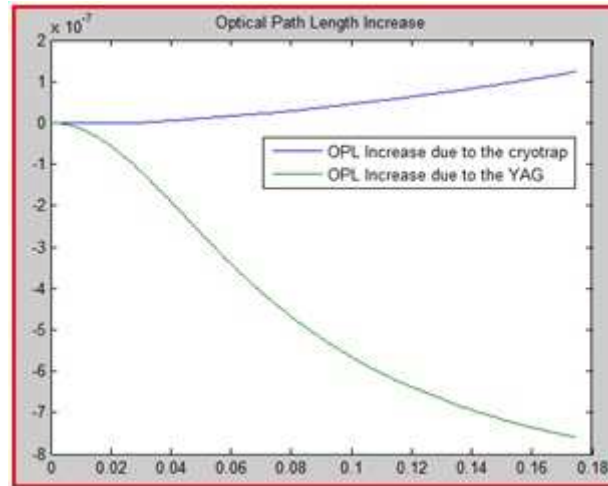


Figure 13.11: OPL increase due to thermal effects in the TM. The blue curve is the OPL increase due to the trap, while the green curve is the OPL increase due to the absorption of YAG power.

13.2.5.3 LN₂ bubbling and suspension system

About 6 liters/hour of liquid nitrogen will evaporate in each cryotrap: the intention is to minimize the mechanical vibrations that could be produced by the boiling process. As it happens in the DT small cryotrap, seismic vibrations are produced in the frequency band 60–120 Hz [421] immediately after the refill operations and tests indicate that they may be caused by the bubbling of the bath enhancing some mechanical resonances of the trap structure.

The analysis of LN₂ boiling process [422] shows that various regimes are possible in general, and that in our design evaporation should occur by ‘natural convection’, taking place at the liquid free surface, without formation of bubbles.

A prudent approach is to consider the occurrence of bubbling and a proper way to mitigate the transmission of seismic vibrations to the tower and to nearby equipment. Attention will be paid to avoid splashing of the LN₂.

A suspension system based on air springs will insulate the outer part of the cryostat from the cold vessel. The system will work in vertical, axial and transversal directions. The resonance frequency of the system will be about 3–4 Hz and the Q factor around 10–20. All the elements of the suspension system are located outside the vacuum vessel to allow modifications and replacement.

If bubbling were to occur, the frequency is expected to be around 50 Hz or above (it is a characteristic of the liquid, with bubble size less than 1 mm). The proposed suspension system would cut them effectively.

The various elements of the suspension system are shown in Figs. 13.12 and 13.13. The silicon rubber spring for horizontal positioning allows movement from thermal contraction/expansion and specifically restricts motion in the xy-plane (transverse). The air-spring system for vertical isolation needs to allow vertical motion e.g. during bake out. The flexible hinges located at the top provide guidance for vertical displacement (but not horizontal).

Bubbling occurrence and vibrations characteristics are largely related to the practical real-

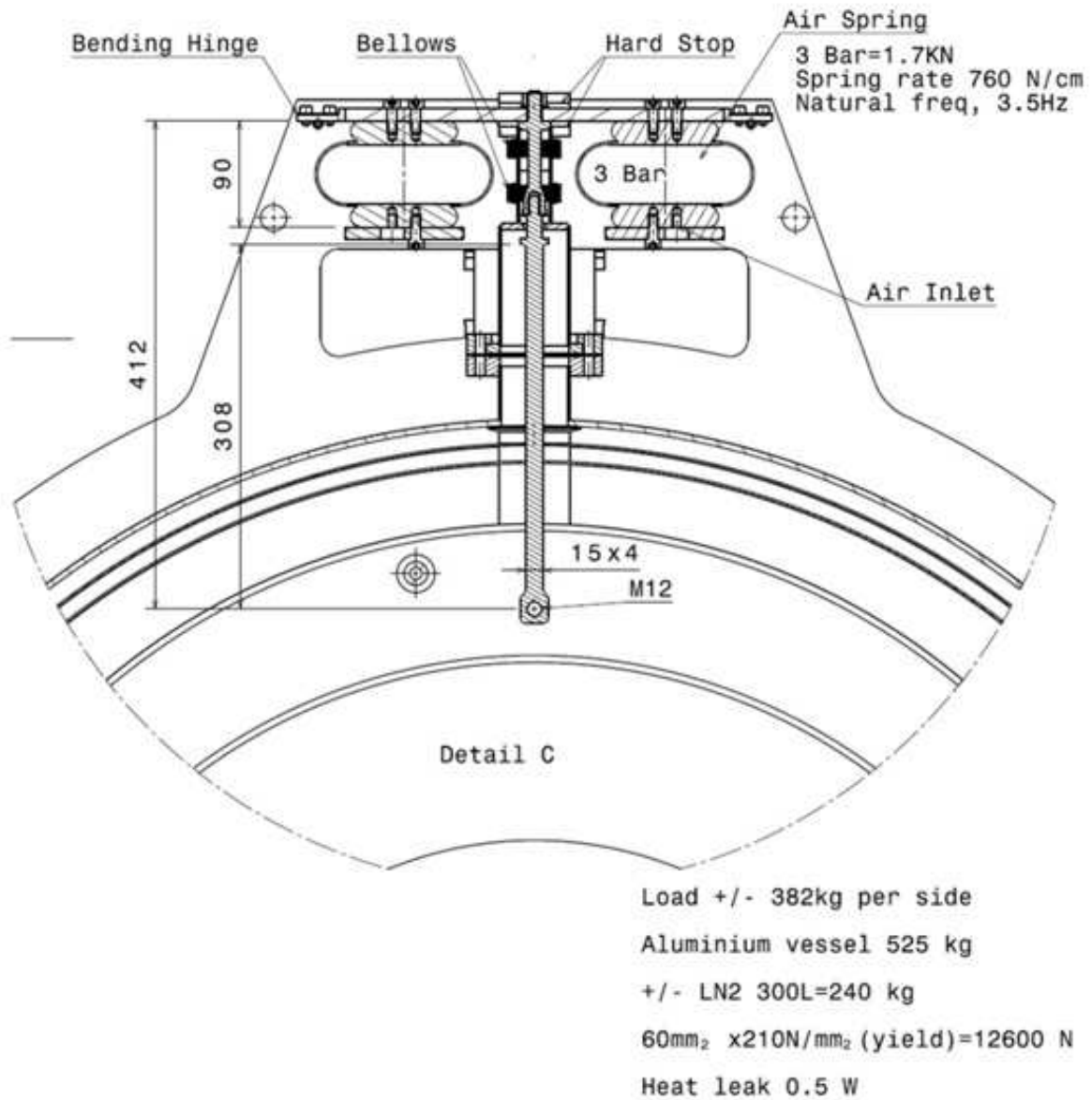


Figure 13.12: The cold vessel of the cryotrap is suspended with air springs in order to isolate AdV from possible bubbling noise produced by the cold vessel itself.

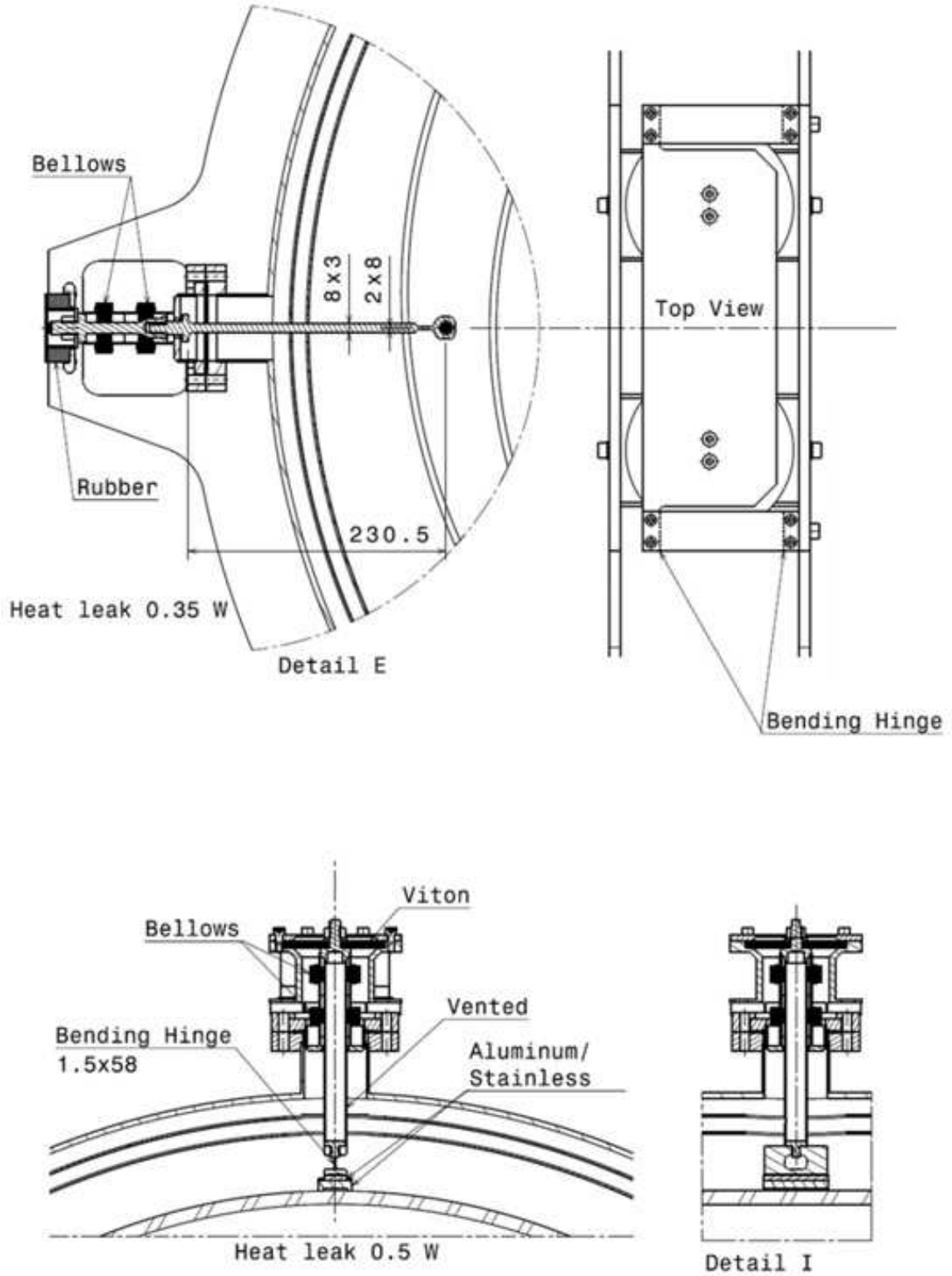


Figure 13.13: Suspension system for the cryotrap. Top left: silicon rubber spring for horizontal positioning. Top right: top view of the air-spring system (bending hinges). Bottom: axial motion damping system. See Fig. 13.12 for a cross section of the central air spring suspension system.

ization of the cryotrap mechanical details, and cannot be completely determined during the design phase. The suspension system, the surface quality, the thermal bridges need to be verified and corrected if needed. The full scale prototype is considered necessary to limit risks of the cryotrap performance.

Other seismic disturbances could come from vibrations of the external LN₂ tanks (see 13.2.6), transmitted by propagation through the soil. Mechanical shocks could be caused by thermal dilatations of metallic structures induced by the daily external temperature change. Strong wind could cause oscillations of the tanks, too.

The expected seismic disturbances emitted from tanks will be characterized by directly testing one tank of similar type among the ones in service near the Virgo site, in collaboration with the present supplier of LN₂.

13.2.6 Liquid nitrogen supply plant

The design of the LN₂ distribution plant is based on the following parameters:

| | | |
|---|---|-----------------------|
| Volume of one trap | : | 300 l |
| Heat load on one trap | : | 300 W |
| Cold mass | : | 500 kg |
| Number of traps | : | 4 |
| LN ₂ input flow in each trap | : | 7.10 l/h |
| Evaporated nitrogen (GN ₂) | : | 4.5 m ³ /h |
| LN ₂ for cool-down | : | 650 l |
| Working hours between tank refilling | : | 840 h (35 days) |

Refilling of a tank has been estimated to take 2 hours. It can be done during a weekly maintenance break of 4 hours. It is foreseen to refill one out of the four tanks every week, so each one will be refilled every 4 weeks (28 days).

The plant consists of the following equipment:

- LN₂ storage tanks;
- LN₂ transfer lines;
- GN₂ venting lines (LN₂ evaporation, cool-down, regeneration and baking);
- Vaporization and heating system for the regeneration and baking of the traps (to be installed in a second phase, if needed).

13.2.6.1 Storage tanks

We considered two hypotheses of storage:

- One storage tank for each trap (four in total), in order to minimize the length of the transfer lines connecting the tank to the cryogenic trap (approximately 25 m);
- One storage tank for each trap in the terminal buildings, and a single storage tank for the two traps in the central building, in order to minimize LN₂ losses for self-consumption.

In this case the transfer line length in the central building will be 52 m for the trap in the West arm, and 54 m for the trap in the North arm.

The chosen baseline solution is a plant with one storage tank for each trap (four in total). The choice is dictated primarily by economics: even if a single tank has lower losses than two tanks of the same total capacity, the savings due to a lower length of the transfer lines (both in the cost of the lines and in their losses) are expected to be much larger.

There are two types of cryogenic tanks of large sizes: tanks insulated with perlite and intermediate vacuum; and super-insulated tanks under high vacuum. The choice of tank type depends essentially on the comparison between the losses of the tanks, integrated over the life of the plant (lower for super-insulated tanks), and the initial investment (higher for super-insulated tanks). With a first estimate of costs (liquid nitrogen at 0.094 euro/l) we envisage the use of perlite tanks, which can be borrowed instead of purchased [423, 424].

13.2.6.2 Liquid nitrogen transfer lines

In order to reduce the evaporation of LN₂ along the path from the storage tank to the cryogenic trap, the transfer line must be super-insulated with intermediate high vacuum (see Fig. 13.14).

The flow rate of LN₂ inside each line will be approximately 8 l/h. The line has to be designed to guarantee at the given LN₂ flow rate low losses, stratified flow (for good gas-liquid separation) and low pressure drop. The optimal trade-off among these requirements is given by the DN15 line, with the following technical parameters:

- inner conduit F 21.3 × 1.65 mm ASTM A312 Tp 304;
- outer conduit F 60.3 × 1.5 mm AISI 304;
- design pressure 16 bar;
- working temperature −196°C;
- linear heat loss 0.4 W/m;
- linear weight 3.7 kg/m.

The GN₂ produced during the normal operation of the traps will be piped to the outside of the buildings by insulated venting lines. The GN₂ produced in the normal operation of the traps is 4.5 Nm³/h. A much higher gas load is foreseen during the cool-down of the trap (500 Nm³/h), and during the regeneration and baking (415 Nm³/h), see paragraph 13.2.7. For this reason the venting lines are dimensioned to withstand these higher fluxes.

The main design parameters are:

| | | | |
|---------------------|---|------------------------|---------------------------|
| max load | : | 4.5 Nm ³ /h | (normal operation) |
| | | 500 Nm ³ /h | (cool-down) |
| | | 415 Nm ³ /h | (regeneration and baking) |
| design pressure | : | 0.5 bar g | |
| design temperature: | | −196 – +150°C | |
| nominal diameter | : | DN80 | |

The automatic regulating valve should be placed near to the trap, as shown in Fig. 13.14. Behind the valve the trap operates at atmospheric pressure, while before the valve the pressure will be the working pressure of the tank plus the pressure due to the height of the column of liquid. In the worst case, in the central building, we will have at the level of the valve on the tank side approximately 1.3 bar. This causes a sudden expansion across the valve with the formation of 0.12 g/s of GN₂, corresponding to 0.08 m³/h. This is negligible compared to the GN₂ produced in the trap under normal operation conditions (4.5 m³/h).

13.2.7 Regeneration and baking

The system will be based on atmospheric vaporizers to evaporate the LN₂ taken from the storage tank, and on an electric heater to heat up the GN₂ to the desired temperature. The same system, shown on Fig. 13.15, will also be used for the bake out of the trap, if needed.

For the regeneration, the following parameters were considered to design the evaporator:

| | | | |
|------------------------------|---|------------------------|-------------|
| temperature | : | 50°C | |
| duration | : | 4 days | |
| transient | : | 6 hours | |
| gas load | : | 415 Nm ³ /h | (transient) |
| | | 50 Nm ³ /h | (regime) |
| LN ₂ consumption: | | 3 800l + 1 870l/d | |

while for the bake out the corresponding parameters are:

| | | | |
|-----------------------------|---|------------------------|--------------------------|
| temperature | : | 140°C | |
| duration | : | 4 days | (warm up phase duration) |
| transient | : | 22 hours | |
| gas load | : | 170 Nm ³ /h | (transient) |
| | | 50 Nm ³ /h | (regime) |
| LN ₂ consumption | : | 5 800l + 1 870l/d | |
| electric heater power: | | 10 kW | |

The regeneration will take about 1 week or slightly more. The cool-down will follow: the temperature will be accurately monitored and the nitrogen flow will be adjusted in order to avoid too fast and non uniform temperature change, potentially dangerous for the mechanical structure and for welds in particular. A He leak test will be repeated after each cool down.

13.2.8 Safety

Risks connected to employing cryogenic fluids are carefully considered both in the construction of the technical equipment construction and in the operation procedures.

Risks are related to:

- development of large quantity of gas from small quantity of liquid;
- physical contact producing injuries similar to burnings;
- excessive nitrogen concentrations in the room atmosphere reduces the Oxygen concentration and may cause asphyxia danger; cold vapors can accumulate in the lower rooms.

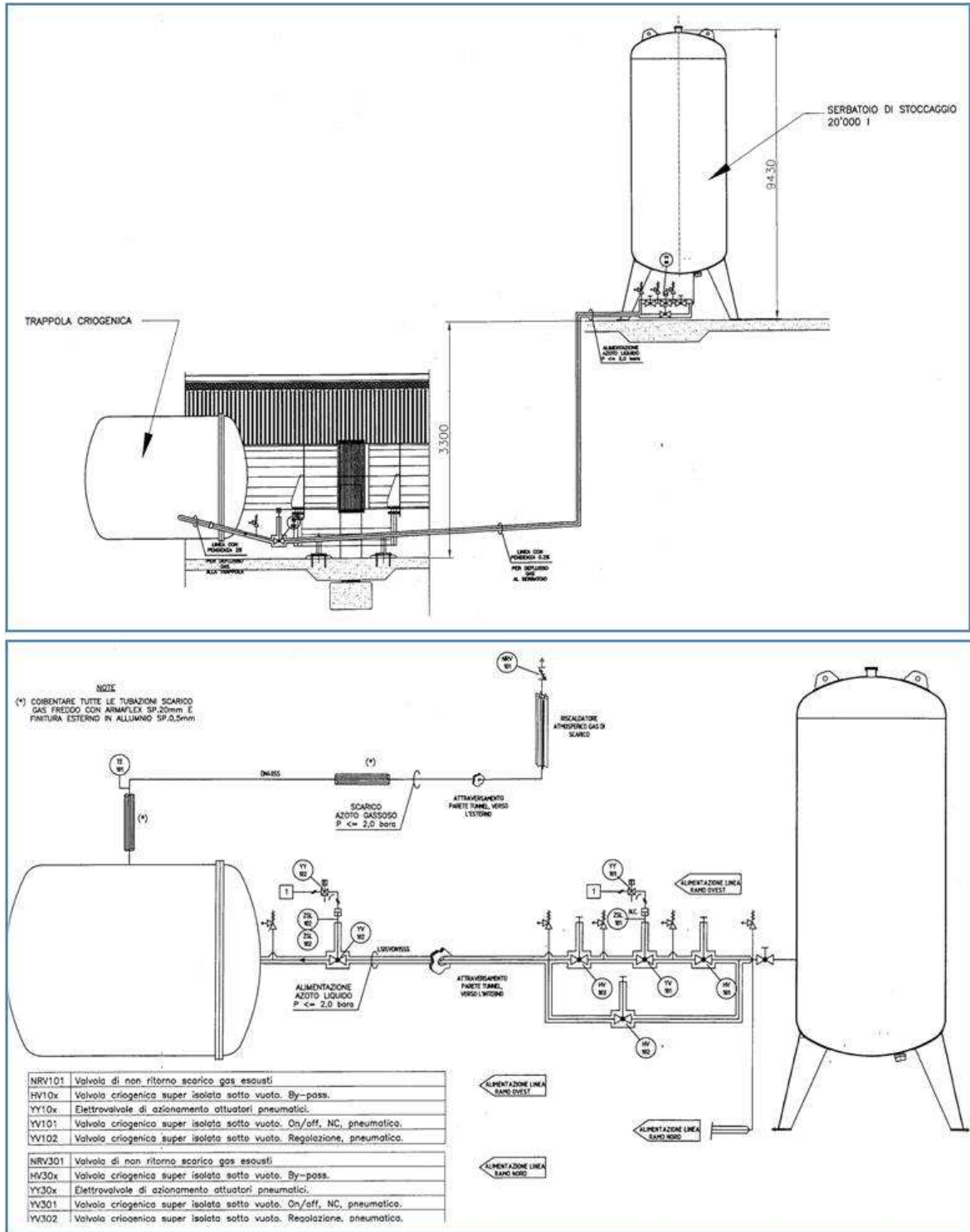


Figure 13.14: LN₂ plant schematic — Central building.

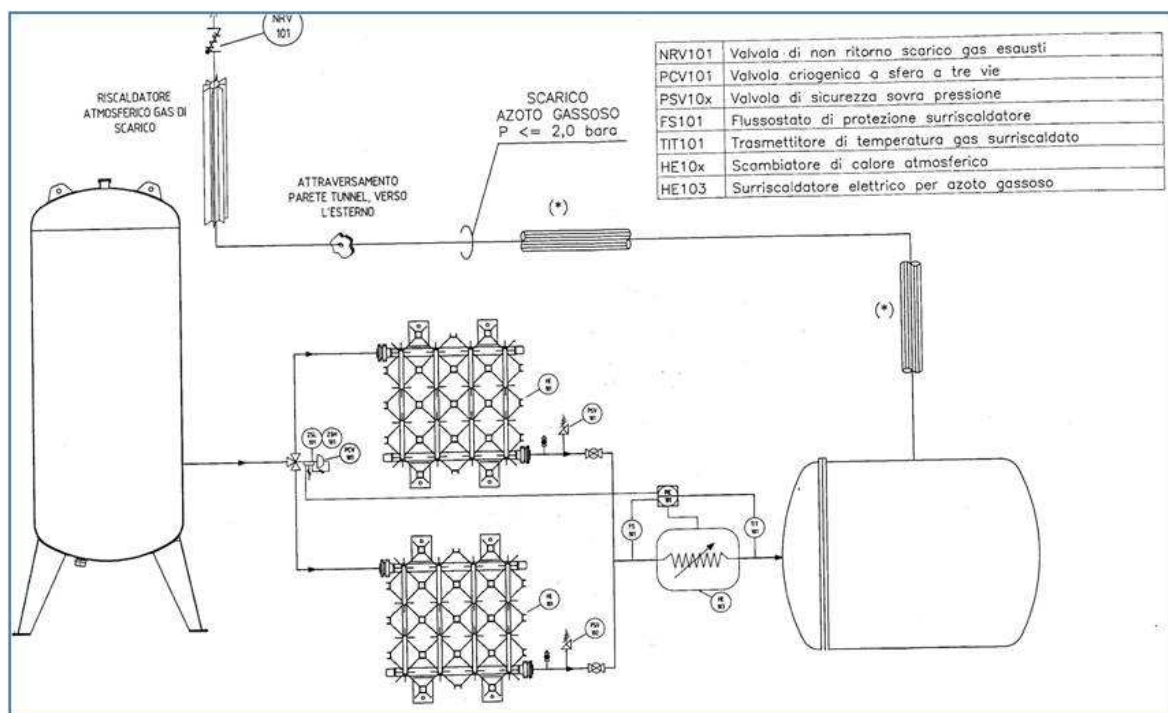


Figure 13.15: Layout of the regeneration and baking system. We note that two vaporizers are needed for each trap in order to insure continuous operation. They will alternate every 8–10 hours to allow heating up to eliminate the frost accumulated on the surface.

The equipment described in the above paragraphs will be produced, inspected and tested in agreement with the Italian laws and European directives relative to pressure vessels for cryogenic service. In particular overpressure relief valves and burst disks are foreseen to prevent explosion hazards, as shown in Sections 13.2.1 and 13.2.6.

The system is designed to keep the pressure inside the cryostat vessel below 1.5 bar absolute.

A pressure relief device will be installed also on the cryotrap vacuum vessel (Fig. 13.16) to cope with the case of accidental leakage of the aluminum cryostat and spreading of LN₂ inside the vacuum tube: this would lead to high pressure in the cryotrap when the large valves are closed. Safety will be insured by a burst disk (all metal, bakeable) mounted in series with a one-flow valve. This arrangement will avoid accidental venting of the cryotrap in case of unintentional rupture of the burst disk.

13.2.9 Prototype action items

The first trap of the series will be built in advance, with a separate contract, to serve as prototype, and will undergo to a sequence of tests.

After extensive testing in the factory and at Nikhef, the first cryotrap will arrive on site by end 2012. It will be installed in the west end hall, where conflicts with other construction activities are not foreseen, and where final tests will be performed.

The remaining three cryotrap will be ordered through a new call for tender.

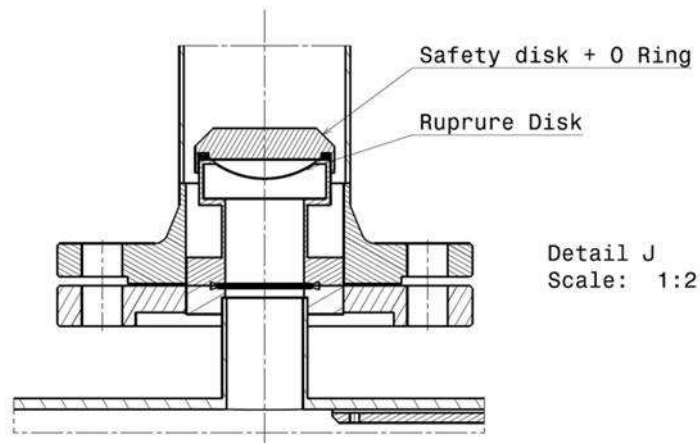


Figure 13.16: A rupture disk in combination with a safety disk on an O-ring are employed as safety device.

Here we give a non exhaustive list of actions to be undertaken with the prototype(1–6 at Nikhef, 8–9 at EGO):

1. LN₂ consumption;
2. vacuum performances and cleanliness;
3. bubbling noise;
4. system performance and damping of mechanical frequencies;
5. LN₂ consumption for different water layer thickness;
6. design changes, if necessary;
7. transportation to Cascina;
8. installation at **WE** position;
9. startup and full functional test.

13.3 Tower vacuum system

13.3.1 Requirements and overview

The **TSPs** presently installed on the central tower links will have to be replaced because they are not suitable for the changed operative conditions required in **AdV**. Actually the tower lower chambers will not to be baked anymore and the **TSPs** (one per mirror tower, 3000l/s each) will be moved downstream of the cryotrap at the beginning of the vacuum tubes (2 **TSPs** per cryotrap). In this location, the vacuum level is more compliant with their design specifications (hydrogen at **UHV** pressure, with a minor percentage of water).

Three new ion pumping groups (3000l/s total speed for hydrogen) will replace them on the links as pumps of the mirror tower lower chambers in the central area. Similarly the **TSPs** of the terminal mirror towers will be moved between the cryotrap and the terminal large valves

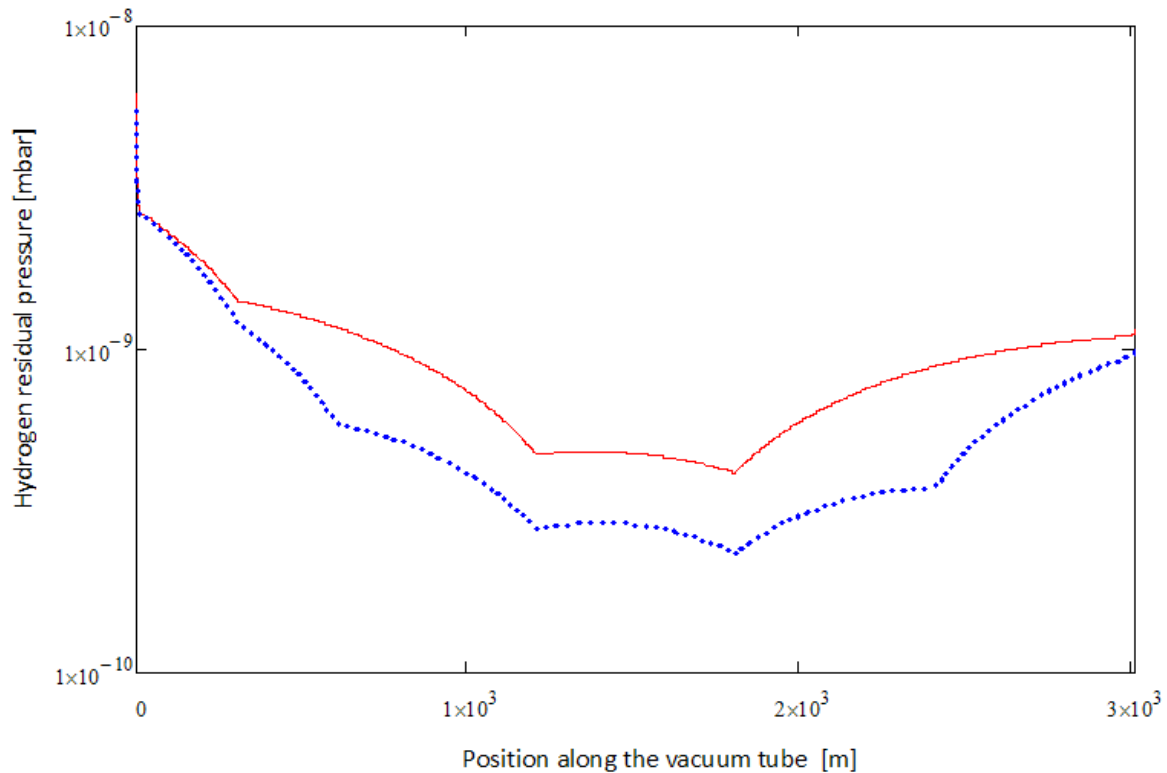


Figure 13.17: Estimated hydrogen pressure along the two arms. On one arm (red) 2 out of 5 tube TSP pumping stations have been assumed off for regeneration (hydrogen gas loads: estimated from DT, IB and MC towers = 10^{-5} mbar l/s each, measured from mirror towers lower part = $3 \cdot 10^{-6}$ mbar l/s each, and from tubes = $1.5 \cdot 10^{-14}$ mbar.l/s.cm².)

and replaced by ion pumps. Fig. 13.17 reports the estimated hydrogen pressure profile along the tubes.

Ion pumps will insure a quiet and reliable operation, without seismic or acoustic emissions, and will work constantly also when TSP groups will be alternatively out of service for the periodical regenerations. Ion pumps have a limited speed, and the hydrogen pressure goal in the arm pipes relies mostly on the TSPs, as in original Virgo.

Close to the AdV design sensitivity the presence of air in the residual gas may prevent reaching the foreseen pressure. There are two possible sources:

- the permeation of the Viton O-rings of the tower bottom lids and of the upper rings of DT, IB and MC towers (in the hypothesis of the injection brewster being replaced by a cryotrap, as considered for the baseline), which are not equipped with separating roof;
- the air outgassed by materials such as the extended surfaces of porous teflon and several other components mounted on detection and injection benches and their suspensions. These parts are recharged of air at any venting and then require several days of pumping to be degassed.

The overall air flux permeating through Viton O-rings (estimated as $2.5 \cdot 10^{-5}$ mbar l/s [411, 425] for N₂ + O₂) will be of the same magnitude as the total hydrogen load, but less efficiently

handled by TSP pumps,[426, 427]. Not being pumped by 77 K cryotraps, air would diffuse in the arm tubes rising above the goal level ($5 \cdot 10^{-10}$ mbar).

The remedy to the permeation of Viton O-rings of UHV towers bottom flanges will be their replacement by metal seals, as already foreseen in Virgo. Their use, however, will affect the interventions in the towers: closing the bottom flanges becomes much more delicate than at present, as in case of a leak it will be necessary to vent one more time to replace the seal, causing a few additional days of downtime.

In Adv metal seals will be needed also for the 2 m diameter upper rings of the IB and DT towers as there is no IVC. This may not be necessary for the MC tower thanks to the MC pipe conductance.

When coming closer to the design sensitivity, a possibility to maintain the present easy access to the DT, IB and MC towers would be to improve the DT/IB cryotraps in order to pump also air. More details are given in the sections DT and IB link.

13.3.2 Enlarged links

Four UHV vacuum pipes link the Beam Splitter (BS) tower to the nearby towers. They include the vacuum valves needed to isolate each tower during venting, the ports for optical services (i.e. TCS and local controls) and for pumping. DT and IB tower links with respectively the SR and Power Recycling (PR) towers are special and described separately as they include cryogenic pumps. A geometrical sketch of the link design is presented in Fig. 13.18.

The main features are: raw material 304L, diameter 300–1000 mm, incorporating large size bellows, one large gate valve per link, flanges with metal seals (conflat or helicoflex type).

The link design is strictly related to the optical requirements in terms of beam clipping, baffles setup for stray light mitigation and parasitic beams trapping (see the section on the Stray Light Control subsystem (SLC)). The design shown is under evaluation and might possibly be modified. A strong effort will be done to find a suitable tradeoff among optical constraints and affordable construction.

The completion of the design is expected for mid 2012, and the installation in 2013. Each link will be realized in three pieces to allow an easy installation, and all these new parts will be baked at 400°C, as is done for almost all the UHV chambers. The installation will be complex, given dimensions and weights. Suitable tools, like chariots and movable beam cranes, are being developed and built in order to handle and position precisely the links. An example is given in Fig. 13.19.

Additional details are given below for the BS–NI tower link, as shown in Fig. 13.20 (note it is slightly different from Fig. 13.18, being not yet frozen). It has a quite large size to accept the secondary beams coming from the Compensation Plate (CP) (in case of the back-up solution of CP macro tilt) and to allow positioning some viewports facing the input mirror at favorable angles. Two more ports are used for the vacuum equipment. The valve has an aperture of 650 mm. The BS–NI and BS–WI links are symmetric.

A detail of the BS–PR link is shown in Fig. 13.21. This is the part designed for the extraction of the pick-off beam: the port size available for each of the two secondary beams is 270 mm. One of the two ports will be connected, through a glass separation, to the PR–Pickoff (PO)

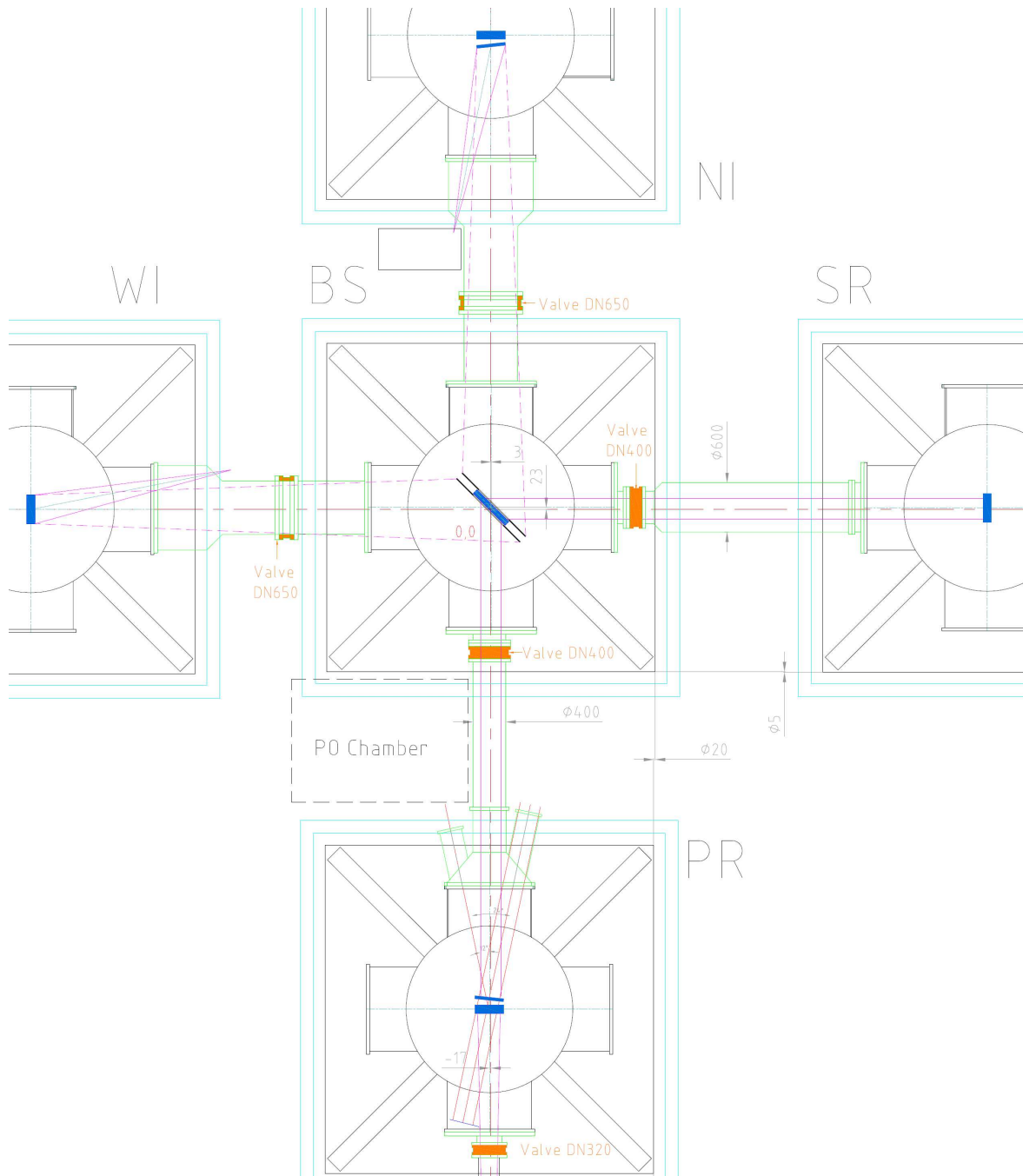


Figure 13.18: Sketch of the link geometry. The solid red lines represent approximately the main beam (width = 5 times the average radius).

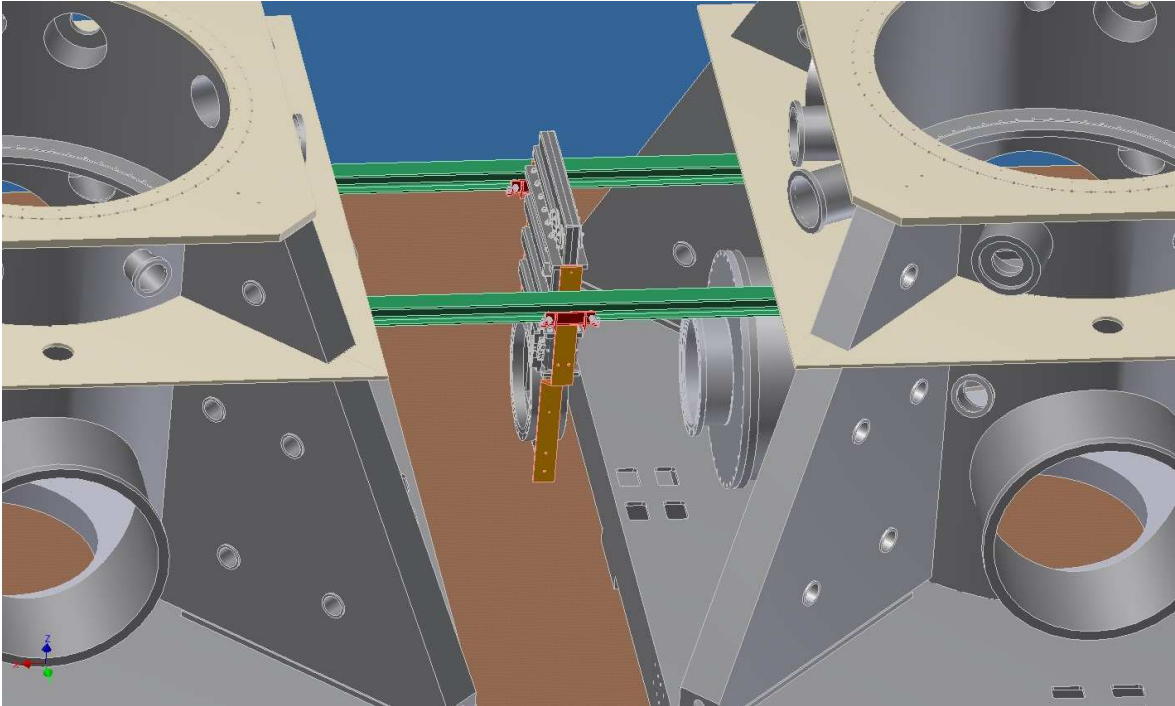


Figure 13.19: Example of a tool designed to install cryotrap, valves and tower flanges in central towers.

minitower. The other beam will be dumped. The aperture available for the main beam is here 400 mm, (corresponding to 8 times the average beam radius), currently under revision concerning optical acceptance (SLC). Being not constrained by beam extraction ports, the link **BS-SR** will be wider to accommodate more easily the most favorable baffling.

Tab. 13.3 shows the aperture of the different valves needed for the tower links.

| Valve aperture | Quantity | Position (notes) |
|------------------------|----------|---|
| 651 mm | 2 | BS-WI link and BS-NI link |
| 400 mm | 2 | BS-SR link and BS-PR link (inside BS oven) |
| 300 mm | 1 | DT-SR link (same for IB-PR) |
| 250 mm or 300 mm (TBC) | 1 | DT-SR link (same for IB-PR) |

Table 13.3: List of main valves installed on links between towers.

13.3.3 Detection tower and injection bench links

The present **DT-SR** link includes a cryogenic trap with a free aperture of 155 mm shown in Fig. 13.22; it will be replaced by a new one (aperture = 240 mm) of larger size to fit with the new beam dimensions.

The cryotrap captures on the 77 K (LN₂) surfaces most of the condensable gases (water

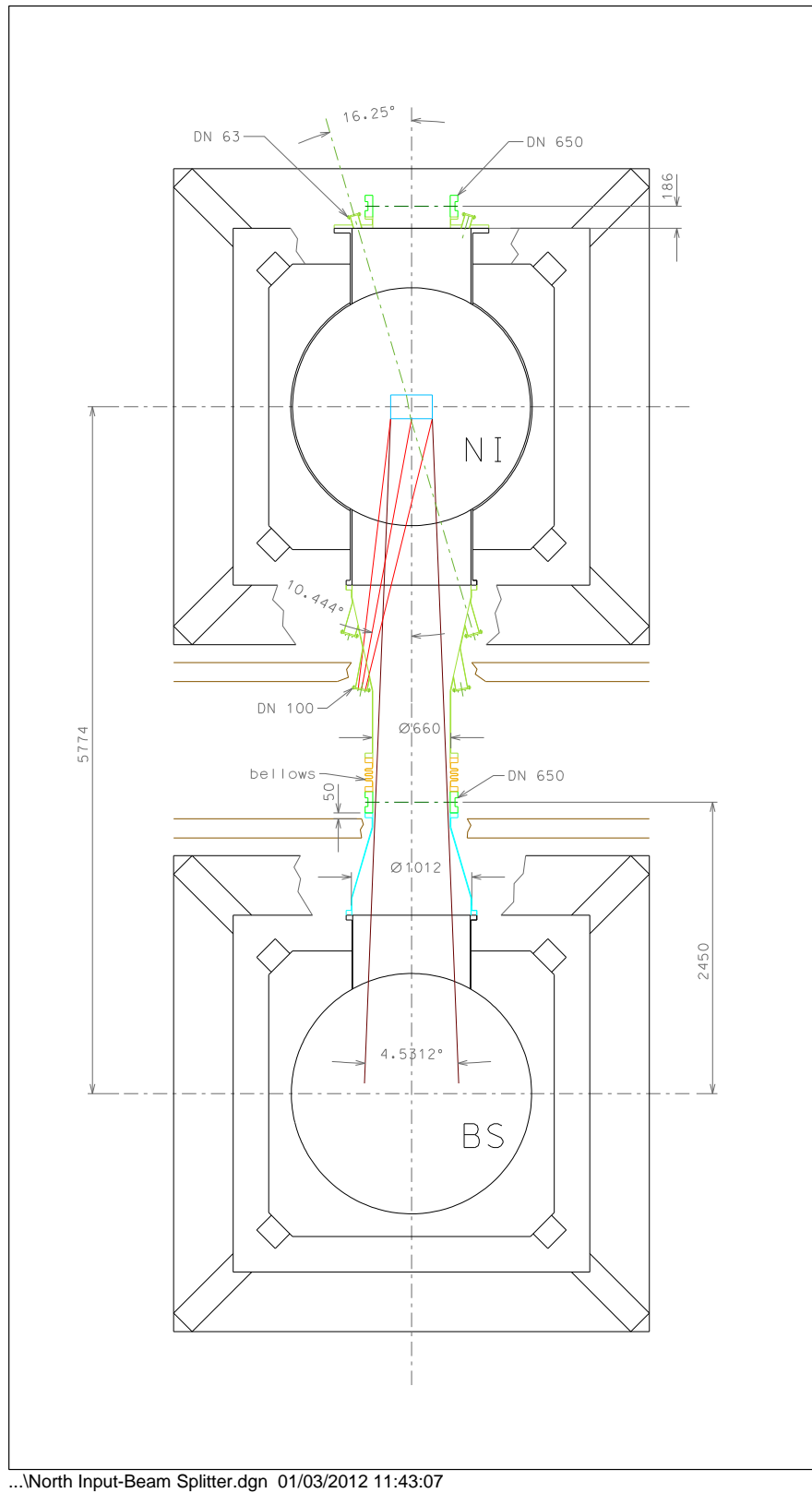


Figure 13.20: Geometry of BS – NI tower link: one port is for the CO₂ laser input; another one is for local control; two other ports are for spare.

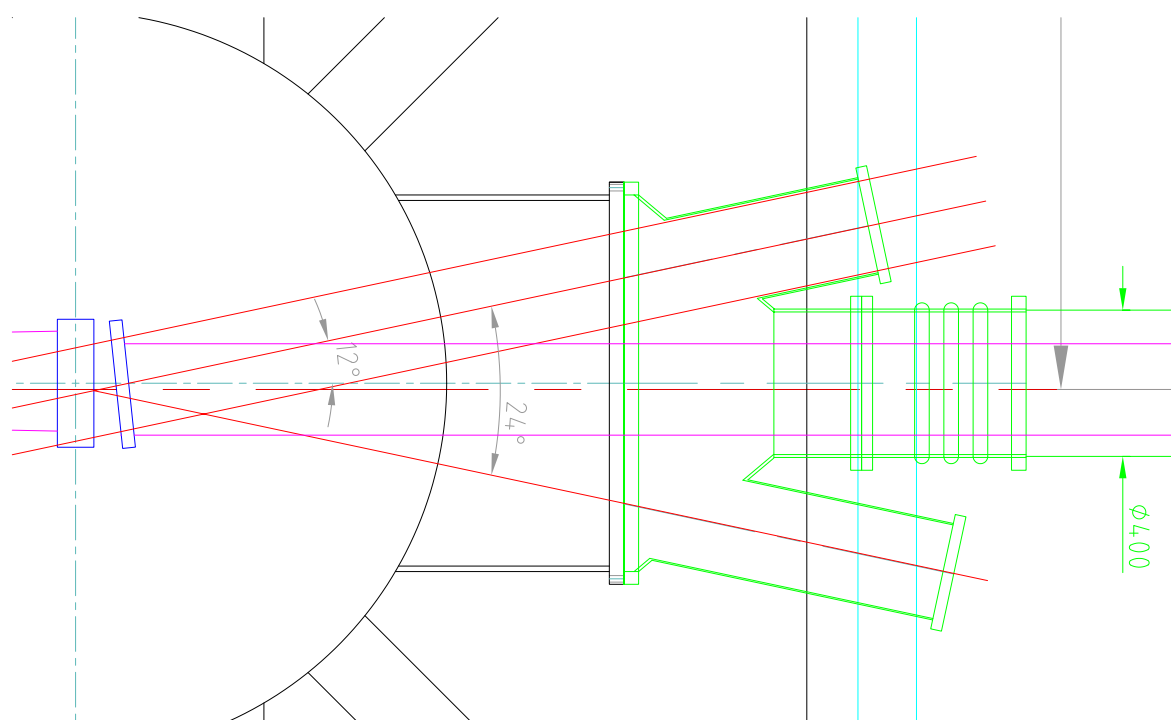


Figure 13.21: BS – PR tower link. Detail of the geometry of pick-off extraction.

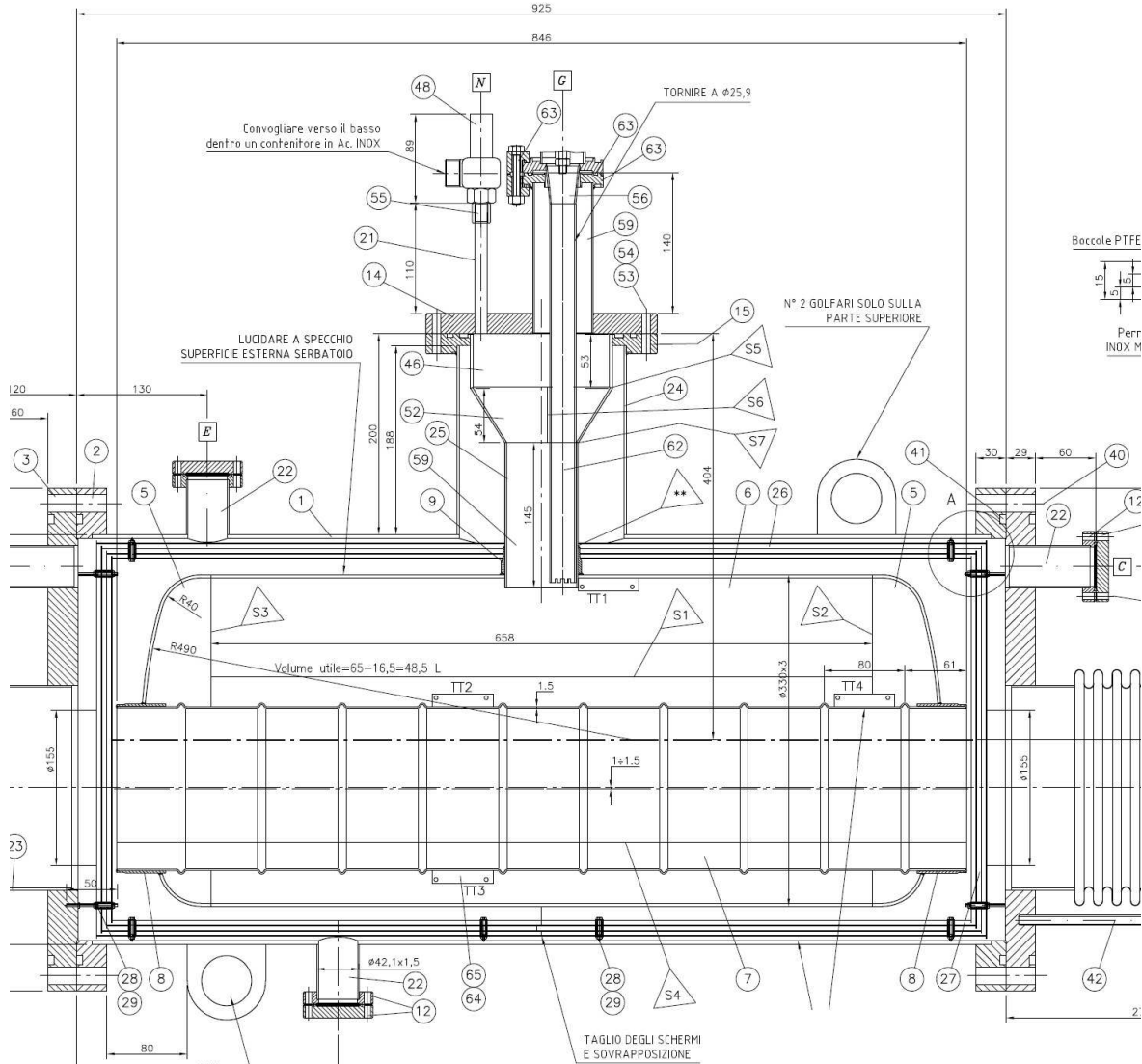


Figure 13.22: The present DT cryotrap, which will be enlarged for AdV.

and hydrocarbons) coming from the DT tower (an escaping fraction of a few % can be attained, depending on the final aperture and length) to preserve the base pressure in the UHV chambers and as a precaution against the major risk of contamination of the mirrors. In Virgo, suspensions and benches actually include components incorporating polymeric materials with lower cleanliness requirements with respect to the mirror chambers. The PR-IB link will be similar to the DT-SR one. A spare port for an extra turbo-molecular pump will be installed on the MC pipe close to the IB tower.

Close to the AdV design sensitivity it may be necessary to improve the pumping speed for air due to Viton permeation and to frequent tower ventings. In this case DT-SR and PR-IB cryotrap will be replaced by new ones incorporating colder surfaces (< 20 K) to pump also air. Classical technologies are available; basically there will be a double stainless steel standard cryostat cooled by LN_2 and Liquid Helium (LHe). In this case, the surfaces at 4.2 K will pump also hydrogen. A pumping speed of about 6000 l/s or larger could be obtained for nitrogen

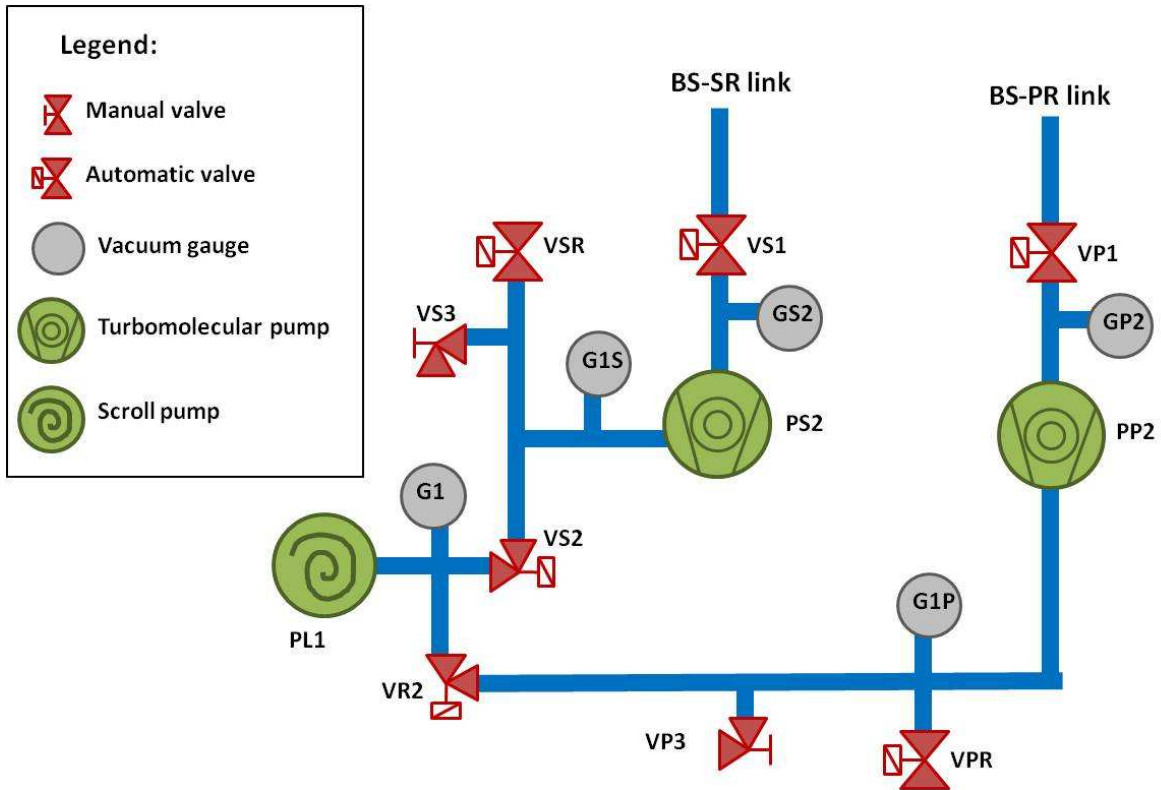


Figure 13.23: Sketch of the two turbomolecular pumping groups.

(cold surfaces of 0.2 m^2), and the flux coming from the **DT** and **IB** towers reduced to a fraction of 0.2 or less. In a preliminary study, the radiative heat loss of the low temperature part results at the order of 0.2 Watt or less ($< 10 \text{ l/day}$); this cooling power would be affordable with a portable **LHe** dewar cyclically substituted during maintenance breaks.

13.3.4 Central towers pumping

During the commissioning phase two turbo stations will be installed on links (**PR-BS** and **SR-BS**) in order to shorten the recovery of the vacuum level after venting. They will be switched off during data taking periods, and ion pumps will then be engaged. Scheme and specifications of these pumps are reported in Figs. 13.23 and 13.24 and Tabs. 13.4 and 13.5. The turbopumps are of the hybrid type with magnetic bearings (1600 l/s nominal speed, the same as the tower ones) and exist already. They will be fixed to ground and installed with bellows that proved effective in reducing vibrations already in **V+** [428, 429]. Cooling fans are not needed thanks to the continuously running remote scroll group [430].

There will be a single scroll pump for both turbos, to be used for evacuations and start-up. The turbos will be backed by the remote scroll system, and the local scroll pump will be off.

During data taking periods the turbos will be stopped and ion pumps will be used in order to lower the mechanical vibration noise. There will be 3 ion pump groups, with a total pumping speed of 3000 l/s (nominal speed = 3000 l/s for H_2 , 1500 l/s for N_2) installed on the links around **BS** (**BS-SR**, **BS-NI**, **BS-WI**). The **PR-BS** link will not be equipped for space reasons,

| Item | Quantity | Description |
|--------------------|----------|--|
| PL1 | 1 | Dry pump (scroll) |
| PP2, PS2 | 1 | Turbo-molecular pump , DN250CF hybrid magnetic (existing) |
| VS1, VP1 | 1 | DN250CF 24VDC electro-pneumatic UHVgate valve with position indicator |
| VS3, VP3 | 1 | DN25KF HV manual angle valve with position indicator, for venting and leak detection |
| VS2, VP2, VSR, VPR | 4 | Backing pump valves, DN25KF 24VDC HV electro-pneumatic angle valve with position indicator |
| G1, G1S, G1P | 2 | Pirani gauge |
| GS2, GP2 | 4 | Cold cathode gauge |

Table 13.4: List of equipment of the two turbomolecular pumping groups

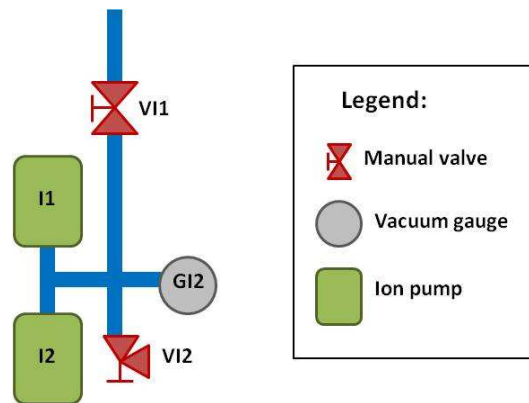


Figure 13.24: Sketch of the ion pumping group.

as there is already a turbopump and the pick-off equipment.

As they are only needed for quiet data taking, the ion pumps could also be purchased and installed in a second step, after commissioning, in order to optimize the AdV spending profile.

The pumping system of the upper parts of the towers will remain as it is except for the remote scroll pumps (sect. 13.3.6).

13.3.5 Minitowers integration

In Virgo acoustic noise was found to couple with all external benches. The mitigation strategy acts on both reducing noise emission of sources and minimizing noise coupling paths (stray light control, SLC subsystem). After the V+ experience of acoustic enclosures, found to be of little effectiveness at low frequencies, AdV features in-vacuum benches.

| Item | Quantity | Description |
|--------|----------|--|
| VI1 | 1 | DN250CF UHV gate valves with position indicator (manual or automatic, To Be Confirmed (TBC)) |
| VI2 | 1 | DN40CF manual all metal angle valve for service |
| I1, I2 | 2 | Ion pump Triode 500 l/s H ₂ nominal speed |
| GI2 | 1 | Cold cathode gauge |

Table 13.5: List of equipment of one ion pumping group.

A rough vacuum level is already providing a significant acoustic isolation [431]. At the pressure of 1 mbar a reduction factor of 1000 is expected, even neglecting the additional shielding effect of the chamber walls.

Hence the minitower chambers will normally operate at a rough vacuum level, in static vacuum, separated by a glass window from the rest of the vacuum chambers. Nevertheless the chambers have been designed with additional ports (see Suspended Benches subsystem (**SBE**) chapter) to connect a turbo-molecular pump and high vacuum sensors, in case it would be necessary to decrease the pressure. An additional port is available to install an ion pump, which has no moving parts, in case the seismic emissions produced by the turbo-molecular pump would disturb the interferometer. The minitower pumping system is reported in Fig. 13.25, and the pumping equipment is listed in Tab. 13.6. It is envisaged to purchase the full pumping set just for one minitower, in order to perform tests. The control system will be ready to include the full equipment in case this will be required for any of the minitowers.

One of the integration issues is the reduced space available especially for the central building minitowers. As a consequence, a comprehensive design study taking into account the installation and operation needs of infrastructure, optics, vacuum, and safety is ongoing. For the **PR-PO** minitower, the chamber design will be adjusted to the available space constraints.

It will take about 1.5 hr to evacuate a minitower to 1 mbar using a normal scroll pump (one could add a second pump if necessary). The procedure for the intervention on benches will be easy; venting and restarting could take place within a single day allowing a few hours of work on the bench.

If necessary, a turbo pump could be installed up to a DN250mm size (typical nominal speed 1500 l/s). Assuming a gas load similar to the bench towers, it will allow to go below 10^{-6} mbar. Fig. 13.26 shows a minitower with the turbo pump (800 l/s DN200). It includes the bellows to reduce the transmission of mechanical vibrations from the pump to the chamber. The installation at the end buildings will be eased by the larger space available, and the turbo-molecular pump will be normally mounted with the bellows. The ion pump, if needed, could be installed on the ground.

Link pipes will be built to connect the various minitowers to the towers. The links will be equipped with bellows for thermal expansion, if needed, and with transparent windows to separate the different vacuum/cleanliness levels of towers and minitowers. The windows will be made of material of optical grade and mounted on double O-rings; they will withstand a 1 bar pressure difference in both directions. The link pipes for the terminal minitowers will

| Item | Quantity | Description |
|---|----------|---|
| P1 | 1 | Scroll dry pump |
| P2 | 1 | Turbo-molecular pump, magnetic bearings (*) |
| V21 | 1 | DN250CF 24 VDC electro-pneumatic gate valve with position indicator (*) |
| Ve1 | 1 | DN63CF manual gate valve with position indicator (*) |
| Ve2 | 1 | DN40CF manual angle valve with position indicator (*) |
| V24 | 1 | DN25KF manual angle valve with position indicator, for remote scroll (*) |
| V23 | 1 | DN25KF manual angle valve with position indicator, for venting |
| V22 | 1 | DN40KF 24 VDC electro-pneumatic angle valve with position indicator |
| V1 | 1 | DN40CF electro-pneumatic angle valve with position indicator for roughing |
| Ion | 1 | Ion pump 300 – 500 l/s (*) |
| Ge1, G1 | 2 | Pirani gauges (1 *) |
| Ge4 | 1 | RGA (*) |
| Ge2 | 1 | Capacitance gauge |
| Ge3, G2, Gi1 | 3 | Cold cathode gauge (*) |
| (*) these items are only needed for UHV operation and can be purchased later. | | |

Table 13.6: Pumping system equipment list. Most of them are optional, not foreseen for starting of AdV

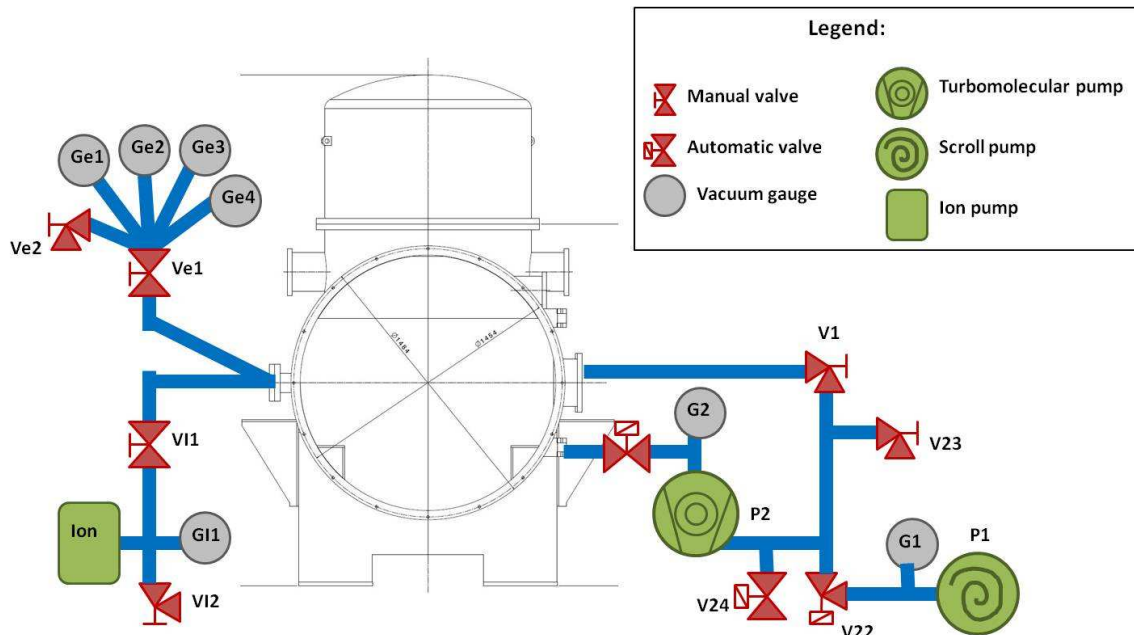


Figure 13.25: Minitower pumping system schematic.

have a free aperture in the range of 400 mm and will be supported from ground, being several meters long.

If during the **AdV** commissioning the glass separation of the **DT** minitower (or Injection subsystem (**INJ**) one) will be found to perturb the interferometer, it might have to be removed.

At least one valve must be installed on the link between **DT** tower and minitower to allow the venting of the minitower while keeping the rest of the system under vacuum. The valve(s) will have a glass window on the gate to allow the beam passage.

If it is not possible for optical reasons to have small size links, the **DT** cryotrap (installed between the **DT** tower and **SR** tower) will help in reducing the impact on the general vacuum level. However, in this case the **ITF** recovery time after venting of a minitower and interventions on the bench will take a few days, and the impact of an access to the minitowers on the schedule will become similar to the access of one of the large towers.

13.3.6 Remote scroll pumping

In **AdV** the scroll pumps will run continuously backing the tower turbomolecular pumps, and not only occasionally, as in Virgo. This gives two advantages: an improvement of the vacuum level and a limitation of the environmental noise by allowing to stop the turbo pump cooling fans, thanks to the lower discharge pressure. Since the scroll pumps are noisy, they will be placed far away in a separate room, in such a way that they cannot deteriorate the interferometer sensitivity. To limit the number of running pumps, all turbomolecular fore-lines will be lead to a single scroll pump group, composed by two pumps running alternatively. A sketch of the vacuum equipment is given in Fig. 13.27 and a list of the necessary vacuum equipment in Tab. 13.7. The connection pipe has a diameter of 50 mm, and a length of less

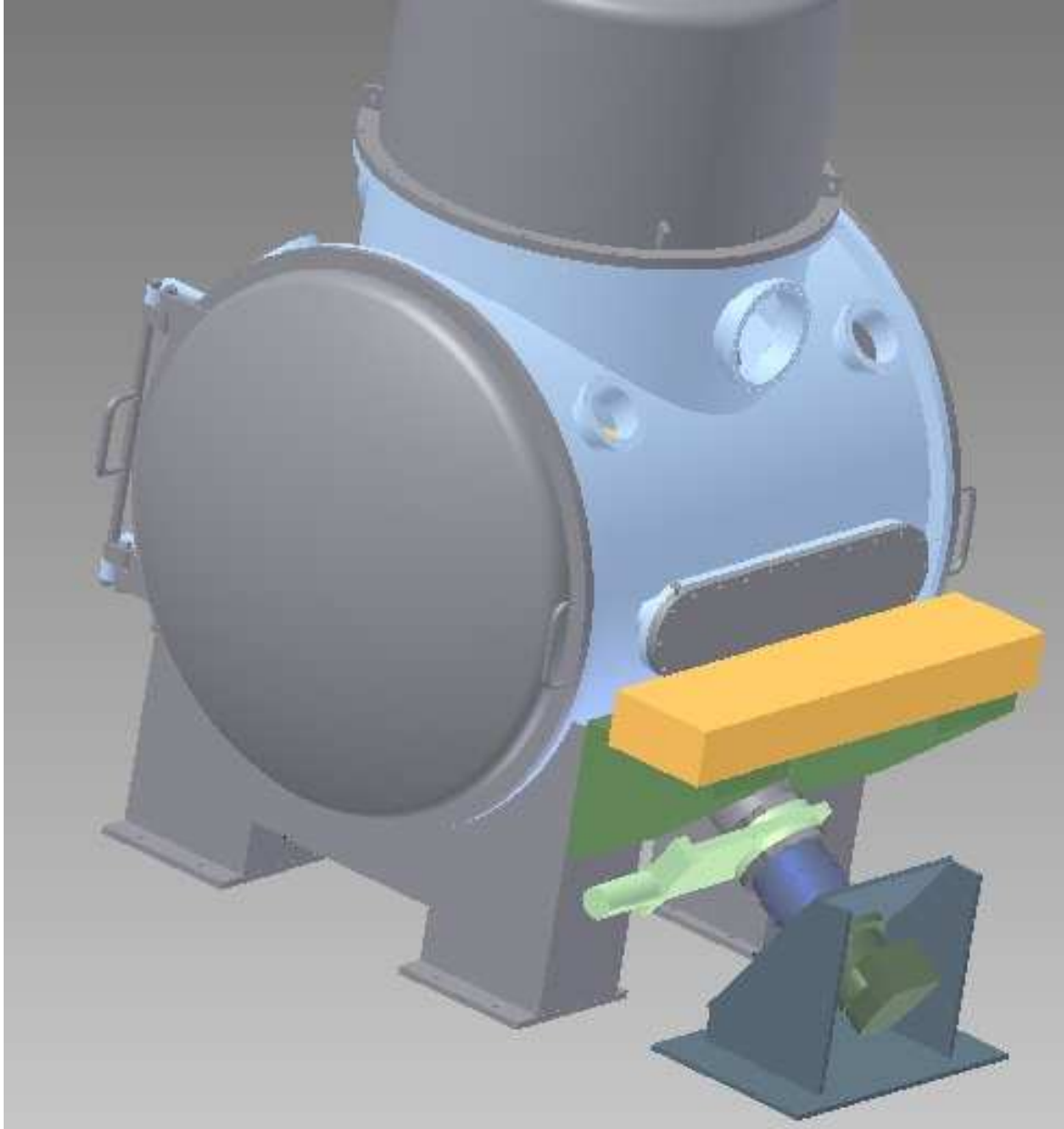


Figure 13.26: View of a turbo-pump mounted with its bellows on a minitower.

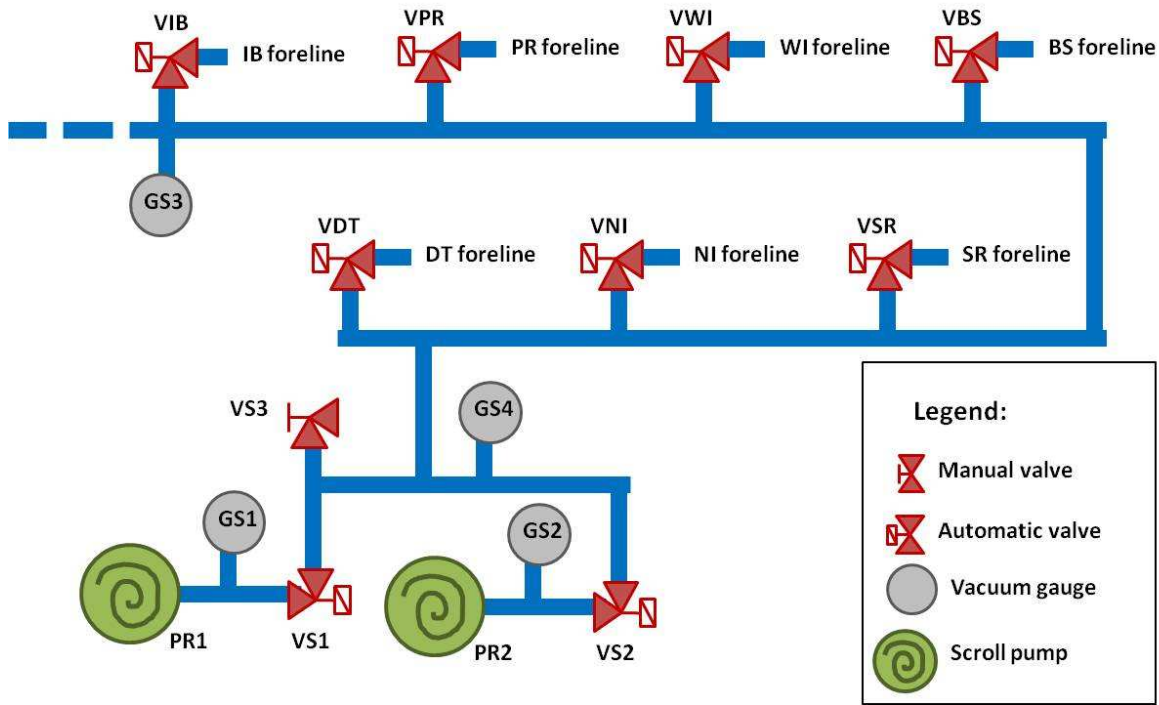


Figure 13.27: Sketch of the remote scroll system.

than 50 m (the vacuum conductance is estimated at 1 l/s). The pressure at the far extremities will be maintained below 1 mbar. Possibly, a small turbo-pump will be added to help the scroll pumps in evacuating hydrogen.

| Item | Quantity | Description |
|--|----------|--|
| Pr1, PR2 | 2 | Dry pump, 30 m3/hr scroll type |
| Gs1—Gs4 | 4 | Pirani sensor |
| Vs1, Vs2 | 2 | DN40KF electro-pneumatic angle valve with position indicator, 24 VDC |
| VNI, VBS, . . . , minitowers, 'links' turbos | 9 to 11 | DN40KF electro-pneumatic angle valve with position indicator, 24 VDC |
| Vs3 | 1 | DN16KF manual angle valve with position indicator |

Table 13.7: List of vacuum equipment of the remote scroll system

The central building scroll pumps will be placed either in the electronics room on the 1st floor, or in the room next to it. This positioning, together with Sorbothane supporting pads, has experimentally shown to be sufficiently effective [508]. To increase the isolation performances a present glass wall will be replaced by a concrete one.

The moderate heat dissipation of the scroll group (a few 100 W) will not require ventilation apertures, eventually creating an acoustic bypass. An 'office-like' air-conditioning unit may

be installed inside the room.

13.3.7 Signal recycling tower upgrade

In order to host a full size super-attenuator, the **SR** tower has to grow by 4 vertical rings, simple replicas of existing objects.

13.3.8 New intermediate vacuum chamber for mirror towers

In order to improve the seismic insulation performances, the Filter 7 (**F7**) will become an integrated part of the payloads of the **BS** and of the Fabry-Perot cavity mirrors (see the Payload section). The separating roof (also called **IVC**) which contains only a small conductance aperture for the passage of the main supporting wire (Fig. 13.28) cannot stay any more between **F7** and the marionette. To solve this issue, all the separate parts of the **IVC** will be removed to allow the free passage of the various legs and wires of the new payload. The wall separating the upper tower **HV** volume from the lower **UHV** mirror volume will be raised above the **F7**. This separation will consist of a lower cylindrical part and of an upper conical hat (Fig. 13.28 and 13.29). The lower rim of the cylinder will be equipped with a suitably shaped Viton gasket, to obtain the best possible tightness, resting on the upper surface of the old **IVC**. At the cone top, the hole for the passage of the main pendulum chain wire will be extended by a 80 cm long tube to reduce the conductance, plus a short bellows to allow some flexibility. The tube will have a diameter of 30 mm to allow the passage of the 15 mm diameter main wire, composed by the maraging steel supporting wire, surrounded by several tenths of electric conductors. The computed residual conductance will be about 1.8 l/s. Halfway along the tube, a chamber that can be pumped through a soft bellows, allows to reduce the conductance to about 0.4 l/s.

The overall performances should be practically equivalent to those of the present **IVC**. Also mirror pollution and arm tube base pressure should be preserved, provided that all the components of the new Payload are selected and conditioned according to the mirror chamber cleanliness prescriptions. The construction of a new full size separating roof is started and will be tested within a few months.

13.3.9 Displacement of towers

The change of the interferometer optical configuration and the control strategies require to change the position of the main mirrors of up to about 0.6 m (**NE**, **NI**) (See Optical Simulation and Design subsystem (**OSD**) chapter 2). The displacement of the towers involves considerable work and is subject to infrastructural constraints. The main limitation comes from the structure of the central building. Each tower has one bottom flange of 2 m diameter, corresponding to the tower diameter, with a smaller 1 m diameter lid in the center. Only the 1 m lid is opened to install the payload. The large 2 m flange has been conceived for exceptional needs that never happened up to now. The 2 m flanges of **NI** tower will not remain completely inside the corresponding rectangular aperture in the floor; hence it will not be demountable anymore. This has been considered acceptable since there are no plans for introducing payloads larger than 1 m. The development of leaks is also considered very

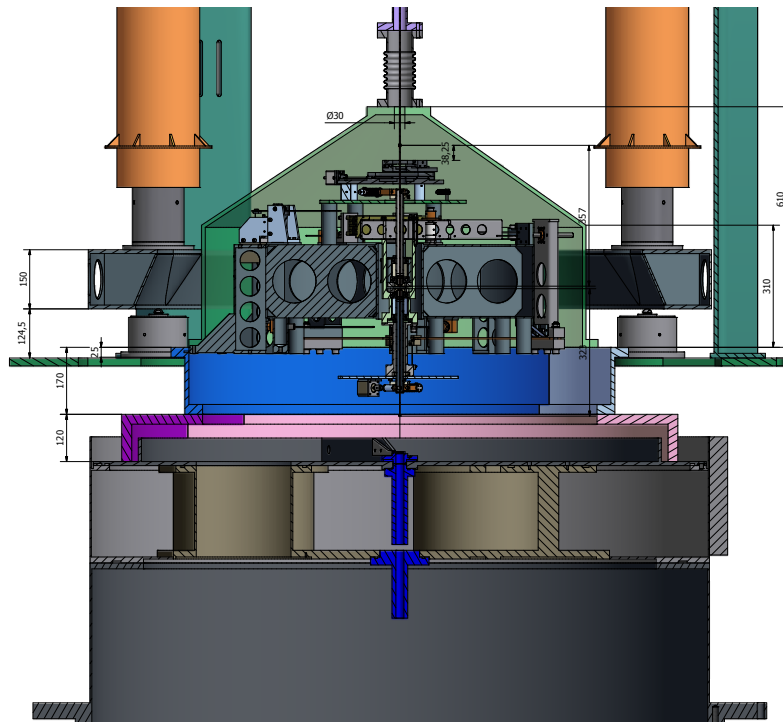


Figure 13.28: Section of the new IVC of the BS tower. The present IVC is visible still in place, with the new 'hat' parts standing on it and embracing the filter. The suspension wire is not shown here.

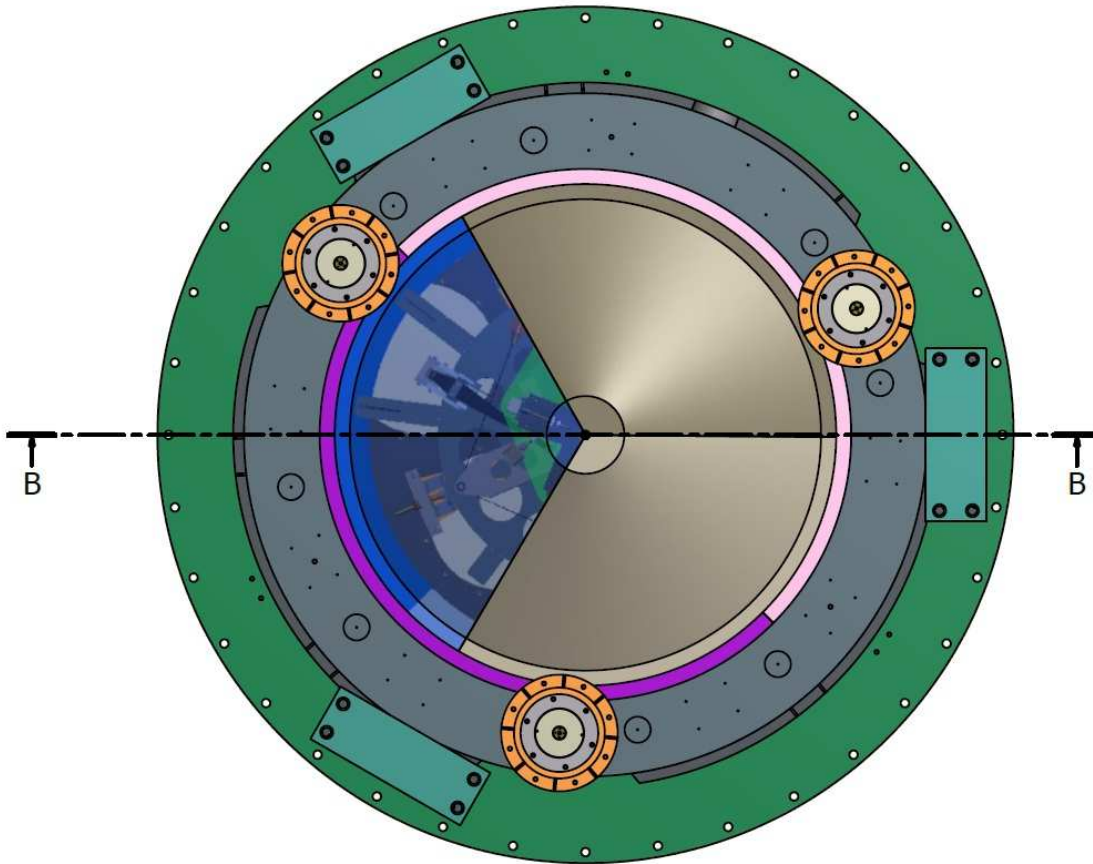


Figure 13.29: Top view of new IVC of the BS tower. The top hat can be dismantled in three sections to give access to F7 for tuning operations.

unlikely, since bake out is not considered anymore an option for the towers. The displacements are reported in Tab. 2.5. Significant work will be necessary for the towers: **NE**, **NI**, **PR**, **SR**, **DT**, **MC**.

Preparatory works necessary before the tower displacement include:

- geometry survey;
- removing parts of scaffoldings and stiffening beams;
- removing oven walls;
- removing the air tight connections between tower bottom and basement clean room;
- removing clean air ducts;
- rearrangement of cables and cable trays, related electrical cabinets and electronics racks;
- removing the concerned platform parts;
- removing the link between towers.

Cabling issues must be considered with much care, and the possibility to avoid removing and reinstalling all cables has been studied. The real displacement will be done by moving the entire tower on special sliders, once having removed the payloads and having blocked the super-attenuators. A similar operation has been already performed successfully in the past, displacing twice the **MC** tower of about 800 mm. All the preparatory works will have to be recovered at the end in the opposite sequence.

The metallic structures surrounding the towers (ovens, platforms) will have to be adjusted to fit with the new towers positions and to allow for the installation of enlarged link vacuum valves and cryotrap. Fig. 13.30 shows the situation for the **NE** tower where the oven has to be modified in order to integrate the cryotrap and its valve.

13.4 Pumping system configuration

Special care has been taken to make the pumping system residual environmental emissions to comply with **AdV** goals [428] (see also the Infrastructure subsystem (**INF**) chapter 15).

The different pumps running when the **ITF** is in science mode are reported in Fig. 13.31. The turbomolecular pumps are linked to the towers upper part, mechanically insulated by bellows and with cooling fans normally off. In the central building they are backed by a remote scroll pump (see 13.3.6) located in an insulated room, and in the **MC** and End buildings by a remote scroll pump located in the tunnel. As a precaution, the possibility to substitute the turbos with ion pumps is foreseen as well on the tower upper parts. It will be done independently for each tower, depending on commissioning needs.

In the baseline solution, no pump is foreseen to be running in science mode for the minitowers (mInj, mPO, mDT, mWE in Fig. 13.31) as they will be separated from the rest of the system by a glass separation and left under static vacuum. Ports are however foreseen to add turbomolecular pumps (linked to the remote scroll system) or ion pumps if this turns out to be necessary (see 13.3.5).

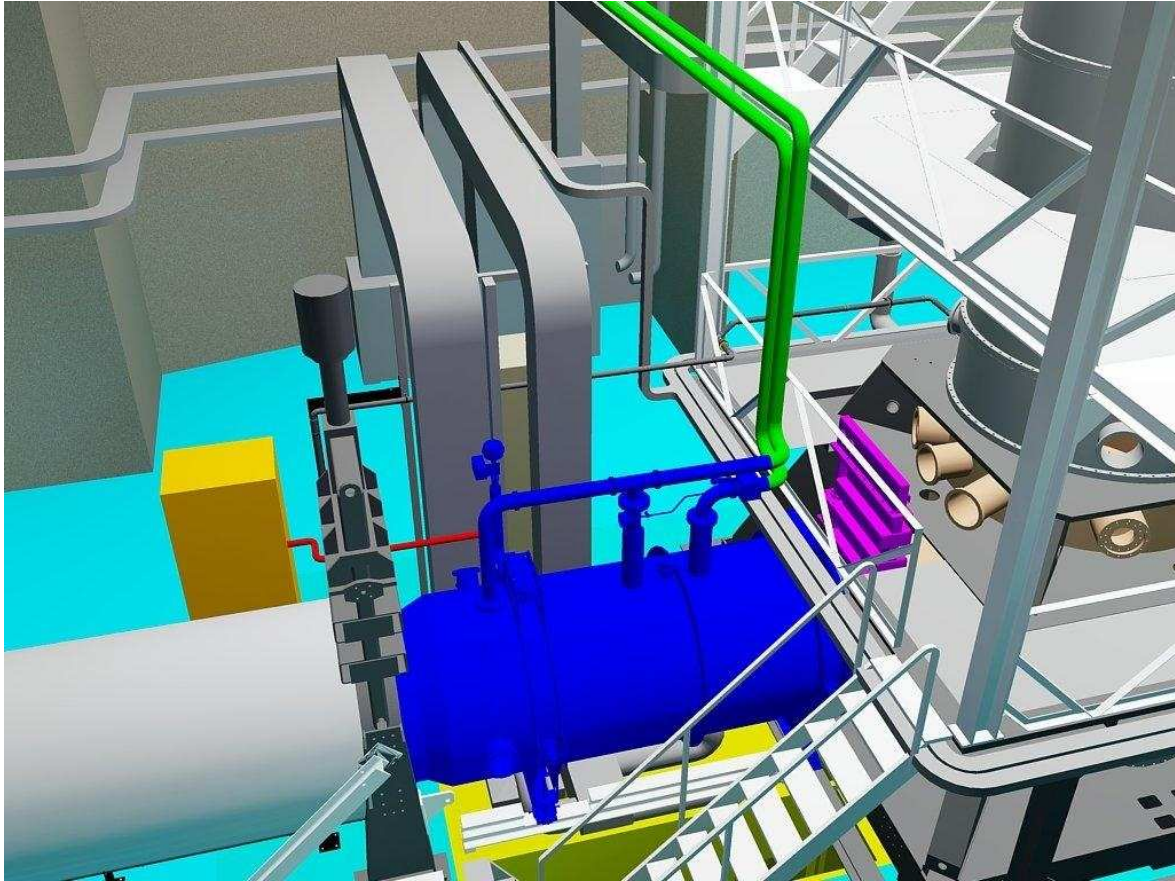


Figure 13.30: Tower installation: cryotrap (blue) and valve (pink) are to be installed in 2013. The oven structure has to be adapted.

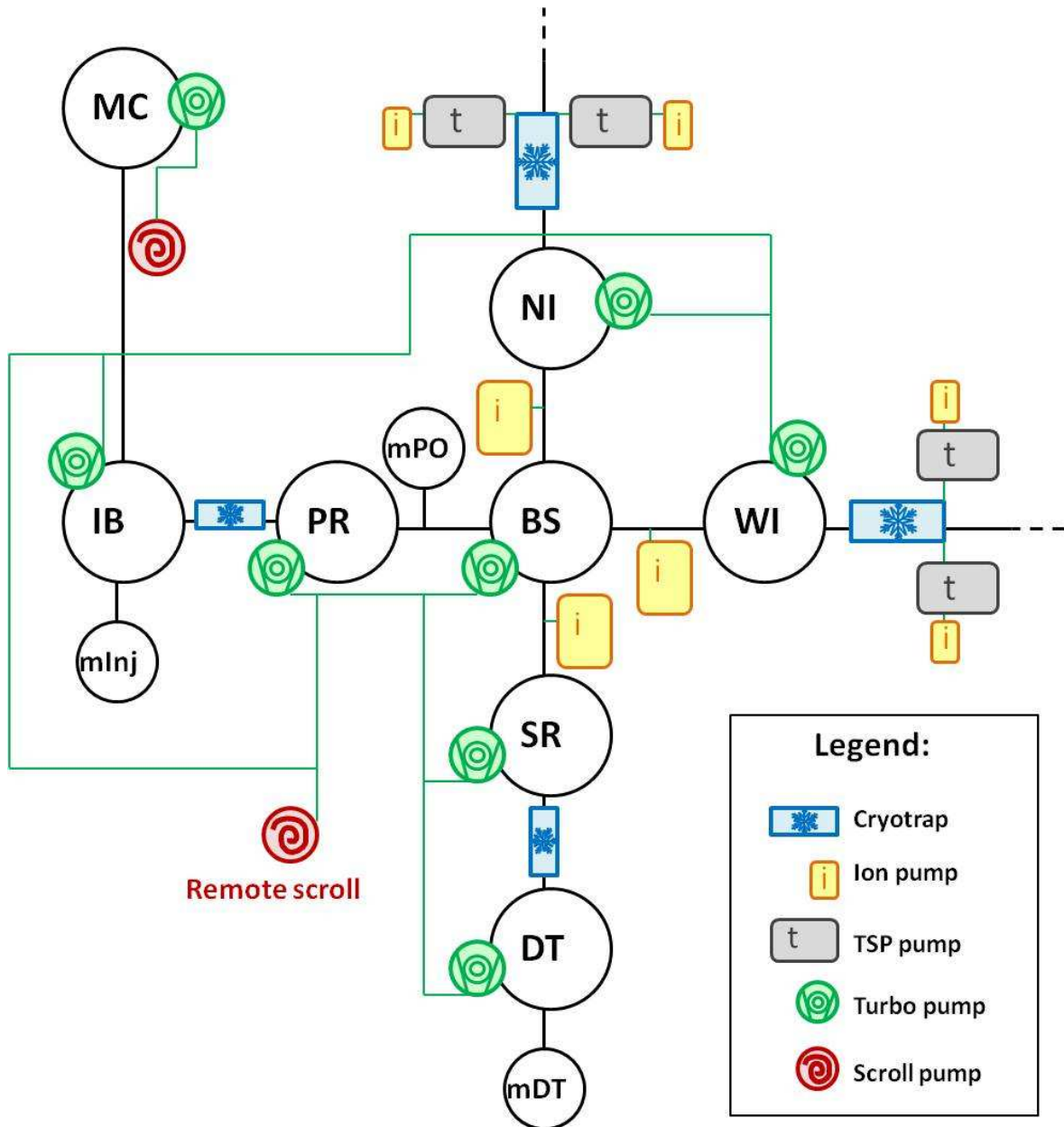


Figure 13.31: Pumping system used in science mode for the MC and central building, and for the tubes and end buildings.

Extra pumps (scroll pumps, turbomolecular pumps) will be used during tower evacuation (and possibly commissioning) phases.

13.5 Control system

The vacuum control system is made up of 22 main control stations and several other components installed along the entire vacuum system. It includes also the supervisor software used to drive the vacuum system. It must be revised, since it has been designed more than 10 years ago and it is based on the OS-9 standard, using components no longer available on the market. Besides the new hardware, it will be necessary to upgrade also the control logic, and supervisory software, for more versatility and to include future devices, such as new pumping stations and pump types. New interlocks and loops will be added to actively control the improved vacuum conditions. The selected solution is based on **PLCs**, extensively tested by industry and specifically studied for the operation of critical systems. The plan is to reuse many of the compliant hardware already existing (main cabinets, parts of the power relays and cabling). The environmental noise aspects have been considered through all the design.

13.5.1 Architecture overview

The control system for **AdV** has to handle the existing Virgo vacuum hardware and the new needed stations (cryotrap, minitowers etc.) We keep the same philosophy used in Virgo: each independent vacuum volume will be controlled by a dedicated station. Low level securities will be insured by hardware while higher level ones will be insured at a software level, either in each station or in supervision itself when information coming from several stations will be required to take a decision. As it is in Virgo, each station can be controlled in local or distant mode, the switch between modes being without impact on the vacuum status itself.

The software part of each station (old or new) will be housed in a Bekhoff CX1020 **PLC**. A wide survey of available **PLCs** has been done and it should be underlined that vacuum needs are quite demanding, in particular due to the large numbers of serial ports and the large numbers of variables to be handled. Extensive tests have been performed using the Bekhoff **PLC** and all current controllers run properly either using the RS connections or HMS anybus Modbus/Serial Link bridge. The possibility to directly use ModBus is important for integrating future hardware and insure as much as possible as “plug-and-play” functionalities. One of the advantages of the choice for **PLCs** is the long term maintenance, compatibility and reliability as they are industrial products.

13.5.2 Update of existing control stations and new control stations

New vacuum systems, thus new control stations and modifications of the existing ones, are needed for **AdV**. The general design is still evolving, for the links in particular, so that some changes may still happen. A summary of the new and already existing vacuum system and of the relevant control stations is given in the Tab. 13.8. The control stations can be also arranged differently, grouping the devices to be controlled as it is more convenient for the control system realization.

| Number of control stations | Name of vacuum equipment | Description |
|----------------------------|---------------------------------|---|
| 4 | Cryotraps | Each station will include the needed cryotrap vacuum equipment (pumps, gauges, valves . . .) and cryogenics devices (essentially temperature and LN ₂ level signals readout and feeding valve status) |
| 0 | Link pumps | New pumps on enlarged links, their sensors and the valves will be integrated in the corresponding existing racks of the towers (NI , WI , PR , SR), in the place of the removed pumps (TSP groups). |
| 0 | LN ₂ tanks | Readout of level and pressure inside the LN ₂ storage tanks, and related alarms. Integrated in the cryotraps control stations. |
| 1 | Remote scroll | It will be a simple separated rack. Interlocks between the different towers are anyway needed. |
| 5 | Minitowers | Normally one control station per minitower. Possibly integrated into the nearby tower control station. A ‘remote’ driving console for ‘local’ operation is foreseen. |
| 2 | 300 m tube stations | To control a TSP added at 300 m along the tubes; this should be very simple. |
| 2 | IB , DT cryotraps | As the present one, to be integrated in the system |
| 10 | Tower stations | Already present — To control the different pumps and sensors present in each tower pumping station |
| 12 | Tubes stations | Already present — To control the different pumps and sensors present in each tube pumping station |
| 4 | Large valves | Already present |
| 6 | Link valves | Already present |

Table 13.8: Summary of new and already existing vacuum systems and relevant control stations for **AdV**

Additional minor changes will affect the existing vacuum equipment of towers and tubes; for example, some pumps will be removed from towers (**TSPs**) and a **TSP** station will be placed on the tubes at 300 m from the input towers.

Of course, the production of new stations is the priority and the upgrade of existing ones will be done in agreement with the available funding and manpower, keeping in mind the constraints of the integration and commissioning. Thus, it is possible that the current and the new control system will have to cohabit at some period.

13.5.3 SCADA control software and DAQ interface

Our plan for supervision is to use TANGO [438] which is used at the large research centres such as ESRF, DESY or SOLEIL. It is based on CORBA and has been already successfully tested at EGO and LAL. It will allow an easy and efficient way to monitor and control all vacuum stations. A dedicated tool will be developed in order to connect TANGO and the **AdV DAQ** but it has to be underlined that this point has a larger impact than the vacuum control itself and is interesting for any slow control. Discussions have already started with the collaboration to find the best solution.

13.5.4 Environmental noise aspects

Measurements of the magnetic field noise [435] show the necessity to remove the vacuum power supplies far from the mirrors (≥ 15 m from the mirrors, the input mirrors are the most sensitive). Noise projections show that in the central hall (where magnetic noise is far more important than in the **NE**, **WE** and **MC** buildings), increasing their present distance to 15 m would reduce the magnetic noise effects by two orders of magnitude as required for **AdV**. The power supplies of the central towers will be relocated in the **DAQ** room. Moreover, modifications and/or shielding of the electronics can add further safety. Transporting the DC power to the racks by point-to-point cables is not a problem; if the voltage drops are too big, power supplies with sensing input can be used; on the other hand the affected electronics (relays and similar) should also work with significant voltage drops. Acoustic and seismic noise emissions will be mitigated by choosing appropriate cooling fans [433, 434] and adopting specific tools (rubber mounts) for their installation inside the rack. Furthermore the racks themselves will be seismically isolated. A prototype installation of a rack fixed to the concrete wall through rubber pads, rather than installing it on a platform, has proven effective to reduce seismic effects. Disturbances of cooling fans resulted below the seismic background noise, no more visible on environmental sensors [439]. Concerning the effect on the interferometer, in general, acoustic and seismic levels will be also less harmful, thanks to the choice of suspending benches in vacuum.

Chapter 14

Data acquisition, general purpose electronics and software (DAQ)

14.1 Introduction and requirements

14.1.1 Subsystem definition

This chapter describes all the needed activities starting from the output of the front-end electronics up to the data ready to be analyzed for Gravitational Waves (GW) searches. It covers different fields:

- the digitization electronics to interface the front-end electronics to both the data acquisition and the fast control loops of the detector (section 14.2): ADC and DAC channels, digital demodulation, video system;
- the network for the exchange and processing of the digital fast control loops (section 14.2);
- the front-end electronics of the environmental monitoring system (section 14.5);
- the data collection system (DAQ), used to collect all the information needed for the control and monitoring of the detector and the extraction of the GW signal (section 14.3);
- the specifications for the online software and communication between the different online processes (section 14.4);
- the calibration support, with online tools for calibration measurements and online/offline tools for the GW $h(t)$ reconstruction (section 14.6).

Some specific digital electronics of the suspension actuators is described in section 11.

14.1.2 Requirements

The main requirements for the digital electronics and data collection system are described hereafter.

- Constraint on the **data flows**:
 - the number of channels to be acquired is of the order of 15000, with about 2500 “fast” channels ($f > 1$ Hz, up to 800 kHz for a few channels) and about 12000 “slow channels” ($f \leq 1$ Hz). This translates into a maximum data rate of up to 100 MBytes/s uncompressed;
 - the front-end camera flow will be of the order of 400 MBytes/s.
- Constraints on **real-time fast controls**:
 - the DARM servo-loop put constraints on the maximum delay introduced by electronics and digital controls: it can be as low as $100 \mu\text{s}$ (for dual recycled interferometer configuration). It pushes for running the loop at a frequency of the order of 20 kHz to 40 kHz.
- Constraints on the **timing system** (both on the timing distribution system and on local oscillators):
 - constraints on the absolute timing come from the data analysis, from the stochastic analysis where coherent analysis between different detectors are done up to few kHz [442], and from the CBC and burst searches for source sky localization¹. This sets an absolute timing accuracy of $30 \mu\text{s}$ between LIGO and Virgo. As a consequence, the absolute timing accuracy for a single detector is of the order of $10 \mu\text{s}$;
 - constraints on the relative timing of the Virgo data (within kilometer lengths) come from the speed of the loops, the maximum unity gain frequency of the loops being of the order of 200 Hz. Assuming the signal at 100 Hz is of the order of 5% of the full scale input, having 19 effective bits for the 10 kHz control signals requires the timing jitter to be lower than $0.12 \mu\text{s}$ ²;
 - constraints on the local timing jitter at the level of the photodiode ADCs come from the frequency of the analog anti-aliasing filter, around 100 kHz, and the effective number of bits: 16. The required timing jitter of the local ADC clock should be kept below 0.02 ns;
 - constraints on the timing jitter at the level of the ADCs used for the digital demodulation sampling at ~ 500 MHz. The lock clock of such ADCs must have a jitter below ~ 300 fs (see section 14.2.6.1).
- **General constraints**:
 - a latency from the real-time processes to the automation processes, user interfaces and data visualization of the order of 1 s;
 - full data provided for archiving;

¹ The time resolution of the CBC searches is slightly lower than 1 ms. Aiming at an error of the order of 1% gives again a timing precision of $\sim 10 \mu\text{s}$. It was shown that such an error, achieved in initial Virgo and LIGO, had not impact on the source parameter estimation [441].

² In the Virgo $h(t)$ reconstruction process, where different signals are added together similarly to the DARM loop, similar constraints on the relative timing of the different channels, of below $\sim 1 \mu\text{s}$, have been found [480].

- data selection and tools to provide reduced datasets for the subsystems commissioning and data analysis;
- a system easy to reconfigure (add channels, change frequencies, add new data streams, ...) and to use on test benches;
- good reliability and maintainability.

14.1.3 Main interfaces with other subsystems

14.1.3.1 Data collection and digital electronics

The **DAQ** subsystem is interfaced with all the subsystems that need to collect data (section 14.3). The main interface is with the subsystems where digital electronics is needed (section 14.2). In particular, the number of digital electronics boards or boxes provided by the **DAQ** subsystem has been evaluated and the front-end electronics must be properly interfaced (connectors, signal types, ...).

The **VAC** subsystem is interfaced with the **DAQ** for the data collection of slow channels. The following subsystems are also interfaced since they need digital electronics (ADC and/or DAC channels) for monitoring, control and data collection: **PAY**, **SAT**, **TCS**, **DET**, **INJ**, **PSL**, **SBE** and **ISC**. Furthermore, the **DET**, **INJ**, **TCS** subsystems will need digital cameras.

14.1.3.2 Others interfaces with subsystems and groups

- **INF** – The locations of the electronics racks must be discussed with the **INF** subsystem to foresee the mains power supplies, the cable trays. Another topics can be the cooling of the electronics: the idea of bringing fresh air from the air conditioning system close to the racks using flexible tubes is being discussed.
- **ISC** – Real-time PCs and software framework is provided to the **ISC** subsystem to run the ITF control servo-loops. Interactions are needed in the design of the real-time control system by the **DAQ** subsystem and the design of the servo-loop by the **ISC** subsystem since the overall delay must be kept low enough for the loop to be stable (section 14.2.7). The design of a digital SSFS loop is a possible option to be evaluated.
- **PAY** – Calibration of the mirror actuator demands that a minimum force is applied on the mirrors via the electro-magnetic actuators in high-power mode (section 14.6).
- **SAT** – Actuator calibration is done by transferring measurements from high-power to low-noise electronics modes (section 14.6). The electronics used to monitor the current flowing in the coils of the mirror actuators must be sensitive enough to have the same configuration for couples of consecutive modes.
- **EGO computing** – The **DAQ** subsystem will provide needs and specifications to the **EGO computing** service on the Ethernet network (access ports, speed, ...), the storage farm, the access to the filesystem and the servers used for online processing and detector monitoring web pages.

14.2 Digital electronics and control

The digital electronics has two roles:

- the interface between the front-end electronics and the system for data collection and distribution;
- the distribution of the signals between the different controlled subsystems with a very low latency for the fast control-loops of the detector. The locking and alignment loop signals are going from the injection and detection photodiodes, to the driving electronics of the suspensions. A set of digital cameras are also used for beam imaging and local controls of the suspended optical benches and mirrors, with a specific image distribution system.

In this section, the requirements, architecture and details of the electronics are discussed in relation with the controls. The electronics seen as the interface with the data collection system will be described in the section 14.3.

The timing distribution system is first described in section 14.2.1.

A general overview of the digital control of the Interferometer (ITF) is given in section 14.2.2. The digital network components and foreseen electronics developments are discussed in sections 14.2.3, 14.2.4, 14.2.5 and 14.2.6. An estimation of the data propagation delay in the control network is given section 14.2.7 and the foreseen control network topology is shown section 14.2.8.

In section 14.2.9, the video system and its components are introduced.

Finally, in section 14.2.10, some general specifications for all the electronics to be installed in AdV are given.

14.2.1 Timing system

14.2.1.1 The timing distribution network

A central timing system is used to synchronize the ITF controls, the servoloops and the readout systems. It is based on the GPS time-stamp which is used for synchronization with other experiments as LIGO.

Figure 14.1 shows the diagram of the timing network with its star configuration. A GPS receiver (SW1050-R from MICROSYSTEMES³) generates an IRIG-B signal [444]. This 1 kHz signal contains a 1 PPS signal, the associated GPS time and some extra data. The IRIG-B signal is sent to the master Timing Distribution Box (TDBox) which distributes the signal to TDBoxes located in most of the racks through optical fibers and other TDBoxes. The connections between the TDBoxes and the front-end digital electronics (real-time PCs, ADC, DAC, ...) are made with network-like cables (LVDS signal) of length between 1 and 3 meters. The IRIG-B signal is used to lock the local oscillators of the digital electronics and to time stamp the sampled data with the GPS time.

The timing system [442] was deployed in summer 2008 for Virgo+ and will be used for AdV. Some modifications will be done due to the new locations of the racks. The lengths of the fibers

³<http://www.microsystemes.com>

and adjustable delays in the TDBoxes have been adjusted to produce the same propagation delay within better than 50 ns, such that all the data sampling clocks are synchronous⁴.

Figure 14.2 shows the timing jitter introduced by the timing distribution system, both at the level of the TDBoxes (green) and at the level of the internal clocks of digital electronics (red). Above 1 Hz, the timing jitter of the digital electronics clocks is below 0.1 ns.

14.2.1.2 Timing distribution box (TDBox)

TDBoxes are 19" wide 1U height⁵ rack-mount modules (see Fig. 14.3). Two types of TDBoxes are available (A and B), depending on their outputs.

The input timing signal (IRIG-B or 10 MHz clock) can enter via a BNC, a RJ-45 connector or an optical transceiver⁶. A manual selector allows to choose the input used. The input signal is then transmitted to 1 BNC and 16 RJ-45 outputs (TDBox-A and -B). A delay line

⁴ With the system deployed in Virgo+, all the data sampling clocks were delayed from the clock of the GPS receiver by a known and fixed value of 16.041 μ s (due to the 3-km optical fiber length). This delay is taken into account in the reconstruction of the gravitational wave signal $h(t)$.

⁵ 1 U = 44.45 mm

⁶ Two other signals, called *running* and *sampling*, can also enter from the BNC or RJ-45 connectors. They are only output to the RJ-45 connectors. They were not used during Virgo+.

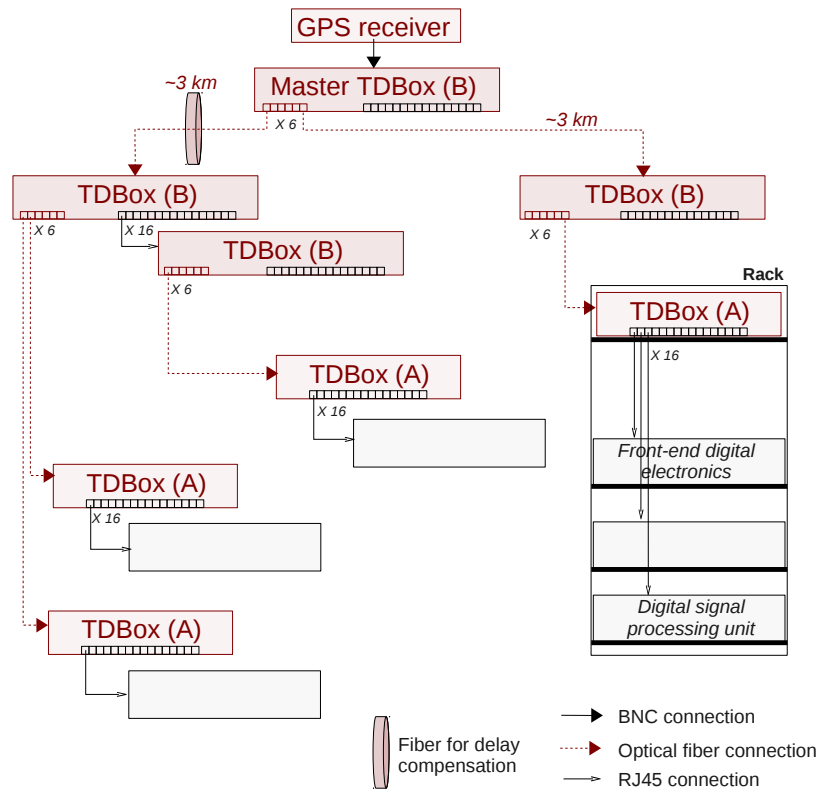


Figure 14.1: Diagram of the AdV timing distribution network, from the GPS receiver to the front-end digital electronics and processing units.

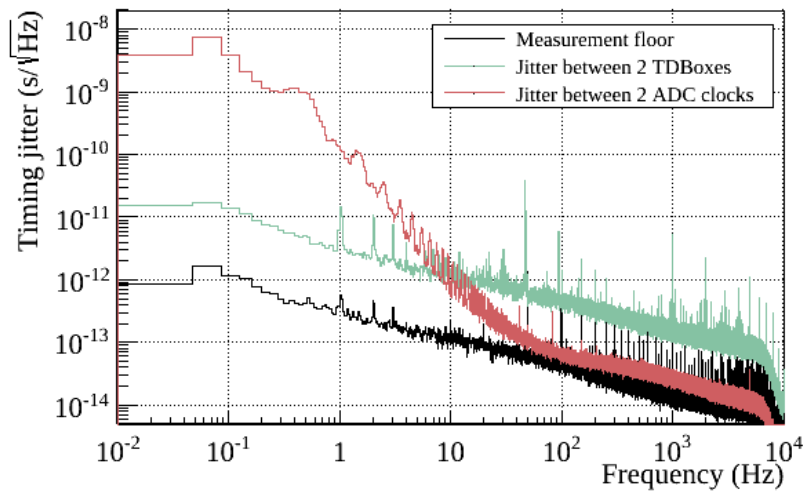


Figure 14.2: Jitter noise of the timing distribution system, measured in fall 2011. Green: jitter between the 10 MHz signals provided by two TDBoxes driven by the same central clock. Red: jitter between the 10 MHz signals generated by two different ADC boards, each of them having its own clock, locked on two different TDBoxes driven by the same central clock. For reference, the measurement noise floor is shown in black.

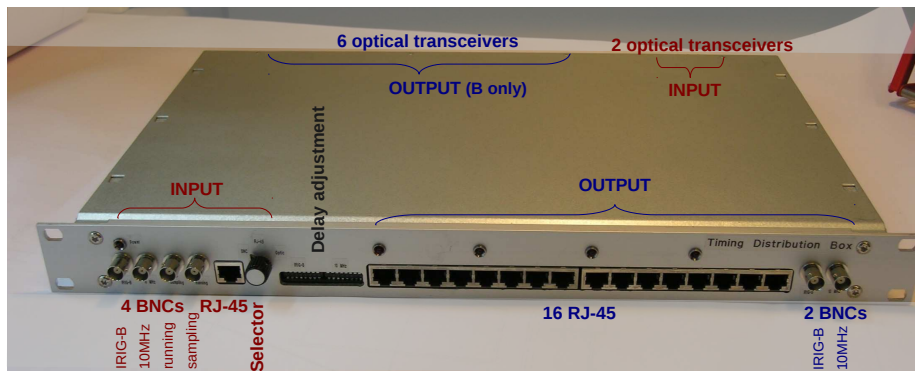


Figure 14.3: Photo of a Timing Distribution Box.

permits to adjust the propagation delay in the TDBox between 10 ns and 255 ns. It is used to fine-tune the delays between the racks. In the TDBox-B, the selected input signal is also transmitted, without adjustable delay, to 6 optical transceivers.

TDBoxes have been produced in 2008, with 10 and 27 TDBoxes available for AdV, of types B and A respectively. The foreseen setup of the timing distribution network for AdV will use 8 and 22 TDBoxes respectively.

14.2.1.3 Monitoring of the timing system

Different ways to monitor the timing system will be provided, some of them were already used during Virgo+ [445]. They will be important for the data analysis of the network of GW detectors:

- an auxiliary GPS receiver of the same type as the main one is used to cross-check the main GPS receiver stability. It is also a spare in case the main one fails;
- a receiver of a different type than GPS (Galileo for example) will be used to cross-check the main GPS receiver stability⁷;
- the time received from the distribution system by a real-time PC will be compared to the local time locked on an external **NTP** server in order to check the absolute time-stamp at the 10 ms level;
- the timing jitter of the distribution system is monitored using a free atomic clock;
- the error signals of the local clocks from each front-end digital electronics board are monitored.

14.2.1.4 Developments of the timing system for AdV

The system installed for Virgo+ will be used for AdV, updating the TDBox network to the modified hardware locations. No hardware developments are foreseen for the core of the AdV timing system. The number of produced TDBoxes is enough for the foreseen timing network, with a few spares available.

In the long run, in order to simplify the installation of additional boards and test benches and to possibly increase the number of monitoring channels, some developments are foreseen, with some options. The timing signal can be distributed via optical fibers down to the front-end electronics. This could be done via the TOLM network (see section 14.2.2). Another solution for isolated DAQ-boxes (see section 14.2.6) is to synchronize them via **NTP**.

14.2.2 Online Architecture for ITF fast controls

The longitudinal and angular global controls of the **ITF** are performed through synchronous fast digital loops (running at ~ 20 kHz). The so-called *TOLM network* has been built in order to exchange and process the data from the sensing electronics (cameras and **ADCs**

⁷ The old Virgo auxiliary GPS receiver, based on a VME crate, will be removed.

channels from injection and detection systems) to the driving electronics (DACs channels of the actuation of the suspensions and benches). A data format has been defined for the communication, the so-called *TOLM format*. A diagram of the network, interfaced with the timing distribution network, is shown Fig. 14.4.

For global control, the signals are collected by the sensing electronics in the different locations of the ITF. They are sent through optical fibers to real-time processing units (real-time PCs, DSPs, ...) that run the digital servoloops and send the data to other processing units or to the driving channels of the different ITF suspensions. A series of multiplexer/demultiplexer (Mux/Demux) boards is used to route the packets in the network.

Local controls can be implemented sending the data directly from the sensing to the driving part.

The centralized timing system previously described is used to synchronize the readout systems, the data exchanges over the TOLM network, the ITF controls and the servoloops.

The new components of the TOLM network for AdV will be designed with an Ethernet connection for easier configuration and monitoring (while it is done through the TOLM network for the Virgo+ electronics).

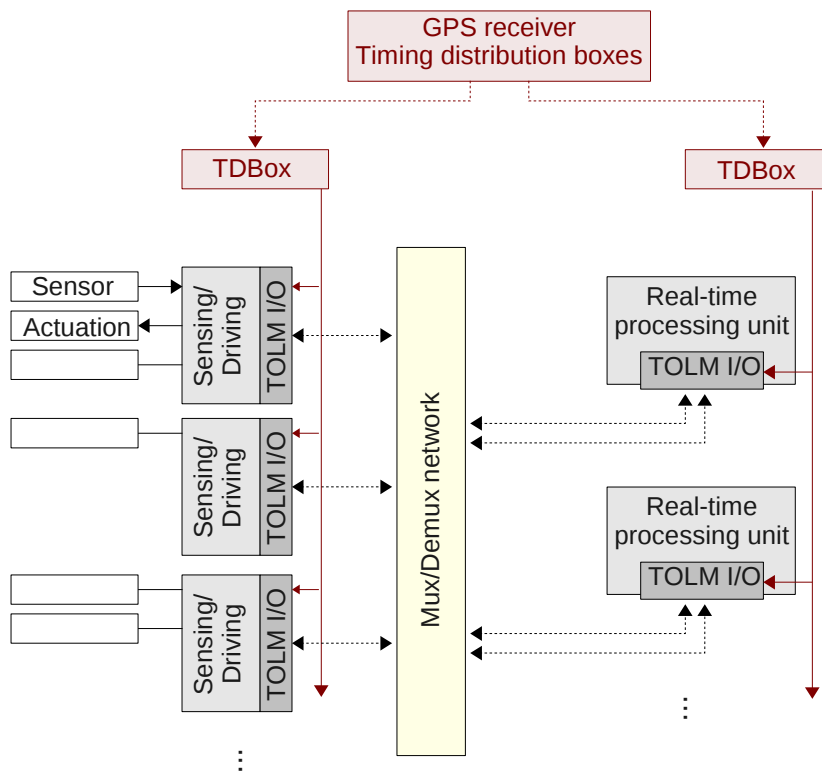


Figure 14.4: Online architecture of the ITF control through the TOLM network: diagram. Sensing and driving channels are distributed at different locations along the detector. Red: timing distribution. Grey: Digital electronics interfaced with TOLM network. Yellow: Mux/Demux network used to route the data packets. Dotted lines indicate optical fibers while continuous lines indicate copper cables.

14.2.3 The TOLM network

In this section, details are given about the hardware components used in the architecture of the online **ITF** control. The principle of the Timing and Optical Link Module (**TOLM**) interface is first given. The main characteristics of the components of the TOLM network are then discussed.

14.2.3.1 TOLM interface (Timing and Optical Link Module)

The TOLM interfaces are designed to interface both the timing system and the communications between the optical fiber network components to the front-end digitization electronics or to the real-time processing units. The common input/output of all the TOLM interfaces are:

- optical transceiver(s) (Small Form factor pluggable (**SFP**) format) with one input fiber and one output fiber for the configuration and data transfers;
- a timing RJ-45 input to receive a clock synchronized on the GPS (in general the IRIG-B signal from a **TDBox**);
- a specific interface to digital electronics (real-time PC, **DSP**, **FPGA**, ...).

The input timing signal is used to lock a local clock and to time-stamp the output data with the GPS time.

TOLM-based electronics receive and send data packets in the TOLM format through the optical fibers, the format of the TOLM packets is described in [455].

As shown by Fig. 14.4, the TOLM network is based on **different components** detailed in the following sections. Specific TOLM mezzanines have been built to interface some components to the TOLM network ; other components have on-board interface.

- At the network end-points, ADC and DAC channels are used for sensing and driving. Such front-end digital electronics has on-board interface with the TOLM network.
- Different types of real-time processing units are used.
 - Real-time PCs are processing units interfaced with the network through **TOLM-PCI** mezzanines (see Fig. 14.5(b)). The real-time PCs are used to run the online control-loop software in real-time, but also to format the data to the frame format and send them to the data collection system.
 - For the suspension actuation, the processing units are DSPs, interfaced with **TOLM-PMC** mezzanines (Fig. 14.5(a)). They do not format the data for the data collection system: their data are thus sent through the TOLM network to real-time PCs.
- The data packets are routed in the network through Mux/Demux boards.

Developments of the TOLM interfaces for AdV

The principle of the TOLM interface will not be modified and enough mezzanines of both types, TOLM-PCI and TOLM-PMC, have been produced (see table 14.1).

However, the current TOLM-PCI mezzanines installed in Virgo+ real-time PCs are based on the **PCI-X** standard. Since the PC standard has evolved to PCI-express (**PCIe**) in the new

computers, the new mezzanines built for AdV will use the PCIe standard.

| Mezzanine type | N_{prod} | N_{labs} | $N_{available}$ | $N_{foreseen}$ | |
|----------------|------------|------------|-----------------|-----------------|--------------|
| | | | | $N_{installed}$ | N_{spares} |
| TOLM-PMC | 44 | 2 | 42 | 20 | 22 |
| TOLM-PCI | 35 | 12 | 27 | 17 | 10 |
| TOLM-PCIe | 0 | 0 | 0 | 17 | 10 |

Table 14.1: Summary of the use of TOLM interfaces needs for AdV. N_{prod} : produced boards. N_{labs} : boards used in Virgo labs. $N_{available}$: boards available for AdV. $N_{installed}$: foreseen number of boards to be installed for AdV. N_{spares} : foreseen number of spare boards for AdV.

14.2.3.2 Mux/Demux

The Mux/Demux boards [455] are used to route packets of data which travel in the TOLM network. The boards have been deployed for Virgo+ in 2008.

The Virgo+ Mux/Demux board has the format of a VME 6U board. A view of the board is shown Fig. 14.5(c). Board interfaces are (i) 2 VME connectors for power supplies only (5 V), (ii) 8 bidirectionnal optical links (SFP transceivers) for data input and output, and (iii) a reset button, as well as leds to visualize the board status. It receives packets of data in the TOLM format at its input and routes them to the correct outputs. A "broadcast" capability exists: the same packet can be sent to several outputs.

The information needed to route the packets is contained in the header of each packet, configured by the user when a new packet is added to the network. Up to three Mux/Demux boards can be cascaded. The addresses of the outputs of the Mux/Demux are written in the packet header, as well as the "broadcast" option.

Foreseen evolution for AdV – For the first phase of AdV, the foreseen number of Mux/Demux boards to be installed is 25, with 2 spares available. The Virgo+ boards will thus be used. However, the speed of the communication, defined by the transceivers for serial communications, will be increased from 1.6 Gbit/s to 2.5 Gbits/s.

In the long run (for dual recycled configuration), in order to minimize the propagation time in the TOLM network, and to gain flexibility in the network architecture, developments of new boards will be needed. The following modifications are foreseen:

- use a box format instead of a VME board;
- increase the number of input/output channels from 8 to 16 or 32;
- add Ethernet connection for debugging, configuration and monitoring purposes;
- a local clock can be used for timing distribution over optical fibers.

14.2.4 Real-time processing units

14.2.4.1 Real-time PC (RTPC)

The Real-Time PCs (**RTPCs**) are processing units of the TOLM network. They are used to run, for example, the locking and alignment servoloops, or the generation of synchronous excitations for calibration purposes, but also to process the camera raw images and as front-end for data collection.

The diagram of the data interface in the real-time PCs is shown in Fig. 14.6(a). Data packets from the TOLM network are stored in a **FIFO** memory in the TOLM interface. On interrupt, synchronized with the timing system, the TOLM software transfers the data to a channel buffer. It also awakes the real-time processes in a predefined order, and they write their output channels to the channel buffer. Finally, the TOLM software put the data in the TOLM format and send them to the network through the TOLM interface. The whole sequence of real-time processing must last less than a period of the servoloop ($50\ \mu\text{s}$ for a loop running at 20 kHz).

The TOLM software also sends the data to the data collection system.

The real-time processing is based on the RTAI/Linux operating system [446]. The TOLM and global control softwares running on the RTPC are described in [447, 448]. The RTPCs selected in 2007 were Transtec X2100OAT55-B [449].

Foreseen evolution for AdV – Presently, the real-time processes are started by an interrupt sent by the TOLM interface when data are received. There is a few (6) μs delay between the interrupt generation and the start of the processes, with at some random times a larger delay (up to $\sim 15\ \mu\text{s}$). Another way to get the incoming data is based on *polling*. This method could help to contain the time distribution to within a few μs . It will be studied for AdV.

Other ways to optimize the use of CPUs and to reduce the latency will also be studied.

17 RTPCs are foreseen for the first phase of AdV. The current ones, bought end 2007, will be used for the commissioning of AdV. However, due to aging, they will be replaced by new selected ones during the first commissioning phase (thus before the first run of AdV). Their interface with the TOLM network will be done through TOLM-PCIe mezzanines. The new RTPCs used for ITF control will be installed and tested in parallel to the old ones such that the transition will be smooth.

14.2.4.2 Real-time DSPs

The DSPs used in the driving part of the suspensions are described in the SAT chapter. As described in Fig. 14.6(b), the input data are processed and sent to a DAC for driving. The processed data are sent back to the data collection system via the TOLM network.

For AdV, the DSP boards will be interfaced with the TOLM network with the existing TOLM-PMC mezzanines. 20 DSPs are foreseen to be installed in the first phase of AdV.

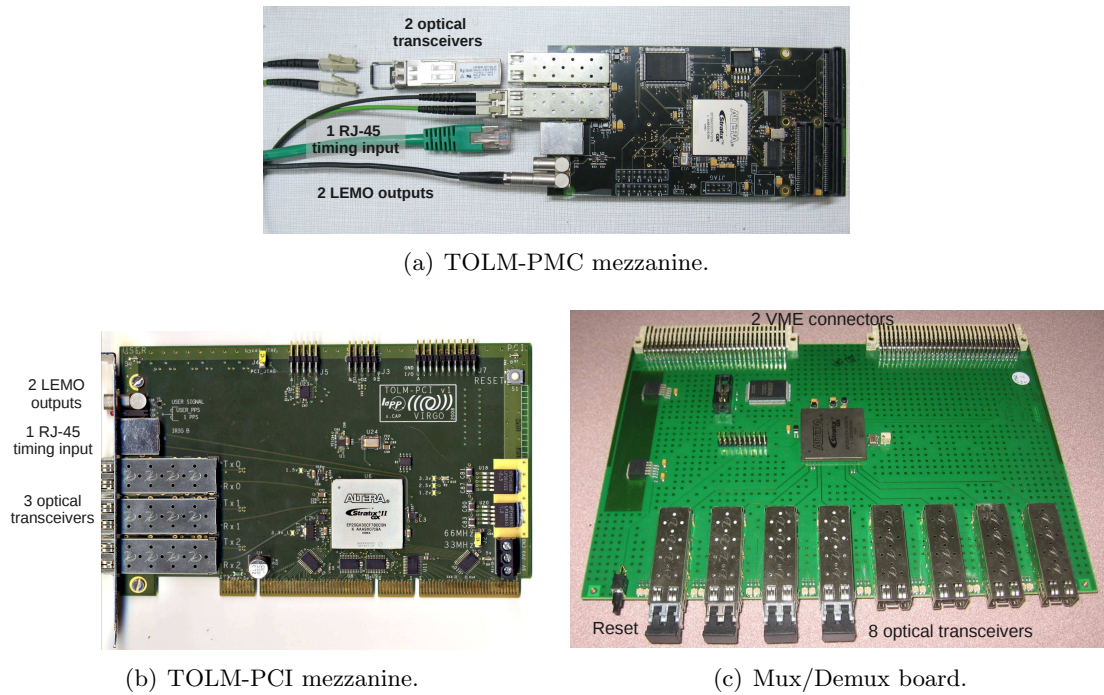


Figure 14.5: Pictures of the base components of the TOLM network developed for Virgo+.

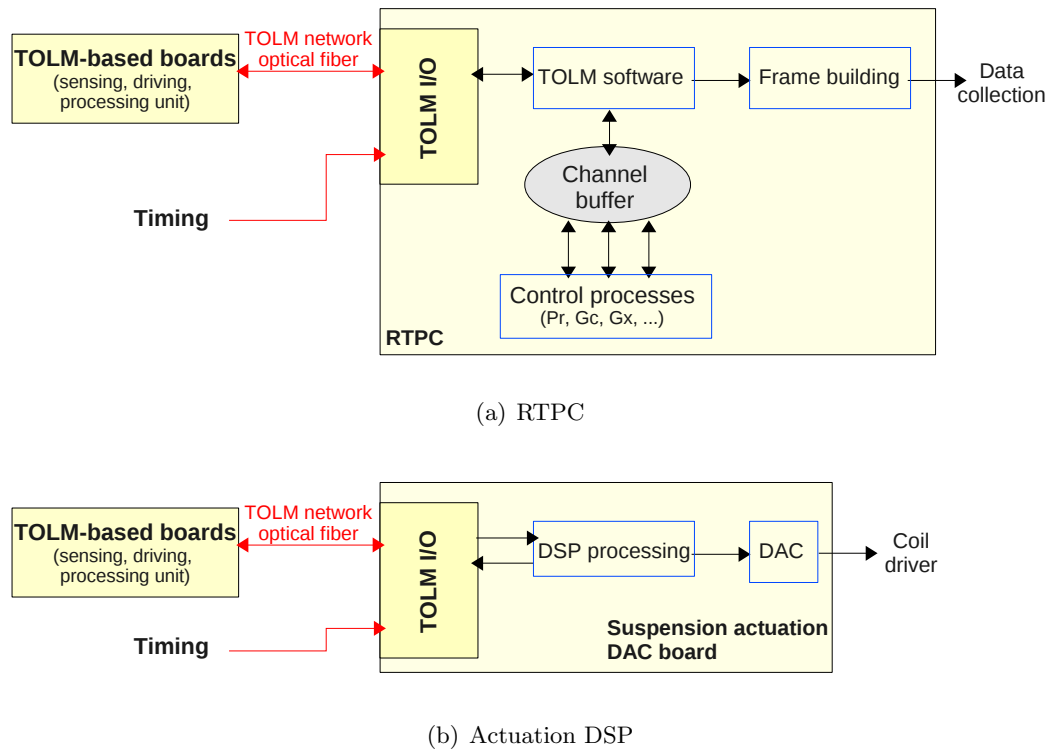


Figure 14.6: Diagram of the main processing units of the TOLM network: real-time PCs and DSPs for suspension actuation.

14.2.4.3 DAQ-boxes

The DAQ-Boxes, described in section 14.2.6, will contain DSPs and FPGAs that can be used as real-time processing units.

14.2.5 ADC7674 boards

The fast (800 kHz) ADC7674 boards [450], installed for Virgo+, are used to digitize up to 16 channels, to process them and to send them to the TOLM network. They are to the timing system (RJ-45 input) in order to generate a sampling clock synchronous within Virgo and to time-stamp the data with the GPS time. Views of the ADC7674 board are given in Fig. 14.7(a). It is a 3U VME size board, the VME being used only for power supplies (+12 V, -12 V, +5 V).

The diagram of one ADC7674 channel is shown in Fig. 14.7(b). The analog input signal (differential or single-ended, 3-pin LEMO connector) is sent to an analog mezzanine [451] with signal conditioning electronics (gain, anti-alias filters, compression filters, ...). The signal is then digitized at up to 800 kHz by the ADC7674 [452]. Data are low-passed by digital anti-alias filters (usually 8th order Butterworth filters) and decimated in order to reduce the frequency of the output signal down to its requested value. This processing is performed in DSPs and FPGAs. A so-called "main FPGA" receives the 16 digital signals from the 16 ADC channels, puts them together in the TOLM format along with their time-stamp, and sends the packets to the TOLM network through the optical SFP transceiver.

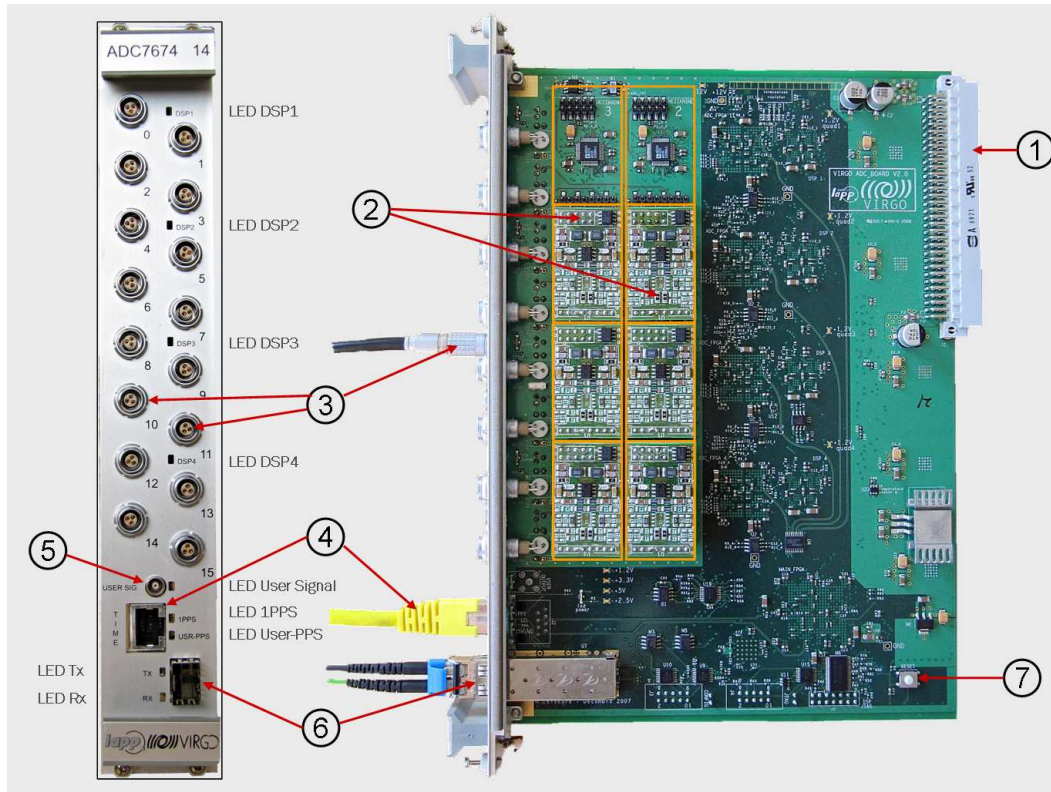
Different **clocks** are needed on the board. They are all generated on-board from a main clock, locked on the Virgo timing system. In particular, the clock that defines the sampling frequency of the ADCs (800 kHz in general) is built and distributed to all the ADC chips such that no delay is introduced between them.

The noise of an ADC channel with a flat mezzanine (anti-alias filter, but no compression filter), has been measured at the level of $200 \text{ nV}/\sqrt{\text{Hz}}$ above 100 Hz, for a full scale input range of $\pm 20 \text{ V}$ (see Fig. 14.7(c)). The noise in the region 1 Hz to 10 Hz comes from the analog preamplification stage of the mezzanine and from the nonlinear noise of the ADC depending to the shape of the input signal [453].

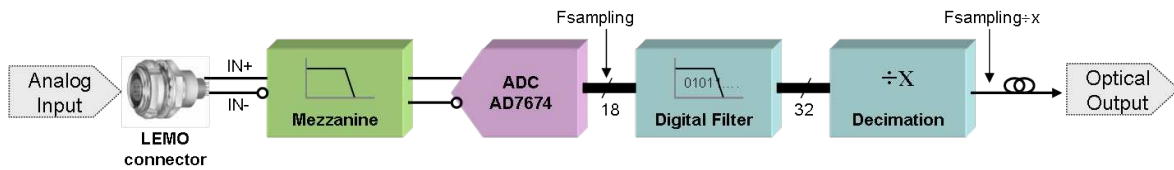
Foreseen evolution for AdV – The ADC7674 boards can be used as they are in AdV, increasing the speed of the optical link from 1.6 Gbit/s to 2.5 Gbit/s. Among the 60 produced ADC7674 boards, 40 are foreseen to be installed in AdV. Some specific noise issues will be taken into account when building new ADC channels for the DAQ-box.

14.2.6 DAQ-box general design

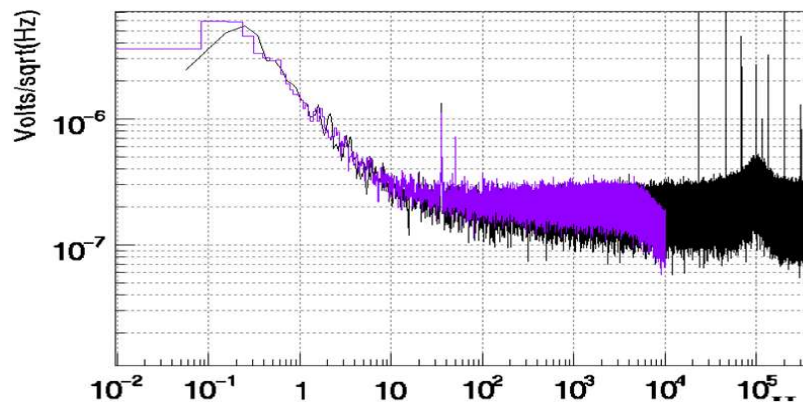
The DAQ-box [454] is being designed to host the digital demodulation channels needed by DET, the new general purpose ADC and DAC channels and the slow monitoring and control channels. A mother board will contain the common interfaces, i.e. a TOLM interface for timing and data distribution, and an Ethernet link for board management. The mezzanines will contain the specific functionalities.



(a) Views of the ADC7674 board (front panel and top view). 1: VME connector for power supply. 2: analog mezzanines. 3: 3-pin LEMO input cables. 4: RJ-45 timing input. 5: LEMO user output. 6: optical SFP transceiver for TOLM network I/O. 7: Reset.



(b) Overview of a ADC-channel of the ADC7674 board [450]



(c) Measured noise floor of an ADC channel of the ADC7674 board, as function of frequency (Hz). Black:channel sampled at 800 kHz. Purple: channel decimated to 20 kHz.

Figure 14.7: Overview of the Virgo+ ADC7674 board.

The preliminary design is to use a 19" 2U size box. The schematic of the box is shown Fig. 14.8(a). A box can include four mezzanines, which can be different. If needed, double-width mezzanines can be used.

The usual RJ-45 input will be used to receive the timing signal. The option to have optical fiber input is kept for future developments of the timing system. SFP optical transceivers will be available to connect the box to the TOLM network. An Ethernet connection is planned to manage the board, with RJ-45 and optical fiber connectors.

On the **mother board**, a main **FPGA**⁸ is used to manage the board configuration and the inputs/outputs. An embedded **ARM** processor interfaced with Ethernet will be used for board configuration, control, monitoring and firmware upgrade. The temperatures, voltages and currents of the board will be monitored to check of the electronics status and power consumption. The DAQ-Box will be able to send, through Ethernet, slow data to the data collection system (as a slow monitoring station). On-board frame builders could be run in the processor in order to send faster data, already formatted, to the data collection servers (see section 14.3.3.2). It might also be possible to build trend data from the measured channels.

Mezzanines are connected on the mother board via 170 pins **AMC**s connectors. A possible size for the mezzanines is 180.6 mm × 73.5 mm × 17 mm, with a custom front panel of 76 mm × 46 mm. Such a front panel could contain up to eight 3-pin LEMO connectors as the ones of the ADC7674 board.

For each mezzanine, an FPGA is used for versatile interfaces between the mother board and the mezzanine. A DSP is used to process the data sent by the mezzanine. For a given channel, the processing power is expected to be similar to the one available in the ADC7674 boards DSPs (one possibility is ADSP-21488 from Analog Devices, running at 400 MHz). The foreseen power supply levels available for the mezzanines are +3.3 V, +12 V, −12 V. Different interfaces are available. An **I2C**-bus is used for mezzanine monitoring (temperature, voltage, current). Management signals can be exchanged to reset the mezzanine, or check its presence and its type. A JTAG-bus permits debugging of the mezzanine. Finally, input/output are done through the FPGA. Different formats are supported for data input/output (LVTTL, LVDS, ...).

Following the electronics specifications (section 14.2.10.1), the DAQ-box will have two inputs for the power supply: the mains supply and an optional external DC power supply.

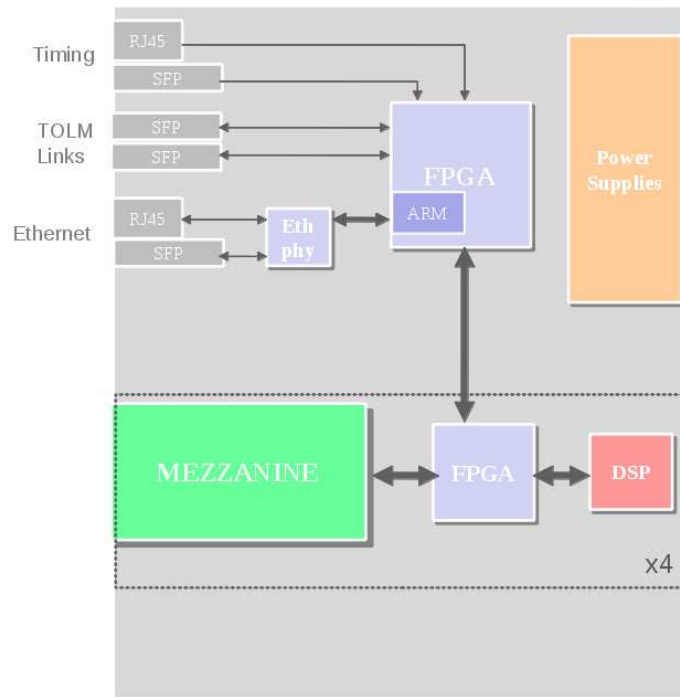
14.2.6.1 Mezzanine for digital demodulation

Digital demodulation of the photodiode signals at frequencies between 6 MHz and 132 MHz is foreseen for the AdV control (see the ISC chapter). Studies are on-going by the DET subsystem in order to validate the noise level of such a digital demodulation with respect to the constraints (see the DET chapter).

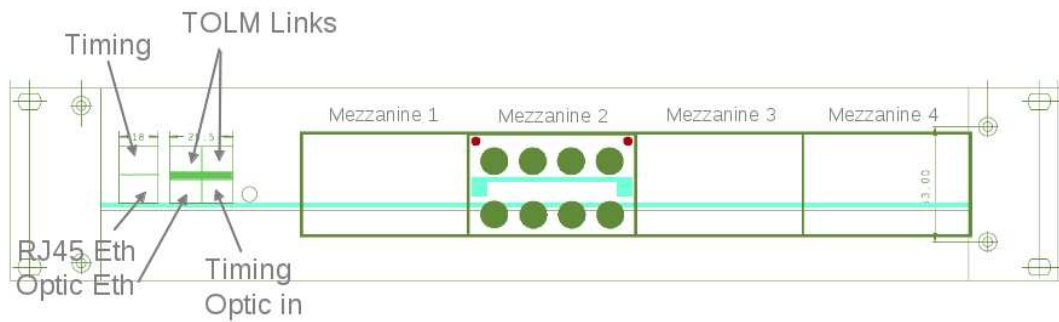
In such a mezzanine, the input RF analog signal will be low-pass filtered (around 100 MHz) and sampled at 400 MHz or 500 MHz by an ADC⁹. A software signal built in the DAQ-box will be used in a first step of the demodulation. The demodulation computations using this

⁸The foreseen FPGA is Cyclone V SX SoC.

⁹ The ADCs to be tested are the ADS5474 from Texas Instruments and the ISLA214P50 from Intersil.



(a) Diagram of the DAQ-box



(b) Foreseen view of the DAQ-box front-end.

Figure 14.8: Diagram and front-end view of the DAQ-box.

local clock will then be performed in a FPGA¹⁰ on the mezzanine, as well as a first decimation so that the output signal frequency will be lower than 1 MHz. The motherboard FPGA and DSP associated to the mezzanine will then complete the digital filtering and decimation of the data.

To be able to correct the jitter of the local clock of the DAQ-box relative to the modulation frequency, the distributed LO signal will have also to be acquired and demodulated by the local clock of the DAQ-box¹¹. Input connector type could be single-ended SMA connectors.

Digital demodulation induces strong constraints on the timing jitter of the clocks distributed to the mezzanine ADC and FPGA. The signal-to-noise ratio of the ADC being of the order of 70 dB and the maximum input frequency of the analog signal of ~ 160 MHz, the total jitter of the sampling must be below ~ 300 fs. Since the aperture jitter of the ADC is of the order of 100 fs, the clock jitter must be kept below ~ 280 fs. The expected noise of the clock jitter cleaner (LMK048XX) used on the 500 MHz ADC demodulation board prototype is shown in Fig. 14.9: the expected timing jitter RMS is below 200 fs, in agreement with the constraints.

In the following, the number of such mezzanines has been estimated assuming that a mezzanine has four input RF signals. The signal from a photodiode that enters on a mezzanine on a single input cable can be demodulated at all needed frequencies. However, limitations might come from the number of processed output channels to be managed by the mother

¹⁰ The foreseen FPGA is from Altera, Stratix IV EP4SGX70HF35C3N.

¹¹ Note that the different LO signals are synchronous and therefore we need to monitor the phase jitter of only one modulation frequency. Furthermore, the goal to lock them on the timing system would help digital demodulation.

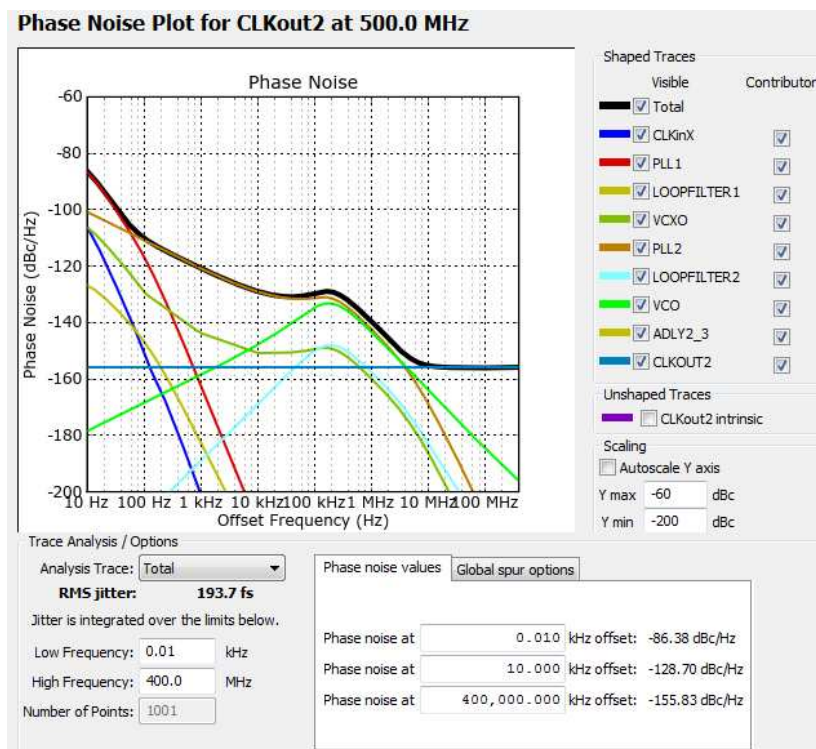


Figure 14.9: Expected jitter of a clock at 500 MHz (simulation).

board DSPs (for a given photodiode signal, the number of frequencies to be demodulated can go up to 5, which results in 10 processed channels after demodulation). This might decrease the number of possible input RF signals for some mezzanines.

One of the main advantage of digital demodulation instead of analog demodulation is its flexibility: adding (or removing) a demodulation frequency to a beam signal can be done loading new parameters on the demodulation mezzanine FPGA, with no or limited hardware intervention. The other big advantage of digital demodulation is the reduction of the front-end connections. For example, in the case of signals from the photodiodes at the level of the detection benches, 7 photodiodes signals are demodulated, for a total of 29 frequencies. It induces the following needs:

- analog demodulation: 29 RF inputs on analog demodulation boards, and 58 ADC channels (for the two quadrature signals);
- digital demodulation: 8 RF inputs on digital demodulation mezzanines¹².

In this case, the use of digital instead of analog demodulation thus removes the cabling of numerous demodulation boards, and reduces the number of needed ADC channels by more than a factor 7.

The principle of the digital demodulation is under test and will be validated end 2012. In case of excessive noise, analog demodulation boards and more ADC channels will be needed.

14.2.6.2 Mezzanine for fast DAC channels

General purpose fast-DAC channels will be used in particular to control the new SAS suspensions, the output mode-cleaner, the galvanometers, the locking auxiliary laser, the thermal compensation system, the noise injections for calibration and noise hunting.

The general purpose fast-DAC mezzanine will manage up to 8 DAC channels. The digital data from the TOLM network are processed by the FPGA/DSP associated to the mezzanine, sent to the mezzanine where they are converted by the DAC. The analog signal is low-pass filtered and sent to the driving as a differential signal via a the 3-pin LEMO.

The foreseen DAC chips are 400 kHz, 24-bit DACs (AD1955 from Analog Devices). Output analog anti-image filters will be similar to the input anti-alias filters used in ADC7674 channels.

14.2.6.3 Mezzanine for fast ADC channels

With the development of the DAQ-Box, new fast ADC channels, similar to the ones of the ADC7674 board, will be provided. The principle will thus be the same as described in section 14.2.5 and Fig. 14.7(b). A mezzanine will manage 8 ADC channels. It thus contains the analog input filters (anti-alias and compression filters), and the ADC chips (similar to the ADC7674, 800 kHz 18-bit ADCs). The input analog signal (differential or single-ended, 3-pin LEMO connector) is filtered and sampled, at 800 kHz maximum, by the mezzanine. It

¹² assuming that a beam signal incoming on a mezzanine can be demodulated at all the needed frequencies in a single mezzanine.

is then sent to the associated mother board FPGA/DSP for digital filtering and decimation. The data are then sent to the main FPGA.

This mezzanine will provide extra ADC-channels that will allow more flexible electronics installation, in particular for channels to be acquired under vacuum by the DET subsystem. Its development will also ease the future upgrades of the ADC channels. A new ADC chip could be selected to build the new ADC channels. Analog filters will also be studied. Specific upgraded mezzanines could be developed during AdV to replace some channels, when noise is limiting the detector sensitivity, improving the ADC chip and/or the analog electronics.

14.2.6.4 Mezzanine for slow control and monitoring

Power supply and slow monitoring and control of electronics is needed for AdV. The main need comes from the DET subsystem, which will provide electronics to supply the power and control the photodiodes (both longitudinal and quadrant). DAC channels are needed to control the photodiode polarization voltage (V_{bias}), the gain selection of the preamplifier and a shutter in front of the photodiode. ADC channels are needed to monitor the V_{bias} and the current flowing in the photodiode (power monitoring). For photodiodes on benches under vacuum, ADC channels for temperature and pressure monitoring are foreseen. All this could be implemented as a mezzanine for the DAQ-Box. We expect that several photodiodes could be managed by a single mezzanine¹³. Slow ADCs and DACs of this mezzanine could be used for other slow monitoring and control purposes (environmental monitoring or power supply and trigger of digital cameras for example, see section 14.2.9).

If sufficiently slow, the input/output of such a mezzanine could be done only through the Ethernet network (already with the frame format), instead of the TOLM network.

14.2.6.5 DAQ-box: planning and foreseen needs

The specification of the mother board and mezzanines interfaces (mechanical and electronics, [454]) has been completed in March 2012. In order to develop the mezzanines in parallel, a testboard will be designed and built at LAPP by mid-2012, with a main FPGA to manage the TOLM interface and the mezzanines. This testboard will allow to test the mechanical structure of the mezzanine and the performances of the mezzanines and FPGA management.

In parallel, a prototype of a fast DAC mezzanine will be designed and built for summer 2012. The mezzanine performances will be tested at LAPP and then used at Nikhef to control the SAS system.

A testboard for digital demodulation will be tested at LAPP in 2012 to study the 400 MHz and 500 MHz 14-bit ADCs and the digital demodulation performances. It will be the base for the developments of the demodulation mezzanine in 2013.

The detailed design of the motherboard will start beginning of 2013, when a new low-consumption FPGA will be available. The phases of designing, building and testing the prototype are foreseen to last about one year.

¹³We assumed that a mezzanine could manage 4 photodiodes in the estimation of the DAQ-box needs.

The fast ADC mezzanine as well as the slow control and monitoring mezzanine will be developed in 2013 and 2014.

At least 30 DAQ-boxes are foreseen to be installed in the first phase of AdV, with about 20 mezzanines for digital demodulation, 25 mezzanines for fast DAC channels, 40 mezzanines for fast ADC channels and 17 mezzanines for slow control and monitoring.

14.2.7 Delay of the digital control loop system

In this paragraph, we give an estimation of the delay introduced by the system from the sensing signal to the actuation signal. This is an important parameter for the design of the **ITF** locking servoloop filters [440] that will run on the real-time PCs (the phase margin must be kept high enough, which is easier with a small delay from electronics). After an estimation of the delay of the Virgo+ system, we give preliminary ideas to reduce the delay for AdV.

14.2.7.1 Case of Virgo+

The Virgo+ longitudinal control loop (DARM) was running at 10 kHz. The delay from photodiode sensing to actuation signal was estimated to:

- Sensing in Analog-to-Digital Converter (**ADC**) channel: 115 μ s. Anti-aliasing filter in analog mezzanine: 6 μ s ; digital anti-aliasing filter (8th order Butterworth for channel sampled at 20 kHz): 109 μ s. The ADC clock is in phase with the main 10 kHz clock.
- Transfer from ADC to real-time PC: ~ 30 μ s. Transfer itself: ~ 20 μ s and real-time PC clock delayed by ~ 30 μ s from the main clock.
- Processing and transfer from real-time PC to actuation: 100 μ s. Processing in the real-time PC (~ 60 μ s) and data transfer to the **DSP** actuator (~ 20 μ s): the DSP gets the data at the next clock tick (clock delayed by ~ 30 μ s from the main clock).
- Driving (processing): 100 μ s, from processing in the DSP and Digital-to-Analog Converter (**DAC**) settling.
- Driving (**DAC** channel): 180 μ s, from anti-imaging filter.

The total delay is ~ 550 μ s.

14.2.7.2 Possible improvements for AdV

Such a delay would limit the performance of the DARM loop for AdV in the dual recycling configuration. An option to reduce the delay could be to run the loop at 40 kHz (instead of 10 kHz), to use the foreseen new Mux/Demux boxes with less stages and to reduce the order of the anti-alias and anti-image filters (see next paragraph). In this case, the delay would be of the order of 100 μ s (20 + 10 + 25 + 16 + 10 + 20 μ s coming from the ADC anti-alias filter, the data transfer to the RTPC, the computation time in the RTPC, the data transfer to the end mirrors, the computation in the new actuation DSPs developed by SAT and the DAC anti-image filter). The hardware and software improvements to fit this delay will be further studied before the SR mirror is installed.

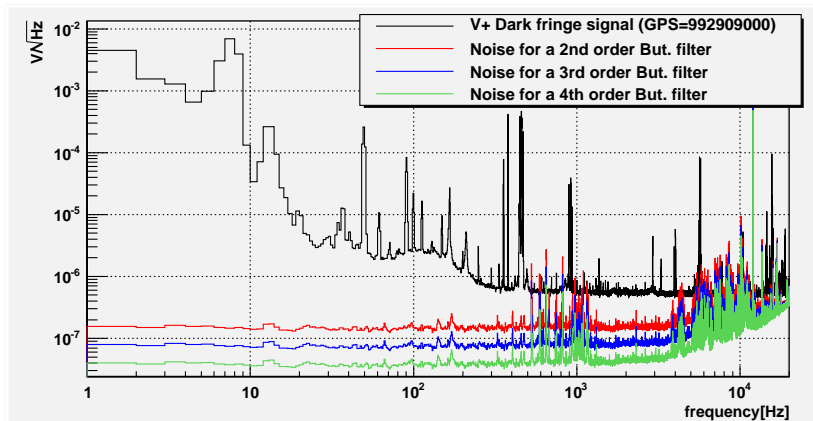


Figure 14.10: Estimation of the aliasing noise on the Virgo+ dark fringe signal (*Pr_B1_Acp*). Black: initial channel, sampled at 80 kHz. Red/blue/green: level of noise coming from aliasing in the case the channel is sampled at 40 kHz, after a 2nd/3rd/4th order Butterworth filter is applied.

Assuming that the order of the ADC anti-alias filter used by the control loop is reduced to three (instead of eight in Virgo+), the corresponding delay will be reduced to 17 μ s. The reduction of the order of the ADC anti-alias and DAC anti-image filters will slightly increase the noise of the control loop. The excess noise is illustrated by Fig. 14.10 which shows the effect of a reduced filter for Virgo+, if the anti-aliasing was only a second, third or fourth order filter with a 20 kHz cutoff frequency. The plot has been made with VSR4 data sampled at 80 kHz in science mode. Of course, the unity gain frequency was much lower than the foreseen AdV DARM frequency and, at 200 Hz (300 Hz), the DARM signal was already a factor 3 (10) below the sensitivity. In this case, the contribution from the aliasing of the high part of the spectrum would be negligible. In addition, since the $h(t)$ reconstruction uses an algorithm which subtracts the control signals, any additional noise in the control signal is further reduced in the final data. Translating this signal to a higher unity frequency gain, like 200 Hz, means that the bump will be at a slightly higher frequency, still with the noise due to aliasing much lower than the sensitivity.

Finally, it should be reminded that a similar anti-aliasing filter is done by the DSP of the ADC, after the ADC digitization. Therefore, the frequency cut of the filter could easily be tuned during commissioning to move a possible large resonance out of the control band. Furthermore, the signal used for the $h(t)$ processing could be acquired in parallel with a more aggressive anti-aliasing filter to keep the $h(t)$ signal clean of any folding effect.

14.2.8 Possible topology of the AdV TOLM network

The deployment of the timing and TOLM networks for Virgo+ is described in [443]. With the present Mux/Demux boards, the constraints to build the TOLM network are:

- maximum of 8 links per Mux/Demux board;
- cascade of at most 3 consecutive Mux/Demux board along a signal transmission;
- for the driving, the tidal control imposes a direct link between the suspensions of a same cavity: IB/SAS-IB, NI/NE/SAS-NE, WE/WE/SAS-WE, BS/PR/SR/SAS-PR and OB/SAS-OB;

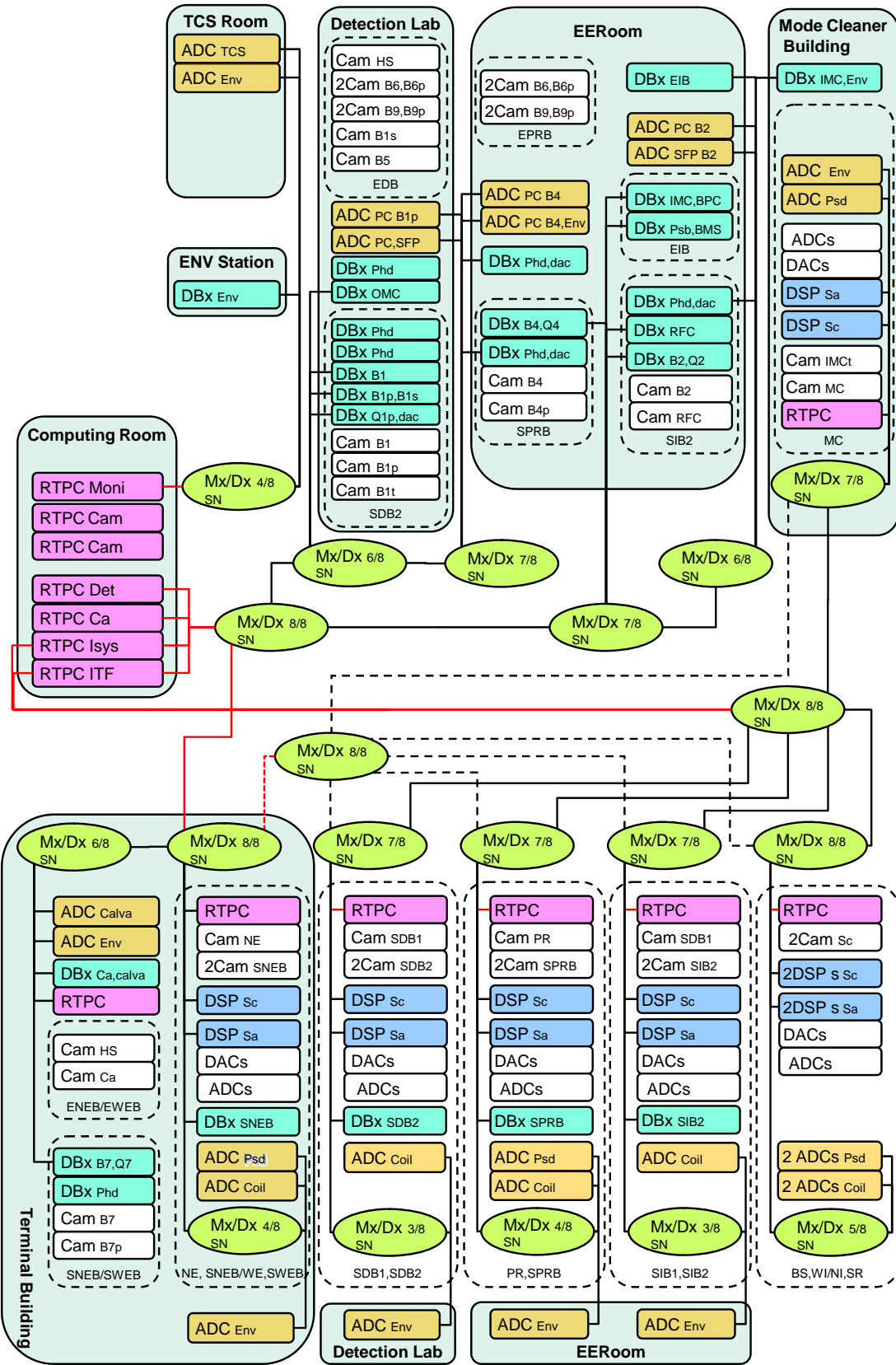


Figure 14.11: Foreseen topology of the TOLM network for AdV.

- 3 bi-directional mono-mode optical fibers for the TOLM network are installed between each terminal building and the DAQ room.

It results in the foreseen topology shown in Fig. 14.11. This topology allowed to estimate the number of digital electronics components to be installed in AdV, as summarized in the previous sections. It is foreseen to install all the real-time PCs of the central area in the computing room.

14.2.9 Components of the camera acquisition

Cameras and visualization tools are needed for beam imaging and for local controls. They provide digital images at frequencies up to 50 Hz.

The system used for Virgo will be upgraded [456] for AdV following the general layout sketched in Fig. 14.12: the digital cameras will be replaced ; they will be power-supplied and controlled by the so-called *CameraBoxes* [458], the data being collected and distributed to real-time PCs through a dedicated gigabit Ethernet ("GigE") network. The CameraBox is remotely programmable via Ethernet and can manage up to 8 cameras. It generates the trigger signals for the cameras synchronized with the AdV timing system and it provides the camera power supply. Camera configuration and image visualization are performed through the Ethernet network using as interface the *Imaging* and *Telescreen* softwares.

Ethernet switches will be used so that a single computer can work with several cameras. The **real-time PC** has a TOLM interface in order to send the result of the imaging processing

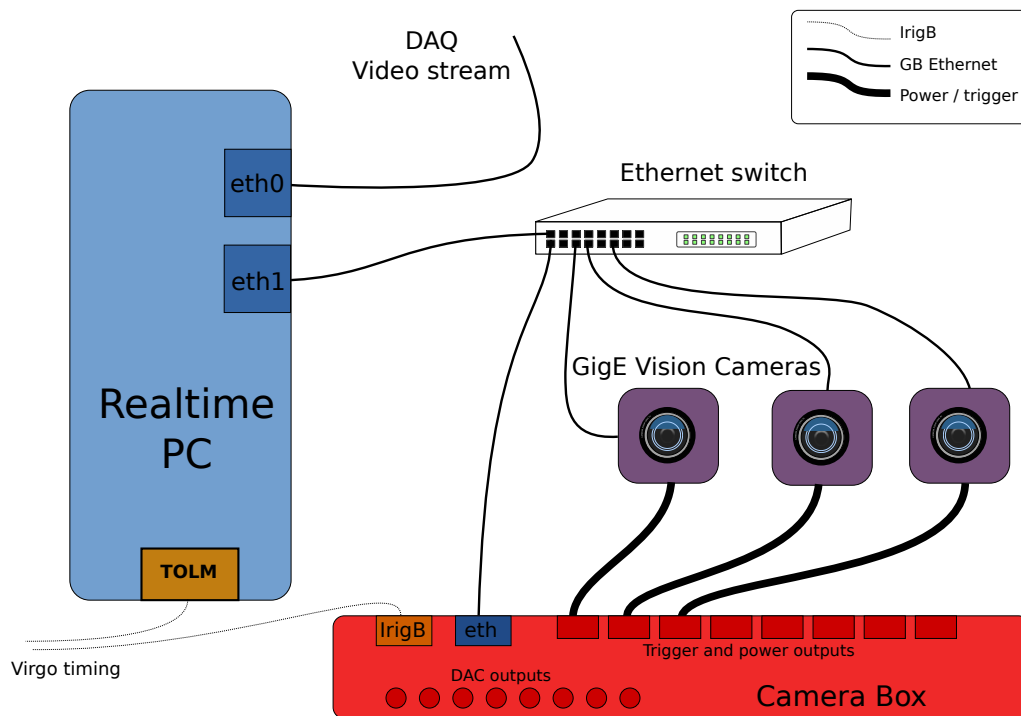


Figure 14.12: Camera network diagram.

to the relevant devices synchronically with the timing system. In Fig. 14.4, the cameras are *sensors* and the real-time PC are *sensing* devices.

On-site commissioning of the new system has started in fall 2011, at the end of Virgo+.

14.2.9.1 Digital camera

The digital cameras are used for different types of applications, with different constraints:

1. Beam imaging: the camera is located on an optical bench and the beam is directly sent to the CCD without any lens. A large CCD is convenient to collect the full beam without the need of a precise camera alignment.
2. Local controls: the camera is equipped with a lens to image a target on the bench. The resolution on the position is better when there are more pixels in the CCD, when the pixels are thinner and when the pixel noise is lower. The size of the CCD is not a strong constraint.
3. Test mass monitoring: cameras are foreseen to monitor the light diffused on the mirrors. The same cameras as for local controls will be used.
4. Thermal Compensation System subsystem (TCS): cameras are needed to image the TCS beams and others are needed for the Hartman sensors.
5. monitoring of the locking auxiliary lasers (ISC subsystem)

Foreseen evolution for AdV – Cameras for beam imaging have been selected [457]: the Smartek GC1392M have been chosen and 10 have been bought. The cameras needed for the AdV controls are summarized in Fig. 14.13, excluding cameras for video monitoring. The different cameras will be selected and bought.

14.2.9.2 CameraBox

The CameraBox is used to supply power and provide a trigger signal to the AdV cameras, synchronized on the Virgo timing system. Its design is generic enough in order to be able to connect different cameras from different vendors. The box is a 19" rack-mount 2U module. A CameraBox can supply up to 8 cameras with +12 V DC, either from the mains supply with an internal AC-DC converter (with a maximum power of 80 W) or from an external +12 V DC source.

The trigger sent to the cameras can be synchronized with the incoming IRIG-B signal from the Virgo timing system. In order to reduce the noise, the internal DC-DC converter is synchronized with the Virgo timing system.

The CameraBox also provides 8 analog outputs driven by 16-bit DACs (0.025 to 11.92 V output). They provide local control for devices like the camera illumination or a camera shutter. The camera box temperature can be read through the Ethernet network.

For a given tower or optical bench where cameras will be used, a CameraBox and an Ethernet switch will be placed near them. This will ease the installation of additional cameras and reduce the cabling work.

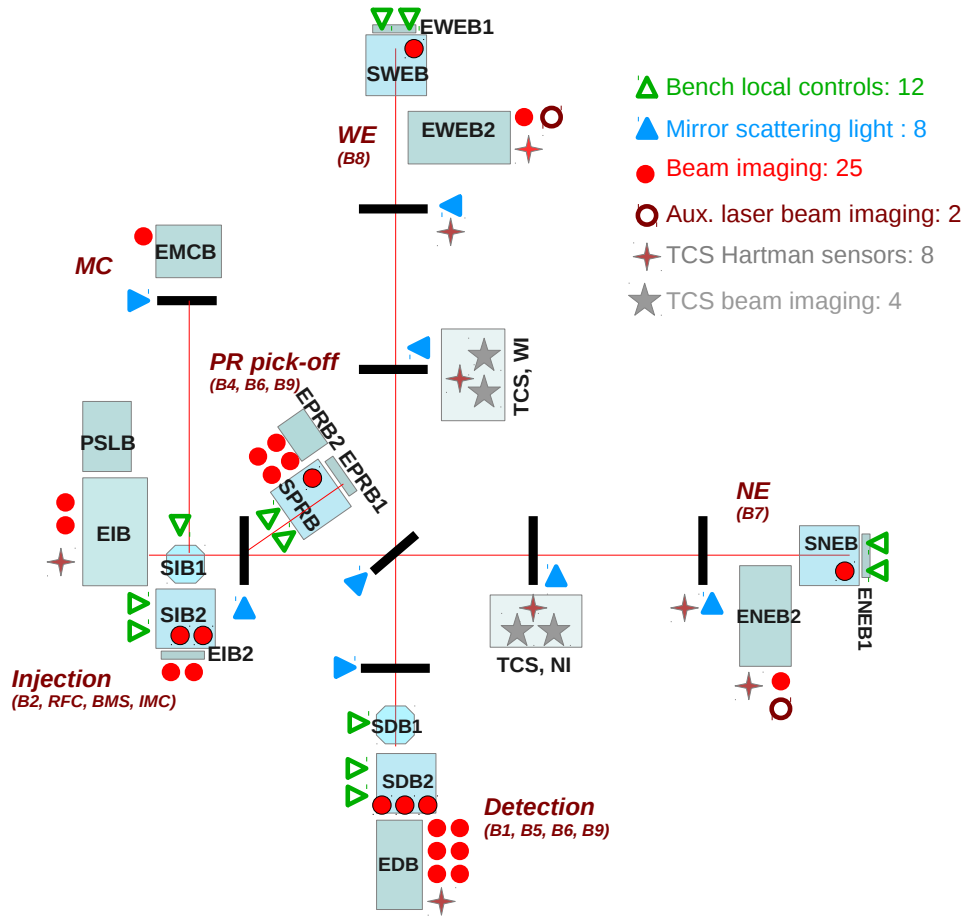


Figure 14.13: Foreseen locations of the different types of digital cameras in AdV. The mirrors and optical benches are represented.

Foreseen evolution for AdV – The foreseen number of CameraBoxes to be installed in the first phase of AdV is ~ 15 . 5 have been produced in 2011 for their commissioning and 15 additional ones are already planned to be produced. This is enough for the start of AdV. In the long run, it could be useful to have DAQ-box mezzanines that handle the power supply and trigger of a few cameras (2 – 4). This could be done by the slow monitoring and control mezzanines, or specific ones.

14.2.9.3 Software and data flows

When a camera receives a trigger from the CameraBox, it sends an image to a real-time PC through the Ethernet network.

A real time image analysis is performed by the software *Imaging*: computation of errors signals for local controls, selection of the interesting zones in the image, data compression. The processed information is then sent to the data collection and, for the local control, to the actuators through the TOLM network. For one camera, the raw data flow of ~ 13 MBytes/s is reduced down to ~ 2.5 kB/s. Compared to Virgo, Imaging replaces the old GxServer software. Imaging has been designed to be compatible with the existing tool used to visualize and process the camera images, *GxClient*. However, GxClient will have to be upgraded.

In parallel, the images can be transferred to a task providing a compressed video stream such that the output images use a much reduced network bandwidth (the compression factor is estimated to ~ 20). A system called *Telescreen*, based on gstreamer¹⁴, is used to multiplex the video streams to provide images for the big screens in the control room, to record on demand some of the video sequence, and to forward the streams to other remote displays on demand.

The estimation of the front-end data flow from the cameras is done assuming:

- 20 cameras are used for bench local controls and mirror monitoring, with 50 Hz images of 512×512 8 bits pixels;
- 25 cameras are used for beam imaging, with 10 Hz images of 512×512 8 bits pixels.

It results in 250 MBytes/s for the mirrors and local controls data and 65 MBytes/s for the beam imaging data. However, this flow is divided between different local subnetworks and processed by the associated real-time PC in order to select the interesting zones of the image and to compress them. The video output flow after the image compression can be estimated to ~ 20 MBytes/s.

14.2.10 Electronics specifications

In this section, we give the main recommendations and specifications for custom electronics design and installation. More detailed specifications are given in [459] and [460].

14.2.10.1 Cabling recommendations

Two options are available for the overall view of the electronics installation.

¹⁴<http://gstreamer.freedesktop.org/>

1. **Put all the possible electronics as far away from the detector as possible.** In this option, the conditioning and digital electronics is put far away from the detector, in a centralized area. Long cables with analog signals are then used to connect the front-end electronics of the different subsystems to the centralized electronics. Possible noise could come from crosstalks in the cables or from ground loops between the different subsystems.
2. **Put all the digital electronics close to the front-end electronics.** In this option, short cables are used to transmit the analog signals inside each subsystem, and long cables only transmit the digital signals between the different subsystems. Possible noise could come from the presence of electronics close to the detector parts. The option to use DC power supplies located away from the electronics area should be provided to reduce noise if necessary.

The second option has been chosen, which implies the following specifications for the electronics:

- the digital and ADC/DAC electronics will be put close to the front-end electronics (analog cables will be less than ~ 5 m);
- optical fibers will be used for digital transfers along long distances between subsystems (more than ~ 5 m).

Standard cables, connectors and philosophies shall be used for every class of signals: for **RF** signals, coaxial cables and connectors shall be used, while for "low frequency" signals (below 100 kHz), shielded twisted pair cables driven differentially shall be the norm. Details about cable segregation in trays and standard connectors are given in [459], section 5.5, and in [460], section 6.7.

14.2.10.2 Power supply

Two solutions are possible to power AdV electronics systems: (i) the AC mains, or (ii) DC power supplies at system level wherever needed (in particular in case the internal AC-DC converters generate noise for the detector).

Given the overhead of the construction of a general DC distribution system and the limited proof of benefit, the first solution will be used. However, in order to have the option to cure specific problems, specification for the custom designed electronics is to have the two power supply inputs available: the AC mains and a DC input. The choice between them is done via a manual selector on the electronics. An example of such device is the CameraBox (section 14.2.9.2). In principle, commercial equipment can be simply plugged in the available main outlets.

The specifications on the crates for both options are described in [459], section 5.1. In case of DC power supply, linear power supplies could be put "far" from the racks/detector sensitive area, and DC-DC converters could provide the needed DC voltages at the rack level.

DC-DC converters can also be a source of noise, both for on-board converters or for bigger rack-level converters. They should have their switching frequency synchronized with the

Virgo timing system such that the noise, if present, is well controlled at a fixed and known frequency¹⁵.

14.2.10.3 Electronics cooling and power consumption

If possible, electronics cooling should be done by radiative and convection means, aiming at using only crates without fans. If small on-board fans are needed, remote tuning of the speed could help noise hunting (however, this would decrease the acoustic noise but increase the electro-magnetic noise). They should have low electromagnetic noise coupling inside the board. The use of fans can be reduced by *minimizing the power consumption* of the designed electronics.

Possible improvement of the cooling without fan would be to build flexible hoses to bring fresh air from air conditioning close to the racks (interface with INF subsystem).

Temperature monitoring of the electronics boards should be available with two aims. First, it can be used to monitor the boards status. Second, it can be used to optimize the board cooling by switching off un-necessary fans, or decreasing their speed in order to reduce the fan noise introduced in the ITF signals.

14.2.10.4 Racks specifications

The main purpose of the racks is to hold and operate electronics. In addition, they can be used as shields if it is wrapped into a closed metallic enclosure. Some old racks (220 cm high, 60 cm wide, 60 deep) dedicated to host 19" wide equipments will be used for AdV. However, new racks will be needed and slightly larger version is recommended: 220 cm × 80 cm × 80 cm. They have internal provision for cable routing on the side of the rack, and some extra-room on the back to ease internal cabling. The use of such wider racks would help to keep their doors shut for a better shielding.

The reference solution presented in [460], section 5.4, is a Schroff Varistar Zone 3 rack.

Of the order of 50 racks are foreseen to be installed for the first phase of AdV.

14.2.10.5 Installation monitoring: hardware and inventory database

An HardWare Inventory and Installation database (HWII)¹⁶ has been developed (see section 14.4.2.1) in order to track the status and history of the different parts constituting Virgo. To fulfil this goal, all the electronics (and any hardware) installed on the detector will have to be inserted in this database.

14.2.10.6 General specifications

A large fraction of custom electronics will be hosted in chassis and crates located inside 19" racks. All of them should share the following common characteristics: (i) an on/off switch

¹⁵ For reference, ltm4606ev converters have been used for the CameraBoxes (0.6 to 5 V. maximum 6 A, ~ 20 euro each). ltm4628 will be used for DAQ-box test boards (0.6 to 5 V. maximum 16 A, ~ 23 euro each).

¹⁶<https://pub3.ego-gw.it/itf/hwii>

and a green LED clearly indicating the presence of power; (ii) power connectors on the back, with a fuse on each power line (if more than one); (iii) a yellow LED in parallel with the fuse that lights on when the power is tripped; (iv) a crowbar circuit shall protect the unit from power supply failures wherever applicable.

The enclosure containing the electronics shall be metallic, rack-mountable, and all of them shall be grounded.

Crates should be designed to allow removal of the modules by sliding them out from the front. To improve reliability, all functional connectors shall be left alone once the integration of the units is validated. Designers shall therefore add diagnostic provisions to their units to monitor relevant signals and parameters without interfering with the normal operation of the electronics.

14.3 Data collection system

The tasks of the data collection system (the so-called **DAQ** system) are:

- to collect all the information needed for the control, the monitoring of the detector and the extraction of the gravitational wave signal in a coherent way;
- to build different data streams for online processing and online access;
- to provide the data streams to the storage system.

The data acquisition is synchronized over kilometer lengths, and the expected front-end data flow is of the order of 400 MBytes/s : 300 MBytes/s from the camera images (mirrors and benches local controls and beam imaging, see section 14.2.9.3) ; the other 100 MBytes/s come from all the other sensors and control loops. Data reduction (decimation, compression, image processing, ...) must be processed in order to limit the flow in the Ethernet network and to keep reasonable storage disk space. Reduction factors higher than 3 and 20 will be obtained for the time series data and for the camera data, respectively.

For reference, excluding the camera data, the last Virgo+ run (VSR4) provided 36 MBytes/s of uncompressed data (12 MBytes/s after compression). The addition of new systems (more suspended benches, more TCS, ...) in AdV will increase the data flows.

14.3.1 Data format: frame

The format of the detector data has been defined in 1996, the so-called *frame* format. It has been developed in collaboration within the Virgo and LIGO experiments and is being used to exchange the data for coincident data analysis. Specifications on the common format and rules for revisions have been defined [467]. The frame library is defined in the package Fr [468]. The Virgo detector generates a continuous data flux. The frame format is based on the definition of time slices of the data flow, with slices of a few seconds. Every time slice contains different types of data: times series, images, spectra, events.

All the data structures are related to a central structure, the *frame header*, which contains the high-level information such as the frame GPS time, the frame duration, the frame number, the data quality...

A frame file¹⁷ usually contains several frames and terminates with a *table of content* (TOC) which is created when the data are written on disk. When reading the file, the TOC allows a fast random access to the frames and the different data.

ASCII files are used to ease the data access: the *ffl*, or *frame files list*. It contains basic information about the data files written on disk: location, GPS time of the first frame, duration of data content, number of events in the data file. Programs can then easily access any data file, and thanks to the TOC, they can rapidly access any data vector in the file.

¹⁷Frame file extension is gwf

14.3.2 Architectural description

The general architecture of the data collection is described in Fig. 14.14.

The data to be collected come from the front-end electronics. It is the vacuum data, environmental and **ITF** monitoring data, control signals coming from the local and ITF loops and calibration signals. The raw data are collected, formatted and merged in the front-end data acquisition. Part of the data can be provided to the automation system used to control the ITF, or reduced to build different data streams. At this level, the data can be accessed online by experts for data acquisition debugging and by ITF commissioners with low latency¹⁸ (< 1 s).

The data are then used for detector monitoring, online reconstruction of the **GW** signal $h(t)$ and online data processing (data quality, data analysis). They are available online for users access within less than¹⁹ 30 s (this will be reduced for AdV, optimizing the $h(t)$ reconstruction).

The raw data and data produced by the different intermediate processes are finally put in different streams for storage. The final files are readable on disk with latencies from 2 to 30 minutes depending on the streams. They are then available for offline use.

The typical data collection flows and stream storage expected for AdV at the different levels are given in the left column of the Fig. 14.14. AdV raw data is expected to represent a storage of 1 to 2 TBytes/day.

14.3.3 Data assembly and distribution

The data exchange between the different servers must be done through the software framework used for communication between the servers. In this section, the current software for communication, Cm [466], is used as the baseline. However, other softwares are under study (see section 14.4.1).

14.3.3.1 Frame data exchange between servers: Fd library

A library, called Frame Distribution (**Fd**) [469], has been developed in order to manage the data exchange with the frame format between the different servers of the DAQ system. It is based on the use of shared memories [470] to put the data in common areas and of the Cm library which deals with the **TCP/IP** protocol on the Ethernet network. Using the Fd library, the frames can be sent and received through different means: the Ethernet network, shared memories, or on disk space.

FdIOserver is a tool that reads and writes data from and to Ethernet, disks or shared memories and offers signal processing features like data compression, channel selection or frame merging. In the data acquisition pipeline, it is mainly used to send via the Ethernet

¹⁸ We define the latency as the duration between the time of the first data sample of a *frame* and the time when it is accessible.

¹⁹ At present, there is no theoretical constraint below 1 min on the time gap between gravitational waves and electromagnetic light.

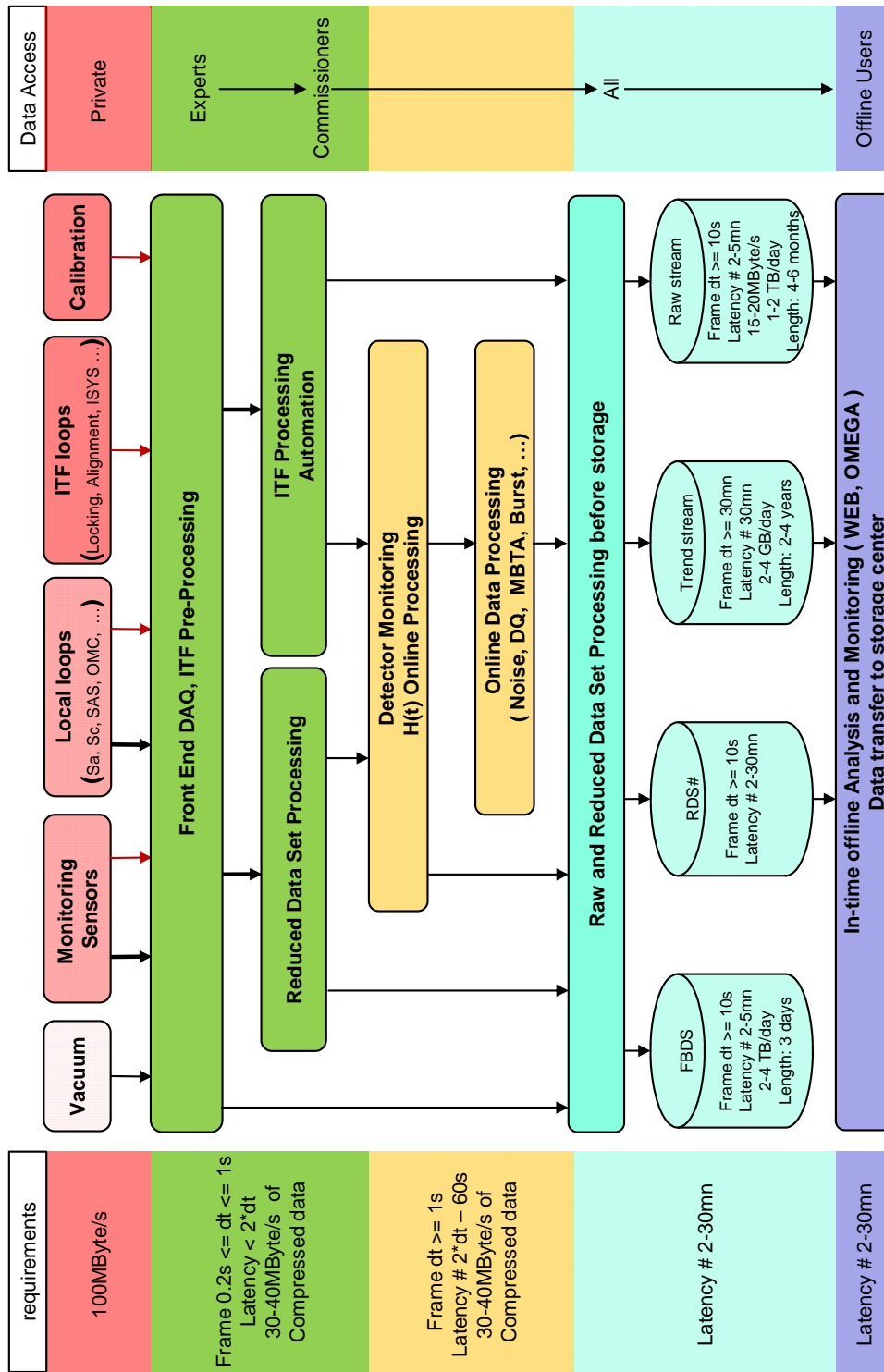


Figure 14.14: AdV data collection general architecture. See text for details. dt is the length of the frames. FBDS: full bandwidth raw data stream. RDS: reduced data stream. The LIGO data transferred at Cascina are not shown in this diagram.

network frames read from a shared memory, or to distribute frames received through Ethernet by writing them into a shared memory.

Fd evolutions for AdV. Maintenance and updates will of course be necessary for AdV. In case the general DAQ framework is changed, the Fd tools will be upgraded to interface properly the new framework (in place of Cm).

14.3.3.2 Data collection general overview

An overview of the data collection principle is shown in Figure 14.15.

The **front-end data collectors** collect, time-stamp and send the data to the frame building stage. The front-end data are separated into two flows, depending on their sampling frequencies:

- the data sampled at frequencies higher than 1 Hz are acquired in **TOLM**-based boards and sent to the DAQ through optical fibers;
- the data sampled at lower frequencies are taken from the "slow monitoring stations" and sent to the DAQ through Ethernet network.

The **front-end frame building** stage receives the data from the front-end collectors, puts them in the frame format, compresses them and pushes them to the main frame building stage through the Ethernet network. Different software tools (slow frame builder and TOLM frame builder) are used to write the data in the frame format.

The **main frame builder** receives asynchronously the frames sent by the different frame providers. It merges them into a single frame and writes them into a shared memory. Different consumers (FdIOServers) can then be plugged onto this shared memory in order to process the data and/or send the frames or part of the frames to other locations. In particular, a FdIOServer is used to write the frames on disk for storage.

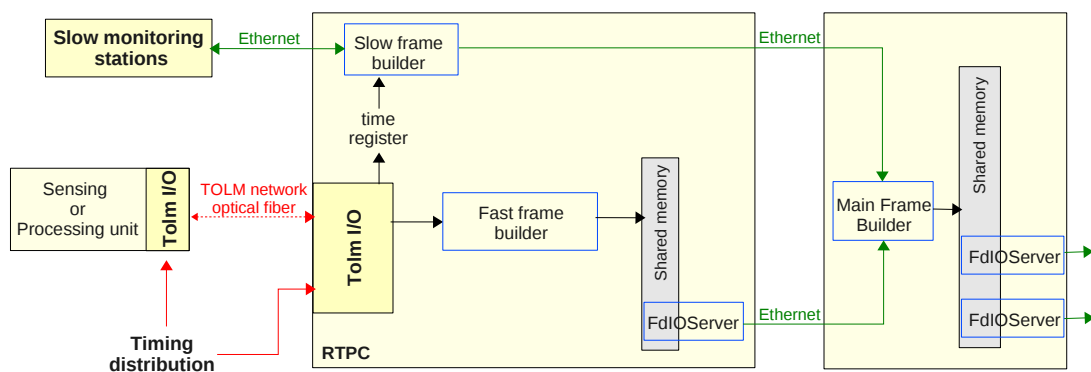


Figure 14.15: Data collection principle. See text for details.

14.3.3.3 Data from slow monitoring stations

The **Slow Monitoring Stations (SMSs)** send digital data with sampling frequency lower than 1 Hz. Only sampling frequencies sub-multiple of 1 Hz are available. Such data are provided by the vacuum system, the environment monitoring, and the laser, detection and suspension slow controls. The data collection is performed through the Ethernet network. Each subsystem has one or more SMSs that acquire the data. As SMS servers are not synchronized with the timing system, they receive Cm requests including the GPS time of the request. On reception, each SMS server formats the data as text string (the so-called *SER data*), builds a Cm message that includes the GPS time stamp and the text string, and sends this message to the requester.

The requesters are **Slow Frame Builders (FBSs)**. At the frame frequency, the FBS receives a software interrupt (from the local CPU or, in real-time PC, from the timing system), with the GPS timestamp. It forwards it to the SMS according to their sampling frequencies. On SMS data reception, the FBS builds a frame and stores all the SMS data as serial channels (defined as a key and a series of channel names and values). If one serial channel is shared between different SMS, the FBS merges the SMS data in a unique serial channel. When the frame is complete or when the waiting time is expired, the FBS sends the frame to a main frame builder.

14.3.3.4 Data from the TOLM network

Data with sampling frequencies higher than 1 Hz are sent to the front-end frame builder stage, located in real-time PC, through the **TOLM** network (see section 14.2.3.1). These data are used in-loop for locking (10 – 40 kHz) and for alignment (500 – 2000 Hz), but also for fast monitoring of the environment and different subsystems. The main control loops components are the photodiode readout, the global control and the suspension control.

In a real-time PC, the data are received through the TOLM board and processed by the TOLM Frame Builder (**TFB**). It writes the data into frame format and pushes them into a shared memory. A FdIOServer is used as a consumer of the shared memory to send the frames to a main frame builder.

The DAQ-Box (section 14.2.6) should include the frame building processing. The ones with slow ADCs could be used as a SMS stations.

14.3.3.5 The frame collectors (main frame builders)

The main frame building stage merges the frames built by the different frame providers, and distributes the data for sub-data streams, displays and detector monitoring facilities.

The **Main Frame Builder (FBM)** [471] receives frames sent by the different frame providers and merges them using their GPS time. When one frame is complete or a time-out has been reached, the frame is written into a shared memory and made available for consumers. The

consumers take their frames from the shared memory and perform dedicated operations (as filtering, channels selection) before sending them to the archiving system, display facilities or additional frame processing.

The DAQ architecture is based on a set of **FBMs** put in a tree-like architecture in order to provide different data flows to different locations.

14.3.4 Data streams

In order to monitor the interferometer, different data streams are built in the data collection system architecture. They can be accessed online for DAQ debugging, **ITF** or subsystems commissioning, or any other needs, with latencies as indicated Figure 14.14. Short frames (~ 1 s) are used to reduce the access latency to a few seconds. The main streams are finally stored on disk for offline use. In general, the frame length of data on disk is increased to speed up the data access from files.

The main stream keeps mainly all the collected data, it is the so-called raw data stream. In order to monitor the ITF, other streams are built with reduced data sets or statistical informations on the collected data. Compared to the raw data stream, the size of these streams is lower and the length of the frames larger in order to have faster offline data access. The stream definition can easily be adjusted to fit the needs.

Raw data stream . The raw data stream is built from all the collected data, with possibly some channel selection and decimation to reduce the disk storage space. The online raw data from the front-end DAQ are accessible online with frames of 1 s and a latency lower than 2 s. It is stored on disk with frames of 10 s (to speed-up the data access). Data are stored on a circular buffer at the Virgo site. Virgo has shown that a buffer depth of 6 month is useful for commissioning. Users can need to store some interesting data for longer than 6 months. A storage space must be foreseen for users to copy segments of the raw data. The length of the buffers will be discussed during the commissioning phase and adapted to the needs.

Trend data . In order to quickly visualize the interferometer signal variations over long time periods (weeks or months), the minimum, maximum, mean value and rms of every fast channels is computed every second and stored in the trend data stream. The trend frame builder server receives the whole data stream from a dedicated consumer running on the main acquisition line. It computes the trend data for each raw channel present in the frame. The trend frame builder also computes statistical information about the DAQ system, such as the number of compressed bytes and channels recorded, and the DAQ latency (3500 channels during VSR4). The trend data frames cover 30 minutes. When complete, the frame is compressed and stored on disks at the Virgo site for about three years. They are also stored in the computing centers.

For Adv, minute trend data could be helpful to study time evolutions over longer periods.

50 Hz data . In order to increase the efficiency of the analysis of the low frequency band (mHz to 25 Hz), the fast channels mainly acquired at 10 kHz and 20 kHz are resampled

at 50 Hz after low-pass filtering (7th order filter with cut-off at 20 Hz). A dedicated data acquisition pipeline is defined for this stream: specific frame consumers are defined on each pipeline and perform in parallel the filtering and the building of the 50 Hz frame. The different 50Hz frame consumers then send their frames to a dedicated 50Hz main frame builder which merges, compresses and writes the frames (10 s long). The data are stored on disks at the Virgo site for about one year. They are also stored in the computing centers.

This stream could evolve to a *reduced data set* (*RDS*) stream for AdV, with a selection of channels decimated at different frequencies.

Spectra data . A set of spectrograms over one day or one week is periodically updated and available on web pages within WebMonitoring area. They are computed for a set of data channels chosen according to the commissioning or noise monitoring needs. The spectra are computed online and stored on disk under frame format in a specific "spectro" data stream (not linked with the raw data) with a rate of about 1.2 GBytes/day. The circular buffer lasts for about one year.

Other streams . Other streams could be useful for AdV.

A *full bandwidth raw data* stream will be built from the front-end DAQ and directly stored on disk without any data selection nor decimation. It could be used as a debugging dataset. A circular buffer of few days should be enough.

In Virgo+, a *reduced data set* is built offline and exchanged with LIGO for noise studies and data analysis. Streams are also built with data from the $h(t)$ reconstruction or from online analysis like MBTA (multi-band template analysis).

14.3.5 DAQ system monitoring

Tools have been developed to monitor the data collection system and the data storage. Some tools are used to monitor the status of the data collection servers online, with a latency of a few seconds. Others permit a long term estimation of the data collection performances.

Monitoring of the data propagation . Some slow monitoring channels are built in order to monitor the data collection from the front-end. Each TOLM element provides data about the timing errors of its clock with respect to the timing distribution system. Data in the TOLM packets allow to monitor the data propagation in the TOLM network (such as the propagation time, the number of words in the packet, the presence of errors in the propagation). In the data collection tree, all frame processing servers produce slow monitoring channels to follow the size of the frames, the delays introduced in the chain or the number of stored channels. Slow monitoring channels are also produced by the **TOLM** online processes running on the real-time PCs (latency, memory use, ...). Such information are important since any large variation indicate a risk of data loss in the data collection chain. They are stored in the data. In order to monitor the data collection evolution online, some of these information is available on web pages²⁰.

²⁰ <https://www-cascina.virgo.infn.it/MonitoringWeb/DAQ>

Online monitoring of the data collection . In practice, this monitoring is done first through the detector monitoring system (section 14.3.6.1). But in addition, graphical interfaces (CI) are used by experts to control and monitor the data collection servers: it permits to start or stop the server, to check its status, to modify its configuration or to access to additional information. The same information is available remotely via the web²¹.

Monitoring of the data storage . Every data file is checked by the Fm software as soon as it is closed. The file status is checked thanks to a "checksum" realized on the bytes of the file. Then, the presence of some channels in all the frames of the file are verified in order to estimate the data losses that could have happened in the data collection chain, before the data storage.

For AdV, this information could be put in a web monitoring page.

14.3.6 Online detector monitoring and data visualization

The AdV detector will be in operation 24 h per day while being sensitive to detector malfunctioning and to instrumental and environmental noises. This induces that the data quality is precisely selected in the GW search data analysis and that the data collection is reliable. Permanent online monitoring of the detector is thus needed, in order to give the needed diagnostic information in the control room with low latency, and then to help for the data selection in the GW search analysis.

Monitoring tools are used for the commissioning of the detector and by the operators for online monitoring (automation, data display, web monitoring, ...). Additional monitoring are mainly used during science runs (data quality epochs, online analysis outputs, ...) and are described at the end of the section.

14.3.6.1 Detector monitoring

Discriminating quantities, called "quality flags", are defined in the *Detector Monitoring System*. They are stored as slow data and visualized in the control room. They give a general view of the status of the detector subsystems et allow a fast reaction of the operators in case of detector malfunctioning.

Software tools have been developed to configure data quality algorithms and to generate such **quality flags**. For each AdV subsystem (detection benches or photodiodes, beam injection, suspensions, environmental monitoring, ITF alignment and locking, TCS, vacuum, data collection, ...), an algorithm is used to monitor the defined signals and build the initial quality flags from different conditions on the signals. Different initial quality flags are generally combined to obtain a more general flag for an easier visualisation in control room.

The DMS Graphical User Interface (GUI) is a web page. The flags are seen in the control room with a latency of a few seconds: as shown by Fig. 14.16, the GUI is a set of red or green buttons that summarize the status of the different general flags. Clicking onto a button open another window with the status of the associated initial flags. This GUI is available through the web, in the control room via a private network, but is also available remotely.

²¹ <https://www.casina.virgo.infn.it/MonitoringWeb/Process>

14.3.6.2 Data visualization

The dataDisplay tool [474] allows to browse through the available channels and to visualize various types of plots (signal versus time, spectra, spectrograms, transfer function, coherence, 1d or 2d distributions ...) for all the channels available online at the output of frame builders or offline in the various data streams written on disk. It is used from control room or remotely to visualize with a few seconds of latency any signal useful to be monitored. Data can be read online through a Cm connection with a frame provider or by a direct connection to a shared memory. Data can be read offline from disk or through a Cm connection to a dataSender, a dedicated server allowing remote access to the data stored on disk.

The dataDisplay software uses a few libraries (Xforms for the GUI, Fr for the data access, Cm for the online data access and ROOT²² for the plots visualization).

Foreseen evolutions . In the coming year, it will be upgraded, improving items like:

- remove some limitations when plotting channels with different frequencies;
- speed-up and add channel processing (use of anti-aliasing filters when downsampling, computing of bandrms values, ...);
- speed-up the visualisation by optimizing the ROOT plots refresh;
- if possible, speed-up the connection with dataSenders;

²²<http://root.cern.ch>

| Detector Monitoring System | | | | | | | | | | | | | | |
|--|------------------|------------|--------------|---|-----------------|---------------|---|-----------------|--------------|---|-----------|---------|---------|-------|
| SHELVED PAGE UTC Wed Feb 15 14:15:50 2012 Latency 3.00 GPS 1013350565 Frame No 105 | | | | MUTE DMS [current status: NOT MUTED] Switch to UNSHELVED page Stop refresh Switch to internal view Contracts / HELP | | | Admin DMS Flag list Alarm Log DMS / FLAG Log View XML files | | | ITE STATUS Mode: Not locked 2358 h 3 mn DMS: 0 2311 h 38 mn - AutoReleack: OFF - AutoScience: OFF - Horizon_NISNS AVG: 0.0 Last event (2011-11-09 09:18:58 LT): Lock sequence reset | | | | |
| Automation | Atp_Host | | | | | | Test | | | | | | | |
| Alignment | All_host* | | | | | | All_temp* | | | | | | | |
| Detection | OB_ID | OB_IC | OB_Vert | OB_TE | OB_Guardians | OB_Servers | OB_PIOs | Det_Servers* | | | | | | |
| | Gx_B1 | Gx_B1p | Gx_B5 | Gx_B7 | GxServer* | Det_PIOs | | | | | | | | |
| | Pr* | Pr_Align | Lo* | Vb* | Sr* | Pi | OMC | | | | | | | |
| Injection | IB_ID | IB_IC | IB_AA | IB_Vert | IB_TE | IB_Guardians | IB_Servers | IB_PIOs | IB_Light | | | | | |
| | MC_ID | MC_IC | MC_AA | MC_Vert | MC_TE | MC_Guardians | MC_Servers | MC_PIOs | MC_Light | | | | | |
| | Laser | LaserAmpli | LaserChiller | LaserChillerDiodes | Laser_Interlock | BMS | EIB_SAS | | | | | | | |
| | Modulation* | PFC | MC_Power | MC_zControl | MC_Noise | IMC_Lock | PMC | ActuatorServers | Inj_PIOs | | | | | |
| Locking | CoilDrnMode | | | CoilRelay | | DSP* | Gc_temp* | Gc_host | | | | | | |
| Suspensions | PR_ID | PR_IC | PR_Vert | PR_F7 | PR_TE | PR_Guardians | PR_Servers | PR_PIOs | | | | | | |
| | BS_ID | BS_IC | BS_Vert | BS_F7 | BS_TE | BS_Guardians | BS_Servers | BS_PIOs | | | | | | |
| | NI_ID | NI_IC | NI_Vert | NI_F7 | NI_TE | NI_Guardians | NI_Servers | NI_PIOs | | | | | | |
| | NE_ID | NE_IC* | NE_Vert | NE_F7 | NE_TE | NE_Guardians | NE_Servers | NE_PIOs | | | | | | |
| Vacuum | LinkValves | TubeValves | TowerServers | TubeServers | TurboPumps | ScrollPumps | TubePumps | Pressure | BackPressure | CompressedAir | CryoTrap | OSRboot | CHRoCCs | 1500N |
| Environment | Central_Building | | MC_Building | NE_Building | WE_Building | LaserLab | Ext_Inj_Bench | Dead_Sensor | Env_hosts | | | | | |
| | EE_Room | DaqRoom | NE_Bench | Laser_Bench | Ext_Det_Bench | External | Env_ADCs | | | | | | | |
| Infrastructures | UPS_TB | UPS_MC* | UPS_NE | UPS_WE | ACS_CB | ACS_TB* | ACS_MC | ACS_NE | ACS_WE | ACS_COB | Generator | | | |
| Servers | Olserver | ADC7674* | DAQ | Decl_Moni | Storage | InfraServers* | WEB_App | DAQ_Host | RIO_temp | | | | | |

Figure 14.16: Screen shot of the Detector Monitoring System web page (during Virgo+ dismounting, February 2012).

- if possible, have a continuous reading of stored files and online streams;
- get independency between the GUI library (currently Xforms) and the data processing code.

14.3.6.3 Monitoring web pages

Monitoring from few minutes to hours is available through the web²³, the so called *monitoring web page*. This system uses the data that are written on disk and computes some plots to give an overview of the detector status but also of the data analysis status. For example, it outputs the sensitivity curve every 5 minutes, the detector range for binary neutron stars plotted over a day and refreshed every 15 minutes, the mirror alignment, the powers of the photodiodes, some **GW** reconstruction parameters, the number of events detected by online GW searches for bursts or binary coalescences. The choice of the main figures of merits to be shown will be discussed with the LIGO experiment.

This system is based on the ROOT software, interfaced to the Fr and Frv libraries used to manage the frames and the data vectors. It uses also specific scripts which manage the plots and organise the access to the archived web pages.

14.3.7 Online processing

Some online processing that is more related to data analysis is mainly used during science run periods, in addition to the other detector monitoring tools.

14.3.7.1 Online data quality flags

A first set of online data quality flags is computed and used by the Detector Monitoring System. A second set of online data quality flags is computed for data analysis purpose. Those flags often use combination of channels and result of rms computed in various frequency bands. The flags values are put in the raw data stream. In parallel, they are used to compute data quality segments which are stored online in the LIGO database (segdb) and the Virgo Database (**VDB**). Those segments can be used by offline or online analyses to veto time periods or noise events [475].

14.3.7.2 Online analysis

Online processing such as NoiseMonitoring, $h(t)$ -reconstruction (section 14.6.4), Kleine-Welle, Omega and online analysis (MBTA) are not directly related to the DAQ system but use the DAQ tools, and sometimes provide data that are added to the data streams stored on disk.

In particular, $h(t)$ -reconstruction provides a channel with the ITF range for coalescence of binary neutron stars. It is visualized online in the control room to monitor the detector sensitivity. It is also stored in the raw and trend data streams on disk.

²³ <http://wwwcascina.virgo.infn.it/MonitoringWeb>

Another example is Omega, which provides web pages where a *trigger rate* is shown as function of time. It permits to visualize the presence of glitches in the data, which are transient signals spoiling the detector sensitivity. For commissioning, it is used to track some glitch family, trying to understand their origin in order to fix their source in the detector hardware.

Additional online analysis developed for AdV can easily be plugged into the data collection architecture.

14.3.8 Automation with the Alp software

Software has been developed to automatize the detector operations and monitoring, the so-called Alp code. Different Alp servers can work with different configurations. It has been largely used in Virgo for the automation of the detector operations (locking, alignment, calibration, ...). It can also be used to generate quality flags.

Foreseen evolutions . Alp will still be used for AdV. The evolution toward the support of Matlab and the addition of new functionalities will be studied, as well as the use of python in Alp.

14.3.9 Storage and online network needs

14.3.9.1 Data storage

The estimated data flow and buffer length for AdV are summarized in the table 14.2. The main streams data flow have been estimated assuming they are twice as large as during VSR4.

| Stream | Data flow (GB/day) | Number of channels | Buffer length (year) | Disk space (TB) |
|-----------|-----------------------|-----------------------|-------------------------|--------------------|
| Raw | 2000 | 14000 | 0.5 | 370 |
| Trend | 4 | 32000 | 3 | 5 |
| 50 Hz/RDS | 30 | 2000 | 3 | 30 |
| Spectro | 2.5 | 300 | 1 | 1 |
| $h(t)$ | 7 | 10 | 1 | 3 |
| mbta | 2 | | 1 | 1 |
| Total | 2050 | - | - | 410 |

Table 14.2: Foreseen data flows and storage needs for the main streams of AdV. The flows and frame sizes are for the compressed data written on disk.

14.3.9.2 Online data collection networks

While the fast data collection is done through the TOLM network, the Ethernet network is used to collect the slow data, to provide the video streams and to provide the boot and NFS accesses.

A Gigabit Ethernet network will be used to collect the camera raw data down to the associated real-time PCs. The same network will be used for the monitoring and control of the DAQ-Boxes and the camera boxes.

14.4 DAQ software environment

14.4.1 Framework for communication between servers

14.4.1.1 Framework currently used in Virgo

The Virgo framework is based on the Cm software [466] and its associated name server to manage the communications between the different processes (servers). Cm allows to drive and configure the different servers. Cm is used by the Fd package (see section 14.3) in order to exchange data between the servers.

A parser has been defined in the Cfg package in order to have a general way to configure the servers. ASCII configuration files are written with the format defined in Cfg, based on a set of keys with associated values. Each server has additionnal specific keys.

Each server generates a log file in a location defined in the configuration file (in general in the /virgoLog area). The generation of error messages is done using Cfg functions.

Graphical user interfaces, base on the Cl package, are used as clients to monitor and control the different servers. A GUI permits to control various servers.

In Virgo, the server and client configuration files are put in the /virgoData area and saved in a database.

The servers are organized in such a way they were mostly "independent": a server could start in any case, an would gives an error message in the GUI client if another needed server or data were not available. A flag is also set in the Detector Monitoring to provide status information.

14.4.1.2 Possible evolutions for AdV

The Cm package, initially developed by LAL, is not anymore maintained by them and is being used by the Virgo collaboration only. If still used for AdV, it will need maintenance and further developments. Another option is to use another software for server communication. A somehow "light" tool with similar messaging skills than Cm, but more widely used, could be 0MQ²⁴. Another option is to use a full *Supervisory Control and Data Acquisition (SCADA)* framework, as Tango²⁵. It provides tools for communication (based on Corba), but also for overview of all servers and processes, for data display, configuration, error loggers, alarm handling, graphical user interfaces. In any case, if Cm is replaced by another tool, the transition will not be easy and both systems will be running in parallel for some period, and probably still at the start of AdV, evolving towards the new framework with time.

²⁴<http://www.zeromq.org/>

²⁵<http://www.tango-controls.org/>

14.4.2 DAQ-oriented software tools

14.4.2.1 Hardware inventory and integration database

The Virgo HWII²⁶ is used to track the status and history of the different parts constituting Virgo²⁷. Parts are instances of specific Part Types, e.g. crates, racks, timing distribution boxes, wave plates, viewports. They are added to a parent-child tree structure, which can also be displayed topographically (Figure 14.17). Image and other files can be associated to each Part, while Group Administrators can configure the interface in such a way as to enable the storage of custom information in relation to specific Part Types. Each change to a Part made by a user is automatically recorded in the associated Worklog (Figure 14.18), explaining which action has been undertaken, when, by whom and where.

²⁶<https://pub3.ego-gw.it/itf/hwii>

²⁷ It is also used to track parts involved in the CALVA experiment.

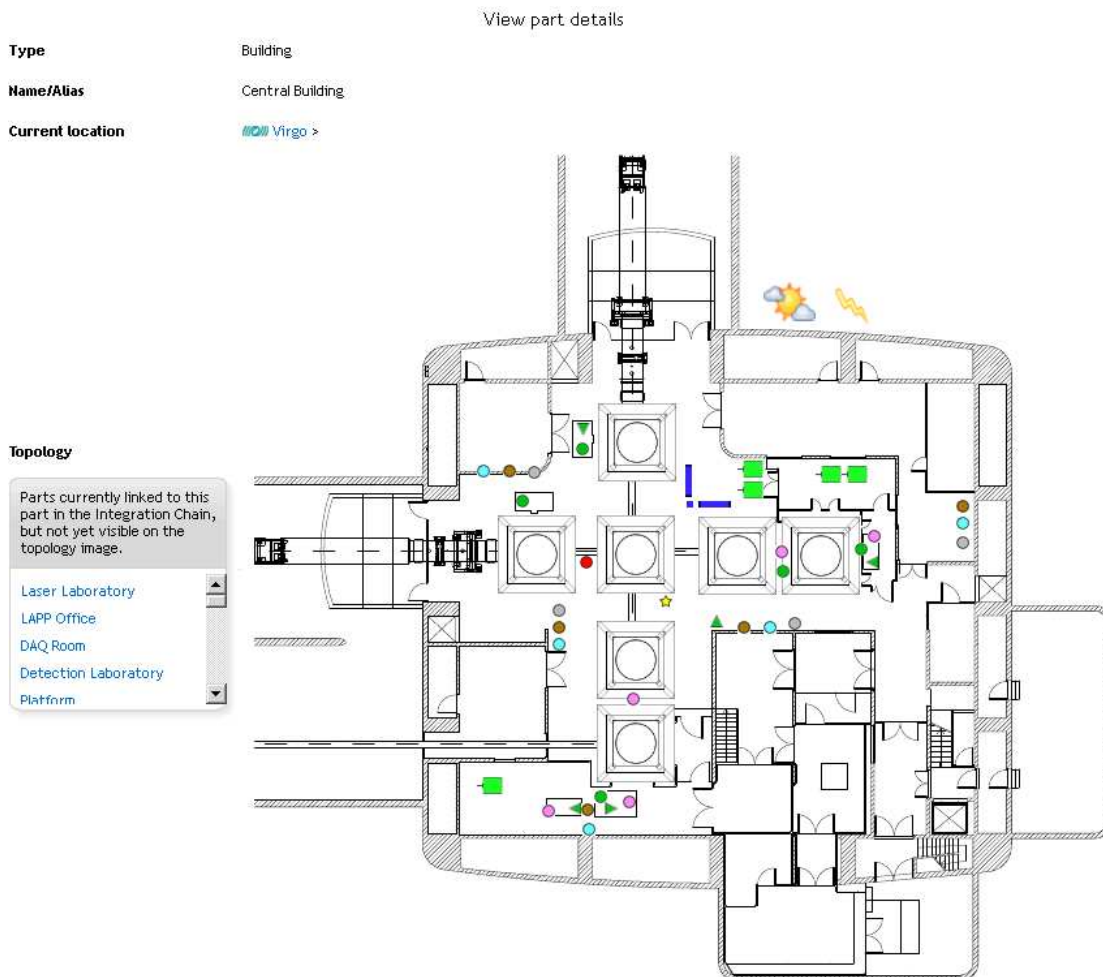


Figure 14.17: The Central Building in View Part Detail mode, showing locations of environmental sensors.







At the end of Virgo+, the **HWII** database contains records relating to 3376 individual Parts in use in Virgo or in storage. These Parts are associated to 205 different Part Types.

The **HWII** is extensively used by the DAQ, EGO Optics, Vacuum and Data and Noise Analysis groups. Close collaboration with these groups has improved this application. One recent modification involved the creation of a "Part Type Discussions" section, which enables all instances of a specific Part Type to be displayed, along with their Topographical view, together on the same page.

Foreseen evolutions for AdV Plans for further development of the **HWII** involve: connecting it to the upcoming Connections Database (CDB) application, which will enable closer integration between itself and other Virgo PHP-MySQL environment applications, such as the Virgo Logbook, Technical Documentation System (TDS) and Procedures database; continuing to work with users and actors important to the application in the addition of Parts and Part Types, rendering the process ever more simple; experimenting with the process of automatic updating, via the uploading of external application-specific configurations, which would enable a user to update all related parts without having to manually enter information.

14.4.2.2 Channels database

The Channels database stores, for each channel acquired by the data acquisition or produced by the online processing, some information useful for data analysis or ITF's commissioning: channel's name, units (Volts, Decibels, mbar, ...), sampling rate (in Hz), mean value over

| Worklog | | | |
|----------------|---------|---|------------------------------|
| Date | User | | |
| 16:24 24/09/08 | maillet | Part attached to Wall-MC-W | |
| 15:55 23/09/08 | maillet | Part moved to: Wall-MC-W | |
| 11:59 17/09/08 | maillet | On the polariscope, the vie | |
| 11:55 17/09/08 | maillet | File  points (1).jpg (v001 | |
| 11:55 17/09/08 | maillet | File  points.jpg (v001) at | |
| 11:55 17/09/08 | maillet | File  Y01b.jpg (v001) att | |
| 11:54 17/09/08 | maillet | File  Y01a.jpg (v001) att | |
| 11:54 17/09/08 | maillet | File  Y01-vacuum-side.pn | |
| 11:54 17/09/08 | maillet | File  Y01-air-side.png (v001) attached to this part. Map of defects on air | New Building > Virtual store |
| 11:53 17/09/08 | maillet | Dusty surfaces but no particular defect on air side. May have a bubble on | New Building > Virtual store |
| 11:52 17/09/08 | maillet | Part added to database. | New Building > Virtual store |




Figure 14.18: A Viewport-associated Worklog, showing one of the uploaded photos of the Part, taken immediately following its installation in Virgo.

the last second, min and max values over the last second, type of channel (ADC, PROC, SMS), source of the channel (Cm Name of the server, name of a contact person, ...) and the description of the channel (and any additional useful information like anti-alias filter used). The MySQL database is filled automatically every few minutes by scripts that read the table of content of the raw data file. It permits that some of the information provided by the Channels database are automatically updated (channel obsolete or not, sampling rate, units, mean value, ...).

A web interface²⁸ has been designed for the users to get information from the Channels database or to fill in the "source" and "description" fields of the selected channels.

14.4.3 AdV online software management

14.4.3.1 Configuration management

The software must be stored in a centralized archive and accessible by each software developer. It must be possible to track and identify previous system configurations. For release preparation in particular, code freezing or "tagging" is required i.e. a simple notification by the package responsible, that a certain version of the corresponding package has achieved its planned objectives and may be taken from the repository for the release.

The configuration management tool must enable:

- identification of items;
- traceability of changes (who did what, when);
- accessibility of previous configurations for any item.

Both source code and documentation must be subject to strict version control. The software package constitutes the main configuration item.

Configuration management item: software package A software package is a piece of software (code and documentation) able to perform functions and having an interface available to an external user to access the functions provided. Technically a package is a way to organize functions in homogeneous groups. The interface hides the implementation and system dependencies from the user. Managementwise, the package is the basic unit for planning, software project control and configuration control. There is no rule to define how big a package shall be. Common sense and programming experience should be enough to identify what can be gathered and treated as a unique item. Each package shall have one responsible person, who will be entitled to delegate activities on the package but shall retain responsibility at all times. Descriptive, non-empty comments are required for each file/package at check in. They must be complete and readable, avoiding "standard" phraseology like "fixed typo" or "fixed bug".

Package identification .

A package is identified by its name and its version mnemonics. The version identification model is based on :

²⁸<https://tds.ego-gw.it/itf/channelsdb/>

- A version is defined with a mnemonic comprising at least two numbers for the major (v) id and the minor (r) id (a third number can be present representing a patch (p) id)
- The increase of these two numbers during a development has to follow those rules:
 - if the changes in the libraries of package A are not backward compatible (it is necessary to change something in packages which are using A) then the major id number must be increased by one unit.
 - if the change does not imply any modifications in the other packages, the minor id number must be increase by one unit

A patch version is sometimes useful to isolate a change in the code during a temporary test for instance. The package version is then labelled vXrYpZ and is not meant to be included into a software release.

Package structure .

Each package version should contain the following directories: (i) /src for the source files (for example .c and .h files), (ii) /doc for all the documentation, (iii) /cmt for CMT files, (iv) /mgr for script files, (v) one or more platform dependant directory containing the libraries and executable for this computer and (vi) /tests for the test validation suite and the related input and reference output files.

Configuration management tool The tool currently in use is **CVS** [472] a public domain tool which has been available for many years and offers sufficient guarantees of reliability and stability (however, it is no more maintained). A tool called **SCVS**, made by a thin layer of Sh scripts, has been developed on top of CVS in order to provide an easy and structured approach to software configuration management. It manages packages more than files, and blocks the access whenever a package is being modified. By archiving a package the developer tells the others that a new consistent set of files is ready for use.

Read only access to the CVS archive in Cascina is also possible via **CVSweb**²⁹.

For AdV, we plan to migrate to the successor of CVS, the **SVN tool**. The philosophy of SVN is the same as CVS, with some additional features, so that the transition should be smooth. We will evaluate wether the SCVS layer is still useful or abandoned.

14.4.3.2 Build tools and development environment

In Virgo, the tool **CMT** [473] has been used to provide a standard common software development environment. It provides those main features:

- a structured make usage for software build;
- management of the relationships among packages;
- easy encapsulation of third party tools and libraries;
- standardization of the users UNIX environment set-up;

²⁹<http://wwwcascina.virgo.infn.it/cgi-bin/cvsweb/cvsweb.cgi/>

- fully interoperable with CVS and SVN.

Discussions are ongoing on CMT future and evolution. Its version will be updated soon to the latest one. A very interesting set of tools is the one corresponding to CMake/CPack/CTest/CDash. This toolchain constitutes a complete software management solution and allows to build the software and package distributions (tar, rpm and deb files supported), and support automated test and report via dedicated web page.

A possible solution would be to keep CMT as front end so that nothing changes for the developers, but at the level of software manager a translator to CMake is used in order to exploit the whole toolchain features (in particular for what concerns software distribution packaging). CMake is being evaluated. The results will be discussed in order to decide if it is abandoned, used for managing only, or used instead of CMT in all Virgo software.

Software disk areas in cascina Several disk areas will be used to manage and operate the software. The following areas are foreseen:

- The development area will be the *home* directory of the developers who can create and delete subdirectories under it.
- The staging area (*/virgoStaging*): this is a temporary area for integration phases of the packages. Users can install or remove archived packages, but will not be able to modify them. The package versions are removed from this area if they failed the tests or when they are installed in the production area. This area being new for AdV, this idea will be tested before final validation.
- The production area (*/virgoApp*): this directory is the primary repository where all reference versions are provided for actual Virgo operations. The ownership and permission of the files in */virgoApp* do not allow users different from the software manager (*swmgr*), who performs the installations, to modify that area.
- The release area (*/virgo*): This area contains the Virgo software releases named using the acronym **VCS** (Virgo Common Software) followed by a numerical identification id split in major id and minor id. The Virgo release directory structure is mainly as follows:
 - The *ext* directory containing a "plain" installation of external packages resulted from native installation procedures (typically from *configure*, *make*, *make install*). Each of them will have a corresponding CMT wrapper in VIRGOSW. The possibility to provide the full package via CMT is being evaluated.
 - The VIRGOSW directory containing the Virgo basic and application software baseline defined using symbolic links on top of the production area */virgoApp*. So the baseline is simply a different view of the same software.

14.4.3.3 Software problem report system

Keeping track of faults in software products whenever these are discovered is of fundamental importance. The Software Problem Report (**SPR**) System³⁰ is meant to be used by internal

³⁰ https://www.cascina.virgo.infn.it/sDoc/software/spr_overview.html

or external users of Virgo to report problems/errors, submit change requests or to require clarification on software, hardware or documentation. Users can submit requests via a Web Browser Interface or sending email to the SPR address.

14.5 Environmental monitoring

The Environmental Monitoring system provides a large variety of sensors, together with the relative conditioning electronics, that are used to record all the physical parameters that can modify the ITF working conditions or response. In fact, due to the sensitivity of the ITF and to the weakness of the expected signals, a lot of external perturbations can degrade the interferometer performances. The weather condition, lightning events, and detector temperature, pressure and humidity are monitored at slow frequencies, namely lower or equal to 1 Hz. At higher frequencies, the ITF mechanical vibrations, the acoustic, magnetic and power supply noises are monitored.

All the signals collected by the environmental monitoring system are sent to the data collection system. As shown in Fig. 14.19, the transmission can occur in two ways, depending on the signal frequency: (i) the slow signals, analog or digital, sampled at 1 Hz or less, are sent to the data collection directly as digital data using slow monitoring stations (see section 14.3.3.3); (ii) for faster analog signals, the output of the conditioning electronics is connected to the TOLM network through standard fast ADC channels (see section 14.3.3.4). All the slow monitoring channels are sent to the slow frame building stage at 1 Hz, even if the true sampling frequency can be lower, in particular for commercial probes with digital output. On the other hand, the sampling frequency of the fast channels strongly depends on the probes as well as on the conditioning electronics: it is fixed on the basis of the desired frequency band.

The general architecture of the environmental monitoring system foreseen for AdV is very similar to the Virgo and Virgo+ one [461, 462]. Nevertheless some significant difference exists, mainly due to the aging of components and to the stronger requirements for the environmental quality in the advanced detector.

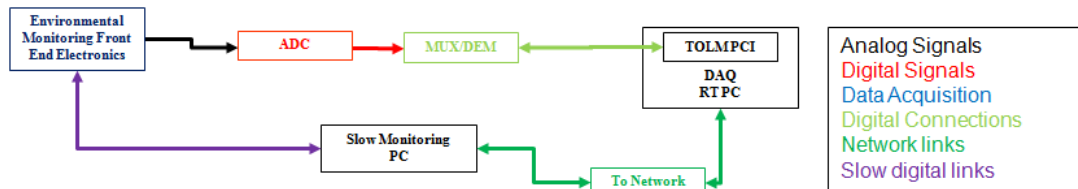


Figure 14.19: Environmental Monitoring simplified scheme

14.5.1 Slow channel monitoring

The slow channel monitoring manages the acquisition of several outdoor and indoor parameters at frequencies up to 1 Hz: weather conditions, lightning events, temperature, pressure and humidity.

For data collection, the data are directly sent to the slow frame builder, with two possible cases:

1. the probes directly provide digital data that are collected by a serial or a network link. This is the case for the weather conditions and lightning sensors;
2. the probes provide analog data: a simple acquisition system is necessary to convert

them to digital data which are then collected by a serial or a network link. This is the case for general purpose temperature, humidity and pressure sensors.

In both cases, the slow channel monitoring is still based on a distributed-server architecture, where each server has the double task to manage and get data from a probe and to send them to the slow frame builder.

In the remaining part of the section the different elements are described with some details.

14.5.1.1 Weather station

The weather station is used to monitor the external conditions since, in particular cases, they can affect the **ITF** performances. The selected weather station is an improved version of the model used for Virgo and Virgo+: a *Vantage Pr 2* by *Davis*, equipped with an anemometer, a rain rate probe, a thermometer, an hygrometer and a barometer. The sensors have to be placed, of course, in a suitable external place, while the station console, connected with the external integrated sensor suite with a communication cable, has to be located indoor. The new console can accommodate a new kind of data-logger directly connected with the network, while the old model was connected by a RS232 serial link. In this way the architecture is simplified, since no element is needed between the console and the computer running the server of this probe.

The weather station provides data with an internal sampling frequency of 1/3 Hz and can be partially configured from the network.

14.5.1.2 Lightning detector

The lightning detector used in Virgo/Virgo+ was a commercial radio frequency detector, model *LD-250* from *Boltek*, that is able to detect events and recognize them as strikes up to a distance of 400 km. The lightning sensor has to be placed as close as possible to the external area, but it can be mounted also inside the building. In Virgo it was mounted on the roof of the central building, but a better place should be used for AdV in order to have a better accessibility to the sensor for maintenance. The sensor console communicates with the computing hosting the server via a serial to Ethernet converter in order to simplify the architecture³¹.

The detector console sends, through the serial link, the information about the events recognized as lightning: distance and angle respect to a fixed direction. Usually, during a storm, several lighting events happen in a short time; in this case the console sends the information about each event in sequence. This feature does not allow an optimal data storing inside the **SMS** data, since the timing information about each event are lost. Moreover the recognition mechanism, integrated inside the detector, is not perfect and can fail.

To overcome these two problems, the possibility of using an existing European network of lighting detector [463] is under investigation. By installing on the AdV site a suitable detector, one also gains the possibility to use, with a minimal latency, the data coming from the large sensor network (more than 300 detectors placed in several European Countries), with detailed

³¹ An RS232 serial link is also available.

and precise information about the timing and position of the events. The plan is to use both kinds of detectors during normal operations.

14.5.1.3 Temperature probes

The temperature probes are the same as used in Virgo: *AD 590 MF* from *Analog Device*. They are 2-terminal integrated circuit temperature transducers that produce an output current proportional to the absolute temperature. Their nominal sensitivity is $1 \mu\text{A}/\text{K}$: the current output needs to be conditioned before the acquisition. The measured temperature ranges from -55°C to 150°C . The probes will be powered at 5 V.

The probes are vacuum compatible. Some are installed in the high-vacuum section of the suspension tower to monitor the temperature stability of the suspension.

14.5.1.4 Humidity probes

The humidity probes are the same as used in Virgo: model *G-CAP 2* from *GE Measurement & Sensing Technologies*. They are relative humidity sensors based on polymer capacitance, with a sensitivity of about $0.333 \text{ pF}/\text{RH}$, where RH is the relative humidity percentage. The measured RH ranges from 0% to 100%. The probes will be powered at 10 V.

Since this probe is a capacitor, it needs a *close* conditioning electronics to reduce any effect due to the capacitance of the connection cable. This is an important point if the probe has to be placed near critical equipments of the **ITF**. In this case, to avoid electromagnetic interferences, it is mandatory to achieve a suitable conditioning electronics, with a negligible electromagnetic emission.

14.5.1.5 Pressure probes

The pressure probes are the same as used in Virgo: *MPX4115A* from *Motorola*. They are piezoresistive transducers with integrated temperature compensation. Their nominal sensitivity is $45.9 \text{ mV}/\text{kPa}$ and the measured range is 15-115 kPa.

Since they have voltage output, no special conditioning electronics is required. Nevertheless they contain some integrated electronics and have to be powered at 5 V.

14.5.1.6 Read-out electronics and slow data acquisition

The read-out conditioning electronics and digitization electronics are the basic elements of the *environmental slow monitoring module*, whose scheme is shown Fig. 14.20. The digital data are then sent to the data acquisition system. Modules will be 19" 1U boxes to easily integrate them in standard racks.

The read-out electronics needed for the slow monitoring sensors must convert the different probe analog outputs (current, capacity and voltage) to provide voltage output signals. It has to be designed according to the sensor specifications and taking into account the slow sampling frequency. Moreover, some probes need voltage bias or additional voltage power.

In order to standardize the read-out front-end, a configurable conditioning electronics, able to manage up to 16 slow monitoring probes, will be used. The probe side of the front-end will provide the required bias and voltage power by using simple manual jumper-selection. In this way it will be possible to host also future probes, with compatible outputs, or to use the same front-end to connect other AdV equipments with analog outputs.

After the conversion to voltage, and to prevent aliasing in the digitization, the analog data are low-pass filtered with a low cutoff frequency, around 10 to 20 Hz, and strong roll-off (at least eight orders). This is required to avoid aliasing when the conversion to digital happens.

The data are then sampled and sent to the slow frame builder. For Virgo and Virgo+, this task was performed using a commercial system with distributed architecture [464, 465]. In order to simplify the architecture and to improve the performance for AdV, a new slow monitoring electronics was developed in the environmental slow monitoring module. It uses an **ARM** processor to manage the acquisition of the 16 inputs coming from the conditioning read-out electronics. through a multiplexed true differential 18-bit ADC. The internal sampling frequency is fixed around 50 Hz. The digital data are filtered and down-sampled by the processor that periodically sends the data, on request, to the slow frame builder.

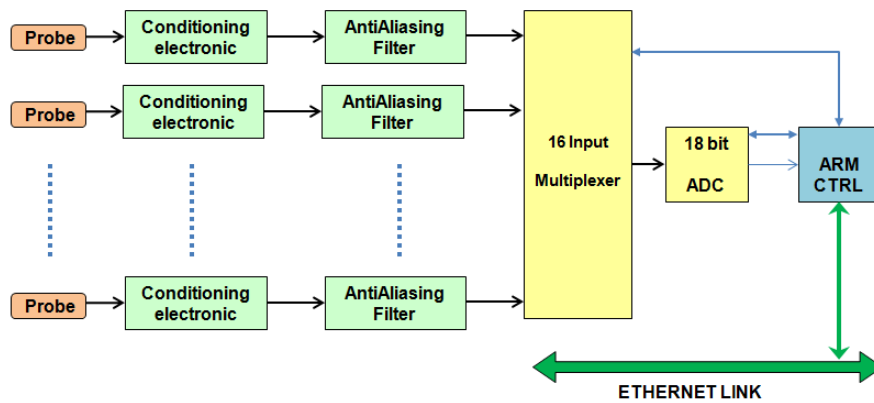


Figure 14.20: Environmental Slow Monitoring Module

14.5.1.7 Probe and electronics location

Apart from the external probes, like weather station and lightning detector, all the other sensors are placed inside the buildings, for general monitoring, or close to critical equipments or systems that require careful monitor. Temperature and humidity sensors are expected to be mounted close to, or on the optical benches, while temperature probes will be also mounted inside each suspension tower.

Monitoring types and location of the slow monitoring modules in racks can be listed as specific tasks, shown as full green shapes in Fig. 14.21

1. *Building monitoring*: a set of twelve temperature probes set vertically, one humidity and one pressure probes will be managed by one module (green full squares). 9 modules, with no need of rack, will be installed close to the sensors: one on each wall of the Central Building, one for the Mode Cleaner Building, two for each End Building.
2. *Suspension monitoring*: for each suspension filter (10), two temperature probes (green

full circles) placed inside the towers will be managed by one module located in the corresponding suspension rack. 6 additional modules will be installed to monitor the temperature in the suspended benches.

3. *Lab monitoring:* for each optical bench and laboratory, one temperature and one humidity sensors (green full triangles) will be managed by one module located in suitable DAQ racks. At least 8 modules are needed: DAQ room, Detection Lab, Laser Lab, EE room, Locale Pompe (TCS benches), Mode Cleaner, North and West End Benches.
4. *External Monitoring:* no module is foreseen in the actual configuration, only lightning detectors and weather station.

14.5.2 Fast channels

The fast channel monitoring system manages all the sensors and the related conditioning electronics, that need to be acquired with sampling frequencies higher than 1 Hz. They measure seismic, acoustic, magnetic and mains power supply noises.

The probe analog voltage signals, properly amplified to fit the voltage input range of the standard ADC channels [450], are directly connected to the data collection front-end in the TOLM network. No particular anti-aliasing filtering is required before the ADC channels, since they have a simple input low-pass filter, a high sampling frequency (800 kHz), and a digital filtering for data-decimation. On the other hand, since the input stage of the board is differential, the output of the conditioning electronics of *all* fast monitoring channels, should be differential. This is not possible for commercial conditioning electronics that use standard single-ended output. In these cases a dedicated connection is required.

A list of the selected probes with their main characteristics is given in table 14.3.

| Monitor | Probe | Type | Freq. (Hz) | Driving | Conditioning | No. of output |
|-------------|------------------|-----------|------------|---------|--------------|---------------|
| Seismic | Velocimeter | CMG-40-T | 0.033-50 | Custom | Embedded | 3 |
| | Episensor | FBA-ES-T | 0.1-200 | Custom | Embedded | 3 |
| Vibration | Accelerometer | 393B12 | 0.1-1000 | | Nexus | 1 |
| | Accelerometer | 8340 | 0.1-1500 | | Nexus | 1 |
| Magnetic | Magnetometer | MFS-06 | 4-10000 | Custom | Embedded | 1 |
| Acoustic | Standard Mic. | 4190+2660 | 3.15-20000 | | Nexus | 1 |
| | Infra-sound Mic. | 4193+2660 | 0.1-20000 | | Nexus | 1 |
| Radio Freq. | Antenna | ARA-60 | 4-120 MHz | Custom | Mixer | 4 |
| Mains | Transformer | Custom | DC-1000 | N/A | Custom | 1 |

Table 14.3: Fast probe types and characteristics.

14.5.2.1 Seismic probes

A large variety of seismic probes have been used in Virgo and Virgo+ operation, since no single probe, with suitable sensitivity and frequency band, is available for the ITF mechanical vibration monitoring. To overcome this problem, several sensors will be used for AdV also.

The very **low frequency** part of the seismic noise is covered by tri-axial broadband velocimeters, model *CMG-40T* from *Güralp*. The sensitivity of this probe can be selected from 140 V/(m/s) to 200 V/(m/s) in the frequency band from 0.033 Hz to 50 Hz.

The **medium frequency band** is measured by tri-axial accelerometers (*epi*sensors), model *FBA ES-T* from *Kinematics*. The probe sensitivity can be selected from $2.5 \text{ V}/(\text{m}/\text{s}^2)$ to $40 \text{ V}/(\text{m}/\text{s}^2)$. It works in the frequency range 0.1 Hz to 200 Hz.

Both kinds of sensors need dedicated conditioning electronics. They provide differential output.

The **upper part of the frequency band** is covered by piezoelectric accelerometers. Two models are foreseen, with very similar characteristics. The model *393B12* from *PCB* was already used in Virgo. It has a sensitivity of $10 \text{ V}/\text{g}$ and a measurement band that ranges from 0.1 Hz to 1 kHz; The model *8340* from *Brüel and Kjaer* has a sensitivity of $10 \text{ V}/\text{g}$ and a frequency band from 0.1 Hz to 1.5 kHz. For both sensors, a commercial conditioning amplifier is foreseen.

14.5.2.2 Magnetic probes

The magnetic probes will be the same as used in Virgo/Virgo+. They are induction coil magnetometers, with embedded calibration facility and feed-back for self resonance reduction, model *MFS-06* from *Metronix*. The sensitivity of these devices is $0.8 \text{ V}/\text{nT}$, the standard measurement ranges from 4 Hz to 10 kHz, but they can be also used, enabling the embedded chopping system, in the 2.5 mHz to 500 Hz band, of course with a little sensitivity loss. Such sensors being sensitive to the magnetic field along a single axis, they are installed in group of three in order to monitor the magnetic field variation along all the directions. Like the seismic sensors, these probes are equipped with an embedded calibration system. A dedicated electronic is required to manage each probe.

14.5.2.3 Acoustic probes

The acoustic sensors are used to monitor pressure noise in the audio and infra-audio frequency bands. For standard building monitoring, the foreseen audio sensors are *Falcon type 4190*, equipped with preamplifier model 2660, both from *Brüel and Kjaer*. They are condenser microphones with a sensitivity of $50 \text{ mV}/\text{Pa}$ and a frequency band ranging from 3.15 Hz to 20 kHz. For monitoring the most critical parts of the **ITF**, where lower frequency noise can be effective, infra-sound microphones, model *4193*, also from *Brüel and Kjaer*, are available. Their frequency band extends from 70 mHz to 20 kHz, but the low frequency cut-off raises again to 100 mHz if the same preamplifier of the other model is used. In any case, such a little difference between the nominal and the effective frequency band is not enough to justify the use of a different preamplifier.

Since both microphones require an high voltage polarization of 200 V, a dedicated conditioning electronic is required for their driving also. The standard solution is to use a commercial amplifier.

14.5.2.4 Radio frequency probe

The standard magnetometer are suitable for measuring the magnetic field up to 10 kHz. In AdV, however, some radio frequencies sources are used for phase modulation of the laser

beam, for locking and alignment purposes (cfr. ISC and OSD sections). The main modulation frequencies will be in the range 5 MHz to 80 MHz. To monitor the quality of the environment, a dedicated probe has to be used. For Virgo+, the selected sensors was an **RF** antenna: model *ARA-60* from *Dressler*. Its measurement band spans from 4 MHz to 120 MHz, with a gain of 10 dB. The sensors characteristics allow its use in AdV also.

This probe requires dedicated electronics for power and signal conditioning. The antenna output is band-passed around the selected frequency and demodulated to allow the signal acquisition with a standard **ADC**.

14.5.2.5 Voltage sniffer

One of the most important contribution to the environmental electronics noise is the 50 Hz contamination due to the mains voltage power. In order to monitor this important source, a set of simple, home-made, voltage sniffers will be used. The sniffers are directly connected to the mains and provide a low voltage signal proportional to the input. The output consists of a single-ended signal to be acquired with standard **ADC**.

14.5.2.6 Read out electronics

All the fast probes require dedicated conditioning electronics to convert the output signal in a voltage level with adequate amplitude and frequency band. For **piezoelectric accelerometers and microphones**, the use of the commercial conditioning amplifiers, model *Nexus* from *Brüel and Kjaer*, represent the standard solution, even if a feasibility study of an home-made amplifier, with similar characteristics in terms of gain, noise and frequency band is ongoing. The output of the commercial amplifiers is single-ended, while a differential output could be implemented in the home-made devices.

For the **other seismic probes and for magnetometers**, equipped with an embedded electronics for signal conditioning, the power supply is the only needed additional electronics. The magnetometers have a single-ended output, consequently, for these probes, an additional differential driver has to be added at the output. Finally an optional line to manage the calibration capabilities of episensors and magnetometers can be added. A conditioning board, able to drive up to 2 tri-axial seismic sensors and 3 magnetometers, with minimal filtering capabilities and differential output, is foreseen to manage these kinds of sensors. This electronics will consist in a 19" 1U box to easily arrange it in standard racks. With respect to the previous version, a small reduction in the dimensions, from 2U to 1U, is foreseen.

For **RF probes**, a commercial mixer, with multiple output, will be used to extract the limited band signals around each modulation frequency. Also in this case, the mixer output is single-ended. The use of digital demodulation from DAQ-box instead of the mixer has to be studied.

Finally, simple transformers will be used for the **voltage sniffers**.

14.5.2.7 Probe and electronics location

The fast monitoring probes will be located in the experimental halls for the general monitoring of the building environment, Different sensor sets are shown as red empty shapes in Fig. 14.21.

The conditioning electronic will be placed near to the closest ADC system to minimize the cabling to the DAQ side. The plan is to use the same racks used for general acquisition purposes also for the probe signal conditioning. The foreseen number of fast probes and conditioning electronics is given in table 14.4, with the following task distribution.

1. *Building Monitoring*: a set of three magnetometers, one slow frequency seismic probe (episensor or velocimeter), one microphone and one RF antenna (red empty squares) are foreseen for each building. The associated electronics, 1 conditioning board, 1 Nexus amplifier and 1 mixer, will be hosted in a suitable DAQ rack.
2. *Suspension and Suspended Bench Monitoring*: one piezoelectric accelerometer (red empty circle) will be installed on each tower and suspended bench, managed by a Nexus amplifier. Since each amplifier can manage up to 4 sensors, the reference solution is to place all the conditioning electronics on the platform or in the DAQ room for the central building, and to share the amplifier with the acoustic monitoring in the other buildings.
3. *Standard Bench Monitoring*: one mid-frequency seismic probe and one infra-sound microphone (red empty triangle) will be put on each standard bench, managed by 1 conditioning board and 1 Nexus amplifier. Also in this case, depending on the total number of conditioning boards or commercial amplifiers, it will be possible to share some electronics with empty channels already available for other tasks. On the other hand, the extra electronics should be hosted in a suitable DAQ rack corresponding to the laboratory where the probes are placed.
4. *Laboratory Monitoring*: a voltage sniffer is foreseen to monitor the main voltage used to power the racks placed in the laboratories.

| Monitoring | Probe | Number of probes |
|-------------------|------------------|-------------------|
| Buildings | Velocimeter | 4 |
| | Standard Mic. | 4 |
| | Magnetometer | $4 \times 3 = 12$ |
| | Antenna | 4 |
| Towers | Accelerometer | 10 |
| Suspended Benches | Accelerometer | 5 |
| Standard Benches | Episensor | 8 |
| | Infra-sound Mic. | 8 |
| Laboratories | Voltage Sniffer | 6 |

Table 14.4: List and number of foreseen fast probes for environmental monitoring.

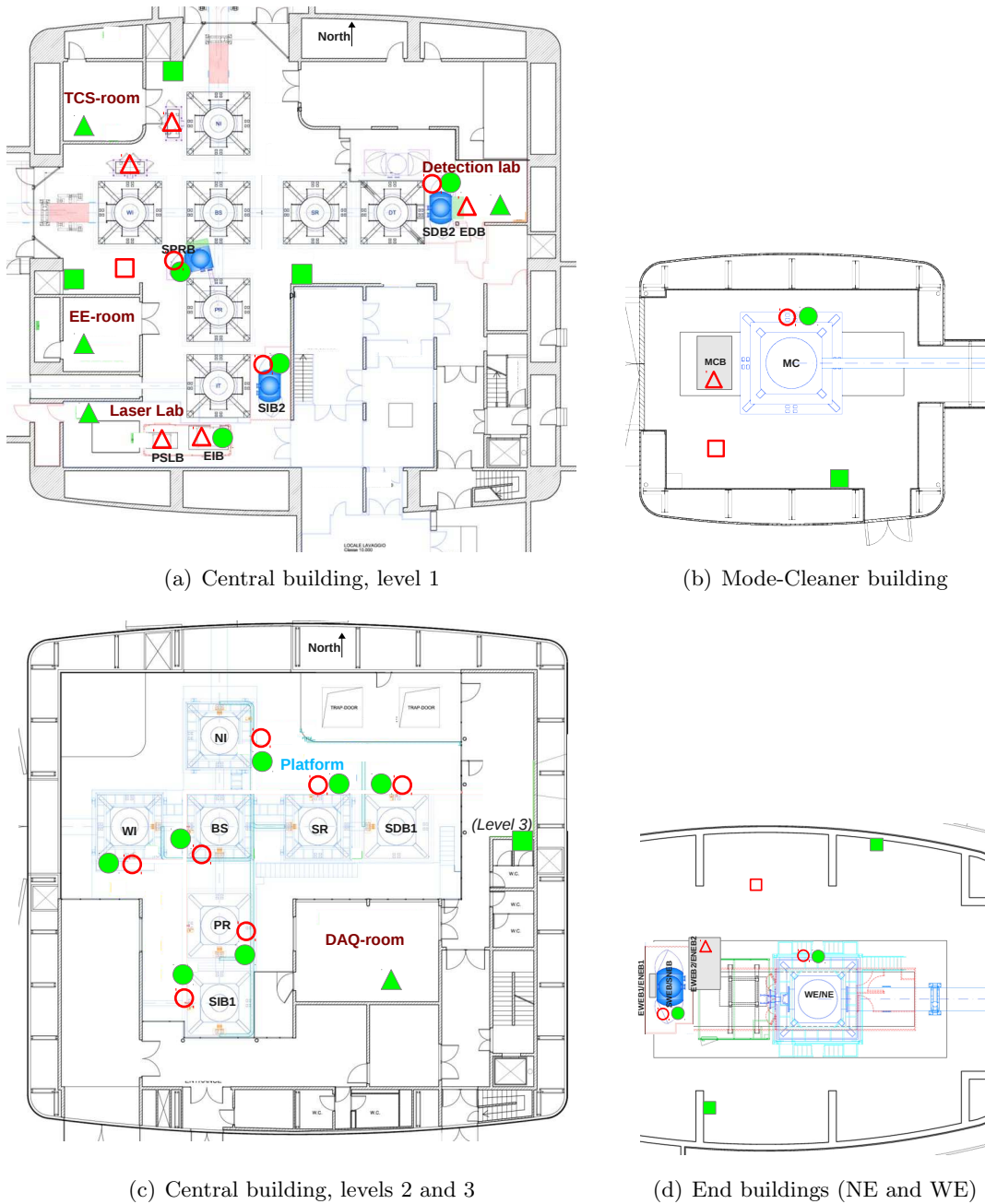


Figure 14.21: Foreseen locations of the sets of probes for environmental monitoring. Slow monitoring: green full shapes. Fast monitoring: red empty shapes. See text for details.

14.6 Calibration and $h(t)$ reconstruction

Calibration and reconstruction deal with the conversion of the detector signals to the physical signal: the gravitational wave amplitude time series $h(t)$.

The goal of the ITF calibration is to determine the frequency response of the dark fringe sensing and mirror actuators, and the ITF optical response to differential arm motion. The different transfer functions must be known within few % in modulus and within few 10 mrad/1 μ s in phase and delay. Absolute timing of the data must also be carefully studied.

The calibration parameters are then used as input to compute the $h(t)$ signal from the ITF time series.

The calibration also deals with the so-called **hardware injections**: the ITF mirrors are moved in a controlled way to simulate a GW signal in the detector. Such injections can be made coherently in different detectors (LIGO-Virgo) in order to simulate a GW signal in the array of detectors. The hardware injections are performed to check the calibration/reconstruction compatibility, to study the robustness of the quality flags and the safety of the vetos applied by the data analysis. It is also possible to perform *blind* injections in order to test the full analysis pipeline and GW detection procedure.

Two calibration methods are performed in order to have independent estimations of systematic errors. The standard calibration is first described. The auxiliary method, the so-called *photon calibration*, is then introduced. The hardware injections system is also presented. Finally, the principle of the $h(t)$ reconstruction is given.

14.6.1 Signal injection system for the calibration

The way the excitation of the mirrors are injected during the calibration data taking, or during the hardware injections, have been modified for Virgo+ and will be used for AdV. An excitation signal is generated and it is added to the control signal of the mirror in order to be applied.

Two possible ways, using two types of real-time process, are used to generate the excitation, as shown in figure 14.22.

- A calibration *Pr process*. It generate sines or wide-band noises signals. It is used to inject the calibration permanent lines when the ITF is running.
- Calibration *injector processes*. They read $h(t)$ channel from frame files and are able to generate the excitation signal to be injected such that the given $h(t)$ signal is simulated in the ITF, at a predefined time given by the frame file. The response of the actuators, with absolute timing calibration³², must be given as an input to such injectors. They are used for hardware and blind GW signal injection in common with other detectors. If needed, they can also generate sines or wide-band noise signals.

These processes run on a real-time PC and produce channels in a shared memory. Then the TOLM software sends the data to the corresponding mirror (or marionette) actuators, in addition to the Global Control signals. They are also sent to the data collection system.

³² The propagation delay of the generated channel to the actuator inside the TOLM network must also be taken into account.

The same principle is used to perform signal injection with the photon calibrator laser. In the context of *noise hunting*, it is planned to use the same system to provide some excitation channels to different locations of the AdV detector.

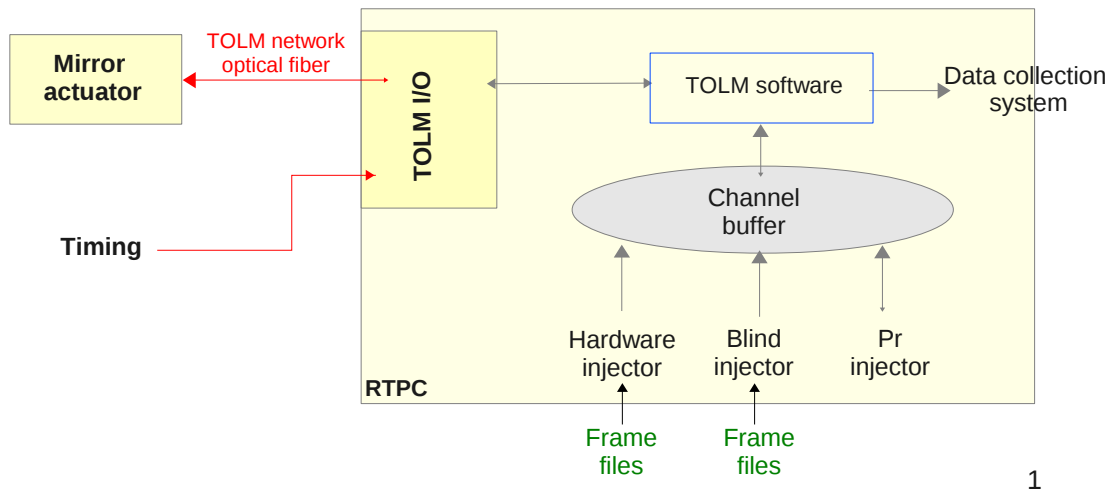


Figure 14.22: Principle of the system for calibration signals injection.

14.6.2 Standard calibration

14.6.2.1 Overview

Calibration methods developed for Virgo are described in [477, 476].

The different types of measurements need specific configurations and alignment of the ITF, as well as different excitations sent to the mirrors or marionettes. They are automated using the Alp software. The data taking is started and controlled as an Alp server. Data analysis is done with the Cali package, largeley based on the ROOT software³³.

The typical calibration errors obtained during Virgo science runs are summarized in table 14.5. The errors were dominated by the systematic errors coming from the transfer of the mirror actuation response from high-power to low-noise mode. This measurement is done excited the different coil actuators in high-power and low-noise modes, and to compare the current flowing in the coils in the different configurations. The challenging and key point of such measurement is to use the same electronics to sense the current in the different modes.

| | Range | Modulus | Phase / Timing |
|--------------------|--------------|---------|---------------------|
| Absolute timing | < 10 kHz | - | 4 μ s |
| Arm and BS mirrors | 5 Hz-1 kHz | 3% | 10 mrad / 5 μ s |
| PR mirror | 5 Hz-300 Hz | 5% | 50 mrad |
| Arm marionette | 10 Hz-200 Hz | 3% | 30 mrad |

Table 14.5: Summary of the typical Virgo calibration errors.

³³<http://root.cern.ch>

14.6.2.2 Frequency domain sensitivity

One of the main output of the calibration process is the sensitivity curve of the detector. It can be computed in the frequency domain from the ITF output signal at dark port, and knowing the ITF response in closed-loop. The permanent excitation (one of the so-called *permanent calibration lines*) of an end mirror at a fixed frequency is needed to monitor the ITF response gain. The sensitivity curve is shown on the monitoring web pages every few minutes.

The same method is also used to estimate a figure of merit of the detector sensitivity, the so-called *detector range*. An online server allows to compute the range every few seconds. The processed channel is added to the data collection raw data stream and is stored in the raw and trend data files. The evolution of the range as function of time is also shown on a monitoring web page.

14.6.2.3 Foreseen evolution for AdV and constraints on hardware

With the method described above, similar calibration errors as for Virgo+ are expected for the first phase of AdV. Lower errors will be required for source parameter estimation when regular detections will happen. Other methods will have to be developed.

Simulations will be needed to validate that such methods will still be valid for actuation calibration with the optical configuration of AdV. In particular, the excitation of the mirrors must be high enough to be visible in the free swinging Michelson configurations. This puts constraint on the minimum force being applied on the mirror magnets from the coils of the actuators, inducing interactions with the **PAY** subsystem.

Coil current measurement in the Virgo+ coil drivers was performed using the same sensing electronics for high power and low noise modes. It will be important to keep this feature in any upgrade of the coil driver electronics for AdV by the **SAT** subsystem.

Ways to measure the optical response of the ITF in dual recycled configuration have to be developed. Nonlinearities in the ITF optical response due to the DC detection need to be studied. If necessary, ways to measure and correct them will have to be developed.

Permanent monitoring of the timing calibration will be setup, probably in the WebMonitoring pages.

14.6.3 Photon calibration

14.6.3.1 Overview

The Photon Calibrator (**PCal**) system aims at acting on a mirror using the radiation pressure of an auxiliary laser with a wavelength different from 1064 nm and maximum power of about 1 W. The force applied on the mirror, and hence the mirror motion, are proportionnal to the power reflected by the mirror. Absolute calibration of the reflected power is performed as function of the output of a photodiode that receives about 1% of the beam [478].

The PCal is used as a mirror actuator, completely independent of the main detector control loops and actuation systems. It can be used to:

- check the $h(t)$ -reconstruction (modulus and phase), comparing the reconstructed $h(t)$ to the applied calibrated excitation;
- perform calibration of the electro-magnetic actuators, comparing the response of the locked ITF to an excitation via the standard actuator and via the photon calibrator;
- perform hardware injections, since the excitation could simulate a GW-like signals.

In Virgo, the design of the viewports around the tower is such that the PCal beam, injected through a viewport towards the center of the mirror, hits the mirror with an incidence angle of about 40° . The beams that are reflected and transmitted by the mirror output through other viewports (see figure 14.23) could also be monitored.

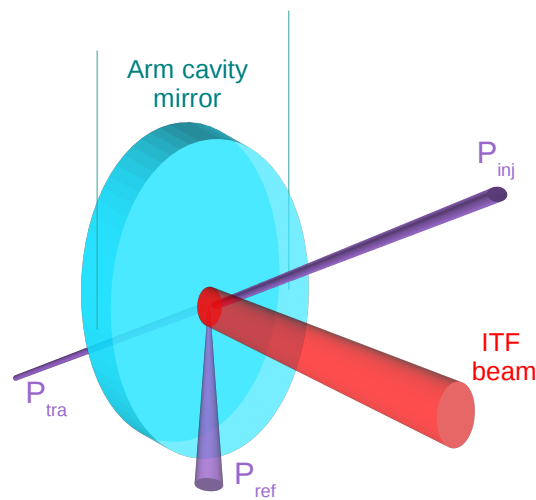


Figure 14.23: Photon calibration beams around the suspended mirror: injected, reflected and transmitted.

In Virgo and Virgo+, the PCal was installed around the NI mirror. The laser diode had a wavelength of 915 nm with maximum power of 1.2 W. The availability of the three beams for power measurements allowed to estimate power losses in the setup. This was the main systematic errors for the PCal calibration. The overall systematic errors on the amplitude of the force applied by the PCal were of the order of 8%. The timing of the setup has been calibrated within $5 \mu\text{s}$ to the GPS time.

During Virgo and Virgo+, the PCal was mainly used to validate the $h(t)$ -reconstruction independently than with the standard actuators, but with less accuracy ($\sim 8\%$ instead of $\sim 3\%$). Moreover, this validation was limited to frequencies below few hundreds of hertz: the PCal force on the mirror induces both a motion of the mirror body, but also a deformation of its surface [479] and the excitation of the drum mode, at few kHz. Both effects made the direct use of the PCal for high frequency calibration more difficult and limited.

During VSR4, the PCal was also used to inject permanent calibration lines to cross-check the ITF optical gain monitoring with the standard actuators.

14.6.3.2 Foreseen developments for AdV

For AdV, PCal will still be useful as an independent cross-check of the standard calibration within better than 10%. Different improvements of the system can be foreseen in order to ease the calibration of the PCal setup and to reduce systematic errors of the ITF calibration using the PCal:

- install the PCal setup on end mirrors, with different advantages:
 - the response of the detector to the PCal-induced arm elongation would be the same as for a GW; When acting on an input mirror, the response was modified within a few percent since also the short Michelson lengths were varied.
 - at 980 nm and 40° incidence angle, the expected mirror reflections are $> 99.99\%$ and ~ 0.25 on the HR and AR faces respectively. The full injected beam power could therefore be used to calibrate the induced force. The transmitted power could be neglected and the reflected power used to estimate systematic errors: it would simplify the absolute power calibration campaigns.
- improve the PCal laser:
 - use a better collimated laser beam, with reduced size (of the order of 1 mm at the three viewports): this will ease the absolute power calibration and reduce systematic errors;
 - select a laser with a wavelength closer to 1064 nm (possibly 980 nm) in order to maximize the mirror reflectivity.
- install a shutter to completely stop the laser beam remotely;
- install quadrant photodiodes to monitor the beam alignment (or a camera);
- install two PCals, one on both end mirrors, in order to have independent cross-checks of their absolute calibration;
- a possible option is to separate the PCal beam into two or three beams that hit the mirror symmetrically around its center, possibly close to the circle that is a node of the mirror drum mode. This would reduce the deformations of the center of the mirror, sensed by the main ITF beam, and allow to use the PCal up to few kHz.

For power calibration purposes, some possible improvements are:

- before their installation, measure the reflection of the end mirrors at the wavelength and incidence angle of the PCal beam;
- depending on the beam size, it could be useful to use powermeters with larger sensor heads;
- setup a digital loop to control the power of the PCal laser, such that it is more stable during the power calibration measurements. This would also reduce the possible harmonics in the mirror permanent excitation applied with the PCal.

Such improvements should allow to slightly reduce to systematic errors of the PCal calibration to below 5%, i.e. close to the level of the standard actuator calibration errors.

The overall use of viewports around the end mirror vacuum chamber has to be discussed with other subsystems. The installation of the PCal systems at new viewports with incidence angle lower than 40° could be helpful.

14.6.4 $h(t)$ reconstruction

14.6.4.1 Overview

The goal of the reconstruction is to provide a calibrated $h(t)$ stream of data, free of instrumental biases. This means to convert the volts measured by the ADCs of the photodiodes readout to displacement in meters or in strain and also to correct for the frequency dependent effects of Virgo like the cavity response and the feedback loops of the locking system.

The procedure is based on a subtraction of the control signals [480, 481]. Since the interferometer is controlled in such a way that it stays on its operating point close to the dark fringe, the $h(t)$ signal is reconstructed from different signals:

- the dark fringe signal, corrected by the calibrated sensing response and the ITF optical response, gives the effective differential arm length value.
- the control signals sent to the mirrors and marionettes to keep the cavity lengths at the operating point, knowing the calibrated actuation, give the differential arm length due to the controls.
- the sum of the two effects gives the differential arm length of the equivalent free ITF: it is the $h(t)$ time series.

$h(t)$ time series must be time-stamped on the GPS time for multi-detector analysis, with precision better than few 10th of micro-seconds.

Since the optical response of the ITF slowly varies with time, the so-called *permanent calibration lines* are injected. They are used to monitor the optical response at few frequencies. Such lines are then subtracted within few percents and do not appear in the $h(t)$ stream.

The package for $h(t)$ -reconstruction is called Hrec. The Hrec server runs online: it reads data from a shared memory and the processed data are sent to another shared memory. The data are stored in specific files, but are also added to the main stream of the data collection and stored in the raw data files. The $h(t)$ data are available with a latency of the order of 30 s. The daily amount of data during VSR4 was 17 GBytes/day (0.2 MBytes/s). It is expected to be similar for AdV.

14.6.4.2 Time domain sensitivity

The detector sensitivity is defined as the FFT of the reconstructed $h(t)$ signal. The sensitivity curve is shown on the monitoring web pages every few minutes, and compared to the one measured in the frequency domain for monitoring. A detector range is also computed from the $h(t)$ channel: it is also shown on web pages, and stored in the raw and trend data files.

14.6.4.3 Foreseen developments for AdV

The core of the Hrec software will be still used for the start of AdV, in the power-recycled configuration. However, it will have to be upgraded to deal with DC detection: the level of non-linearities in the ITF optical response will have to be investigated. It will then have to be upgraded to cope with the dual recycling configuration. Hrec will be upgraded in advance and tested on simulations of the detector in dual-recycling configuration.

The online $h(t)$ data are available with a latency of ~ 30 s. This duration is dominated by the computation of FFTs over 20 s long windows in the reconstruction process. Studies will have to be done if lower latency is required for online multi-detector GW analysis (to provide triggers to electro-magnetic observatories).

Chapter 15

Infrastructures (INF)

15.1 INF Subsystem overview

The infrastructure subsystem (INF) is the evolution of the former subsystem Infrastructure Modifications for Environmental noise reduction (IME) included in the baseline project. In that scenario, the subsystem purpose was mostly dedicated to the realization of the civil engineering works aimed to reduce the level of environmental noise into the experimental buildings. For the Advanced Virgo final optical configuration (Marginally Stable Recycling Cavities (MSRC)), the needs of modification of the current infrastructures in the experimental buildings have significantly increased in addition to the expected works for the environmental noise mitigation. In fact, modifications and arrangements of the current spaces and facilities should be implemented in order to make possible the installation of several parts of the new scientific apparatus.

The first part of the chapter is dedicated to the scientific results and requirements for the environmental noise reduction. With reference to the experience gained in the Virgo/Virgo+ commissioning during the past years, Sec.15.2 describes, for each noise source: the noise reduction goals, the noise reduction requirements and the general criteria to be adopted for this purpose. However, the proposed mitigation actions, which have been considered in the basic design process, should be carefully evaluated during the detailed design phase in order to verify the impact on the budget as well the trade-off between cost and benefits.

The next section gives the requirements of environmental noise reduction, the goals, and the criteria for mitigation. The descriptions reported in Sec.15.3 to 15.7 are based on the basic design of the expected modification works and treat the different systems which are affected and the works foreseen.

15.2 Requirements of environmental noise reduction

15.2.1 Introduction

Experience with Virgo evidenced the necessity to operate the Interferometer (ITF) in a quiet environment. Seismic, acoustic and electromagnetic disturbances can couple significantly

to the interferometer in several and subtle ways and degrade the detector sensitivity. The noise eventually impacts on Gravitational Waves (GW) signal searches [482]. Sources of periodic noise (i.e. persistent vibration of pump engines or cooling fans) can affect searches of GW continuous signals from neutron stars, as well as GW stochastic backgrounds. Non-stationary periodic noise as well as fast noise transients (i.e. electro-magnetic noise pulses from a switching large electric load such as for example a water chiller engine) add noise to GW burst signals searches. As example, Fig.15.1 illustrates the impact of coherent vibration noise in Virgo Science Run 4 (VSR4), the last Virgo+ scientific run. This is the minimum noise impact achieved with a continuous and attentive mitigation work through Virgo and Virgo+ commissioning, as documented for example in references [482, 483, 484, 485].

Major noise sources and preferred environmental noise paths to the interferometer have been studied in Virgo [483]. Primary noise sources are part of the service infrastructures needed for the interferometer operation, in particular: 1) the Heating, Ventilation and Air Conditioning (HVAC) systems both because of vibration noise produced by moving mechanical parts (engines, fans, water chiller compressors, water circulation pumps) and because of acoustic noise generated in air turbulence processes at the fan and in the air ducts; 2) electronic devices, both because of seismic and acoustic noise generated by the fan cooling system, and because of electro-magnetic emissions of power supplies; 3) vacuum pumps, because of seismic and acoustic emissions.

The goal of Advanced Virgo (AdV) is to reduce environmental noise in the GW channel a safe factor ten below the design sensitivity. The noise projection in Fig.15.1 roughly sets the overall noise reduction goal at about a factor one hundred. This ambitious goal needs acting at the same time on: 1) reducing the coupling factor of the disturbance to the interferometer; 2) reducing the emitted noise; 3) limiting the noise transmission paths.

AdV detector design has put extreme care in reducing environmental noise coupling. In Virgo vibration noise was found to couple significantly at in-air and ground-connected external optical benches, optical windows, and in-vacuum absorbing light baffles. In AdV, beam paths in air and through ground connected optics are minimized by adopting in-vacuum suspended optical benches and cryogenic vacuum traps. Nevertheless exposed parts remain, like: in-air injection benches and ground-connected glass window links.

In Virgo electromagnetic disturbances were found to couple significantly to mirror test masses (because of force exerted on the actuation magnets) and to the control and readout electronics (because of cross-talk between offending sources and sensitive electronics). In AdV, reducing magnetic actuators strength of core optics is also strategic to minimize exposure to environmental magnetic fields (see Payload subsystem (PAY) chapter).

Concerning mitigation of sources and transmission paths, in Virgo several *a-posteriori* patch solutions were adopted which often provided just a limited benefit. Now AdV gives the unique opportunity to improve the environmental noise climate close to the interferometer implementing more radical and effective solutions. This means substituting or modifying identified noisy devices or relocating them in new properly isolated places, or improving the shielding of ITF sensitive parts. The final designed solutions shall take into account various factors: 1) noise reduction benefits to the detector sensitivity; 2) new detector design needs and constraints, such as the new clean laboratories, constraints on the location of additional vacuum and electronic equipments; 3) specific needs of the new infrastructure devices (new HVAC sizing, energy savings, ease of machine operation and maintenance); and 4) attention

to costs.

Sec.15.2.2 describes the expected impact of **ITF** infrastructure devices on the **AdV** interferometer sensitivity and defines noise reduction goals. Sec.15.2.3 describes noise mitigation guidelines and tentative action plans.

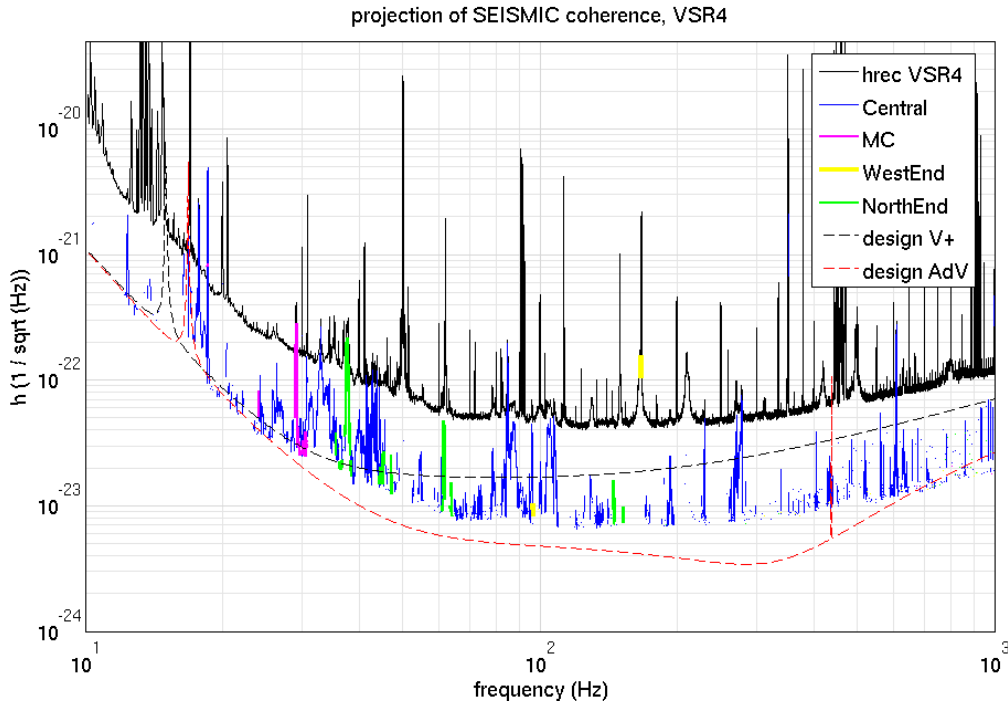


Figure 15.1: Projected seismic noise contributing to **VSR4** strain sensitivity (black) estimated from coherence with monitoring probes. Solid colored curves are projections of the maximum coherence value among acoustic and seismic probes. Blue = **CB** hall, purple = **MC** hall, green = **WE** hall, yellow = **NE** hall. Dashed curves are the Virgo+ (black) and **AdV** (red) design sensitivities.

15.2.2 Noise reduction goals

We consider here the following devices: **HVAC** systems, cooling fans and power supplies for electronic equipments, and vacuum pumps. However, just the **HVAC** systems are strictly of Infrastructure subsystem (**INF**) competence and their mitigation project is described in Sec.15.3. Electronics and vacuum pumps mitigation projects are discussed, respectively, in the Data Acquisition (**DAQ**) chapter and Vacuum subsystem (**VAC**) chapter of this Technical Design Report. However, these actions require some infrastructure modification works which are described in Sec.15.5 and 15.6.

The indicated noise reduction goals are defined at a few noise receptor locations which are chosen close to identified critical **ITF** noise coupling locations. However, it has to be stressed that the intensity of both acoustic and seismic noise depends to some extent on the probe location (for example because of sound waves interference with walls, or amplification of vibrations at resonant modes of mechanical parts). Therefore, the goals indicated here are admittedly to some extent subjective; for example, the limits indicated in Fig.15.4 for the

CB are aimed on eliminating all seismic noise produced by the Virgo installation and its machinery itself, and to reduce the noise level in proximity of the **ITF** to almost the natural ground seismic activity. This step can relatively easily be achieved, whereas reducing seismic activity further would be very costly. Similarly, the need to protect the External Injection Bench (**EIB**) and other systems within the **CB** of acoustic noise is evident (see Sec.15.2.2.2). For other locations, such as End Buildings (**EBs**) and **MC** building, the noise reduction goals are minimal and meant to set a safe margin motivated by the experience with Virgo and Virgo+ commissioning work. These relatively small noise reductions can be reasonably achieved with limited modifications of the existing machines (i.e. at the **EBs**) or by the careful choice and installation of new machines (as it would be the case of the Injection subsystem (**INJ**) lab and the **MC**).

We stress that the impact of the suppression of a specific source, or the mitigation at a specific receptor, on the signal of **AdV** is impossible to predict exactly for seismic and especially for acoustic noise. However, experience with Virgo and Virgo+ has shown that all improvements are helpful or even required to achieve the ultimate design sensitivity.

15.2.2.1 Seismic noise

Sources of seismic noise

Primary sources of seismic noise at Virgo are: air conditioners engines and fans, cooling fans of electronic equipments, and vacuum pumps [483]. Also water pumps and water chillers located in the technical building of the central area, **MC** and **EBs** produce vibration noise which is sensed inside the experimental halls [486, 487].

Fig.15.2 illustrates the characteristics of this noise. Frequency stability of the motors is $f_0/\Delta f \simeq 200$, thus FFT spectra with 20s time windowing typically resolve them completely. The generated noise mainly consists of periodic lines from 10 Hz up, corresponding to devices rotation frequency and harmonics. The noise is significantly above the natural seism displacement spectrum, which for $f \geq 10$ Hz models as $s(f) = 10^{-7}/f^2$ m/ $\sqrt{\text{Hz}}$ [488].

Cooling fans produce seismic lines at typically 40-45 Hz and harmonics; air conditioners noise is associated to the fundamental rotation frequency of the fan (typically 10 Hz to 20 Hz) and engine (24 Hz); water pumps and water chillers produce noise at the fundamental frequency (24 Hz or 48 Hz) and occasionally also the second and fourth harmonics have relevant intensity.

These seismic lines propagate with little attenuation throughout the building floors and walls [489] and are well visible as vibrational noise of ground connected **ITF** parts (vacuum tower tanks and external optical benches) as they are often amplified at structural modes.

Seismic noise paths

The major path of vibration noise in Virgo has been stray light [490, 491]. Because of optics imperfections tiny fractions of light are scattered off the main beam path and then back into the interferometer after having impinged on seismically excited surfaces, like optics on external benches or in-vacuum optical links not completely protected by light absorbing baffles. The back-scattered beam adds to the interferometer a phase noise modulated by this seismic

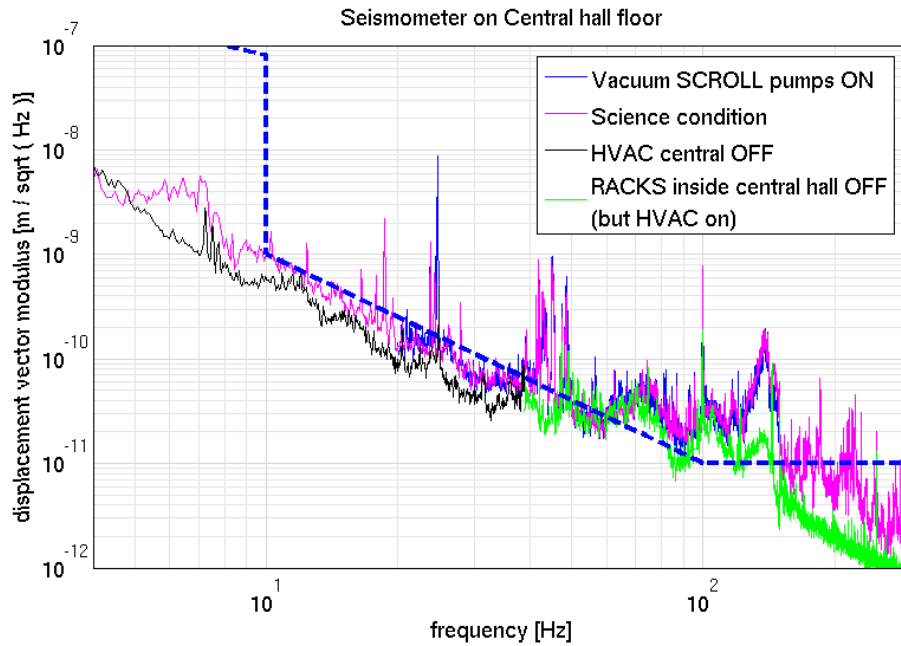


Figure 15.2: Seismic activity of the central hall measured at the ground floor (low frequency tri-axial seismometer Guralp-40T next to the **BS** tower). The displayed quantity is the FFT amplitude spectrum of the displacement vector modulus measured with 20s time windowing. The purple line represents the reference Virgo science-mode noise condition (vacuum scroll pumps switched off). Noise contributions from single infrastructure devices are evidenced: air conditioning of the **CB** (purple to black), racks in the hall (purple to green), and vacuum scroll pumps of central towers (purple to blue). These data were collected in September 2008 when exceptionally all Virgo electronics was switched off to allow electric re-cabling works. For reference purposes, the dashed blue line is the seismic noise reduction goal defined hereafter.

excitation. Both sound pressure and vibrations transmitted through the ground contribute to seismically excite optically exposed parts. Most critical stray-light noise coupling locations in Virgo have been in-air and ground-connected optical tables, Brewster window vacuum links, and output windows.

The minimization of diffused light noise coupling to **AdV** is pursued by several means, namely by the seismic isolation in vacuum of the main external optical benches (see Suspended Benches subsystem (**SBE**) chapter), by the selection of low-diffusing optics (see Detection Subsystem (**DET**) chapter), and by the accurate design and positioning of stray light baffles to protect exposed parts (see Stray Light Control subsystem (**SLC**) chapter). However, potential stray light noise paths remain, in particular: 1) the optical windows between the **ITF** and mini-towers designed to separate the different vacuum levels; 2) possibly the phase camera system of the external detection bench if it will be used in science mode; 3) small in-air and ground connected benches designed to carry the sensors of the Hartmann thermal compensation system or digital cameras, although of less concern because they receive very small laser beam intensity.

Virgo experience taught that a careful approach to the stray-light noise is mandatory. Besides reducing noise coupling, it is also necessary to pursue the reduction of vibration noise reaching interferometer critical locations. A proposition for a tentatively safe requirement for vibration noise reduction is described hereafter.

Seismic noise reduction goals

Stray light coupling is nonlinear and setting a limit is not straight forward. An intrinsically safe limit on the displacement of the light scatterer can be placed for frequencies below 10 Hz by requiring that the maximum frequency of up-converted noise ($f_{max} = 2 \cdot v/\lambda$, v =scatterer velocity, see [491]) is below 10 Hz, thus not polluting AdV detection band:

$$\tilde{s} < \frac{\lambda}{4\pi f} \cdot 10 \simeq \frac{\lambda}{4\pi f} \text{ m}/\sqrt{\text{Hz}}, \text{ for } f \leq 10\text{Hz}$$

where \tilde{s} is the 20s time-windowed FFT spectrum of the modulus of the 3-component displacement vector. Note that this limit holds independently from the amount of stray light coupling at the scatterer. Fig.15.3 illustrates this limit and compares it to typical floor displacement noise of Virgo experimental buildings.

For frequencies above 10 Hz the limit depends on the magnitude of stray light coupling. For reference, Fig.15.3 also illustrates the seismic limit required to reduce the scattered light measured in Virgo+ (VSR4) in one of the maximally coupled location to ten times below AdV sensitivity. Although couplings in AdV are expected to be sufficiently small, a safe approach to stray light is necessary. It is thus required that vibration produced at ITF sensitive parts by local infrastructure devices is reduced to almost the natural ground seismic activity. This requirement is modeled as $s(f) \leq 10^{-7}/f^2 \text{ m}/\sqrt{\text{Hz}}$ for frequencies $10 \text{ Hz} < f < 100 \text{ Hz}$, also shown in Fig.15.3.

For frequencies above 100 Hz, because of the flattening of the AdV design sensitivity curve, a constant frequency independent displacement requirement is sufficient: $s(f) \leq 10^{-11} \text{ m}/\sqrt{\text{Hz}}$, for $f \geq 100 \text{ Hz}$. The displacement noise requirement for the frequency full band is illustrated in Fig.15.3.

Below 10 Hz floor vibrations produced by the present ITF infrastructure devices satisfy the limit. It shall be verified to be met also by new installations. In addition, attention must be paid that critical ITF components (ground connected refractive or reflective optics) do not amplify low frequency ground seism at any internal mechanical resonant mode. Mechanical modes of new components exposed to beams (optical mounts, light baffles, cryogenic-traps, etc.) will be carefully evaluated and damped if necessary.

Above 10 Hz displacement noise of buildings floor at present exceeds the limit by a factor of 10. Note that at vacuum links (i.e. tower flanges where output windows or cryogenic traps are installed) the floor noise is often amplified by mechanical resonances. Fig.15.4 illustrates the measured vibration noise and identified sources in the CB and shows its contribution to the Virgo+ noise budget in VSR4. The noise (below $\simeq 50 \text{ Hz}$) is measured by a tri-axial seismometer (*Kinematics* mod. *Episensor FBA-ES*) at the base of the DT while above 50 Hz a seismometer (*Piezotronics* mod. *393B12*) at the detection tower output flange oriented along the beam is used. These sensors are part of the Virgo permanent environmental monitoring network [492]. See reference [493] for sensor locations. The comparison between the measured seismic noise and the goal set in Fig.15.4 gives the following reduction requirements: 1) for the hall HVAC a factor of 10 from about 10 to 100 Hz; 2) for the clean rooms HVAC a factor of about 20 on emitted seismic tones around 15 to 20 Hz; 3) for the DAQ room HVAC a factor of 5 for tones around 24 Hz. Similarly, Fig.15.5 and Fig.15.6 illustrate the Virgo+ seismic noise status at the MC and EBs (see figure captions for defined seismic receptor locations).

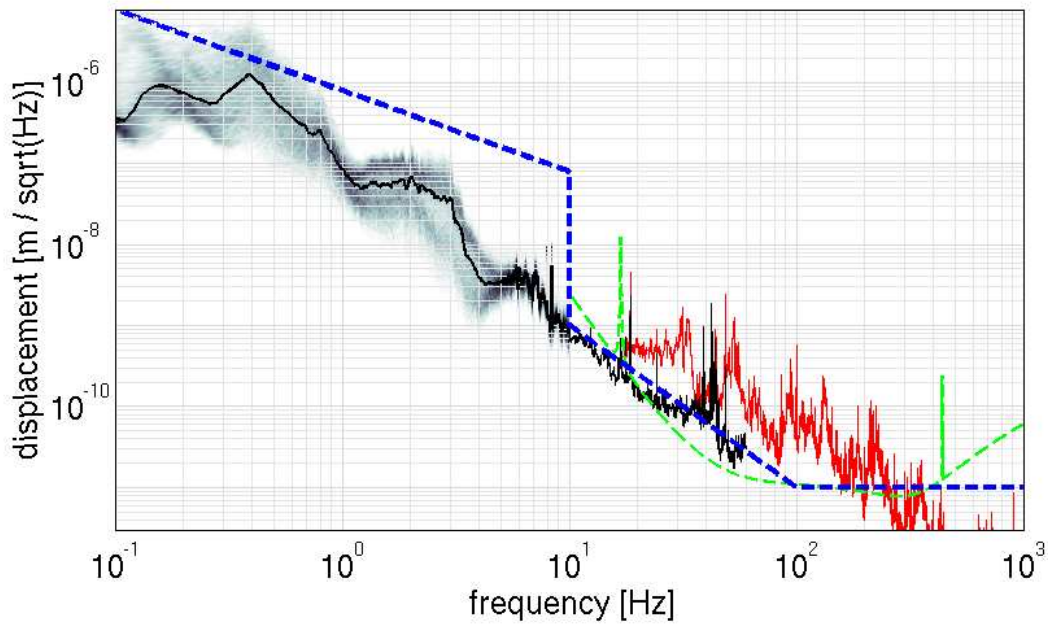


Figure 15.3: Displacement noise measured at the central building floor (black) and at the tower vacuum tanks (red) (maximum measured spectral noise among the central towers for which seismic isolation of the turbo-molecular vacuum pump has been implemented: DT, PR and NI). The measured noise is compared to the set seismic noise requirement (dashed blue). The amplification of floor seism at tank walls can be seen (black to red). The grey shading illustrates the variation of ground displacement measured over one year. Low frequency seism variation is due to natural causes (wind and sea activity up to $\simeq 1$ Hz) and traffic noise (approximately 1 Hz to 5 Hz). Above 5 Hz seismic noise is due to infrastructure machines, and it is quite stationary. The green curve is for reference and represents the limit required for safely reducing the stray-light measured in Virgo+ to 10 times below the AdV design sensitivity (the coupling factor is the one measured in Virgo+ for the BS tower, eLog 28904).

15.2.2.2 Acoustic noise

Sources of acoustic noise

Slow (less than 1 Hz) air pressure variations inside experimental halls are associated to external atmospheric conditions and presence of wind. Above 1 Hz and up to $\simeq 100$ Hz the dominant source of acoustic noise in the buildings is the air conditioning and air distribution system. The generated noise is broadband with wide bumpy structures and, for some machines, also a few narrowband tonal components above $\simeq 50$ Hz. The noise is presumably produced in air turbulence processes near the fan or inside the ducts and transmitted through air or duct vibrations. Above $\simeq 100$ Hz the main acoustic noise source in the building are the small cooling fans of electronics racks. Acoustic noise from cooling fans consists of a broadband background and intense tonal components at the fan frequency, blade-pass frequency and its harmonics (most intense tonal components are measured around 45 Hz and its multiples). Fig.15.7 shows the impact of the running equipment (HVAC and racks) on the acoustic noise in the CB.

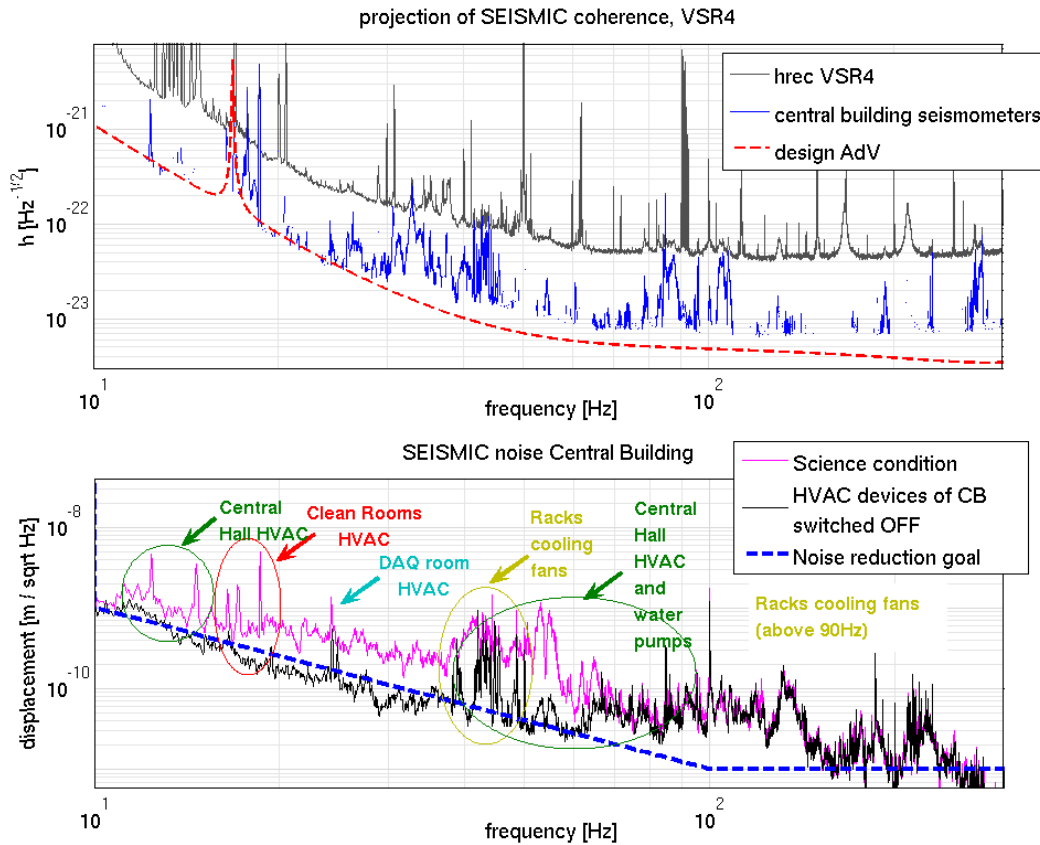


Figure 15.4: Top: projection of coherent noise measured in **VSR4** already shown in Fig.15.1. Only coherent noise with **CB** seismometers is shown. This plot highlights the correspondence with the seismic noise shown in the bottom plot. Bottom: purple: seismic noise of the **CB**. Displayed data is the modulus of the 3-component displacement vector at the **DT** base (channels Em_SEBDCE13,14,15). Above 100 Hz the data are from a single-axis piezoelectric accelerometer at **DT** East flange (channel Em_SETODE01). Black: residual noise after switching off all the central building air conditioning devices including water pumps. The arrows point to identified sources of tonal components. Blue: dashed curve: limits for **AdV**.

Acoustic noise paths

It has been shown that sound pressure noise induces vibrations of mechanical parts (i.e. optical mounts, in-air optical benches or optical links) of the **ITF**. Thus, ultimately acoustic noise coupling paths are the same as those for seismic noise. One outstanding example are acoustically induced vibrations of the old detection Brewster window ([494]). Also acoustic coupling at external benches was found to be critical [495]. To mitigate acoustic coupling during Virgo sound shielding enclosures have been installed around all external in-air benches carrying control optics [496, 497]. Tab.15.1 lists the measured performances of the Virgo acoustic enclosures. These offer reasonably good acoustic isolation (about a factor 10 in sound pressure) above $\simeq 100$ Hz, but poor isolation at lower frequencies. Presumably performances are limited by the enclosure stiffness at low frequency and by apertures (needed for cables and beams) at high frequency.

In **AdV**, acoustic coupling will be minimized by placing most crucial optical benches under vacuum. However, exposed elements remain. The most critical one is the in-air **EIB**, which

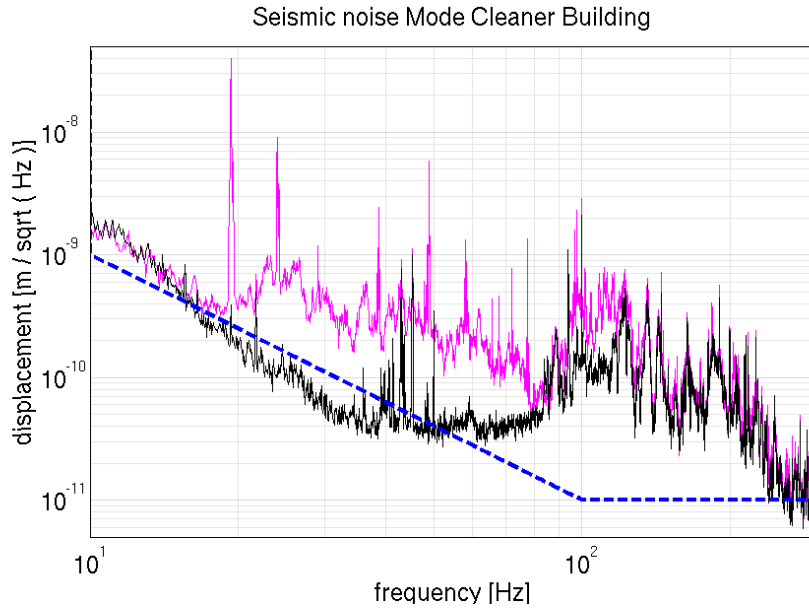


Figure 15.5: Seismic activity at MC building. Displayed quantity is the modulus of the 3-component displacement vector measured by the *Episensor* probe located at MC floor (channels Em_SEBDMC01,2,3). Above 100 Hz the single-axis piezoelectric accelerometer located at the MC tower West flange is used instead (channel Em_SETOMC01). The purple curve describes the science mode condition. The black curve is the noise when the building HVAC machine is switched off. The blue dashed line is the limit for AdV.

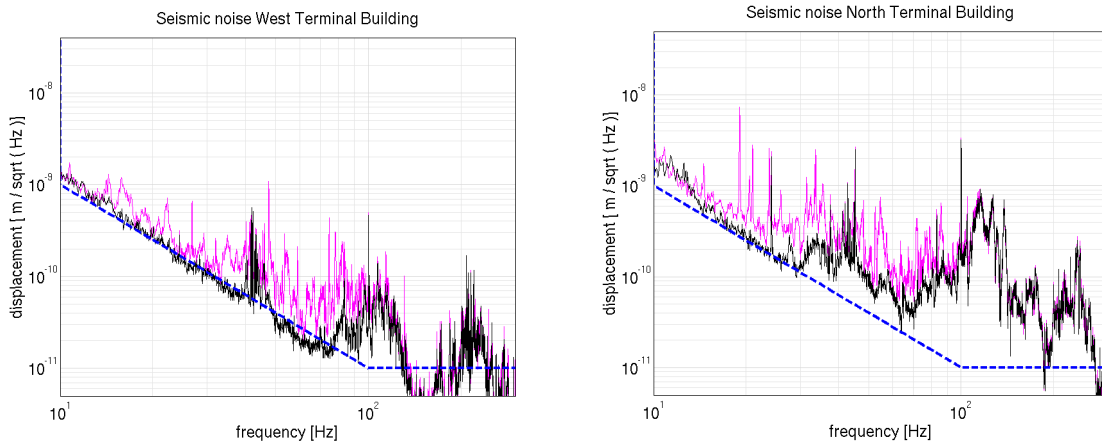


Figure 15.6: Seismic activity at the WEB (left) and NEB (right). Shown is the single axis horizontal displacement of the west (north) tower east (south) flanges (channels Em_SETOWE01 and Em_SETONE01). The purple curve describes the science mode condition, the black curve is the noise when the building HVAC machine is switched off. Below 40 Hz, the measurement is limited by sensor noise. The blue dashed line is the limit for AdV. The difference in intensity of seismic activity between NEB and WEB above $\simeq 100$ Hz is due to the vacuum turbomolecular pumps: the NE tower features a turbo pump of the same model as those in the central towers, but not seismically isolated, while the WE tower features a less noisy turbo pump model.

is discussed below.

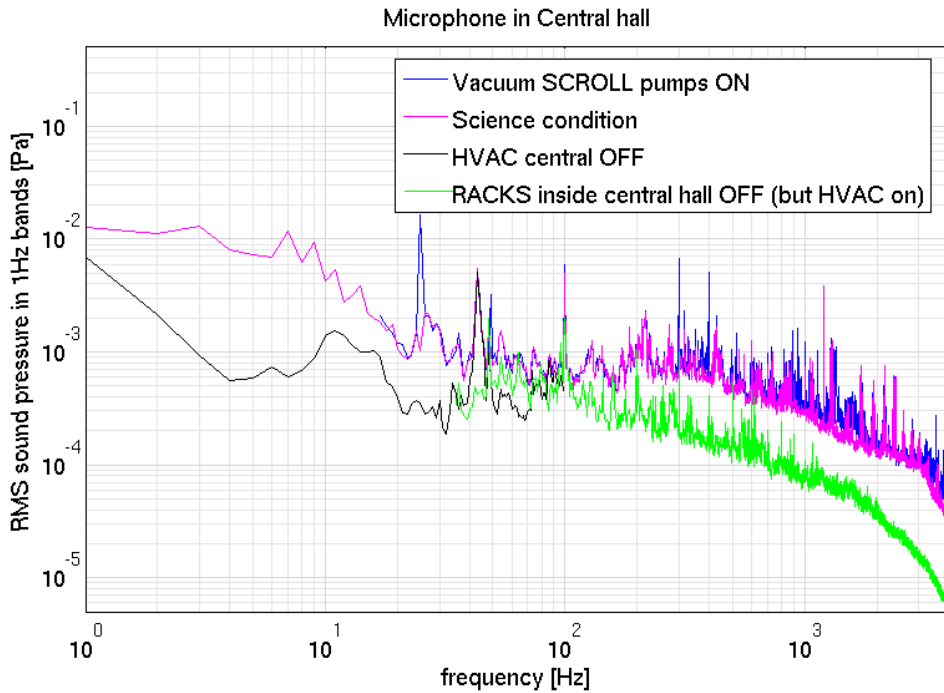


Figure 15.7: Acoustic noise in the Virgo CB (channel Em_ACBDC01). The displayed quantity is the RMS of the sound pressure in 1 Hz wide frequency bands. The purple line represents the reference Virgo science mode noise condition (vacuum scroll pumps off). Noise contributions from single infrastructure devices are visible by comparing the purple line to the different curves: air conditioning off (black line), racks in the hall off (green line), and vacuum scroll pumps of central towers on (blue line). These data were collected in September 2008 when exceptionally all Virgo electronics was switched off to allow electric re-cabling works.

While the reader is referred to **SBE** chapter for more details, it is briefly recalled here that another important path of vibration noise evidenced in Virgo was the jittering of the input beam (Beam Jitter (**BJ**)). Jitter noise of the beam at the interferometer input depends on longitudinal and angular motion of the **EIB** and the optics on it. The need for some reduction of vibration noise of **EIB** was demonstrated in Virgo and Virgo+, and holds for **AdV** as well [498]. The designed seismic isolation stage for the Advanced Virgo external injection bench is the External Injection Bench-Seismic Attenuation System (**EIB-SAS**), described in section **SBE**.

Tests of **EIB-SAS** in the Virgo+ injection system (December 2011 to February 2012) showed that the bench isolation performance is ultimately limited (from 1 Hz up to at least 500 Hz) by coupling to sound pressure fields. This is illustrated in Fig.15.8 [499]. This figure compares the residual bench vibration noise with the seismic requirement¹. An additional factor of 10 reduction of bench vibration noise above 10 Hz is necessary to meet the requirement.

It has been demonstrated that the residual bench motion (from 1 Hz up to at least 500 Hz)

¹The **EIB-SAS** seismic noise requirement described in reference [500] has been set for Virgo+. Simulation effort is ongoing to convert beam jitter noise requirements at the **MC** input (see chapter) to vibration requirements for the optics on the bench, and eventually set the **EIB-SAS** seismic requirement tailored for **AdV**. However, the **AdV** requirement is considered to not differ significantly from the Virgo+ requirement, which is provisorily taken as reference.

| Center frequency of octave bands | Enclosure of External Injection Bench | Enclosure of Detection lab | Enclosure of North End Bench | Enclosure of West End Bench |
|----------------------------------|---------------------------------------|----------------------------|------------------------------|-----------------------------|
| Frequency [Hz] | $D[dB]$ | $D[dB]$ | $D[dB]$ | $D[dB]$ |
| 16 | 4 | 4 | NA | NA |
| 31.5 | 3 | 15 | 6 | 6 |
| 63 | 6 | 12 | 12 | 10 |
| 125 | 16 | 13 | 15 | 17 |
| 250 | 15 | 20 | 16 | 17 |
| 500 | 12 | 23 | 21 | 21 |
| 1000 | 15 | 23 | 25 | 19 |
| 2000 | 19 | 23 | 24 | 23 |
| Reference | eLog 30592 | eLog 16008 | eLog 16309 | eLog 16309 |

Table 15.1: Acoustic isolation of Virgo bench enclosures. The measured quantity is $D \equiv 20 \cdot \log_{10}(P_{before}/P_{after})$ where P_{before} and P_{after} are the RMS sound pressure fields at the bench location measured respectively before and after the enclosure installation (above 50 Hz the isolation has been measured also by adding white noise following prescriptions of UNI EN ISO 11546-2:1997). More details in referenced Virgo electronic logbook entries.

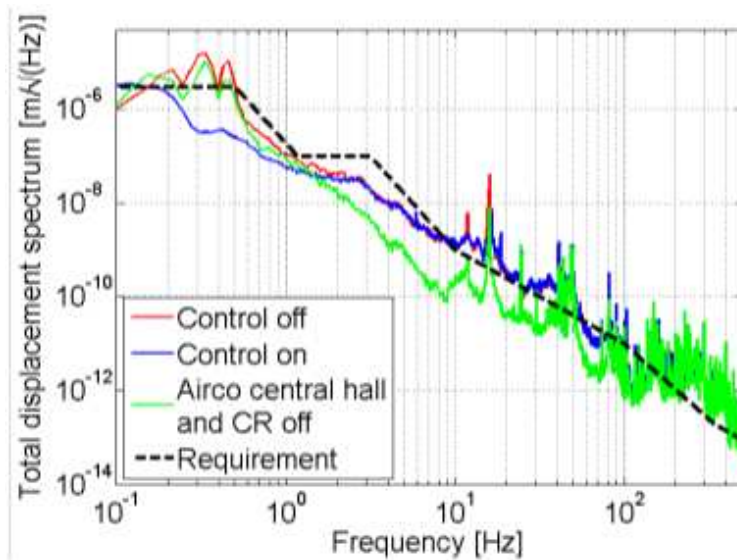


Figure 15.8: Displacement noise of EIB on the SAS suspension. The displayed quantity is the modulus of the displacement vector. The blue curve corresponds to the bench inertial damping control on. The green curve corresponds to air conditioners of the CB off. The black dashed curve is the seismic noise requirement ([500]).

is due to the differential action of sound pressure on the bench and reduces proportionally to the sound pressure field intensity [499]. Fig.15.9 illustrates the EIB-SAS noise reduction as the intensity of the sound pressure field and its gradient reduces when switching off the air conditioners of the building. The clean room air conditioner is the most relevant source below 100 Hz, while above 100 Hz residual noise originates from rack cooling fans located in

the main experimental hall.

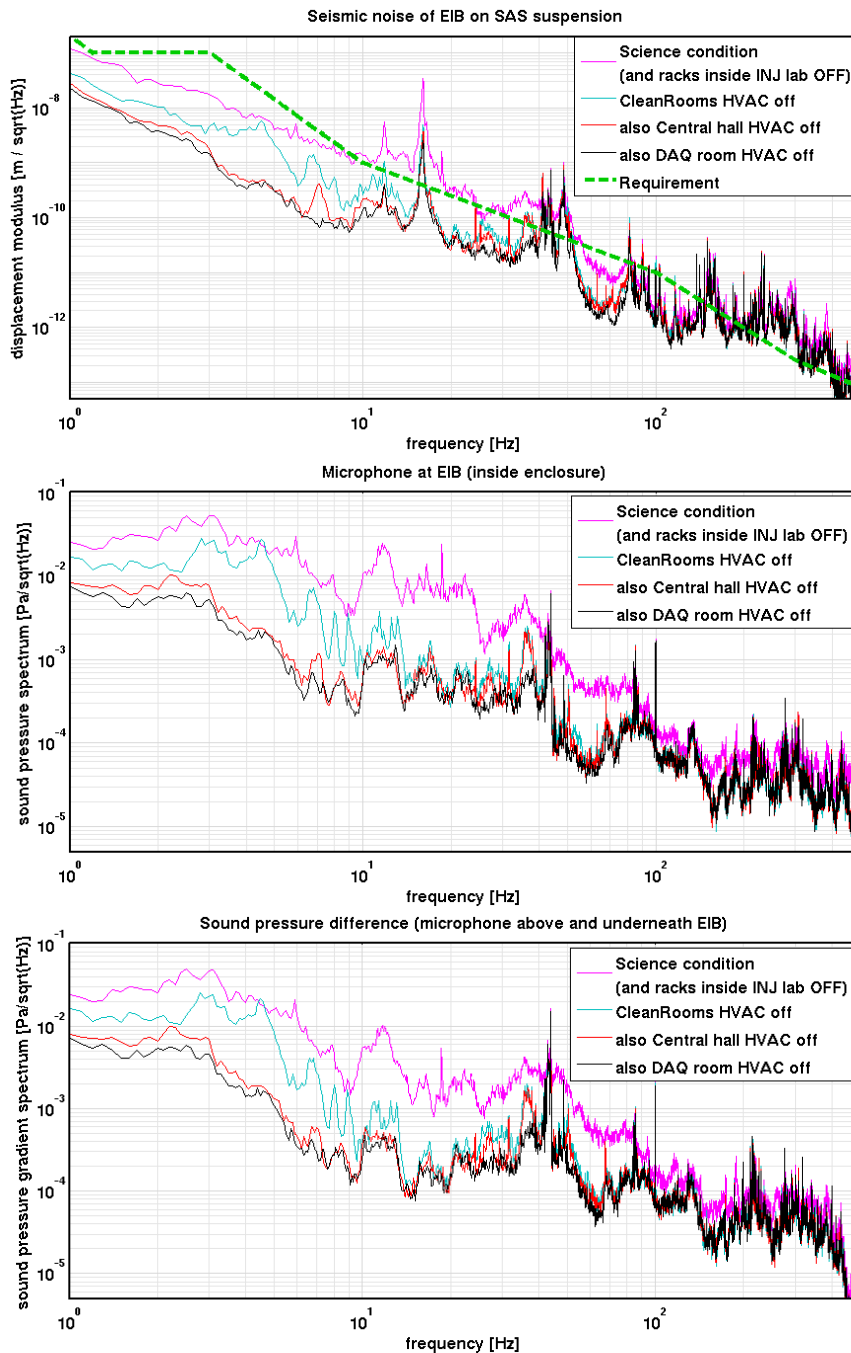


Figure 15.9: Noise reduction as the sound pressure field intensity at **EIB-SAS** reduces when switching off one by one in sequence all air conditioners of the building (see legend). Top: Displacement noise of **EIB** on the **SAS** suspension. Centre: sound pressure field measured by one microphone probe above the bench (probe *Em_AC_EIB*). Bottom: sound pressure difference between the probe above the bench and another probe placed underneath the bench, at a distance of 1 m from the other probe.

Acoustic noise reduction goals

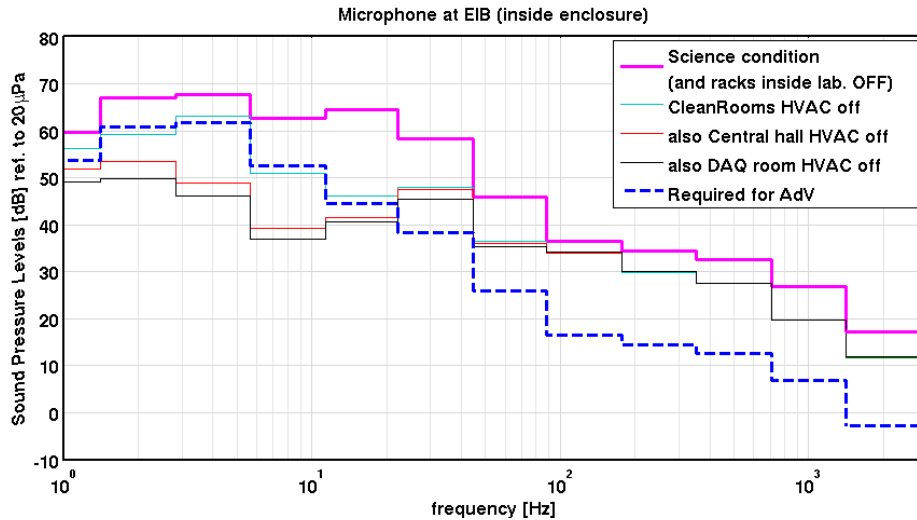


Figure 15.10: Acoustic noise at **EIB-SAS** inside the Virgo acoustic enclosure (same data as in Fig. 9 top) shown here as **SPL** $L_p \equiv 20 \cdot \log_{10}(P_{RMS}/P_0)$, where P_{RMS} is the **RMS** value of sound pressure in octave bands, and P_0 is the conventional sound pressure reference of 20 μPa . The dashed blue line is the **SPL** at the **EIB-SAS** location required in **Adv**.

- **EIB-SAS**

The major objective is to mitigating the acoustic pressure field at the location of the **EIB**. The acoustic noise requirement is illustrated in Fig.15.10 expressed as **SPL** in octave frequency bands (see Fig.15.10 caption for definitions). In Sec.15.2.3.1 a strategy is presented to achieve this goal.

- **Other locations**

A safe approach requires that also optical links and small external benches are exposed to less acoustic induced vibration. Because of the obvious limited performance of acoustic enclosures and also of the possible difficulty in installing shields around some sensitive components, the most promising strategy is to realize a more silent environment in the entire experimental hall by reducing acoustic emission from identified sources. The main concern is tonal noise above $\simeq 50$ Hz.

- **Central building hall:** a factor of 4 reduction of **RMS** sound pressure intensity (-12 dB) above $\simeq 50$ Hz is needed in the **CB** hall where most links and sensitive components are located. Fig.15.11 left illustrates the Central hall acoustic noise in Virgo.
- **Detection lab:** acoustic noise in the new **DET** lab should benefit of the hall noise reduction. However acoustic noise in proximity of the external bench and optical links, must certainly not be worse than it was in Virgo inside the external detection bench enclosure (Tab.15.2).
- **End building halls:** a similar reduction (about -12 dB in **RMS** sound pressure intensity above $\simeq 50$ Hz) is strongly advised also for the **EBs**. Fig.15.12 illustrates the acoustic noise measured at the Virgo **EBs**. To reach this goal mainly muffling sound emissions from cooling fans is needed, as detailed in Sec.15.2.3. Between about 50 Hz and 100 Hz some mitigation is necessary also on the **HVAC** side, mainly aimed

at removing tonal noises.

- **Mode cleaner:** there is no noise evidence to motivate specific acoustic mitigation in the **MC** building. However, a safe approach suggests some mitigation is pursued mainly aimed at reducing the intense sound tones emitted by both the **HVAC** and racks cooling fans (in Fig.15.11-right). A reduction factor of 4 is advised.

Tab.15.2 summarizes **SPLs** in octave bands measured at all reference locations and noise reduction requirements. Microphone probe locations are documented in the online map at [493].

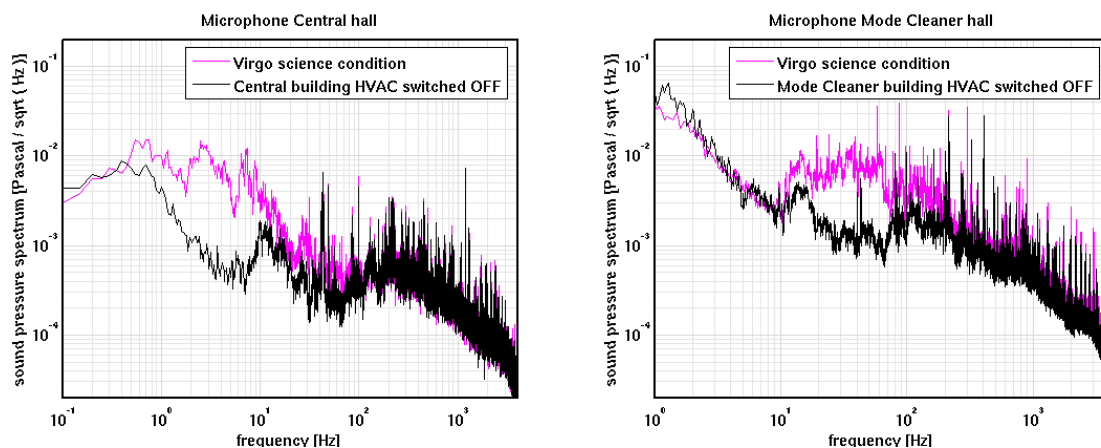


Figure 15.11: (left) Sound pressure field measured in the **CB** (*probe Em_ACBDCE01*); (bottom) sound pressure field measured in the **MC** hall (*probe Em_ACBDMC01*). Science mode environment condition in purple; residual noise after **HVAC** devices are switched off in black.

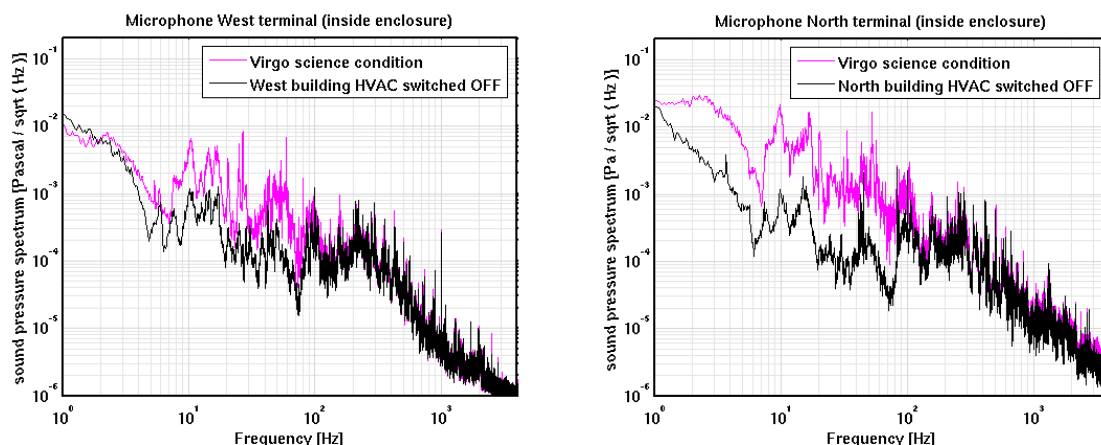


Figure 15.12: (left) Sound pressure field measured inside the West acoustic enclosure (*probe Em_ACBDWE01*); (right) sound pressure field measured inside the North acoustic enclosure (*probe Em_ACBDNE01*). Science mode environment condition in purple; residual noise after **HVAC** devices are switched off in black.

| Center frequency of octave bands | INJ lab at EIB | | Central hall | | DET lab at EDB | | Mode Cleaner hall | | North End hall | | West End hall | |
|----------------------------------|-----------------|---------------|-----------------|---------------|-----------------|-----------------|-------------------|-----------------|-----------------|-----------------|-----------------|--|
| Virgo probe name | <i>AC_EIB</i> | | <i>ACBDCE01</i> | | <i>ACDBDL01</i> | | <i>ACBDMC01</i> | | <i>ACBDNE01</i> | | <i>ACBDWE01</i> | |
| Notes | (2,3) | | (1) | | (1,3) | | (1) | | (1,3,4) | | (1,3,4) | |
| Frequency [Hz] | <i>SPL</i> [dB] | <i>D</i> [dB] | <i>SPL</i> [dB] | <i>D</i> [dB] | <i>SPL</i> [dB] | <i>SPL</i> [dB] | <i>D</i> [dB] | <i>SPL</i> [dB] | <i>D</i> [dB] | <i>SPL</i> [dB] | <i>D</i> [dB] | |
| 1 | 60 | -6 | 52 | | 60 | 62 | | 62 | -10 | 52 | | |
| 2 | 67 | -6 | 55 | | 62 | 61 | | 63 | -10 | 51 | | |
| 4 | 68 | -6 | 55 | | 67 | 55 | | 60 | -10 | 46 | | |
| 8 | 63 | -10 | 57 | | 60 | 52 | | 60 | -10 | 50 | | |
| 16 | 65 | -20 | 50 | -10 | 51 | 61 | -10 | 60 | -10 | 51 | | |
| 31.5 | 58 | -20 | 50 | -10 | 38 | 66 | -10 | 58 | -10 | 54 | -6 | |
| 63 | 46 | -20 | 46 | -12 | 33 | 67 | -12 | 65 | -12 | 58 | -6 | |
| 125 | 37 | -20 | 49 | -12 | 35 | 66 | -12 | 64 | -12 | 58 | -6 | |
| 250 | 35 | -20 | 53 | -12 | 31 | 64 | -12 | 60 | -12 | 58 | -10 | |
| 500 | 33 | -20 | 52 | -12 | 30 | 61 | -12 | 59 | -12 | 54 | -6 | |
| 1000 | 27 | -20 | 52 | -12 | 25 | 59 | -12 | 55 | -12 | 44 | -6 | |
| 2000 | 17 | -20 | 47 | -12 | 24 | 54 | -12 | 48 | -15 | 38 | -6 | |

Table 15.2: Black: Sound Pressure Levels (SPL) computed in octave bands from 1 Hz to 2 kHz at defined acoustic receptors ($SPL \equiv 20 \cdot \log_{10}(P_{RMS}/P_0)$, P_{RMS} is the pressure field RMS in the specified frequency band and $P_0 = 20 \mu Pa$). Red: required noise reduction, $D \equiv 20 \cdot \log_{10}(P_{Adv}/P_{Virgo})$. Green: advised noise reduction. Notes: (1) data collected during of **VSR4** science mode on June 15, 2011; (2) data collected on January 23, 2012 during **EIB-SAS** tests, with respect to science mode environmental noise condition also racks inside the **INJ** lab were switched off; (3) microphone is located at the external optical bench inside the acoustic shield enclosure; (4) **SPL** is estimated outside of the enclosure, by adding to the measured **SPL** the measured enclosure acoustic isolation listed in Table 15.1. Consult reference [493] for details on probes location.

15.2.3 General criteria for noise mitigation

In this section we describe tentative mitigation strategies to meet the noise reduction goals specified in Sec.15.2.2. General criteria are given for purchasing machines and installing equipment, and rules for the **executive** design to be elaborated by the external contractor firm. Our preference is based exclusively only on the presumed noise impact on the interferometer sensitivity. For some items other aspects (i.e. energy saving, operating conditions) might provide an important motivation for upgrades, these will be discussed in Sec.15.3. Sec.15.2.3.1 proposes a strategy for reducing acoustic noise inside the **INJ** lab. Sec.15.2.3.2 concerns mitigation actions for the **HVAC** machines; each machine is treated separately for both seismic and acoustic aspects. Sec.15.2.3.3 briefly describes mitigation of seismic and acoustic emission from rack cooling fans. Sec.15.2.3.4 briefly describes the noise concerns and mitigation actions foreseen for vacuum scroll pumps. Finally, Sec.15.2.3.5 motivates and proposes a strategy for monitoring switching noisy devices. For each item we briefly recall the mitigation goal stated in the previous Sec.15.2.2.

15.2.3.1 INJ lab silencing

The main concern for the **INJ** lab is acoustic noise because it limits **EIB-SAS** performance, while seismic noise is not of primary concern because **EIB-SAS** performs a good isolation from ground seism. As stated in Sec.15.2.2.2, at the **EIB** location **RMS** sound pressure noise above 10 Hz shall reduce by at least 20 dB with respect to Virgo. Some smaller noise reduction (6 to 10 dB) is advised also below 10 Hz as detailed in Fig.15.10 and Tab.15.2.

A tentative strategy for silencing the **EIB** consists of the following steps (see [501]):

- **Enclosure.** One new larger acoustic enclosure covering both laser and injection bench is planned to allow easy access and interventions on the optical benches [502]. The acoustic isolation provided by the Virgo acoustic enclosure around the injection benches was very poor below ≈ 100 Hz and modest (≈ 15 dB) above 100 Hz (Tab.15.1). Probably the isolation performance will be improved by connecting it tightly to the concrete floor instead of setting it on the floating floor as it was done in Virgo. However, ultimately enclosure performance might be limited by the presence of unavoidable holes for cables and beams. Thus, the optimal strategy to achieve the noise reduction goal seems to be not just improving the enclosure performance, but instead primarily aiming at creating a more silent environment inside the laboratory, mitigating all identified sources. This is detailed in the following steps. It should be also reminded that one established problem of the Virgo enclosures was air flux likely caused by temperature gradients [496]. Care must be taken to guarantee temperature uniformity within the new enclosure volume and between the inside and the outside of the enclosure, for example by properly positioning and sizing acoustically isolated air grids.
- **Cooling fans.** The interior of the **INJ** lab will be freed from fan-cooled electronic equipment. New electronic racks will be placed in a dedicated room separated from the sensitive locations (i.e. **INJ** lab) by heavy and rigid walls made of concrete or equivalent material with excellent acoustic isolation properties also in the 10–100 Hz frequency region. A proposal is made in [502] and further discussed in Sec.15.7.1.
- **Air conditioner.** In Virgo the same machine was adopted for conditioning both the clean rooms and the **INJ** lab. This machine is the primary source of acoustic noise inside the laboratory over the whole relevant frequency band. This is evidenced also in Fig.15.10 which shows results of a selective switch off. A new, smaller and properly sized machine will be dedicated to only the **INJ** lab. The new machine must guarantee air renewal rate and filtering quality for the clean room class ISO 7/8, as well as humidity and temperature stability as specified in [503]. The new machine will have an adjustable air flux over the widest possible range in order to operate at *full* range when access to the laboratory is made, while it will slow down according to needs during data taking [503]. The air distribution ducts layout also needs modification to adapt to the new organization of the **INJ** lab (i.e. presence of minitower). Particular care shall be put in limiting as much as possible air turbulence inside the **INJ** lab room and in the under-floor.
- **Separating walls.** The acoustic isolation of the **INJ** lab from the **CB** is poor. The residual acoustic noise above 100 Hz is transmitted from the **CB** through the separating wall [501]. This wall will be replaced by a wall with better acoustic isolation performance. This is further discussed in Sec.15.7.1.

- **Other sources.** We will verify that all other possible sources of acoustic noise outside the laboratory individually produce noise which is at least a factor of 3 (10 dB) below the set limit. To this end, as can be seen in Fig.15.10, some reduction of acoustic noise from the **CB** air conditioner (i.e. 10 dB between 10 and 100 Hz) is needed. Also acoustic noise emission from racks in the hall need mitigation as explained in Sec.15.2.3.3.

15.2.3.2 HVAC systems

The executive design implementation of the **AdV HVAC** systems is outsourced to an external engineering firm. Here and in Sec.15.3 the baseline choices are presented, while the operative choices and implementation details are left to the expertise of the engineering firm.

Hereafter the characteristics of the existing machines and mitigation experience are recalled, in order to define some basic mitigation actions. These actions will be adequate to meet the set noise reduction requirement as well as other important requirements: 1) the oversize or undersize of some existing machines; 2) the need to have machines with flexibility of their working conditions; 3) the need of independent systems allowing the modification of the operating parameters in experimental rooms with different characteristics and requirements; 4) the need to simplify machine installation, improve their operating conditions and maintenance; 5) the energy saving by improving the thermal insulation of the air distribution ducts. Finally, the designing has to take into account the impact on the project both in terms of cost-benefit analysis and of the **AdV** general planning.

- **The new HVAC**

New air handler machines and air distribution systems are certainly needed for the new **DET** lab and the **INJ** lab (see Sec.15.2.3.1). New machines are envisaged also for the **CB** hall (because currently oversized with respect to needs) and the **MC** hall (see motivation below). In selecting new machines general well known criteria for reducing seismic and acoustic noise emissions will be followed, among which: 1) careful sizing to avoid oversizing; 2) adopt slow fans to reduce both seismic and acoustic noise, eventually choose slower but larger diameter fans to guarantee needed air flux; 3) optimize fans for low air turbulence (i.e. reverse blades by an airfoil profile type); 4) air turbulence in the ducts can be minimized keeping air speed low, possibly below 6 m/s; 5) seismically isolate moving parts (engine/fan) with a low cut-off ($f_c \leq 4$ Hz) and well damped ($Q \leq 5$) isolation stage; 6) care of mechanical balancing of the engine-fan system; 7) minimize seismic shortcuts through isolation of pipes and ducts; 8) minimize air turbulence caring of the smooth layout of ducts in and out of machines; 9) insert acoustic silencers on the ducts close to the machine body to reduce noise above several tens of Hz. It is also desired that new machines allow some flexibility in regulating the air flux and speed of the fan, in order to permit reducing noise if proven necessary and compatible with air conditioning needs. For conditioning electronic rooms of small volume (like the one foreseen for additional **INJ** racks, see Sec.15.7.1 and Fig.15.32) a wall fan-coil air cooling system is advised. A similar system (two fan-coil units of 3400 W chilling power each) has been adopted for the Electronic Equipment (**EE**) room hosting the Virgo **INJ** lab electronics racks. The system proved effective and particularly silent (eLog 21180).

- **HVAC of CB hall**

The main concern of this machine is seismic noise (broadband and at tones) from about 10

to 100 Hz (Sec.15.2.2.1) which needs a reduction of a factor of 10. In the same frequency range a 10 dB reduction of acoustic noise should be achieved as well (Sec.15.2.3.1).

This machine is oversized with respect to AdV needs and thus should be replaced. In addition, there are other motivations for replacing it. The machine has a large size and does not fit easily into a room which is part of the main building. Some seismic noise mitigation was obtained in Virgo by implementing a passive spring isolation stage underneath the engines, and fans reducing the vibration noise of the moving parts transmitted to the building floor and walls [483]. It was realized that further noise reduction needs mitigating auxiliary seismic transmission paths like water pipes and ducts, which presently short-circuit the machine body to the building floor and walls. Some reduction of acoustic noise has been obtained in Virgo by slowing down the inlet and outlet fans by 25 % [483]. This modification brought the machine to the limit of its designed operation range. Further slowing down would require substitution of the fans with larger ones, and consequently major modifications on the ducts aperture. The acoustic noise contribution of the air distribution system could not be disentangled. However, sharp duct turns are present at the inlet and outlet of the hall HVAC machine body and are a suspected source of air turbulence. The hall machine has no acoustic silencers, since they cannot fit in the restricted space available.

- **HVAC of CB clean rooms**

The main concern of this machine is seismic noise: it is responsible for intense seismic tones around 15 to 20 Hz associated with the engines and fans, and a reduction of about a factor of 20 is needed (Sec.15.2.2.1). As explained in Sec.15.2.3.1, in Virgo this machine was serving both the clean rooms and the INJ lab. One option is to keep this machine (which is still in good condition and properly sized) and dedicate it to the clean rooms only. However, seismic isolation of the machine needs to be improved. As well, it has to be assured that the residual acoustic noise it might introduce in the INJ lab is negligible.

- **Possible relocation of CB hall and clean room machines**

The current location and installation of both the hall and clean room machines make it difficult to implement effective solutions. Their relocation outside the building would make this implementation easier. The new machines can be placed on isolated platforms. A sketch of the new installation and of the isolated platform is illustrated in Fig.15.14 and 15.16. Commercial damping systems with cut-off frequencies of a few Hz are a feasible and adequate solution. Vibration noise transmitted through water pipes can be cured in a more effective way. Flexible joints can be inserted on pipes to and from the machine, and used to suspend air ducts to walls.

- **HVAC of DAQ room**

The main concern of this machine is seismic noise. Residual seismic tonal noise around 24 Hz needs a factor of about 5 in amplitude reduction (Sec.15.2.2.1). During Virgo+ commissioning, this machine has been already subject to successful mitigation with encouraging results, achieved by slowing down the fan speed by 15% (eLog 27767).

It is possible that only minor mitigation actions can be implemented in the existing machine. Possible actions are: 1) improving seismic isolation of moving parts, and 2) possibly further slowing down of the fan, if the thermal load of the new DAQ room will be reduce as anticipated.

- **HVAC of MC building**

The **MC** air conditioner is responsible for intense seismic tones starting from 20 Hz. The impact of this noise on the Virgo+ sensitivity is small and limited to a few lines. However (see Fig.15.5) the produced seismic noise is quite intense and some mitigation is required. Some reduction of acoustic noise to mainly reduce intense tonal emissions is needed as well. But the major concern of this machine is electro-magnetic noise, as briefly explained hereafter.

The **HVAC** machine of the **MC** building in use for Virgo implements an electric heating system. Building temperature regulation occurs by means of continuous switching of a high current resistor. This is an identified source of magnetic noise inside the **MC** building (i.e. intense magnetic lines below 100 Hz) and noise in the power line which affects also the **CB**. Also the water chillers were found to produce intense voltage noise transients each time they switch on, which causes correlated noise transients in the interferometer **GW** signal [504]. The power voltage noise seems to propagate to the **CB** because of a not sufficiently isolated electric path between the two buildings and the medium to low voltage transformer located in the central area Technical Building (**TB**) [505].

One possibility is to replace the current machine with a water based heating system. The new machine of likely larger dimensions would not fit into the tight space in the building occupied by the present machine, and an external installation is needed. This would also allow reducing the noise transmitted into the hall and to the floor by implementing a seismic isolation of the moving parts (currently absent) and adopting a low acoustic emission fan type. There might be margin to reduce the hall air flux needs so to possibly slow down the air fan.

- **HVAC of North and West End buildings**

The **NEB HVAC** machine contributes to coherent seismic noise in the Virgo+ sensitivity in the range from 30 Hz to 60 Hz (in Fig.15.1), and some mitigation is required. Also the acoustic tonal noise between 50 and 100 Hz needs to be reduced by about a factor of 5 (see Sec.15.2.2.2).

It seems possible to achieve this with limited modifications of the existing machines. A significant reduction of emitted acoustic and seismic noise has been achieved by slowing down by almost -50% the **WE** machine fans (compare left to right plots in Fig.15.6 and Fig.15.12).

Further noise reduction can be achieved by: 1) replacing the current **HVAC** fans which are not optimized for low noise emissions; 2) further reducing the air flow speed; 3) improving the acoustic isolation of the air handler machine technical room from the experimental hall; but before deciding on this point the acoustic isolation of this panel wall will be evaluated, as was done for the **INJ** lab (eLog 30613 and 30614); 4) improving the seismic isolation of the **HVAC** engine fans and water pumps and curing seismic shortcuts (water pipes, ducts).

15.2.3.3 Electronics racks

Cooling fans of electronic equipment placed in the experimental halls in close proximity to the interferometer are responsible for considerable amount of seismic tonal noise around 40-50 Hz and harmonics (Fig.15.2). The **CB** electronic racks are of particular concern because of the evident noise coupling to Virgo+ (Fig.15.4). It is necessary to reduce seismic noise emitted

by the rack cooling fans and reaching the **ITF** sensitive parts (i.e. external not suspended benches and vacuum tanks carrying optical links) through common base ground by at least 10 times.

The cooling fans also emit acoustic noise, mainly tonal noise and are the main source of acoustic noise in the experimental halls above about 50 Hz. As stated in Sec.15.2.2.2, a factor of 4 reduction of the **RMS** sound pressure intensity (-12 dB) above 50 Hz is required for the **CB** and advised also in the **EBs**, possibly in the **MC**.

In **AdV** it is expected that, with respect to Virgo, a larger number of electronic devices and racks need to be located in the experimental hall close to the **ITF**. The adopted strategy (see **DAQ** chapter) is to reduce the number of cooling fans by adopting wherever possible convection cooled type of electronics. However, a safe approach requires the following actions to be also adopted: 1) select more silent fans (slower and larger fan models have been tested for the vacuum racks, see [506, 507] and the **VAC** chapter); 2) improve fan installation in their casings to reduce rattling (i.e. use rubber mounts); 3) implement seismic isolation of racks placing or suspending them through a seismic isolation stage with cutoff frequencies smaller than 4 Hz and good damping ($Q \leq 10$). A custom implementation has been realized and tested for vacuum racks (eLog 30694, see also the **VAC** chapter).

Particular attention shall be paid to muffling acoustic sources placed in the proximity of the separation wall between the **CB** and the **INJ** lab, to minimize noise transmission.

15.2.3.4 Vacuum pumps

A concern is the intense acoustic and seismic tonal noise (24.5 Hz and harmonics) produced by scroll pumps. In Virgo scroll pumps were located in the experimental hall, one per tower. Scroll pumps emit intense seismic and acoustic noise (see in Fig.15.2 the scroll pump noise measured by a ground seismometer, and in Fig.15.6 the acoustic signal measured by the hall microphone). The noise was proven to be troublesome for the interferometer and scroll pumps were kept off during science runs, and shortly operated during dedicated maintenance periods.

In **AdV** one continuously running pump per building is needed to preserve the required vacuum cleanness (see **VAC** chapter). These pumps will be confined to properly acoustically and seismically isolated spaces, so to assure that they contribute negligibly to seismic and acoustic noise within the experimental halls.

Effective acoustic shielding at 25 Hz requires a dedicated room with massive and rigid walls and adequate sound absorption treatment. Acoustic isolation requirement is particularly strict for the scroll pump serving the **CB**, while it can be a bit relaxed for **EBs**. A possible satisfactory solution for the **CB** has been tested (see [508]). This solution is further discussed in Sec.15.5.2 below and addressed in the **VAC** chapter. The vacuum connection of the pump to each tower will be done with flexible pipes to minimize transmission of vibrations.

Turbo molecular pumps (one per tower) need to be close to the tower vacuum tank. A seismic isolation of the pump and cooling fans similar to those adopted in Virgo [509] is foreseen. Sound emissions can be silenced if necessary with acoustic shield covers. Magnetic emission of turbo pumps have been evaluated and found tolerable [510].

15.2.3.5 Switching devices

Virgo infrastructure counts several devices, e.g. water chillers, air compressors, etc., which are subject to high current when switched on or off. These are potential sources of noise transients. It is necessary that their on/off status is monitored. A measurement of the electric current intensity flowing through the device can provide additional information on the healthy condition of some machines. A possible implementation consists of current probes whose slow signals are managed by the Infrastructure Machine Monitoring System (**IMMS**) system (see Sec.15.4). The system has been tested in Virgo for some water chiller devices (eLog 27793).

15.3 HVAC systems modification works

15.3.1 Central Building

15.3.1.1 Introduction

The major part of the **HVAC** systems modification works concerns the **CB**: a new external technical area, located to the east of the building, will be implemented to house the air handler machines (5 in total), and two technical rooms will be realized in that area. The **HVAC** system of the **INJ** lab will be independent from the one of the clean rooms. A new **HVAC** system will serve the **DET** laboratory that will be transformed into a new clean room area. All the air distribution systems will be completely new or rebuilt, except for the path inside the clean rooms.

15.3.1.2 Facility description

The new external technical area covers an area of about 10×15 m² and has a useful height of 5 m. It will have a light metallic structure supporting a simple circular arc-shaped cover. The foundation of the structure consists of a reinforced concrete slab, 35 cm thick, on which will be realized a concrete industrial type floor. The part hosting the air handler machines (about 110 m²) is open, while there are two closed technical rooms, one of about 25 m² for the pumps and the hot and cold water distribution manifold, another of about 15 m² for the electric power switchboards. The works also include the infrastructures connecting the new external technical area with the existing facilities: the realization of the cold water lines (inlet and outlet, each 95 m long, mostly with underground path - polyethylene pipes) to the **TB**, where are placed the centralized chillers; the realization of the hot water lines (inlet and outlet, each about 30 m long - polyethylene pipes) joining the lines already implemented in 2009; the realization of underground electrical ducts to the main substation in the **TB**. Finally, the works will be completed by the external arrangements linking the new facility to the existing roads and sidewalks.

Fig.15.13 reports a picture of the **CB**, describing the new infrastructures to be realized.



Figure 15.13: Perspective view of the CB with the external technical area.

15.3.1.3 HVAC equipments description

All the air handler machines will be placed in the new external technical area each of them serving a single CB HVAC system, respectively: the experimental hall, the DAQ room, the clean rooms, the INJ lab and the DET lab. The following list shows the actions which will be performed for these machines.

- The old experimental hall machine will be replaced with a new one, given its age and over-sizing with respect to the real needs experienced during the years. This allows a rationalization and a reduction of the air flow and of the air speed in the ducts. In addition, the new machine will have better performances in terms of soundproofing and energy saving.
- For the DAQ system, the existing machine will be reutilized; in order to adjust the machine to the flow resistance of the new air ducts distribution, it will have a new fan of suitable characteristics.
- Also for the clean rooms system it is foreseen to place the existing machine, which is still in good condition and has sufficient characteristics for the new configuration of the air distribution into the new location.
- The INJ lab will have a new properly sized machine in order to maintain the design

conditions [503] within the lab and make the system completely independent from the operation of the clean rooms, an improvement over the current configuration.

- The **DET** lab will be upgraded to become a clean room, having the same characteristics of the **INJ** lab (ISO 7/8); for this reason also this lab shall be served by a new properly sized **HVAC** machine.

The general parameters considered for the designing are the following:

External conditions: winter $T_e = -5^\circ C$, $RH = 80\%$; summer $T_e = 32^\circ C$, $RH = 50\%$.

Internal conditions (experimental hall): winter/summer $T_i = 22 \pm 0.3^\circ C$, $RH = 50 \pm 5\%$.

Air speed in the ducts: $v_{air} < 9.0$ m/s.

Air speed outlet (diffusers): $v_{air} < 3.5$ m/s.

The characteristics of the air handler machines are listed in Tab.15.3.

| System | | CB experimental hall | | Data Acquisition | Clean Rooms | INJ lab | | DET lab |
|-------------------------------------|---------|----------------------|----------------------|------------------|----------------|---------|---------------------|---------|
| | | design | current | design/current | design/current | design | current | design |
| inlet air flow rate | m^3/h | 30000 | 42000 ⁽²⁾ | 5000 | 21000 | 5000 | 4800 ⁽³⁾ | 2500 |
| outlet air | m^3/h | 28000 | 38000 ⁽²⁾ | 5000 | 19000 | 5000 | 4800 ⁽³⁾ | 2500 |
| % of air renewal | % | 10% | 10% | 0% | 20% | 20% | — ⁽³⁾ | 20% |
| max heat exchanger heating capacity | kW | 121 | n.a. | — | — | 25 | 23 ⁽³⁾ | 10 |
| max heat exchanger cooling capacity | kW | 294 | n.a. | 34.6 | 130 | 35 | — ⁽³⁾ | 15 |
| power supply | V | 400 | 400 | 400 | 400 | 400 | — ⁽³⁾ | 400 |
| total input electric current | A | 27 | n.a. | 2 | 22 | 2 | — ⁽³⁾ | 2 |
| sound pressure ⁽¹⁾ | dB(A) | 72 | n.a. | 61 | 86 | 61 | — ⁽³⁾ | 60 |

(1) From the machine data sheet.

(2) Progressively reduced during Virgo and Virgo+ operation.

(3) Current system included in the Clean Rooms **HVAC** system.

Table 15.3: Main technical parameters of the **CB** design air handler machines (for comparison we reported the current ones).

General design characteristics, in order to optimize the systems, improve their efficiency and comply with the general design criteria described in Sec.15.2, are the following:

- all the machines will be installed on special anti-vibration supports ($f_{cut} \leq 4$ Hz; $Q < 5$) for the limitation of seismic noise transmitted;
- the manifolds of the hot and cold water pipes for the distribution to the various machines will be positioned into a proper room, realized in the new technical area;
- in the same room, there will be the pumps for balancing each circuit (if really needed, otherwise they will be eliminated); adequate flexible joints will be installed for the

mitigation of the seismic noise transmitted by such equipment;

- for each air handler machine, the electromagnetic compatibility of installing an inverter for the speed control of each fan will be checked, in order to have the possibility of adjusting the air flow depending on eventual changes within the internal conditions of the served areas;
- the chillers and the heat generator in the **TB** are able to insure the redundancy for the continuous operation of the systems.

New input power lines will be realized for the **HVAC** systems; the main distribution will take place through underground power lines deriving from the general substation in the **TB**; the electrical distribution panels for the machines and other equipments will be placed into a proper room in the new technical area.

15.3.1.4 HVAC air distribution

Because of the displacement of the machines outside the building and the need of improving their seismic and acoustic isolation performances, the air distribution systems of the **CB** will be almost completely new or rebuilt. Inside the building, the air distribution system for the experimental hall will be completely rebuilt and a new distribution system will be implemented for the **DAQ** room and the **DET** lab. Only the air distribution system within the clean rooms, placed in the false ceiling and below the floating floor, will be unchanged; in contrast, the air distribution system within the **INJ** lab, being independent from the clean rooms one, will be modified and optimized in order to limit the air turbulences inside the room.

The air ducts will have circular section in order to avoid angles and minimize turbulences and losses. They are made from steel and properly insulated thermoacoustically. Tab.15.4 summarizes the design parameters of the various circuits.

| HVAC system | | duct diameters [mm] | air speed v_{air} [m/s] | air flow G [m ³ /h] |
|----------------------|--------|------------------------|------------------------------|-----------------------------------|
| CB experimental hall | supply | 450÷1250 | 3.2÷6.8 | 30000 |
| | return | 630÷1120 | 7.9÷8.3 | 28000 |
| Clean Rooms | supply | 1000 | 7.4 | 21000 |
| | return | 900 | 8.3 | 19000 |
| Data Acquisition | supply | 560 | 5.6 | 5000 |
| | return | 560 | 5.6 | 5000 |
| INJ lab | supply | 560 | 5.6 | 5000 |
| | return | 560 | 5.6 | 5000 |
| DET lab | supply | 400 | 5.5 | 2500 |
| | return | 400 | 5.5 | 2500 |

Table 15.4: Main design parameter of the **CB** air duct circuits.

Outside the building the air ducts are supported by proper metallic frames, while inside the building, their paths are mainly distributed in the external hollows, as those currently installed. In the joints between each air handler machine and the air distribution ducts proper fabric bellows and silencers will be installed in order to minimize the seismic noise and reduce the acoustic noise transmitted through this paths. Particular care will be adopted for the air

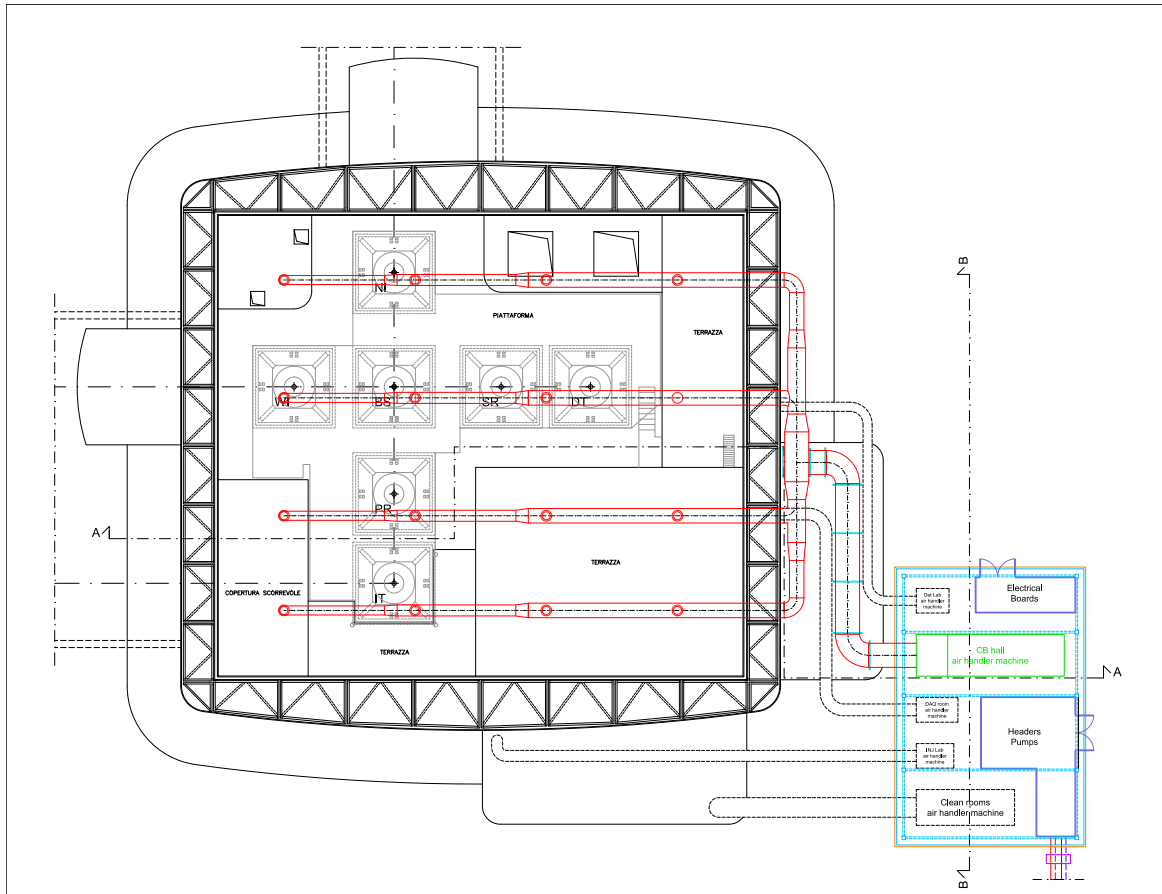


Figure 15.14: CB hall HVAC system; supply air ducts.

duct supports fixed to the metallic structures, installing special clamping systems available on the market for the isolation of such structures (damping supports, suspensions, etc.).

Fig.15.14 to 15.19 are extracted from the basic design of the project and shown the paths of the supply air distribution (Fig.15.14, 15.15 and 15.16) and the return (Fig.15.17, 15.18 and 15.19) for each HVAC machine at the corresponding level, while the cross sections are shown in Fig.15.20 and 15.21.

15.3.2 Mode Cleaner

15.3.2.1 Introduction

The design choice has considered the complete rebuilding of the HVAC system, in order to satisfy the mitigation noise requirements (replacing the electric resistive heating system, limiting the seismic noise transmitted by the HVAC machines actually located in the building's hollow), and improve both the functionality and efficiency of the system, as well as the maintainability of the equipments. As for the CB, the realization of a new external technical area to the west of the building is foreseen to host the machines and the auxiliary equipments. Also the air distribution system will be completely rebuilt.

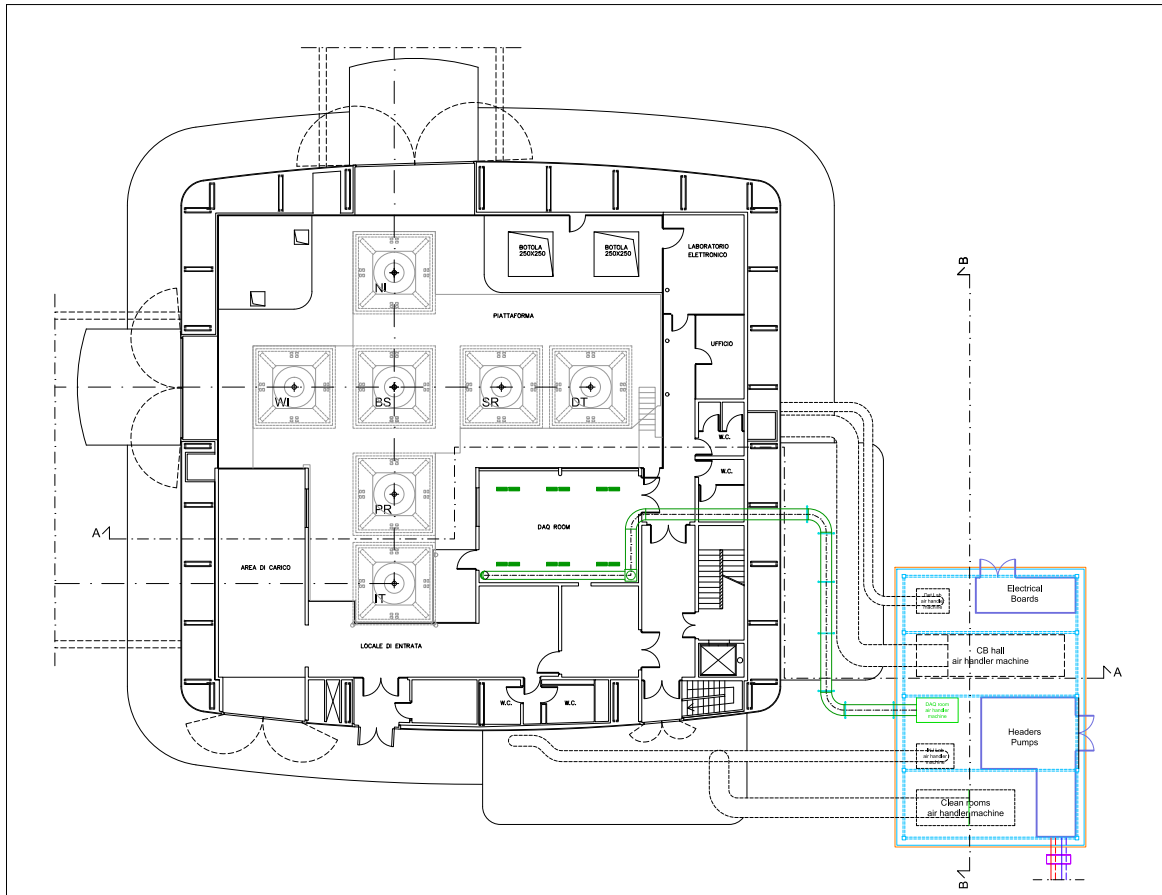


Figure 15.15: DAQ HVAC system; supply air ducts.

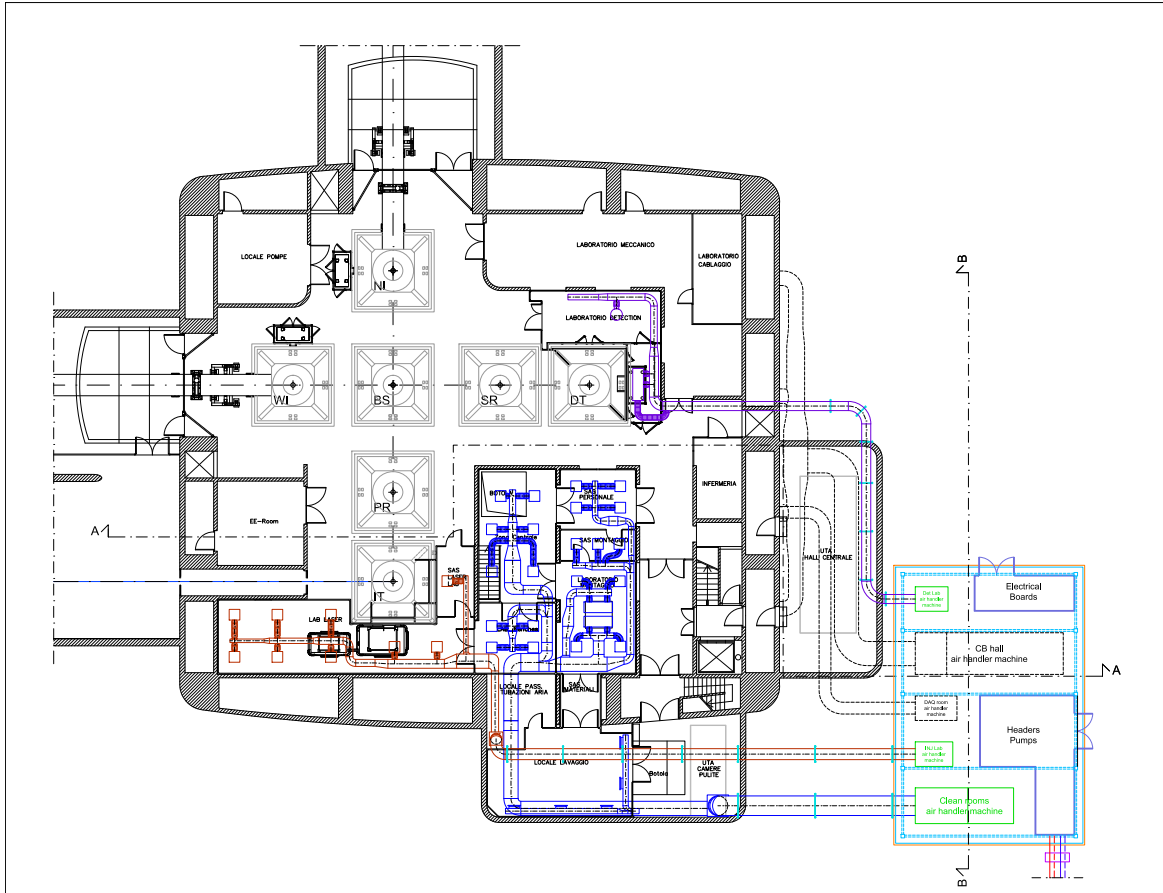


Figure 15.16: Clean rooms, INJ lab and DET lab HVAC systems; supply air ducts.

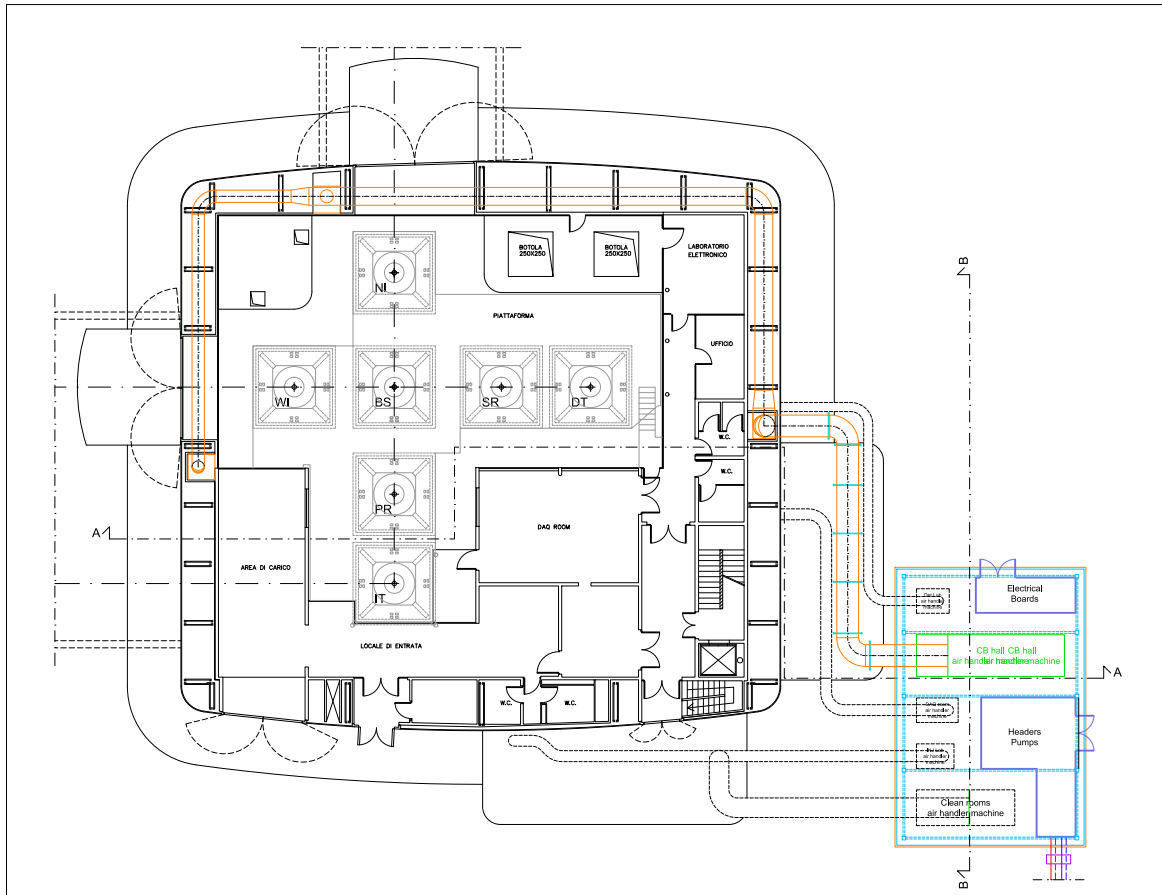


Figure 15.17: CB hall HVAC system; return air ducts.

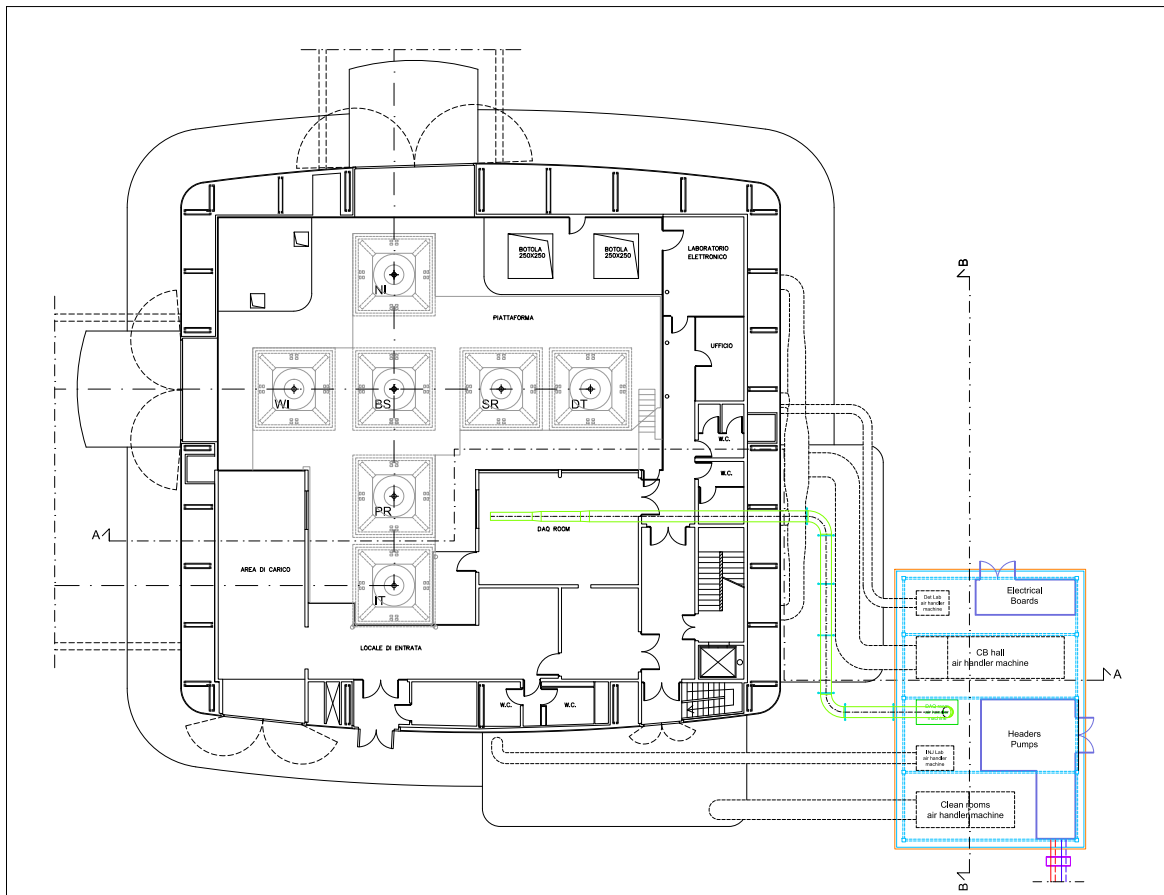


Figure 15.18: DAQ HVAC system; return air ducts.

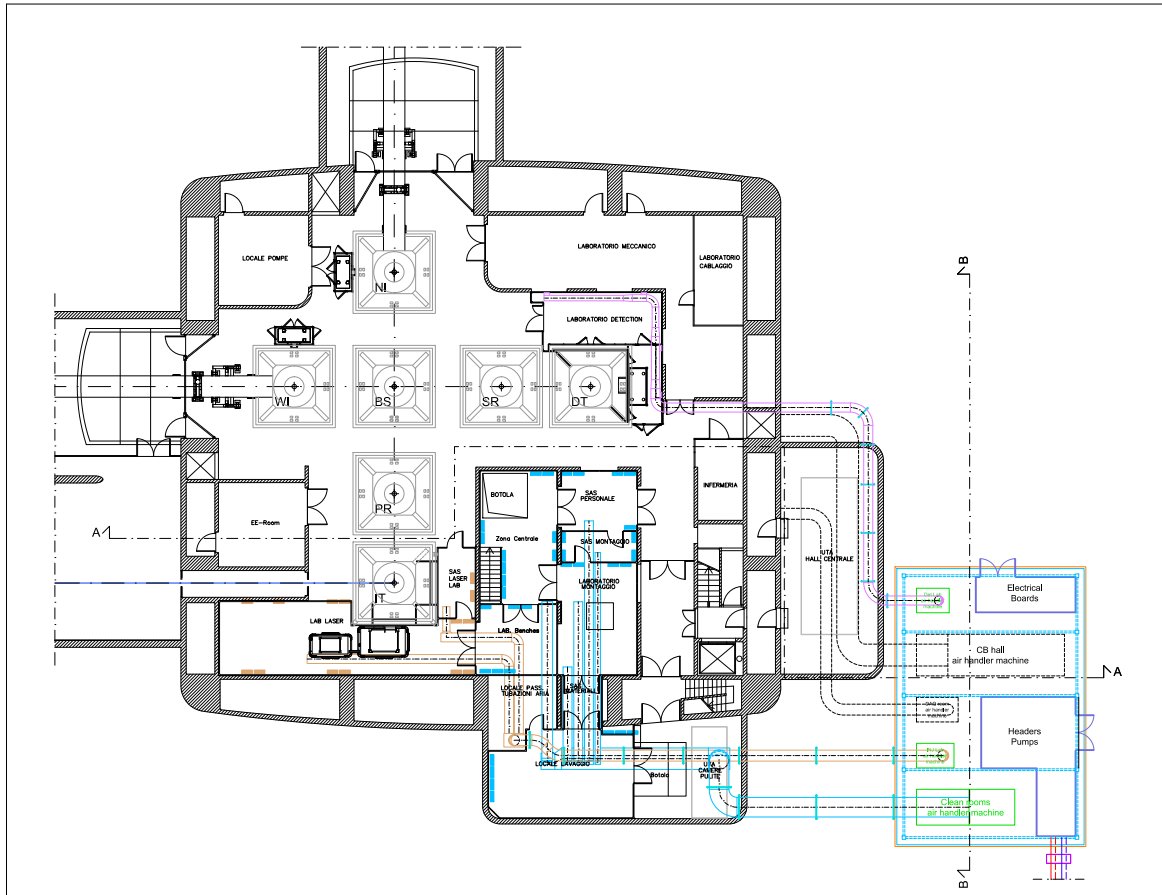


Figure 15.19: Clean rooms, INJ lab and DET lab HVAC systems; return air ducts.

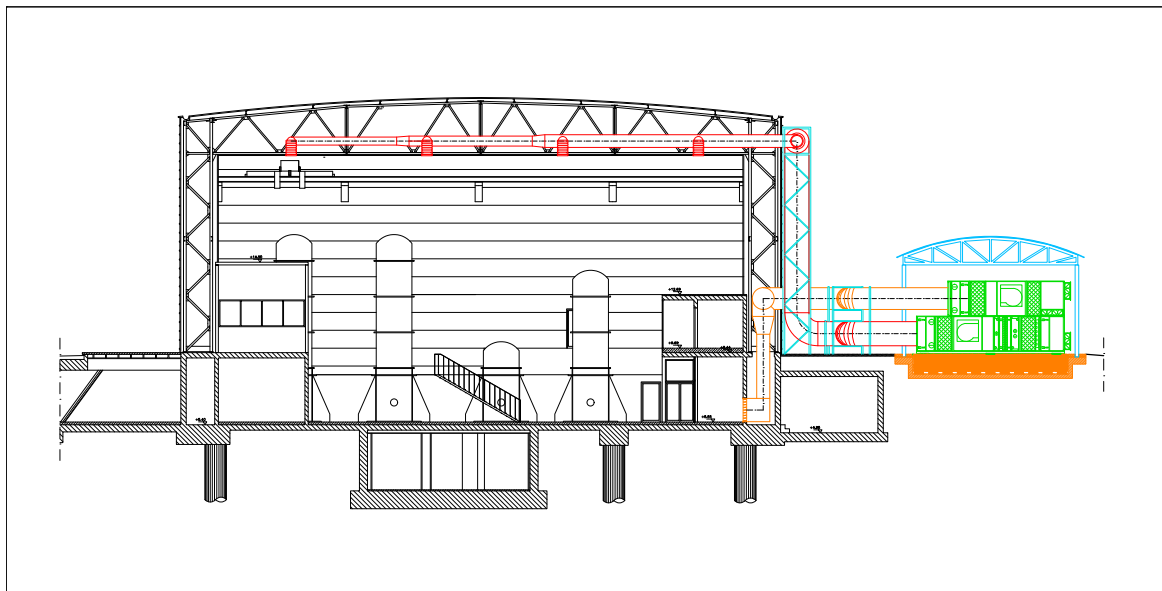


Figure 15.20: Cross section of the CB and the external technical area showing the new air distribution systems.

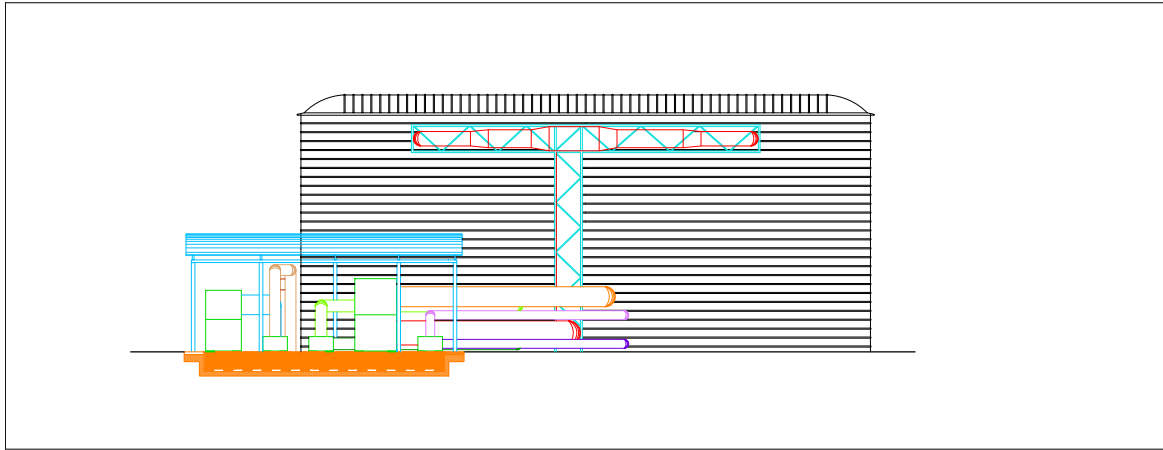


Figure 15.21: East view of the **CB** and the external technical area showing the new air distribution systems.

15.3.2.2 Facility description

The new external technical area has the same structural characteristics (concrete basement and metallic structure) as the correspondent facility of the **CB**. It covers an area of 6.5×5.5 m² and has a useful height of 3.2 m. In this technical area both the cooling and heating machines and the air handler machine will be installed, as well as the other equipments (pumps, manifolds, inertial tanks and electric boards). The external works include the underground infrastructures connecting the technical area to the general networks, such as water and power supply and the external arrangements needed to complete the works (sidewalks and square linking to the existing roads).

Fig.15.22 reports a general pictures of the **MC** with the new infrastructures to be realized, while Fig.15.23 and 15.24 shown the path of the air distribution system.

15.3.2.3 HVAC equipment description

The **HVAC** system consists of the heating machines (one heat pump and one chiller supplying the warm and the cold water, respectively) and of the air handler machine. In order to assure the continuous operation of the systems, there will be a spare chiller for redundancy, while for the warm water the installation on an emergency electric heating system (after the check of its compatibility with the **ITF**) is foreseen. The two machines already serving the existing **HVAC** system will be reused. The characteristics of these machines are listed in Tab.15.5.

All the pipes connecting the machines with the auxiliary equipments will be completely rebuilt and properly insulated. The same measures for the mitigation of the seismic and acoustic noise transmitted from the machines and described for the **CB** technical area will be implemented. In order to increase the efficiency of the system and for energy saving, a solar panel system on the roof of the technical facility might be integrated.

In addition to the seismic and acoustic noise mitigation, the project is also based on the following technical aspects and general considerations:



Figure 15.22: Perspective view of the MC Building with the external Technical Area.

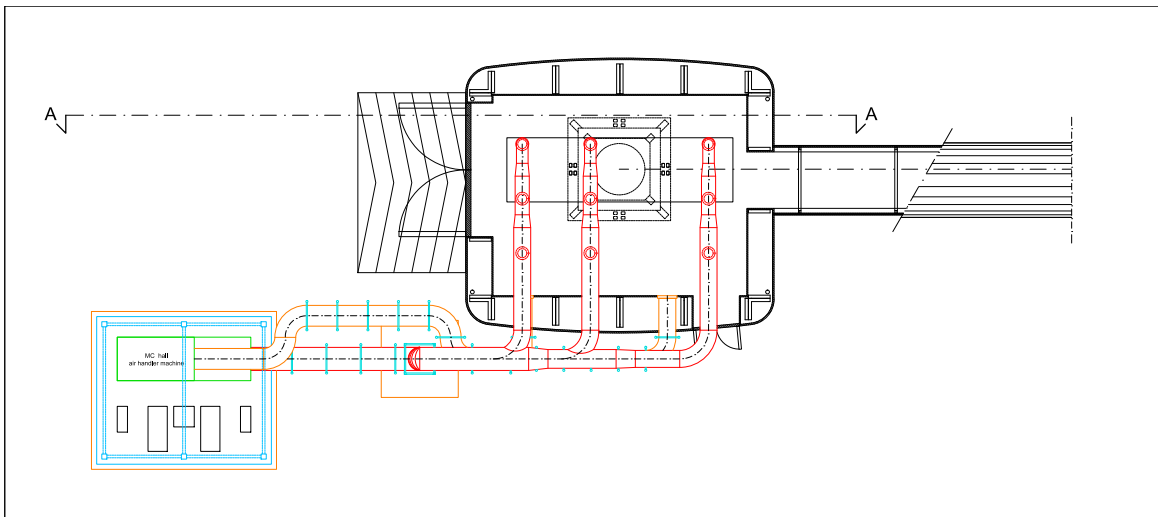


Figure 15.23: Plan view of the MC building; experimental hall HVAC system.

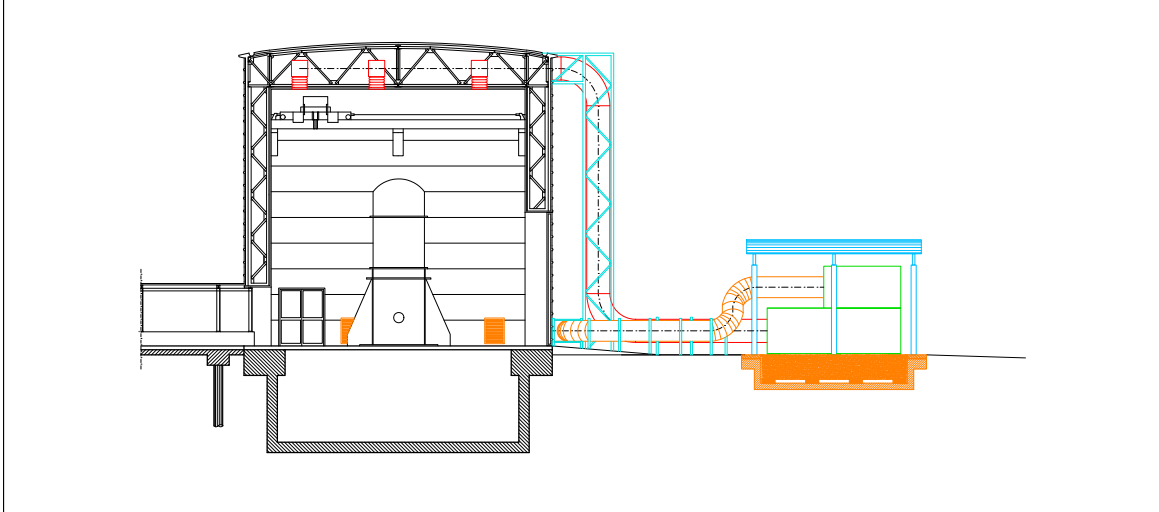


Figure 15.24: Cross section of the MC building; experimental hall HVAC system.

| MC HVAC machine | | MC heat pump | MC chiller | MC spare chiller |
|-------------------------------------|-------|--------------|------------|------------------|
| heating/cooling capacity | kW | 40 | 40 | 40 |
| power supply | V | 400 | 400 | 400 |
| total input electric current | A | 29 | 29 | n.a. |
| no. of compressors | n. | 1 | 1 | 1 |
| type of compressors | — | Scroll | Scroll | Alternative |
| sound pressure level ⁽¹⁾ | dB(A) | 47 | 47 | 47 |

(1) From the machine data sheet.

Table 15.5: Main technical parameters of the MC HVAC machines.

- the need to improve the air distribution inside the experimental hall decreasing the vertical temperature gradients;
- the need to improve the control and the stability of the relative humidity;
- the need to improve the accessibility of the air handler machines (now placed in the narrow hollow of the building) for improving their functionality and maintenance.

The general parameters considered for the designing are the following:

External conditions: winter $T_e = -5^\circ\text{C}$, $RH = 80\%$; summer $T_e = 32^\circ\text{C}$, $RH = 50\%$.

Internal conditions: winter/summer $T_i = 22^\circ\text{C}$, $RH = 50 \pm 5\%$.

Air speed in the ducts: $v_{air} < 9.0$ m/s.

Air speed outlet (diffusers): $v_{air} < 3.5$ m/s.

The main characteristics of the air handler machine are listed in Tab.15.6.

| System | | MC experimental hall | |
|-------------------------------------|-------------------|----------------------|-------------------|
| | | design | current |
| inlet air flow rate | m ³ /h | 8000 | 6000 |
| outlet air flow rate | m ³ /h | 6000 | 6000 |
| % of renewal air | % | 10% | 0% |
| max heat exchanger heating capacity | kW | 70 | 60 ⁽²⁾ |
| max heat exchanger cooling capacity | kW | 58 | 30 |
| power supply | V | 400 | 400 |
| total input electric current | A | 10 | 114 |
| sound pressure ⁽¹⁾ | dB(A) | 63 | n.a. |

(1) From the machine data sheet.

(2) Consisting of a resistive heating system.

Table 15.6: Main technical parameters of the MC air handler machine (for comparison we reported the current one).

15.3.2.4 HVAC air distribution

The air distribution system of the MC will be completely renewed because of the displacement of the machines outside the building and the need to improve its seismic and acoustic isolation performances. The air ducts, their path and the support structures have the same characteristics of those described for the CB (Sec.15.3.1.4), as well all the same measures for the noise mitigation will be implemented.

Tab.15.7 summarizes the main design parameters of the circuit:

| HVAC system | | ducts diameter [mm] | air speed v_{air} [m/s] | air flow G [m ³ /h] |
|----------------------|--------|------------------------|-------------------------------|-----------------------------------|
| MC experimental hall | supply | 355÷800 | 2.5÷4.4 | 8000 |
| | return | 560÷710 | 3.4÷4.2 | 6000 |

Table 15.7: Main designl parameters of the MC airduct circuit.

15.3.3 End Buildings

15.3.3.1 General requirements

The data collected and analyzed until now for the EBs show that the noise transmitted from the HVAC system has a less important effect than the other experimental buildings. For this reason the improvement works planned for these facilities will be focused mainly to the isolation of noise sources, through:

- the optimization of the air flow, replacing the fans with ones of less noisy characteristics (lower revolving speed, reverse blades fans) and dimensioned for 14.000 m³/h, 15% less than the present value;
- the optimization of the outlet air speed inside the experimental hall;
- the installation of more efficient silencers in the link between the air handler machine and the air ducts;
- the installation of proper damping systems for the air ducts supports at the joint between them and the building structures;
- the installation of proper damping supports for the air handler machine;
- the improvement of the passive acoustic isolation of the structures separating the technical room hosting the air handler machine from the experimental hall.

Fig.15.25 and 15.26 shown the EBs HVAC system.

15.4 IMMS upgrades and improvements

The IMMS of Virgo and Virgo+ aims at collecting equipment data from building installations, including air conditioning machines, Uninterruptible Power Supply (UPS) machines, temperature, humidity, air flow and pressure sensors. Various industrial communication protocols are involved depending on the manufacturers and constitute the primary data access connection layer. At a higher level, data are gathered in Virgo frames by dedicated servers communicating through the internet network. IMMS data are timestamped and archived together with other Virgo data at a frequency of 1 Hz. Infrastructure alarms and email notification to on-call experts are based on the IMMS data collection and are managed by the detector monitoring system. For AdV, IMMS will follow the infrastructure upgrades integrating new machines and building sensors data. This activity will include writing the technical specifications for the integration of the primary layer protocols from the machine manufacturers and the sensor controllers in the Virgo framework. In addition to the data

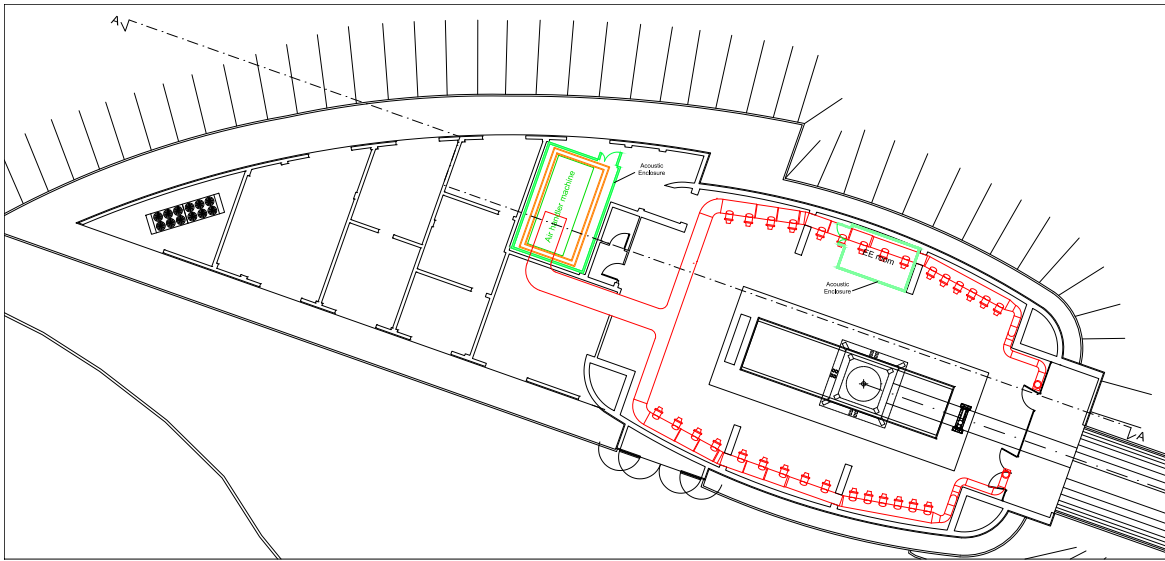


Figure 15.25: Plan view of the WEB building; experimental hall HVAC system.

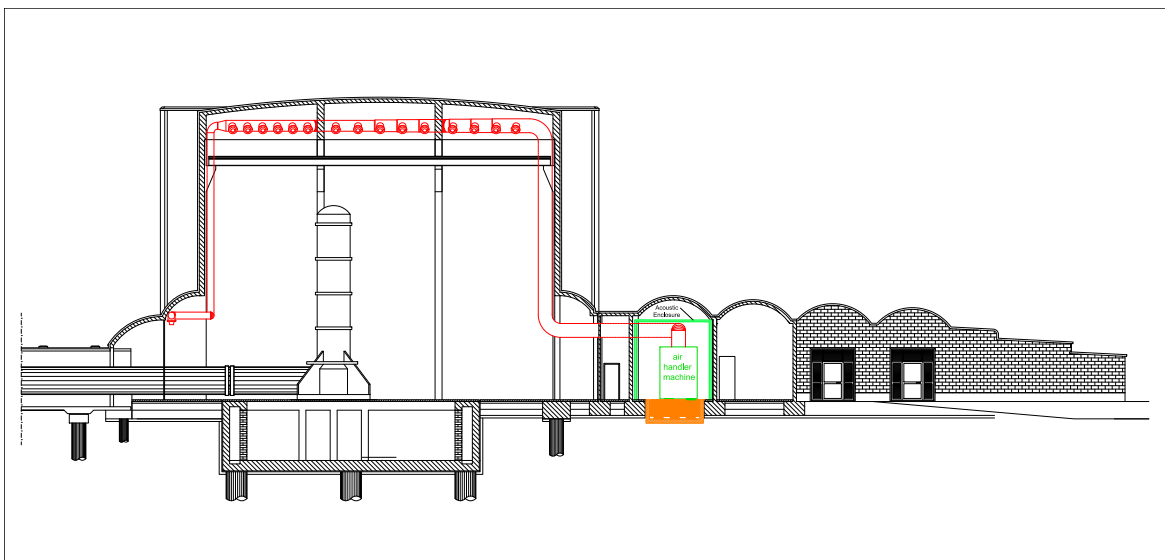


Figure 15.26: Cross section of the WEB building; experimental hall HVAC system.

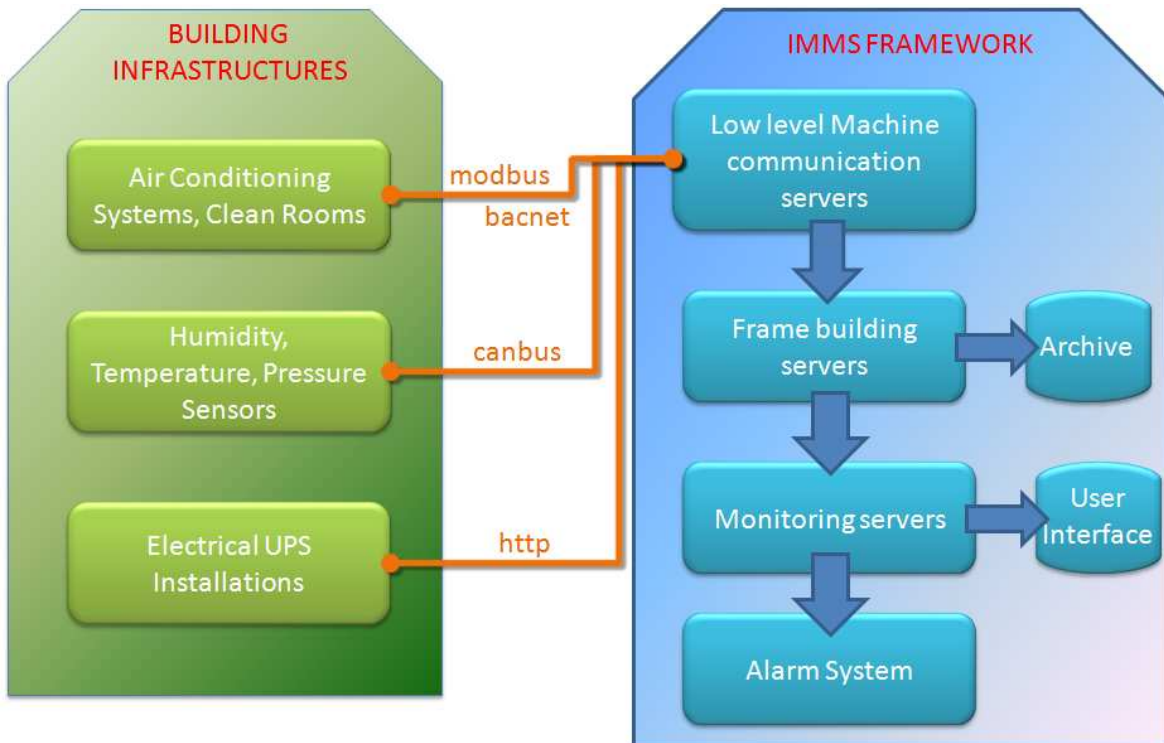


Figure 15.27: IMMS System architecture.

monitoring, it is foreseen to add control functionalities to the servers, allowing experts to configure and operate machines remotely. A centralized monitoring and control interface will be developed, and the alarm system will be upgraded, in particular studying the possibility to set up automatic emergency and recovery procedures. Fig.15.27 shows the schematic architecture of the IMMS.

15.5 Infrastructure modifications for vacuum systems

15.5.1 Tower displacements geometry

In order to comply with the AdV optical configuration, the towers will be displaced in two directions with respect to their current position; the range of these displacements varies from a few mm up to about 0.6 m (see Optical Simulation and Design subsystem (OSD) and VAC chapters). The related geometry is based on the existing reference point network, commonly used in the past years for the alignment activities of the interferometer equipments as well for the monitoring of the building displacements. The topographic instruments to be used are those already available (Leica TDA5000 total station and Leica DNA03 digital level).

The geometry activity for each tower to be displaced will consist in: 1) the initial survey to verify the tower position; 2) the determination of the final position and the tracking of the references for the displacement; 3) the final survey to check that the position is correct.

15.5.2 Scroll pumps room

Different with respect to now, the vacuum scroll pumps will run continuously for **AdV**. In order to limit the noise transmitted by such equipments, they will be displaced far from the towers in an acoustically isolated room. This might be either the electronics room on the first floor or the room next to it [508].

The heat dissipation of the scroll pumps will not require ventilation; possibly an air conditioning unit may be installed in the room. Proper acoustic enclosures will be realized (rough dimensions 1.5x1.5x2.0 m), provided with air ducts directly connected to the outside the building to facilitate heat dissipation. The installation will be completed with the needed new electrical power systems. Finally, in order to further reduce the seismic noise transmitted, the pumps will be installed on proper damping support systems.

15.5.3 Cryotrap power systems and data cable trays

For each of the 4 main cryotrap to be installed, an electric power cabinet will be installed nearby to supply the vacuum pumps and cryogenic devices. Limited power is needed (3-4 kW, 220V AC). Being a critical system for the experiment, the power will be connected to an **UPS**.

Cable trays, from the control racks to the instruments, will also be installed, normally with double channels (signals, power). Also local network connection plugs will be needed to connect the control system racks.

15.5.4 Liquid nitrogen tanks external areas

The **AdV** vacuum system will require the installation of 4 cryogenic traps at each end of the 3 km vacuum tube in order to improve the present vacuum level. Each apparatus will be cooled to 77K by liquid nitrogen stored in external tanks (See **VAC** chapter) installed in proper external areas and located near the experimental buildings (2x15000 liter tanks for the traps installed in the **CB**, a 15000 liter tank each for the **EB**'s ones).

External arrangement works must be implemented for these installations, consisting essentially in: 1) preparation of the ground in the areas identified for the location of the tanks; 2) realization of the reinforced concrete foundations of the tanks; 3) support works to integrate the liquid nitrogen transfer lines into the existing buildings; 4) installation of an electric power cabinet next to the external tank; and 5) realization of the safety protection fence delimiting each external storage area. Fig.15.28 shows a sketch of one of the future installations.

15.6 Infrastructure modifications for electronics

15.6.1 Electronics room realization

A larger numbers of electronic devices will be used in **AdV** compared with Virgo; especially the **CB**, with the installation of minitowers, will see a sensible increase of demand in terms of

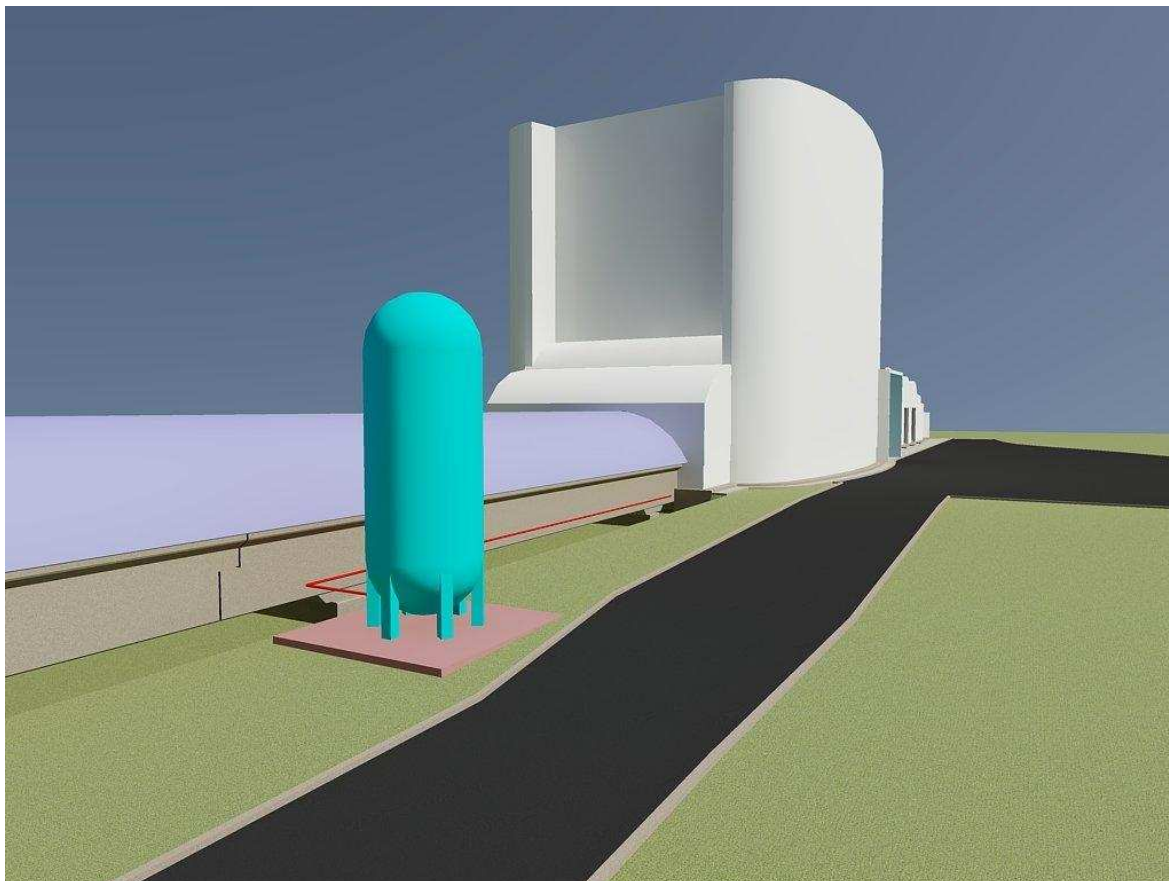


Figure 15.28: Perspective view of the NEB with the LN₂ tank external area.

dedicated room for electronics installation. This will likely imply that one or more additional rooms need to be built; more specifically the area for hosting them has to be identified and the separation walls erected. For example, this can be done for the modified **INJ** lab; the area hosting the **INJ** lab electronics will be moved out both of the laboratory itself and out of the **EE** room and located right before the new laboratory's safety access system entrance. Similar things will happen in other instances and for other subsystems.

15.6.2 Data cable trays for new installations

The main modifications to **AdV** electronics having an impact on infrastructure will likely be the addition of provisions for cable segregation connecting racks. The typical rack uses up to four different signal classes which need to be kept at given distances from each other to avoid Electromagnetic Interference (**EMI**); it is then necessary to make room for these conductive trays or containments, which in turn need to be grounded (i.e., connected to the already existing facility grounding, Fig.15.29). A more detailed list of guidelines and rationale for requirements regarding the electronic installation can be found in [511].

A possibility still not ruled out is the adoption of a Direct Current (**DC**) power distribution scheme to power custom electronics. Its scope and impact is still undetermined at this time, but it is safe to assume that, in some form, it will exist in Advanced Virgo. The idea behind it is that convenient **DC** voltage levels (such as ± 24 V) will be made available for subsystems to use. Details about their generation are available in the document mentioned above. This solution aims at removing potential sources of **EMI** from sensitive antenna points; this choice implies that the power supplies themselves will be located in a dedicated area (i.e. **DAQ** room) sufficiently far from the sensitive region. This as well will have an impact on infrastructures, realistically more for its (potentially) widespread distribution than for any other reasons.

From the point of view of air conditioning system capabilities all this should not have measurable consequences, since present guidelines point towards designs characterized by much lower power dissipation.

15.7 Infrastructure modifications for minitowers installation

15.7.1 INJ lab rearrangements

Important changes are planned for the current configuration of the **INJ** lab, in order to: 1) improve the acoustic insulation of the room from the experimental hall; and 2) allow the installation of a new vacuum chamber, the minitower, close to the Injection Tower (**IT**). The previous Sec.15.2.3.1 has already described the motivations and the expected interventions in relation to the first point. In addition, the new configuration will require a different accessibility (through a safety access system placed on the west side) and a new layout for the laboratory, implying several modifications for both the concrete walls and the internal paneling as well the false ceiling of the existing structures. Moreover, the **HVAC** air distribution system will be completely rearranged in function of the new layout. In this case, the installation of an independent **HVAC** system from the clean room for the laboratory is essential to improve the possibility to control the internal conditions and meet the requirements.

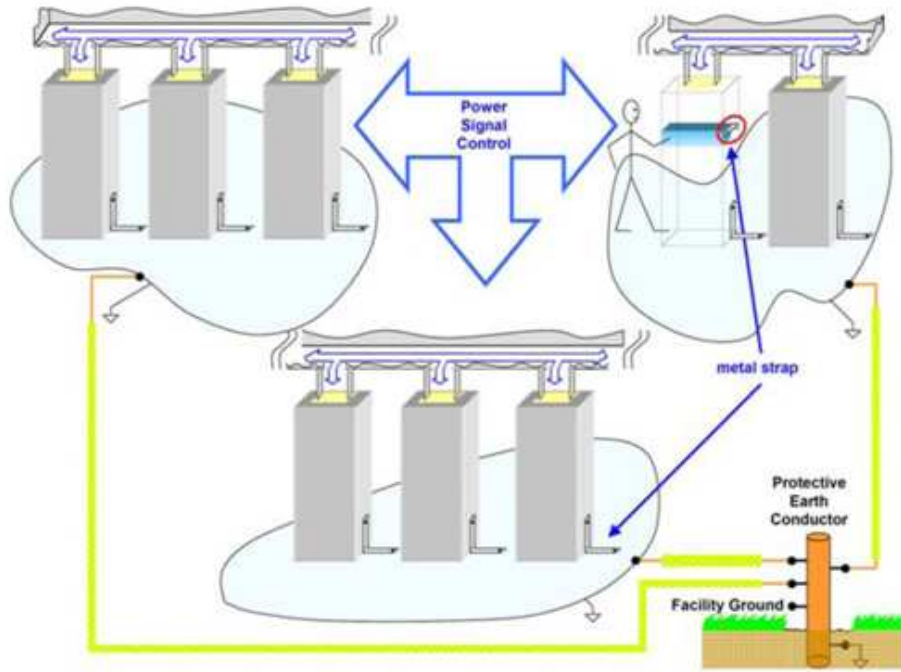


Figure 15.29: Correct scheme for equipment grounding.

Fig.15.30 reports an extract of the CB plan view, describing the modifications to be realized.

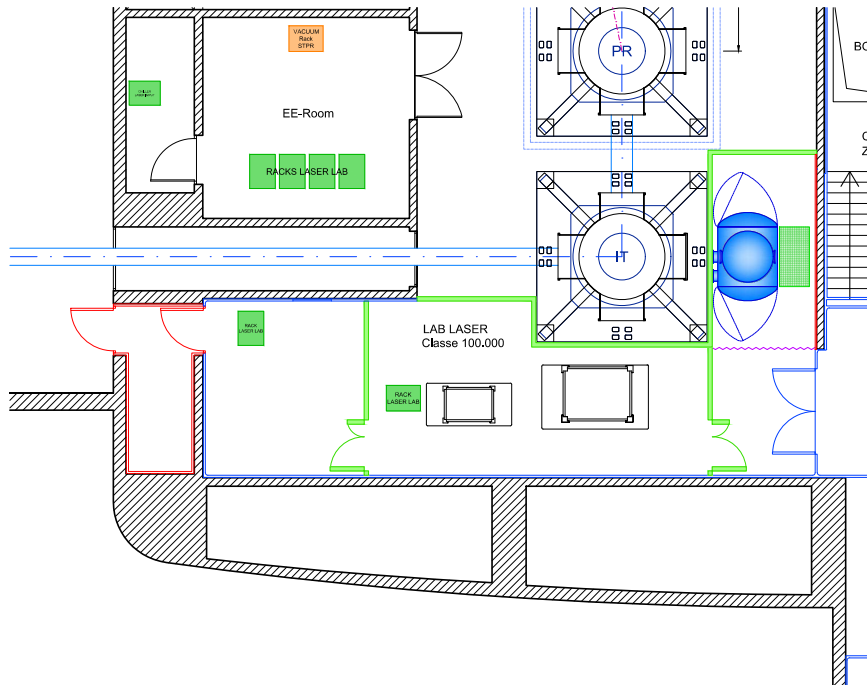


Figure 15.30: Plan view of the new INJ lab layout.

15.7.2 DET lab re-arrangements

The new **DET** lab configuration foresees the complete reconstruction of the laboratory, enlarging the available service space to allow the installation of the **DET** minitower (and the future squeezing minitower, if it will be needed). The laboratory will be transformed into a new clean room area, having the same requirements of the **INJ** lab (ISO 7/8 class). To this end, the access to the laboratory must be through a dedicated safety access system. In addition, a subsidiary room, the **DET** electronic lab, will be realized, hosting all the electronics racks. This new room, outside the clean area, will be separated from the **DET** lab (direct access and no link between the electronic room and the **DET** lab). Fig.15.31 shows the new layout of the **DET** area.

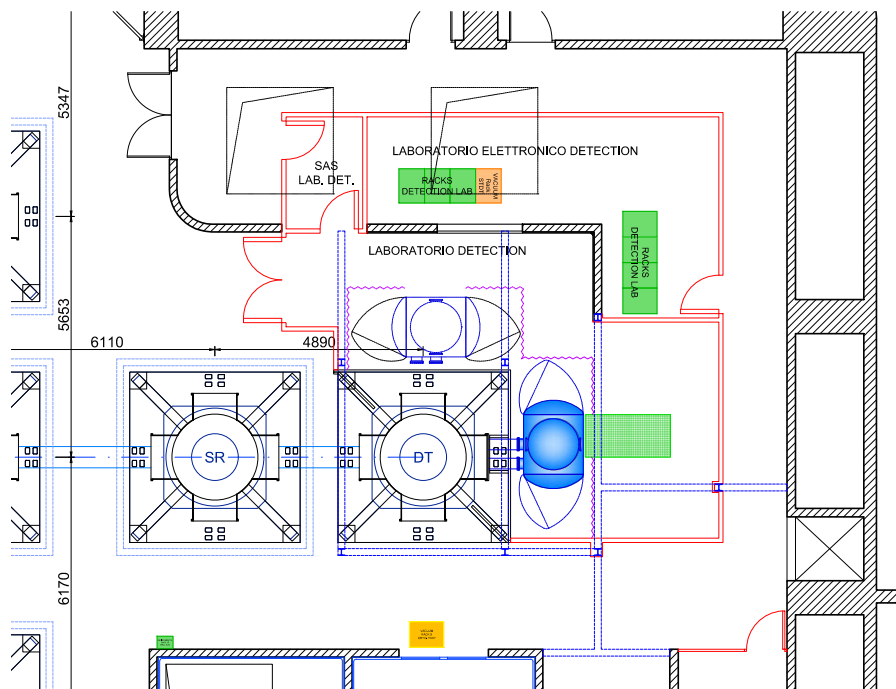


Figure 15.31: Plan view of the new **DET** lab layout.

The new **DET** lab configuration implies the implementation of heavy works inside the experimental hall. For this reason special care must be followed and suitable protections will be installed, in order to limit the work impact and the dust diffusion. Such works can be grouped into the following categories: 1) cutting and demolition of the existing reinforced concrete walls; 2) construction of a new metallic structure to restore the stability of the upper floor of the building; 3) modification and raising of the metallic platform around the **DT** to extend the internal height of the laboratory (allowing the installation and the operation of the minitowers and setting up the space for the air ducts and the other plants); 4) realization of the clean room paneling. In addition, the existing cabling lab will be dismantled and transferred in order to leave room for the **DET** electronics lab and enable the access to the experimental hall on that side of the building. Fig.15.32 reports some pictures of the described modifications.

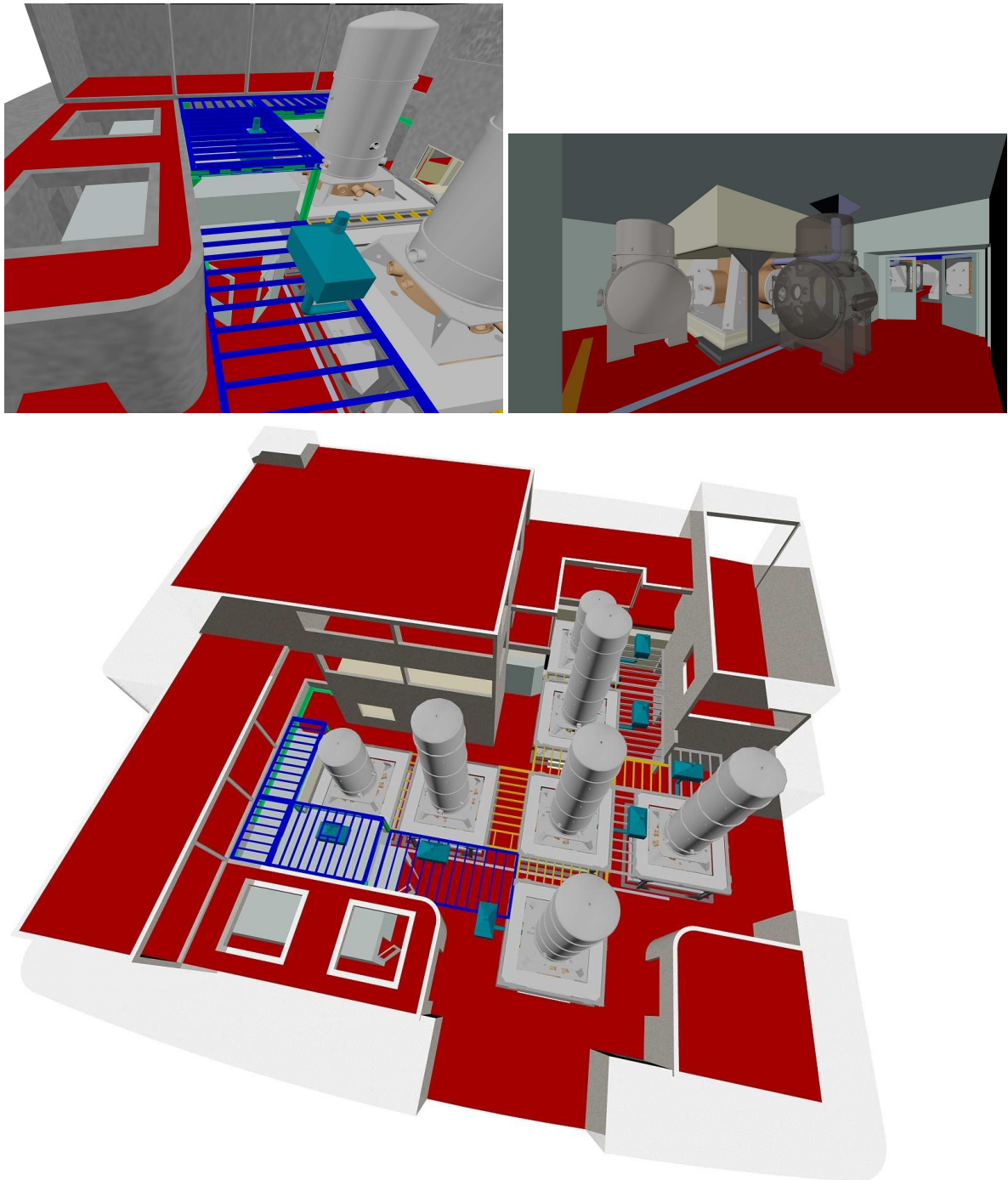


Figure 15.32: Perspective views inside and outside the **DET** lab; in blue the part of the metallic platform to be modified.

15.7.3 End buildings rearrangements

The installation of the **EB** minitowers will require, for both the **NEB** and **WEB**, the realization of a proper enclosure to implement the needed clean environment around this new vacuum chamber. The modification works can be listed as: 1) the modification of the current trap

door interfacing with the foreseen position of the equipment; 2) the realization of the new structure and the paneling for the enclosure separating the minitower lab with respect to the experimental hall; 3) the readjustment of the current clean room system to the new layout; 4) the realization of the dedicated electric power system and data cable trays distribution.

Acronyms

AA Automatic Alignment

ACA Actuator Cage (a rigid frame attached to F7)

AC Alternating Current

ACC Accelerometer

ADC Analog-to-Digital Converter

AdV Advanced Virgo

ALP Automation of the Locking Procedure

AMC Advanced Mezzanine Card

AMU Atomic Mass Unit

AOM Acousto-Optic Modulator

AR Anti-Reflective

ARM Advanced RISC Machine

BBH Binary Black Holes

BJ Beam Jitter

BNS Binary Neutron Stars

BPC Beam Pointing Control

BRDF Bidirectional Reflectance Distribution Function

BS Beam Splitter

CB Central Building

CC Corrective Coating

CCD Charge-Coupled Device

CHRoCC Central Heating Radius of Curvature Correction

CITF Virgo Central Interferometer (6 m arm length test interferometer)

COM Center of Mass

CMRF Common Mode Rejection Factor
CP Compensation Plate
CVS Concurrent Versions System
DAC Digital-to-Analog Converter
DAQ Data Acquisition (in fact, data collection)
DAS Double Axicon System
DARM Differential Arm Length
DC Direct Current
DET Detection Subsystem
DLC Diamond-Like Carbon
DOF Degree(s) of Freedom
DSP Digital Signal Processor
DT Detection Tower
EB End Building
EDB External Detection Bench
EE Electronic Equipment
EIB External Injection Bench
EIB2 Second External Injection Bench
EIB-SAS External Injection Bench-Seismic Attenuation System
EM End Mirror for the arm cavities
EMC Electromagnetic Compatibility
EMI Electromagnetic Interference
ENEB1 External North End Bench 1
ENEB2 External North End Bench 2
EO Electro-Optical
EOM Electro-Optical Modulator
EPRB1 External Power Recycling Pickoff Bench 1
EPRB2 External Power Recycling Pickoff Bench 2
ETM End Test Mass
F0 Filter 0
F7 Filter 7 (also defined steering filter)
FBM Main Frame Builder

FBS Slow Frame Builder
Fd Frame Distribution
FEA Finite Element Analysis
FI Faraday Isolator
FIFO First In First Out
FIR Finite Impulse Response
FOM1 Figure of Merit 1
FP Fabry-Perot
FPGA Field-Programmable Gate Array
FSR Free Spectral Range
GAS Geometric Anti-Springs
Gc Global control
GIPC Global Inverted Pendulum Control
GN₂ Gaseous Nitrogen
GO General Optics
GPS Global Positioning System
GUI Graphical User Interface
GW Gravitational Waves
HOM High Order Mode
HPBD High Power Beam Dump
HP High Power
HPIO High Power Input Optics
HR High Reflectivity
HSF High Spatial Frequency
HV High Vacuum
HVAC Heating, Ventilation and Air Conditioning
HWII HardWare Inventory and Installation database
HWS Hartmann Wavefront Sensor
IB Injection Bench
IBJM Input Beam Jitter Monitoring
IBMS Input Beam Monitoring System
ID Inertial Damping

IM Input Mirror for the arm cavities
IMC Input Mode Cleaner
IME Infrastructure Modifications for Environmental noise reduction
IMMS Infrastructure Machine Monitoring System
INJ Injection subsystem
INF Infrastructure subsystem
IP Inverted Pendulum
IPC Input Power Control
IRIG-B Inter-Range Instrumentation Group type B
ISC Interferometer Sensing and Control
IT Injection Tower
ITF Interferometer
ITM Input Test Mass
IVC Intermediate Vacuum Chamber
I2C Inter Integrated Circuit
LB Large Baffle
LC Local Control
LED Light-Emitting Diode
LHe Liquid Helium
LLab Laser Laboratory
LMA Laboratoire des Matériaux Avancés
LN₂ Liquid Nitrogen
LSF Low Spatial Frequency
LVDS Low Voltage Differential Signal
LVDT Linear Variable Differential Transformer
MC Mode cleaner
MIMO Multiple Input Multiple Output
MMT Mode Matching Telescope
MSPS Mega-Samples Per Second
MSRC Marginally Stable Recycling Cavities
MTBF Mean Time Before Failure
NDRC Non-Degenerate Recycling Cavity

NE North End
NEB North End Building
NI North Input
NTP Network Time Protocol
OL Optical Lever
OMC Output Mode Cleaner
OMC-MMT Output Mode Cleaner Mode Matching Telescope
OPL Optical Path Length
OSD Optical Simulation and Design subsystem
PAY Payload subsystem
PCal Photon Calibrator
PCIe PCI-Express
PCI-X PCI-Extended
PDH Pound-Drever-Hall
PE cold cathode
PI Pirani
PLC Programmable Logic Controller
PMC Pre-Mode Cleaner
PO Pickoff
POP Pickoff Plate
POSD Position Sensing Device
PPS Pulse Per Second
Pr Photo-diode read-out
PR Power Recycling
PRC Power Recycling Cavity
PR Power Recycling Mirror
PSD Power Spectral Density
PSL Prestabilized Laser
PV Peak-to-Valley
PZT Piezo-electric Transducer
QPD Quadrant Photodiodes
RC Recycling Cavity

RF Radio Frequency
RFC Reference Cavity
RGA Residual Gas Analyzer
RH Ring Heater
RIN Relative Intensity Noise
RM Reference Mass
RMS Root Mean Square
RoC Radius of Curvature
RSE Resonant Sideband Extraction
RTL Round Trip Losses
RTP Rubidium Tytanil Phosphate
RTPC Real-Time PC
SA Superattenuator
SAFE Superattenuator Facility at EGO
SAS Seismic Attenuation System
SAT Superattenuator subsystem
SATCS Superattenuator Control System
SBE Suspended Benches subsystem
SCADA Supervisory Control and Data Acquisition
SDB Suspended Detection Bench
SDB1 Suspended Detection Bench 1
SDB2 Suspended Detection Bench 2
SER Serial data
SF Standard Filter
SFP Small Form factor pluggable
SIB Suspended Injection Bench
SIB1 Suspended Injection Bench 1
SIB2 Suspended Injection Bench 2
SiC Silicon Carbide
SLC Stray Light Control subsystem
SLED Superluminescent Diode
SM Single-Mode

SMA SubMiniature version A connector
SMS Slow Monitoring Station
SNEB Suspended North End Bench
SNR Signal to Noise Ratio
SPL Sound Pressure Level
SPR Software Problem Report
SPRB Suspended Power Recycling pickoff Bench
SR Signal Recycling
SRC Signal Recycling Cavity
SRCL Signal Recycling Cavity Length
SR Signal Recycling Mirror
SSFS Second Stage of Frequency Stabilization
SVN Subversion (Apache Software)
SWEB Suspended West End Bench
TB central area Technical Building
TBC To Be Confirmed
TCS Thermal Compensation System subsystem
TCP/IP Transmission Control Protocol/Internet Protocol
TDBox Timing Distribution Box
TDR Technical Design Report
TF Transfer Function
TFB TOLM Frame Builder
TIS Total Integrated Scattering
TM Test Mass
TOLM Timing and Optical Link Module
TOLM-PCI Timing and Optical Link Module, Peripheral Component Interconnect
TOLM-PMC Timing and Optical Link Module, PCI Mezzanine Card
TSP Titanium Sublimation Pump
UHV Ultra-High Vacuum
UPS Uninterruptible Power Supply
V+ Virgo+
VAC Vacuum subsystem

VCS Virgo Common Software

VDB Virgo Database

VLAN Virgo Local Area Network

VME Versabus Module Eurocard

VSR4 Virgo Science Run 4

WE West End

WEB West End Building

WI West Input

Bibliography

All the Virgo notes (documents with a code of the kind *VIR-xxx*) in this reference list are available in the Virgo Technical Documentation System: <https://pub3.ego-gw.it/itf/tds/>.

- [1] R. Flaminio, A. Freise, A. Gennai, P. Hello, P. La Penna, G. Losurdo, H. Lueck, N. Man, A. Masserot, B. Mours, M. Punturo, A. Spallicci, A. Viceré, *Advanced Virgo White Paper*, Virgo Internal report VIR-NOT-DIR-1390-304 (2005). [1](#)
- [2] The Virgo Collaboration, *Advanced Virgo Conceptual Design*, Virgo Internal report VIR-042A-07 (2007). [1](#)
- [3] The Virgo Collaboration, *Advanced Virgo Preliminary Project Execution Plan*, Virgo Internal report VIR-043A-07 (2007). [1](#)
- [4] The Virgo Collaboration, *Advanced Virgo Preliminary Design*, Virgo Internal report VIR-089A-08 (2008). [1](#)
- [5] The Virgo Collaboration, *Advanced Virgo Baseline Design*, Virgo Internal report VIR-027A-09 (2009). [1](#)
- [6] H.Heitmann, G.Losurdo, AdV SSM, *AdV selected milestones*, Virgo Internal report VIR-0496B-09 (2009).
- [7] Advanced LIGO team, *Advanced LIGO Reference Design*, LIGO-M060056-06-M (2006).
- [8] <http://lhocds.ligo-wa.caltech.edu:8000/advligo/GWINC> . [7](#)
- [9] S. Hild and G. Losurdo: *Advanced Virgo design: Comparison of the Advanced Virgo sensitivity from Bench 4 and GWINC (v1)*, Virgo note, VIR-055A-08 (2008). [7](#)
- [10] Punturo M.: *Advanced Virgo sensitivity document*, Virgo note VIR-0073A-12 (2012). [7](#)
- [11] S. Hild, A. Freise and G. Losurdo: *Sensitivity Options for the Advanced Virgo Baseline Design*, Virgo note, VIR-026A-09 (2009).
- [12] Virgo Technical Documentation System <https://pub3.ego-gw.it/itf/tds/> [13](#)
- [13] The Virgo Collaboration, *Advanced Virgo baseline design*, Virgo internal document VIR-027A-09 (2009) [14](#), [53](#)
- [14] G. Losurdo, *Advanced Virgo report to the STAC*, Virgo internal document VIR-0341A-11 (2011) [14](#)

- [15] H. Yamamoto, SIS (Stationary Interferometer Simulation) manual, LIGO technical document, LIGO-T070039-v2 (2009) [20](#), [21](#)
- [16] M. Laval and J-Y. Vinet, Guide for DarkF Users, Virgo internal document VIR-0007A-08 (2008) [20](#)
- [17] J. Degallaix, OSCAR a Matlab based optical FFT code, Journal of Physics: Conference Series, Vol. 228, No. 1, Pag. 012021 (2010) [19](#), [20](#), [54](#)
- [18] P. Saha, Fast estimation of transverse fields in high-finesse optical cavities, J. Opt. Soc. Am. A, vol. 14, No. 9, Pag. 2195-2202 (1997) [19](#), [21](#)
- [19] B. Caron, L. Derome, R. Flaminio, X. Grave, F. Marion, B. Mours, D. Verkindt, F. Cavalier, A. Viceré, SIESTA, a time domain, general purpose simulation program for the Virgo experiment, Astroparticle Physics, vol. 10, Pag. 369-386 (2008) [21](#), [54](#)
- [20] R. Bonnard, M. Galimberti, J. Degallaix, R. Flaminio, Advanced Virgo Mirror specifications cavities, Virgo internal document, VIR-0571A-10 (2010) [21](#)
- [21] R. Bonnard, M. Galimberti, J. Degallaix, Q. Benoit, R. Flaminio, L. Pinard, Simulations for Advanced Virgo Mirrors Roughness Specifications, Virgo internal document, VIR-0571A-10 (2010) [21](#)
- [22] R. Bonnard, M. Galimberti, J. Degallaix, R. Flaminio, L. Pinard, Simulations for AdV. Mirror Specification: High Spatial Frequency and Corrective Coating, Virgo internal document, VIR-0088A-11 (2011) [21](#)
- [23] R. Bonnard, J. Degallaix, M. Galimberti, R. Flaminio, L. Pinard, Simulations for the specifications of mirror flatness for Advanced Virgo, Virgo internal document, VIR-0104A-11 (2011) [21](#)
- [24] M. Galimberti, SIESTA simulations of a power-recycled interferometer, Virgo internal document, VIR-0715A-11 (2011) [21](#)
- [25] <https://www.cascina.virgo.infn.it/sDoc/VirgoReleases/Distributions/index.html> [21](#)
- [26] <cvs.ego-gw.it:/cvsroot/siesta/> [21](#)
- [27] R. Day, G. Vajente, J. Marque, AdV optical layout:new parameters proposal, Virgo internal document, VIR-0377B-11 (2011) [23](#)
- [28] The interferometer simulation tool finesse <http://www.gwoptics.org/finesse/> [20](#), [21](#)
- [29] A. Chiummo, R. Day, J. Marque, Validation of the use of mirror defect maps with Finesse, Virgo internal document, VIR-0432A-10 (2010) [22](#)
- [30] A. Chiummo, R. Day, J. Marque, Use of Mirror Defect Maps with Finesse, Virgo internal document, VIR-0572A-10 (2010) [22](#)
- [31] A. Chiummo, Convergence of Finesse simulations with MSRCs: current status, Virgo internal document, VIR-0491A-11 (2011) [22](#)
- [32] G. Vajente, Modal Interferometer Simulation Tool, Virgo internal document, VIR-0332A-10 (2010) [20](#), [22](#)

- [33] Optickle web site: http://ilog.ligo-wa.caltech.edu:7285/advligo/ISC_Modeling_Software 20, 22
- [34] Gwinc web-site <https://awiki.ligo-wa.caltech.edu/aLIGO/GWINC> 20, 22
- [35] Optocad web site: <http://home.rzg.mpg.de/~ros/optocad.html> 20, 23
- [36] A. Pasqualetti, Towers displacement range, Virgo internal document VIR-0607A-09 (2009) 23
- [37] M. Barsuglia, Macroscopic wedge on the BS - SIS simulation, Virgo internal document VIR-0313A-11 (2011) 33
- [38] from Heraeus data sheet 36
- [39] H. Yamamoto, Optics, Cavity and Loss: What we learned in aLIGO, LIGO technical document, LIGO-G1100857 (2011) 35
- [40] A. Rocchi and V. Fafone, TCS aspects of CP tilt, Virgo internal document VIR-0483A-11 (2011) 33
- [41] G. Vajente, Requirements on PO power leaking to dark port, Virgo internal document VIR-0447B-11 (2011) 35, 38, 43
- [42] M.Mantovani, personal communication (2011) 36
- [43] J. Degallaix, OSD news, VIR-0050B-12 (2012) 38
- [44] J. Degallaix, OSD news, VIR-0011A-12 (2012) 39
- [45] J. Degallaix, News and results, VIR-0030A-12 (2012) 39
- [46] J. Sidles and D. Sigg, Optical Torques in suspended Fabry-Perot interferometers. Physics Letters A, 354(3):167-172 (2006) 47
- [47] R. Ward, Re-evaluating the choice of the Advanced Virgo arm cavity finesse, VIR-0268A-10 (2010) 47, 50
- [48] R. Ward, SIS update - MSRC, VIR-0312A-11 (2011) 50
- [49] R. Bonnard and R. Flaminio, Simulation of Thermal Effects in Adv. Virgo, VIR-0267A-10 (2011) 50
- [50] R. Day, G. Vajente, J. Marque, Adv optical layout: new parameters proposal, VIR-0311B-11 (2011) 51
- [51] G. Losurdo, Advanced Virgo sensitivity curve: cavity finesse and signal recycling tuning, VIR-0024A-07 (2007) 51
- [52] R. Bonnard, J. Degallaix, M. Galimberti, R. Flaminio and L. Pinard, Simulations for the specifications of mirror flatness for Advanced Virgo, Virgo internal document VIR-0104A-11 (2011) 54
- [53] J. Degallaix, M. Galimberti, R. Bonnard and Q. Benoit, Defining the arm cavity loss for Advanced Virgo, Virgo internal document VIR-706A-10 (2010) 53
- [54] R. Bonnard and J. Degallaix, Advanced Virgo arm mirror specifications, RTL or RTL00?, Virgo internal document VIR-706A-10 (2010) 53

- [55] R. Bonnard et al., Simulations for AdV. Mirror Specification: High Spatial Frequency & Corrective Coating, Virgo internal document VIR-0088A-11 (2011) [56](#)
- [56] M. Galimberti, FFT simulations at LMA: state of the art, Virgo internal document VIR-0007A-10 (2010) [20](#)
- [57] R. Bonnard et al, Simulations of the specifications of mirror flatness for Advanced Virgo, VIR-0104A-11 (2011) [59](#)
- [58] R. Ward, A study of cold ITF defects in MSRC with SIS, VIR-0326A-11 (2011) [58](#), [61](#), [63](#)
- [59] R. Ward, Update on MSRC studies with SIS, VIR-0659A-11 (2011)
- [60] R. Day, Update on Simulations of ITF with roughness maps, VIR-0575A-2011 (2011) [62](#), [63](#), [64](#)
- [61] R. Day, E. Genin, and J. Marque, Influence of mirror roughness on clipping losses in optical cavities, VIR-0398A-10 (2010) [58](#)
- [62] R. Ward, MSRC SIS update: compensated cold ITF defects, VIR-0391A-11 (2011) [65](#)
- [63] A. Chiummo, et al., AdV design: MSRC degeneracy mitigation, VIR-0311A-11 (2011) [50](#)
- [64] R. Ward, MSRC SIS study: impact of cold ITF defects on squeezing, Virgo internal document VIR-0392A-11 (2011) [69](#)
- [65] R. Lawrence, Adaptive thermal compensation of test masses in Advanced LIGO, Classical and Quantum Gravity, 19, 1803 (2002) [66](#)
- [66] J. Degallaix, OSD: simulation comparisons, VIR-0705A-11 (2011) [61](#)
- [67] G. Losurdo, Mirror metrology upgrade - Project overview, VIR-0051A-12 (2012)
- [68] R. Ward, Squeezing the LSPR, VIR-0580A-10 (2010) [71](#)
- [69] M. Galimberti, Analysis of the deformation of AdV mirrors in phase map measurement, VIR-0707A-11 (2010) [61](#)
- [70] H. Vahlbruch, A. Khalaidovski, N. Lastzka, C. Gräfelf, K. Danzmann and R. Schnabel, The GEO 600 squeezed light source, Classical and Quantum Gravity, Vol. 27, P. 084027 (2010) [68](#)
- [71] A. Khalaidovski, H. Vahlbruch, N. Lastzka, C. Gräfelf, K. Danzmann, H. Grote and R. Schnabel, Long-term stable squeezed vacuum state of light for gravitational wave detectors, <http://arxiv.org/abs/1109.3731> (2011) [69](#)
- [72] T. Corbitt and N. Mavalvala, Review: Quantum noise in gravitational-wave interferometers, Journal of Optics B, Vol. 8, P. S675 (2005) [67](#)
- [73] The LSC, A gravitational wave observatory operating beyond the quantum shot-noise limit, Nat Phys, Vol. 7, P. 962 (2011) [68](#)
- [74] K. McKenzie, D. A. Shaddock, D. E. McClelland, B. C. Buchler, and P. K. Lam. Experimental demonstration of a squeezing-enhanced power-recycled michelson interferometer for gravitational wave detection. Phys. Rev. Lett., 88:231102, (2002) [68](#)

- [75] K. Goda, O. Miyakawa, E. E. Mikhailov, S. Saraf, R. Adhikari, K. McKenzie, R. Ward, S. Vass, A. J. Weinstein, and N. Mavalvala. A quantum-enhanced prototype gravitational-wave detector. *Nat Phys*, 4, 472 (2008) **68**, **277**
- [76] C. M. Caves, Quantum-mechanical noise in an interferometer, *Phys. Rev. D* 23(8):1693-1708, (1981) **68**, **69**
- [77] S. S. Y. Chua, M. S. Stefszky, C. M. Mow-Lowry, B. C. Buchler, S. Dwyer, D. A. Shaddock, P. K. Lam, and D. E. McClelland. Backscatter tolerant squeezed light source for advanced gravitational-wave detectors. *Opt. Lett.*, 36(23):4680 (2011) **69**
- [78] K. McKenzie, N. Grosse, W. P. Bowen, S. E. Whitcomb, M. B. Gray, D. E. McClelland, and P. K. Lam. Squeezing in the audio gravitational-wave detection band. *Phys. Rev. Lett.*, 93:161105 (2004) **69**
- [79] H. Vahlbruch, S. Chelkowski, B. Hage, A. Franzen, K. Danzmann, and R. Schnabel. Coherent control of vacuum squeezing in the gravitational-wave detection band. *Phys. Rev. Lett.*, 97:011101 (2006) **69**
- [80] A. Buonanno and Y. Chen. Quantum noise in second generation, signal-recycled laser interferometric gravitational-wave detectors. *Phys. Rev. D*, 64(4):042006 (2001) **70**
- [81] S. Chelkowski, H. Vahlbruch, B. Hage, A. Franzen, N. Lastzka, K. Danzmann, and R. Schnabel. Experimental characterization of frequency-dependent squeezed light. *Phys. Rev. A*, 71:013806 (2005) **68**
- [82] H. J. Kimble, et al. Conversion of conventional gravitational-wave interferometers into quantum non demolition interferometers by modifying their input and/or output optics. *Phys. Rev. D* 65 022002 (2001). **68**
- [83] B. Mours et al., *Thermal noise reduction in interferometric gravitational wave antennas using high-order TEM modes*, *Class. Quantum Grav.* 5777 (2006) **71**
- [84] E.D'ambrosio et al., *Reducing thermoelastic noise in gravitational-wave interferometers by flattening the light beams*, <http://arxiv.org/pdf/gr-qc/0409075> **72**
- [85] M. Bondarescu et al., *Phys. Rev. D* 78, 082002 (2008) **72**
- [86] H. Kogelnik and T. Li, *Appl. Opt.* **5**, 1550, (1966) **72**
- [87] J.-Y.Vinet, *Reducing thermal effects in mirrors of advanced gravitational wave interferometric detectors*, *Classical and Quantum Gravity* 24 (2007) **72**
- [88] J. Franc et al., *Role of high-order Laguerre-Gauss modes on mirror thermal noise in gravitational wave detectors*, Einstein Telescope internal note ET-0002A-10 (2010) **72**
- [89] S.Chelkowski et al., *Prospects of higher-order Laguerre-Gauss modes in future gravitational wave detectors*, *Phys. Rev. D* 79, 122002 (2009) **72**
- [90] M.Barsuglia, *Some considerations on HOLM for Virgo*, Advanced Virgo presentation, July 2008, at <http://wwwcascina.virgo.infn.it/advirgo/biweekly.html> **72**
- [91] P.Fulda et al., *Experimental Demonstration of higher-order Laguerre-Gauss mode interferometry*, *Phys. Rev. D* 82, 012002 (2010) **72**

- [92] M.Granata et al., *Higher-Order Laguerre-Gauss Mode Generation and Interferometry for Gravitational Wave Detectors*, PRL 105, 231102 (2010) [72](#)
- [93] P.Fulda et al., *Review of the Laguerre-Gauss mode technology research program at Birmingham*, arXiv:1112.4388 (2011) [72](#)
- [94] M.Galimberti et al, *Surface specifications for ET mirrors: state of the art*, talk at the 3rd annual ET workshop, Budapest, Nov. 2010 [73](#)
- [95] T.Hong et al.,*Effects of mirror aberrations on Laguerre-Gaussian Beams in Interferometric Gravitational-Wave Detectors*, Phys. Rev. D 84, 102001 (2011) [73](#)
- [96] C.Bond et al., *Higher order Laguerre-Gauss mode degeneracy in realistic, high finesse cavities*, Phys. Rev. D 84, 102002 (2011) [73](#)
- [97] G. Vajente, *Advanced Virgo Length Sensing and Control steady state design*, Virgo note VIR-0738A-11 (2011) [78](#), [83](#)
- [98] E. Calloni, G. Vajente, *Conceptual design of the second stage of frequency stabilization for Advanced Virgo*, Virgo note VIR-0013A-12 (2012) [79](#)
- [99] D. J. Richardson, J. Nilsson, and W.A. Clarkson, *High power fiber lasers: current status and future perspectives*, JOSA B, Vol. 27, Issue 11, pp. B63-B92 (2010) [80](#)
- [100] A. Chiummo, *Requirements for technical noise with ITF asymmetries*, Virgo note VIR-0517A-11 (2011) [83](#)
- [101] Innolight Mephisto laser datasheet. [84](#)
- [102] C.N.Man and A. Brillet, *Injection locking and coherent summation of argon ion lasers*, Lecture Notes in Physics, 1984, Volume 212, Gravitation, Geometry and Relativistic Physics, p. 222-225 [87](#)
- [103] https://wwwcascina.Virgo.infn.it/optics/doc/PMC_datasheet_270208.pdf [88](#)
- [104] The Virgo collaboration,*AdV Baseline design*,VIR-0027A-09,(2009). [93](#), [141](#)
- [105] E. Genin, C.N. Man,*Advanced Virgo Interface Control Document: INJ-PSL*,VIR-0019A-10,(2010). [96](#)
- [106] I. Fiori, E. Genin, J. Marque,*IME/INJ: Laser laboratory air conditioning preliminary requirements for AdV*,VIR-0019A-10,(2010). [99](#)
- [107] J.D. Mansell et al, *Appl.Opt.*, 40, 366-374, (2001). [104](#)
- [108] G. Vajente, *Advanced Virgo Length Sensing and Control steady state design*, VIR-0738A-11 (2011) [104](#), [109](#)
- [109] G. Vajente, *Simulation of Advanced Virgo Length Sensing and Control system*, VIR-068B-08, (2008). [104](#)
- [110] G. Vajente, *Advanced Virgo Length Sensing and Control steady state design*, VIR-0738A-11, (2011). [104](#)
- [111] B. Canuel, R. Day, E. Genin, P. La Penna, M. Mantovani, J. Marque, F. Paoletti, *AdV INJ: Preliminary design study*, VIR-0023A-09, (2009). [104](#), [141](#)

- [112] B. Canuel, R. Day, E. Genin, F. Nocera, F. Paoletti, *High power input optics R&D: Final report*, VIR-0296A-10, (2010). [105](#), [106](#), [107](#), [115](#), [116](#), [149](#)
- [113] E. Genin, *Considerations on input beam jitter, MC AA noise and IMC length noise for AdV.*, VIR-0602A-10, AdV workshop, November 2010, <https://tds.ego-gw.it/ql/?c=7906>. [111](#)
- [114] E. Genin, *Installation of new Beam Monitoring System and results.*, VIR-0196A-08, Commissioning weekly meeting, Janvier 2008, <https://tds.ego-gw.it/ql/?c=3241>. [112](#)
- [115] The Virgo collaboration, *Noise from scattered light in Virgo's second science run data*, Class. Quantum Grav. 27 (2010) 194011. [116](#)
- [116] B. Canuel, J. Marque, E. Genin, *A High power, low diffusing and vacuum compatible beam dump for dumping B1s on SDB*, VIR-0620A-10,(2010). [119](#)
- [117] B. Swinkels, *Commissioning during and after VSR4*, VIR-0667A-11,(2011). [121](#)
- [118] Th.S. Bauer, R. Day, E. Genin, J. Marque, L. Pinard, *AdV INJ: IMC flat mirrors specifications.*, Virgo internal note, VIR-0506A-11, <https://tds.ego-gw.it/ql/?c=8562>. [124](#)
- [119] R. Day, E. Genin and J. Marque, *Influence of mirror roughness on clipping losses in optical cavities*, Virgo internal note, VIR-0398A-10, <https://tds.ego-gw.it/ql/?c=7643>. [125](#)
- [120] E. Genin et al., *INJ status*, Presentation at Virgo Coll. Meeting July 2011 , VIR-0411A-11, <https://tds.ego-gw.it/ql/?c=8466>. [125](#)
- [121] E. Genin, Th.S. Bauer, B. Canuel , I. Fiori, F. Frasconi, J. Marque, P. Ruggi , *Dihe-dron support substitution: Installation and commissioning*, Presentation at Virgo Coll. Meeting November 2011, VIR-0668A-11, <https://tds.ego-gw.it/ql/?c=8726>. [126](#), [127](#)
- [122] R. Day, *INJ - Specs of the IMC end mirror* Presentation at Virgo Coll. Meeting February 2012, VIR-0083A-12, <https://tds.ego-gw.it/ql/?c=8887>. [132](#)
- [123] M. Mantovani, *Suspended Injection bench requirements - MC Automatic Alignment noise projection*, VIR-0598A-10, (November 2010). [139](#)
- [124] R. Day, E. Genin, M. Mantovani and J. Marque, *AdV INJ: Why we have to change the IMC end mirror in AdV*, VIR-0688A-10, 2010. [135](#)
- [125] P. Fritschel, *Notes on the laser frequency stabilization*, VIR-NOT-LAL-1380-51, <https://tds.ego-gw.it/ql/?c=433> [142](#)
- [126] B. Canuel, R. Day, E. Genin, J. Marque, P. La Penna, *AdV INJ: Design Requirements document*, VIR-0628A-09, (2009). [148](#)
- [127] The Virgo collaboration, *Results of the Virgo central interferometer commissioning*, Class. Quantum Grav. 21 (2004) S395-S402. [148](#)
- [128] E.Genin, P.La Penna, J.Marque, *Suspended Injection Bench Faraday in-vacuum isolation measurement*, VIR-0026A-07, (2007). [148](#)

- [129] R. Day, E. Genin, M. Mantovani and J. Marque, *AdV INJ: Why we have to change the IMC end mirror in AdV.*, VIR-0688A-10, (2010). 122
- [130] E. Khazanov et al, *Investigation of self-induced depolarization of laser radiation in terbium gallium garnet*, IEEE Journ. Quant. Electr., 35 (8), (1999). 149
- [131] E. Khazanov et al, *Compensation of Thermally Induced Modal Distortions in Faraday Isolators*, IEEE Journ. Quant. Electr., 40 (10), (2004). 149
- [132] D.Tanner et al, *The LIGO input optics*, LIGO-G070296-00-R 149
- [133] E.A. Khazanov, Quantum Electronics, 29(1), 59-64(1999) 149
- [134] The Virgo collaboration, *In-vacuum optical isolation changes by heating in a Faraday isolator Appl. Opt.*, Vol. 47, Issue 31, pp. 5853-5861 (2008) 149
- [135] V. Zelenogorsky, O.Palashova and E. Khazanova, Optics Communications Volume 278, Issue 1, 2007, 8-13 149
- [136] Khazanov et al., *AdV Faraday isolator design study*, VIR-0245A-10, (March 2009). 149
- [137] B. Canuel, E. Genin, *AdV INJ: Faraday isolator prototype characterization*, VIR-0455A-11, (2011). 150, 151
- [138] E. Genin, *AdV: MSRC configuration: preliminary study of input MMT*, VIR-0114A-11, (2011). 155
- [139] M. Barsuglia, C. Buy, B. Canuel, R. Day, E. Genin, G. Vajente, *AdV INJ: Mode matching telescope configuration choice for the ITF input telescope.*, VIR-0010A-12, (2011). 97, 156, 157, 159, 160, 161, 162
- [140] R. Day, E. Genin, V. Fafone, G. Vajente, J. Marque, *AdV design: MSRC case (summary)*, VIR-0139A-11, (2011). 155
- [141] E. Genin, *AdV MSRC: progress on pick-off extraction*, VIR-0166A-11, (2011). 156
- [142] C. Buy, M. Barsuglia, *AdV input/output mode matching telescopes for the MSRC. Update of the preliminary study*, DET/INJ joint meeting on telescopes, (2011). 155
- [143] E. Genin, *AdV: MSRC configuration: preliminary study of input MMT*, VIR-0114C-11, (2011). 159
- [144] E. Genin, *Towards the choice of Mode matching telescopes configuration*, VIR-0546A-11, (2011). 160
- [145] P. La Penna, O. Francois, J. Marque, E. Genin, *Note on Virgo parabolic telescope: design, installation and commissioning*, VIR-0504A-10, (2010). 160
- [146] G. Vajente, *Simulation of back-reflection from injection and detection mode-matching telescopes*, VIR-0179D-11, (2011). 162
- [147] S. Braccini, *Measurement of suspension performance*, VIR-NOT-PIS-1390-191 (2002), <https://tds.ego-gw.it/ql/?c=1339> 162
- [148] B. Canuel, E. Genin, J. Marque, P. Ruggi, *Towards the choice of Mode matching telescopes configuration*, VIR-0546A-11, <https://tds.ego-gw.it/ql/?c=8602> 162

- [149] R. Day, *Update on Diffused light from MMT optics with FFT code*, VIR-0549A-11, <https://tds.ego-gw.it/ql/?c=8605> 162
- [150] B. Swinkels, *Scattered light from the OB*, VIR-0143A-11, <https://tds.ego-gw.it/ql/?c=8197> 163
- [151] C.Comtet et al., *Proceedings of the 42th Rencontres de Moriond*, 2007. 171, 179
- [152] Z. Yan, Li Ju, *et al.*, *Applied Optics* 45 (2006) 2631-2637 172
- [153] http://www.virgo.optique.espci.fr/Virgo_Mirrors/ 174
- [154] A.Brillet, *et al.*, *Phys. Rev. D*, **67**(10), 102006 (2003) 174
- [155] F. Bondu, M. Laval and J.-Y. Vinet *Virgo Note VIR-054A-07* (2007). 174
- [156] L. Pinard, R. Flaminio, D. Forest: *Bulk absorption measurement at 1064 nm of the new Heraeus ultra pure fused silica used for the Advanced Virgo Test Mass: effect of the annealing*, *Virgo note VIR-0091A-10* (2010). 172
- [157] K. Numata, K. Yamamoto, H. Ishimoto, S. Otsuka, K. Kawabe, M. Ando, K. Tsubono: *Systematic measurement of the intrinsic losses in various kinds of bulk fused silica*, *Physics Letters A* 327 (2004) 263-271. 172
- [158] Q. Benoit *Effect of mirror roughness in Advanced Virgo cavity*, *Virgo internal document VIR-0643B-09* (2009).
- [159] R. Bonnand *Simulations for AdV. Mirror Specification: High Spatial Frequency and Corrective Coating*, *Virgo internal document VIR-88A-11* (2011).
- [160] R. Bonnand *Simulations for the specifications of mirror flatness for Advanced Virgo*, *Virgo internal document VIR-104A-11* (2011). 177
- [161] R. Day, E. Genin, J. Marque *Influence of mirror roughness on clipping losses in optical cavities*, *Virgo internal document VIR-0398A-10* (2010).
- [162] R. Bonnand *Calculation of the flatness specifications for the Advanced Virgo arm mirrors*, *Virgo internal document VIR-0020A-12* (2012). 175, 177
- [163] L. Pinard *Presentation for the technical readiness review of the new wet cleaning machine*, *Virgo internal document VIR-0789A-09* (2009). 184
- [164] B. Cimma, D. Forest, P. Ganau, B. LAGRANGE, J.M. Mackowski, C. Michel, J.L. Montorio, N. Morgado, R. Pignard, L. Pinard, A. Remillieux: *on beam sputtering coatings on large substrates: towards an improvement of the mechanical and optical performances*, *Applied Optics*, vol. 45 (2006) 1436-1439. 180
- [165] R. Day, V. Fafone, J. Marque, M. Pichot, M. Punturo, A. Rocchi *Virgo Input Mirrors thermal effects characterization*, *Virgo Note VIR-0191A-10* (2010). 174
- [166] M. Galimberti *Analysis of the deformation of AdV mirrors in phase maps measurements*, *Virgo internal document VIR-707A-11*(2011). 184
- [167] R. Bonnand, J. Degallaix, *Advanced Virgo arm mirror flatness specification, RTL or RTL00?*, *Virgo internal document VIR-0032A-12*, (2012) 175

- [168] J.Y. Vinet, *Thermal issues in mirrors - October 2008*, VIR-0224A-10 (2010). 189, 201, 202
- [169] R.C. Lawrence, Ph.D. thesis, MIT, 2003, LIGO-P030001-00-R. 189
- [170] R. Day, E. Genin, and J. Marque, *Influence of mirror roughness on clipping losses in optical cavities*, VIR-0398A-10 (2010). 189
- [171] A. Rocchi, VIR-480A-07, (2007). 189
- [172] V. Fafone and A. Rocchi, *AdV TCS: effect of non-uniform absorption - thermal simulations*, VIR-0207A-11 (2011). 189
- [173] V. Fafone and A. Rocchi, *AdV TCS: effect of substrate non-uniformities - thermal simulations*, VIR-0351A-11 (2011). 191, 203
- [174] V. Fafone, talk at the Advanced Virgo Meeting, Cascina March 12, 2009; https://wwwcascina.virgo.infn.it/advirgo/biweekly/2009/2009-03/fafone_090312.ppt. 192
- [175] G. Vajente, *Advanced Virgo Length Sensing and Control steady state design*, VIR-0738A-11 (2011). 193
- [176] J. Degallaix, C.Zhao, L. Ju and D. Blair, *Thermal tuning of optical cavities for parametric instability control*, Journal of the Optical Society of America B (2007), Vol 24, p 1336-1343 195
- [177] G. Parguez, A. Pasqualetti, V. Fafone, A. Rocchi, *Vacuum test of Phosphor bronze insulated wire for the ring heater*, VIR-0584A-10 (2010). 198
- [178] G. Parguez and A. Pasqualetti *Vacuum test: Al coated with alumina samples*, VIR-0060A-12 (2012). 200
- [179] INFN Roma Tor Vergata, VIR-0298A-10, (2010). 201
- [180] J. Degallaix, Ph.D. thesis, UWA, 2006. 202
- [181] V. Fafone, *AdV Thermal Compensation System*, VIR-0115A-10 (2010). 202, 208
- [182] V. Fafone and A. Rocchi, *AdV TCS: Considerations on actuation and sensing for the correction of high order aberrations in MSRC*, VIR-0373A-11 (2011). 207, 208
- [183] P. Willems, LIGO-T060224-v4 (2010). 209, 210, 212, 215
- [184] V. Fafone and A. Rocchi, *TCS noise: general concepts and application to the Virgo/Virgo+ case*, VIR-0615B-09 (2009). 213
- [185] P. Willems, LIGO-T1000093-v4 (2010). 214
- [186] V. Fafone for the TCS Group, *TCS R&D progress*, VIR-0090A-11 (2011). 215
- [187] V. Fafone and A. Rocchi, *AdV TCS: PRM e ITM RoC tuning*, VIR-0550A-11 (2011). 216, 217, 218, 219, 221
- [188] V. Fafone and A. Rocchi, *Input from TCS to OSD: ITM RoC tuning & PR substrate*, VIR-0573A-11 (2011). 216, 217

- [189] V. Fafone and A. Rocchi, *Correction of RoC by CO₂ central heating*, VIR-0625A-10 (2010). 218
- [190] R. Day and A. Chiummo, *Radius of Curvature Correction (CHRoCC)*, VIR-0555A-11 (2011). 218
- [191] The Virgo Collaboration, *Advanced Virgo Baseline Design*, VIR-0027A-09 (2009). 222
- [192] A.F. Brooks, *et al.*, Opt. Express **15** (16), 10370-10375 (2007). 222
- [193] A.F. Brooks, Ph.D. thesis, University of Adelaide (Australia), (2007). 224
- [194] A.F. Brooks, *et al.*, Appl. Opt. **48**, 355-364 (2009). 225
- [195] R. Day, *Simulation of use of phase camera as sensor for correcting common high order aberrations in MSRC*, VIR-0389A-11 (2011). 229
- [196] V. Fafone and A. Rocchi, *AdV TCS: preliminary investigation on the HWS telescope on the End Benches*, VIR-0022A-12 (2012). 234
- [197] R. Flaminio, H. Heitmann, *Interferometer locking scheme*, VIR-NOT-LAS-1380-66. 235
- [198] L. Rolland, R. Gouaty, B. Mours, E. Tournefier, *Constraints on the Advanced Virgo detection bench jitter from OMC alignment*, VIR-0685A-10. 242, 260, 261
- [199] L. Rolland, R. Gouaty, B. Mours, *Constraints on the Advanced Virgo detection bench jitter from OMC alignment: an update*, VIR-0650A-11. 242, 260, 261
- [200] G. Vajente, *OMC requirements from ISC considerations*, VIR-0541A-11. 243, 244
- [201] E. Tournefier, *Advanced Virgo output mode cleaner: specifications*, VIR-0071A-08. 243, 248, 249, 252
- [202] R. Gouaty, G. Le Corre, B. Mours, L. Rolland, E. Tournefier, *Advanced Virgo output mode cleaner: revision of the specifications*, VIR-0020A-11. 243, 245, 251, 252, 258
- [203] https://tds.ego-gw.it/itf/osl_virgo/index.php?callRep=28357 245
- [204] R. Gouaty, *The Virgo Output Mode Cleaner*, VIR-0465A-11. 245
- [205] K. Numata *et al.*, Phys. Rev. Lett. **93**, 250602 (2004). 245, 258
- [206] J. Marque, G. Vajente, *Proposal of an alternative design of the OMC to improve filtering performance*, VIR-0713A-11. 259
- [207] A. Dominjon, *Recherche des ondes gravitationnelles avec l'interféromètre Virgo: étude et conception de l'ensemble de détection du signal*, Ph.D Thesis, Université de Savoie (1996). 246
- [208] L. Derome, *Le système de détection de l'expérience Virgo dédiée à la recherche d'ondes gravitationnelles*, Ph.D Thesis, Université de Savoie (1999). 246, 248, 258
- [209] L. Derome, *New mode cleaner support test*, VIR-0045A-07. 246, 248, 258
- [210] F.J. Raab, S.E. Whitcomb, LIGO-T920004-00-R (1992). 251
- [211] P. Fritschel, LIGO-T060303-00-D (2006). 251
- [212] R. Day, *Simulations of ITF with roughness maps*, VIR-0536A-11 (2011). 249, 251, 300

- [213] R. Day, *Update on Simulations of ITF with roughness maps*, VIR-0575A-11 (2011). 249, 251, 300
- [214] N. Smith-Lefebvre, S. Ballmer, M. Evans, S. Waldman, K. Kawave, V. Frolov, and N. Mavalvala, *Optical alignment sensing of a readout mode cleaner cavity*, Optics Letters, Vol. 36, Issue 22, pp. 4365-4367 (2011). 261
- [215] https://tds.ego-gw.it/itf/osl_virgo/index.php?callRep=30268 264
- [216] https://tds.ego-gw.it/itf/osl_virgo/index.php?callRep=30270 264
- [217] B. Canuel, E. Genin, J. Marque, *High power, Low diffusing and vacuum compatible beam dump - application to B1s dumping on SDB*, VIR-0586A-10 (2010). 264
- [218] M. Barsuglia, C. Buy, B. Canuel, R. Day, E. Genin, J. Marque, G. Vajente, *AdV INJ: Mode matching telescope configuration choice for the ITF input telescope*, VIR-0010B-12 (2012). 286, 292
- [219] https://tds.ego-gw.it/itf/osl_virgo/index.php?callRep=28729 290
- [220] B. Canuel, E. Genin, *Determination of back scattering and direct reflection recoupling from single optics - application to the End Benches*, VIR-0375A-10 (2010). 292
- [221] B. Swinkels, *Scattered light from the OB*, VIR-0143A-11 (2011). 293
- [222] M. Mantovani, *FoM for end benches telescope optimization for AA purposes*, VIR-0058A-12 (2012).
- [223] C. Buy, M. Barsuglia, *End bench telescopes for AdV - Optical design*, VIR-0628A-10 (2010).
- [224] C. Buy, *AdV End Bench Telescopes-QPD sensitivity*, VIR-0059A-12 (2012). 303
- [225] H. Heitmann, E. Genin, J. Marque, *End bench redesign*, VIR-0066A-10 (2007). 304
- [226] A. Belletoile, *Selection and DC characterization of the control photodiodes for Advanced Virgo*, VIR-0478A-10 (2010). 265
- [227] F. Beauville et al, *A camera based position control of a suspended optical bench used in a gravitational wave detector*, Review of Scientific Instruments vol 74, 4, p2564 (2003). 301
- [228] M. Mantovani, *SBE suspension requirements for Automatic Alignment purposes*, VIR-0101A-12 (2012). 242
- [229] M. Mantovani, 'Automatic Alignment Sensing and Control Scheme for Advanced Virgo MSRC configuration', VIR-0201A-11, April 18, 2011. 268, 270
- [230] See VIR-0377B-11 for details. 270
- [231] M. Mantovani, 'Automatic Alignment Sensing and Control Scheme for Advanced Virgo MSRC configuration Advanced Virgo MRSC simulations related to Angular control: EDB suspension requirements - CP tilt requirement - central area pick off', VIR-0370A-11, June 29, 2011. 275
- [232] M. Mantovani, 'Automatic Alignment Control Scheme and Terminal bench requirement update', VIR-0444A-11, July 28, 2011.

- [233] R. Gouaty, B. Mours, P. Mugnier, L. Rolland, E. Tournefier, ‘*DET space constraints and vacuum needs*’, VIR-0388A-11, July 7, 2011.
- [234] B. Mours, P. Mugnier, ‘*Detector Bench Vacuum Enclosure*’, VIR-0023A-11, January 13, 2011.
- [235] M. Mantovani, ‘*EDB suspension requirements*’, VIR-0456A-11, August 23, 2011.
- [236] J.F.J. van den Brand, A. Bertolini, E. Hennes, M. Doets, ‘*Requirements for SAS systems for Advanced Virgo*’,
- [237] Z. Barbaric, ‘*Position Error Estimation of a Laser Illuminated Object*’, Scientific Publications of the State University of Novi Pazar, Appl. Math. Inform. and Mech., Vol. 3, 1 (2011), 59 - 69.
- [238] Z. Barbaric, A.S. Marincic and L.M. Manojlovic, ‘*Measurement error estimation of a light spot position on a quadrant photodiode*’, 16th Telecommunications forum TELFOR 2008, Serbia, Belgrade, November 25 - 27, 2008.
- [239] Nergis Mavalvala, ‘*Alignment Issues in Laser Interferometric Gravitational-Wave Detectors*’, PhD thesis, MIT, January, 1997.
- [240] H.L. Groenstege, J.D. Schipper, A.H. Kruijer, ‘*Four quadrant diode front end module for the Virgo Linear Alignment 3/30 mW, plus configuration*’, Nikhef Department of Electronic Technology, 2009.
- [241] J.F.J. van den Brand, H. Groenstege, ‘*Electronics: Demod + 4Q FE*’, VIR-0433A-07, April 3, 2007. 271
- [242] J.F.J. van den Brand, ‘*Technical review of 4Q FE design for Virgo+*’, December 12, 2007. 271
- [243] H. Heitmann, ‘*Alignment plans & status*’, VIR-0421A-07, April 2, 2007. 271
- [244] H. Heitmann, ‘*The 2nd modulation frequency project*’, VIR-0367A-07, February 5, 2007. 271
- [245] H. Heitmann, ‘*LA commissioning plans*’, VIR-0310A-07, November 19, 2007. 271
- [246] H. Heitmann, ‘*Alignment status & plans*’, VIR-0262A-07, March 6, 2007. 271
- [247] Application note AN118, Rev. 1.2 12/03, ‘*Improving ADC resolution by oversampling and averaging*’, Silicon Laboratories, 2003. 271
- [248] J. Betzwieser, *Analysis of spatial mode sensitivity of a gravitational wave interferometer and a targeted search for gravitational radiation from the Crab pulsar*, Ph.D. thesis (2007). 277
- [249] S. Bigotta, *Phase camera 1 status and measurements*, Virgo internal document: VIR-0125A-09, (2009). 277, 282
- [250] A. Di Lieto, *Phase camera*, Virgo internal document: VIR-0230-09, (2009). 277
- [251] J. Marque, *Review of past experiences with Virgo Phase camera*, Virgo internal document: VIR-0343A-11, (2011). 277

- [252] D. Rabeling, *Nikhef phase camera: project update*, Virgo internal document: VIR-0354A-11, (2011). 277, 282
- [253] R. Day, *Simulation of use of phase camera as sensor for correcting common high order aberrations in MSRC*, Virgo internal document: VIR-0389A-11 (2011). 277, 280, 282
- [254] F. Guzman Cervantes, *Real-Time Spatially Resolving Phasemeter for LISA Pathfinder*, Masters of Science thesis (2004). 277, 279, 280, 282
- [255] A. Freise, et al., *Frequency domain interferometer simulation with higher-order spatial modes*, Class. Quant. Grav. 21 (2004) S1067 [arXiv:gr-qc/0309012] 311, 340
- [256] Optickle home-page, http://ilog.ligo-wa.caltech.edu:7285/advligo/ISC_Modeling_Software 193, 311, 314, 340
- [257] H. Yamamoto et al., *End to End time-domain optical simulator* <http://www.ligo.caltech.edu/~e2e/> 312, 335
- [258] CALVA home-page, <http://calva.lal.in2p3.fr/> 355
- [259] R. Gouaty, *Requirements for longitudinal and quadrant photo-diodes*, VIR-0438A-11 (2011) 313, 316
- [260] G. Vajente, *Advanced Virgo Length Sensing and Control steady state design*, VIR-0738A-11 (2011) 314, 317, 320, 321, 358
- [261] L. Barsotti and M. Evans, *Lock Acquisition Study for Advanced LIGO*, LIGO technical note LIGO-T1000294-v1 (2011) 336, 357
- [262] G. Vajente, R. Day, J. Marque, *AdV optical layout: new parameters proposal*, VIR-0377B-11 (2011) 314, 339
- [263] M. Mantovani, *Differential offset vs Automatic Alignment control*, VIR-0737A-11 317, 344, 345, 357
- [264] E. Tournefier, *Advanced Virgo output mode cleaner: specifications*, VIR-0071A-08 (2008) 319
- [265] J. Marque, G. Vajente, *Proposal of an alternative design of the OMC to improve filtering performance*, VIR-0713A-11 (2011) 319
- [266] B. Swinkels, E. Campagna, G. Vajente, L. Barsotti and M. Evans, *Longitudinal noise subtraction: the alpha-, beta- and gamma-technique*, VIR-0050A-08 (2008) 320
- [267] E. Tournefier, *High frequency noise in the recycled ITF*, VIR-0154A-05 (2005) 321
- [268] A. Chiummo, *Coupling of frequency and power noise vs. ITF asymmetries: preliminary results*, VIR-0485A-11 (2011) 325
- [269] A. Chiummo, *Requirements for technical noise with ITF asymmetries*, VIR-0517A-11 325
- [270] R. Gouaty, *OMC design & specifications for side band transmission*, VIR-0581A-11 325
- [271] F. Bondu, *L'interferometre Virgo: proprietes optiques, stabilisation en frequence du laser*, Memoire d'habilitation a diriger des recherches, Observatoire de la Cote d'Azur (2008) 325, 337

- [272] E. Calloni, G. Vajente, *Conceptual design of the second stage of frequency stabilization for Advanced Virgo* VIR-0013A-12 [315](#), [331](#), [334](#)
- [273] B. Swinkels, P. Ruggi and G. Vajente, *Lock acquisition of the Advanced Virgo arm-cavities with reduced force*, VIR-0019A-12 (2012) [332](#)
- [274] F. Acernese et al., *Lock acquisition of the Virgo gravitational wave detector*, *Astroparticle Physics* vol. 30 p. 29, (2008) [332](#)
- [275] F. Cavalier, *Lock acquisition for the arms*, VIR-0656A-10 [337](#)
- [276] B. Canuel et al, *AdV INJ: Preliminary Design Study document*, VIR-0023A-09 [337](#)
- [277] D. Sigg *et al.*, *Phys. Lett. A* **354** 3 (2006) 167-172 . [340](#)
- [278] M. Mantovani, *Automatic Alignment control scheme & Terminal bench requirements update*, VIR-0444A-11 [340](#)
- [279] M. Mantovani, *Automatic Alignment Sensing and Control scheme for Advanced Virgo MSRC configuration*, VIR-0201A-11 [341](#)
- [280] M. Mantovani, G. Vajente, *Alignment accuracy requirements for Advanced Virgo*, VIR-0247A-10 [341](#)
- [281] M. Mantovani, *Stable Recycling Cavities : L.R.C. vs S.R.C. angular requirements*, VIR-0029B-11 [341](#)
- [282] M. Mantovani for the Virgo Collaboration, *Automatic Automatic Alignment for the first science run of the Virgo interferometer*, *Astroparticle Physics* Volume 33, Issue 3, April 2010, Pages 131-139 [341](#)
- [283] M. Mantovani for the LIGO-Virgo Collaboration, *Automatic Alignment system during the second science run of the Virgo interferometer*, *Astroparticle Physics* Volume 34 (2011) 327-332 [341](#), [343](#), [344](#)
- [284] M. Mantovani, *Automatic Alignment status for VSR2 and plans toward V+ sensitivity*, VIR-0513A-09 (2009) [343](#)
- [285] M. Mantovani, *AA electronics status and future installations*, VIR-0208A-10 (2010) [343](#)
- [286] M. Mantovani, A. Masserot, Virgo logbook entry 24766 (2009); M. Mantovani, Virgo logbook entry 25217 (2009); M. Mantovani, A. Masserot, F. Paoletti, Virgo logbook entry 26695 (2010) [343](#)
- [287] L. Barsotti, M. Evans, *Modeling of Alignment Sensing and Control for Advanced LIGO*, LIGO-T0900511-v4 [343](#)
- [288] B. Mours, *Beams centering using cameras*, VIR-0654A-11 [344](#), [350](#)
- [289] M. Mantovani, *SEB displacement requirements update*, VIR-0523A-11 [347](#)
- [290] R. Gouaty, *OMC design & specifications for side band transmission*, VIR-0581A-11 (2011) [356](#)
- [291] R. Abbott, R. Adhikari, S. Ballmer, L. Barsotti, M. Evans, P. Fritschel, V. Frolov, G. Mueller, B. Slagmolen, S. Waldman, *AdvLIGO Interferometer Sensing and Control Conceptual Design*, LIGO-T070247-00-I (2008)

- [292] H. Grote, *High power, low-noise, and multiply resonant photodetector for interferometric gravitational wave detectors*, Rev. Sc. Instr. **78**, 054704 (2007)
- [293] E. Tournefier, *Technical noises for Virgo+: DC and AC readout cases*, VIR-NOT-LAP-1390-338 **313**
- [294] The Virgo Collaboration, *Advanced Virgo Baseline Design*, VIR-027A-09 **313**
- [295] V.B. Braginsky, S.E. Strigin, and S.P. Vyatchanin, Phys. Lett. A **287**, 331 (2001). **350**, **351**
- [296] C. Zhao *et al.*, Phys. Rev. A **78**, 023807 (2008). **351**
- [297] C. Molinelli *et al.*, in preparation (2012). **351**
- [298] S. Gras, C. Zhao, L. Ju, J. Degallaix, and D.G Blair, Phys. Rev. Lett. **94**, 121102 (2004). **351**, **352**
- [299] M. Evans, L. Barsotti, and P. Fritschel, Phys. Lett. A **374**, 665 (2010). **351**
- [300] J. Degallaix, C. Zhao, L. Ju, and D. Blair, “Thermal tuning of optical cavities for parametric instability control,” J. Opt. Soc. Am. B **24**, 1336 (2007) **352**
- [301] J. Miller *et al.*, Phys. Lett. A **375**, 788 (2011). **352**
- [302] <http://usa.autodesk.com/autodesk-inventor/> **367**
- [303] <http://www.radiantzemax.com/en/design/> **195**, **367**
- [304] Vinet J-Y, Brisson V, Braccini S, “Scattered light noise in gravitational wave interferometric detectors: Coherent effect”, *Phys. Rev. D* **54** 1276 (1996) **369**
- [305] Vinet J-Y, Brisson V, Braccini S, Ferrante I, Pinard L, Bondu F, Tournie E, “Scattered light noise in gravitational wave interferometric detectors: a statistical approach”, *Phys. Rev. D* **56** 6085 (1997) **369**
- [306] V. Brisson, J.Y. Vinet, “Summary of scattered light noise calculations and baffle design in the long cavities”, Virgo internal document VIR-NOT-LAL-1390-123 (1998), <https://tds.ego-gw.it/ql/?c=721> **369**
- [307] Braccini S, “Pipe baffle shaking tests”, Virgo internal document VIR-0172A-08 (2007), <https://tds.ego-gw.it/ql/?c=3217> **369**
- [308] E. Genin, “Study of Back-reflected/back-scattered light from MMT telescope optics. Next steps toward the choice of the telescope configuration”, Virgo internal document, presentation at INJ/DET meeting June 6, (2011) **373**
- [309] R. Ward, M. Evans, “The Optickle optical modeling tool”, presentation at the QND workshop in Hannover (2005), <http://www.ligo.caltech.edu/~rward/presentations/QND/Optickle.pdf> **374**
- [310] Fiori I for the Virgo collaboration, “Noise from scattered light in Virgo’s second science run data”, *Class. Quantum Grav.* **27** 194011 (2010)
- [311] T. Tomoru *et al.*, “Study of optical dumpers used in high vacuum system of interferometric gravitational wave”, *J. Phys.: Conf. Ser.* **32** 476 (2006) **375**

- [312] M. Smith, V. Sannibale, N. Nguyen, "AOS SLC Arm Cavity Baffle FDR", LIGO internal document T1000747-v3 (2011), <https://dcc.ligo.org/cgi-bin/private/DocDB/ShowDocument?docid=29694> 375
- [313] M. Smith, "Trade-off: porcelain coating vs. oxidized polished stainless steel for ACB", LIGO internal document L1100197-v4 (2011), <https://dcc.ligo.org/cgi-bin/private/DocDB/ShowDocument?docid=70021> 375
- [314] VIR-0435A-09 (2009). 380
- [315] P. Ruggi, https://tds.ego-gw.it/itf/osl_virgo/index.php Entry: 30433 (2011). 383
- [316] A. Gennai et al. "Advanced Virgo Suspension Control System", VIR-0174A-11 (2011). 383
- [317] Di Fiore, Majorana, P. Ruggi https://tds.ego-gw.it/itf/osl_virgo/index.php Entry:30724 (2012). 384
- [318] P. Ruggi, "Modeling multipendulum suspension", VIR-0501A-09 (2009). 394, 395
- [319] ECM Engineered Ceramic Materials GmbH, Am Bleichbach 10, 85452 Moosinning; Germany. 390
- [320] L. Abadie, et al., "Beating the spin-down limit on gravitational wave emission from the Vela pulsar", *Astrophys. Jou.* 737:93 (16pp) (2011). 395
- [321] P.Puppo et al., "Virgo+ Thermal Noise Study", VIR-0074A-12 (2012). 395, 399
- [322] M. Tacca, "Tests and understanding of the V+ monolithic suspensions: 02", Thermal Noise Workshop, 23-24 Feb 2012, Cascina Italy, <http://agenda.infn.it/contributionListDisplay.py?confId=4429> (2012). 395, 396
- [323] VIR-0622A-10, M. Colombini, "Q measurements on Monolithic Suspension" (2010). 395
- [324] VIR-0031A-11, M. Colombini, "Q measurements on Monolithic Suspension" (2011). 395
- [325] G. Cagnoli, L. Gammaitoni, J. Hough, J. Kovalik, S. McIntosh, M. Punturo, and S. Rowan, *Phys. Rev. Lett.* **85**, 2442 2445 (2000). 396
- [326] H. Vocca VIR-643A-08, "Status of monolithic suspensions" (2008). 400
- [327] G.Cagnoli and P.Willem. *Phys. Rev. B* **65** (2002). 401
- [328] P.Willem, *Phys. Lett. A* 300 (2002). 401
- [329] F. Piergiovanni, *J. Phys. Conf. Ser.* 228 (2010). 403
- [330] Virgo collaboration, *Virgo Final Design*, Virgo Note VIR-TRE-DIR-1000-13 (1997). 416, 434, 451
- [331] G. Ballardin et al., *Measurement of the Virgo superattenuator performance for seismic noise suppression*, *Rev. Sci. Instrum.* 72, 3643 (2001). 416, 419
- [332] G. Losurdo et al., *Inertial control of the mirror suspensions of the Virgo interferometer for gravitational wave detection*, *Rev. Sci. Instrum.* 72 (9), 3653 (2001). 417

- [333] G. Losurdo, *Ultra-low frequency inverted pendulum pre-isolator for the Virgo test mass suspension*, PhD Thesis (1999). 417
- [334] A. Gennai, G. Losurdo, A. Marin, D. Passuello, *Superattenuator Inertial Damping*, Virgo Note VIR-NOT-PIS-4900-104, (1999). 417
- [335] M. Beccaria et al., *Extending the Virgo gravitational wave detection band down to a few Hz: metal blade springs and magnetic antisprings*, Nucl. Instr. and Meth. A394, 397-408 (1997). 420
- [336] S. Braccini et al., *Measurement of the seismic attenuation performance of the Virgo Superattenuator*, Astrop. Phys. 23 (6), 557-565 (2005). 420
- [337] F. Acernese et al., *The commissioning of the central interferometer of the Virgo gravitational wave detector*, Astrop. Phys. 21 (1), 1-22 (2004). 420
- [338] F. Acernese et al., *Measurements of Superattenuator seismic isolation by Virgo interferometer*, Astrop. Physics, vol. 33 (3), 182-189 (2010). 420
- [339] S. Braccini on behalf of the ET-WG2, *Einstein Telescope - Seismic Isolation Design Study*, Talk at the WP2-WP3 joint meeting (Jena), (2010). 420
- [340] L. Holloway, I. Fiori, *Study of the seismic motion at Virgo*, Virgo Note VIR-NOT-FIR-1390-246, (2003). 421
- [341] L. Holloway, I. Fiori, F. Paoletti, *Study of 1-4 Hz seism*, Virgo Note VIR-NOT-FIR-1390-246, (2003). 421
- [342] E. Marchetti, M. Mazzoni, I. Fiori, *Seismic investigation of the response of the 3 km arms of Virgo Interferometer*, Virgo Note VIR-NOT-FIR-1390-297, (2005). 421
- [343] G. Losurdo et al., *The control of the Virgo Superattenuator revised (I). Inertial Damping: present and future*, Virgo Note VIR-NOT-FIR-1390-318 (2006). 421
- [344] *Superattenuator Facility at EGO: Proposal*, Virgo Note VIR-0047A-07 (2007). 421
- [345] *Superattenuator Facility at EGO: Proposal ADDENDUM*, Virgo Note VIR-0048A-07 (2007). 421
- [346] SAT Group, *AdV Plan for R&D, SR Construction and Short SA Upgrade*, Virgo Note VIR-091A-08 (2008). 422, 434, 459
- [347] A. Gennai, *Advanced Virgo - Suspension Control System*, Virgo Note VIR-0174A-11 (2009). 422, 459
- [348] H. Tariq et al., *The linear variable differential transformer (LVDT) position sensor for Gravitational Wave Interferometer low-frequency controls*, Nucl. Instr. and Meth. A489, 570-576 (2002). 423, 445
- [349] P. Ruggi, F. Frasconi, S. Braccini, *Measurements of the Filter 7 prototype*, Virgo Note. 425
- [350] G. Ballardini et al., *Measurement of the transfer function of the steering filter of the Virgo super attenuator suspension*, Rev. Sci. Instrum. 72 (9), 3635 (2001). 425

- [351] C. Bradaschia, V. Dattilo, F. Frasconi, P. Mugnier, Z. Zhang, *Conductance pipe for the Virgo IVC*, Virgo Note [VIR-TRE-PIS-3400-171](#) (1998) [426](#)
- [352] G. Vajente, *Requirements for the Advanced Virgo Length Sensing and Control System*, Virgo Note [VIR-0083A-08](#), (2008). [434](#)
- [353] A. Gaddi, F. Raffaelli, *Standard filters specifications*, Virgo Note [VIR-SPE-PIS-4600-105](#), (1996). [436](#)
- [354] PHILIPS, Datasheet of Ferroxdure 330 (FXD 330) in the "Handbook of PHILIPS Components" (1991). [438](#)
- [355] R. Del Fabbro, *Magnetic antisprings*, Virgo Note [VIR-NOT-PIS-1380-71](#), (1993). [438](#)
- [356] S. Braccini et al., *An improvement in the Virgo Superattenuator for interferometric detection of gravitational waves: the use of magnetic antisprings*, Rev. Sci. Instrum. 64 (2), 310 (1993). [438](#)
- [357] S. Braccini, C. Casciano, R. De Salvo, L. Holloway, G. Losurdo, *Extending the Virgo detection band down to few Hz: metal blade springs and a magnetic antispring system*, Nucl. Instr. and Meth. A394 397-408 (1997). [438](#)
- [358] V. Dattilo, *Direct characterization of the antispring system*, Virgo Note. [438](#)
- [359] S. Braccini, C. Casciano, R. De Salvo, F. Fidecaro, *Temperature Stabilization requirement of the Virgo towers*, Virgo Note [VIR-NOT-LAP-1390-35](#) (1996). [439](#)
- [360] M. Bernardini, C. Bradaschia, H. B. Pan, A. Pasqualetti, R. Poggiani, Z. Zhang, *Out-gassing measurement of VAC-SEAL vacuum epoxy*, Virgo Note [VIR-TRE-PIS-3400-59](#) (1996). [439](#)
- [361] S. Malik, S. Braccini, R. De Salvo, *Effect of heating on the antispring system (magnets & glue)*, Virgo Note [VIR-NOT-PIS-4600-115](#), (1997). [439](#)
- [362] S. Malik, S. Braccini, *Role of the centering wires in determining the main resonant frequency of the mechanical filter*, Virgo Note [VIR-TRE-PIS-4600-112](#) (1996). [440](#)
- [363] F. Raffaelli, *Virgo blade springs mechanical aspects*, Virgo Note [VIR-TRE-PIS-4600-111](#) (1997) [440](#)
- [364] S. Braccini, C. Casciano, R. De Salvo, F. Paoletti, F. Fidecaro, *Evidence of creep in the superattenuator mechanical filters*, Virgo Note [VIR-NOT-PIS-1390-49](#) (1996). [440](#)
- [365] S. Braccini et al., *The Maraging-steel blades of the Virgo superattenuator*, Meas. Sci. Technol. 11, 467-476 (2000). [440](#), [441](#)
- [366] S. Braccini, R. De Salvo, G. T. Feng, F. Paoletti, G. Gennaro, *Behavior measurement and analysis for Virgo suspension wires*, Virgo Note [VIR-SCH-PIS-4600-114](#) (1997). [442](#)
- [367] S. Malik, S. Braccini, R. De Salvo, *Measurements of creep in the suspension wires*, Virgo Note [VIR-NOT-PIS-4600-116](#). [442](#)
- [368] S. Braccini et al., *Seismic vibrations mechanical filters for the gravitational waves detector Virgo*, Rev. Sci. Instrum. 67 (8), 3904 (1996). [442](#)

- [369] S. Braccini, C. Casciano, R. De Salvo, L. Holloway, G. Losurdo, *Extending the Virgo detection band down to few Hz: metal blade springs and a magnetic antisping system*, Nucl. Instr. and Meth. A394 397-408 (1997). 442
- [370] S. Braccini, C. Casciano, R. De Salvo, *Crossbar and blades dampers* Virgo Note VIR-NOT-PIS-4600-108 (1996). 442
- [371] M. Bernardini, C. Bradaschia, H. B. Pan, A. Pasqualetti, R. Poggiani, G. Torelli, Z. Zhang, *Outgassing measurements of a third AML motor*, Virgo Note VIR-TRE-PIS-3400-56 (1996). 443
- [372] V. Dattilo, *State of the work and definition of the aspects related to cabling interfaces*, Virgo Note VIR-MOM-PIS-4600-81 (1997). 443
- [373] V. Dattilo, *Virgo vacuum cabling*, Virgo Note VIR-TRE-PIS-4600-145 (1998). 445
- [374] S. Braccini et al., *Low noise wideband accelerometer using an inductive displacement sensor*, Rev. Sci. Instrum. 66 (3), 2672 (1995). 445
- [375] M. Ciardelli, N. Menzione, F. Gherardini, *Clean Operations*. 451
- [376] A. Gennai, *New DSP final design document*, Virgo Note VIR-SPE-PIS-4900-120 (2005). 452
- [377] V. Boschi et al., *A state observer for the Virgo inverted pendulum*, Rev. Sci. Instrum. 82, 094502 (2011). 454
- [378] A. Gennai, *New Coil Driver Measurements*, Virgo Note VIR-010C-08 (2008). 458
- [379] A. Giazotto, *Tilt metres as a tilt independent accelerometer*, Phys. Lett. A, 376- 5, 667-670 (2012). 460
- [380] A. Gennai, *Technical Requirements for a HRG Sensor Prototype*, Virgo Note VIR-0661A-11 (2011). 460
- [381] J. van den Brand, M.Beker, A.Bertolini, M.Blom, H.J.Bulten, E.Hennes, F.Schimmel *EIB-SAS performance document draft*, Virgo note, VIR-0578B-11 (2011). 477, 484, 492
- [382] V. Fafone et al. *The noise budget of Virgo+ with monolithic suspensions*, Virgo note, VIR-0677E-10 (2010). 477
- [383] I.Fiori *Vibration noise requirement for EIB in Virgo+*, Virgo note, VIR-029A-12 (2012). 477
- [384] A.Stochino et al. *The Seismic Attenuation System (SAS) for the Advanced LIGO gravitational wave interferometric detectors*, NIM A598:737-753 (2009). 477, 501
- [385] S.Go”sler et al. *The AEI 10 m prototype interferometer*, Class.Quant.Grav.27:084023 (2010). 477
- [386] S.Braccini et al. *The maraging-steel blades of Virgo superattenuator*, Meas.Sci.Technol.11:467-476, (2007). 481
- [387] A.Bertolini, G.Cella, R. DeSalvo, V. Sannibale *Seismic noise filters, vertical resonance frequency reduction with geometric anti-springs: a feasibility study* NIM A435:475-483 (1999). 483

- [388] A. Takamori *Low frequency seismic isolation in gravitational wave detectors*, University of Tokyo, PhD Thesis, LIGO-P030049-00-R (2002). 483
- [389] S. Marka et al. *Anatomy of the TAMA SAS seismic attenuation system*, *Class.Quant.Grav.* **19**:1605-1614 (2002). 483
- [390] G. Cella, V. Sannibale, R. DeSalvo, A. Takamori *Monolithic geometric anti-spring blades* NIM A **540**:502-519 (2005). 484, 502
- [391] N. Virdone et al. *Extended-time-scale creep measurement on maraging cantilever blade springs* NIM A **593**:597-607 (2008). 484
- [392] M. Mantovani *Minimizing the resonant frequency of MGAS springs for seismic attenuation in low frequency gravitational wave detectors*, Università di Pisa, Tesi di Laurea Specialistica, LIGO-P040025-00-D (2004). 484
- [393] H. Tariq et al. *The linear variable differential transformer (LVDT) position sensor for gravitational wave interferometer low-frequency controls* NIM A **489**:570-576 (2002). 488
- [394] C. Wang et al. *Constant force actuator for gravitational wave detectors seismic attenuation systems* NIM A **489**:563-569 (2002). 488
- [395] I. Fiori et al. *Acceptance criteria for EIB-SAS*, Virgo note, VIR-0077A-11 (2011). 492
- [396] A. Takamori et al. *Inverted pendulum as low-frequency pre-isolation for advanced gravitational wave detectors*, NIM A **582**:683-692 (2007). 501
- [397] P. Ruggi *Modeling multi-pendulum suspensions*, Virgo note, VIR-0501A-09 (2009). 502
- [398] A. Stochino et al. *Improvement of the seismic noise attenuation performance of the Monolithic Geometric Anti-Spring Filters for gravitational wave interferometric detectors* NIM A **580**:1559-1564 (2007). 502
- [399] G. Losurdo, D. Passuello, P. Ruggi, *The control of the Virgo Superattenuator revised (I). Inertial damping: present and future*, Virgo note, VIR-NOT-FIR-1390-318 (2006). 515
- [400] B. Mours, P. Mugnier, *Modeling of the minitower vacuum chambers*, Virgo note, VIR-0646A-11 (2011). 520
- [401] F. Beauville et al. *A camera based position control of a suspended optical bench used in a gravitational wave detector*, *Rev.Sci.Instrum.* **74**:2564-2570 (2003). 516
- [402] G. Cella, *Residual pressure noise evaluation*, 2008, Virgo internal document, http://wwwcascina.virgo.infn.it/advirgo/biweekly/2008/2008-06/cella_190608.ppt 525
- [403] The Virgo collaboration, *Advanced Virgo Baseline Design*, 2009, Virgo internal document, VIR-0027A-09, <https://tds.ego-gw.it/itf/tds/file.php?callFile=VIR-0027A-09.pdf> 525
- [404] The Virgo collaboration, *Advanced Virgo Preliminary Design*, 2008, Virgo internal document, VIR-089A-08, <https://tds.ego-gw.it/itf/tds/file.php?callFile=VIR-089A-08.pdf> 526

- [405] A. Pasqualetti, *VAC-TRG report: Small cryotrap proposal: Scientific motivations and vacuum requirements*, 2009, Virgo internal document, <https://workarea.ego-gw.it/ego2/virgo/advanced-virgo/vac/internal-review-group/> 526
- [406] F. Ricci, B. Canuel, V. Fafone, M. Punturo, *Final report of the internal review committee for the Advanced Virgo Vacuum system*, Virgo internal document, http://wwwcascina.virgo.infn.it/advirgo/docs/VAC_IRCreport.pdf 526
- [407] The Virgo collaboration, *Virgo Final Design*, Virgo internal document, VIR-TRE-DIR-1000-13, <https://pub3.ego-gw.it/itf/tds/file.php?callFile=VIR-TRE-DIR-1000-13.pdf> 527, 528
- [408] W. Viehmann, A.G. Eubanks, *Effects of surface contamination on the infrared emissivity and visible light scattering at cryogenic temperatures*, 1972 Eubanks Goddard Space Flight Center NASA, NASA technical note TND6585NASA 533
- [409] R.G.Jr. Ross, *Cryocooler load increase due to external contamination of low-emissivity cryogenic surfaces*, *Cryocoolers*, 2003, **12**, 727–736 533
- [410] K.M. Welch, *Capture pumping technology*, Elsevier, 2001 534
- [411] J.E. O’Hanlon, *A User’s Guide to Vacuum Technology*, Wiley, 2003 534, 550
- [412] A. Pasqualetti, D. Le Galliot, G. Parguez, P. Rapagnani, *Increased vacuum pumping for Virgo+*, 2008, Virgo internal document VIR-0231A-10 (change request), page 4, <https://pub3.ego-gw.it/itf/tds/file.php?callFile=VIR-0231A-10.pdf> 534
- [413] P.A. Redhead, *Modeling the pump-down of a reversibly adsorbed phase. I. Monolayer and submonolayer initial coverage*, *Journal of Vacuum Science and Technology A*, 1995, **13**, 2, 467–475 535
- [414] C.G. Smith, G. Lewin, *Free Molecular Conductance of a Cylindrical Tube with Wall Sorption*, *Journal of Vacuum Science and Technology*, 1996, **3**, 92 534
- [415] A. Pasqualetti, *Evaluation of cryotrap for Advanced Virgo*, 2010, Virgo internal document VIR-0077B-10, <https://tds.ego-gw.it/itf/tds/file.php?callFile=VIR-0077B-10.pdf> 534
- [416] Virgo Vacuum team, *Cryotrap vacuum behaviour*, 2010, Virgo Logbook entry 27082, <https://pub3.ego-gw.it/logbook/main.php?area=logbook&ref=search&searchrecid=27082> 535
- [417] A. Pasqualetti, M. Barsuglia, G. Losurdo, V. Lorette, R. Ward, H. Heitmann, V. Brisson, J. Van den Brand, C. Bradaschia, G. Parguez, I. Fiori, J. Marque, S. Braccini, E. Genin, M. Doets, T. Zelenova, *Discussion about baffle aperture at tube extremities*, 2010, Virgo internal documents, <https://workarea.ego-gw.it/ego2/virgo/advanced-virgo/vac/diffused-light-cryotrap-30jun2010/>, minutes: https://workarea.ego-gw.it/ego2/virgo/advanced-virgo/vac/diffused-light-cryotrap-30jun2010/Minute_30_Jun.txt/ 538
- [418] J.-Y. Vinet, *Backscattering noise from cryotrap*, 2010, Virgo internal document VIR-0344A-10, <https://pub3.ego-gw.it/itf/tds/file.php?callFile=VIR-0344A-10.pdf> 540

- [419] J.-Y. Vinet, *Cryostat, baffles, scattered light and noise*, 2010, Virgo internal document VIR-0765B-09, <https://pub3.ego-gw.it/itf/tds/file.php?callFile=VIR-0765B-09.pdf> 540
- [420] A. Rocchi, E. Hennes, *Thermal effects of the cryotrap on AdV TMs*, 2009, Virgo internal document - ppt presentation, https://workarea.ego-gw.it/ego2/virgo/advanced-virgo/vac/internal-review-group/presentations-for-the-04mar/090304_crioeffects.pptx/ 540
- [421] I. Fiori, *On the problem of scattered light noise from AdV CryoTraps*, 2010, Virgo internal document, https://workarea.ego-gw.it/ego2/virgo/advanced-virgo/vac/diffused-light-vs-cryotrap-11feb2010/minidocIrene_AdV_CryoT_BSnoiseProjection.doc/ 541
- [422] P. Di Marco, S. Filippeschi, *Some technical notes on LN₂ boiling*, 2010, Virgo internal document VIR-0264A-10, <https://pub3.ego-gw.it/itf/tds/file.php?callFile=VIR-0264A-10.pdf> 541
- [423] G. Gemme, *LN₂ distribution plant*, 2010, Virgo internal document VIR-0346A-10, <https://pub3.ego-gw.it/itf/tds/file.php?callFile=VIR-0346A-10.pdf> 545
- [424] G. Gemme, D. Milani, G. Roveta, *LN₂ plant design - Cryotrap interface*, 2010, Virgo internal document VIR-0266A-10, <https://pub3.ego-gw.it/itf/tds/file.php?callFile=VIR-0266A-10.pdf> 545
- [425] R. N. Peacock, 1980, *J. Vac. Sci. Technol.*, **17**, 1, 330 550
- [426] A. K. Gupta, J. H. Leck, 1975, *Vacuum*, **25**, 362 551
- [427] D. J. Harra, 1976, *J. Vac. Sci. Technol.*, **13**, 471 551
- [428] J. Marque, *Detection turbo pump: bellow effect*, 2008, Virgo logbook entry 20157, <https://pub3.ego-gw.it/logbook/main.php?area=logbook&ref=search&searchrecid=20157> 557, 567
- [429] I. Fiori, D. Huet, F. Paoletti, EGO Vacuum team, *Shut off test of the turbo cooling fans*, 2009, Virgo logbook entry 25072, <https://pub3.ego-gw.it/logbook/main.php?area=logbook&ref=search&searchrecid=25072> 557
- [430] I. Fiori, D. Huet, F. Paoletti, EGO Vacuum team, *Noise from turbo cooling fans*, 2009, Virgo document VIR-0571A-09, <https://tds.ego-gw.it/itf/tds/index.php?callContent=2&callCode=6997&title=fans&startPage=> 557
- [431] K. Chi Thi Ngo, A. J. Zuckerwar, *Acoustic isolation vessel for measurement of the background noise in microphones*, 1993, *Acoust. Soc. Am.* **93**, 2974 559
- [432] Virgo OSD subsystem, *OSD status and plans*, 2011, Virgo week presentation, <https://tds.ego-gw.it/itf/tds/file.php?callFile=VIR-0676A-11.pdf>
- [433] I. Fiori, *Acoustic tests on larger fans*, 2011, Virgo meeting presentation, <https://tds.ego-gw.it/itf/tds/file.php?callFile=VIR-0733A-11.pdf> 572
- [434] D. Miller, I. Fiori, A. Pasqualetti, D. LeGalliot, R. Cosci, *New cooling fans for Advanced Virgo (AdV) Vacuum Racks: first measurements of acoustic emission*, 2011,

- Virgo meeting presentation, <https://tds.ego-gw.it/itf/tds/file.php?callFile=VIR-0602A-11.pdf> 572
- [435] I. Fiori, A. Pasqualetti, F. Paoletti, *Magnetic noise of Vacuum rack components: measurement and distance constraints for Advanced Virgo*, 2011, Advanced Virgo document, VIR-0261B-11, <https://tds.ego-gw.it/itf/tds/index.php?callContent=2&callCode=9156&title=magnetic&startPage=> 572
- [436] T. Zelenova, A. Pasqualetti, *Proposal of the displacements*, 2011, Virgo drawing EGO-DWG-VAC-ADV-600, <http://www.ego-gw.it/reserved/documents/codifier/download.aspx?Code=EGO-DWG-VAC-ADV-600>
- [437] I. Fiori, *analysis of Brewster shaking tests: (1) diffused light*, 2011, Virgo logbook entry 30387, https://tds.ego-gw.it/itf/osl_virgo/index.php?callRep=30387
- [438] TANGO SCADA website <http://www.tango-controls.org/> 572
- [439] I. Fiori, A. Pasqualetti, *EGO Vacuum team shaking tests of seismically isolated vacuum rack*, 2012, Virgo logbook entry 30694 https://tds.ego-gw.it/itf/osl_virgo/index.php?callRep=30694 572
- [440] G. Vajente, Virgo note VIR-0738A-11 (2011) Advanced Virgo Length Sensing and Control steady state design. 592
- [441] S. Vitale et al., arxiv 1111.3044 (2012) Effect of calibration errors on Bayesian parameter estimation for gravitational wave signals from inspiral binary systems in the Advanced Detectors era. 574
- [442] N. Letendre, A. Masserot and B. Mours, Note Timing VIR-073B-08 (2008) Virgo+ Timing Deployment. 574, 576
- [443] T. Bouedo et al, Virgo note VIR-0022C-07 (2007) Virgo+ Control and DAQ Electronic Deployment. 593
- [444] <http://irigb.com> 576
- [445] L. Rolland, N. Letendre, A. Masserot and B. Mours, Virgo note VIR-0354A-10 (2010) Stability of the timing system during VSR2. 579
- [446] E. Pacaud, T. Bouedo, N. Letendre, A. Masserot and B. Mours, Virgo note VIR-NOT-LAP-1390-335 (2007) Characterization of RTAI/Linux real-time performance on i386 hardware for the Virgo control loops. 583
- [447] D. Sentenac, Virgo note VIR-0080A-10 (2010) Software Requirements Specification for the Global Control. 583
- [448] T. Bouedo, F. Carbognani, N. Letendre, A. Masserot et al., Virgo note VIR-0056A-08 (2008) New Global Control. 583
- [449] E. Pacaud, T. Bouedo, N. Letendre, A. Masserot and B. Mours, Virgo note VIR-0052A-07 (2007) Selection Tests for the Virgo+ Control and DAQ Real-time PC. 583
- [450] N. Letendre et al., Virgo note VIR-0109A-12 (2012) ADC Board Specifications. 585, 586, 625

- [451] S. Vilalte, Virgo note VIR-0096A-12 (2010) Circuit design of the Virgo+ filtering mezzanine. [585](#)
- [452] T. Bouedo et al., Virgo note VIR-NOT-LAP-1390-329 (2006) ADC tests for the general purpose acquisition board. [585](#)
- [453] R. Gouaty et al, Virgo talk VIR-0358A-11 (2011) ADC7674 non-linear noise. [585](#)
- [454] N. Letendre et al., Preliminary DaqBox Specifications, VIR-0108A-12 (2012) Preliminary DAQ-Box Specifications. [585](#), [591](#)
- [455] N. Letendre et al., Virgo note VIR-NOT-LAP-1390-321 (2006) Mux/Demux optical card specifications. [581](#), [582](#)
- [456] B. Mours et al, Virgo note VIR-0134B-11 (2011) Digital Camera Upgrade. [595](#)
- [457] E. Pacaud, Virgo note VIR-0493A-11 (2011) GigE Vision Camera Selection Tests. [596](#)
- [458] N. Letendre et al., Virgo note VIR-0445A-11 (2011) CameraBox Guide. [595](#)
- [459] F. Nocera and F. Paoletti, Virgo note VIR-0737B-09 (2011) Electronics for Advanced Virgo: Guidelines and Requirements for Electronics Installation – a proposal. [598](#), [599](#)
- [460] F. Nocera, F. Paoletti and R. Cavaliera, Virgo note VIR-0545B-10 (2011) Electronics for Advanced Virgo: Guidelines and Requirements for Electronics Systems – a proposal. [598](#), [599](#), [600](#)
- [461] A. Anastasio, F. Barone, A. Eleuteri, F. Garufi, L. Milano, in Gravitational Waves Proceedings of the 3rd Amaldi Conference, S.M. eshkov editor, AIP Conference Proceedings 523, Pasadena, California, (USA), 17-19 July, 1999, p. 463-464 The Environment Monitoring of the Virgo Antenna for gravitational wave detection. [621](#)
- [462] F. Barone, R. De Rosa, A. Eleuteri, L. Milano, K. Qipiani, IEEE Trans. Nucl. Sci. 49, 2002, p. 405-410 The Environmental Monitoring System of Virgo Antenna for Gravitational Waves Detection. [621](#)
- [463] See <http://www.blitzortung.org> and the documentation therein. [622](#)
- [464] F. Barone, R. De Rosa, F. Garufi, Virgo note VIR-MAN-NAP-5800-108 (1999) Building Control User Manual. [624](#)
- [465] F. Barone, R. De Rosa, F. Garufi, Virgo note VIR-MAN-NAP-5800-109 (1999) Building Control Technical Manual. [624](#)
- [466] C. Arnault, P. Massart, Virgo note VIR-MAN-LAL-5600-107 (1998) Cm: a multitask communication package. [603](#), [614](#)
- [467] LIGO DCG and Virgo DAQ, note VIR-0671-08 (2008) Specification of a Common Data Frame Format for Interferometric Gravitational Wave Detectors [602](#)
- [468] <http://lappweb.in2p3.fr/virgo/FrameL/> Web documentation about the FrameLib. [602](#)
- [469] F. Bellachia, D. Verkindt, et al, Virgo note VIR-SPE-LAP-5400-105 (2008) The Virgo Online Frame Distribution (Fd/FdIO) Documentation. [603](#)
- [470] D. Verkindt, Virgo note VIR-0086B-08 (2008) Frames Shared Memory Library User's Documentation. [603](#)

- [471] D. Verkindt, Virgo note VIR-0093A-08 (2008) Main Frame Builder Users Documentation. 606
- [472] F. Carbognani, Virgo note EGO-MAN-COM-4 (2003) SCVS: Simple Concurrent Version System User Manual. 618
- [473] C. Arnault (2005), <http://www.cmts.site.org> CMT (Configuration Management Tool) web site. 618
- [474] D. Verkindt and D. Buskalic, Virgo note VIR-0008A-08 (2008) Data Display Users Manual. 610
- [475] M-A. Bizouard and D. Verkindt, Virgo presentation VIR-0610A-11 (2011) VDB roadmap for AdVirgo. 611
- [476] T. Accadia et al., (Virgo collaboration), *Class. Quantum Grav.* 28 (2011) 025005 Calibration and sensitivity of the Virgo detector during its second science run. 631
- [477] A. Masserot, B. Mours and L. Rolland, Virgo note VIR-0028B-08 (2008) Timing calibration during VSR1. 631
- [478] T. Accadia, L. Rolland and B. Mours, Virgo note VIR-0404A-10 (2010) Power and timing calibration of the Photon Calibrator for VSR2. 632
- [479] T. Accadia, L. Rolland and B. Mours, Virgo talk VIR-0670A-11 (2011) NI Drum mode study with the Photon Calibrator 633
- [480] B. Mours and L. Rolland, Virgo note VIR-0340A-10 (2010) $h(t)$ reconstruction for VSR2. 574, 635
- [481] B. Mours and L. Rolland, Virgo note VIR-0056A-11 (2011) $h(t)$ reconstruction for VSR3. 635
- [482] The Virgo collaboration, "Virgo data characterization and impact on gravitational wave searches", arXiv:1203.5613v1 (2012) <http://arxiv.org/abs/1203.5613> 638
- [483] Fiori I, "Environmental noise: experience with Virgo commissioning", Virgo internal document VIR-0019B-09 (2009), <https://tds.ego-gw.it/ql/?c=2203> 638, 640, 654
- [484] Calloni E and Virgo Commissioning team, "Commissioning progress Report for the STAC and the EGO council", Virgo internal document VIR-0325A-11 and EGO-STC-200-2011 (2011), <https://tds.ego-gw.it/ql/?c=8380> 638
- [485] The Virgo Collaboration, "Commissioning progress report for the STAC and the EGO council", EGO-STC-167-2010 (2010), <https://tds.ego-gw.it/ql/?c=> 638
- [486] Accadia T et al., Characterization of the Virgo seismic environment , *Class. and Quantum Grav.* 29 (2012) 640
- [487] Fiori I, "A measurement of attenuation in soil of seismic noise from Virgo infrastructure machines at North End Terminal", Virgo internal document VIR-0028A-12 (2010), <https://tds.ego-gw.it/ql/?c=8830> 640
- [488] The Virgo Collaboration, "Virgo: a laser interferometer to detect gravitational waves", submitted to *Journal of Instrumentation* (2012) 640

- [489] Fiori I and Pasqualetti A, Seismic noise tests for the AdV Vacuum equipment (a report) , eLog 30498 (2011), Seismic noise tests for the AdV Vacuum equipment (a report) , https://tds.ego-gw.it/itf/osl_virgo/index.php?callRep=30498 640
- [490] Vinet J-Y, Brisson V, Braccini S, "Scattered light noise in gravitational wave interferometric detectors: Coherent effect", *Phys. Rev. D* **54** 1276 (1996) 640
- [491] Accadia T et al., Noise from scattered light in Virgo's second science run data , *Class. and Quantum Grav.* **27** 194011 (2010) 640, 642
- [492] Barone F, Garufi F, Milano L, Environment monitoring probes , Virgo internal document VIR-MAN-NAP-5800-102, <https://tds.ego-gw.it/ql/?c=800> 642
- [493] The Virgo Environmental Monitoring system online map, https://wwwcascina.virgo.infn.it/EnvMon/websensormain_i.htm 642, 650, 651
- [494] Flaminio R, Brewster window noise , ILIAS meeting, VIR-0227A-07 (2007), <https://tds.ego-gw.it/ql/?c=644>
- [495] Marque J et al. Back-scattered light on terminal benches: Measurement Analysis and Proposal for mitigations , Virgo internal document VIR-0837A-07 (2007), <https://tds.ego-gw.it/ql/?c=6809> 644
- [496] Fiori I, et al. Acoustic Enclosure Performance, INJ benches , Virgo internal document VIR-0188B-06 (2006), <https://tds.ego-gw.it/ql/?c=2844> 644, 652
- [497]] Richard F, Acoustic Isolation of End Benches , Virgo internal documents VIR-291A-07 and VIR-202A-08 (2008), <https://tds.ego-gw.it/ql/?c=3247> 644
- [498] Genin E, Considerations on input beam jitter, MC AA noise and IMC length noise for AdV, Virgo internal document VIR-0602A-10 (2010), <https://tds.ego-gw.it/ql/?c=7906> 646
- [499] Blom M, the Nikhef group, EIB-SAS installation and first results, Virgo internal document VIR-0077A-12 (2012), <https://tds.ego-gw.it/ql/?c=8881> 646, 647
- [500]] Fiori I , Vibration noise requirement for EIB in Virgo+, Virgo internal document VIR-0029A-12 (2012), <https://tds.ego-gw.it/ql/?c=8831> 646, 647
- [501] Fiori I and Ruggi P, Acoustic noise in Laser Lab mitigation priority list, Virgo internal document VIR-0035A-12 (2012), <https://tds.ego-gw.it/ql/?c=652>
- [502] Genin E et al., LL modifications for AdV, first proposal from INJ, Virgo internal document VIR-0038A-12 (2012), <https://tds.ego-gw.it/ql/?c=8840> 652
- [503] Fiori I, Genin E, Marque J, IME/INJ: Laser laboratory air conditioning preliminary requirements for AdV , Virgo internal document VIR-0766A-09 (2009), <https://tds.ego-gw.it/ql/?c=7090> 652, 659
- [504] Meeting MC chiller glitches minutes, Virgo internal document VIR-0156A-10 (2010), <https://tds.ego-gw.it/ql/?c=7289> 655
- [505] Swinkels B, et al. MC building powered by generator n.2 , eLog 26758 and MC chiller glitches eLog 26761 (2010), https://tds.ego-gw.it/itf/osl_virgo/index.php?callRep=26761 655

- [506] Miller D, et al. Noise emission tests of new fans for AdV vacuum racks , Virgo internal document VIR-0602A-11 (2011), <https://tds.ego-gw.it/ql/?c=8659> 656
- [507] Fiori I and the EGO Vacuum team, Acoustic tests on larger fans , Virgo internal document VIR-0733A-11 (2011), <https://tds.ego-gw.it/ql/?c=8792> 656
- [508] Fiori I and Pasqualetti A, Scroll room noise tests , Virgo internal document VIR-0054A-12 (2012), <https://tds.ego-gw.it/ql/?c=8858> 563, 656, 674
- [509] Marque J for the EGO Vacuum Team, Detection turbo pump: bellow effect , eLog 20157 and Virgo internal document VIR-0268A-08-1 (2008), <https://tds.ego-gw.it/ql/?c=3313> 656
- [510] Fiori I, Pasqualetti A, Paoletti F, Magnetic noise of vacuum rack components, measurements and distance constraints for AdV , Virgo internal document VIR-0261B-11 (2011), <https://tds.ego-gw.it/ql/?c=8316> 656
- [511] Nocera F and Paoletti F, Electronics for Advanced Virgo: Guidelines and Requirements for Electronics Installation , Virgo internal document VIR-0737A-09 (2009), <https://tds.ego-gw.it/ql/?c=7061> 676